



# Research in Pulsed Power Plasma Physics

Final Report

Volume II  
Section Four

August 1996

Prepared by:

Steve Swanekamp  
David Rose

Prepared for:

Naval Research Laboratory  
4555 Overlook Avenue, SW  
Washington, DC 20375-5000

Contract Number: N00014-93-C-2086

19970103 116

DTIC QUALITY INSPECTED 2

1410 Spring Hill Road • Suite 300 • McLean, Virginia 22102 • (703) 847-4000

APPROVED FOR PUBLIC RELEASE  
DISTRIBUTION UNLIMITED

## TABLE OF CONTENTS

### VOLUME I

#### SECTION ONE OVERVIEW

#### SECTION TWO INTENSE ION BEAM GENERATION

- 2.1 Applied-B Ion Diode Development ..... II-1
- 2.2 Pulser Development for the Active Plasma Source ..... II-2

#### SECTION THREE INTENSE BEAM TRANSPORT

- 3.1 Transport of Intense Ion Beams in Gas ..... III-1
- 3.2 Analysis of Ion Beam Transport Constraints ..... III-1
- 3.3 Diagnostic Development ..... III-2
- 3.4 Additional Beam Transport Work ..... III-2
- 3.5 List of Papers ..... III-2

### VOLUME II

#### SECTION FOUR MICROSECOND CONDUCTION TIME PLASMA OPENING SWITCHES

- 4.1 Plasma source development ..... IV-2
- 4.2 Microsecond POS operation ..... IV-2
- 4.3 POS-Load Coupling ..... IV-3
- 4.4 The ZFX Facility ..... IV-3
- 4.5 List of papers ..... IV-3

## SECTION FOUR

### MICROSECOND CONDUCTION TIME PLASMA OPENING SWITCHES

One type of opening switch that is currently under development at the Naval Research Laboratory for terawatt applications is the plasma opening switch (POS). In its simplest form the POS consists of a series of plasma guns spaced around the azimuth of a coaxial transmission line. These guns are used to inject plasma between the anode and cathode of a coaxial transmission line that connects the pulsed-power generator with the load. The desired plasma conditions in the POS are varied by adjusting the time delay between the POS plasma sources and the main power pulse. During the conduction phase, the impedance of the switch is low and magnetic energy is stored in the circuit inductance as the discharge current increases. Since magnetic energy is stored at relatively low voltage, the insulation problems associated with capacitive systems are significantly reduced. The elimination of water and oil insulation sections combined with the higher energy density available in an inductive energy store (IES) systems has the potential to substantially reduce both the size and cost of pulsed-power machines. To achieve high output powers, the switch must open to an impedance that is large compared to the load impedance and deliver the stored magnetic energy to a load on a time scale that is short compared to the conduction time.

During the conduction phase of the POS, current from the generator, which initially flows through the plasma as electrical energy, is converted into magnetic energy. During the conduction phase, the current through the plasma abruptly decreases (i.e. the POS opens) allowing magnetic energy to flow past the POS and to the load. The present understanding of POS operation is that the plasma is redistributed by  $J \times B$  forces during the conduction phase. As a result of this redistribution, a low density region forms in the plasma creating a gap as the POS opens. There is considerable evidence that when the POS opens the gap size is limited to several millimeters for a wide range of POS parameters. The limit on gap size severely limits the maximum impedance that can be achieved by the open POS and restricts the overall efficiency for energy transfer between the POS and load. Although some progress has been made, the limitations of POS gap size is not very well understood.

Typically the POS must conduct megampere currents for times approaching  $1 \mu s$ . This requires plasma densities of  $>10^{15} \text{ cm}^{-3}$  and switch lengths of several centimeters. During this contract period several different plasma sources were investigated for use in POS applications. The geometry of the POS can also play a significant role in the overall operation of the POS. Several different geometry variations were tried during this reporting period. The power delivery phase is generally accompanied by large amounts of vacuum electron flow. This current flow represents a reasonable fraction of the total energy available to drive the load. For this reason, a considerable amount of effort was devoted to the study of POS-load coupling during this contract period.

The outline of this section is as follows: Section 4.1 describes the work on development of plasma sources for POS applications; Section 4.2 describes the work on understanding the operation of a microsecond POS; Section 4.3 presents the work on POS-load coupling; and Section 4.4 describes the work to complete and take the first shots on the ZFX facility.

#### 4.1 Plasma source development

High density plasma experiments were performed on the NRL's Hawk pulsed-power generator during this reporting period. In these experiments an array of 36 cable gun plasma sources were used to produce plasma densities in the mid  $10^{16} \text{ cm}^{-3}$  to low  $10^{17} \text{ cm}^{-3}$  range. The switch radius was 1.25 cm with an A-K gap spacing of 2 cm and switch lengths of 3-8 cm were used. These experiments made 1.5 MV (a record for a straight center conductor) after a conduction time of 0.9 ms. In addition, two geometry variations (the "Plasma Anode" and "Anode Step") that had shown improvements on DPM1 at Physics International were shown to have no noticeable effect on the Hawk voltage. The two-color interferometer was used to measure the electron and neutral densities from the flashboards used on ACE IV at Maxwell Laboratories Incorporated. Electron density in the  $10^{15} \text{ cm}^{-3}$  range as measured and no significant neutral component was detected except very near the cathode. A gas gun plasma source was developed that allows, in principle, a selection of plasma ion species through the selection of the gas introduced into the gun. The electron density was measured using a six-chord He-Ne laser interferometer. Line-integrated densities in the range of  $3 \cdot 10^{16} \text{ cm}^{-2}$  were measured. The gas gun sources were not very reproducible and did not significantly improve the output of the Hawk generator. Cable guns were developed and fielded on Hawk during this reporting period. The objective of these experiments was to compare the operation of Hawk with cable gun sources to that using flashboards.

#### 4.2 Microsecond POS operation

Because most POS experiments are performed in coaxial geometry they provide little diagnostic access in the azimuthal direction. For this reason a parallel plate POS experiment was developed with the hope that the POS would operate in much the same way as the coaxial switch. The density in the POS was mapped out over a series of shots measured using a multi-chord He-Ne interferometer. These measurements were used to produce a movie of POS operation that, coupled with visible light images, provided an unprecedented view of POS operation.

Work was performed with tapered cathodes during this contract period. This was shown to produce very high power (0.7 TW) output pulses. The good switch performance was presumably because the large radius on the generator side permitted long conduction times while the small cathode on the load side permitted better opening. Switch performance was seen to deteriorate when the small anode radius in the POS region was extended.

Particle-in-cell simulations (PIC) of the gap formation process near an electrode were performed. In these simulations the opening phase is studied by idealizing the plasma distribution predicted by an MHD code and loading it into a PIC code. These simulation results used realistic POS densities ( $10^{14}$ - $5 \cdot 10^{15} \text{ cm}^{-3}$ ) and show the propagation of a 2-D potential hill along the cathode. This leaves a preformed gap in its wake. Opening occurs when this potential hill reaches the load side of the POS. The radial size of the POS gap is shown to be proportional to  $B/n$  where  $B$  is the magnetic field and  $n$  is the electron density. Gap formation away from an electrode has also been simulated using the PIC method. These preliminary results show good agreement with the simulations of gap formation near an electrode.



The first kinetic treatment (using the PIC) demonstrating fast magnetic field penetration due to the Hall electric field were performed during this reporting period. These simulations agree well with many aspects of fluid treatments of the problem. However, the PIC analysis also shows the formations of paramagnetic vortices in the electron flow. The radial size of these vortices are on the order of the electron skin depth. It is seen that, when ions can move, that magnetic field penetration due to the Hall effect followed by radial  $J \times B$  ion motion can produce a gap in the plasma that occurs away from the electrodes.

Investigations into conduction time scaling for a microsecond conduction time POS were performed during this contract period. This work examines the dependence of the conducted current in Hawk and Gamble II on density, length, radius, and the rate at which the generator current rises. Hawk follows a scaling predicted by MHD and EMH conduction limit derivations. Gamble II, with a current rise rate ten times greater than Hawk, shows a non-MHD or EMH scaling.

#### **4.3 POS-Load Coupling**

Significant progress was made in understanding how a microsecond POS couples with a Bremsstrahlung diode load during this contract period. This work included efforts in understanding how magnetic energy flows past the POS to the load and in characterizing the energy delivered to a load through an analysis of the x-ray production. The power-flow work employed both PIC simulations and anode and cathode current measurements to characterize the current flow pattern in the section of transmission line between the POS and load. Differences between simulation and experiment were attributed to the presence of plasma between the POS and load. The radiation analysis supports this picture since the amount of load energy predicted by the radiation transport simulations is too high to be explained by vacuum electron flow alone. The radiation transport simulations also showed that, for the range of voltages for Decade, the absorbed x-ray dose has a linear dependence on energy.

#### **4.4 The ZFX Facility**

The ZFX facility at NRL was completed during this reporting period. The ZFX pulsed-power generator featured an advanced parallel plate water capacitor technology. To minimize the field stresses near the edge of the plates, a series of plastic field attractors. The facility was successfully operated at 750 kV for several discharges before a damaging electrical breakdown in the capacitor ended operations. The failure was most likely caused by debris in the water at the time of firing. Because of the complex design, it was extremely difficult to locate and remove debris and air bubbles. An extensive engineering redesign and a simplification of the fabrication procedures are needed to correct these design flaws.

#### **4.5 List of papers**

- 4.5.1 "High density ( $> 10^{17} \text{ cm}^{-3}$ ) POS experiments on Hawk," B. Weber, R. Comisso, P. Goodrich, and R. Riley, Pulsed-Power Physics Technote 95-15.
- 4.5.2 "POS plasma and neutral density measurements," B.V. Weber, R. Comisso, P. Goodrich, D. Hinshelwood, and R. Riley, Pulsed-Power Physics Technote 95-14.

- 4.5.3 "Maxwell slow flashboard density measurements using two-color interferometry," B. Weber, P. Goodrich, R. Riley, and M. Sucey, Pulsed-Power Physics Technote 94-04.
- 4.5.4 "Interferometric studies of gas gun plasmas," D. Hinshelwood, Pulsed-Power Physics Technote 93-09.
- 4.5.5 "Cable gun POS experiments with diode load on Hawk," B. Weber, and M. Sucey, Pulsed-Power Physics Technote 93-07.
- 4.5.6 "Parallel plate POS performance on Hawk," R.A. Riley, B.V. Weber, R.J. Commisso, D.D. Hinshelwood, and J.M. Grossmann, Pulsed-Power Physics Technote 95-09.
- 4.5.7 "Parallel plate POS Experiments on Hawk," R.A. Riley, B.V. Weber, R.J. Commisso, D.D. Hinshelwood, J.M. Grossmann, and S.B. Swanekamp, Pulsed-Power Physics Technote 94-27.
- 4.5.8 "Magnetostatic analysis of parallel plate POS," R. Riley, J. Grossmann, S. Swanekamp, and B. Weber, Pulsed-Power Physics Technote 94-20.
- 4.5.9 "Refractive index of bound electrons," R. Riley, D. Hinshelwood, and B. Weber, Pulsed-Power Physics Technote 94-10.
- 4.5.10 "Positive polarity POS operation on Hawk," D. Hinshelwood, and R. Fisher, Pulsed-Power Physics Technote 93-10.
- 4.5.11 "High power plasma opening switch operation on Hawk," P.J. Goodrich, R.J. Commisso, J.M. Grossmann, D.D. Hinshelwood, R.A. Riley, S.B. Swanekamp, and B.V. Weber, Tenth International Conference on High Power Particle Beams, (San Diego, CA, June 1994), p. 299.
- 4.5.12 "High power opening switch operation on Hawk," P.J. Goodrich, D.D. Hinshelwood, R.J. Commisso, J.M. Grossmann, J.C. Kellogg, and B.V. Weber, Ninth IEEE Pulsed-Power Conference, (Albuquerque, NM, June 1993), p. 190.
- 4.5.13 "Plasma opening switch experiments on Hawk with tapered cathodes and cable gun plasma sources," P.J. Goodrich, Pulsed-Power Physics Technote 94-02.
- 4.5.14 "Particle-in-cell simulations of fast magnetic field penetration into plasmas due to the Hall electric field," S.B. Swanekamp, J.M. Grossmann, A. Fruchtman, B.V. Oliver, and P.F. Ottinger, to be published in Phys. Plasmas, October 1996.
- 4.5.15 "Conduction phase to opening phase transition on the plasma opening switch," J.M. Grossmann, S.B. Swanekamp, R.J. Commisso, P.J. Goodrich, D.D. Hinshelwood, Tenth International Conference on High Power Particle Beams, (San Diego, CA, June 1994), p. 199.
- 4.5.16 "Gap formation processes in a high density plasma opening switch," J.M. Grossmann, S.B. Swanekamp, P.F. Ottinger, R.J. Commisso, D.D. Hinshelwood, and B.V. Weber, Phys. Plasmas **2**, 299 (1995).

- 4.5.17 "Simulations of gap formation processes in plasma opening switches," J.M. Grossmann, S.B. Swanekamp, A. Fruchtman, J. Huba, R. Mason, B. Oliver, P.F. Ottinger, R.J. Commisso, R. Riley, and B.V. Weber, Pulsed-Power Physics Technote 95-07.
- 4.5.18 "EMH effects in plasma opening switches," Steve Swanekamp, John Grossmann, Amnon Fruchtman, and Bryan Oliver, Pulsed-Power Physics Technote 94-28.
- 4.5.19 "MHD and EMH effects in plasma opening switches," J.M. Grossmann, S.B. Swanekamp, A. Fruchtman, J. Huba, B.V. Oliver, Pulsed-Power Physics Technote 94-29.
- 4.5.20 "Modeling of long-conduction time POS," J.M. Grossmann, S.B. Swanekamp, J.D. Huba, C.R. DeVore, P.F. Ottinger, R.J. Commisso, B.V. Weber, and P.J. Goodrich, Pulsed-Power Physics Technote 93-17.
- 4.5.21 "Relativistic Child-Langmuir law," B. Weber and S. Swanekamp, Pulsed-Power Physics Technote 94-30.
- 4.5.22 "Chordal line-integrals and the 2-D snowplow model of the microsecond plasma opening switch," Randall Ingermanson, D. Parks, Eduardo Waisman, Dave Hinshelwood, and Bruce Weber, Tenth International Conference on High Power Particle Beams, (SanDiego, CA, June 1994), p.202.
- 4.5.23 "Plasma opening switch conduction scaling," B.V. Weber, R.J. Commisso, P.J. Goodrich, J.M. Grossmann, D.D. Hinshelwood, P.F. Ottinger, and S.B. Swanekamp, Phys. Plasmas 2, 3893 (1995).
- 4.5.24 "Microsecond conduction time plasma opening switch research at NRL," B.V. Weber, R.J. Commisso, G. Cooperstein, P.J. Goodrich, J.M. Grossmann, D.D. Hinshelwood, P.F. Ottinger, R.A. Riley, and S.B. Swanekamp, Tenth International Conference on High Power Particle Beams, (SanDiego, CA, June 1994), p. 8.
- 4.5.25 "POS conduction dependence on current rise time," B.V. Weber, R.J. Commisso, P.J. Goodrich, J.M. Grossmann, D.D. Hinshelwood, J.C. Kellogg, P.F. Ottinger, S.J. Stephanakis, and J.R. Goyer, Pulsed-Power Physics Technote 93-04.
- 4.5.26 "Characterization of Bremsstrahlung from the DM1 generator," F.C. Young, R.J. Commisso, D.V. Rose, and S.B. Swanekamp, Proceedings of the 1996 HEART conference which appears in the Proceedings of the Government Microcircuit Applications Conference, (Orlando, FL, March 1996), p. 581.
- 4.5.27 "Experimental and theoretical investigations of 2-D vacuum power flow," S.B. Swanekamp, J.M. Grossmann, D.D. Hinshelwood, S.J. Stephanakis, J.R. Boller, and R.J. Commisso, Ninth IEEE Pulsed-Power Conference, (Albuquerque, NM, June 1995), p. 216.
- 4.5.28 "Modeling of DM1 POS and load performance," R.J. Commisso, J.R. Boller, S.B. Swanekamp, J.M. Grossmann, P.F. Ottinger, B.V. Weber, F.C. Young, and G. Cooperstein, Ninth IEEE Pulsed-Power Conference, (Albuquerque, NM, June 1995), paper 6-6.

- 4.5.29 "Simulations of vacuum electron flow in inductive energy store pulsed-power systems," S.B. Swanekamp, J.M. Grossmann, R.J. Commisso, P.J. Goodrich, P.F. Ottinger, and B.V. Weber, Tenth International Conference on High Power Particle Beams, (SanDiego, CA, June 1994), p. 198.
- 4.5.30 "Bremsstrahlung yield simulations for DM1," D.V. Rose, S.B. Swanekamp, F.C. Young, and R.J. Commisso, NRL Memorandum Report NRL/MR/6777-95-7748, 1995.
- 4.5.31 "Circuit simulations of DM1 with and Electron-Beam load," R.J. Commisso, J.R. Boller, D.V. Rose, and S.B. Swanekamp, NRL Memorandum Report NRL/MR/6770-95-7750, 1995.
- 4.5.32 "Joint NRL/CEG plasma-filled diode experiment," B. Weber, Pulsed-Power Physics Technote 95-34.
- 4.5.33 "Numerical simulations of Bremsstrahlung diode experiments on Gamble II," D.V. Rose, R.J. Commisso, F.C. Young, S.J. Stephanakis, J.M. Grossmann, J.C. Kellogg, S.B. Swanekamp, and G. Cooperstein, Pulsed-Power Physics Technote 95-25.
- 4.5.34 "Krypton density measurements for the Saturn solid PRS nozzle," B. Weber, J. Kellogg, G. Peterson, R. Spielman, and M. Sucy, Pulsed-Power Physics Technote 95-23.
- 4.5.35 "Experimental and theoretical investigations into 2-D vacuum power flow," Steve Swanekamp, John Grossmann, Dave Hinshelwood, and Bob Commisso, Pulsed-Power Physics Technote 95-22.
- 4.5.36 "Modeling of DM1 performance," R.J. Commisso, J.R. Boller, D.V. Rose, S.B. Swanekamp, F.C. Young, P.F. Ottinger, B.V. Weber, and G. Cooperstein, Pulsed-Power Physics Technote 95-21.
- 4.5.37 "Review of Hawk power-flow experiments," R.J. Commisso, B.V. Weber, P.J. Goodrich, J.M. Grossmann, S.B. Swanekamp, P.F. Ottinger, and R.A. Riley, Pulsed-Power Physics Technote 95-12.
- 4.5.38 "POS-Load coupling theory," Steve Swanekamp, John Grossmann, Bob Commisso, Phil Goodrich, Ron Riley, and Bruce Weber, Pulsed-Power Physics Technote 95-11.
- 4.5.39 "Progress on front to back POS simulation," Steve Swanekamp, John Grossmann, Joe Huba, Jim Geary, Larry Ludeking, and David Smithe, Pulsed-Power Physics Technote 95-10.
- 4.5.40 "Decade circuit modeling with a PRS load," J.R. Boller, R.J. Commisso, D. Mosher, P.F. Ottinger, and S.B. Swanekamp, Pulsed-Power Physics Technote 94-13.
- 4.5.41 "Cathode current measurements on Hawk," B. Weber, and M. Sucy, Pulsed-Power Physics Technote 93-11.

- 4.5.42 "Aluminum wire array implosions on ZFX," G.G Peterson, J.R. Boller, R. Fisher, J.C. Kellogg, D. Mosher, F.C. Young, and R.J. Commisso, Pulsed-Power Physics Technote 95-19.
- 4.5.43 "Evaluation of the ZFX 240 kJ parallel-plate water capacitor: Lessons learned," J.C. Kellogg, J.R. Boller, R.J. Commisso, K.A. Gerber, J.D. Sethian, G.G. Peterson, and S.B. Swanekamp, to appear in the proceeding of the 1995 IEEE Pulsed-Power Conference Proceedings.
- 4.5.44 "ZFX small-scale module tests," J.R. Boller, J.C. Kellogg, R.C. Fisher, M.M. Sucky, and R.J. Commisso, Pulsed-Power Physics Technote 94-26.
- 4.5.45 "Failure analysis of ZFX shot 36," J.C. Kellogg, J.R. Boller, R. Fisher, and M. Sucky, 94-07.
- 4.5.46 "ZFX- A pulsed-power driver using a parallel plate water capacitor," J.D. Sethian, J.R. Boller, R.J. Commisso, J.C. Kellogg, B.V. Weber, P.J. Goodrich, and D.D. Hinshelwood, Pulsed-Power Physics Technote 93-13.
- 4.5.47 "Three dimensional electrostatic simulations of the ZFX water capacitor," S. Swanekamp, R. Boller, and J. Kellogg, Pulsed-Power Physics Technote 94-03.
- 4.5.48 "Initial cable gun POS experiments on Hawk," B. Weber, D. Hinshelwood, and R. Commisso, Pulsed-Power Physics Technote 93-06.

PULSED POWER PHYSICS TECHNOTE NO. 95-15

TITLE:       **HIGH DENSITY ( $> 10^{17} \text{ cm}^{-3}$ ) POS EXPERIMENTS ON HAWK**

AUTHORS:   **B. Weber, R. Commisso, P. Goodrich, and R. Riley**

DATE:       **6 April 1995**

ABSTRACT:       This talk was presented at the DNA POS Workshop on March 30, 1995. This work was initially inspired by the Jupiter project to investigate density limits for POS operation, namely voltage generation. Coincidentally, the geometry used on Hawk for these experiments is almost identical to the SAB (small area Bremsstrahlung) configuration on DM-1. 36 plasma guns were used to produce densities in the high- $10^{16}$  to mid- $10^{17} \text{ cm}^{-3}$  range, as required to conduct the Hawk current with the small radius (1.25 cm), and the short plasma lengths (3-8 cm) used. Anode geometry modifications were investigated, with all cases compared by plotting switch voltage as a function of conduction time. One configuration was superior to the others, using an 8-cm length and a 2 cm radial gap in the POS region. For this case, 1.5 MV was generated after 0.9  $\mu\text{s}$  conduction, a record for Hawk with a straight center conductor (similar to results with a tapered center conductor, and presumably lower density). "Plasma Anode" and "Anode Step" configurations did not result in increased voltage on Hawk as they did on DPM1.

THIS REPORT REPRESENTS UNPUBLISHED  
INTERNAL WORKING DOCUMENTS AND SHOULD  
NOT BE REFERENCED OR DISTRIBUTED WITHOUT  
THE AUTHORS' CONSENT

# High Density ( $>10^{17} \text{ cm}^{-3}$ ) POS Experiments on Hawk

B. Weber, R. Comisso, P. Goodrich,\* R. Riley\*\*

Naval Research Laboratory  
Washington DC 20375

DNA/RAST POS Workshop  
NSWC White Oak,  
March 28-30, 1995

\* JAYCOR, Vienna, VA  
\*\* NRL/NRC Research Associate

## Can high voltage generation be maintained at high density?

NRL

- Long conduction and fast opening seem exclusive
  - Required density increases with conduction current and time
    - »  $n \sim I^2 \tau^2 / l^2 r^2$  (MHD scaling)
  - Gap opening is inversely related to density
    - » erosion,  $dD/dt \sim 1/n$
    - » magnetic pressure,  $dD/dt \sim 1/nM$

but...

- At  $\sim \mu\text{s}$ , MA, conduction, density can decrease significantly during conduction
  - plasma thinning, density redistribution during conduction  
ref: *Hinshelwood, et al., Phys. Rev. Lett. 68, 3567 (1992)*
- Is there a density limit?

DNA POS Workshop  
NSWC, 28-30 March 1995

## Previous experiments show voltage limits with $< 10^{16} \text{ cm}^{-3}$ density

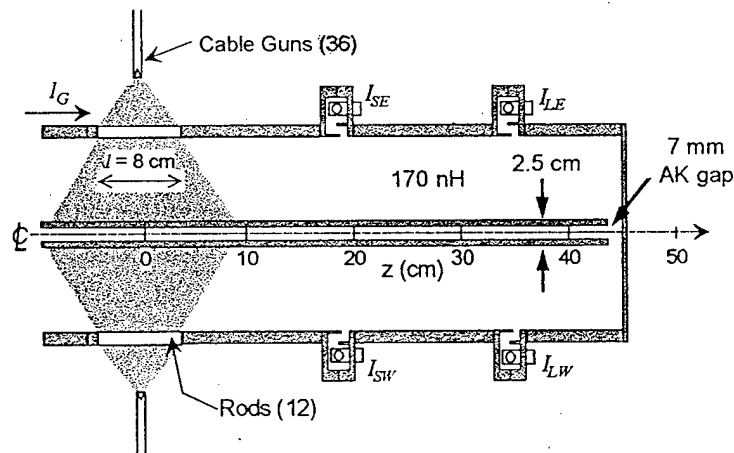
NRL

- PI experiments
  - $V$  decreases for conduction times  $> 0.4 \mu\text{s}$  (EYESS)
    - ref: Goyer, et al., *J. Appl. Phys.* **72**, 1275 (1992)
    - » ion loss current increases with density required for longer conduction
  - anode geometry change extends conduction time to  $> 0.6 \mu\text{s}$  (DPM1)
    - ref: Goyer, et al., *IEEE Trans. Plasma Sci.* **22**, 242 (1994)
    - » "plasma anode" + "anode step" increase  $V$  at long  $\tau$
- Hawk experiments with  $10^{15}$ - $10^{16} \text{ cm}^{-3}$  densities
  - $V$  increases with  $\tau$  then falls rapidly, depending on  $r$ 
    - ref: Goodrich, et al., *Proc. Beams '94*, 299 (1994)
    - »  $0.9 \mu\text{s}$  for  $r = 5 \text{ cm}$
    - »  $0.75 \mu\text{s}$  for  $r = 1.25 \text{ cm}$
- High density Hawk experiments
  - small radius (1.25 cm), short length (3 cm) requires  $> 10^{17} \text{ cm}^{-3}$
  - varied anode geometry (plasma anode, anode step)
  - high voltage (1.5 MV) at  $0.9 \mu\text{s}$  conduction for some conditions

DNA POS Workshop  
NSWC, 28-29 March 1995

## High Density POS experiment on Hawk

NRL

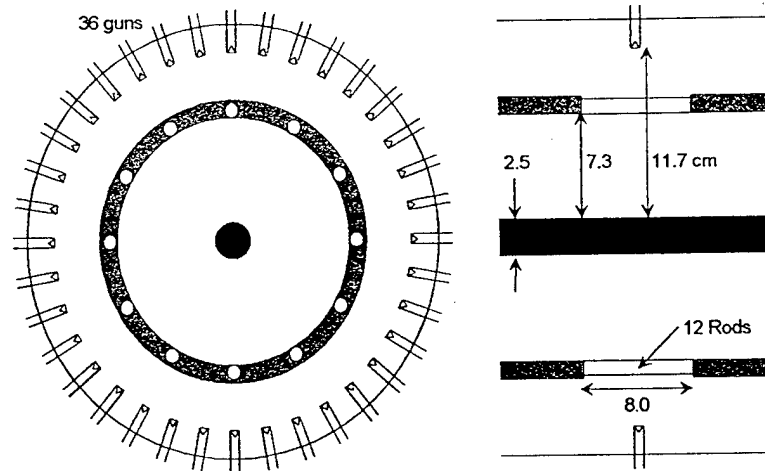


DNA POS Workshop  
NSWC, 28-30 March 1995



## 36 plasma guns are used to produce high density

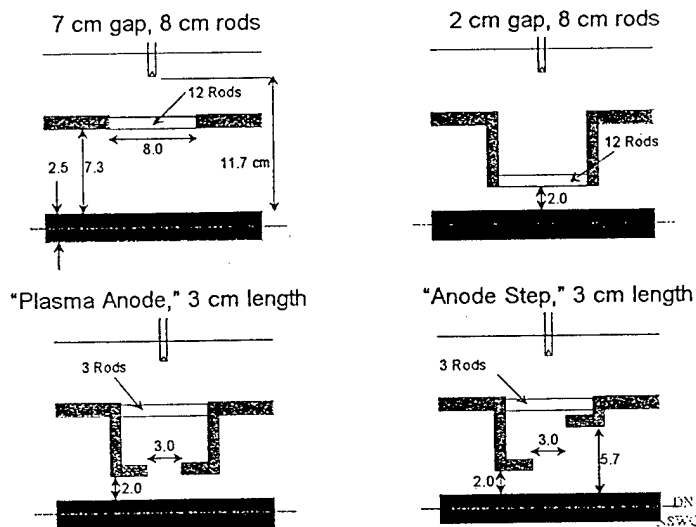
NRL



LNA PDS Workshop  
NSWC, 28-30 March 1995

## Anode geometry variations

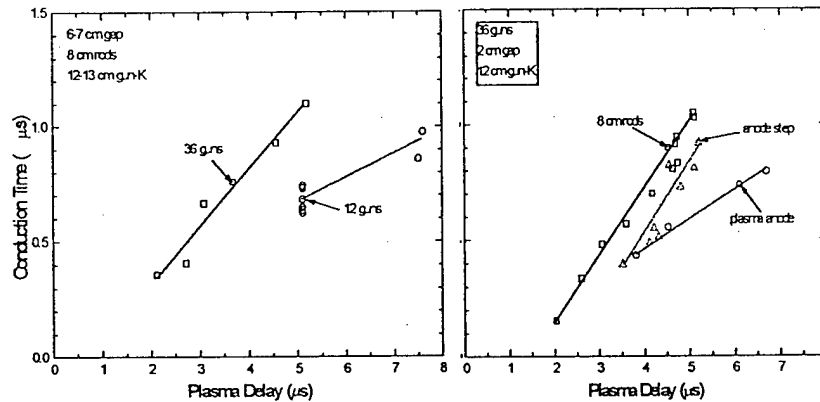
NRL



LNA PDS Workshop  
NSWC, 28-30 March 1995

## The conduction time varies for the different anode configurations

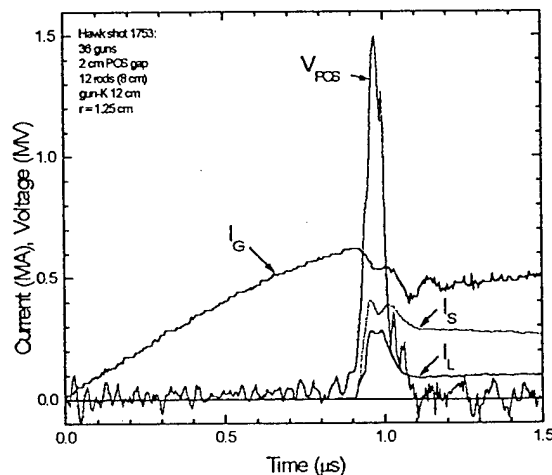
NRL



PNA PDS Workshop  
NSWC, 28-30 March 1995

## High voltage (1.5 MV) obtained after 0.9 μs conduction (at $\sim 10^{17} \text{ cm}^{-3}$ )

NRL



- density estimated from previous cable gun experiments (TN 93-06)

$$n \cong \frac{1.6 \times 10^{20}}{r^2 l^2} \iint I^2 dt^2$$

- for shot 1753 parameters:

$$n \sim 6 \times 10^{16} \text{ cm}^{-3}$$

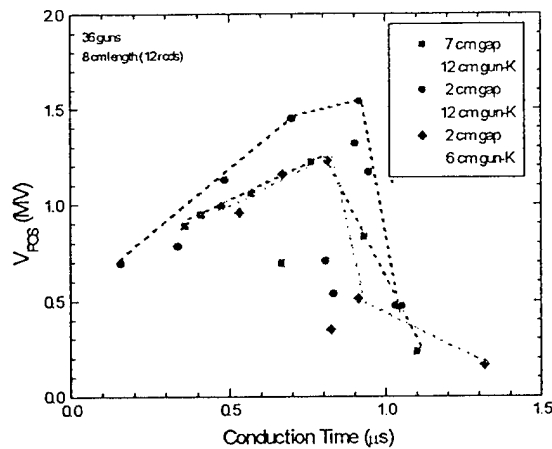
- same conduction time, smaller length (3 cm):

$$n \sim 4 \times 10^{17} \text{ cm}^{-3}$$

PNA PDS Workshop  
NSWC, 28-30 March 1995

## Radial POS gap size and gun distance make a difference

NRL



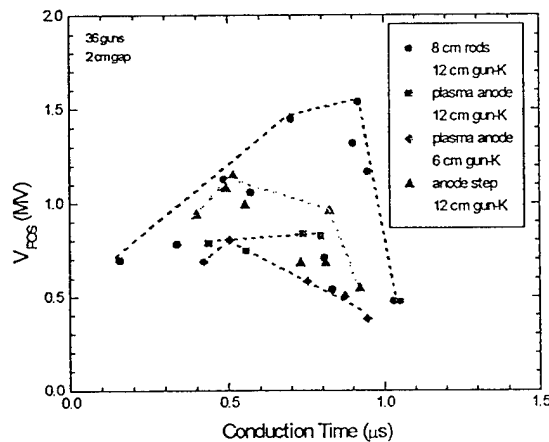
- 1.5 MV at 0.9 μs conduction time is a record for Hawk with a straight center conductor

- similar (or better) results obtained using tapered center conductors (lower density ?)

DNA POS Workshop  
NSWC, 28-30 March 1995

## Plasma anode and anode step do not increase the voltage on Hawk

NRL



- "Plasma anode" and "anode step" configurations have  $l = 3$  cm, so  $n > 10^{17} \text{ cm}^{-3}$  for long conduction times

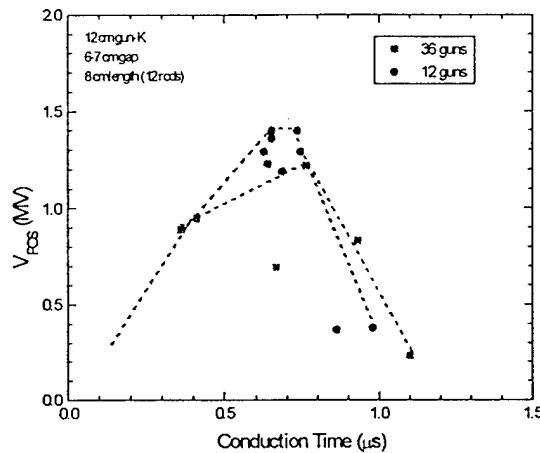
- Lower  $V$  with higher  $n$ ?

— axial, radial plasma distributions different too

DNA POS Workshop  
NSWC, 28-30 March 1995

## 36-gun data is similar to previous 12-gun data

NRL



- Longer delay time required with 12 guns does not result in lower  $V$
- Other configurations?

DNA POS Workshop  
NSWC, 28-30 March 1995

## Summary and Conclusions

NRL

- Unclear if there is a "density" limit on Hawk
  - 1.5 MV at 0.9  $\mu s$  conduction time,  $n \sim 6 \times 10^{16} \text{ cm}^{-3}$
  - lower voltage with  $l = 3 \text{ cm}$ ,  $n > 1 \times 10^{17} \text{ cm}^{-3}$
- "Plasma anode" and "anode step" do not enhance voltage on Hawk as on DPM1
  - longer conduction time on Hawk (900 vs. 600 ns)
  - plasma anode used smaller plasma length (3 cm, higher density) than POS with 8-cm-rod anode
- 12- and 36-gun results are very similar
- Plasma distribution (axial and radial) may be dominant
  - multi-chord axial interferometry would help

DNA POS Workshop  
NSWC, 28-30 March 1995

# HIGH DENSITY PLASMA OPENING SWITCH EXPERIMENTS ON HAWK<sup>†</sup>

B. V. Weber, R. J. Commisso, P. J. Goodrich,<sup>\*</sup> and R. A. Riley, Jr.<sup>\*\*</sup>

Pulsed Power Physics Branch, Plasma Physics Division  
Naval Research Laboratory, Washington, DC 20375

## ABSTRACT

Previously, plasma opening switch (POS) experiments<sup>1</sup> on Hawk have shown fast opening ( $< 100$  ns) into electron-beam diode loads, generating 1-2 MV after 0.5-1  $\mu$ s conduction time. The plasma density measured in these experiments was in the  $10^{15}$  -  $10^{16}$   $\text{cm}^{-3}$  range. Plasma thinning by  $J \times B$  forces during conduction<sup>2</sup> reduces this density, ultimately leading to gap formation in the low density region. The Hawk experiments described here were designed to investigate this switching phenomenon with higher initial densities, in the  $10^{17}$   $\text{cm}^{-3}$  range, to determine whether fast switching and high voltage could be sustained. This scaling is important for POS applications on future, higher energy generators. Experiments were performed with a relatively small center conductor radius (1.27 cm) and small plasma length (3 cm or 8 cm). Either 36 or 12 cable gun plasma sources were used to inject plasma into the coaxial switch region. The anode structure was varied to investigate techniques to increase the voltage when the switch opens. High voltage (1.5 MV) switching was observed at  $\sim 0.9$   $\mu$ s conduction time when the radial gap between the inner and outer conductors in the switch region was reduced from 7 cm to 2 cm. Two techniques that improved switching on the DPM1 experiment<sup>3</sup> at conduction times  $< 600$  ns were investigated on Hawk: (1) removing the physical connection on the anode through the switch plasma, and (2) varying the radius of the anode conductor on the load side of the switch. These changes had no noticeable effect on the switch voltage for the longer conduction time scale of Hawk. The number of plasma sources had little effect on the voltage. These experiments demonstrate that, at least for some geometrical configurations, POS operation at  $10^{17}$   $\text{cm}^{-3}$  density is similar to operation at one or two orders-of-magnitude lower density. Presumably, the plasma thinning mechanism results in a similar gap in all cases.

## INTRODUCTION

Long conduction time ( $\sim 1$   $\mu$ s) plasma opening switches (POS) are the subject of intense research for pulsed power development. Successful implementation of such switches will enable inexpensive, compact pulsed power generators without water lines. The Hawk generator at the Naval Research Laboratory (NRL) is a testbed for long conduction time POS development. Hawk consists of a 250 kJ Marx with typical output voltage of 640 kV and a vacuum inductor, initially shorted by a POS as shown schematically in Fig 1. The current through a short circuit at the POS location is a sine wave with 750 kA amplitude and a quarter period of 1.2  $\mu$ s. In previous POS experiments on Hawk, the injected plasma density was in the  $10^{15}$  -  $10^{16}$   $\text{cm}^{-3}$  range, resulting in 0.5-1.0  $\mu$ s conduction times and voltages as high as 2 MV.<sup>1</sup>

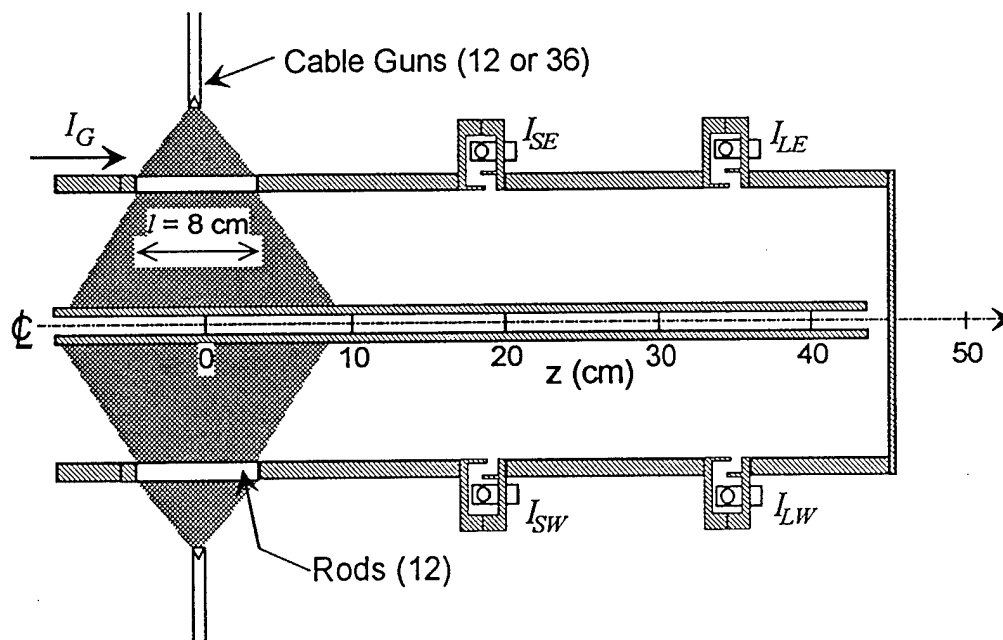


Figure 1. High density POS experiment on Hawk.

The fast switching in these experiments is believed to be related to a "plasma thinning" mechanism, where the plasma is redistributed by  $J \times B$  forces during conduction resulting in a low density region where gap opening can occur, by a combination of erosion and magnetic pressure. The physical size of the gap calculated from simple magnetic insulation relations is about 2-3 mm. The density reduction during conduction has been observed in some experiments using laser interferometry.<sup>2</sup> The density, averaged along an axial line of sight, becomes smaller than the sensitivity of the instrument (about  $10^{14} \text{ cm}^{-3} \times 10 \text{ cm}$ ) at the time of opening. This density reduction by more than two orders of magnitude is probably required to obtain high voltage switching. Without this density decrease, the POS would conduct the generator current and eventually propagate axially to the load as a plasma flow switch.

POS operation may be limited at higher density. If the plasma thinning mechanism only decreases the initial density by a fixed factor, the density prior to opening may be too high to allow vacuum gap formation, resulting in low voltage generation. If, on the other hand, higher density allows higher conducted current density, the plasma thinning may be expected to continue until vacuum gap formation occurs, similar to that obtained in the lower density cases. The conditions for productive plasma thinning are not well known, and may depend on many factors including the plasma distribution and the electrode shapes. In the Hawk experiments reported here, high density ( $\sim 10^{17} \text{ cm}^{-3}$ ) POSs were investigated for several anode configurations, showing that at least for one configuration, high voltage (1.5 MV) can be obtained after 0.9  $\mu\text{s}$  conduction time.

### HIGH DENSITY POS EXPERIMENTS ON HAWK

The POS plasma sources shown in Fig. 1 are cable guns, constructed from semi-rigid coaxial cable with an inverted cone drilled into the end. Current from a capacitor is discharged across the insulator (Teflon, C2 F4), creating a plasma that flows into the region between the inner and outer

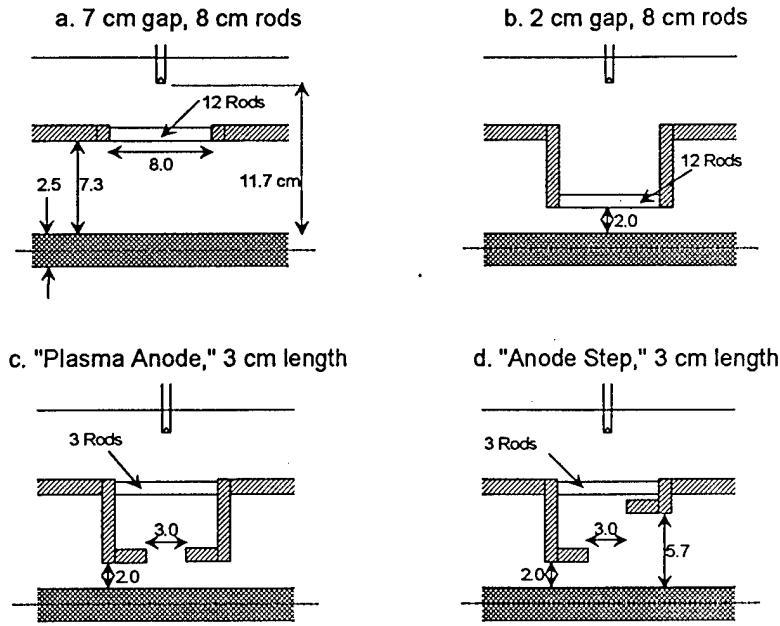


Figure 2. Anode variations used in high density POS experiments on Hawk: a) 8 cm length, 7 cm radial gap in POS region, b) 8 cm length, 2 cm radial gap in POS region, c) "plasma anode" configuration, where plasma connects the 3 cm long break in the anode in the POS region, and d) the "anode step" configuration, where the radial gap is increased on the load side of the POS to 5.7 cm.

conductors with a flow velocity of a few cm/ $\mu$ s. For these experiments, either 12 or 36 guns were arranged azimuthally in one ring to provide the high density plasma.

The density,  $n$ , required to conduct the Hawk current,  $I(t)$ , depends on the center conductor radius,  $r$ , and the plasma length,  $l$ ,

$$n \cong \frac{1.6 \times 10^{20}}{r^2 l^2} \iint I^2 dt^2 \quad (1)$$

where cgs units are used except  $I(\text{amps})$ .<sup>4</sup> This scaling relation has been determined from other cable-gun and flashboard POS experiments on Hawk where the plasma density was measured during shots using a He-Ne laser interferometer. High density will be required when  $r$  and  $l$  are small. For the experiments reported here, the center conductor radius was 1.27 cm and the plasma length was either 8 cm or 3 cm.

The geometry of the outer (anode) conductor was varied as shown in Fig. 2. The two variations in the top half of Fig. 2 utilize 12, 8-cm-long rods to connect the two sides of the plasma injection region. These two configurations differ by the distance between the center conductor and the rods. The configurations in the bottom half of Fig. 2 depend on the injected plasma to connect the two sides of the anode, therefore the name "plasma anode." These two configurations differ on the load end, where the distances between the center conductor and anode are changed. The increased radial distance on the load side of the plasma injection region is called the "anode step." The distance between the guns and the center conductor was either 12 cm or 6 cm.

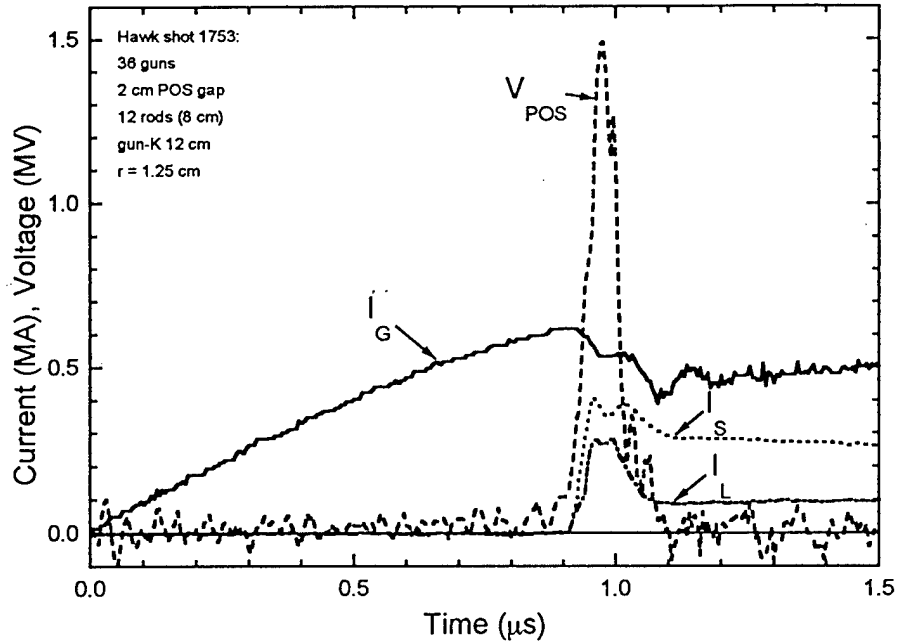


**Figure 3.** Electrical measurements for Hawk shot 1753, using the configuration shown in Fig. 2b. The conduction time is  $0.9 \mu\text{s}$  on this shot. The voltage rises when the POS opens, with a maximum of 1.5 MV. The currents measured on the load side of the POS ( $I_S$  and  $I_L$ ) indicate current loss in the POS-load region.

## RESULTS

Sample electrical data from a high voltage, long conduction time shot are shown in Fig. 3. This shot used the anode geometry illustrated in Fig. 2b (2 cm gap, 8 cm rods). The generator current,  $I_G$  in Fig. 3, rises to 620 kA in  $0.9 \mu\text{s}$  while the POS is “closed.” The POS voltage,  $V_{\text{POS}}$ , increases to 1.5 MV when the POS “opens,” beginning at  $t = 0.9 \mu\text{s}$ . Current measurements between the POS and the load,  $I_S$  and  $I_L$  indicate current losses that occur because the load impedance and POS-load inductance are higher than optimum for the POS. In principle, the POS-load inductance and load impedance could be reduced to optimize the power and energy delivered to the load.

The POS density inferred from Eq. 1 for the shot in Fig. 3 is  $6 \times 10^{16} \text{ cm}^{-3}$ . For the same conduction time but a shorter length of 3 cm (as with the anode configurations in the bottom of Fig. 2), the required density is  $4 \times 10^{17} \text{ cm}^{-3}$ . Therefore, the POS experiments with different anode configurations should be able to investigate POS operation with densities in the  $\sim 10^{17} \text{ cm}^{-3}$  range.

Results from the two configurations in the top half of Fig. 2 are compared in Fig. 4. These configurations have 8 cm rods located either 2 cm or 7 cm from the center conductor. The distance between the guns and the cathode was either 12 cm or 6 cm for the 2 cm gap case. The plot shows the maximum POS voltage as a function of conduction time. The highest point corresponds to the shot in Fig. 3.

The “best” configuration, from the point of view of voltage generation, is the 2 cm gap, 12 cm gun-cathode distance configuration. The voltage decreases abruptly for conduction times greater than  $0.9 \mu\text{s}$ , possibly because the plasma dynamics during conduction are different, leading to smaller gap



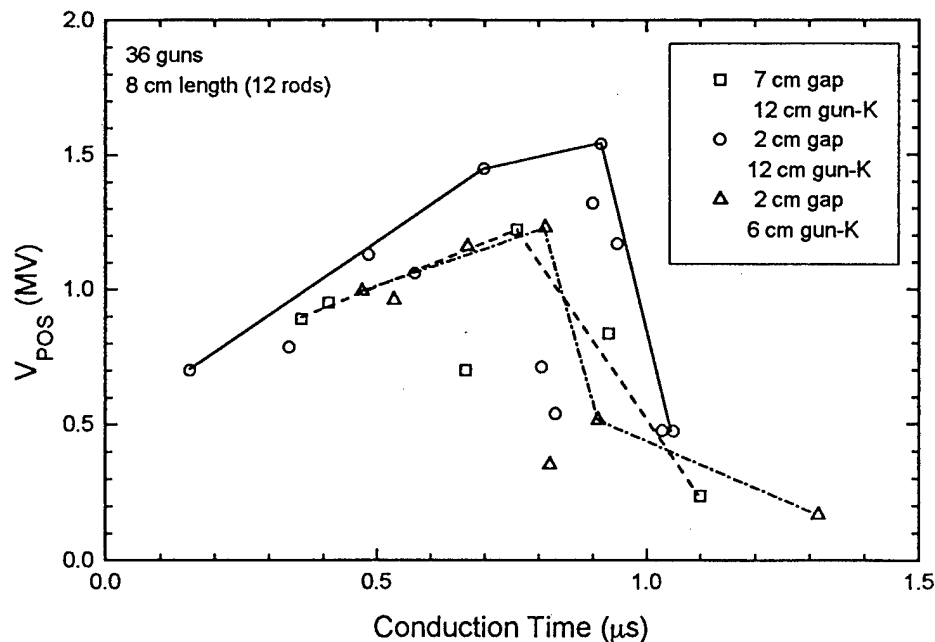


Figure 4. Maximum POS voltage is plotted versus conduction time for the three variations indicated in the plot. Decreasing the gun-cathode distance from 12 cm to 6 cm results in decreased voltage, as does increasing the distance between the cathode and the rods from 2 cm to 7 cm.

formation. The desirable high voltage performance is somewhat irreproducible as evidenced by the two low points at 0.8 μs conduction time.

The voltage decreases noticeably when the gun-cathode distance is decreased to 6 cm. This result is probably related to the change in plasma distribution. The results with a larger gap between the center and outer conductors are similar to those with the decreased gun-cathode distance.

Results from the "plasma anode" and "anode step" configurations are compared with the 2 cm gap results in Fig. 5. The plasma anode configuration results in lower voltage than the other configurations. The anode step results in somewhat increased voltage, but is significantly lower than the 2 cm gap configuration. These configurations differ in both the density required to conduct the generator current and the plasma length. Both of these changes may contribute to the decreased voltage generation for these configurations.

## CONCLUSIONS

Experiments have been performed on Hawk to explore POS operation with plasma densities in the  $10^{17} \text{ cm}^{-3}$  range, one to two orders of magnitude higher than in previous Hawk experiments. Parameters that influence the voltage generated when the switch opens include the plasma source locations and the outer conductor configuration. Of the four outer conductor configurations investigated, one is superior in the sense that the voltage generated (1.5 MV) is highest at the longest conduction time (0.9 μs). Configurations using the "plasma anode" and "anode step" configurations, similar to those that proved superior on the DPM1 experiment,<sup>3</sup> resulted in lower voltage than the best configuration, an 8-cm long aperture connected with rods, located 2 cm from the cathode.

In order to design an optimum POS configuration for a given generator (or, to design an optimum generator for a given POS) requires a model that explains these results. Future work has this

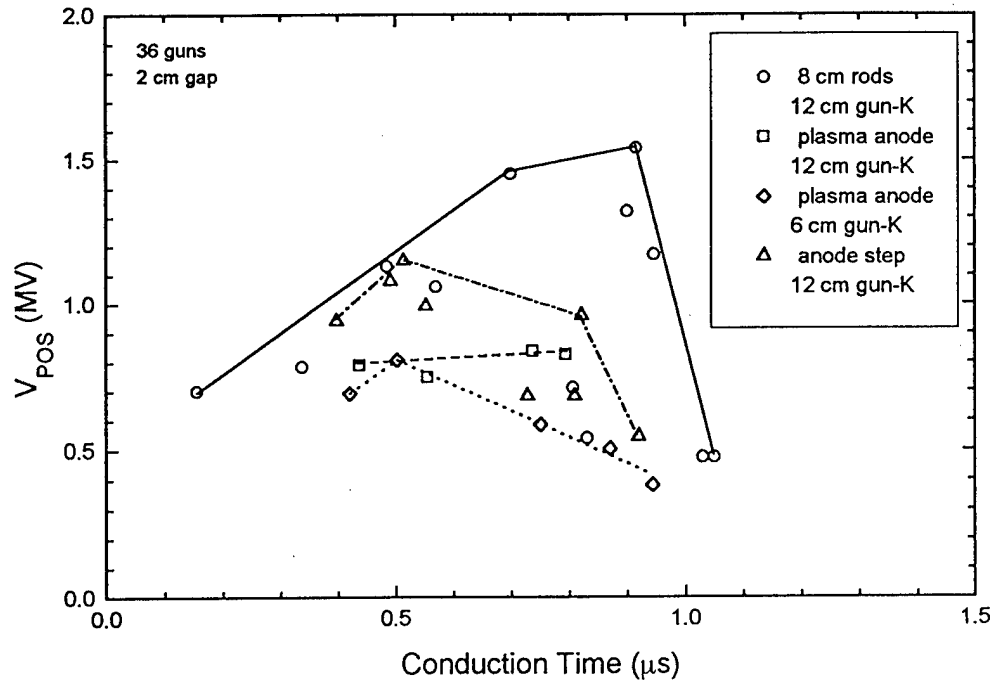


**Figure 5.** Maximum POS voltage versus conduction time are compared for the best configuration in Fig. 4 and the plasma anode and anode step configurations. The plasma anode and anode step configurations result in decreased voltage relative to the 8 cm rods, 2 cm gap case.

objective, using experimental measurements of plasma dynamics and combined MHD/Hall modeling of the conduction phase coupled with particle modeling of the opening phase.

## ACKNOWLEDGMENTS

The authors are pleased to acknowledge the support of Dr. J. Rowley of the Defense Nuclear Agency. The Hawk experiments were performed with the expert technical assistance of M. Sucky.

+ Work Supported by DNA

\* JAYCOR, Vienna VA

\*\* National Research Council Associate

1. R. J. Comisso, P. J. Goodrich, J. M. Grossmann, D. D. Hinshelwood, P. F. Ottinger, and B. V. Weber, *Phys. Fluids B* 4, 2368 (1992). P. J. Goodrich, R. J. Comisso, J. M. Grossmann, D. D. Hinshelwood, R. A. Riley, S. B. Swanekamp, and B. V. Weber, in *Proc. 10<sup>th</sup> Intl. Conf. on High Power Particle Beams*, W. Rix and R. White, eds., NTIS PB95-144317, p. 299.
2. D. D. Hinshelwood, B. V. Weber, J. M. Grossmann, and R. J. Comisso, *Phys. Rev. Lett.* 68, 3567 (1992).
3. J. R. Goyer, D. Kortbawi, and P. S. Sincerny, *IEEE Trans. Plasma Sci.* 22, 242 (1994).
4. B. V. Weber, R. J. Comisso, P. J. Goodrich, J. G. Grossmann, D. D. Hinshelwood, P. F. Ottinger, and S. B. Swanekamp, *Phys. Plasmas* 2, 3893 (1995).

TITLE: POS PLASMA AND NEUTRAL DENSITY MEASUREMENTS

AUTHORS: B. Weber, R. Commisso, P. Goodrich, D. Hinshelwood, and R. Riley

DATE: 6 April 1995

ABSTRACT: This talk was presented at the DNA POS Workshop on March 29, 1995. Interferometric diagnosis of POS plasmas is discussed, with examples from experiments at NRL. Different wavelengths have been used, from 2 mm microwaves to 0.5 micron lasers. Different techniques have been developed, including direct phase detection, heterodyne phase detection, multi-chord interferometry, and two-color interferometry. These measurements have had an important influence on our thinking about POS physics, and many labs have adopted these techniques for diagnosing their POS experiments. These measurements will undoubtedly lead to improved understanding of POS physics in the future.

THIS REPORT REPRESENTS UNPUBLISHED  
INTERNAL WORKING DOCUMENTS AND SHOULD  
NOT BE REFERENCED OR DISTRIBUTED WITHOUT  
THE AUTHORS' CONSENT

# POS Plasma and Neutral Density Measurements

B. Weber, R. Commisso, P. Goodrich,\*  
D. Hinshelwood,\* R. Riley\*\*

Naval Research Laboratory  
Washington DC 29375

DNA/RAST POS Workshop  
NSWC White Oak  
March 28-30, 1995

\* JAYCOR, Vienna, VA  
\*\* NRL/NRC Research Associate

## Outline

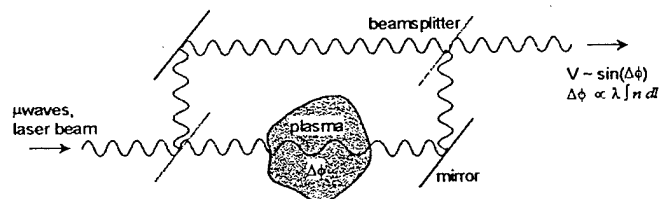
NRL

- Old days (80's)
  - 140 GHz microwave interferometry
    - › Mendel guns, MIP source
  - CO<sub>2</sub> laser interferometry
    - › NRL flashboards, PI flashboards & cable guns
- Recent Past (90's)
  - He-Ne laser interferometry: first *n* msmts during shots
    - › density thinning during conduction
    - › POS conduction scaling
  - Multi-chord He-Ne: gas plasma sources
- Present
  - two-color interferometer (SRL SBIR funded by DNA)
    - › plasma and neutral measurements
    - › very high sensitivity for measuring low density in POS-load region

DNA POS Workshop  
NSWC, 28-30 March 1995

## Interferometry is a powerful tool for diagnosing the POS plasma

NRL



### Advantages

line-integrated  
can use multi-chord  
sensitive to free electrons  
non-intrusive  
electrically isolated  
~ ns time resolution  
~ mm spatial resolution

### Disadvantages

line-integrated  
single line-of-sight  
insensitive to neutrals, ions

DNA POS Workshop  
NSWC, 28-30 March 1995

## Microwave and CO<sub>2</sub>-laser interferometers were used to diagnose plasma sources

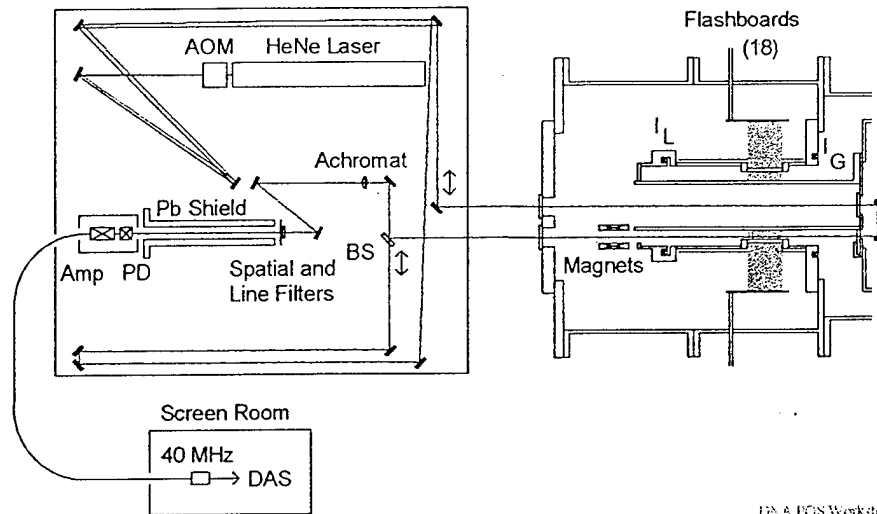
NRL

- 140 GHz (2 mm) μwave interferometer used to measure plasma source density and to infer conduction scaling  
ref: Weber, et al., IEEE Trans. Plasma Sci. 19, 757 (1991)
  - Mendel guns as used on Gamble I
  - MIP flashboards as used on PBFA II
  - short (~ 50 ns) conduction time,  $I \propto n$
  - limited to  $< 2 \times 10^{14} \text{ cm}^{-3}$  densities
  - density in POS-load region on Pawn, Hawk
- CO<sub>2</sub> laser (10.6 μ) interferometer used for higher densities
  - 40 MHz heterodyne, better signal/noise
  - cutoff  $10^{19} \text{ cm}^{-3}$ , practical limit determined by refraction
  - plasma source measurements:
    - NRL flashboards
    - PI flashboards & cable guns
  - measurements on Hawk and Gamble II (without pulsed power)

DNA POS Workshop  
NSWC, 28-30 March 1995

## A He-Ne laser interferometer made the first measurements during shots on Hawk

NRL

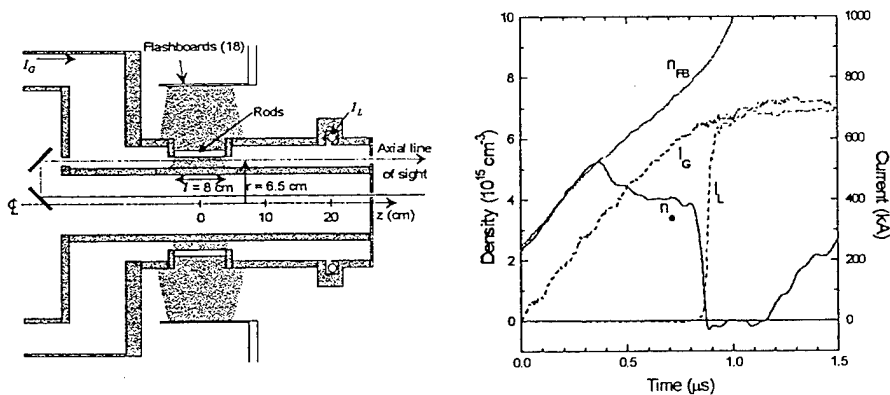


ref: Weber and Hinshelwood, *Rev. Sci. Instrum.* **63**, 5199 (1992)

DNA FOS Workshop  
NSWC, 28-30 March 1995

## The line-integrated density decreases at the time of opening

NRL

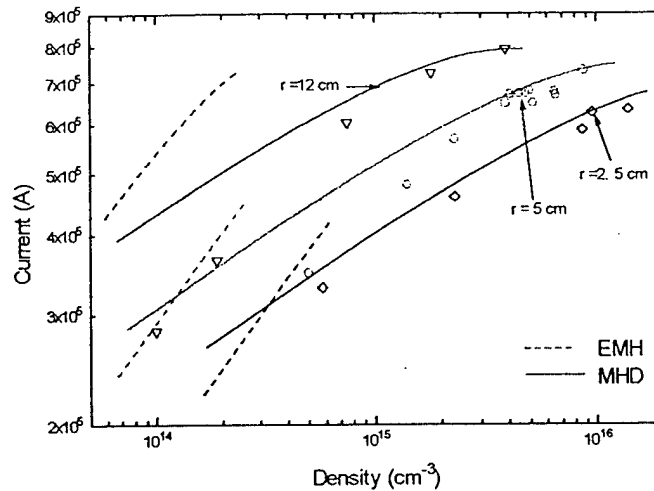


ref.: Hinshelwood, et al., *Phys. Rev. Lett.* **68**, 3567 (1992)

DNA FOS Workshop  
NSWC, 28-30 March 1995

## Conduction scaling was determined using the He-Ne interferometer on Hawk

NRL

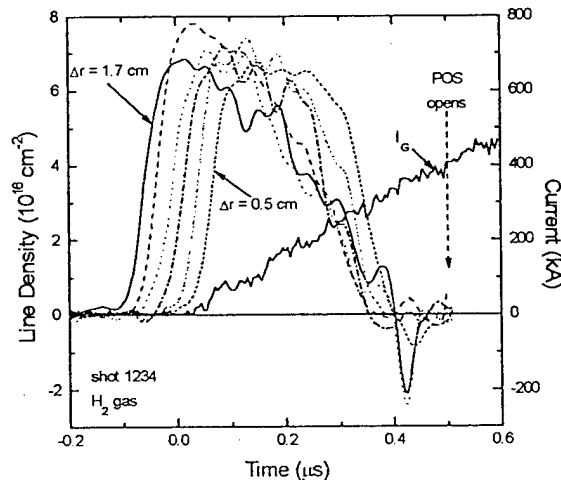
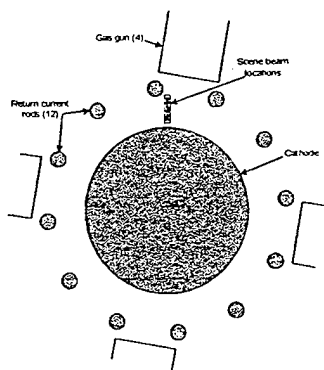


ref: Weber, et al., Proc. Beams '92

DNA POS Workshop  
NSWC, 28-30 March 1995

## A multi-chord version of the He-Ne interferometer was demonstrated on Hawk using gas plasma sources

NRL

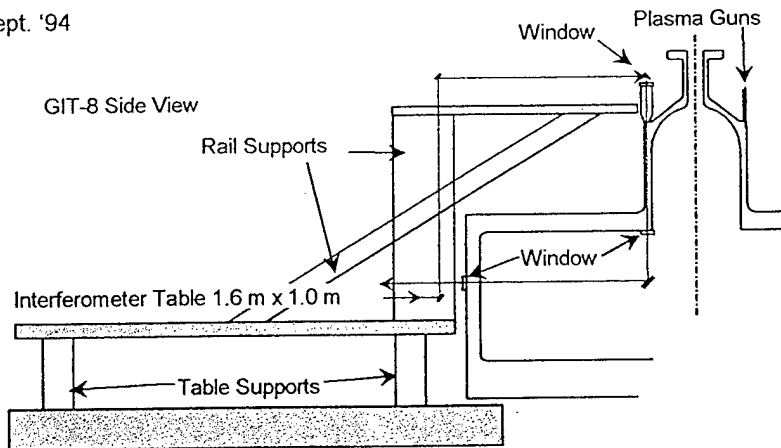


DNA POS Workshop  
NSWC, 28-30 March 1995

# A He-Ne interferometer went to Tomsk!

NRL

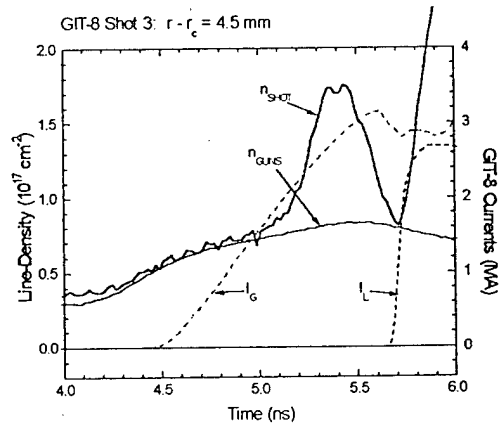
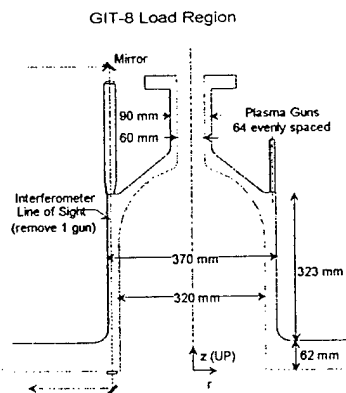
Sept. '94



DNA FOS Workshop  
NSWC, 28-30 March 1995

## Density measured during 3 MA, 1 $\mu$ s conduction time shots on GIT-8

NRL



DNA FOS Workshop  
NSWC, 28-30 March 1995



## Two-color, high sensitivity interferometer extends our ability to measure plasma and neutrals

NRL

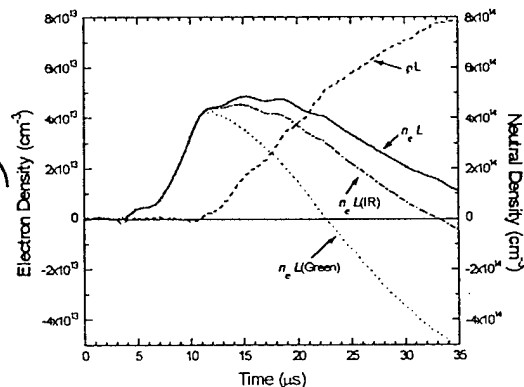
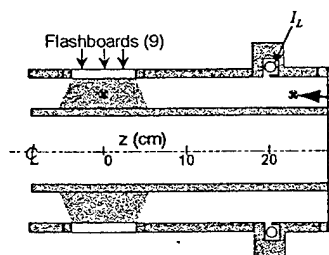
- Designed and built for Hawk by SRL (DNA SBIR)
  - operational September '93
- Two cw YAG lasers,  $\lambda = 1.064$  &  $0.532 \mu$ 
  - two independent Mach-Zender interferometers
- Sophisticated vibration isolation, optics in vacuum
- Motorized mirror mounts for remote overlap control
- PZT to set initial phase close to  $0^\circ$ , or to change phase by several  $\lambda$  to calibrate
- Photodiode detector bridge to cancel common mode
- $\sim$  ns time response,  $\sim$  mm spatial resolution
- With high gain, can measure  $10^{-5} \lambda$  phase change!
- Two wavelengths, can distinguish electron and "neutral" densities

DNA FOS Workshop  
NSWC, 28-30 March 1995

## Example of neutral measurement

NRL

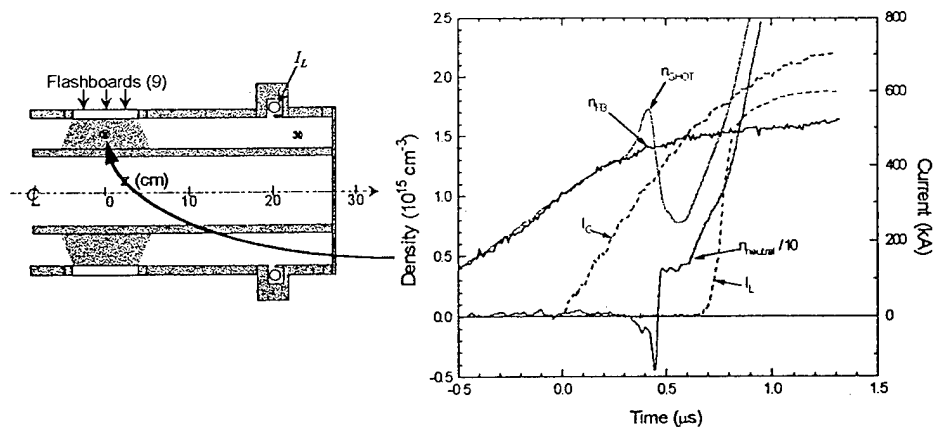
- FB sources only, laser beams in load region



DNA FOS Workshop  
NSWC, 28-30 March 1995

## A large neutral density is detected during conduction on Hawk shots

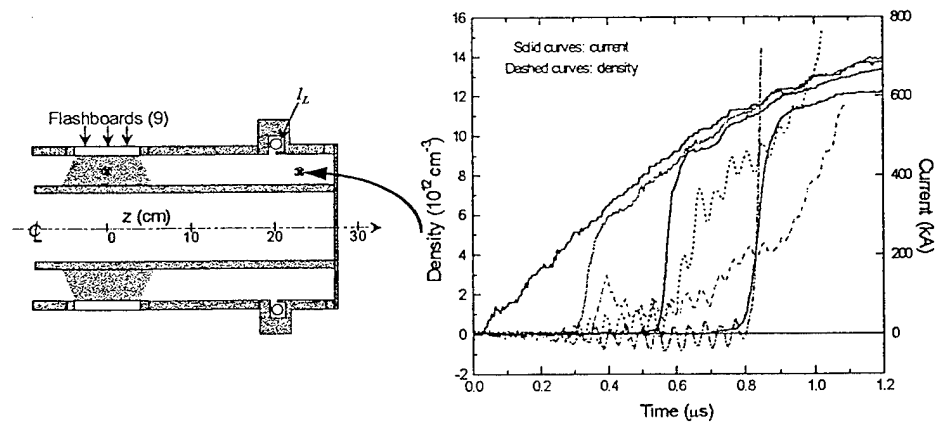
NRL



DNA FOS Workshop  
NSWC, 28-30 March 1995

## A low density plasma reaches the load region after load current rises

NRL



DNA FOS Workshop  
NSWC, 28-30 March 1995

## Plans

NRL

- **Exploit interferometry to improve POS understanding**
  - two-color & multi-chord HeNe interferometers on Parallel Plate POS experiment (Hawk)
  - measure low density plasma in e-beam diode load (2 color)
  - measure evolution of radial plasma distribution in coax POS (multi-chord HeNe)
- **Continue technology transfer**
  - 140 GHz interferometer transferred to Sandia
  - HeNe techniques adapted at MLI
  - PI, MLI, NRL plasma sources diagnosed at NRL
  - if it can go to Tomsk, it can go anywhere!
- **Spinoffs**
  - gas distribution from PRS nozzles
    - » Phoenix Ar nozzle diagnosed

DDA POS Workshop  
NSWC, 28-30 March 1995

## Summary and Conclusions

NRL

- **Interferometry is a powerful tool for POS diagnosis**
- **Variety of techniques for different applications**
  - CO<sub>2</sub>,  $\mu$ wave: low density
  - HeNe laser: easy, cheap, good for phase shifts  $\gg 1^\circ$
  - SRL technique: good for very small phase shifts  $\ll 1^\circ$
  - 2-color: measure electrons and neutrals
- **Results from past few years have affected our thinking**
  - density thinning, opening in low density region
  - MHD conduction scaling
  - possibly high  $n$  neutrals near POS electrodes at opening
  - low density downstream plasma
- **Room for *much* more work to understand POS physics**

DDA POS Workshop  
NSWC, 28-30 March 1995

TITLE:       **MAXWELL "SLOW" FLASHBOARD DENSITY MEASUREMENTS  
              USING TWO-COLOR INTERFEROMETRY**

AUTHORS:   **B. Weber, P. Goodrich, R. Riley, M. Sucy**

DATE:       **6 April 1994**

ABSTRACT:       A flashboard from ACE 4 is diagnosed using the two-color SRL interferometer installed on the Hawk vacuum chamber. Measurements are made using a mockup of the ACE experimental hardware. The objective is to determine whether neutrals evolve from either the flashboard, the anode mesh or the cathode metal that could have an adverse effect on POS operation.

Electron densities in the  $\sim \text{few} \times 10^{15} \text{ cm}^{-3}$  range were measured, with maximum densities near the cathode plate. The phase shift from the electrons is large compared with the phase shift from bound electrons in ions and neutrals, limiting the accuracy of the neutral measurements. At all locations, a slow rising neutral density is observed late in time (later than times used in ACE 4 experiments). At early times, the neutral density is relatively small ( $< 5 \times 10^{15} \text{ cm}^{-3}$ ) or not measurable except near the cathode. Near the cathode, two peaks in "neutral density" are detected that cannot be attributed to any known noise sources. One possibility is that some species that has an anomalously large index of refraction evolves then disappears.

These measurements demonstrate that electron densities inferred from He Ne interferometry are not in error due to neutrals, and that no anomalously high neutral density is present in the POS gap, except possibly near the cathode.

THIS REPORT REPRESENTS  
UNPUBLISHED INTERNAL  
WORKING DOCUMENTS AND  
SHOULD NOT BE REFERENCED  
OR DISTRIBUTED

## I. Experimental setup

The Maxwell "slow" flashboard was diagnosed using the SRL two-color interferometer on the Hawk vacuum chamber. The setup is a mockup of the configuration used in recent ACE 4 POS experiments. A sketch of the setup is shown in Figure 1. The return current wires are in front of the flashboard gaps to impede the expansion of the plasma from the surface. The flashboard is driven by a 2.2  $\mu\text{F}$  capacitor, charged to 25 kV for the data reported here.

The goal of these tests is to measure neutrals that may evolve from the flashboard surface, the anode mesh, or the cathode surface. It is assumed that a large source of neutrals could affect POS performance, at least to the extent that the electron density measured in a test stand is not the density in an actual experiment during current conduction. These flashboards have been diagnosed at MLI using a He-Ne interferometer to measure electron densities *in situ* in ACE 4, but without pulsed power. Measurements with pulsed power are in progress.

## II. Two-color interferometry

The two-color interferometer uses two cw lasers, a 1.064  $\mu\text{m}$  YAG (IR) and a 0.532  $\mu\text{m}$  frequency-doubled YAG (green). The interferometer optics are suspended in a vacuum chamber which is isolated from the surrounding structures by air pads. This isolation allows the initial phase to be set near a zero-crossing of the  $\sin(\phi)$  signal, where  $\phi$  is the relative phase difference between the reference and plasma legs of the interferometer. The vibration isolation and lack of thermal and acoustic effects result in impressively slow baseline drifts of about  $10^\circ$  per second, corresponding to relative mirror motion of about 1 mm per day. This allows precise measurements of phase shifts at both wavelengths.

Each laser beam is phase shifted by both plasma electrons and by bound electrons in neutrals and ions (referred to here as "neutrals"). The phase shift from plasma electrons is given by:

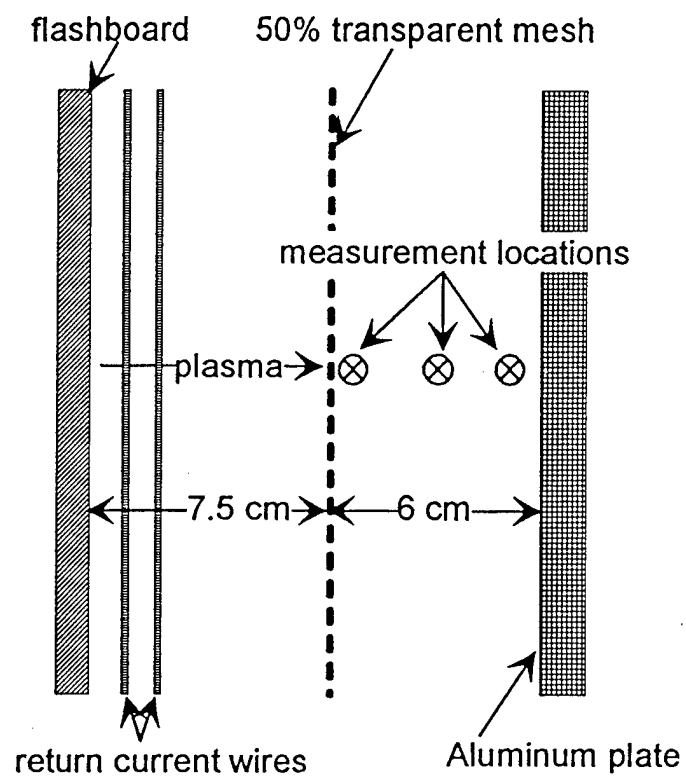
$$\phi_e = -r_e \lambda \int n_e dl \quad (1)$$

where  $r_e = 2.82 \times 10^{-13}$  cm,  $\lambda$  is the wavelength of the probe laser, and the electron density,  $n_e$ , is integrated along the laser line of sight. The phase shift from "neutrals" has the opposite sign and is inversely proportional to wavelength:

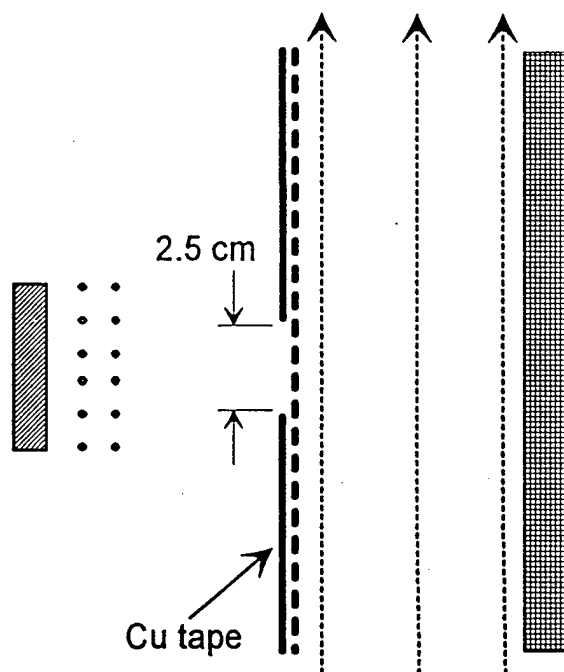
$$\phi_n = \frac{2\pi\beta}{\rho_o} \frac{1}{\lambda} \int \rho dl \quad (2)$$

where  $\rho$  is the "gas" density, assumed here to be air (for convenience instead of science), for which  $\beta = 3 \times 10^{-4}$  and  $\rho_o = 2.5 \times 10^{19}$  cm<sup>-3</sup>. Plasma electrons cause 40 times the phase shift of an equal density of "neutrals" for the IR wavelength, and 10 times the phase shift at the green wavelength. (Note that this depends on the exact species that constitute the "neutrals".)

The phase shift is measured for the two probe beams,  $\phi_I$  (for IR) and  $\phi_G$  (for green). The electron and neutral phase shifts are given by:



Side View



Top View

Figure 1. MLI slow flashboard setup for 2-color interferometry

$$\phi_{el} = \frac{4}{3}\phi_I - \frac{2}{3}\phi_G \quad (3)$$

$$\phi_{eG} = \frac{2}{3}\phi_I - \frac{1}{3}\phi_G \quad (4)$$

$$\phi_{nl} = \frac{2}{3}\phi_G - \frac{1}{3}\phi_I \quad (5)$$

$$\phi_{nG} = \frac{4}{3}\phi_G - \frac{2}{3}\phi_I \quad (6)$$

Here, the terms on the right hand sides are measured directly by the interferometer. The quantities on the left are the shifts caused by electrons and neutrals, assuming the wavelength dependencies in Eqs. 1 and 2.

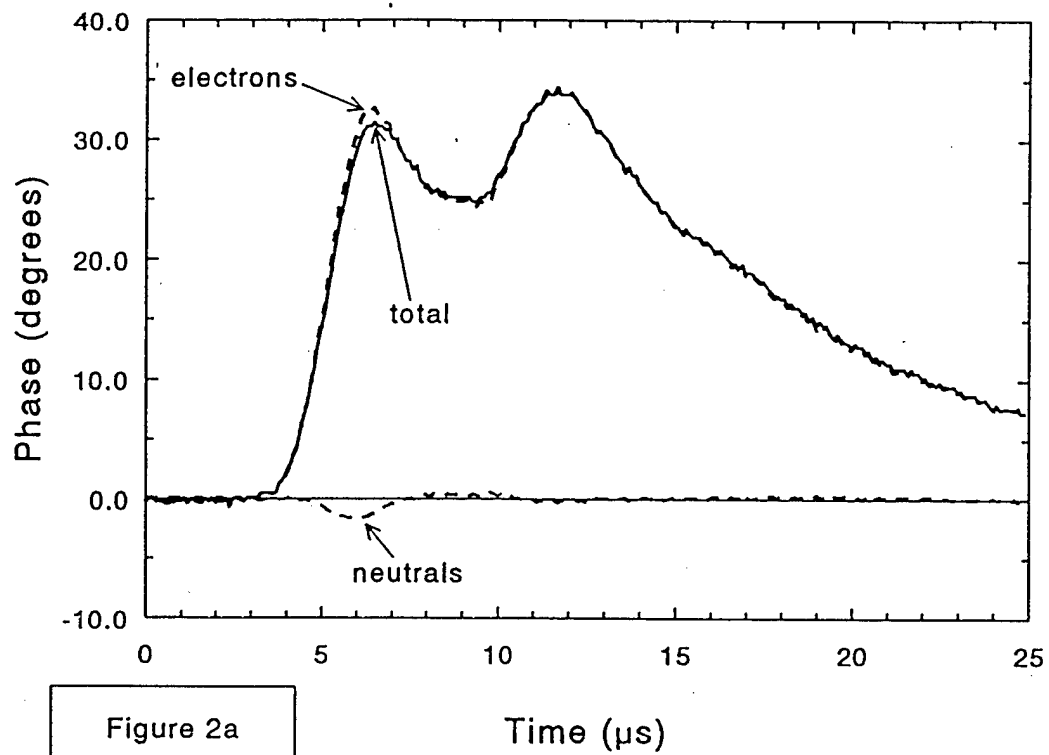
An illustration of the technique is shown in Figs. 2a and b. The laser line-of sight is about 5 mm from the plate, with a 2.5-cm long plasma aperture on the mesh. The origin of time corresponds to the onset of flashboard current. The solid curves (labeled "total") are the phase shifts for the IR and green beams, each of which is a combination of a positive phase shift from electrons and a negative shift from "neutrals." (This sign convention is the opposite of Eqs. 1 and 2 so the plots will result in primarily positive numbers.) The phase shifts from electrons and neutrals are calculated for each wavelength using Eqs. 3-6. The "total" phase shifts are very close to the "electron" shifts, except at the first peak at  $t = 6 \mu\text{s}$ . There, the IR shifts differ by about  $1.5^\circ$  while the green shifts differ by about  $3^\circ$ . These differences are significant in that they cannot be attributed to standard sources of "noise" such as: baseline shifts, plasma light, electronic interference in the laser intensity, electronic differences in the detection circuitry, etc. More subtle sources of noise that have not been ruled out include refraction (leading to decreased contrast on the detectors) and nefarious species that have strong transitions at wavelengths between the two probe lasers (such as  $H_\alpha$  at  $0.654 \mu$ ). These types of effects may explain the non-physical positive neutral phase shift (corresponding to a negative neutral density) of about  $+1^\circ$  for the green beam for  $t > 8 \mu\text{s}$ .

### III. Results

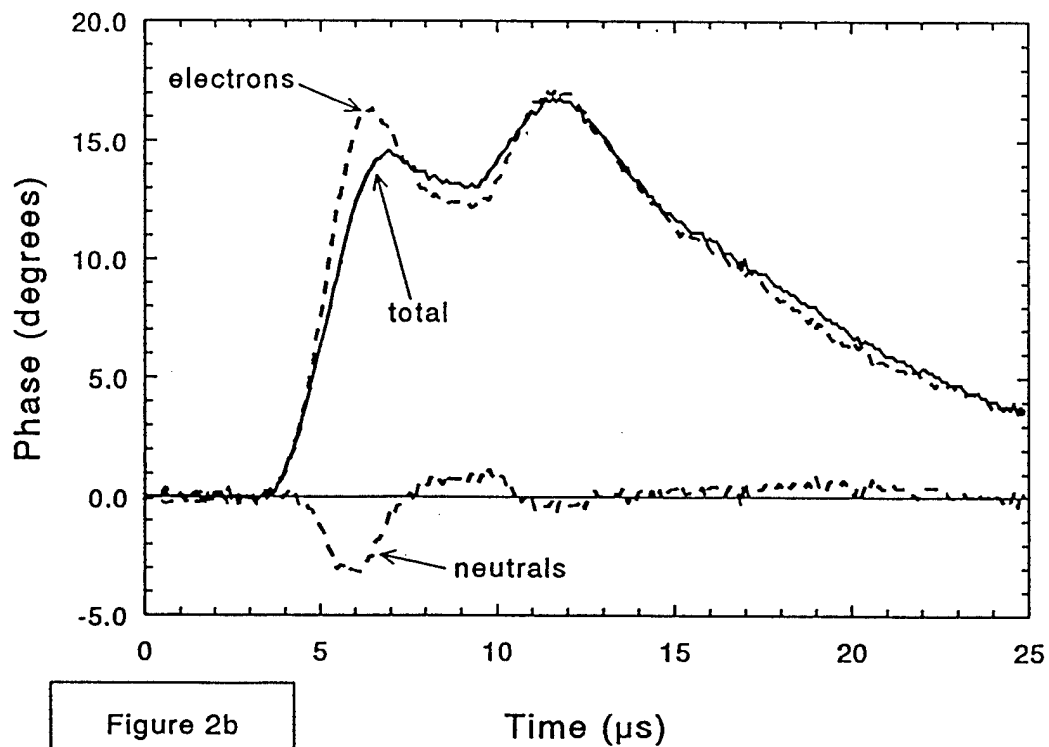
The phase shifts are converted into line-integrated densities using Eqs. 1 and 2, where for "neutrals," the index of refraction of air is used. Measurements were made at the three locations indicated in Fig. 1: 5 mm from the cathode plate, 5 mm from the mesh, and 30 mm from both the mesh and plate (mid gap). To limit the phase shift to a manageable value, the mesh was covered with copper tape leaving a 2.5-cm wide slot for the plasma to flow through. The most troublesome measurement location was near the aluminum plate. In Fig. 3a, the electron density (line integrated, averaged for 5 shots) is plotted vs. time along with the standard deviation to indicate the shot-to-shot variation. The flashboard current begins at  $t = 0$ . The electron density would be the same, within a few percent, if either laser were used alone (i.e., without the two-color correction, see Fig 1).

The "neutral" density is another story. The 5-shot average and standard deviation are plotted in Fig. 3b for the location near the plate. Late in time,  $> 25 \mu\text{s}$ , a slow-rising density appears that seems reasonable. The early time peaks at  $8 \mu\text{s}$  and  $14 \mu\text{s}$  are more difficult to understand. One possibility is that certain species appear and disappear that contribute an

Phase shifts for IR beam  
measurements near plate

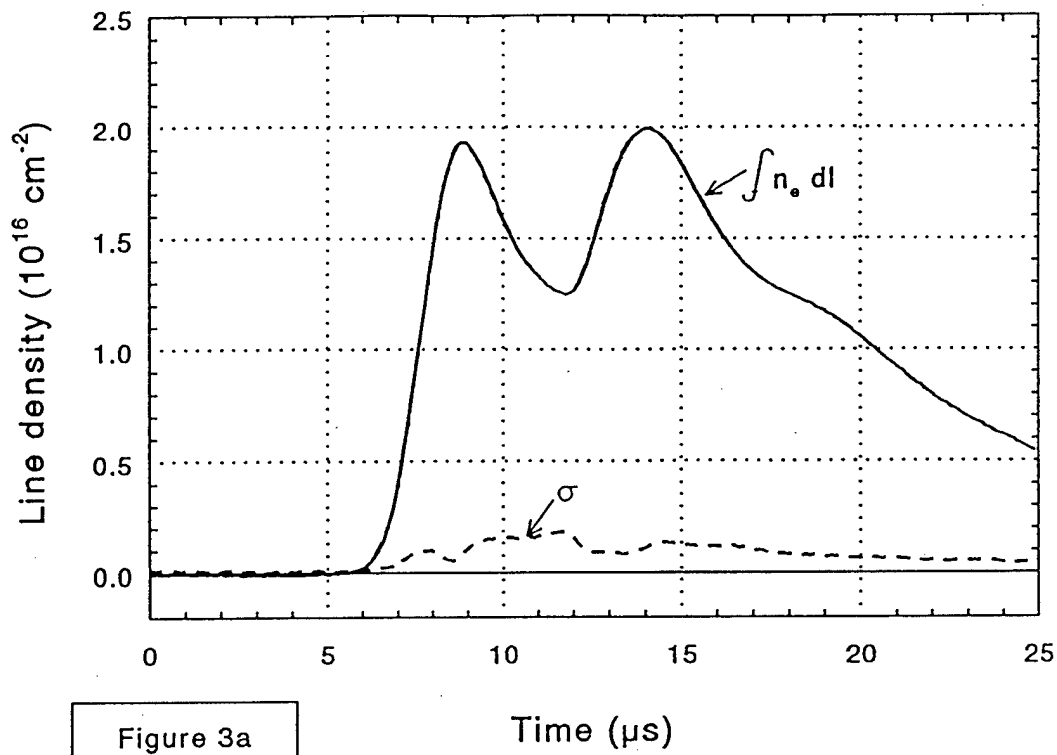


Phase shifts for green beam  
measurements near plate

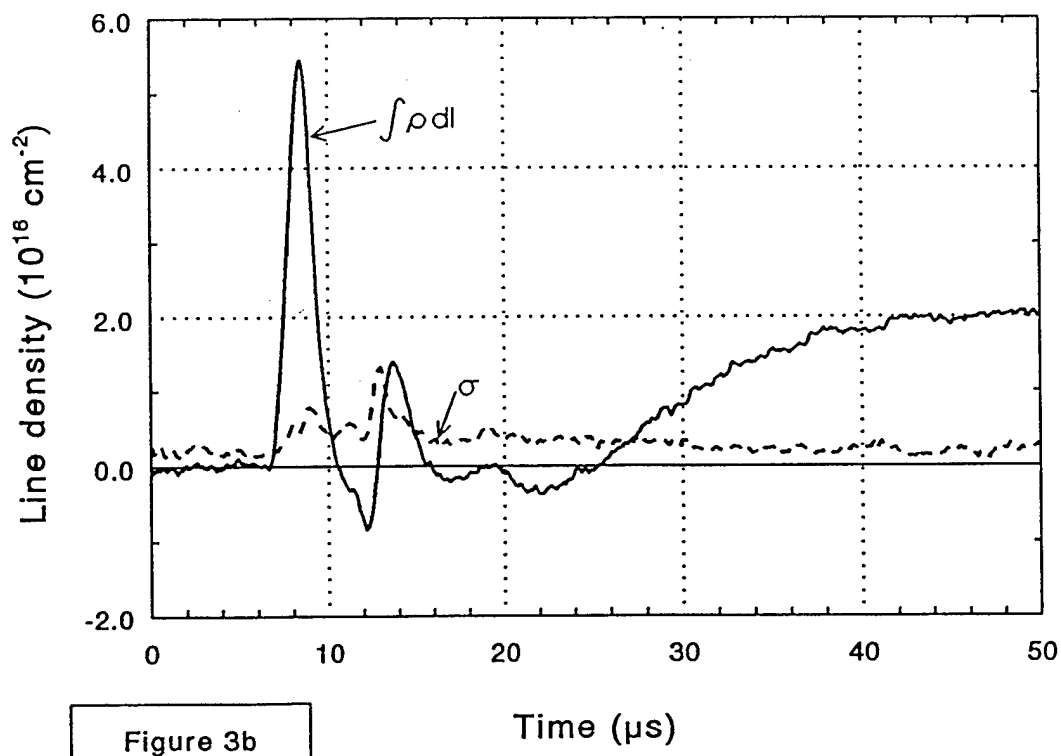




Electron density 5 mm from plate  
5-shot avg and std deviation



"Neutral" density 5 mm from plate  
5-shot avg and std deviation

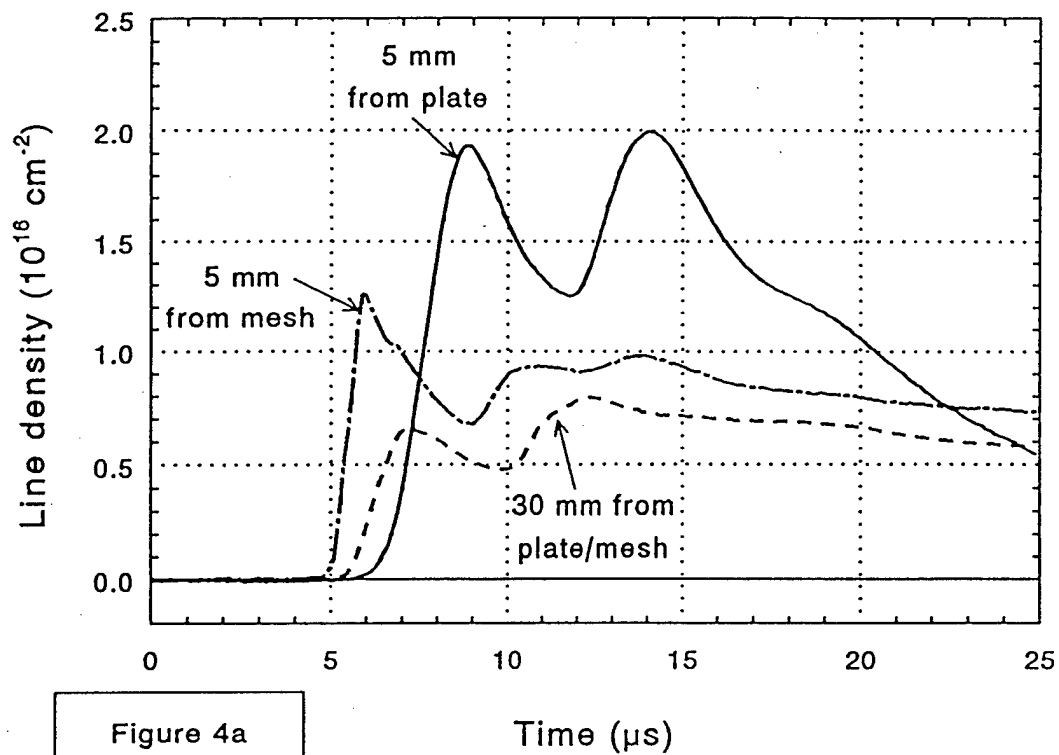


unusually large phase shift. This effect is not nearly as strong at the other two measurement locations (see below).

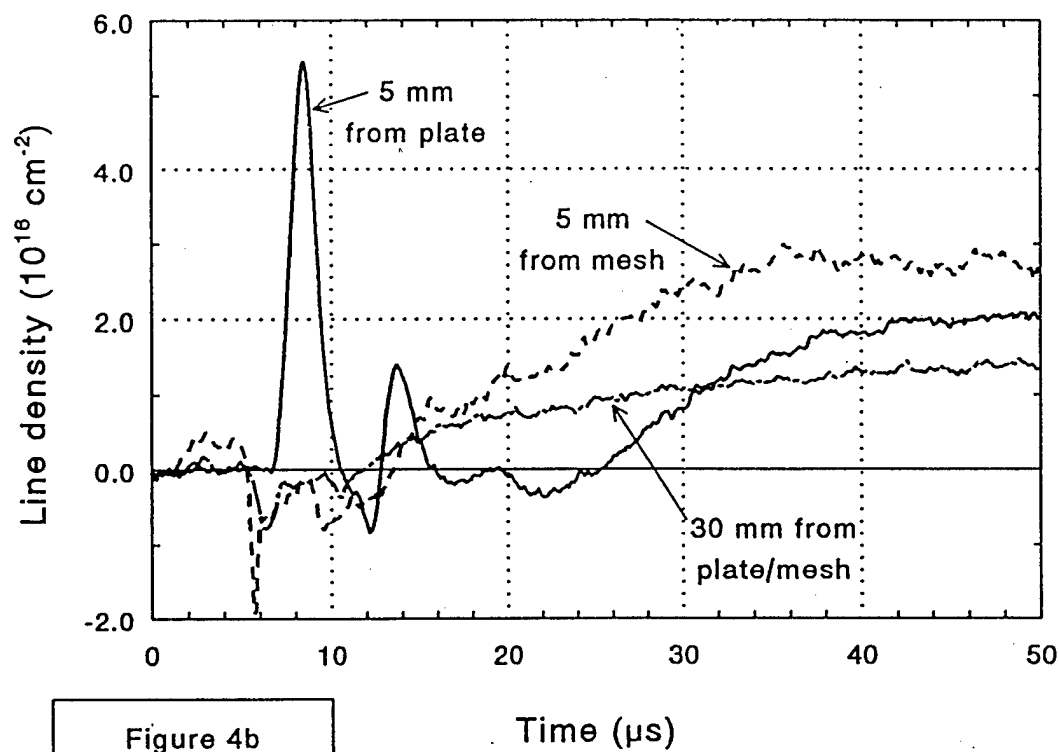
The electron densities are compared at the three locations in Fig. 4a. The mid-gap and near-mesh data are two-shot averages that were very similar. The density is higher at the mesh than in the gap, but is highest near the plate after about  $t = 7.5 \mu\text{s}$ . This density increase near a plate is a universal feature of all plasma sources we have tested, and is probably related to the generation of species causing the anomalous "neutral" density near the plate.

The neutral densities are compared at the three locations in Fig. 4b. The mid-gap and near-mesh data seem reasonable; a slow density increase is observed beginning at about  $t = 10$  to  $15 \mu\text{s}$ . The inferred neutral density has some wiggles for  $t < 10 \mu\text{s}$ , probably the result of subtraction errors. For times of interest in ACE 4 ( $t < 12 \mu\text{s}$ ), there does not appear to be a "large" density of neutrals that would affect POS operation, except possibly near the plate.

Electron density  
between mesh and plate



"Neutral" density  
between mesh and plate



PULSED POWER PHYSICS TECHNOTE 93-09

TITLE: INTERFEROMETRIC STUDIES OF GAS GUN PLASMAS

Author: D. Hinshelwood

Date: April 28, 1993

Abstract: This is the first in a series of three technotes describing our work with gas guns. This note presents results from a few brief studies of the mechanical valve and of gas breakdown in the guns, and measurements of the electron density, obtained with our six-chord interferometer, both for the guns alone and during short circuit shots. The gas guns are seen to produce radial density profiles that range from similar to, to very different from, those produced by flashboard sources. Data taken during machine shots are consistent, both qualitatively and quantitatively, with what we would expect based on our MHD picture of conduction current limitation. Reproducibility is seen to be poor, and possible ways to improve it are discussed. The results of this work suggest improved ways of fielding these sources in the future. While further investigation of these sources is likely a low priority, with some changes in the source arrangement, these sources have the potential to allow further relevant physics experiments

## INTRODUCTION

This is the first in a series of three technotes describing our work on gas gun plasma sources. Results from a few brief studies, of the mechanical valve and of gas breakdown in the guns, are presented first. Then, measurements of the electron density, obtained with our six-chord interferometer, both for the guns alone and during short circuit shots, are presented. The gas guns are seen to produce radial density profiles that range from similar to, to very different from, those produced by flashboard sources. Data taken during machine shots are compared both qualitatively and quantitatively with what we would expect based on our MHD picture of conduction current limitation. Reproducibility, and possible ways to improve it, is discussed. The results of this work suggest improved ways of fielding these sources in the future. Two companion technotes, presently under preparation, present the results of initial interferometric, test stand studies of the guns (Jim Kellogg) and the results of about 80 shots with diode loads (Phil Goodrich). So far, the use of gas gun plasma sources has not improved operation of the POS on Hawk. However, some useful physics information has been obtained and with some changes in the source arrangement, these sources have the potential to allow further, relevant physics experiments

## GAS GUN DESIGN AND TESTING

A machine drawing of the gas gun we developed is shown at the top of Fig. 1. The gun geometry is based on the guns first used by Yasha Krasik in his work at Tomsk. Here, however, an automobile fuel injector is used as the mechanical valve. We learned of this technique from a paper by Michael Brown of Cal Tech (JAP 69, 6302 [1991]). Each valve is driven by a 200  $\mu\text{F}$ , SCR-switched pulser built by Jim. For most of this work the pulsers were charged to 170 V. The plasma discharge itself is driven by two of our standard doghouses, with one, type-C cable connected to each of the six capacitors. Typically, the valve is pulsed several hundred microseconds before the doghouses are fired. Further details will be presented in Jim's note; in general the insulation and inductive isolation worked quite well and the guns were found to be quite reliable from this standpoint.

In the first test of the valves themselves, they were fired in vacuum toward, and at various distances from, a Penning gauge. This gauge can measure pressures up to a few microns ( $\sim 10^{14} \text{ cm}^{-3}$ ) with a response time of about 50  $\mu\text{s}$ , and so is sensitive to the first front of the expanding gas. With 100 V on the pulser and over a range of back pressures of air, the gas front moves at about 0.07  $\text{cm}/\mu\text{s}$ , consistent with the mean thermal velocity of 0.05  $\text{cm}/\mu\text{s}$ . Extrapolation of the data shows that the valve begins to open at 325  $\mu\text{s}$ .

Next, mechanical operation of the valve was examined directly. A small sliver of paper was attached to the valve plunger in such a way that the paper blocked a HeNe beam from reaching a photodiode. Retraction of the plunger was measured by the increase in photodiode signal. The backing pressure, pulser voltage, and pulser capacitance were varied. The capacitance was seen to have a negligible effect on the initial signal rise so that similar results would be expected with the 200  $\mu\text{F}$  used in Hawk experiments and the 100  $\mu\text{F}$  used here. Typical data is shown in the center of Fig. 1. (The

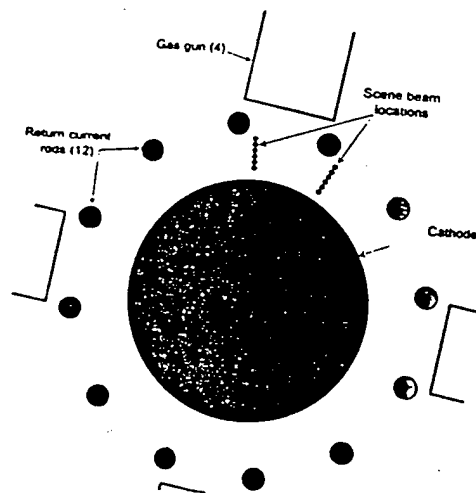
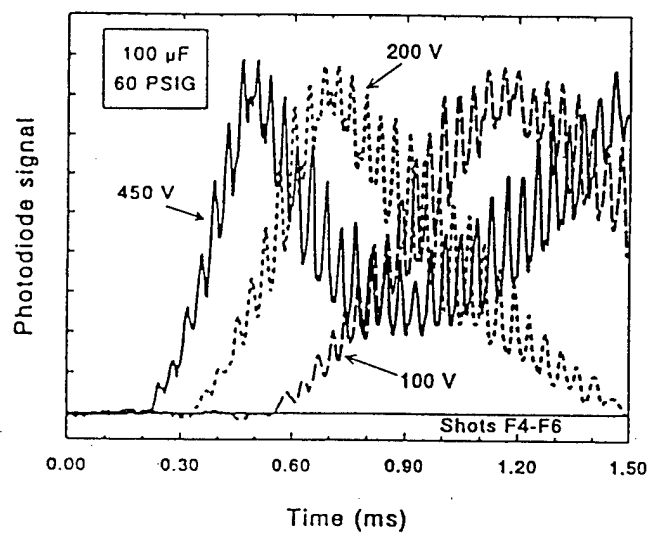
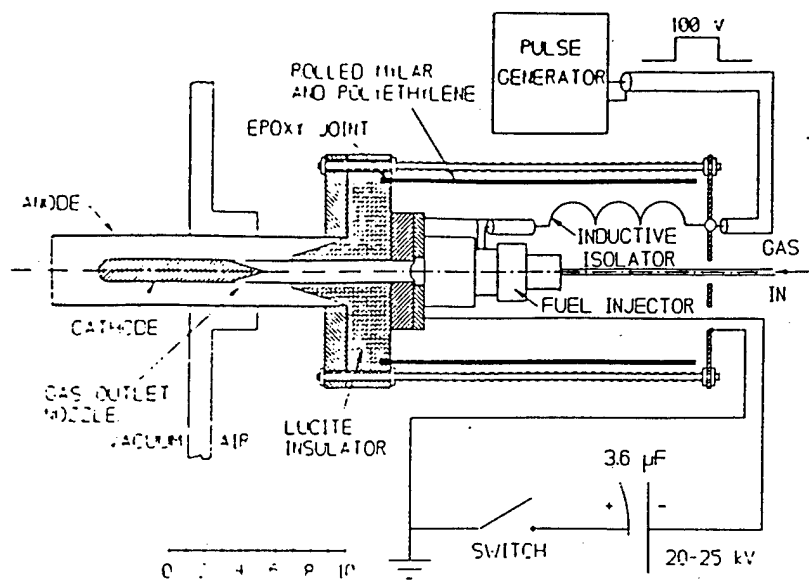


Figure 1: (top) Gas gun schematic; (middle) Measurement of the mechanical valve action; (bottom) Switch and scene beam arrangement.

fast oscillations on the signals do not occur in the absence of backing pressure and thus they are likely caused by a vibration of the plunger.) As the pulser voltage is raised, the valve opens sooner and more quickly. Unfortunately, this test was not set up to record the very first opening of the valve: for example at 100 V the valve begins to open at 325  $\mu$ s but the motion is not noticeable here until 525  $\mu$ s. By extrapolation of this data and that from the Penning measurements, at the 170 V used in the Hawk experiments the valve begins to open at about 250  $\mu$ s and opens completely at 800  $\mu$ s. This shows that the valves had only just begun to open at the timings used in the experiments. The limited data taken here show a good reproducibility in the mechanical action of one valve, but valve-to-valve reproducibility was not examined. The data here suggest that in the future the valves should be operated at higher voltages in order to sharpen the opening and hopefully reduce dispersion of gas in the guns prior to the discharge. They should also be operated with lower capacitance: reducing the capacitance does not change the initial rise but greatly reduces the duration of opening and thus reduces the pressure rise in the system after firing the guns.

Breakdown in the guns was diagnosed briefly using framing photography. A 4-mm wide slit was machined along the length of one gun barrel. The gun was operated with H<sub>2</sub> at 55 PSIG back pressure, using valve-to-discharge delays of 350-510  $\mu$ s. These were the timings used on Hawk. For all delays, light is observed first at the location of the holes in the center conductor. The luminous region then expands toward the gun exit at roughly 5 cm/ $\mu$ s for 430  $\mu$ s delay and at 10 cm/ $\mu$ s for 350  $\mu$ s delay. By 1-2  $\mu$ s, a slight difference in luminosity distribution is seen for different delays - for 350  $\mu$ s the light is brighter near the center electrode tip while for 430  $\mu$ s the light remains brighter near the holes.

## INTERFEROMETRIC ARRANGEMENT

This experiment was the first to make use of our multichord interferometer. Briefly, two cylindrical lenses are used to expand in one direction the beam from a 35-mW HeNe laser (gracefully lent to us by John Thompson at MLI). The lens pair is located beyond the AOM so that both beams are expanded together. The resulting, roughly 2-cm-wide strip beams are directed along our usual interferometer arrangement. The combined output beam is observed by an array of six short fiber optic segments coupled to photodiodes. The experimental arrangement on Hawk, along with the scene beam locations in the switch region, is shown in the drawing at the bottom of Fig.1. Four guns were used in the Hawk experiments and in most cases they were located very close to the anode rods as shown. This gives rise to a large azimuthal asymmetry when the 10-cm-diam cathode is used, which as a minimum complicates interpretation of the data. In future experiments they should probably be backed off. The 10-cm-diam cathode was used for all of the interferometric measurements.

The scene beams were located 0.24 cm apart in radius between 0.5 and 1.7 cm from the cathode. This setup did not have the beam-aligning paddle that was used in previous measurements, so that beam alignment could not be determined as accurately as before. There is probably a 0.1-0.15 cm uncertainty in the radial position of the beam

array in this work. Shots were taken with two locations of the gun collar, giving the two scene beam locations shown in the figure.

## SOURCE-ONLY STUDIES

Figure 2 shows data taken using 430  $\mu\text{s}$  valve-to-discharge delays with  $\text{H}_2$  gas. Unless noted, a back pressure of 55-60 PSIG was used for all shots presented here. The top graph shows data taken with the scene beams under the gun (Fig. 1). The middle graph shows the same data on an expanded time scale. Note that in all of the graphs in this note the line-averaged electron density is given, because the axial length is less well determined than when flashboards were used. Also, in all graphs here time zero corresponds to the start of the gun discharge (doghouse) current. Density is observed first by the scene beam closest to the gun at 2.45  $\mu\text{s}$ . This location is about 12 cm from the gas exit holes, giving an average velocity of 0.5 cm/ $\mu\text{s}$  which is in consistent with the framing photographic data. A sharp front is observed, moving at a faster velocity of about 10 cm/ $\mu\text{s}$ . Evidently the plasma observed here was either accelerated along the gun or originated later than the start of the discharge. A slight density decrease is seen behind the front. Shortly after the front reaches the cathode, a larger density increase is seen which propagates out from the cathode at 1-2 cm/ $\mu\text{s}$ . The last graph in Fig. 2 shows data taken with the scene beams offset from the gun. Here density is observed first close to the cathode, which is also closer to the gun as seen in Fig. 1. The later arrival time is consistent with the 10 cm/ $\mu\text{s}$  front velocity. The initial density behavior at this timing, with its very large spatial and temporal gradients, differs greatly from that observed with flashboards. The later-time, secondary plasma is typical of flashboard data and may be unrelated in composition to that supplied from the guns. By varying the gun-to-generator time delay it is possible to vary greatly the initial radial profile of the electron density. For the first 400 ns the secondary plasma appears to be absent, so that during this time the plasma composition can be controlled. However, this is shorter than the typical conduction time. At much greater gun-to-cathode separations it may be possible to stretch out the early density behavior and allow more controllable physics experiments. During this time the density ranges from strongly peaked near the anode to evenly distributed. By moving the guns farther away and operating in parallel-plate geometry with different injection directions, it should be possible to study the effect of plasma species and profile on switch operation.

The minimum delay for which the discharge could be driven was about 340  $\mu\text{s}$ . This time is consistent with the fact that the valve barely begins to open at 250  $\mu\text{s}$ , and  $\text{H}_2$  moving at the thermal speed of about 0.2 cm/ $\mu\text{s}$  requires 50  $\mu\text{s}$  to reach the holes in the gun center conductor. The top graph in Fig. 3 shows data taken for 350  $\mu\text{s}$  discharge delays. At this timing the density behavior differs markedly from that seen in Fig. 2. Density is first observed at 1.7  $\mu\text{s}$ , suggesting a faster plasma which is consistent with the framing photographic data. In this case, measurable density is seen simultaneously at all radial locations, and at both the center and offset azimuthal locations. After 1  $\mu\text{s}$  the density is slightly larger both near the cathode and near the guns than it is in the middle of the gap. This is all indicative of a fast, low density plasma that impacts the cathode and



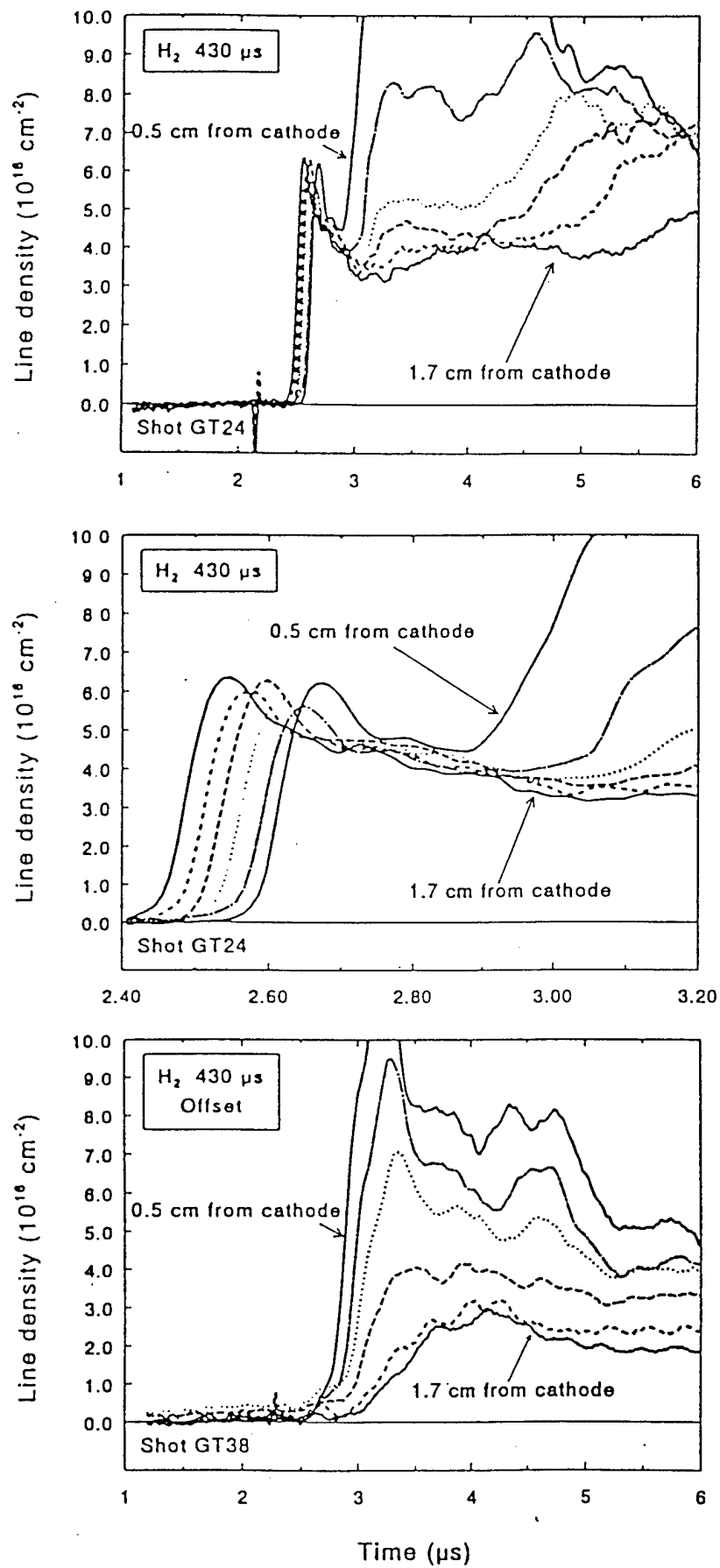


Figure 2: Density distributions from the sources alone.

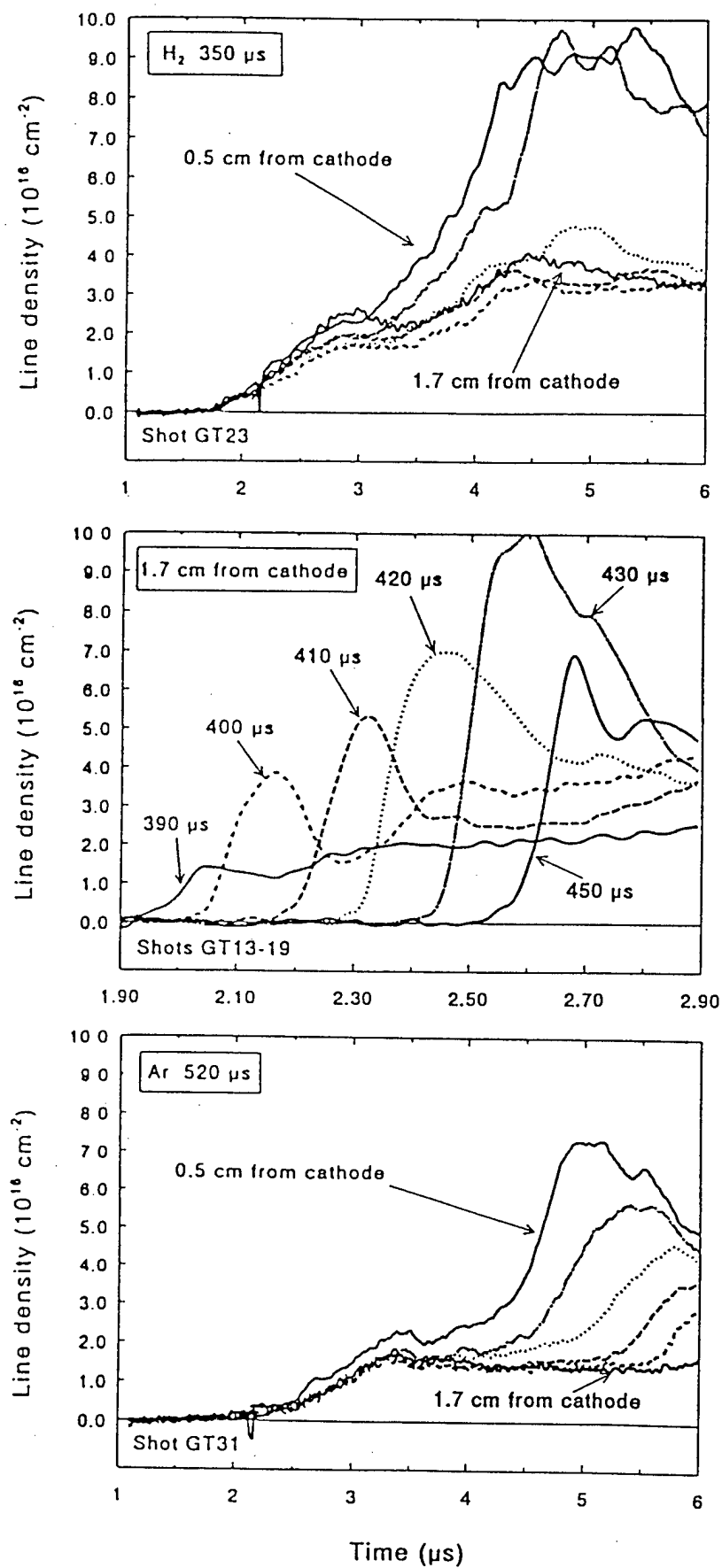


Figure 3: Density distributions from the sources alone.

bounces around, allowing the density to equilibrate within the switch region more rapidly than it increases with time. Later in time the profile is similar to that seen in Fig. 2.

At intermediate timings the density profile evolution varies smoothly between that shown here and that in Fig. 2. This is shown in the second graph in Fig. 3. Here data observed at 1.7 cm from the cathode is compared for a variety of timings. As the timing is increased beyond 430  $\mu\text{s}$ , the steepness of the density front decreases.

The last graph in Fig. 3 shows density data for Ar gas. For Ar, 520  $\mu\text{s}$  is about the minimum timing at which the discharge can be driven. With a thermal speed of roughly 0.04 cm/ $\mu\text{s}$ , Ar should require 200  $\mu\text{s}$  longer to transit from the valve to the holes than  $\text{H}_2$ , so that this minimum time is consistent with that for  $\text{H}_2$ . The density data are qualitatively similar to the early-timing data for  $\text{H}_2$  shown in the top graph.

Reproducibility of these sources is discussed in the section after next.

## MEASUREMENTS DURING MACHINE SHOTS

Interferometric measurements were performed during 11 machine shots with short circuit loads. Hydrogen gas was used for all shots with discharge delays of 430  $\mu\text{s}$ . This timing was chosen because of the resulting initial density behavior. The graphs in Fig. 4 show data from shots with generator delays of 2.3  $\mu\text{s}$ . Several interesting features are seen. On both shots the density at the start of conduction is very small. (Because of the weaker signals in this experiment, the noise-equivalent density is roughly a factor of two greater than in previous work.) Density increases during conduction as plasma flows into the switch region. On shot 1247 (top graph), opening appears to occur close to the cathode. Since the initial density is lowest there, this would be expected based on our MHD picture of conduction current limitation. On shot 1248, opening is a long, protracted process. This type of behavior was also observed on POP when the guns were placed very close to the cathode, and is believed to occur because the plasma influx increases rapidly over the conduction time. In this case, plasma can be supplied to the switch region as fast as it is distorted and/or eroded.

Figure 5 shows data from shots with 2.6- $\mu\text{s}$  generator delays. Shot 1249 (top graph) shows a density profile evolution typical of that observed on shots with flashboards: the density decreases during conduction at all locations except close to the anode, where it increases. The density minimum is located at 1.5 cm from the cathode. Shot 1234, by comparison, shows different behavior. Here the density decreases to the measurement limit at all locations. It is not immediately obvious why this shot is different from shot 1249. On this shot the load current was not recorded and the time of opening is estimated from the switch voltage. Despite the encouraging, broad density reduction, the switch voltage does not indicate a rapid opening. (In fact, all of the short circuit shots in this run exhibit rather slow openings.) The last graph shows data taken with the scene beams at the offset location. Here also the density decreases at all observed radial locations during conduction. In this case the azimuthal asymmetry may cause azimuthal pinching of the switch plasma.

The top graph in Fig. 6 shows data from a shot with a 3  $\mu\text{s}$  generator delay. At this time the secondary plasma density is much greater and opening appears to occur close

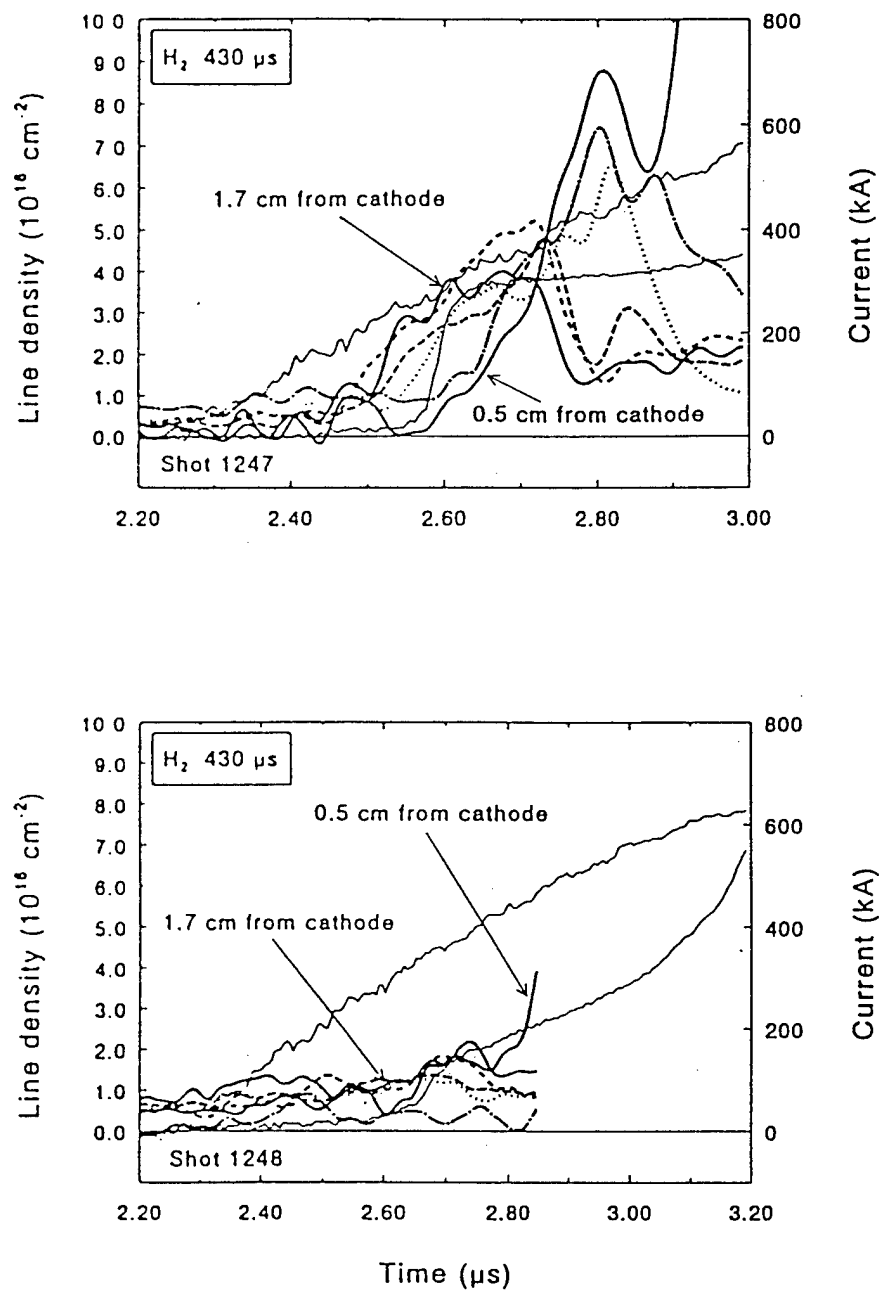


Figure 4: Density distributions from Hawk shots with early generator time delays.

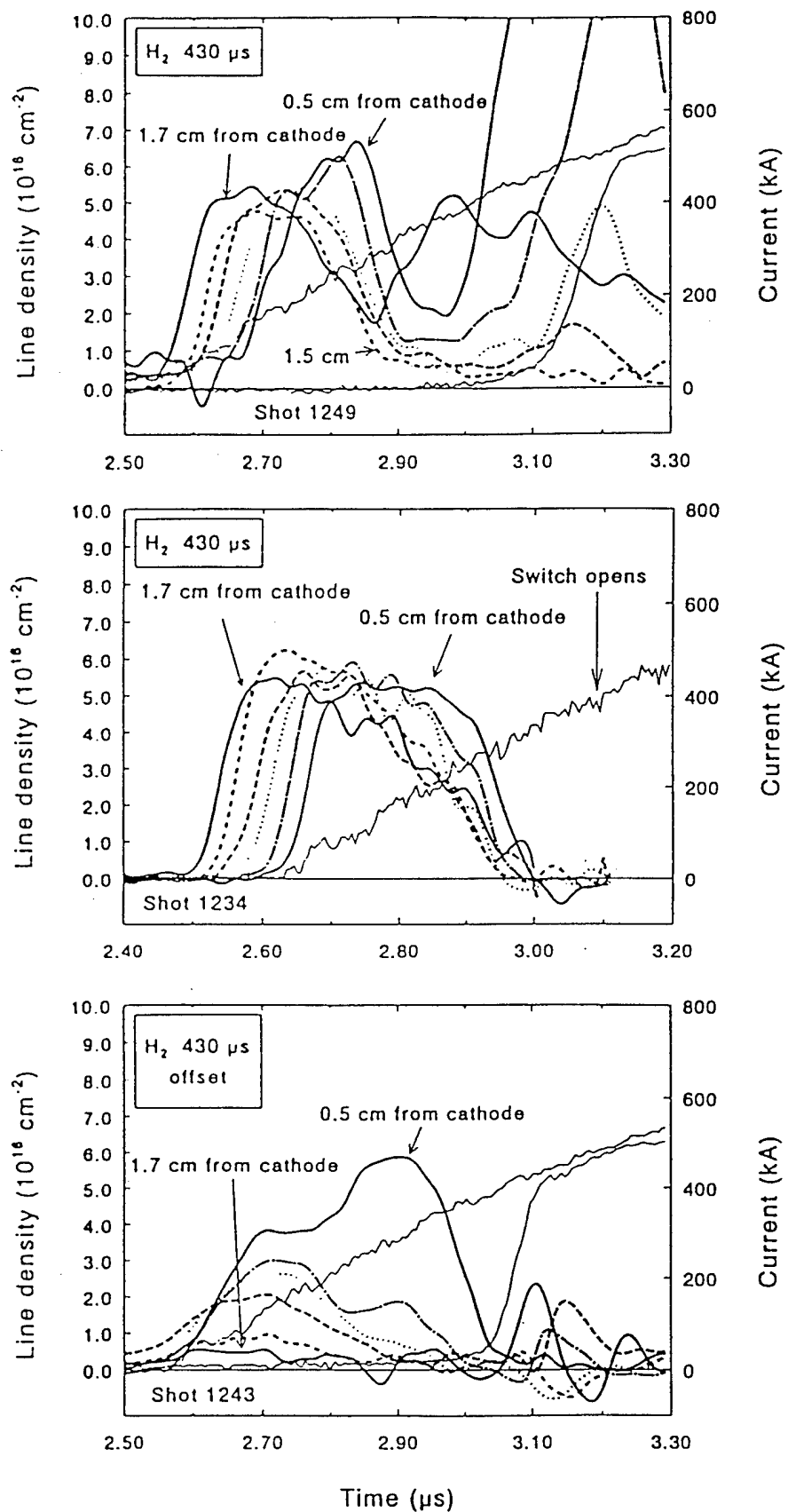


Figure 5: Density distributions from Hawk shots with somewhat later generator time delays.

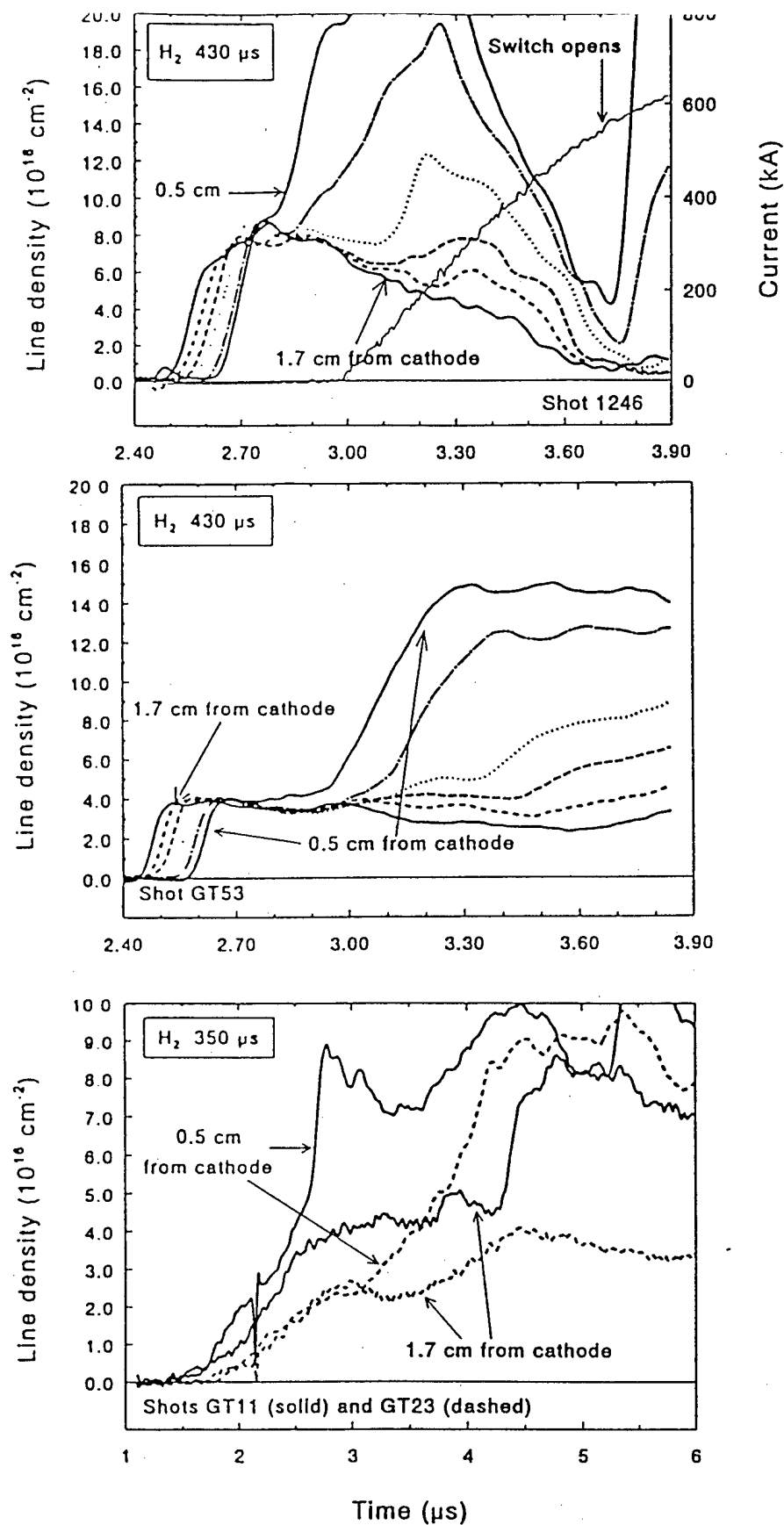


Figure 6: (top) Density distribution from a Hawk shot at a still later generator time delay; (middle) Distribution from the sources alone immediately prior to shot 1246; (bottom) Source irreproducibility.

to the anode. This would be expected based on our MHD picture because of the large radial density gradient away from the cathode.

## REPRODUCIBILITY

In general, the data here show poor reproducibility, as illustrated in the last two graphs in Fig. 6. The middle graph shows data from the source-only shot immediately preceeding shot 1246. The density profiles track well at first, but then become greatly different by the time generator current begins. With this irreproducibility it is not possible to compare directly shots with and without firing the generator, for example. The bottom graph compares data from two source-only shots taken with short discharge delays. Again, a large difference is exhibited. Such variation was not always observed, for example the data from the sequence of shots in Fig. 3 shows a smoothly-varying trend that is indicative of more reproducible behavior. Operation of these guns involves several processes which may vary shot-to-shot: action of the mechanical valve; gas breakdown and discharge intiation; interaction of the discharge with surfaces in the gun; and interaction of the injected plasma with the cathode surface. Some of the variation encountered may have resulted from incomplete purging and/or conditioning when the gas was changed or when the guns were brought up to air. The mechanical valves appear to be reliable and with further study, an operational/conditioning proceedure could likely be developed that would allow reasonably reproducible operation of these guns.

## COMPARISONS WITH OUR MHD PICTURE

As stated above, the results here are qualitatively consistent with our understanding of conduction current limitation. The switch is seen to open at the radial location of the density minimum (since the density gradients here dominate the weak magnetic field gradient): opening either at the cathode, at the anode, or in between, depending on the radial density profile.

The data are also quantitatively consistent. The diode shots Phil took with  $H_2$  and Ar comprise mainly  $H_2$  shots with 430 and 345  $\mu s$  discharge delays, and Ar shots with 520  $\mu s$  delays. For the early delay, the data here suggest that it is reasonable to assume azimuthal uniformity. In this case the measured density can be used to predict the conduction current. The diode shots at this early timing are found to have conduction currents that agree with those predicted, assuming a protonic plasma. Predictions for many of the  $H_2$  shots at 430  $\mu s$  discharge delays are also consistent. However, in this case the rapid variation in density during conduction, and the observed azimuthal asymmetry complicate the interpretation. There are a few shots, such as shot 1247 in Fig. 4, for which the density is small-to-negligible at the start of the generator pulse. That conduction is observed indicates that either plasma flow into the switch region continues during conduction, or else new plasma is formed by ionization of neutrals that may be present along with the injected plasma. The Ar shots that Phil took also show conduction currents that are consistent with predictions assuming a doubly to triply ionized Ar plasma. In all of the above, the uncertainty in the density, azimuthal distribution, and composition have a relatively small effect on the predicted conduction current because of

its weak dependence on density in the MHD regime. By the same token, however, it is difficult to use the observed conduction current to deduce the plasma composition, or the existence of neutrals, etc.

## RELEVANCE TO DIODE SHOTS

As discussed in Phil's Technote, switch performance with gas guns and diode loads was not very exciting. The data presented here indicate that at the generator delay times used in most of the diode shots taken with  $H_2$  and Ar, either little current conduction occurred (as would have been expected), or the secondary plasma would have dominated, with a density profile similar to that on flashboard shots. Only a few shots with  $H_2$  were taken under conditions corresponding to the rapidly varying density profile, and considering the lack of reproducibility it is not obvious what the exact density profiles were on these diode shots.

## CONCLUSIONS

Considering the unexciting results with diode loads, further investigation of these sources would seem to be a relatively low priority within the POS program. However, they do have the potential of enlarging the available parameter space obtainable from POS plasma sources, and thus facilitating relevant physics experiments. If work on these sources were to continue, the first step should be a careful study of conditioning effects to improve the source reproducibility. As mentioned before, the valves should probably be driven with higher voltage, lower capacitance pulsers. The switch should be operated with more guns at a large distance from the cathode. Under these conditions, experiments could be performed that would add to our understanding of POS physics.



PULSED POWER PHYSICS TECHNOTE NO. 93-07

TITLE: CABLE GUN POS EXPERIMENTS WITH DIODE LOADS ON HAWK

AUTHORS: B. Weber, M. Sucky

DATE: 18 May 1993

ABSTRACT: This technote summarizes results of POS experiments on Hawk using cable guns and diode loads. This research is intended to complement DPM1 experiments to diagnose power flow and improve our understanding of the cable gun POS for Decade applications. In this series of about 100 shots, several parameters were varied, including the center conductor radius, the anode structure ("anode pocket"), plasma length, and load impedance. There is limited evidence that removing the anode pocket results in increased voltage. The conduction time is a (weak) function of the plasma length. The voltage is increased using a smaller radius center conductor, and is relatively independent of the length, similar to previous Hawk results using flashboard and gas gun plasma sources. The possibility of small conduction time jitter ( $920 \pm 12$  ns) is demonstrated for a sequence of seven shots, although over the entire run, greater jitter is typical (for example,  $719 \pm 79$  ns). A simple implementation of the PI PIN diode array proves to be a good backup for the electrical voltage measurement. The current measured near the load side of the POS rises before the load current. This delay is a consistent feature of this shot sequence, and is relatively independent of the experimental parameters. Current loss is indicated by current monitors near the load and by side-on x-ray photos. Improved current measurements, including cathode monitors, should allow meaningful comparisons with power flow calculations.

THIS REPORT REPRESENTS  
UNPUBLISHED INTERNAL  
WORKING DOCUMENTS AND  
SHOULD NOT BE REFERENCED  
OR DISTRIBUTED

## Experimental Setup

The experimental variations on Hawk are illustrated in Fig. 1. The 12 cable guns are located 14 cm from the axis. Center conductor diameters of 4 inches and 1 inch were used. The plasma injection aperture was varied, using the traditional "anode pocket" (PI jargon) illustrated in the top half of Fig. 1, or using a continuous extension of the outer conductor illustrated in the bottom half of Fig. 1. The plasma aperture was 8 cm long, or was masked to a length of 2.5 cm. Six B-dot current monitors located between the POS and the load measure the up/down symmetry and the location of current losses.

X-ray signals are recorded using two PIN diodes, filtered by 2 mm thick lead and 10 mm thick lead. The ratio of the PIN signals is used to infer the endpoint voltage. Pinhole cameras record end-on and side-on views of the x-rays for comparison with measured current losses.

About 100 shots were taken, 70% with diode loads and 30% with short circuits. Several observations can be made from this data set including the effect of the anode pocket, POS length dependence, conduction time jitter, radius scaling and current losses.

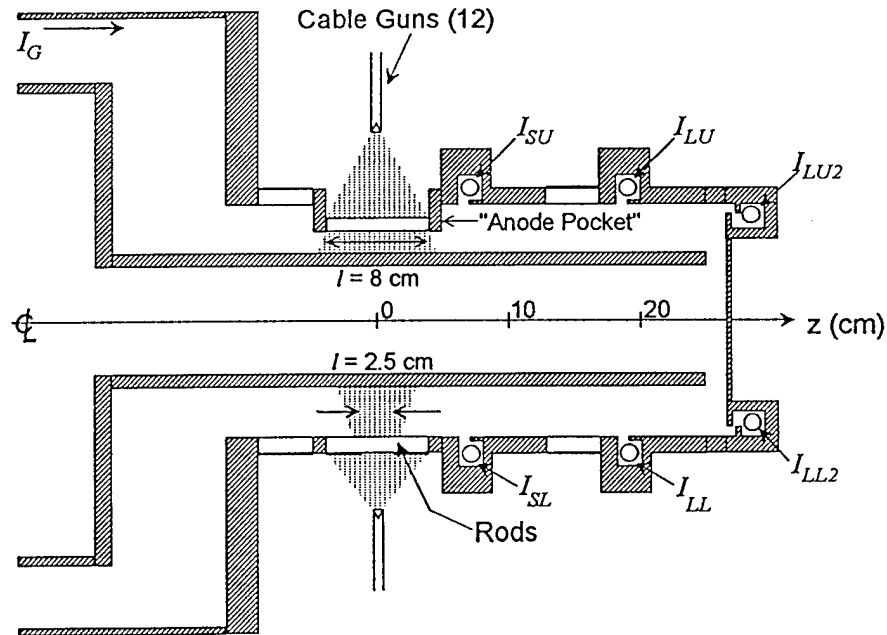


Figure 1. Hawk cable gun POS experimental setup

### Effect of "anode pocket"

Experiments on DPM1 at PI have indicated a strong dependence of voltage on the POS anode structure. The shots taken on Hawk are a small sample that show similar, but weaker trends. Figure 2 shows the insulator voltage (VDC) as a function of conduction time for shots with and without the anode pocket, with all other parameters the same ( $r = 5$  cm,  $l = 8$  cm).

Apparently, the voltage increases from a maximum of about 500 kV when the anode pocket is present, to about 800 kV when it is removed. The difference in AK gaps and the spread in the data limit this conclusion, but the effect may be an interesting one to pursue with more convincing experiments.

The anode pocket had no apparent effect on the voltage when the smaller radius (1.27 cm) center conductor was used, probably because the anode pocket was far from the center conductor surface. (Again, the set of comparable data was small and somewhat inconclusive.)

The rest of the data reported below will be for the case without the anode pocket.

### Conduction dependence on length

Two plasma injection aperture lengths were used,  $l = 2.5$  and 8 cm. The conduction times are compared for the two lengths in Fig. 3 for  $r = 5$  cm. The horizontal axis is the knob setting that determines the time delay between the gun current and Hawk. (The actual time delay is about  $0.3 \mu\text{s}$  greater than the knob setting.) The error bars are standard deviations for cases with enough data points. Assuming the density is the same for a given delay, the scaling of conduction time (or current) with "length" is  $l^{0.2-0.5}$ . The expected scaling for MHD-limited conduction is  $l^{1/2}$ . The actual length change was not determined (for example, by interferometry), so the precise scaling is somewhat uncertain. It is clear, however, that the conduction time depends on length to a small power ( $<1$ ).

The error bars in Fig. 3 represent the jitter obtained over this 100-shot sequence. For example, 24 shots were taken for the  $l = 2.5$  cm case with a delay setting of  $3 \mu\text{s}$ . The resulting conduction time is  $719 \pm 79$  ns, a rather large jitter compared with results from DPM1. For a more controlled set of seven consecutive shots with short circuit loads (used for a radial scan of the density, see TN 93-06), the conduction time was  $920 \pm 12$  ns, demonstrating the possibility of small jitter with microsecond conduction time. To assess the jitter,

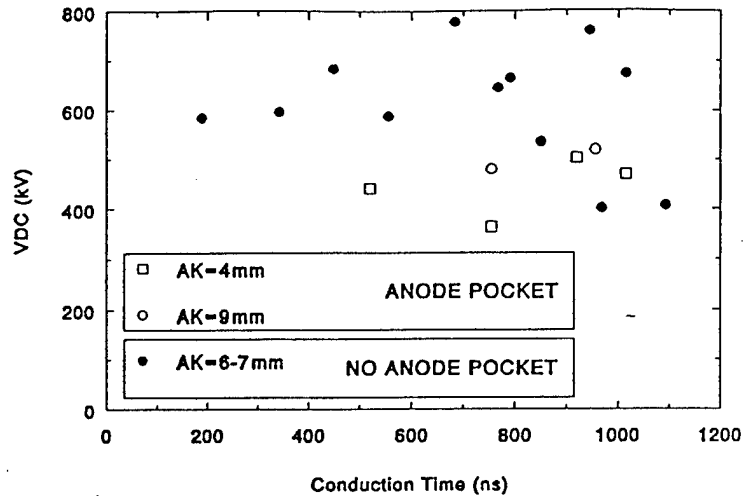


Figure 2. Evidence that the anode pocket affects the voltage.

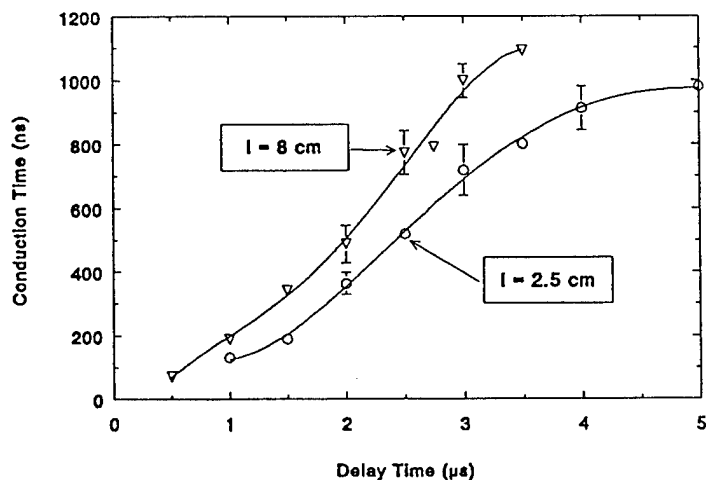


Figure 3. Conduction time dependence on length ( $r = 5$  cm)

its causes and limitations, requires a more thorough set of experiments than these.

### Comparison of different configurations

Figure 4 is a scatter plot of voltage (VDC) versus conduction time for all diode shots without the anode pocket. The parameters varied are:  $r$  (1.3 or 5 cm),  $l$  (2.5 or 8 cm) and the diode AK gap (4-10 mm). The voltage is higher (up to 1.3 MV) using the 1" diam center conductor compared with the 4" diam center conductor (up to 800 kV). The voltage increases weakly with AK gap (6 mm results in higher voltage than 4 mm) and is relatively independent of length. These conclusions are in general agreement with previous Hawk POS results using flashboards and gas plasma sources.

The voltage plotted in Fig. 4 is measured at the insulator, VDC. The inferred endpoint voltage from the PIN diode ratio is compared with VDC in Fig. 5 for all shots where data are available. Most of the data points (73%) lie within the  $\pm 10\%$  lines, indicating pretty good agreement. The data points are skewed a little toward  $V_{PIN} > VDC$ , possibly an indication that the diode voltage is a little higher than VDC because of inductive effects.

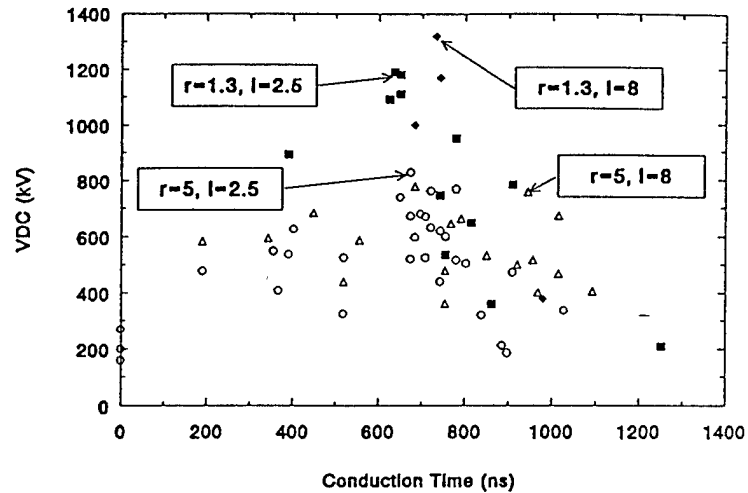


Figure 4. Voltages for different configurations

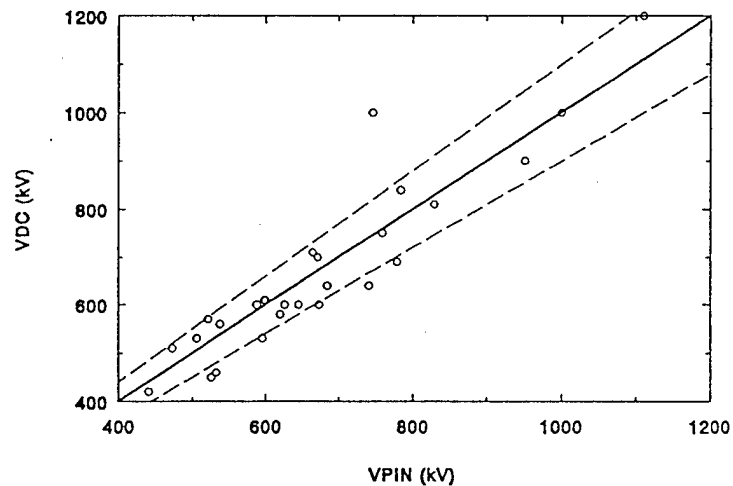


Figure 5. Insulator voltage and voltage inferred from ratio of PIN diode signals

### Current loss and x-rays

Figure 6 shows data from shot 1314, where  $r = 5$  cm,  $l = 8$  cm, and the AK gap = 6 mm. This is an example of a high voltage shot for these parameters. The conduction current is 650 kA and the conduction time is 940 ns. The upper and lower B-dots are averaged to obtain the currents  $I_S$  (near switch),  $I_L$  (between switch and load), and  $I_{L2}$  (at load). The current increases at the  $I_S$  location first, then rises almost simultaneously at the  $I_L$  and  $I_{L2}$  locations. This is generally true for all the shots in this series; there is a significant time delay between the current measured at the  $I_S$  and  $I_L$  locations, and no noticeable delay between the  $I_L$  and  $I_{L2}$  locations. The  $I_S$ - $I_L$  delay is usually  $60 \pm 30$  ns, independent of  $l$ ,  $r$ , or AK gap, with a slight trend of increasing delay with conduction time. This indicates that the current is connecting to the anode

in the vicinity of  $IS$  before opening occurs. The amplitude of  $IS$  is less than  $IL$ , probably because the slot is partially shorted by plasma, indicating a smaller current than actually exists. The current at the load,  $IL2$ , is significantly smaller (by 200 kA) than at the intermediate location,  $IL$ , indicating current loss to the walls (or shielding of the current monitors). X-ray photos show emission from the walls in the vicinity of the load, consistent with the current measurements. The difference (100 kA) between  $IL$  and the generator current,  $IG$ , may represent losses in the POS (or shielding of the current monitor). These measurements are a starting point for diagnosing power flow in Hawk, and comparing with the numerical calculations of Steve Swanekamp. (Similar measurements were made previously for the flashboard POS.)

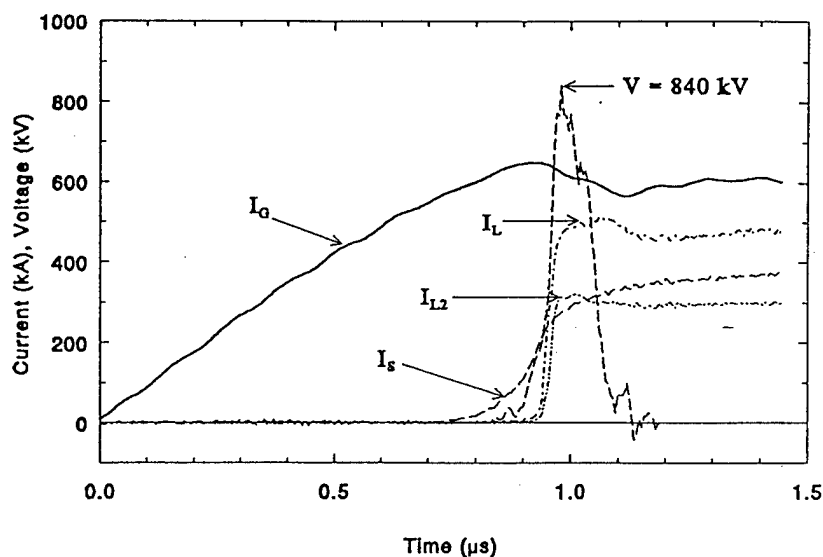


Figure 6. Current and switch voltage waveforms for a "high voltage"  $r = 5$  cm shot

### Future plans

To improve the understanding of power flow, surface B-dots will be installed inside the center conductor to measure the electron flow current (by subtracting the anode and cathode currents). These diagnostics will be used with short circuit, e-beam diode, and plasma-filled diode loads to determine the effect of the load impedance (and its time history) on the power flow. John Grossmann has found in simulations that the flow can be influenced by the impedance time history. We may be able to obtain data relevant to John's analysis and to address general power flow issues for Decade.

PULSED POWER PHYSICS TECHNOTE NO. 95-09

TITLE: PARALLEL-PLATE POS PERFORMANCE ON HAWK

AUTHORS: R.A. Riley, B.V. Weber, R.J. Comisso, D.D. Hinshelwood, and J.M. Grossmann

DATE: April 3, 1995

ABSTRACT:

Results of parallel-plate plasma opening switch (POS) experiments on HAWK are presented and compared to similar coaxial POS experiments. The parallel plate geometry provides much better diagnostic access of the switch plasma than the standard coaxial POS, but does not open as well as a coaxial POS.

The poorer opening of the parallel-plate POS was assumed, based on 3-D magneto-static calculations, to be due to high current densities on the edge of the plates, leading to strong fringing fields and, possibly, pinching in the  $\theta$ -like direction. In order to reduce these effects, we use a tri-plate, rather than a bi-plate, geometry and have cut a current-constricting "notch" in the cathode just upstream of the switch plasma. These modifications have had little effect on performance.

Time integrated images of the tri-plate switch plasma's visible emissions show bright electrode plasmas just down-stream of the switch region that are produced late in time. Time-resolved images of the downstream edge of the injected plasma region show a current snowplow advancing toward the load side of the injected plasma and the gap opening near the cathode electrode.

Initial interferometry data integrated along the  $\theta$ -like direction, near the middle of the A-K gap of the switch region, show that the snowplow removes all plasma until  $\sim 2\mu\text{s}$  after opening and that no plasma is measured near the load until  $\sim 1\mu\text{s}$  after opening.

In future experiments, multi-chord interferometry will be used to study how the plasma within the switch and between the switch and load are related to the switch's conduction and opening characteristics.

THIS REPORT REPRESENTS UNPUBLISHED INTERNAL WORKING  
DOCUMENTS AND SHOULD NOT BE REFERENCED OR DISTRIBUTED

Plasma opening switches (POS) allow pulsed-power systems to store energy in the magnetic field of an inductor while the switch is closed, then when the switch opens this energy is directed to a load. How these switches open is an active area of research. Coaxial plasma opening switches, such as shown in Figure 1(a), perform well for peak currents of  $\sim 1\text{MA}$ , conduction times  $\tau \leq 1\mu\text{s}$ , and load impedance  $\sim 1\Omega$ . This performance may be dependent on the  $1/r$  gradient in the magnetic field resulting from its cylindrical geometry.

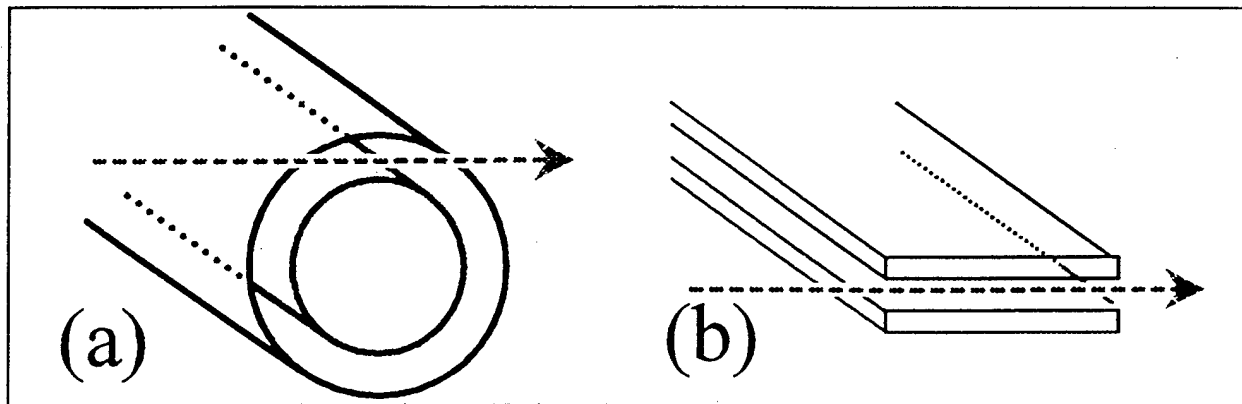


Figure 1. POS geometries: (a) coaxial and (b) parallel-plate.

As shown in Figure 1(b), a parallel-plate POS offers obvious advantages for diagnostic access. However, parallel-plate geometry requires a break in the  $\theta$ -like direction, leading to edge effects and has very little gradient in magnetic field except near the edges.

Chordal interferometry of a coaxial switch measures the plasma density integrated over a line-of-sight that spans a continuum of radii, but can be Abel inverted to find the plasma density as a function of radius and axial position. However, as shown in Figure 2, it is very difficult to construct a coaxial POS with the degree of  $\theta$ -symmetry needed to resolve a small ( $\delta r \sim 1\text{mm}$ ) gap in a high density ( $n \sim 10^{15}\text{ cm}^{-3}$ ) plasma.

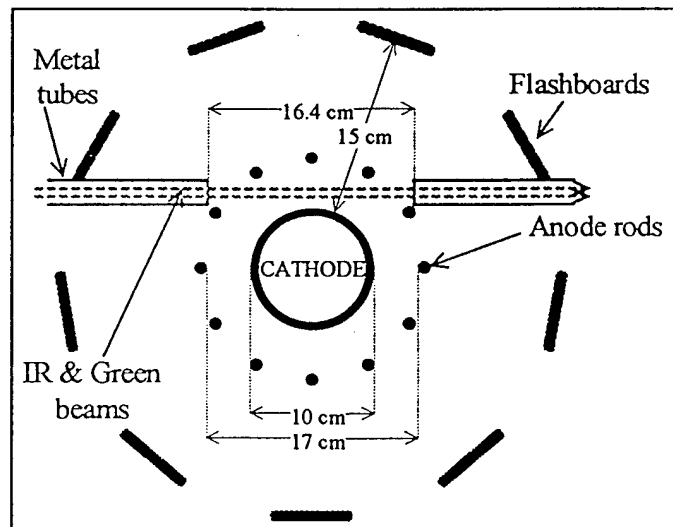


Figure 2. Not so  $\theta$ -symmetric coaxial POS.

We are attempting to construct a parallel-plate POS that will work as a coaxial POS with the hope that what is learned from observing this switch can be generalized to the coaxial case. The tri-plate geometry used in our experiments is given in Figure 3. Unfortunately, this switch does not operate as well as an equivalent coaxial POS.

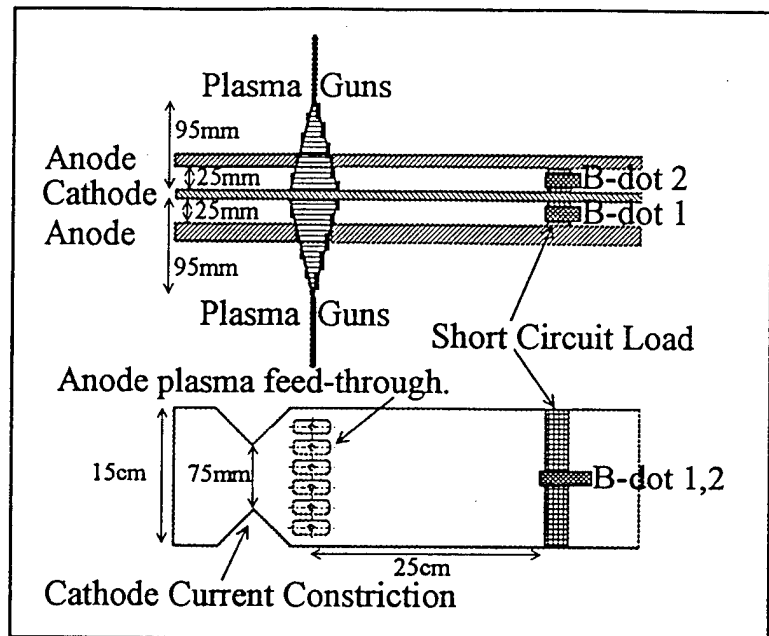


Figure 3. Tri-plate POS geometry.

The short-circuit load currents of the tri-plate switch are compared to the load currents for a similar coaxial switch, with the associated generator currents in Figure 4. Both experiments use twelve guns and have similar magnetic field strengths. The coaxial POS conducts for 1  $\mu$ s then opens in  $\sim 50$  ns and the load carries the entire generator current. The tri-plate load currents switch in  $\sim 100$  ns, for conduction times up to

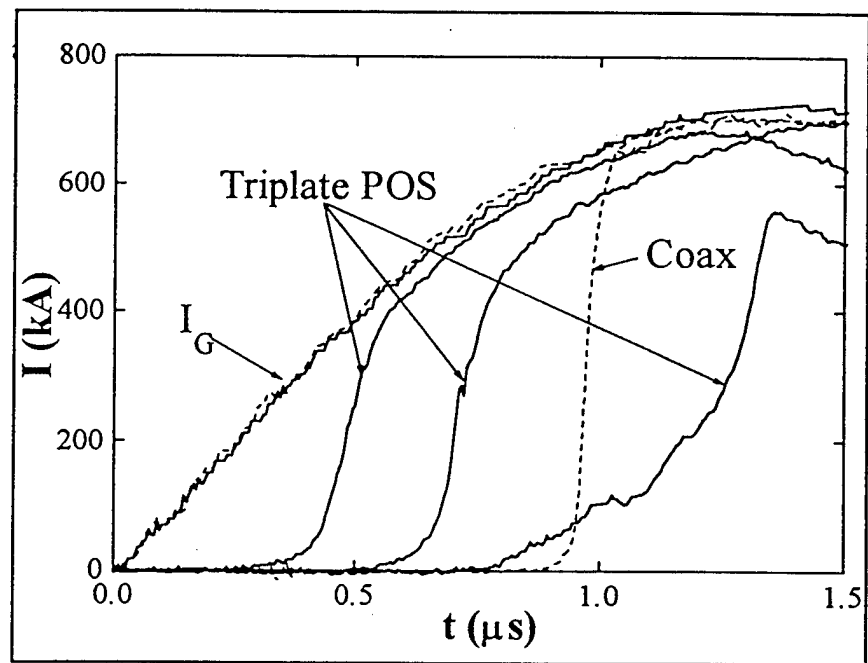
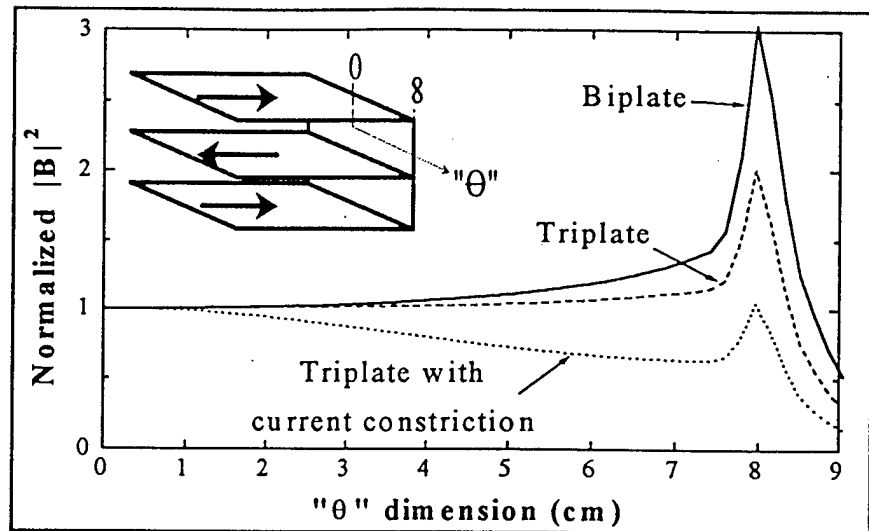


Figure 4. Comparison of tri-plate and coaxial short-circuit load shots.

for conduction times up to  $\sim 650$  ns. For longer conduction times, the tri-plate POS opens very slowly if at all.



The code QUICK-SILVER was used to calculate the magneto-static field for the bi-plate and tri-plate geometries. The square of the magnetic field at the surface of the plasma, half way between the anode and cathode are plotted in Figure 5. The curves are normalized to the value at the center of the electrode.



**Figure 5.** Normalized magnetic pressure at the surface of the switch plasma in the center of the A-K gap.

The fields are strongly peaked on the edge of the electrodes/plasma at 8 cm. These calculations were also performed with a current constricting notch in the cathode to try to reduce the strength of the peak of the field at the edge of the switch.

We have made a direct comparison of the bi-plate and tri-plate POSs by removing the bottom anode from the tri-plate and running the experiment at half the charge voltage and so half the generator current. For this physics comparison, the bi-plate and tri-plate POS perform equivalently, as shown in Figure 6.

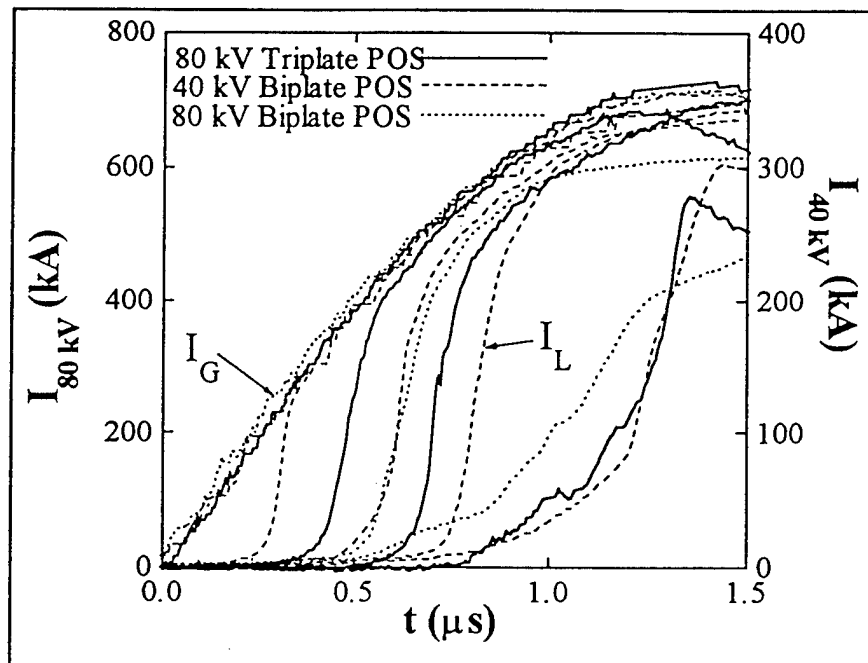


**Figure 6.** Comparison of tri-plate and bi-plate short circuit load currents.

The fact that there

does not seem to be any improvement in switch performance in going from bi-plate to tri-plate or notched tri-plate suggests that fringing effects are not the dominant reason that the parallel-plate switch does not perform as well as the coaxial switch. Perhaps the  $1/r$  gradient in the magnetic field is a more important difference.

Figure 7 displays time integrated images of the emission of the plasma in the tri-plate switch for shot 1778 with a conduction time of  $\sim 400$  ns. When the plasma reaches a given axial position cannot be determined from these images. Most of the light is probably emitted during a restrike of the plasma shortly after opening. Time resolved images of the opening of the tri-plate switch are given in Figures 8, 9, and 10. Figure 8 shows the switch opening near the cathode at  $\sim 550$  ns into the generator current. Figure 9 shows the plasma remaining straight in the  $r$ -like direction even when the snowplow reaches the back surface of the injected plasma and starts to open (poorly) at 700 ns. Figure 10 shows opening on the top and then the bottom at a faster framing speed.

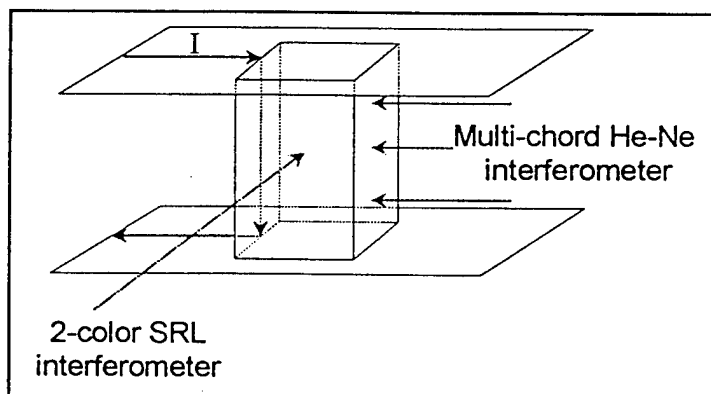
Figure 11 compares chordal interferometry between the coaxial and tri-plate POSs near the center of the injected plasma region. The inferred density of the coaxial POS never returns to zero after the snowplow passes because it also samples the dense shell of plasma near the anode.

Figure 12 shows the snowplow moving through the center of the A-K gap of the tri-plate POS. The densities peak just before the switch opens. The densities at the center of the injection region and at 1 and 2 cm toward the load are given.

Figure 13 shows that little if any plasma arrives near the load until  $\sim 1 \mu$ s after opening.

We conclude that the parallel-plate POS has better diagnostic access but does not switch as well as a coaxial POS. This lack of performance may not be due to fringing effects as we first suspected, but may be due to the lack of  $1/r$  gradient in the magnetic field found in coaxial geometries.

Future plans include fast framing of the switch plasma looking through the load to see if the plasma pinches in the  $\theta$ -like direction during conduction or opening and a multi-chord HeNe



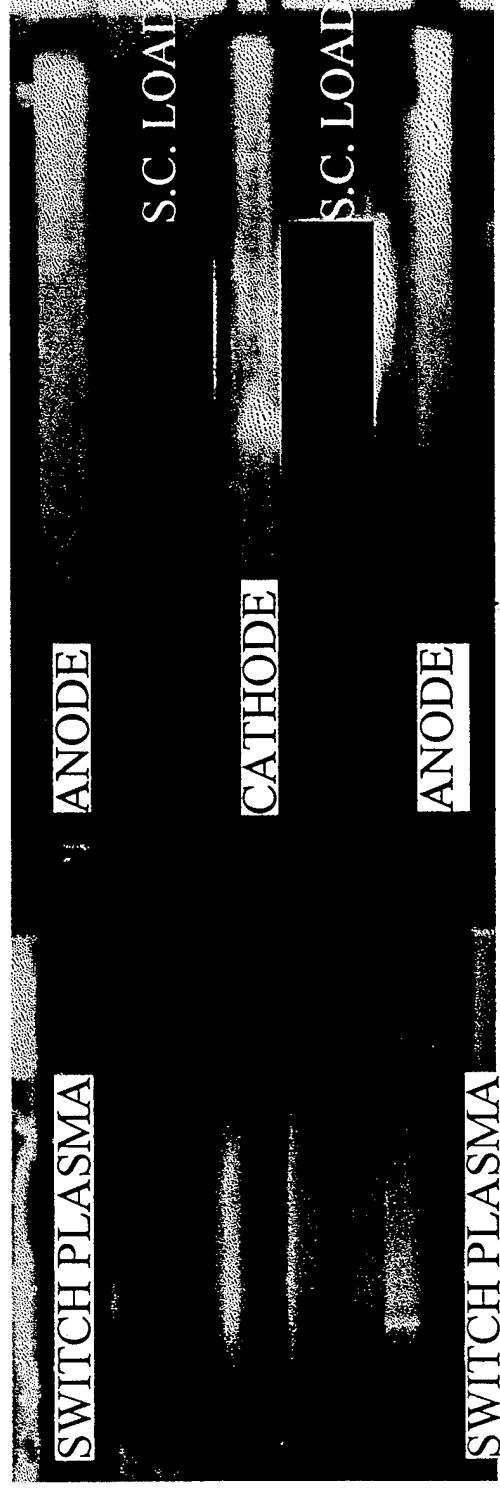
interferometer to measure the density integrated in the  $\theta$ -like direction and along the axis of the switch. The SRL interferometer will be used to make more sensitive measurements of how much plasma arrives near the load in the first few micro-seconds after the switch opens. We also plan to install more B-dot probes. Spectroscopy is also a possibility.

As more data is acquired it will be compared to PIC and fluid simulations.

# Time-integrated images show bright, late-time electrode plasmas

**NRL**

- SHOT 1778, Conduction time  $\sim 400$  ns.



SHOT  
1778

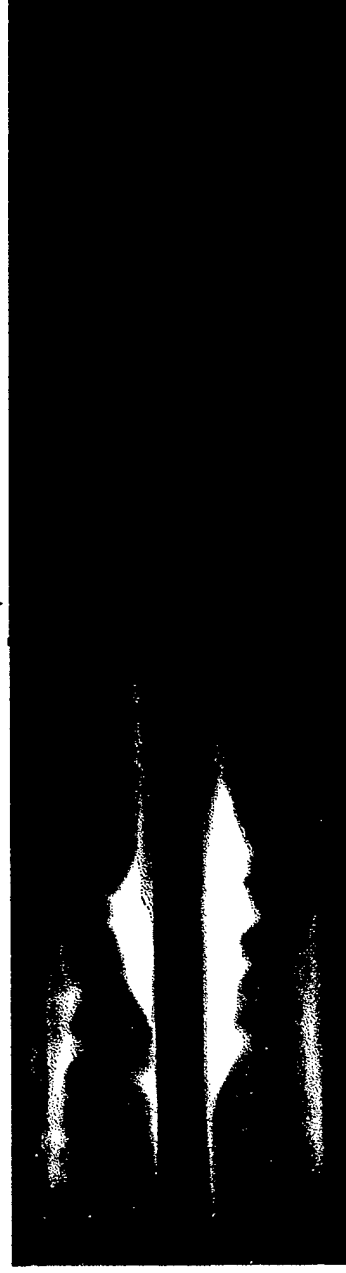
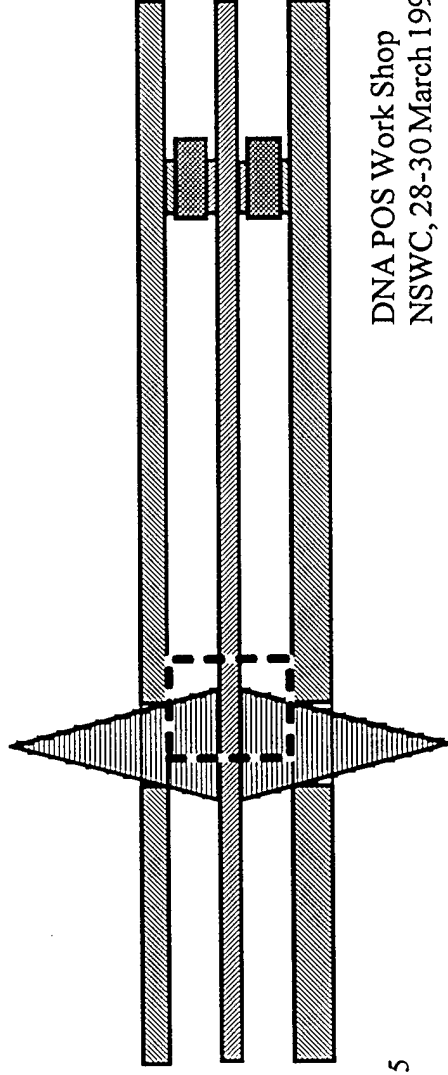
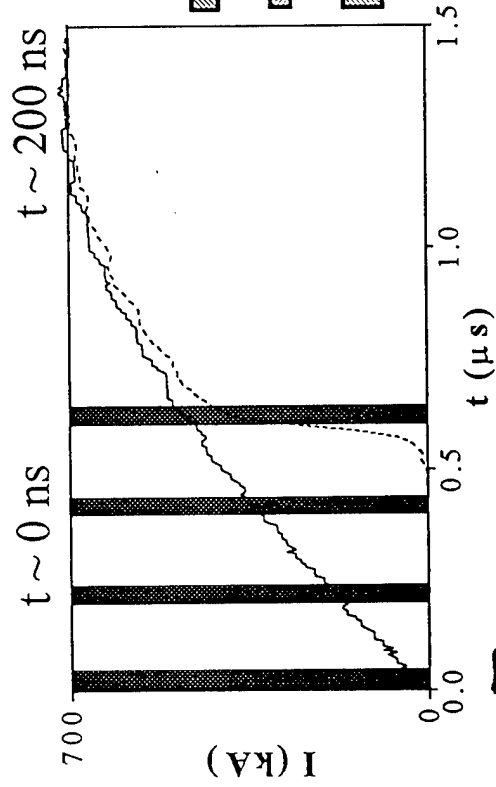
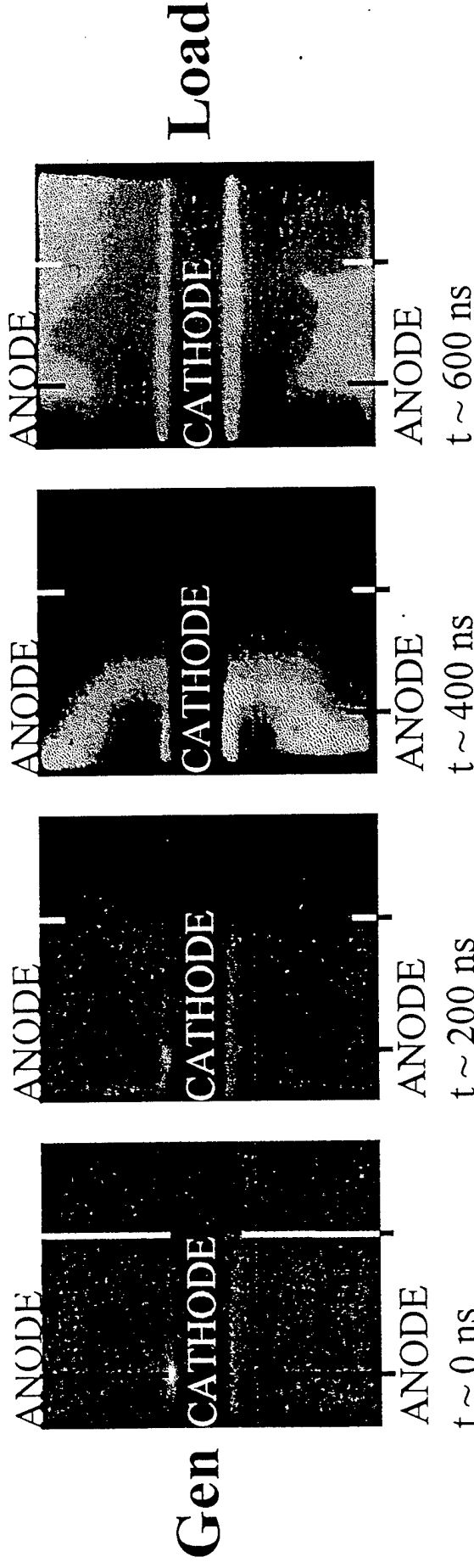


**Figure 7.**

# Time-resolved images of tri-plate showing opening near cathode

NRL

- Shot 1842, 40ns exposures, opening begins at  $t \sim 550$  ns



DNA POS Work Shop  
NSWC, 28-30 March 1995

Figure 8.

# VRL

- Figure 1 displays four fluorescence images of a microfluidic device, showing the movement of a fluorescent species (likely a dye or ion) over time. The images are arranged in a 2x2 grid, with the top row labeled 'Gen' and the bottom row labeled 'Load'. The left column shows the 'ANODE' and the right column shows the 'CATHODE'. The time points for each image are indicated on the right side of the grid:

  - Top-left (Gen, ANODE):  $t \sim 100$  ns
  - Top-right (Gen, CATHODE):  $t \sim 300$  ns
  - Bottom-left (Load, ANODE):  $t \sim 500$  ns
  - Bottom-right (Load, CATHODE):  $t \sim 700$  ns

The images show a bright, elongated region of fluorescence that moves from the anode towards the cathode as time progresses, indicating the transport of the fluorescent species under the applied load.

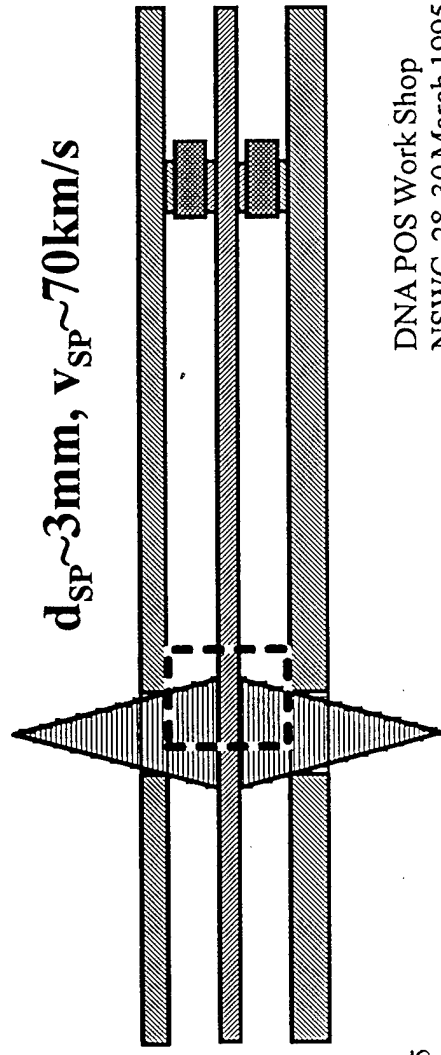
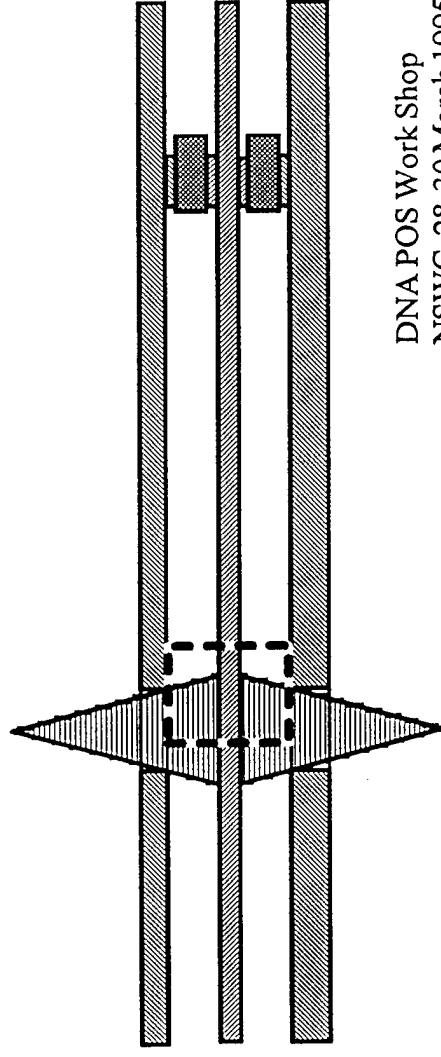
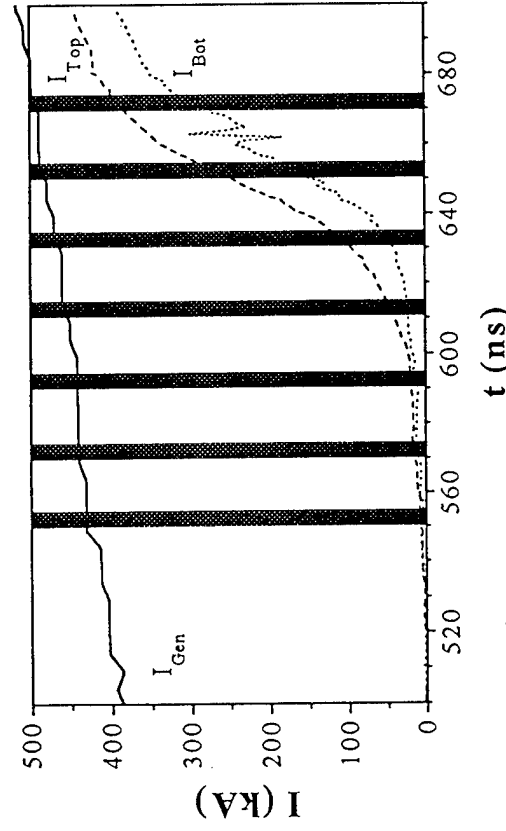
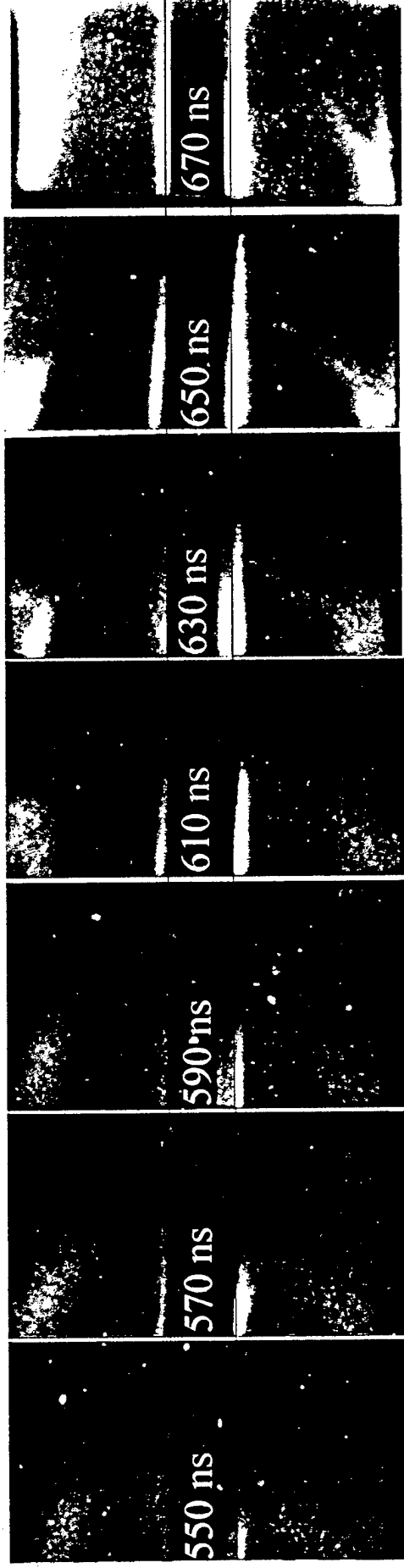


Figure 9.

# Time-resolved images of tri-plate showing opening on top, then bottom

NRL

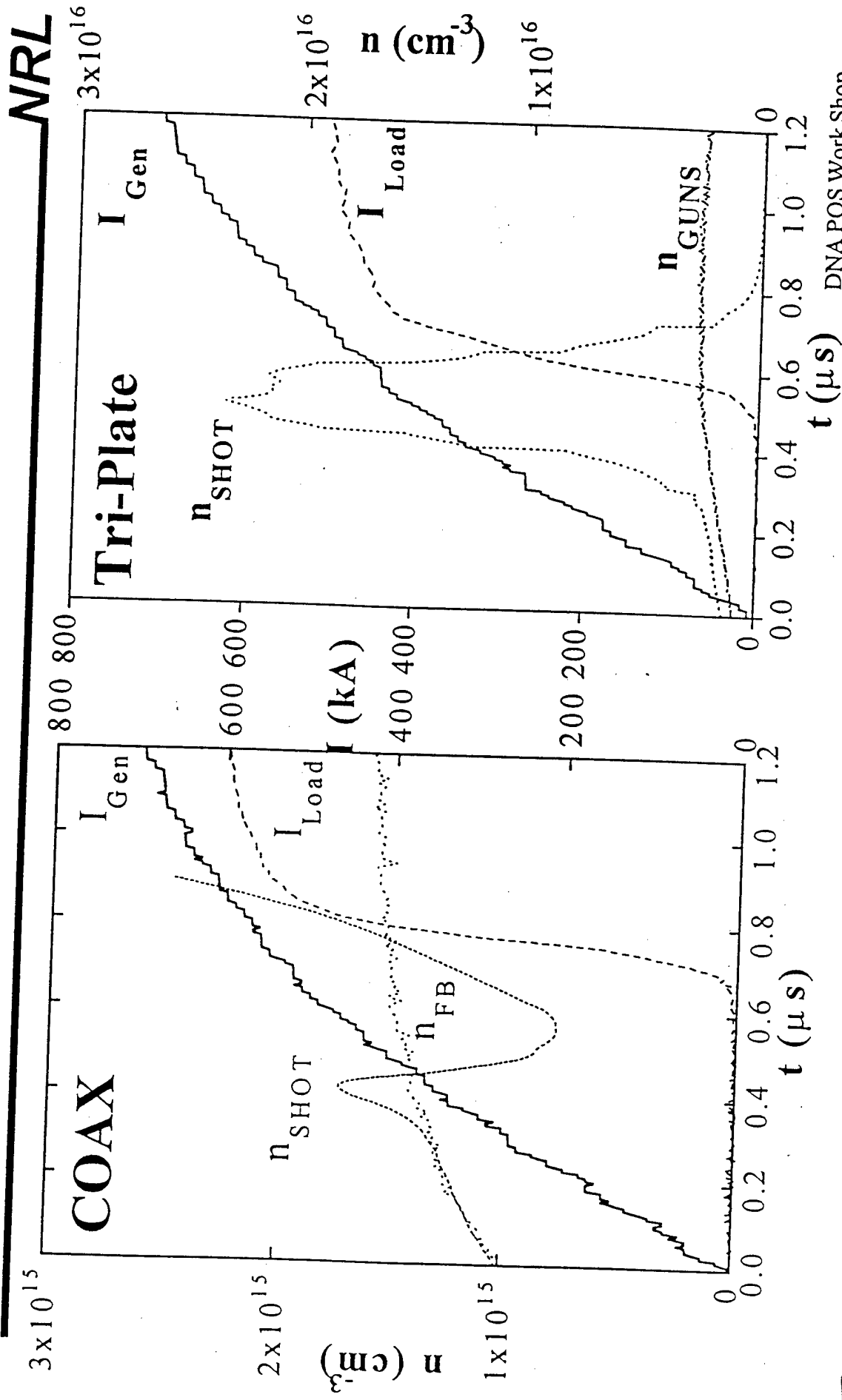
- Shot 1844, 4ns exposures, opening begins at  $t \sim 600$  ns



DNA POS Work Shop  
NSWC, 28-30 March 1995

Figure 10.

# Chordal interferometry on coax POS does not show zero density in switch



DNA POS Work Shop  
NSWC, 28-30 March 1995

**Figure 10.**



# “Theta” line-of-sight interferometry shows snow-plow motion in switch

NRL

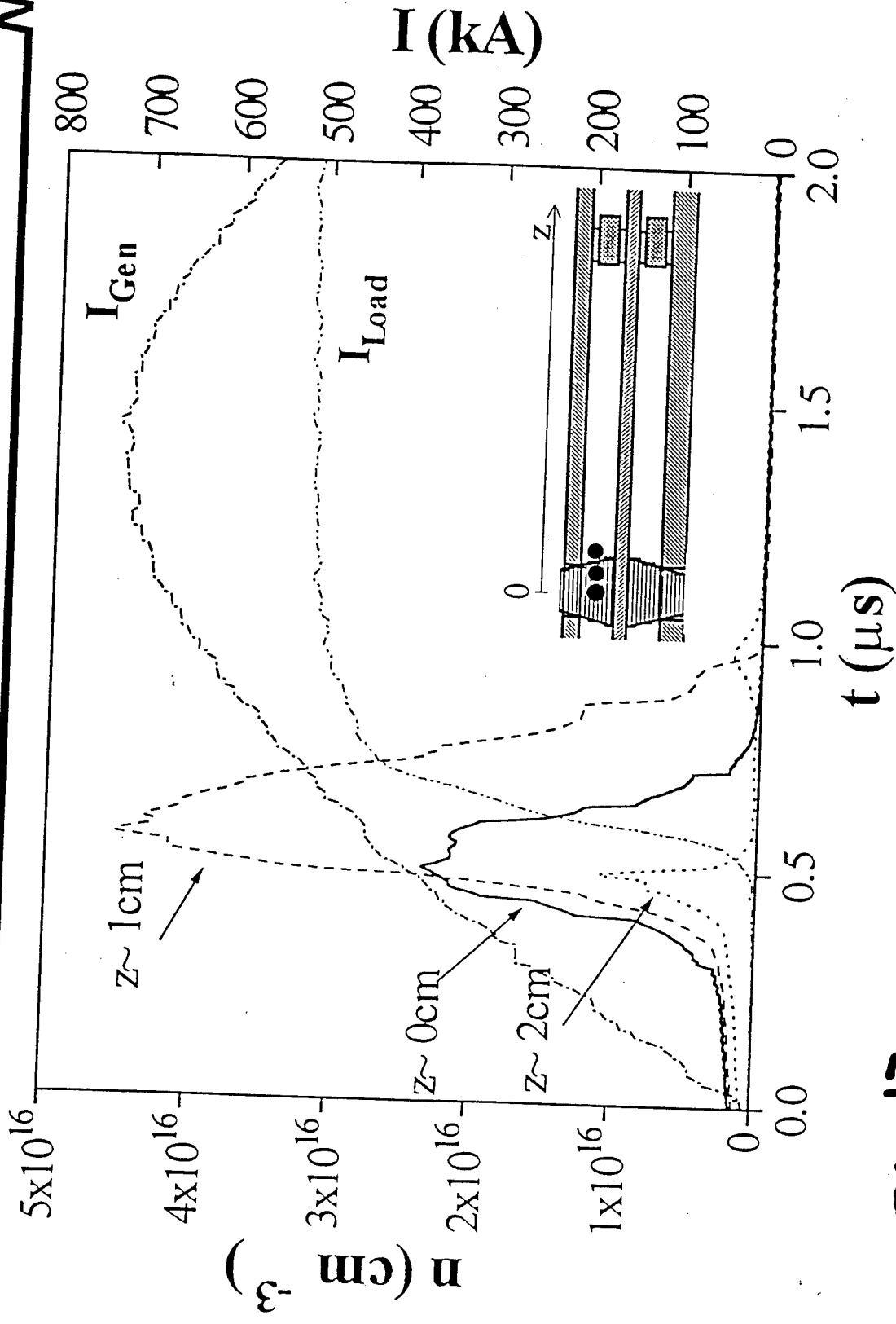


Figure 12.

# Plasma arrives downstream after opening

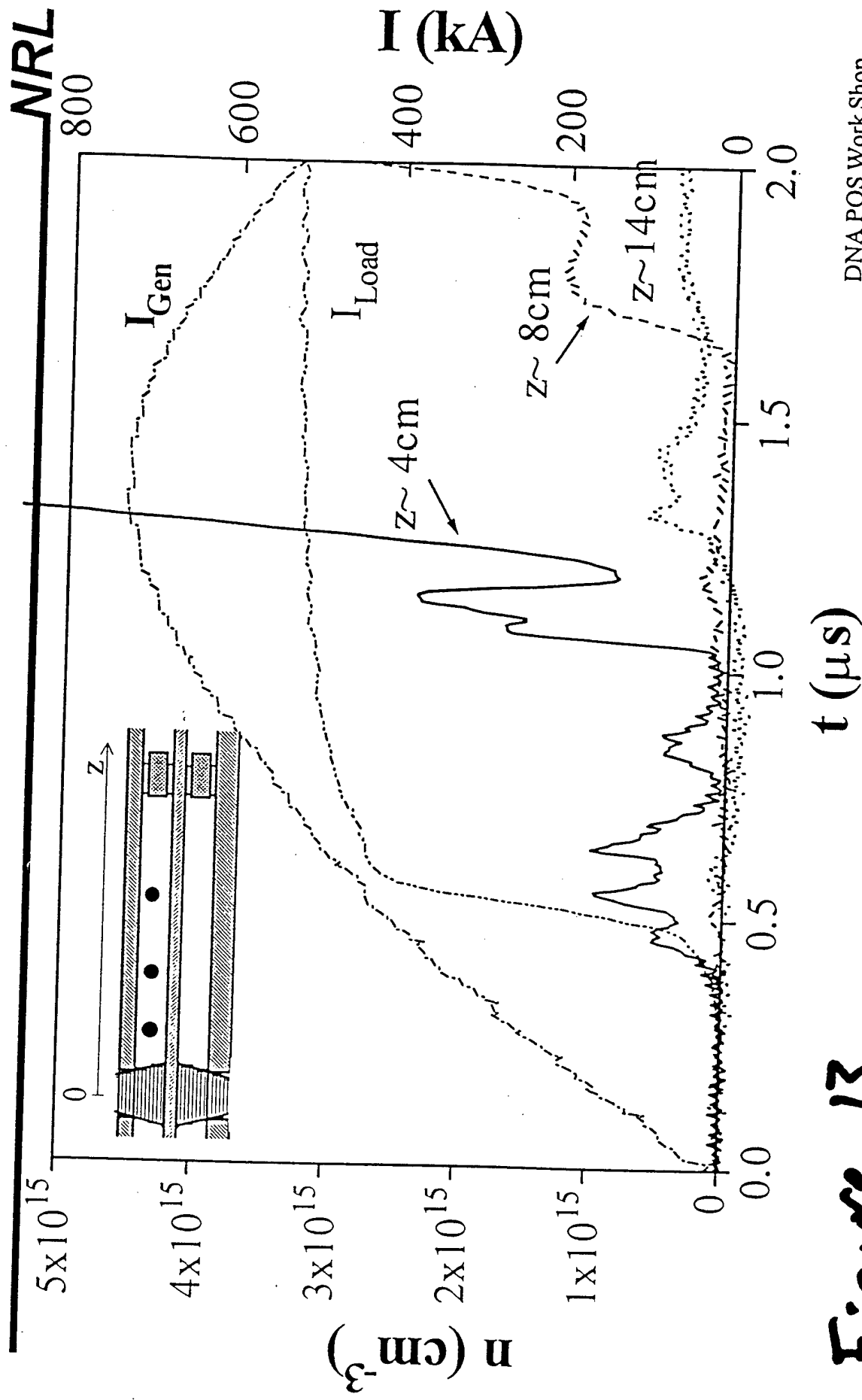


Figure 13.

TITLE: PARALLEL-PLATE PLASMA OPENING SWITCH EXPERIMENTS ON HAWK

AUTHORS: R.A. Riley, B.V. Weber, P.J. Goodrich, D.D. Hinshelwood, R.J. Comisso, J.M. Grossmann, and S.B. Swanekamp

DATE: December 5, 1994

ABSTRACT:

Results of parallel-plate plasma opening switch (POS) experiments on HAWK are presented and compared to similar coaxial POS experiments. The Hawk generator produces a sinusoidal output current of amplitude  $\sim 750$  kA and quarter period  $\sim 1.2$   $\mu$ s. The parallel plate geometry provides much better diagnostic access of the switch plasma than the standard coaxial POS. Power flow diagnostics include a number of B-dot current probes and a wire volt meter to record the POS voltage.

The switch plasma has been experimentally observed to pinch in the  $\theta$ -like direction. This is explained, based on 3-D magneto-static calculations, to be due to high current densities on the edge of the plates, leading to strong fringing fields.

In future experiments, interferometry will be used to study how the plasma within the switch and between the switch and load are related to the switch's conduction and opening characteristics.

## I. Introduction

Plasma opening switches (POS) allow pulsed-power systems to store energy in the magnetic field of an inductor while the switch is closed, then when the switch opens this energy is directed to a load. Coaxial plasma opening switches, such as shown in Figure 1, perform well for peak currents of  $\sim 1\text{MA}$ , conduction times  $\tau \leq 1\mu\text{s}$ , and load impedance  $\sim 1\Omega$ . How these switches open is an active area of research. Interferometry performed on a  $\theta$ -symmetric geometry can be Abel inverted to find the plasma density as a function of radius and axial position. However, it is very difficult to construct a coaxial POS with the degree of  $\theta$ -symmetry needed to resolve a small ( $\delta r \sim 1\text{mm}$ ) gap in a high density ( $n \sim 10^{15}\text{ cm}^{-3}$ ) plasma.

As shown in Figure 2, a parallel-plate POS offers obvious advantages for diagnostic access. It is hoped that such a POS could be made to work as a coaxial POS and that what is learned from observing this switch can be generalized to the coaxial case. Unfortunately, these switches do not operate as well as the coaxial POSs, probably due to fringing effects and pinching.

The short-circuit load currents measured for the coaxial switch illustrated in Figure 3 are compared to the load currents for similar bi-plate (Figure 5) and tri-plate (Figure 9) switches. The load current for the coaxial POS is shown in Figure 4 with the associated generator current. The coaxial POS conducts for  $1.0\mu\text{s}$  then opens in  $\sim 50\text{ ns}$  and the load carries the entire generator current. The load currents for the bi-plate, shown in the lower halves of Figures 6, 7, and 8, switch more slowly ( $\sim 100\text{ ns}$ ) and do not reach full generator current even at much shorter conduction times. The tri-plate load currents in Figure 12 also switch in  $\sim 100\text{ ns}$ , but the switch continues to operate for longer conduction times than the bi-plate. Figure 13 compares the bi-plate and tri-plate for a conduction time of  $\sim 650\text{ ns}$ .

We have recently made a more direct comparison of the bi-plate and tri-plate POSs by removing the bottom anode from the tri-plate and running the experiment at half the charge voltage and so half the generator current. For this physics comparison, the bi-plate and tri-plate POS perform equivalently.

Figures 10 and 11 are time integrated images of the emission of the plasma in the tri-plate switch for shots 1774, 1775, 1777, and 1778 whose load currents are given in Figure 12. When the plasma reaches a given axial position cannot be determined from these images. Much of the light

could be emitted during a restrike of the plasma. We plan to implement time resolved imaging very soon to remove this ambiguity.

The code QUICK-SILVER was used to calculate the magneto-static field for the bi-plate and tri-plate geometries shown in Figure 14. The square of the magnetic field at the surface of the plasma, half way between the anode and cathode are plotted in Figure 15. The curves are normalized to the value at the center of the electrode. The fields are strongly peaked on the edge of the electrodes/plasma at 8 cm. These calculations were also performed with a current constricting notch in the cathode to try to reduce the strength of the peak of the field at the edge of the switch.

Future plans include putting a current constricting notch into the cathode of the tri-plate, installing a time resolve imaging diagnostic of the switch plasma, using the SRL interferometer shown in Figure 16 and a multi-chord HeNe interferometer along the axis of the switch.

We conclude that the parallel-plate POS has better diagnostic access but suffer from strong fringing effects and pinching.

# Interferometer line-of-sight in POS region

---

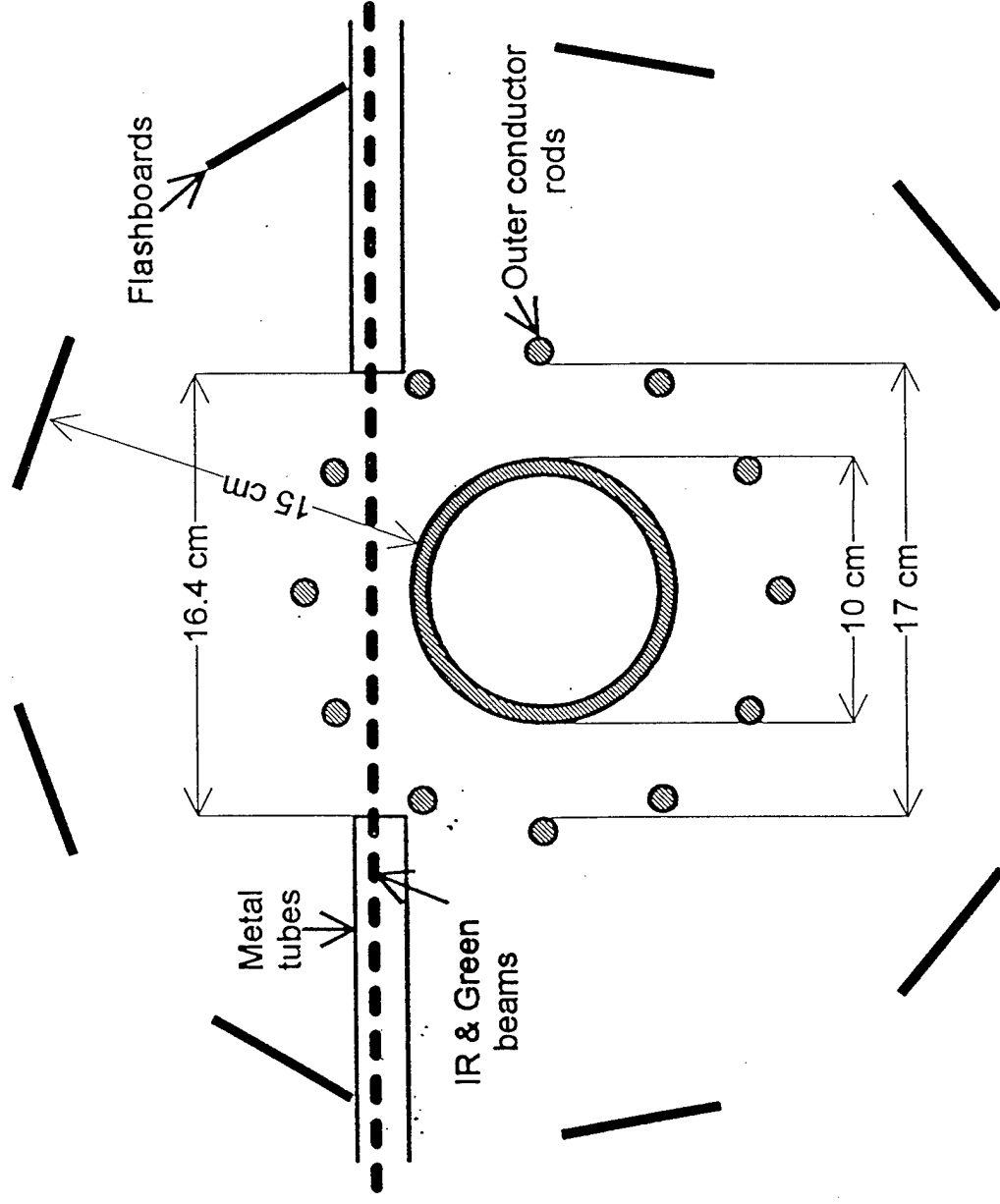


Figure 1.

# Parallel plate POS experiment

---

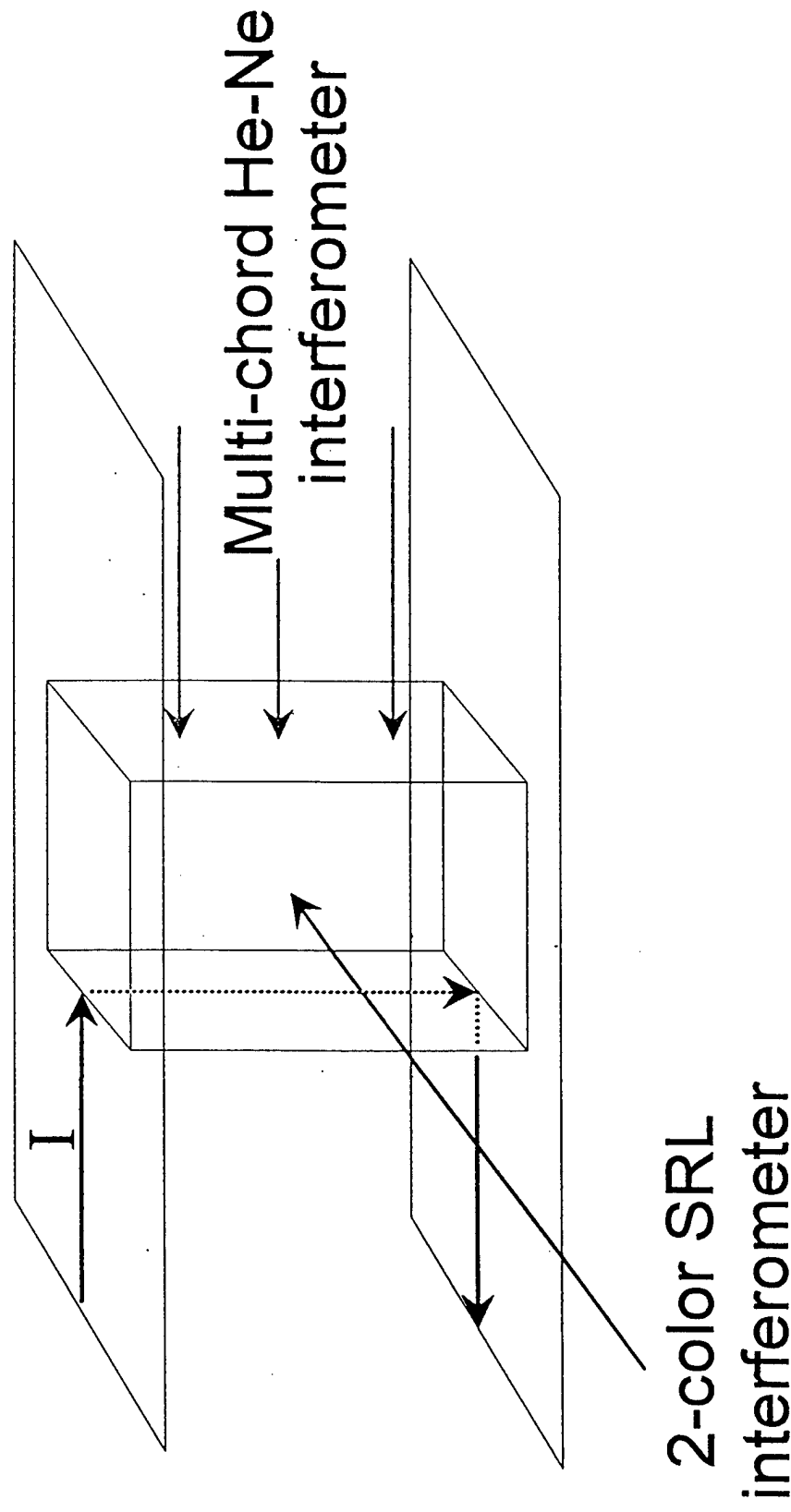
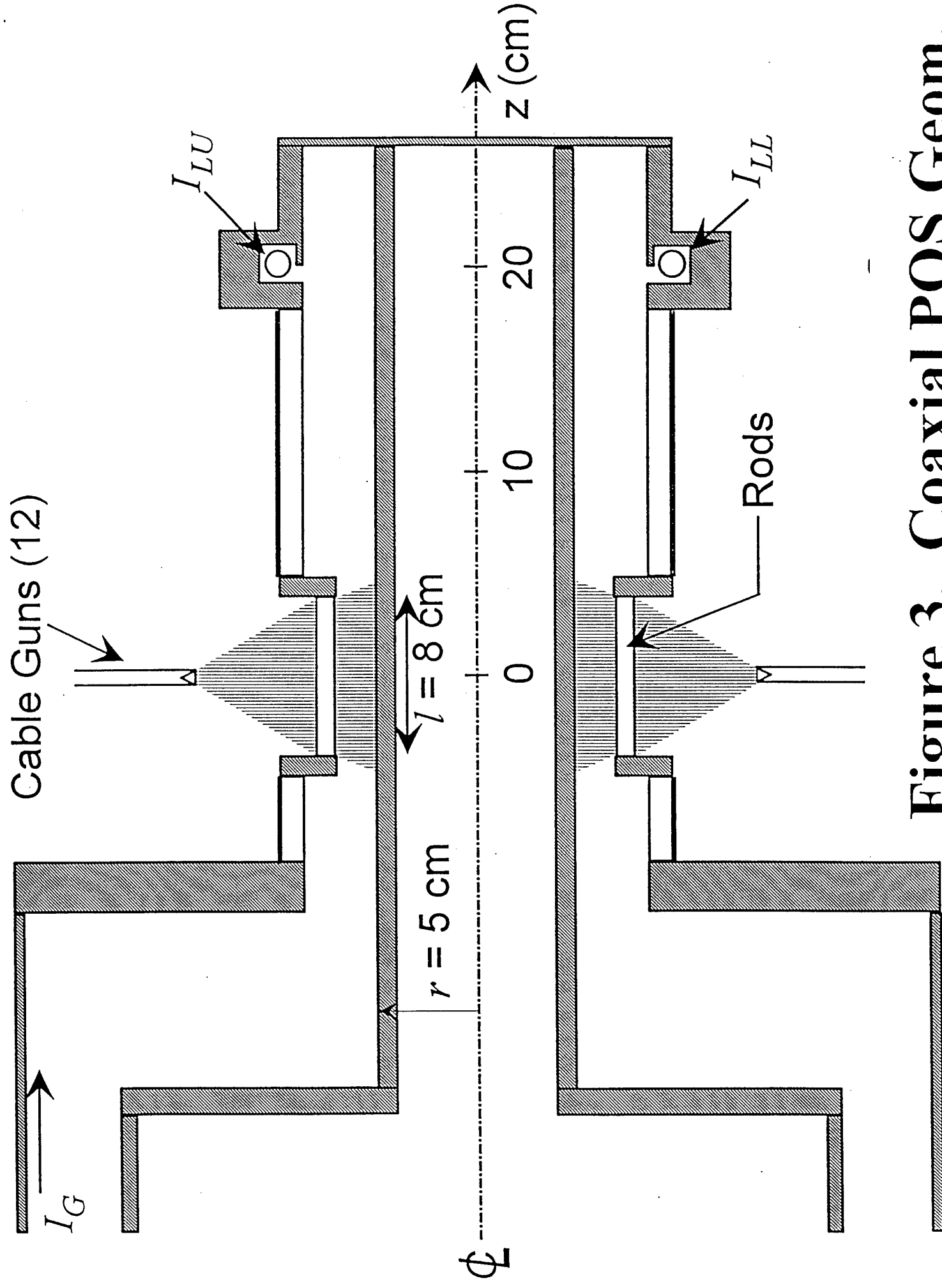
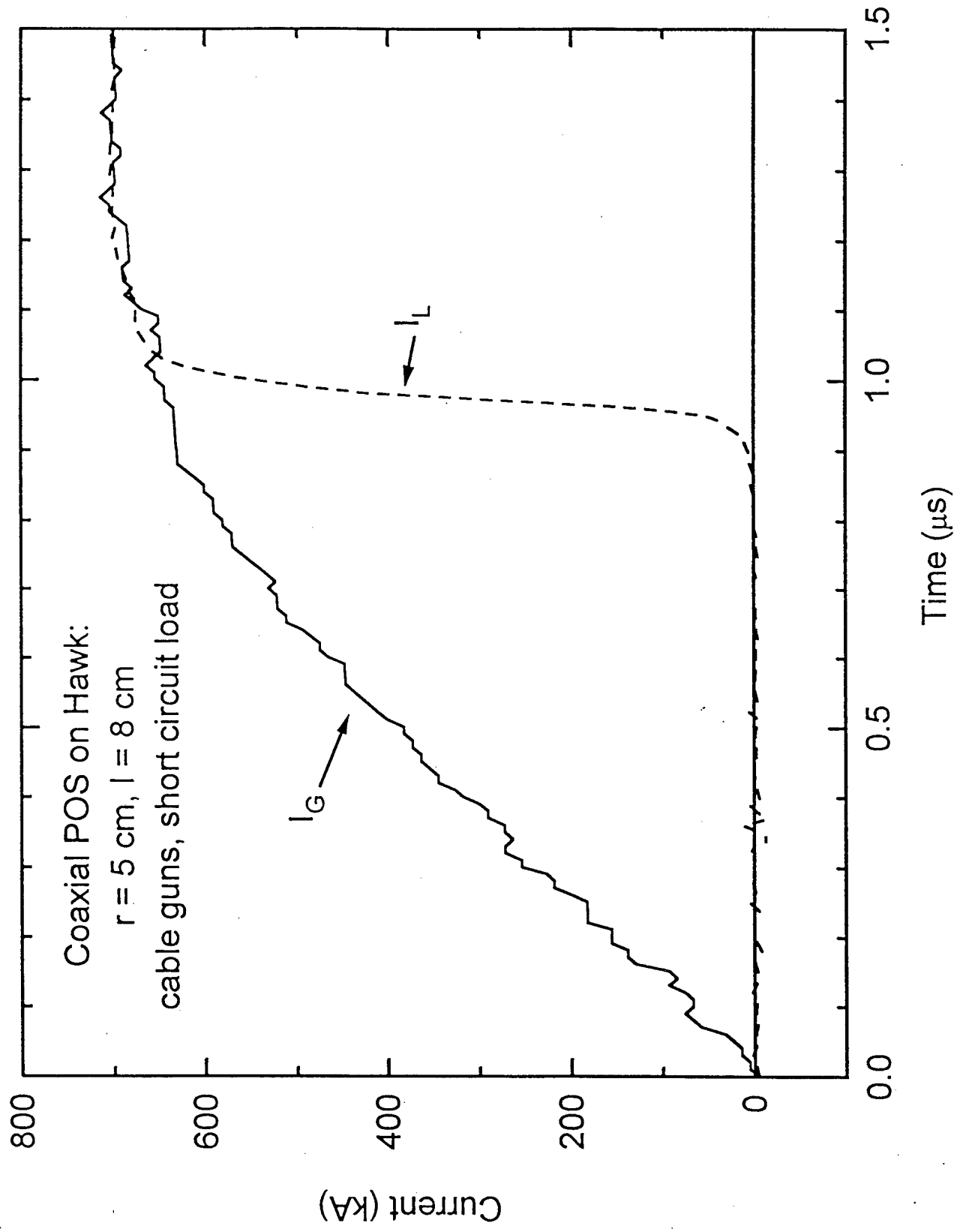


Figure 2.



**Figure 3. Coaxial POS Geom.**





**Figure 4. Coax Load Current.**

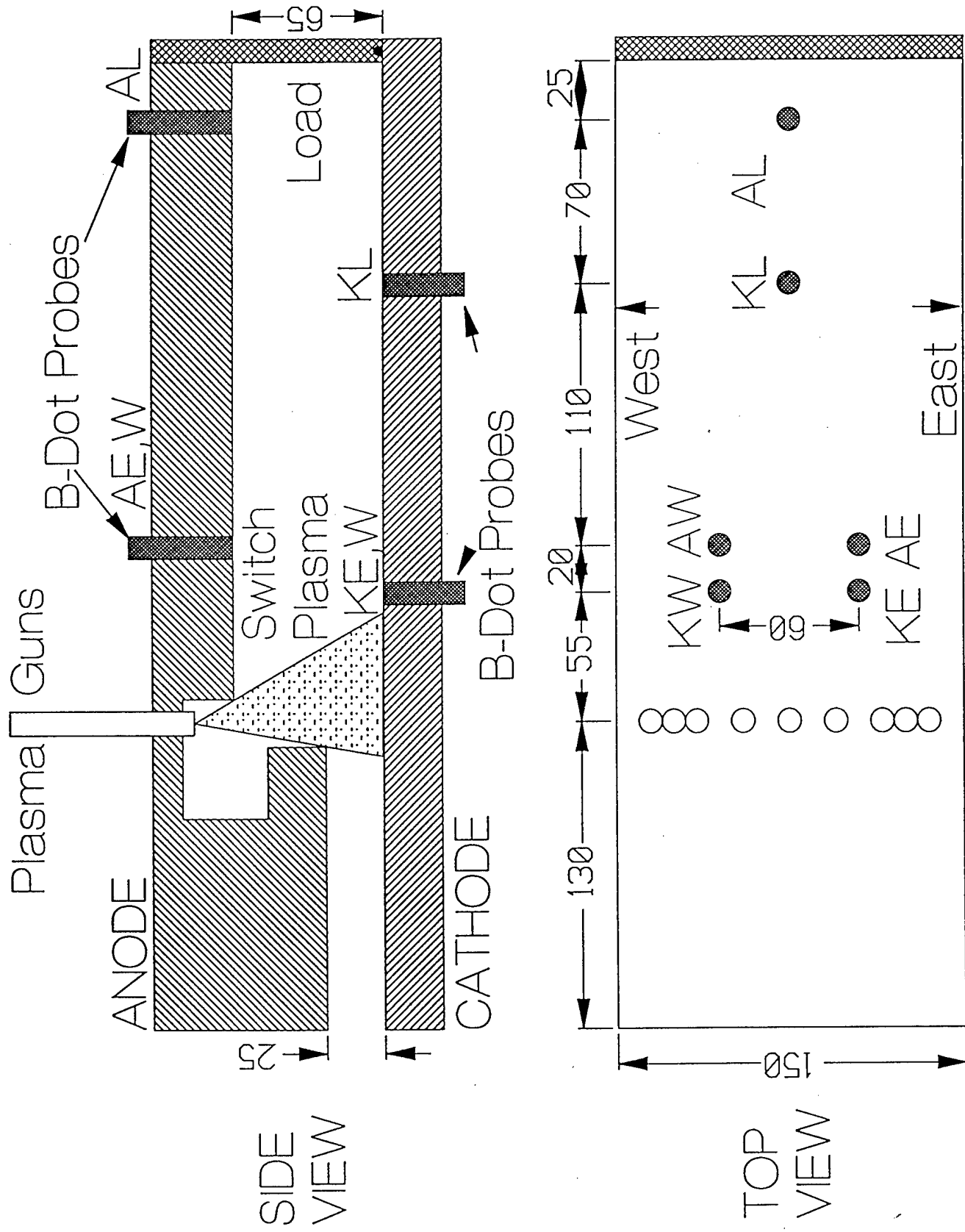


Figure 5. Bi-Plate POS Geom.

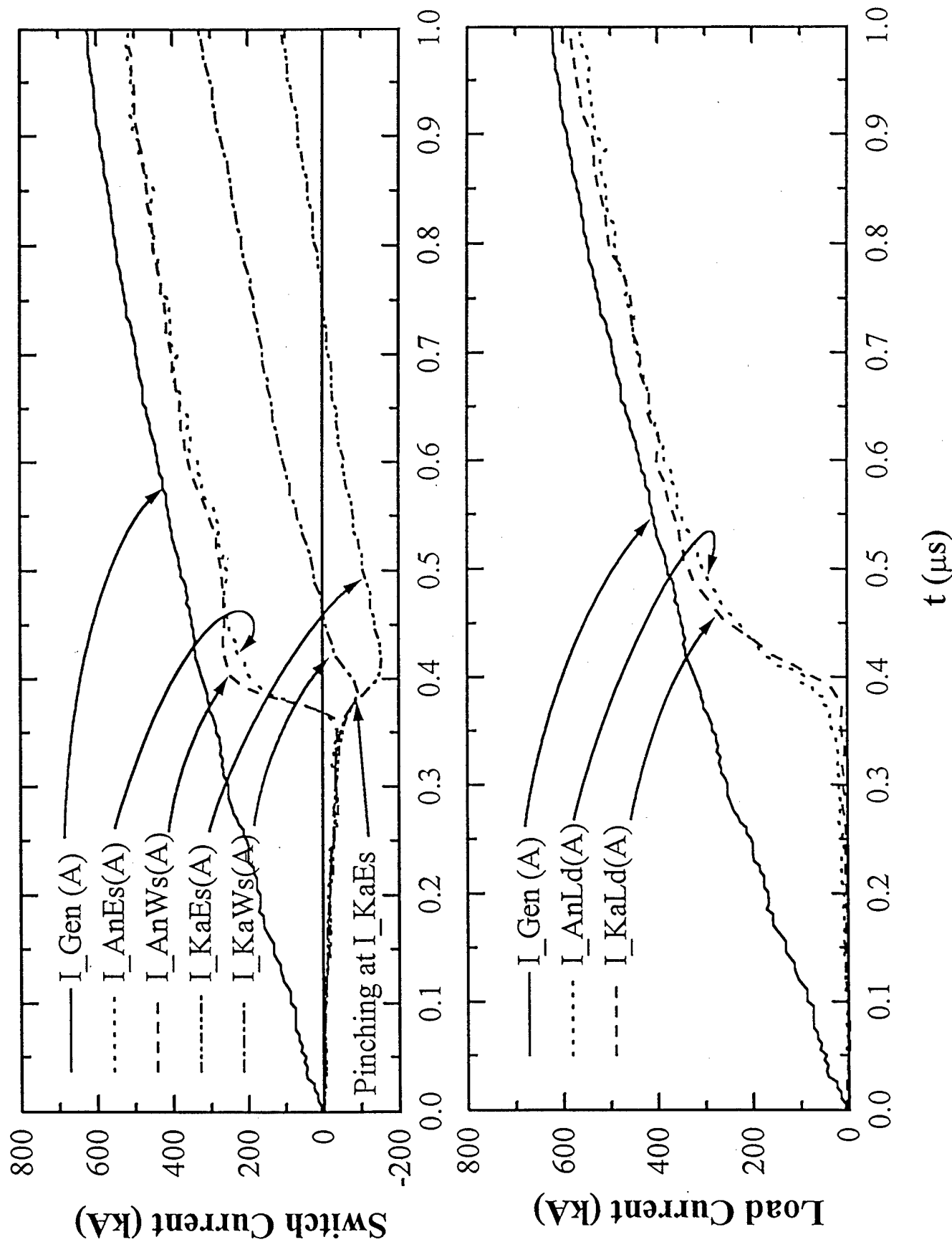


Figure 6. Bi-Plate Switch and Load Currents for Shot 1740.

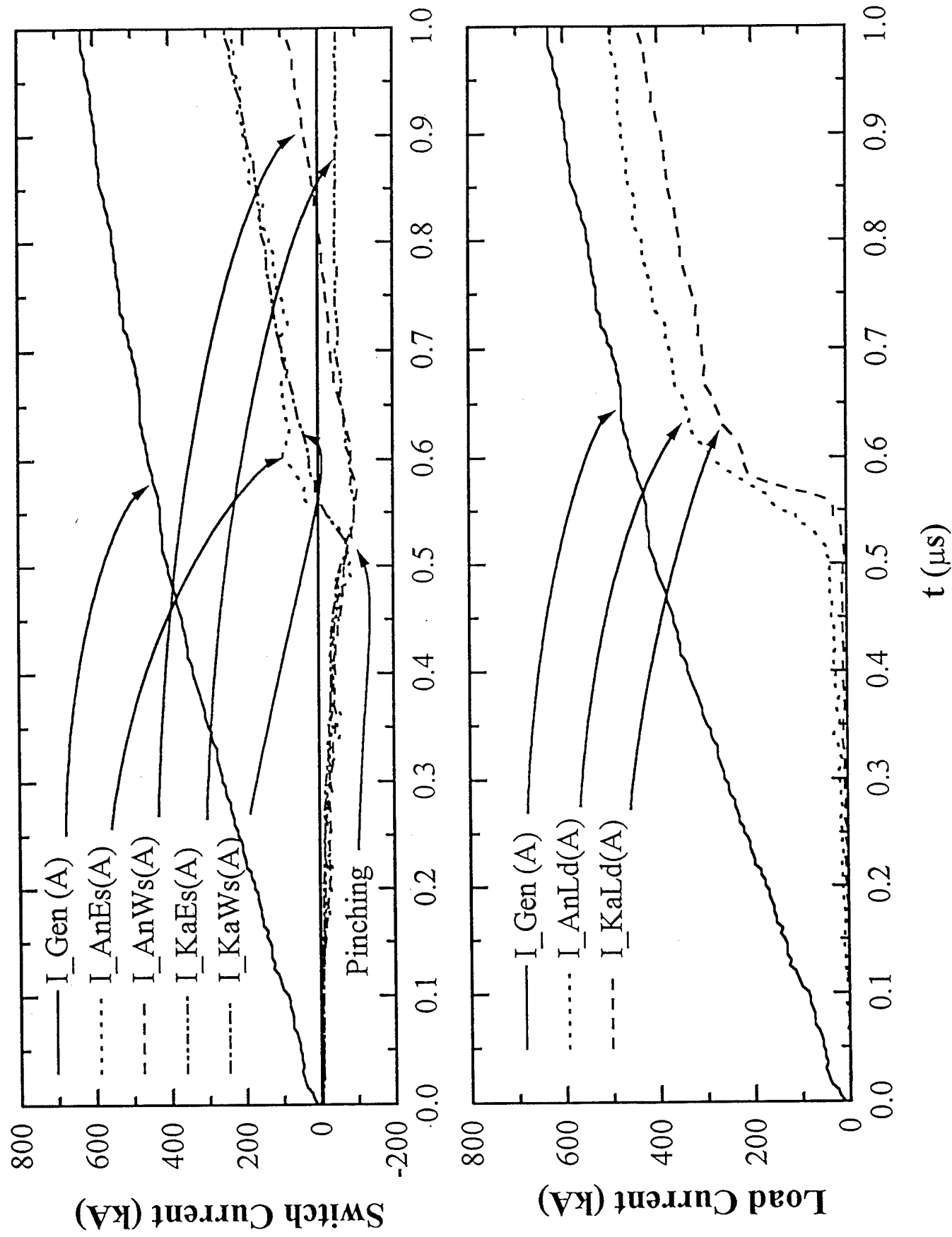


Figure 7. Bi-Plate Switch and Load Currents for Shot 1741.

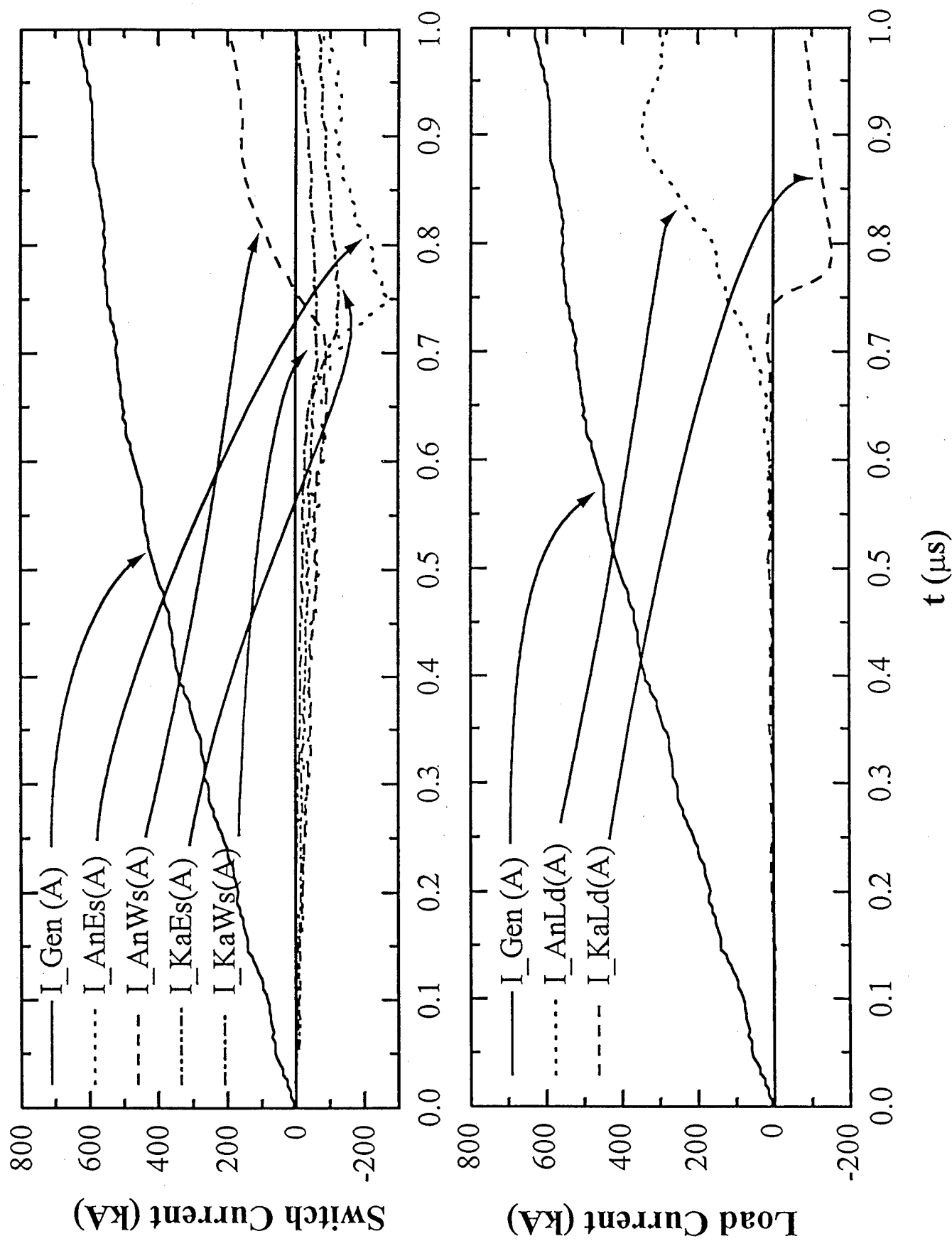


Figure 8. Bi-Plate Switch and Load Currents for Shot 1742.

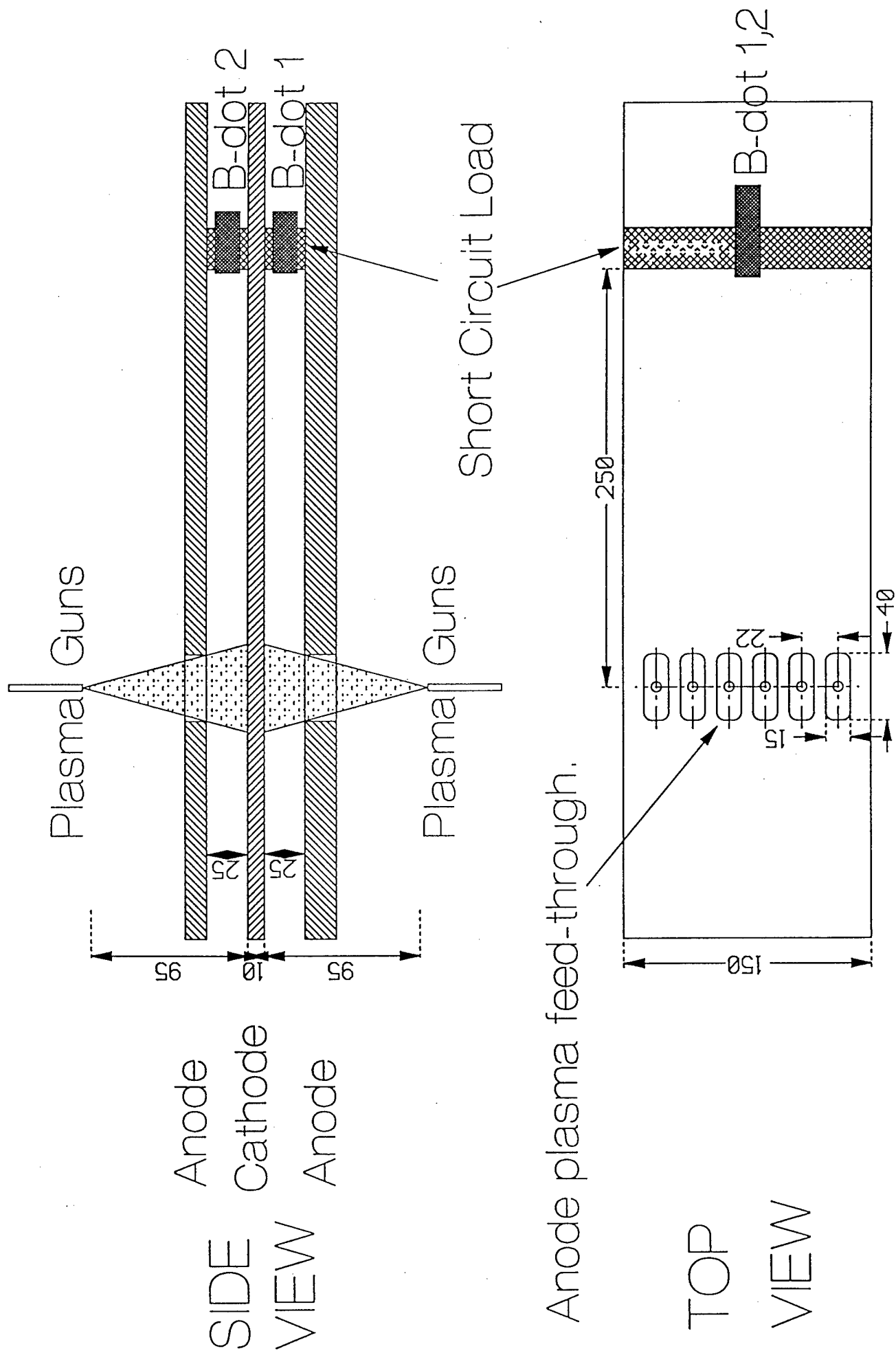
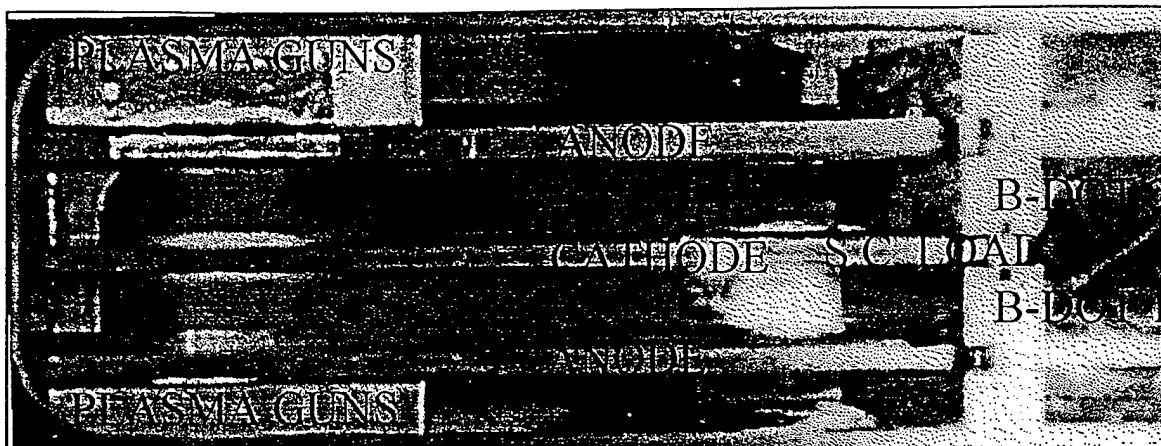
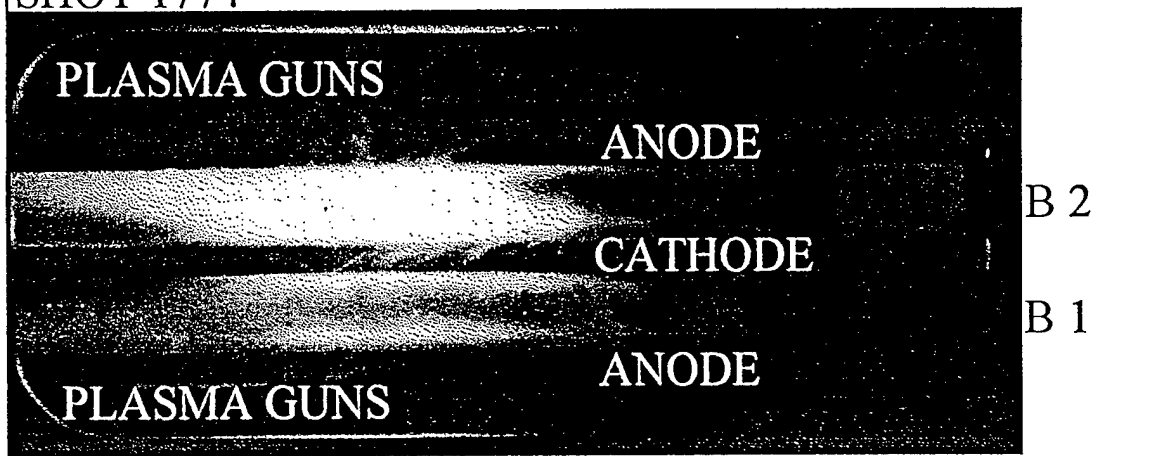


Figure 9. Tri-Plate POS Geom.



SHOT 1774



**Figure 10. Tri-Plate Image  
(Shot 1774).**

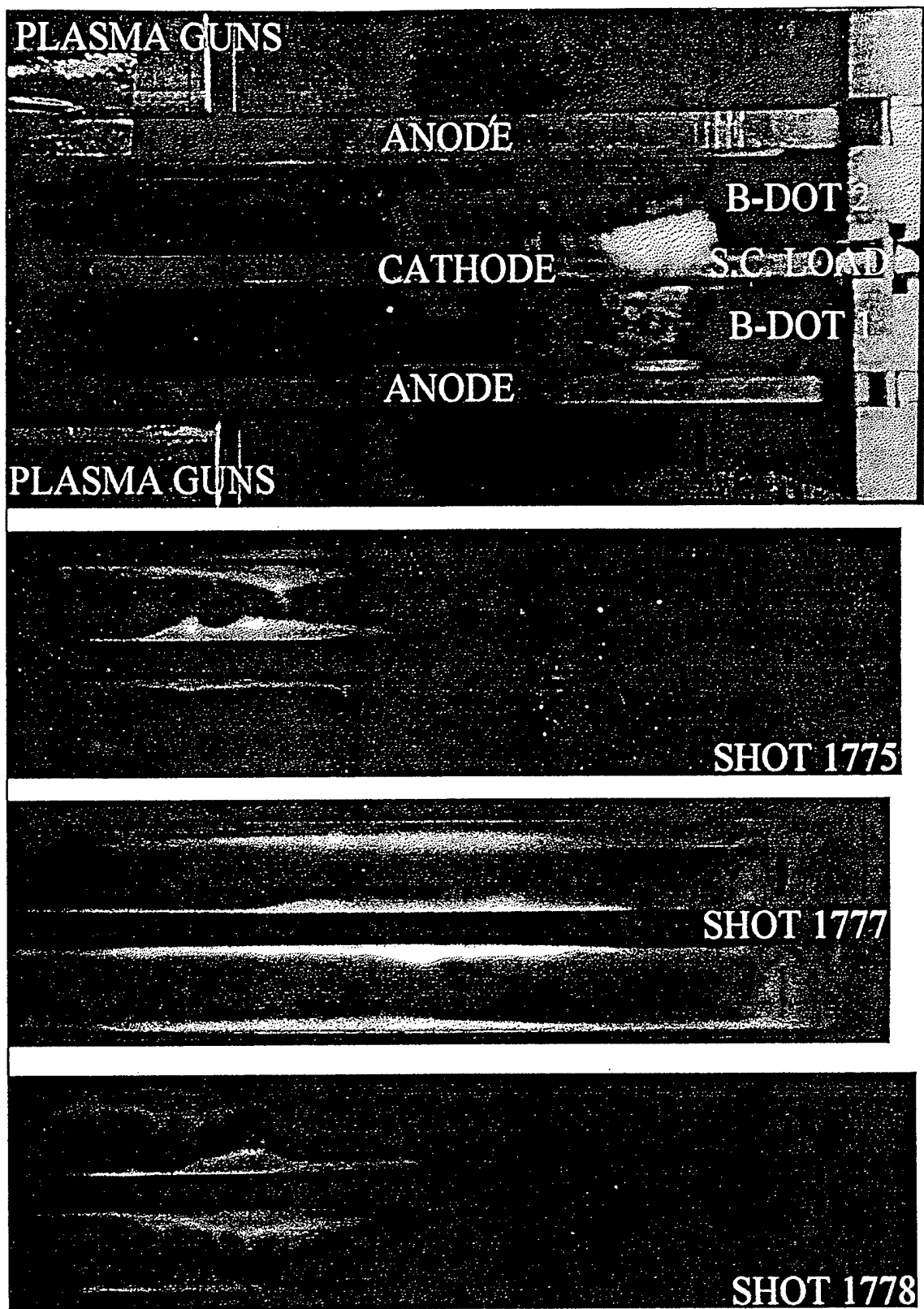


**Figure 11. Tri-Plate Image  
(Shots 1775,7,8).**



### Figure 12. Tri-Plate Load Currents

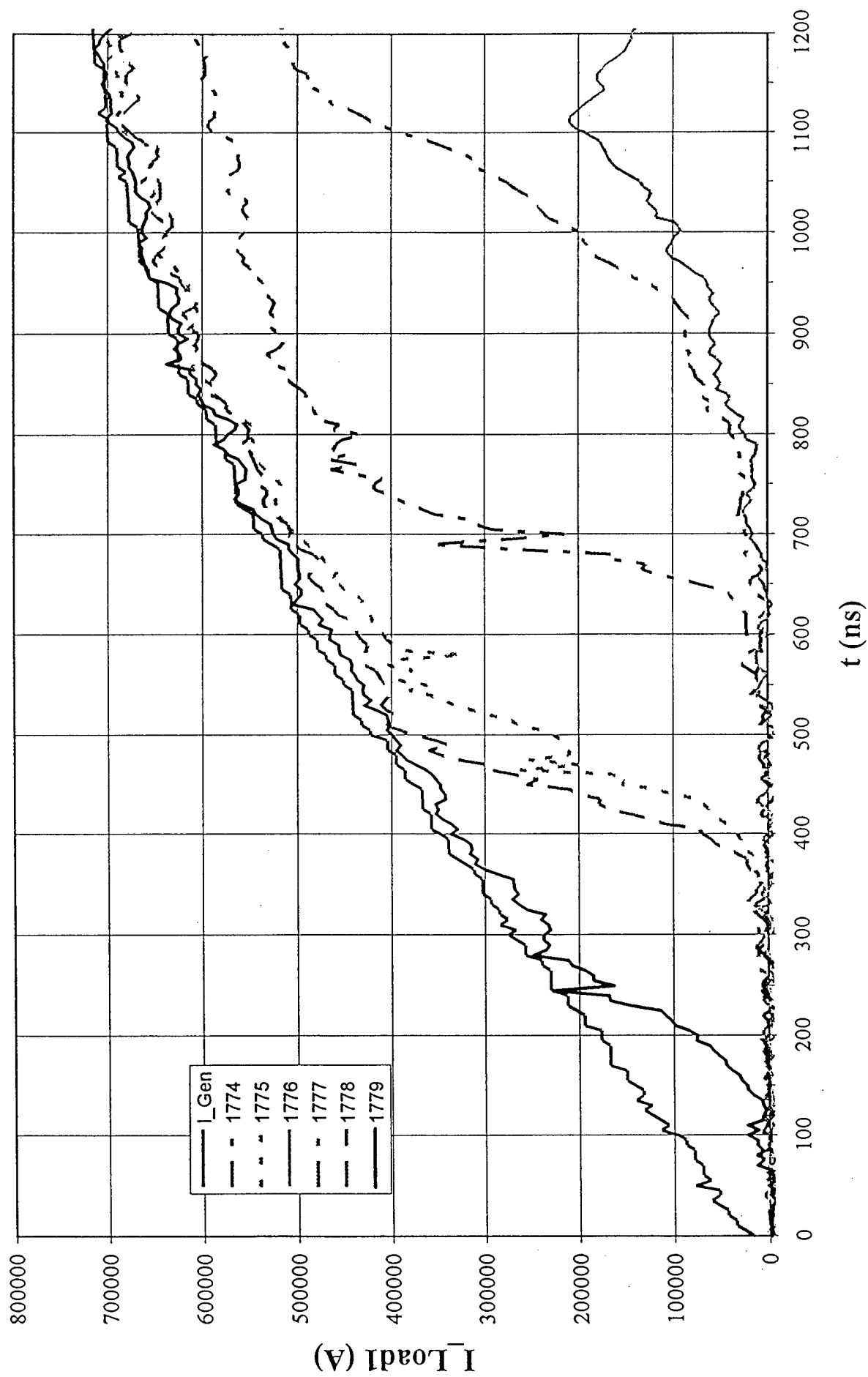
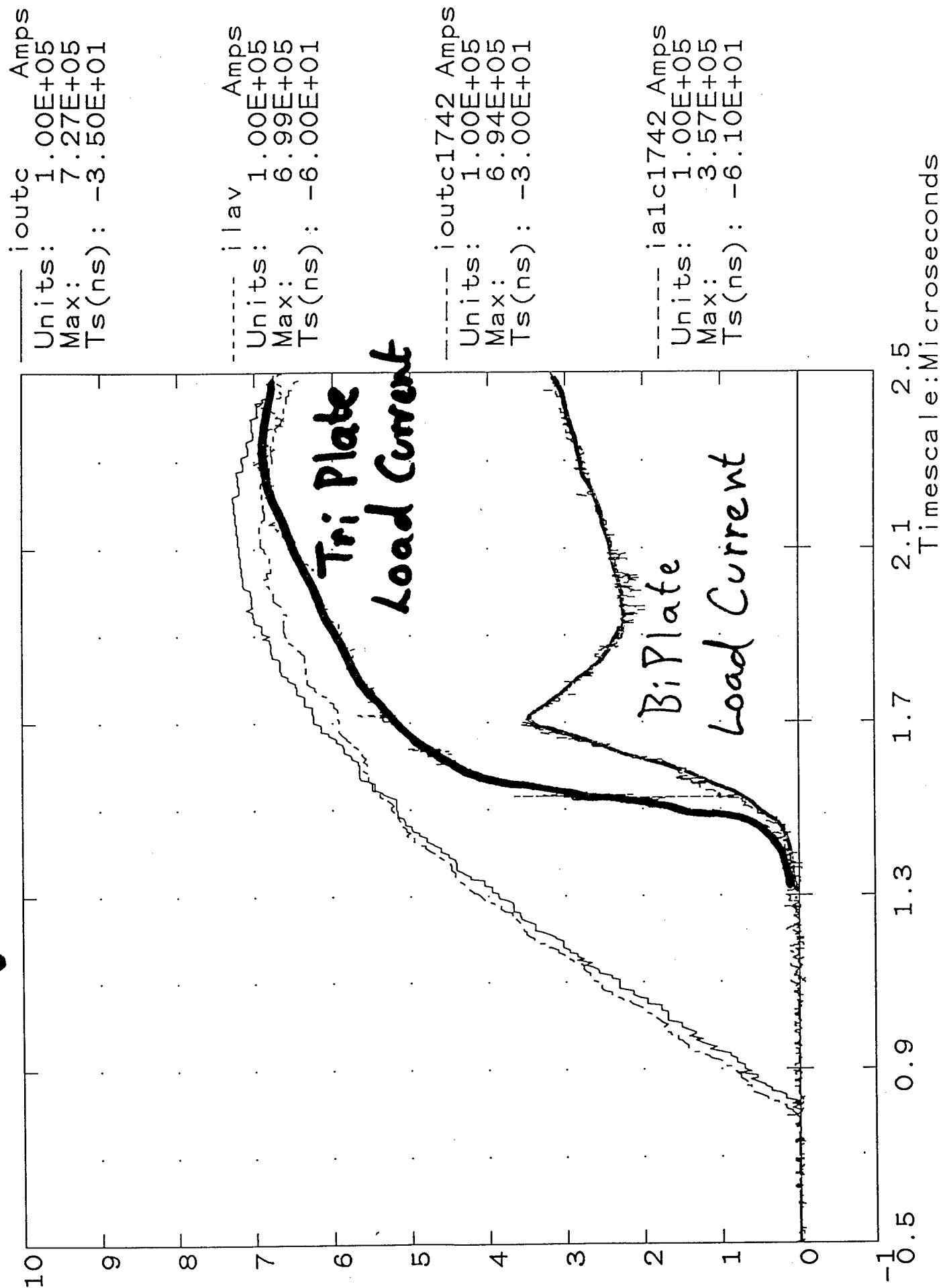


# Figure 13.

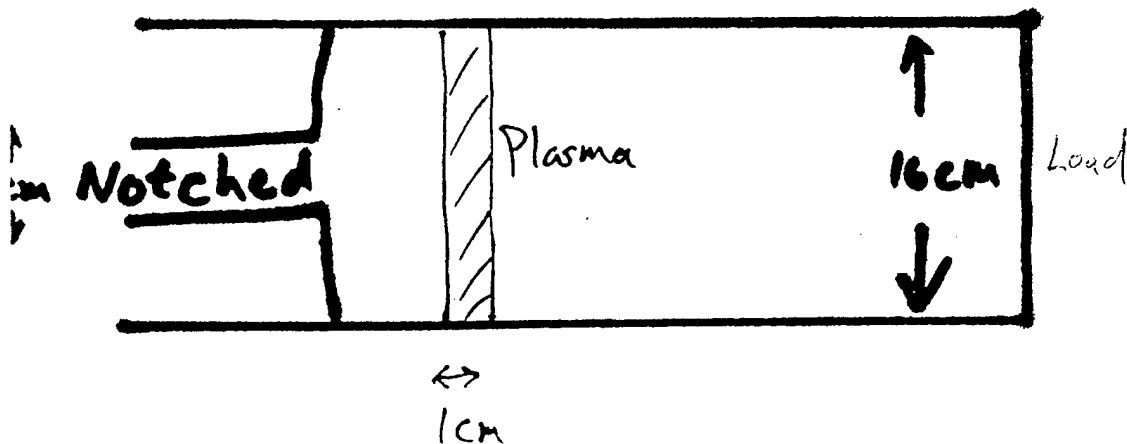
Shot 1774



# Bi-Plate

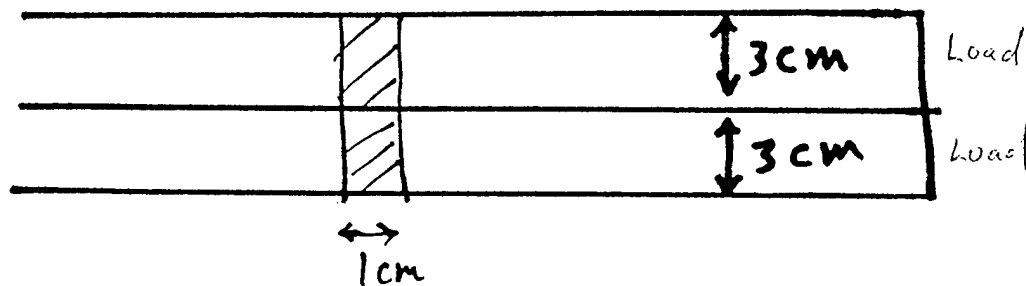


← 7cm →



↔  
1cm

# Tri-Plate



↔  
1cm

← 7cm →

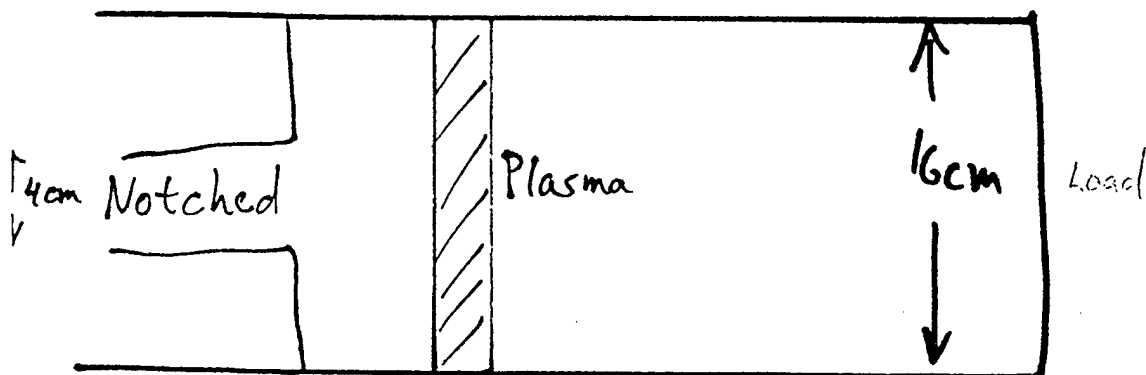
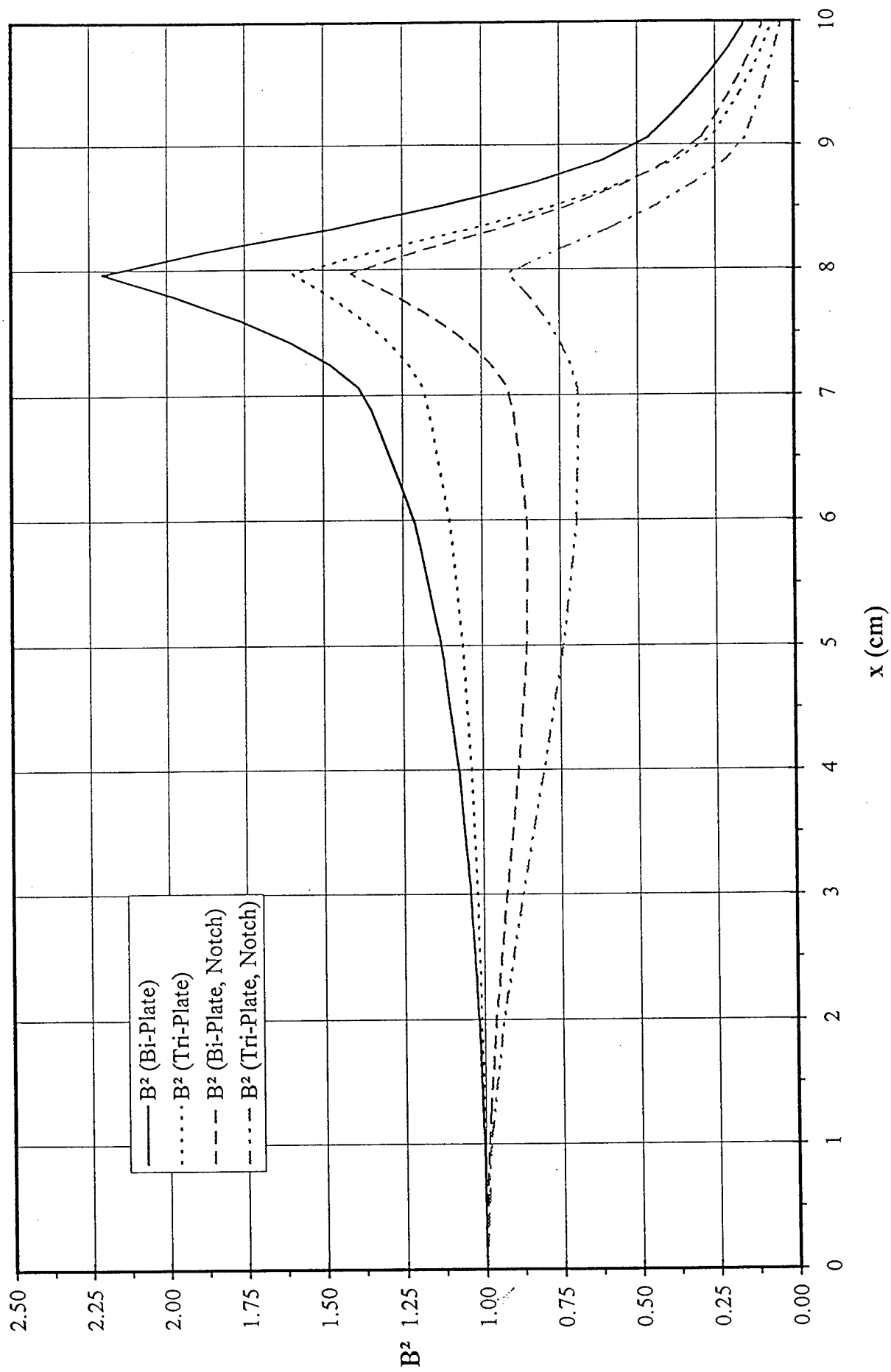


FIGURE 14.  
Geometries for Mag-Stat Calcs

Figure 15. Computed  $B^2$  on Plasma Middle of A-K



# **A 2-color interferometer is installed on Hawk for improved density measurements**

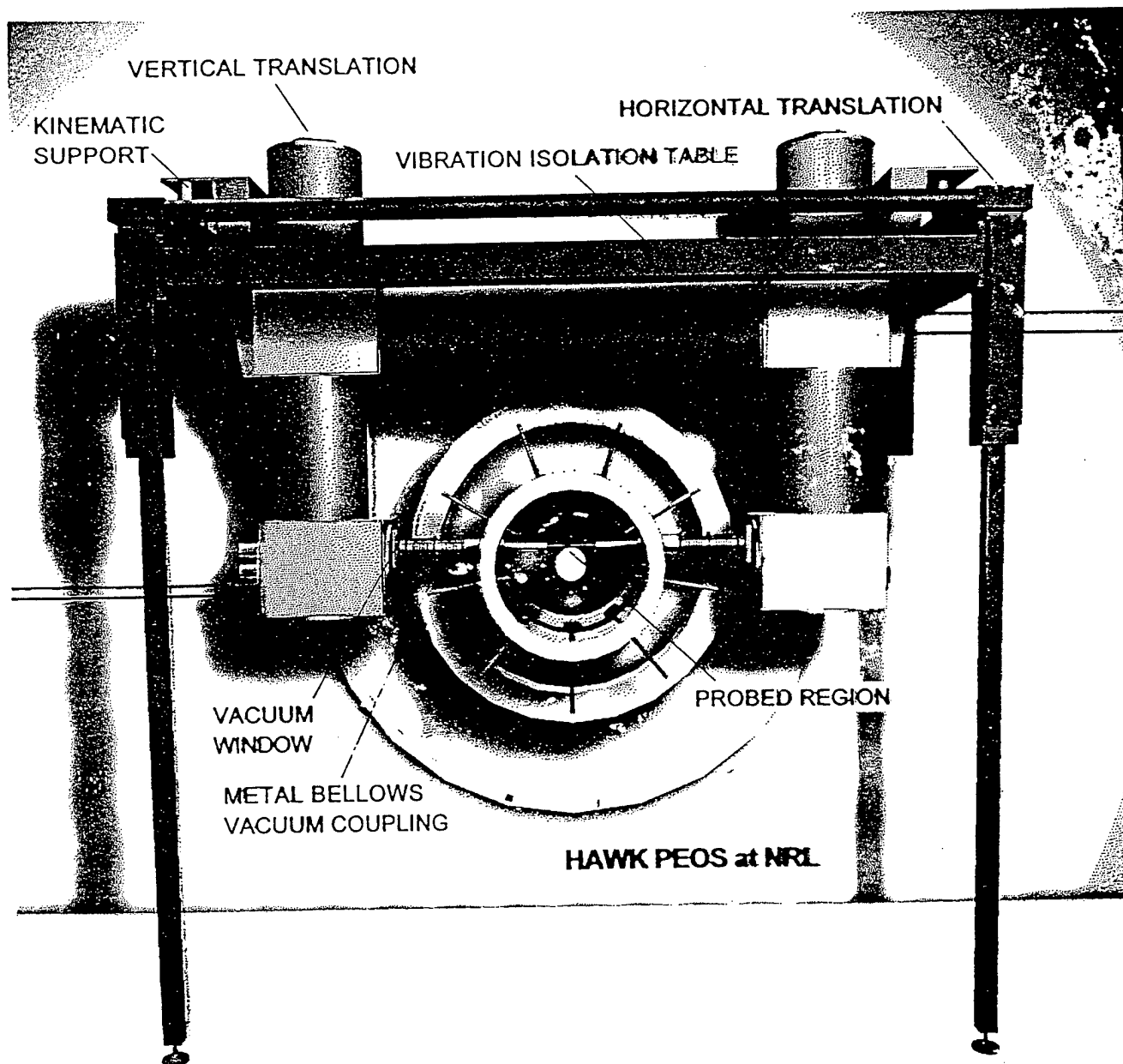
**NRL**

---

- SRL technique uses 1.06  $\mu$  and 0.53  $\mu$  lasers, vibration stabilized, optically isolated
- 10<sup>-5</sup> wave phase sensitivity, ns time response
  - corresponds to 2x10<sup>12</sup> cm<sup>-2</sup> density limit
- 2-color technique allows independent measurement of electron and neutral densities
  - neutral density strongly dependent on species
- device is limited to transverse line of sight (no mirrors attached to machine)

# Figure 16.

## SRL Two-Color Interferometric Plasma Diagnostic



The vacuum housing containing the interferometer is kinematically supported on a vibration isolation table which is rigidly attached to the HAWK structure.

TITLE:       **MAGNETOSTATIC ANALYSIS OF PARALLEL-PLATE POS**

AUTHORS:   **R. Riley, J. Grossmann, S. Swanekamp, B. Weber**

DATE:       **October 3, 1994**

**ABSTRACT:**

Experiments with parallel-plate plasma opening switches (POS) on NRL's HAWK pulsed-power facility have shown evidence of pinching of the plasma in the switch region. This document presents a magnetostatic analysis of the parallel plate POS to explain this pinching behavior and to suggest design options to minimize it.

Our goal in designing a parallel plate POS is to reduce the pinching forces on the edges of the plasma and to make the current profile at the switch plasma as uniform with respect to  $x$  ( $\theta$ ) as possible. This search includes triple-plate and rectangular coax geometries.

The current distributions of various rectangular geometries are examined based on two-dimensional magnetostatics to determine the best geometry to deliver current to the switch plasma. The current distribution of an infinite flat strip is derived analytically and is found to be strongly peaked at the outer edges.

A computer model based on dividing the metal surfaces into a finite number of wires oriented parallel to the power-flow direction ( $z$ ) is used to study the current distribution for more complex geometries, including various single conductors, bi-plate, triple-plate, and rectangular-coax.

**THIS REPORT REPRESENTS UNPUBLISHED INTERNAL WORKING  
DOCUMENTS AND SHOULD NOT BE REFERENCED OR DISTRIBUTED**

## I. Introduction

Experiments with parallel-plate plasma opening switches (POS) on NRL's HAWK pulsed-power facility have shown evidence of pinching of the plasma in the switch region. This document presents a magnetostatic analysis of the parallel plate POS to explain this pinching behavior and to suggest design options to minimize it.

The goal of the parallel plate POS experiments is to create an opening switch which operates similar to, and ultimately as well as, the standard coaxial POS, and which allows much improved diagnostic access. The operation of this switch will then be observed to gain a better understanding of the physics of the coaxial switch's operation.

Pinching is not observed in coaxial switches and is thought to be the main reason that parallel plate switches do not perform as well as coaxial switches. The plasma density, current density and magnetic field in coaxial switches are, ideally, independent of the angular position ( $\theta$ ) around the axis of the coaxial switch. The angular position in the coaxial switch corresponds to the displacement transverse to the power flow and parallel to the surface of the plates ( $x$ ) in the parallel plate switch, as shown in Figure 1. Near the edges of the parallel plate

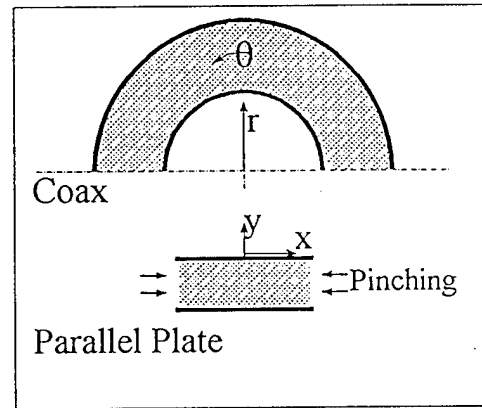


Figure 1. Comparison of coax and parallel switch geometries.

switch, the surfaces of the conductors are discontinuous with respect to  $x$ . The currents and fields at these edges are similarly discontinuous, leading to fringing effects.

Our goal in designing a parallel plate POS is to reduce the pinching forces on the edges of the plasma and to make the current profile at the switch plasma as uniform with respect to  $x$  ( $\theta$ ) as possible.

## II. Magnetostatics

The basic differential laws of magnetism, in MKS units, are<sup>1</sup>

$$\vec{\nabla} \cdot \vec{B} = 0 \quad \text{and} \quad \vec{\nabla} \times \vec{H} = \vec{J} \quad (1)$$

The corresponding boundary conditions at a metal surface are



$$\hat{n} \cdot \vec{B} = 0 \quad \text{and} \quad \hat{n} \times \vec{H} = \vec{K} \quad , \quad (2)$$

where  $\hat{n}$  is the unit vector normal from the metal surface and  $\vec{K}$  is the idealized surface current density.

In the vacuum outside the conductors, the current density is zero,  $\vec{J} = 0$ . This permits the introduction of a magnetic scalar potential  $\Phi_M$  such that

$$\vec{H} = -\vec{\nabla} \Phi_M \quad (3)$$

and which satisfies the Laplace equation

$$\nabla^2 \Phi_M = 0 \quad . \quad (4)$$

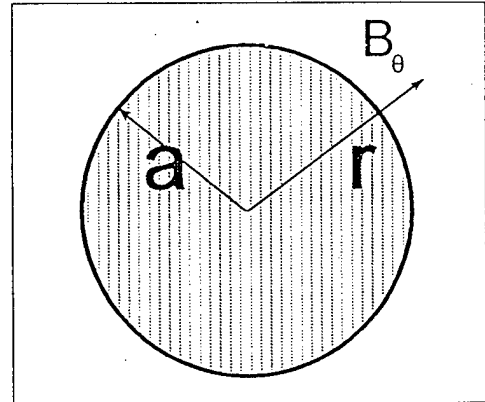
### III. Infinite Circular Rod, Single Conductor

The magnetic field due to an infinite circular rod of radius  $a$ , carrying a current  $I$  in the  $z$  direction is known from Ampère's Law

$$\oint_C \vec{H} \cdot d\vec{\ell} = I \quad (5)$$

to be

$$\vec{H} = \frac{I}{2\pi r} \hat{\theta} \quad \text{for } r > a \quad ,$$



(6) Figure 2. Infinite rod geometry.

where  $\hat{\theta}$  is the unit vector in the  $\theta$  direction. The magnetic scalar potential of this geometry based on Eq. (3) is then

$$\Phi_M = -\frac{I\theta}{2\pi} \quad (7)$$

where, in cylindrical coordinates

$$\vec{\nabla} = \hat{r} \frac{\partial}{\partial r} + \frac{\hat{\theta}}{r} \frac{\partial}{\partial \theta} + \hat{z} \frac{\partial}{\partial z} \quad . \quad (8)$$

#### IV. Conformal Map from Rod to Flat Strip

The inverse of the Joukowski transform<sup>2,3,4</sup>

$$w = \frac{z + \sqrt{z^2 - 4a^2}}{2}, \quad (9)$$

where  $z = x + iy$  and  $w = re^{i\theta}$ , conformally maps a line segment on the  $x$  axis of the complex plane ( $-2a < x < 2a$ ), as shown in **Figure 3**, to the upper half of a circle of radius  $a$ , as shown in **Figure 2**.

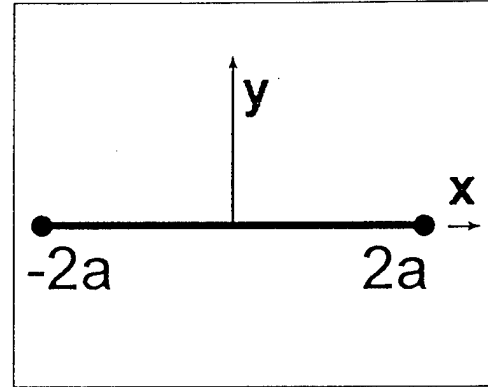


Figure 3. Flat strip geometry.

Because the magnetic scalar potential satisfies the Laplace equation, it can be mapped from the cylindrical geometry to the flat geometry as

$$\Psi_M(w) = -\frac{I}{2\pi} \arg(w) = -\frac{I}{2\pi} \arctan \left[ \frac{\text{Im}(w)}{\text{Re}(w)} \right], \quad (10)$$

where  $\arg(w) = \theta$  for  $w = re^{i\theta}$ .

The real and imaginary components of  $w$  in terms of  $x$  and  $y$  in the first quadrant ( $x \geq 0, y \geq 0$ ) are

$$\text{Re}(w) = \frac{x}{2} + \frac{1}{2\sqrt{2}} \sqrt{\sqrt{(4a^2 - x^2 + y^2)^2 + 4x^2y^2} + (4a^2 - x^2 + y^2)} \quad (11)$$

and

$$\text{Im}(w) = \frac{y}{2} + \frac{1}{2\sqrt{2}} \sqrt{\sqrt{(4a^2 - x^2 + y^2)^2 + 4x^2y^2} - (4a^2 - x^2 + y^2)} \quad (12)$$

where the complex square root is defined as  $\sqrt{w} = \sqrt{r} e^{i\theta/2} = \sqrt{r} [\cos(\theta/2) + i \sin(\theta/2)]$ .

The mapped magnetic scalar potential in the first quadrant is then

$$\Psi_M(w) = -\frac{I}{2\pi} \arctan \left\{ \frac{\sqrt{2}y + \sqrt{\alpha^2 + \beta^2 + \alpha}}{\sqrt{2}x + \sqrt{\alpha^2 + \beta^2 - \alpha}} \right\}, \quad (13)$$

where  $\alpha = 4a^2 - x^2 + y^2$  and  $\beta = 2xy$ . This analysis assumes that all results derived in the first quadrant can be generalized to the other three quadrants based on symmetry, such as the magnetic field  $B_x(x,y) = B_x(-x,y) = -B_x(x,-y)$  and  $B_y(x,y) = -B_y(-x,y) = B_y(x,-y)$ .

In the limit as  $y \rightarrow 0$  and  $|x| < 2a$ , the transform reduces to

$$w = \frac{x + i \sqrt{4a^2 - x^2}}{2}, \quad \text{Re}(w) = \frac{x}{2}, \quad \text{Im}(w) = \frac{\sqrt{4a^2 - x^2}}{2}. \quad (14)$$

For the limit as  $y \rightarrow 0$  and  $|x| > 2a$ , the imaginary component of the transform reduces zero, which is consistent with the boundary conditions and symmetry of the magnetic field.

### V. Current Profile for Flat Strip, Single Conductor

The current distribution can be found by taking the limit as  $y \rightarrow 0$  of the magnitude of the  $x$  component of the magnetic field

$$K_z(x) = -\lim_{y \rightarrow 0} H_x(x, y) = -\frac{I}{2\pi} \frac{\partial}{\partial x} \arctan \left[ \frac{\sqrt{4a^2 - x^2}}{x} \right], \quad (15)$$

where we have assumed  $|x| < 2a$ . For  $|x| > 2a$ , the result reduces to zero. Note that integrating this result gives the correct total current

$$2 \int_0^{2a} dx K_z(x) = \frac{I}{\pi} [\arctan(\infty) - \arctan(0)] = \frac{I}{2}, \quad (16)$$

which is that of the upper half of the circle. In the flat geometry, we must multiply the current distribution by a factor of two to normalize the result.

Evaluating the derivative and multiplying by the normalization factor, we find the current distribution in the flat strip geometry to be

$$K_z(x) = \frac{I}{\pi \sqrt{(2a)^2 - x^2}}. \quad (17)$$

where  $d/dx \arctan(u) = [1+u^2]^{-1} du/dx$ . The current density is infinite at  $x = \pm 2a$ .

This current density has the same form as the derivative of the current on the upper surface of a circular rod with respect to  $x = a \cos(\theta)$

$$\frac{dI}{dx} = \left( \frac{dI}{d\theta} \right) \left( \frac{d\theta}{dx} \right) = \frac{I}{2\pi \sqrt{a^2 - x^2}}. \quad (18)$$

### VI. Magnetic Field at Surface of a Flat Strip

The  $x$  component of the magnetic field at the surface of the strip was given in the previous section by Eq. (15) and (17) as

$$H_x(x) = \frac{-I}{\pi \sqrt{(2a)^2 - x^2}} \quad (19)$$

The y component must be zero at the surface ( $y=0$ ,  $|x|<2a$ ) to satisfy the boundary conditions. Taking this limit of the derivative of the magnetic scalar with respect to y

$$\lim_{y \rightarrow 0} H_y(x, y) = \frac{I}{2\pi} \left( \frac{x}{2a} \right)^2 \lim_{y \rightarrow 0} \frac{\partial}{\partial y} \left[ \frac{\sqrt{2} y + \sqrt{\alpha^2 + \beta^2 + \alpha}}{\sqrt{2} x + \sqrt{\alpha^2 + \beta^2 - \alpha}} \right], \quad (20)$$

and deleting the terms of the derivative that go to zero

$$\lim_{y \rightarrow 0} H_y = \frac{I}{2\pi} \frac{x}{4a^2} \lim_{y \rightarrow 0} \left[ 1 - \frac{\sqrt{2} \alpha}{2x \sqrt{\alpha^2 + \beta^2 - \alpha}} \frac{\partial}{\partial y} (\sqrt{\alpha^2 + \beta^2 - \alpha}) \right]. \quad (21)$$

Using L'Hospital's rule<sup>5</sup> to evaluate the limit of the form 0/0

$$\lim_{y \rightarrow 0} H_y = \frac{I}{2\pi} \frac{x}{4a^2} \lim_{y \rightarrow 0} \left[ 1 - \frac{2\sqrt{2}xy}{\sqrt{1 + (\beta/\alpha)^2 - 1}} \right] = 0, \quad (22)$$

we find that the solution satisfies the boundary conditions at the surface of the flat strip.

## VII. Two-Dimensional Magnetostatic Numerical Calculation

The magnetic field of geometries more complex than a single circular rod or a flat strip is difficult to compute analytically. In this section, the analytic result for the flat strip's current distribution is compared to a simple 2-D magnetostatic numerical calculation.

The metal surfaces are represented by arrays of equally spaced wires which carry current in the z direction. The current in these wires must be distributed such that the normal component of their combined magnetic field is zero at the surfaces of the conductor.

The flat strip geometry is symmetric about the y axis, so only the current distribution on the right side is calculated. The enforcement of boundary conditions assumes this mirror symmetry. The current distribution on the right side is divided into N elements spaced out at intervals of  $dx=L/(N-1/2)$ , as shown in

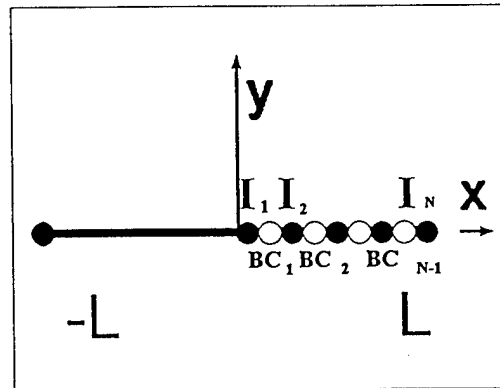


Figure 4. Flat strip wires and BC's.

Figure 4. These current elements must sum to half the total current

$$\sum_{i=1}^N I_i = \frac{I}{2} \quad (23)$$

To form a set of N equations in N unknowns, the boundary condition is enforced at N-1 positions,

$$\sum_{i=1}^N I_i \left[ \frac{1}{x_j - u_i} + \frac{1}{x_j + u_i} \right] = 0 \quad \text{for } j = 1, \dots, N-1, \quad (24)$$

where the BC is enforced at  $x_j = L[j/(N-1/2)]$  and the magnetic field is due to the 2N wires at  $\pm u_i = L[(i-1/2)/(N-1/2)]$ . The BC is also satisfied at  $x=0$  by the assumed symmetry. The position of the last current sample must be outside all of the positions where the BC is enforced to permit a solution to this set of equations.

The set of equations can be written in matrix form as

$$\begin{bmatrix} 1 & \dots & 1 \\ \left( \frac{1}{x_1 - u_1} + \frac{1}{x_1 + u_1} \right) & \dots & \left( \frac{1}{x_1 - u_{N-1}} + \frac{1}{x_1 + u_{N-1}} \right) \\ \vdots & \ddots & \vdots \\ \left( \frac{1}{x_N - u_1} + \frac{1}{x_N + u_1} \right) & \dots & \left( \frac{1}{x_N - u_{N-1}} + \frac{1}{x_N + u_{N-1}} \right) \end{bmatrix} \cdot \begin{bmatrix} I_1 \\ I_2 \\ \vdots \\ I_N \end{bmatrix} = \begin{bmatrix} \frac{I}{2} \\ 0 \\ \vdots \\ 0 \end{bmatrix} \quad (25)$$

The solution of this system of linear equations for  $N=15$  is compared to the analytic result in Figure 5.

The simulation provides a good approximation to the analytic current distribution except at the edge of the strip. The strength of this singularity at the edge is partly due to the non-physical zero thickness of the strip. The next section examines how the current distribution on the surface of an

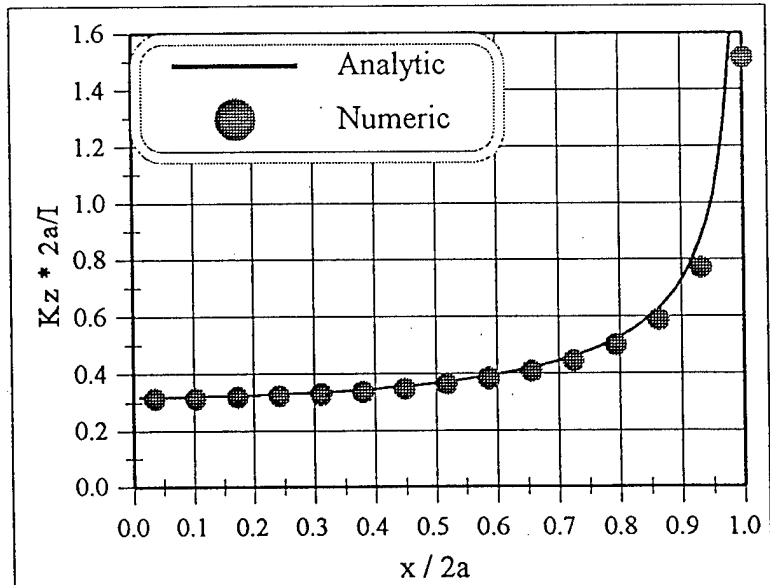


Figure 5. Analytic and numeric results for flat-strip current distribution.

infinite conducting bar varies with thickness.

### VIII. Rectangular Bar, Single Conductor

An infinite conducting bar is more physical than the flat strip described above. The analytic solution to this geometry is much more difficult to obtain than that for the flat strip. An analytic solution based on conformal mapping of this geometry would require inverting the Schwarz-Christoffel transform<sup>6,7,8</sup>

$$z = \int_0^z \frac{dw}{\sqrt{(1-w^2)(k^2-z^2)}} \quad (26)$$

which maps the lower half plane to the outside of a rectangle. An analytic solution of this form would not be useful for gaining physical insight.

The 2D simulation assumes a mirror symmetry about the x axis and about the y axis as shown in Figure 6. The simulation solves for  $N_x$  ( $N_y$ ) wires equally spaced over the half of horizontal (vertical) surface of the rectangular bar in the first quadrant, where  $N_x = \text{int}[N(L/h) + 1/2]$  and  $N+1 = N_x + N_y$  due to the wire at the corner that is part of both the horizontal and vertical surfaces. This choice of  $N_x$  and  $N_y$  ensures that  $dx \sim dy$ .

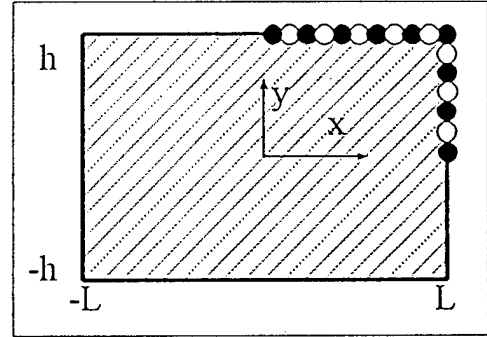


Figure 6. Rectangular bar geometry.

Since this only covers a quarter of the surface of the bar, the first equation is

$$\sum_{i=1}^N \mathbb{I}_i = \frac{I}{4} \quad (27)$$

The boundary condition is enforced at  $N_x - 1$  positions on the horizontal surface as

$$\sum_{i=1}^N \mathbb{I}_i \left[ \frac{x_j - u_i}{(x_j - u_i)^2 + (y_j - v_i)^2} + \frac{x_j + u_i}{(x_j + u_i)^2 + (y_j - v_i)^2} + \frac{x_j - u_i}{(x_j - u_i)^2 + (y_j + v_i)^2} + \frac{x_j + u_i}{(x_j + u_i)^2 + (y_j + v_i)^2} \right] = 0 \quad (28)$$

and at  $N_y - 1$  positions on the vertical surface as

$$\sum_{i=1}^N \mathbb{I}_i \left[ \frac{y_j - v_i}{(x_j - u_i)^2 + (y_j - v_i)^2} + \frac{y_j + v_i}{(x_j - u_i)^2 + (y_j + v_i)^2} + \frac{y_j - v_i}{(x_j + u_i)^2 + (y_j - v_i)^2} + \frac{y_j + v_i}{(x_j + u_i)^2 + (y_j + v_i)^2} \right] = 0 \quad (29)$$

where the BC's are enforced at  $x_j, y_j$  and the wires are located at  $u_i, v_i$ .

The analytic result for the flat strip is compared to the solutions to this set of equations for  $N=100$  for  $L/h=1, 10$  in Figure 7. The current density is plotted with respect to the displacement along the surface of the conductor (s) in units of  $L$ . The plot continues  $h/L$  beyond the end of the horizontal surface.

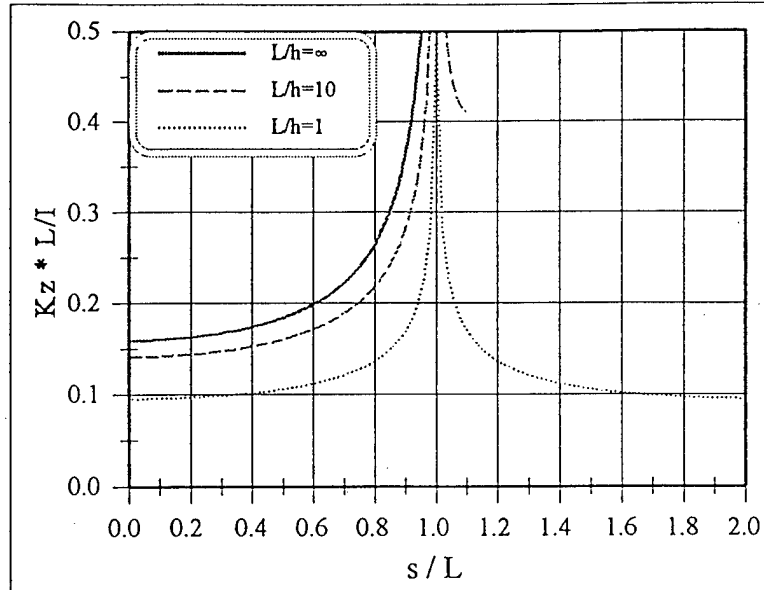


Figure 7. Current distributions for rectangular rods with  $L/h=\infty, 10, 1$ .

The current density has an infinite peak at the sharp corners of the rectangle but the peak is narrower than for the flat strip. This is analogous to the infinite charge density at sharp edges in electrostatics. This suggests that rounding the corners of the rectangular bar would remove the singularities in the current density.

The simulation was also run with the end of the rectangle rounded to a half-circle. One of the wires was placed at the corner where the flat and rounded surfaces connect to avoid having a BC at this discontinuity.

These results for rounded and squared rectangular rods with  $L/h=10$  are compared to the constant current density of a circular rod ( $L/h=1$ ) in Figure 8.

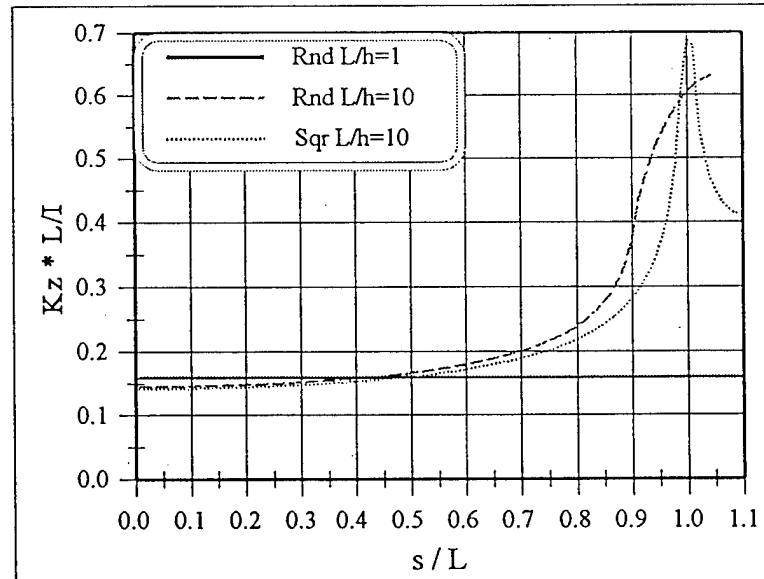


Figure 8. Current distributions for rounded and squared rectangular rods with  $L=10h$ .

### IX. Bi-Plate, Parallel Plate Conductors

The simplest parallel plate configuration is a flat strip carrying a current  $I$  in the  $z$  direction and a second strip with a separation  $2H$  carrying the same current in the opposite direction, as shown in Figure 9. This geometry is symmetric about the  $y$  axis and anti-symmetric about the  $x$  axis.

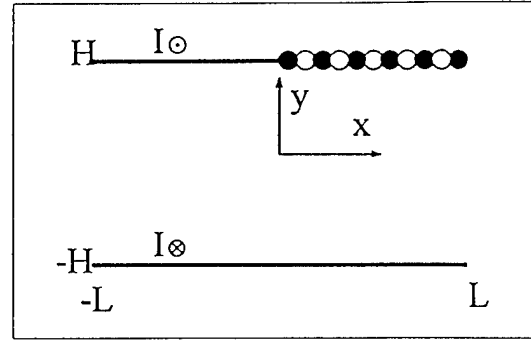


Figure 9. Flat-strip pair geometry.

The 2-D simulation solves for  $N$  wires evenly spaced over half the length of one of the conductors. Since this only covers half of one of the strips, the first equation is

$$\sum_{i=1}^N I_i = \frac{I}{2} \quad (30)$$

The boundary condition is enforced at  $N$  positions on the horizontal surface as

$$\sum_{i=1}^N I_i \left[ \frac{1}{x_j - u_i} + \frac{1}{x_j + u_i} - \frac{x_j - u_i}{(x_j - u_i)^2 + 4H^2} - \frac{x_j + u_i}{(x_j + u_i)^2 + 4H^2} \right] = 0 \quad (31)$$

where the wires on the other strip carry current in the opposite direction.

The results of this calculation for  $N=100$  are compared with the analytic solution for a single flat strip in Figure 10. The current distribution becomes more uniform as the separation goes to zero. The width of the current-density spike seems to be proportional to the separation.

How small this separation can be in experiments is limited by how well these strips can be insulated from each other in a vacuum. For experiments on HAWK, this limit seems to be in the range of  $2H \sim 2-3$  cm.

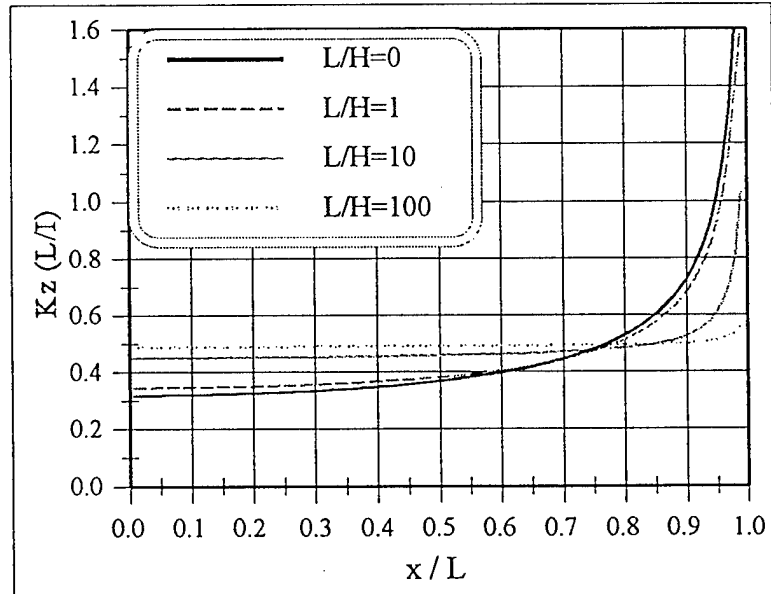


Figure 10. Current distribution of single flat-strip and pairs with different separations.



For the conducting surfaces of the surrounding vacuum chamber to be considered a small perturbation on the fields created by this pair of strips, their width must be smaller than the radius of the vacuum chamber ( $2L < R$ ). Experiments in HAWK's vacuum chamber are limited to aspect ratios of  $L/H < 10$ . A larger vacuum chamber would be of little use in improving the aspect ratio, because the width is also limited by the need to maintain high current densities in the switch plasma for the switch to open correctly.

### X. Triple-Plate

A more symmetric parallel plate geometry is the triple-plate with one flat strip carrying current  $I$  in the  $z$  direction and two other flat strips at  $y = \pm H$  each carrying half the current ( $I/2$ ) back in the negative  $z$  direction, as shown in Figure 11. This geometry is symmetric about the  $x$  axis and about the  $y$  axis.

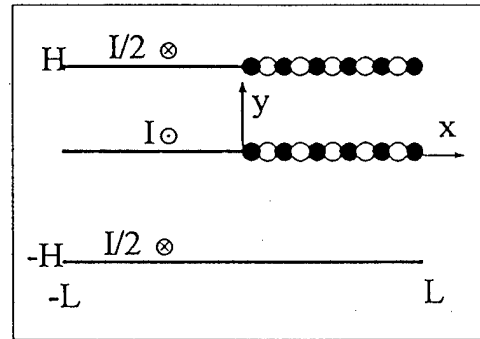


Figure 11. Triple-plate geometry.

The 2-D simulation solves for  $N$  wires evenly spaced over half the length of the inner conductor and over half of the top conductor. This requires two normalization equations

$$\sum_{i=1}^N I_i = \frac{I}{2} \quad \text{and} \quad \sum_{i=N+1}^{2N} I_i = -\frac{I}{4}, \quad (32)$$

where the first  $N$  wires are on the inner surface and the second  $N$  wires are on the top plate. This ordering of the currents makes the matrix more diagonal, reducing the need for pivoting in the linear equation solver. The boundary condition is enforced at  $N-1$  positions on the inner surface as

$$\sum_{i=1}^N I_i \left[ \frac{1}{x_j - u_i} + \frac{1}{x_j + u_i} \right] + 2 \sum_{i=N+1}^{2N} I_i \left[ \frac{x_j - u_i}{(x_j - u_i)^2 + H^2} + \frac{x_j + u_i}{(x_j + u_i)^2 + H^2} \right] = 0, \quad (33)$$

and on the outer surface as

$$\sum_{i=1}^N I_i \left[ \frac{x_j - u_i}{(x_j - u_i)^2 + H^2} - \frac{x_j + u_i}{(x_j + u_i)^2 + H^2} \right] + \sum_{i=N+1}^{2N} I_i \left[ \frac{1}{x_j - u_i} + \frac{1}{x_j + u_i} + \frac{x_j - u_i}{(x_j - u_i)^2 + 4H^2} + \frac{x_j + u_i}{(x_j + u_i)^2 + 4H^2} \right] = 0. \quad (34)$$

The results of this calculation for  $N=100$  and  $L/H=5$  are compared with the current distribution of a bi-plate with  $L/H=10$  in Figure 12. In both cases the separation between plates with opposite current directions is  $H=L/5$ .

There is only a very minor difference among the three plots. The triple-plate geometry is effectively two bi-plates stacked with the center plates merged into

one. This halves the current density on both surfaces relative to a single bi-plate, but has three-dimensional symmetry advantages that will be describes in section XII.

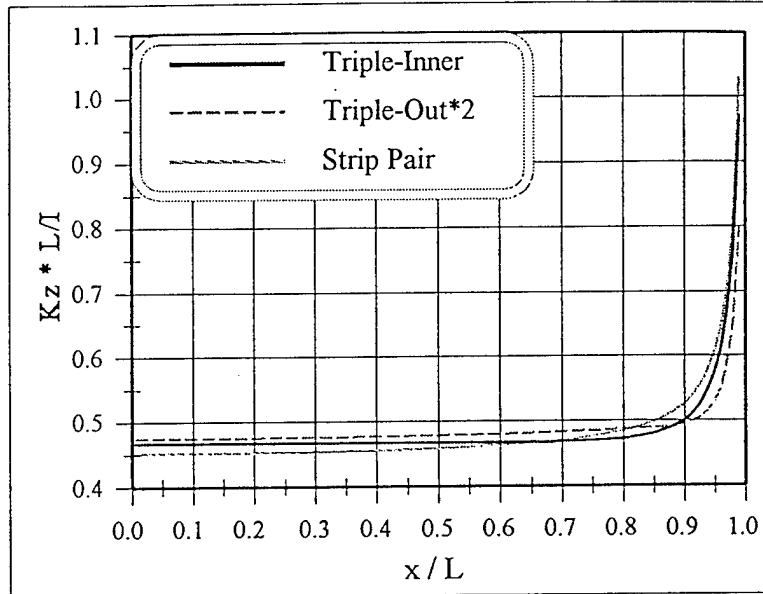


Figure 12. Current distribution on inner and 2\* outer surfaces of triple-plate ( $L/h=5$ ) and on bi-plate ( $L/h=10$ ).

## XI. Rectangular Coax

A geometry more like circular coax is the rectangular coax (aka tri-plate) with one flat strip,  $2L$  wide, carrying current  $I$  in the  $z$  direction and a surrounding rectangular box with vertical spacing  $h$  and horizontal spacing  $\ell$  carrying the same current back in the negative  $z$  direction, as shown in Figure 13. This geometry is symmetric about the  $x$  axis and about the  $y$  axis.

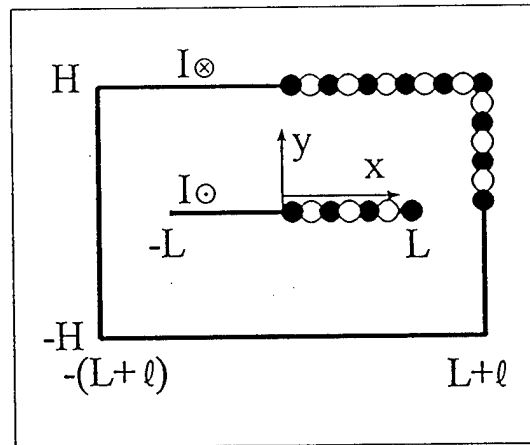


Figure 13. Rectangular-coax geometry.

The 2-D simulation solves for  $N$  wires evenly spaced over half the length of the inner conductor and over the top-right corner of the outer conductor. This requires two normalization equations

$$\sum_{i=1}^N I_i = \frac{I}{2} \quad \text{and} \quad \sum_{i=N+1}^{2N} I_i = -\frac{I}{4}, \quad (35)$$

where the first  $N$  wires are on the inner strip and the second  $N$  wires are on the outer conductor. This ordering of the currents makes the matrix more diagonal, reducing the need for pivoting in the linear equation solver. The boundary condition is enforced at  $N-1$  positions on the inner surface as

$$\sum_{i=1}^N \mathbb{I}_i \left[ \frac{1}{x_j - u_i} + \frac{1}{x_j + u_i} \right] + 2 \sum_{i=N+1}^{2N} \mathbb{I}_i \left[ \frac{x_j - u_i}{(x_j - u_i)^2 + v_i^2} + \frac{x_j + u_i}{(x_j + u_i)^2 + v_i^2} \right] = 0, \quad (36)$$

where  $v_i$  is the vertical position of the wire on the outer conductor. On the horizontal part of the outer surface ( $j < N_x$ )

$$\sum_{i=1}^{2N} \mathbb{I}_i \left[ \frac{x_j - u_i}{(x_j - u_i)^2 + (y_j - v_i)^2} + \frac{x_j + u_i}{(x_j + u_i)^2 + (y_j - v_i)^2} + \frac{x_j - u_i}{(x_j - u_i)^2 + (y_j + v_i)^2} + \frac{x_j + u_i}{(x_j + u_i)^2 + (y_j + v_i)^2} \right] = 0, \quad (37)$$

and on the vertical surface ( $j \geq N_x$ )

$$\sum_{i=1}^{2N} \mathbb{I}_i \left[ \frac{y_j - v_i}{(x_j - u_i)^2 + (y_j - v_i)^2} + \frac{y_j - v_i}{(x_j + u_i)^2 + (y_j - v_i)^2} + \frac{y_j + v_i}{(x_j - u_i)^2 + (y_j + v_i)^2} + \frac{y_j + v_i}{(x_j + u_i)^2 + (y_j + v_i)^2} \right] = 0, \quad (38)$$

where there are  $N_x$  ( $N_y$ ) wires on the horizontal (vertical) surface and  $N = N_x + N_y - 1$  due to the wire at the corner which is part of both surfaces of the outer conductor.

The results for a vertical separation of  $H=L/5$ , and horizontal separations of  $\ell=L$ ,  $L/10$  are compared to those for a bi-plate with the same vertical separation  $H=L/5$  in **Figure 14**. The current densities are plotted with respect to the displacement along the surfaces from their positive intercept with the  $x$  axis, in units of the inner conductor's half width  $L$ .

The current distribution on the inner conductor of the

rectangular coax is almost identical to that of the bi-plate for horizontal separations greater than vertical separation ( $\ell > H$ ). As seen in **Figure 14**, even when  $\ell = H/2$  there is little difference from the bi-plate current density.

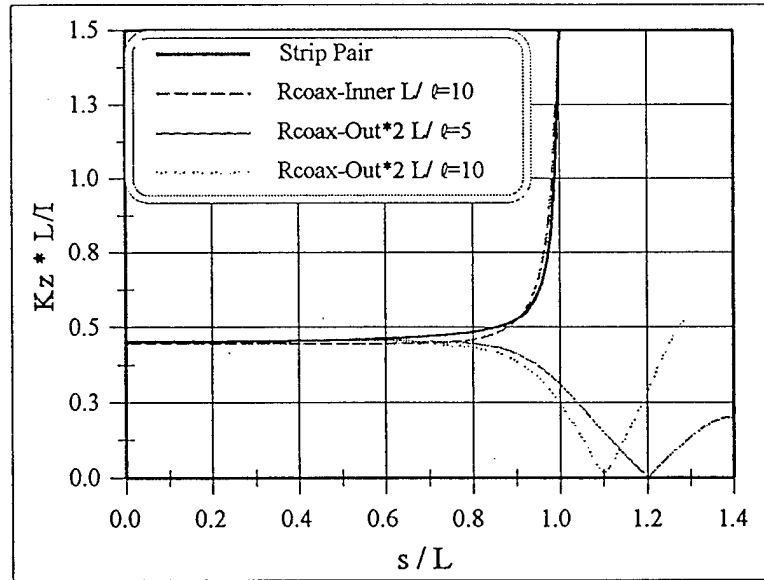


**Figure 14.** Current distribution on inner and 2\* outer surfaces of rectangular-coax with  $H/L=5$  and on bi-plate with  $H=L/10$ .

For small horizontal separations, the current density on the inner conductor is more sharply peaked at the edge for the rectangular coax than for the bi-plate. As with the single flat strip, the current on the edge must balance the vertical components of the magnetic field due to all of the current to the left. In the rectangular coax, the edge current must also balance the field due to currents to the right which are in the opposite direction.

The current density on the outer surface mirrors that of the inner conductor until slightly to the right of the inner conductor's edge where it goes to zero as it approaches the corner. The current on the vertical surface of the outer conductor then rises slowly as it reaches the vertical position of the inner conductor, mirroring the inner conductor in the vertical plane as in the horizontal. For the larger horizontal separation, the peak current density on the vertical face of the outer conductor is smaller.

## XII. 3D Considerations

The analysis above is two dimensional, concerning how the current is delivered to the plasma in a POS. The region in which plasma is introduced requires a full three-dimensional analysis which is beyond the scope of this document. This section presents a few hand-waving arguments about how the current delivered to the plasma will redistribute in the plasma and how this current distribution affects the switch dynamics.

There are two idealizations about how the plasma is introduced into the switch. In both cases, we will assume that the plasma's thickness in the power-flow ( $z$ ) direction is small compared to the vertical separation of the switch ( $H$ ). We will further assume that the plasma is a perfect conductor. The first idealization is that the plasma is a rectangular sheet conductor with a width comparable to that of the inner conductor of the switch ( $L$ ); we will refer to this

idealization as the parallel-plasma model, as illustrated in Figure 15. The second, competing, idealization is that the plasma sheet is uniform throughout the switch, making contact with all conducting surfaces of the switch; we shall refer to this as the coax-plasma model, as illustrated in

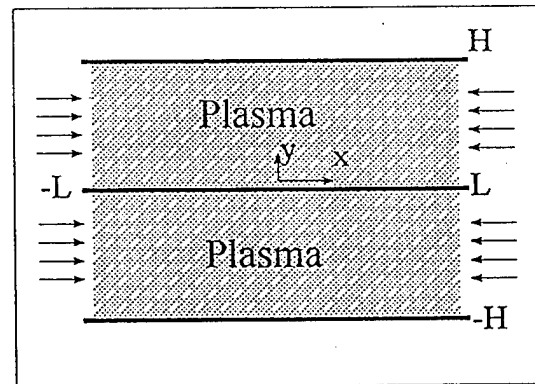


Figure 15. Parallel-plasma model.

**Figure 16.**

The main advantages of the parallel-plasma model are that diagnostics of the plasma are not corrupted by edge effects of plasma outside of the switch region. The main disadvantage is that the edge of the plasma is subject to pinching forces that can change the width of the plasma in the  $x$  ( $\theta$ ) direction during the conduction phase of switch operation. This is thought to disrupt the switch plasma and may be the main reason that the switch does not operate as well as the circular-coax POS.

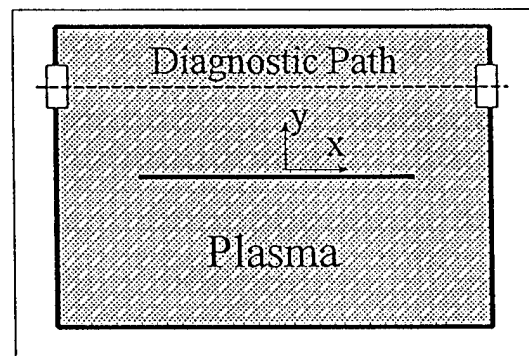
The 2D magnetostatic analysis predicts that the current density is strongly peaked on the outer edges of the plates of bi-plate and triple-plate geometries. It is likely that this will translate into similar current density peaks on the edges of the plasma, exacerbating the pinching.

By constricting the inner and outer conductors to a small horizontal width, shortly before the switch region, the current delivered to the switch plasma can be concentrated more toward the middle of the switch region. Unfortunately, this may also reduce the uniformity of the current density away from the edges.

The pinching forces can be reduced, relative to a bi-plate, by using a triple plate geometry because the  $z$  component of the magnetic field generated by the plasma below the inner conductor partially cancels that due to the plasma above the inner conductor at the edge of the plasma. Unfortunately the triple plate geometry also halves the current density in the plasma and doubles the number of plasma sources required, relative to a bi-plate.

The pinching-force effects may also be balanced by increasing the plasma density near the edge of the plasma sheet. Preliminary bi-plate experiments on HAWK with smaller plasma source separations nearer the edge of the plasma sheet still showed evidence of pinching.

The main advantages of the coax-plasma model are that there are no plasma edges and no pinching forces (at least until the switch starts to open and a gap forms in the plasma.) The main disadvantage is that the switch may not open the plasma that is to the left and right of the inner conductor. The horizontal separation may be chosen to reduce this possibility, but the large area in the corner of the outer conductor with

**Figure 16.** Coax-plasma model.

low current density will add uncertainties to the diagnostics which interrogate the switch plasma.

### XIII. Conclusions

Based on 2-D magnetostatics and some 3-D intuition, the best parallel plate configuration seems to be a triple-plate with a plasma sheet with approximately the same width as that of the switch plates. The plate separation should be as close as possible (~3cm) and the plates should be as wide as possible (~30cm) and still maintain a current density high enough for switch operation. The plates should be constricted down to a narrow neck shortly before the switch region. How narrow this neck should be and how close it should be to the switch plasma will have to be determined experimentally.

---

### REFERENCES

1. J. D. Jackson, Classical Electrodynamics, 2nd ed. (John Wiley & Sons, Inc., New York, 1975) pp. 190-1922.
2. M. D. Greenberg, Foundations of Applied Mathematics, (Prentice-Hall, Inc., New Jersey, 1978) p. 302.
3. Z. Nehari, Conformal Mapping, (Dover Publications, Inc., New York, 1975) pp. 266-271.
4. E. B. Saff, A. D. Snider, Fundamentals of Complex Analysis for Mathematics, Science, and Engineering, (Prentice-Hall, Inc., New Jersey, 1976) pp. 360-262.
5. J. M. H. Olmsted, Advanced Calculus, (Prentice-Hall, Inc., New Jersey, 1961) pp. 95-96.
6. Z. Nehari, Conformal Mapping, (Dover Publications, Inc., New York, 1975) p. 280.
7. E. B. Saff, A. D. Snider, Fundamentals of Complex Analysis for Mathematics, Science, and Engineering, (Prentice-Hall, Inc., New Jersey, 1976) p. 341.
8. L. V. Ahlfors, Complex Analysis, 2nd ed. (McGraw-Hill Book Co., New York, 1966) p. 230.

TITLE:       **REFRACTIVE INDEX OF BOUND ELECTRONS**

AUTHORS:   **R. Riley, D. Hinshelwood, B. Weber**

DATE:       **May 12, 1994**

**ABSTRACT:**

A two-color interferometer (developed by SLR) measures the line-integrated particle densities of electrons and neutrals in plasmas produced on the HAWK pulsed-power facility at NRL. This method assumes the neutrals have the same refractive properties as air. Under this assumption, data collected near metal surfaces sometimes imply negative neutral densities.

Refractive indices are calculated from the line spectra of a number of species likely to be found in the plasma. These values are compared with tabulated values measured at STP. The refraction due to neutrals in their ground state is roughly constant with respect to wavelength for  $1100 \text{ nm} > \lambda > 400 \text{ nm}$  and is a small fraction ( $< 10\%$ ) of that due to free electrons.

Excited ions with radiation lines nearly resonant with the probing beam, such as  $H_{\alpha}$  at  $6563 \text{ \AA}$  or excited carbon, are strongly refractive. Some of these radiation lines are between the wavelengths of the two lasers probing the plasma and provide a reasonable explanation for the anomalous results based on assuming the neutrals refract as air.

The Saha calculated excitation and ionization, which assumes local thermodynamic equilibrium, predicts a small fraction of excited neutral hydrogen. Even a small density of hydrogen in this excited state will have a noticeable effect on the inferred neutral density. The anomalous refraction due to the  $H_{\alpha}$  line is a small correction to measured electron densities at  $1064$  and  $532 \text{ nm}$  but is a significant effect at  $6328 \text{ \AA}$  (HeNe laser). Excited states of neutral carbon are a more likely explanation due to lower excitation energies.

**THIS REPORT REPRESENTS UNPUBLISHED INTERNAL WORKING  
DOCUMENTS AND SHOULD NOT BE REFERENCED OR DISTRIBUTED**

## I. Introduction

SRL has developed a two-color interferometer to measure the line-integrated particle densities of electrons and neutrals of plasmas. The interferometer measures the change in optical path length caused by traversing the same chord through a plasma probed by a Nd:YAG laser ( $\lambda=1064$  nm) and a frequency-doubled Nd:YAG laser ( $\lambda=532$  nm). The neutral density derived from the data assumes that the neutrals have the same refractive properties as air.

This diagnostic has been used on the HAWK pulsed-power facility at NRL to monitor plasmas with an electron density of  $\sim 10^{22}$  m<sup>-3</sup>. The plasma ejected by flashboards impacts with an aluminum plate perpendicular to its direction of travel. Data collected by this diagnostic at 5 mm from the surface of the Al plate give negative densities under the assumption that the neutrals refract as air.

The refraction of neutrals and ions of elements likely to be found in the plasma are calculated based on their line spectra at a number of excitations. This tests the assumption that neutrals refract as air and shows the implications when this assumption is not valid.

## II. Refraction Calculation Method

A plane wave with an angular frequency  $\omega$  (rad/s) propagating through a plasma will be refracted by the free electrons as<sup>1</sup>

$$\eta_e - 1 \approx - \frac{e^2}{2 \epsilon_0 m_e} \frac{n_e}{\omega^2}, \quad (1)$$

where  $\eta_e = c/v$  is the index of refraction,  $e^2/(2\epsilon_0 m_e) \approx 1591$  m<sup>3</sup>/s<sup>2</sup> and  $n_e$  is the particle density of free electrons in the plasma in m<sup>-3</sup>.

Ignoring attenuation, the refractive index due to bound electrons can be calculated based on their line spectra as<sup>2</sup>

$$\eta_b - 1 \approx \frac{e^2}{2 \epsilon_0 m_e} \sum_i n_i \sum_j \frac{f_{ij}}{\omega^2 - \omega_{ij}^2}, \quad (2)$$



where  $n_i$  is the density of ions in  $\text{m}^{-3}$  with an electron excited to the  $i$ 'th state, and  $\omega_{ij}$ ,  $f_{ij}$  are the angular frequency and line strength of the transition from the  $i$ 'th to the  $j$ 'th state. The line strengths of each excited state  $i$  must satisfy the summation rule<sup>3</sup>

$$\sum_j f_{ij} \equiv Z_i \quad (3)$$

where  $Z_i$  is the number of electrons bound to the ion. This sum includes transitions from inner shells and forbidden transitions which do not contribute to refraction. For excited states, the line strengths of absorption and emission are related as

$$f_{ij} = -\frac{g_i}{g_j} f_{ji} \quad (4)$$

where  $g_i$  is the degeneracy of the  $i$ 'th state.

Typically only the line spectra of the valence electrons is used and  $Z_i$  is taken to be the number of identical electrons in the outermost shell. As a computational convenience, only a finite number of lines are used and a line with energy equal to the ionization potential is given a line strength which satisfies the summation rule

$$f_{i,\infty} \equiv Z_i - \sum_{j=0}^n f_{ij} \quad (5)$$

The results given below assume that  $Z_i \approx 1$  is taken to be the smallest integer greater than the sum of the line strengths used.

The refraction due to bound electrons as a fraction of the refraction due to free electrons is

$$\frac{\eta_b - 1}{1 - \eta_e} \approx \sum_i \frac{n_i}{n_e} \sum_j \frac{f_{ij}}{\omega_{ij}^2 / \omega^2 - 1} \quad (6)$$

### III. Neutral Hydrogen vs. Free Electron Refraction

As an example of this method, the line spectrum used to calculate the refraction of hydrogen is given in Table 1 for its ground and first excited states<sup>4</sup>. The photon wavelength in Å, energy in eV and line strengths are given for the first lines of the spectrum. The last line corresponds to the full ionization energy and is given the line strength needed to satisfy the summation rule. The degeneracies of the states are also given. The first line of the spectrum of the first excited state is for the de-excitation to the ground state.

Table 1 Hydrogen line spectra of the ground and first excited states.

$\lambda_{0J}$ (Å)	$E_{0J}$ eV	$g_j$	$f_{0J}$	$\lambda_{1J}$ (Å)	$E_{1J}$ eV	$g_j$	$f_{1J}$
1215.67	10.199	8	0.4162	1215.67	10.199	2	-0.2081
1025.72	12.088	18	0.0791	6562.80	1.889	18	0.6407
972.537	12.749	32	0.02899	4861.32	2.550	32	0.1193
949.743	13.055	50	0.01394	4340.46	2.856	50	0.04467
937.803	13.221	72	0.007799	4101.73	3.023	72	0.02209
930.748	13.321	98	0.004814	3970.07	3.122	98	0.01270
926.226	13.386	128	0.003183	3889.05	3.188	128	0.008036
923.150	13.431	162	0.002216	3835.38	3.233	162	0.005429
920.963	13.463	200	0.001605	3797.90	3.265	200	0.003851
919.352	13.486	242	0.001201	3770.63	3.288	242	0.002835
918.129	13.504	288	0.000921	3750.15	3.306	288	0.002151
917.181	13.518	338	0.000723	3734.37	3.320	338	0.001672
916.429	13.529	392	0.000577	3721.94	3.331	392	0.001326
911.29	13.595	2	0.4388	3645.2	3.396	2	0.3413

The plots in Figure 1 show the refraction by atomic hydrogen in its ground and first excited states divided by the refraction by an equal density of free electrons over the visible and near IR range of wavelengths. The wavelengths of three laser lines (532, 633, and 1064 nm) are marked by vertical lines. Ground state hydrogen produces a small fraction of the refraction by free electrons. The  $H_\alpha$  line at 6563 Å of the first excited state of hydrogen has a refraction comparable to that of free electrons at 532 and 1064 nm and eight times as large at 633 nm. The refraction at 532, 633 nm has the same sign as electrons unlike the refraction at 1064 nm which is the same sign as the ground state.

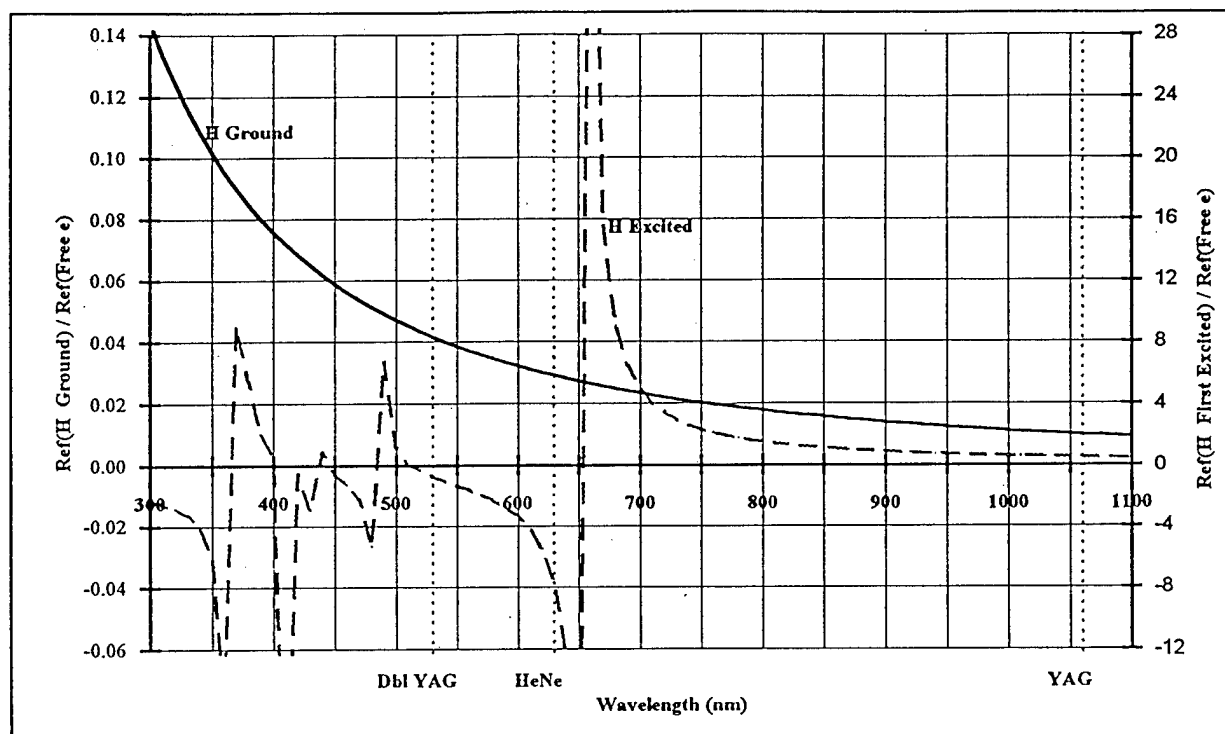


Figure 1 Refraction of visible light by atomic hydrogen in its ground and first excited states as a fraction of the refraction by free electrons.

#### IV. Comparison with Measured Values of Refraction

To benchmark this calculation method, calculated refractions are compared with the measured values tabulated by Gardiner, *et. al.*<sup>5</sup>. The calculated and measured refractive index of visible light for a number of gases at STP ( $T=273$  K,  $P=1.013 \times 10^5$  Pa,  $n=2.69 \times 10^{25}$  m<sup>-3</sup>) are given in Table 2. The refraction of molecules were taken as a simple sum of the refractions of the constituent atoms. The agreement between the measured and calculated refractions is within 25%. Ground states are assumed at STP. No reference is given for measured refraction of excited states and ions.

Table 2 Index of refraction of a number of selected gases for 600-nm light at STP.

Gas	$\eta_{\text{Meas}}$	$\eta_{\text{Calc}}$
e <sup>-</sup>	0.995680	0.995664
Ar	1.00028	1.00025
CO	1.00033	1.00033
He	1.00003	1.00003
H	1.00013	1.00014
N <sub>2</sub>	1.00029	1.00026
O	1.00027	1.00021

A plasma will contain a number of elements at various excitation levels and ionization states. The refractive index of selected elements and ions in their ground and first excited states is given in **Table 3** at the laser lines of interest. The table also contains the number of lines and summation of line strengths used to calculate these refractions. The energy of each state is also given.

For the majority of excited and ionization states the refractive indices are very flat over the visible spectrum and are within a factor of two of air ( $\sim N_2$ ). The notable exceptions are highlighted and are much more refractive and are negative at one or more of the laser frequencies.

### V. Local Thermodynamic Equilibrium and Saha Calculations

The levels of ionization of ions in a plasma can be calculated based on Saha equilibrium if the plasma is in local thermodynamic equilibrium (LTE). LTE requires that the densities of excited states and ionization states be in thermal equilibrium with the free electrons. Electron collisions with ions maintain the populations of these states. LTE does not require the radiation to be thermal (i.e., blackbody). A plasma can be assumed to be in LTE if it satisfies the inequality<sup>6</sup>

$$n_e > 10^{19} \sqrt{T_e} (\Delta E)^3 \text{ (m}^{-3}\text{)} , \quad (7)$$

where  $\Delta E$  is the energy difference in eV between states and  $T_e$  is the electron temperature in eV.

For an electron density of  $10^{22} \text{ m}^{-3}$  and an electron temperature of 2 eV, only transitions of energies  $\Delta E < 9 \text{ eV}$  can be considered to be in LTE. This may seem to exclude the upper excited states of many elements such as hydrogen with a ground state ionization potential of 13.6 eV. In the presence of a free electron density comparable to the expected ion density, the populations of the upper excited states can be thought of as in equilibrium with the free electrons rather than the ground state of the ion.

The particle densities of ionization states in a plasma in LTE can be calculated by the Saha equation<sup>7</sup>

Table 3 Refraction of a number of selected excitations at laser wavelengths ( $n=10^{22} \text{ m}^{-3}$ ).

Ion	IP eV	Ex. eV	Lines	$\Sigma f$	$Z_{\text{eff}}$	$\eta_{532} - 1$	$\eta_{633} - 1$	$\eta_{1064} - 1$
e <sup>-</sup>						-1.27e-06	-1.79e-06	-5.07e-06
H-I	13.595	0	13	0.56	1	5.26e-08	5.19e-08	5.09e-08
		10.205	13	0.65	1	-1.02e-06	-1.56e-05	2.47e-06
		12.088	10	0.82	1	-9.49e-07	4.05e-06	-1.18e-05
He-I	24.580	0	11	0.47	1	1.29e-08	1.28e-08	1.28e-08
		20.612	8	0.30	1	2.03e-06	9.66e-07	6.44e-07
C-I	11.264	0	11	0.68	1	7.53e-08	7.37e-08	7.15e-08
		1.264	9	0.20	1	8.65e-08	8.46e-08	8.18e-08
		2.683	5	0.21	1	1.31e-07	1.26e-07	1.19e-07
		4.183	3	0.13	1	1.47e-06	1.42e-06	1.35e-06
		7.485	7	0.76	1	-1.28e-05	-2.55e-05	-2.41e-03
		7.685	9	0.38	1	-6.04e-06	-1.04e-05	-1.68e-04
		7.946	2	-0.05	1	1.29e-06	1.02e-05	7.49e-06
		8.537	4	0.92	1	-1.31e-05	-2.67e-05	-9.29e-05
		8.644	3	0.97	1	-9.10e-06	-1.56e-05	1.21e-03
		8.771	2	0.66	1	2.31e-05	1.95e-06	-1.15e-04
		8.849	3	-0.06	1	9.54e-05	3.56e-05	-7.16e-05
C-II	24.376	0	5	1.15	2	6.27e-08	6.20e-08	6.09e-08
		5.336	1	0.16	2	4.31e-08	4.29e-08	4.25e-08
		9.286	2	0.31	2	7.60e-08	7.52e-08	7.40e-08
C-III	47.864	0	3	1.08	2	4.05e-08	4.01e-08	3.95e-08
		6.499	4	0.83	2	2.68e-08	2.66e-08	2.62e-08
		12.690	5	0.86	2	1.54e-07	1.45e-07	1.33e-07
N-I	14.530	0	2	0.48	1	4.91e-08	4.85e-08	4.76e-08
		2.384	7	0.40	1	5.99e-08	5.90e-08	5.76e-08
		3.576	6	0.21	1	7.17e-08	7.04e-08	6.84e-08
N-II	29.593	0	6	1.05	2	3.60e-08	3.58e-08	3.54e-08
		1.899	5	1.15	2	3.32e-08	3.30e-08	3.28e-08
		4.052	2	0.72	2	2.94e-08	2.96e-08	2.94e-08
O-I	13.614	0	7	0.14	1	4.00e-08	3.96e-08	3.90e-08
		1.967	4	0.14	1	5.34e-08	5.28e-08	5.18e-08
		4.190	1	0.13	1	8.11e-08	7.96e-08	7.73e-08
F-I	17.418	0	15	0.00	0	~7.00e-08	~7.00e-08	~7.00e-08
		12.717	3	0.93	1	-8.96e-6	3.74e-09	5.97e-07
		12.999	3	0.98	1	-2.55e-6	-6.67e-6	4.94e-06
Ar-I	15.755	0	6	0.55	3	9.41e-08	9.34e-08	9.23e-08
		11.548	8	1.09	3	-1.43e-06	-4.51e-06	8.96e-06
		11.624	10	1.08	3	-1.34e-06	-4.26e-06	1.00e-05

$$\frac{n_{i+1}}{n_i} = \frac{z_{i+1}}{z_i} \frac{2}{n_e} \left[ \frac{m_e e T_e}{2 \pi \hbar^2} \right]^{3/2} e^{-\frac{\Delta E_i}{T_e}} \approx \frac{6.04 \times 10^{27}}{n_e} \frac{z_{i+1}}{z_i} T_e^{3/2} e^{-\frac{\Delta E_i}{T_e}} \quad (8)$$

where  $\Delta E_i$  is the ionization potential in eV of an ion in its  $i$ 'th ionization state, and the partition function for the  $i$ 'th ionization state is<sup>8</sup>

$$z_i = g_{i,0} + \sum_{j=1}^n g_{i,j} e^{-\Delta E_{i,j}/T_e}, \quad (9)$$

where  $j$  is the index over excitation states and  $g_{i,j}$  are the statistical weights of the excitation states. A nondegenerate state has  $g=1$  and a free electron has  $g=2$  due to its spin degeneracy. The form of the partition function assumes that the excited states are in thermal equilibrium with the ground state

$$\frac{n_i}{n_0} = \frac{g_i}{g_0} e^{-\Delta E_i / T_e}. \quad (10)$$

## VI. Saha Weighted Refraction.

The plots in **Figure 2** show the refractive indices due to neutral carbon at 532, 633, 1064 nm predicted by Saha equilibrium for electron and carbon ion densities of  $10^{22} \text{ m}^{-3}$  and electron temperatures between 0.5 and 1.5 eV. The refraction of the Nd:YAG IR wavelength (1064 nm) is negative and a strong function of temperature. At higher electron densities the assumption of LTE is more valid and only shifts the critical temperature up by a fraction of an eV.

The refraction due to carbon remains flat at 532 and 663 nm for higher temperatures as the carbon becomes more ionized. This calculation includes the refraction due to all excitations of carbon listed in **Table 3**. The refraction of higher ionizations for an electron density of  $10^{22} \text{ m}^{-3}$  only becomes significant for electron temperatures greater than 2 eV.

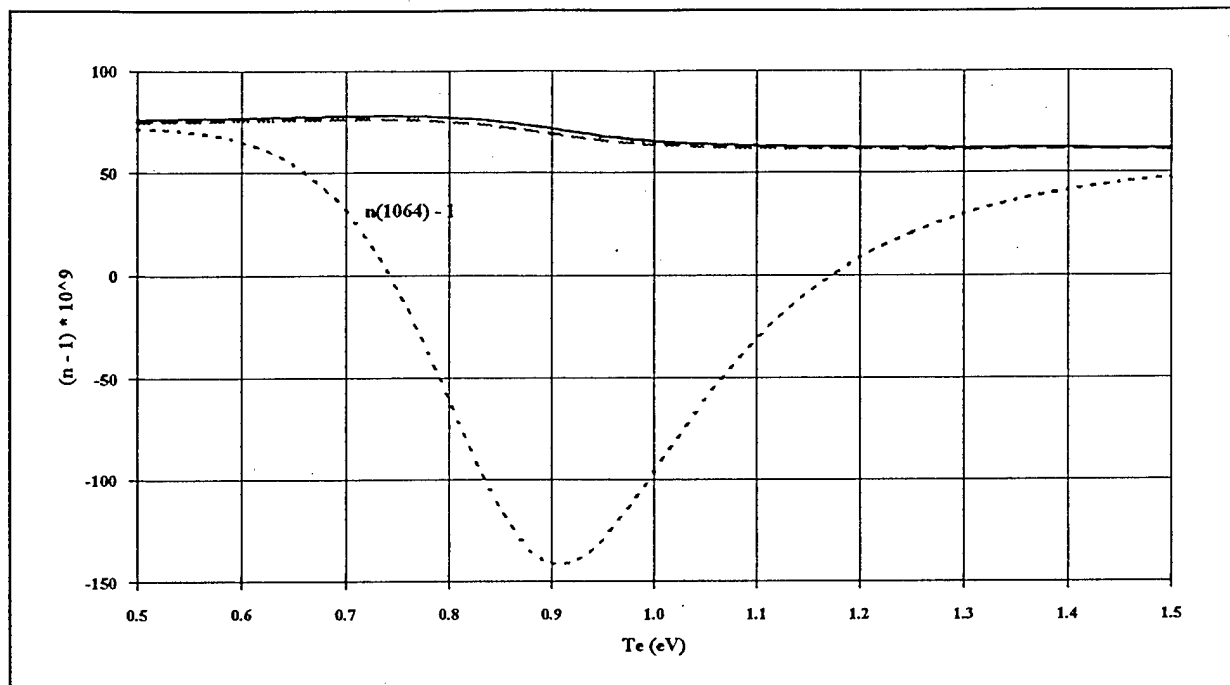


Figure 2 Refraction due to carbon at laser wavelengths based on Saha calculations for  $n_e = n_c = 10^{22} \text{ m}^{-3}$  and  $0.5 \text{ eV} < T_e < 1.5 \text{ eV}$ .

The narrowness of the range of temperatures for which carbon has a refraction significantly different from air at 1064 nm is consistent with the transient nature of the density anomalies recorded by the SLR interferometer on HAWK experiments. This suggests that the plasma striking a metal plate may have its directed kinetic energy thermalized to raise the temperature of the plasma or the plasma may be cooled by coming into thermal contact with the metal.

A similarly weighted refraction for hydrogen shows only a small deviation between the three different laser wavelengths. This is because hydrogen becomes ionized before a significant fraction of the neutral hydrogen is in an excited state.

## VII. Conclusions

This diagnostic may reasonably assume that a low temperature ( $< 0.5 \text{ eV}$ ), low density ( $< 10^{22} \text{ m}^{-3}$ ) plasma refracts as air to differentiate between electron and neutral densities. Under these conditions the electrons tend to be either in the continuum or in ground states of ions or neutrals and

their populations are described by coronal equilibrium. At the other extreme, a fully ionized plasma will have a refraction dominated by the free electrons and negligible bound state contributions.

Within these extremes, some knowledge of the electron temperature and relative densities of the plasma species must be assumed. Using two probing wavelengths requires that the refraction of the bound electrons be known in order to measure ion and electron densities although the electron density is still good to a few percent. The addition of a probe at a third wavelength would only serve to measure the density of one extra excited state.

The most reasonable method would seem to be to limit the number of elements in the plasma to as few as possible and to probe the plasma at wavelengths as far from the resonances of these elements as possible. For a small number of plasma species, the calculated refractive indices (such as given in Table 3) can be used to re-analyze interferometry data to provide consistent (if not unique) densities for the electrons and ions.

#### REFERENCES

1. H. R. Griem, Plasma Spectroscopy (McGraw-Hill Book Co., New York, 1964) p. 12.
2. H. R. Griem, Plasma Spectroscopy (McGraw-Hill Book Co., New York, 1964) pp 42,299.
3. H. R. Griem, Plasma Spectroscopy (McGraw-Hill Book Co., New York, 1964) p. 58.
4. W. L. Wiese, M. W. Smith, and B. M. Glennon, Atomic Transition Probabilities (National Bureau of Standards, 1966)
5. W. C. Gardiner, Jr., Y. Hidaka, and T. Tanzawa, "Refractivity of Combustion Gases", in Combustion and Flame 40, (1981) 213-9.
6. R. McWhirter, in Plasma Diagnostic Techniques, edited by Huddelstone and Leonard (Academic Press, New York, 1965).
7. H. R. Griem, Plasma Spectroscopy (McGraw-Hill Book Co., New York, 1964), p. 137.
8. Y. B. Zel'dovich and Y. P. Raizer, Physics of Shock Waves and High-Temperature Hydrodynamic Phenomena, 1 (Academic Press, New York, 1966), p. 194.



## PULSED POWER PHYSICS TECHNOTE 93-10

TITLE: POSITIVE POLARITY POS OPERATION ON HAWK

Author: D. Hinshelwood and R. Fisher

Date: May 4, 1993

Abstract: This note gives the results from a handful of shots taken in June, 1992 where Hawk was operated in positive polarity. The conduction current as a function of generator delay was compared with that obtained in negative polarity using short circuit loads. A few shots were taken with a diode load. Conduction appears seen to be slightly greater in positive polarity. It is speculated that the apparent, longer conduction time may be related to a greater delay in establishing magnetic insulation between the switch and the load. This issue could be resolved with further experiments and PIC simulations, leading to an increase in our understanding of the POS.

Positive polarity POS operation was investigated with a small number of shots on Hawk in June, 1992. For these shots a 5-cm diam center conductor (anode) was used with a 4.5-cm radial gap in the switch region, i.e., the standard anode rod arrangement for the 10-cm diam center conductor was used. The standard-length configuration was used, with 13-cm-long anode rods connecting the load  $dB/dt$  collar to the switch anode rod assembly. Most of the run consisted of short circuit shots in alternate polarities. Only the usual machine electrical diagnostics were used. Reversing the polarity of Hawk is a simple procedure which requires only that the main and mini-Marx power supply leads be reversed. This run comprised shots 1009-1029 and the data is stored in [HAWK.PLUS].

The first five graphs on the page after next compare generator and load currents for both polarities, at five different generator delays. For each set of shots the delay was the same within the resolution of the data. With these delays the conduction current and time ranged from 250 kA at 300 ns to 670 kA at 1  $\mu$ s. The two load currents are averaged together in these graphs for clarity. Unless noted, both load  $dB/dt$ 's agree fairly well with one another on these shots. At the earliest timing the switch appears to open at the same time on all three shots taken, although a small foot on the load currents in positive polarity causes opening to be delayed. At the next three timings, the switch appears to conduct slightly longer in positive polarity (on two of the positive polarity shots, shot 1024 at 1.6  $\mu$ s and shot 1014 at 2.1  $\mu$ s, the two load  $dB/dt$  signals differed by about 40%). The load currents in positive polarity also show a slight dip before opening, and this dip can almost be imagined to start when the load current begins in negative polarity. For these shots, the rise in switch voltage, associated with switching to the load inductance, also occurs later in positive polarity. At the latest timing, the load current starts at the same time in both polarities (on each shot one of the load  $dB/dt$ 's lost it, so that the actual load currents were larger than shown).. A polarity-dependent foot is also seen on both load current traces.

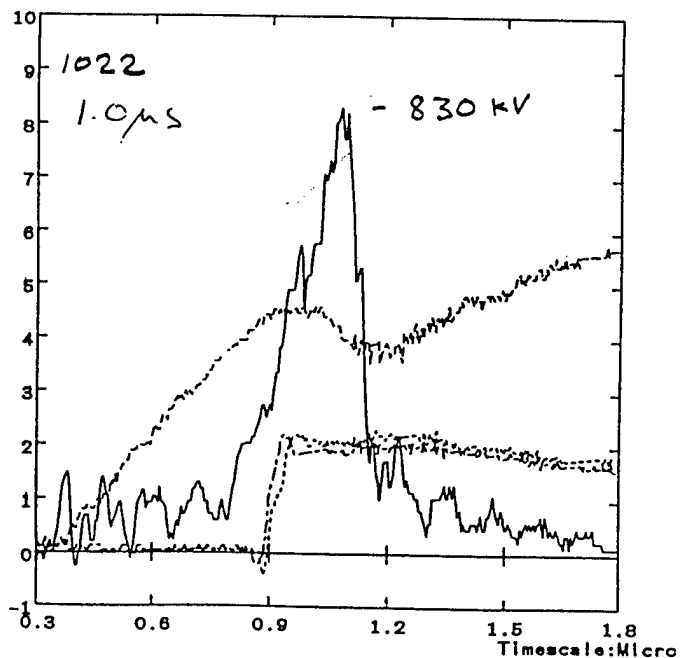
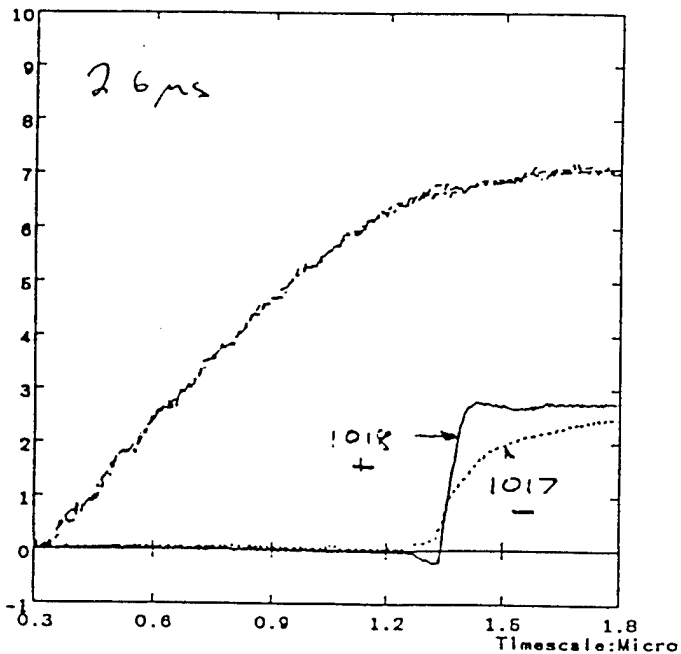
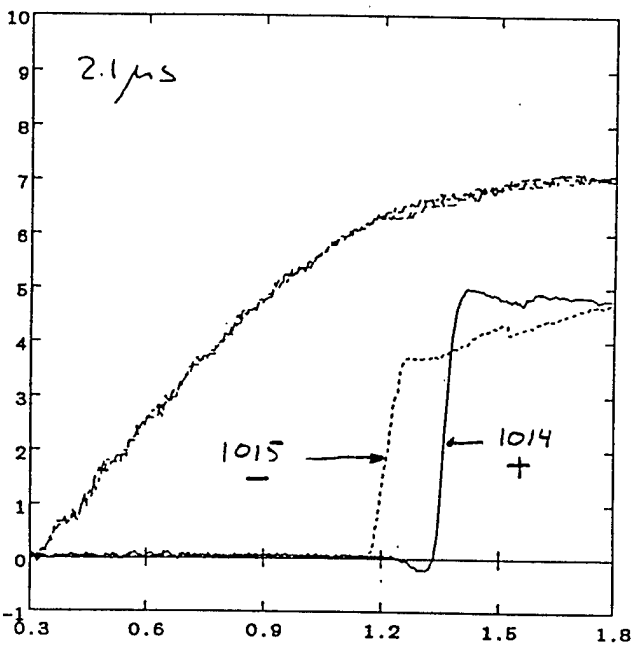
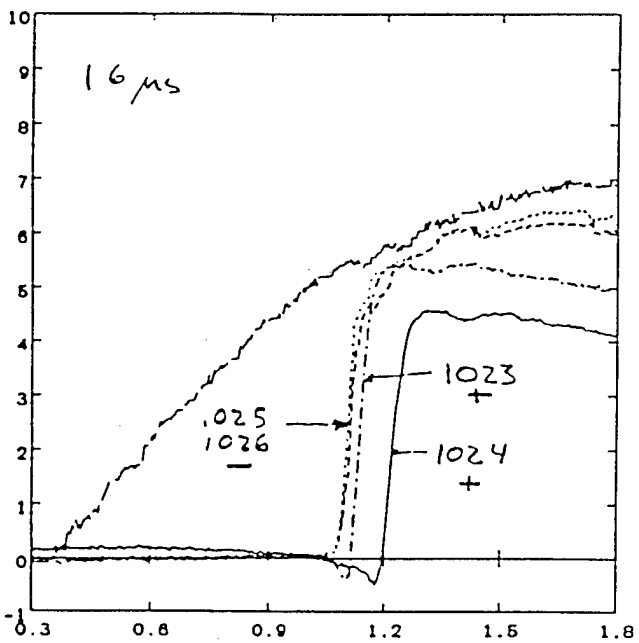
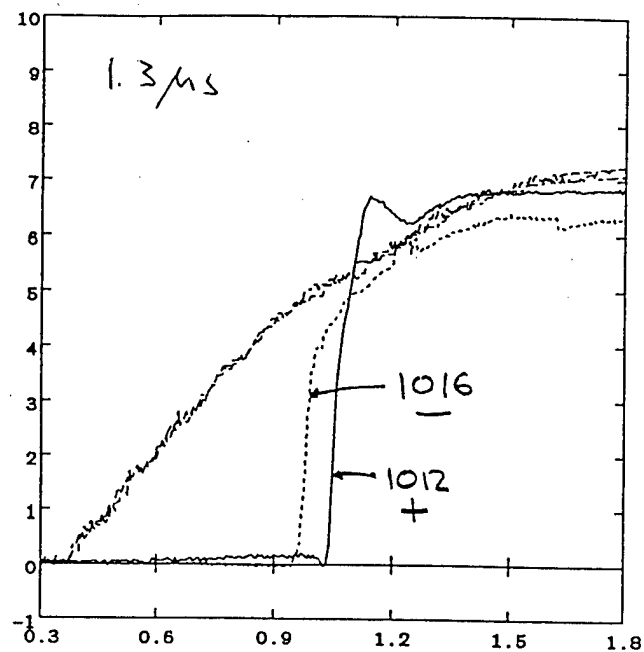
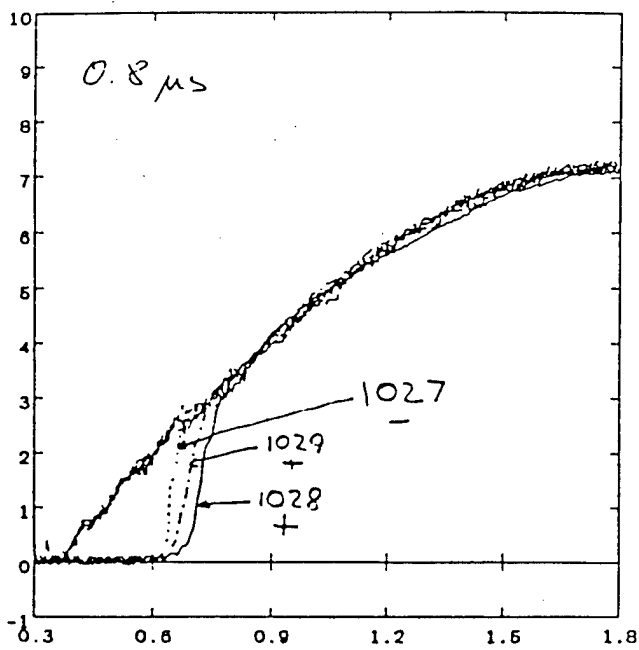
The last graph shows data from one of the few shots with a diode load. The center conductor was terminated in a butt end to form the anode, and another short section of 5-cm-diam hollow tube was installed in the short-circuit plate to form the cathode. The diode gap was about 1 cm. This shot was taken with a rather short delay; two other shots, taken at longer delays, exhibited much lower load impedance. The results from this shot are far from spectacular.

Interpretation of these results is complicated by the fact that in positive polarity the load current monitors are located on the cathode. The data Bruce is taking now show that both the anode and cathode load currents start at the same time. Therefore, the later load currents observed here for positive polarity shots are probably not the result of this monitor asymmetry. On the other hand, we would not expect switch opening in the MHD regime to be polarity dependent. A possible explanation is that in positive polarity there is a greater delay between switch opening and current transfer to the load. This delay is related to the establishment of magnetic insulation between the switch and the load and might well be polarity dependent in the cylindrical geometry of this experiment.

Since the total current into the diode load on shot 1022 was not measured, it is difficult to say whether the system was in the switch- or load-limited regime. Thus, the data here are insufficient to judge positive polarity operation of the switch into a diode

load. Like the dog on his hind legs, however, it is encouraging that the positive polarity switch works at all.

This polarity comparison should be continued with a limited number of shots as part of the current run on Hawk, where both anode and cathode monitors are installed, both immediately past the switch and at the load. If a polarity dependence is observed and can be attributed to phenomena beyond the switch, then the effect of polarity should be studied using PIC simulation. As a minimum, reproducing this effect with simulation would constitute a good benchmarking of the code, and may even lead to a greater understanding of POS operation.



## HIGH POWER PLASMA OPENING SWITCH OPERATION ON HAWK

P.J. Goodrich\*, R.J. Commisso, J.M. Grossmann, D.D. Hinshelwood\*,  
R.A. Riley\*\*, S.B. Swanekamp\*\*\*, and B.V. Weber  
Pulsed Power Physics Branch, Plasma Physics Division  
Naval Research Laboratory, Washington DC 20375

### Abstract

*The Hawk pulsed power generator is used in plasma opening switch (POS) experiments in the 1- $\mu$ s conduction time regime to study long conduction time switch physics. Cathode and anode geometries, especially in the switch region, can have a major impact on switch performance. There is a tradeoff between higher voltage and lower conducted current as the radius of the cathode center conductor is decreased. Tapering the cathode over the switch length has produced the best performance to date: 0.7 TW at 0.75  $\mu$ s conduction times with flashboard plasma sources and 1.6 MV has been generated at 1  $\mu$ s conduction times with cable gun sources. There is a limit on the minimum radial gap in the switch and downstream region below which voltage and current transfer are reduced. Switch performance deteriorates as the anode outer conductor just downstream of the switch, but at the same radius as the switch rods, is extended toward the load. As observed in past experiments, POS performance is independent of the plasma source used (flashboards, cable guns, or gas guns) in a given switch/load configuration. A helical center conductor in the switch region, which increases the total insulating magnetic field by a factor of 2.3, resulted in dramatically degraded switch opening for conduction times greater than 0.35  $\mu$ s.*

### Introduction

The Hawk generator is a 600 nH, 1- $\mu$ F Marx bank that stores 225 kJ with an erected voltage of 640 kV at 80-kV charge to deliver up to 720 kA in 1.2  $\mu$ s to a plasma opening switch (POS). Previous experiments<sup>1</sup> with flashboard plasma sources have identified hydrodynamic plasma distortion as the dominant mechanism that controls much of the POS operation. Maximum load power is determined by an effective gap for magnetic insulation in the POS. Empirically, this gap is limited to about 3 mm in size in Hawk. Above a critical load impedance--the switch limited regime--current is lost between the switch and the load, typically nearer the load, with the

voltage remaining constant; at lower impedance--the load limited regime--the voltage decreases in proportion to the load impedance. Maximum load power is obtained at this critical impedance.

In general, increasing the cathode magnetic field--by conducting more current or decreasing the cathode radius--allows the fixed gap POS to remain insulated at a higher voltage (V~B). However, for a given plasma density, the switch opens earlier for smaller radius cathodes (larger magnetic fields, a consequence of MHD-limited conduction<sup>2,3</sup>). In this manner, up to 2 MV at 0.6  $\mu$ s conduction, with ~0.6 TW load power at 7  $\Omega$  critical impedance, was generated with a 2.5 cm diameter cathode.<sup>4</sup> Using the same plasma delay, the voltage was

850 kV but at  $0.9 \mu\text{s}$  conduction, with 0.4 TW load power at  $1.7 \Omega$  impedance, with a 10 cm diameter cathode.<sup>4</sup>

In this paper, recent Hawk experiments with further modifications to the POS electrode geometry--tapered cathodes, changing the anode downstream of the switch, and a helical center conductor--are discussed. Three plasma sources are used: flashboards (FB), cable guns (CG), and gas guns ( $\text{H}_2$ , He, and Ar).

### Tapered Cathodes

Tapering the cathode center conductor in the switch region optimizes the tradeoff between a higher voltage but a lower conducted current for a given plasma delay as the switch radius is reduced. A larger radius on the generator side allows longer conduction while the smaller radius on the load side, which is probably near the plasma center-of-mass location at opening, generates higher POS voltage.

Figure 1 shows a 10 cm to 5 cm diam cathode taper through the 8 cm length switch. The cathode tip shown here is flared to  $\sim 9.5$  cm diam, one technique used to reduce the load impedance at peak power. Figure 2 is a plot of peak switch voltage as a function of load impedance at peak power on shots with a 10 to

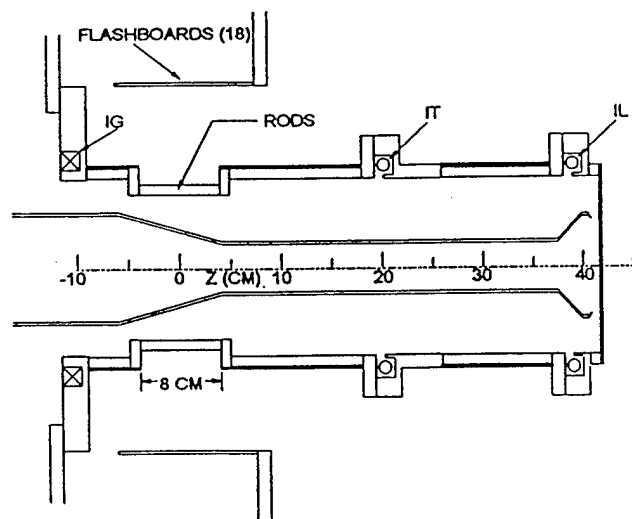


Figure 1. Hawk POS configuration with a 10 to 5 cm diam cathode taper in the switch region.

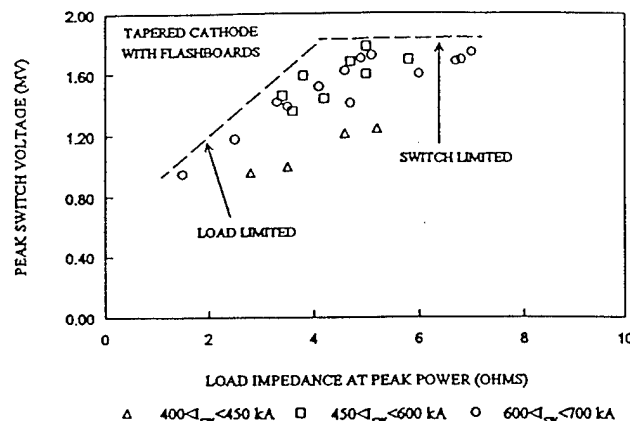


Figure 2. The switch operational regimes depend on the load impedance. Cathode is a 10 to 2.5 cm diam taper.

2.5 cm diam cathode taper and flashboard plasma sources. The operational regime depends on the load impedance. In switch-limited operation, above about  $4 \Omega$ , the voltage is 1.7 MV on the longest conduction shots.

The highest load power to date has been produced in this taper geometry operating near the critical impedance. Figure 3 is a  $0.75 \mu\text{s}$  conduction time shot where 0.7 TW was produced and 55 kJ delivered to the load--20% energy efficiency--at a  $3.5 \Omega$  load impedance. Above this impedance, in switch-limited operation, the load current is lower. For example, load power is about 0.5 TW at  $5 \Omega$  load impedance.

In typical switch-limited operation, this current loss occurs closer to the load than the switch (figure 4). Subsequent experiments with

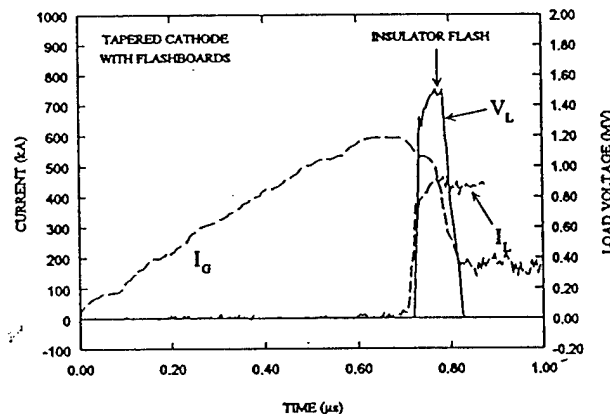


Figure 3. Tapered cathodes have produced the highest power, 0.7 TW at  $3.5 \Omega$  critical load impedance.

cathode current monitors at the load (and a resistive wire voltmeter near the load) suggest the load current, at least at peak power, is primarily cathode current. This is consistent with PIC code simulations of Hawk.<sup>5</sup> Current which is lost upstream of the load, but near the load, is probably vacuum electron flow.

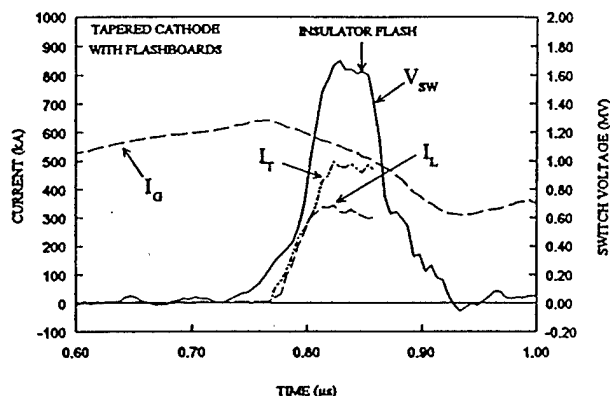


Figure 4. Current losses typically occur near the load in switch-limited operation.

Figure 5 shows peak switch voltage versus conduction time for shots using a 10 to 2.5 cm diam taper, 10 cm diam, and 2.5 cm diam cathodes with flashboard, cable gun, and gas gun plasma sources. Tapered cathodes produce higher voltage than straight cathodes especially at longer conduction times ( $> 0.8 \mu s$ ). Conduction times above  $0.75 \mu s$  were not pursued with the faster plasma velocity flashboards since sufficient switch plasma reaches the load on longer plasma delay shots and results in load-limited operation.

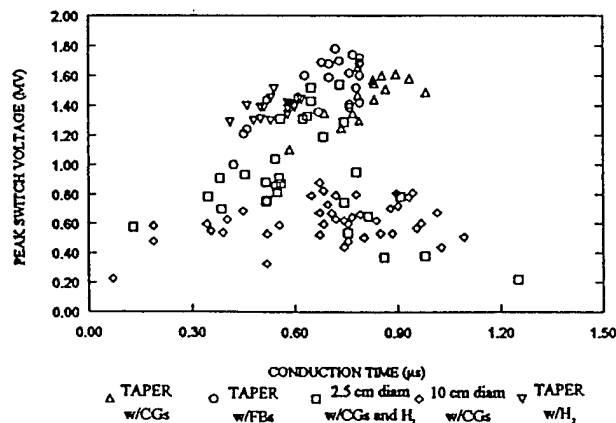


Figure 5. Tapered cathodes produce higher voltage than straight cathodes at longer conduction times.

This plot shows that switch performance is independent of the plasma source (flashboards, cable guns, or gas guns) in a given geometry, i.e. switch/load configuration, consistent with previous results<sup>4</sup>. As is also typical, the smaller radius cathodes (2.5 cm diam) generally generate higher voltage than the larger cathodes (10 cm diam) at a given conduction time. In figure 6, "flow impedance", defined here as  $V_{sw}/I_G$ , is plotted as a function of conduction time for the data in figure 5. This is a lower limit on the flow impedance because the downstream cathode current is not included here. The tapered cathodes are associated with higher flow impedance and maintain this flow impedance at longer conduction times ( $\sim 3 \Omega$  at  $1 \mu s$ ).

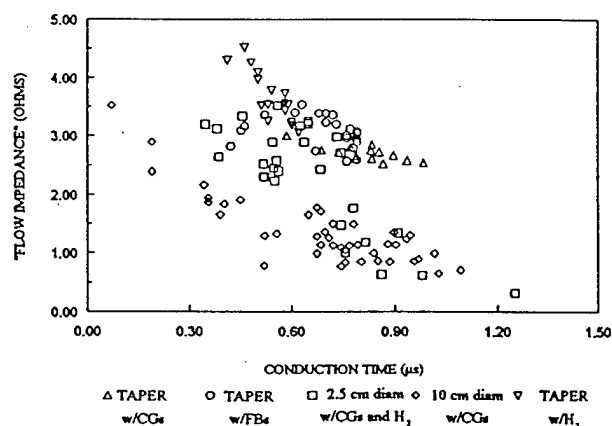


Figure 6. Tapered cathodes are associated with higher flow impedance than straight cathodes and maintain this flow impedance at longer conduction times.

## Anode Modifications

Changes to the anode outer conductor can also effect switch opening. One modification was to add an extension to the anode just downstream of the switch at the same radius as the switch rods, providing a radial gap of 2 cm in this region with the straight 10 cm diam cathode. The usual configuration is to expand out to a 4 cm gap immediately downstream of the switch rods (see figure 1).

Switch performance--switch voltage and load current--deteriorated with the extension, as shown in figure 7. This figure shows data from three shots with a 6 cm, 2 cm, and no extension and the same 0.95  $\mu$ s conduction time. There is clear evidence that electrons are lost at this anode switch extension. Simulations show that the vacuum electrons flow primarily near the anode as the switch opens,<sup>5</sup> so current loss at this reduced radius location is not unreasonable.

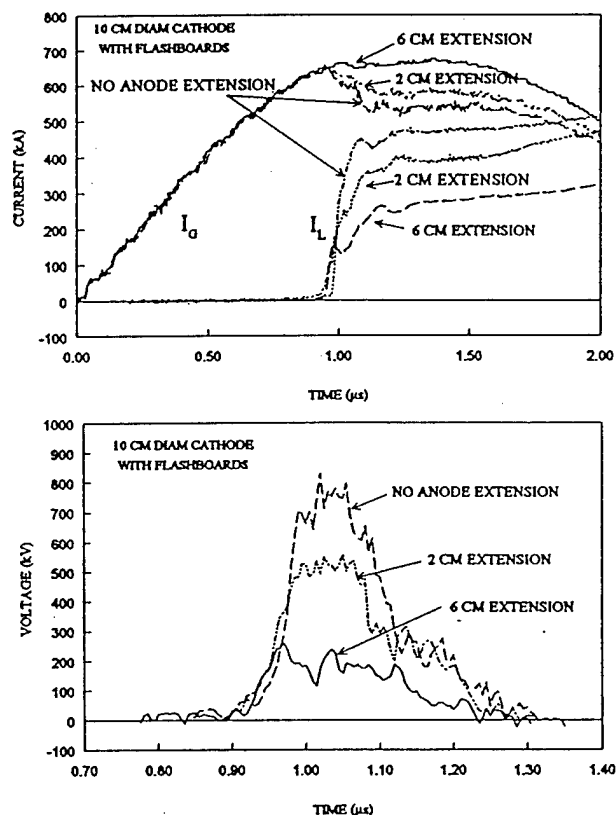


Figure 7. An extension added to the anode just downstream of the switch, but at the same radius as the switch, degrades switch opening.

### Helical Center Conductor

A helical center conductor with a pitch of four and a 10 cm diam was tested in the switch region. The helix increases the total insulating magnetic field in the switch by a factor of 2.3. Conduction time for a given plasma delay was the same as the solid 10 cm diam cathode, suggesting that the additional  $B_z$  field does not contribute to hydro forces limiting conduction.

However, switch opening was very poor, with both short circuit and diode loads, for conduction times greater than 0.35  $\mu$ s. For conduction times less than 0.35  $\mu$ s with short circuit loads, results with the helical center conductor were similar to results with the solid 10 cm diam cathode.

### Summary

These experiments illustrate the importance of the electrode geometry on switch conduction and opening. Tapering the cathode over the switch length optimizes the tradeoff between a higher voltage but lower conducted current as the cathode radius is decreased. In this manner, 0.7 TW load power was produced at 0.75  $\mu$ s conduction as well as 1.6 MV generated at 1  $\mu$ s conduction. There is a limit on the minimum radial gap between electrodes in the switch region and also downstream of the switch below which voltage and current transfer efficiency are reduced. A helical center conductor in the switch region resulted in dramatically degraded switch opening for conduction times over 0.35  $\mu$ s.

- \* JAYCOR, Vienna, VA
- \*\* NRC Research Associate
- \*\*\* SAIC, McLean, VA

- <sup>1</sup>D.D. Hinshelwood, et al., Phys. Rev. Lett., **68**, 3567 (1992).
- <sup>2</sup>R.J. Comisso, et al., Phys. Fluids B **4**, 2368 (1992).
- <sup>3</sup>B.V. Weber, et al., IEEE Trans. Plasma Sci., **19**, 757 (1991).
- <sup>4</sup>P.J. Goodrich, et al., in *Proc. 9th Int. Conf. on High Power Particle Beams*, 609 (1992).
- <sup>5</sup>S.B. Swanekamp, et al., these *Proceedings*.



P.J. Goodrich and D.D. Hinshelwood  
Jaycor, Vienna, VA 22182-2270

R.J. Commisso, J.M. Grossmann, J.C. Kellogg, and B.V. Weber  
Pulsed Power Physics Branch, Plasma Physics Division  
Naval Research Laboratory, Washington D.C. 20375-5346

### Abstract

The Hawk pulsed power generator is used in plasma opening switch (POS) experiments in the 1- $\mu$ s conduction time regime to study long conduction time switch physics. Experiments reported here include modifying the POS electrode geometry, injecting plasma into the e-beam diode, using gas gun plasma sources (with  $H_2$ , He, and Ar gases), and using a helical cathode center conductor in the switch region to increase the total insulating magnetic field. Tapering the cathode center conductor over the 8 cm POS length from 10 cm to, typically, a 2.5 cm diam produced peak load powers of 0.7 TW with 55 kJ delivered to the diode—20% energy efficiency—with carbon-coated flashboards as the plasma source. Performance (voltage, power generated) with a straight 10 cm diam cathode deteriorated when the POS anode outer conductor just downstream of the switch was extended toward the load at the same radius as the switch. Load power was up to 70% higher with a plasma-filled diode (PFD) used in conjunction with the POS for short POS conduction times (400 ns and less). Use of a helical center conductor resulted in dramatically degraded switch performance for >350 ns conduction times. Switch performance with gas guns was generally comparable to that with flashboards in a given switch/load configuration and was independent of the gas ( $H_2$ , He, and Ar) used.

### Introduction

The Hawk generator<sup>1</sup> is a 600 nH, 1- $\mu$ F Marx bank that stores 225 kJ at 80-kV charge to deliver up to 720 kA in 1.2  $\mu$ s to a plasma opening switch (POS). Past experiments and analyses<sup>2</sup> have identified hydrodynamic plasma distortion as the dominant mechanism that controls much of the POS operation.<sup>3</sup> A high density plasma is used to conduct the current pulse, while the opening phase is characterized by a rarefied plasma resulting from redistribution during the conduction phase. The maximum load power is determined by an effective gap for magnetic insulation in the POS. This earlier data indicated that above a critical load impedance the effective gap in the POS, as determined from magnetic insulation arguments, is limited to 3 mm. Above this critical impedance, called the switch-limited regime, current is shunted into the transition section between the switch and the load with the voltage remaining constant. At impedances lower than the critical value, the voltage decreases in proportion to the load impedance, the so called load-limited regime. Maximum load power is obtained at this critical impedance. Increasing the cathode magnetic field ( $I/r$ )—by conducting more current ( $I$ ) or decreasing the cathode radius ( $r$ )—allows the fixed-gap POS to remain insulated at a higher voltage. In this way, load voltages up to 2 MV were achieved with a 2.5 cm diam cathode, a factor of 2.8 higher than the Marx voltage.

In this paper, recent Hawk experiments with further modifications to the POS electrode geometry, plasma-filled diodes (PFD), and gas gun plasma sources are discussed.

### Tapered Cathodes

Tapered cathodes were employed in the switch region and upstream and downstream of the switch. The larger cathode magnetic

field in tapered regions may insulate the electron flow better and allow higher load powers. Only tapering in the switch region had an effect on performance with significant improvement observed with a taper like that shown in Fig. 1. This gradual 10 to 2.5 cm diam taper through the 8 cm length switch produced load powers up to 0.7 TW (1.5 MV and 465 kA, see Fig. 2) and 55 kJ—20% energy efficiency from the energy stored in the Marx—delivered to the load. Such a taper generated voltages close to those possible with a 2.5 cm diam cathode but with the longer conduction/higher currents associated with a 10 cm diam cathode, producing the high load powers. The importance of geometry on switch performance is illustrated by the fact that when the tapering starts just a few cm further downstream, near the middle of the switch instead of at the upstream end, performance becomes identical to a straight 10 cm diam cathode, i.e. 850 kV and 0.4 TW load power at 900 ns conduction.

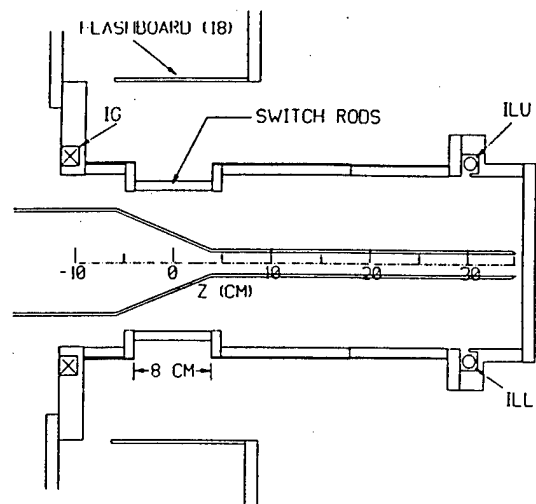


Fig. 1. Hawk front end vacuum section with a 10 cm to 2.5 cm diam cathode taper in the switch region.

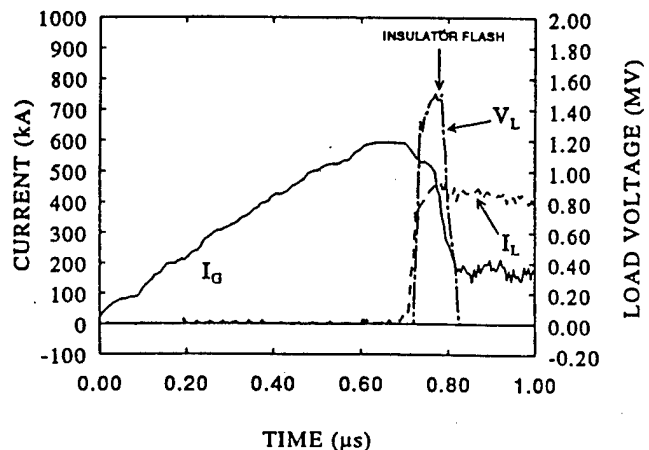


Fig. 2. Generator and load currents and load voltage for the tapered cathode in fig.1. Peak load power is 0.7 TW.

Figure 3 shows the peak switch voltage as a function of load impedance at peak power for shots with the taper depicted in Fig. 1. Above  $\sim 4 \Omega$  the voltage is roughly constant for a given conduction current—the switch-limited regime. Voltage increases with conduction current and is over 1.6 MV on the longest conduction (600 to 700 kA) switch-limited shots. The  $4 \Omega$  impedance is the critical impedance for this geometry, producing 0.7 TW on 600-700 kA conduction shots.

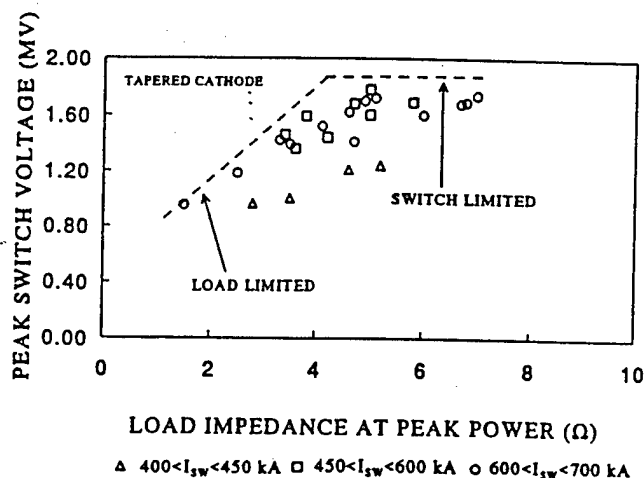


Fig. 3. Peak voltage as a function of load impedance at peak power with the tapered cathode.

The influence geometry can have on switch operation is further illustrated in Fig. 4 where two tapered cathode shots with the same conduction time (same plasma conditions) are shown. In one case, the setup is with the standard 26 cm switch-to-load length in load-limited operation—good current transfer, relatively low voltage—because sufficient switch plasma is accelerated to the load by  $J \times B$  forces during conduction with this small radius cathode to limit the load impedance at peak power. On the other shot (with the same diode gap) the transition section was extended to 40 cm, allowing high load impedance—switch-limited—operation with higher voltage but lower load current.

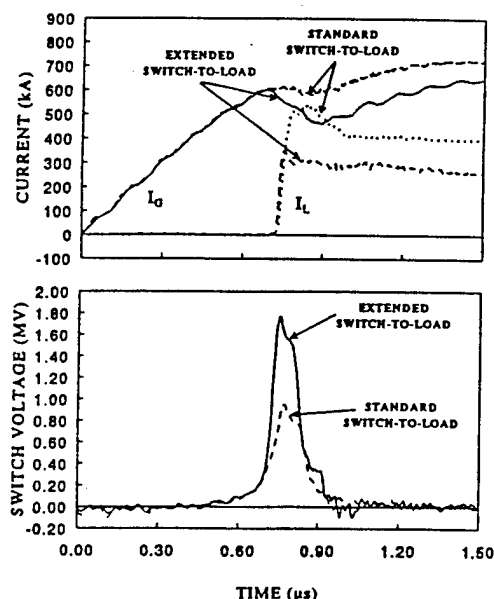


Fig. 4. Two shots with the tapered cathode and the same conduction time and diode gap, but with different switch-to-load lengths.

## Anode Modifications

Changes to the anode structure can have a substantial effect on switch opening. One modification was to add a 6 cm long extension to the anode just downstream of the switch at the same radius as the switch rods, providing a 2 cm radial gap in this region with a 10 cm diam cathode. The usual configuration is to expand out to a 4 cm radial gap immediately downstream of the switch rods.

Figure 5 shows data from shots with 6 cm, 2 cm, and no extension for the same 950 ns conduction time. Switch opening with the 6 cm extension is very poor. Most of the current is lost over the last 3 cm length of the extension, with the location where the anode damage begins corresponding to the downstream edge of the switch at opening if the switch translates about half the switch length during the conduction phase. Opening actually improved somewhat as the plasma delay was shortened—an atypical result. A 2 cm extension resulted in better switch opening than the 6 cm extension (for the same conduction time) but still not as good as the no extension standard setup, where current transfer efficiency is 80% and voltages of 800 kV are produced for 950 ns conduction, performance typical of a 10 cm diam cathode.

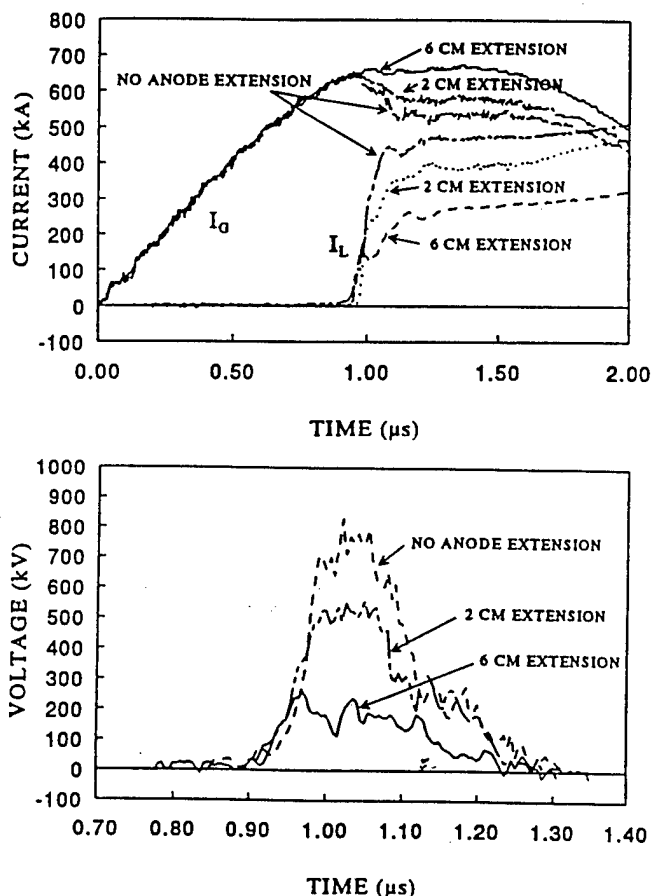


Fig. 5. Changes to the anode geometry can have a substantial effect on switch performance: an extension added to the anode just downstream of the switch but at the same radius as the switch rods degrades switch opening. The cathode is 10 cm in diameter.

## Plasma-Filled Diodes

PFD experiments were done by injecting plasma from a flashboard downstream of the diode into the diode gap through holes in the anode strike plate. The PFD was used in three cathode configurations: a straight 5 cm diam cathode, a 10 to 5 cm diam switch taper, and a

tapered cathode which was flared out to a 10 cm diam at the diode as shown in Fig. 6. Flaring the cathode at the diode was a convenient way of reducing the load impedance at peak power for a given diode gap, operating closer to the critical impedance. On long POS conduction time shots, peak load power was up to 30% higher with the PFD. However, some switch plasma reached the load on these long conduction shots—the impedance rises from zero even with no independent PFD plasma—so there are no true vacuum diode shots for comparison.

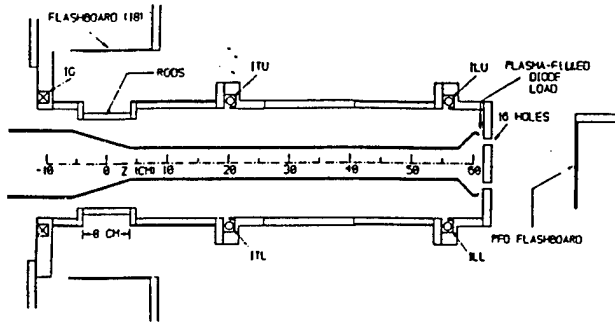


Fig. 6. One of the (cathode) configurations used with a plasma-filled diode load.

For short POS conduction times, where switch plasma does not reach the load and the load with no PFD behaves as a vacuum diode, the enhancement in load power using the PFD was greater. Figure 7 shows peak load power on shots with 400 ns POS conduction times was up to 70% higher with the PFD (for similar load impedance at peak power). With the PFD, somewhat higher voltage is produced (indicating a larger switch gap) and more current reaches the load. This is consistent with the reduced vacuum electron flow with a PFD load that is seen in simulations. Also, the PFD shots showed strong on-axis beam pinching in the diode, evident from x-ray pinhole pictures and damage on the anode plate. This is probably because the plasma is a source of ions necessary for pinching. (Shots with a small radius cathode at the diode—2.5 cm and 5 cm diam—and no PFD also show pinching although it is not as intense.)

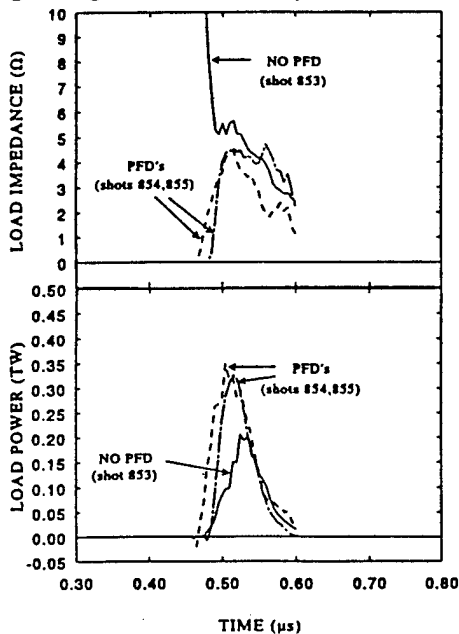


Fig. 7 Load power on PFD shots is up to 1.7 times higher than vacuum diode shots for short POS conduction times and the same load impedance at peak power.

The control of load impedance provided by the PFD is illustrated in Fig. 8. This figure shows two PFD shots with the same POS conduction time and large diode gap, but different PFD delays. Peak load power is the same on these two shots—just over 0.5 TW. In the upper graph, the PFD delay is short and opening is switch-limited: the load impedance at peak power ( $\sim 4 \Omega$ ) and the voltage generated are high, current transfer is fairly low. In contrast, in the bottom graph the PFD delay is long and performance is load-limited: the impedance at peak power ( $\sim 2 \Omega$ ) and the voltage generated are limited, while the current transfer efficiency is good.

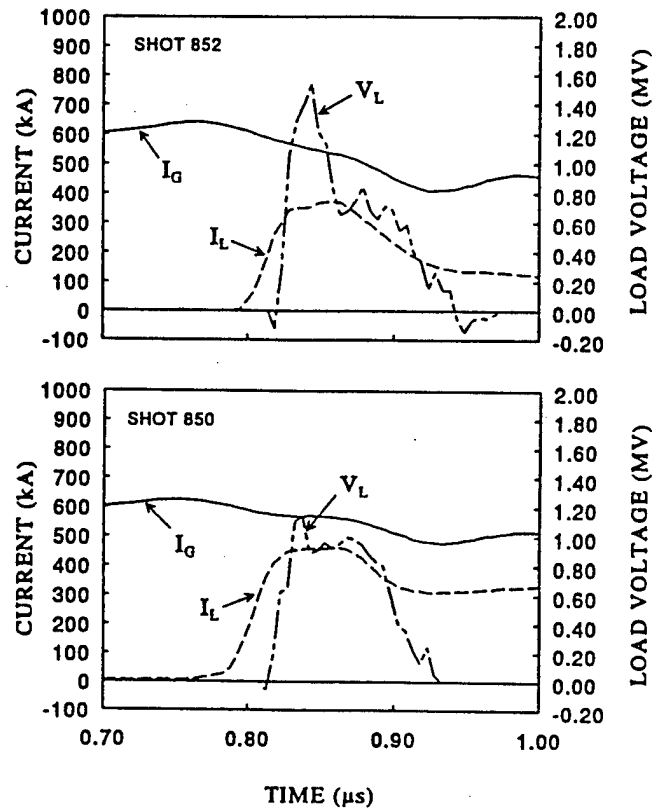


Fig. 8. Control of load impedance at peak power and thus load voltage and current is possible with an independent PFD. With a) short PFD delays performance is switch-limited; with b) long PFD delays performance can be load-limited.

### Helical Center Conductor

A helical cathode center conductor with a pitch of four and a nominal 10 cm diam was used in the switch region. The helix is 20 cm long and has four slots. Each rib makes  $\sim 2.5$  turns around the helix. It was not centered under the flashboards/anode rods, but displaced about 4 cm downstream. This was done so that the center-of-mass of the plasma, which may translate downstream about half the switch length or 4 cm during conduction, is at the center of the helix (where the field is highest) at opening. The additional axial field increases the total insulating magnetic field in the central region of the helix a factor of 2.3 above that from a solid cathode of the same diameter.

Switch opening with the helix was generally very poor, although there appeared to be different "regimes" of operation. Conduction times for a particular plasma delay were typical of solid 10 cm diam cathodes. For long delays of  $\geq 1 \mu\text{s}$  the switch conducts for  $\sim 1 \mu\text{s}$ , but with small load currents and low voltage generated upon opening with

both short circuit and diode loads. Most of the current stays in the switch. With intermediate delays, from 0.5 to 1  $\mu$ s, the switch did not open at all for both short circuit and diode loads. For short delays, less than 0.5  $\mu$ s, the switch conducts for 350 ns and less. With short circuit loads switch opening was much improved and all the current reached the load. (No data was taken with diode loads at these short conduction times.) Current appeared to be flowing in the helix ribs on the short plasma delay shots, because the ribs were deformed by magnetic forces during the pulse. This did not occur with the longer plasma delays and suggests that in this case current is carried in the plasma, not the helix, for most of the pulse. The fact that switch opening here is inferior to the solid cathode suggests that it is not simply a matter of the helical turns shorting out. Also, the  $B_z$  field decreases to zero at the ends of the helix and this may result in additional electron losses downstream of the switch. To retrap some of this flow, the cathode just downstream of the helix was reduced to 5 cm diameter on some shots, resulting in a slight improvement in performance.

### Gas Gun Plasma Sources

Four gas guns, similar to those in ref. 4, were used as an opening switch plasma source with  $H_2$ , He, and Ar gases. The gas, at 60 psig back pressure, was fed into the region between the coaxial electrodes, where the plasma discharge is initiated, through an automobile fuel injector used as the mechanical valve<sup>5</sup>. Typically, the valve is pulsed at least several hundred microseconds before the discharge is initiated in the gun by a capacitor bank. This minimum gas puff delay is needed to initiate the gun discharge and involves the time it takes for the valve to start opening and the transit time of the gas from the valve to the location near the front of the gun where gas breakdown occurs. Best performance with  $H_2$  and He gases occurred with gas puff delays of 400 to 450  $\mu$ s. For Ar, gas puff delays of  $\sim$ 500  $\mu$ s resulted in best performance, consistent with its slower thermal velocity. The plasma produced by the guns typically has a slower velocity and is more localized than flashboard plasma.

Tapered cathodes, as well as 10 cm diam and 2.5 cm diam straight cathodes, were used with the gas guns. The gun to cathode distance was varied from 3.5 to 10 cm. Two B-dot current monitors, ILU2 and ILL2 which are located behind the diode, were used on these gas gun shots in addition to the standard load current monitors, ILU and ILL, which are 5 cm upstream of the diode. In typical operation, these two sets of current monitors agree: little current is lost over the 5 cm distance from the standard current monitors to the load. Even in switch-limited operation, most of the current loss, which can be a substantial fraction of the total current, occurs near the load but upstream of the standard load current monitors ILU and ILL.

Switch performance with a 10 cm diam cathode was equivalent for the different gases (but at different gas puff, plasma delays). In addition, performance is very similar to flashboards: voltage and load power improve with conduction time and at 900 ns conduction the switch voltage is  $\sim$ 800 kV. Figure 9 shows the peak switch voltage as a function of load impedance at peak power for shots with He gas. On the longest conduction shots, the voltage is 800 kV at load impedances of  $\sim$ 2  $\Omega$  and above (similar to flashboards). Highest load power, about 0.4 TW, occurs at this 2  $\Omega$  critical impedance, also comparable to flashboards.

Performance with a 2.5 cm diam cathode was, again, independent of the gas used. Voltage and load power improve with conduction time up to 600 ns, similar to flashboards. In Fig. 10, the peak switch voltage is plotted versus load impedance at peak power for shots with  $H_2$  gas. For these shots, switch-limited operation may not have been reached and voltages higher than 1.3 MV may be possible if the load impedance is increased above 5.5  $\Omega$ .

For the 10 to 2.5 cm diam tapered cathode (tapering in switch) the voltage is 1.4 MV at the  $\sim$ 4  $\Omega$  critical impedance and above (Fig. 11 with  $H_2$  gas). This is also similar to flashboards with tapered cathodes. However, in what is atypical behavior, the switch-limited voltage does not increase with conduction current, but is constant at 1.4 MV over a range of conduction currents from 350 to 550 kA.

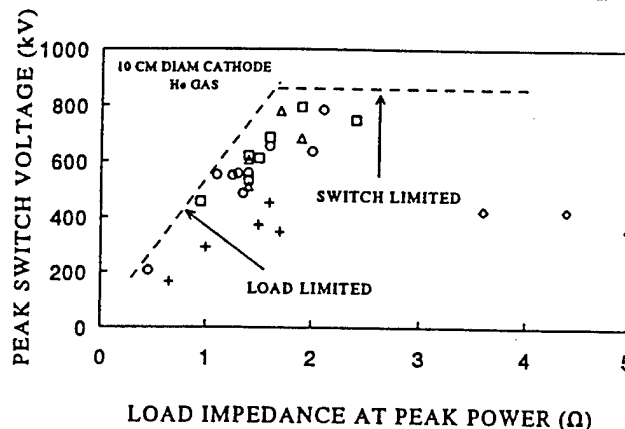


Fig. 9. Peak voltage as a function of load impedance at peak power with a 10 cm diam cathode and gas gun plasma sources (He gas here).

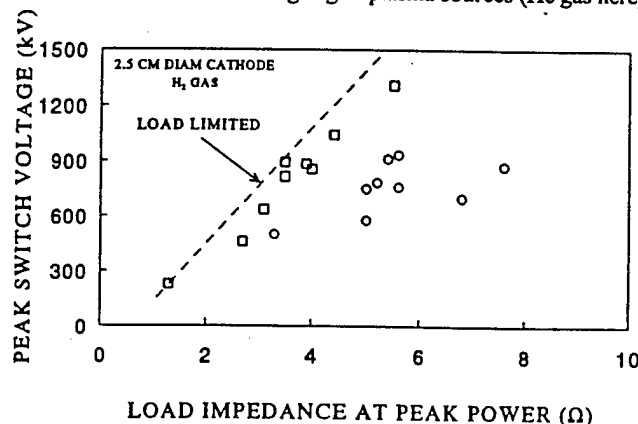


Fig. 10. Peak voltage as a function of load impedance at peak power with a 2.5 cm diam cathode and  $H_2$  gas.

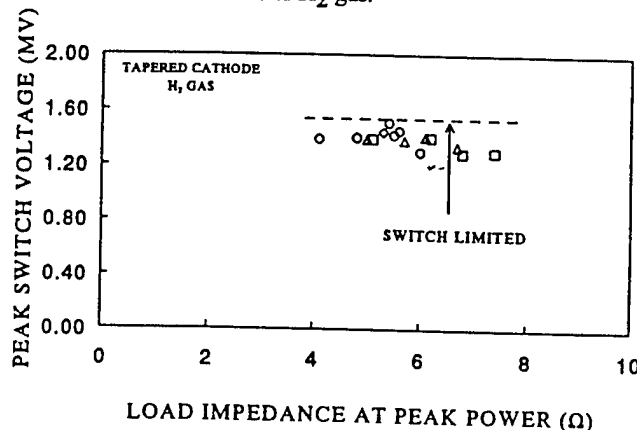


Fig. 11. Peak voltage as a function of load impedance at peak power with a tapered cathode and  $H_2$  gas.

### Summary

Recent experiments on Hawk illustrate the importance of the electrode geometry on switch performance. Cathode and anode

configurations have an impact on switch opening. Tapering the cathode over the 8 cm POS length from 10 cm diam to a 2.5 cm diam is a good compromise between the high voltage generated with a small radius cathode and the longer conduction/higher currents associated with the larger cathodes, producing load powers of 0.7 TW (1.6 MV, 450 kA) with 55 kJ—20% energy efficiency—delivered to the diode. There is a limit on the minimum radial gaps in the switch and downstream of the switch below which voltage and current transfer efficiency are reduced. For example, switch opening with a straight 10 cm diam cathode deteriorated when the radial gap downstream of the switch was reduced to that used in the switch.

The load power was up to 70% higher with a PFD used in conjunction with the POS for short conduction times (400 ns and less), where switch plasma does not reach the load. On longer conduction time shots, the effect was less pronounced, with about a 30% enhancement with the PFD. In this case, however, some switch plasma reached the load so there were no true vacuum diode shots for comparison.

A helical center conductor in the switch region, designed to increase the total insulating magnetic field for a given cathode radius, resulted in dramatically degraded switch opening (low voltage, poor current transfer) for >350 ns conduction times with both short circuit and diode loads. Opening was good for <350 ns conduction with short circuit loads. Indications were that current was carried in the helix only on the short conduction time (low plasma density) shots, because the helical ribs were deformed by magnetic forces on these shots.

Switch/load performance with gas guns was generally comparable to that with flashboards in a given switch/load configuration. Performance was independent of the gas ( $H_2$ , He, and Ar) used.

#### References

- [1] J.R. Boller, NRL Memorandum Report 6748, January 1991.
- [2] P. J. Goodrich, et al., 8th IEEE Pulsed Power Conference, San Diego, CA, 1991, IEEE Cat. No. 91CH3052-8, p. 515, also see P.J. Goodrich, Proceedings of the 9th International Conference on High Power Particle Beams, Washington D.C., 1992.
- [3] D.D. Hinshelwood, et al., "Density Redistribution in a Microsecond-Conduction-Time Plasma Opening Switch," Physical Review Letters, vol. 68, p. 3567, June 15, 1992.
- [4] P.S. Ananjin, et al., "Application of Pulsed Gas Vents for Plasma Opening Switches," IEEE Trans. on Plasma Sci., vol. 20, p. 537, October 1992.
- [5] M.R. Brown, et al., J. Appl. Phys., vol. 69, p. 6302, (1991).

TITLE: PLASMA OPENING SWITCH EXPERIMENTS ON HAWK  
WITH TAPERED CATHODES AND CABLE GUN PLASMA SOURCES

AUTHORS: P. J. Goodrich

DATE: 23 February 1994

ABSTRACT:

This experiment is a continuation of plasma opening switch (POS) work on Hawk with tapered cathodes but with cable gun plasma sources instead of flashboards. Cathodes tapered in the switch region, typically from 10 cm to 2.5 cm diam, have produced the highest load power to date, 0.7 TW (e.g. 1.5 MV load voltage and 465 kA load current out of 500 kA total system current at the time of peak voltage and before insulator flashover) with 55 kJ delivered to the diode--20% energy efficiency--using flashboard plasma sources. Conduction was typically ~700 ns, conducting 600 kA with modest flashboard plasma delays of ~1.5  $\mu$ s. Conduction time was up to 775 ns for a 2  $\mu$ s plasma delay, the longest delay used with the flashboards. In the present experiment, a more complete timing scan was done with cable guns. A plasma delay of 5.8  $\mu$ s, for example, produced conduction times of 1  $\mu$ s. Voltages of 1.5 MV were generated at these conduction times with flow impedances of at least 3  $\Omega$ . A series of shots with a 5  $\mu$ s plasma delay resulted in conduction times of 850 to 900 ns with a (consistent) switch voltage of 1.55 MV. This is the conduction time for best performance with a straight 10 cm diam cathode. Two cathode current monitors located at the diode had the same amplitude at peak voltage as the anode load current monitors, suggesting little vacuum electron flow near the load at peak power. Vacuum flow, if any, could be lost upstream of the load (where there are no cathode current monitors). Current, whether cathode or vacuum flow, is certainly lost to the anode upstream of the load because anode current monitors closer to the switch typically showed higher currents than the anode load monitors. Total current delivered to the load was fairly low, at most 300 kA or 50% current transfer efficiency. Load impedance was typically about 7  $\Omega$  at peak power with a 7 mm diode gap and a 2.5 cm diam cathode tip, about 6  $\Omega$  with the same gap and a 5 cm diam cathode at the diode. Similar results were found with flashboards where the "critical" impedance--the impedance for maximum load power--occurred at ~4  $\Omega$ . (Peak load power was 0.7 TW at this impedance with flashboards). This lower impedance was produced by 1) closing the diode gap although this can lead to gap closure problems, 2) reducing the switch-to-load distance, or 3) flaring the cathode at the diode out to a ~9.5 cm diameter. None of these techniques was tried during this experimental run with cable guns. They will be looked at in the future as well as optimizing the switch-to-load inductance by reducing the downstream anode radius which may also increase the energy delivered to the load. One difference between flashboard and cable gun plasma sources (using tapered cathodes) was the hollow x-ray profile seen on the cable gun shots. The beam does not pinch except on very long plasma delay shots (conducting at or past peak current) where switch plasma may reach the load and contribute to pinching. Conversely, shots with flashboards always showed a uniform radiation distribution.

## I. Introduction

Various cathode tapers have been used in the past with flashboard plasma sources. These included tapers in the region between the switch and the load and in the switch itself. Both abrupt and gradual tapers were tried in these regions (see TN 92-03). A gradual 10 cm diam to either a 5 cm, 2.5 cm, or 1.3 cm diam taper over the 8 cm switch length or over the first 4 cm of the switch produced the best performance in terms of switch voltage generated and current conducted in the switch. Voltages of 1.5 MV at 700 ns conduction times with 470 kA delivered to the load were achieved at the critical load impedance of  $\sim 3.5 \Omega$  (peak load power of 0.7 TW; see Beams '92 and Pulsed Power Conf. '93). The total system current was 500 kA at the time of peak voltage and before insulator flashover, so the 470 kA of anode load current represents excellent current transfer efficiency. Such a taper generated voltages close to those possible with a 2.5 cm diam cathode but with the longer conduction/higher currents at modest plasma delays associated with a 10 cm diam cathode, producing the high load powers. This conduction time occurred using a standard 1.5  $\mu$ s plasma delay. No shots were fired with plasma delays greater than 2  $\mu$ s with conduction times over 775 ns.

Figure 1 shows peak switch voltage as a function of load impedance at peak power for shots with a gradual 10 cm to 2.5 cm diam cathode taper over the 8 cm switch length and flashboard plasma sources. Voltage increases with conduction current and is over 1.6 MV on the longest conduction (600 to 700 kA) switch-limited shots. Above  $\sim 4 \Omega$  the voltage is roughly constant for a given conduction current--the switch-limited regime. Load impedances of  $\sim 5 \Omega$  and above were the result of an extended length geometry--40 cm or more switch-to-load length--with at least a 7 mm diode gap. Lower impedances at peak power were obtained by reducing the switch-to-load distance to the standard 26 cm length, by gradually flaring out the cathode tip to a 9.5 cm diameter, or by reducing the diode gap.

In these present experiments with cable guns, the cathode had either a 10 to 5 cm diam taper over the 8 cm switch length (figure 2) or a 10 to 2.5 cm diam taper (figure 3). The switch-to-load length was 46 cm and the diode gap was 7 mm. A vacuum wire (resistive) voltmeter was used to measure the load voltage (the wire was 3 cm from the cathode tip). An end-on x-ray pinhole camera and the PI pin diode array were also fielded. A total of six anode B-dot current monitors were used downstream of the switch, as shown in figures 2 and 3, and in the case of the 10 to 5 cm diam taper two cathode B-dot monitors were located at the load.

## II. Results with a 10 to 5 cm Diam Taper

The 10 to 5 cm diam taper produced voltages of 1.1 to 1.45 MV with conduction times ranging from 0.58 to 0.85  $\mu$ s, respectively, using cable gun plasma delays of 3.35 to 4.25  $\mu$ s. Improvement in switch performance, i.e. the voltage generated, with longer conduction times (up to a limit) is a typical result. But longer plasma delays, with longer conduction times possibly resulting in higher voltages, were not tried with this taper. This is, nevertheless, superior performance to a straight 5 cm diam cathode where performance degraded--voltage drops below  $\sim$ 1 MV--for conduction times greater than 0.75  $\mu$ s. Indeed, conduction was generally limited to 0.7  $\mu$ s with the straight 5 cm diam cathode using flashboard plasma sources; to conduct longer required a very large increase in flashboard plasma delay and subsequent degradation in performance.

Figure 4 shows current traces on a typical shot with a 10 to 5 cm diam taper, shot 1498. This shot has a 4.1  $\mu$ s plasma delay and a conduction time of 0.79  $\mu$ s. The IS2S signal is the average of the intermediate anode B-dots ISW2 and ISE2, the ILAVS signal the average of the two load anode B-dots ILW and ILE, and IKAVS is the average of the two load cathode B-dots IKLW and IKLE. It is usually the case that the two monitors at a given axial location ( $180^\circ$  apart) agree, except possibly for ISW1 and ISE1. These two suffer the most from plasma shielding as they are the current monitors nearest the switch; they are routinely lower in amplitude than the monitors farther downstream. On this shot, about 85% of the current, (cathode current plus vacuum flow), reaches the intermediate anode B-dots and about half of this reaches the load. The cathode load current is smaller than the anode load current until peak voltage where the two agree, which at least suggests little vacuum flow near the load at peak power. Of course, the  $\sim$ 50% current loss between the intermediate anode B-dots and the load B-dots (according to the data) may result precisely because it consists of vacuum flowing electrons, readily lost to the anode; without cathode current monitors upstream of the load one cannot be certain.

Figure 5 shows shot 1497 in this sequence with a 0.75  $\mu$ s conduction time and a 3.75  $\mu$ s plasma delay. Here significantly more current is lost between the switch and the intermediate B-dots than on shot 1498. But according to the data, there is little additional loss between the intermediate monitors and the load. Also, the cathode load current is somewhat less than the anode load current at peak voltage.

Shot 1500 is similar to shot 1498 showing significant current loss between the intermediate B-dots and the load (figure 6). Figure 7 gives the voltage on this modest 0.78  $\mu$ s conduction time shot: VDC is the capacitive voltmeter in the oil behind the insulator and WVM is the vacuum wire voltmeter at the load. The data show the load voltage rising quickly after switch opening at  $t \approx 1.5 \mu$ s. As is typical on Hawk shots, the peak load voltage (here 1.2 MV) is close to the peak



voltage on VDC. From this data, the load impedance at peak power is  $\sim 5.5 \Omega$ , representative of these taper shots with a 7 mm diode gap (typically 5.5 to 6  $\Omega$ ). Figure 8 shows IV--the anode load current ILAVS multiplied by the load voltage WVM--plotted with pin diode signal PIN7. Interestingly, the x-ray pinhole pictures show a hollow profile with the deposition on the anode plate occurring at the radius of the cathode tip (5 cm diam). Though there is sometimes a hot spot on axis this profile is significantly different from past shots in this geometry with flashboard plasma sources where the beam pinched and the radiation distribution was uniform.

No attempt was made in this run to improve the current transfer efficiency by reducing the load impedance at peak power. Three hardware changes made in the past with tapered cathodes and the flashboards to reduce the load impedance and increase power coupled to the load were: 1) closing the diode gap, 2) reducing the switch-to-load distance, or 3) flaring the cathode at the diode out to  $\sim 9.5$  cm diameter. In this manner, peak load powers of 0.7 TW were achieved with tapered cathodes and flashboard plasma sources.

Of course, the interpretation of the B-dot current monitor signals in the present run must be viewed cautiously because of plasma shielding, frequency response, etc. problems associated with this new style of surface B-dot monitors. This can mean, for example, that current is higher than B-dot signals suggest. Also suspicious are current traces like shot 1498, figure 4, where the start times of the downstream currents, IS2S, ILAVS, and IKAWS, are different. Work on improving the current monitors is in progress.

### III. Results with a 10 to 2.5 cm Diam Taper

After only a handful of shots with a 10 to 5 cm diam taper, and no conduction times longer than 0.85  $\mu$ s, a 10 to 2.5 cm diam taper was installed (figure 3). The magnetic field is higher at the downstream end of the switch with the 10 to 2.5 cm taper due to the smaller cathode radius here. This leads to somewhat better switch performance (voltage generated) for a given conduction time. Shots were taken with conduction times up to 1  $\mu$ s (with a 5.8  $\mu$ s cable gun plasma delay).

Figures 9, 10, and 11 show shots with conduction times ranging from 0.83 to 0.86  $\mu$ s, conducting about 650 kA, and plasma delays from 4.8 to 5.3  $\mu$ s. The anode load current, ILAVS, is low--current transfer efficiency is under 50% at peak voltage--giving load impedances at peak power of 6 to 7  $\Omega$ . The diode gap was also 7 mm which is a 16  $\Omega$  vacuum diode impedance and, again, no attempt was made to improve the current coupled to the load by reducing the load impedance at peak power, etc. Best switch performance with a straight 10 cm diam cathode occurs at 0.8 to 0.9  $\mu$ s conduction times. The voltage generated at this conduction time with the tapered cathode,  $\sim 1.6$  MV, is more than a factor of 2 higher (figure 12). Shots with small radius

straight cathodes (5 cm and 2.5 cm diam) have shown in the past even higher voltages but at shorter conduction times, 0.6 to 0.7  $\mu$ s. Longer conduction than this, with longer plasma delays, resulted in degraded switch performance (voltage). However, figures 13 and 14 show that 1.5 MV can be generated using the tapered cathode at 1  $\mu$ s conduction times (this is shot 1510: 715 kA conduction current, 5.8  $\mu$ s plasma delay). The advantage of the taper is that voltages close to those possible with a small radius cathode can be generated, but at the longer conduction times/higher currents associated with best performance using a 10 cm diam cathode. Figures 15 and 16 show switch voltage waveforms for shots 1506 through 1509 which had comparable conduction times around 0.85  $\mu$ s. The switch voltage is consistently 1.5-1.6 MV.

Scatter plots of peak switch voltage as a function of conduction current and conduction time are shown in figures 17 and 18, respectively, for shots with tapered cathodes, a 10 cm diam straight cathode, and a 2.5 cm diam cathode. In the case of the 10 cm diam cathode, this data set (there are many more 10 cm diam shots) shows improving switch performance (voltage) with conduction up to about 0.9  $\mu$ s. The 2.5 cm diam cathode shows voltage increasing with conduction time up to  $\sim$ 0.7  $\mu$ s--in fact a factor of two higher voltage than the 10 cm cathode for 0.7  $\mu$ s conduction times--at which point performance falls off. A few things of note with the 10 cm and 2.5 cm diam cathode data: 1) the plasma delay necessary for a given conduction time is significantly longer with the 2.5 cm cathode than the 10 cm cathode, 2) the (limited) data with the 2.5 cm diam cathode were taken in the standard configuration with a 26 cm switch-to-load length where past experiments using flashboards showed load-limited (low voltage) operation; hence, the voltage on these shots at 0.7  $\mu$ s conduction times is lower than on flashboard shots in the extended configuration and 3) there is scatter in the data, more than is typical.

The data with the tapered cathodes, however, show voltage increasing with conduction through 1  $\mu$ s conduction times. Voltage is close to the voltage generated with the 2.5 cm diam cathode up to conduction times of  $\sim$ 0.75  $\mu$ s, at which point the 2.5 cm cathode voltage degrades, but the tapered cathode voltage continues to increase and is 1.5-1.6 MV at 0.9-1  $\mu$ s.

A lower bound on the switch flow impedance (which is all the rage these days) for these data is shown in figures 19 and 20 as a function of conduction current and conduction time, respectively. It is a minimum value because downstream cathode current is not included ( $I_c = 0$ ) in the flow impedance formula. The "flow impedance" is about 3  $\Omega$  at conduction times of 0.6  $\mu$ s and less with the 2.5 cm cathode, falling for longer conduction. It is also about 3  $\Omega$  at short conduction times with the 10 cm cathode, falls with longer conduction, but does plateau at about 1.25  $\Omega$  over conduction times of 0.6 to 1  $\mu$ s. In contrast, the tapered cathode "flow impedance" is roughly constant at nearly 3  $\Omega$  on long conduction time shots from 0.6 to 1  $\mu$ s.

The x-ray pinhole pictures again show a hollow profile like the 10 cm to 5 cm diam tapered cathode. There is no pinch and the deposition on the anode plate occurs at the radius of the

cathode tip (here 2.5 cm diam). Pinching does occur in this geometry with flashboard sources as well as with a straight 2.5 cm diam cathode and cable guns. The last two shots in the present run had unintentionally long plasma delays, due to problems with the doghouses, and did pinch. However, they conducted past peak with poor switch performance--very low voltage--and possibly sufficient switch plasma reached the load to facilitate pinching (which may be more like the case with tapered cathodes and flashboards).

#### IV. Future Work

Using this basic tapered geometry, where 1.5 MV at 1  $\mu$ s conduction times can be generated, it would be productive to attempt to improve the current delivered to the load and thus the load power. This was accomplished in the past with precisely this taper geometry and flashboards by reducing the load impedance at peak power from  $\sim 7 \Omega$  (like it is in the present experiment) to  $\sim 3\text{--}4 \Omega$ . The hardware changes that reduced this impedance were: 1) closing the diode gap from 7 mm although gap closure could become a problem, 2) reducing the switch-to-load distance, or 3) flaring out the cathode tip to a  $\sim 9.5$  cm diameter. In this way, 0.7 TW peak load power was achieved at 0.7  $\mu$ s conduction times (figure 21). Although the cathode current was not measured in the tapered shots with flashboards and so the actual amount of vacuum electron flow was not known, the vacuum flow may in fact be minimal (not a popular view) given that: 1) total current transfer efficiency to the load was high based on the anode load current (see figure 21) and 2) side viewing x-ray pinhole pictures did not show loss upstream of the load and end-on pictures showed a good centered pinch in the diode.

The experiments with flashboards employed the anode "hats" to measure the anode current. These monitors do not suffer from plasma shielding when used at a switch-to-load distance of 20 cm or greater out to 1  $\mu$ s conduction times. The "hat" can be located closer than 20 cm distances for short enough plasma delays. Because the cable gun plasma velocity is slower it may be possible to use these monitors closer than the 20 cm distance with cable guns without suffering plasma shielding effects at long conduction times. In addition, it does not appear that there is a frequency response problem with the anode "hats", a problem that is becoming evident with the surface B-dot probes. That the anode "hats" appear to work basically means that the signal has a fast risetime and shows 100% current transfer with short circuit loads; about 80% current transfer with diode loads operating at critical impedance, lower transfer efficiency running above the critical impedance at peak power.

I propose using this basic anode "hat" design, maybe somewhat modified to be less bulky, at appropriate locations on the anode and a sufficiently modified version to work in the cathode to measure cathode current. Using cable guns, believable downstream current monitors, and the

aforementioned ways of reducing the load impedance at peak power to  $\sim 3 \Omega$  it may be possible to approach 1 TW peak load powers at 1  $\mu\text{s}$  conduction times (say 1.6 MV load voltage and 600 kA load current, conducting 725 kA). Finally, optimizing the switch-to-load inductance by reducing the anode radius to make, say, the typical  $\sim 4$  cm radial gap between the electrodes downstream of the switch may also increase the power delivered to the load.

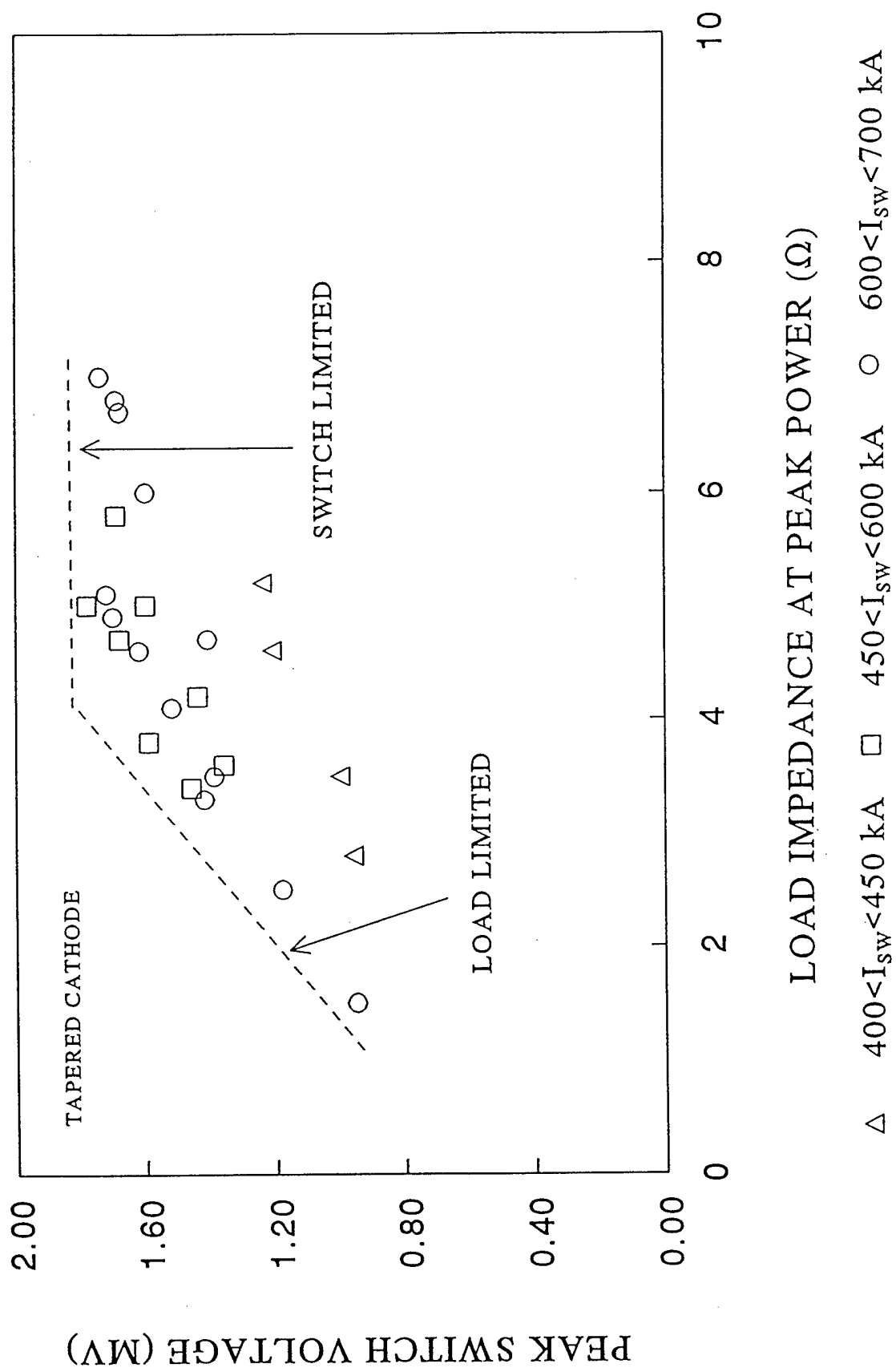


Fig. 1

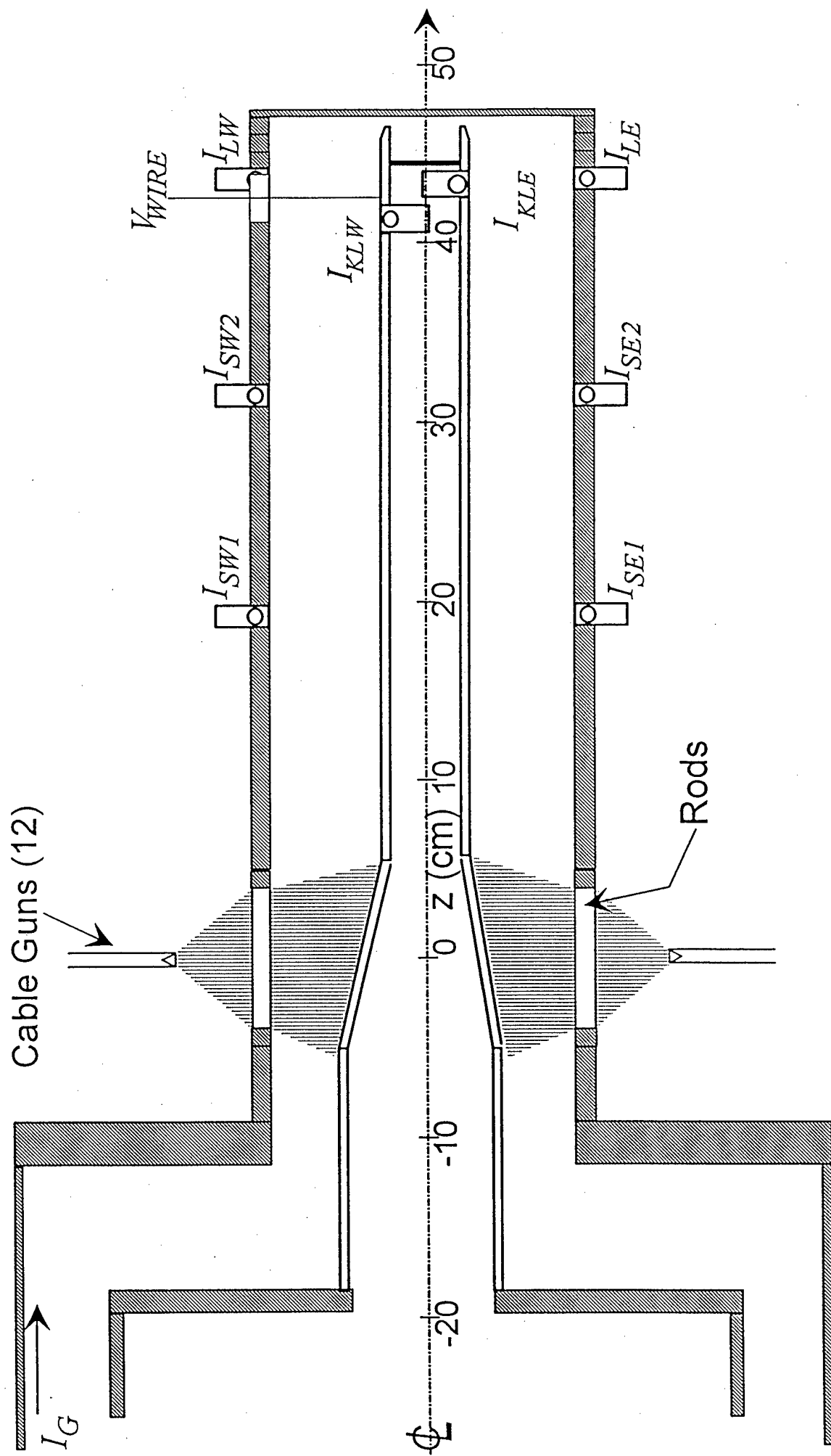


Fig. 2

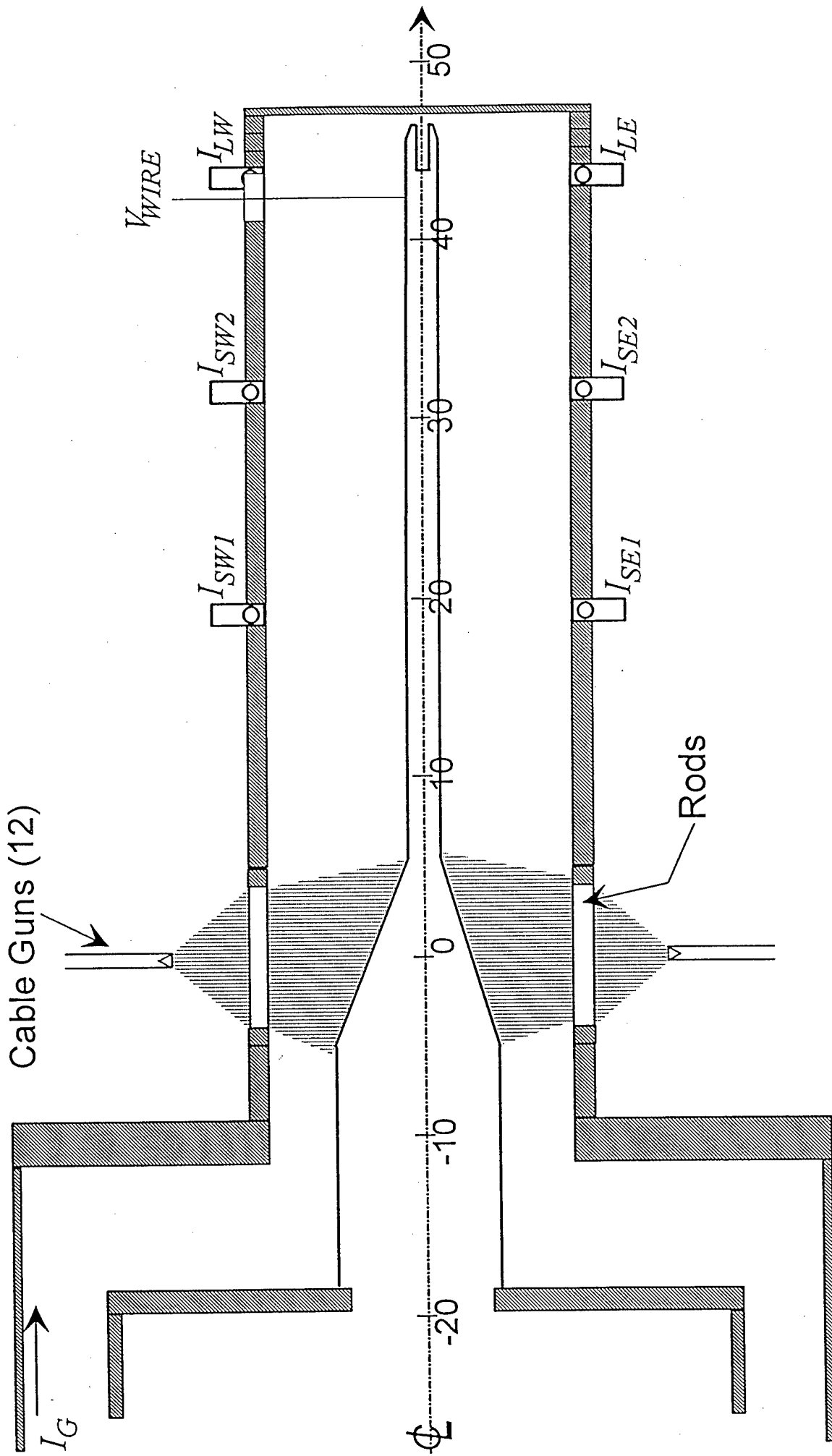


Fig. 3

Shot 1498

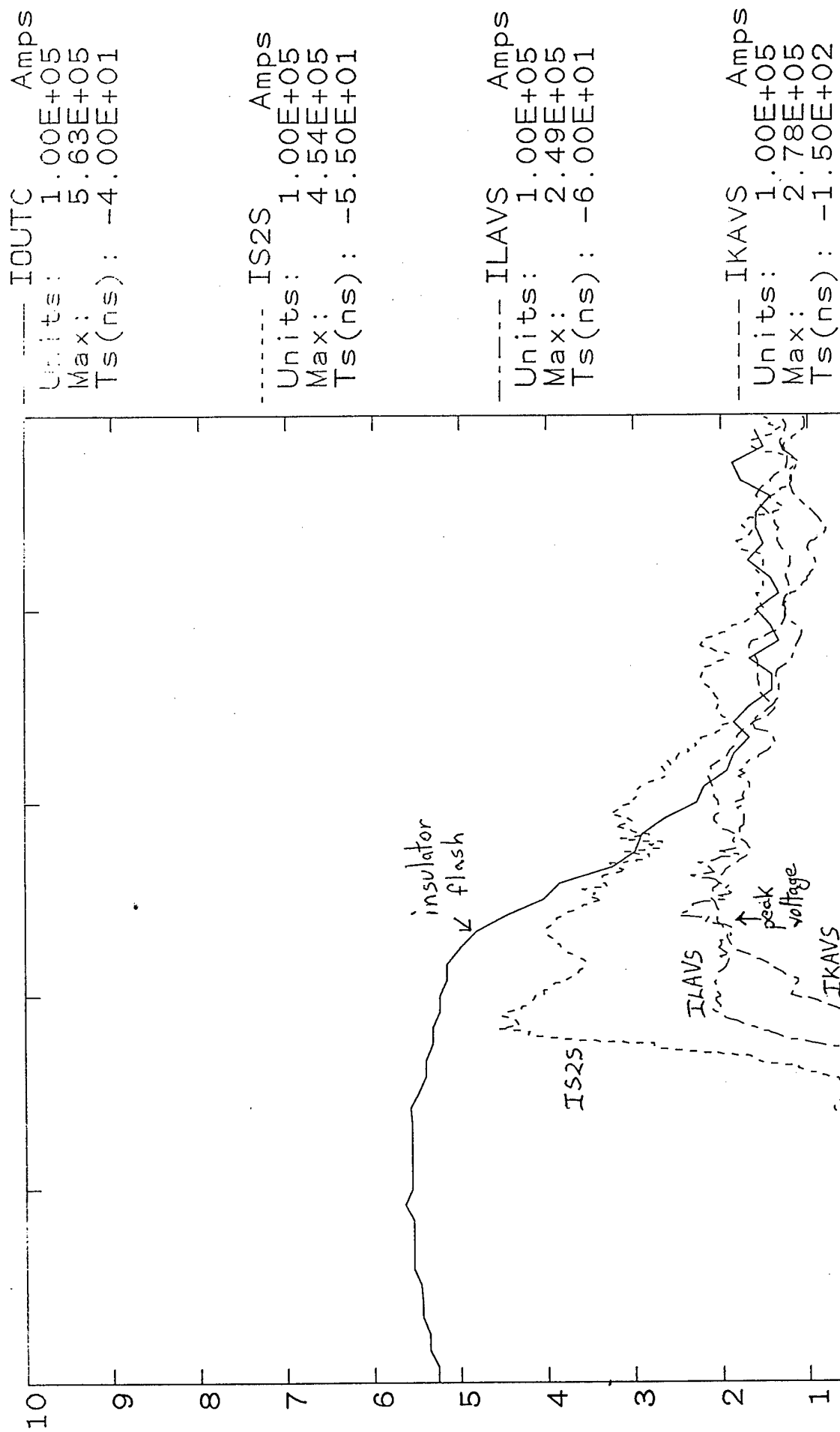


Fig. 4



Shot 1497

IOUTC Amps  
 Units: 1.00E+05  
 Max: 5.35E+05  
 Ts(ns): -4.00E+01

IS2S Amps  
 Units: 1.00E+05  
 Max: 2.86E+05  
 Ts(ns): -5.50E+01

ILAVS Amps  
 Units: 1.00E+05  
 Max: 2.53E+05  
 Ts(ns): -6.00E+01

IKAVS Amps  
 Units: 1.00E+05  
 Max: 4.00E+05  
 Ts(ns): -1.50E+02

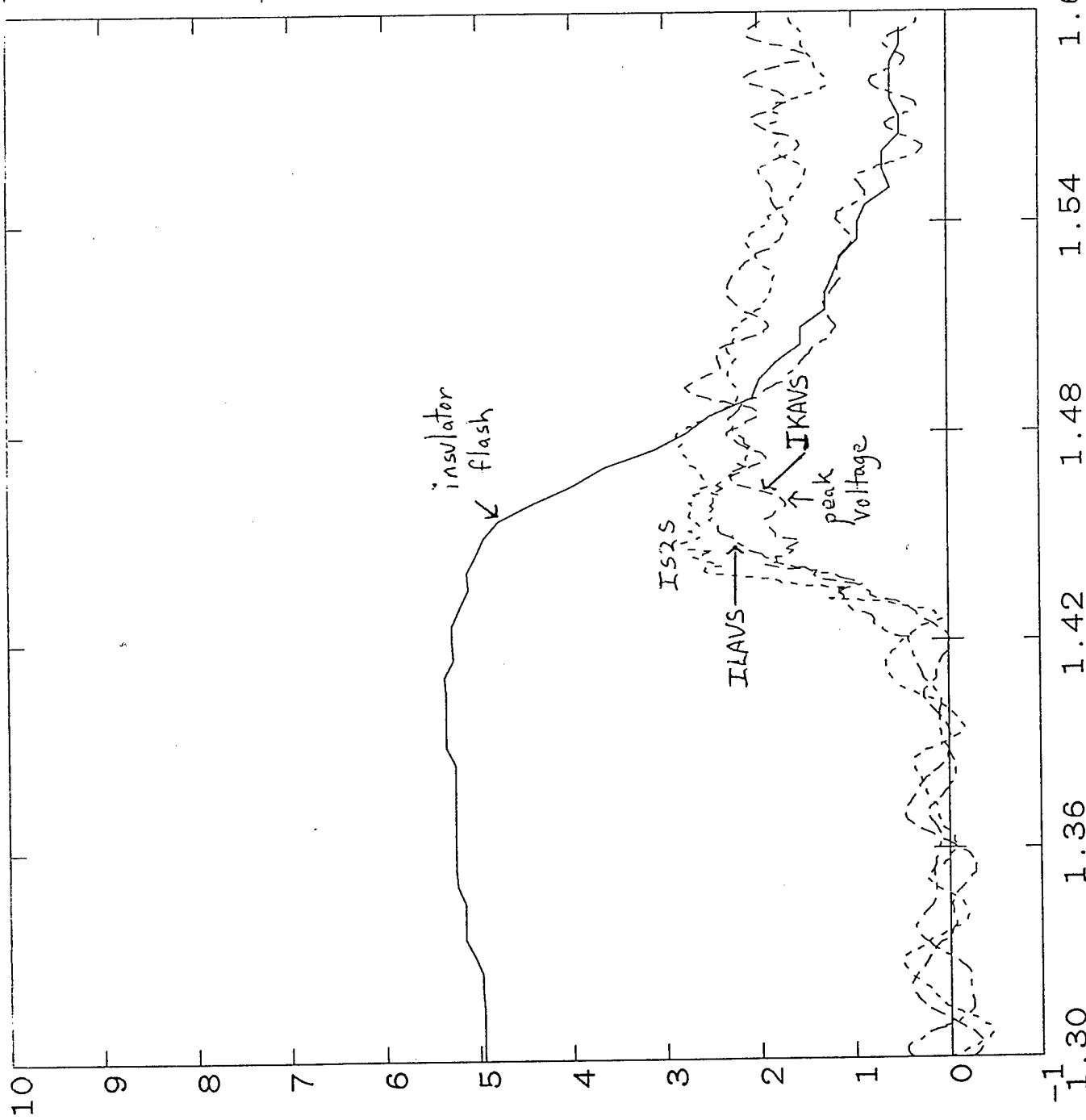


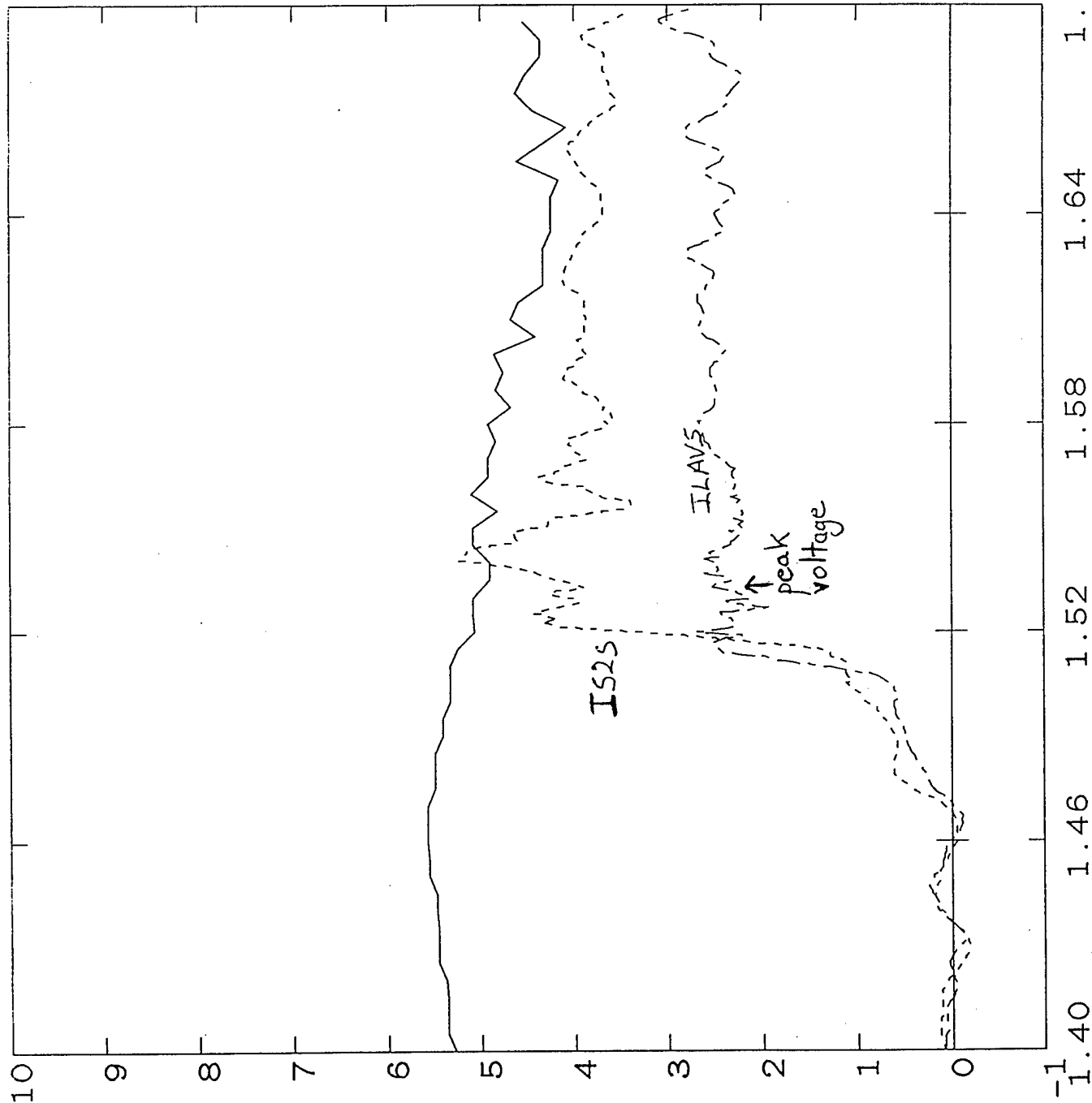
Fig. 5 Timescale: Microseconds

Shot 1500

----- IOUTC      Amps  
Units: 1.00E+05  
Max: 5.56E+05  
Ts(ns): -4.00E+01

----- IS2S      Amps  
Units: 1.00E+05  
Max: 5.23E+05  
Ts(ns): -5.50E+01

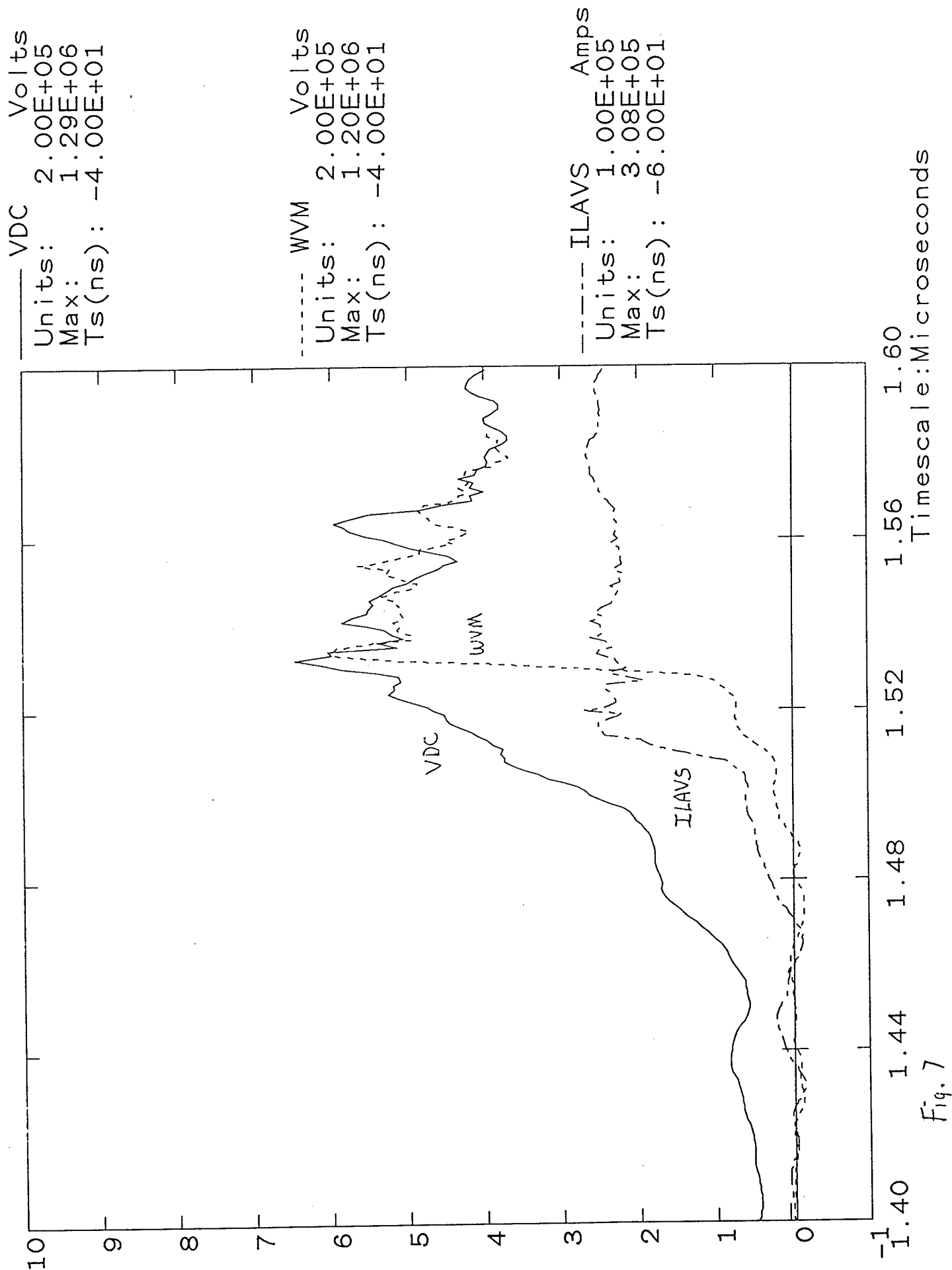
----- ILAVS      Amps  
Units: 1.00E+05  
Max: 3.08E+05  
Ts(ns): -6.00E+01



Timescale: Microseconds

Fig. 6

Shot 1500



Shot 1500

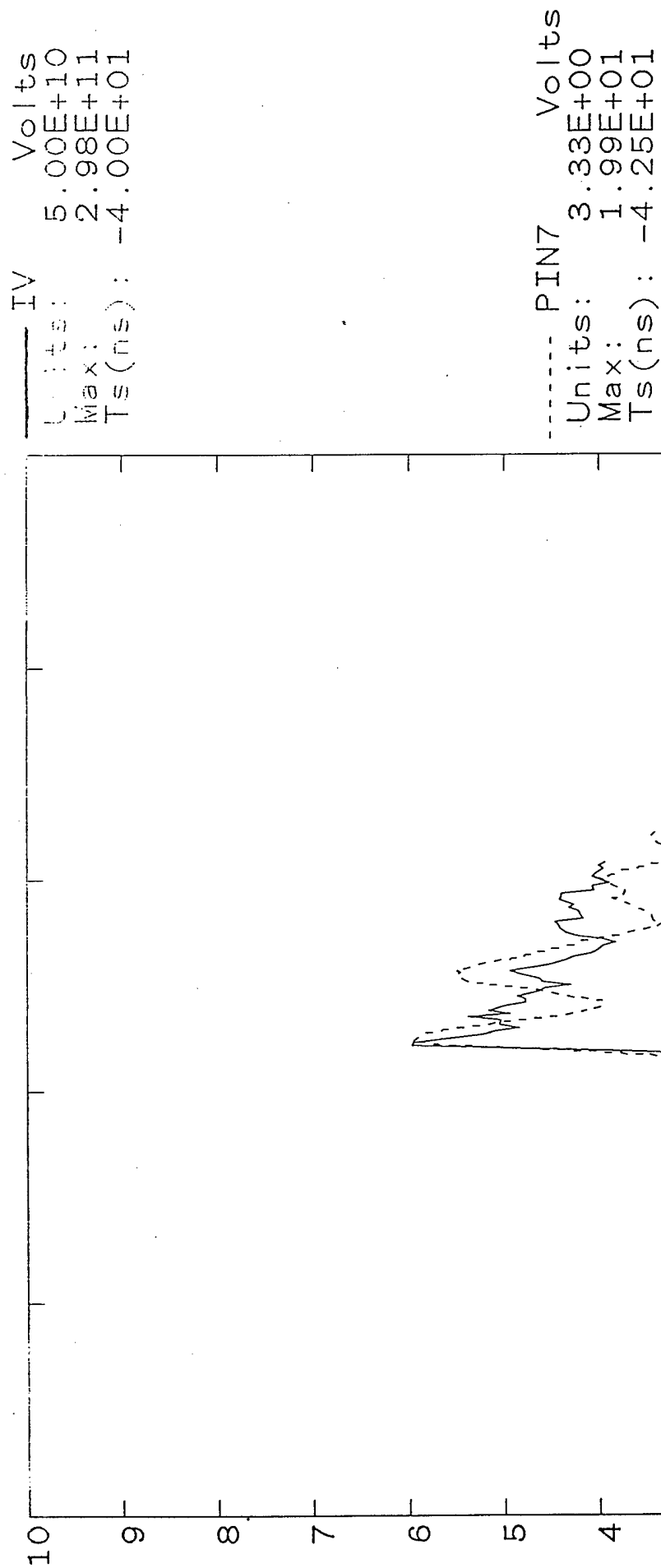
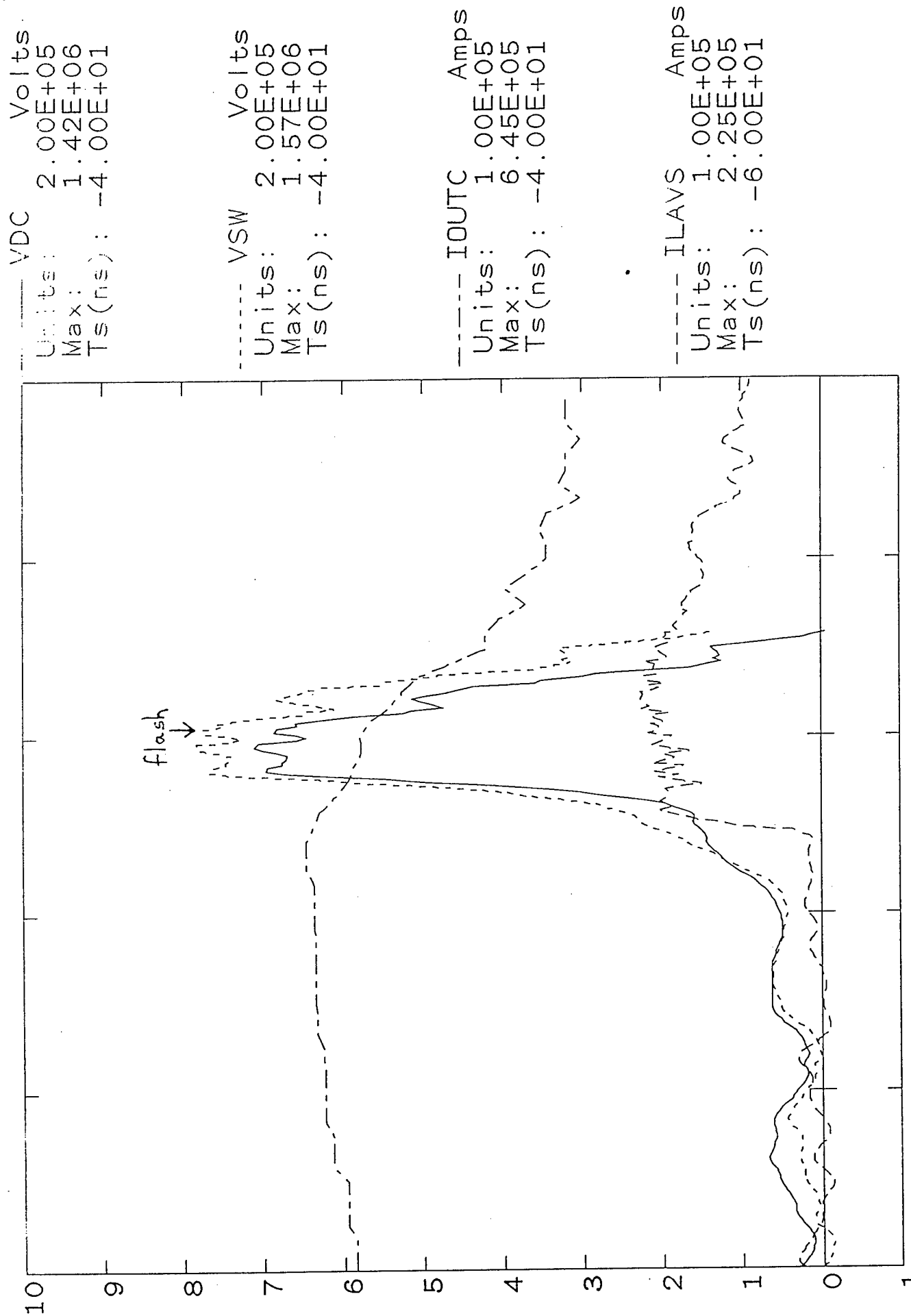


Fig. 8

Shot 1503



Timescale: Microseconds

Fig. 9

Shot 1504

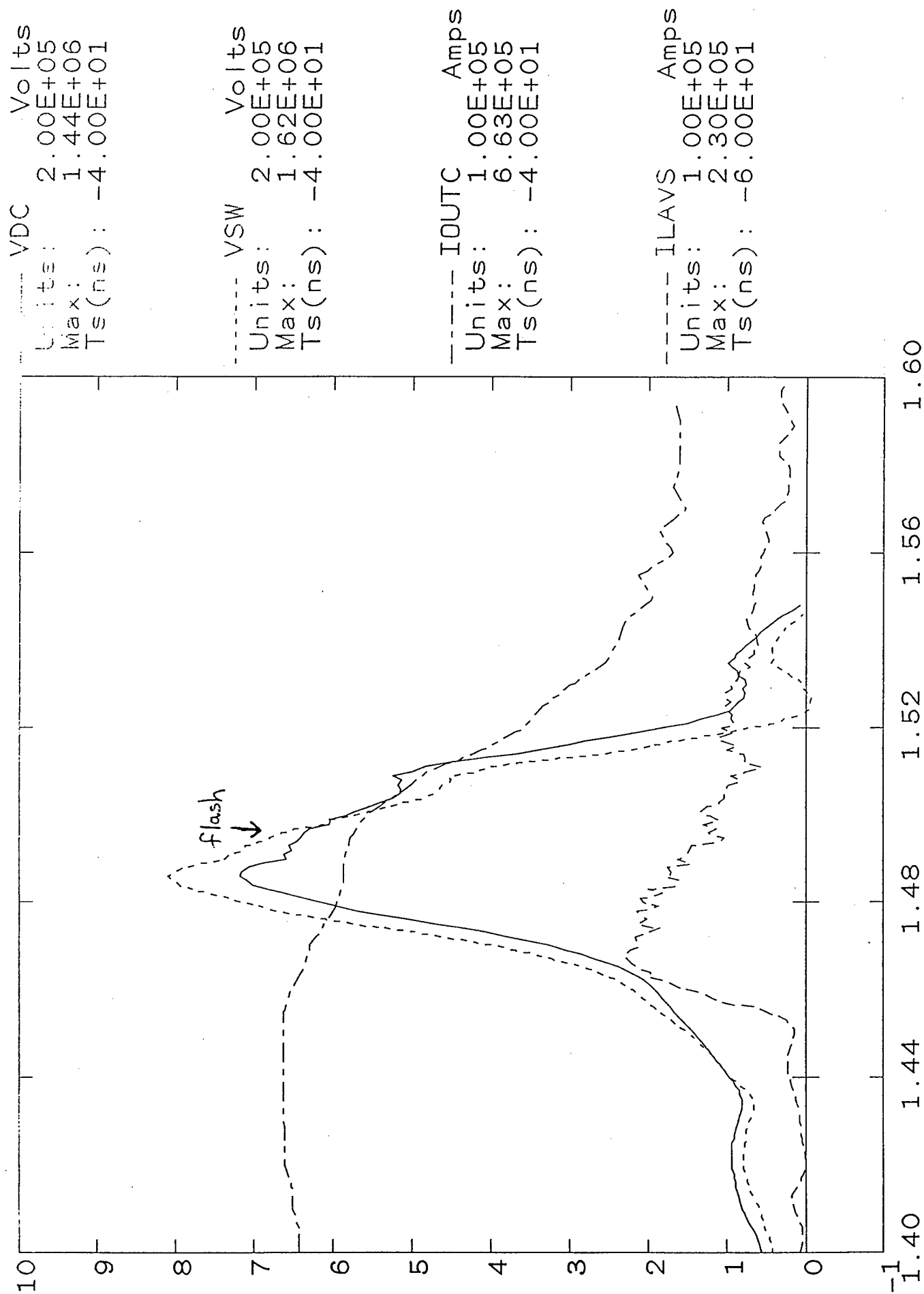


Fig. 10

Timescale: Microseconds

Shot 1507

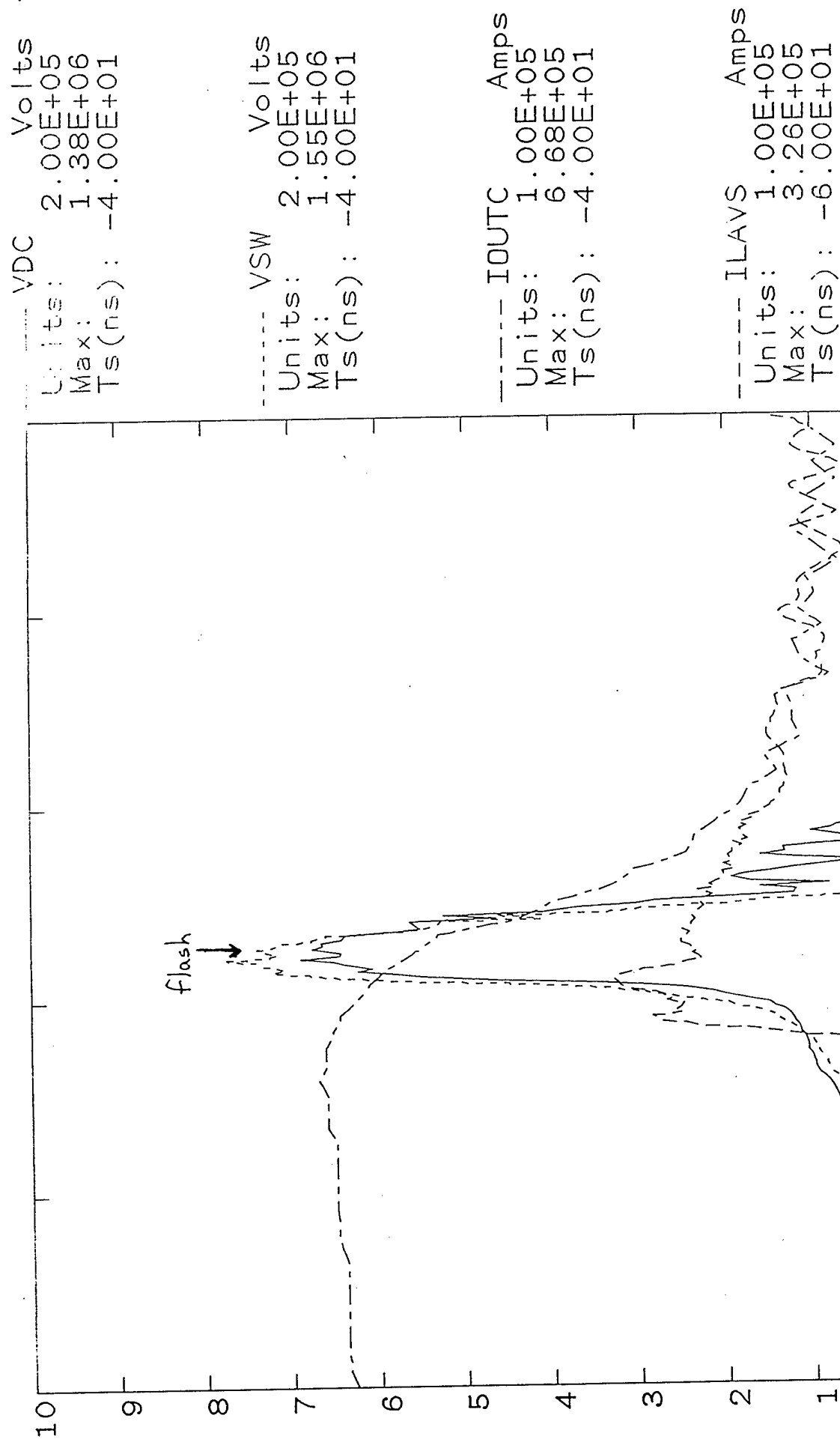


Fig. 11

Shot 1493

VSW1507 Volts  
Units: 2.00E+05  
Max: 1.55E+06  
Ts(ns): -4.00E+01

----- VSWT Volts  
Units: 2.00E+05  
Max: 7.07E+05  
Ts(ns): -2.65E+02

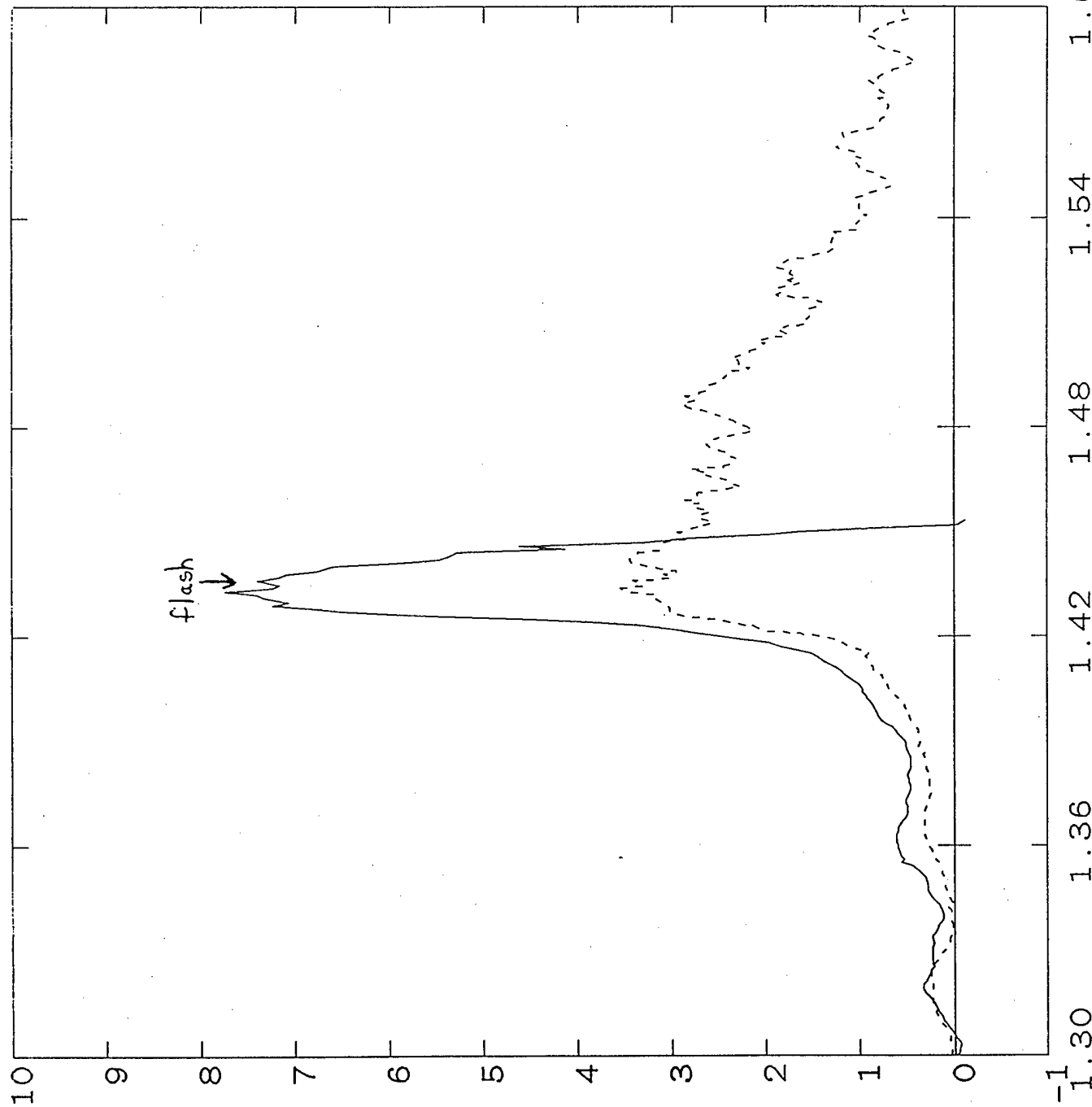


Fig.12  
Timescale:Microseconds



Shot 1510

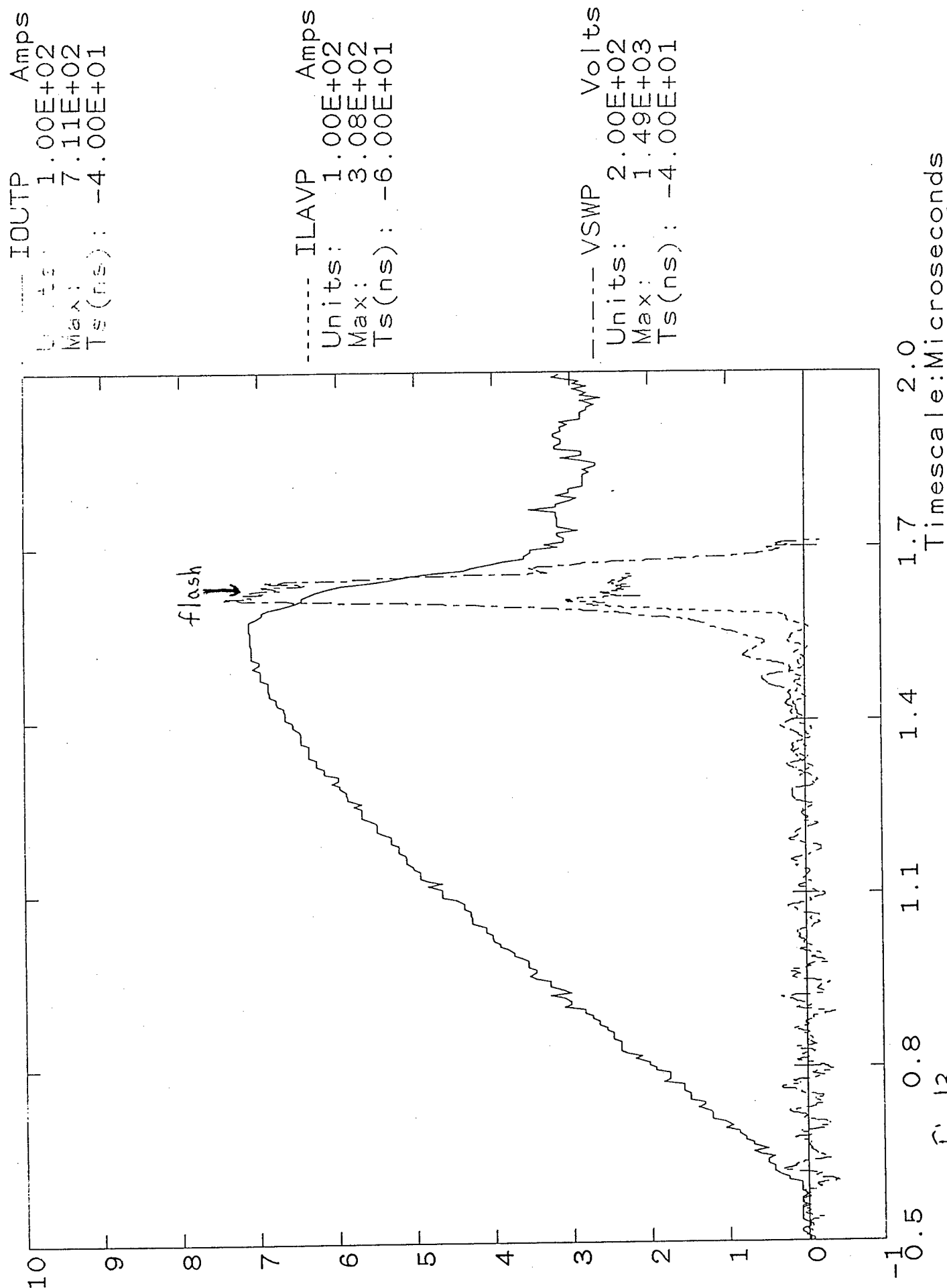


Fig. 13

Shot 1510

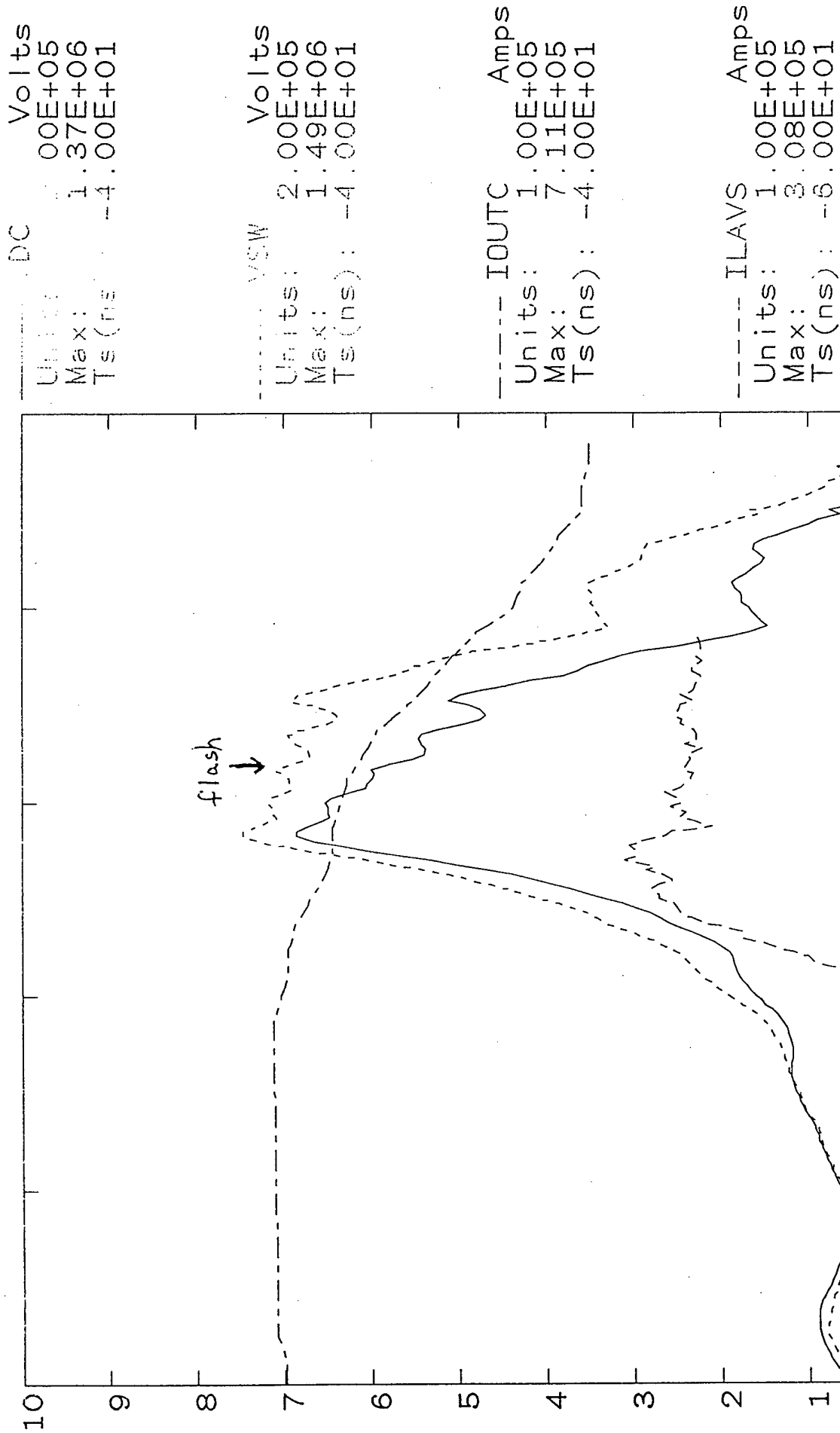


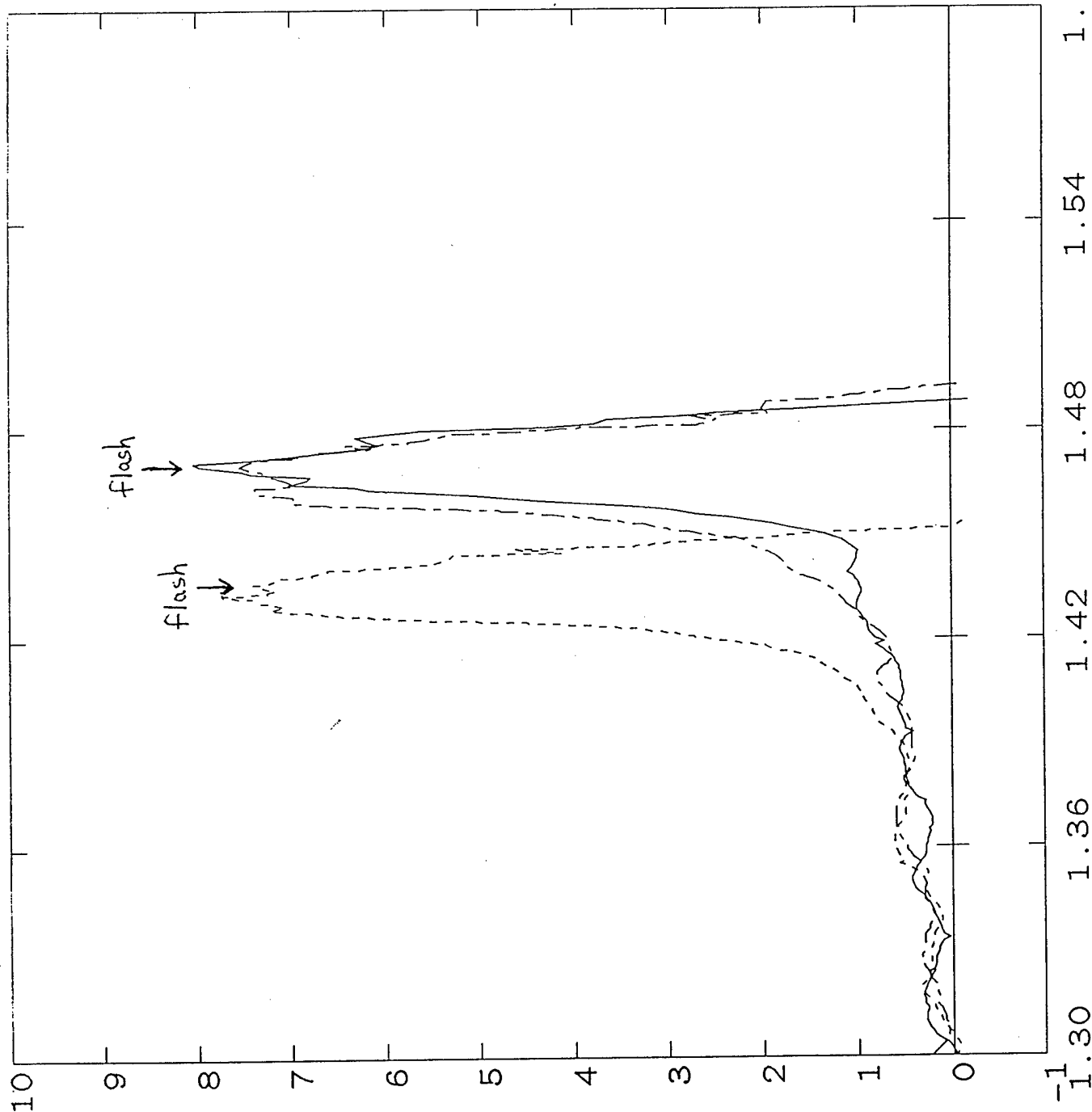
Fig. 14 Timescale: Microseconds

Shot 1508

----- VSW1506 Volts  
Units: 2.00E+05  
Max: 1.61E+06  
Ts(ns): -4.00E+01

----- VSW1507 Volts  
Units: 2.00E+05  
Max: 1.55E+06  
Ts(ns): -4.00E+01

----- VSW Volts  
Units: 2.00E+05  
Max: 1.51E+06  
Ts(ns): -4.00E+01



Timescale: Microseconds

Fig. 15

# Shot 1509

VSW  
Units: 2.00E+05  
Max: 1.47E+06  
Ts(ns): -4.00E+01

----- VSW1508 Volts  
Units: 2.00E+05  
Max: 1.51E+06  
Ts(ns): -4.00E+01

----- VSW1507 Volts  
Units: 2.00E+05  
Max: 1.55E+06  
Ts(ns): -4.00E+01

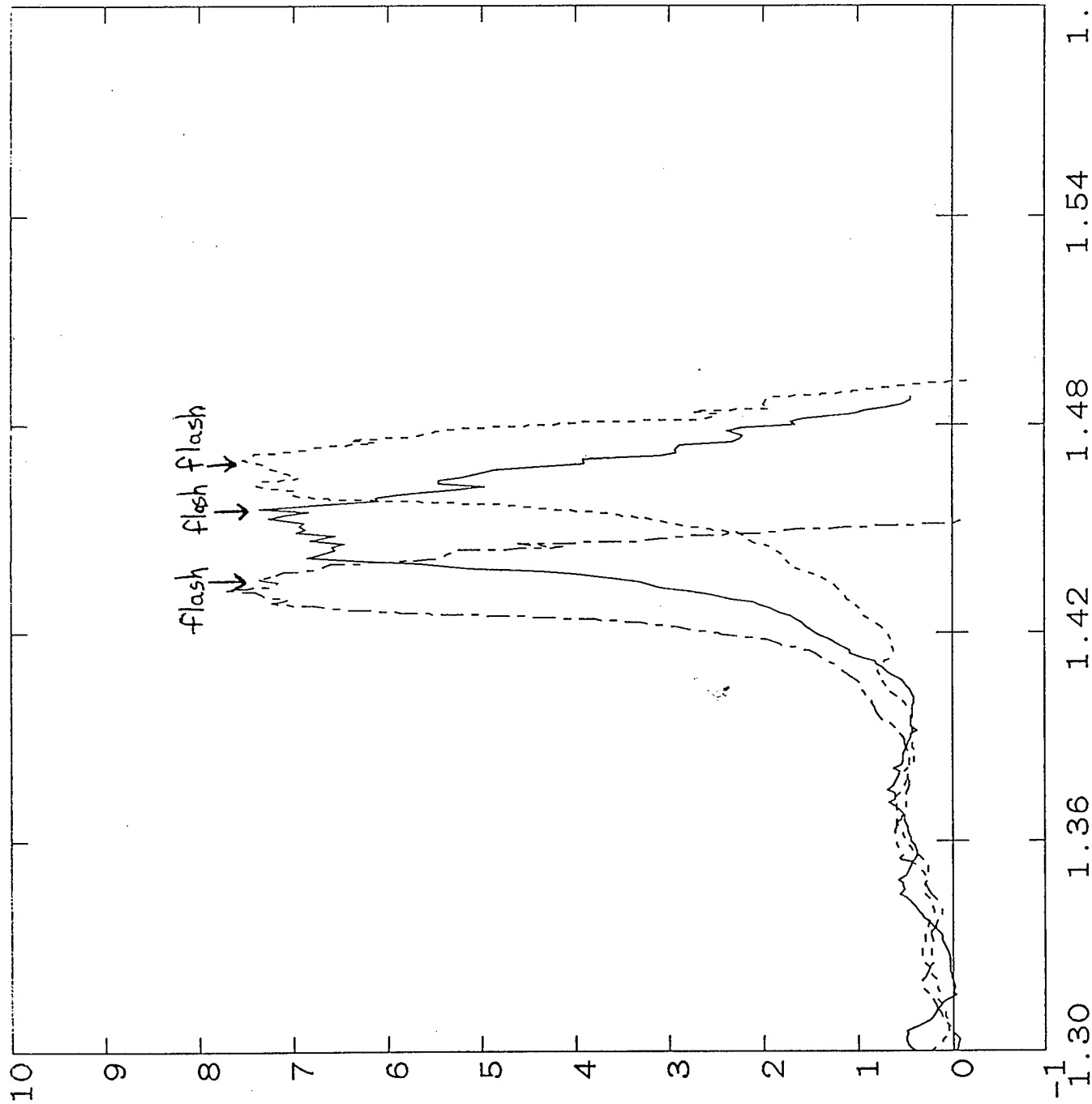


Fig. 16

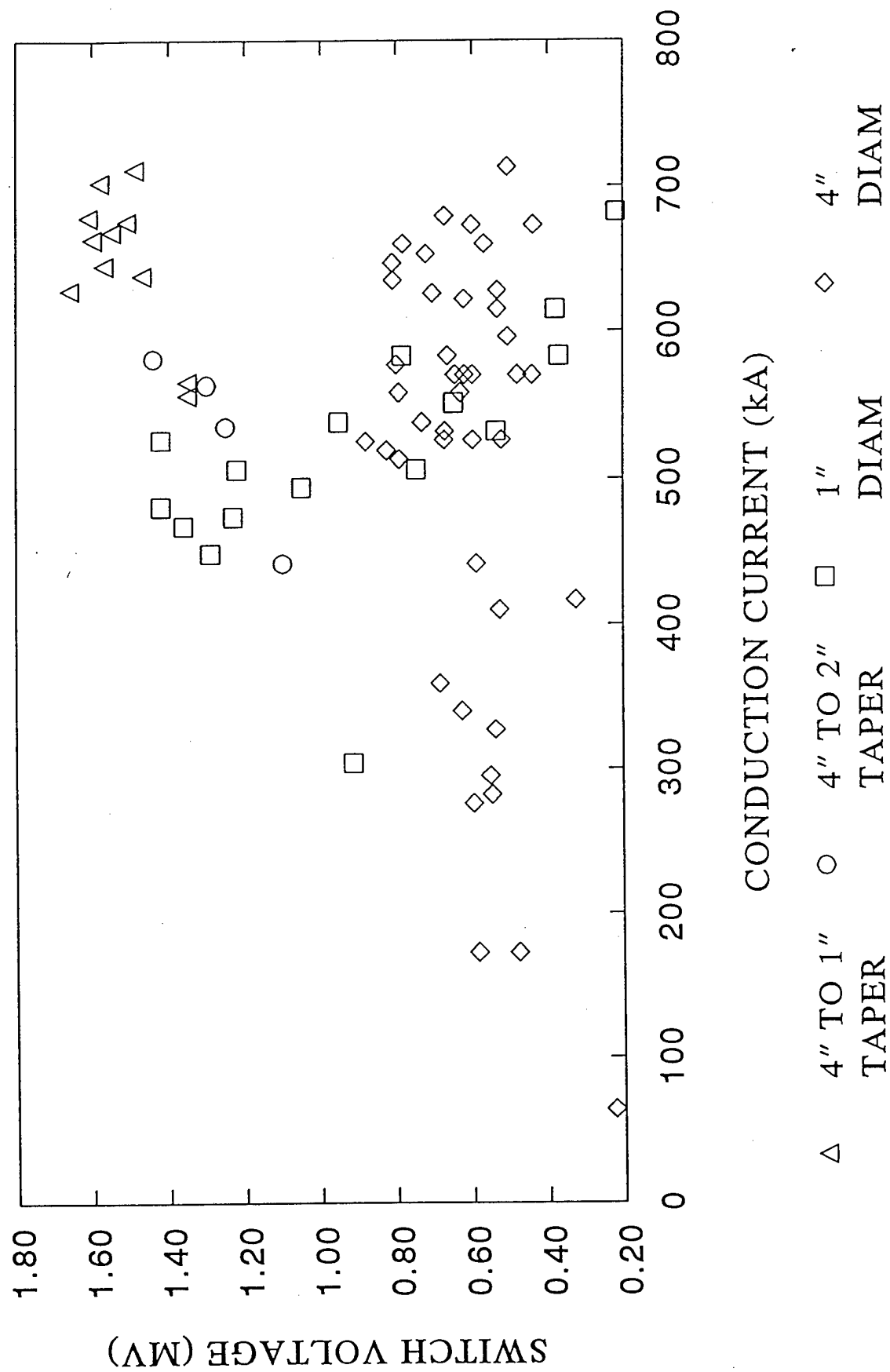


Fig. 17

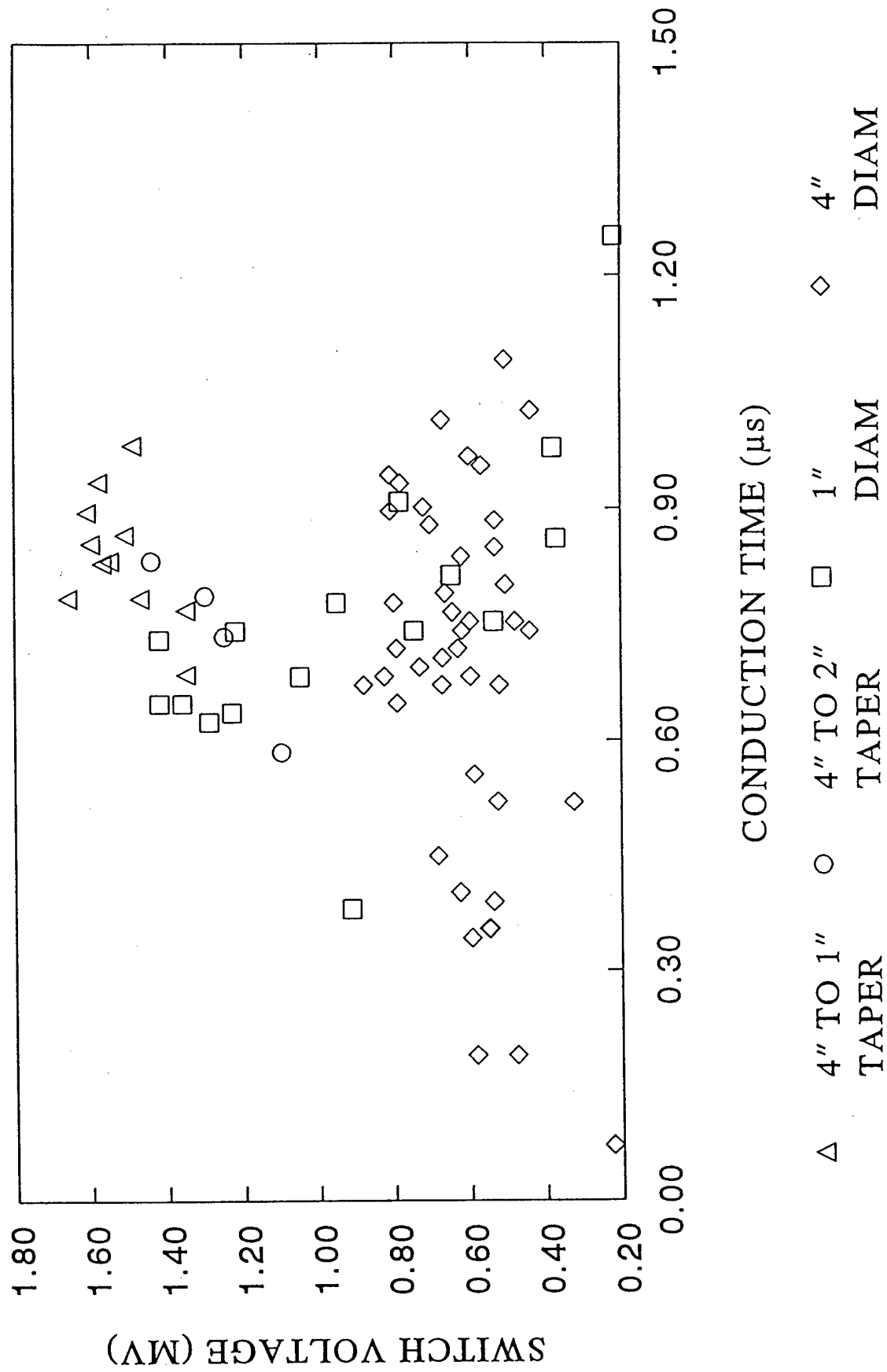


Fig. 18

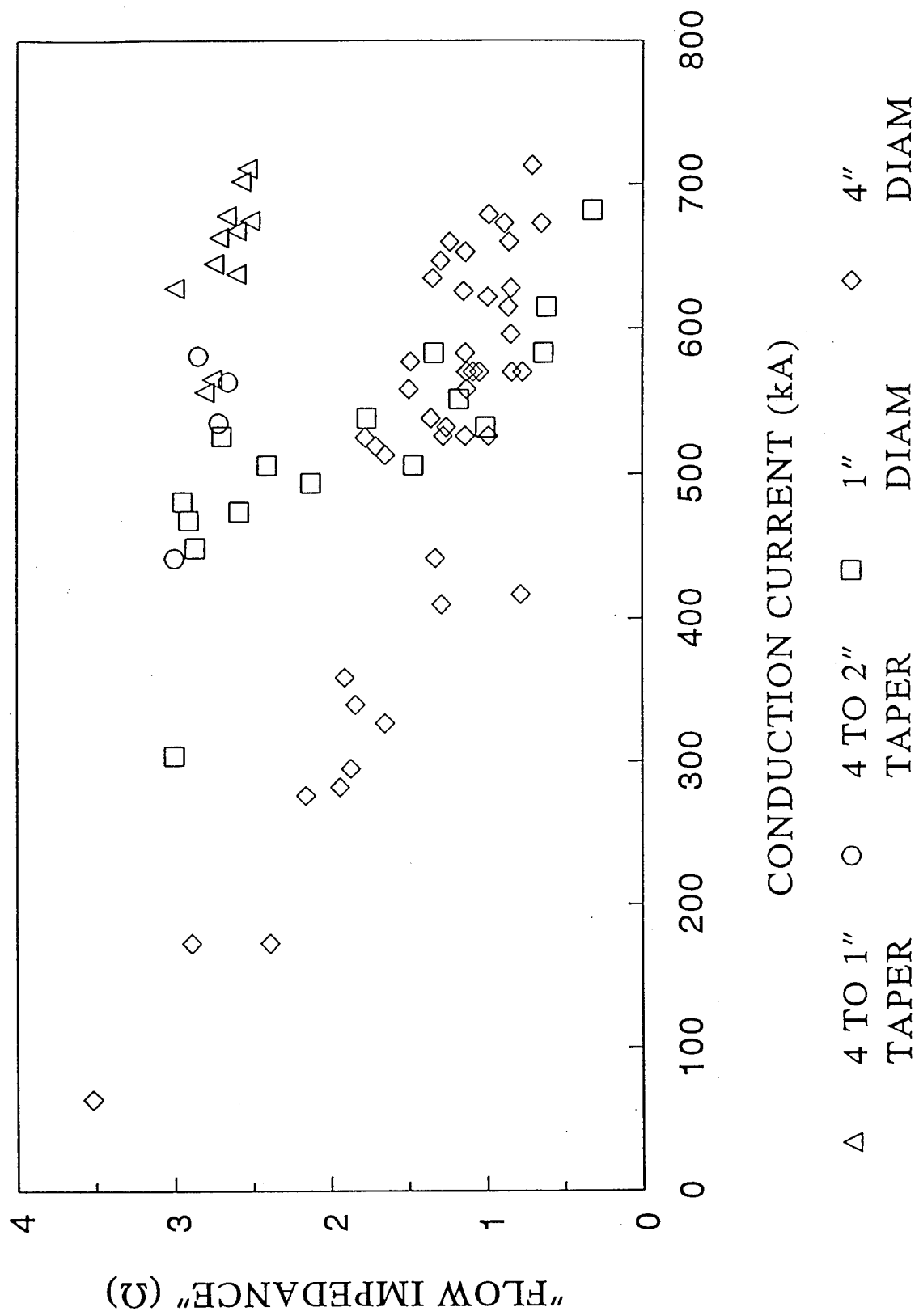


Fig. 19

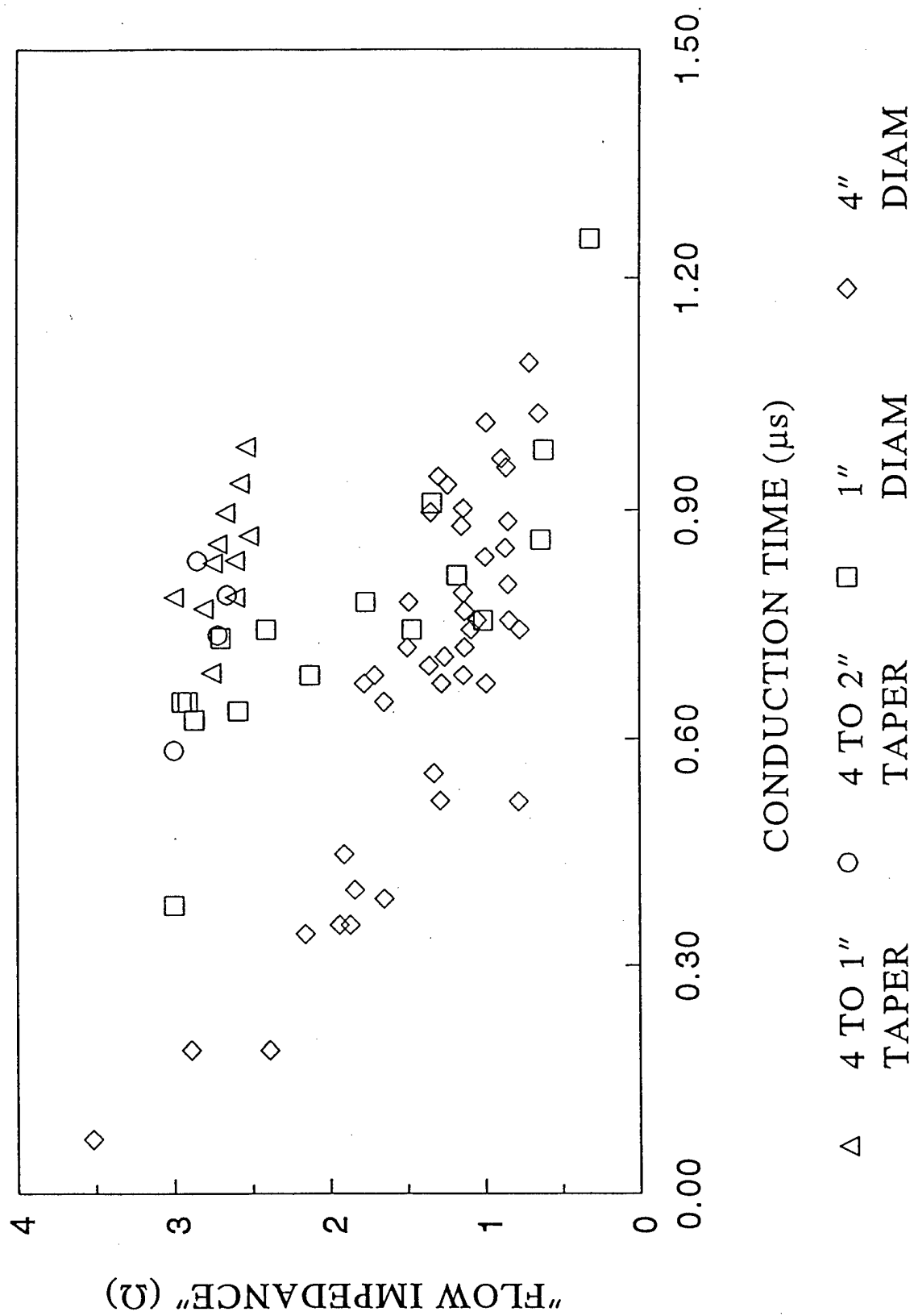


Fig. 20



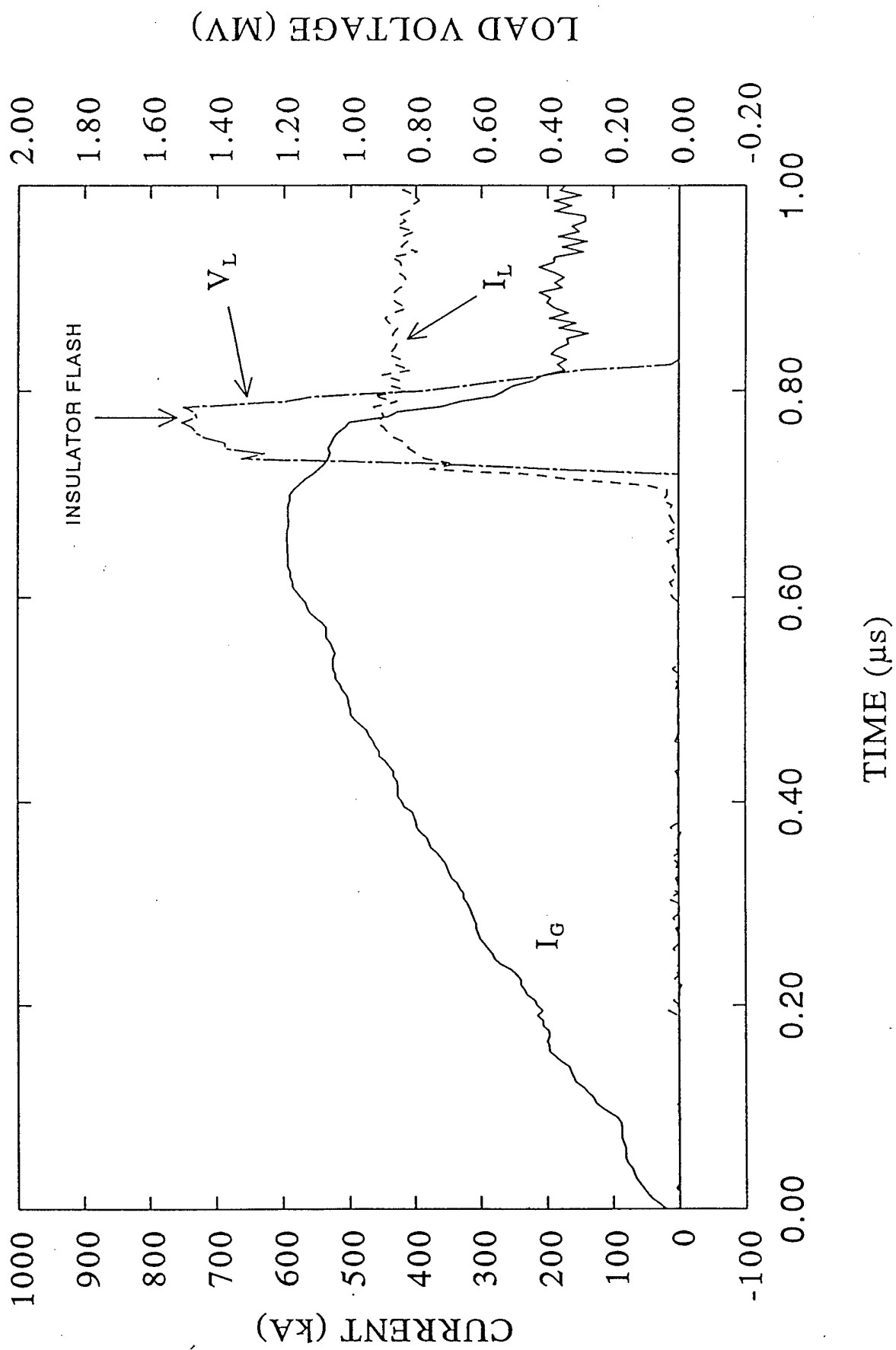


Fig. 21

**PARTICLE-IN-CELL SIMULATIONS OF FAST MAGNETIC FIELD PENETRATION  
INTO PLASMAS DUE TO THE HALL ELECTRIC FIELD**

S.B. Swanekamp<sup>#</sup>, J.M. Grossmann, A. Fruchtman<sup>\*</sup>, B.V. Oliver<sup>+</sup>, and P.F. Ottinger  
Plasma Physics Division  
Naval Research Laboratory  
Washington, DC 20375

<sup>#</sup>JAYCOR, Vienna, VA 22812.

<sup>\*</sup>SAIC, McLean, VA and Princeton Plasma Physics Laboratory, Princeton, NJ.

<sup>+</sup>National Research Council Research Associate at the Naval Research Laboratory.

PACS Numbers: 52., 52.30.-q, 52.65.Kj, 52.65.Rr, 52.75.Kq

### Abstract

Particle-in-cell (PIC) simulations are used to study the penetration of magnetic field into plasmas in the electron-magnetohydrodynamic (EMHD) regime. These simulations represent the first definitive verification of EMHD with a PIC code. When ions are immobile, the PIC results reproduce many aspects of fluid treatments of the problem. However, the PIC results show a speed of penetration that is between 10% and 50% slower than predicted by one-dimensional fluid treatments. In addition, the PIC simulations show the formation of vortices in the electron flow behind the EMHD shock front. The size of these vortices are on the order of the collisionless electron skin depth and are closely coupled to the effects of electron inertia. An energy analysis shows that one-half the energy entering the plasma is stored as magnetic field energy while the other half is shared between internal plasma energy (thermal motion and electron vortices) and electron kinetic energy loss from the volume to the boundaries. The amount of internal plasma energy saturates after an initial transient phase so that late in time the rate that magnetic energy increases in the plasma is the same as the rate at which kinetic energy flows out through the boundaries. When ions are mobile it is observed that axial magnetic field penetration is followed by localized thinning in the ion density. The density thinning is produced by the large electrostatic fields that exist inside the electron vortices which act to reduce the space-charge imbalance necessary to support the vortices. This mechanism may play a role during the opening process of a plasma opening switch.

## I. Introduction.

Magnetic field penetration into plasma is one of the most fundamental issues studied in plasma physics. Although the results of this paper are presented in the context of the plasma-opening switch (POS),<sup>1, 2</sup> the results have a wide range of other applications including space plasmas,<sup>3</sup> fast Z-pinches,<sup>4</sup> charged particle beam propagation in plasmas,<sup>5,6</sup> and basic laboratory experiments<sup>7</sup>. Much of the early work on this subject was performed within the realm of magnetohydrodynamic (MHD) theory where ions move under the influence of  $\mathbf{J} \times \mathbf{B}$  forces and magnetic field is convected with the ion fluid.<sup>8</sup> In this case, the characteristic ion speed is given by the Alfvén speed,  $V_A = B / (4\pi n_i m_i)^{1/2}$ , where  $B$  is the magnetic field strength,  $n_i$  is the ion density, and  $m_i$  is the ion mass. If the plasma is collisional, magnetic field can penetrate due to resistive diffusion at a rate given by  $V_D = c^2 \eta / (4\pi L_D)$ , where  $c$  is the speed of light,  $\eta$  is the resistivity (arising from either classical or anomalous collisions), and  $L_D$  is the characteristic diffusion length.<sup>9</sup> Recent theoretical studies have shown that magnetic field can penetrate into initially unmagnetized plasma on a time scale faster than either the Alfvén speed or resistive diffusion.<sup>10</sup> This penetration results from the addition of the Hall electric field in Ohm's law in ideal MHD theory. In this case the magnetic field is convected with the electron fluid with a characteristic speed given by  $V_H = cB / (4\pi n_e e L_H)$ , where  $n_e$  is the electron density,  $e$  is the magnitude of the electron charge, and  $L_H$  is the characteristic scale length for Hall penetration. The ratio of the Alfvén speed to the Hall speed can be written as  $V_A/V_H = L_H/(c/\omega_{pi})$ , where  $\omega_{pi} = (4\pi Z n_i e^2/m_i)^{1/2}$  is the ion plasma frequency and  $c/\omega_{pi}$  is the collisionless ion skin depth. Therefore, Hall penetration is faster than magnetic field convection due to ion motion when the characteristic Hall length is small compared with the ion collisionless skin depth. Similarly, it can be shown that Hall penetration is faster than resistive diffusion provided  $v < \Omega_\theta L_D/L_H$  where  $v$  is the collision frequency,  $\Omega_\theta = eB_\theta/m_e c$  is the electron cyclotron frequency, and  $m_e$  is the electron rest mass.

This paper presents the first verification of Hall penetration using the particle-in-cell (PIC) method.<sup>11</sup> The simulations are performed using the MAGIC code developed at Mission Research Corporation.<sup>12</sup> Many of the earlier studies of Hall penetration were performed with a fluid approach with various approximations.<sup>13,14,15,16</sup> Some of the approximations that are necessary to close the fluid equations, such as the form for the pressure tensor and the equation of state, make solutions of the fluid equations questionable. In addition, much of the past work required a small amount of collisionality to remove singularities. However, even this small amount of collisionality can lead to difficulties. For example, a small amount of collisionality can lead to unphysically large plasma heating for the drive currents expected in a POS. The PIC method can provide answers to these questions since it is a collisionless, kinetic approach, that requires no assumptions regarding the pressure tensor or plasma equation of state. When there are no collisions, it would be interesting to understand how energy is partitioned between magnetic field energy and internal plasma energy.

Previous PIC simulations of gap formation in the POS have shown evidence of magnetic field penetration and vortices in the electron flow during the gap formation process.<sup>17</sup> However, because several competing mechanisms associated with ion motion occur simultaneously, it has been difficult to verify that this penetration is connected to the Hall effect. Vortices in the electron flow have also been predicted analytically<sup>18,19,20,21</sup> and observed with the two fluid code Anthem<sup>22</sup>.

The PIC results presented in this paper show that vortices in the electron flow accompany magnetic field penetration and these vortices are a natural consequence of the electron inertia. These vortices are similar in many aspects to the vortices observed in PIC simulations of vacuum electron flow in magnetically insulated transmission lines (MITL).<sup>23</sup> Much of the theory developed in Sec. II applies to vacuum flow in MITLs as well.

The outline of the paper is as follows. In Sec. II a brief discussion of the fluid treatment of Hall penetration is presented as well as some of the key results from the fluid approach. In Sec. III results are presented from several PIC simulations that show magnetic field penetration into the plasma. It is shown that the observed penetration agrees very well with the fluid description in many aspects. However, the PIC simulations also show paramagnetic vortices in the electron flow and the penetration speed is slower than that predicted by the fluid theory. Section IV presents a detailed discussion of the partition of energy in the plasma between magnetic energy, thermal and directed electron energy, and energy loss to the boundaries. Because the main concern of the paper is the regime where Hall penetration dominates ( $L_H \ll c/\omega_{pi}$ ), the ion mass is taken to be infinite for much of the paper. However, the role of ion motion is addressed in Sec. III by comparing simulation results for a case where ions can move with the case where ion mass is infinite.

## II. Fluid theory of magnetic field penetration into plasmas due to the Hall electric field.

In this section, the theory of magnetic field penetration into a plasma is presented using a fluid approach. To get a solution to these equations it is necessary to make several questionable assumptions regarding the form of the pressure tensor, the role of displacement current, and the importance of electron inertia. As the basic equations for magnetic field penetration are developed, the key assumptions of the fluid approach are highlighted and compared with the physics contained in the PIC approach. In addition, the main results of the fluid theory are developed for comparison with the PIC simulations presented in the next section.

The geometry considered in this paper is that of the plasma opening switch shown in Fig. 1. In this geometry, a plasma of axial length  $l$  is placed between the anode and cathode of a coaxial transmission line. Current ( $I_G$ ) is driven through the plasma in the form of a transverse electromagnetic (TEM) wave that is applied from the left boundary. In the analysis presented below azimuthal symmetry is assumed and only the TM mode set is retained with field components  $E_r(r,z,t)$ ,  $E_z(r,z,t)$ , and  $B_\theta(r,z,t)$ .

The evolution of the electron fluid is governed by the continuity and momentum balance equations which are given by

$$\frac{\partial n_e}{\partial t} + \nabla \cdot n_e \mathbf{V}_e = 0 \quad , \quad (1)$$

$$\frac{\partial \gamma \mathbf{V}_e}{\partial t} + \mathbf{V}_e \cdot \nabla \gamma \mathbf{V}_e = -\frac{e}{m_e} \left( \mathbf{E} + \frac{\mathbf{V}_e \times \mathbf{B}}{c} \right) - \frac{\nabla \cdot \mathbf{P}}{n_e m_e} + \frac{e}{m_e} \eta \mathbf{J} \quad , \quad (2)$$

where  $\gamma = (1 - V_e^2 / c^2)^{-1/2}$  is the relativistic mass factor,  $\mathbf{V}_e$  is the electron fluid velocity,  $\mathbf{P}$  is the pressure tensor, and  $\mathbf{J}$  is the current density. In fluid treatments it is common to neglect the off diagonal terms in the pressure tensor and treat the pressure as a scalar. Since the PIC method allows for orbit crossings, no assumption regarding the form of the pressure tensor is needed. PIC simulations of the POS have shown that the off diagonal terms can be important in regions of the plasma where there is magnetic field penetration.<sup>24</sup>

When azimuthal symmetry is assumed, Eqs. (1) and (2) can be combined with Faraday's Law,

$$\nabla \times \mathbf{E} = -\frac{1}{c} \frac{\partial \mathbf{B}}{\partial t} , \quad (3)$$

to give the following equation describing the evolution of the electron fluid vorticity and magnetic field,

$$n_e r \frac{D}{Dt} \left( \frac{\omega_\theta - \Omega_\theta}{n_e r} \right) = - \left( \nabla \frac{1}{m_e n_e} \times \nabla p \right)_\theta + \frac{e}{m_e} (\nabla \times \eta \mathbf{J})_\theta . \quad (4)$$

In this last equation  $D/Dt = \partial/\partial t + \mathbf{V}_e \cdot \nabla$  is the convective derivative,  $p$  is the scalar pressure,  $\Omega_\theta = eB_\theta/m_e c$  is the electron cyclotron frequency, and  $\omega_\theta = (\nabla \times \mathbf{V}_e)_\theta$  is the electron fluid vorticity. If the scalar pressure is a function of the density, then the first term on the right hand side of Eq. (4) is zero. If collisions are also ignored, then Eq. (4) describes the constancy of  $\Gamma/n_e r$  along an electron trajectory, where  $\Gamma = \omega_\theta - \Omega_\theta$  is the generalized electron vorticity. For example, the electrons in the plasma prefill are initially unmagnetized and at rest so that their initial generalized vorticity is zero. As magnetic field penetrates into the plasma these electrons seek regions of the plasma that keep their generalized vorticity zero along their trajectory.

The appearance of vorticity in solutions to the fluid equations is a direct consequence of electron inertia. In much of the previous work on Hall theory, electron inertia is ignored. This is equivalent to assuming that electrons are  $\mathbf{E} \times \mathbf{B}$  drifting and results in the neglect of the fluid vorticity ( $\omega_\theta = 0$ ) in Eq. (4). When electron inertia is ignored, Eq. (4) can be written as<sup>25</sup>

$$\frac{D}{Dt} \left( \frac{r \Omega_\theta}{n_e r^2} \right) = 0 , \quad (5)$$

where the pressure and collision terms have been dropped. Equations (4) or (5) apply regardless of the details of the ion motion. Therefore, they are appropriate not only to electron flows in plasmas but also apply to vacuum electron flows in magnetically insulated transmission lines. If there is ion motion, then the electron density will evolve in a complicated manner as ions redistribute themselves. If the electron fluid remains in quasi-equilibrium, then Eq. (5) implies that the electron fluid will evolve to keep  $r \Omega_\theta / n_e r^2$  constant along the electron trajectories as the ion density evolves in time.

In electron magnetohydrodynamics (EMHD) it is customary to ignore ion motion and assume that the plasma is space charge neutral ( $n_e = Z n_i$ ). This simplifies the fluid equations because the electron density is constant and determined by the initial ion distribution. With these assumptions, an equation describing Hall penetration can be derived by expanding the convective derivative in Eq. (5) and using Ampere's Law (displacement current is neglected) to eliminate the electron fluid velocity ( $\mathbf{V}_e = -\frac{c}{4\pi Z n_i e} \nabla \times \mathbf{B}$ ). This equation can be written as

$$\frac{\partial B_\theta}{\partial t} - \frac{c r B_\theta}{4\pi e} \left( \nabla r B_\theta \times \nabla \frac{1}{Z n_i r^2} \right)_\theta = 0 . \quad (6)$$

A stable, non-linear solution to Eq. (6) predicts a shock wave for  $r B_\theta$  which propagates along the  $n_i r^2$  contours.<sup>14, 26</sup>

As a special case of Eq. (6), consider the situation where the ion density is independent of  $z$  [i.e.  $n_i(r, z) = n_i(r)$ ]. In this case the  $Z n_i r^2$  contours are parallel to the  $z$  axis and shock

propagation is expected to occur in the  $z$  direction. For this special case, Eq. (6) can be expressed as<sup>13</sup>

$$\frac{\partial B_\theta}{\partial t} - \frac{c B_\theta}{4\pi Z n_i e L_H} \frac{\partial B_\theta}{\partial z} = 0, \quad (7)$$

where

$$L_H = \left[ (1 / Z n_i r^2) d(Z n_i r^2) / dr \right]^{-1} \quad (8)$$

is the characteristic length for Hall penetration. The penetration speed of the shock front can be expressed as<sup>13,27</sup>

$$V_H(r) = \alpha \frac{c(-r B_\theta)}{4\pi Z n_i e r L_H}, \quad (9)$$

where  $\alpha$  is a constant on the order unity that depends on the time dependence for the applied current,  $I_G(t) = cr B_\theta(r, z=0, t)/2$ . Two cases of practical importance include the constant applied current and the linearly rising current for which  $\alpha = 1/2$  and  $3/8$  respectively.

It is important to note that magnetic field will penetrate only in regions of plasma where the Hall speed is positive. When  $V_H \leq 0$ , Eq. (7) predicts evanescent waves that do not propagate. Furthermore, if the plasma is initially magnetized then expulsion of magnetic field is expected in regions where  $V_H \leq 0$ .<sup>15,22</sup> For a POS in negative polarity ( $-r B_\theta > 0$ ), Eq. (7) predicts magnetic field penetration in regions where  $d(Z n_i r^2)/dr > 0$ . Exclusion of magnetic field is expected in regions where  $d(Z n_i r^2)/dr \leq 0$ . In positive polarity ( $r B_\theta > 0$ ) the regions of penetration and exclusion are reversed. In general it can be shown that magnetic field penetration occurs in the  $\mathbf{B} \times \nabla(Z n_i r^2)$  direction.<sup>16</sup>

### III. Simulation Results

Since Hall penetration dominates ion motion when  $L_H/(c/\omega_{pi}) \ll 1$ , ion motion is assumed negligible in the majority of this section by taking ions to be infinitely massive. The role of ion motion will be addressed later in this section by comparing the infinitely-massive-ion case with a case where the ions can move.

One of the fundamental weaknesses of the PIC method is the so called "grid" instability that produces numerical plasma heating. This instability saturates when<sup>11</sup>

$$\lambda_D \sim \Delta x / \pi, \quad (10)$$

where  $\Delta x$  is the grid size,  $\lambda_D = (k_B T_e / 4\pi n_e e^2)^{1/2}$  is the plasma Debye length,  $k_B$  is the Boltzmann constant, and  $T_e$  is the electron temperature. Artificial plasma heating from the grid instability severely limits the plasma densities that can be accurately simulated with the PIC method. To limit the numerical heating to 10-100 eV, grid sizes of 0.005 to 0.01 cm were used with plasma densities ranging between  $10^{12} \text{ cm}^{-3}$  and  $3 \times 10^{13} \text{ cm}^{-3}$ . For these densities the electron mass was reduced from the normal electron mass to keep the collisionless electron skin depth small compared to the dimensions of the plasma (typically a few cm). At the end of this section, it is demonstrated that the results from the reduced electron mass are equivalent to those with normal electron mass and a corresponding higher magnetic field and electron density.

The simulations presented in this section are set-up as shown in Fig. 1. Space-charge-limited emission of electrons is allowed from the entire cathode surface. The emitted electrons are given an initial velocity of  $10^8 \text{ cm/s}$ . This corresponds to an initial energy of energy of about 3 eV. Plasma is loaded between  $z=2 \text{ cm}$  and  $z=5 \text{ cm}$  between the cathode radius of  $r_c=2.5 \text{ cm}$  and the anode radius of  $r_a=5.0 \text{ cm}$ . A linearly rising current ramp with  $dI_G/dt=10 \text{ kA/ns}$  is

applied on the left hand boundary. The electron mass used in these simulations was 1/10 the normal electron mass. Two slightly different density profiles were used. These profiles are shown Fig. 2a. The first profile is a parabolic density profile with the minimum density of  $10^{12} \text{ cm}^{-3}$  at  $r=3.75 \text{ cm}$  rising to  $3 \times 10^{13} \text{ cm}^{-3}$  at the electrodes. For this density profile the characteristic Hall scale length is 0.2 cm. The second profile is a uniform-parabolic profile that is uniform at  $10^{12} \text{ cm}^{-3}$  between the cathode and  $r=3.75 \text{ cm}$  and then rises parabolically to  $3 \times 10^{13} \text{ cm}^{-3}$  at the anode. The instantaneous Hall speed profiles for these two density profiles in negative polarity ( $-rB_\theta > 0$ ) are shown in Fig. 2b. Recall from the discussion in Sec. II that magnetic field penetration is expected only in regions where the Hall speed is positive. Therefore, exclusion of magnetic field is expected for  $r \leq 3.75 \text{ cm}$  in negative polarity for the parabolic profile. Magnetic field penetration is expected for  $r > 3.75 \text{ cm}$  with maximum penetration occurring near  $r=4 \text{ cm}$ . In positive polarity the regions of penetration and exclusion are reversed. For the uniform-parabolic profile, magnetic field is expected to penetrate the entire plasma in negative polarity. Since the regions of penetration and exclusion are reversed in positive polarity ( $rB_\theta > 0$ ), no magnetic field penetration is expected in positive polarity for the uniform-parabolic profile since the Hall speed profile is negative everywhere.

The fluid theory of Hall penetration is tested with several PIC simulations. One of the most useful diagnostics from these simulations are the contours of  $rB_\theta(r,z)$ . From Ampere's Law  $rB_\theta(r,z)$  is proportional to the current enclosed within a radius  $r$  at axial location  $z$  and which is expressed as  $I(r,z) = 2\pi r B_\theta(r,z) / \mu_0$ . With this definition, the difference between the contour levels of  $I(r,z)$  represents current flow in the plasma parallel to the contours.

Current enclosed contours at  $t=2 \text{ ns}$  are shown in Fig. 3 for the parabolic profile in negative polarity. As predicted, rapid magnetic field penetration takes place at a radial position where the maximum Hall speed occurs and no magnetic field penetration takes place in regions where the Hall speed is negative. Simulation results (not shown) also show that the regions of penetration and exclusion are reversed in positive polarity. However, the penetration speed predicted by the PIC method is about 50% slower than predicted by fluid theory. A one dimensional analysis of Eq. (4) indicates that electron inertia does not change the penetration speed.<sup>28</sup> Therefore, it is speculated that the slower penetration is caused by either strong two-dimensional effects or by the effects of electron pressure that are not included in the fluid analysis.

Figure 4 shows the current enclosed contours for the uniform-parabolic density profile in positive polarity. As predicted by theory, no magnetic field penetration into the bulk plasma deeper than a collisionless skin depth is observed. Rapid penetration of magnetic field is observed at the anode in both Figs. 3 and 4. Anode penetration occurs because the conductor boundary condition ( $E_{||}=0$ ) causes electrons to  $\mathbf{E} \times \mathbf{B}$  drift parallel to the anode.<sup>29</sup> Therefore, this penetration is strongly coupled to the anode boundary conditions and is different from the Hall penetration observed in the body of the plasma.

Figure 3 also shows that magnetic field penetration is accompanied by a train of vortices in the electron flow. The radius of the vortices is about 0.25 cm which is comparable to both the characteristic Hall scale length ( $L_H$ ) and the collisionless skin depth ( $c/\omega_{pe}$ ). Magnetic flux is compressed inside each vortex producing eddy currents in the center that are larger than the drive current. A one-dimensional analysis of Eq. (4) predicts oscillations in the magnetic field behind the shock front that can also be larger than the drive field.<sup>28</sup> The wavelength of these oscillations is proportional to the collisionless electron skin depth.



The center of a vortex is charged positively which is produced by a reduction in the number of electrons in the center of the vortex. This space charge imbalance produces an electric field that allows the electrons to  $\mathbf{E} \times \mathbf{B}$  drift in a counter-clockwise direction around the positively charged center. The detailed electron dynamics inside a vortex is beyond the scope of this paper. However, since the vortices are observed to be paramagnetic, the conservation of generalized vorticity prohibits the vortices from being comprised entirely of electrons from the plasma prefill when pressure and collision terms are neglected in Eq. (4). To see this assume the that pressure term can be neglected so that  $\Gamma=0$  for the electrons in the plasma prefill. For these electrons

$$(\nabla \times \gamma \mathbf{V}_e)_\theta = \Omega_\theta . \quad (11)$$

If Eq. (11) is integrated across the area of a vortex then it is possible to write

$$R\gamma(R)V_\phi(R) = \int_0^R \Omega_\theta R' dR' , \quad (12)$$

where  $R$  is vortex radius, and  $\phi$  is the coordinate direction around the vortex. Since  $\Omega_\theta < 0$  in these simulations, Eq. (12) predicts that  $V_\phi < 0$ . This direction of rotation is such as to produce diamagnetic vortices. However, the vortices are observed to be paramagnetic which implies that our assumption that the pressure term is negligible and the vortices contain only electrons from the initial plasma prefill is false. Therefore, either the pressure terms are important or the vortices must contain a sufficient number of emitted electrons with positive initial generalized vorticity. These issues will be investigated in a future paper.

To better understand the role of ion motion, a simulation was run with the parabolic density profile in negative polarity and an ion mass  $1/4$  the proton mass. For this choice of parameters,  $c/\omega_{pi}=8$  cm at the radial position where the most rapid penetration of magnetic field is expected. Because  $c/\omega_{pi} \gg L_H$  the simulation is still in a regime where Hall penetration is expected to dominate. The current enclosed contours for this simulation at  $t=2$  ns are shown in Fig. 5. Figure 5 demonstrates that, when ions can move, the vortices exhibit a smaller degree of paramagnetism than the infinitely massive case shown in Fig. 3. In the simulations depicted in Fig. 3, the maximum electric field in a vortex at  $t=2$  ns is 250 kV/cm. This electric field is sufficient to move ions several mm in this time and thus significantly reduces the space charge imbalance necessary to support the vortices. Magnetic field penetration followed by the removal of ions due to the electrostatic forces has been shown to lead to gap opening in a POS.<sup>17</sup> The details of this process and the role of the Hall electric field will be the subject of a future paper.

As mentioned above, the size (radius) of the vortices in Fig. 3 is comparable to both the collisionless skin depth and the characteristic Hall scale length. It is of interest to understand whether the vortex size scales with the characteristic Hall scale length,  $L_H$ , or the collisionless electron skin depth,  $c/\omega_{pe}$ . To examine this question, a simulation was run with a density profile for which the Hall speed is independent of  $r$ . This profile is given by

$$n(r) = \frac{n_c r_c^2}{r^2} \frac{1}{1 - f \ln(r/r_c)} , \quad (13)$$

where  $0 < f < 1/\ln(r_a/r_c)$  is a parameter that sets the Hall speed. The penetration speed for the density distribution given by Eq. (13) can be written as

$$V_H = \alpha \frac{c(-r_c B_c)}{4\pi n_c e r_c^2} f , \quad (14)$$

where  $\alpha$  is defined in the text following Eq. (9). The solid curve in Fig. 6 shows the density profile for  $f=1/2$ ,  $r_c=1$  cm,  $r_a=5$  cm, and  $n_c=5 \times 10^{12}$  cm<sup>-3</sup>. For this choice of parameters the characteristic Hall scale length is about 2 cm while the collisionless electron skin depth is about 0.3 cm. The density profile used in the simulations is given by the dashed curve in Fig. 6 which shows a slightly modified density distribution near the cathode. This slightly altered profile was chosen to avoid problems associated with magnetic field penetration right at the cathode boundary. Since  $d(Znr^2)/dr < 0$  near the cathode, field penetration is not expected there. The simulations for the density profile shown in Fig. 6 were done in negative polarity with an electron mass 1/90 the normal electron mass. The applied current rose from 0 to 5 kA in approximately 1.5 ns and then was held constant.

The current enclosed contours at  $t=5$  ns and  $t=10$  ns from a simulation with the density profile depicted in Fig. 6 are shown in Fig. 7. The current enclosed contours at  $t=5$  ns (Fig. 7a) show the formation of a line of vortices along the plasma/magnetic field boundary. Each of these vortices has a diameter of about two collisionless electron skin depths. These results show that the vortex size scales with  $c/\omega_{pe}$  and not  $L_H$ . The penetration speed in this simulation is only 10% slower than that predicted by fluid theory. The current enclosed contours at  $t=10$  ns (Fig. 7 b) show that this initial line of vortices propagates into the plasma at approximately the same axial speed. As the initial line of vortices propagates into the plasma, additional lines of weaker vortices form along the plasma/magnetic field boundary. Each line of the additional lines of vortices propagates with the same axial speed as the initial line of vortices but exhibit a smaller degree of paramagnetism. Notice that the vortices drift slightly radially upward as they propagate into the plasma. This radial drift may be caused by either interactions with other vortices or by interactions with a boundary.

The simulations presented thus far have been with an electron density that is much smaller than those expected in a real POS. This density was chosen to keep the numerical plasma temperature as low as possible. In addition, the electron mass was reduced to keep the electron collisionless skin depth small compared to the size of the plasma. In the remainder of this section it is demonstrated that the simulations with reduced density, magnetic field and electron mass are essentially equivalent to simulations with normal electron mass with density and magnetic field increased by  $\kappa=m_e/m$  where  $m$  is the artificially light electron mass. That this is true can be seen by multiplying Eqs. (1)-(3) and Ampere's Law by  $1/\kappa$ . These new equations describe the dynamics of a species with mass  $m=m_e/\kappa$ . The dynamics of this new species is unchanged provided the drive magnetic field and density are increased by the factor  $1/\kappa$ .

The relative importance of the numerical plasma heating can be estimated by comparing the electron velocity in the current channel with the thermal speed. To first order the electron speed in the current channel can be estimated from Ampere's Law to be

$$|V_e| = \frac{c}{4\pi en_e} |\nabla \times B| \cong \frac{c|B|}{4\pi en_e} \frac{\omega_{pe}}{c}, \quad (15)$$

where it has been assumed that the width of the current channel in the plasma is  $c/\omega_{pe}$ . The ratio of the electron speed in the current channel to the electron thermal speed [ $V_{th}=(2k_B T/m_e)^{1/2}$ ] can be written as

$$V_{th} / V_e = \left( \frac{n_e k_B T}{B^2 / 8\pi} \right)^{1/2}. \quad (16)$$

Equation (16) shows that the relative importance of numerical plasma heating is small provided the ratio of kinetic pressure to magnetic pressure is small. It is important to note that, for a fixed grid, the numerical temperature is proportional to the density [see Eq. (10)]. Therefore, the relative importance of numerical plasma heating is unchanged if  $B$  and  $n_e$  are increased by the same factor.

To test these ideas a simulation was run with the density profile given by Eq. (13) using normal electron mass,  $n_e=4.5 \times 10^{14} \text{ cm}^{-3}$ , and  $I_G=450 \text{ kA}$ . This simulation should be similar to the simulation with  $m=m_e/90$ ,  $n_e=5 \times 10^{12} \text{ cm}^{-3}$ , and  $I_G=5 \text{ kA}$  shown in Fig. 7. Current enclosed contours for this simulation at  $t=5 \text{ ns}$  and  $10 \text{ ns}$  are shown in Fig. 8. Although there are minor differences between the simulation results depicted in Figs. 7 and 8, the size of the vortices and the speed of penetration remain unchanged. This shows that the simulations with reduced electron mass are essentially equivalent to simulations with normal electron mass with a corresponding higher density and magnetic field.

#### IV. Energy considerations.

It is of considerable interest to investigate the flow of energy as the magnetic field penetrates into the plasma. For the simulations described in this paper, conservation of energy over the plasma volume can be expressed as

$$E_{\text{IN}} = E_B + E_E + E_P + E_A \quad (17)$$

where  $E_{\text{IN}} = \frac{c}{4\pi} \int dt \int \mathbf{E} \times \mathbf{B} \cdot \hat{n} dA$  is the energy flowing into the plasma through the generator

boundary,  $E_B = \int \frac{B^2}{8\pi} d^3x$  is the magnetic-field energy,  $E_E = \int \frac{E^2}{8\pi} d^3x$  is the electric-field energy,

$E_P = \sum_{i=1}^{N_p} (\gamma_i - 1)mc^2$  is the total internal energy of the plasma,  $E_A = \sum_{i=1}^{N_A} (\gamma_i - 1)mc^2$  is the

particle energy that flows out through the anode,  $N_p$  is the number of plasma particles in the simulation at time  $t$ , and  $N_A$  is the total number of particles leaving the volume through the boundaries. For the simulations described here, the energy flow out of the plasma occurs by the electrons in the current channel that flow to the anode. Terms describing the flow of electromagnetic energy out of the plasma and the flow of particle energy into the plasma from the cathode have been omitted in Eq. (17) since the simulations show that these terms are negligible.

For an applied current that is constant in time the Hall model predicts that the rate at which energy flows into the plasma is<sup>30</sup>

$$\frac{dE_{\text{IN}}}{dt} = \frac{c}{2} \int E_r B_\theta r dr = \frac{c r_c B_c(t)}{16\pi Z n_e} \left( 1 - \frac{n_c r_c^2}{n_a r_a^2} \right). \quad (18)$$

It can also be shown from fluid theory that half the energy that flows into the plasma goes into magnetic field energy.<sup>31</sup> The other half of the energy that flows into the plasma is either dissipated in the plasma or flows out of the plasma to the boundaries. In Ref. 31 it was shown that, if there is a small amount of resistivity, electrons are heated in the shock front where large magnetic field gradients exist. In this case the dissipated energy stays in the plasma and goes into electron thermal motion. For the parameters expected in a POS, this picture would lead to unrealistically large electron temperatures. Therefore, it is likely that a large fraction of the energy is convected out of the plasma to the anode by the electrons in the current channel.<sup>32,33</sup> In addition to plasma heating and convection to the anode, the simulation results shown in Figs. 3,

7, and 8 show that energy can also go into the electron vortex motion (i.e. the kinetic energy associated with the electron rotation around the center of a vortex).

The partition of energy for the simulation depicted in Fig. 7 is shown in Fig. 9. It is well known that PIC codes do not exactly conserve energy.<sup>11</sup> In this simulation great care was taken so that energy conservation was obeyed to within 10%. As Fig. 9 shows, nearly half the energy that flows into the plasma goes into magnetic field energy. The majority of the remaining energy is convected to the anode by the electrons in the current channel. However, Fig. 9 also shows that a significant amount of energy goes into increasing the internal plasma energy. The internal plasma energy appears primarily in the form of vortices. The internal plasma energy initially rises rapidly as the initial line of vortices is created but increases much more slowly once the initial vortices get established. Once the initial line of vortices is established, the rate at which energy is convected to the anode is about the same as the rate at which magnetic energy increases in the plasma. The electric field energy is not shown in Fig. 9 since the simulations show it is much smaller than both the magnetic field energy and the internal energy of the plasma. In Sec. III it was shown that large electrostatic electric fields exist inside a vortex. However, the total electrostatic energy associated with this field is small because  $|\mathbf{E}|/|\mathbf{B}| \sim |\mathbf{V}_e|/c < 1$  (i.e.  $E^2 < B^2$ ) inside a vortex and the electric field is confined to this region which occupies only in a small fraction of the entire plasma volume.

## V. Conclusions

This paper has used a PIC code to demonstrate fast magnetic field penetration into a plasma associated with the Hall term in fluid theory. This is an improvement over traditional fluid treatments since the PIC method makes no *a priori* assumptions about the plasma equation of state, form of the pressure tensor, or the importance of displacement currents. In addition, fluid treatments generally require a small amount of collisionality to remove singularities in the solutions. Since the PIC technique is inherently collisionless, the PIC results described in this paper treat the collisionless transport of magnetic field into the plasma.

The simulations reproduce many aspects of magnetic field penetration that are consistent with fluid treatments. However, the speed of penetration observed in the simulations is somewhat slower than analytic estimates. This is caused by either strong two-dimensional effects or by the effects of the pressure tensor ignored in the fluid analysis. The simulations show the formation of vortices behind the EMHD shock front that are a natural consequence of electron inertia. These vortices are paramagnetic in nature and their size is a few collisionless electron skin depths.

Most of the results described in this paper are for the case of infinitely massive ions. When ions can move, axial magnetic field penetration is followed by ion motion produced by the large electrostatic force that exists in the center of a vortex. In this case, the vortices in the electron flow are much weaker since the ion motion acts to reduce the space-charge separation that is necessary to support the vortices. The reduction of ion space-charge in regions where the magnetic field penetrates may also lead to gap formation in a POS.

It is observed that half the energy flowing into the plasma goes into magnetic energy. The majority of the remaining energy is convected to the anode by the electrons in the current channel. A significant amount of energy also goes into the internal energy of the plasma while the initial line of vortices are being established. However, once the initial line of vortices is

created, very little additional energy appears as internal plasma energy and the rate at which energy is convected to the anode is approximately the same as the rate of increase in the magnetic field energy in the plasma.

## VI. Acknowledgments

The authors would like to acknowledge Dr. Joe Huba of the Naval Research Laboratory (NRL) for many interesting discussions pertaining to this problem. In addition, many thanks to Drs. Bob Commisso and Bruce Weber at NRL for their continued interest in this work. The authors also profited greatly from the careful reading and technical discussions of this manuscript provided by Mr. David Rose. The first author also benefited from discussions with Drs. Larry (Lars) Ludeking and David Smithe of Mission Research Corporation. Simulation results were obtained using the MAGIC code under the Air Force Office of Scientific Research sponsored MAGIC User's Group. This work was supported by Defense Nuclear Agency.

## LIST OF FIGURES

Figure 1: The geometry used in the simulations is that of the plasma opening switch.

Figure 2: (a) The parabolic and uniform-parabolic density profiles used to demonstrate EMH effects in a PIC code. (b) The Hall speed profiles for the density profiles shown in Fig. 2a.

Figure 3: Current enclosed contours ( $I = -2\pi r B_\theta / \mu_0 = \text{constant}$ ) at  $t = 2$  ns in negative polarity for the parabolic density profile. The contours are normalized so that the units are kA with  $I_G = 20$  kA and an interval of 4 kA between contour levels.

Figure 4: Current enclosed contours ( $I = 2\pi r B_\theta / \mu_0 = \text{constant}$ ) at  $t = 2$  ns in positive polarity for the uniform-parabolic density profile. The contours are normalized so that the units are kA with  $I_G = 20$  kA and an interval of 4 kA between contour levels.

Figure 5. Current enclosed contours ( $I = -2\pi r B_\theta / \mu_0 = \text{constant}$ ) at  $t = 2$  ns in negative polarity for a case where ions can move ( $c/\omega_{pi} = 8$  cm) with the parabolic density profile. The contours are normalized so that the units are kA with  $I_G = 20$  kA and an interval of 4 kA between contour levels.

Figure 6: The density profile for which the Hall speed is independent of  $r$ . The solid curve is the density profile described by Eq. (13). A slightly modified version of this profile near the cathode given by the dashed curve was used in the simulations.

Figure 7. Current enclosed contours ( $I = -2\pi r B_\theta / \mu_0 = \text{constant}$ ) at (a)  $t = 5$  ns and (b)  $t = 10$  ns in negative polarity for the density profile depicted in Fig. 6. The contours are normalized so that the units are kA with  $I_G = 5$  kA and an interval of 1 kA between contour levels.

Figure 8. Current enclosed contours ( $I = -2\pi r B_\theta / \mu_0 = \text{constant}$ ) at (a)  $t = 5$  ns and (b)  $t = 10$  ns in negative polarity for the density profile given by Eq. (13). These results are for normal electron mass with the density and applied magnetic field scaled up by a factor of 90 over that used in obtaining the results shown in Fig. 7. The contours are normalized so that the units are kA with  $I_G = 450$  kA and an interval of 90 kA between contour levels.

Figure 9. The partition of energy in the plasma for the simulation shown in Fig. 7. The energy flowing into the plasma is  $E_{in}$ , the magnetic energy is  $E_B$ , the energy convected to the boundary by electrons is  $E_A$ , and the internal plasma energy is  $E_p$ .

---

<sup>1</sup> R.J. Commisso, P.J. Goodrich, J.M. Grossmann, D.D. Hinshelwood, P.F. Ottinger, and B.V. Weber, Phys. Fluids **B4**, 2368 (1992).

<sup>2</sup> See IEEE Trans. Plasma Sci. special issue on Plasma Opening Switches **PS-15**, (1987).

<sup>3</sup> P.A. Bernhardt, Phys. Fluids **B4**, 2249 (1992).

<sup>4</sup> P. Sheehey, J.E. Hammel, I.R. Lindemuth, D.W. Scudder, J.S. Schlachter, R.H. Lovberg, and R.A. Riley, Phys. Fluids **B4**, 3698 (1992).

- 
- <sup>5</sup> A. Fruchtman and Y. Maron, Phys. Fluids **B3**, 1546 (1991).
- <sup>6</sup> K. Gomberoff, and A. Fruchtman, Phys. Plasmas **1**, 2480 (1994).
- <sup>7</sup> R.L. Stenzel, J.M. Urrutia, and C.L. Rousculp, Phys. Rev. Lett. **74**, 702 (1995).
- <sup>8</sup> M. Rosenbluth, in Plasma Physics and Thermonuclear Research, eds. C.L. Longmire, J.L. Tuck, and W.B. Thompson, (Pergamon Press, London, 1963), p.217.
- <sup>9</sup> J.D. Jackson, *Classical Electrodynamics*, John Wiley and Sons, New York, pp. 472-473 (1975).
- <sup>10</sup> A.S. Kingsep, K.V. Chukbarm and V.V. Yankov, in Reviews of Plasma Physics, edited by B.B. Kadomstev (Consultants Bureau, New York, 1990), Vol. 16, p. 243.
- <sup>11</sup> C.K. Birdsall, and A.B. Langdon, *Plasma Physics via Computer Simulation*, (McGraw Hill, New York, 1985), p. 179.
- <sup>12</sup> B. Goplen, L. Ludeking, D. Smithe, and G. Warren, Comp. Phys. Comm. **87**, 54 (1995).
- <sup>13</sup> A.S. Kingsep, L.I. Rudakov, and K.V. Chukbar, Sov. Phys. Dokl. **27**, 140 (1982).
- <sup>14</sup> A.S. Kingsep, Y.V. Mokhov, and K.V. Chukbar, Sov. J. Plasma Phys. **10**, 495 (1984).
- <sup>15</sup> A. Fruchtman, Phys. Fluids **B3**, 1908 (1991).
- <sup>16</sup> J.D. Huba, J.M. Grossmann, and P.F. Ottinger, Phys. Plasmas **1**, 3444 (1994).
- <sup>17</sup> J.M. Grossmann, S.B. Swanekamp, R.J. Commisso, P.J. Goodrich, D.D. Hinshelwood, J.D. Huba, P.F. Ottinger, and B.V. Weber, Proceeding of the 10th International Conference on High Power Particle Beams, edited by W. Rix and R. White, San Diego, CA, June 20-24 1994, NTIS document No. PB95-14437, p. 280. Copies can be ordered from NTIS, PO Box 1425, Springfield, VA 22151.
- <sup>18</sup> L.I. Rudakov, C.E. Seyler, and R.N. Sudan, Comments on Plasma Phys. and Controlled Fusion **14**, 171 (1991).
- <sup>19</sup> P.M. Bellan, Phys. Fluids **B5**, 1955 (1993).
- <sup>20</sup> M.B. Isichenko, and A.M. Marnachev, Sov. Phys. JETP **66**, 702 (1987).
- <sup>21</sup> A. Fruchtman, and K. Gomberoff, Phys. Fluids **B5**, 2371 (1993).
- <sup>22</sup> R.J. Mason, P.L. Auer, R.N. Sudan, B.V. Oliver, C.E. Seyler, and J.B. Greenly, Phys. Fluids **B5**, 1115 (1993).
- <sup>23</sup> B. Church and R.N. Sudan, Phys. Plasmas **2**, 1837 (1995).
- <sup>24</sup> J.M. Grossmann and D. Mosher private communication (1991).



- 
- <sup>25</sup> R. Kulsrud, P.F. Ottinger, and J.M. Grossmann, *Phys. Fluids* **31**, 1741 (1988).
- <sup>26</sup> K. Gomberoff, and A. Fruchtman, *Phys. Fluids B* **5**, 2841 (1993).
- <sup>27</sup> B.V. Weber, R.J. Comisso, P.J. Goodrich, J.M. Grossmann, D.D. Hinshelwood, P.F. Ottinger, and S.B. Swanekamp, *Phys. Plasmas* **2**, 299 (1995).
- <sup>28</sup> Y.L. Kalda and A.S. Kingsep, *Sov. J. Plasma Phys.* **15**, 508 (1989).
- <sup>29</sup> J.M. Grossmann, S.B. Swanekamp, P.F. Ottinger, R.J. Comisso, D.D. Hinshelwood, and B.V. Weber, *Phys. Plasmas* **2**, 299 (1995).
- <sup>30</sup> A. Fruchtman, *Phys. Rev. A* **45**, 3938 (1992).
- <sup>31</sup> A. Fruchtman and K. Gomberoff, *Phys. Fluids B* **4**, 117 (1992).
- <sup>32</sup> A. Fruchtman and L.I. Rudakov, *Phys. Rev. E* **50**, 2997 (1994).
- <sup>33</sup> J.M. Grossmann, P.F. Ottinger, and R.J. Mason, *J. Appl. Phys.* **16**, 2307 (1989).

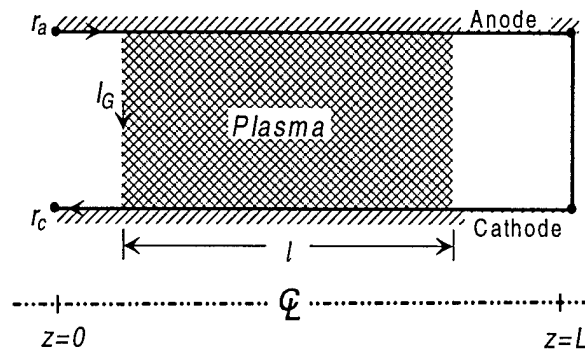


Figure 1  
Swanekamp et. al

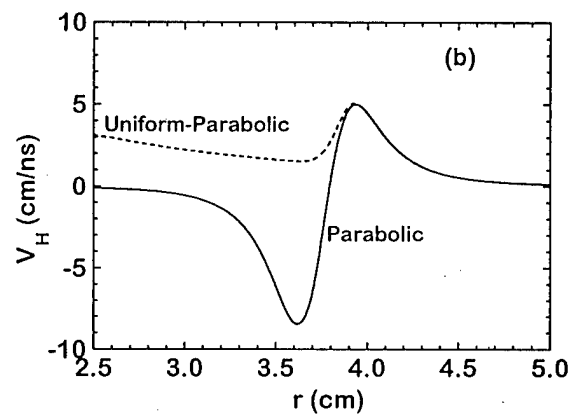
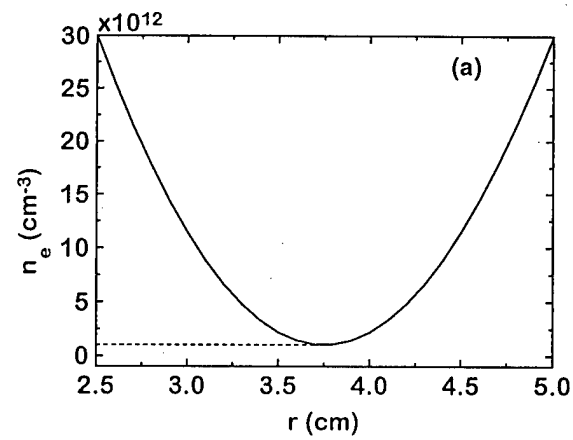


Figure 2  
Swanekamp et. al

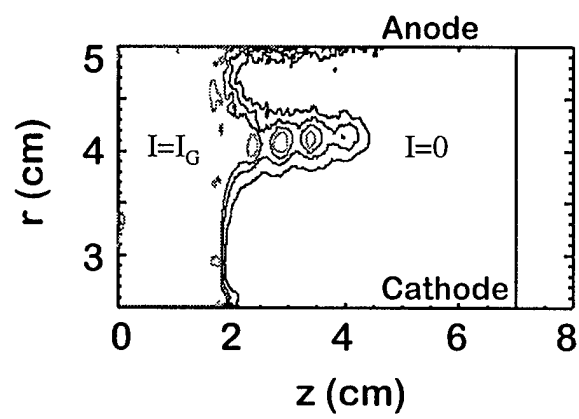


Figure 3  
Swanekamp et. al

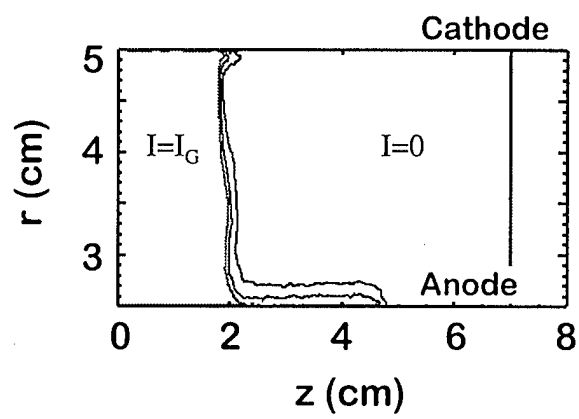


Figure 4  
Swanekamp et. al

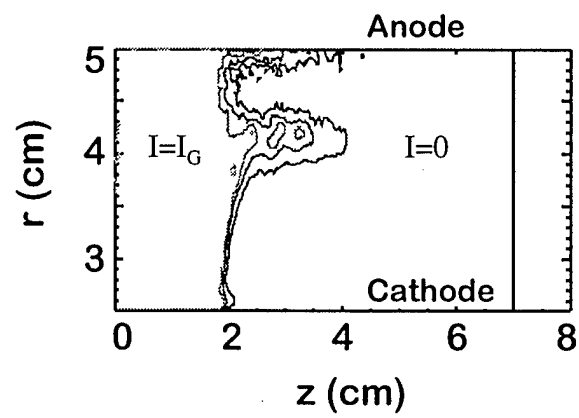


Figure 5  
Swanekamp et. al

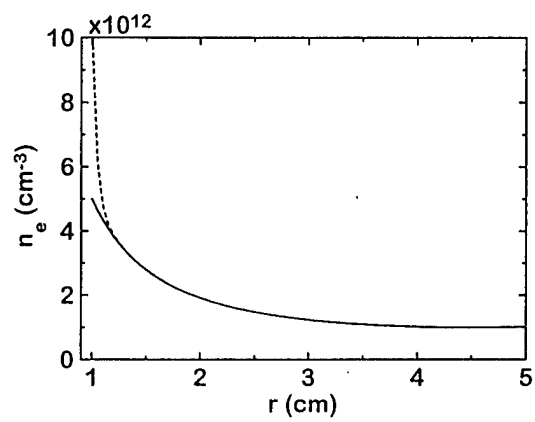


Figure 6  
Swanekamp et. al

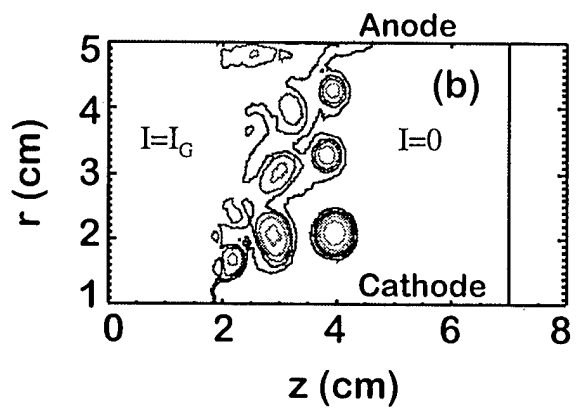
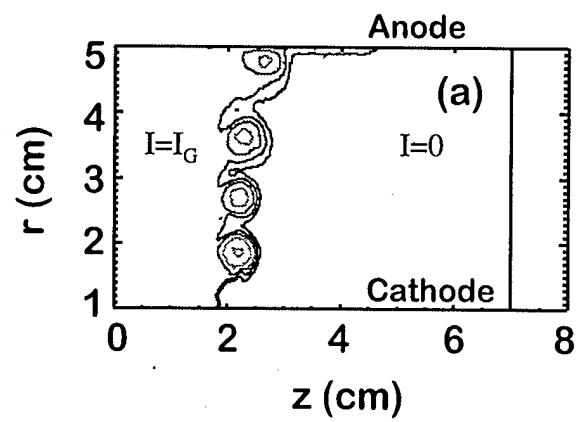


Figure 7  
Swanekamp et. al



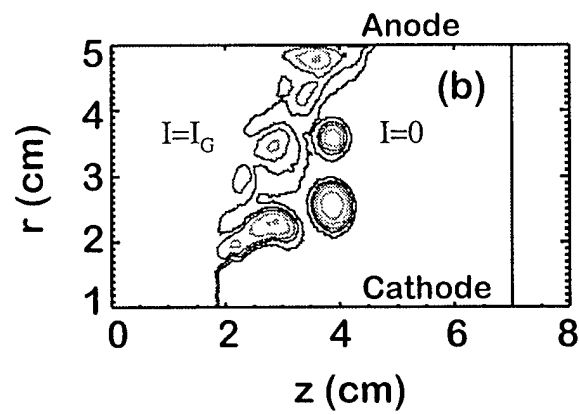
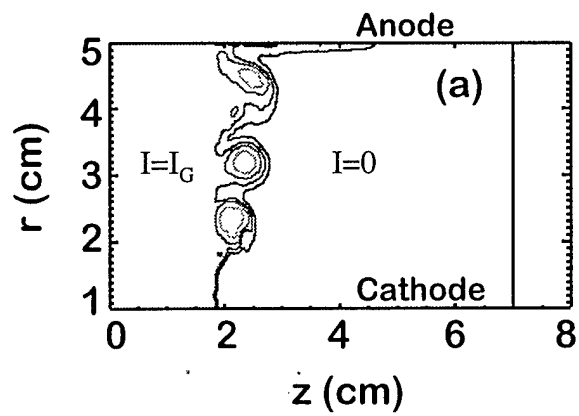


Figure 8  
Swanekamp et. al

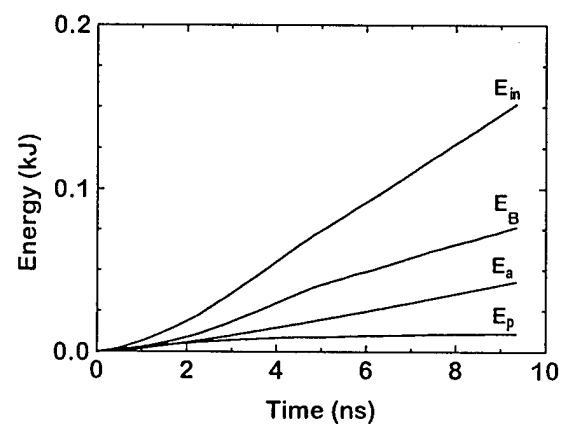


Figure 9  
Swanekamp et. al

## Conduction phase to opening phase transition in the plasma opening switch

J.M. Grossmann, S.B. Swanekamp\*, R.J. Comisso, P.J. Goodrich#, D.D. Hinshelwood#,  
J.D. Huba, P.F. Ottinger, and B.V. Weber

Plasma Physics Division, Naval Research Laboratory, Washington, DC 20375

\* Science Applications International Corporation, McLean VA 22102

# JAYCOR, Inc., Vienna, VA 22182

### Abstract

*The transition between the conduction phase and opening phase of a long-conduction-time plasma opening switch (POS) is examined with the aid of numerical simulations. Evidence of three physical mechanisms is observed: magnetic pressure, magnetic field transport, and gap erosion resulting from ion acceleration out of electrostatic potential hills. Gap erosion occurs in the radial middle of the POS where the quantity  $B^2/n$  is at its largest.*

### I. Introduction

An integral part of inductive energy storage systems is the plasma opening switch (POS), which bridges the anode-cathode gap of a section of transmission line as the storage inductor charges with current.<sup>1</sup> During the conduction phase, the POS conducts all of the generator current, allowing none to pass to the load. During the POS opening phase, an increasing fraction of generator current is delivered to the load. Several physical mechanisms control the conduction and opening phases of POS operation. These include magnetic pressure, magnetic field transport, and electrostatic gap formation. Magnetic pressure deforms and displaces the plasma by  $\mathbf{J} \times \mathbf{B}$  forces.<sup>2,3</sup> Magnetic field transport mechanisms allow magnetic field (current) to penetrate into the plasma rather than being shielded out of the plasma. These mechanisms include the Hall effect (EMH),<sup>4,5,6</sup> electron inertia,<sup>7</sup> and resistive diffusion.<sup>8</sup> Electrostatic gap formation has been described in earlier numerical investigations of short-conduction-time POS, where a potential hill is observed to form near the cathode on the generator side of the plasma fill.<sup>9</sup> Large electrostatic forces accelerate ions out of the potential hill region and the potential hill migrates along the cathode toward the load, leaving a magnetically insulated gap in its wake. When the potential hill reaches the load side of the plasma fill, current begins to flow to the load.

Two of the most important unresolved issues in POS research are how the POS transitions between the conduction and opening phases and how gaps form in the plasma. This paper will describe PIC simulations of this transition in the context of long-conduction-time POS operation. The simulations exhibit all three of the mechanisms mentioned above. Electrostatic gap opening is observed for the first time to occur away from the cathode and in the radial middle of the plasma.

### II. Simulation set-up

Since the simulations described here focus on the transition between the conduction and opening phases of POS operation, a density profile similar to the one found at the end of the conduction phase in fluid simulations of the POS is used as an initial condition to the PIC simulations. Experimentally, the POS opens and the conduction phase ends roughly when the current reaches the load end of the POS.<sup>10</sup> Fluid code simulations yield a generic picture of the conduction phase of long-conduction-time POS in which  $\mathbf{J} \times \mathbf{B}$  forces deform and displace the plasma both radially and axially.<sup>3,11,12</sup> When the current reaches the load end, the density profile is shaped like a saddle with a radial density minimum in the middle of the POS fill region and density rising toward the electrodes. Similar density distributions are used here as initial distributions in PIC simulations of the transition to .

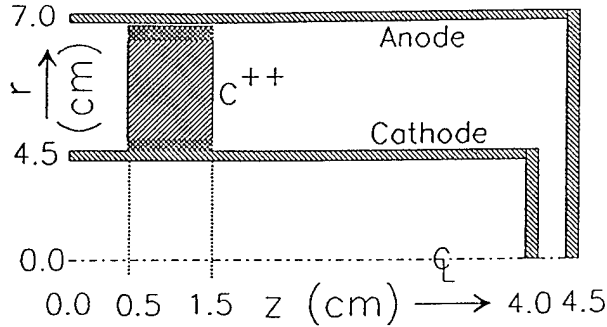


Fig. 1. Schematic of simulation region.

opening. The geometric configuration of the simulations is shown in Fig. 1. The left side of the simulation region is connected to a capacitor-inductor circuit designed to mimic a typical generator. The capacitor is assumed to be almost completely discharged so that the circuit is preloaded with current and the POS plasma carries 1.2 MA from the beginning of the simulation. A short section of transmission line connects the POS to a diode load on the right. The diode impedance is nominally  $4 \Omega$ , but drops to about  $1 \Omega$  late in time when a significant amount of electron flow enters the diode region. The diode impedance is set by introducing a resistive material in the diode gap with a prescribed resistivity.

The axial length of the initial plasma fill is 1 cm and the axial density profile is taken to be uniform. Several initial radial density profiles were investigated, all of which had the same electron density at the cathode, but different minimum densities in the middle of the plasma and/or a choice of whether the density rose again toward the anode or remained uniform. While most of the plasma ions consist of doubly ionized carbon, immobile ions are placed in regions of radial width 2 mm from both electrode surfaces. The gap formation process in the radial middle of the plasma is independent of the use of immobile ions near the electrodes. However, when carbon ions are used near the electrodes at densities accessible to simulations, gaps can form at the electrodes that are nearly as large as the gap in the radial middle of the plasma (depending on the relative magnitudes of the electrode vs. intra-electrode plasma densities). Long-conduction-time POS experiments strongly suggests gap formation in the radial

middle of the plasma,<sup>3</sup> not near the electrodes. It is assumed that this is due to the presence of large plasma densities near the electrodes. The use of immobile ions reduces the size of gaps near the electrode surfaces and brings them closer to those expected in experiment and may be interpreted as a computationally convenient means of modeling high density electrode plasmas.

### III. Simulation Results

The results reported here are for the specific case where the density at the cathode ( $r = 4.5$  cm) is  $10^{15} \text{ cm}^{-3}$ , then drops smoothly to  $2 \times 10^{14} \text{ cm}^{-3}$  at  $r = 5.5$  cm, and then remains uniform to the anode radius of  $r = 7.0$  cm. Results obtained for the same density profile for  $r \leq 6.0$  cm, but thereafter rising to  $10^{15} \text{ cm}^{-3}$  toward the anode, are similar to those in which the density remains uniform all the way to the anode. Other results for which the density minimum is  $10^{14} \text{ cm}^{-3}$  rather than  $2 \times 10^{14} \text{ cm}^{-3}$  are similar except that larger gaps form in the lower density plasma and the time during which the POS remains in the conduction phase is shorter.

Early in simulation, the plasma is accelerated axially toward the load by the  $\mathbf{J} \times \mathbf{B}$  force. Magnetic field also begins to penetrate the plasma and a current channel front migrates axially through the plasma. In the region,  $5.5 \text{ cm} \leq r \leq 7.0$  cm (where the plasma was initially radially uniform), the magnetic front travels with the penetration speed,  $v_H = cB/(4\pi n e r) \approx 2 \text{ mm/nsec}$ , associated with the Hall effect due to cylindrical curvature.<sup>5</sup> In the region near the cathode,  $4.5 \text{ cm} \leq r \leq 5.5$  cm (where the initial plasma density gradients are negative), a current channel front is also observed to penetrate axially into the high density plasma. The rate of penetration is slightly slower than in the region  $5.5 \text{ cm} \leq r \leq 7.0$  cm. This magnetic penetration near the cathode cannot be explained by the Hall effect since the combination of cylindrical curvature and density gradient effects<sup>4</sup> are in a direction to expel magnetic field rather than allow penetration. The magnetic field penetration may be associated either with electron vorticity<sup>13, 6</sup> or electron inertia effects.<sup>7</sup> Electron vortices are observed near the cathode in these

particular simulations and are a recurring feature of POS simulations in general.

At about the point that the current channel reaches the load edge of the plasma, potential hills begin to form in the region  $5.5 \text{ cm} \leq r \leq 5.8 \text{ cm}$  and propagate axially through the plasma. Large electrostatic electric fields in the potential hills accelerate ions out of the potential hills. This process of ion acceleration has the effect of eroding a radial gap in the plasma. The gap extends through the axial length of the plasma and has a radial width of about 3 mm. The term gap is used here to mean a region largely evacuated of plasma in which a large fraction of electrons are magnetically insulated. After the gap forms, electron flow is observed downstream (toward the load) of the POS region. The electron current flow runs axially in the POS region, but turns radially toward the anode in the region downstream of the POS.

Some of the effects described above can be seen in the next two figures. In Fig. 2, the electron density just before and after gap formation is shown. The minimum density in these iso-density

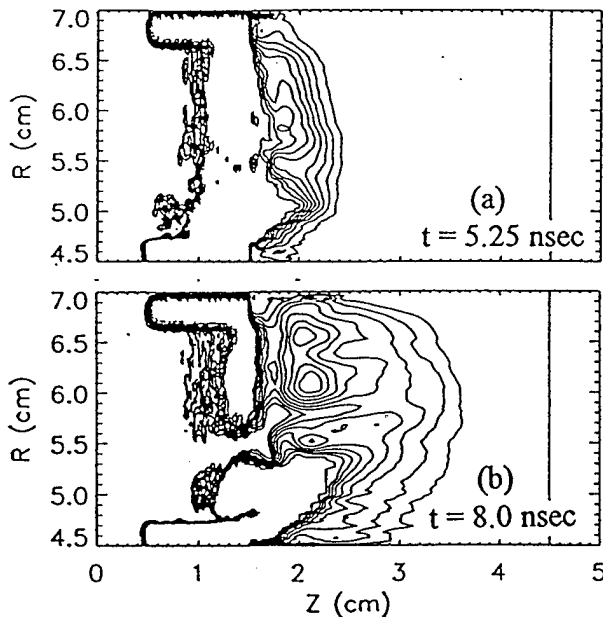


Fig. 2. Iso-density contours in the POS plasma

contours is chosen to be  $10^{13} \text{ cm}^{-3}$  and the maximum density is  $10^{14} \text{ cm}^{-3}$ . Higher and lower densities exist, but are not shown for clarity. The

interval between contour lines is  $10^{13} \text{ cm}^{-3}$ .

Initially, the plasma occupies the region  $0.5 \text{ cm} \leq z \leq 1.5 \text{ cm}$ . In Fig. 2a, the left boundary of the plasma has been displaced axially by  $\mathbf{J} \times \mathbf{B}$  forces. The right boundary shows a low density cloud of plasma flung downstream of the initial fill region in a bow-shaped cloud. The appearance of small density depressions inside the plasma in the region near  $r = 5.5 \text{ cm}$  shows the density thinning effect of potential hills that have formed in that region. In Fig 2b, a gap has fully eroded in the plasma, and the cloud of low density plasma has been further accelerated into the downstream transmission line.

Contours of the current streamlines ( $2\pi r B / \mu_0$ ) are shown in Fig. 3 just before and after gap formation. The maximum contour is 1.2 MA

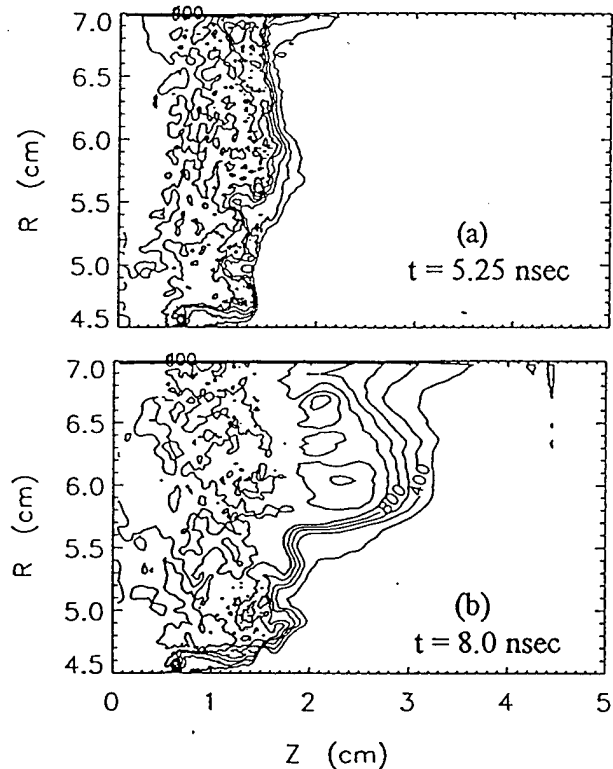


Fig. 3. Current streamlines

and the minimum is 200 kA with an interval between contours of 200 kA. In Fig. 3a, a narrow current channel is seen to have penetrated to the load edge of the plasma. The current has penetrated axially throughout the plasma except in parts of the immobile ion region near the cathode. In Fig. 3b, the current in regions on the cathode

side of the gap (Fig. 2b) is seen to flow in the high density POS plasma, while the current on the anode side of the gap flows in the low density plasma cloud axially downstream of the original POS fill region.

The electron flow downstream of the POS immediately after POS opening is not magnetically insulated away from the anode because the downstream region is filled with a cloud of ions that have been flung downstream of the POS during the conduction phase. These ions tend to be dragged axially toward the load and radially toward the cathode by the electric fields associated with electron  $E \times B$  drift. As the ion cloud is removed in this manner from the downstream transmission line, the electron flow becomes increasingly insulated from the anode and flows into the load.

#### IV. Summary

The transition between the conduction phase and the opening phase has been examined with 2-D PIC simulations. A current channel is observed to migrate axially through the initial plasma fill region while the POS is still in its conduction phase. The plasma is displaced by  $J \times B$  forces at the same time that magnetic transport effects allow current channel penetration. When the channel reaches the load end of the initial plasma fill, gap formation is observed. For the densities used here, gap sizes are roughly consistent with Hawk experiments.<sup>10</sup> These preliminary results show good agreement with previous simulations<sup>14</sup> of gap formation near the cathode where gap sizes and potential hill magnitudes scaled as  $d \text{ (cm)} \approx 10^9 B/n_e$  and  $\phi \text{ (MV)} \approx 5 \times 10^4 B^2/n_e$ , with  $B$ (Gauss) and  $n_e \text{ (cm}^{-3}\text{)}$  is the electron density. These scaling results predict gap sizes  $d \approx 2.7 \text{ mm}$  and potential hills of magnitude  $\phi \approx 700 \text{ kV}$ , in agreement with the present simulations. Gap formation in these and previous simulations occurs before the POS plasma has any information about the load. The radial position of the gap coincides with the location of largest  $B^2/n_e$ . This is where potential hill magnitudes are largest and where magnetic pressure forces are expected to produce the most axial plasma displacement.

Many issues remain to be resolved. Understanding the physical mechanism(s) that

define the transition between the conduction phase and the electrostatic gap formation phase, as well as the gap formation process itself, could lead to experimental techniques to increase the gap size. More work is also needed on the interactive coupling of the POS and load and on understanding the mechanism that allows magnetic field transport in the region near the cathode where the density decreases with radius.

#### V. Acknowledgments

Simulations were performed with the MAGIC<sup>15</sup> code supported through the AFOSR's sponsored MAGIC Users Group. This work is supported by DNA.

#### VI. References

- <sup>1</sup> See Special Issue on Fast Opening Vacuum Switches, IEEE Trans. Plasma Sci. PS-15, 629 (1987).
- <sup>2</sup> W. Rix, D. Parks, J. Shannon, J. Thomson, E. Waisman, IEEE Trans. Plasma Sci. PS-19, 400 (1991).
- <sup>3</sup> D.D. Hinshelwood, B.V. Weber, J.M. Grossmann, R.J. Comisso, Phys. Rev. Lett. 68, 3567 (1992).
- <sup>4</sup> A.S. Kinsep, Yu.V. Mokhov, K.V. Chukbar, Sov. J. Plasma Phys. 10, 495 (1985).
- <sup>5</sup> A. Fruchtman, Phys. Fluids B 3, 1908 (1991).
- <sup>6</sup> R.J. Mason, P.L. Auer, R.N. Sudan, B.V. Oliver, C.E. Seyler, J.B. Greenly, Phys. Fluids B 5, 1115 (1993).
- <sup>7</sup> B.V. Oliver, L.I. Rudakov, R.J. Mason, P.L. Auer, Phys. Fluids B 4, 294 (1992).
- <sup>8</sup> R.M. Kulsrud, P.F. Ottinger, J.M. Grossmann, Phys. Fluids 31, 1741 (1988).
- <sup>9</sup> J.M. Grossmann, P.F. Ottinger, R.J. Mason, J. Appl. Phys. 66, 2307 (1989).
- <sup>10</sup> R.J. Comisso, P.J. Goodrich, J.M. Grossmann, D.D. Hinshelwood, P.F. Ottinger, B.V. Weber, Phys. Fluids B 4, 2368 (1992).
- <sup>11</sup> J.D. Huba, J.M. Grossmann, P.F. Ottinger, to be published in Phys. of Plasmas (1994).
- <sup>12</sup> J.J. Watrous, M.H. Frese, private communication.
- <sup>13</sup> A. Fruchtman, K. Gomberoff, Phys. Fluids B 5, 2371 (1993).
- <sup>14</sup> J.M. Grossmann, S.B. Swanekamp, P.F. Ottinger, R.J. Comisso, D.D. Hinshelwood, B.V. Weber, submitted to Phys. of Plasmas (1994).
- <sup>15</sup> B. Goplen, L. Ludeking, D. Smithe, G. Warren, MAGIC Users Manual, Mission Research Tech. Report No. MRC/WDC-R-282.

# Gap formation processes in a high-density plasma opening switch

J. M. Grossmann, S. B. Swanekamp,<sup>a)</sup> P. F. Ottinger, R. J. Commisso,  
D. D. Hinshelwood,<sup>b)</sup> and B. V. Weber  
*Pulsed Power Physics Branch, Plasma Physics Division, Naval Research Laboratory,  
Washington, D. C. 20375-5000*

(Received 7 March 1994; accepted 15 September 1994)

A gap opening process in plasma opening switches (POS) is examined with the aid of numerical simulations. In these simulations, a high density ( $n_e = 10^{14} - 5 \times 10^{15} \text{ cm}^{-3}$ ) uniform plasma initially bridges a small section of the coaxial transmission line of an inductive energy storage generator. A short section of vacuum transmission line connects the POS to a short circuit load. The results presented here extend previous simulations in the  $n_e = 10^{12} - 10^{13} \text{ cm}^{-3}$  density regime. The simulations show that a two-dimensional (2-D) sheath forms in the plasma near a cathode. This sheath is positively charged, and electrostatic sheath potentials that are large compared to the anode-cathode voltage develop. Initially, the 2-D sheath is located at the generator edge of the plasma. As ions are accelerated out of the sheath, it retains its original 2-D structure, but migrates axially toward the load creating a magnetically insulated gap in its wake. When the sheath reaches the load edge of the POS, the POS stops conducting current and the load current increases rapidly. At the end of the conduction phase a gap exists in the POS whose size is determined by the radial dimensions of the 2-D sheath. Simulations at various plasma densities and current levels show that the radial size of the gap scales roughly as  $B/n_e$ , where  $B$  is the magnetic field. The results of this work are discussed in the context of long-conduction-time POS physics, but exhibit the same physical gap formation mechanisms as earlier lower density simulations more relevant to short-conduction-time POS. © 1995 American Institute of Physics.

## I. INTRODUCTION

Inductive energy storage (IES) is considered a lower cost, smaller size alternative pulsed power technology compared with conventional capacitive energy storage.<sup>1</sup> An integral part of an IES system is the plasma opening switch (POS), which bridges the anode-cathode (A-K) gap of a section of transmission line as the storage inductor charges with current. In its simplest form, the POS consists of a plasma injected between the electrodes of this line. More complex designs incorporate external applied magnetic fields.<sup>2</sup> During the conduction phase of the POS, the plasma conducts all of the generator current, allowing none of it to pass to the load. During the opening phase of the POS, an increasing fraction of the generator current is allowed to pass to the load. Several physical mechanisms have been proposed to be responsible for the conduction and opening phases of POS operation. These mechanisms include the magnetohydrodynamic (MHD) displacement and deformation of plasma by  $J \times B$  forces,<sup>2-6</sup> the penetration of magnetic field by electron-magnetohydrodynamic (EMH) effects<sup>7,8</sup> or anomalous resistivity,<sup>9</sup> and electrostatic gap formation.<sup>10-13</sup> Any of these mechanisms may be active singly or in concert during either the conduction phase or opening phase depending on the experimental regime. This paper focuses primarily on electrostatic gap formation processes near a cathode. This mechanism is considered primarily in the context of long-conduction-time (about 1  $\mu\text{s}$ ) POS, although the scaling results are applicable to short-conduction-time ( $\leq 100 \text{ ns}$ ) POS.

Although the work presented in this paper is motivated by the long-conduction-time POS, its main contribution to POS understanding is the extension of earlier PIC simulations, motivated by short-conduction-time POS experiments, by more than 2 orders of magnitude in density to  $5 \times 10^{15} \text{ cm}^{-3}$ . The applicability of the present results to long-conduction-time experiments remains to be demonstrated, pending observations that confirm or disprove them. The paper describes in detail a new 2-D model for gap formation including the dynamics of a potential hill. The concept of a preformed gap at the time of POS opening is also introduced that may explain experimental observations concerning inferred gap sizes. And finally, density and magnetic field scaling for the preformed gap size and the maximum potential associated with the potential hill are derived that can be compared with experimental observations. These scaling results agree with the scalings of the earlier, lower density simulations. What follows in this section of the paper is (1) a review of long-conduction-time POS investigations which have motivated this work, (2) a discussion of terminology which will be used in the paper, and (3) a discussion of the proposed model and results from the simulations based on it that contrasts them with previous models in order to highlight significant differences. These differences must be compared with future experiments to determine the validity of these models.

Recent results on the HAWK generator<sup>14</sup> at the Naval Research Laboratory (NRL) suggest that the POS conduction phase in these experiments is dominated by MHD (i.e., magnetic pressure or  $J \times B$ ) effects.<sup>4-6</sup> The evidence supporting this conclusion consists of experiments investigating the scaling of the conduction current with plasma density at various cathode radii, plasma lengths, and current rise times.<sup>5,6,15</sup>

<sup>a)</sup>Science Applications International Corporation, McLean, Virginia.

<sup>b)</sup>Jaycor, Inc., Vienna, Virginia.

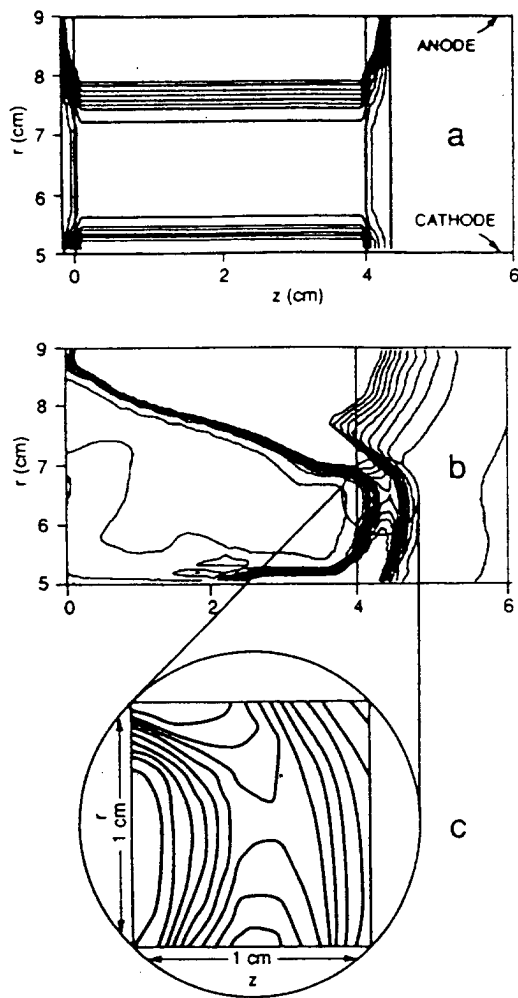


FIG. 1. Plasma density contours at the beginning (a) and end (b) of the conduction phase of a long-conduction time POS. A blowup of the density saddle is shown in (c). Typical experimental dimensions are shown. The generator is on the left, the load is on the right.

The experimental conduction current can be predicted with simple scaling laws based on center of mass motion under the action of magnetic pressure forces. Typical long-conduction-time POS experiments on HAWK have plasma densities of several times  $10^{15} \text{ cm}^{-3}$  with currents rising to 0.7 MA in  $1 \mu\text{s}$ . Simulations of the POS using the two-fluid code ANTHEM<sup>16</sup> demonstrate the deformation of plasma by  $J \times B$  forces and suggest the following picture of the conduction phase. Shown in Figs. 1(a) and 1(b) are density contours of the plasma at the beginning and end of the conduction phase. During the conduction phase, a current channel develops along the generator edge of the plasma. As magnetic pressure displaces and distorts the original plasma column, this current channel moves toward the load. The current channel front acts like a piston displacing the plasma. Both radial and axial displacement of the plasma occurs because of the radial variation of magnetic field resulting from cylindrical geometry and because of radial density gradients in the initial plasma fill.<sup>5,6</sup> The magnetic pressure is largest near the cathode where the plasma density is also largest because of

stagnation at the surface. The current channel can also penetrate into the plasma by resistive diffusion and EMH effects, but for the parameters of interest here, MHD displacement dominates.<sup>15</sup>

At roughly the point where the current front reaches the load edge of the original plasma fill region, the POS is observed to open.<sup>6</sup> Interferometric measurements along an axial line-of-sight confirm that there is a rapid drop in the axial line-integrated density at a certain radial location just as the POS opens.<sup>5</sup> This suggests that the plasma has been thinned out along a large fraction of that line of sight, if not along all of it. The radial location of this thinned density region is determined by the radial gradients in both the magnetic field and density and lies somewhere in between the two electrodes. Interferometric measurements also show that on either side of the thinned region, the plasma density rises as the line of sight moves radially in either direction toward the electrodes.<sup>5</sup> This observation suggests that gap opening in the long-conduction-time POS does not occur at the cathode as may have been the case in the short-conduction time POS.<sup>13</sup> Diagnostic measurements of the line integrated density in two-dimensional (2-D) snowplow models,<sup>17</sup> 2-D ANTHEM simulations,<sup>5,15</sup> and MHD simulations<sup>18,19</sup> show results similar to those above. ANTHEM simulations indicate a density "saddle" in the plasma at the end of the conduction phase, as shown in Fig. 1(b) and in detail in Fig. 1(c). Since the density in the POS is lowest in the saddle, this is where gap formation is assumed to occur.

While an MHD code can be used to simulate most of the conduction phase of a long-conduction-time POS, a particle-in-cell (PIC) code is better suited to simulate the last stages of the conduction phase if the underlying physics of POS behavior changes from being dominated by MHD effects to being controlled by electrostatic gap opening processes. In this paper, PIC simulations of the gap formation process are performed by examining a very small fraction of the total plasma volume [Fig. 1(c)]. Cylindrical geometry with azimuthal symmetry is assumed. The simulation plasma is meant to represent the plasma in the density saddle generated by magnetic pressure forces during the conduction phase. This plasma region thus represents the final volume of plasma carrying the generator current just before POS opening. Radial dimensions of the simulation are chosen to be at least twice the radial gap size that develops in the simulated plasma, and axial dimensions are chosen to be many times wider than the current channel width that develops in the simulated plasma. For simplicity, uniform density profiles in  $r$  and  $z$  are chosen in the simulation because the expected gap sizes are a fraction of the dimensions of the saddle region. Nonuniform density profiles will be tested in future work. The dense plasma on the cathode side of the density saddle in Fig. 1(c) is modeled as a space-charge-limited source of electrons in the simulations and will be called the "effective cathode." In the simulations a radius of 4.5 cm is chosen for the effective cathode rather than the 6.5 cm radius of the density saddle depicted in Fig. 1(b). Either choice is representative of typical HAWK experimental parameters.

The simulations show the development of a 2-D, localized, magnetized sheath in the POS plasma. It is localized



because it occupies a limited region near the effective cathode that is a small fraction of both the axial and radial dimensions of the original POS plasma fill region. It is considered magnetized for two reasons; one is that electron orbits in the sheath are bent by the magnetic field after being accelerated across some fraction of the sheath potential. The other reason is that two-fluid simulations of the POS show that the development of a localized 2-D sheath (rather than a 1-D sheath along the entire axial length of the plasma) is related to the  $\mathbf{v} \times \mathbf{B}$  force on the electrons.<sup>20,21</sup>

Scaling properties of the sheath potential and size with magnetic field and density are examined here and compared with simple analytic estimates. In addition, the self-consistent process of POS gap formation is studied. The term "gap" will be used to refer to a region largely evacuated of plasma electrons and ions. A good example of a gap is a region bounded radially above by a plasma, below by an emitting cathode, and in which emitted electrons are either magnetically insulated, or their drifts are largely in the axial direction. (Radial drifts and electron current loss from the cathode to the plasma may occur.) The term "sheath" will refer to a region still populated by ions, but locally non-neutral and across which current is carried by ions and electrons that are accelerated by electrostatic forces. In a sheath, the emission of electrons and their subsequent motion are strongly influenced by the presence of the local ion space charge. Examples of sheaths are a region of bipolar Child–Langmuir flow,<sup>22</sup> or a region of space-charge-limited electron emission from a cathode in a uniform ion background.<sup>23,24</sup>

The simulations show that a gap forms in the wake of the 2-D sheath while the POS is still in the conduction phase (i.e., before current is diverted to the load). To avoid confusion with load-driven gap formation processes which may occur during POS opening, and because the gap forms during POS conduction, this gap will be referred to as the "preformed" gap. While the 2-D sheath is limited in axial length, the axial length of the preformed gap grows and becomes as long as the POS plasma fill region as the 2-D sheath migrates toward the load. The preformed gap exists along the effective cathode between the generator side of the POS fill region up to the location of the 2-D sheath. Electrons emitted in the preformed gap do not radially cross the gap because they are magnetically insulated. Some ions are radially accelerated into the preformed gap from the plasma toward the effective cathode. The presence of this sparse population of ions in the preformed gap makes it hard to precisely determine the radial location of the plasma–gap boundary, but the size (radial extent) of the preformed gap is roughly one to two times the radial size of the 2-D sheath. The size of the preformed gap scales with plasma density and magnetic field in the same way as the 2-D sheath.

The simulations described here suggest a picture that differs from previous models of gap formation.<sup>10,13,25–27</sup> These models were essentially one dimensional in that uniformity in the axial direction was assumed, while gap opening occurred in the radial direction. The NRL model<sup>10,13,27</sup> was originally applied to the short conduction time ( $\leq 100$  ns) POS and assumed that during the conduction phase an

equilibrium Child–Langmuir bipolar sheath developed at the cathode and grew in axial length as the generator current rose. Current in the bipolar sheath was carried in the radial direction. The end of the conduction phase was determined by the point when the sheath extended along the entire axial length of the POS plasma. At the end of the conduction phase, the current carried by the sheath was larger than it could carry in equilibrium and the now axially uniform sheath grew in radial size. Subsequent modeling of this sheath growth showed that it can be very rapid at high sheath potentials.<sup>12</sup> If radial sheath growth proceeded beyond a certain point, the sheath size became large enough that the magnetic field could produce significant electron orbit bending within the sheath. Following the nomenclature of the present paper, the sheath becomes a gap at this point. The gap was uniform in  $z$  and grew rapidly in radial size by enhanced ion erosion as long as the current remained near the critical current.<sup>10</sup> In enhanced erosion, plasma ions are rapidly accelerated into the gap by the additional electron space charge in the gap produced by electron flow at the critical current. Goyer developed a variation on the NRL model by finding conditions for which the end of the conduction phase is determined by the formation of a magnetically insulated gap rather than by the bipolar sheath limit.<sup>25</sup> Parks *et al.* developed a model similar to the enhanced erosion model in which the ion current density is determined by energy and momentum conservation.<sup>26</sup> In addition to being 1-D, all of these models assumed that sheath and gap voltage are equal to the POS voltage (the voltage measured across the A–K gap in the POS region). To the extent that the POS voltage is inductively coupled to the load voltage, the load influences gap growth in these models. Finally, these models assumed that during periods of rapid gap growth the electron flow in the gap is critically insulated, i.e., that the gap size, gap voltage, and magnetic field are related by the critical, or saturated current formula.<sup>28</sup> In a critically insulated gap, electron orbits extend across the entire gap so vacuum electron flow fills the gap.

In contrast to 1-D models, 2-D simulations of the end of the conduction phase show that a localized 2-D sheath forms during the conduction phase. This sheath migrates axially toward the load, creating a magnetically insulated preformed gap in its wake. Previous simulations of the entire conduction phase of a short-conduction-time POS showed similar sheath and gap development, and indicated that the axial migration of the 2-D sheath is not determined by equilibrium bipolar sheath physics.<sup>29</sup> Those simulations differ from the present in that the densities were 2 to 3 orders of magnitude smaller and the current was not constant but rose in time. More recent simulations of Gamble *et al.*<sup>30</sup> short-conduction-time POS experiments<sup>4</sup> with electron densities of  $0.5\text{--}1.75 \times 10^{13} \text{ cm}^{-3}$ , current rises of 250 kA in 80 ns, and with a plasma of axial length 10 cm, showed the 2-D sheath migrating from the generator to the load side of the POS plasma in 20–30 ns. This migration time is roughly consistent with the conduction times of experiments run at the same densities as those simulated. These results, and results from the present simulations, show axial penetration of magnetic field is limited to the site of the potential hill and that

the full generator current is not carried at the load side of the POS early in the conduction phase of the POS. Rapid penetration of magnetic field along the cathode and current conduction to the load end of the POS are assumed in a model of the type of POS that incorporates external applied magnetic fields.<sup>2</sup> The resulting magnetic field pressure in the radial direction is assumed to open a gap in the POS along the entire cathode. In contrast, the present simulation and Gamble I simulation results show gap formation that is localized to the site of a potential hill which migrates relatively slowly toward the load. In addition, the gap formation mechanism is the electrostatic acceleration of ions predominantly toward the cathode, rather than the  $J \times B$  acceleration of ions toward the anode.

In the present simulations the radial size of the preformed gap remains fairly uniform in  $z$  and constant while the POS conducts current. Since the preformed gap is created before current is diverted to the load, it is concluded that the radial size of the preformed gap is independent of the load. In addition, 2-D simulations show that the electrostatic potential measured in the sheath is much larger than the POS voltage measured across the A-K gap. Electron orbits in the preformed gap behind the sheath are confined close to the cathode, so that electron flow fills only a small fraction of the gap. This demonstrates that the preformed gap is strongly insulated (unsaturated), and not just critically insulated. The preformed gap exists before the beginning of the POS opening phase, and thus represents the smallest gap that can form in the POS, since the presence of a nonzero impedance load (or large inductance in the load transmission line) could result in further gap growth during the POS opening phase. A nonzero impedance load will increase the POS voltage and could produce electron flows that are more saturated than the strongly insulated flows seen in these short-circuit load simulations. This saturated flow can cause further opening of the gap by enhanced erosion.<sup>10</sup> Thus the final gap size, meaning the gap size after the POS is fully open, could be larger than the preformed gap. In fact, for large enough load impedances (or large downstream inductances), it may be sufficient to model gap growth from the preformed to the final gap by assuming that the gap is critically insulated and that the POS voltage and gap voltage are the same. These possibilities will be the subject of future work. In the present simulations, where the load is a low inductance short circuit, the final gap and the preformed gap are of the same size, and both are strongly insulated.

In Sec. II, the design of the simulations is described. These are the first high density (up to  $5 \times 10^{15} \text{ cm}^{-3}$ ) simulations of the POS extending previous results at lower densities ( $< 2 \times 10^{13} \text{ cm}^{-3}$ ). Results of the simulations are also discussed in Sec. II, including descriptions of the formation of the 2-D sheath and preformed gap. In Sec. III scaling relations, in terms of electron density and magnetic field, are derived for the magnitude of the potential in the sheath and the radial size of the sheath. The scaling relations are then compared with simulation results. Finally, conclusions drawn from this work are discussed in Sec. IV.

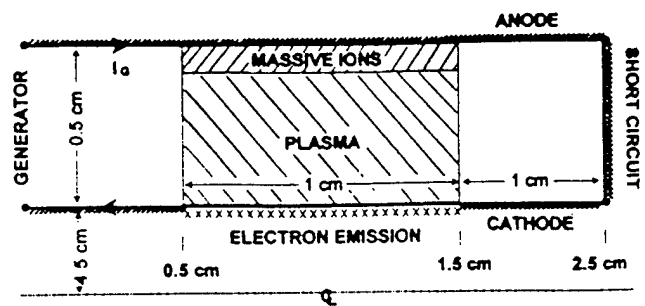


FIG. 2. Schematic diagram of the simulation region. The effective cathode radius is 4.5 cm. The plasma ions consist of  $C^{++}$ , but a massive ion species is introduced near the anode to prevent gap opening there.

## II. SIMULATION SETUP AND RESULTS

A schematic diagram of the numerical simulations is shown in Fig. 2. A section of transmission line is connected to a series LC circuit designed to mimic the primary energy source (generator) in a typical long-conduction-time POS experiment. The A-K gap of a portion of the axial length of the transmission line is filled with plasma. A carbon plasma is used, with the carbon ions doubly ionized.<sup>27</sup> On the load side of the POS, the transmission line is terminated with a short circuit (a conductor connects the anode and cathode of the transmission line).

Typical dimensions used in the simulations are shown in Fig. 2. Because these simulations are motivated by the long-conduction-time POS problem and only the final stages of the POS conduction phase are being modeled, the simulation is started by preloading the generator circuit and transmission line on the generator side of the POS with the full generator current. Since the focus of this paper is on the gap formation processes in the POS at the end of the conduction phase rather than on the interaction of the POS with a load, the POS-to-load distance is kept short.

As described in Sec. I, the simulation represents a small subregion of the original POS plasma volume [see Figs. 1(b) and 1(c)]. An emitting cathode boundary condition (the effective cathode) is used at the lower boundary of the simulation and models the dense plasma on the cathode side of the subregion. A modification of a conducting anode boundary condition is used at the upper boundary of the simulation. This modification consists of placing a small layer of immobile ions near the conducting anode surface. The actual anode in an experiment is far removed from the simulation region. Therefore the boundary condition at the upper surface of the simulation region should represent a continuation of the plasma rather than a conducting surface. Experiments and ANTHEM simulations show that the plasma at the anode side of the density minimum being simulated has a positive radial density gradient.<sup>5</sup> Simulations of such a plasma show axial penetration of the magnetic field and current into the plasma (by EMH effects) with electron currents in the radial direction. Simulations of a conducting anode on the other hand, also allow axial penetration of the magnetic field and current, but with the current in the axial direction near the anode.<sup>31-34</sup> This axially directed current produces a radial

TABLE I. Simulation setup and results. Rows 2–6 are input parameters, while rows 7–9 are simulation results. Input parameters shown are the density, current, magnetic field at the cathode, radial anode–cathode spacing, and axial plasma length. Results are the maximum sheath potential, radial sheath size, and an estimate of the preformed gap size. These results are dependent on the input density and magnetic field (current) only, not on the geometric parameters of rows 5 and 6. The cathode radius in all cases is 4.5 cm.

Case	1	2	3	4	5
$n_e (\times 10^{14} \text{ cm}^{-3})$	10	10	10	1	50
$I$ (MA)	1.2	0.6	2.4	1.2	1.2
$B (\times 10^4 \text{ G})$	5.33	2.66	10.66	5.33	5.33
$\Delta_{A-K}$ (cm)	0.5	0.5	1.0	2.5	0.28
$l$ (cm)	1.0	1.5	1.0	3.0	0.5
$\varphi$ (MV)	0.2	0.06	0.5	1.2	0.03
$d_{2D}$ (cm)	0.07	0.05	0.15	0.7	0.01
$d_{PF}$ (cm)	0.1	0.1	0.15	0.7	0.02

$J \times B$  force on the plasma that opens a gap near the anode. For this reason the behavior of a conducting anode boundary is unlike the behavior of the dense plasma on the anode side of the density minimum. To make the conducting anode boundary condition behave more like the appropriate plasma boundary, a massive ion species is introduced in the region immediately adjacent to the simulation boundary. The massive ion plasma still allows the magnetic field to penetrate, but prevents gap formation at the anode boundary because the ions do not move. The intent here is to remove the possibility of extraneous gap opening at this boundary so that it will not obscure the gap function physics on the cathode side. In addition, the upper simulation boundary is placed far enough from the effective cathode and cathode potential hill that the upper boundary condition has no effect on the processes being studied in this paper.

The results reported in this paper are obtained using the 2½-D electromagnetic particle-in-cell (PIC) code MAGIC<sup>35</sup> in cylindrical geometry. A series of numerical simulations is run at various plasma densities and current levels. Simulation input parameters are shown in Table I. The anode–cathode spacing,  $\Delta_{A-K}$ , and plasma length,  $l$ , are varied somewhat both to reflect the different gap sizes expected when the density and magnetic field are varied, and to keep the problem numerically tractable. However, the effective cathode radius,  $r_c$ , is kept the same and the results reported here are independent of the geometrical variations used.

To illustrate the main features of the simulations, the case of a  $10^{15} \text{ cm}^{-3}$  plasma carrying 1.2 MA is used as an example. Shown in Fig. 3 is a series of snapshots in time of contours of  $2\pi rB/\mu_0$  in increments of 100 kA ( $\mu_0$  is the permeability of free space). These contours represent surfaces of constant enclosed current and are referred to as current streamlines. In Figs. 3–5 the initial plasma fill occupies the region  $0.5 \text{ cm} \leq z \leq 1.5 \text{ cm}$  and the load is at  $z=2.5 \text{ cm}$ . Figure 3 shows current flowing in a wedge-like pattern near the effective cathode and that the wedge migrates axially in time. The radial extent of the wedge, that is the radial distance between the effective cathode and where the current flows axially back toward the generator in the plasma above the cathode, is about 1–2 mm. This distance can be associated later with approximately twice the radial size of the electrostatic sheath that develops in the plasma (see Fig. 5).

The POS begins to open at about 3 ns. At about 3.5 ns, the POS allows half the generator current, or 600 kA to reach the load. At about 4 ns, the POS is fully opened. Notice that at  $t=3 \text{ ns}$  there are very few current streamlines in the gap between  $4.5 \text{ cm} < r < 4.6 \text{ cm}$  for  $z < 1.3 \text{ cm}$ . This indicates that electrons emitted in the gap are well insulated before the POS opens. After opening, the streamlines also show little or no vacuum electron current launched on the load side of the POS. Because there is little or no vacuum flow launched near the POS, these simulations demonstrate that a gap can form in the plasma that is significantly larger than the minimum necessary to magnetically insulate the electron flow before and after opening. Here, strongly insulated flow after opening is due to the proximity of the short circuit load to the POS.

In Fig. 4, a series of particle snapshots shows the positions of the carbon ions at various times during the creation of the preformed gap. The snapshots show the removal of ions from a region of plasma near the effective cathode. Electron particle snapshots are very similar to the ion plots and are not shown. For ease of viewing only one in ten of the simulation ions is plotted in Fig. 4. The development of a preformed gap (or region of low ion density) along the effective cathode in the POS region is seen. Ions are accelerated across the preformed gap from the plasma to the effective cathode. Referring back to Fig. 3, little or no electron current exists in the gap on the generator side of the 2-D sheath. Electrons emitted into the preformed gap from the effective cathode are thus strongly magnetically insulated until they reach the region of large radial current density (see Fig. 3) at the load side of the gap. In order to understand the process that creates this preformed gap, the potentials that develop in the plasma will be examined.

Figure 5 shows a series of time snapshots of the electrostatic potential contours that develop in the POS plasma just before POS opening. The minimum contour level is 75 kV with increments of 25 kV between contour levels. The development of a localized 2-D sheath near the cathode is seen. These contours should be compared with the current streamlines of Fig. 3. Electrostatic potential contours are shown because the voltages that develop in the plasma during the

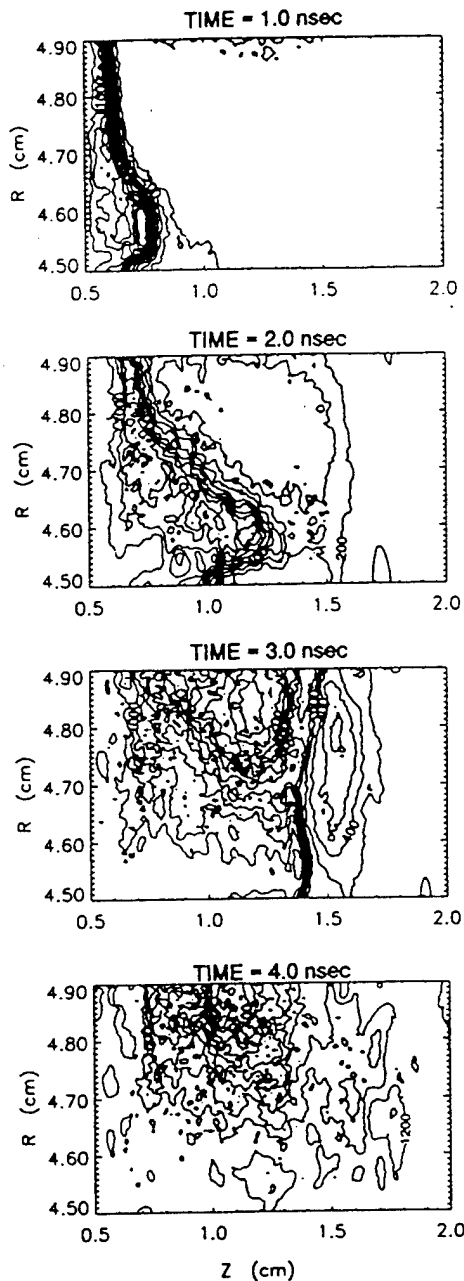


FIG. 3. Current streamline contours. The minimum contour level is 100 kA and the increment between contour levels is 100 kA. The initial plasma fill is between  $0.5 \text{ cm} \leq z \leq 1.5 \text{ cm}$ . The figure shows the penetration of a wedge-like current structure near the effective cathode.

conduction phase are predominantly electrostatic in nature—the inductive contribution is negligible. Notice that large potentials and potential gradients develop near the main electron-emission site at the effective cathode where the large current densities exist (see Fig. 3). The POS voltage (the A–K voltage in the POS region) is very close to zero while the POS is in the conduction phase ( $t \leq 30 \text{ ns}$ ). In contrast, the sheath floats to potentials up to about 200 kV. These potentials are positive, indicating the presence of non-neutralized ion space charge. Because the electron emission site and the region of ion space charge are non-neutral and

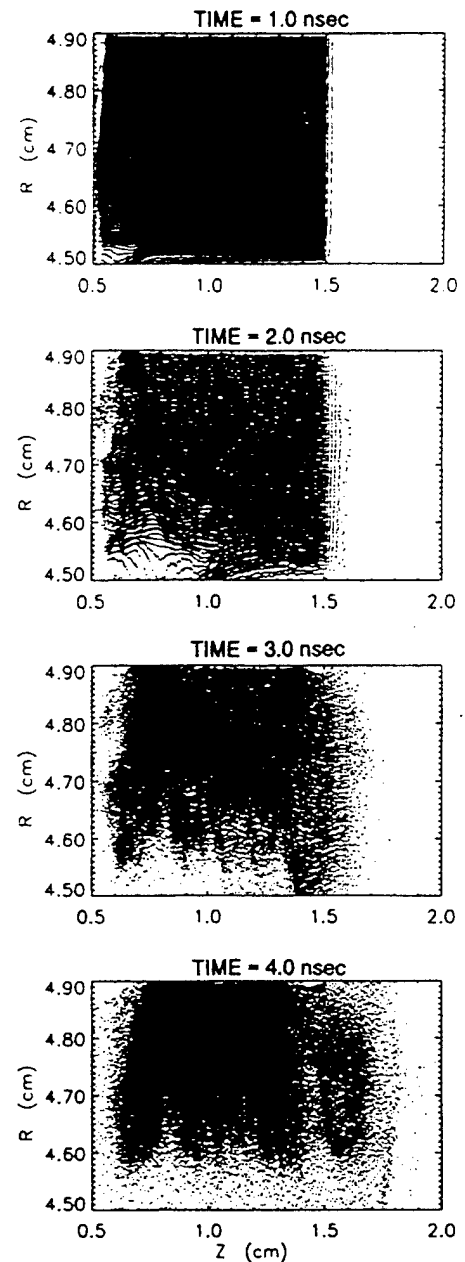


FIG. 4. Ion particle positions at various times. Only one in ten of the total number of simulation ions is shown. The opening of a gap and the progressive increase in its axial length is seen.

because of its limited axial and radial extent, this phenomenon is collectively referred to as the 2-D sheath. Just on the generator side of the main emission site, the potential contours form closed concentric loops that indicate a local maximum. This portion of the 2-D sheath has been referred to as the potential hill.<sup>11</sup> Near the potential hill, large electrostatic electric fields draw electrons from the effective cathode, and also accelerate ions out of the hill, mostly toward the effective cathode. The electrostatic fields also allow current-carrying electrons to  $E \times B$  drift around the hill after they are accelerated radially across a fraction of the 2-D sheath. As ions are accelerated out of the hill, a region evacuated of plasma is left behind (see Fig. 4). The potential hill migrates

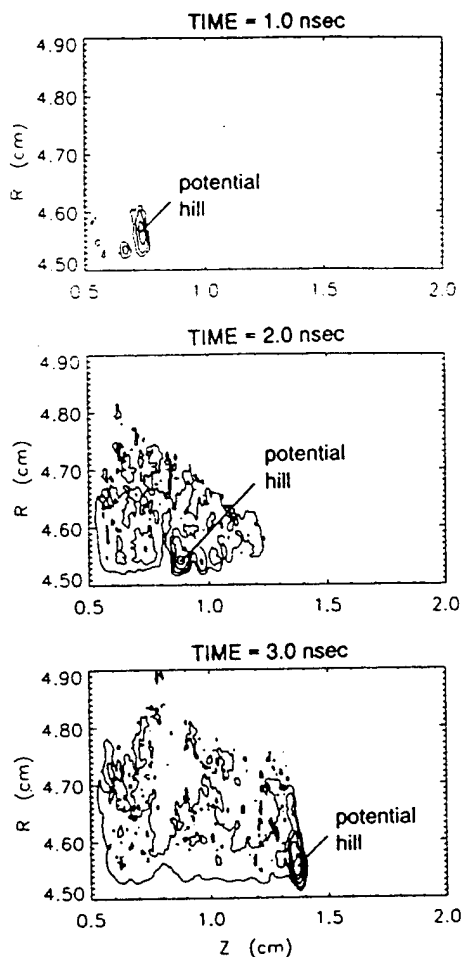


FIG. 5. Electrostatic potential contours before POS opening. These isopotential contours are shown in increments of 25 kV between contours with minimum contour level of 75 kV. Comparing with Fig. 3, the development of a potential hill immediately on the generator side of the main emission site is seen. The potential reaches a maximum of 200 kV at  $t = 3$  ns.

toward the load as new ions are uncovered on the load side to replace those accelerated out of the potential hill on the generator side. In this way, both the potential hill region and emission site migrate toward the load, leaving a preformed gap in their wake. For the cases examined in this paper, there is a rough correlation between the gap size, defined as the radial extent of the evacuated region, and the sheath size  $d_{2D}$ , defined as the radial distance between the effective cathode and the sheath potential maximum. By examining Figs. 4 and 5 before opening ( $t \leq 3.0$  ns) it is found that, for this particular case, the potential maximum is about 200 kV, the sheath size is about 0.7 mm, and the gap size is roughly 1 mm. Radial electric fields near the potential hill are close to 2–4 MV/cm and current densities of emitted electrons of about  $0.8 \text{ MA/cm}^2$  are seen.

The preformed gap size and potential hill are independent of the load because they form before the POS has any information about the load. As noted before, as the POS opens, further gap growth by enhanced erosion is possible especially in the case of nonzero impedance or large inductance loads. However, in this paper only the case of a short-

circuit load is considered and, on the time scales considered here (few ns), no further gap growth is seen as the current is diverted to the load. Another consequence of the short-circuit load is that very little or no vacuum electron flow is launched downstream of the POS after it is opened. The effect of non-zero load impedance on further gap opening as well as power flow to the load<sup>36</sup> will be the subject of future work.

The transition from the end of the POS conduction phase to the beginning of the POS opening phase in these simulations occurs when the 2-D sheath reaches the load end of the POS and is accompanied by a rapid rise in the load current. The opening transition can be best understood in terms of the rapid removal of the remaining ions out of the preformed gap. When the potential hill, or 2-D sheath reaches the load end of the POS, a block of ions still fills the radial extent of the gap at the load end. This block is small in axial length compared with the axial length of the POS. Initially there is enough ion space charge to allow electrons to flow across the gap so that no current reaches the load. As these ions are removed by the large electrostatic forces in the potential hill, insulation of the electron flow begins. Eventually all these ions are removed and the electron flow is magnetically insulated in the gap.

In the simulation described above, the size of the preformed gap and the maximum potential that develops in the 2-D sheath was found at one particular POS plasma density and current. To determine the scaling of the 2-D sheath potential, the sheath size, and the preformed gap size with density and current, a series of numerical simulations were run with different plasma densities and currents at fixed effective cathode radius. At the current level of 1.2 MA, three different electron densities,  $10^{14}$ ,  $10^{15}$ , and  $5 \times 10^{15} \text{ cm}^{-3}$ , were used for the initial plasma fill. For an initial plasma with electron density of  $10^{15} \text{ cm}^{-3}$ , three different current levels were simulated, 600 kA, 1.2 MA, and 2.4 MA. The results of these simulations are shown in Table I. In each case, the 2-D sheath size that forms during the gap opening process is recorded, together with the maximum potential that develops in the sheath structure near the effective cathode. A rough estimate of the preformed gap size,  $d_{PF}$ , that develops in the plasma is also shown. The 2-D sheath size is much easier to identify than the preformed gap size because the location of the sheath potential maximum is well defined (see Fig. 5) while the boundary between the preformed gap and the plasma above it can only be approximated (see Fig. 4). Scaling of the sheath size and sheath potential with density and magnetic field are compared to simple analytic estimates in the next section.

### III. SCALING RELATIONS

Attempts to understand the fundamental physical mechanisms underlying the formation of potential hills and some of their properties have been made in earlier work.<sup>11,20,21,37</sup> Some qualitative similarity exists between the potential hills seen here and the 1-D potential structures found in simulations of plasma-filled diodes (PFD),<sup>38–41</sup> although the magnetic field plays a more important role in the development of the 2-D potential hills. For simplicity, it is assumed in the following discussion that potential hills are magnetized

sheaths that develop near plasma/electrode interfaces. An approximate scaling law for the magnitude and radial size of these sheaths can be derived from the following 1-D analysis.

In this analysis, it is assumed that the ion background density at the electron emission site is roughly uniform. This is justified by the observation that as soon as a substantial number of ions are accelerated out of the sheath at one axial location, the sheath migrates axially into a region where ions have not yet moved. So even though ions are eventually accelerated, it is assumed that the sheath forms on a time scale short compared to the ion response time. Assuming space-charge-limited emission of electrons in a uniform, stationary background of ions, a relation between the plasma ion density,  $n_i$ , sheath potential,  $\phi$ , and electron current density,  $j_e$ , can be found by a simple modification of the technique developed by Child.<sup>42</sup> Poisson's equation is integrated once in the relativistic limit using the boundary condition that the electric field vanishes at both ends of the sheath, yielding

$$j_e = n_i Z e c \left( \frac{e \phi / m c^2}{2 + e \phi / m c^2} \right)^{1/2}, \quad (1)$$

where  $Z$ ,  $e$ ,  $c$ , and  $m$  are the ion charge state, electron charge, speed of light, and electron mass, respectively. For the purposes of deriving simple scaling relations and because the relativistic correction to Eq. (1) is not large for the cases considered in this paper, the nonrelativistic limit of the equation above will be used. This relation is

$$j_e = \alpha_\phi \frac{n_i Z e}{2} \left( \frac{2 e \phi}{m} \right)^{1/2}, \quad (2)$$

where the term  $\alpha_\phi$  is a multiplier of the formula. A value of  $\alpha_\phi < 1$  will be used later because empirically, electron magnetization prevents electrons from achieving the maximum sheath potential. Notice that the term under the square root is the velocity of the electron beam accelerated in the full sheath potential, so Eq. (2) (with  $\alpha_\phi = 1$ ) implies that the beam electron density after acceleration is half the original plasma electron density,  $n_e = n_i Z$ . In the nonrelativistic limit, Poisson's equation can be integrated once more to yield the following modification of the Child-Langmuir formula:<sup>23,24</sup>

$$j_e = \alpha_\phi \frac{\pi}{16} \left( \frac{2 e}{m} \right)^{1/2} \frac{\phi^{3/2}}{d^2}, \quad (3)$$

where  $d$  is the radial sheath size and the multiplier  $\alpha_\phi$  is used as it was in Eq. (2). The current density in Eq. (3) (with  $\alpha_\phi = 1$ ) is  $9\pi^2/16$  times larger than the unipolar and about three times larger than the bipolar Child-Langmuir formulas. Note that equating Eqs. (2) and (3) and solving for  $d$  yields an expression for the sheath size that scales like the Debye length with an effective temperature given by  $e\phi$ .

If it is assumed that the beam electrons carry all of the current and that the axial width of the current channel scales as the collisionless skin depth associated with the beam density, then

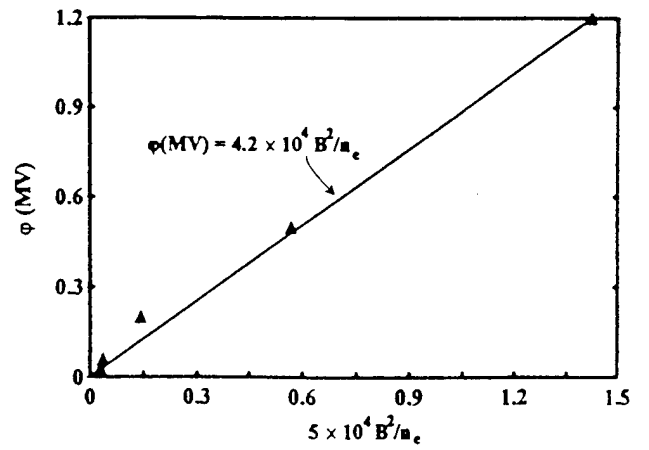


FIG. 6. The scaling of the maximum sheath potential as a function of the normalized parameter  $5 \times 10^4 B^2 / n_e$  is shown. This parameter is the right-hand side of Eq. (6) with multiplication factors set = 1.0. Simulation results of the potential are plotted, together with a straight-line fit of the data.

$$j_e \approx \frac{I}{2\pi r_c (\alpha_\omega c / \omega_{pb})} = \left( \frac{n_b}{\pi m} \right)^{1/2} \frac{eB}{2\alpha_\omega}, \quad (4)$$

where  $B$  is the magnetic field at the effective cathode,  $n_b$  is the beam density of the electrons in the current channel,  $\omega_{pb}$  is the plasma frequency associated with the beam, and  $\alpha_\omega$  is a multiplier of the collisionless skin depth. A value of  $\alpha_\omega > 1$  will be used because current channel widths seen in simulations are typically a few collisionless skin depths. Eliminating  $j_e$  from Eqs. (2) and (4), and assuming  $n_b \approx Zn_i/2$  [consistent with Eq. (2)], we find in Gaussian units that,

$$\phi \approx \frac{B^2}{8\pi n_b e \alpha_\omega^2 \alpha_\phi^2}, \quad (5)$$

or in mixed units,  $B$  (G),  $\phi$  (MV),  $n_b$  ( $\text{cm}^{-3}$ ),

$$\phi(\text{MV}) \approx \frac{5.0 \times 10^4 B^2}{\alpha_\omega^2 \alpha_\phi^2 n_e}. \quad (6)$$

The last approximation is obtained by again assuming that the plasma electron density,  $n_e \approx 2n_b$ .

An estimate of the radial size of the 2-D sheath,  $d_{2D}$ , can be made by assuming that the 2-D sheath scales as a multiplicative factor,  $\alpha_D$ , times the 1-D sheath size from Eq. (3). A value of  $\alpha_D > 1$  will be necessary to obtain agreement with simulation results. Combining Eqs. (2), (3), and (5) to find the 1-D sheath size in terms of  $B$  and  $n_e$ , the following is obtained:

$$d_{2D} \approx \alpha_D d = 3.7 \times 10^8 \frac{\alpha_D}{\alpha_\omega \alpha_\phi n_e} B. \quad (7)$$

The scaling relation derived from the 1-D analysis above for the voltage and sheath size are now compared to the 2-D simulation results. In Figs. 6 and 7, simulation results for the potential and sheath size are plotted, together with straight line fits of the data. An analytic expression for the straight line fit is given in each figure. The horizontal axis parameter in Fig. 6 corresponds to the right-hand side of Eq. (6) with

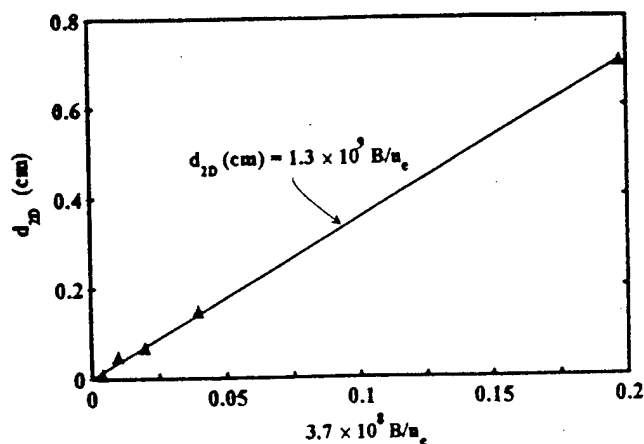


FIG. 7. The scaling of the 2-D sheath size as a function of the normalized parameter  $3.7 \times 10^8 B/n_e$  is shown. This parameter is the right-hand side of Eq. (7) with multiplication factors set=1.0. Simulation results of the sheath size are plotted, together with a straight-line fit of the data.

the multiplication factors set to 1. The horizontal axis parameter in Fig. 7 corresponds to the right-hand side of Eq. (7) with the multiplication factors set to 1. Figure 6 demonstrates that the simulation data fits the scaling relations of Eq. (6) with the product  $\alpha_\omega \alpha_\phi \approx 1$ . Checking with simulations, it is found that values of  $\alpha_\phi \approx 0.3$ , and  $\alpha_\omega \approx 3$  are typical. A value of  $\alpha_\phi < 1$  may be a manifestation of the magnetization effect on the electrons since electron orbit bending in the magnetic field prevents them from penetrating to the core (maximum potential) of the potential hill region. (If they could reach the core, they would neutralize the ion space charge and the potential hill would cease to exist.) Assuming  $\alpha_\omega \alpha_\phi \approx 1$ , Fig. 7 demonstrates that the good agreement with simulation can be found with  $\alpha_D \approx 3.5$ . Earlier MASK PIC code<sup>43</sup> simulations of the POS<sup>29</sup> in the lower density regimes of  $n_e = 4 \times 10^{12} - 10^{13} \text{ cm}^{-3}$  and with magnetic fields comparable to those used here obtained results that agree with the general scaling laws shown in Figs. 6 and 7 to within 20%.

It should be noted that the simple analytic model described above is not unique. Arguments based on the assumption that the electron current density is related to electron  $E \times B$  drift can be used to derive the same scaling for the potential. Another method based on magnetic and electric pressure balance<sup>44</sup> can also be used to arrive at the scaling,  $\phi \propto B^2/n_e$ . These analyses, together with the model presented here, provide some confidence that basic plasma physics principles apply, but do not illuminate the fundamental physical origin of potential hills.

#### IV. CONCLUSIONS AND DISCUSSION

In a series of simulations of a POS coupled to a low inductance transmission line terminated with a short-circuit load, the formation of a gap in the plasma near the effective cathode is observed. This gap is associated with the development and migration of a localized 2-D sheath in the plasma during the POS conduction phase. The process of sheath formation and ion evacuation out of the sheath occur before information about the load or downstream transmis-

sion line is available to the POS plasma, so that development of this preformed gap in the POS is independent of the load. The simulation results also differ from previous models of sheath and gap formation in that the sheath potential can be much larger than the POS voltage and that the preformed gap that forms is strongly insulated during the conduction phase. This suggests that the description of the initial gap formation process in previous models is not appropriate. Previously it was assumed that the gap forms during the POS opening process effectively starting with zero radial size at the end of the conduction phase. These simulations suggest that a preformed gap has formed at the end of the conduction phase, so that during POS opening a gap of nonzero size already exists. Because of the voltage that a load imposes on the POS, further gap growth can occur by the interaction of the POS with a nonzero impedance load if the electron flow in the gap is not strongly insulated.

Scaling of the sheath and preformed gap with density and magnetic field shows that the maximum potential that develops in the sheath scales as  $\phi \text{ (MV)} \approx 4 \times 10^4 B^2/n_e$ , while the sheath size scales as  $d_{2D} \text{ (cm)} \approx 10^9 B/n_e$ , where  $B$  is in G and  $n_e$  is measured in  $\text{cm}^{-3}$ . The preformed gap size is up to a factor of two larger than the sheath size and scales similarly. These simulations show that when the POS is closely coupled to a short-circuit load, the vacuum electron flow launched by the fully opened POS is negligible and that the final gap is significantly larger than the critically insulated gap. The final gap is the same size as the preformed gap because of the proximity of the short-circuit load to the POS. The preformed gap represents the minimum gap size of the opening POS since POS/load interactions can drive this gap to larger sizes during opening by processes such as enhanced erosion.

The results presented here extend previous short-conduction-time POS simulations in the  $n_e = 10^{12} - 2 \times 10^{13} \text{ cm}^{-3}$  density regime to the higher density regimes of  $10^{14} - 5 \times 10^{15} \text{ cm}^{-3}$  expected in long-conduction-time experiments. In the short-conduction-time POS simulations, the axial length of the POS plasma was 10 cm, the current rises to 250 kA in 80 ns, and the 2-D sheath structure migrated axially through the plasma on a time scale of 20–30 ns. These low-density simulations also showed the development of a 2-D sheath and a preformed gap. Scaling of the gap size and sheath potentials with magnetic field and density was the same as that reported here.

For long-conduction-time POS experiments, a conceptual model is presented describing the transition of POS dynamics from the MHD-dominated conduction phase to the erosion-dominated opening phase. The simulations described here are intended to model the end of the conduction phase after MHD redistribution of the plasma. An assumption is made in this paper that the dense plasma at the cathode side of the density saddle in Fig. 1(c) can be modeled as a cathode (the effective cathode). More work is needed to verify this assumption. In future work the final stages of the POS conduction phase will be simulated using a density profile like that shown in Fig. 1(c), with a smaller density in the middle of the POS and much larger densities near the electrodes. These simulations could reveal problems with the ef-



fective cathode assumption. For example, gap opening may always occur at the actual cathode, not in the radial middle of the POS. Experimental observations seem to contradict this, and the scaling results of this paper suggest that a gap at the actual experimental cathode would be too small to hold off much voltage because of the large plasma density there.

In experiments, an inferred gap size<sup>6</sup> can be defined from the POS voltage and generator current at the time of peak load power by using a critical,<sup>10</sup> or saturated<sup>28</sup> current formula relating these three parameters. However, when the electron flow in the real gap is well insulated (unsaturated), the inferred gap size is related more closely to the electron gyro radius, or the electron sheath size within the gap, than the gap size itself.<sup>45</sup> Experimental studies on HAWK have been made of the parametric dependence of the inferred gap size on the load impedance.<sup>6,46</sup> In the switch-limited regime,<sup>6,46</sup> where the POS voltage is limited by the POS rather than the load, the inferred gap size is weakly dependent on the load impedance. In the load-limited regime,<sup>6,46</sup> where the POS voltage is limited by the load impedance, the inferred gap size increases from a minimum size as the load impedance,  $Z_L$ , is increased from 0  $\Omega$ . As the load impedance increases further, the value of the inferred gap reaches a peak at the transition between the load and switch-limited regimes. For the POS parameters studied on HAWK (e.g.,  $r_c = 2.5$  cm,  $l = 8$  cm, conduction current  $I = 0.65$  MA, conduction time  $\tau = 0.85$   $\mu$ s), the inferred gap rises from a minimum of about 0.5 mm for a short-circuit load to about 3 mm for  $Z_L > 1.5$   $\Omega$ . The nonzero minimum inferred gap at zero load voltage results from the inductive voltage drop between the POS and the load (POS to load inductance  $\approx 25$  nH). Because the inferred gap size could be interpreted either as the real gap size or as the electron gyroradius within a larger gap, the inferred gap is a lower bound on the true gap size. It is therefore possible that in the load-limited regime, the true gap size remains close to its switch-limited value (i.e., it does not fall from 3 to 0.5 mm) as the load impedance decreases. This would suggest that the true gap size is only weakly dependent on the load impedance in the load-limited regime. The simulation results presented here provide one possible explanation of this interpretation by suggesting a mechanism for the formation of a gap that is independent of the load in the limit of low load impedances.

Experimental values of the inferred gap<sup>6,46</sup> described above depend on the load impedance but seem insensitive to the effective density<sup>6</sup> during the POS conduction phase or to the corresponding conduction current. This is true despite a variation in the effective density from  $n_e = 10^{15}$  to  $9 \times 10^{15}$   $\text{cm}^{-3}$  (this corresponds to a variation in the conduction current from about 0.4 to 0.8 MA). During the conduction phase, the plasma is redistributed by  $J \times B$  forces so that the plasma density in the region of opening at the time of opening could be considerably different from the effective density during conduction. The relationship (if any) between these two densities remains to be established. Neither of them has yet been directly measured. The axially line-averaged density throughout POS conduction and opening has been measured, but the effective axial length of the plasma during conduction is inferred from the aperture limiting the axial length of

the plasma injection region. The effective axial length of the plasma at opening is unknown. In Fig. 1, the plasma length as predicted by ANTHEM when the POS is close to opening is almost an order of magnitude less than the initial plasma length. Using this, and assuming that the line-averaged density at opening drops roughly 2 orders of magnitude from its value during conduction,<sup>5,6,15</sup> it can be estimated that the density at opening is on the order of  $n_e = 10^{14} - 10^{15}$   $\text{cm}^{-3}$ . For assumed densities at opening in the range  $n_e = 10^{14} - 10^{15}$   $\text{cm}^{-3}$ , and with corresponding conduction currents ranging from 0.4–0.8 MA, the scaling relation of Fig. 7 (assuming the gap size  $= d_{2D}$  and that  $r_c = 5$  cm) predicts preformed gaps ranging from 2.0–0.4 mm, respectively. This range of gap sizes gives an estimated range of preformed gaps that might be predicted by simulations; they should not be interpreted to suggest a gap size dependence on conduction density or conduction current. Such a dependence would only hold if the density at opening were related to the effective density during conduction. If the simple estimates made above are valid, the predicted results from the scaling relation of Fig. 7 are reasonably close to the inferred gaps from experiments ( $d = 0.5$  mm at  $Z_L = 0$   $\Omega$ ,  $d = 3$  mm for  $Z_L > 1.5$   $\Omega$ ).

Future work will study the relation between the effective density during conduction and the density at opening, the nature of the electron flow launched from the POS with more realistic load geometries, the effect of nonuniform density profiles and nonzero impedance loads on gap formation, and the validity of the effective cathode assumption. The scaling of the preformed gap with  $B$  and  $n_e$  found here suggests that improvements in POS performance (i.e., larger gaps) would be obtained either with greater thinning of the plasma at the end of the conduction phase and/or with higher magnetic fields. It remains to be seen whether these parameters can be controlled independently in actual experiments, where experiments at higher magnetic fields (currents) also require higher injected plasma densities to obtain the appropriate conduction time.

## ACKNOWLEDGMENTS

The assistance of Larry Ludeking at Mission Research Corporation with MAGIC is gratefully acknowledged.

Simulation results in this work were obtained using the Mission Research Corporation MAGIC code under the AFOSR-sponsored MAGIC User's Group. This work was supported by the Defense Nuclear Agency.

<sup>1</sup>A good overview is provided in the Special Issue on Fast Opening Vacuum Switches, IEEE Trans. Plasma Sci. PS-15, 629 (1987).

<sup>2</sup>C. W. Mendel, Jr., M. E. Savage, D. M. Zagar, W. W. Simpson, T. W. Grasser, and J. P. Quintenz, J. Appl. Phys. 71, 3731 (1992).

<sup>3</sup>W. Rix, D. Parks, J. Shannon, J. Thompson, and E. Waisman, IEEE Trans. Plasma Sci. PS-19, 400 (1991).

<sup>4</sup>B. V. Weber, R. J. Comisso, P. J. Goodrich, J. M. Grossmann, D. D. Hinshelwood, J. C. Kellogg, and P. F. Ottinger, IEEE Trans. Plasma Sci. PS-19, 757 (1991).

<sup>5</sup>D. D. Hinshelwood, B. V. Weber, J. M. Grossmann, and R. J. Comisso, Phys. Rev. Lett. 68, 3567 (1992).

<sup>6</sup>R. J. Comisso, P. J. Goodrich, J. M. Grossmann, D. D. Hinshelwood, P. F. Ottinger, and B. V. Weber, Phys. Fluids B 4, 2368 (1992).

<sup>7</sup>A. S. Kingsep, Yu. V. Mokhov, and K. V. Chukbar, Sov. J. Plasma Phys. 10, 495 (1984).

<sup>8</sup>A. Fruchtman and Y. Maron, Phys. Fluids B 3, 1546 (1991).



- <sup>9</sup>R. M. Kulsrud, P. F. Ottinger, and J. M. Grossmann, *Phys. Fluids* **31**, 1741 (1988).
- <sup>10</sup>P. F. Ottinger, S. A. Goldstein, and R. A. Meger, *J. Appl. Phys.* **56**, 774 (1984).
- <sup>11</sup>J. M. Grossmann, P. F. Ottinger, D. Mosher, and R. J. Mason, *Bull. Am. Phys. Soc.* **35**, 2055 (1990).
- <sup>12</sup>J. M. Grossmann, S. B. Swanekamp, and P. F. Ottinger, *Phys. Fluids B* **4**, 44 (1992).
- <sup>13</sup>B. V. Weber, R. J. Commisso, R. A. Meger, J. M. Neri, W. F. Oliphant, and P. F. Ottinger, *Appl. Phys. Lett.* **45**, 1043 (1984).
- <sup>14</sup>P. J. Goodrich, J. R. Boller, R. J. Commisso, D. D. Hinshelwood, J. C. Kellogg, and B. V. Weber, *8th IEEE International Pulsed Power Conference*, San Diego, CA, edited by R. White and K. Prestwich (Institute of Electrical and Electronic Engineers, Piscataway, NJ, 1991), p. 515, IEEE Catalog number: 91CH3052-8.
- <sup>15</sup>B. V. Weber, J. R. Boller, R. J. Commisso, P. J. Goodrich, J. M. Grossmann, D. D. Hinshelwood, J. C. Kellogg, P. F. Ottinger, and G. Cooperstein, *9th International Conference on High Power Beams*, Washington, D.C., May 25–29 1992, edited by D. Mosher and G. Cooperstein, p. 375. See National Technical Information Service Document No. PB92-206168. Copies may be ordered from the National Technical Information Service, Springfield, Virginia 22161. All orders must be prepaid.
- <sup>16</sup>R. J. Mason, M. E. Jones, J. M. Grossmann, and P. F. Ottinger, *Phys. Rev. Lett.* **61**, 1835 (1988).
- <sup>17</sup>R. Ingermanson, D. Parks, and E. Waisman, *9th IEEE International Conference on Pulsed Power*, Albuquerque, NM, 1993, June 21–23, edited by K. Prestwich and W. Baker (Institute of Electrical and Electronic Engineers, Piscataway, NJ, 1993), p. 165.
- <sup>18</sup>J. D. Huba, J. M. Grossmann, and P. F. Ottinger, *Phys. Plasmas* **1**, 3444 (1994).
- <sup>19</sup>J. J. Watrous and M. Frese (private communication, 1993).
- <sup>20</sup>B. V. Oliver, L. I. Rudakov, R. J. Mason, and P. L. Auer, *Phys. Fluids B* **4**, 294 (1992).
- <sup>21</sup>R. J. Mason, P. L. Auer, R. N. Sudan, B. V. Oliver, C. E. Seyler, and J. B. Greenly, *Phys. Fluids B* **5**, 1115 (1993).
- <sup>22</sup>I. Langmuir and K. B. Blodgett, *Phys. Rev.* **22**, 347 (1923); *I. Langmuir, Phys. Rev.* **2**, 450 (1913).
- <sup>23</sup>T. A. Voronchev, *Elektronnaya Tekhnika*, Ser. 3, *Gazorazryadnye Prib.* **3**, 36 (1971).
- <sup>24</sup>V. I. Koshelev and N. A. Ratakhin, *Sov. Phys. Tech. Phys.* **23**, 84 (1978).
- <sup>25</sup>J. Goyer, *IEEE Trans. Plasma Sci.* **PS-19**, 920 (1991).
- <sup>26</sup>D. Parks, E. Waisman, R. Ingermanson, and E. Salberta, in Ref. 15, p. 553. See National Technical Information Service Document No. PB92-206168. Copies may be ordered from the National Technical Information Service, Springfield, Virginia 22161. All orders must be prepaid.
- <sup>27</sup>B. V. Weber, R. J. Commisso, G. Cooperstein, J. M. Grossmann, D. D. Hinshelwood, D. Mosher, J. M. Neri, P. F. Ottinger, and S. J. Stephanakis, *IEEE Trans. Plasma Sci.* **PS-15**, 635 (1987).
- <sup>28</sup>J. M. Creedon, *J. Appl. Phys.* **46**, 2946 (1975).
- <sup>29</sup>J. M. Grossmann, R. Kulsrud, J. M. Neri, and P. F. Ottinger, *J. Appl. Phys.* **64**, 6646 (1988).
- <sup>30</sup>G. Cooperstein, J. J. Condon, and J. R. Boller, *J. Vac. Technol.* **10**, 961 (1973).
- <sup>31</sup>E. Waisman, P. G. Steen, D. E. Parks, and A. Wilson, *Appl. Phys. Lett.* **46**, 1045 (1985).
- <sup>32</sup>J. M. Grossmann, P. F. Ottinger, J. M. Neri, and A. T. Drobot, *Phys. Fluids* **29**, 2724 (1986).
- <sup>33</sup>R. J. Mason, J. M. Wallace, J. M. Grossmann, and P. F. Ottinger, *IEEE Trans. Plasma Sci.* **PS-15**, 715 (1987).
- <sup>34</sup>P. L. Auer and R. J. Mason, *Phys. Plasmas* **1**, 481 (1994).
- <sup>35</sup>B. Goplen, L. Ludeking, D. Smithe, and G. Warren, Mission Research Corporation (private communication).
- <sup>36</sup>S. G. Swanekamp, J. M. Grossmann, P. F. Ottinger, R. J. Commisso, and J. R. Goyer, *J. Appl. Phys.* **76**, 2648 (1994).
- <sup>37</sup>J. M. Grossmann, P. F. Ottinger, and R. J. Mason, *J. Appl. Phys.* **66**, 2307 (1989).
- <sup>38</sup>R. J. Kares, *J. Appl. Phys.* **71**, 2155 (1992).
- <sup>39</sup>R. J. Kares, J. L. Geary, and J. M. Grossmann, *J. Appl. Phys.* **71**, 2168 (1992).
- <sup>40</sup>S. B. Swanekamp, J. M. Grossmann, P. F. Ottinger, and J. L. Geary, *Phys. Fluids B* **4**, 3608 (1992).
- <sup>41</sup>S. B. Swanekamp, S. J. Stephanakis, J. M. Grossmann, B. V. Weber, J. C. Kellogg, P. F. Ottinger, and G. Cooperstein, *J. Appl. Phys.* **74**, 2274 (1993).
- <sup>42</sup>C. D. Child, *Phys. Rev.* **32**, 492 (1928).
- <sup>43</sup>A. T. Drobot, *Bull. Am. Phys. Soc.* **29**, 1379 (1984).
- <sup>44</sup>C. W. Mendel, Jr. and J. P. Quintenz, *Comments Plasma Phys. Controlled Fusion* **8**, 43 (1983).
- <sup>45</sup>R. V. Lovelace and E. Ott, *Phys. Fluids* **17**, 1263 (1974).
- <sup>46</sup>P. J. Goodrich, R. C. Fisher, D. D. Hinshelwood, J. R. Boller, R. J. Commisso, and B. V. Weber, in Ref. 15, p. 609. See National Technical Information Service Document No. PB92-206168. Copies may be ordered from the National Technical Information Service, Springfield, Virginia 22161. All orders must be prepaid.

*This is  
revised by  
4-26-95*

**PULSED POWER PHYSICS BRANCH TECH-NOTE NO. 95-07**

**TITLE:** SIMULATIONS OF GAP FORMATION IN PLASMA OPENING  
SWITCHES

**DATE:** MARCH 29, 1995

**AUTHORS:** J.M. GROSSMANN, S.B. SWANEKAMP, A. FRUCHTMAN, J. HUBA,  
R. MASON, B. OLIVER, P.F. OTTINGER, R.J. COMMISSO, R. RILEY,  
AND B.V. WEBER

**ABSTRACT:** Magneto-hydrodynamic (MHD) and electron magneto-hydrodynamic (EMH or Hall) effects in POS gap opening are examined. A review of earlier work (BEAM'S 94) on gap opening in the radial middle of the POS is given. More detailed studies of these processes are described. In particular, a study is initiated of how EMH effects may control the gap formation process. Two cases are studied, the extreme EMH regime and the MHD dominated regime. Three codes are used, Hall/MHD, ANTHEM, and MAGIC. Hall/MHD is a one-fluid code with Hall effects included. ANTHEM is a two-fluid code, and MAGIC is a particle-in-cell (PIC) code. Evidence is presented that suggests the importance of electron inertia effects and the unmagnetized ion Rayleigh-Taylor instability on gap formation.

THIS REPORT REPRESENTS UNPUBLISHED INTERNAL  
WORKING DOCUMENTS AND SHOULD NOT BE  
REFERENCED OR DISTRIBUTED.

Fig. 1. Title and Authors.

Fig. 2. Outline. First we'll give a review of our previous PIC simulations of the POS. Our simulations are self-consistent simulations of POS opening intended for use in understanding POS opening physics and as input to the POS opening models employed by Steve Swanekamp and Bob Commisso et al. in their studies of load coupling.

Although EMH effects may not be very evident in the conduction phase of the POS, we will show evidence that suggests the importance of EMH effects in the opening phase. We illustrate these effects using two regimes, an extreme EMH regime where ions are immobile, and an MHD dominated regime where ion motion dominates.

Finally we will summarize our work and discuss the application of these ideas to improving POS performance. The difficulties of exploiting EMH effects are also discussed.

Fig. 3. HAWK experimental results. The conduction current in HAWK experiments scales with density, radius and length as predicted by the scaling equation shown here. The scaling equation is obtained from a center-of-mass motion equation. The picture we have of the POS is of a snowplow pushing the plasma axially and radially until the snowplow reaches some point near the load end of the plasma, at which point the POS opens. The density profile in the bottom left figure shows that at the point of POS opening, a gap has formed in the radial middle of the switch. This radial density profile is obtained using axial-line-of-sight interferometry through the switch plasma. It is not a general result, however. In some HAWK shots with plasma gun sources, the opening seems to occur very near the cathode. Ron Riley's picture of the parallel plate POS also shows a picture consistent with the idea of an axially moving snowplow followed by gap formation away from the cathode, although how far away is arguable.

Fig. 4. In contrast to the experimental observation that opening can occur away from the electrodes, PIC simulations of the POS, when left to their own devices, always open at the electrode surfaces. The nature of the opening is different at each of the electrodes. At the cathode, a potential hill or electron vortex forms early during the current rise. This potential hill migrates axially along the cathode leaving a magnetically insulated gap in its wake. When the gap reaches the load end of the POS, the POS opens. Some properties of the potential hill are listed. The magnitude, physical size and axial velocity of the potential hill are shown.

The anode in simulations is modeled as a solid, perfect conductor. Since such a conductor shorts out the axial electric field, electrons cannot drift radially into the anode and are forced to drift axially along the anode. This drift causes rapid penetration of magnetic field, followed by  $\mathbf{J} \times \mathbf{B}$  acceleration of the plasma away from the anode. The subsequent gap can open the POS. The penetration of current and magnetic field is very rapid. Its velocity is given in the figure. This velocity, as well as the cathode penetration velocity are approximate ballpark numbers good to a factor of two.

Fig. 5. To bring the simulations in closer agreement to experiments, it is necessary to suppress electrode opening. This is done by placing an immobile ion species near the electrode surfaces. Justifications for this technique are discussed in the figure.

Fig. 6. When electrode opening is suppressed, you see results from the PIC code that are in closer qualitative agreement with exp't. Looking at the density contours in this figure, JxB pushing of the plasma is seen, followed by gap opening in the radial middle of the POS plasma, which in turn is followed by POS opening and power delivery to the load. These results are from the BEAMS '94 meeting and feature a  $2 \times 10^{14} \text{ cm}^{-3}$  carbon ( $\text{C}^{++}$ ) plasma being driven with 1.2 MA of current.

Fig. 7. Another interesting feature of the results presented at the BEAMS meeting, was evidence of EMH effects in the gap opening process. The simulations showed that a potential hill formed inside the gap as the POS gap was opening. The potential hill moved through the gap and then up the load edge of the plasma. A new potential hill formed in the gap behind the first. Although not shown, an electron vortex accompanied each of the potential hills. Other EMH effects seen in these simulations include magnetic field penetration and density structuring, terms which will be defined in the following figures. The nature of these effects were not understood until Steve Swanekamp recently performed a series of numerical experiments in which the effects were demonstrated to be due to EMH. Some of these numerical experiments are described in NRL Tech. Note. 95-10.

Fig. 8. The results above were a review of past PIC results and are summarized in this figure.

Fig. 9. The main thrust of this talk is to present evidence of the importance of EMH effects in POS opening and gap formation. So first we should define some of the terms that will be used. The term EMH refers to effects associated with terms generally ignored in the generalized Ohm's law. The first four terms in the law are usually included in non-ideal MHD descriptions of plasmas, while the 3rd and 4th terms on the RHS are ignored. In the equation shown in this figure,  $u$  is the ion velocity while  $J$  is the sum of the ion and electron current densities. The 3rd term on the RHS is called the Hall term. It, together with Faraday's law gives you mechanisms for magnetic field transport into a plasma. The 4th term is associated with electron inertia. The 3rd and 4th terms collectively lead to EMH effects, and describe electron effects on the current distribution in the plasma. Another term we'll use frequently is 'density structuring' or 'density structures'. These are depicted in the two bottom left figures showing a uniform snowplow and then a snowplow with density structures. The term density structures will have this specific meaning in this talk. A density structure looks like a snowplow that has been passed through a comb. A more general definition of density structuring is given in Joe Huba's paper. In a density structure the ion and electron densities are very nearly equal so that the quasi-neutrality assumption built into the MHD equations is obeyed. A vortex is a current spiral that appears in certain PIC simulations of the POS, and is depicted in the bottom right figure. Vortices and density structures are both EMH effects, but are completely independent. You can have either one independently of the other. We will show that one is a Hall effect, while the other is an electron inertia effect. In a vortex, the quasi-neutrality assumption is violated. While the electron density is definitely non-uniform in a vortex, the vortex can form whether or not the ion density is structured. So a vortex can form with or without an underlying ion density structure. However, if a vortex forms in a region that was structured, the region can no longer be referred to as a density structure, since it is no longer quasineutral. The electron density in the middle of the

vortex is lower than the local ion density, while the electron density in the outer edge of the vortex is higher than the local ion density.

Fig. 10. We will illustrate the importance of EMH effects by looking at two regimes: 1) the extreme EMH and 2), the MHD-dominated regimes. These regimes are determined by choosing the ion mass so that either EMH effects or MHD effects dominate. This can be done because the relative importance of these effects can be estimated by comparing the Alven velocity with the Hall penetration velocity. Both cases have the same current rise and initial density profile.

Fig. 11. We have obtained results from three different codes. Hall/MHD is a one fluid code with Hall effects, ANTHEM is a two-fluid code, and MAGIC is a PIC code. The latter two codes should show Hall and electron inertia effects self-consistently. We'll show results of these code by drawing either current streamlines or density contours. In the bottom of this figure we are showing examples of both early in time.

Fig 12. First, we'll look at the extreme EMH regime by using an immobile ion background in the plasma. This figure shows current streamlines late in time after the current and magnetic field have penetrated to the load side of the plasma. Hall/MHD shows pure Hall penetration. ANTHEM shows the development of one vortex in addition to the magnetic field penetration. It is able to resolve the vortex because ANTHEM includes electron inertial effects. The PIC code is able to resolve a train of vortices that fill in the penetrating finger of current. The differences between the PIC code's train of vortices versus ANTHEM's single vortex is thought to be due to deficiencies in ANTHEM. The vortices are significant because: 1) they are strongly paramagnetic, that is the current enclosed and magnetic field is 50 % stronger inside the vortex than the current or magnetic field supplied by the generator, and 2) because large electrostatic fields build up in the vortices, and these electrostatic fields could accelerate ions out of the potential hills that form in the vortex. For this reason, a vortex is a gap opening mechanism that results from EMH effects. In this figure, ions are infinitely massive, so they cannot be accelerated out of the vortex by electrostatic fields. In a real plasma, the formation of vortices depends on whether ions remain in the vortex long enough for it to exist in the first place. A vortex can only exist around a positively charged region of plasma because electrons have to  $\mathbf{E} \times \mathbf{B}$  drift in order to spin in the vortex. If ions are quickly accelerated out of the potential hill at the center of the vortex, the vortex cannot form.

Fig. 13. Next we will examine the MHD-dominated regime where  $m_i = m_p/20$ . The first set of figures shows the evolution of the ion density as predicted by the Hall/MHD code with the Hall effect turned off. What you see is a classic snowplow  $\mathbf{J} \times \mathbf{B}$  accelerating through the initial plasma fill.

Fig 14. Now we'll use the same code on the same problem, only turn the Hall effect on. This time we see the snowplow again, but with density structures inside the snowplow. The fact that we are seeing different results now than in the previous figure demonstrates the importance of Hall effects even in an MHD dominated regime. The structuring in the snowplow is due to the unmagnetized ion Rayleigh-Taylor instability, or more colloquially, the Hall Rayleigh-Taylor instability. (See Joe Huba's Physics of Plasmas paper, October 1994, p. 3444). The density

valleys that form in the structures could be precursors of the final gap that opens in the POS. In future work, we will try to make the connection between gaps and valleys more rigorous by following the evolution of these structures from conduction to opening using a PIC code. We tried to use the ANTHEM code on this same problem but were unable to duplicate the results Hall/MHD, at least in the case of very low resolution. This could be because of ANTHEM's inherent numerical diffusivity or because the resolution of the code must be made higher.

Fig. 15. Next we will look at the same MHD-dominated regime again, only this time with a PIC code. A snowplow is again evident, as well as density structures in the snowplow. A gap forms in the radial middle of the POS just before POS opening. The claim we are making that EMH effects could be involved in POS opening hangs on the following argument. The Hall/EMH code and the PIC code show very similar results up to POS opening (compare Fig. 14 and 15). The fluid code develops structures, and it does so only with the Hall effect turned on. The PIC code shows density structures too. At least one of these structures evolves into a gap which opens the POS. It is possible that the same physical mechanisms that produce density structures in the fluid code also produce them in the PIC code and are thus involved in gap formation. That's one piece of evidence that suggests that EMH effects are involved in PIC opening. Additional evidence of the importance of EMH effects was demonstrated in the PIC results discussed in Figs. 6 and 7, where we observed vortices in the gap in the higher density,  $C^{++}$  results reported at the BEAM's 94 meeting.

Fig 16. Summary of the results so far. We are exploring the possibility that gap precursors and vortices determine the gap size. Theoretical analysis of these effects is underway. Scaling results not presented here suggest that you might get bigger gaps for lower density, more uniform plasmas at opening. We are also examining detailed physics of vortices including a detailed analysis of where the electromagnetic and kinetic energy is partitioned and how vorticity conservation theorems apply. This work is being done in collaboration with Amnon Fruchtman.

Fig. 17. We would like to use our knowledge of gap opening mechanisms to improve POS performance. One method of exploiting EMH effects is to somehow make the plasma density as low and as uniform as possible at opening. Perhaps by shaping the electrode surfaces in some favorable way, this can be achieved. Another method may be to delay EMH effects so that  $J \times B$  forces have more time to thin out the plasma and then larger density structures or vortices will open larger gaps. A few ideas on how to do this are discussed in this figure. One of these ideas is to apply an external magnetic field. A preliminary study of this idea showed that an external field prevented the formation of vortices in the plasma in the extreme EMH regime. If these approaches do not work, maybe we should try to make our switches open at the electrodes where the physical opening mechanisms are simpler to understand because they do not rely on complicated effects such as Hall Rayleigh Taylor instabilities or vortices (the MCPOS is one example of such an approach, but it introduces another set of complications in the form of applied magnetic fields). Speaking purely hypothetically, based on observed plasma behavior in simulations, if you could suppress opening in the body of the plasma, the POS would exhibit rapid penetration of magnetic field along the cathode by cathode potential hills, followed by radial  $J \times B$  acceleration of plasma. The gap formed by the potential hill alone would not be large enough to open the POS because the large density near the cathode produces a small gap. However, the

subsequent radial  $J \times B$  acceleration of the plasma would open a much larger cathode gap, sufficient to open the switch. A similar effect would be observed at the anode if the anode were a solid perfect conductor.

Fig. 18. We have shown results from both fluid codes and PIC codes on time scales where both can be applied to the same problem. In practice, however, PIC and fluid codes each have distinct domains of usefulness. PIC code are better for short time scales, fluids better for long time scales. We are working on marrying the two types of code so that the output of a fluid code can be directly inputted into a PIC code. That way we can run the fluid code during the conduction phase of the POS and then run the PIC code during the opening phase.

Since we will be using fluid codes extensively, we would like to see further development of the codes. Each of our fluid codes needs improvements, as described in the figure. In addition, we think that more work on the MCPOS would be very beneficial in improving our understanding of both DNA and SANDIA style switches. There may be aspects of the MCPOS that can be exploited in more conventional switches.

mskew

## Simulations of gap formation in a POS

NRL

John Grossmann, Steve Swanekamp,<sup>+</sup>  
Amnon Fruchtman,<sup>#</sup> Joe Huba,  
Rod Mason,<sup>@</sup> Bryan Oliver,<sup>\*</sup>  
Paul Ottinger, Bob Commisso,  
Ron Riley,<sup>\*</sup> and Bruce Weber

DNA POS WORKSHOP  
NSWC, March 29 1995

<sup>+</sup> Jaycor, <sup>#</sup> SAIC, <sup>@</sup> LANL, <sup>\*</sup> NRC/NRL Research Associate

DNA POS Workshop  
29 March 1995

Fig. 1

## OUTLINE

NRL

- **Review** - POS simulations using PIC codes.
- **Focus on EMH effects**
  - Evidence that EMH controls POS opening and gap size.
  - Illustrate EMH effects in two regimes-
    - Extreme EMH (no ion motion).
    - MHD dominated.
- **Summary**
  - Improving POS performance.
  - Difficulties in exploiting EMH effects.

DNA POS Workshop  
29 March 1995

Fig. 2



## Hawk Experimental Results

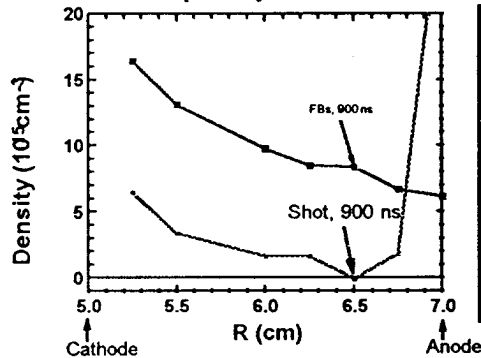
NRL

Conduction phase is MHD dominated

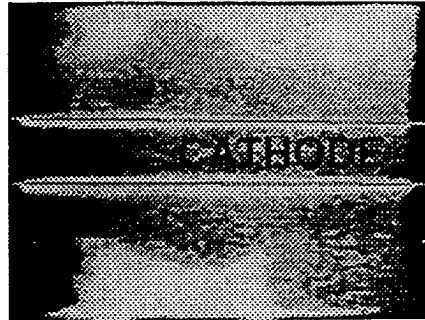
$$\iint I^2 dt dt = 100 \pi m_i n_e r^2 \ell_o^2 / Z_i$$

See gap formation at opening

Coax POS can open away from electrodes



Parallel Plate POS



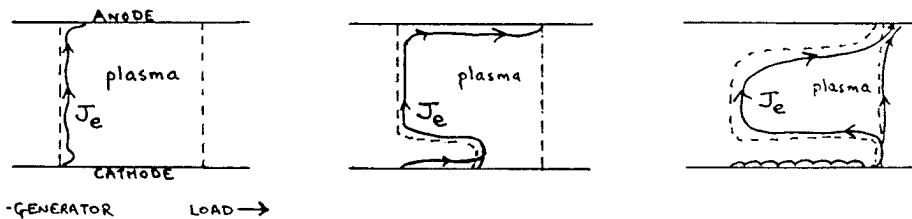
DNA POS Workshop  
29 March 1995

Fig. 3

## PIC Simulations of POS

NRL

Electrode Opening dominates PIC simulations



Cathode gap formation by vortices, potential hills.

$$\phi(\text{MV}) = 5 \times 10^4 B^2 / n_e, \quad d(\text{cm}) = 10^9 \times B / n_e, \quad V_z = 3 \times 10^8 \text{ cm/s}$$

Anode gap formation by radial  $J \times B$  forces.

$$\text{Current penetrates along anode with } V_z \approx 5 \times 10^9 \text{ cm/s}$$

DNA POS Workshop  
29 March 1995

Fig. 4

## Electrode opening can be suppressed

NRL

- Place massive ions near electrode surfaces
  - Justification:
    - » empirically, opening can occur away from electrodes
    - » expt'l anode is not a solid conductor
    - » cathode plasma densities may be very high in exp't
- Effect is to allow other physics mechanisms to play role

DNA POS Workshop  
29 March 1995

Fig. 5

## Gap opening in plasma

SS62,  $m_i = C^{++}$  in plasma,  $m_i = \infty$  near electrodes

NRL

Electron density contours:

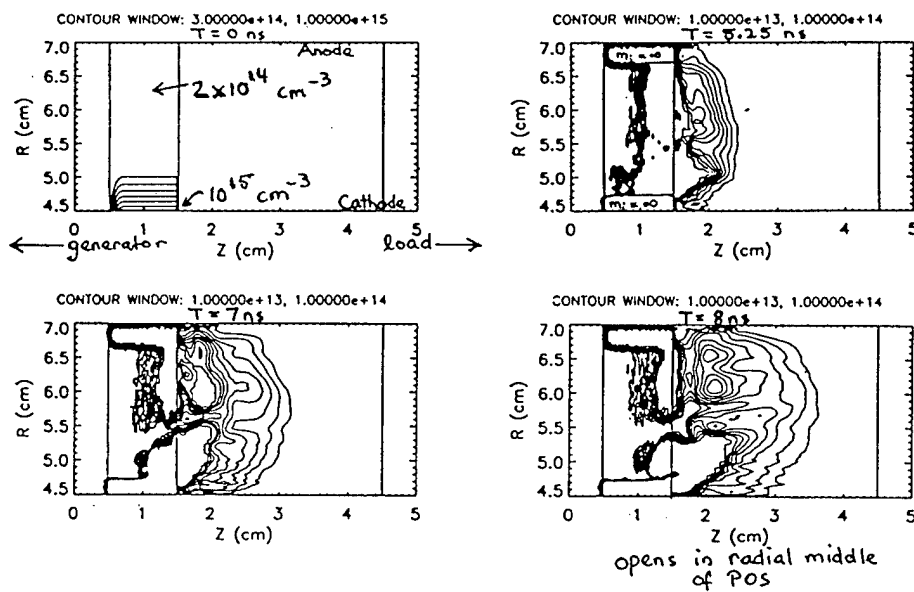


Fig. 6

## Life-cycle of a potential hill

SS62

NRL

iso-potential contours, increments of 100 kV

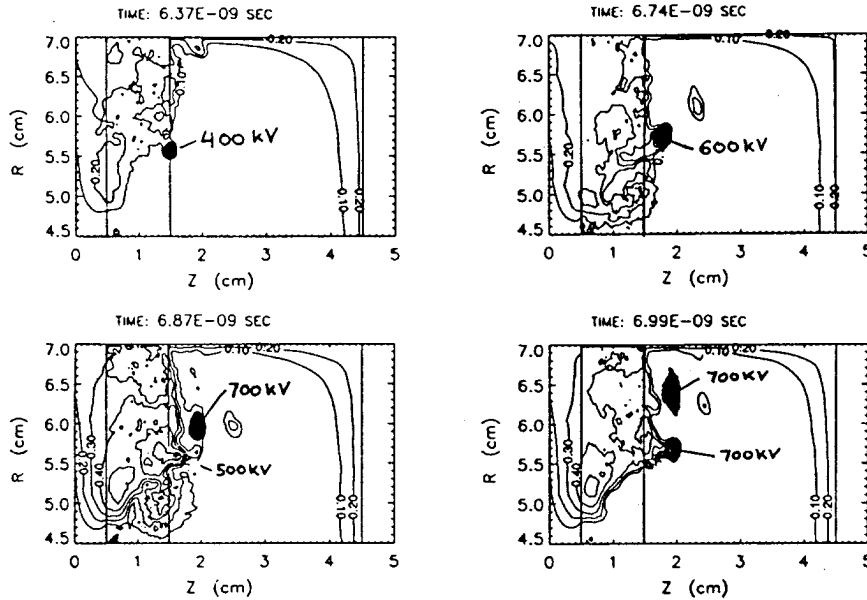


Fig. 7

## Review of past PIC Results

NRL

### Qualitative agreement with exp't

- Axial translation of plasma by  $J \times B$  force
- Gap opening in radial middle of plasma

### Observed EMH effects

- Magnetic field penetration into plasma
- Electron vortices
- Density structuring

DNA POS Workshop  
29 March 1995

Fig 8

## Some definitions

NRL

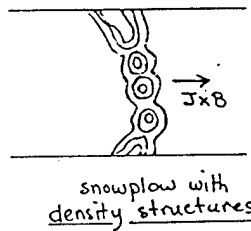
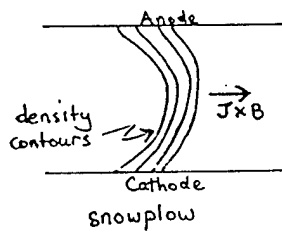
**EMH** - Electron Magneto-Hydrodynamics.

Effects associated with terms in generalized Ohm's law:

$$E + u \times B = \eta J - \nabla p / en_e + \underbrace{J \times B / en_e}_{\text{HALL}} + \underbrace{\frac{m_e}{e} \frac{\partial}{\partial t} \left( \frac{J}{n_e} \right)}_{\text{Electron inertia}}$$

EMH

### DENSITY STRUCTURING



### VORTEX



DNA POS Workshop  
29 March 1995

Fig 9

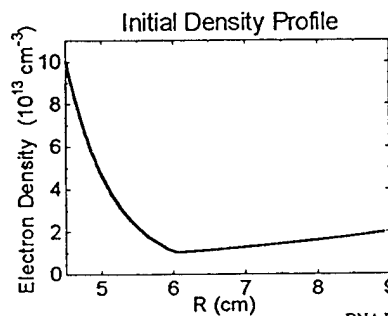
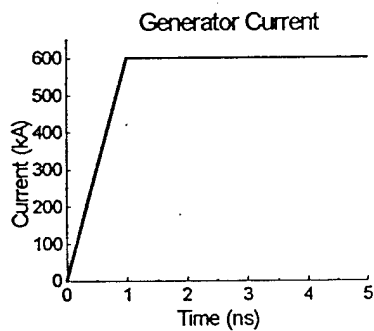
## Two Cases Illustrate EMH Effects

NRL

- A. Extreme EMH regime ( $m_i = \infty \Rightarrow V_A \ll V_H$ ).
- B. MHD dominated regime ( $m_i = m_p/20 \Rightarrow V_A \approx 3V_H$ ).

$$V_A = B / \sqrt{4\pi n_i n_e}, \quad V_H = \frac{cB}{8\pi m_e} \left( \frac{2}{r} + \frac{1}{n_e} \frac{\partial n_e}{\partial r} \right)$$

Both cases have same current risetime and initial density profile



DNA POS Workshop  
29 March 1995

Fig 10

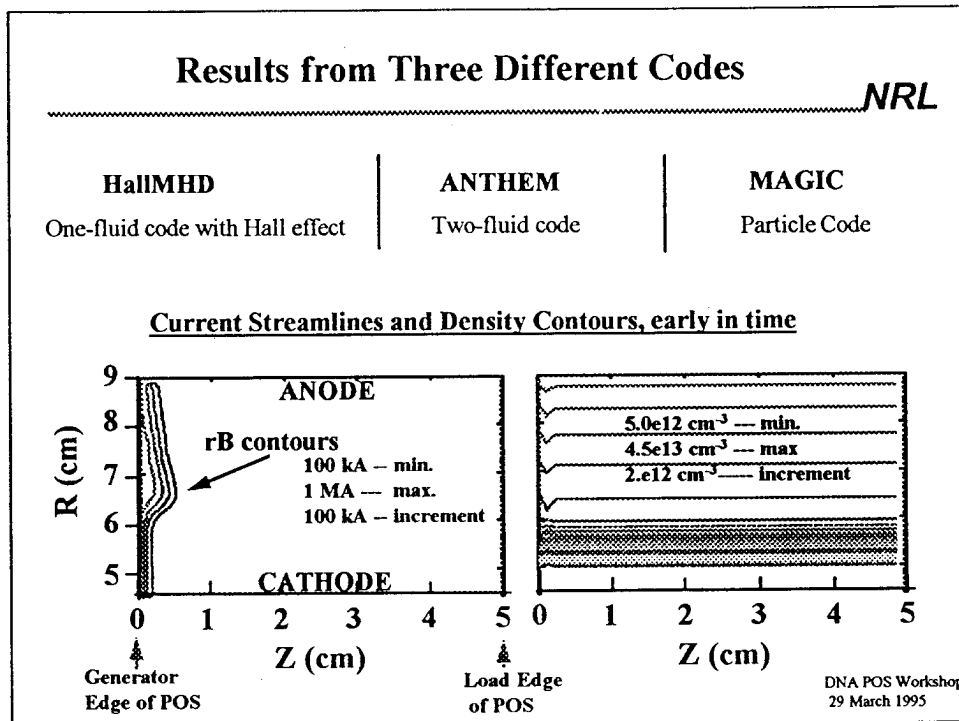


Fig 11

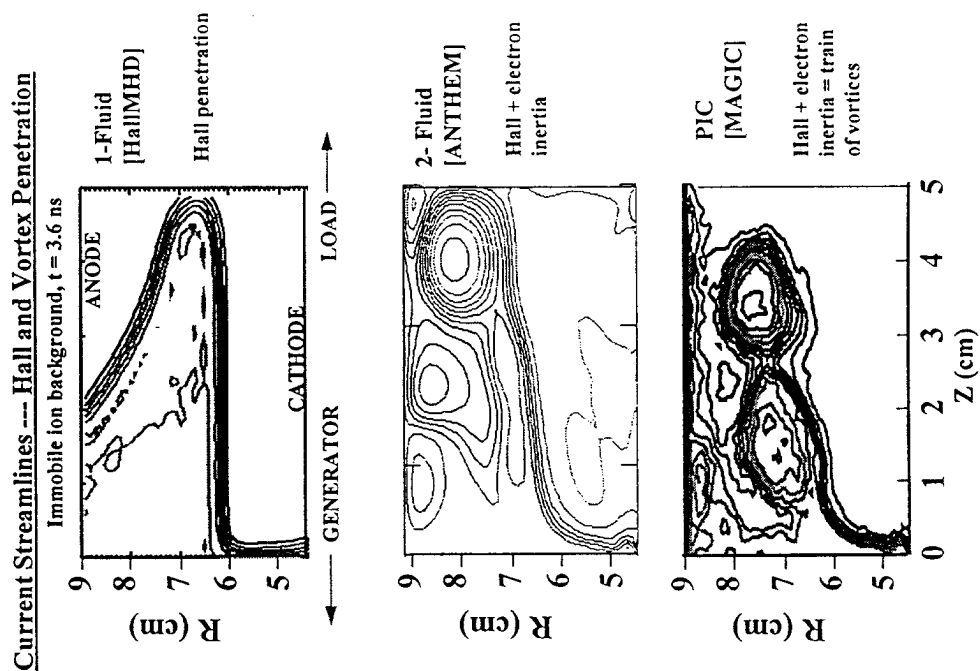


Fig. 12

# Density Contours -- Snowplow and Hall

$m_i = m_p/20$ , Hall = on in HallMHD code

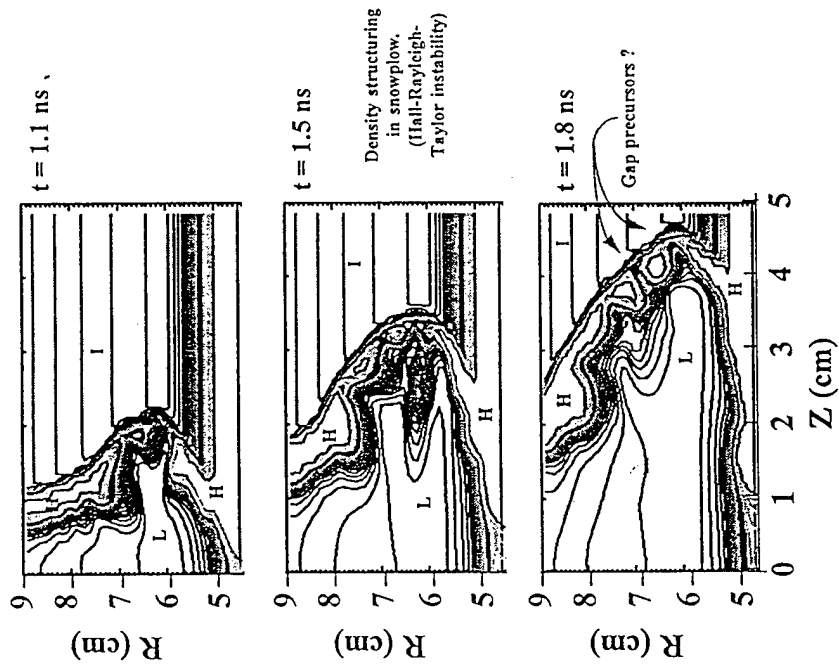


Fig 14

# Density Contours -- Snowplow only, no Hall

$m_i = m_p/20$ , Hall = off in HallMHD code

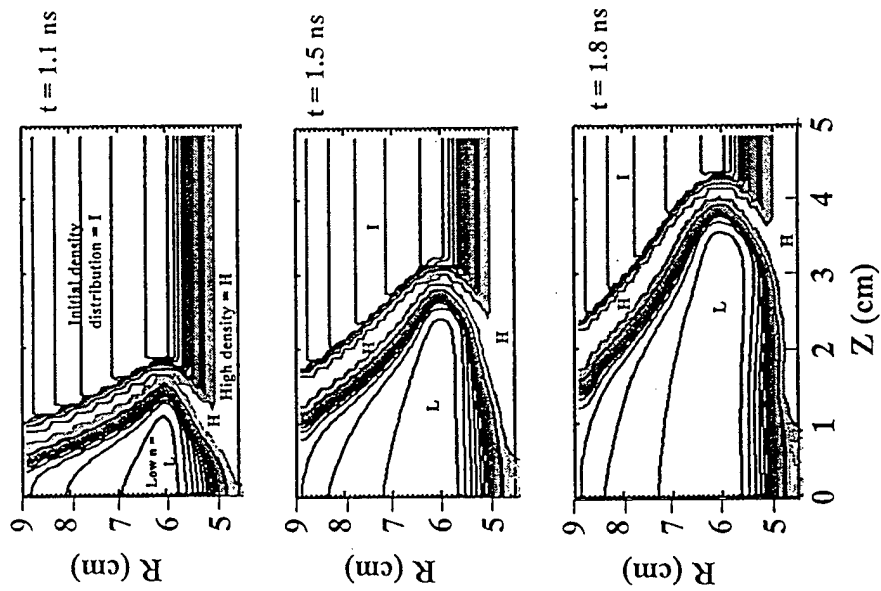


Fig. 13

## Density Contours -- Snowplow and EMH

$m_i = m_p/20$ , PIC code

$m_i = \infty$  near electrodes to suppress electrode opening

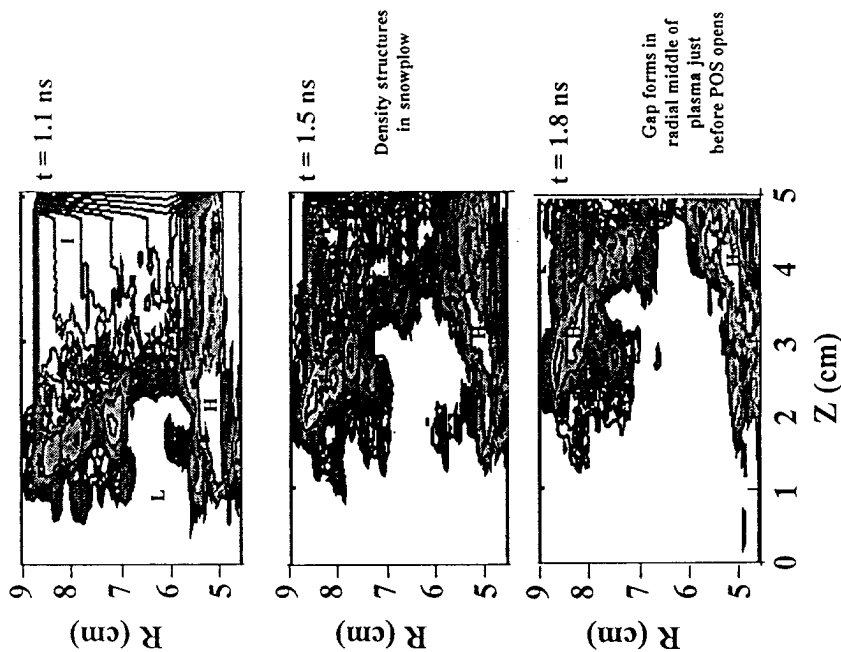


Fig. 15

## Summary

NRL

### • Results

- Vortices in EMH-only regime
- Smooth snowplow in MHD regime when Hall = off
- Density structures in snowplow when Hall = on
- Good correlation between PIC and HallMHD codes

### • Simulations suggest:

- EMH effects (vortices, density structuring) involved in POS opening
- Density structures form gap precursors
- Gap precursors, vortices determine gap size at opening?

### Theoretical analysis of density structuring and vortices is underway

- Density controls growth rate of Hall Rayleigh-Taylor instability
- $\left(\frac{1}{n_e} \frac{\partial n}{\partial r}\right)^{-1}, \frac{c}{\omega_p}$  control size of vortices, structures
- Bigger gaps with more uniform, lower density plasmas at opening

DNA POS Workshop  
29 March 1995

Fig. 16

## Improving POS Performance

NRL

### 1. Exploit EMH effects

- Experimentally control density uniformity at opening.
  - Size of density structures and vortices depend on  $n$ ,  $dn/dr$ .
  - Electrode geometry may affect density uniformity at opening.
- » More uniform plasma at opening  $\Rightarrow$  bigger gaps ?

### 2. Reduce EMH effects

- Inject plasma fill with negative density gradient
  - Apply axial magnetic field.
- » Force more JxB thinning of plasma before opening

### 3. Exploit electrode opening

DNA POS Workshop  
29 March 1995

Fig 17

## Future work

NRL

- PIC codes good for opening and load coupling, but short time scales (10's ns).
- Fluid codes can treat long time scales (1  $\mu$ s).

### Marriage of two types of code:

Fluid code for conduction phase.

Fluid results coupled directly to PIC for opening phase.

### Further development of fluid codes:

HallMHD does Hall effect, but needs electron inertia effects.

ANTHEM does electron inertia effects, but Hall effects are diffused.

### Further work on MCPOS

Applied magnetic field may turn off EMH effects in beneficial way.

DNA POS Workshop  
29 March 1995

Fig. 18



PULSED-POWER PHYSICS TECHNOTE NO. 94-28

TITLE:       **EMH Effects in Plasma Opening Switches**

AUTHORS:   **Steve Swanekamp+, John Grossmann, Amnon Fruchtman#, and Bryan Oliver\***

DATE:       12 December 1994

ABSTRACT: PIC simulations have been performed with parabolic density profiles that show magnetic field penetration into a plasma at depths much greater than the collisionless skin depth. These simulations represent the first time these effects have been observed in a PIC code. In this technote we describe the simulations and, based on these simulations, we speculate on the role of EMH effects in the plasma opening switch.

THIS REPORT REPRESENTS  
UNPUBLISHED INTERNAL  
WORKING DOCUMENTS AND  
SHOULD NOT BE REFERENCED  
OR DISTRIBUTED

+JAYCOR, Vienna VA

#Weizmann institute of science, Rehvolt, Israel

\*NRL-NRC postdoctoral research associate

Figure 1. Title and authors.

Figure 2. Motivation. One of the current areas of POS research is in understanding the differences between the EMH and MHD conduction regimes. In addition to understanding the conduction mechanisms it is also of interest to understand the differences between the opening process in these two regimes. Once the conduction and opening mechanisms are understood we can then begin to devise ways of making bigger switch gaps.

Figure 3. Outline. PIC simulations of the conduction phase of the POS show three competing mechanisms that control the opening; sheath effects at the electrodes, electron-magneto-hydrodynamics (EMH), and magneto-hydrodynamics (MHD). In this work sheath effects at the electrodes are suppressed by making the plasma density at the electrodes high compared the density in the radial center of the switch. Penetration of magnetic field due to the hall effect (EMH) is expected when there is a strong density gradient while MHD effects are expected to be more pronounced when there is alot of ion motion due to  $J \times B$  forces. In simulations with strong density gradients and immobile ions vortices are observed in the electron current streamlines. Properties of these vortices will be described by John Grossmann. In simulations where ions are allowed to move we see distortion and deformation of the plasma.

Figure 4. Application of MHD theory to conduction-phase physics. This view graph outlines the MHD equations and is shown to stress that what we are going to discuss is strongly influenced by the presence of the Hall term in Ohm's law.

Figure 5. Ion motion can be ignored when the relevant time scales are small compared to the ion cyclotron period and relevant space scales are small compared to the ion skin depth. In this regime Faraday's law, Ampere's law and Ohm's law can be combined to give an equation which determines the transport of magnetic field into the plasma. The equation is hyperbolic predicts shock-like penetration of magnetic field into the plasma. To see this consider the term that multiplies the  $\partial B / \partial z$  term. If this term were constant then the solution to this equation would be simple traveling wave. However, since the speed of the wave depends on the magnetic field, if the magnetic field increases in time wavelets launched later in time catch up with the wavelets launched earlier in time. This gives rise to a shock-like penetration of magnetic field into the plasma. The speed of the wave for a magnetic field that rises linearly in time is given in the third equation. We see that the penetration speed depends strongly on  $L_n$ . This term arises from curvature effects and density gradients. The EMH conduction current can be defined as the current in the POS when the magnetic field has penetrated the entire length of the POS plasma. It is important to note that in the EMH limit the current scales as  $n^{1/2}$  and is independent of ion mass.

Figure 6. MHD effects are expected to dominate EMH effects when the center of mass velocity of the plasma is large compared with the hall speed. The MHD conduction limit is defined as the current in the POS when the axial displacement of the center of mass is  $1/2$  the switch length. In the MHD limit the conduction current scales as  $(nM)^{1/4}$ . Notice that the MHD limit depends on ion mass. We will exploit this in the simulations.

Figure 7. This figure shows the conduction current scaling for HAWK for different center conductor radii. The solid curves are the MHD scaling curves while the EMH curves are the light lines. The data show that MHD scaling predicts the observed conduction current on

HAWK at high density. At lower densities MHD scaling no longer is obeyed and the data indicate that EMH could possibly explain the deviation from MHD scaling.

Figure 8. Comparison of experimental and PIC code regimes. POS experiments typically use densities in the range of  $10^{14}$ - $10^{16}$  cm<sup>-3</sup>, switch lengths of 3-10 cm, anode-cathode gap spacing of 3-5 cm, with conduction times between 0.3-1.0  $\mu$ s. Because of numerical plasma heating difficulties PIC simulations of the POS conduction and opening phases are limited to densities of  $10^{12}$ - $10^{14}$  cm<sup>-3</sup>, switch lengths of 3-10 cm, anode-cathode gap spacing of 3-5 cm, with conduction times between 10-100 ns. Simulations of the opening phase alone have been run in the  $10^{14}$ - $10^{15}$  cm<sup>-3</sup> density regime with plasma lengths on the order of 1 cm and run times typically less than 10 ns. Can the pertinent physics that is expected to play a role in the POS be scaled to fit into a regime that the PIC code can treat comfortably? Yes. By suppressing sheath effects at the electrodes, fixing the density, and changing the ion mass.

Figure 9. Simulation set-up. The density profile that was chosen for the simulations presented in this technote is shown on the left hand side of this figure. The density has a parabolic profile that is  $10^{12}$  cm<sup>-3</sup> in the center of the A-K gap and rises to  $3 \times 10^{13}$  cm<sup>-3</sup> at the electrodes. The density is taken to be uniform in the z-direction. The simulation geometry is shown on the right hand side of the figure. Plasma is preloaded between the A-K gap between  $z=1.8$  and  $4.7$  cm. The load impedance is  $Z_L=0$ . The electron mass used in the simulation was taken to be  $1/10$  the normal electron mass. This artificially light electron mass was chosen so that  $c/\omega_{pe}$  be small compared to relevant length scales in the POS. The ion mass was taken to be  $A m_p$  where  $m_p$  is the proton mass. Typical values of  $A$  range from  $0.05 \leq A \leq 1$ . The rate of rise of the current for these simulations was taken to be 10 kA/ns which is about a factor of two faster than DM1.

Figure 10. PIC simulations with immobile ions show vortices in the electron flow. The hall speed profile at  $t=2$  ns is shown on the left hand side of the figure. Magnetic field penetration into the plasma is expected where the hall speed profile is positive. In regions where the hall speed profile is negative EMH theory predicts evanescent behavior. The current streamlines are shown at  $t=0.6$  ns and  $t=2.0$  ns are shown on the right hand side. The current streamline at  $t=0.6$  ns shows that current initially flows in a very narrow region of the plasma. However, at  $t=2.0$  ns the simulation shows very rapid penetration of the magnetic field into the plasma at precisely the location where the hall speed profile is a maximum. Behind the shock front vortices in the electron flow are observed.

Figure 11. PIC simulations with  $M_i = m_p/4$  show penetration due to EMH and gap opening due to radial  $J \times B$  forces. In this simulation the ions are allowed to move by choosing an ion mass that is  $1/4$  the proton mass. In this simulation we see rapid penetration due to EMH followed by radial  $J \times B$  motion of the ions. This radial  $J \times B$  motion eventually opens a gap in the plasma which allows magnetic energy to flow past the POS and into the load.

Figure 12. PIC simulations with  $M_i = m_p/4$  show plasma distortion due to  $J \times B$  forces. In this simulation a lot of displacement of the center of mass is observed. This is accomplished by making the ion mass  $1/20$  the proton mass. The current stream lines at  $t=3$  ns show MHD motion and magnetic field penetration due to EMH effects occur at approximately the same rate. The current streamlines at  $t=5$  ns show a bubble in the MHD front at approximately  $r=3$  cm. It also shows some current in the load from EMH penetration. This occurs because the hall resistance is

large compared to the load impedance. However, a short time later the bubble breaks a gap forms and the bulk of the current now flows through this gap.

Figure 13. This figure shows a comparison between the scaling of the conduction current vs. mass density. The solid curve is the curve from MHD scaling and the diamonds are the values obtained from simulation. The simulation shows good agreement with MHD scaling for low mass densities and not so good agreement for high mass densities where EMH effects play a role.

Figure 14. Outstanding issues. The PIC simulations showed about 50% slower speeds of penetration than predicted by analytic EMH theory. We are looking at the role of boundary conditions and electron inertia as possible explanations. Because collisionless EMH theory does not conserve energy, another interesting issue is how energy is divided between magnetic field energy, electron vortex energy, and sheath losses. Of course our ultimate goal is to understand what are the mechanisms that control gap opening and provide insight into how to make bigger POS gaps. This will come only with a more detailed understanding of the physics of the conduction and opening processes.

# EMH Effects in Plasma Opening Switches

Steve Swanekamp<sup>#</sup>

John Grossmann

Amnon Fruchtman<sup>\*</sup>

Bryan Oliver<sup>+</sup>

Talk presented to NRL pulsed-power group

December 9, 1994

<sup>#</sup>Jaycor, Vienna VA

<sup>\*</sup>Weizmann Institute of Science

<sup>+</sup>NRC-NRL Research Associate

# Motivation

---

- What are the differences in plasma dynamics between the EMH and MHD conduction regimes?
- How does the POS transition from conduction to opening phases?
- How do we make bigger gaps?

# Outline

---

- Conduction phase physics
  - Sheath effects at the electrodes
  - Electron Magneto-Hydrodynamics (EMH)
    - $I_c \sim n^{1/2}$
  - Magneto-Hydrodynamics (MHD)
    - $I_c \sim M^{1/4} n^{1/4}$
- PIC simulations of EMH-MHD transition
  - Immobile ions (EMH)
    - Vortices in the current streamlines
  - Very mobile ions (MHD)
    - Plasma distortion due JxB forces
- Properties of the electron vortices (JMG)

# Application of MHD theory to conduction-phase physics

---

$$\frac{\partial n}{\partial t} + \nabla \cdot nu = 0$$

continuity

$$\frac{\partial u}{\partial t} + u \cdot \nabla u = \frac{J \times B}{nMc}$$

momentum balance

$$\frac{\partial B}{\partial t} = c \nabla \times E$$

Faraday's Law

$$\nabla \times B = \frac{4\pi}{c} J$$

Ampere's Law

$$E = \eta J - \frac{u \times B}{c} + \frac{J \times B}{Znec}$$

Ohm's Law



# Conduction current scaling in the EMH limit

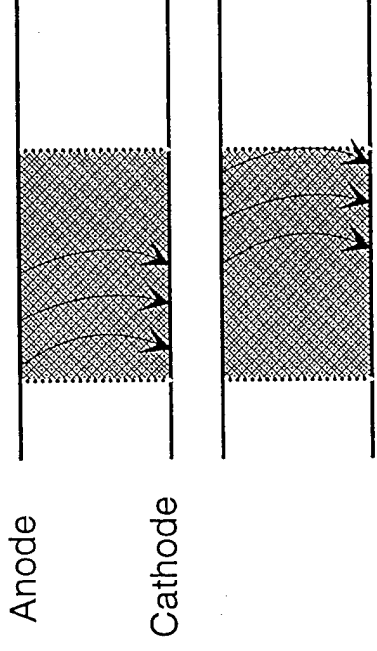
---

- When ion motion can be ignored ( $\tau \ll \tau_{ci}$  and  $L_n \ll c/\omega_{pi}$ )

$$\frac{\partial B}{\partial t} - \frac{cB}{4\pi enL_n} \frac{\partial B}{\partial z} = 0$$

$$L_n^{-1} = \frac{2}{r} + \frac{1}{n} \frac{dn}{dr}$$

$$V_{hall} = \frac{3}{8} \left( \frac{cB}{4\pi enL_n} \right)$$



B penetration by  
Hall effect

- Conduction current is defined as the current when the magnetic field penetrates the length of the POS

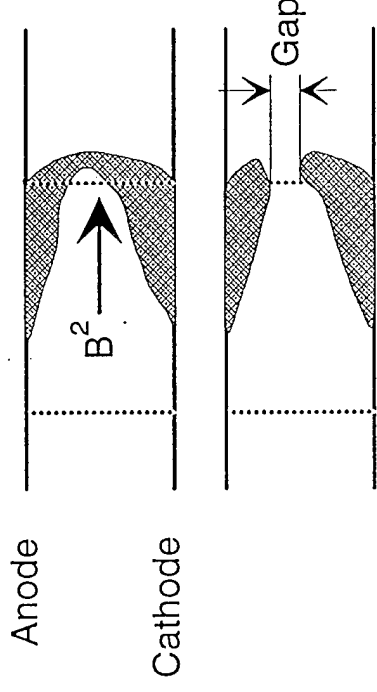
$$I_{EMH} \sim (r L_n n \ell dI_G / dt)^{1/2}$$

# Conduction current scaling in the MHD limit

---

- When magnetic pressure dominates over the hall term  
( $V_{com} \gg V_{hall}$ )

$$\ell n M V_{com} = \int \frac{B^2}{8\pi} dt$$



Plasma distortion by  
 $J \times B$  forces

- Conduction current is defined as the current when the center-of-mass moves  $1/2$  the switch length

$$I_{MHD} \sim (nM)^{1/4} (r \ell dI_G / dt)^{1/2}$$

# Conduction current in Hawk follows MHD/EMH scaling

---

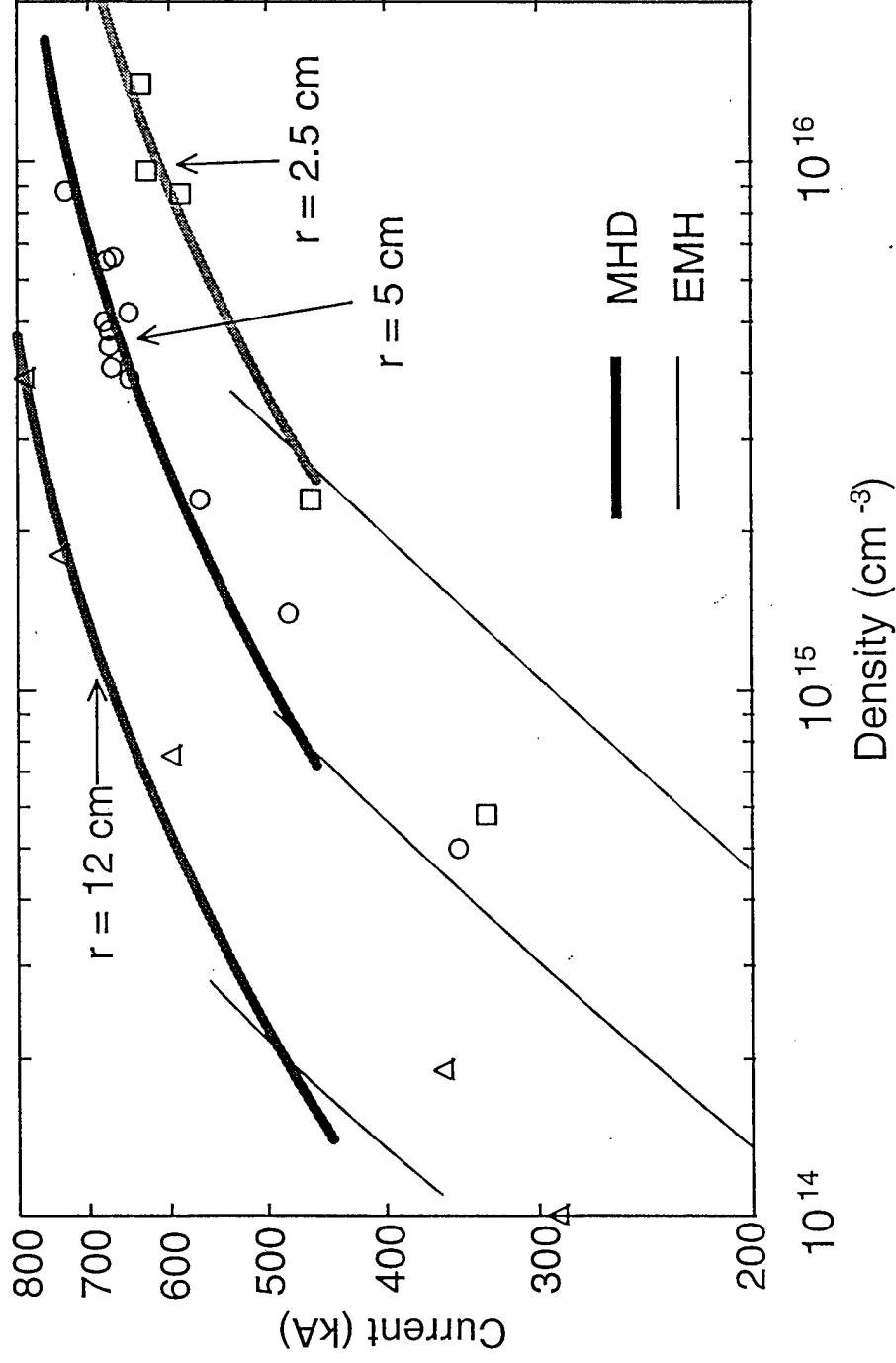


Fig. 7

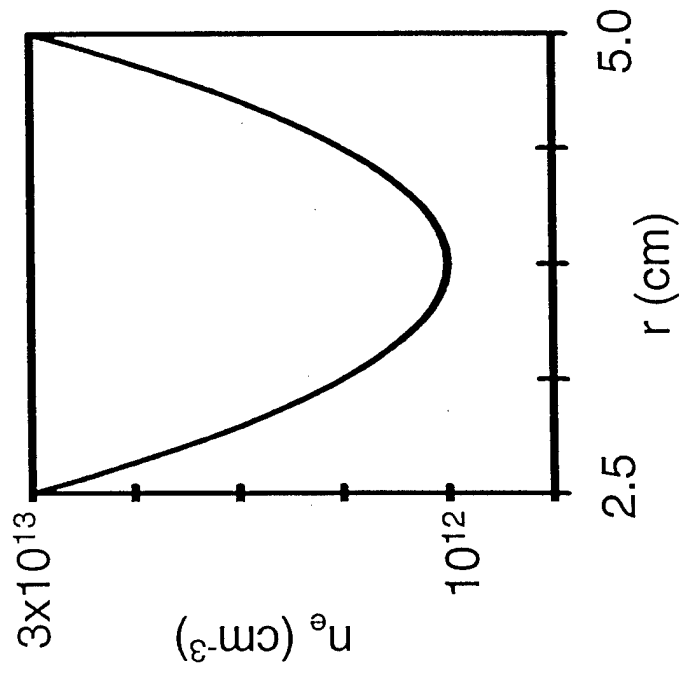
# Comparison of Experimental and PIC Codes Regimes

---

- Experiments (Hawk, DM1)
  - $n_e \sim 10^{14} - 10^{16} \text{ cm}^{-3}$ ,  $\ell \sim 3-10 \text{ cm}$ ,  $\Delta r = r_a - r_c \sim 3-5 \text{ cm}$ ,  $\tau_c \sim 0.3-1.0 \mu\text{s}$
- PIC codes
  - Conduction and opening
    - $n_e \sim 10^{12} - 10^{14} \text{ cm}^{-3}$ ,  $\ell \sim 3-10 \text{ cm}$ ,  $\Delta r = r_a - r_c \sim 3-5 \text{ cm}$ ,  $\tau_c \sim 10-100 \text{ ns}$
  - Opening phase
    - $n_e \sim 10^{14} - 10^{15} \text{ cm}^{-3}$ ,  $\ell \sim 1 \text{ cm}$ ,  $\Delta r \sim 3 \text{ cm}$ ,  $\tau < 10 \text{ ns}$
- Can the EMH and MHD conduction physics be scaled to fit in the PIC regime? Yes! By suppressing sheath effects at the electrode, fixing  $n_e$ , and changing  $M_i$

# Simulation Set-up

---



$$M_e = m_e / 10, M_i = A m_p$$

$$dI/dt \approx 10 \text{ kA/ns}$$

$$Z_L = 0$$

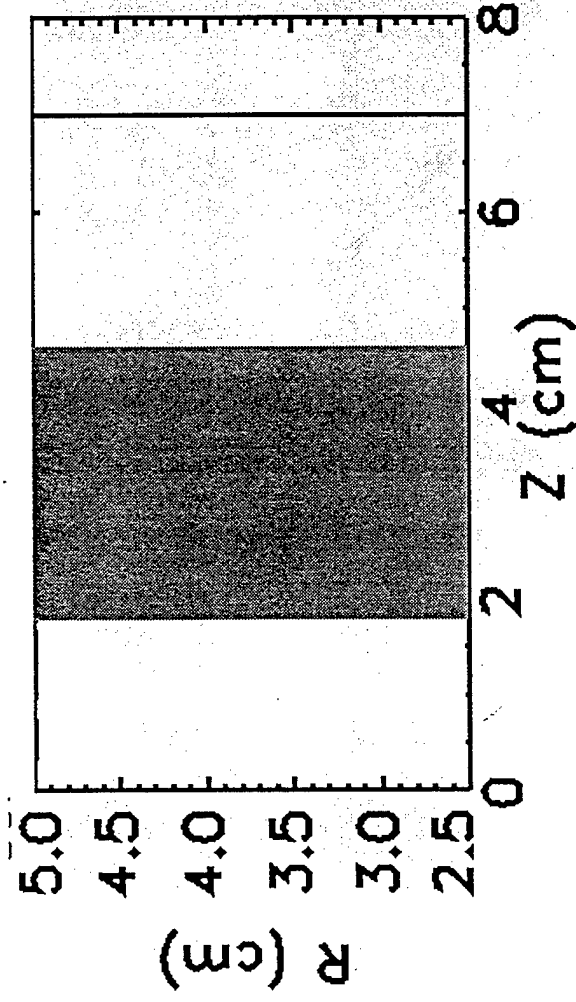
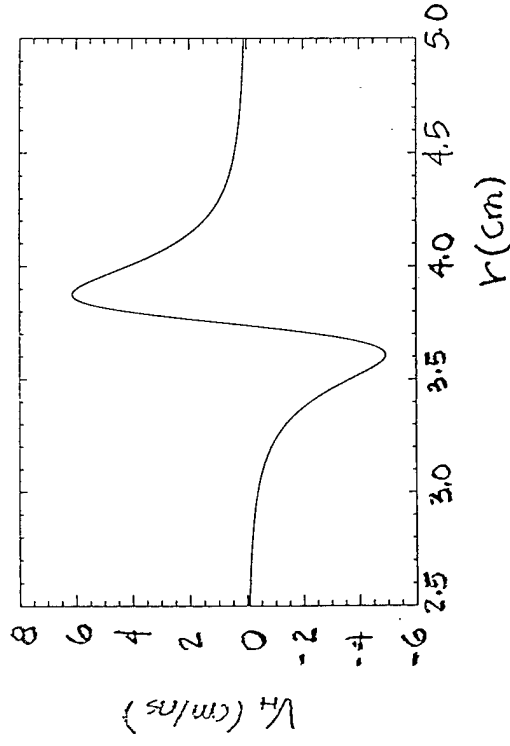
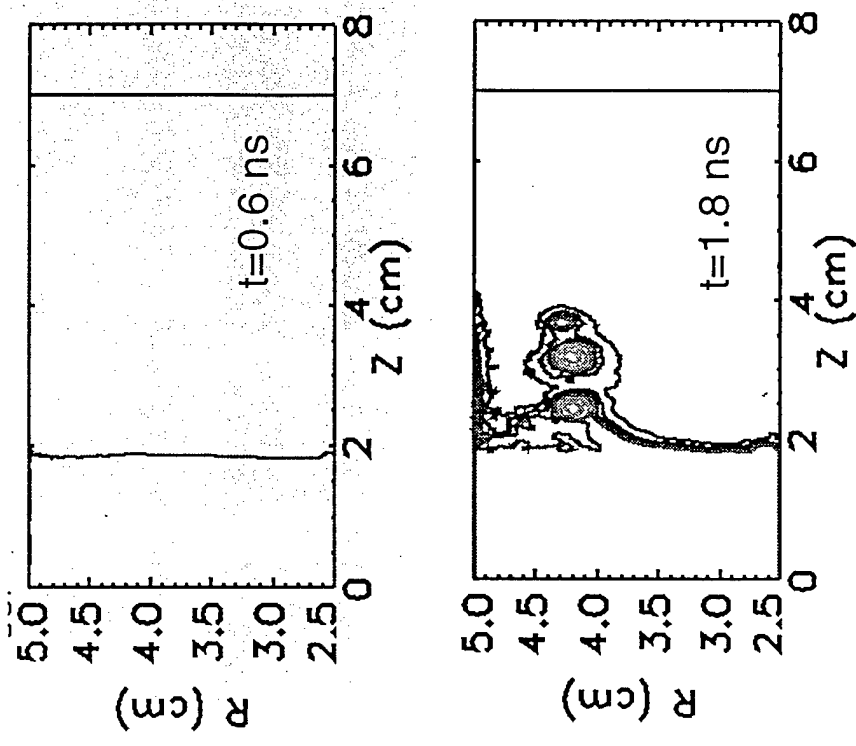


Fig. 9

# PIC simulations with immobile ions show vortices in electron flow

---

Current enclosed contours



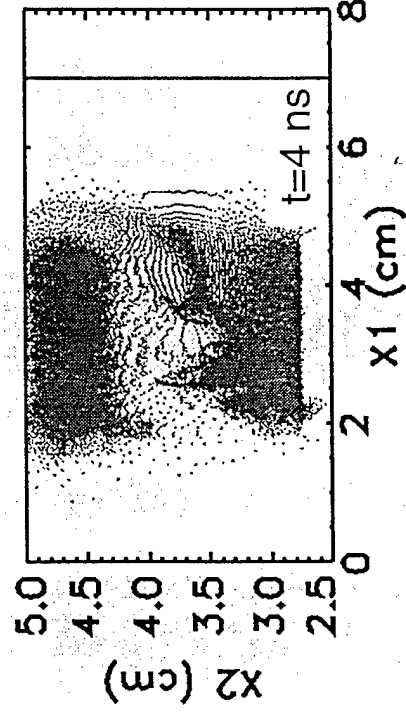
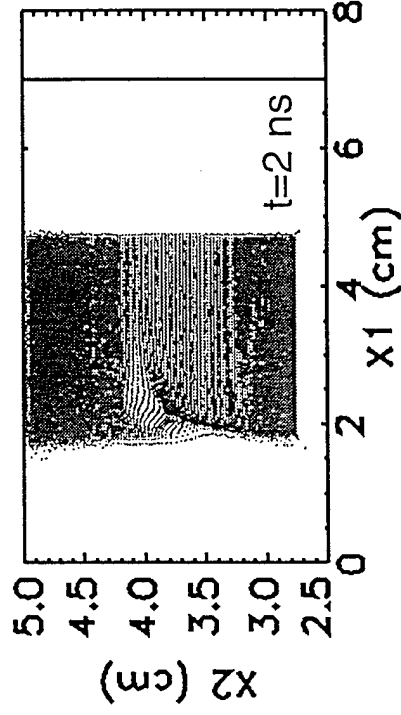
$$V_H = \frac{3}{8} \frac{cB}{4\pi en} \left( \frac{2}{r} + \frac{1}{n} \frac{dn}{dr} \right)$$

Fig. 10

# PIC simulations with $M_i=m_p/4$ show penetration due to EMH and gap opening due to radial $\mathbf{J} \times \mathbf{B}$ forces

---

Ion positions ( $M_i=m_p/4$ )



Current enclosed contours

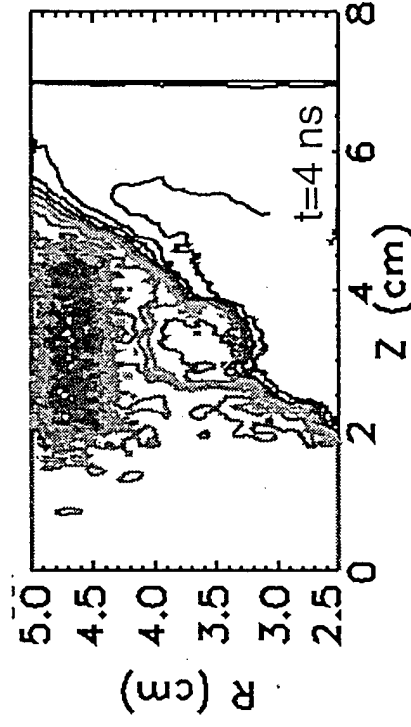
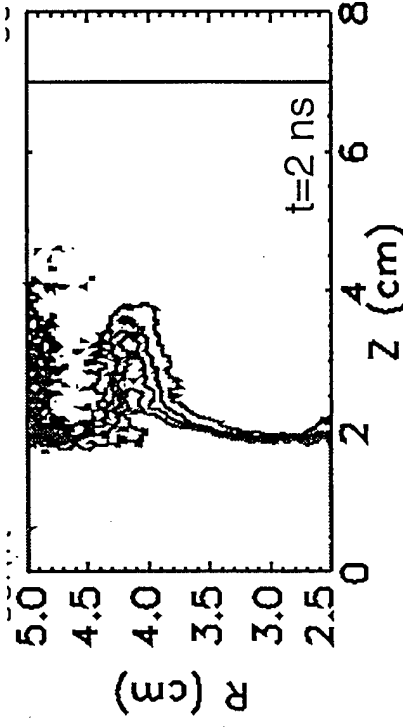
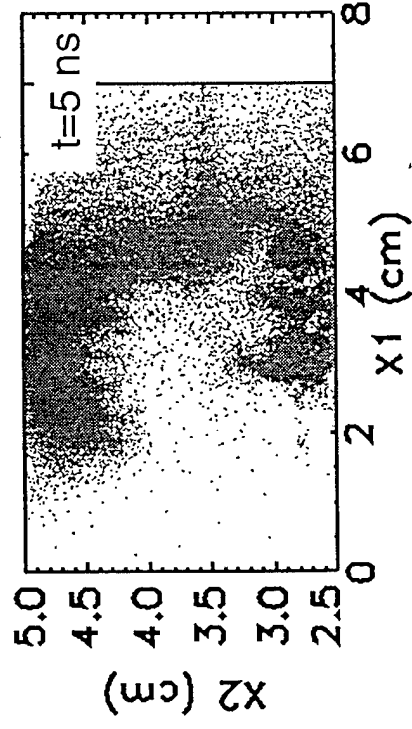
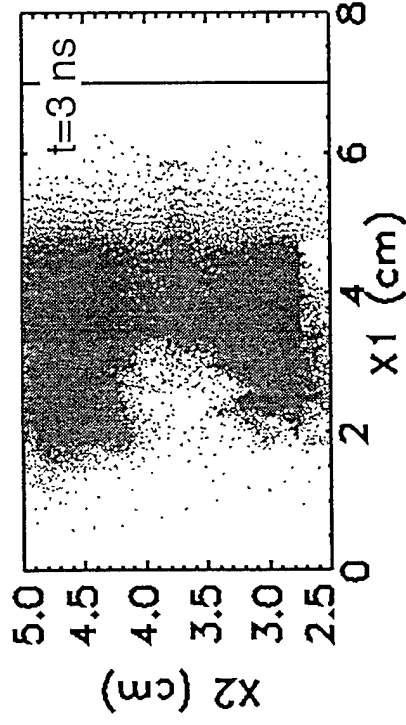


Fig. 11

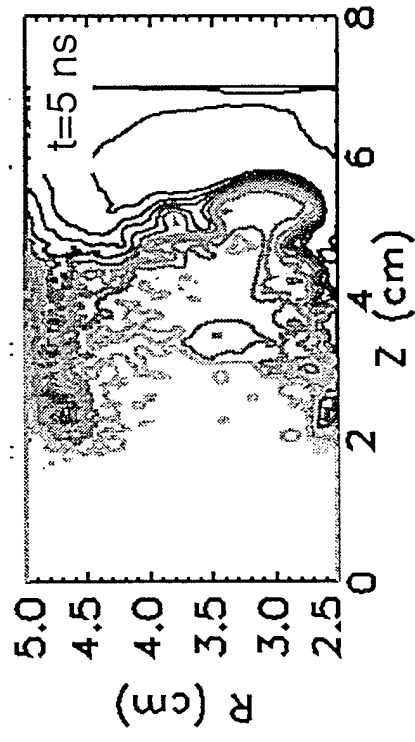
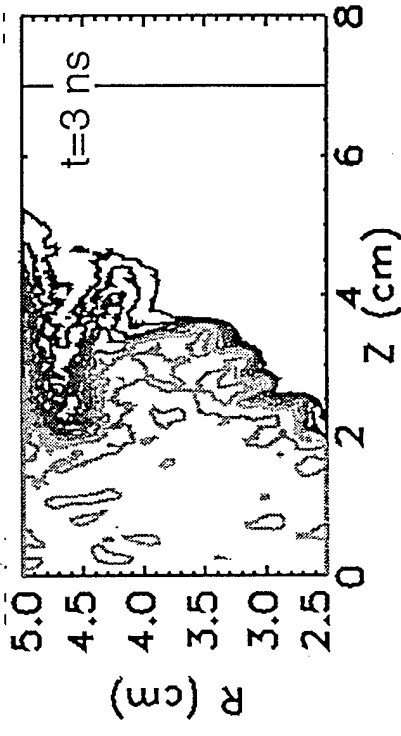
# **PLC simulations with $M_i=m_p/20$ show plasma distortion due to $\mathbf{J} \times \mathbf{B}$ forces**

---

Ion positions ( $M_i=m_p/20$ )



Current enclosed contours





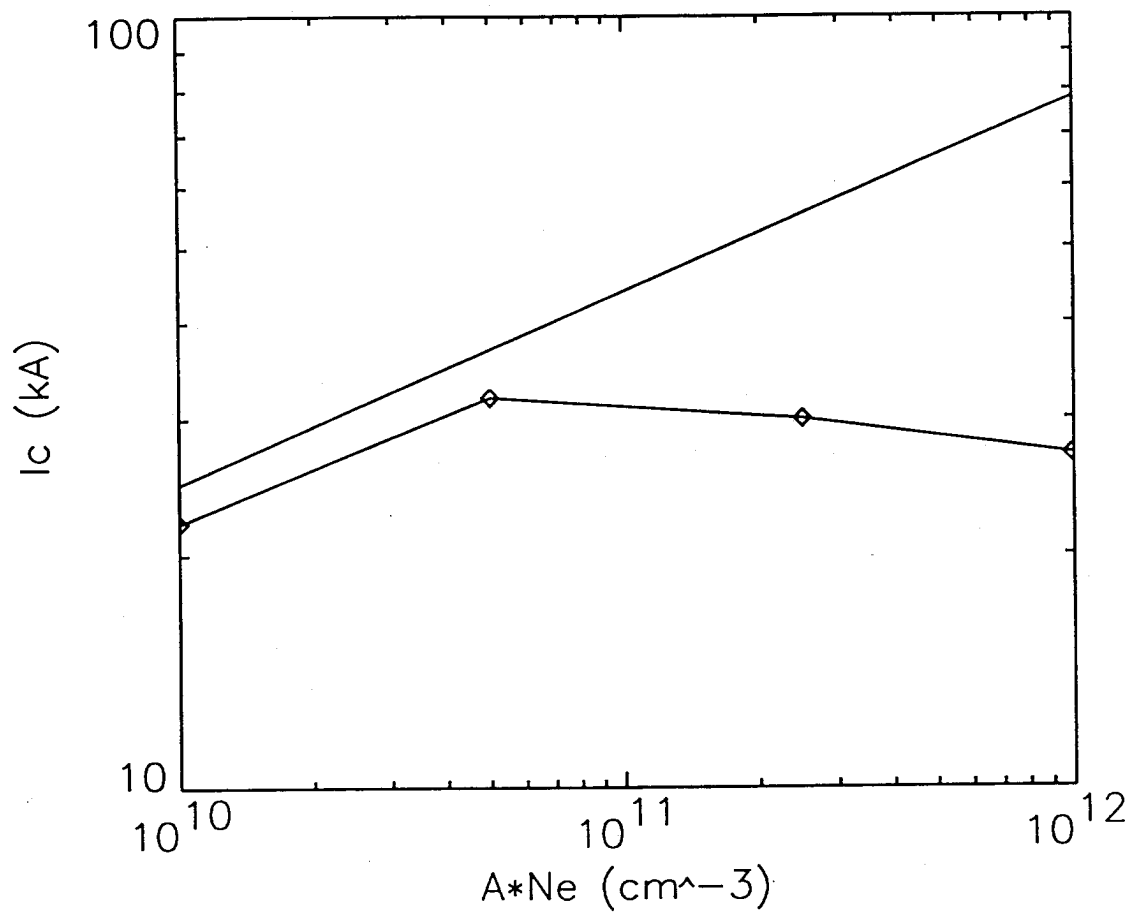


Fig. 13

# Outstanding issues

---

- Why does PIC predict slower penetration speeds than EMH theory?
  - Boundary conditions
  - Electron inertia
- How is energy partitioned between magnetic energy, electron vortex energy, and sheath losses?
  - Collisionless EMH theory does not conserve energy
  - Can show  $1/2$  energy flow from vacuum goes into magnetic energy and the other half is dissipated
- What limits gap size and how can we make bigger gaps?

PULSED POWER PHYSICS BRANCH TECH-NOTE NO. 94-29

TITLE: MHD AND EMH EFFECTS IN PLASMA OPENING SWITCHES

DATE: DEC 09 1994

AUTHORS: J.M. GROSSMANN, S.B. SWANEKAMP, A. FRUCHTMAN, J. HUBA,  
AND B. OLIVER

ABSTRACT: Magneto-hydrodynamic (MHD) and electro-magneto-hydrodynamic (EMH or Hall) effects in POS gap opening are examined. Much of this note recalls earlier work (BEAM'S 94) on gap opening processes in the radial middle of the POS. More detailed studies of these processes are described. Attempts are made to understand how EMH effects may be controlled experimentally.

THIS REPORT REPRESENTS UNPUBLISHED INTERNAL  
WORKING DOCUMENTS AND SHOULD NOT BE  
REFERENCED OR DISTRIBUTED.

Fig. 1. Title and authors.

Our new results concerning POS gap opening are presented and compared to earlier work.

Fig. 2. The standard cathode potential hill and gap formation cartoon. This form of gap opening was the focus of our last paper (due out in *Physics of Plasmas*, January 1995). The main idea behind this gap opening mechanism is that a 2-D sheath forms near the cathode around which electrons circulate in a vortex. The potential hill is positively charged and large electrostatic fields form to accelerate the ions out of the hill. When ions have been removed from the potential hill at one axial location, the hill and its electron vortex migrate further along the cathode and toward the load. The new potential hill location provides a region of fresh ions around which the electrons can circulate (largely by  $E \times B$  drifting). These fresh ions are then themselves removed from the potential hill region by the local electrostatic forces and the hill migrates further, leaving a magnetically insulated gap in its wake. Eventually the 2-D sheath reaches the load end of the POS and the switch opens.

Fig. 3. Some physical properties of cathode potential hills. The rate of migration along the cathode and subsequent opening of the POS in simulations is roughly consistent with the conduction time in Gamble I POS experiments. The geometric size of the potential hill is roughly  $10^9$  B/n (all CGS units) and the potential hill magnitude scales like  $\phi$  (MV) =  $5 \times 10^4$  B<sup>2</sup>/n (CGS except  $\phi$ ). The question we sought to answer subsequently was whether the same gap opening mechanism applies in a POS when the opening occurs away from the cathode, say in the radial middle of the POS.

Fig. 4. Set-up of simulations of opening in the radial middle of the POS. Current is assumed to rise instantaneously to 1.2 MA. Physical dimensions of the simulations are shown together with the two different types of density profile to be discussed in this tech. note. In one case the density stays flat near the anode (curve labeled ss62), while in the other the density rises as you move toward the anode (curve labeled ss52). In both cases, the main body of the plasma consists of doubly ionized Carbon and an infinitely massive ion species occupies regions near the electrodes. These regions are used to prevent POS opening at the electrode surfaces. This technique can only be weakly justified by arguing that perhaps opening does not occur at the cathode in some experiments because of large electrode densities there and by arguing that opening near the anode as seen in simulations does not occur in experiments where the anode is not a solid conductor.

Fig. 5. Results of simulation ss62 with flat density profile at the anode. The plasma is pushed axially by  $J \times B$  forces during the first 5-7 ns of conduction. At about 6 ns, electron vortices begin to form in the radial middle of the plasma and a gap opens in the plasma at around  $r = 5.5$  cm. The actual gap opening mechanism is unknown, but the presence of vortices at the same time as gap opening suggests that they are involved. Large electric fields and potential hills are associated with these vortices. These electric fields could open a gap in the plasma.

Fig. 6. An interesting feature of the vortices is that they stream axially through the plasma until they reach the load end of the plasma and then move radially toward the load. As one vortex

travels through the plasma, another forms behind it and begins to migrate. This is very suggestive of the types of vortex that form when magnetic field penetrates a plasma via electro-magneto-hydrodynamic effects (EMH). More on that in a following figure. It is also interesting to contrast the migration of these vortices/potential hills with potential hills that form near a cathode. In contrast to vortices/potential hills that form in the middle of the POS, those that form near a cathode only migrate after they have removed ions from the core of the potential hill.

Fig. 7. This next set of figures shows the results of simulations (ss52) very much like the last set, except that the density profile rises as you move radially toward the anode (please refer to Fig. 4 and the density profile labeled 'ss52'). In this figure, particle positions are shown at three different times during a simulation. Three different effects are seen. Although not apparent in Fig. 7(a), a certain amount of density thinning has occurred at the radial location of the arrow. In addition, the plasma has been displaced axially by  $J \times B$  forces at all radial locations between the immobile ions. This density thinning is more apparent in Fig. 7(b), where displacement and distortion of the plasma in the radial middle of the POS is also shown with a second arrow. Finally, in Fig. 7(c), a gap opens in the middle of the POS and the POS opens.

Fig. 8. Current streamlines at the same times as Fig. 7. These figures are shown blown-up in the next set of view graphs.

Fig. 8(a). This shows the result of magnetic field penetration into the plasma by EMH effects. The most rapid penetration occurs in regions of high density gradients. The penetration of magnetic field produces current streamlines that lead to  $J \times B$  forces on the plasma that thins the plasma locally.

Fig. 8(b). Later in time, the effects of MHD plasma pushing on the main body of the plasma becomes more important. Although one snapshot of the current streamlines cannot give the same information as watching a movie of the process, it is clear from a movie of the current streamlines and particle positions that MHD forces displace the plasma in the radial middle of the POS and then vortices appear near the region of low density. As in Figs. 5 and 6 (from simulation ss62), the final gap opening appears to occur where the vortices stream through the plasma. Gap opening could be produced by the large electrostatic fields produced in the potential hills associated with the vortices.

Fig. 8(c). Current streamlines after the POS opens into a 2 Ohm load.

Fig. 9. Next we will study some of the properties of the vortices. The idea is to understand how their geometric size scales and how fast they can penetrate into a plasma. If their size is correlated to the gaps that form in the plasma, then perhaps some control of the POS gap is possible. In the next set of figures, simulation results will be shown for cases which differ from the set-up described in Fig. 4. The plasma length will be 4 cm instead of 1 cm, the density profile will be exponential instead of parabolic, immobile ions will be used everywhere, and densities will be roughly 1/4 of those used in Fig. 4.

Fig. 10. First we will examine the scaling of magnetic field penetration with density. Two simulations (ss89 and ss90) were run with density profiles shown in this figure. Below each density profile is the profile of the local Hall velocity (cm/ns) predicted from a solution of a 1-D

Burger's equation with instantaneously rising magnetic field at the plasma boundary. Because the density is a factor of two lower in ss90, the Hall velocity is a factor of 2 higher.

Fig. 11. Current streamlines for the two cases at the point in time where the magnetic field penetrates to the load end of the POS. Below each streamline contour plot is the velocity at which the magnetic field penetrated, and well as the maximum Hall velocity from Fig. 10. Not only is there a discrepancy with the Hall velocity in absolute terms, but the relative velocity of magnetic field penetration does not scale as a factor of two as expected

Fig. 12. Next we will examine how the geometric size of the vortex scales with density gradients. Three different cases are considered, labeled ss93, ss92, and ss94. Below each density profile is the Hall velocity profile.

Fig. 13. Current streamlines in each of the three cases. The density gradient appears to have some effect on the size of the vortex. There may be a correlation of the vortex size with the Hall velocity profile.

Fig. 14. Some of our conclusions. The EMH vortices are similar to the potential hills that form near a cathode, but also have some different physical properties and may arise for different reasons. For example, the geometric size of a cathode potential hill is more closely related to local magnetic field and density and does not scale with density gradients as the vortices do. In addition, cathode potential hills only migrate axially if ions are mobile, while vortices can migrate independent of ion motion.

There may be two different ways in which gaps form away from electrode surfaces. The EMH vortices produce current streams that could form a gap by  $\mathbf{J} \times \mathbf{B}$  forces or (perhaps equivalently) by the large electrostatic forces that develop in the vortex. Another way is that MHD displacement and distortion of the plasma could produce density gradients favorable to EMH penetration and vortex formation, which in turn produces gap opening.

We have done some simulations to examine magnetic field penetration and vortex size scaling with density and density gradients.

Fig. 15. Some of the many remaining issues and problems that should be addressed.

Fig. 16. The effect of adding an external applied  $B_z$  field on magnetic field penetration. The run on the left is ss93, described in Figs. 9, 12, and 13. The run on the right uses the same defining parameters, but a uniform external field of magnitude  $1/2$  of the generator field is applied. The figures show current streamlines obtained from the  $B_\theta$  field only (i.e. contours of  $rB_\theta$ , normalized to current). Notice that magnetic field still penetrates, but the character of the penetration is much more uniform.

# EMH Effects in POS

John Grossmann  
Steve Swanekamp  
Amnon Fruchtmann  
Joe Huba  
Bryan Oliver

Fig. 1

## B. Potential hills

(cathode gap formation)

short conduction time PDS simulations, uniform density

NRL

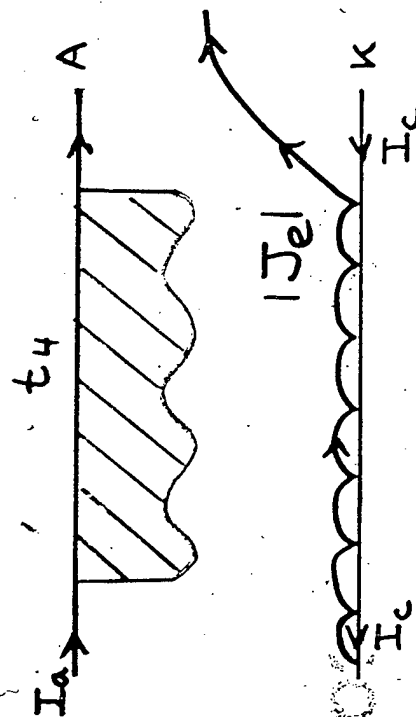
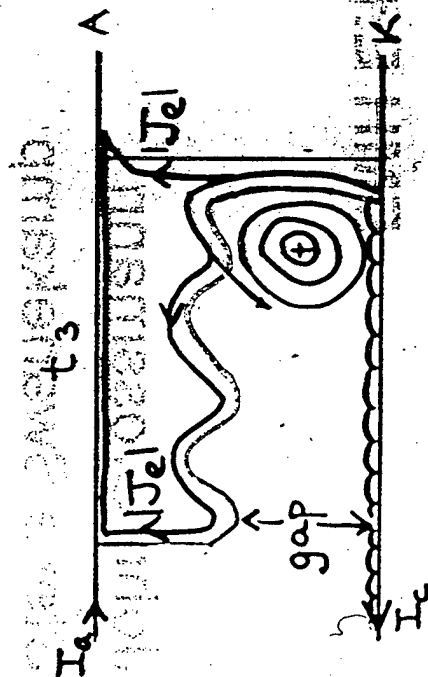
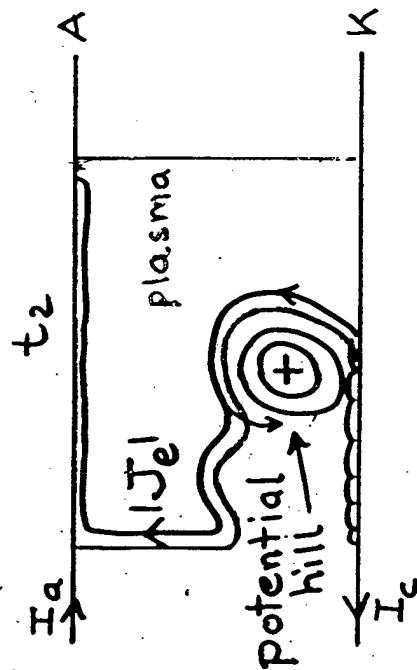
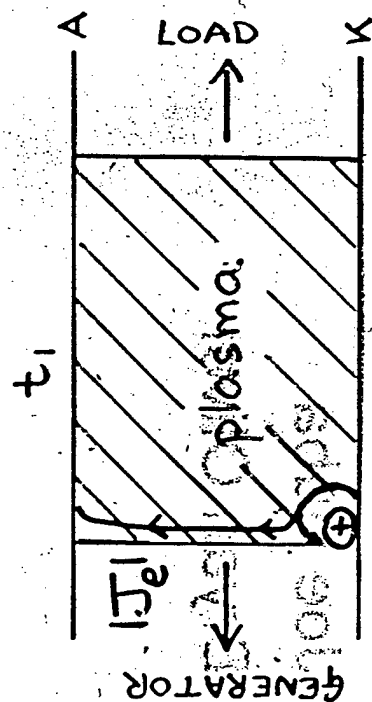


Fig 2



# Potential hills

(cathode gap formation)

NRL

- Results from Gamble I POS simulations consistent w/ expt:  
linearly rising generator current: 250 kA in 80 ns  
plasma length: 5 - 10 cm  
penetration time of cathode potential hill scales with density and length:  
 $\tau \propto n^{1/2}, \tau \propto \ell^{1/2}$ .  
 $\tau = 17 \text{ ns for } n = 5 \times 10^{12} \text{ cm}^{-3}$   
 $\tau = 30 \text{ ns for } n = 1.75 \times 10^{13} \text{ cm}^{-3}$
- gap size  $d(\text{cm}) = 10^9 B/n$ , potential  $\phi(\text{mV}) = 5 \times 10^4 B^2/n$
- Does same mechanism open gaps in long-cond.-time POS where opening occurs away from cathode ??

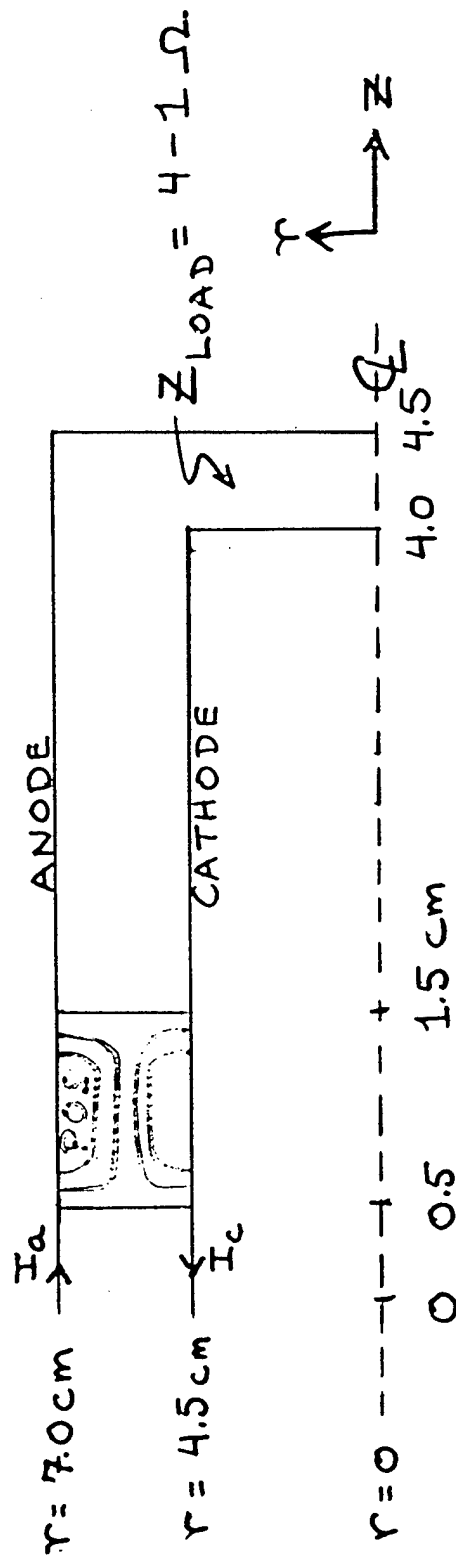
Fig.

W

# Simulation Set-up

simulate end of conduction phase of long conduction time Pos

NRL



$I_{\text{GENERATOR}} = 1.2 \text{ MA}, t \geq 0$

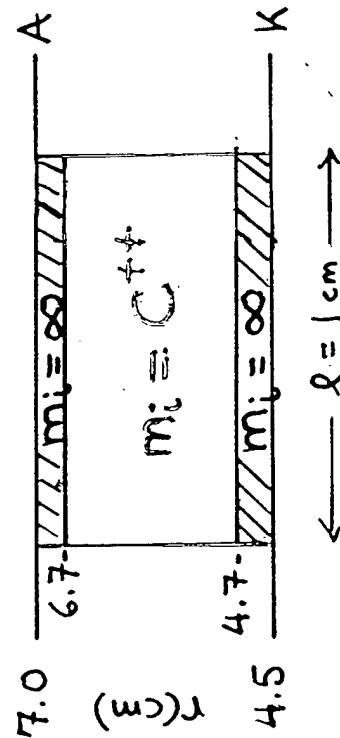
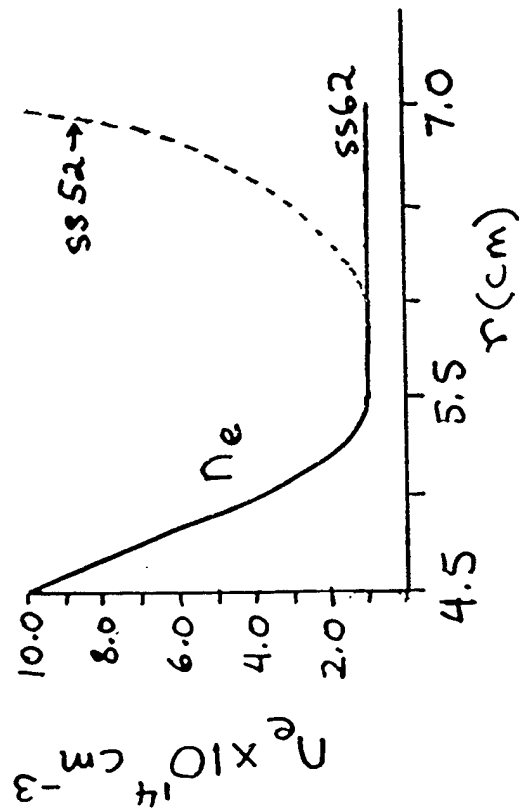


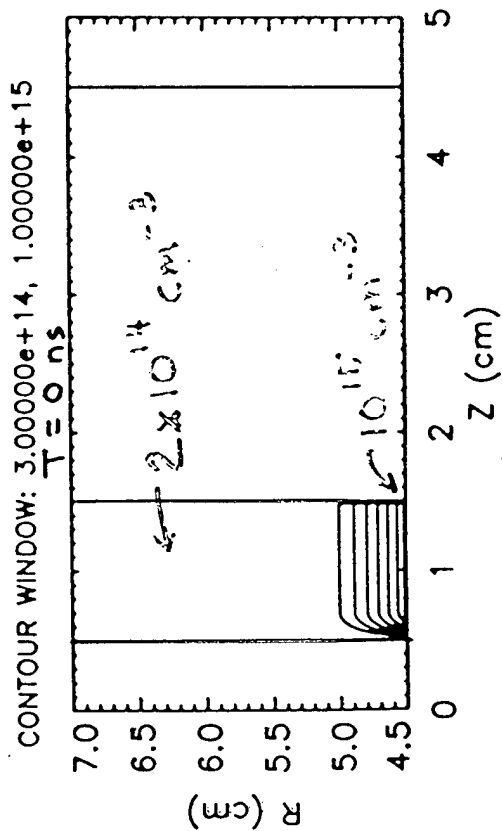
Fig. 4

# Gap opening in plasma

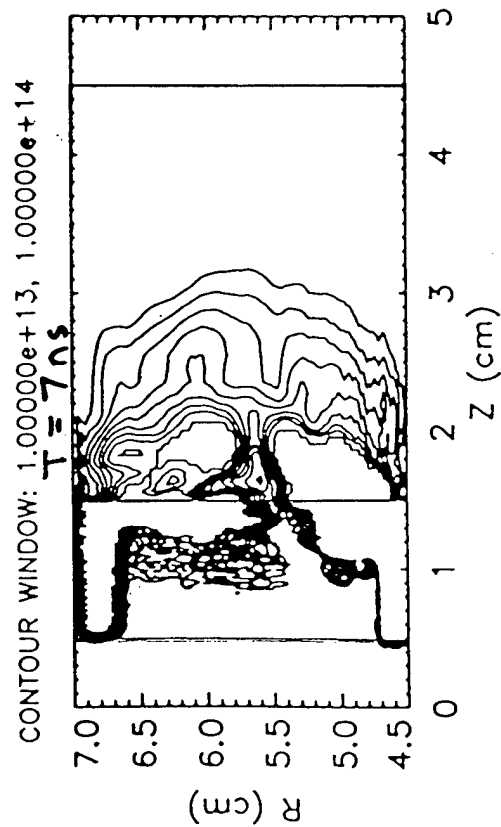
SS62

NRL

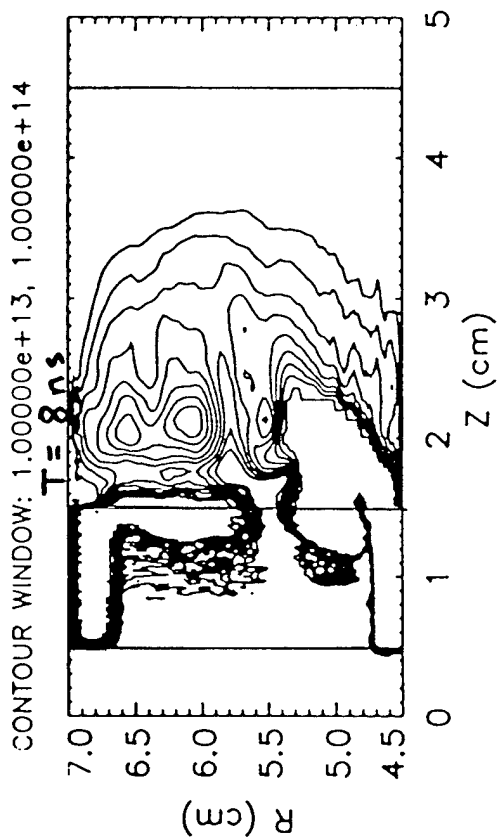
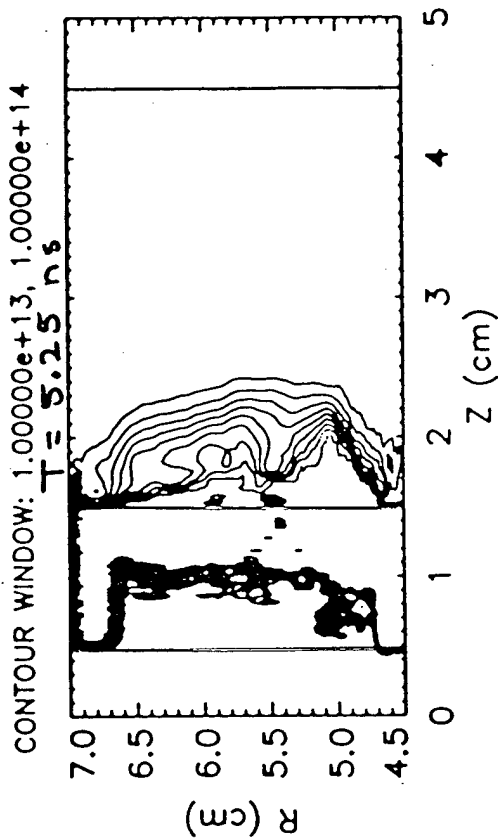
Electron density contours:



Ti  
ig



5



# Life-cycle of a potential hill

5562

NRL

iso-potential contours, increments of 100 kV

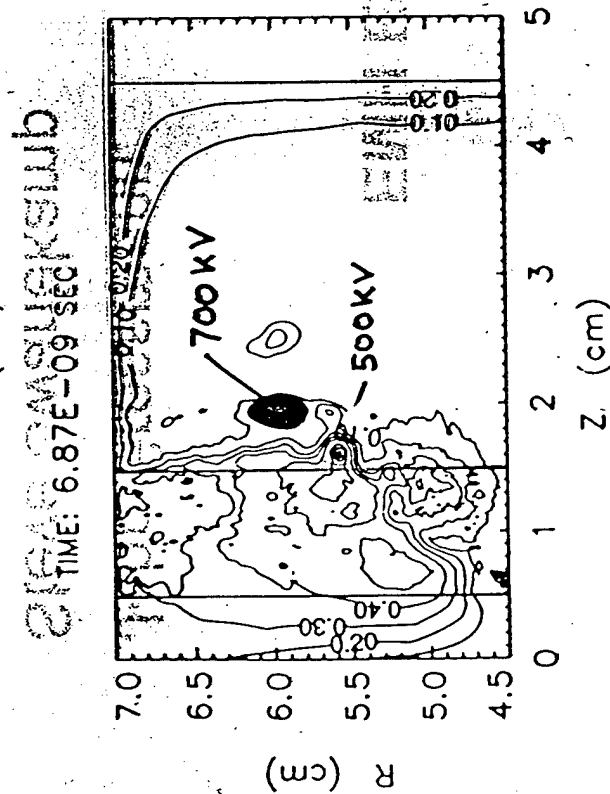
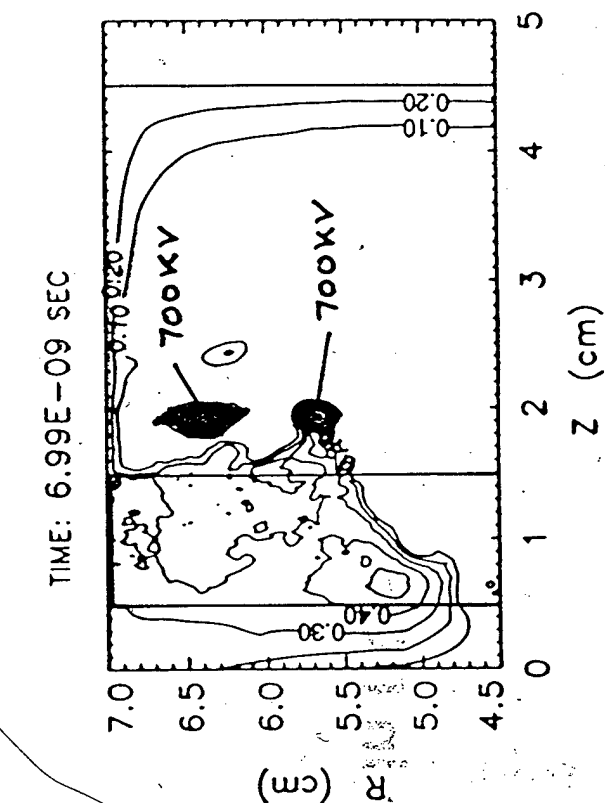
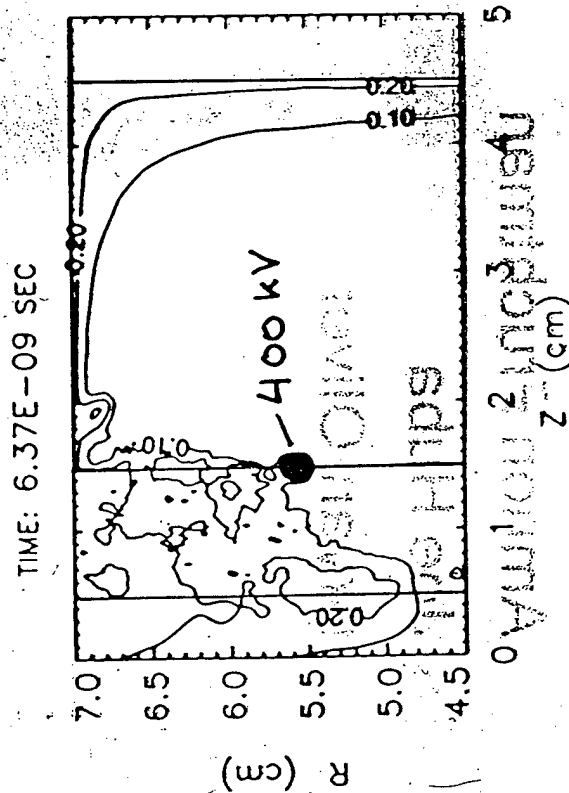
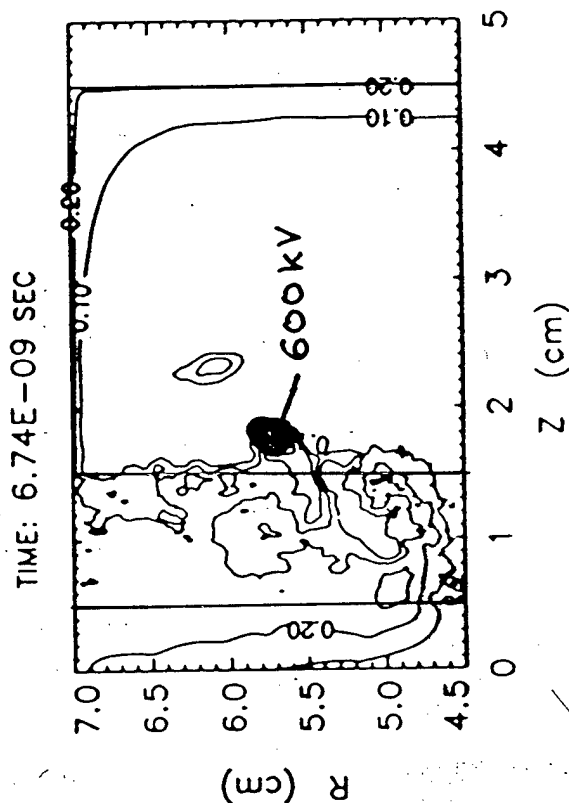


Fig 6

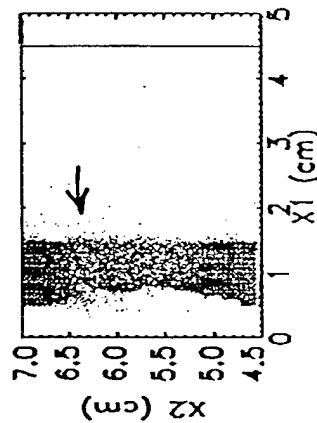
# Simultaneous EMH and MHD effects ss52

$t = 1 \text{ ns}$

$t = 3.25 \text{ ns}$

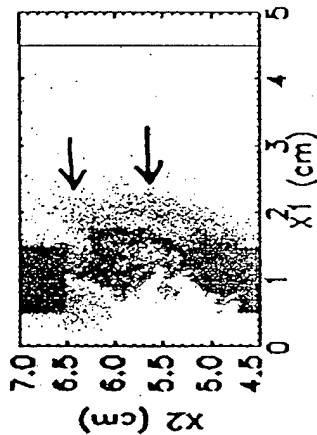
$t = 7.0 \text{ ns}$

ss52, axis of symmetry incl.  
PHASESPACE PLOT OF X2 vs X1 TIME: 1.00 NS  
SPECIES: ELECTRON Q/M RATIO: -1.759E+11



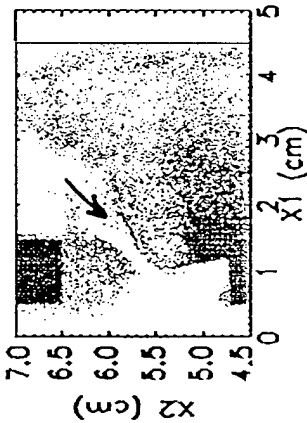
(a)

ss52, axis of symmetry incl.  
PHASESPACE PLOT OF X2 vs X1 TIME: 3.50 NS  
SPECIES: ELECTRON Q/M RATIO: -1.759E+11



(b)

ss52, axis of symmetry incl.  
PHASESPACE PLOT OF X2 vs X1 TIME: 7.00 NS  
SPECIES: ELECTRON Q/M RATIO: -1.759E+11

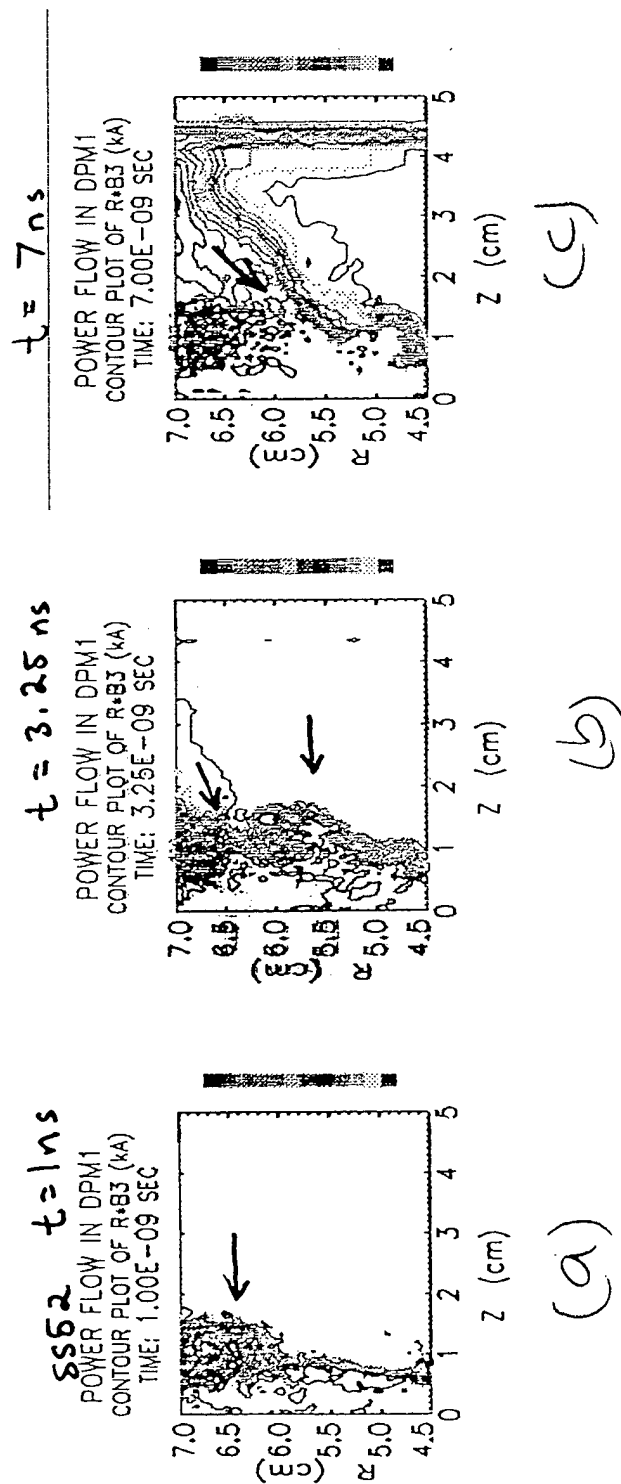


(c)

Fig 7 (a), (b), (c)

# Simultaneous EMH and MHD effects

Fig. 8 (a), (b), (c)



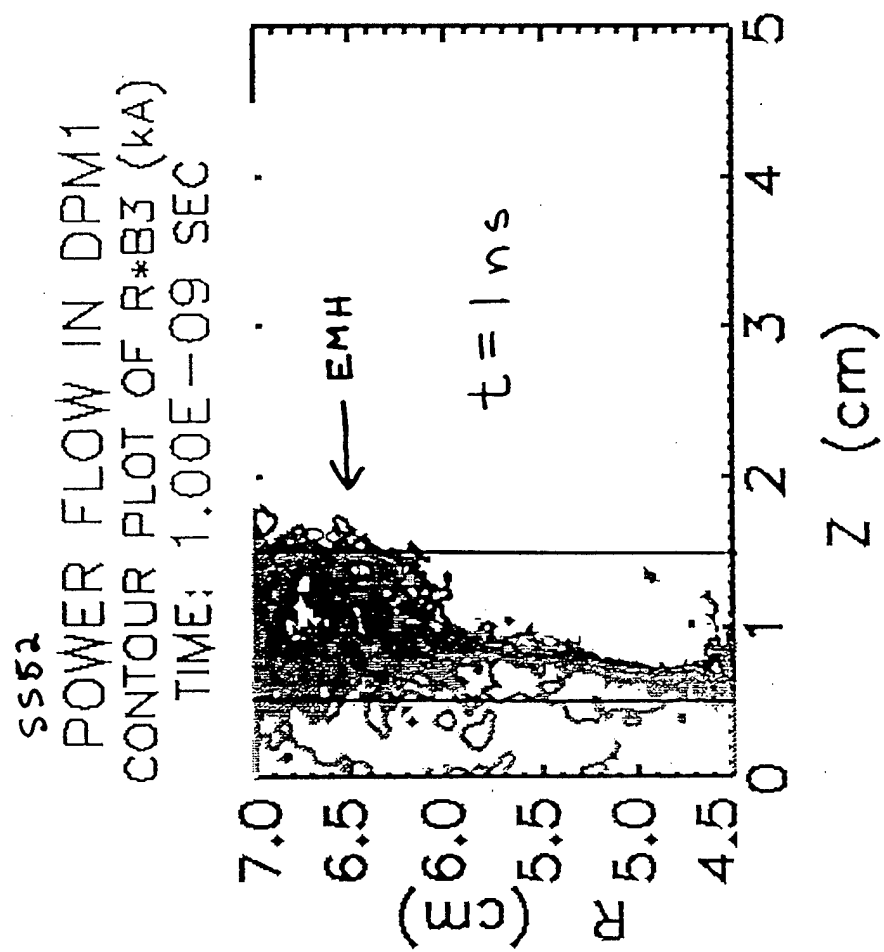


Fig 8(a)

Simultaneous EMH and MHD effects  
 ss52

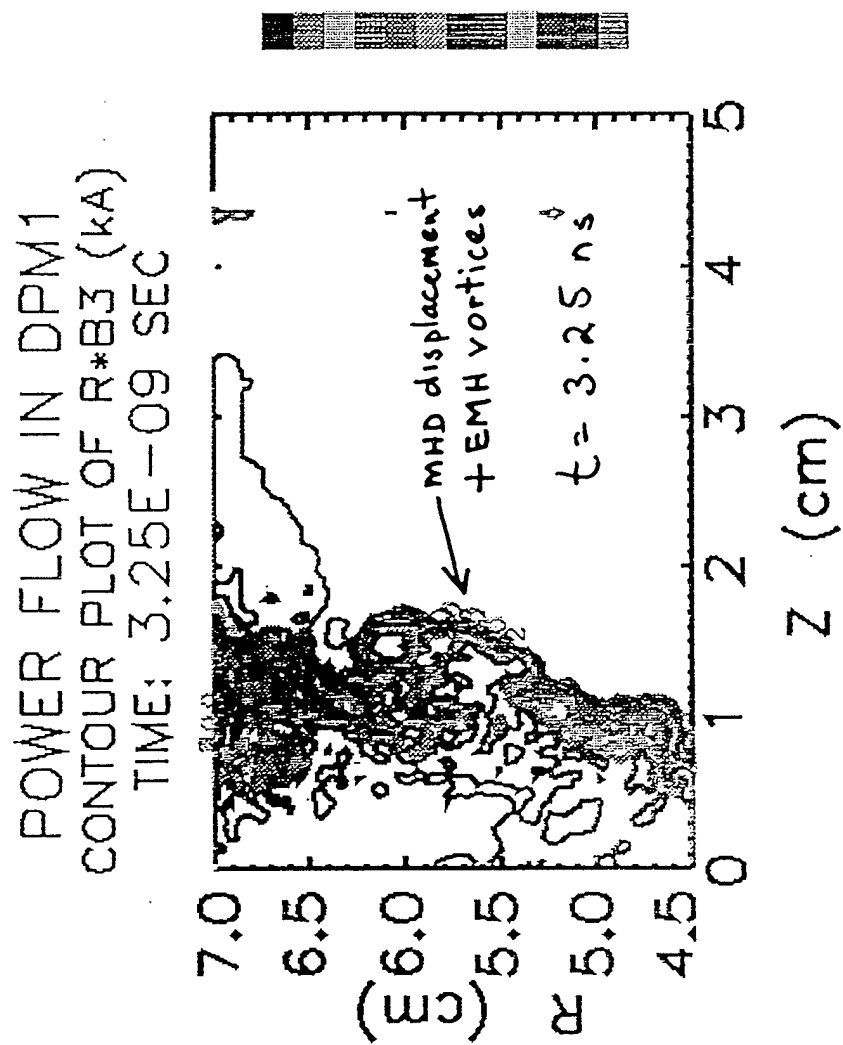


Fig 8 (b)



Simultaneous EMH and MHD effects  
 SS52

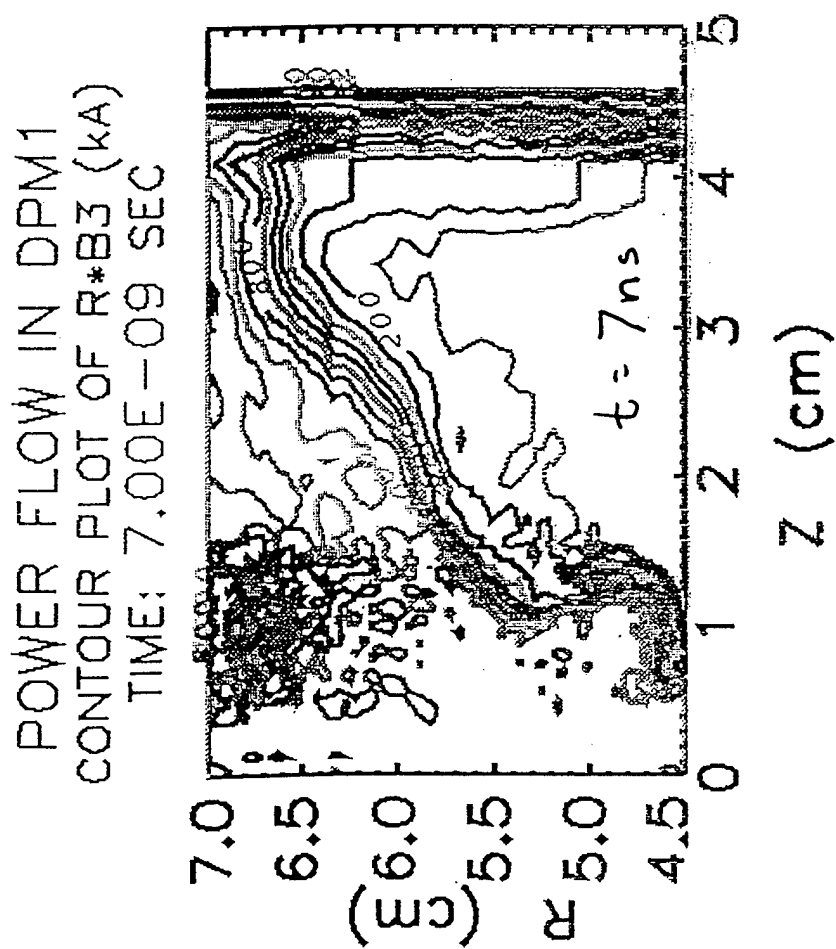


Fig 8c

## Study Properties of EMH vortices

### More recent results:

same set up as before, except :-

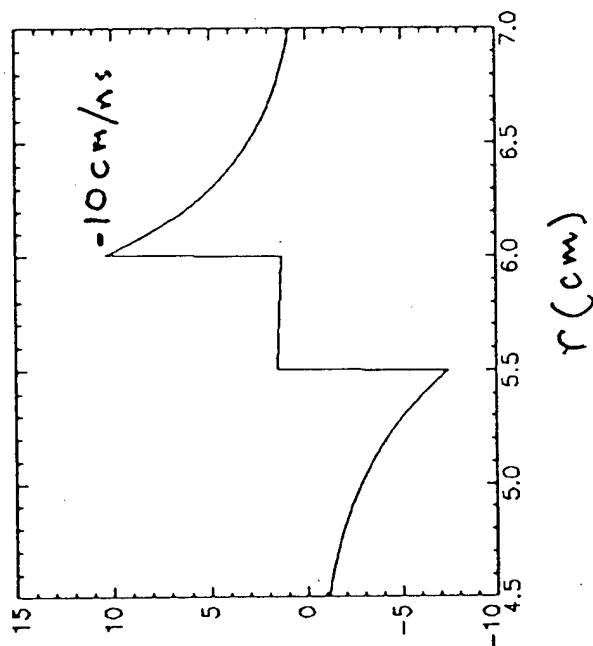
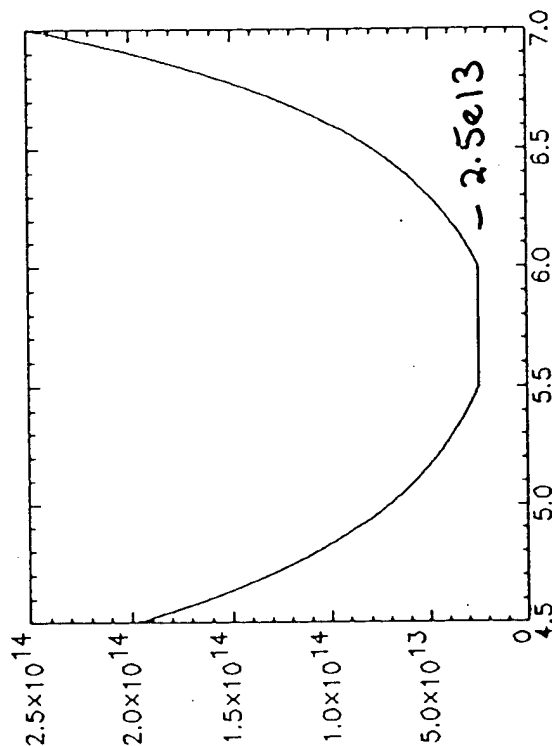
$$\begin{array}{ll} l = 4 \text{ cm} & (\text{rather than } l = 1 \text{ cm}) \\ n(r) = n_0 e^{kr} & (n(r) \sim n_0(1+kr^2)) \\ m_i = \infty \text{ everywhere} & (m_i = \infty \text{ near electrodes}) \end{array}$$

densities factor of 4 smaller

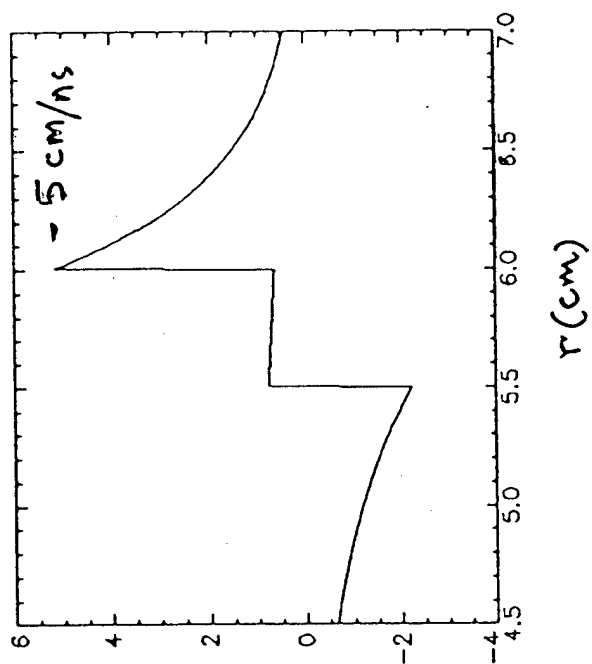
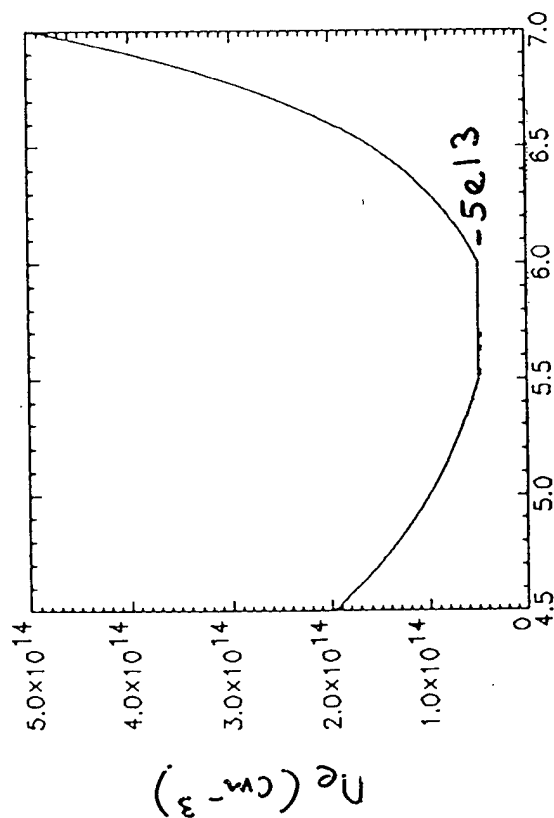
Fig 9

Fig 10

ss 90

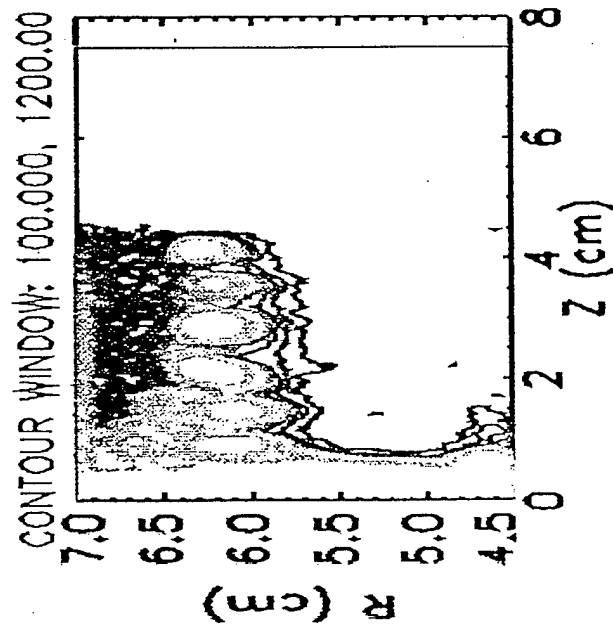


ss 89

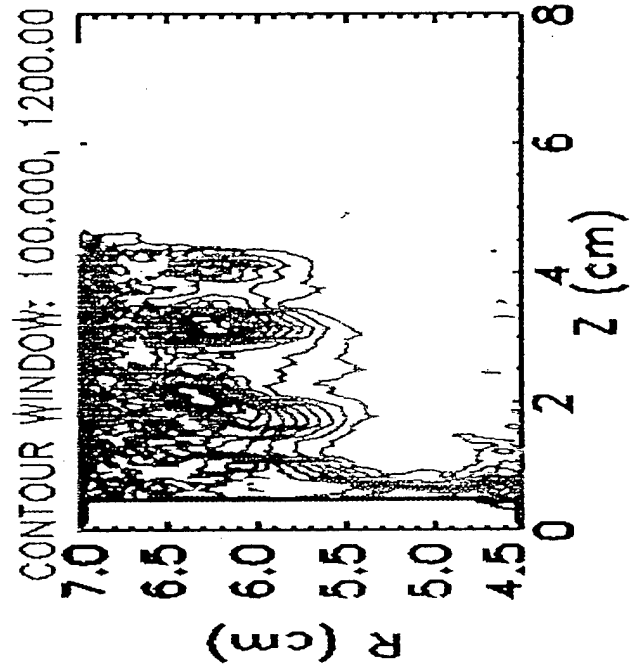


# Scaling of B-field penetration with density

ss89, EMH test, Nmin=5e13 cc      ss90, EMH test, Nmin=2.5e13 cc  
 Current Enclosed Contours at TIME: 2.619      Current Enclosed Contours at TIME: 2.1177 NS



$V \approx 1.5 \text{ cm/ns}$   
 $V_H \approx 5 \text{ cm/ns}$



$V \approx 1.9 \text{ cm/ns}$   
 $V_H \approx 10 \text{ cm/ns}$

Fig 11

# Scaling of vortex size with density gradients

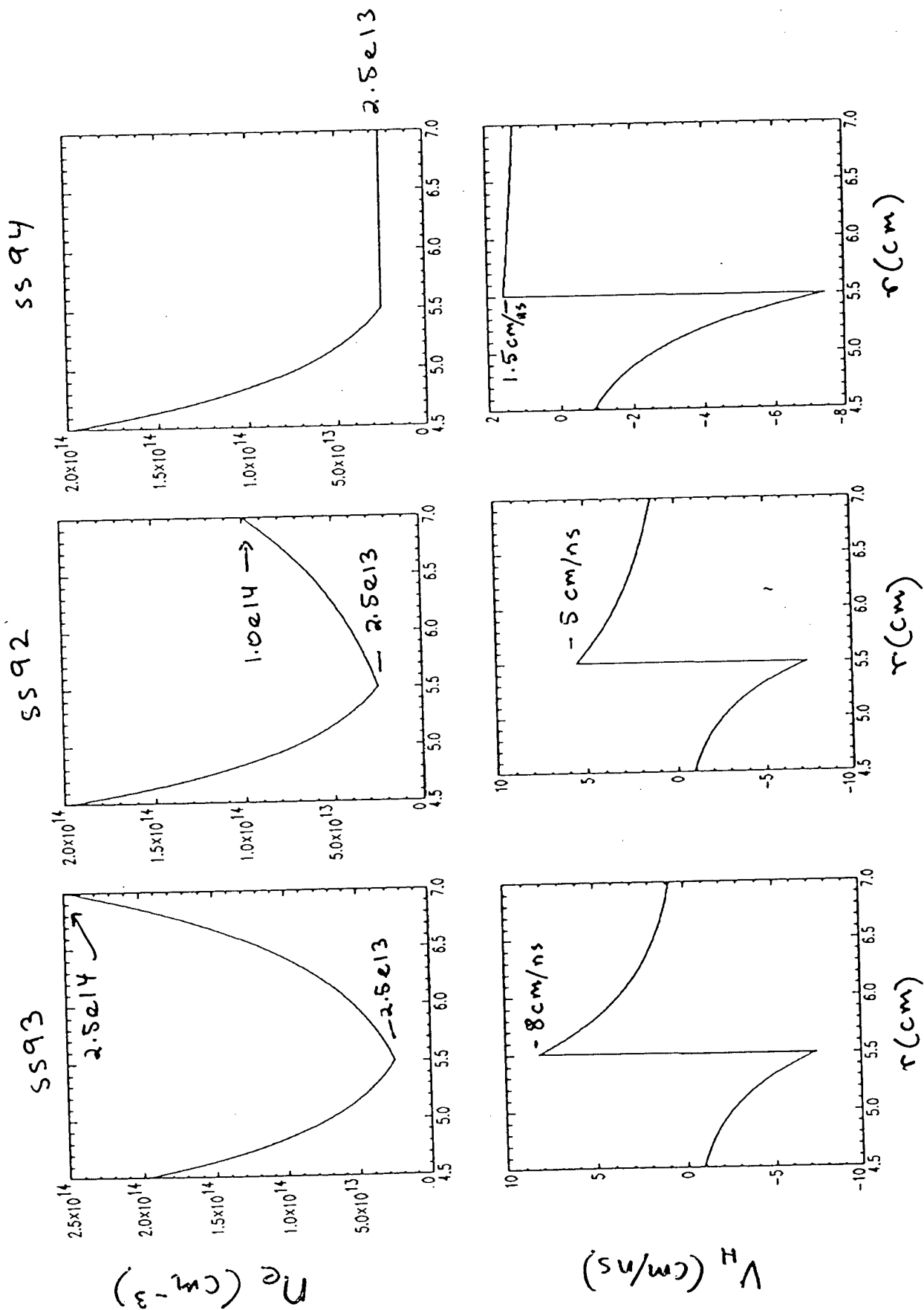
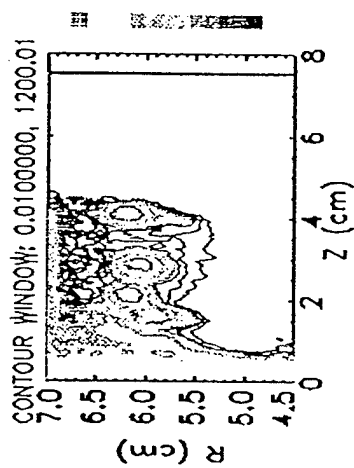


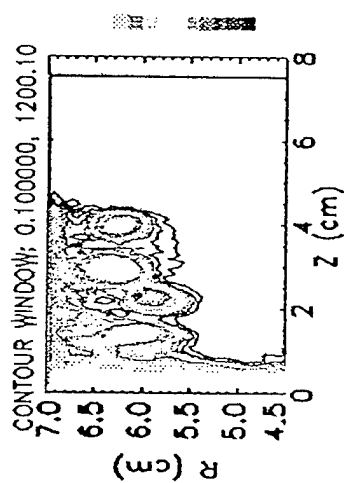
Fig 12

# Vortex size scaling with density gradients

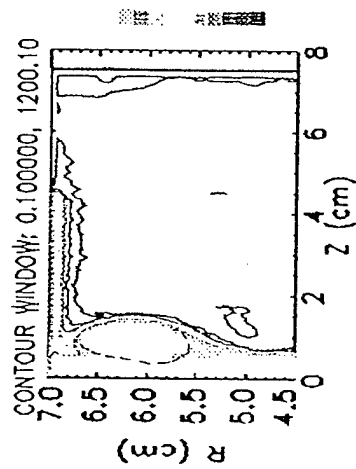
ss93, EMH test,  $N_{min}=2.5e13$  cc  
Current Enclosed Contours at TIME: 2.4996 NS



ss92, EMH test,  $N_{min}=2.5e13$  cc  
Current Enclosed Contours at TIME: 2.7431 NS



ss94, EMH test,  $N_{min}=2.5e13$  cc  
Current Enclosed Contours at TIME: 2.9989 NS



## Conclusions

- EMH vortices are not cathode potential hills.  
geometric size and penetration have different physical properties
- Two types of gap formation in the middle of the plasma  
MHD deformation and displacement of plasma, then EMH vortices ?  
EMH field penetration, then vortices and opening of plasma gap ?
- Vortex size scales depends on  $n^{-1}dn/dr$ ,  $v_H(r)$  profile
- B field penetration depends on  $n$ ,  $n^{-1}dn/dr$

TI  
25

11

# Future Directions

## Physics Issues

Test:

- equipartition of energy and vorticity conservation laws
- Importance of electron inertia, boundary conditions, 2-D effects
- B-field penetration scaling

## Exploiting EMH/vortices

Examine:

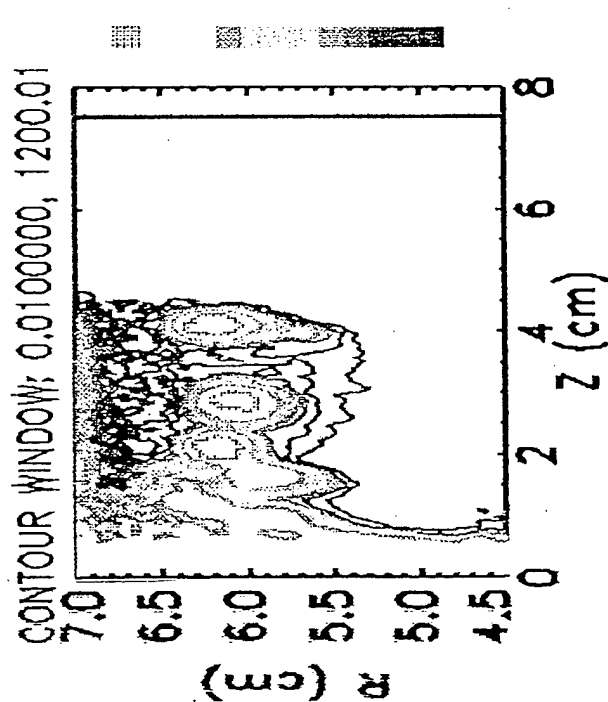
- Correlation between POS gap and vortex size
- Possibility of xpt'l control of vortex size ( $B$ ,  $n$ ,  $dn/dr$ )
- Effect of external solenoidal B fields (CT-POS)

Fig 15



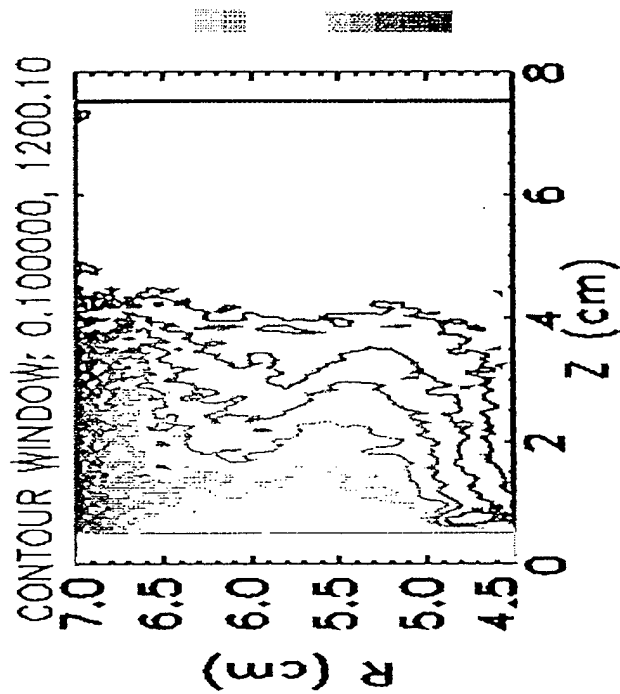
Can vortex formation be controlled ?

ss93, EMH test, Nmin=2.5e13.cc  
Current Enclosed Contours at TIME: 2.4996 NS



applied  $B_z = 0$

ss95, EMH test, Nmin=2.5e13 cc  
Current Enclosed Contours at TIME: 1.9999 NS



$B_z \approx 0.5 B_0$   
 $B_z(r, z)$  uniform

Fig 16

PULSED-POWER PHYSICS TECH. NOTE NO. 93-17

**TITLE:     Modeling of long-conduction time POS**

**AUTHORS:** J.M. Grossmann, S.B. Swanekamp, J.D. Huba, C.R. DeVore, P.F. Ottinger, R.J. Commisso, B.V. Weber, and P.J. Goodrich

**DATE:** 3 November, 1993

**ABSTRACT:** Synopsis of talk presented at APS - DPP meeting, St. Louis, Mo., Nov. 1 - 5, 1993. Talk was 5F3, and is listed in APS Bulletin Vol. 38, p. 1988, (1993). Theoretical and numerical modeling of long-conduction-time opening switches is presented. Emphasis is placed on the hydrodynamic compression and displacement of plasma during the conduction phase, together with the final opening of a gap in the resulting plasma configuration.

This report represents unpublished internal working documents and should not be referenced or distributed

Figure 1. Copy of submitted abstract.

Figure 2. Title and author list.

Figure 3. Overview of talk. Two separate topics will be addressed, conduction phase physics and the physics of final gap formation. The main mechanisms that may be active during the conduction phase are plasma displacement and distortion by magnetic pressure forces, and the penetration of magnetic field into the plasma by electro-magneto-hydrodynamic (EMH) effects. The mechanisms of final gap formation are 2-D magnetized sheath formation, and subsequent gap opening behind the sheath. The importance of the gap is that it controls the optimum load current and voltage as well as the electron flows launched downstream of the POS region. The topics of conduction phase physics and gap opening are related in that the mechanisms active during the conduction phase prepare the plasma for final opening. The density profiles determined by magnetic pressure and EMH effects determine the nature of the gaps that open in the POS plasma. In our simple picture of this process (depicted in the cartoons of this figure), the plasma is axially and radially displaced by magnetic pressure until all the current is concentrated in a small volume at the load edge of the original plasma fill. In this small volume, the physics of final gap opening dominates late in the conduction phase of the POS.

Figure 4. The three core experimental observations found in long-conduction time experiments at NRL. These results should be reproduced by simulations of the conduction phase. Although POS experiments have been conducted at several different laboratories, the experiments at NRL have been especially well diagnosed and provide a great deal of data for comparison to theory.

Figure 5. Theoretical analysis of the conduction phase has included 1-D center-of-mass calculations as well as 1 and 2-D fluid simulations. Some of the numerical codes used in these simulations are listed here. For the most part, good agreement is found between experiment and simulation. We hope to use these simulations to predict conduction current scaling and to obtain detailed density profiles at the end of the conduction phases. These density profiles will be used in PIC simulations of final gap opening.

Figure 6. As an example of one of the fluid codes listed above, results are shown in this figure from the Huba/Lyon MHD/EMH code. The code is in Cartesian geometry, so we will compare to experiments at large cathode radius where cylindrical effects are less important. Contours of the density, magnetic field, and current density at various times are shown. The initial plasma density has a radial profile but is uniform in  $z$ . The initial density profile is valley-like, similar to experiment, with a minimum value at  $10^{15} \text{ cm}^{-3}$ . The figures show the axial and radial displacement of plasma by  $\mathbf{J} \times \mathbf{B}$  (magnetic pressure) forces and the evacuation of plasma behind the current front. Although not shown here, we find that the axial line-of-sight, line-averaged density drops as the current channel reaches the load end of the plasma. The inclusion of EMH effects results in faster current penetration than with magnetic pressure alone, and the interface between high and low density regions at the generator side of the evolving plasma shows the development some sort of surface instability.

Figure 7. To obtain scaling results for comparison to experiment and to understand the effect of EMH on the conduction time, we ran the fluid code at three different densities and recorded the time it took for the current channel to reach the load end of the original plasma fill. We call this time the penetration time. In the figure, the solid circles represent data from the code run with Hall effects turned off (i.e. magnetic pressure alone). Squares represent data when Hall and magnetic pressure effects are both switched on. The crosses represent experimental data from a HAWK shot with cathode radius of 12 cm. The data shows fairly good agreement with experiment, and that Hall effects are not important at larger densities. (The Hall/MHD and ideal MHD results coincide at  $n = 10^{16} \text{ cm}^{-3}$ .)

Figure 8. Next we will examine the issue of gap opening in the POS. PIC simulations will be used to examine gap opening in a small plasma region at the end of the conduction phase. We will refer to this small region as the opening region, shown circled in this figure. Note the different spatial and time scales of the conduction phase compared to the opening phase. In these particular simulations we will assume the plasma is uniform and that the POS is connected to a low inductance downstream transmission line terminated with a short-circuit load. Since we are looking at the opening phase, the plasma carries the full generator current at the start of the simulation. The dense plasma at the cathode side of the opening region is modeled as a space-charge-limited emitter. We use the MAGIC code in this case, but other codes (ANTHEM and MASK) show similar results. A large range of densities and currents have been simulated.

Figure 9. Plots of the ion positions at various times during the gap opening process. These show the radial and axial development of a 1 mm gap in the plasma near the effective cathode. By gap we mean a region largely evacuated of plasma (although space-charge-limited emission of ions from the plasma above the gap can send ions into the gap, and if the electrons emitted from the cathode are not fully magnetically insulated, they can occupy some fraction of the gap).

Figure 10. The physical mechanism for the gap opening process of Fig. 9 is examined in this and the next two figures. Figure 10 shows the evolution of current streamlines during the opening process. A localized emission site migrates axially along the cathode as time progresses. By emission site we mean the region near the effective cathode where there are large gradients in the current streamlines, and therefore large current densities. These large current densities are created by electrons accelerated radially in a local 2 - D sheath near the cathode. By sheath we mean a non-neutral region of the original plasma fill. Before  $t = 3 \text{ ns}$ , the electrons then flow back toward the generator in the plasma above the gap and then flows up the generator edge of the plasma. At  $t = 3 \text{ ns}$ , the current flows along the load edge of the plasma after being accelerated in the sheath. At  $t = 4 \text{ ns}$ , current has been diverted to the load. The current no longer crosses between electrodes in the switch region, although it does flow inside the remaining plasma in an arc near the anode. Notice that there is no launched electron flow downstream of the POS region. All of the load current flows in the cathode.

Figure 11. In this figure we superimpose iso-potential contours of the electrostatic potential that develops near the emission sheath on top of the current streamline plots of Fig. 10. The potential plots show that a localized 2-D sheath develops near the cathode and that the sheath

floats to positive potential. The emission sheath is characterized by circular potential contours that we call potential hills. Large electric fields develop near these potential hills and accelerate ions toward the cathode. The electrostatic removal of ions from the potential hill region creates the gap that forms behind (on the generator side of) the potential hill.

Figure 12. In the interest of clarity, this figure shows the electrostatic potentials used as an overlay of Fig. 11. These plots should be compared with Figs. 10 and 11.

Figure 13. The main results of our PIC simulations of gap opening. We have examined the formation of a preformed gap in the case of a POS terminated by a low inductance transmission line and a short circuit load. We call the gap "preformed" because technically, it forms during the conduction phase, not during the opening phase. The gap forms before it has any information about the load, which is why we claim that the preformed gap forms independent of the load. However, further gap growth can be expected when the POS is coupled to higher impedance loads. We have conducted several simulations to find how the preformed gap scales with plasma density and magnetic field. The results of these runs are summarized in the scaling laws shown in this figure.

Figure 14. Analytic estimates of gap scaling. By assuming that the electron current density can be estimated from the formula for space-charge-limited emission into a uniform ion background, that the current channel width scales like the collisionless skin depth, and that the sheath size is related to the Debye length associated with the sheath potential, the empirical scaling laws of Fig. 13 can be approximately recovered.

Figure 15. Summary and future work. We hope in the future to investigate the effect of realistic density profiles and realistic loads on gap opening. The density profiles can be obtained from fluid simulations of the conduction phase or from direct experimental measurements. Gap opening will be examined in both the load limited regime (load impedance controls load voltage) and in the switch limited regime (switch gap controls load voltage). Depending on the densities and load impedances, we expect to see further gap growth from its preformed levels. The size of the gap will determine the optimum load currents and voltages and the types of electron flow launched downstream of the POS.

**35th Annual Meeting, APS Division of Plasma Physics  
1-5 November 1993—St. Louis, MO**

**ABSTRACT SUBMITTAL FORM**

Subject Classification Category

4.2 Plasma Switches ☒ Theory ☐ Experiment

**Theoretical Modeling and Simulation of Long-Conduction-Time Plasma Opening Switches.** J.M. GROSSMANN, C.R. DEVORE,\* S.B. SWANEKAMP, P.F. OTTINGER, and J.D. HUBA, Plasma Physics Division, Naval Research Laboratory. — A comprehensive model of long-conduction-time plasma opening switches (POS) is presented. This model includes a mixture of hydrodynamic, electro-magneto-hydrodynamic, and gap formation mechanisms. The first of these mechanisms is associated with the radial and axial compression and/or displacement of the plasma by  $J \times B$  forces. The second, commonly referred to as EMH, or the Hall effect, is associated with the transport of magnetic field into the plasma. Gap formation in the plasma takes place due to enhanced erosion or the electrostatic expulsion of ions out of a potential hill. It is proposed that all of these mechanisms are active during the conduction and opening phases of the POS. However, each of them takes on more or less significance during different phases of POS operation. Analytic and numerical tools developed to study these processes and their relative importance are described. These techniques are used to model various experiments. PIC simulation results will be shown of the final opening of the POS for densities  $\geq 10^{15} \text{ cm}^{-3}$ . Results of a 2-D fluid code with EMH effects will also be presented.

\* Laboratory for Computational Physics and Fluid Dynamics.

☐ Prefer Poster Session

☒ Prefer Oral Session

☒ This poster/oral should be placed in the following grouping: (specify order)

First of three talks preceding

S.B. Swanekamp, et al.

☐ Special Facilities Requested  
(e.g., movie projector)

☐ Other Special Requests

Submitted by:

John Grossmann  
(Signature of APS Member)

John M. Grossmann  
(Same Name Typewritten)

NRL Code 6771  
Naval Research Laboratory  
Washington, D.C. 20375  
(Address)

This form, or a computer generated form, plus TWO XEROX COPIES, must be received by Friday, 2 July 1993, at the following address:

Saralyn Stewart  
The University of Texas at Austin/Institute for Fusion Studies  
26th and Speedway—RLM 11.234  
Austin, TX 78712  
Telephone (512) 471-4378

Fig. 1

Fig. 2

# Modeling of Long-Conduction Time POS

NRL

J.M. Grossmann

S.B. Swanekamp\*\*

J.D. Huba

C.R. DeVore\*

P.F. Ottinger

R.J. Comisso

B.V. Weber

P.J. Goodrich+

Plasma Physics Division, Naval Research Laboratory

\* Laboratory for Computational Physics and Fluid Dynamics, NRL

\*\* Science Applications International Corporation

+ Jaycor

# Motivation: Physics of Conduction and Gap Opening

NRL

- Conduction Current Scaling with  $n, L, r, dl/dt$

Mechanisms studied:

- ♦  $\nabla B^2$  (MHD)
- ♦ EMH ( $\nabla B$  and  $\nabla n$ )

- Final Gap Formation

POS gap: 1) determines load voltage and current.  
2) controls electron vacuum flow, losses.

Mechanisms studied:

- ♦ 2-D, magnetized sheaths
- ♦ Gap formation behind sheaths

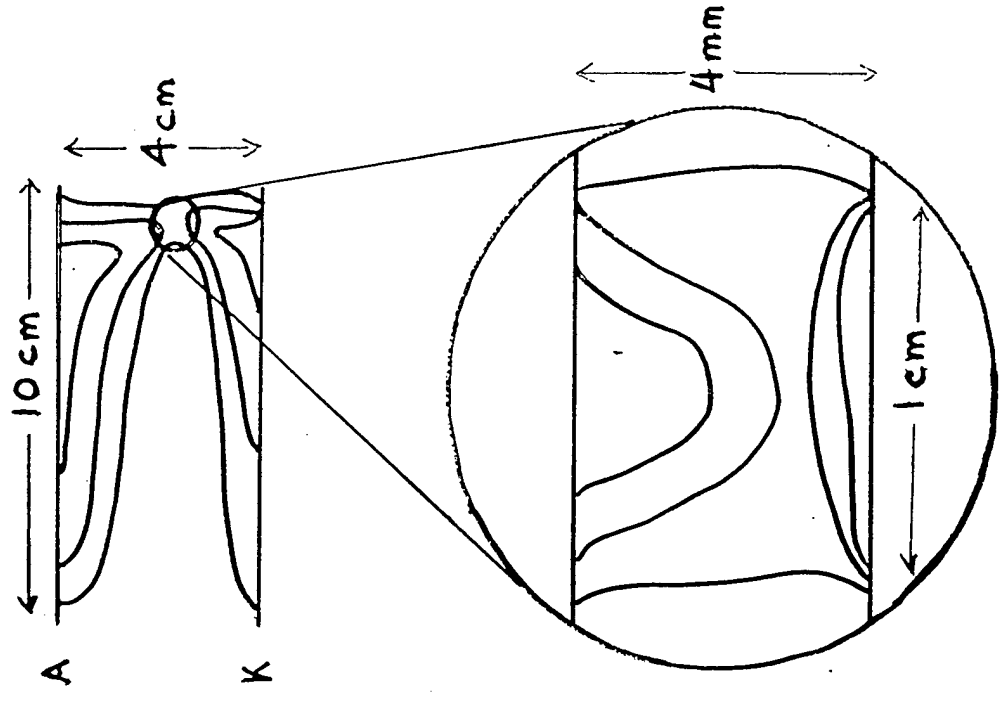


Fig. 3



# Long conduction time POS ( $\leq \mu\text{sec}$ ) - Xp't

NRL

- Axial migration of current channel.  
POS opens approx. when channel reaches load end of POS  
- Commisso et al., Phys. Fluids B 4, 2368 (1992)
- Conduction current scaling consistent with  $\nabla B^2$ .  
results may also indicate EMH effects at lower  $n$  ?  
- Weber et al., in preparation
- Line-averaged density drops rapidly at opening.  
- Hinshelwood et al. Phys. Rev. Lett. 68, 3567 (1992)

Fig. 4

# Long-conduction time POS - theory

NRL

Fluid simulations of the conduction phase:

ANTHEM (Mason, LANL)  
MHD/EMH (DeVore, Huba, NRL)  
S3SNOW, DELTA (Ingermanson, Salberta, Waisman, S-Cubed)  
MACH2 (Watrous, Frese, Numerex)

Simulations show:

- $\nabla B^2$  forces displace and distort plasma axially and radially
- EMH (Hall) effects at lower densities
- Good qualitative agreement w/ exp't

Use fluid simulations to:

- predict conduction current scaling
- obtain density profiles  $n(r,z)$  at end of conduction phase for PIC simulations of final gap opening.

# HALL MHD (Cartesian)

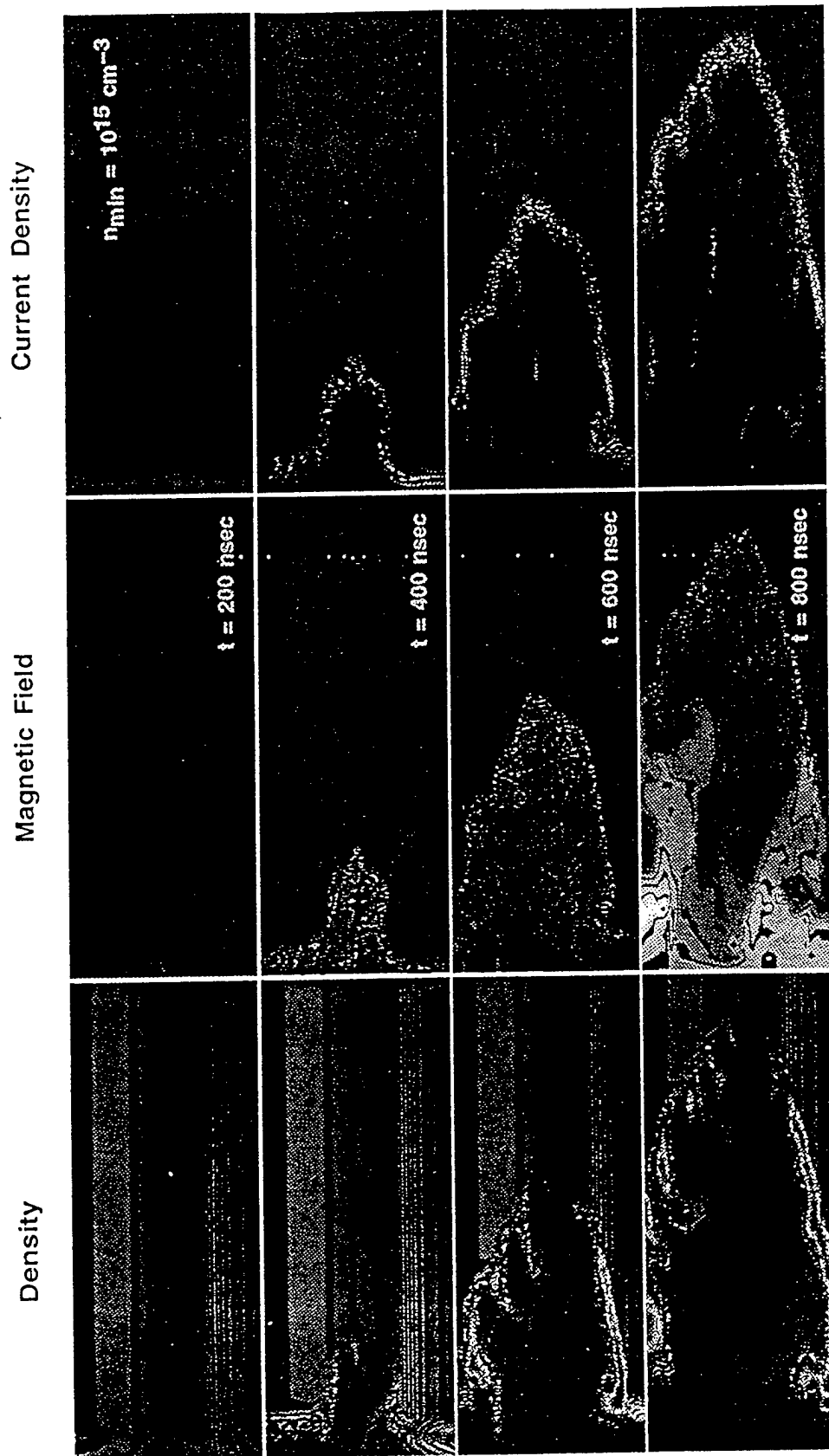


Fig. 6

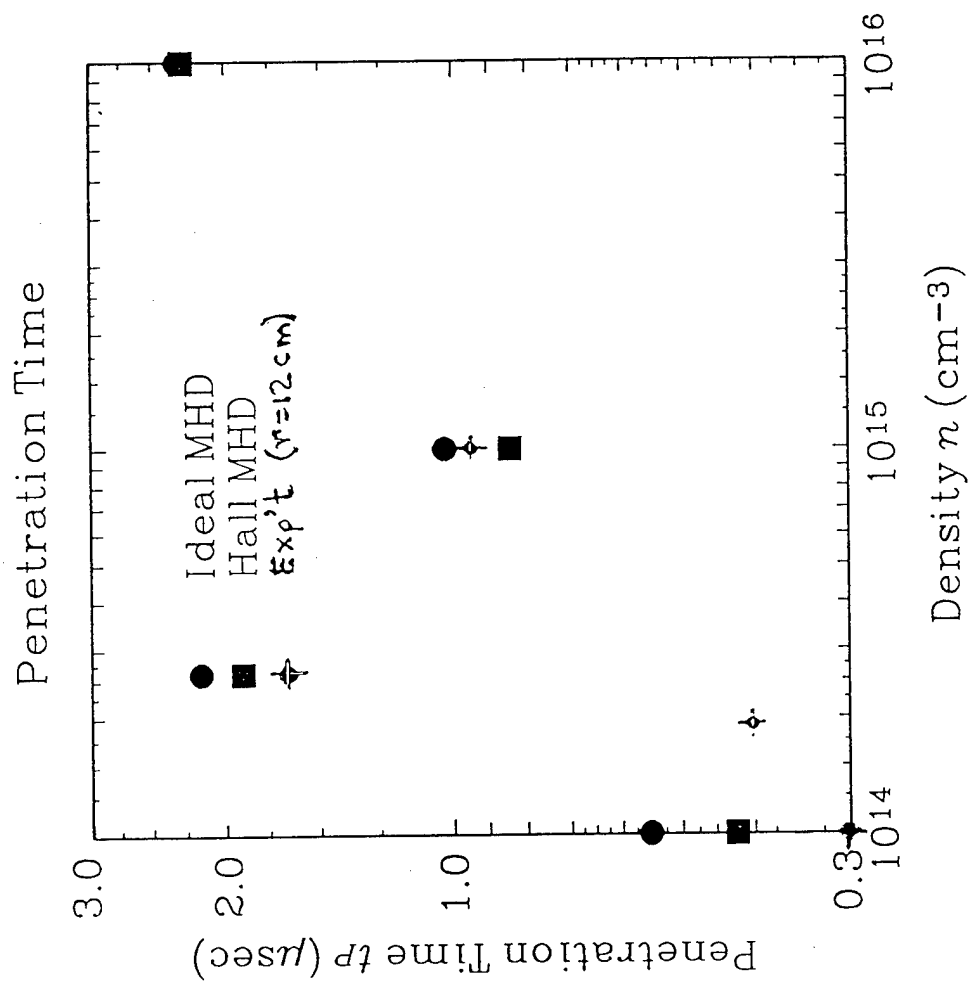


Fig. 7

# PLC simulations of final gap opening

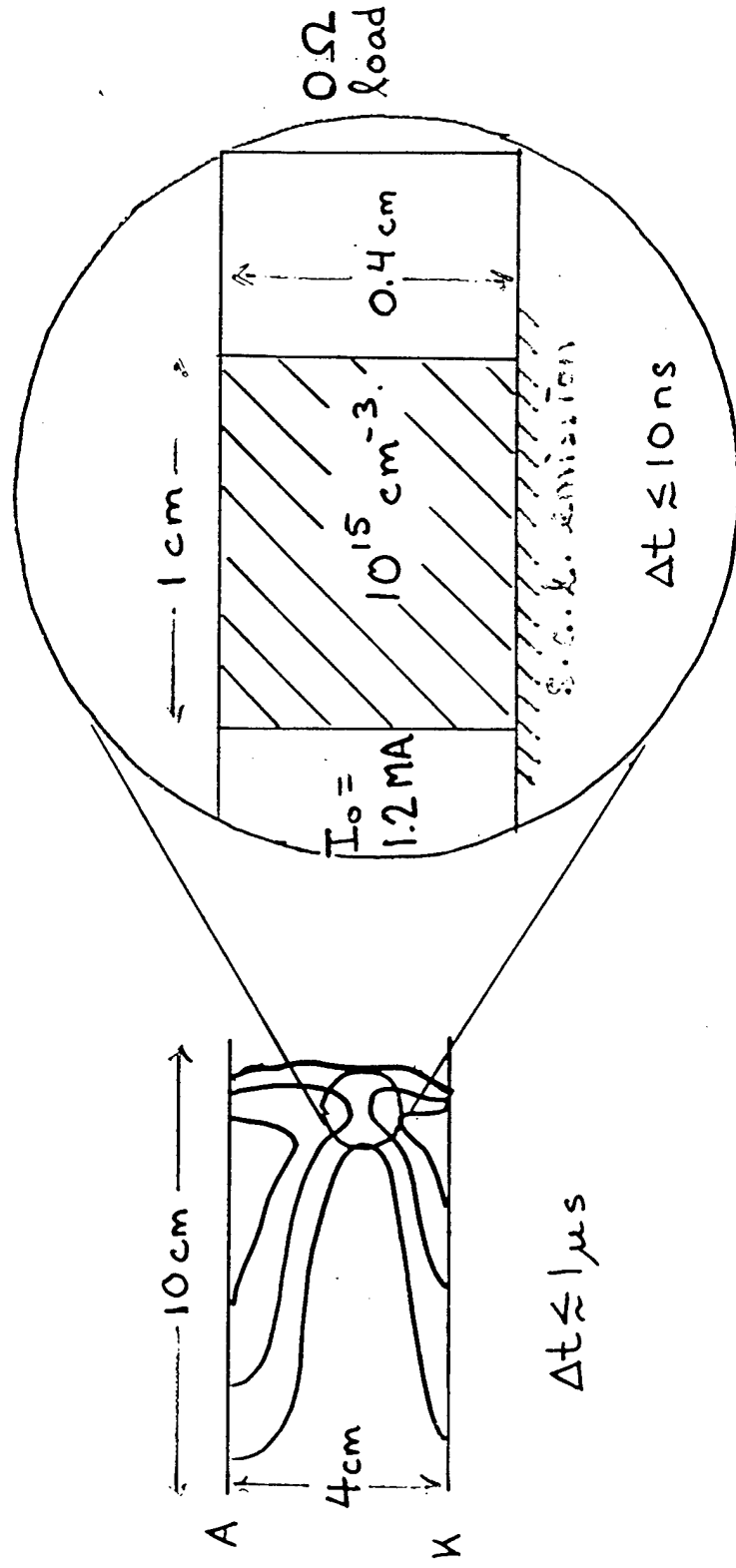
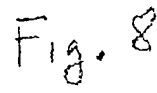
Plasma carries maximum generator current at start of simulation.

Denser plasma at cathode side modeled as space-charge-limited emitter.

Uniform initial plasma densities assumed.

MAGIC 2-D PIC code used (Goplen, Barker et al.) (MASK, ANTHEM show similar results)

Simulations have been run with densities  $4 \times 10^{12}$  -  $5 \times 10^{15} \text{ cm}^{-3}$ , and with currents ranging from 100 kA to 1.2 MA. Ions -  $\text{C}^{++}$ .



# Gap formation at site of effective cathode

NRL

$n_e = 10^{15} \text{ cm}^{-3}$ ,  $I = 1.2 \text{ MA}$ ,  $r_c = 4.5 \text{ cm}$ ,  $C^{++}$ ,  $0 \Omega$  load.  $\Delta r = 4 \text{ mm}$ ,  $\Delta z = 1 \text{ cm}$   
 Ion particle plots

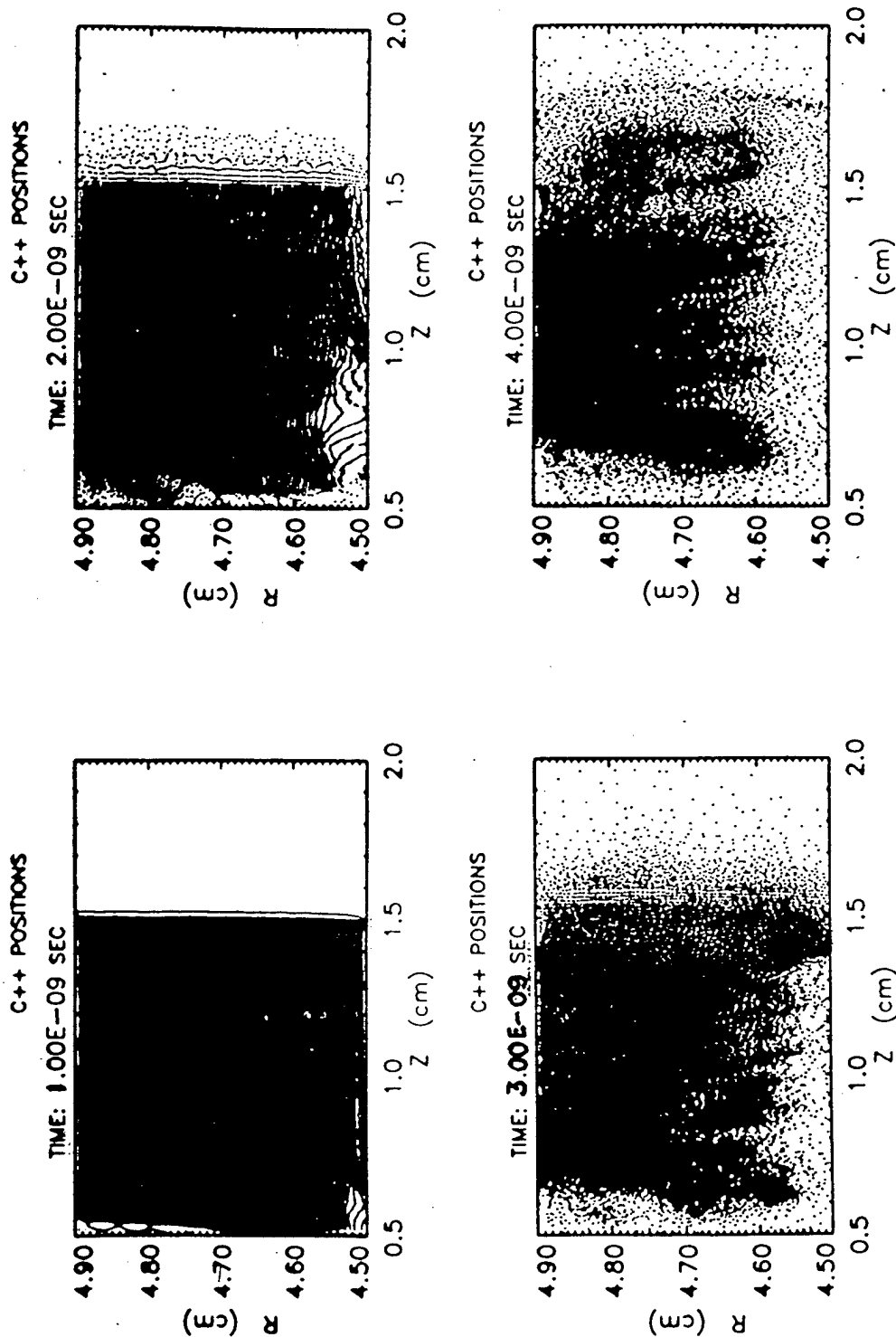


Fig. 9

# Sheath development ahead of gap

NRL

Contours of constant current enclosed

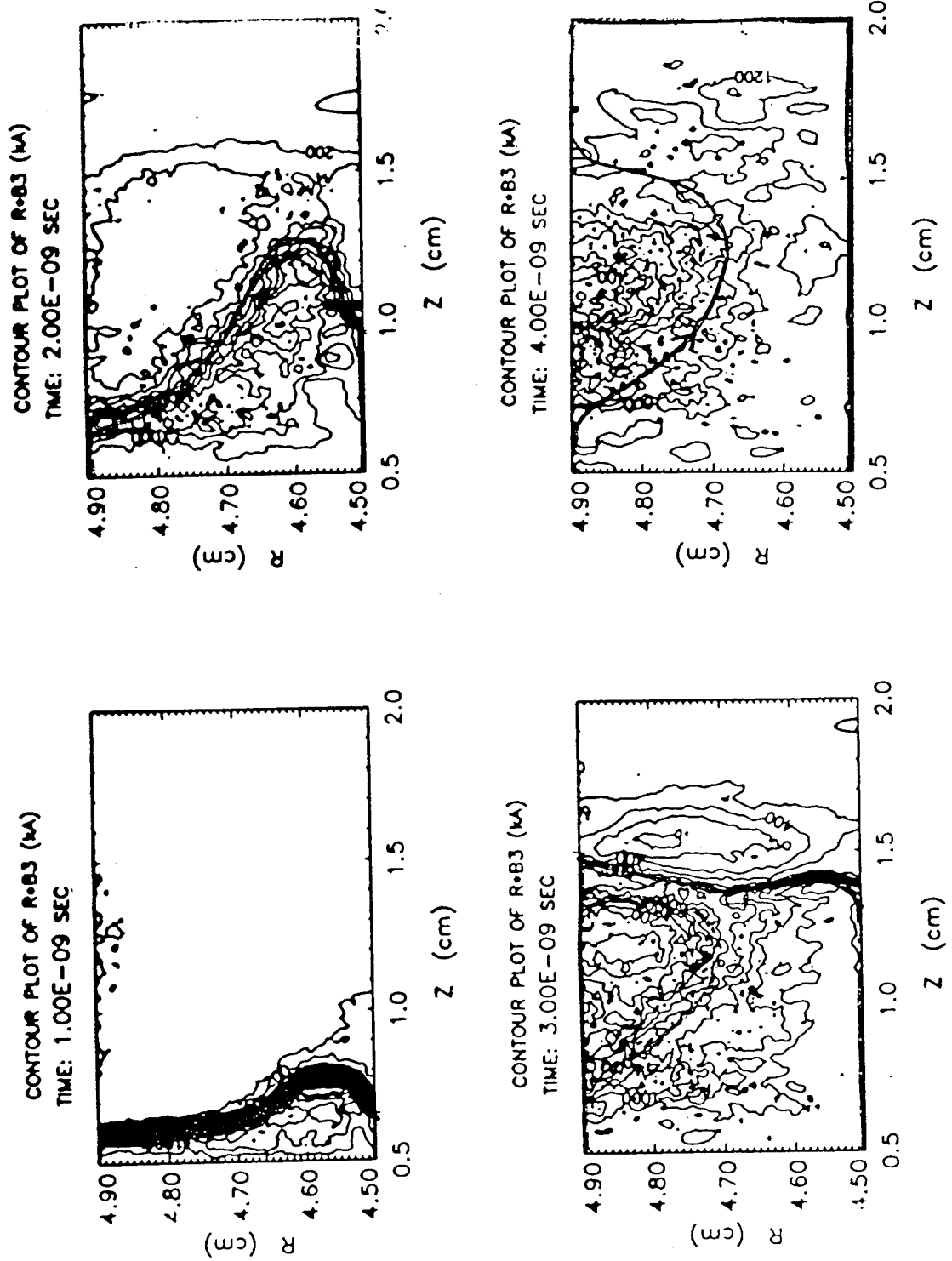


Fig. 10

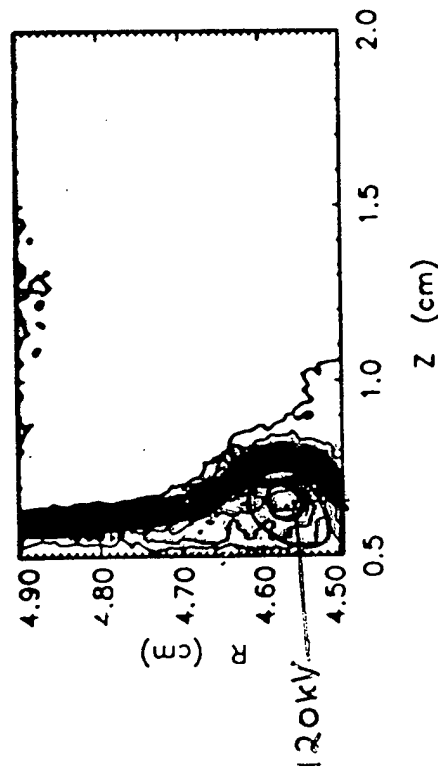
# Sheath development ahead of gap

NRL

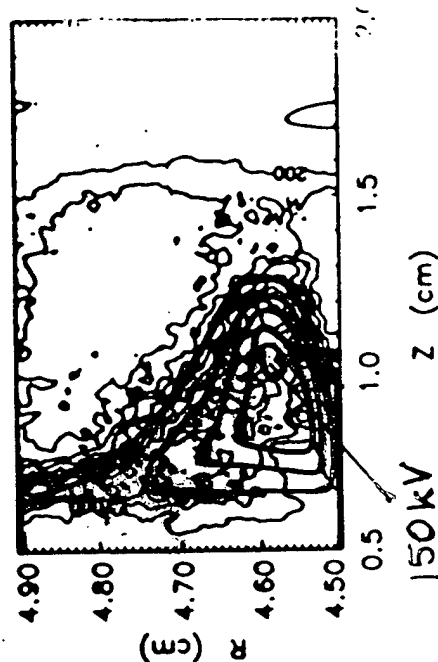
## Contours of constant current enclosed

Electrostatic Potential Contours

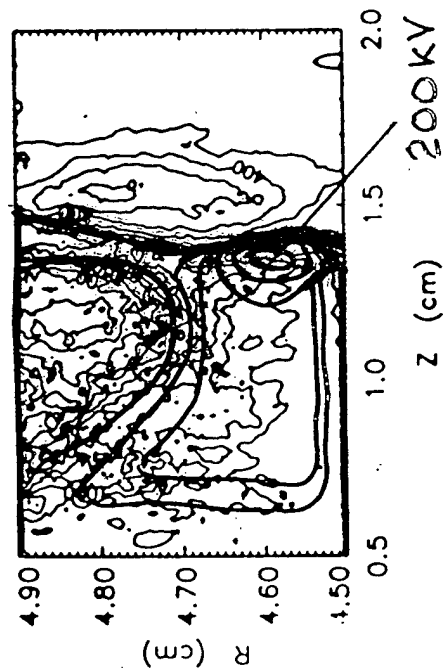
CONTOUR PLOT OF R=83 (kA)  
TIME: 1.00E-09 SEC



CONTOUR PLOT OF R=83 (kA)  
TIME: 2.00E-09 SEC



CONTOUR PLOT OF R=83 (kA)  
TIME: 3.00E-09 SEC



CONTOUR PLOT OF R=83 (kA)  
TIME: 4.00E-09 SEC

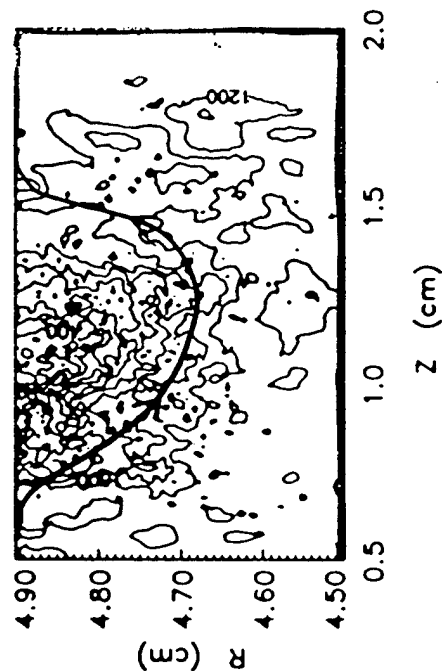


Fig. 11



Electrostatic Potential Contours

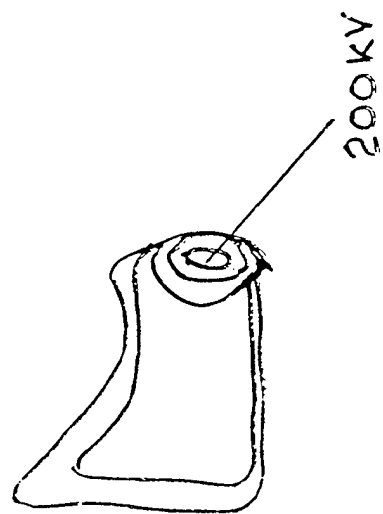
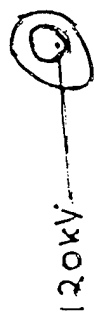
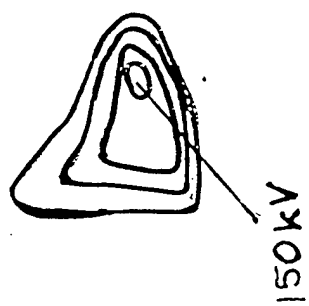


Fig. 12

# Results of gap opening simulations

NRL

- ◆ Formation and axial migration of local 2-D magnetized sheath
- ◆ Magnetically insulated gap forms in wake of sheath
- ◆ "Pre-formed" gap, independent of load

In this  $0 \Omega$  load case -

- ◆ Electrons are well insulated after POS opens- no vacuum current
- ◆ Gaps much larger than necessary for magnetic insulation

Scaling of pre-formed gap and sheath potential with  $B$ ,  $n$

- ◆  $d \text{ (cm)} \approx 10^9 B/n_e$
- ◆  $\phi \text{ (MV)} \approx 4 \times 10^4 B^2/n_e$  }  $B \text{ (Gauss)}, n_e \text{ (cm}^{-3}\text{)}$

Scaling holds within 20% for density range  $4 \times 10^{12} - 5 \times 10^{15} \text{ cm}^{-3}$ ,  
magnetic field range 10 - 50 kG.

# Simple analytic estimates of gap scaling

NRL

Assume uniform ion background, 1-D space-charge-limited electron emission,

$$j_e = \frac{n_i Z e}{2} \left( \frac{2 e \varphi}{m} \right)^{1/2} \quad (\text{non-rel. limit}) \quad (1)$$

Assume electrons carry generator current in channel of width  $\Delta z \approx c/\omega_p$

$$j_e \approx \frac{I}{2 \pi r_c (c/\omega_p)} = \left( \frac{n_e}{4 \pi m} \right)^{1/2} e B \quad (2)$$

Equate (1) and (2) to get,  $\varphi (\text{MV}) \approx 2.5 \times 10^4 \frac{B^2}{n_e}$ .

Assume:  $d(\text{cm}) \approx 10 \lambda_D \cong 7.43 \times 10^6 \left( \frac{\varphi}{n_e} \right)^{1/2} \approx 1.2 \times 10^9 \frac{B}{n_e}$  (3)

Discrepancies could be due to 2-D effects - electron magnetization.

TH  
as. I

# Summary, future work

NRL

- At opening, codes show pre-formed gap independent of load

For 0  $\Omega$  loads:

- Gap larger than critical
- Electrons well insulated, no vacuum flow

Scaling of gap, sheath potential:

- $d \text{ (cm)} \approx 10^9 B/n_e$
  - $\phi \text{ (MV)} \approx 4 \times 10^4 B^2/n_e$
- } Agrees w/ simple analytic model

Future Work:

- Continue work with fluid/EMH codes. Use realistic density profiles from codes (or xp't), and realistic loads to:
- study gap scaling in load limited and switch limited regimes
  - study vacuum electron flow launched by POS gap

Fig. 15

TITLE:       **RELATIVISTIC CHILD-LANGMUIR LAW**

AUTHORS:   **B. Weber and S. Swanekamp**

DATE:       **23 December 1994**

**ABSTRACT:**

The relativistic version of the Child-Langmuir law is derived and compared with the non-relativistic case. At 0.5 MV, the non-relativistic law overestimates the emission current by about 10%. This discrepancy increases with voltage. The relativistic emission law is not amenable to a simple power law expression, but fits of this form are given for different voltage ranges: 0.1-1 MV, 0.3-3 MV, and 1-10 MV.

The non-relativistic Child-Langmuir law is  $J \text{ (A/cm}^2\text{)} = 2.33 \text{ V(MV)}^{3/2} / \text{D(cm)}^2$ . A simple, easily-remembered formula for the relativistic case is shown to be  $J = 2 \text{ V}^{4/3} / \text{D}^2$ , more accurate than the "3/2" law for voltages greater than 0.4 MV, and within -0.2% and +7% in the range  $0.4 < V < 5 \text{ MV}$ . These formulae may be useful for incorporation in circuit models of diodes.

THIS REPORT REPRESENTS UNPUBLISHED INTERNAL  
WORKING DOCUMENTS AND SHOULD NOT BE  
REFERENCED OR DISTRIBUTED WITHOUT THE  
AUTHORS' CONSENT

## INTRODUCTION

The non-relativistic Child-Langmuir law relates the current density, voltage and gap size for a vacuum diode. The assumptions include space-charged limited emission (meaning the electric field is zero at the emitting cathode surface) and 1D electron motion. The standard derivation results in the following power law expression (1994 NRL Plasma Formulary pg. 47):

$$J = 2.34 \times 10^3 \frac{V^{3/2}}{D^2} \frac{A}{cm^2}$$

Here, the voltage  $V$  is in MV, and the gap  $D$  is in cm. This formula is incorrect at high voltage when relativistic effects increase the effective electron mass, approximately when the voltage exceeds the electron rest mass energy of 0.511 MeV. We are interested in vacuum diodes at voltages in the 0.1-10 MV range, and so need to know the corresponding space-charge limited emission for these diodes.

This note contains a derivation of the relativistic Child Langmuir law and gives numerically-derived fitting functions that may be used in calculations and simulations of vacuum diodes. The derivation of the non-relativistic law is included for completeness, and because the derivation for the relativistic case is closely related.

## NON-RELATIVISTIC CHILD-LANGMUIR LAW

An electron moves in the electric field between two parallel conductors with a voltage difference  $V$  and separation  $D$ . The relevant equations are:

$$e\phi = \frac{1}{2}mv^2$$

$$J = nev$$

$$\frac{d^2}{dx^2}\phi = \frac{ne}{\epsilon_0}$$

Here,  $\phi(x)$  is the potential at a point  $x$  in the gap;  $n$ ,  $e$ ,  $m$ , and  $v$  are the electron density, charge, mass and velocity, and  $\epsilon_0$  is used in the Poisson equation in mks units. The velocity  $v$  is eliminated using the first two equations and the density  $n$  is eliminated in the Poisson equation resulting in:

$$\frac{d^2}{dx^2}\phi = \frac{J}{\epsilon_0} \sqrt{\frac{m}{2e\phi}}$$

Multiplying both sides by  $d\phi/dx$  and integrating once gives:

$$\left(\frac{d\phi}{dx}\right)^2 = \frac{4J}{\epsilon_o} \sqrt{\frac{m\phi}{2e}}$$

Here, it was assumed that  $d\phi/dx = 0$  and  $\phi = 0$  at the cathode ( $x=0$ ). Taking the square root of both sides and separating the variables results in an equation that can be integrated from  $x = 0$  to  $D$  ( $\phi = 0$  to  $V$ ). The result is solved for  $J$  to give the familiar 3/2 power law:

$$J = \frac{4\epsilon_o}{9} \sqrt{\frac{2e}{m}} \frac{V^{3/2}}{D^2} = 2334 \frac{V_{MV}^{3/2}}{D_{cm}^2} \left(\frac{A}{cm^2}\right)$$

(Note that the numerical value of the coefficient, 2334, is slightly different from the value in the NRL Plasma Formulary,  $2.34 \times 10^3$ . I think the number in the formulary is wrong.)

### RELATIVISTIC CHILD-LANGMUIR LAW

The first two equations above are different in the relativistic case, where now  $v = \beta c$  and  $\beta^2 = (\gamma^2 - 1)/\gamma^2$ :

$$e\phi = mc^2(\gamma - 1)$$

$$J = ne\beta c$$

$$\frac{d^2}{dx^2}\phi = \frac{ne}{\epsilon_o}$$

The equations are combined, eliminating  $\phi$ ,  $n$ , and  $\beta$  resulting in:

$$\frac{d^2}{dx^2}\gamma = \frac{e}{mc^2} \frac{J}{\epsilon_o c} \frac{\gamma}{\sqrt{\gamma^2 - 1}}$$

This equation can be partially solved by multiplying both sides by  $d\gamma/dx$  and integrating once:

$$\left(\frac{d\gamma}{dx}\right)^2 = \frac{2e}{mc^2} \frac{J}{\epsilon_o c} \sqrt{\gamma^2 - 1}$$

Separating the variables and integrating results in an equation for  $J$ :

$$J = \frac{mc^3 \epsilon_o}{2e} \frac{I^2}{D^2} = 678.2 \frac{I^2}{D^2}$$

$$\text{where } I \equiv \int_1^{\gamma_o} \frac{d\gamma}{(\gamma^2 - 1)^{1/4}}$$

The voltage dependence is in the integral expression for  $I$ , where  $\gamma_0$  is evaluated at the full gap voltage  $V$ .

The integral  $I$  is evaluated numerically for voltages between 0.01 and 10 MV using a sophisticated numerical integration technique. The tricky part of the numerical integral is the singularity in the integrand at  $V = 0$  ( $\gamma = 1$ ). This was handled by starting the numerical integral at  $V = \epsilon$ , and calculating the integral to  $V = 0.01$  MV, then decreasing  $\epsilon$  until the integral was accurate to one part in  $10^6$ . The integral from 0.01 to 10 MV was performed by increasing the spacing between points by a constant factor of 1.1. The resulting  $J \cdot D^2(V)$  values are compared with the non-relativistic values in Fig. 1. Also plotted is the percent deviation of the non-relativistic values to the relativistic ones.

The error, plotted in Fig. 1, shows that the non-relativistic Child-Langmuir law varies noticeably from the more accurate relativistic values at voltages greater than 0.1 MV. For example, the non-relativistic value is 10% greater at 0.52 MV, 20% greater at 1.2 MV and at 10 MV, the non-relativistic value is greater by a factor of two.

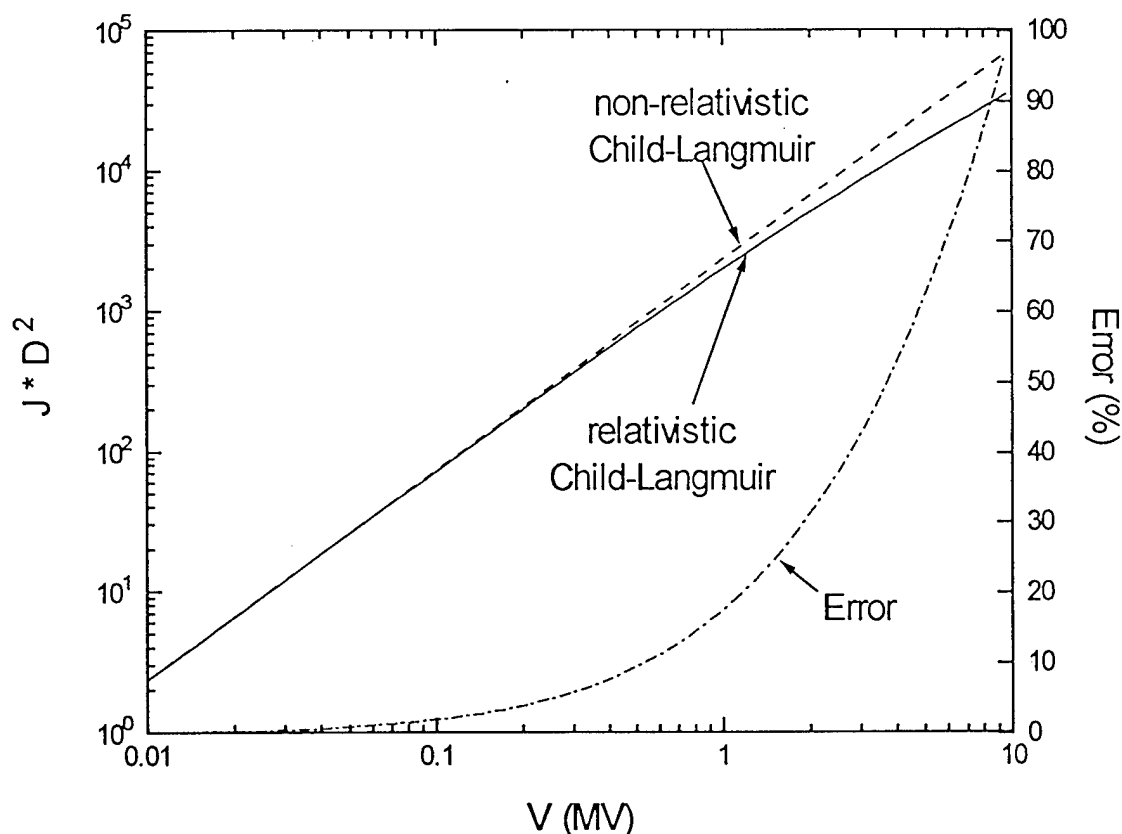


**Figure 1.** Comparison of relativistic and non-relativistic Child Langmuir laws.  $J$  is in units of  $A/cm^2$ , and  $D^2$  is in units of  $cm^2$ . The "error" is the percent difference between the two traces.



# POWER LAW FITS TO RELATIVISTIC CHILD LANGMUIR LAW

Very accurate power law fits can be made to the relativistic Child-Langmuir law data in Fig. 1. The fit functions below are for the indicated overlapping voltage ranges.

Voltage range	Power law	error (%)
0.1-1 MV	$JD^2 = 2030 V^{1.440}$	+2,-1
0.3-3 MV	$JD^2 = 1952 V^{1.374}$	+3,-2
1-10 MV	$JD^2 = 2069 V^{1.268}$	+4,-2

These fits are plotted in Fig. 2. The circles are the calculated values of  $J \cdot D^2$  for the relativistic case, and the solid lines are the power law fits for each voltage range.

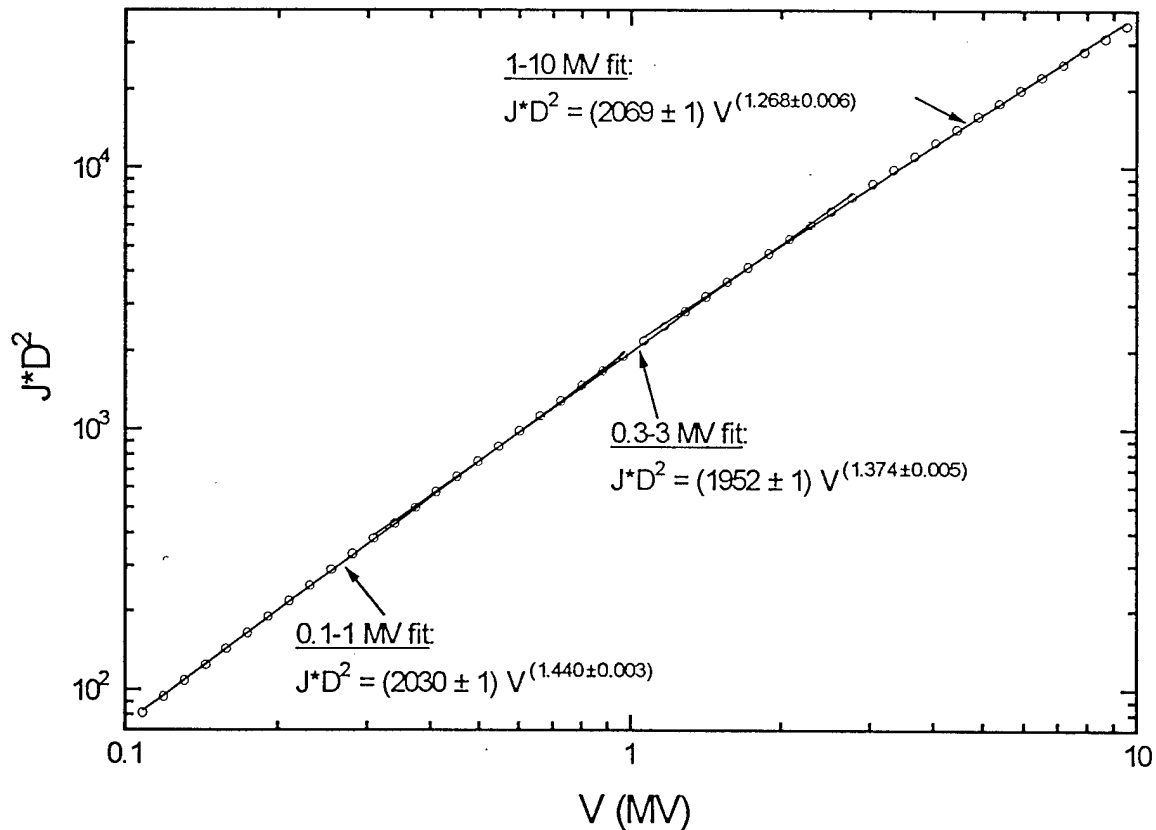


**Figure 2.** Calculated relativistic Child Langmuir law values (circles) and power law fits in selected voltage ranges (lines). The parameters of the fits have associated standard deviations as shown.

These fits are high at the ends of the range and low in the center of the range. The error, defined to be  $\{(\text{fit value}) - (\text{calculated value})\} / (\text{calculated value})$  is plotted for the three power law fits in Fig. 3. Also plotted is the percent error in the non-relativistic Child-Langmuir law. The fits are accurate to within a few percent over the specified voltage range, as indicated in the table above.

A simpler power law is a “round number” average of the fits:

$$J \cdot D^2 = 2000 V^{4/3}$$

This simple expression has the advantage that it is easy to remember and is probably accurate enough for most uses. The percent deviation of this “4/3” law from the calculated relativistic values is included in Fig. 3. The deviation is reasonably small over a large voltage range, within +7%, -0.2% for voltages in the 0.4-5 MV range. For voltages greater than 0.4 MV, the “4/3” law is more accurate than the “3/2” law.

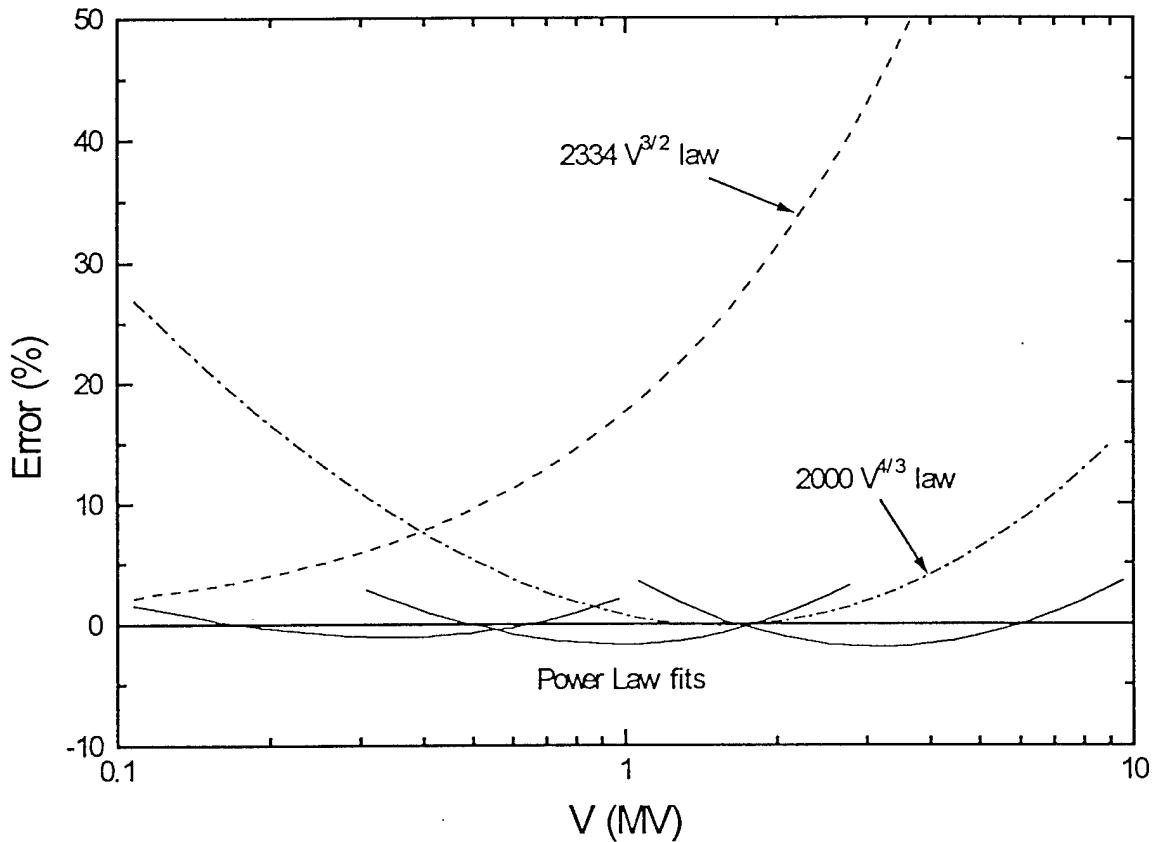


**Figure 3.** Percent error for the non-relativistic Child-Langmuir law, the three power law fits, and a simple “4/3” law.

## SUMMARY

The difference between the non-relativistic and relativistic Child Langmuir laws has been computed and parameterized in the 0.1-10 MV range. Simple power laws are given, accurate within a few percent over order-of-magnitude voltage ranges. These power laws can be used in vacuum diode calculations and circuit codes to more accurately represent the space-charge-limited phase. A simple scaling law approximating the relativistic case is  $J = 2 V^{4/3} / D^2$ , preferable to the non-relativistic Child-Langmuir law,  $J = 2.33 V^{3/2} / D^2$  for voltages above 0.4 MV.

## CHORDAL LINE-INTEGRALS AND THE 2-D SNOWPLOW MODEL OF THE MICROSECOND PLASMA OPENING SWITCH

Randall Ingermanson, Don Parks, Eduardo Waisman  
S-Cubed, Division of Maxwell Laboratories, Inc.  
3398 Carmel Mountain Road  
San Diego, CA 92121-1095

Dave Hinshelwood, Bruce Weber  
Naval Research Laboratory, Code 6773  
4555 Overlook Avenue, SW  
Washington, D.C. 20375

### Abstract

*In recent years, it has become clear that MHD processes dominate the conduction phase of microsecond plasma opening switches such as HAWK and ACE-4. A useful tool for analyzing this phase is the 2-D snowplow model. The model provides an efficient way to predict the thinning of density line-integrals observed in experiments.*

*Two main questions remain to be addressed: 1) What is the thickness of the snowplow front? 2) Does the snowplow model accurately predict the position of the snowplow front as a function of time? Both of these issues can be resolved by a careful analysis of the chordal density line-integrals measured on HAWK.*

*Here we extend the model to include a finite snowplow thickness, and we refine the computer code to compute chordal line-integrals. By comparing the results to measurements made on HAWK, we estimate the thickness and position of the snowplow front as functions of time.*

### I. Introduction

Until recently, the conduction phase of the microsecond plasma opening switch was poorly understood. When interferometric measurements of the plasma density in HAWK were published in 1991, it became clear that the dominant conduction mechanism is controlled by MHD processes. Weber, et. al., [1,2] showed that a simple 1-D snowplow model explained the conduction times over a broad range.

Soon afterward, it was shown [3] that a 2-D snowplow model could give quantitative predictions of the detailed behavior of the measured density line-integrals. In order to construct a practical computer code incorporating this model, it was necessary to solve certain technical problems: how to impose boundary

conditions and how to implement adaptive mesh refinement along the snowplow front.

Initially, only axial density line-integral measurements were available. More recently, chordal line-integral data has been taken, and this allows a more refined analysis of the experiments. In particular, two new questions can be studied:

- 1) What is the thickness of the snowplow front?
- 2) Does the snowplow model accurately predict the position of the snowplow front as a function of time?

Both of these issues can be resolved by a careful analysis of the chordal density line-integrals measured on

HAWK. In this paper, we extend the 2-D snowplow model to include a finite snowplow thickness, and we refine the computer code to compute chordal line-integrals. By comparing the results to measurements made on HAWK, we estimate the thickness and position of the snowplow front as functions of time.

## 2. HAWK Geometry

In the HAWK experiments studied here, the geometry is shown in Figures 1 and 2.

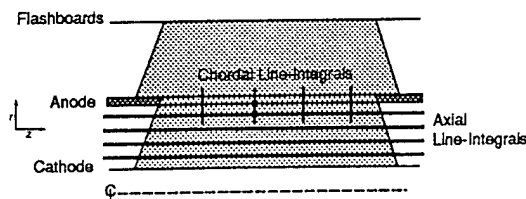


Figure 1.

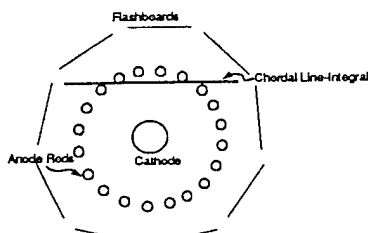


Figure 2.

The anode rods are at a radius of 7 cm, the cathode radius is 2.5 cm. The switch is 8 cm long. The plasma is generated by flashboards, and its density is assumed constant in the Z direction. The radial density distribution is measured by taking axial line-integrals of the electron density by interferometry and dividing by the switch length. Axial line-integrals are taken at radii of 3, 3.5, 4, 5.5, and 6.5 cm. Chordal line-integrals are taken at positions 1, 3, 5, and 7 cm down the switch. The chordal line of sight has an outer radius of 8.1 cm, and an inner radius of 5.1 cm. Both axial and chordal line-integrals are taken without pulsed power, and then with pulsed power.

The axial line-integrals allow us to extrapolate a density distribution in the region  $r_c < r < r_a$ . If we compute the

expected chordal line-integral without pulsed power, we find a large discrepancy with the measured chordal line-integral. This, we attribute to plasma between the anode rods.

We assume that with pulsed power, there will again be a contribution from this plasma, which we can approximate by the discrepancy measured without pulsed power.

## 3. 2-D Snowplow Model

The 2-D snowplow model [4,5,3] is a cartoon of the plasma dynamics. It makes the following simplifying assumptions: 1) Perfect cylindrical symmetry, 2) Current flows only on the surface of the plasma, 3) Magnetic pressure acts normal to the plasma surface 4) Mass is scooped up inelastically and accumulates in a thin front with zero pressure.

We can then use the measured current to compute the magnetic field, and the measured axial line-integrals (without pulsed power) to compute the density of the interior plasma (with pulsed power).

The model then reduces to a coupled set of mass and momentum equations, which can be discretized on a 1-D curve representing the snowplow front. No energy equation is solved, because the process is assumed inelastic. Because the model is so simple, a microsecond conduction time POS can be simulated on a low-end workstation in less than a minute.

The boundary conditions of the model are non-trivial, as noted in [4]. The first reasonable suggestion for boundary conditions was made in [3], and we use the same technique here.

The model assumes a front of zero thickness, leading to an infinite density at the surface (and therefore, possible singularities in computing the line-integrals). In reality, one expects the front to be smeared out by some unknown form-function. We will show that an exponential function

with characteristic length  $\lambda$  roughly matches the data, where  $\lambda$  is of order 1 cm.

#### 4. The Current Sheath Follows a Snowplow Trajectory

The concept of the "trajectory" of a 2-D snowplow front is poorly defined. In this section, we adopt the following strategy: 1) Tentatively define the trajectory using the positions of the chords and the measured times of the peaks in chordal line-integrals, 2) Find the meaning of these peak times in the context of the snowplow model, and assign a meaning to "trajectory" within the model, 3) Compute the theoretical trajectory and fit it to the measured one.

The measured chordal line-integrals with pulsed power are plotted in Figure 3.

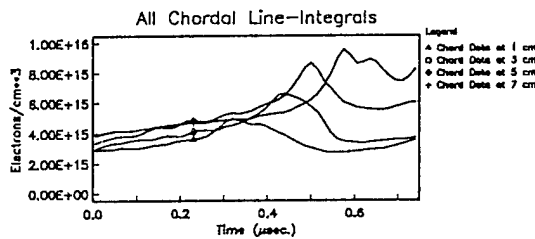


Figure 3.

From these plots, we extract the peak times corresponding in some sense to the arrival at the points  $Z_i = \{1, 3, 5, 7\}$  cm. The resulting "experimental trajectory" is plotted in Figure 4.

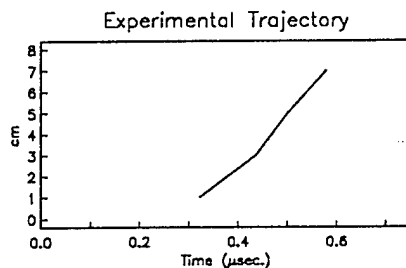


Figure 4.

Now what does the peak in the chordal line-integral really mean? For the real physical device, we have no way of saying for sure; but in the snowplow model, we can. Consider the computed

chordal line-integral at  $Z = 5$  cm, shown in Figure 5. The peak time is 503 nsec.

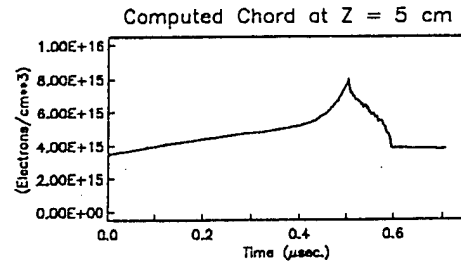


Figure 5.

Figure 6 shows that at 503 nsec, the computed position of the snowplow front is just contacting the line-of-sight of the chordal line-integral, at the minimum radius  $R_{\min} = 5.1$  cm. We therefore define the "trajectory" of the snowplow model as the  $Z$  position of that point on the snowplow front at  $R = R_{\min}$ .

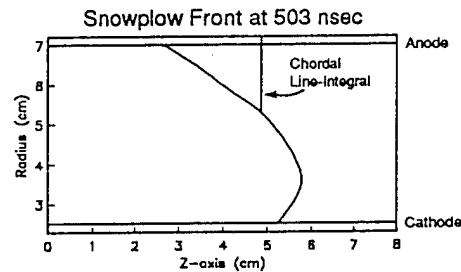


Figure 6.

Figure 7 shows a fit of the theoretical trajectory to the measured trajectory. The fitting parameters are as follows. The plasma has an initial spread, both upstream and downstream, of  $\Delta z = 1.65$  cm; the plasma continues to spread outward with velocity  $v_z = 3.0 \times 10^6$  cm/sec; the ratio of atomic mass to ionization is  $A/Z = 8.0$ .

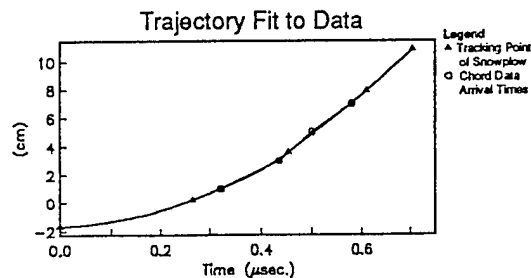


Figure 7.

## 5. Measurement of the Snowplow Thickness

As shown in the previous section, the peak time of the chordal line-integral corresponds to the arrival of the snowplow front at the chord's Z position. Prior to this arrival time, the chordal line-integral can be regarded as the sum of the undisturbed plasma and the plowed plasma. Since the line-integral of the undisturbed plasma was also measured, we can subtract the two curves and obtain an estimate of the line-integral of the snowplowed material alone.

This estimate is the difference of two experimental curves. Using the results of the snowplow model, we can correct for the time-dependent effects due to mass accretion. And knowing the trajectory of the front, we can relate position to time. The result is a rough estimate of the (line-integrated) spatial density distribution, which we normalize to a peak value of 1, since the interpretation of the amplitude is unclear. Figure 8 shows the results obtained at the four chordal positions. These curves roughly approximate the form-function we mentioned in Section 3. As time progresses, the front thickness increases from a few mm to a couple of cm.

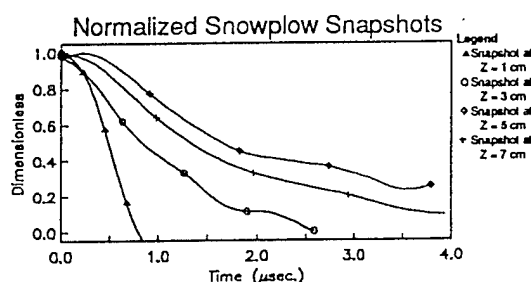


Figure 8.

## 6. Chordal Line-Integrals

In Figure 9, we show a comparison between a computed and a measured chordal line-integral, at  $Z=5$  cm. The difference in amplitude of the peaks is probably due to increased ionization in the snowplow front, an effect not yet accounted for by our model. Note that the tail that begins at 600 nsec is *entirely* due to the residual plasma between the anode

rods, as discussed in Section 2.

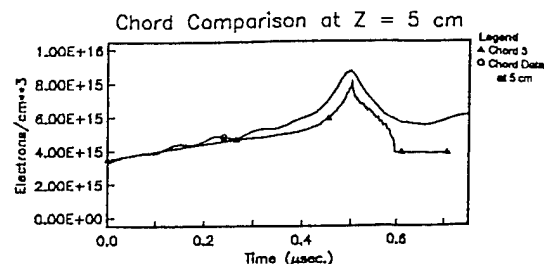


Figure 9.

## 7. Conclusions

The current sheath within the POS follows a snowplow trajectory with reasonable parameters. The snowplow front has a thickness of order 1 cm. The 2-D snowplow model provides a fast and reasonably accurate method of studying the time-evolution of the POS conduction phase.

## References

- 1 Weber, B.V., J.R. Boller, R.J. Commisso, P.J. Goodrich, J.M. Grossmann, D.D. Hinshelwood, and P.F. Ottinger, "Conduction Limits and Scaling of Microsecond-Conduction-Time Plasma Opening Switches," APS Plasma Physics Annual Meeting, 1991.
- 2 Hinshelwood, D.D., R.J. Commisso, P.J. Goodrich, J.M. Grossmann, J.C. Kellogg, and B.V. Weber, "Density Measurements of Microsecond-Conduction-Time POS Plasmas," BEAMS '92.
- 3 Ingermanson, R.S., D.E. Parks, E.R. Salberta, and E. Waisman, "Two-Dimensional Studies of Current Conduction in Plasma Opening Switches," BEAMS 92.
- 4 Hussey, T.W., M.K. Matzen, and N.G. Roderick, "Large-Scale-Length Non-Uniformities in Gas Puff Implosions," J. Appl. Phys. **59** (8), 1986.
- 5 Salberta, E., D. Parks, and E. Waisman, "General Solution for Asymmetric Snowplow in Z-Pinch-Like Geometry," Phys. Fluids B4 (10) 3440, Oct. 1992.

# Plasma opening switch conduction scaling

B. V. Weber, R. J. Commisso, P. J. Goodrich,<sup>a)</sup> J. M. Grossmann, D. D. Hinshelwood,<sup>a)</sup>  
P. F. Ottinger, and S. B. Swanekamp<sup>a)</sup>

Pulsed Power Physics Branch, Plasma Physics Division, Naval Research Laboratory,  
Washington, D.C. 20375-5000

(P)218

(Received 19 April 1995; accepted 6 July 1995)

Plasma opening switch (POS) experiments performed on the Hawk generator [Commisso *et al.*, Phys. Fluids B 4, 2368 (1992)] (750 kA, 1.2  $\mu$ s) determine the dependence of the conduction current and conduction time on plasma density, electrode dimensions, and current rise rate. The experiments indicate that for a range of parameters, conduction is controlled by magnetohydrodynamic (MHD) distortion of the plasma, resulting in a low density region where opening can occur, possibly by erosion. The MHD distortion corresponds to an axial translation of the plasma center-of-mass by half the initial plasma length, leading to a simple scaling relation between the conduction current and time, and the injected plasma density and POS electrode dimensions that is applicable to a large number of POS experiments. For smaller currents and conduction times, the Hawk data suggest a non-MHD conduction limit that may correspond to electromagnetohydrodynamic (EMH) field penetration through the POS plasma. © 1995 American Institute of Physics.

## I. INTRODUCTION

A plasma opening switch (POS) can be used to conduct current from a pulsed power generator or a high voltage Marx bank, then open on a faster time scale to deliver a high power pulse to a load (for example, an electron- or ion-beam diode).<sup>1</sup> An example of a POS on the Hawk generator<sup>2</sup> is sketched in Fig. 1. Plasma is injected into the electrode region between the inner and outer conductors using flashboard<sup>3</sup> plasma sources. Current from the generator initially flows through the plasma as magnetic energy accumulates in the circuit inductance. At some point during the current waveform, the current through the plasma decreases rapidly (the POS "opens") and the generator current can flow to a downstream load. This technique is attractive for pulsed power applications because of the advantages of inductive energy storage over more conventional capacitive energy storage, which include: higher energy density, decreased size and cost, and the possibility to scale to higher energy and power.

Various POS configurations have been used in different experiments<sup>1</sup> to conduct currents from 10's of kA to several MA, with conduction times from 10's of ns to over 1  $\mu$ s. It is suspected that different physical processes determine the conduction limit and subsequent opening, depending on the POS parameters and driving current waveform. The experimental evidence for different conduction mechanisms is limited by a lack of precise measurements of the plasma parameters during actual POS experiments. As a result, there is a need for POS scaling experiments that include measurements of the plasma density with adequate time and spatial resolution to distinguish different conduction mechanisms.

In this paper, measurements are reported that quantify the conduction scaling for the Hawk POS with conduction currents from 300–800 kA and conduction times from 0.3–

1.9  $\mu$ s. The key element of these experiments is an *in situ* density measurement during shots using a He-Ne laser interferometer. As will be shown, the conduction limits agree with simple scaling relations derived from physical models. Within some limits, these scaling relations are applicable to a large number of high current, long conduction time POS experiments.

The rest of this paper is organized as follows. The Hawk POS experiment is described and the results of density measurements during shots are summarized. Examples of conduction limits based on theory are discussed, and scaling relations are derived. The Hawk data are then compared with these scaling relations.

## II. HAWK CONDUCTION SCALING EXPERIMENT

Hawk consists of a high current, 1- $\mu$ F Marx bank<sup>4</sup> with a typical output voltage of 640 kV and stored energy of 0.23 MJ at 80-kV charging voltage. The discharge of the Marx into the circuit inductance, shorted by a POS, results in a sinusoidal current with 750 kA peak amplitude and 1.2  $\mu$ s quarter period. When the POS opens, current is transferred in 20 ns to an electron-beam diode load, with resulting load powers as high as 0.7 TW (450 kA, 1.6 MV).<sup>5</sup> A review of POS research on Hawk, including preliminary conduction scaling results, has been published previously.<sup>2</sup>

A sketch of the POS conduction scaling experiment on Hawk is shown in Fig. 1. The POS plasma is injected between the coaxial conductors using 18 flashboards, each driven by a capacitor circuit generating about 35 kA in 0.6  $\mu$ s. The Hawk current is measured on the generator ( $I_G$ ) and load ( $I_L$ ) sides of the POS. A short circuit load is used to simplify the measurement of conduction current, to minimize debris, and to prevent high voltages that could adversely affect the density measurements.

A He-Ne laser interferometer<sup>6</sup> is used to measure the line-integrated electron density in the Hawk POS during shots. Two lines-of-sight are illustrated in Fig. 1. The axial line-of sight is used to measure the line-density at a selected

<sup>a)</sup>Permanent address: JAYCOR, Vienna, Virginia 22180.

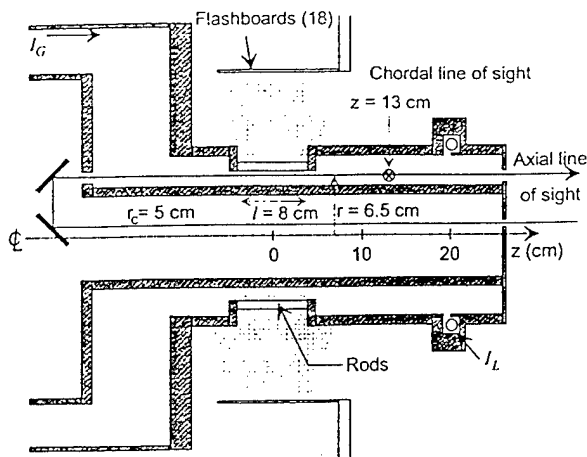


FIG. 1. POS experiment on Hawk. Plasma is injected between the coaxial conductors using flashboard plasma sources. The current is measured on the generator ( $I_G$ ) and load ( $I_L$ ) sides of the POS. The plasma density is diagnosed using axial and chordal lines-of-sight using a He-Ne laser interferometer.

radial location (for example,  $r = 6.5$  cm in Fig. 1). The length of the plasma injection aperture ( $l = 8$  cm in Fig. 1) is used to convert the line-integrated density to more conventional density units ( $\text{cm}^{-3}$ ). The precision of the density measurement using the axial line-of-sight is about  $\pm 1 \times 10^{14} \text{ cm}^{-3}$ .

Figure 2 shows data from three Hawk shots using an  $r = 5$  cm center conductor using the axial line-of-sight located at  $r = 6.5$  cm, 1.5 cm from the center conductor and 0.5 cm from the outer conductor in the POS region (as shown in Fig. 1). The plasma density was varied by changing the time delay between firing the plasma sources and the Hawk generator. A typical generator current,  $I_G$ , and three load currents,  $I_{L1}$ ,  $I_{L2}$ , and  $I_{L3}$  are shown in Fig. 2a; the corresponding densities,  $n_1$ ,  $n_2$ , and  $n_3$  are shown in Fig. 2b. For the time delay of shot 2, the density measured firing only the flashboards,  $n_{FB}$ , is shown. For all three cases, the density peaks during conduction, then decreases to a low value prior to opening. The conduction current and conduction time increase as the peak density increases.

For about the first half of the conduction time, the density measured during a Hawk shot is equal to the density measured firing the plasma sources alone (compare  $n_2$  and  $n_{FB}$  in Fig. 2b for  $t < 0.4 \mu\text{s}$ ). The density then becomes smaller than the source-only density (compare  $n_2$  and  $n_{FB}$  in Fig. 2b for  $0.4 < t < 0.8 \mu\text{s}$ ), sometimes exhibiting a double-humped structure ( $n_3$  in Fig. 2b). The density decreases rapidly prior to the onset of the load current, becoming relatively small at the time opening begins.<sup>7</sup> The plasma source density is generally an increasing function of time for the time range of interest. The decrease in density during conduction shown in Fig. 2b is typical of all Hawk data discussed in this paper.

Table I lists the parameters of the five different configurations used in this study. The parameters varied include the center conductor (cathode) radius,  $r_c$ , the plasma length,  $l$ , and Marx charge voltage,  $V$ . For all cases, the radial separa-

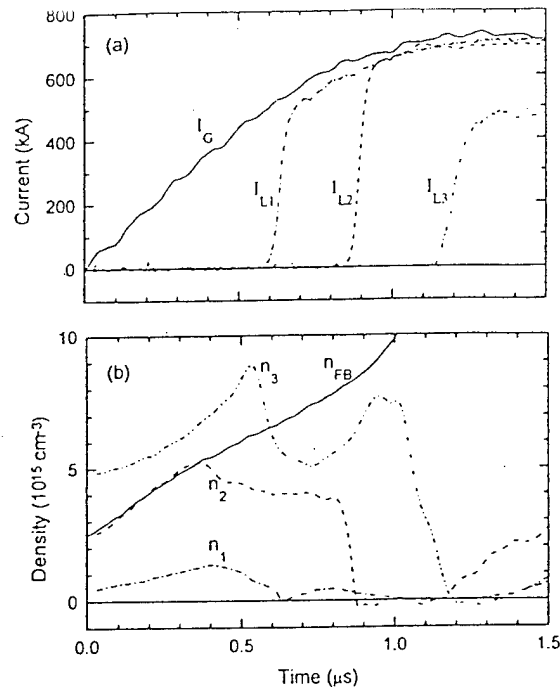


FIG. 2. Current and density waveforms for three Hawk shots with parameters of case 1 in Table I. (a) Generator ( $I_G$ ) and load currents ( $I_{L1}$ ,  $I_{L2}$ ,  $I_{L3}$ ) for three different plasma injection time delays, showing increased conduction time (onset of load current) and conduction current ( $I_G - I_L$ ) as the time delay increases. (b) Electron densities ( $n_1$ ,  $n_2$ ,  $n_3$ ) measured using the axial line-of-sight for the three shots in (a). The density measurements were made 1.5 cm from the surface of the  $r = 5$  cm center conductor. The density measured firing the plasma sources alone ( $n_{FB}$ ) is shown for the time delay of shot 2.

tion between the inner and outer conductors in the POS region was 2 cm. Eighteen flashboard plasma sources were used except for case 5, where 9 flashboards were used. The radial location of the density measurement,  $r$ , was chosen based on a radial scan of the density for each value of  $r_c$ ; this shot-to-shot density scan was performed for a single conduction time (in the range 0.9–1.1  $\mu\text{s}$ ) for each of the three cathode radii. At the time of opening, the density has a minimum at the radius indicated in Table I, and increases toward both conductors. Presumably, opening occurs in this low-density region. The same measurement location was used at other conduction times, charging voltages and lengths, with the assumption that opening occurs close to the same radial location. This assumption needs to be checked in the future using a multi-chord interferometer technique to measure the density distribution on a single shot.

TABLE I. POS configurations for conduction scaling experiments.

Case #	$r_c$ (cm)	$l$ (cm)	$V$ (kV)	$r$ (cm)	$n_{FB}$
1	5	8	80	6.5	18
2	5	8	50	6.5	18
3	5	4	80	6.5	18
4	2.5	8	80	4	18
5	11.8	8	80	12.7	9



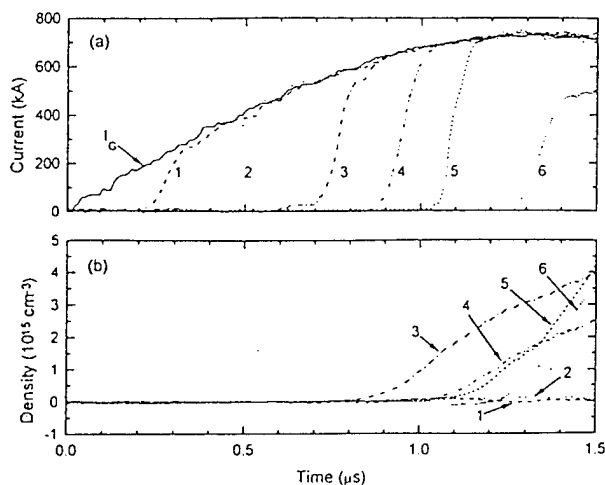


FIG. 3. Current and density measurements for six Hawk shots with parameters of case 1 in Table I. (a) Load currents (1–6) for six shots with conduction times varying from 0.2–1.3  $\mu s$ . (b) Chordally-integrated densities (1–6) at  $z=13$  cm (9 cm from the load edge of the plasma injection aperture).

The chordal line-of-sight shown in Fig. 1 is used to diagnose plasma translation from the plasma injection region toward the load. Sample data are shown in Fig. 3 for six shots with conduction times of 0.2–1.3  $\mu s$ , and the POS parameters corresponding to case 1 in Table I. In Fig. 3a, currents are shown for different plasma timings; Fig. 3b shows the corresponding densities, averaged over the 11-cm chord length. The density is measured at  $z=13$  cm (9 cm from the edge of the plasma injection aperture), 1 cm from the center conductor. The data indicate that opening occurs before plasma is displaced to this location for conduction times less than 1.1  $\mu s$ . This situation can be contrasted with a plasma flow switch,<sup>8</sup> where switching occurs when a plasma armature moves past a gap or into an imploding load. A large plasma density, comparable to the density in the POS region, appears at this location *after* opening for shots 3–6, that is, for conduction currents greater than 500 kA. For conduction currents less than 500 kA (shots 1 and 2), the measured densities at  $z=13$  cm are negligible (much smaller than the density in the POS region during conduction). This phenomenon may be indicative of different conduction mechanisms, discussed below. The downstream plasma is moving with an axial velocity of about 30 cm/ $\mu s$ , a value consistent with  $J \times B$  acceleration of a  $C^{++}$  plasma with the measured line density.

### III. THEORETICAL CONDUCTION LIMITS

POS conduction limits can be separated into three general categories based on different physical phenomena that precede opening: gap formation at switch electrodes, magnetic field penetration through the plasma, and plasma distortion by  $J \times B$  forces. Each conduction limit predicts different dependencies on POS parameters and driving current waveform. For a given set of parameters, one conduction limit could dominate the others. This condition defines different conduction regimes for the POS. Scaling relations are

derived for representative conduction-limiting mechanisms in each category, and special cases are compared to separate the conduction regimes for generic, coaxial POS experiments, for which Hawk is one example.

For all cases discussed below, current (current density) is expressed in units of A ( $A/cm^2$ ), lengths in units of cm, time in units of seconds, mass in units of grams, and the proton charge  $e=1.6 \times 10^{-19}$  C.

#### A. Gap formation at an electrode: Bipolar and modified bipolar

One of the first conduction limits hypothesized for a POS was space-charge-limited bipolar conduction.<sup>9</sup> The cathode electrode is assumed to be a space-charge-limited electron emitter, and ions are drawn from the POS plasma, with the ratio of electron and ion current densities determined by the bipolar relation,  $J_e/J_i = \sqrt{M/Zm}$ , where  $J_e$  and  $m$  ( $J_i$  and  $M$ ) are the electron (ion) current density and mass, and  $Z$  is the ion charge state. For the  $C^{++}$  ions typical of flashboard plasmas,<sup>10</sup>  $J_e/J_i = 105$ . For ions flowing into the cathode with velocity  $v$ , the steady state ion current density,  $J_i$ , is at most  $nev$ , where  $n$  is the plasma electron density and quasineutrality is assumed. If the ion current density exceeds this value, ions must be accelerated out of the plasma, resulting in plasma erosion and the onset of the opening phase. This bipolar conduction limit,  $I_{BP}$ , occurs at a current level determined by the maximum ion current that can be conducted without erosion:

$$I_{BP} = \sqrt{M/Zm}(2\pi r l)nev \quad (1)$$

where  $r$  is the cathode radius and  $l$  is the plasma length. This conduction limit, in principle, is independent of the conduction time.

The scaling in Eq. (1) was compared<sup>11</sup> with experiments using measurements of the plasma density (using microwave interferometry) in short-conduction-time ( $\sim 50$  ns) POS configurations used on the Gamble I<sup>12</sup> and Particle Beam Fusion Accelerator (PBFA) II<sup>13</sup> generators. The conduction current in both the Gamble I POS and the PBFA II "Magnetically Injected Plasma (MIP)"<sup>14</sup> experiments were found to be roughly proportional to the plasma density measured firing the sources alone, and the magnitude of the current agreed with Eq. (1) assuming the plasma composition was mostly  $C^{++}$  and the average ion velocity was 3.6 cm/ $\mu s$ , reasonable values based on the limited measurements available. Other Gamble I experiments<sup>15</sup> showed that for constant  $nl$ , but changing  $n$  and  $l$  by a factor of three, resulted in the same conduction current, supporting the linear dependence on  $l$ . These experiments did not test the predicted scaling with  $v$  or  $M/Z$ , or the independence of  $I_{BP}$  on conduction time.

Another conduction limit, called modified bipolar (MBP) is derived<sup>16</sup> by calculating the sheath size during conduction and comparing this to the electron orbit. When the electron orbit is comparable to the sheath size, it is expected that an enhanced erosion opening will begin. This condition can occur before the bipolar current limit is reached. An analysis<sup>17</sup> of this condition leads to the approximate current limit:

$I_{MBP}$  is (relatively) independent of length, velocity, and conduction time.<sup>16</sup>

Experimental evidence for the MBP current limit include  $I(n)$  data from Falcon<sup>16</sup> and Eyess,<sup>17</sup> with densities measured in a separate vacuum chamber that show  $\sqrt{n}$  scaling and weak scaling with length, and Omni experiments<sup>18</sup> that show<sup>16,17</sup> similar dependencies on  $n$  and  $l$ .

## B. Magnetic field penetration: Electromagnetohydrodynamics

Another proposed conduction limit<sup>19</sup> is based on magnetic field penetration by the Hall effect for time scales shorter than  $\omega_{pi}^{-1}$ . A penetration speed based on electromagnetohydrodynamic (EMH) equations can be derived assuming ion motion is negligible and that radial current is conducted by electrons executing  $E \times B$  drifts. This situation has been analyzed<sup>20</sup> for the special case of a current ramp ( $dl/dt = \text{constant}$ ), and a negative polarity center conductor, appropriate for the Hawk experiments discussed here. The application of this formalism to the Hawk experiment (given in the Appendix) results in the axial penetration velocity,  $u$ :

$$u = \frac{3}{8} \times \frac{I}{2\pi enr} \left[ \frac{1}{n} \frac{dn}{dr} + \frac{2}{r} \right], \quad (3)$$

where  $r$  is the radius where opening occurs. The first term in brackets is the penetration speed related to radial density gradients, and the second term is related to the  $l/r$  magnetic field gradient. The initial density distribution in the 2 cm radial POS gap in Hawk has  $dn/dr < 0$  within 1 cm from the center conductor, and  $dn/dr \approx 0$  within 1 cm from the outer conductor.<sup>7</sup> The fastest penetration speed in Hawk will occur, according to Eq. (3), where  $dn/dr \approx 0$  and  $r$  is minimum.

For comparison with POS conduction scaling experiments, opening is assumed to begin when the field penetrates to the load side of the plasma. A simple EMH conduction limit for the case  $dn/dr \approx 0$  (appropriate for Hawk) is found by setting  $\int u dt = l$ , and setting  $dn/dr = 0$  in Eq. (3). The resulting conduction limit is:

$$\int I_{EMH} dt = \frac{8}{3} \pi e r^2 l n. \quad (4)$$

Experimental evidence for the EMH conduction limit includes experiments<sup>21</sup> where varying the number of plasma sources (and thereby the average density) and the current rise rate indicate that  $\int I dt \propto n$ , in agreement with the scaling predicted by Eq. (4), however, the plasma density was not measured.

## C. Plasma displacement by $J \times B$ forces: Magnetohydrodynamics

The MHD limit occurs when ion motion is not negligible and the plasma is displaced and distorted by  $J \times B$  forces, resulting in a low density region where opening can occur by an erosion mechanism. This "plasma thinning" can occur after the plasma center-of-mass is displaced to the load end

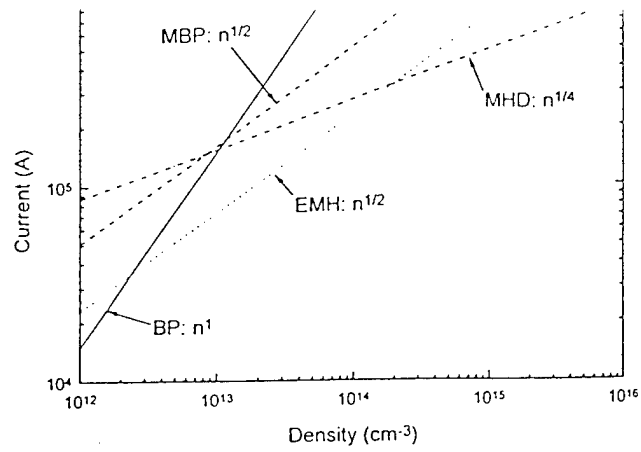


FIG. 4.  $I(n)$  scaling models for a linear ramp current and typical Hawk parameters:  $r=5$  cm,  $l=8$  cm,  $i=10^{12}$  A/s, and  $C^{++}$ . The four conduction scaling models are bipolar (BP), modified bipolar (MBP), electromagnetohydrodynamics (EMH) and magnetohydrodynamics (MHD). For a given density, the smallest current threshold determines the dominant conduction limit.

of the POS<sup>22</sup> (or equivalently, when a snowplow reaches the load end of the plasma).<sup>23</sup> This results in an MHD conduction limit:

$$\int \int I_{MHD}^2 dt^2 = \frac{100\pi r^2 l^2 M n}{Z}. \quad (5)$$

Previous evidence for MHD-limited conduction has been obtained in long conduction time (0.5–1  $\mu$ s) POS experiments, but without direct measurement of the plasma density, on generators at the Naval Research Laboratory,<sup>22</sup> generators at the Institute of High Current Electronics<sup>24,25</sup> and on the Advanced Concept Experiment (ACE) generators at Maxwell Laboratories, Inc.<sup>26</sup>

## D. Comparison of conduction limits for a linear current ramp

The BP, MBP, EMH and MHD conduction limits are easily compared for the special case of a linear current ramp:  $I(t) = \dot{I}t$ , where  $\dot{I}$  is constant. The conduction limits in Eqs. (1) and (3)–(5) (assuming  $C^{++}$  and  $v=3.6$  cm/ $\mu$ s) are then:

$$\begin{aligned} I_{BP} &= 3.80 \times 10^{-10} r l n, \\ I_{MBP} &= 1.02 \times 10^{-2} r n^{1/2}, \\ I_{EMH} &= 1.64 \times 10^{-9} r (\dot{I} l n)^{1/2}, \\ I_{MHD} &= 1.39 \times 10^{-5} (r^2 \dot{I}^2 n)^{1/4}. \end{aligned} \quad (6)$$

The conduction current limits are plotted as a function of  $n$  in Fig. 4 using parameters appropriate for a typical POS configuration on Hawk ( $r=5$  cm,  $l=8$  cm,  $\dot{I}=10^{12}$  A/s,  $C^{++}$ ). For a given density, the lowest current threshold would determine the conduction current. For the example in Fig. 4, the MHD limit would apply for currents greater than 350 kA, the EMH limit would apply for currents between 35 and 350 kA, and the BP limit would apply for currents less than 35 kA. The MBP limit would not be encountered at any

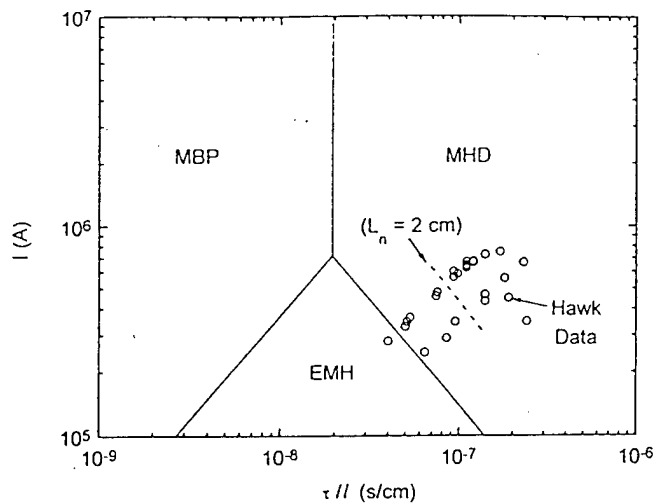


FIG. 5.  $I(\tau/l)$  diagram separating the MBP, EMH and MHD conduction regimes for a linear ramp current and a uniform,  $C^{++}$  plasma. In principle, this plot determines the dominant conduction mechanism for any coaxial POS experiment in negative polarity without prior knowledge of the plasma density or radial location of opening (assuming the bipolar conduction limit is excluded). The open symbols are Hawk data. The dashed line is the approximate boundary between EMH and MHD when the density gradient scale length is  $L_n = 2$  cm.

current level. (The Hawk current is sinusoidal, changing these current levels slightly. For a different generator or greatly different POS parameters, the BP or the MBP limit could be the dominant conduction limit.)

A more general diagram separating the MBP, EMH, and MHD conduction "regimes" can be derived using the relations in Eq. (6) to eliminate  $n$  and  $r$  (but still assuming  $C^{++}$ ). Setting  $I_{MBP} < I_{EMH}$  results in the condition  $I > 3.88 \times 10^{13} \tau/l$ , independent of  $r$  and  $n$ , where the conduction time,  $\tau$ , is related to the current derivative,  $\dot{I}$ , by  $\tau = I/\dot{I}$ . For values of  $I$  and  $\tau/l$  satisfying this inequality, the MBP limit would occur before the EMH limit. The EMH limit would occur before the MBP limit when  $I < 3.88 \times 10^{13} \tau/l$ . In a similar way, the condition for the MHD limit to occur before the MBP limit is found by setting  $I_{MHD} < I_{MBP}$ , resulting in  $\tau/l > 1.90 \times 10^{-8}$ , and the condition for the MHD limit to occur before the EMH limit is found by setting  $I_{MHD} < I_{EMH}$ , resulting in  $I \tau/l > 1.40 \times 10^{-2}$ . These three inequalities combine to separate the  $(I, \tau/l)$  space into the three regimes shown in Fig. 5. For example, the "MHD" region in Fig. 5 is the part of the  $(I, \tau/l)$  space where  $I_{MHD} < I_{MBP}$  and  $I_{MHD} < I_{EMH}$ . Since  $I$  and  $\tau/l$  are sufficient to specify the regime of operation it is possible, in principle, to determine the conduction regime for experiments where the density and the radial location of opening are not known. Data from Hawk are included in Fig. 5, showing that most of the data fall in the MHD regime, and some data are close to the EMH regime. (The dashed line is an empirical division between MHD and non-MHD scaling from the Hawk experiments that will be discussed below.) These conduction regimes are hypothetical, and have not been verified or refuted by appropriate experiments. The Hawk experiments described here are a start toward this goal.

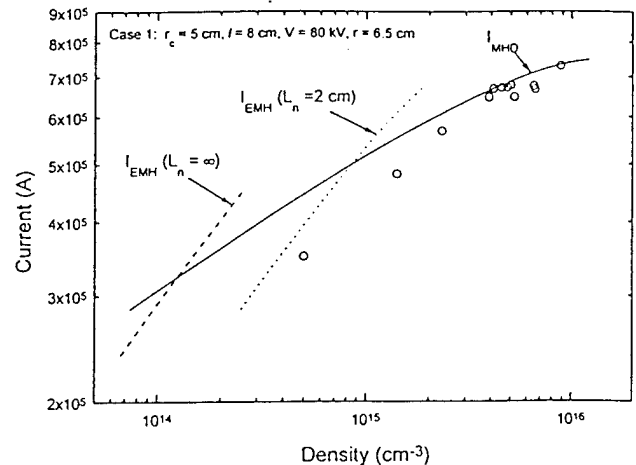


FIG. 6. Hawk data (open symbols) for case 1 compared with MHD (solid line) and EMH (dashed lines) scaling relations.

#### IV. COMPARISON OF EXPERIMENT AND THEORY

This section compares Hawk data with the scaling relations above. For scaling purposes, the *initial* density is not an appropriate parameter because plasma from the flashboards continues to enter the switch region during part of the conduction time (see Fig. 2). Instead, the maximum density during conduction is used as a scaling parameter for comparison with the scaling laws presented above [Eqs. (1)-(5)]. It is assumed that if the plasma sources produced a constant density equal to this maximum value, then switching would occur at approximately the same point during the current waveform. This approximation is useful to explain the results of experiments, but this maximum density is not known *a priori* for a given shot. A snowplow calculation that includes the time dependence of the density will be presented as one technique to predict the conduction limit from *a priori* density measurements.

For the five cases listed in Table I, the density was varied by changing the plasma delay time. For each case, the  $I(n)$  data are compared with the EMH and MHD scaling equations given by Eqs. (4) and (5), where the sinusoidal Hawk current waveform is used to evaluate the conduction limit instead of the linear ramp current used above. The BP limit is not expected to be relevant for Hawk at currents greater than 35 kA, based on Fig. 4, and the MBP limit should not apply for any of the Hawk data shown in Fig. 5.

The Hawk data for case 1 are compared with the MHD and EMH scaling relations in Fig. 6. The data follow the MHD curve at the highest currents and densities. At lower currents, the measured current is well below the MHD limit, approaching the EMH slope as the current decreases. Two EMH curves are shown with different density gradient scale lengths,  $L_n = n/(dn/dr)$ . The curve labeled " $L_n = \infty$ " corresponds to  $dn/dr = 0$  assumed in Eq. (4). The curve labeled " $L_n = 2$  cm" is calculated using a faster penetration speed corresponding to a density gradient scale length equal to the radial gap in the POS [Eq. (2)]. The EMH curve with the 2-cm density gradient scale length is a better match to the data. It should be noted, however, that this density gradient is

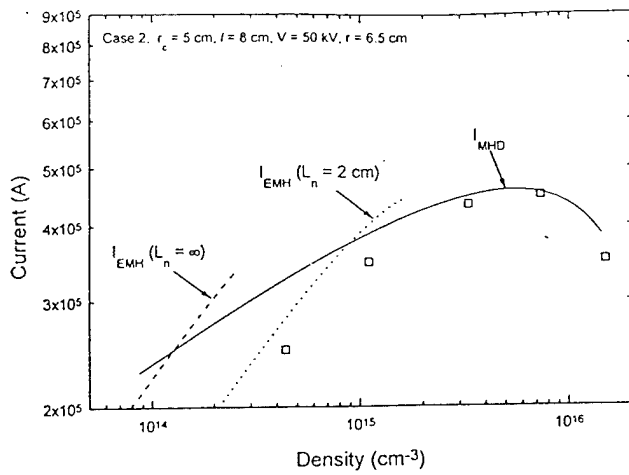


FIG. 7. Hawk data (open symbols) for case 2 compared with MHD (solid line) and EMH (dashed lines) scaling relations.

not present in Hawk in the *injected* plasma distribution. It may be, however, that density gradients result from  $J \times B$  distortion of the plasma during conduction. Direct measurement of the plasma distribution during shots in the non-MHD regime will be a subject of future work. The comparison in Fig. 6 shows that the Hawk current follows MHD scaling ( $I \propto n^{1/4}$ ) for currents greater than about 500 kA and densities greater than about  $10^{15} \text{ cm}^{-3}$ , and a different scaling for smaller currents and densities. EMH scaling ( $I \propto n^{1/2}$ ) may account for the  $<500 \text{ kA}$  data if the penetration speed is increased using a density scale length equal to the radial POS gap size.

For case 2, the current rise rate was reduced, relative to case 1, by decreasing the charge voltage of the Marx from 80 to 50 kV. The conduction scaling data are compared with theory in Fig. 7. The data agree with the MHD scaling for densities greater than  $10^{15} \text{ cm}^{-3}$ , and follow the modified EMH scaling, i.e., assuming an increased penetration speed.

For case 3, the plasma length was halved, relative to case 1, by masking the generator half of the plasma injection region. The density was computed using  $l=4 \text{ cm}$  instead of  $l=8 \text{ cm}$  used in all other cases. The comparison of experiment and theory in Fig. 8 show a similar trend; the data follow MHD scaling for densities greater than  $2 \times 10^{15} \text{ cm}^{-3}$  and a modified EMH curve for smaller densities.

For case 4, the center conductor radius was reduced from 5 cm to 2.5 cm. The data compare well with the MHD limit, as shown in Fig. 9. These data do not show evidence of EMH scaling.

For case 5, the center conductor radius was increased to 11.8 cm. The number of flashboards was reduced from 18 to 9 to reduce the density at a given time delay. The comparison of experiment and theory is shown in Fig. 10. The data agree with MHD scaling for densities greater than  $6 \times 10^{14} \text{ cm}^{-3}$  and follow the modified EMH scaling for lower densities.

In general, the Hawk data agree with MHD scaling for densities greater than about  $10^{15} \text{ cm}^{-3}$  and follow a different density scaling for lower densities, similar to EMH scaling but with a penetration speed greater than derived from the

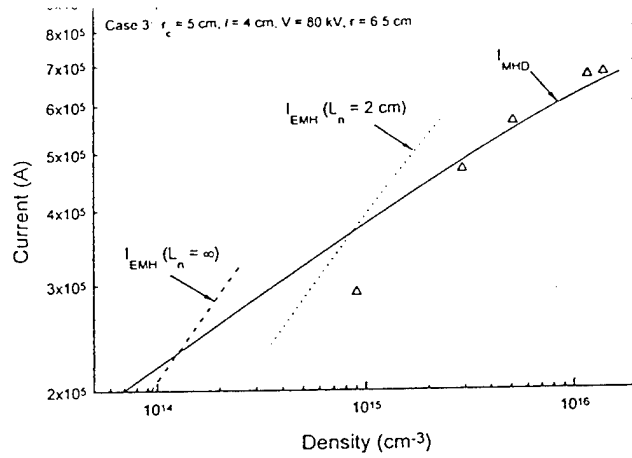


FIG. 8. Hawk data (open symbols) for case 3 compared with MHD (solid line) and EMH (dashed lines) scaling relations.

magnetic field gradient alone. The required increase in penetration speed corresponds to a density gradient scale length roughly equal to the radial electrode gap in the POS. The positive density gradients ( $dn/dr > 0$ ) required to explain this effect may develop during conduction, increasing the penetration speed according to Eq. (3). The observed dependencies on current rise rate (Fig. 7) and plasma length (Fig. 8) are counter to the predicted conduction scaling for the BP and MBP limits, justifying their exclusion in Figs. 7–10.

The downstream density measurements, shown in Fig. 3, are indicative of the different physical manifestations expected of the MHD and non-MHD conduction mechanisms. In the EMH limit, switching occurs before the plasma is translated significantly. Evidently, plasma motion in the axial direction is negligible compared with radial motion for case 1 parameters and  $I < 500 \text{ kA}$  (see traces 1 and 2 in Fig. 3b). In the MHD-dominated case,  $I > 500 \text{ kA}$ , the plasma center-of-mass is translated (about  $l/2$ ) during conduction. The plasma gains axial momentum, and eventually flows downstream (traces 3–6 in Fig. 3b). The division between the

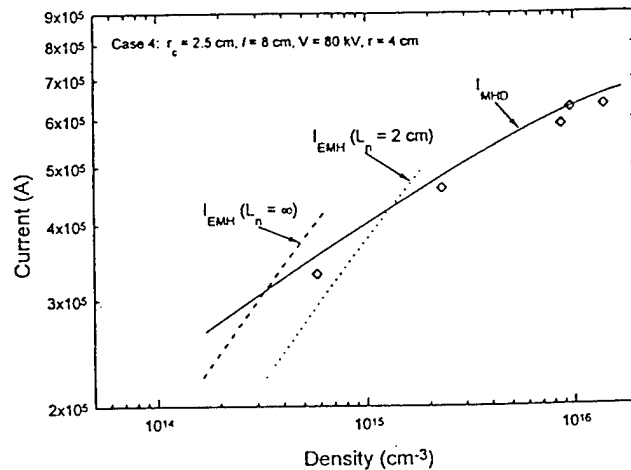


FIG. 9. Hawk data (open symbols) for case 4 compared with MHD (solid line) and EMH (dashed lines) scaling relations.

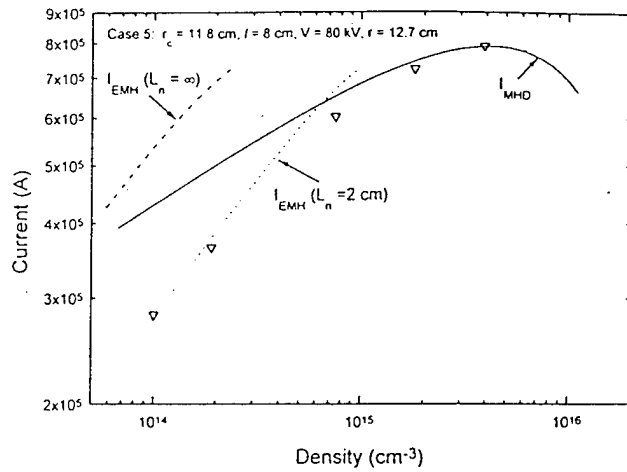


FIG. 10. Hawk data (open symbols) for case 5 compared with MHD (solid line) and EMH (dashed lines) scaling relations.

regimes in Fig. 3 ( $I = 500$  kA) agrees with the departure in the scaling results shown in Fig. 6, further evidence that different conduction mechanisms are related to the observed plasma displacement.

#### A. Snowplow model

The data in Figs. 6–10 show that the MHD limit [Eq. (5)] is a good predictor of the conduction current for Hawk, for currents where the MHD limit dominates the EMH limit. This scaling is based on the peak density during conduction, which in general is unknown *a priori*. In actual experiments (Hawk being one example) the injected plasma density is usually a function of time, and the maximum value during conduction is different from the measured density without pulsed power.

One way to account for the time dependence of the plasma source density for the case of MHD-limited conduction is to use a modified snowplow model.<sup>27</sup> In this model, the current is assumed to flow in a narrow sheet that sweeps up plasma as the sheet progresses axially through the switch region. The magnetic field behind the snowplow is assumed to prevent plasma from entering this region from outside the switch region, but not to affect the density time dependence in the undisturbed region in front of the snowplow. The equation of motion for the snowplow is:

$$F = \frac{d}{dt} \left( M_{sp} \frac{dX_{sp}}{dt} \right), \quad (7)$$

where  $M_{sp}$  is the snowplow mass and  $X_{sp}$  is the snowplow axial location. The equation for the snowplow mass is:

$$\frac{dM_{sp}}{dt} = \frac{2\pi r \Delta r M_i}{Z} n(t) \frac{dX_{sp}}{dt}, \quad (8)$$

where  $\Delta r$  is a small radial section of the snowplow and  $n(t)$  is the time-dependent density in the undisturbed region in front of the snowplow. Substituting the magnetic force  $F = 2\pi r \Delta r (B^2/8\pi)$  into Eq. (7), using  $B(G) = I(A)/5r(\text{cm})$  and eliminating  $M_{sp}$  using Eq. (8) gives an equation for the snowplow position:

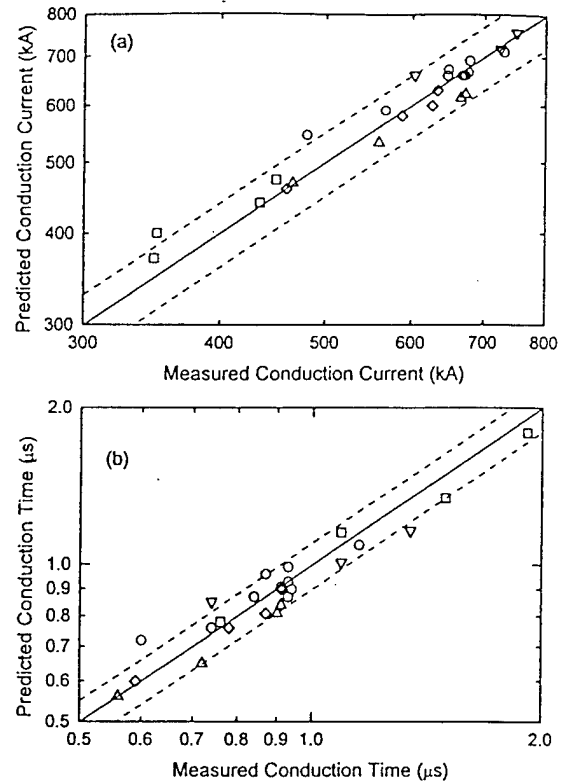


FIG. 11. Comparison of measured and predicted (a) conduction currents and (b) conduction times using a snowplow model. The open symbols correspond to the data points in Figs. 6–10 that follow the MHD scaling curves. The dashed lines are  $\pm 10\%$  deviations from perfect agreement.

$$\frac{dX_{sp}}{dt} = \frac{1}{10r} \sqrt{\frac{Z}{\pi M_i n}} \frac{d}{dt} \left\{ \int dt \left( n \int I^2 dt \right) \right\}^{1/2}. \quad (9)$$

The condition for the end of conduction is  $X_{sp} = l$ , analogous to the more general MHD limit of Eq. (5), where the center-of-mass displacement is  $l/2$ .

With these assumptions, the density measured in Hawk by firing the flashboards alone can be used in Eq. (9) to predict the end of conduction, assuming a  $C^{++}$  plasma. Results of these predictions are compared with the measured conduction currents in Fig. 11a for all of the shots in Figs. 6–10 where the MHD limit is expected to apply. The predicted and measured conduction times are compared in Fig. 11b. The dashed lines in Figs. 11a and 11b are  $\pm 10\%$  discrepancies from perfect agreement. Most of the data fall between these lines. Because the Hawk current is sinusoidal, the current and time are not proportional. The two points at 1.5 and 1.9  $\mu\text{s}$  measured conduction time in Fig. 11b show that the snowplow technique predicts the conduction limit even for conduction well past the peak of the current waveform. For the non-MHD data (not shown in Fig. 11) the measured currents and conduction times are much smaller than the snowplow predictions.

Some Hawk data have been successfully simulated with a two-dimensional (2D) snowplow model<sup>26</sup> and 2D fluid codes.<sup>28</sup> These techniques have promise to predict the radial and axial plasma distributions and to generate the conditions that exist at the start of the opening phase. Particle codes

ing simulations of these kinds with diagnostics of the plasma dynamics during shots should lead to improved understanding of POS physics.

## V. CONCLUSIONS

The scaling of conduction current and conduction time with POS parameters has been determined for the Hawk experiment, including scaling with density, radius, length and current rise rate. For high currents, conduction ends at a point determined by hydrodynamic displacement and distortion of the switch plasma, corresponding to a plasma center-of-mass displacement in the axial direction equal to roughly half the switch length. Measurements indicate that the line-integrated density decreases at a location between the switch electrodes prior to the onset of the opening phase. For these high current cases, the conduction current scaling follows a simple MHD scaling relation [Eq. (5)], where the conduction current scales as  $(r^2 l^2 j^2 n)^{1/4}$ . A snowplow model can be used to predict the conduction limit to account for a time-varying plasma source density.

For smaller currents, conduction ends at a lower current than predicted by the MHD scaling relation. For the Hawk experiments described here, the departure from MHD scaling may be evidence of EMH field penetration to the load side of the plasma. The EMH scaling derived using a penetration speed corresponding to the magnetic field gradient does not match the experimental data; an increased penetration speed (using a density gradient scale length of 2 cm) is needed to better match the Hawk experiment, except for the case with the smallest center conductor radius. Experimentally, POS experiments in this non-MHD regime exhibit very little plasma translation toward the load after switching, in contrast to the MHD case, where density of a similar magnitude to that in the switch region eventually moves many cm downstream after opening. The experimental data for this non-MHD regime on Hawk is far from complete; this is a subject for future research work on Hawk.

These results substantiate the existence of different conduction mechanisms (in particular the MHD, and possibly EMH regimes) for POSs, and suggest that the simple conduction scaling relations [Eqs. (5) and (4)] will apply to other POS experiments with parameters in the corresponding part of  $(I, \tau/l)$  space in Fig. 5. The MHD regime, in particular, is predicted to dominate the other mechanisms for high conduction currents and conduction times; this is a major area of interest for POS applications. Much of the scaling in the  $(I, \tau/l)$  space in Fig. 5 remains to be explored, perhaps by using similar diagnostics as used on Hawk on other POS experiments.

## ACKNOWLEDGMENTS

The authors are pleased to acknowledge R. Fisher for his expert assistance with the Hawk experiments. We are also grateful to R. DeVore for suggesting the derivation of the EMH penetration speed in the Appendix.

This work was supported by the Defense Nuclear Agency.

## SPEED

An EMH magnetic field penetration velocity is derived for comparison with Hawk experiments. This derivation follows previously published work,<sup>20</sup> and makes use of a solution first presented to us by A. Fruchtman.

Faraday's law and Ampère's law are combined, assuming an Ohm's law with zero resistivity, zero plasma flow velocity and zero pressure gradient:

$$E = \frac{J \times B}{en},$$

resulting in a Burgers equation for the magnetic field:

$$\frac{\partial B}{\partial t} = \frac{cB}{4\pi ne} \left( \frac{2}{r} + \frac{1}{n} \frac{\partial n}{\partial r} \right) \frac{\partial B}{\partial z} = aB \frac{\partial B}{\partial z}.$$

Here, cgs units are used and

$$a = \frac{c}{4\pi ne} \left( \frac{2}{r} + \frac{1}{n} \frac{\partial n}{\partial r} \right).$$

The location of a shock front,  $z_f$ , propagating in the axial direction can be found by substituting the above into the integral equation:

$$\begin{aligned} \frac{\partial}{\partial t} \int_{z_f-\epsilon}^{z_f+\epsilon} B(z,t) dz &= \int_{z_f-\epsilon}^{z_f+\epsilon} \frac{\partial B}{\partial t} dz + \dot{z}_f B(z_f+\epsilon, t) \\ &\quad - \dot{z}_f B(z_f-\epsilon, t). \end{aligned}$$

Substituting for  $\partial B/\partial t$ , taking the limit  $\epsilon \rightarrow 0$ , and assuming  $B(z_f+\epsilon, t) = 0$  results in an equation for the penetration speed:

$$\dot{z}_f = -\frac{a}{2} B(z_f-\epsilon, t).$$

(The penetration speed is positive because  $B$  is negative in negative polarity.)

For the special case of a linearly rising magnetic field,  $B(z=0, t) = \alpha t$ , a solution of the Burgers equation is:

$$B(z, t) = \frac{\alpha}{2} \left[ t + \left( t^2 + \frac{4z}{a\alpha} \right)^{1/2} \right], \quad 0 \leq z \leq z_f.$$

This solution can be substituted in the equation for  $z_f$  to give a differential equation for the shock front location:

$$\dot{z}_f = -\frac{a}{2} B(z_f, t) = -\frac{a\alpha}{4} \left[ t + \left( t^2 + \frac{4z_f}{a\alpha} \right)^{1/2} \right].$$

Choosing the particular solution  $z_f = kt^2$ , then  $\dot{z}_f = \frac{3}{8} \times a\alpha t = -\frac{3}{8} aB(0, t)$ . This is the penetration speed in Eq. (3).

<sup>1</sup>G. Cooperstein and P. F. Ottinger, Guest Editorial, IEEE Trans. Plasma Sci. PS-15, 629 (1987) and references therein.

<sup>2</sup>R. J. Comisso, P. J. Goodrich, J. M. Grossmann, D. D. Hinshelwood, P. F. Ottinger, and B. V. Weber, Phys. Fluids B 4, 2368 (1992).

<sup>3</sup>D. G. Colombant and B. V. Weber, IEEE Trans. Plasma Sci. PS-15, 741 (1987).

<sup>4</sup>P. Sincerny, D. Drury, J. Goyer, G. James, M. Krishnan, J. Levine, C. McDonald, and I. Roth, 7th IEEE International Pulsed Power Conference, Monterey, CA, edited by B. H. Bernstein and R. White (Institute of Elec-

- trical and Electronic Engineers, Piscataway, NJ, 1989), p. 275, IEEE Catalog number: 89CH2678-2.
- <sup>5</sup>See National Technical Information Service Document No. PB92-206168 (P. J. Goodrich, R. C. Fisher, D. D. Hinshelwood, J. R. Boller, R. J. Comisso, and B. V. Weber, *9th International Conference on High-Power Particle Beams*, p. 609). Copies may be ordered from the National Technical Information Service, Springfield, Virginia 22161.
- <sup>6</sup>B. V. Weber and D. D. Hinshelwood, *Rev. Sci. Instrum.* **63**, 5199 (1992).
- <sup>7</sup>D. D. Hinshelwood, B. V. Weber, J. M. Grossmann, and R. J. Comisso, *Phys. Rev. Lett.* **68**, 3567 (1992).
- <sup>8</sup>P. J. Turchi, M. L. Alme, G. Bird, C. N. Boyer, S. K. Coffey, D. Conte, J. F. Davis III, and S. W. Seiler, *IEEE Trans. Plasma Sci.* **PS-15**, 747 (1987).
- <sup>9</sup>C. W. Mendel, Jr., and S. A. Goldstein, *J. Appl. Phys.* **48**, 1004 (1977); P. F. Ottinger, S. A. Goldstein, and R. A. Meger, *J. Appl. Phys.* **56**, 774 (1984).
- <sup>10</sup>A. B-A. Baranga, N. Qi, and D. A. Hammer, *IEEE Trans. Plasma Sci.* **PS-20**, 562 (1992).
- <sup>11</sup>B. V. Weber, R. J. Comisso, P. J. Goodrich, J. M. Grossmann, D. D. Hinshelwood, J. C. Kellogg, and P. F. Ottinger, *IEEE Trans. Plasma Sci.* **PS-19**, 757 (1991).
- <sup>12</sup>G. Cooperstein, J. J. Condon, and J. R. Boller, *J. Vac. Sci. and Technology*, **10**, 961 (1973).
- <sup>13</sup>B. N. Turman, T. H. Martin, E. L. Neau, D. R. Humphreys, D. D. Bloomquist, D. L. Cook, S. A. Goldstein, L. X. Schneider, D. H. McDaniel, J. M. Wilson, R. A. Hamil, G. W. Barr, and J. P. VanDevender, *5th IEEE International Pulsed Power Conference*, Arlington, VA, edited by M. F. Rose and P. J. Turchi (Institute of Electrical and Electronic Engineers, Piscataway, NJ, 1985), p. 155, IEEE Catalog No. 85C2121-2.
- <sup>14</sup>G. E. Rochau, D. H. McDaniel, C. W. Mendel, M. A. Sweeney, W. B. S. Moore, G. R. Mowrer, W. W. Simpson, and D. M. Zagar, *7th IEEE International Pulsed Power Conference*, Monterey, CA, edited by B. H. Bernstein and R. White (Institute of Electrical and Electronic Engineers, Piscataway, NJ, 1989), p. 251, IEEE Catalog No. 89CH2678-2.
- <sup>15</sup>B. V. Weber, R. J. Comisso, G. Cooperstein, J. M. Grossmann, D. D. Hinshelwood, D. Mosher, J. M. Neri, P. F. Ottinger, and S. J. Stephanakis, *IEEE Trans. Plasma Sci.* **PS-15**, 635 (1987).
- <sup>16</sup>J. R. Goyer, *IEEE Trans. Plasma Sci.* **PS-19**, 920 (1991).
- <sup>17</sup>J. R. Goyer, *8th IEEE International Pulsed Power Conference*, San Diego, CA, edited by R. White and K. Prestwich (Institute of Electrical and Electronic Engineers, Piscataway, NJ, 1991), p. 520, IEEE Catalog No. 91CH3052-8.
- <sup>18</sup>J. B. Greenly, G. D. Rondeau, H. T. Sheldon, and P. L. Dreike, *IEEE Trans. Plasma Sci.* **PS-15**, 735 (1987).
- <sup>19</sup>A. S. Kingssep, Yu. V. Mokhov, and K. V. Chukbar, *Sov. J. Plasma Phys.* **10**, 495 (1984).
- <sup>20</sup>K. Gomberoff and A. Fruchtmann, *Phys. Fluids B* **5**, 2841 (1993).
- <sup>21</sup>G. I. Dolgachev, L. P. Zakatov, and A. G. Ushakov, *Sov. Fis. Plazmy* **17**, 1171 (1991).
- <sup>22</sup>B. V. Weber, R. J. Comisso, P. J. Goodrich, J. M. Grossmann, D. D. Hinshelwood, J. C. Kellogg, and P. F. Ottinger, *IEEE Trans. Plasma Sci.* **PS-19**, 757 (1991).
- <sup>23</sup>W. Rix, D. Parks, J. Shannon, J. Thompson, and E. Waisman, *IEEE Trans. Plasma Sci.* **PS-19**, 607 (1991).
- <sup>24</sup>See National Technical Information Service Document No. PB92-206168 (A. A. Kim and D. V. Getman, *9th International Conference on High-Power Particle Beams*, edited by D. Mosher and G. Cooperstein, p. 586). Copies may be ordered from the National Technical Information Service, Springfield, Virginia 22161.
- <sup>25</sup>See National Technical Information Service Document No. PB92-206168 (V. M. Bystritskii, I. V. Lisitsyn, and A. A. Sinebryukhov, *9th International Conference on High-Power Particle Beams*, edited by D. Mosher and G. Cooperstein, p. 535). Copies may be ordered from the National Technical Information Service, Springfield, Virginia 22161.
- <sup>26</sup>See National Technical Information Service Document No. PB92-206168 (D. Parks, E. Waisman, R. Ingermanson, and E. Salberta, *9th International Conference on High-Power Particle Beams*, edited by D. Mosher and G. Cooperstein, p. 553). Copies may be ordered from the National Technical Information Service, Springfield, Virginia 22161.
- <sup>27</sup>This analysis was suggested to us by Eduardo Waisman.
- <sup>28</sup>J. D. Huba, J. M. Grossmann, and P. F. Ottinger, *Phys. Plasmas* **1**, 3444 (1994).
- <sup>29</sup>J. M. Grossmann, S. B. Swanekamp, P. F. Ottinger, R. J. Comisso, D. D. Hinshelwood, and B. V. Weber, *Phys. Plasmas* **2**, 299 (1995).

# MICROSECOND CONDUCTION TIME PLASMA OPENING SWITCH RESEARCH AT NRL

B. V. Weber, R. J. Commisso, G. Cooperstein, P. J. Goodrich,\* J. M. Grossmann,  
D. D. Hinshelwood,\* P. F. Ottinger, R. A. Riley,\*\* and S. B. Swanekamp,\*\*\*  
Pulsed Power Physics Branch, Plasma Physics Division  
Naval Research Laboratory, Washington, DC 20375-5346

## Abstract

*Microsecond conduction time plasma opening switch (POS) research is being pursued to improve the understanding of the physical mechanisms responsible for conduction and opening with the goal of improved switching for pulsed power applications. Experiments on Hawk show the dominant effect of MHD distortion for a large range of experimental parameters. Electron and neutral densities are measured in the switch and load regions for comparison with theory. The dependence of the power flow on the load impedance time history is investigated using plasma-filled and vacuum diode loads.*

The goals of microsecond conduction time plasma opening switch (POS) research at the Naval Research Laboratory (NRL) include improved understanding of physical mechanisms and limitations, and improved switching for pulsed power applications. This paper reviews research in several areas of POS physics based on experiments on the Hawk generator<sup>1</sup> and related theory work during the past two years.

Typical POS configurations on Hawk are illustrated in Fig. 1. Three different plasma

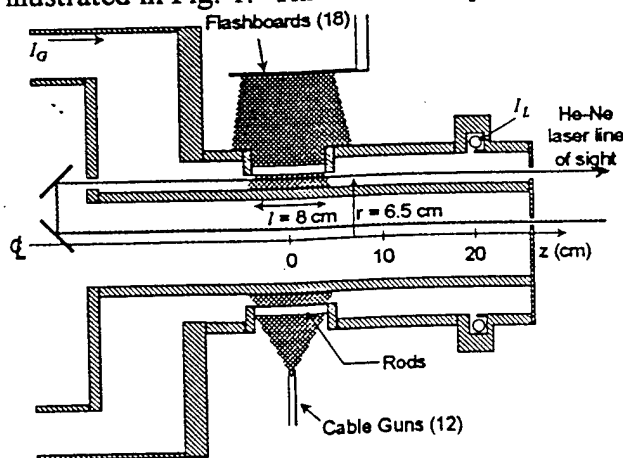


Figure 1. POS configuration on Hawk

sources have been investigated, including flashboards, cable guns, and gas guns. On Hawk, POS operation (voltage, switching time) is essentially independent of plasma source.

POS conduction physics is investigated with interferometry<sup>2</sup>. Fig. 1 shows a line-of-sight for an axially-integrating He-Ne laser interferometer<sup>3</sup>. Typical results of this measurement at different radial locations are shown in Fig. 2a for flashboard plasma sources and in Fig. 2b for cable gun plasma sources. The time  $t = 900$  ns in Figs. 2a and b corresponds to the time of opening, when the upstream (generator) current is about 600 kA. In the flashboard case, a minimum in the line-integrated density (denoted "Shot, 900 ns" in Fig. 2a) occurs at  $r = 6.5$  cm, while in the cable gun case, the density minimum is closer to  $r = 5$  cm, near the cathode surface. The localized density decrease in both cases is the result of MHD displacement and distortion of the plasma.

The traces labeled "FBs" and "CGs" are the densities measured by firing the plasma



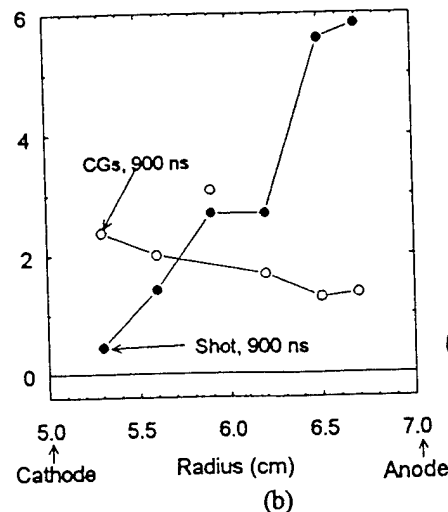
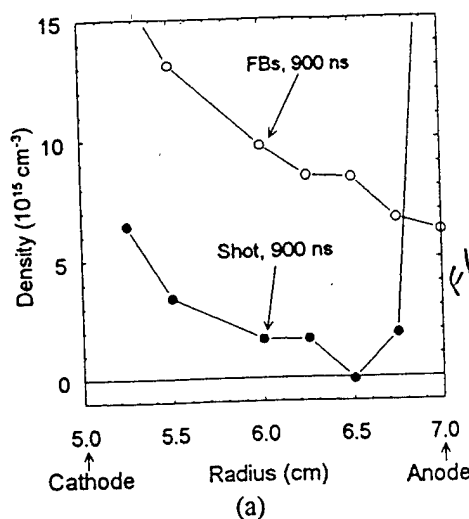


Figure 2. Axially-integrated electron density measurements in Hawk for (a) flashboard plasma sources and (b) cable gun plasma sources.

sources alone, without firing Hawk. The data taken during shots show how these densities are redistributed. The data in Fig. 2 give the impression that the cable gun plasma conducts more current for a given density than does the flashboard plasma, but this is not the case. Plasma redistribution limits the flashboard density to about  $5 \times 10^{15} \text{ cm}^{-3}$  during conduction, while for the cable gun case the electron density inventory approximately doubles during conduction, probably by ionization, resulting in a similar density during conduction for the two cases. The conduction limit in Hawk can be calculated using a simple MHD-based model<sup>4</sup> using the measured plasma distribution.

A sophisticated two-color (1.06 and  $0.53 \mu$ ) laser interferometer<sup>5</sup> was installed on Hawk to measure neutral and electron densities simultaneously, with a line-integrated electron density noise limit of only  $2 \times 10^{12} \text{ cm}^{-2}$ . Data from this new diagnostic on Hawk are shown in Fig 3. The line of sight for the data in Fig 3a is a chord through the axial center of the plasma injection region ( $z = 0$  in Fig 1), approximately 1.5 cm from the center conductor, with a 3.5 cm separation between the inner and outer conductors. Metal tubes shield the laser beams from the flashboard plasma outside the anode rods. The electron density,  $n_{\text{shot}}$ , increases and decreases, evidence of a 2D snowplow with finite axial extent

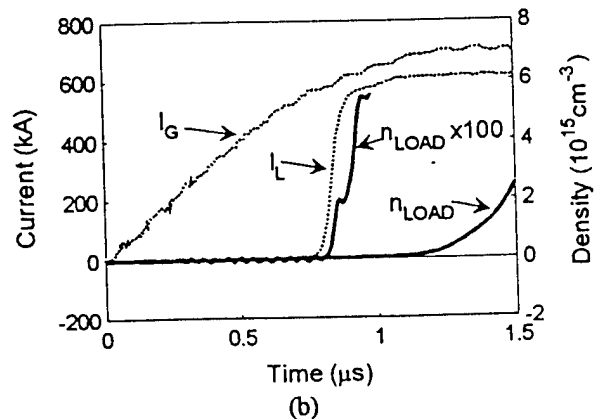
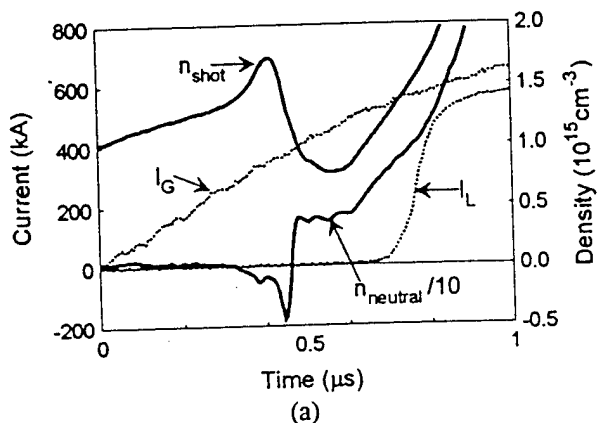


Figure 3. Two-color interferometry of (a) the POS region and (b) the load region.

moving through the POS during conduction. At a similar time, the inferred neutral density increases rapidly and is about five times greater than the electron density at the time of opening. This neutral density can be deleterious to switch opening, depending on its location. Attempts to reduce the neutral density generated during conduction can be diagnosed and evaluated in the future using this two-color technique.

The superior phase sensitivity of the two-color interferometer relative to the He-Ne interferometer was exploited for measuring the density near the load. The data in Fig 3b were taken with the chordal line-of-sight located at  $z = 23$  cm in Fig. 1, about 1.5 cm from the center conductor. The electron density measured with poor ( $1^\circ$ ) phase resolution,  $n_{\text{LOAD}}$ , implies that the high ( $10^{15} \text{ cm}^{-3}$ ) densities in the POS do not reach the load region until 100's of ns after switching<sup>6</sup>. With high phase resolution, densities in the  $10^{13} \text{ cm}^{-3}$  range are measured in the load region beginning  $< 100$  ns after the onset of the load current. This low density can affect power flow between the switch and load, and will be the subject of further investigations.

The Hawk conduction data have been modeled<sup>7,8,9,10</sup> with several fluid codes, including Hall effects. These simulations show good agreement with the measured plasma dynamics in Hawk, and their outputs may be used as inputs to particle codes to determine the physics of gap opening.<sup>11</sup> Understanding the gap formation mechanism and its relation to the conduction phase is the critical area of research for POS improvement.

An important new area of research on Hawk is the investigation of power flow between the POS and an e-beam diode load. The diagnostic setup with a cable gun POS is shown in Fig. 4. The diagnostics include anode and cathode current monitors located between the POS and the load, and a resistive divider to directly measure the load voltage. A

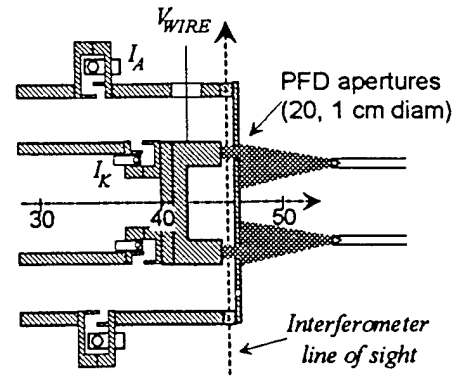


Figure 4. Hawk power flow experiment.

plasma filled diode (PFD) is used to lower the initial impedance of the diode to investigate its effect on power flow. The two-color interferometer is used to diagnose the density in the PFD.

An example of the data obtained in this experiment is shown in Fig 5.  $I_A$  and  $I_K$  are the anode and cathode currents measured in the vicinity of the load,  $V$  is the directly-measured load voltage. Time  $t = 0$  corresponds to the start of the POS conduction current. Density is injected into the 11 mm A-K gap of the diode using cable guns as illustrated in Fig. 4.

The electrical diagnostics indicate that the PFD is initially a short circuit, with  $I_A = I_K$  and  $V = 0$ . When the PFD "opens,"  $V$  increases, and  $I_K < I_A$  indicating current flow in vacuum. Analogous shots with vacuum diodes show different electrical behavior.  $V$  and  $I_A$  rise simultaneously, with a delayed and smaller  $I_K$ .

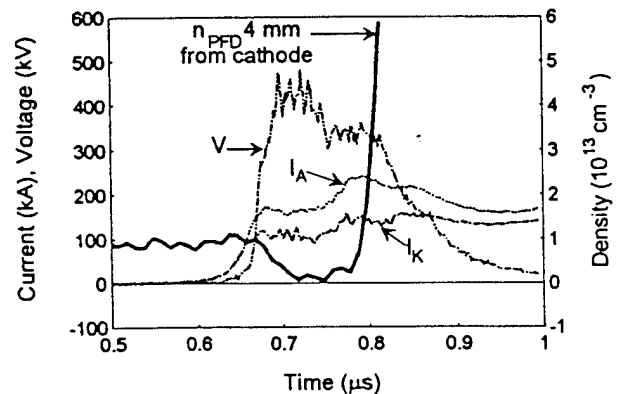


Figure 5. Power flow data with PFD load.

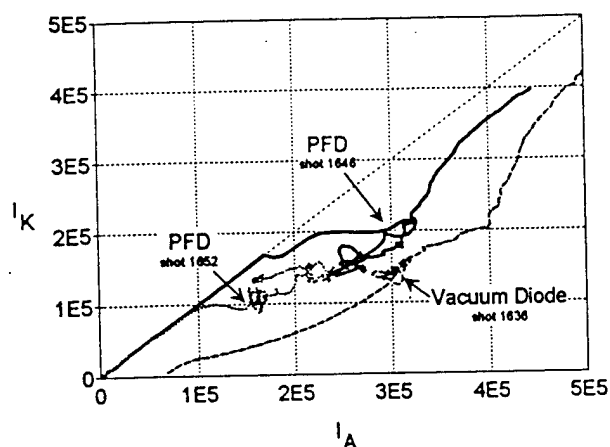


Figure 6. Comparison of PFD and vacuum diode loads.

This indicates the diode is initially an open circuit and all current flows in vacuum.

The initial PFD density in Fig. 5 is about  $1 \times 10^{13} \text{ cm}^{-3}$ . (This phase shift corresponds to  $10^{-4}$  wavelengths!) The density decreases to zero when the PFD opens, 4 mm from the cathode. Similar measurements 8 mm from the cathode show no density decrease. The evolution of the PFD density can be measured with this technique, and compared with PFD theory and PIC simulations.

A comparison of the power flow with and without PFD loads on Hawk is shown in Fig. 6. Data from two PFD shots and one vacuum diode shot are compared, plotting  $I_K$  versus  $I_A$ . These shots were chosen for comparison because they all had similar load impedance at peak power (defined as  $V/I_A$ , the impedance "seen" by the POS). The ratio  $I_K/I_A$  is higher for the PFD shots, a potentially important result for coupling useful power to loads.

The power flow in the Hawk experiment will be compared with PIC simulations<sup>12</sup>. Preliminary comparisons of experiments and simulations indicate the vacuum current in Hawk,  $I_A - I_K$ , is far greater than expected for pure electron flow. A low density plasma (of order  $10^{12} \text{ cm}^{-3}$ ) would support the observed vacuum current.

In summary, MHD-limited conduction holds for a variety of plasma sources and plasma distributions on Hawk. Two-color

interferometry shows high density neutrals in the switch region during conduction and low density plasma in the load region after opening. Power flow experiments indicate increased load cathode current using PFD loads. Simulations of power flow in Hawk are in progress.

Future POS research at NRL will emphasize modeling, combining fluid simulations of conduction with particle simulations of opening. These models will be benchmarked with well-diagnosed experiments, including a parallel plate POS on Hawk to take advantage of the two-color interferometer. This work will help to determine the ultimate limitations of POS systems for pulsed power applications.

\* JAYCOR, Vienna, VA

\*\* NRC Research Associate

\*\*\* SAIC, McLean, VA

<sup>1</sup>R. J. Comisso, *et al.*, Phys. Fluids B 4, 2368 (1992).

<sup>2</sup>D. Hinshelwood, *et al.*, Phys. Rev. Lett. 68, 3567 (1992).

<sup>3</sup>B. V. Weber and D. D. Hinshelwood, Rev. Sci. Instrum. 63, 5199 (1992).

<sup>4</sup>B. V. Weber, *et al.*, in Proc. 9<sup>th</sup> Int. Conf. on High-Power Particle Beams, 375 (1992).

<sup>5</sup>The two-color interferometer was designed and built by S. F. Fulghum of Science Research Laboratory.

<sup>6</sup>see ref. 4.

<sup>7</sup>see ref. 2.

<sup>8</sup>R. Ingermanson, *et al.*, these Proceedings.

<sup>9</sup>J. J. Watrous and M. H. Frese, in IEEE Conf. Record-Abstracts, 139 (1994).

<sup>10</sup>J. D. Huba, *et al.*, in IEEE Conf. Record-Abstracts, 139 (1994).

<sup>11</sup>J. M. Grossmann, *et al.*, these Proceedings.

<sup>12</sup>S. B. Swanekamp, *et al.*, these Proceedings.

TN file

PULSED POWER PHYSICS TECHNOTE NO. 93-04

TITLE: POS CONDUCTION DEPENDENCE ON CURRENT RISE RATE

AUTHORS: B.V. Weber, R.J. Comisso, P.J. Goodrich, J.M. Grossmann,  
D.D. Hinshelwood, J.C. Kellogg, P.F. Ottinger, S.J. Stephanakis, and  
J.R. Goyer (Physics International Co.)

DATE: 19 November 1992

ABSTRACT: This talk was presented at the APS/DPP meeting in Seattle, Washington. Experimental evidence for different POS conduction regimes is presented based on density measurements during shots on Hawk using various POS parameters: density, length, radius, and the generator current rise rate, and *in situ* density measurements on Gamble II (prior to shots) where density and plasma length were varied. The conduction scaling observed on Hawk follows the dependencies predicted by simple MHD and EMH conduction limit derivations. Gamble II POS experiments (ten times greater  $dI/dt$  than Hawk) show scaling more like the modified bipolar (MBP) prediction, where conduction current is independent of plasma length and proportional to the square root of the density. The square root of length dependence predicted by EMH, expected to apply in the Gamble II case, was not evident. Diagnostic limitations and the small range of parameter variations so far limit the conclusiveness of the non-MHD scaling experiments, but the contrast with the MHD-limited conduction on Hawk is evident. Experiments with density measurements during shots on Gamble II with more parameter variations (radius and  $dI/dt$  in addition to  $n$  and  $l$ ) are needed to adequately diagnose the conduction scaling in this important case.

THIS REPORT REPRESENTS  
UNPUBLISHED INTERNAL  
WORKING DOCUMENTS AND  
SHOULD NOT BE REFERENCED  
OR DISTRIBUTED

# Plasma Opening Switch Conduction<sup>\*</sup> Dependence on Current Rise Rate

B.V. Weber, R.J. Commisso, P.J. Goodrich,<sup>\*\*</sup> J.M. Grossmann,  
D.D. Hinshelwood,<sup>\*\*</sup> J.C. Kellogg, P.F. Ottinger, S.J. Stephanakis

Plasma Physics Division  
Naval Research Laboratory  
Washington, DC

J.R. Goyer  
Physics International Co.  
San Leandro, CA

Paper 7E4 APS/DPP  
19 November 1992

\* Work Supported by DNA

\*\* JAYCOR, Vienna, VA

# Motivation: Physics of POS Conduction

---

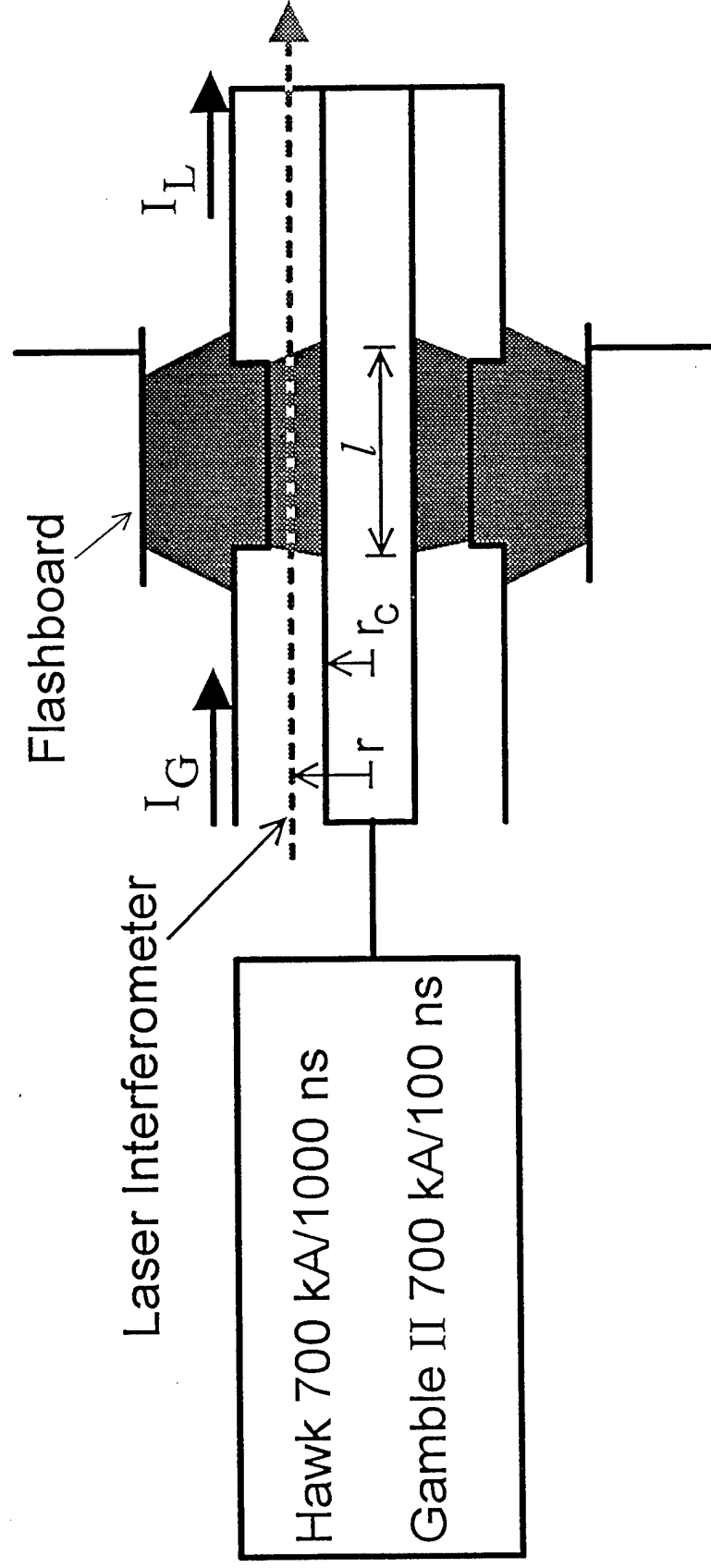
NRL

- Introduction: POS experiments on Hawk and Gamble II
  - ♦ Hawk: 700 kA, 1000 ns
  - ♦ Gamble II: 700 kA, 100 ns

$I(n) \Rightarrow \text{different scaling}$
- Hypothetical conduction models
  - ♦ Bipolar (BP), Modified BP (MBP), EMH, MHD
  - ♦ Experimental regime determined by POS parameters
- Hawk scaling experiments  $I(n, r, l, dI/dt) \Rightarrow \text{MHD, (EMH?)}$
- Gamble II scaling experiments  $I(n, l) \Rightarrow \text{MBP? (EMH)}$
- Conclusions and Future Work

# POS Experiment on Hawk and Gamble II

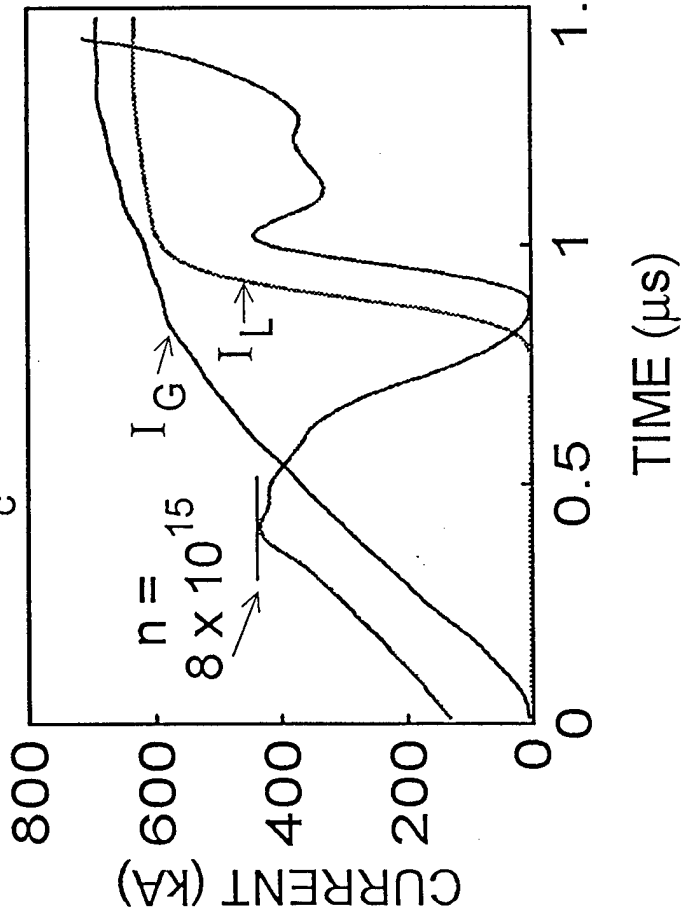
NRL



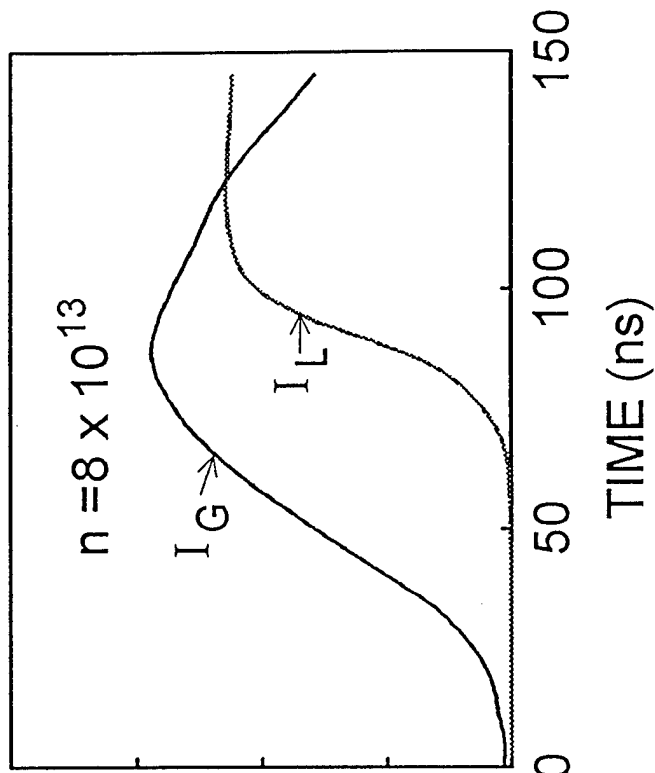
# Higher n required to conduct longer time

NRL

Hawk,  $r_c = 2.5 \text{ cm}$ ,  $l = 8 \text{ cm}$



Gamble II:  $r_c = 2.5 \text{ cm}$ ,  $l = 8 \text{ cm}$



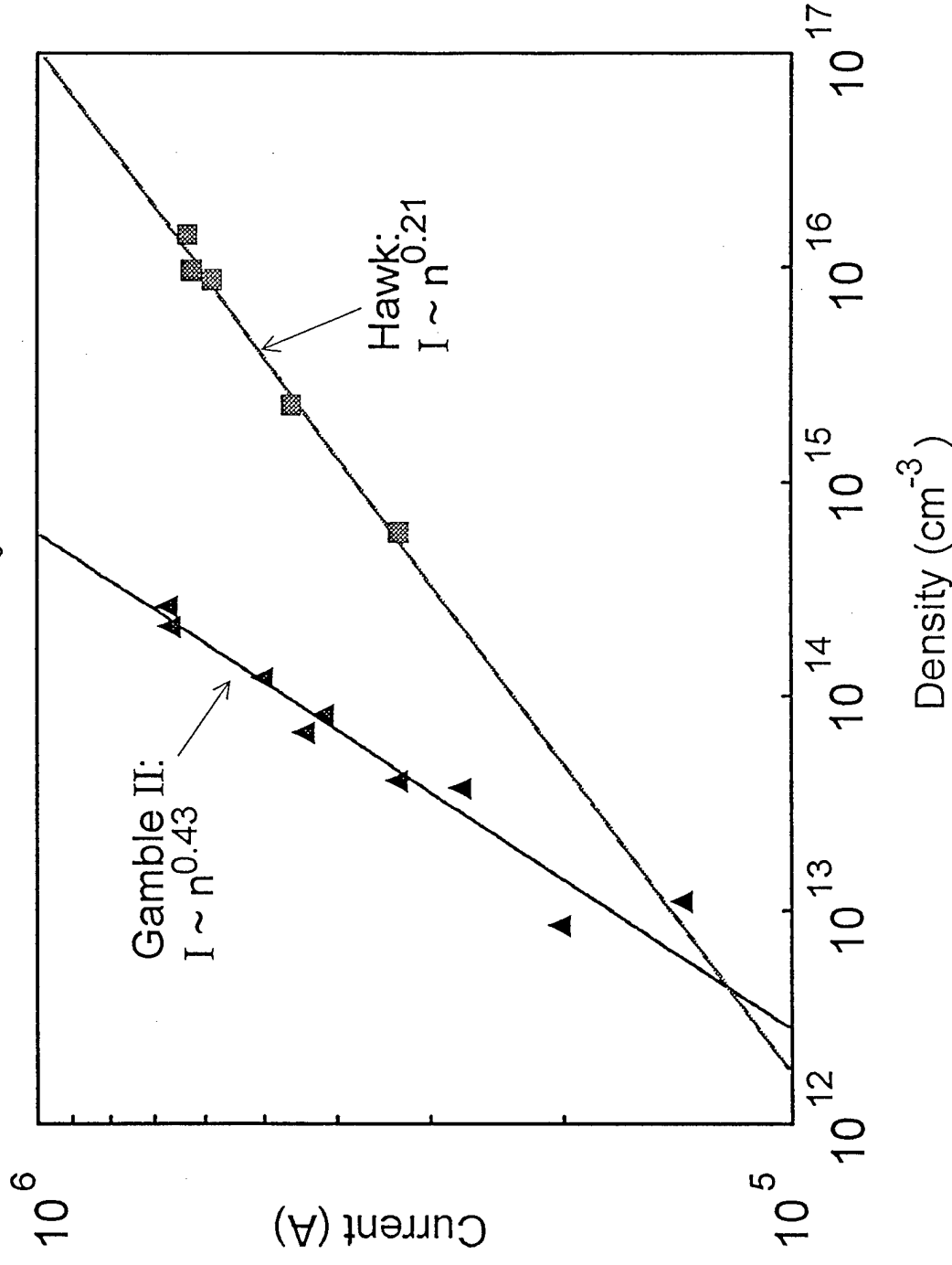
Hawk:	600 kA,	800 ns	$8 \times 10^{15} \text{ cm}^{-3}$
Gamble II:	500 kA,	50 ns	$8 \times 10^{13} \text{ cm}^{-3}$



# I(n) scaling different for Hawk, Gamble II

NRL

POS I(n) scaling:  $r_c = 2.5$  cm,  $l = 8$  cm



# Four scaling laws predict different I(n, r, l, dI/dt) scaling

NRL

1. Bipolar: conduction limit: onset of erosion (P.F. Ottinger, *et al.*, JAP 56, 1984)

$$I = \sqrt{M/Zm}(2\pi r l)nev \quad I_{BP} = 3.77 \times 10^{-10} r l n$$

2. Modified Bipolar: onset of magnetic insulation (J. Goyer, IEEE Trans. Plasma Sci., Oct. 1991)

$$I = 1.02 \times 10^{-2} r \sqrt{n} \quad I_{MBP} = 1.0 \times 10^{-2} r n^{1/2}$$

3. EMH: field penetrates plasma (A.S. Kingsep, *et al.*, Fizika Plazmy 8, 1982)

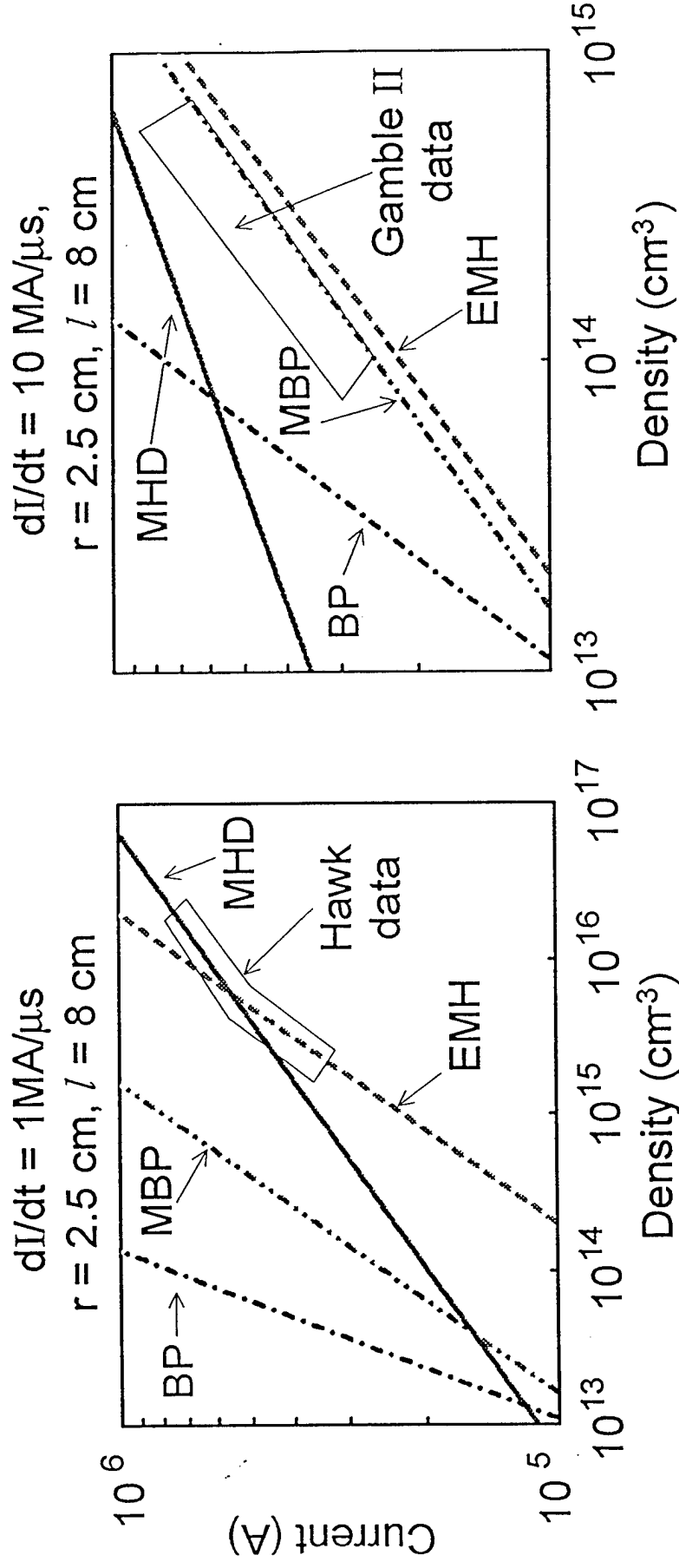
$$\int I \, dt = \pi e r^2 l n \quad I_{EMH} = 1.0 \times 10^{-9} r (l \dot{I} n)^{1/2}$$

4. MHD: plasma displaced/distorted (W. Rix, *et al.*, IEEE Trans. Plasma Sci., 19, 1991)

$$\iint I^2 \, dt^2 = \frac{100 \pi^2 r^2 l^2 M n}{Z} \quad I_{MHD} = 1.4 \times 10^{-5} (r^2 l^2 \dot{I}^2 n)^{1/4}$$

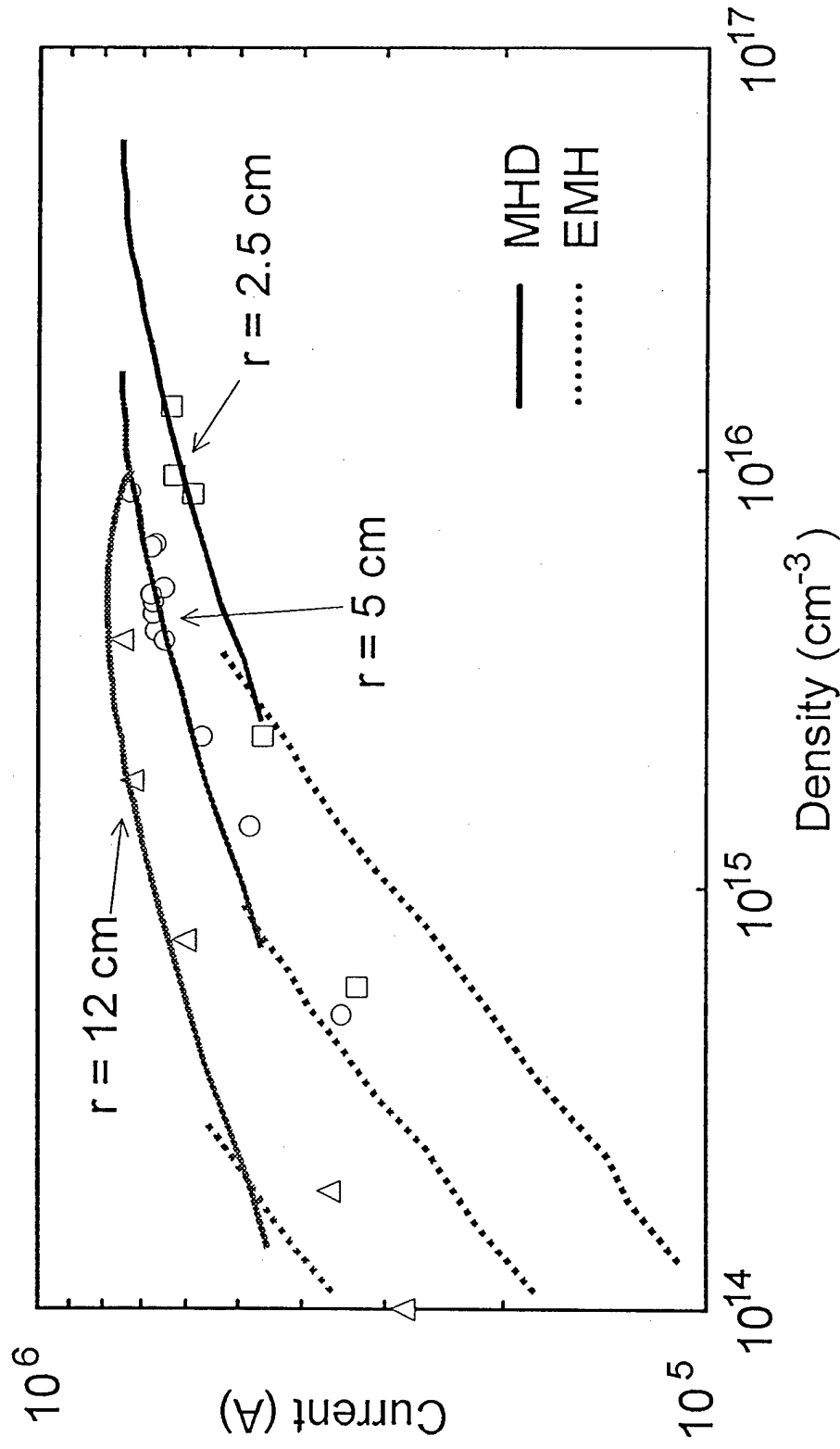
# Different conduction limits apply for Hawk and Gamble II (linear current ramp approx.)

NRL



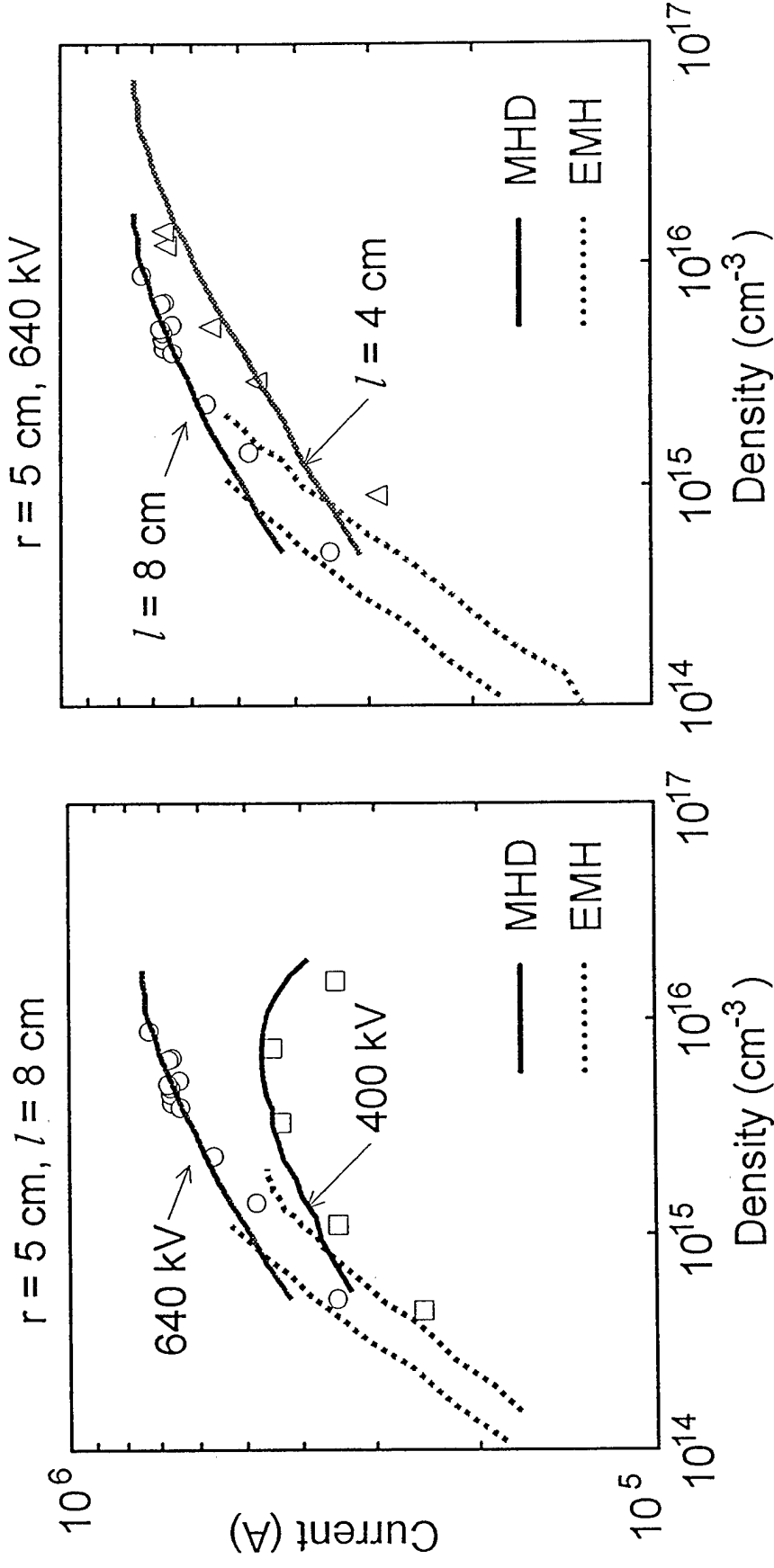
# Hawk $I(n)$ scaling follows MHD for $I > 450$ kA (vary $r = 2.5, 5, 12$ cm)

NRL



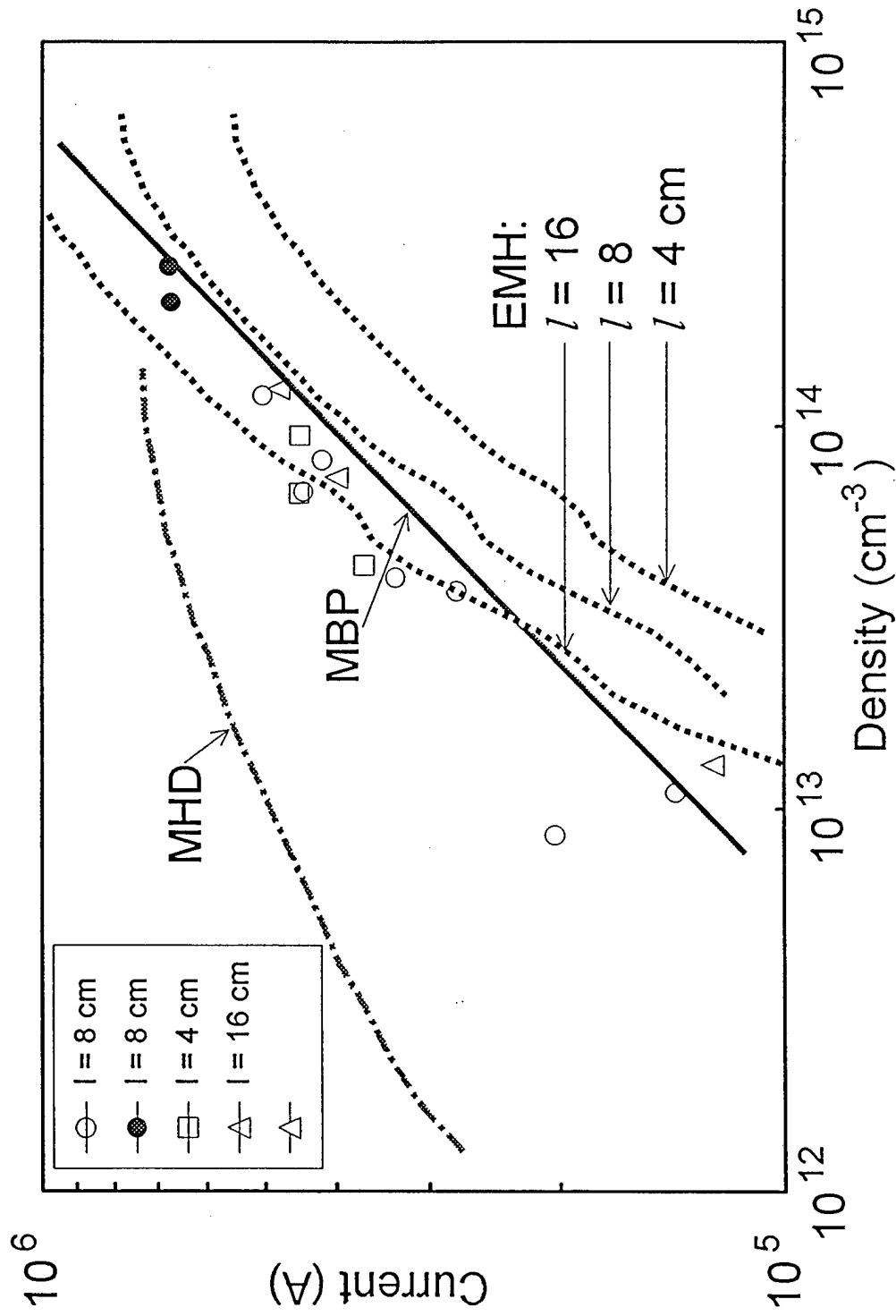
# Hawk $I(n)$ scaling follows MHD for $I > 450$ kA (vary $l$ , $dI/dt$ factor of 2)

NRL



# Gamble II I(n) scaling (vary $l = 4, 8, 16$ cm)

NRL



# Conclusions: POS conduction regime depends on $n$ , $r$ , $l$ , and $dI/dt$

NRL

POS on Hawk and Gamble II operate in different regimes  
different  $I(n)$  scaling

Scaling expts on Hawk  $\Rightarrow$  MHD for  $I > 450$  kA  
non-MHD (EMH?) for  $I < 450$  kA

Scaling expts on Gamble II  $\Rightarrow I \propto n^{1/2}$ , independent of  $l$   
(MBP?, contrary to EMH)

*caveat:* non-MHD regimes not adequately diagnosed

# Future work: More scaling experiments!

---

NRL

Determine scaling in non-MHD regime:  
measure  $n(r,t)$  while varying  $dI/dt$  and  $r$   
scaling expts on other generators (*ie*, DPM1)

Improved density measurements:  
multi-chord He-Ne on Hawk  
CO<sub>2</sub> during shots on Gamble II  
high resolution interferometer (SRL)

Vary plasma sources:  
gas gun sources tested on Hawk  
"slow" plasma guns used at PI



# CHARACTERIZATION OF BREMSSTRAHLUNG FROM THE DM1 GENERATOR\*

F.C. Young and R.J. Comisso  
Plasma Physics Division  
Naval Research Laboratory  
Washington, DC 20375-5346  
and

D.V. Rose and S.B. Swanekamp  
JAYCOR  
Vienna, VA 22182

## Introduction

The DECADE simulator [1], [2] is designed around a radiation requirement of 20 krad deposited in a thickness of 20-mil silicon over an area of  $10^4 \text{ cm}^2$  with a 2:1 spatial uniformity and a 40-ns full-width at half-maximum radiation pulse. The DM1 facility at Physics International (PI) represents one of sixteen generator modules to be used in the DECADE generator. In this paper, bremsstrahlung radiation for experimental conditions relevant to DM1 is simulated with the two-dimensional radiation transport code CYLTRAN, which is part of the integrated TIGER series of Monte-Carlo, electron/photon transport codes [3]. Results of these calculations are used to characterize the bremsstrahlung absorbed in 20-mil silicon for a variety of electron beam diode configurations on DM1 and to evaluate the effect of changes in the bremsstrahlung converter package. A more complete analysis of the DM1 performance based on radiation measurements, including an estimate of the diode electrical energy required to generate the measured dose, can be found in Ref. [4].

Circuit modeling coupled with radiation yield simulations for DM1 can be found in Ref. [5]. An analysis of DM1 performance based on the circuit modeling, 2-D particle-in-cell simulations, and radiation yield simulations can be found in Ref. [6].

## Model for Dose Calculations

Idealized electron-beam diode waveforms (constant current, triangular voltage, 100-ns pulse duration) are used to calculate radiation outputs over a parameter regime appropriate for DM1 bremsstrahlung diode experiments. Current and voltage measurements at the diode are not available on DM1, but the end-point voltage is inferred from bremsstrahlung measurements. The bremsstrahlung source, electron beam-stop and silicon absorber, modeled in the CYLTRAN calculations, are shown in Fig. 1. The electron beam is injected with a  $\cos \theta$  angular distribution truncated at  $\theta_{\max} = 70^\circ$ . These calculations can include the

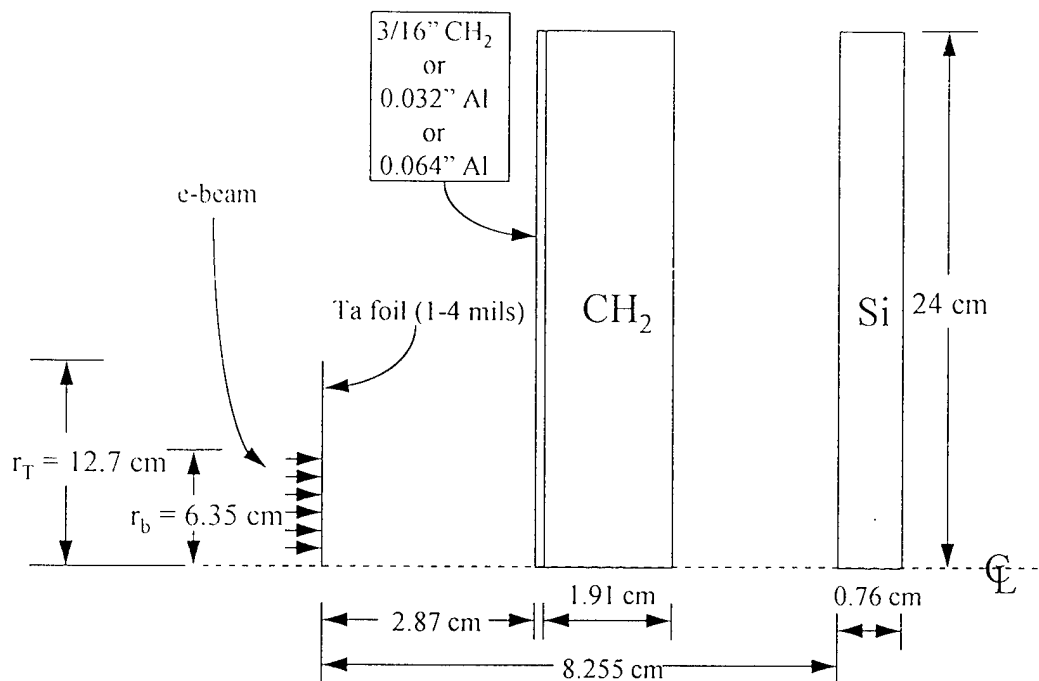


Figure 1. Cylindrical geometry configuration used in CYLTRAN simulations of DM1 bremsstrahlung production.

effects of electron albedo suppression in the diode, but assume no electron reflexing in the diode.

The validity of this source model was tested by comparing calculated dose with bremsstrahlung dose measured on the Gamble II generator at NRL [7]. Measured diode current and voltage waveforms were used to determine the incident electron spectrum for the dose calculation. The peak current (0.5 MA) and voltage (1.3 MV) on Gamble II are similar to values expected for DM1. Good agreement between measured and calculated dose was obtained when albedo suppression is included without reflexing in the calculation.

#### Electron Spectrum

For the DM1 geometry in Fig. 1, the energy spectrum of electrons transmitted through the tantalum converter is calculated for 2- and 3-mil thick tantalum. For these calculations, the injected electron energy spectrum (upstream of the tantalum) is a flat distribution with a cut-off energy of 1.75 MeV. The thicker converter results in a less intense transmitted electron spectrum and a reduced end-point energy, as expected. However, with albedo suppression, the number of low energy electrons in the transmitted spectrum is increased substantially for both converter thicknesses. With albedo suppression, these electron distributions peak at an energy of approximately 1.0 MeV, but have significant intensities extending up to nearly 1.75 MeV. Angular distributions of electrons emerging from the tantalum, including albedo suppression,

are also computed, and these distributions peak in the forward direction, as expected. These electrons are stopped by the polyethylene ( $\text{CH}_2$ ) beam-stop shown in Fig. 1.

#### Comparisons of Measured and Calculated Doses

The bremsstrahlung spectrum transmitted through the beam-stop and absorbed in different thicknesses of silicon is characterized. When albedo suppression is included, the 20 to 200 keV range of the transmitted energy spectrum is enhanced by approximately 50%. Outside of this energy range, the enhancement is less. As shown in Fig. 2, the primary contribution to the dose in 20-mil silicon is from photons with energies less than 100 keV, but a significant contribution is made by higher energy photons. The dose-area product (DAP) in a 20-mil silicon absorber at 8.255 cm from the converter is calculated by integrating the dose out to a radius of 24 cm. Calculated DAP's are in agreement with measured DAP's of 6 to 10 Mrad(Si)- $\text{cm}^2$  for peak end-point voltages of 1.45 to 1.75 MV provided the diode electron current is of 500 to 800 kA.

Two changes in the DM1 diode geometry were modeled with CYLTRAN to evaluate their impact on the DAP in 20-mil silicon. Replacing the first 0.188" portion of the  $\text{CH}_2$  beam-stop with aluminum increases the DAP by no more than 10%. Also, calculations for different tantalum converter thicknesses indicate that the DAP is maximized for a 3- to 4-mil thick converter and is reduced by 10% for a 2-mil thick converter. These changes are reflected in the results of DAP measurements by PI despite

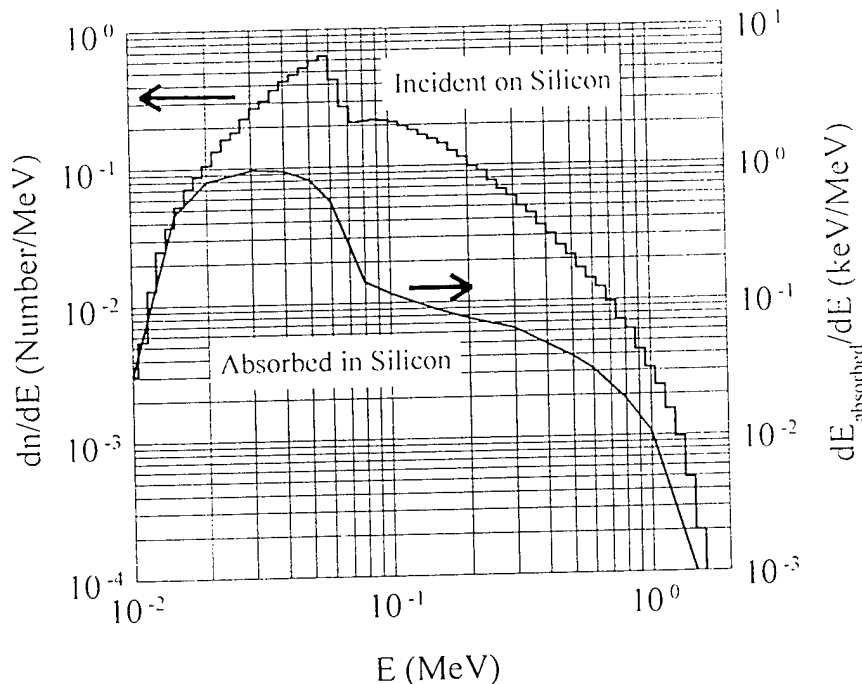


Figure 2. Bremsstrahlung spectra incident on the silicon in Fig. 1 and absorbed in the silicon.

shot-to-shot variations in the measurements. The average DAP and standard deviation for eleven shots on DM1 with a 3-mil tantalum converter and with a 0.938" (2.38 cm) CH<sub>2</sub> beam-stop is  $7.9 \pm 1.3$  Mrad(Si)-cm<sup>2</sup>. On four shots with the front portion of the CH<sub>2</sub> beam-stop replaced with either 0.032" or 0.064" aluminum, this average increases to  $9.4 \pm 0.9$  Mrad(Si)-cm<sup>2</sup>. For four shots with a 2-mil tantalum converter, this average decreases to  $6.4 \pm 0.9$  Mrad(Si)-cm<sup>2</sup>. These changes in the DAP are consistent with changes predicted by CYLTRAN calculations within the DM1 shot-to-shot variations.

Measured and computed radial dose profiles at 8.255 cm from the tantalum converter are in reasonable agreement over the range from  $r = 0$  to 24 cm. Most of the dose is absorbed within a radius of 11 cm which is nearly twice the electron-beam radius. The average peak dose for eleven shots is  $14 \pm 3$  krad(Si). The radial dose profile suggests that a 2-dimensional diode array as planned for DECADE with a diode spacing of about 30 cm can produce a 2:1 uniformity over  $10^4$  cm<sup>2</sup>. However, reproducible centering of the bremsstrahlung source and a factor-of-two increase in the dose are required to achieve the goals envisioned for DECADE.

#### References

\* Work supported under DNA MIPR No. 95-20267.

- [1] C. McDonald, P. Sincerny, and L. Schlitt, "Electrical Modeling of a Fast Charge, Inductive Store Concept for DECADE," in Proceedings of the Eighth IEEE International Pulsed Power Conference, R. White and K. Prestwich, eds. (IEEE, New York, 1991), p. 675.
- [2] P. Sincerny, S. Ashby, K. Childers, C. Deeney, D. Drury, J. Goyer, D. Kortbawi, I. Roth, C. Stallings, and L. Schlitt, "The DECADE High Power Generator," in Proceedings of the Ninth IEEE International Pulsed Power Conference, K.R. Prestwich and W.L. Baker, eds. (IEEE, Piscataway, New Jersey, 1993), p. 880.
- [3] J.A. Halbleib, R.P. Kensck, T.A. Mehlhorn, G.D. Valdez, S.M. Seltzer, M.J. Berger, "ITS Version 3.0: The Integrated TIGER Series of Coupled Electron/Photon Monte Carlo Transport Codes," Sandia National Laboratories Report SAND91-1634, 1992. [Also in Oak Ridge National Laboratory - Radiation Shielding Information Center Report CCC-467, 1994]
- [4] D.V. Rose, S.B. Swanekamp, R.J. Commisso, and F.C. Young, "Bremsstrahlung Yield Simulations for DM1," NRL Memorandum Report No. 7748, 1995.
- [5] R.J. Commisso, J.R. Boller, D.V. Rose, and S.B. Swanekamp, "Circuit Simulations of DM1 with an Electron-Beam Diode," NRL Memorandum Report No. 7750, 1995.
- [6] R.J. Commisso, J.R. Boller, J.M. Grossmann, P.F. Ottinger, D.V. Rose, S.B. Swanekamp, F.C. Young, and G. Cooperstein, "Modeling of DM1 Performance," 10th IEEE International Pulsed Power Conference, Albuquerque, New Mexico, 1995, paper 6.6.
- [7] S.J. Stephanakis, and J.C. Kellogg, private communication, 1995.

EXPERIMENTAL AND THEORETICAL INVESTIGATIONS OF  
2-D VACUUM POWER FLOWS.B. Swanekamp<sup>a)</sup>, J.M. Grossmann, D.D. Hinshelwood<sup>a)</sup>,

S.J. Stephanakis, J.R. Boller, and R.J. Comisso

Plasma Physics Division

Naval Research Laboratory

Washington, DC 20375

*Simulations of vacuum electron flow in a coaxial transmission line with and without ion emission are compared with each other and with experimental data from Gamble II. The simulation without ions shows large current losses just downstream of an impedance discontinuity. Simulations with ions show that the vacuum electron current past the impedance discontinuity is increased by the presence of ions. The losses are much more distributed than in the simulation without ions. The experimental data shows a more distributed current loss that is similar to the case where ion emission is allowed. This suggests that ions may be present and playing a role in the experiment.*

With the trend towards multi-modular high power systems, understanding power flow through complicated two and three dimensional (2-D and 3-D) structures is vital to realizing the full potential of many advanced pulsed-power designs. Some examples of complex 3-D structures used in advanced multi-modular systems include convolutes and transitions between coaxial and triplate transmission lines. One of the main tools for analyzing power-flow in such structures is the particle-in-cell (PIC) code. Before these tools can be used with confidence it is necessary to benchmark these codes with experiments in simple geometries that are very well diagnosed. This paper presents comparisons between 2-D PIC simulations with experimental measurements made on the Gamble II accelerator. The simulations are performed with and without ion emission from the anode. The simulation without ions shows very localized current losses whereas simulations with ion emission from the anode show more distributed current losses and is in better agreement with experimental data.

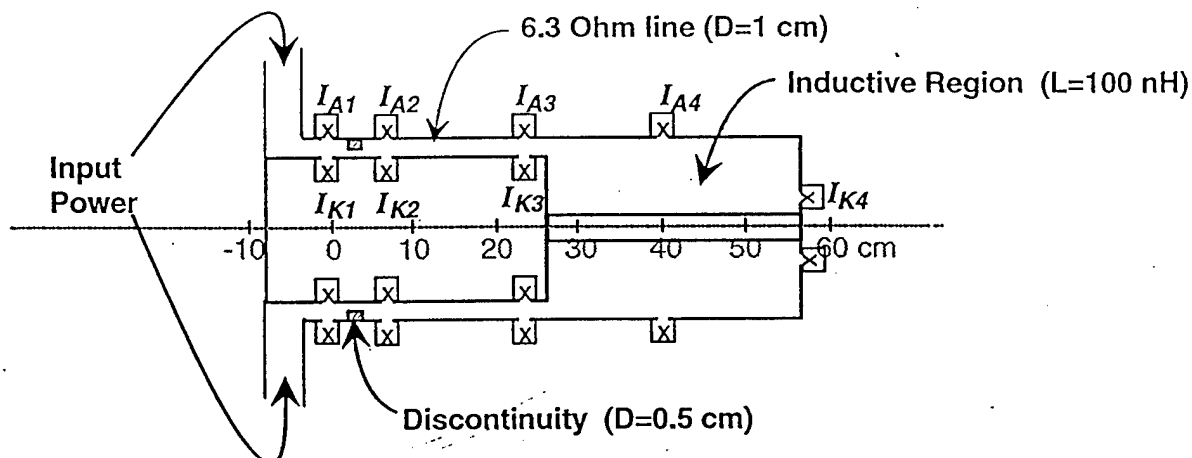


Figure 1. Schematic of the Gamble II power-flow hardware.

A schematic of the power-flow hardware fielded on the front end of Gamble II is shown in Fig. 1. A  $6.3 \Omega$  coaxial transmission line with a 1 cm anode-cathode (A-K) gap is terminated by a

highly inductive section. This high inductance section acts as a high impedance load early in time and gradually becomes a low impedance load late in time as the current derivative approaches zero. Vacuum electron flow is launched into the  $6.3 \Omega$  transmission line at a localized impedance discontinuity where the local gap size is decreased from 1 cm to 0.5 cm. The vacuum electron flow downstream of the impedance discontinuity is diagnosed by a series of anode and cathode B-dot current probes ( $I_{A1-4}$  and  $I_{K1-4}$ ).

A computational model of the geometry depicted in Fig. 1 was setup in the 2-D PIC code MAGIC<sup>1</sup>. A simplified one dimensional transmission line model of the Gamble II accelerator consisting of an open circuit voltage (3 MV, 85 ns FWHM) and an equivalent generator resistance of  $2 \Omega$  was used to drive a TEM wave into the 2-D simulation. In all the simulations described in this paper, the entire cathode surface was treated as a space-charge-limited electron emitter. Simulations results are presented with and without space-charge-limited proton emission from the anode in the  $6.3 \Omega$  line downstream of the impedance discontinuity. Ion emission in the inductive region was not allowed in either of the simulations.

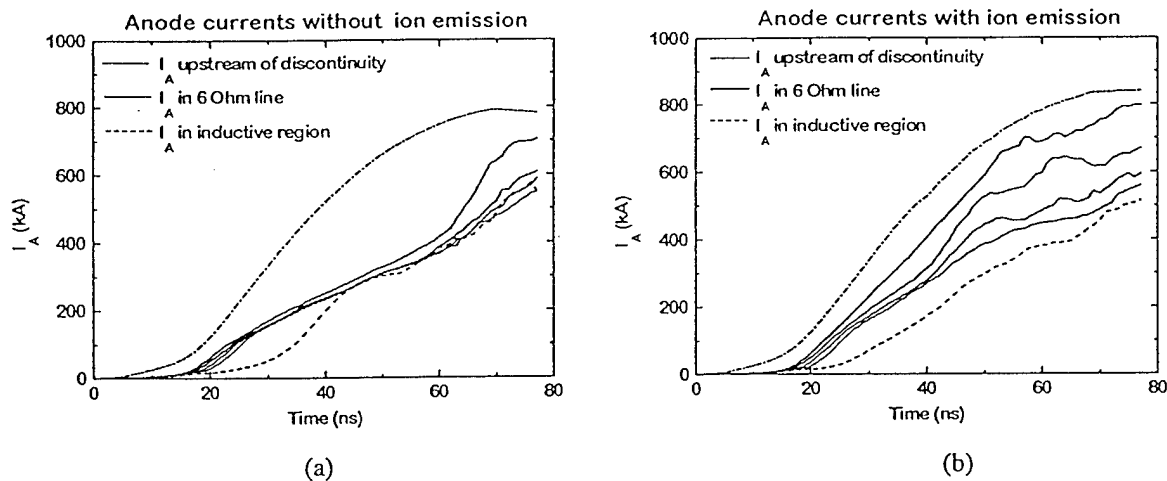


Fig. 2. The calculated anode currents (a) for the simulation without ions and (b) with proton emission in the  $6.3 \Omega$  line. The dashed curves are calculated anode currents in the inductive section.

Figure 2 shows the anode currents at 5 cm intervals starting just upstream of the impedance discontinuity ( $z=0$ ). The anode currents for the simulation without ions, shown in Fig. 2a, indicate large current losses just downstream of the impedance discontinuity and very little current losses elsewhere in the  $6.3 \Omega$  line. The electron loss just downstream of the impedance discontinuity carries a sufficient amount of energy to the anode (hundreds of J/gm) to create an anode plasma.<sup>2</sup> Figure 2a also shows that some current is lost at the transition between the  $6.3 \Omega$  line and the inductive load for  $t < 40$  ns. The anode currents for the simulation with proton emission, shown in Fig. 2b, indicate less current loss associated with the impedance discontinuity. From Fig. 2b it is also seen that, when ions are present, the current losses are distributed throughout the  $6.3 \Omega$  line. Figure 2b further shows that current losses at the transition between the  $6.3 \Omega$  line and the inductive load are present over a longer time scale for the simulation with ions. This current loss is from both electrons and ions. Although ion and electron currents were not distinguished in the simulation,

estimates from the Child-Langmuir<sup>3</sup> (C-L) law predict that, at a peak voltage of 1.2 MV, the ion current is 75 kA for the present geometry. This is a lower bound for the ion current since magnetically insulated electron flow can enhance the ion current over the C-L value.

One possible explanation for the increased vacuum electron current in the 6.3  $\Omega$  line when proton emission is allowed is that the region downstream of the impedance discontinuity behaves similarly to a pinched beam diode.<sup>4</sup> If ion emission does not occur a large fraction of the electron flow strikes the anode about one Larmor radius downstream of the impedance discontinuity. When the electrons deposit enough energy to the anode an anode plasma forms that reduces the anode electric field and provides a space-charge-limited source of ions.<sup>2</sup> The reduced anode electric field allows the magnetic force to prevent the electrons which enter the anode plasma from striking the anode surface. These electrons move axially down the transmission line and strike the anode in a new region where, if enough energy is deposited, plasma forms on a new portion of the anode and electron flow propagates down the transmission line. For simplicity, ion emission in MAGIC is enabled after a specified electric field exists on the anode surface (100 kV/cm) and not turned on by electron beam energy deposition to the surface. Therefore, the simulations with ion emission do not adequately model the detailed process of anode plasma formation but provide insight to the effects of ions in magnetically insulated flows.

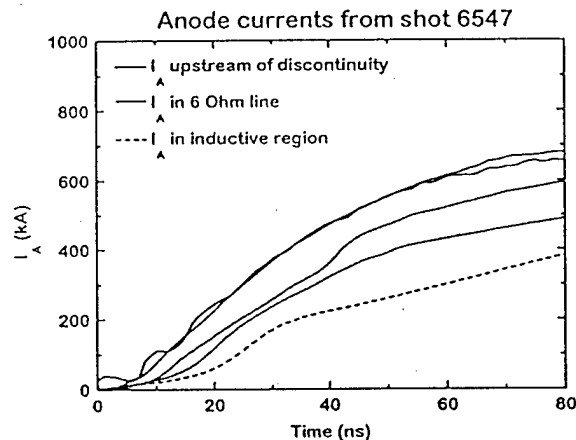


Fig. 3. The measured anode currents in the Gamble II experiment. The dashed curve is in the inductive section.

The anode currents measured on Gamble II are shown in Fig. (3). The measurements show a distributed electron loss in the 6.3  $\Omega$  line. These results are similar to the simulation results with ion emission enabled. This suggests that ions are present in the Gamble II experiment. However, because plasma can magnetically shield the B-dots, there is a reasonably large uncertainty associated with these measurements. Additional experiments are necessary to provide better current measurements and more clearly determine the role of ions. Notice that the peak current in the Gamble II shot is slightly lower than the peak current in the simulation. This difference is due to a slightly higher open circuit voltage used in the simulation than what was produced during the shot.

Current enclosed contours (50 kA between contours) at  $t=50$  ns for (a) the simulation without ions and (b) the simulation with ion emission in the 6.3  $\Omega$  line are shown in Figure 4. At this time

there is about 650 kA upstream of the impedance discontinuity and the cathode current downstream of the impedance discontinuity is approximately 200 kA for both cases. The simulation without ions shows about 300 kA is lost just downstream of the impedance discontinuity. Approximately 150 kA flows in the vacuum with relatively little current loss in the  $6.3 \Omega$  line. By contrast, the simulation with ion emission has only about 50 kA of loss current at the impedance discontinuity and nearly 200 kA of distributed current loss in the  $6.3 \Omega$  line. In addition Fig. 4b shows that the additional vacuum electron current flows primarily near the anode. This might be expected since this is where most of the ion space charge resides. The propagation of vacuum electron current with ions produced on the anode may also occur during the power transfer phase of the plasma-opening switch.

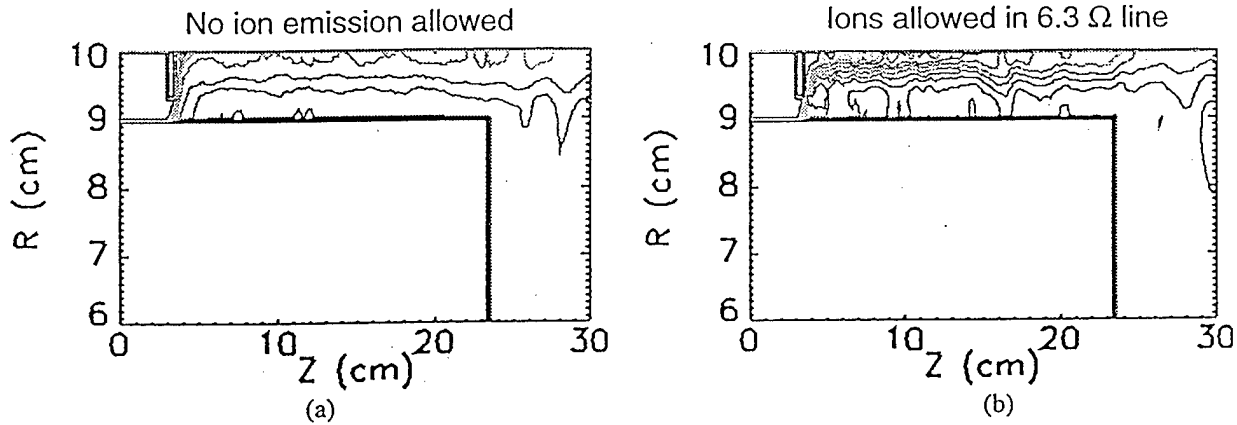


Fig. 4. Current enclosed contours at  $t=50$  ns for (a) the simulation without ions and (b) the case with proton emission in the  $6.3 \Omega$  line.

Vacuum electron flow in the  $6.3 \Omega$  line can be analyzed using the flow impedance concept. If the electrons are  $E \times B$  drifting and there are no ions in the line, then pressure is balanced across the electron flow and the flow impedance can be written as<sup>5</sup>

$$Z_f = \frac{V}{(I_A^2 - I_C^2)^{1/2}}, \quad (1)$$

where  $V$  is the voltage,  $I_A$  is the local anode current and  $I_C$  is the local cathode current. For a localized impedance discontinuity it is customary to use the anode current just upstream of the discontinuity and the cathode current just downstream of the discontinuity. An idealized electron flow pattern is shown in Fig. 5. A physical interpretation of the flow impedance can be described as follows. If the anode-cathode gap spacing,  $D$ , of a coaxial transmission line is small compared to the cathode radius,  $R_C$ , then it can be shown that Eq. (1) is equivalent to the vacuum wave impedance between the centroid of the electron space charge ( $\bar{x}$ ) and the anode ( $Z_f = 60 (D - \bar{x})/R_C$ ).<sup>6</sup> The size of the electron sheath can be estimated from the electron Larmor radius which, in turn, can be estimated from the critical current formula and expressed as

$$D_{CRIT} [cm] = 8500 F_{CR} \frac{R_C [cm]}{I_A [A]} (\gamma^2 - 1)^{1/2}. \quad (2)$$

In Eq. (2)  $\gamma$  is the relativistic mass factor and  $F_{CR}$  is a factor that is weakly dependent on voltage and approximately 1.6 for voltages between 1 and 3 MV.<sup>7</sup> If it is assumed that the electron charge is evenly distributed in the electron sheath, then the charge centroid is approximately  $D_{crit}/2$  and the flow impedance can be written as

$$Z_f \cong 60(D - D_{crit}/2)/R_C. \quad (3)$$

When the vacuum electrons are very well insulated then  $D_{crit}$  is very close zero and the flow impedance is the vacuum wave impedance of the transmission line,  $Z_f \cong 60D/R_C$ . When the electron flow is critically insulated (i.e. the electron gyroradius is comparable to the anode-cathode spacing of the transmission line) then  $D_{crit} = D$  and the flow impedance is half the vacuum wave impedance of the transmission line,  $Z_f \cong 30D/R_C$ . It is important to note that, when ions are present and unmagnetized, the flow impedance defined by Eq. (1) no longer applies since the presence of ions alters the pressure balance relation.

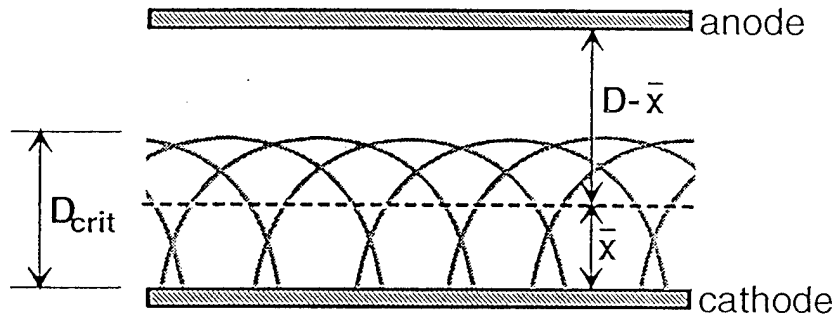


Fig. 5. An idealized electron flow pattern and the relationship between the  $D_{crit}$ ,  $\bar{x}$ , and  $D$ .

The critical gap size and the flow impedance calculated with the voltages and currents from the simulation without ions are shown in Figs. 6a and 6b. The physical gap size and half the vacuum wave impedance for both the impedance discontinuity and the 6.3  $\Omega$  line are also shown by dashed lines in the two figures. Figure 6a shows that  $D_{crit}$  is approximately equal to 0.5 cm in the impedance discontinuity and 1.0 cm in the 6.3  $\Omega$  line indicating that the electron flow is critically insulated over most of the simulation. Therefore, for the simulation without ions, the system sheds precisely enough current near the impedance discontinuity to keep the electron flow critically insulated. The flow impedance is also close to half the vacuum wave impedance over most of the simulation. This is consistent with the conclusion that the electron flow is critically insulated. Late in time, as the inductive load begins to look more like a short circuit, the electron Larmor radius gets smaller. When this happens Eq. (3) predicts that the flow impedance should get larger and approach the vacuum wave impedance of the line. This happens at  $z=20$  cm but does not occur at  $z=5$  cm. The electron density contours late in time indicate that the electron charge at  $z=5$  cm is not evenly distributed in the sheath but more concentrated near the anode. This causes the flow impedance at  $z=5$  cm to decrease late in time even though the Larmor radius is decreasing.

The critical gap size calculated with the voltages and currents from the simulation with proton emission in the 6.3  $\Omega$  line is shown in Fig. 7. Figure 7 shows that the electron Larmor radius with



ions is significantly smaller than the no ion case. This is due primarily to an increase in the anode current in the  $6.3 \Omega$  line when ions are present.

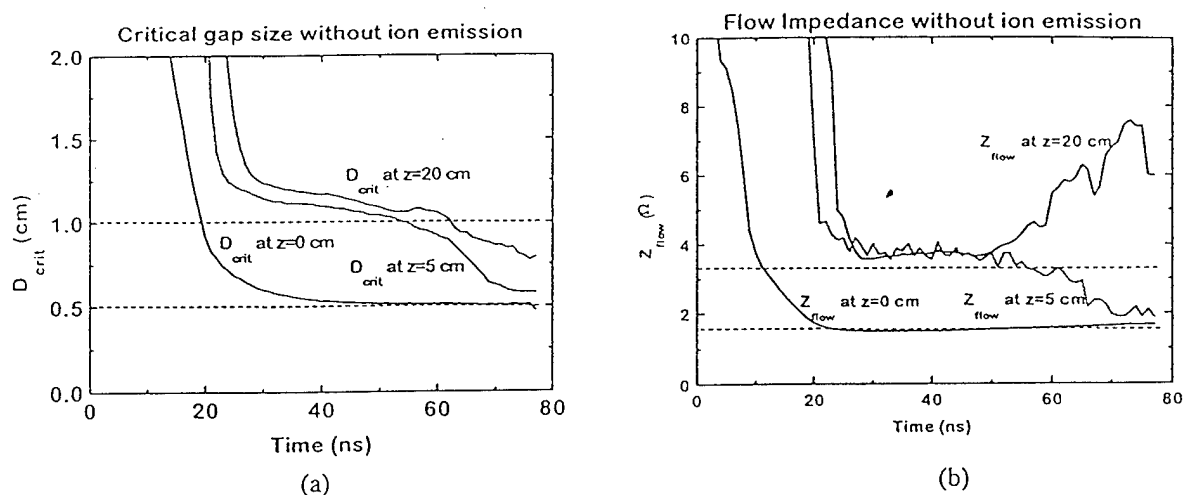


Fig. 6. (a) The critical gap size and (b) the flow impedance at several positions in the  $6.3 \Omega$  line without ions.

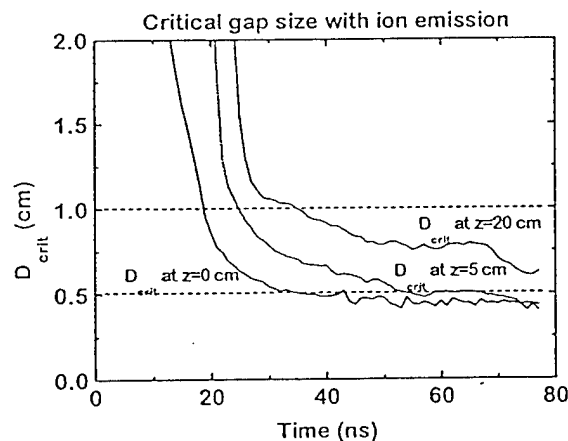


Fig. 7. The critical gap size at several positions in the  $6.3 \Omega$  line with proton emission from the anode.

The authors would like to thank P.F. Ottinger, G. Cooperstein, D. Mosher, Jess Neri and the rest of the Pulsed Power Physics Branch of the Naval Research Laboratory for their interest in this work.

a) JAYCOR, Vienna, VA 22182.

Work supported by DNA.

<sup>1</sup> B. Goplen, L. Ludeking, D. Smithe, and G. Warren, *Computer Physics Communications* **87** (1994), 54.

<sup>2</sup> A. Blaugrund, G. Cooperstein, and S.A. Goldstein, *Phys. Fluids* **20**, 1185 (1977).

<sup>3</sup> C.L. Child, *Phys. Rev.* **32**, 492 (1928). I. Langmuir, *Phys. Rev.* **33**, 954 (1929).

<sup>4</sup> R.B. Miller, *An Introduction to the Physics of Intense Charged Particle Beams*, Plenum Press, New York, pp. 67-70 (1982).

<sup>5</sup> C.L. Mendel, Jr., M.E. Savage, D.M. Zagar, W.W. Simpson, J.W. Grasser, and J.P. Quintenz, *J. Appl. Phys.* **71**, 3731 (1992).

<sup>6</sup> C.L. Mendel, private communication.

<sup>7</sup> R.J. Barker and S.A. Goldstein, *Bull. Am. Phys. Soc.* **26**, 921 (1981).

# MODELING OF DM1 POS AND LOAD PERFORMANCE<sup>+</sup>

R. J. Commisso, J.R. Boller, D.V. Rose,\* S.B. Swanekamp,\* J.M. Grossmann, P.F. Ottinger, B.V. Weber,  
 F.C. Young, and G. Cooperstein  
 Pulsed Power Physics Branch, Plasma Physics Division  
 Naval Research Laboratory, Washington, DC 20375

## ABSTRACT

In this paper, we study the performance of the plasma opening switch (POS) and electron-beam diode load on the DM1 pulsed power generator using the transmission-line circuit code BERTHA, the electron/photon-transport code CYLTRAN, and the 2-dimensional particle-in-cell (PIC) code MAGIC. The results suggest that of the 52 kJ required to be delivered to the load to account for the observed radiation, up to 75% is associated with current not flowing in the cathode. This non-cathode current cannot be explained by electron vacuum flow only, implying the presence of plasma. Further, the inferred experimental diode impedance,  $11 \Omega$ , is much higher than optimum. Assuming no change in the DM1 conduction current/time and POS performance, an optimum diode impedance of  $2 \Omega$ , and a POS-to-load inductance reduced by 75%, the analysis suggests that the load energy on DM1 can range from 54 kJ to 94 kJ, depending on how much non-cathode current reaches the load. The analysis also suggests that to obtain agreement between features of the measurements and calculations, the DM1 flow impedance (gap) must decay after opening and ions must be present in the vacuum transmission line between the POS and load. Understanding of the coupling between the POS and e-beam load remains incomplete.

## INTRODUCTION

DECADE<sup>1</sup> is a proposed 9-MJ, modular pulsed power generator. One such module, DECADE Module 1 (DM1),<sup>2</sup> is now in operation with an electron-beam (e-beam) diode load. Each module uses a coaxial plasma opening switch<sup>3</sup> (POS) for power conditioning. In this paper, we analyze the performance of DM1 during a selected experimental series. The purpose of this work is to try to improve the understanding of POS/load coupling and to suggest ways to optimize the DM1 single shot performance. Three different tools are used in this study. The transmission line code BERTHA<sup>4</sup> is used for circuit modeling that links the pulsed power to the POS and, using physics-based circuit-element models for the POS and e-beam diode load, predict the energy coupled to the load (for the experiments considered here, there are no load-current and only indirect load-voltage measurements). The coupled electron/photon Monte Carlo transport code CYLTRAN<sup>5</sup> is used to link the measured radiation associated with the e-beam load to the energy delivered to the load. The 2-D PIC code MAGIC<sup>6</sup> is used to help understand the electron and ion flow between the POS and load that accompanies the POS opening.

A simplified representation of the DM1 circuit and an illustration of the front-end geometry are given in Fig. 1. An in-depth description of the DM1 circuit can be found elsewhere.<sup>1,7</sup> The front-end geometry shown in Fig. 1 was used in the selected DM1 experiments and, unless otherwise noted, in all the calculations that follow.

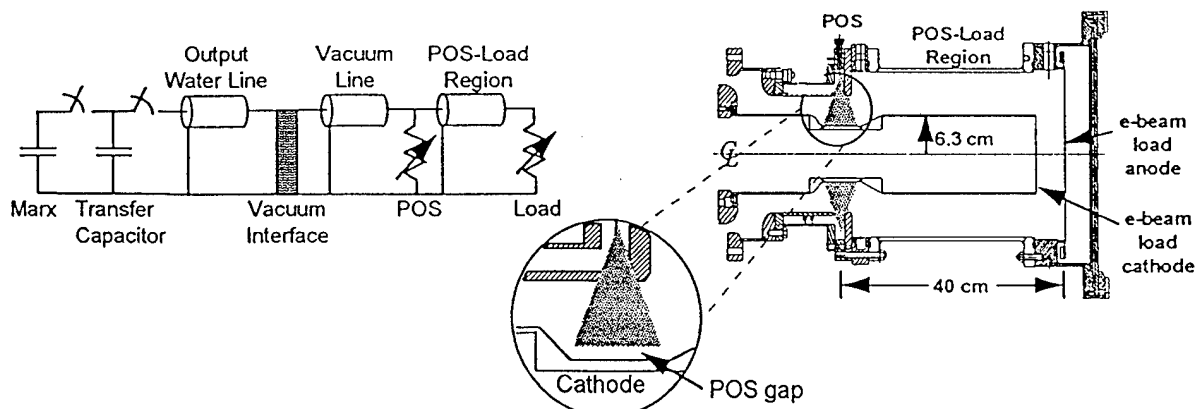


Fig. 1 Representation of the DM1 circuit and sketch of the front-end geometry used in the experiments.

## RESULTS FROM CIRCUIT MODELING

The 48-element circuit model used in BERTHA for these circuit calculations has been successfully benchmarked against other models and successfully (within 10%) compared with measured DM1 electrical waveforms up to the POS.<sup>7</sup> Short descriptions of the circuit-element models for the POS and e-beam load as well as an example of the circuit modeling results follow. Details regarding the circuit-element models and benchmarking work, and complete circuit modeling results, can be found elsewhere.<sup>7</sup> We have assumed the full vacuum inductance for the region between the POS and load. This assumption is discussed later. The Marx charging voltage in the circuit calculations had to be reduced to 90% of the actual charging voltage in all of this work to obtain agreement with measurements.<sup>7</sup>

The circuit-element model for the POS is based on the concept of flow impedance,<sup>8</sup> where the resistance of the POS circuit element,  $R_s$  is related to the flow impedance,  $Z_f$ , by<sup>7</sup>

$$R_s = Z_f \left( \frac{I_{AU} + I_{CD}}{I_{AU} - I_{CD}} \right)^{1/2} \quad (1)$$

Here,  $I_{AU}$  and  $I_{CD}$  are the anode current on the generator side (upstream) and cathode current on the load side (downstream) of the POS, respectively;  $R_s$  is the resistance of the POS ( $R_s = V_s/I_s$ , where  $V_s$  and  $I_s = I_{AU} - I_{CD}$  are the POS voltage and current, respectively), and  $Z_f \equiv V_s/(I_{AU}^2 - I_{CD}^2)^{1/2}$ . In Eq. (1) we have also assumed that all the vacuum electron flow between the POS and load is lost and counted as switch loss. No vacuum electron flow is counted as current available for driving the e-beam load. The load current is  $I_{CD}$ . Because vacuum flow can contribute to the radiation produced in the experiment, we expect this POS circuit model to underestimate the load current. The biggest advantage of this model is that it allows one to differentiate between cathode and anode current reaching the load. However,  $Z_f$  still must be prescribed as a function of time. The physical model for the POS used in this work assumes that the vacuum electrons are always critically insulated (saturated flow) in the time dependent POS gap,  $D_{crit}$ .<sup>3,7</sup> If we further assume that the POS gap forms at the POS cathode radius,  $R_c$ , then one has that  $Z_f \approx 30 D_{crit}/R_c$ .<sup>9</sup>

The circuit-element model<sup>7</sup> for the e-beam load is divided into three phases: 1) an early turn-on phase, 2) a Child-Langmuir (C-L) flow phase, and 3), a critical-current, pinched-beam phase. The model uses as input: the diode cathode outer radius, the cathode inner radius, the radius of curvature of the cathode edges, and the initial anode-cathode (AK) gap,  $D_d$ . The parameters for the load model are: the electric field turn-on threshold, the time duration to reach full C-L current, and the gap closure speed,  $v$ . In the first phase, the current begins to flow in the diode when the mean electric field reaches a preset threshold. Once the field threshold is exceeded, current rises linearly from zero to the full C-L value in the assumed diode "turn-on" time (during which plasma expands to cover the entire cathode area). In the second phase, the full C-L current flows and the diode AK gap closes from electrode plasma motion at a constant speed (closure is initiated at the start of "turn-on"). When the C-L current exceeds the critical current, the third phase begins which limits the diode current to the critical current for the remainder of the simulation. The critical current is expressed as

$$I_{CRIT} = 8500 F_{CR} \frac{R}{D_d - vt} (\gamma^2 - 1)^{1/2} \quad (A), \quad (2)$$

where  $F_{CR}$  is a factor that is weakly dependent on voltage and is approximately 1.6 for voltages between 1 and 3 MV, and  $\gamma$  is the ratio of electron energy to electron rest energy. The values of the diode parameters that best fit the DM1 data, and used here, are 10 kV/cm for the electric field turn-on threshold and 0 ns for the duration to full C-L current. Typical values of the electric field turn-on threshold and duration to full C-L current for similar diodes on the conventional water-line generators are 200-300 kV/cm and 10-20 ns, respectively. Long-conduction-time POS data from Hawk, where POS plasma may be in the e-beam load region at the time of opening, exhibit the same values as used here for DM1.<sup>10</sup> For all of this work, the closure speed was chosen to be 3.5 cm/ $\mu$ s, typical of similar diodes on water-line machines.

For the time dependence of  $Z_f$  in Eq.(1), we assumed a linear rise followed by an exponential decay.<sup>7</sup> This decay is needed to reproduce the measured upstream waveforms. We obtained a good fit to DM1 data when  $Z_f$  linearly increased to 1.38  $\Omega$  (maximum POS gap of about 2.3 mm) in 28 ns, then decreased exponentially (corresponding, e.g., to POS gap closure) with a 1/e time of 55 ns. Comparison of this model with the measured upstream waveforms from a DM1 shot is given in Fig. 2. Also shown in Fig. 2 is the calculated  $I_{AU}$  with a short circuit at the POS. It appears that the present DM1 operation utilizes only about 78% of this available current or

about 60% of the available stored energy if the POS conducted the entire current pulse. Displayed in Fig. 3 are the calculated load-voltage,  $V_L$ , and load-current,  $I_L$ , waveforms along with measured and calculated (using IV and  $IV^{2.8}$  as approximations) x-ray signals. We do not have measured electrical load waveforms to compare with these calculations: however, the peak load voltage of 1.7 MV (inferred from a multi-channel, filtered PIN detector array<sup>11</sup>) agrees with the calculation. The AK gap of 25.4 mm used in the experiment corresponds to a load impedance of  $Z_L = 11 \Omega$ . The calculated peak  $I_L$  is 150 kA and the load energy reaches 12.4 kJ when the measured x-ray pulse reaches zero.

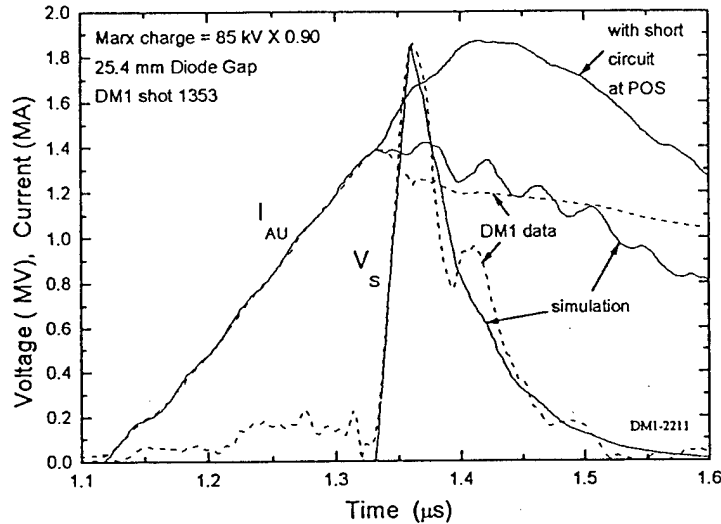


Fig. 2 Comparison of measured and calculated upstream waveforms.

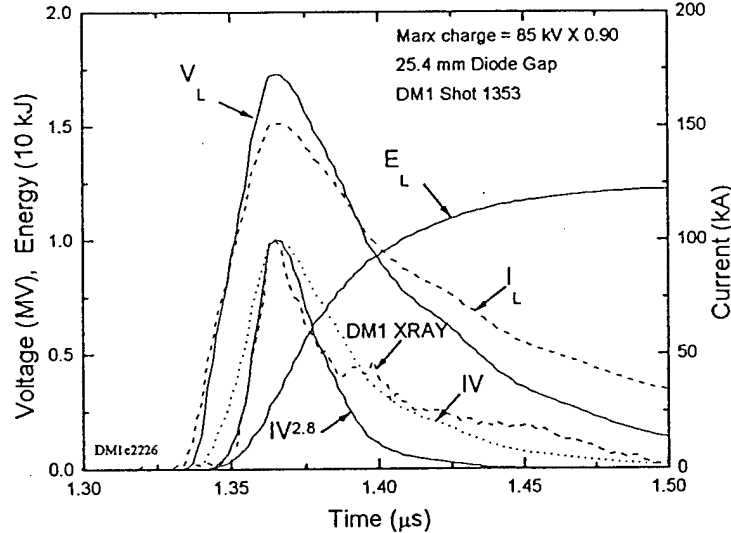


Fig. 3 Calculated load parameters and measured x-ray signal.

## RESULTS FROM CYLTRAN MODELING

A full description of the e-beam diode geometry depicted in Fig. 1 and used in the CYLTRAN simulations, as well as detailed results of the radiation calculations, can be found elsewhere.<sup>12</sup> Briefly, the 12.7-cm radius Ta used as an anode in the e-beam diode was 0.003-in thick and the vacuum window was a 3/16-in thick sheet of polyethylene followed by a 3/4-in slab of polyethylene. The e-beam cathode radius of 6.35 cm was assumed to be the e-beam radius. The incident e-beam angular distribution was forward directed. The calculated dose-area-product (DAP) in the near field is relatively insensitive to this distribution.

Figure 4 contains a plot of the CYLTRAN-calculated DAP in 20 mils of Si as a function of diode energy for a variety of cases. The horizontal line at 7.6 Mrad (Si)-cm<sup>2</sup> is the average measured DAP for the chosen DM1 data set. The standard deviation, maximum, and minimum DAP values are also shown. The open symbols are CYLTRAN calculations for triangular-voltage, flat-current load waveforms. For the circles, the voltage is fixed at 1.75 MV and the current is varied to generate the linear scaling of calculated DAP as a function of load energy. For the two types of triangles, the current is held fixed at either 0.6 MA or 1.2 MA and the voltage is varied between 1 and 2 MV. Note that for these geometries the DAP is an approximately linear function of load

energy. This result means that electrical energy delivered to the diode is a good parameter for optimizing radiation production. The filled squares are calculated DAPs for various BERTHA-generated load waveforms.<sup>7</sup> The point labeled "D<sub>crit</sub>(t) model" corresponds to prescribing  $Z_f$  in Eq. (1) by calculating  $D_{crit}(t)$  from a form of Eq. (2) using the measured upstream waveforms and setting  $Z_f = 30 D_{crit}/R_C$ .<sup>7</sup> The point marked "100 ns" is the result when only the energy in the first 100 ns of the calculated power pulse is used. More energy is delivered to the load when the AK gap and switch-to-load inductance,  $L_{SL}$ , are reduced because the present system is not optimized from a circuit point of view (see next section). The CYLTRAN results for the BERTHA waveforms fall on the same line

as the idealized waveforms, indicating that the DAP in 20 mils of Si for this configuration is relatively insensitive to the shape of the voltage and current waveforms.

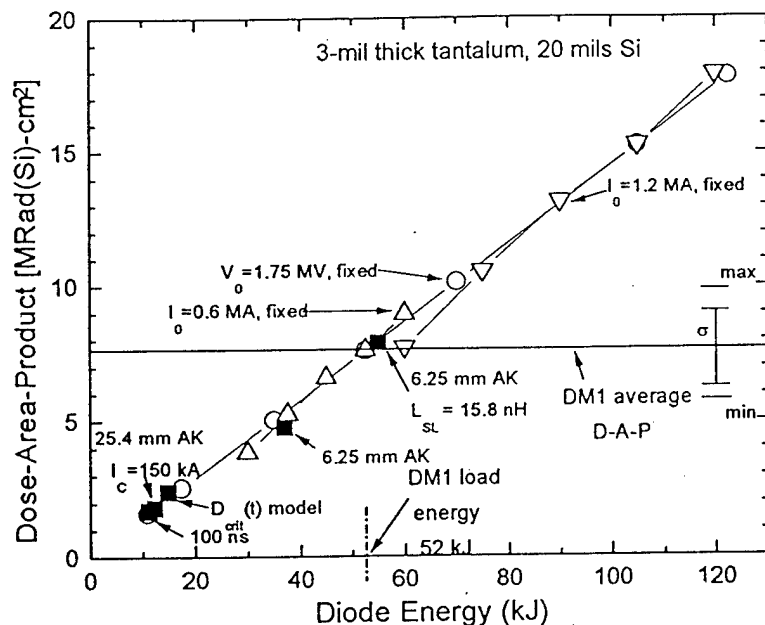


Fig. 4 Dose-area-product as a function of diode energy.

comparisons of measured<sup>11</sup> and calculated radial dose profiles suggest that many electrons hit the anode at a radius well outside the e-beam cathode radius, supporting our conclusion that non-cathode current is present in the experiment.

### RESULTS FROM VARYING CIRCUIT PARAMETERS

Several BERTHA runs were made varying  $D_d$  and  $L_{SL}$  from 25.4 mm and 63 nH to 5 mm and 15.8 nH, respectively (the former values being the ones used in the experiments).<sup>7</sup> These calculations show that the energy delivered to the load has a broad maximum of 37 kJ when  $D_d$  is about 6.3 mm, with an associated  $Z_L$  of about 2  $\Omega$ . This optimization was expected based on the critical gap picture of POS opening, where the optimum load impedance for maximum energy delivery to the load defines the boundary between switch-limited and load-limited operation.<sup>3</sup>

If  $L_{SL}$  is reduced, the load energy is also increased, but only if the load impedance is near the optimum impedance. If  $Z_L$  is large compared to the optimum  $Z_L$ , the beneficial effect of reducing  $L_{SL}$  is negated. For example, with  $D_d = 25.4$  mm, there is no change in the energy delivered to the load as  $L_{SL}$  is reduced. This is because  $Z_L$  is so large (11  $\Omega$ ) it dominates the inductive loading (approximated by  $L_{SL}/t_{open}$ , about 2  $\Omega$  for  $L_{SL}$  of 63 nH and  $t_{open}$  of 28 ns).  $Z_L$  of about 2  $\Omega$  is comparable to the maximum inductive loading and the system can deliver more energy to the load as  $L_{SL}$  is reduced. When  $D_d = 6.3$  mm and  $L_{SL} = 15.8$  nH (25% of the original vacuum inductance), we calculate that 54 kJ is delivered to the load. If we conjecture that the 40 kJ of load energy associated with the non-cathode current is still delivered to the load, then up to 94 kJ (upper bound) might be delivered to the load with this front-end configuration. The real system response must be determined experimentally.

### RESULTS FROM 2-D PIC MODELING

To gain insight into the details of the POS-load coupling, we carried out preliminary 2-D PIC calculations of the behavior of the ion and electron flows using MAGIC. The DM1 front-end geometry (see Fig. 1) was used with the POS modeled by independently moving ions out of a prescribed gap in a prescribed time, as described previously.<sup>9</sup> For the results shown here, the final gap was 1.8 mm and the time for ions to clear the gap was 30 ns. This model, together with a simplified driving circuit, gave a good match to the upstream DM1 waveforms. POS plasma was modeled by allowing ion emission along both sides of the POS. The load for the simulation was an e-

The energy at which the calculated DAP vs. load energy curve intersects the average measured DAP is the energy we infer is producing the observed DAP on DM1 - about 52 kJ. The BERTHA calculation underestimates the energy delivered to the load by approximately 40 kJ. The circuit-element model for the POS assumes only current flowing in the metal cathode, 150 kA peak, reaches the load. Thus we conclude that in the experiment, up to 40 kJ of energy associated with non-cathode current, 525 kA (assuming the experimental load power pulse waveform is comparable with the calculated one), reaches the anode and makes radiation. Electron vacuum flow alone cannot explain this result (see below). Note that

beam diode with no ions, an electric field threshold for electron emission of 100 kV/cm, and a 25-mm AK gap. The full DM1 current flowed in the circuit upstream of POS at time  $t=0$  (initiation of opening).

Measurements on Hawk with downstream current monitors in the anode and cathode suggest that the current propagates to the load nearer the anode first with a speed of the order of 1000 cm/ $\mu$ s, followed by current flowing in the cathode.<sup>13</sup> Recent results from DM1 show similar behavior. On Hawk, the time delay between the current measured near the load and at the anode and the initiation of cathode current flowing, as well as the ratio of anode to cathode current, decrease with decreasing  $Z_L$ . Several possible mechanisms have been proposed to explain the process of current transfer to the load including: vacuum electron flow, electron migration along the downstream anode via plasma production at the anode,<sup>14</sup> and various scenarios involving electron-propagation/current-transport through or by a downstream plasma. In the simulations described here, there is no attempt to include plasma that may be in the POS-to-load region as a result of the POS plasma injection and/or the conduction process. Also, there was no self-consistent algorithm for producing ions at the anode from electron energy deposition. Within the context of these assumptions, the POS-to-load inductance is self-consistently accounted for in the PIC simulations.

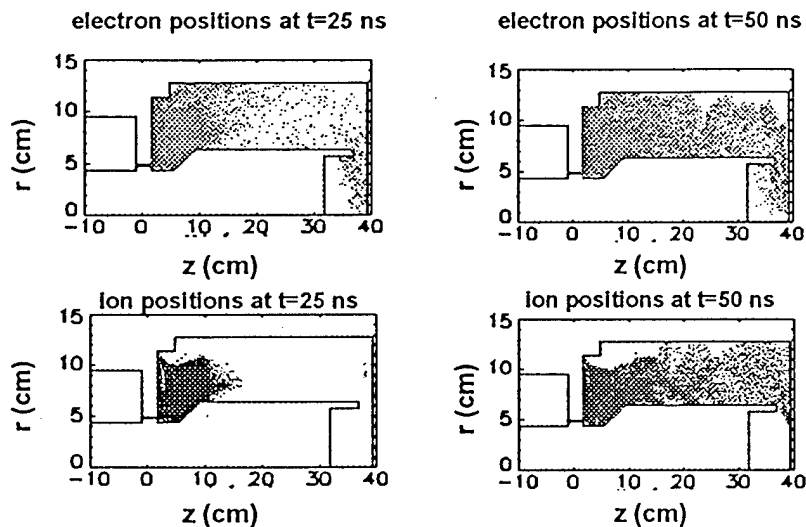


Fig. 5. Electron and ion positions at two times after opening.

In Fig. 5, ion and electron positions are plotted at two different times. At  $t=25$  ns, the electrons fill the downstream region and drag ions associated with the POS plasma into the vacuum line between the POS and load. At  $t=50$  ns, the ions (plasma) also fill the vacuum line. The behavior of the particle flow is distinctly different from that reported in previous simulations,<sup>9</sup> where the electrons hugged the anode of the vacuum line between the POS and load. In this case, the electron flow is more uniformly distributed in radius. The cause of this discrepancy is under

investigation. The onset of significant (anode) current in the diode is associated with the arrival of plasma to the diode. The speed with which the plasma moves depends on the ratio of ion charge to atomic number,  $Z/A$ , which for this simulation was assumed to be 2/5 (corresponding, e.g., to an 18%  $C^{++}/82\% H^+$  plasma - by comparison, purely  $C^{++}$  ions would have  $Z/A=2/12$ ). This  $Z/A$  was chosen to have the anode current and load power peak near the expected time after opening. The cathode current predicted by this simulation is close to the 150 kA predicted by the circuit modeling. Also, the sequencing of anode and cathode monitors observed on Hawk<sup>13</sup> and DM1 is qualitatively reproduced, with the speed of propagation about 1000 cm/ $\mu$ s. However, the total current reaching the load in the simulation was only 200 kA, a factor of 3.5 lower than what was inferred above from the radiation measurements. With a  $Z/A$  of 2/12, the total load current is less than 150 kA. These results will depend on the plasma  $Z/A$  and the existence of other plasma, either injected into or generated in the vacuum line. For example, in a recent simulation ion emission was allowed along the anode (treated as a zero work function ion source) between the POS and load. This resulted in a peak load current of 450 kA, a closer match to the inferred load current, but with the current beginning 15 to 20 ns too early. Here, a model for anode plasma production based on local energy deposition is needed. Additional simulations along with better measurements of plasma density are required to more fully understand the POS/load coupling.

### SUMMARY

We have performed an analysis of a selected set of data from the DM1 pulsed power generator using the transmission-line circuit code BERTHA, the electron/photon-transport code CYLTRAN, and the 2-dimensional particle-in-cell-code MAGIC. The results suggest that up to 75% of the energy delivered to the diode is associated with non-cathode, radiation-producing current. For the experimental series considered, the system is not optimized for energy delivery to the load. The diode impedance of 11  $\Omega$  is much higher than optimum. With the

same DM1 conduction current/time and POS performance considered in this paper, an optimum diode impedance of  $2\ \Omega$ , and a POS-to-load inductance reduced by 75%, this analysis suggests the load energy on DM1 can range from 54 kJ to 94 kJ, depending on how much non-cathode current reaches the load. To obtain agreement between features of the measurements and calculations, the DM1 flow impedance (gap) must decay after opening and ions must be present in the vacuum transmission line between the POS and load. While progress has been made in describing the coupling between the POS and e-beam load, both experimental and theoretical work is required for a fuller understanding of this complex process.

The authors wish to thank Drs. J. Goyer and D. Kortbawi of Physics International for generously giving of their time in providing DM1 data and information on the DM1 operation, Dr. R. Adler for his help in starting and interpreting the CYLTRAN calculations, and Dr. J. Rowley of the Defense Nuclear Agency for his support in this effort.

+ Work Supported by the Defense Nuclear Agency.

\* JAYCOR, Inc., Vienna VA.

### REFERENCES

1. "The DECADE High Power Generator," P. Sincerny, S. Ashby, K. Childers, C. Deeney, D. Drury, J. Goyer, D. Kortbawi, I. Roth, C. Stallings, and L. Schlitt, in Proceedings of the 9th IEEE International Pulsed Power Conference, R. White and W. Rix, eds., San Diego, CA (1993), IEEE Cat. No. 93CH3350-6, p. 880.
2. "Performance of DECADE Module #1 (DM1) and Status of the DECADE Machine," P. Sincerny, S. Ashby, K. Childers, J. Goyer, D. Kortbawi, I. Roth, C. Stallings, J. Dempsey, and L. Schlitt, in Proceedings of this Conference, W. Baker and G. Cooperstein, eds., Albuquerque, NM (1995), paper 12-3.
3. "Characterization of a Microsecond-Conduction-Time Plasma Opening Switch," R.J. Commisso, P.J. Goodrich, J.M. Grossmann, D.D. Hinshelwood, P.F. Ottinger, and B.V. Weber, *Phys. Fluids B* 4, 2368 (1992); and references therein.
4. "BERTHA - A Versatile Transmission Line and Circuit Code," D.D. Hinshelwood, NRL Memorandum Report 5185, (Nov. 1983), unpublished.
5. "ITS: The Integrated TIGER Series of Electron/Photon Transport Codes - Version 3.0," J.A. Halbleib, R.P. Kensek, G.D. Valdez, S.M. Seltzer, M.J. Berger, *IEEE Trans. Nucl. Sci.* NS-39, 1025 (1992).
6. "User Configurable MAGIC for Electromagnetic PIC Calculations," B. Goplen, L. Ludeking, D. Smithe, and G. Warren, *Comp. Phys. Comm.* 87, 54 (1995).
7. "Circuit Simulations of DM1 with an Electron-Beam Load," R.J. Commisso, J.R. Boller, D.V. Rose, and S.B. Swanekamp, NRL Memorandum Rep. 7750 (March 1996), unpublished.
8. "Experiments on a Current-Toggled Plasma-Opening Switch," C.L. Mendel, Jr., M.E. Savage, D.M. Zagar, W.W. Simpson, J.W. Grasser, and J.P. Quintenz, *J. Appl. Phys.* 71, 3731 (1992).
9. "Power Flow between a Plasma-Opening Switch and a Load Separated by a High Inductance Magnetically Insulated Transmission Line," S.B. Swanekamp, J.M. Grossmann, P.F. Ottinger, R.J. Commisso, and J.R. Goyer, *J. Appl. Phys.* 76, 2648 (1994).
10. "Modeling the Hawk POS with a Diode Load," J.R. Boller, R.J. Commisso, and B.V. Weber, *Pulsed Power Physics Branch Technote No. 95-17* (1995), unpublished.
11. J. Goyer and D. Kortbawi, personal communication.
12. "Bremsstrahlung Yield Simulations for DM1," D.V. Rose, R.J. Commisso, S.B. Swanekamp, and F.C. Young, NRL Memorandum Report 7748 (Nov. 1995), unpublished.
13. "Review of Hawk Power Flow Experiments," B.V. Weber, R.J. Commisso, P.J. Goodrich, J.M. Grossmann, S.B. Swanekamp, P.F. Ottinger, and R.A. Riley, presented at the DNA Opening Switch Workshop, NSWC, Silver Spring, MD, March (1995), *Pulsed Power Physics Branch Technote No. 95-12* (1995), unpublished.
14. "Experimental and Theoretical Investigation of 2-D Power Flow," S.B. Swanekamp, J.R. Boller, R.J. Commisso, D.D. Hinshelwood, P.F. Ottinger, and D.V. Rose in Proceedings of this Conference, W. Baker and G. Cooperstein, eds., Albuquerque, NM (1995), paper P2-21.

## SIMULATIONS OF VACUUM ELECTRON FLOW IN INDUCTIVE- ENERGY-STORE PULSED-POWER SYSTEMS

S.B. SWANEKAMP<sup>a</sup>), J.M. GROSSMANN, R.J. COMMISSO,  
P.J. GOODRICH<sup>b</sup>), P.F. OTTINGER, and B.V. WEBER

Plasma Physics Division,

Naval Research Laboratory, Washington, D.C. 20375-5346

*The current understanding of the opening process of a long-conduction-time ( $>300$  ns) plasma opening switch (POS) involves the formation of a fairly small (2-4 mm) vacuum gap. As the switch opens, electrons which are magnetically insulated in the switch gap flow into the downstream magnetically insulated transmission line (MITL). Since the vacuum electron flow can be a large fraction of the net current, it is important to understand the nature of this flow. In this paper the vacuum electron flow into an MITL as the POS opens is studied with the particle-in-cell method. Simulation results are presented for both the Decade Proto-type Module-1 (DPM1) at Physics International and the HAWK inductive energy store accelerator at NRL. The simulations show vacuum electron flow primarily near the anode as the POS opens. The HAWK simulations suggest that a low density plasma ( $\sim 10^{12}$  cm<sup>-3</sup>) can significantly alter the electron flow in the MITL.*

### I. Introduction

In the closed state, the POS must conduct megampere currents for times approaching 1  $\mu$ s.<sup>1</sup> During this time electrical energy is converted into magnetic energy and stored in the primary storage inductor. To achieve high output powers, the POS must open on a time scale short compared the conduction time and deliver the stored magnetic energy to a particle-beam-diode or imploding-plasma load.

Considerable advances have been made in understanding the conduction and opening phases of the  $\mu$ s-conduction-time POS.<sup>2</sup> However, much less is understood about the power flow out of the POS as the switch opens into the magnetically insulated transmission line (MITL) that connects the POS and load. This paper presents results of particle-in-cell (PIC) computer simulations of the vacuum electron flow in the MITL as the POS opens. These simulations are performed for two experimental geometries:

the Decade Prototype Module 1 (DPM1) at Physics International, and the HAWK inductive energy store accelerator at the Naval Research Laboratory.

### II. Power-Flow Simulations for DPM1

In the DPM1 experiment a Marx charges a 0.75  $\mu$ F water capacitor ( $C_{TC}$ ) to an initial voltage of 700 kV. During the conduction phase, the capacitor discharges through the POS as current and magnetic energy build up in the 250 nH primary storage inductor ( $L_S$ ). The quarter cycle of the  $L_S C_{TC}$  discharge is 680 ns and the peak current is approximately 1.2 MA.

A schematic of the DPM1 POS and MITL geometry is shown in Fig. 1. Plasma is introduced into the POS prior to the main pulse by a set of 8 cable guns spaced around the azimuth of a coaxial transmission line.<sup>3</sup> The location of plasma in the switch region is controlled by two masks which limit the axial extent of the plasma introduced into the MITL. Plasma from the cable guns



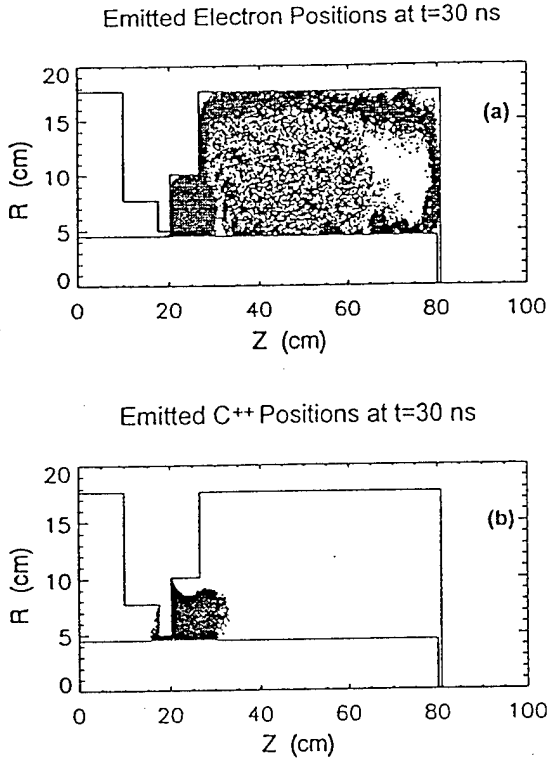


Fig. 3 Emitted electron (a) and  $C^{++}$  (b) positions in the down-stream MITL at  $t=30$  ns.

providing a conductive path between the anode and cathode.

When the series combination of the load impedance and the effective impedance of the MITL inductance [ $Z_{eff} = (L dI_L/dt)/I_L \sim L/t$ ] is large compared to the POS flow impedance, the POS operates in the switch-limited regime.<sup>2</sup> In this regime, the switch behaves as the load and the POS voltage is limited by the size of the switch gap. In the switch-limited regime a significant amount of electron current is lost in the POS. As a result of these losses, many electrons are not insulated at the load end of the POS gap. Those electrons that do flow into the MITL have been accelerated to nearly the full POS potential. If electrons then  $E \times B$  drift along equi-potential lines as they enter the downstream MITL, electron flow from the POS would be concentrated near the anode as seen in the simulations.

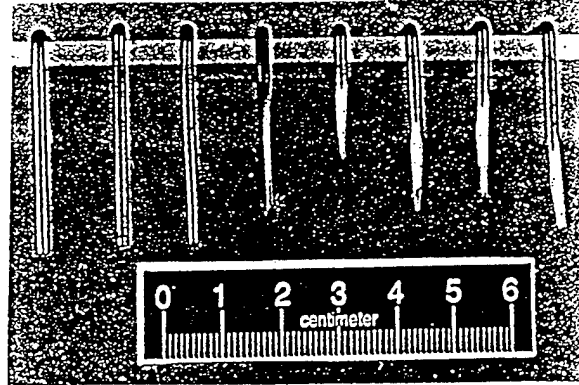


Fig. 4 Damage produced on the wires protruding from the anode.

Damage on the wires<sup>5</sup> protruding from the anode is shown in Fig. 4. Notice that the first few wires are relatively undamaged. This may be the result of plasma in the MITL which can shield the wires from the high energy electrons. The remaining wires show a large amount of damage indicating the presence of high energy electrons near the anode. This agrees qualitatively with the electron flow pattern observed in the simulations.

### III. Power-Flow Simulations for HAWK

A schematic of the HAWK power-flow experiment is shown in Fig. 5. The diagnostics that are of interest for comparison with simulations are the anode ( $I_A$ ) and the cathode ( $I_K$ ) currents nearest the load. The diode voltage and plasma density were also measured. Simulations and experiments have been performed with both plasma-filled and vacuum electron-beam-diode loads. However, since the comparison between experiment and simulation are similar for both PFD and vacuum diode loads, we will only show results from the PFD load. The simulation model for HAWK was very similar to that used for the DPM1 simulations except the geometry was changed to more closely match HAWK.



NRL/MR/6777--95-7748

## Bremsstrahlung Yield Simulations for DM1

D.V. ROSE  
S.B. SWANEKAMP

*JAYCOR, Inc.*  
*Vienna, VA*

R.J. COMMISSO  
F.C. YOUNG

*Pulsed Power Physics*  
*Plasma Physics Division*

November 22, 1995

Distribution authorized to U.S. government agencies and their contractors; administrative or operational use; November 1995  
Other requests shall be referred to Commanding Officer, Naval Research Laboratory, Washington, DC 20375-5320.

REPORT DOCUMENTATION PAGE			Form Approved OMB No. 0704-0188	
Public reporting burden for this collection of information is estimated to average 1 hour per response, including the time for reviewing instructions, searching existing data sources, gathering and maintaining the data needed, and completing and reviewing the collection of information. Send comments regarding this burden estimate or any other aspect of this collection of information, including suggestions for reducing this burden, to Washington Headquarters Services, Directorate for Information Operations and Reports, 1215 Jefferson Davis Highway, Suite 1204, Arlington, VA 22202-4302, and to the Office of Management and Budget, Paperwork Reduction Project (0704-0188), Washington, DC 20503.				
1. AGENCY USE ONLY (Leave Blank)	2. REPORT DATE  November 22, 1995	3. REPORT TYPE AND DATES COVERED  Interim		
4. TITLE AND SUBTITLE  Bremsstrahlung Yield Simulations for DM1			5. FUNDING NUMBERS  PE - 67-0881-04 67-0881-05	
6. AUTHOR(S)  D.V. Rose <sup>1</sup> , R.J. Commisso, S.B. Swanekamp <sup>1</sup> , and F.C. Young				
7. PERFORMING ORGANIZATION NAME(S) AND ADDRESS(ES)  Naval Research Laboratory Washington, DC 20375-5320			8. PERFORMING ORGANIZATION REPORT NUMBER  NRL/MR/6777-95-7748	
9. SPONSORING/MONITORING AGENCY NAME(S) AND ADDRESS(ES)  Defense Nuclear Agency/TDSP 6801 Telegraph Road Alexandria, VA 22310-3398			10. SPONSORING/MONITORING AGENCY REPORT NUMBER	
11. SUPPLEMENTARY NOTES  <sup>1</sup> Jaycor, Inc., Vienna, VA 22182				
12a. DISTRIBUTION/AVAILABILITY STATEMENT  Distribution authorized to U.S. government agencies and their contractors; administrative or operational use; November 1995. Other requests shall be referred to Commanding Officer, Naval Research Laboratory, Washington, DC 20375-5320.			12b. DISTRIBUTION CODE	
13. ABSTRACT (Maximum 200 words)  Recent bremsstrahlung production experiments on the DM1 accelerator are simulated using the integrated TIGER series, Monte Carlo, electron/photon transport codes [J.A. Halbleib, et. al., Sandia National Laboratories Report SAND91 - 1634, 1992]. Idealized bremsstrahlung diode waveforms (constant current, triangular voltage, 100-ns pulse duration) are used to explore radiation output for DM1 over a range of parameters relevant to the experimental conditions. Detailed, cylindrically symmetric models of the DM1 converter package are used throughout. Diode currents between 500 and 800 kA are inferred from measured dose-area-products (6 to 10 MRad(Si)-cm <sup>2</sup> ) and end-point voltages (1.45 to 1.75 MV), by using CYLTRAN calculations that include the re-acceleration of back-scattered electrons. This analysis implies that the total energy coupled to the diode is 40 to 65 kJ. If electron reflexing is included in these simulations, the coupled energy is reduced significantly. Calculations of dose-area-products in lithium fluoride and silicon confirm the factor used to convert measured dose in lithium fluoride to dose in silicon. The calculated radial dose profile for lithium fluoride can be represented by a Gaussian distribution of 10.5-cm radius at half-peak, which is similar to measured radial profiles.				
14. SUBJECT TERMS  Inductive store Pulsed power Radiation production			15. NUMBER OF PAGES  26	
			16. PRICE CODE	
17. SECURITY CLASSIFICATION OF REPORT  UNCLASSIFIED	18. SECURITY CLASSIFICATION OF THIS PAGE  UNCLASSIFIED	19. SECURITY CLASSIFICATION OF ABSTRACT  UNCLASSIFIED	20. LIMITATION OF ABSTRACT  SAR	

## CONTENTS

I. Introduction.....	1
II. Benchmark Calculation.....	2
III. DM1 Bremsstrahlung Yield Simulations .....	6
III. A. Calculational Procedure .....	6
III. B. Comparisons with Experiment.....	8
III. C. Converter and Beam-Stop Variations.....	12
IV. Dose Conversion Factors and Radial Dose Profile .....	13
V. Dose Production Efficiency .....	18
VI. Summary.....	20
VII. Acknowledgments.....	22
VIII. References.....	23

# BREMSSTRAHLUNG YIELD SIMULATIONS FOR DM1

## I. Introduction

The DECADE simulator [1] is designed around a radiation requirement of 20 kRad deposited in a thickness of 20-mils silicon over an area of  $10^4 \text{ cm}^2$  with a 2:1 spatial uniformity and a 40-ns full-width at half-maximum (FWHM) radiation pulse. The DM1 facility [2] at Physics International (PI) represents one of sixteen generator modules to be used in the DECADE generator. In this report, radiation outputs for experimental conditions relevant to DM1 are simulated with the two-dimensional radiation transport code CYLTRAN, which is part of the integrated TIGER series of Monte Carlo, electron/photon transport codes [3]. These results are compared with dose measurements on DM1 as well as with another CYLTRAN analysis [4]. Besides checking the consistency of the DM1 measurements, the main objective of this work is to identify a range of bremsstrahlung diode conditions consistent with the dose measurements. In particular, a major motivation for this work is to obtain an estimate of the energy delivered to the electron beam (e-beam) diode that is required to generate the measured dose. The DM1 experimental data do not include direct measurements of the diode current and voltage. The peak, or end-point, voltage is inferred from a multichannel array of filtered PIN diodes [5], [6]. Such information is crucial for characterizing the power coupling between the DM1 plasma opening switch (POS) [7] and the e-beam diode load [8].

In Sec. II of this report, calculations that model the effects of back-scattering and reflexing electrons [9] are compared with a previous CYLTRAN calculation for DM1 [4]. This is done to benchmark our simulation techniques, and to evaluate the significance of some differences in these two calculations. In this report, the use of the term *back-scattering* means including electrons back-scattered from the converter and re-accelerated into the converter by the diode electric field to make radiation. In Sec. III, these techniques are used to perform a set of simulations that cover a parameter regime appropriate for the DM1 bremsstrahlung diode experiments. It is the purpose of this section to explore limits on the e-beam diode voltage and current consistent with the radiation dose measurements. The effects of varying the tantalum thickness and beam-stop material are also discussed in this section. Lithium fluoride thermoluminescent dosimeters (TLDs) are used for the dose measurements and then are related to dose in silicon by PI. The ratio of silicon dose to lithium fluoride dose, evaluated using CYLTRAN, is presented in Sec. IV. An estimate of the dose production efficiency is given in Sec. V and conclusions are presented in Sec. VI.

## II. Benchmark Calculation

Idealized diode current and voltage waveforms are used as inputs into the CYLTRAN code. A triangular voltage waveform ( $V$ ) and flat current waveform ( $I$ ), illustrated in Fig. 1, are used, similar to previous work [4]. For such waveforms, the radiation dose rate is proportional to  $IV^x$  where the exponent  $x$  is usually between 1 and 3

for forward-directed radiation dose-rate measurements [10]-[18]. The FWHM of the radiated power is given by

$$t_{FWHM} = \tau_o(1 - (1/2)^{1/x}) , \quad (1)$$

where  $\tau_o$  is the full length of the voltage pulse. For  $\tau_o = 100$  ns,  $t_{FWHM} = 22$  ns for  $x = 2.8$ , or  $t_{FWHM} = 29$  ns for  $x = 2.0$ . The shape of the x-ray spectrum may be an important part of validating the inferred voltage [19]. Work is currently underway to estimate this effect from circuit model simulations [20].

The geometry illustrated in Fig. 2 is used for the benchmark calculation with parameters taken from Ref. [4]. An electron beam with a radius,  $r_b$ , of 8 cm is injected onto a 2-mil thick tantalum foil with a radius,  $r_T$ , of 10 cm located at  $z = 0$  cm. A 0.75-cm thick polyethylene ( $\text{CH}_2$ ) beam-stop of 24-cm radius is located at  $z = 5.0$  cm. This is followed by a 0.75-cm thick silicon absorber also of 24-cm radius. The silicon absorber is 7.5 cm from the tantalum foil. For these calculations, the silicon is subdivided into 16 radial zones ( $\Delta r = 1.5$  cm) and 5 axial "slices" ( $\Delta z = 0.15$  cm) for a total of 80 zones. These dimensions are taken from previous CYLTRAN simulations of DM1 [4], with the following important differences. The maximum radius of the silicon absorber is increased from 15 cm to 24 cm, and the number of radial zones is increased from 5 ( $\Delta r = 3.0$  cm) to 16 ( $\Delta r = 1.5$  cm). Consequently, the present calculations have improved radial resolution and encompass a larger radiated area. The electron beam is injected at  $z = 0$  (immediately to the left of the tantalum) with a uniform current density over a radius of  $r_b$  and with a

$\cos(\theta)$  distribution in momentum space, truncated at a maximum angle,  $\theta_{max}$ . Here,  $\theta$  denotes the angle between the axial and injected momentum. Figure 3 illustrates this probability distribution and a schematic of the electron beam injection plane. For the calculations presented in this Section,  $\theta_{max}=70^\circ$ . A discussion of the use of this injected electron distribution is given at the end of Sec. IV.

In the DM1 experiments, electrons back-scattered from the tantalum are most likely re-accelerated into the tantalum by the electric field of the diode. This situation is modeled by placing a constant electric field of sufficient strength to “turn around” electrons with axial energies less than or equal to the maximum diode voltage,  $V_{max}$ , to the left of the tantalum foil in Fig. 2. Unless explicitly stated, this will be the case for all the CYLTRAN calculations presented herein. In addition, electrons that pass through the tantalum foil may be redirected back into the foil if the electron current exiting the foil exceeds the space charge limit. This electron reflexing [9] is modeled by placing an electric field to the right of the tantalum in Fig. 2, equal, but oppositely directed to the back-scattering electric field. The model used here for back-scattering and reflexing electrons is not self-consistent, but for back-scattering we assume that the electric-field magnitude in the diode gap varies slowly relative to the gap crossing time of an average-energy electron. In the case of reflexing, we assume that an idealized virtual cathode is formed between the tantalum and the beam-stop that reflects all electrons back to the tantalum. In contrast, reflexing electrons were modeled in Ref. [4] by trapping the transported electron distribution and re-running the code.



Dose-area products (DAP) as a function of depth in silicon from our simulations are compared with the results of Ref. [4] in Fig. 4, and each data point represents the DAP in that axial zone ( $\Delta z$ ). The DAP is the dose integrated over the area of the silicon absorber. For all the calculations in this Section,  $\tau_o = 100$  ns,  $V_{max} = 1.5$  MV, and  $I_o = 1.0$  MA corresponding to a total energy coupled to the diode of  $E_d = 75$  kJ. Results from the present calculations with and without reflexing (open boxes and circles in Fig. 4) indicate that reflexing increases the DAP by 44%. The results of Ref. [4] are presented as three different sets of data points in Fig. 4. In the first 60-mil layer of silicon, the DAP is 9.5 MRad-cm<sup>2</sup> silicon (solid diamonds in Fig. 4). This result includes a factor of 1.6 to account for back-scattered electrons which were not included in that simulation. An additional 10% was added to the DAP in Ref. [4] because the maximum radius of the silicon absorber was only 15 cm (solid circle in Fig. 4). This result is in agreement with the present simulation results (open circles in Fig. 4), which are obtained with a larger silicon absorber of radius 24 cm. In addition, the increased DAP resulting from single-pass reflexing calculated in Ref. [4] is plotted as a solid square in Fig. 4. This result is also in agreement with the present simulation that includes electrons reflexing through the foil until they fall below the computational threshold energy or are lost radially out of the simulation region. These results show that our methods for treating either back-scattering or reflexing are in reasonable agreement with the previous CYLTRAN analysis [4] of the DM1 experiments, to the precision of the calculations.

One of the most significant differences between the geometry described in this Section and the DM1 experimental geometry, described in Section III (see Fig. 5), is the

thicker CH<sub>2</sub> beam-stop used in the actual experiments. A simulation was performed with the 0.75-cm CH<sub>2</sub> beam-stop increased to 1.91 cm (0.75 inches). Back-scattered electrons (without reflexing) were included using the same parameters as for the open circles in Fig. 4. The overall effect of the thicker beam-stop was to reduce the DAP in silicon by an average of 11%, with the largest decrease (14%) occurring in the first silicon layer. The radial dose profile in the first silicon layer was similar for these two cases; however the on-axis dose in the first silicon layer was reduced by 18% with the thicker beam-stop. In conclusion, the increase in CH<sub>2</sub> beam-stop thickness from 0.75 cm to 0.75 inches produces a modest decrease in the DAP.

### III. DM1 Bremsstrahlung Yield Simulations

#### A. Calculational Procedure

The geometry for the bremsstrahlung measurements on DM1 is illustrated in Fig. 5. An electron beam with a 6.35-cm radius is injected into a 12.7-cm radius tantalum converter of 2- or 3-mil thickness located at  $z = 0$ . This e-beam radius corresponds to the outer radius of the cathode in the DM1 diode. For the experimental configuration considered here, the beam-stop is made up of two distinct sections. The first section, located 2.87 cm from the tantalum foil, is either 0.188-inch thick CH<sub>2</sub>, 0.032-inch thick aluminum, or 0.064-inch thick aluminum. The second section, located immediately after the first section, is 0.75-inch thick CH<sub>2</sub>. In the simulations, a 300-mil thick silicon absorber is placed 3.25 inches (8.255 cm) from the tantalum foil. This absorber is subdivided into 16 radial zones ( $\Delta r = 1.5$  cm), and 8 axial zones of the following

thicknesses: two 10-mil zones, two 20-mil zones, and four 60-mil zones. This finer axial zoning permits a more detailed evaluation of the dose-depth profile than in Sec. II. In order to achieve 2% to 3% statistical accuracy in DAP calculations in 20-mils silicon over a 24-cm radius,  $1.6 \times 10^6$  primary electrons were used in the CYLTRAN calculations. Dose measurements in the DM1 experiments were made with an array of lithium fluoride TLDs located 8.255 cm from the tantalum foil. This TLD array is represented by the silicon absorber in the simulations as shown in Fig. 5. A discussion of the conversion between the measured exposure in lithium fluoride and dose silicon is given in Sec. IV.

As in the previous section, the electron beam is injected with a  $\cos(\theta)$  distribution with  $\theta_{max} = 70^\circ$  unless otherwise noted. In addition, back-scattering of the electrons is included in most of the calculations presented in this section. The energy spectrum of electrons transported through the tantalum foil is shown in Fig. 6 for 2- and 3-mil thick tantalum. For these spectra, the injected beam energy spectrum (upstream of the foil) is a square pulse with an end-point voltage of 1.75 MV and with  $dn/dE$  equal to unity in number of electrons per MeV. The thicker foil results in a less intense spectrum with a reduced, transmitted end-point energy. In addition, the effects of back-scattering on the energy spectrum are evident. For both foil thicknesses, approximately 0.1 electrons/MeV is added to the intensity of the spectrum by including back-scattering. In addition, back-scattering increases the number of low energy electrons in the transmitted spectral distribution. Angular distributions of electrons emerging from the tantalum, including back-scattering, are shown in Fig. 7 (as histograms). These angular distributions have a  $\cos^2(\theta)$  shape, and the tails of the distributions beyond  $\theta_{max} = 70^\circ$  contain scattered

electrons. The transmitted electron distribution as a function of energy and angle is presented in Fig. 8 for a 3-mil tantalum foil and  $V_{max} = 1.75$  MV. This distribution peaks at  $\theta = 0^\circ$  and at an energy of approximately 1.0 MeV.

The impact of back-scattering on the photon distribution transmitted through the beam-stop is shown in Fig. 9. Including back-scattering enhances the photon spectrum over the energy range of 20 to 200 keV by approximately 50%. Outside of this energy range, the enhancement is less. The transmitted photon spectrum including back-scattering is replotted in Fig. 10, along with the spectrum of energy absorbed in 20 mils of silicon. The primary contribution to the dose is from photons with energies less than 100 keV, but a significant contribution is made by higher energy photons.

## B. Comparisons with Experiment

A summary of results from 19 shots on DM1 is presented in Table I. The tantalum converter thickness is listed in the second column. The third column lists the material and thickness used in the first beam-stop (see Fig. 5). The peak voltage, as measured by an end-point voltage monitor [5], [6], is given in column 4. Column 5 lists the peak exposure in kRoentgen measured at 3.25 inches from the tantalum with an array of lithium fluoride TLDs. The factor to convert lithium fluoride exposure in kRoentgen to silicon dose in kRad is listed in column 6. This conversion factor is discussed further in Sec. IV. A two-dimensional distribution  $(r, \theta)$  of the dose was measured for each shot. Interpolation of this distribution in the x- and y-directions was used to determine the center of the radiation pattern and the value of the peak dose at the center. This peak dose is listed in column 7

of Table I. The interpolated center of each radiation pattern is plotted in Fig. 11. The locations of the peak dose in the dose maps are not on axis. This lack of centering is significant and efforts are underway to improve the centering. An effective radius,  $R_{eff}$ , at which the dose is reduced by a factor of two was determined by equating a circular area to the area enclosed by the contour of the x-y interpolation corresponding to one-half of the peak dose. This effective radius is listed in column 8 of Table I.

The following expression was used to fit the radial distribution of the measured dose:

$$D(r) = D_{peak} \exp\left(-\left(\frac{ar}{R_{eff}}\right)^k\right). \quad (2)$$

where  $r = 0$  corresponds to the center as indicated in Fig. 11. The values of the parameters  $a$  and  $k$  in Eq. (2) are 0.83 and 2.0 for most of the calculations presented in this report. Subsequent analysis of the TLD data by Physics International has determined that the best fit is obtained with  $a = 0.8$  and  $k = 1.7$  for the shots listed in Table I [21]. The radial dose distribution, integrated from  $r = 0$  to a maximum radius,  $R_{max}$ , is the DAP,

$$DAP = 2\pi \int D(r) r dr. \quad (3)$$

The DAP in 20 mils silicon was computed for each shot in Table I using  $R_{max} = 24$  cm in Eq. (3). The results are listed in column 9 of Table I for  $a = 0.83$  and  $k = 2.0$ . According

to Eq. (3), with  $R_{eff} = 11.5$  cm (average value from Table I), the DAP lying within a 24-cm radius includes 95% of the DAP calculated with  $R_{max} = \infty$ . The DAP for  $\alpha = 0.8$  and  $k = 1.7$  is listed in Column 10. For this modification, the increase in the DAP ranges from 5% to 12%. Column 11 lists the DAP as computed by Physics International using the  $x$ - $y$  interpolation of the  $r$ - $\theta$  distribution. For this case, changes in the DAP range from -4% to +15%, and the DAP values correspond to areas that are not cylindrically symmetric. The changes in the DAP reflected in columns 10 and 11 in Table I do not alter the conclusions of this report, which are based on the DAP values in column 9.

The DAP was calculated with CYLTRAN for a range of diode currents and voltages for comparison with the results in Table I. The DAP in silicon for  $V_{max} = 1.5$  MV and 3-mil tantalum is plotted in Fig. 12 as a function of depth in silicon for several currents ( $I_o$ ) ranging from 0.6 MA to 1.4 MA. Since the current is constant as a function of time, the electron spectral intensity scales linearly with  $I_o$ . Therefore, the depth-dose profile scales linearly with the current, as shown in Fig. 12. The DAP in silicon for  $I_o = 1.0$  MA is plotted in Fig. 13 for voltages ( $V_{max}$ ) ranging from 1.0 to 2.0 MV. Deep in the silicon absorber (120 to 300 mils), the DAP increases linearly with  $V_{max}$ . Near the surface (i.e., first 20 mils of silicon) the DAP does not scale linearly from 1.0 to 1.25 MV, but does scale linearly with voltage above 1.25 MV. A more detailed discussion of the scaling of dose in 20 mils of silicon with diode energy is given in Sec. 5.

The DAP in silicon for the DM1 geometry calculated with both back-scattering and reflexing is plotted in Fig. 14 as a function of depth in silicon for several values of  $V_{max}$ . Significant increases in the DAP are obtained by including reflexing because all

electrons pass through the tantalum until they are collisionally stopped in the tantalum or scattered radially out of the system. The DAP is enhanced by 10% to 50%, as  $V_{max}$  increases from 1.0 to 2.0 MV. The increase is greater for larger  $V_{max}$  because more passes through the tantalum are possible with higher energy electrons.

In the DM1 experiments, it is envisioned that the peak diode voltage and current may vary from shot-to-shot, but that the total energy coupled the diode ( $E_d$ ) may remain nearly unchanged. Therefore, the DAP in silicon was calculated for several different combinations of  $I_o$  and  $V_{max}$  that give  $E_d = 75$  kJ ( $\tau_o = 100$  ns). Results of these calculations are presented in Fig. 15. The peak voltage dependence of Fig. 13 is apparent only for the range,  $V_{max} = 1.0 - 1.25$  MV, with silicon thicknesses greater than 10 mils. For the range,  $V_{max} = 1.25 - 2.0$  MV, the DAP-depth profiles are essentially the same.

The DM1 results are compared with DAP calculations in Figs. 16 and 17. Contour plots of DAP as a function of diode current ( $I_o$ ) and peak voltage ( $V_{max}$ ) are used. Only back-scattering is included in the contours in Fig. 16, while both back-scattering and reflexing are included in the contours in Fig. 17. In both cases, 3-mil thick tantalum and  $\theta_{max} = 70^\circ$  were used. The DM1 experimental data for 3-mil thick tantalum and 0.188-inch  $CH_2$  first beam-stop are also plotted in these two figures. The end-point voltage is used along with the DAP in silicon (from Table I, column 9) to locate each data point. Limits of the DM1 results form "data windows," shown in Figs. 16 and 17, indicative of current and voltage ranges consistent with the DM1 results. The current inferred from this comparison is based on a pulse duration of  $\tau_o = 100$  ns. At 1.7 MV, a current of 500 to

800 kA is inferred with only back-scattering (Fig. 16), and a current of 350 to 550 kA is inferred with back-scattering and reflexing (Fig. 17).

The DM1 results are compared with contours of energy coupled to the diode in Fig. 18. The "data windows" from Figs. 16 and 17 are superimposed onto a contour map of diode energy as a function of  $I_o$  and  $V_{max}$ . With back-scattering only, the coupled energy ranges from 40 to 65 kJ. With back-scattering and reflexing, the coupled energy ranges from 30 to 50 kJ.

### C. Converter and Beam-Stop Variations

Optimizing the tantalum converter thickness is an important consideration in maximizing the radiation output of DM1. The sensitivity of the DAP to the tantalum thickness is illustrated in Fig. 19, which presents the DAP as a function of silicon thickness for tantalum foils of 1- to 6-mil thickness. For these calculations,  $V_{max} = 1.5$  MV,  $I_o = 1.0$  MA, and back-scattering is included. For the first 10 to 20 mils of silicon, only small differences in the DAP are observed for 2- to 4-mil thick tantalum. However, for 1 mil, the DAP is well below the optimum for the electron energy spectrum considered here. Deeper in the silicon, 1- and 2-mil thick tantalum produce less dose than 3- and 4-mil thick tantalum. For 6-mil thick tantalum, the DAP is reduced near the surface of the silicon, but is not significantly reduced for thicknesses greater than 100 mils. These calculations indicate that the DAP is optimized for 3- to 4-mil thick tantalum converters. The results in Table I are consistent with this conclusion. For the four shots in Table I with a 2-mil tantalum converter, the average DAP is  $6.4 \pm 0.9$  MRad-cm<sup>2</sup>, which is



marginally less than the average DAP for the first eleven shots in Table I with a 3-mil tantalum converter ( $7.9 \pm 1.3$  MRad-cm<sup>2</sup>).

For four shots listed in Table I, the first beam-stop section of 0.188-inch CH<sub>2</sub> was replaced with either 0.032-inch or 0.064-inch aluminum. The effect of this beam-stop change, simulated with CYLTRAN, is presented in Fig. 20 for  $V_{max} = 1.75$  MV,  $I_o = 1$  MA, and 3-mil thick tantalum with back-scattering. With this change, the increase in the DAP is ~10% in the first 10 to 20 mils of silicon, and somewhat less at larger depths. This change is reflected in DAP values from Table I despite shot-to-shot variations in the measurements. The average DAP and standard deviation for eleven shots in Table I with a 3-mil tantalum converter and with a 0.188-inch CH<sub>2</sub> first beam-stop is  $7.9 \pm 1.3$  MRad-cm<sup>2</sup>. For four shots with an aluminum first beam-stop, this average increases to  $9.4 \pm 0.9$  MRad-cm<sup>2</sup>. This change in the DAP is consistent with the change predicted by CYLTRAN calculations within the DM1 shot-to-shot variations.

#### IV. Dose Conversion Factors and Radial Dose Profile

For the DM1 data in Table I, the dose is measured with lithium fluoride (LiF) TLDs at 3.25 inches from the tantalum converter. The LiF TLD response is absolutely calibrated by Physics International personnel with a Cs-137, 662-keV gamma-ray source. The Cs-137 strength in Roentgens is determined with an air-filled ionization chamber. Then the LiF TLD dose in Rads is given by:

$$Rads(LiF) = \frac{(\mu_a/\rho)_{LiF}}{(\mu_a/\rho)_{air}} \left[ \frac{Rads}{100 \text{ erg/g}} \right] \left[ \frac{87 \text{ erg/g}}{Roentgen} \right] Roentgens(air) \quad (4)$$

$$Rads(LiF) = 0.81 \times Roentgens(air), \quad (5)$$

where the mass absorption coefficients ( $\mu_a/\rho$ ) in LiF and air are evaluated at 662 keV. To correct for variations in the absorption coefficients with photon energy from 662 keV to lower energy photons (< 100 keV) which make the primary contribution to the dose on DM1, the conversion factor is increased by 5% to give:

$$Rads(LiF) = 0.85 \times Roentgens. \quad (6)$$

The conversion of absorbed energy from Rad(LiF) to Rad(Si) is sensitive to the thickness of the tantalum converter and to the spectral end-point energy. The following procedure was used by Physics International personnel to determine this conversion factor. The dose at 1 meter from the converter on DM1 was measured with LiF TLDs, calcium fluoride (CaF<sub>2</sub>) TLDs, and with a calibrated silicon PIN diode [22]. Ratios of these dose measurements provide two independent determinations of the LiF-to-silicon conversion factor. Monte Carlo calculations of the doses in these three detectors were performed by Physics International to determine the dependence of the doses on the converter thickness and on the end-point voltage. Representative voltage and current waveforms were used for these calculations. One conversion factor is determined from

the calculated scaling of Rad(Si)-to-Rad(LiF) with end-point voltage. A second conversion factor was determined by comparing the measured  $\text{CaF}_2$ -to-LiF ratio with calculations of doses in  $\text{CaF}_2$ , LiF, and silicon. The conversion factors listed in column 6 of Table I, are averages of these two determinations. Conversion factors from the end-point voltage are 6% to 12% larger and from the  $\text{CaF}_2$  to LiF ratios 6% to 12% smaller than the average values. These conversion factors were used to convert LiF TLD measurements at 3.25 inches from the tantalum to dose silicon.

The conversion from *exposure* in lithium fluoride to *dose* in silicon is cross checked with CYLTRAN simulations by replacing the silicon absorber with lithium fluoride. Individual lithium fluoride TLDs used in the DM1 experiments consist of hollow  $\text{CH}_2$  cylinders, 16-mm long by 5-mm diam outer dimensions and 5-mm long by 3-mm diam inner dimensions. Each TLD contains 0.04 g of lithium fluoride powder, which fills the TLD inner volume, giving a mass density of  $1.13 \text{ g/cm}^3$ . The axis of each TLD cylinder is oriented perpendicular to the beam axis. This TLD geometry was represented in CYLTRAN with the following, equivalent cylindrical geometry. A 1-mm thick layer of  $\text{CH}_2$  was used to simulate the TLD wall thickness. This was followed by a 0.235-cm (92 mils) thick layer of lithium fluoride of mass density  $1.13 \text{ g/cm}^3$ . This thickness of lithium fluoride was obtained by equating a 3-mm by 5-mm rectangular TLD front surface area to a circular area to give a radius of 0.219 cm. The volume of a cylindrical TLD of this area was equated in the actual lithium fluoride volume to give a 0.235-cm thick layer of lithium fluoride.

The DAP in lithium fluoride is calculated with CYLTRAN and compared with the DAP calculated in silicon. For  $V_{max} = 1.75$  MV and  $I_o = 1.0$  MA, these calculations give  $5.8 \text{ MRad(LiF)-cm}^2$  for 92 mils of lithium fluoride and  $12.5 \text{ MRad(Si)-cm}^2$  for 20 mils of silicon. The DAP in lithium fluoride is converted to silicon by combining the conversion from  $\text{Rad(LiF)}$  to Roentgens in Eq. (6) with the conversion from Roentgens to  $\text{Rad(Si)}$  in column 6 of Table I. The average value (1.70) from column 6 is used for the  $\text{Rad(Si)/Roentgen}$  ratio. The DAP, converted to silicon, is  $11.6 \text{ MRad(Si)-cm}^2$ , which is only 7% smaller than the  $12.5 \text{ MRad(Si)-cm}^2$  DAP from the CYLTRAN calculation. This difference is within the uncertainties of the conversion factors in column 6 of Table I. Therefore, these CYLTRAN calculations are consistent with the conversion from lithium fluoride exposure to silicon dose used in Table I.

The radial dose profile in lithium fluoride is calculated with CYLTRAN and represented by a Gaussian profile in order to make comparisons with average values of  $D_{peak}$  and  $R_{eff}$  listed in Table I. Average values for the first eleven shots in Table I are a peak dose of  $8.3 \pm 1.5$  kRoentgens, or  $7.0 \pm 1.3$  kRad(LiF), and an effective radius of  $11.5 \pm 0.8$  cm where the uncertainties represent shot-to-shot standard deviations. The radial dose profile in 92 mils of lithium fluoride, calculated with CYLTRAN for  $V_{max} = 1.75$  MV, is plotted in Fig. 21 along with error bars which represent computed statistical uncertainties. These error bars are larger at small radii because the lithium fluoride area in which the dose is produced is smaller. This profile is scaled to 7.0 kRad(LiF) at the origin for comparison with the average values from Table I. A Gaussian fit to this radial profile, shown in Fig. 21, gives  $R_{eff} = 10.5$  cm. This radius is

reasonably consistent with the average effective radius ( $11.5 \pm 0.8$  cm) from Table I. It should be noted that the effective radius in Table I represents an area that is not necessarily cylindrically symmetric. Also, analysis by Physics International indicates that the measured radial profile is less peaked than a Gaussian distribution [21] so that comparison with a Gaussian may under-estimate the effective radius. A more precise calculation of the radial dose profile may be sensitive to the electron spatial distribution in the diode or to details of the experimental geometry. Work is presently underway to examine the impact of variations in the electron spatial distribution and experimental geometry on the radial dose profile.

The sensitivity of the radial dose profile and the DAP to significant changes in the injected electron distribution was examined in a set of CYLTRAN calculations. The  $\cos(\theta)$  distribution discussed in Sec. II and shown in Fig. 2 was replaced with an electron distribution with a fixed angle of injection. Cases were run for injection angles of  $0^\circ$  (normal to the tantalum),  $70^\circ$ , and  $90^\circ$  (parallel to the tantalum). No significant differences in the radial dose profile or the DAP in 20 mils silicon are observed for any of these changes. This insensitivity to electron injection angle is due primarily to the tantalum thickness. To test this result, a calculation was made with a 0.1-mil thick tantalum foil and a fixed electron injection angle of  $70^\circ$ . In this case, the photon distribution, sampled immediately after the tantalum, peaked at an angle of  $70^\circ$  with respect to the z-axis. Therefore, changes in the injected electron angular distribution are reflected in the photon radial distribution if the converter is sufficiently thin.

## V. Dose Production Efficiency

Results of the CYLTRAN calculations are used to determine the efficiency for producing dose in silicon on DM1 as a function of the energy coupled to the diode. The dose production efficiency is defined as the ratio of energy absorbed in a given thickness of silicon,  $E_{ab}$ , to the energy coupled to the diode,  $E_d$ . The absorbed energy is given by

$$E_{ab} = DAP \times z \times \rho , \quad (7)$$

where  $z$  is the thickness of silicon in which the DAP is computed and  $\rho = 2.42 \text{ g/cm}^3$  is the mass density of silicon. The absorbed energy, like the DAP, is dependent on the geometry of the converter, beam-stop and absorber. The energy absorbed in 20 mils of silicon is plotted in Fig. 22 as a function of coupled energy for the DM1 diode geometry. Results for two different types of diode-energy calculations are presented in this figure. For constant end-point voltage, the absorbed energy scales linearly with the electron current and diode energy, as expected (circles in Fig. 22). For constant current, the absorbed energies are calculated for end-point voltages ranging from 1.0 to 2.0 MV (diamonds and squares in Fig. 22). In this voltage range, the scaling of absorbed energy with energy coupled to the diode is nearly linear, and the efficiency is the slope of this line. For the idealized waveforms in this report, the dose production efficiency in 20 mils of silicon is constant at 0.018%.

The calculated linear scaling of the coupled energy and dose with end-point voltage from 1.0 to 2.0 MV is unexpected. A scaling stronger than linear is usually

observed for pulsed-power generators in this energy range. This linear scaling results in a nearly constant efficiency, contrary to the usual expectations of increasing efficiency with voltage [24], [25], albeit for forward-directed radiation from a thick converter. The reason for this scaling is not obvious, but is probably a consequence of several factors which complicate the interpretation of radiation from DM1. The 3-mil tantalum converter is less than 20% of the electron range at 1.7 MV (not a thick target), and the radiation is generated by a broadened angular distribution represented by a  $\cos\theta$  electron momentum distribution (not forward-directed). Both of these effects tend to reduce the sensitivity of the DAP to the end-point voltage. In addition, the dose is produced primarily by soft radiation ( $< 100$  keV photons) which can be significantly attenuated or spectrally downshifted in the 0.938-inch  $\text{CH}_2$  beam-stop. Monte Carlo codes, such as CYLTRAN, are required to calculate the radiation output under such conditions.

## VI. Summary

Radiation from the DM1 large-area bremsstrahlung diode is evaluated with the electron/photon transport code CYLTRAN. Idealized diode voltage and current waveforms are used because these waveforms were not measured on DM1. Electron back-scattering and/or reflexing, which enhance the bremsstrahlung output, can be treated with this code. Calculations of the dose-area product (DAP) in silicon are benchmarked against previous calculations [4] for DM1 that have less spatial resolution and use different computational techniques to model back-scattering and reflexing. Results from these two calculations are in agreement to within 10%. Also, calculations of energy distributions of electrons transmitted through 2- and 3-mil thick tantalum converters with or without back-scattering scale in intensity and spectral shape as expected. These results indicate that this code can be used to make reliable bremsstrahlung calculations, including back-scattering and reflexing, under conditions relevant to DM1.

Calculations of the DAP for the large-area DM1 converter geometry are compared with measurements to place limits on the e-beam diode current and coupled energy. The DAP is sensitive to the silicon absorber thickness. A thin absorber is normally used to represent the front surface dose. A thickness of 20 mils was chosen as appropriate for bremsstrahlung from the DECADE simulator (based on original specifications). The scaling of the DAP with end-point diode voltage is calculated for silicon thicknesses ranging from 10 to 300 mils. For thicknesses of 20 to 40 mils, the DAP is essentially constant, but decreases slowly as the thickness is increased further. This DAP scales linearly with end-point voltage from 1 to 2 MV; consequently the front-surface DAP is



nearly independent of voltage for a fixed diode energy (i.e., increasing voltage is offset by decreasing current). By comparing the measured DAP and end-point voltage for ten shots on DM1 with CYLTRAN calculations, limits on the diode current of 500 to 800 kA are obtained for diode voltages ranging from 1.45 to 1.75 MV. Also, the energy coupled to the diode is restricted to 40 to 65 kJ. These currents are two to three times smaller than the current measured upstream of the plasma opening switch (POS) on DM1 [20], [23]. Therefore, more efficient transfer of current from the POS to the load should increase the coupled energy and the DAP on DM1.

Two changes in the DM1 diode geometry were modeled with CYLTRAN calculations to evaluate their impact on the DAP. Replacing the first 0.188-inch portion of the CH<sub>2</sub> beam-stop with aluminum increases the DAP by no more than 10%. Also, calculations for different tantalum converters indicate that the DAP is maximized for a 3- to 4-mil thick converter and is reduced by 10% for a 2-mil thick converter (assuming no reflexing).

The absolute bremsstrahlung efficiency and the DAP depend on the precision of the LiF TLD measurements and on the conversion of absorbed energy from LiF to silicon. CYLTRAN calculations for both LiF and silicon were used to cross check the conversion used by Physics International. The CYLTRAN results are consistent with the conversion factor determined by Physics International. The CYLTRAN calculations for back-scattering indicate that the DAP or energy absorbed in 20 mils of silicon scales nearly linearly with diode energy for end-point voltages ranging from 1.0 to 2.0 MV. Consequently, the dose production efficiency is nearly constant. For constant efficiency

and fixed end-point voltage, the DAP can be increased only by increasing the electron current. The CYLTRAN calculations indicate that a significant increase in available electron current and efficiency can result from electron reflexing in the diode. The increase in the DAP with reflexing is sensitive to end-point voltage and ranges from 10% at 1 MV to 50% at 2 MV. The diode on DM1 is configured to allow for reflexing, and the DM1 dose measurements may already be enhanced by reflexing electrons. If reflexing occurs, then the inferred diode current and coupled energy are reduced proportionately.

Measured and computed radial dose profiles show qualitative agreement over the range  $r = 0$  to 24 cm. Most of the dose is absorbed in lithium fluoride at  $z = 3.25$  inches within a radius of 11 cm which is nearly twice the electron-beam radius. The radial dose profile and DAP are insensitive to the electron injection angle for the optimized tantalum converter thickness (3 to 4 mils). These characteristics suggest that a 2-dimensional diode array as planned for DECADE with a diode spacing of about 30 cm can produce a 2:1 uniformity over  $10^4 \text{ cm}^2$ . However, reproducible centering of the bremsstrahlung source and a factor-of-two increase in the current are required to achieve the goals envisioned for DECADE.

## VII. Acknowledgments

The authors wish to thank Dr. R. Adler (Northstar Research) for generously providing his CYLTRAN input deck, and Dr. R. Schneider (PI) and Dr. D. Kortbawi (PI) for help with interpreting the DM1 measurements. Dr. R. Kensek (SNL) provided valuable assistance in modifying the CYLTRAN code. In addition, we wish to thank NRL

colleagues Mr. J.R. Boller, Dr. G. Cooperstein, Dr. J.M. Grossmann, Dr. P.F. Ottinger, Dr. S.J. Stephanakis, and Dr. B.V. Weber for discussions during various stages of this work. The continued support of Dr. J. Rowley (DNA) is greatly appreciated. This work was supported by the Defense Nuclear Agency.

### VIII. References

- [1] C. McDonald, P. Sincerny, and L. Schlitt, "Electrical Modeling of a Fast Charge, Inductive Store Concept for DECADE," in Proceedings of the Eighth IEEE International Pulsed Power Conference, R. White and K. Prestwich, eds. (IEEE, NY, 1991), p. 675; P. Sincerny, S. Ashby, K. Childers, C. Deeney, D. Drury, J. Goyer, D. Kortbawi, I. Roth, C. Stallings, and L. Schlitt, "The DECADE high power generator," in Proceedings of the Ninth IEEE International Pulsed Power Conference, K. Prestwich and W. L. Baker, eds. (IEEE, NY, 1993), p. 880.
- [2] P. Sincerny, S. Ashby, K. Childers, J. Goyer, D. Kortbawi, I. Roth, C. Stallings, J. Dempsey, and L. Schlitt, "Performance of DECADE Module #1 (DM1) and the Status of the DECADE Machine," in the Proceedings of the Tenth IEEE International Pulsed Power Conference, W.L. Baker and G. Cooperstein, eds. (IEEE, NY, 1995), paper 12.3.
- [3] J.A. Halbleib, R.P. Kensek, T.A. Mehlhorn, G.D. Valdez, S.M. Seltzer, M.J. Berger, "ITS Version 3.0: The Integrated TIGER Series of Coupled Electron/Photon Monte Carlo Transport Codes," Sandia National Laboratories

- Report SAND91-1634 (1992). [Also in Oak Ridge National Laboratory - Radiation Shielding Information Center Report CCC-467, 1994]
- [4] R.J. Adler, "Radiation Production Simulations of the DECADE Simulator," 1994, *unpublished*.
- [5] J.C. Riordan, J.E. Faulkner, D. Kortbawi, J.S. Meachum, R.S. Mendenhall, I.S. Roth, and B.A. Whitton, "A differential absorption spectrometer for bremsstrahlung diode voltage measurement," Digest of Tech. Papers, Eighth IEEE International Pulsed Power Conf. (IEEE Publishing Services, NY, 1991), p. 390.
- [6] J.C. Riordan, J.E. Faulkner, J.R. Goyer, D. Kortbawi, J.S. Meachum, R.S. Mendenhall, I.S. Roth, and B.A. Whitton, "A differential absorption spectrometer for bremsstrahlung diode voltage measurement," Rev. Sci. Instrum. **63**, 4792 (1992).
- [7] J.R. Goyer, D. Kortbawi, F.K. Childers, J.A. Dempsey, I.S. Roth, and P.S. Sincerny, "Opening switch research and development for DECADE," in the Proceedings of the 10th International Conf. on High Power Particle Beams, 1994, p.1 (Copies can be ordered from NTIS, P.O. Box 1425, Springfield, Va, 22151; NTIS document number PB95-144317).
- [8] S.B. Swanekamp, J.M. Grossmann, P.F. Ottinger, R.J. Comisso, and J.R. Goyer, "Power flow between a plasma-opening switch and a load separated by a high-inductance magnetically insulated transmission line," J. Appl. Phys. **76**, 2648 (1994).

- [9] B.V. Weber, S.J. Stephanakis, J.R. Boller, G. Cooperstein, J.C. Kellogg, J.M. Neri, and F.C. Young, "Bremsstrahlung X-Ray Source Enhancement Using Reflexing Converters," *J. Radiation Effects, Research and Engineering*, **12**, 232 (1994).
- [10] T.W.L. Sanford, J.A. Halbleib, J.W. Poukey, C.E. Heath, and R. Mock, "Dose-Voltage Dependence of Coaxial Bremsstrahlung Diodes," *Nucl. Inst. Meth. Phys. Research*, **B34**, 347 (1988).
- [11] S.J. Stephanakis, private communication.
- [12] W.F. Oliphant, C.M. Dozier, D.B. Brown, S.J. Stephanakis, J.R. Boller, and G. Cooperstein, "A Characterization and Optimization Study of GAMBLE II as an X-Ray Bremsstrahlung Source," 1982 IEEE Conference on Nuclear and Space Radiation Effects (Las Vegas, NV, July 1982).
- [13] D.E. Beutler, J.A. Halbleib, T.W.L. Sanford, and D.P. Knott, "Experimental verification of bremsstrahlung production and dosimetry predictions as a function of energy and angle," *IEEE Trans. Nucl. Sci.* **NS-41**, 2727 (1994).
- [14] T.W.L. Sanford, J.A. Halbleib, W. Beezhold, and L.J. Lorence, "Experimental verification of non-equilibrated bremsstrahlung dosimetry predictions for 0.75 MeV electrons," *IEEE Trans. Nucl. Sci.* **NS-33**, 1261 (1986).
- [15] T.W.L. Sanford, J.A. Halbleib, and W. Beezhold, "Experimental check of bremsstrahlung dosimetry predictions for 0.75 MeV electrons," *IEEE Trans. Nucl. Sci.* **NS-32**, 4410 (1985).

- [16] T.W.L. Sanford, D.E. Beutler, J.A. Halbleib, and D.P. Knott, "Experimental verification of bremsstrahlung production and dosimetry predictions for 15.5 MeV electrons," IEEE Trans. Nucl. Sci. **NS-38**, 1160 (1991).
- [17] T.W.L. Sanford, J.W. Poukey, J.A. Halbleib, R.C. Mock, and W.H. McAtee, "Voltage dependence of electron dynamics in high-power extended planar-anode diodes," J. Appl. Phys. **73**, 2004 (1993).
- [18] T.W.L. Sanford, J.A. Halbleib, and R.C. Mock, "Dose-rate field of the Hermes III flash x-ray source," IEEE Trans. Nucl. Sci. **NS-37**, 1762 (1990).
- [19] D.L. Fehl, G.T. Baldwin, and L.J. Lorence, Jr., "Cautions in using x-ray measurements derived from broad spectral response functions to determine the peak voltage of flash bremsstrahlung sources," Rev. Sci. Instrum. **63**, 4789 (1992),  
C.M. Dozier, D.B. Brown, J.W. Criss, and L.S. Birks, "Accurate x-ray diagnostics of electron beam x-ray simulators," IEEE Trans. Nucl. Sci. **NS-25**, 1634 (1978).
- [20] R.J. Commisso, J.R. Boller, D.V. Rose, and S.B. Swanekamp, "DM1 Circuit Simulations With an Electron-Beam Load," NRL Memorandum Report # 7750 (1995).
- [21] D. Kortbawi, Physics International, private communication.
- [22] Calibrated PIN provided courtesy of R. Poll, Jaycor, Inc.
- [23] J. Goyer, D. Kortbawi, Physics International, DM1 data base.
- [24] R.D. Evans, *The Atomic Nucleus*, (McGraw Hill, New York, 1955) p. 617.
- [25] H.W. Koch and J.W. Motz, "Bremsstrahlung Cross-Section Formulas and Related Data," Rev. Mod. Phys. **31**, 920 (1959).

Table I

## Summary of Measurements on DM1

(1)	(2)	(3)	(4)	(5)	(6)	(7)	(8)	(9)	(10)	(11)
DM1 Shot #	Ta (mils)	1st Beam Stop	End-point V (MV)	at 3.25" from Ta Peak Exposure (kRoent)	LiF to silicon Conv. Factor	$D_{peak}$ [kRad(Si)]	$R_{eff}$ (measured) (cm)	DAP From Eq. (2) $a = 0.83, k = 2$ 20 mils silicon (MRad-cm <sup>2</sup> )	DAP From Eq. (2) $a = 0.8, k = 1.7$ 20 mils silicon (MRad-cm <sup>2</sup> )	DAP From measurements 20 mils silicon (MRad-cm <sup>2</sup> )
1340	3	0.188" CH <sub>2</sub>	1.45	9.09	1.77	16.1	10.7	8.14	8.95	8.80
1345	3	0.188" CH <sub>2</sub>	1.75	9.77	1.66	16.2	11.3	8.95	9.79	9.52
1346	3	0.188" CH <sub>2</sub>	1.65	5.82	1.66	9.66	12.2	6.06	6.51	6.31
1347	3	0.188" CH <sub>2</sub>	1.7	11.0	1.71	18.8	10.9	9.77	10.8	10.3
1348	3	0.188" CH <sub>2</sub>	1.7	8.54	1.69	14.4	10.2	6.64	7.42	7.66
1349	3	0.188" CH <sub>2</sub>	1.7	7.56	1.70	12.9	12.6	8.49	9.09	8.46
1350	3	0.188" CH <sub>2</sub>	1.6	6.79	1.74	11.8	12.5	7.71	8.23	7.57
1351	3	0.188" CH <sub>2</sub>	1.7	7.92	1.65	13.1	11.1	7.05	7.70	7.53
1352	3	0.188" CH <sub>2</sub>	-	9.15	1.74	15.9	12.1	9.92	10.6	10.1
1353	3	0.188" CH <sub>2</sub>	1.75	8.33	1.65	13.7	11.4	7.76	8.38	8.15
1354	3	0.188" CH <sub>2</sub>	1.65	6.93	1.73	12.0	11.1	6.42	7.06	6.96
1355	2	0.188" CH <sub>2</sub>	1.75	6.79	1.62	11.0	11.1	5.89	6.47	6.28
1356	2	0.188" CH <sub>2</sub>	1.6	7.02	1.71	12.0	12.0	7.33	7.91	7.67
1357	2	0.188" CH <sub>2</sub>	1.5	5.85	1.78	10.4	12.3	6.66	7.09	7.16
1359	2	0.188" CH <sub>2</sub>	1.65	4.68	1.65	7.72	13.5	5.66	5.94	5.45
1341	3	0.064" Al	1.8	10.8	1.72	18.5	10.8	9.52	10.4	10.2
1342	3	0.064" Al	1.65	7.89	1.77	14.0	11.6	8.12	8.79	8.39
1343	3	0.032" Al	1.7	12.1	1.75	21.1	10.5	10.3	11.4	11.3
1344	3	0.032" Al	-	10.1	1.72	17.3	11.4	9.69	10.6	10.3

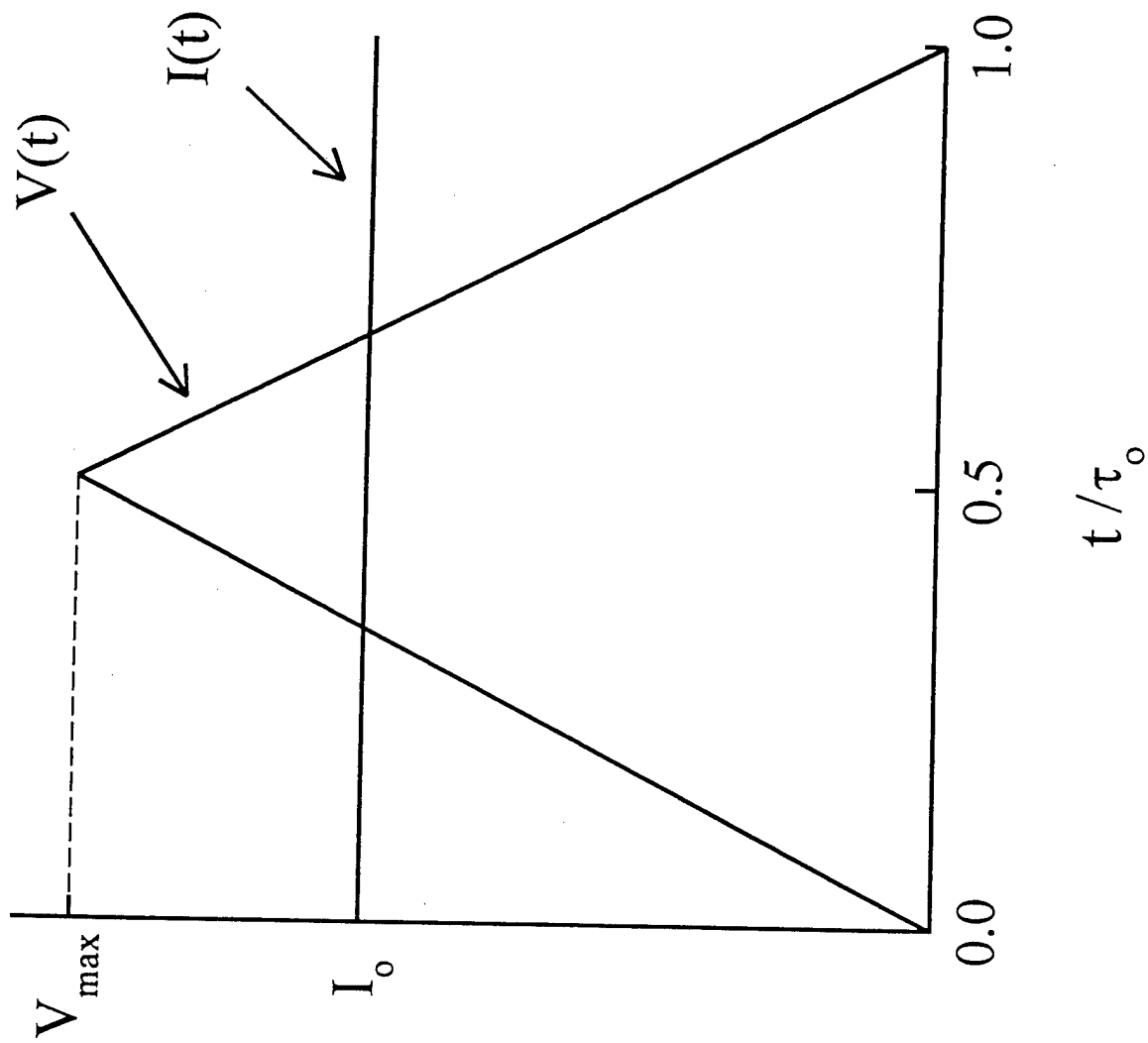


Fig. 1 Idealized diode current and voltage waveforms as a function of a normalized time,  $t/\tau_o$ , that are used as CYLTRAN inputs.



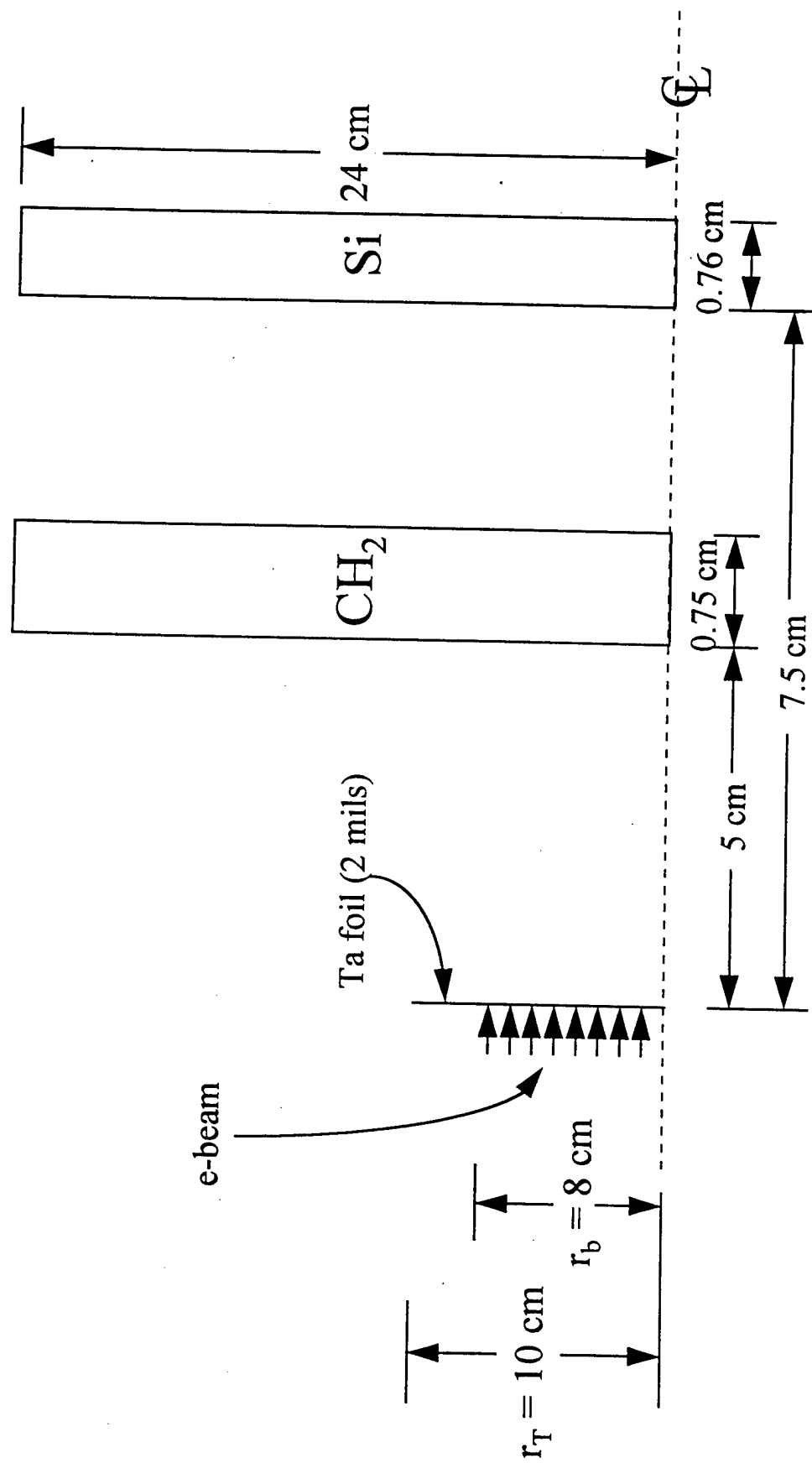


Fig. 2 - Cylindrical geometry for the bremsstrahlung dose calculations in Ref. [4].

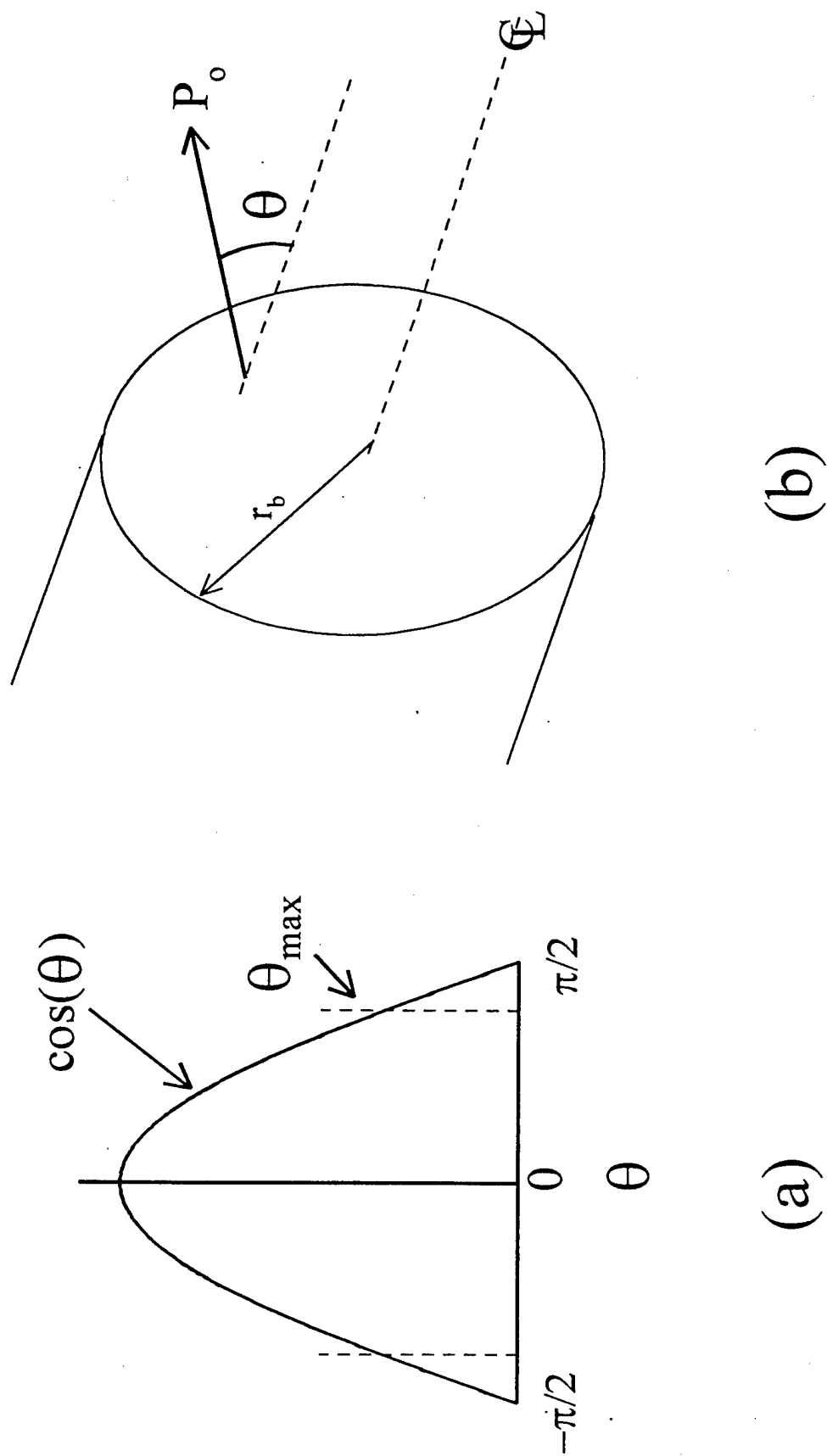


Fig. 3 (a) Momentum space distribution function,  $\cos(\theta)$  with  $\theta_{\max} = 70^\circ$ . (b) Schematic of the injection plane geometry for an electron of momentum  $P_o$  from a surface of radius  $r_b$ .

# 2 mil Ta, 0.75 cm thick beam stop

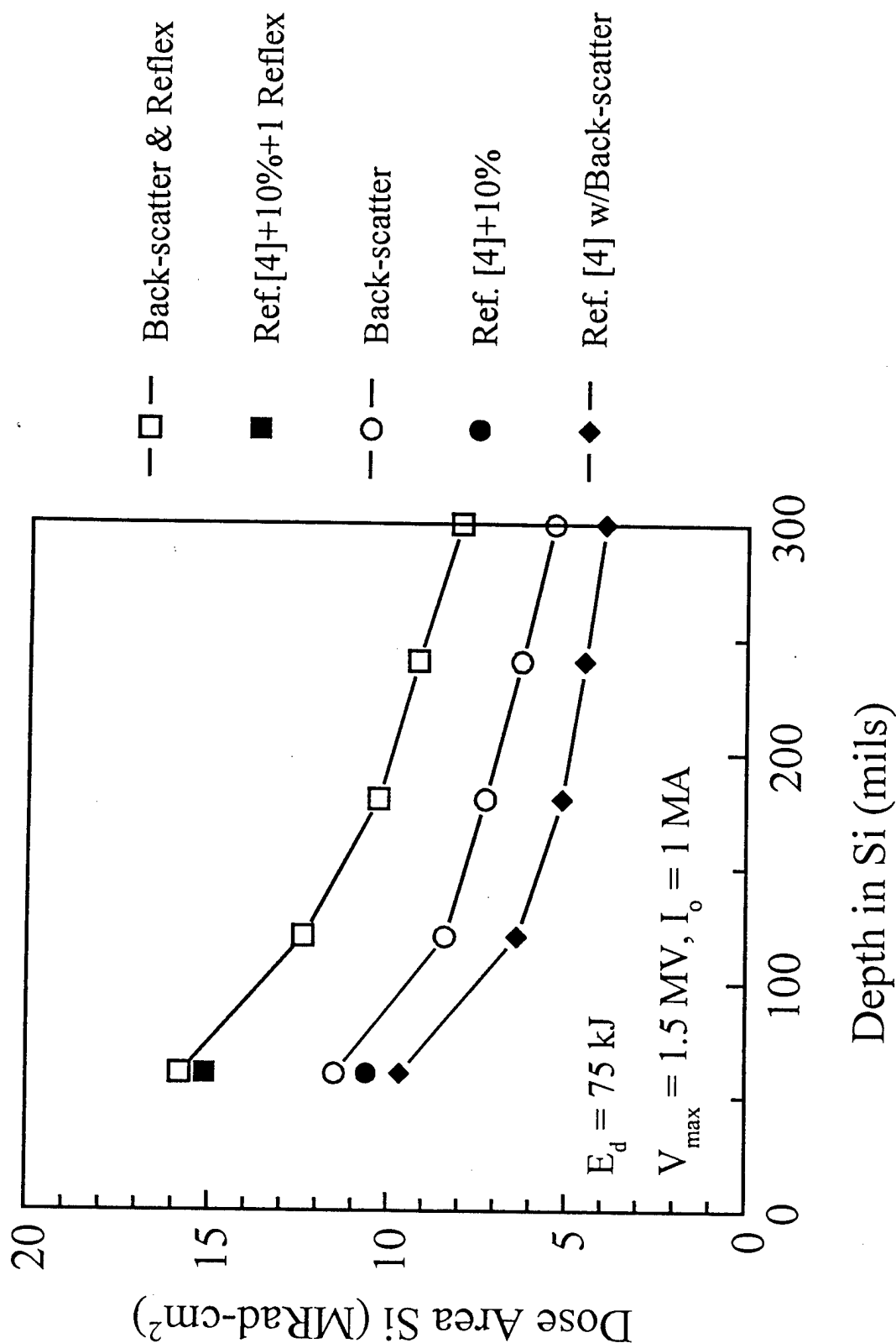


Fig. 4 Benchmark calculation results. Solid data points are from Ref. [4] and open points are from this work.

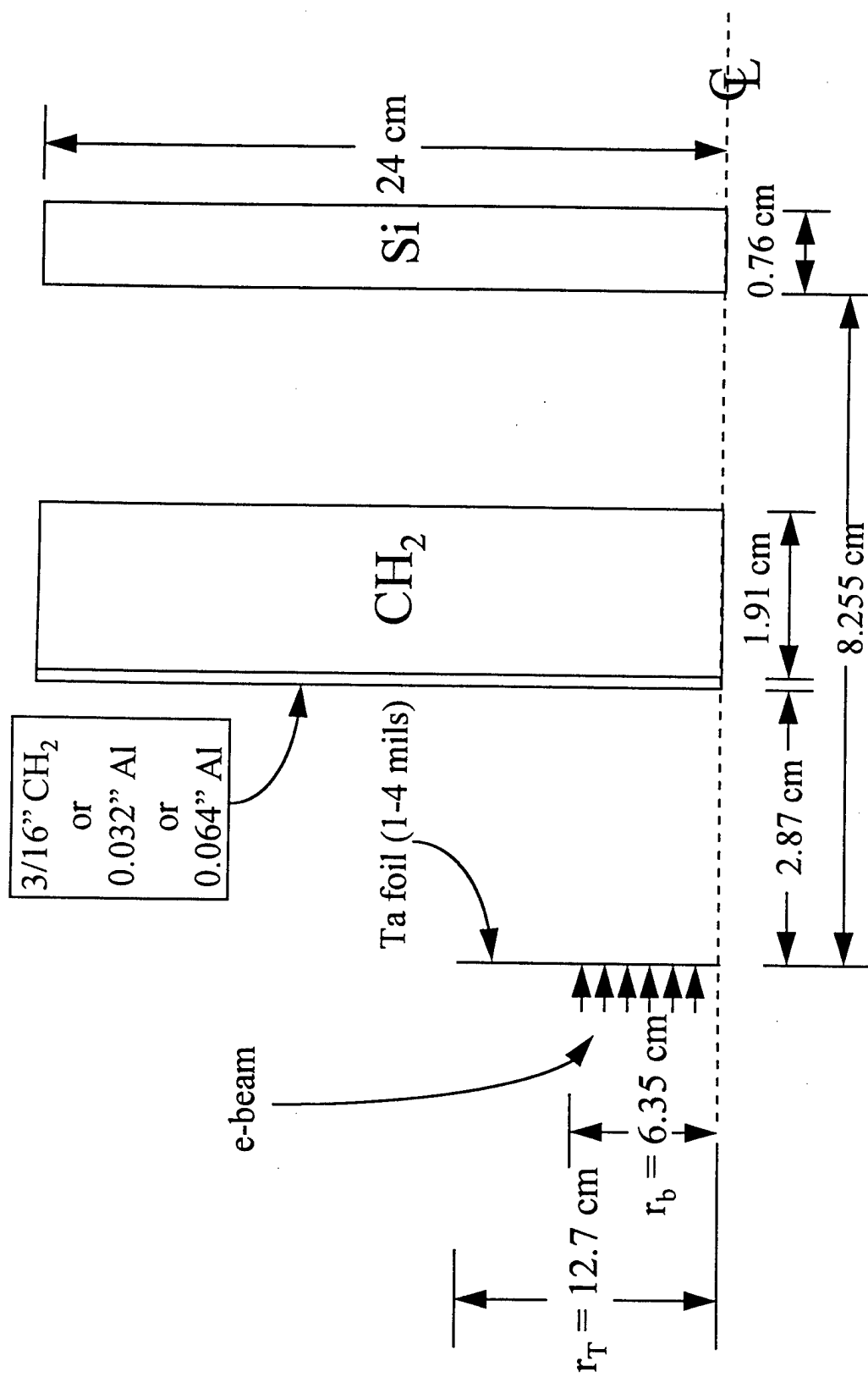


Fig. 5 - Cylindrical geometry used in the CYLTRAN simulations of bremsstrahlung measurements on DM1.

# Normalized To One Electron

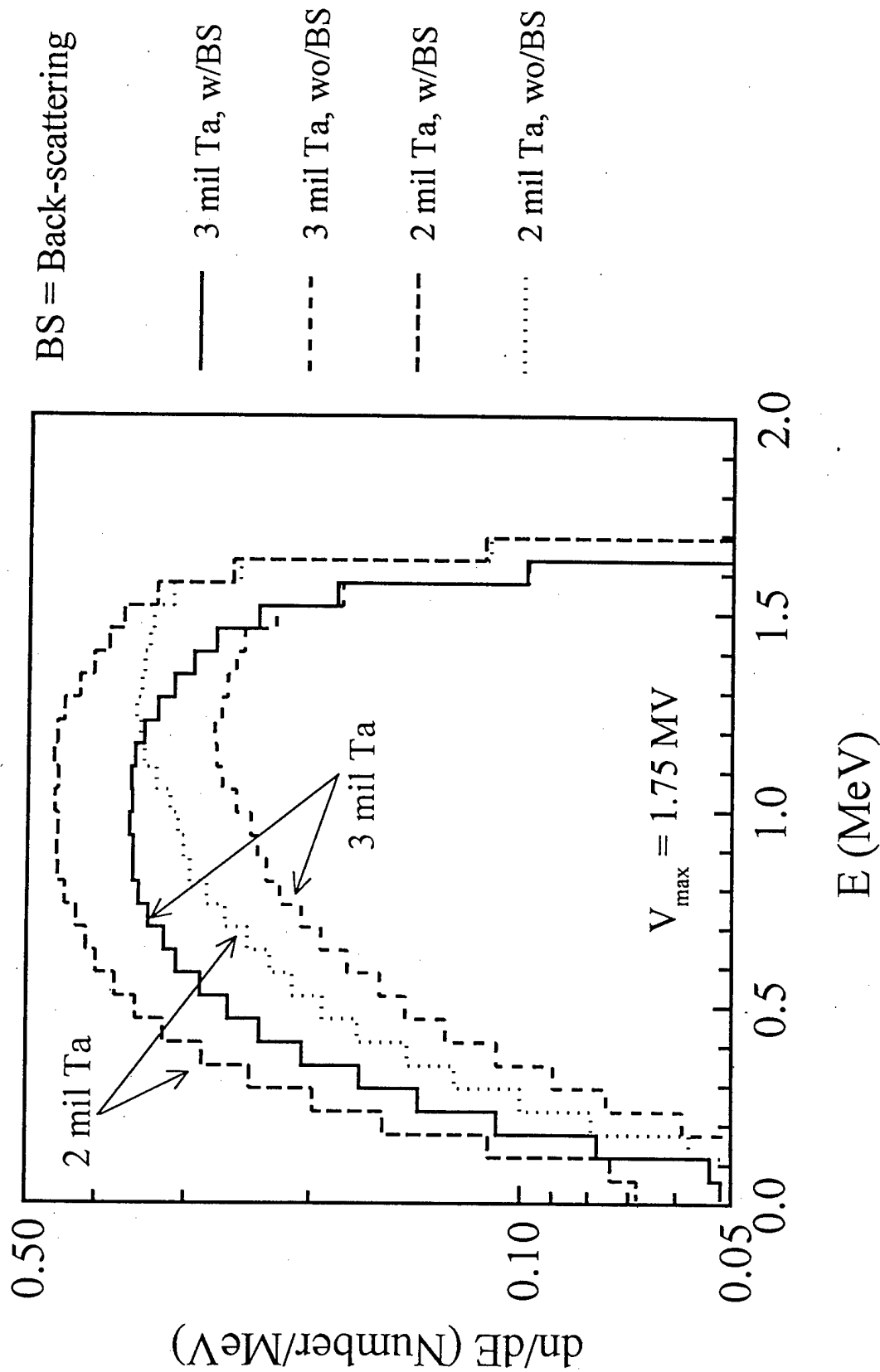


Fig. 6 Energy spectra of electrons transmitted through 2- and 3-mil tantalum foils, with and without back-scattering. For these calculations,  $V_{\max} = 1.75 \text{ MV}$ , and the input electron beam has a  $\cos(\theta)$  distribution truncated at  $\theta_{\max} = 70^\circ$ .

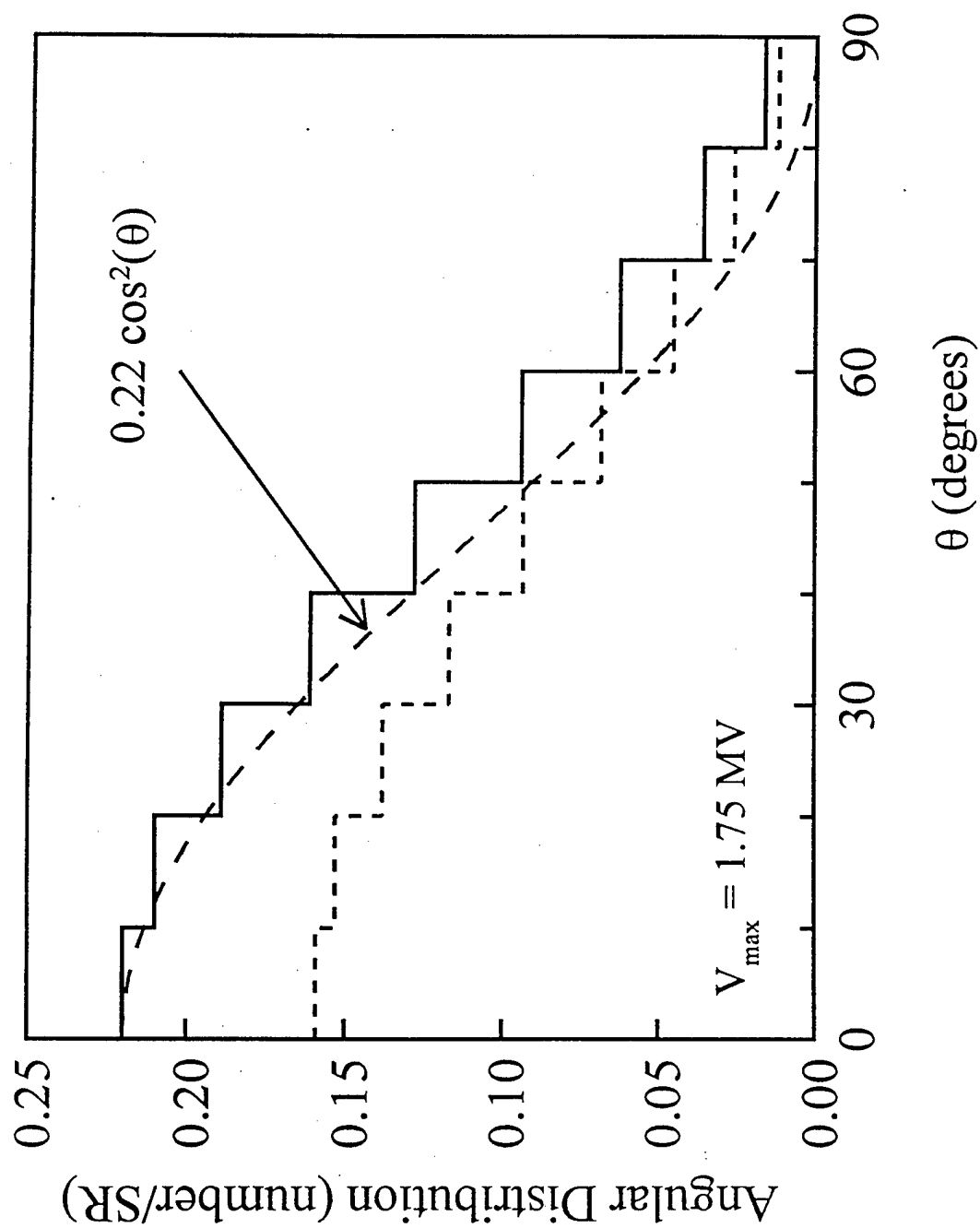


Fig. 7 Angular distributions of electrons transmitted through 2- and 3-mil tantalum foils. For these calculations,  $V_{\max} = 1.75 \text{ MV}$ , and the input electron beam has a  $\cos(\theta)$  distribution truncated at  $\theta_{\max} = 70^\circ$ .

# Normalized to One Electron

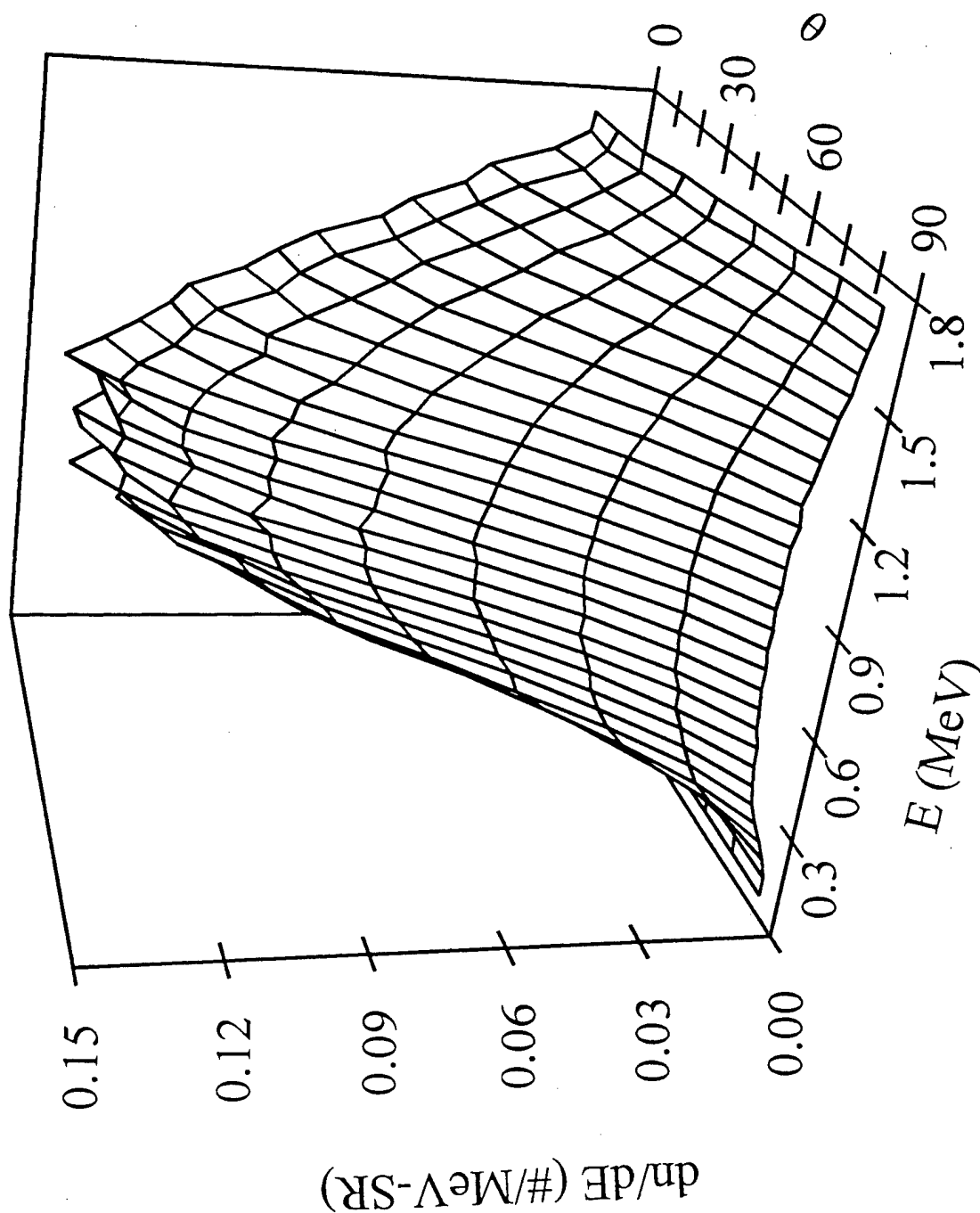


Fig. 8 Electron distribution as a function of energy and angle after transport through 3-mil tantalum. For this calculation,  $V_{max} = 1.75$  MV, and the input electron beam has a  $\cos(\theta)$  distribution truncated at  $\theta_{max} = 70^\circ$ .

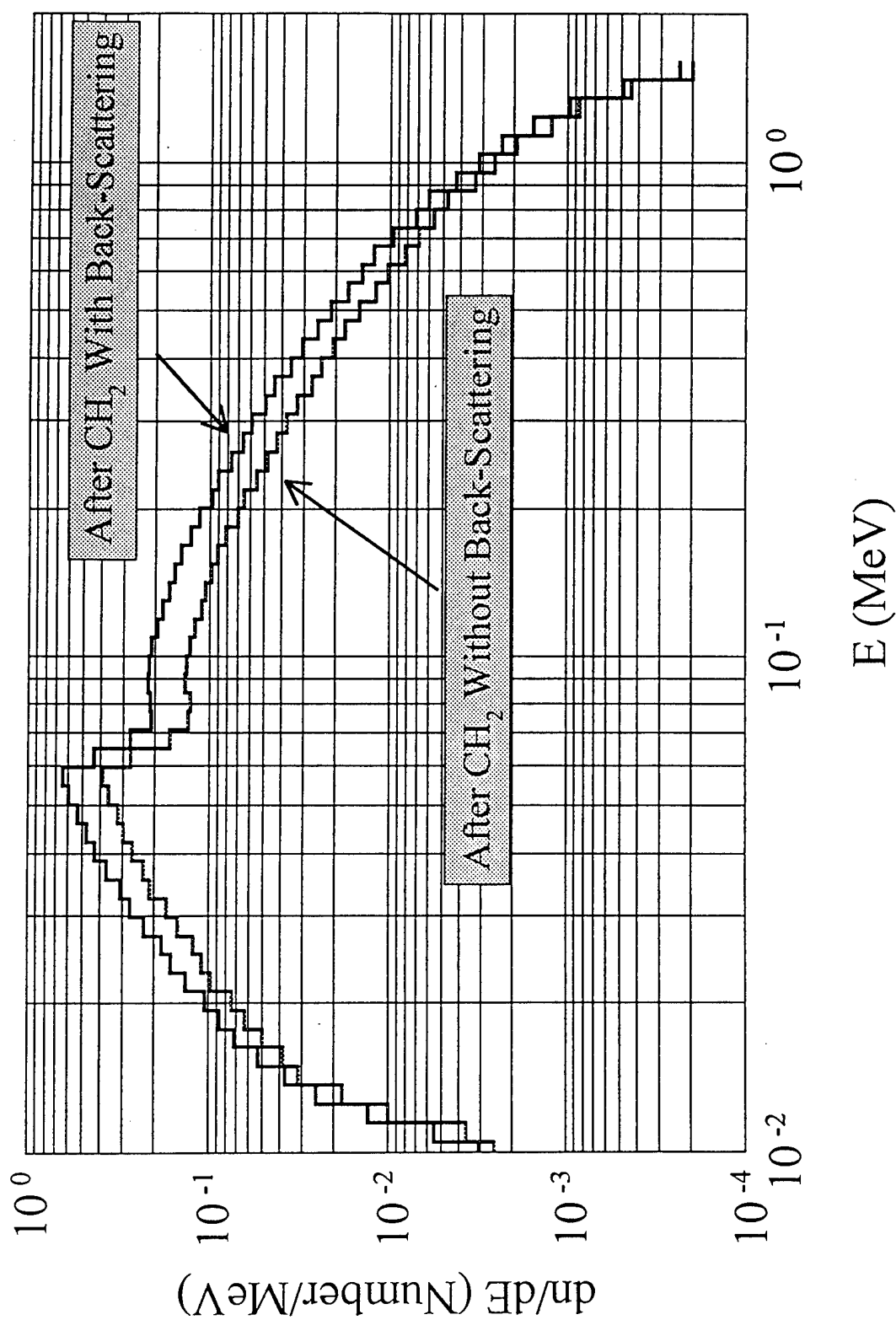


Fig. 9 Transmitted photon spectrum as a function of energy with and without back-scattering after transport through 3-mil tantalum and the beam-stop (0.188-inch + 0.75-inch  $CH_2$ ). For this calculation,  $V_{max} = 1.75$  MV, and the input electron beam has a  $\cos(\theta)$  distribution truncated at  $\theta_{max} = 70^\circ$ .



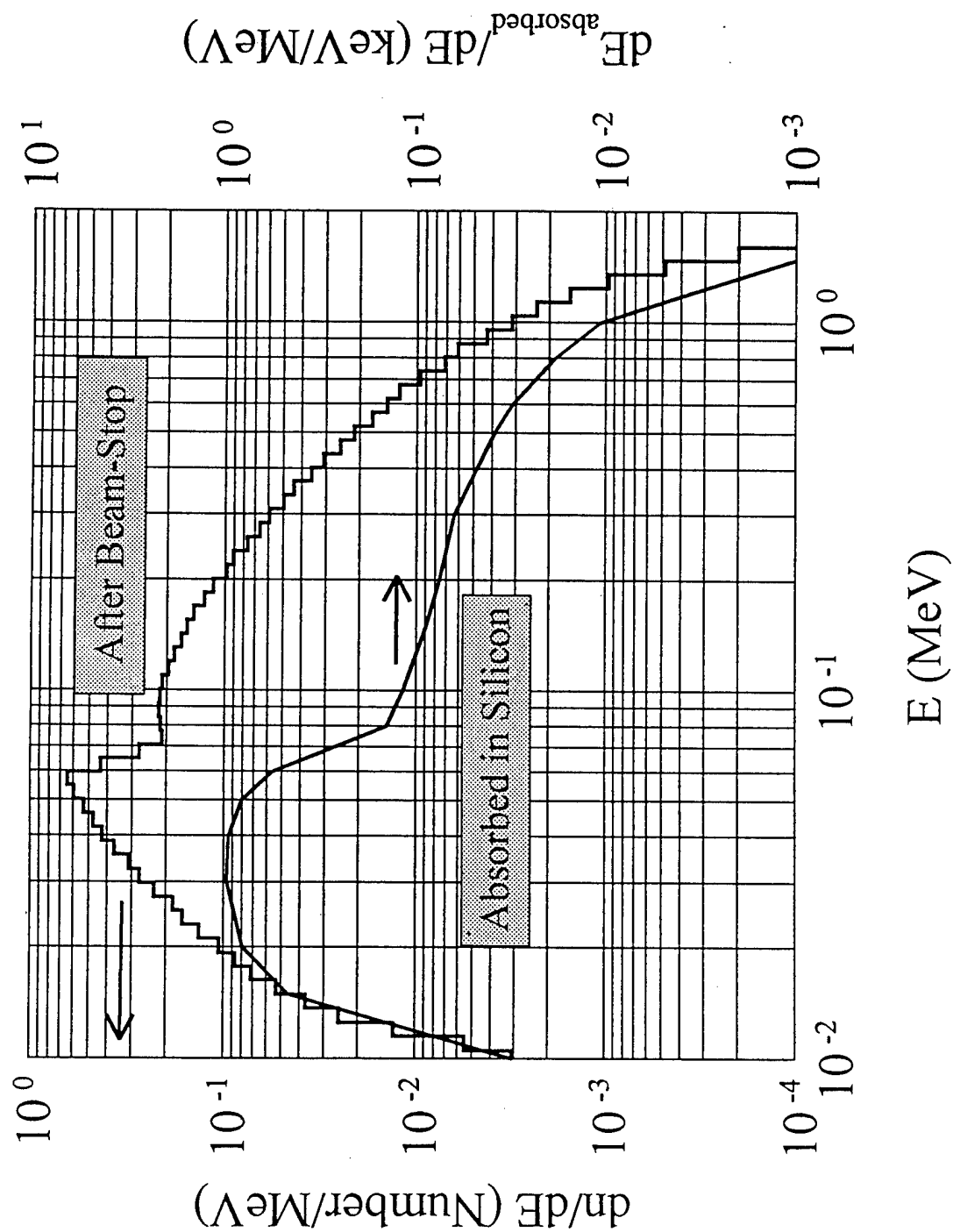


Fig. 10 Transmitted photon spectrum as a function of energy with back-scattering after transport through 3-mil tantalum and the beam-stop (from Fig. 9) and the absorbed energy spectrum in 20-mils silicon. For this calculation,  $V_{\text{max}} = 1.75$  MV, and the input electron beam has a  $\cos(\theta)$  distribution truncated at  $\theta_{\text{max}} = 70^\circ$ .

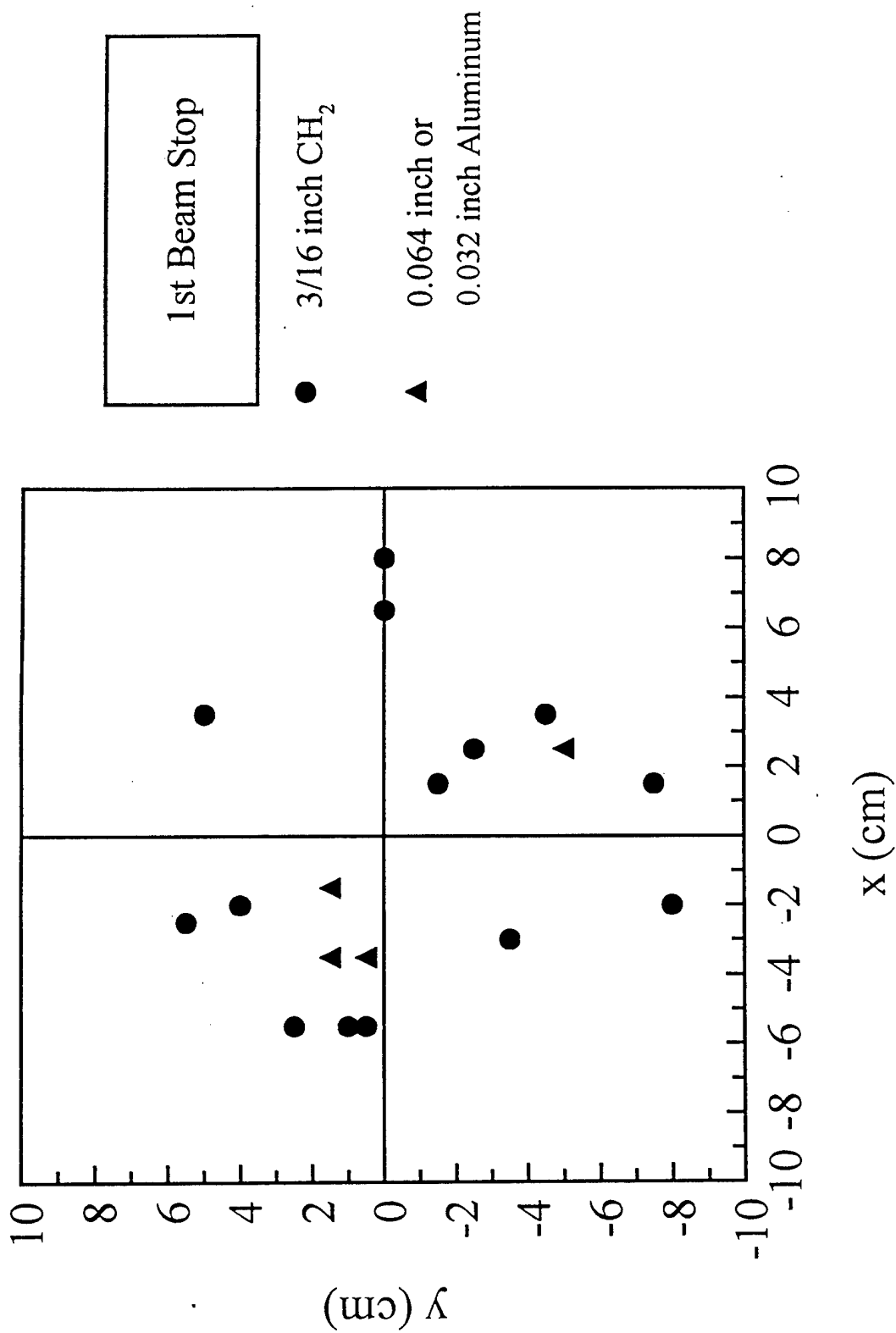


Fig. 11 Position of the fitted peak exposure 3.25 inches downstream of the tantalum converter for the DM1 shots given in Table I.

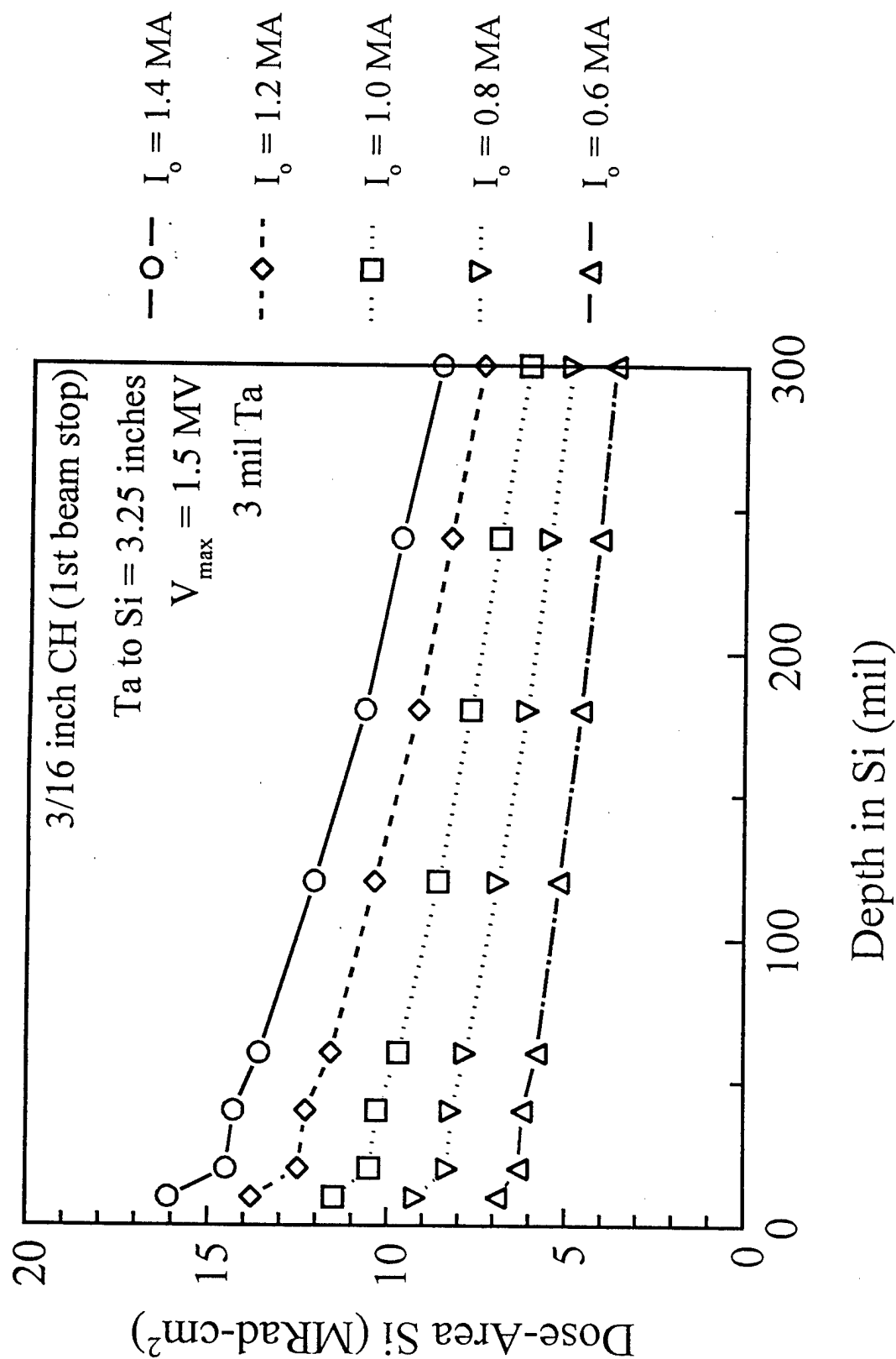


Fig. 12 Plots of DAP versus silicon thickness for several values of  $I_0$ . For these calculations,  $V_{\max} = 1.5 \text{ MV}$ , back-scattering is included, and the converter is 3-mil thick tantalum.

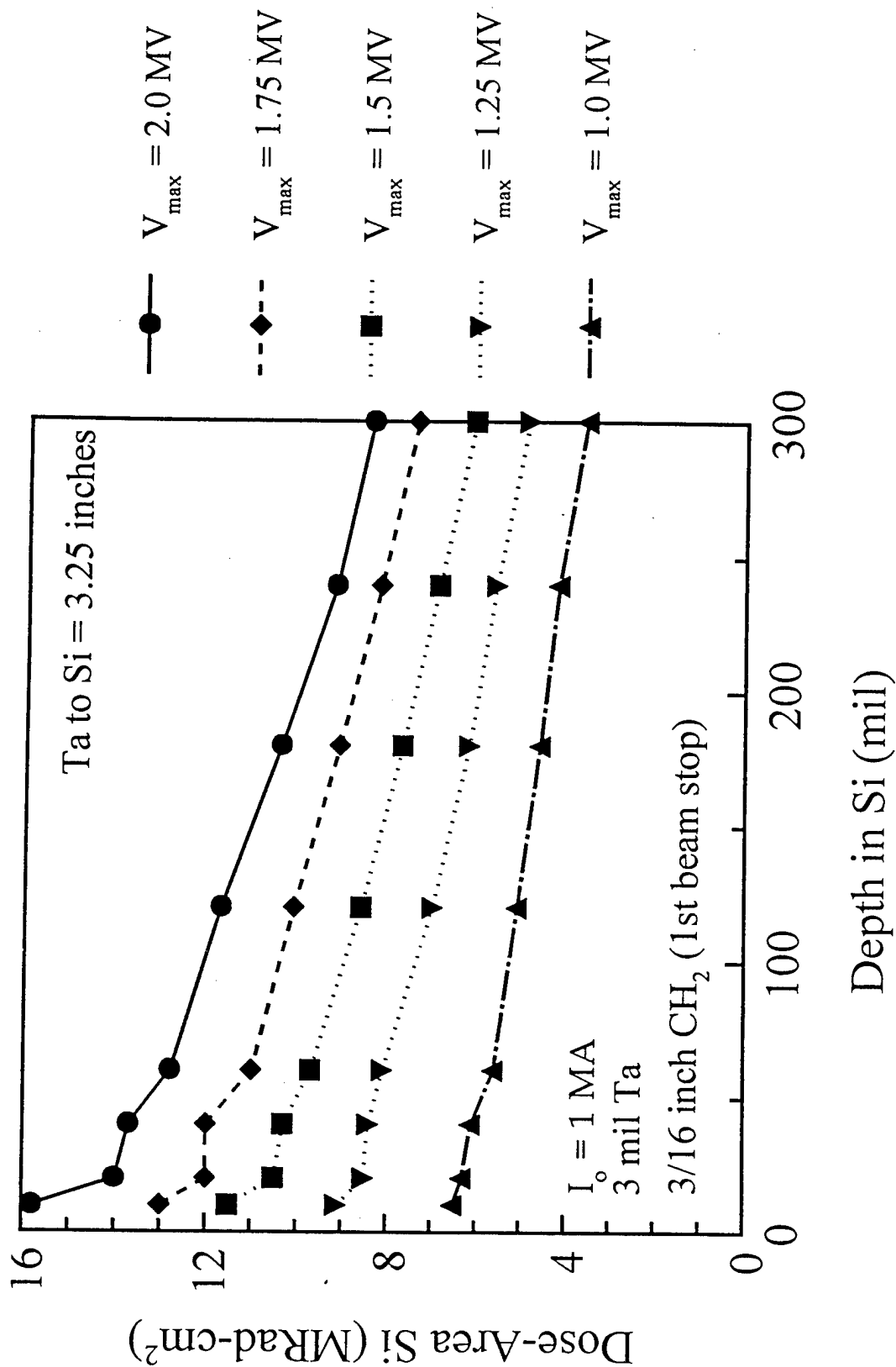


Fig. 13 Plots of DAP verses silicon thickness for several values of  $V_{\max}$ . For these calculations,  $I_o = 1.0 \text{ MA}$ , back-scattering is included, and the converter is 3-mil thick tantalum.

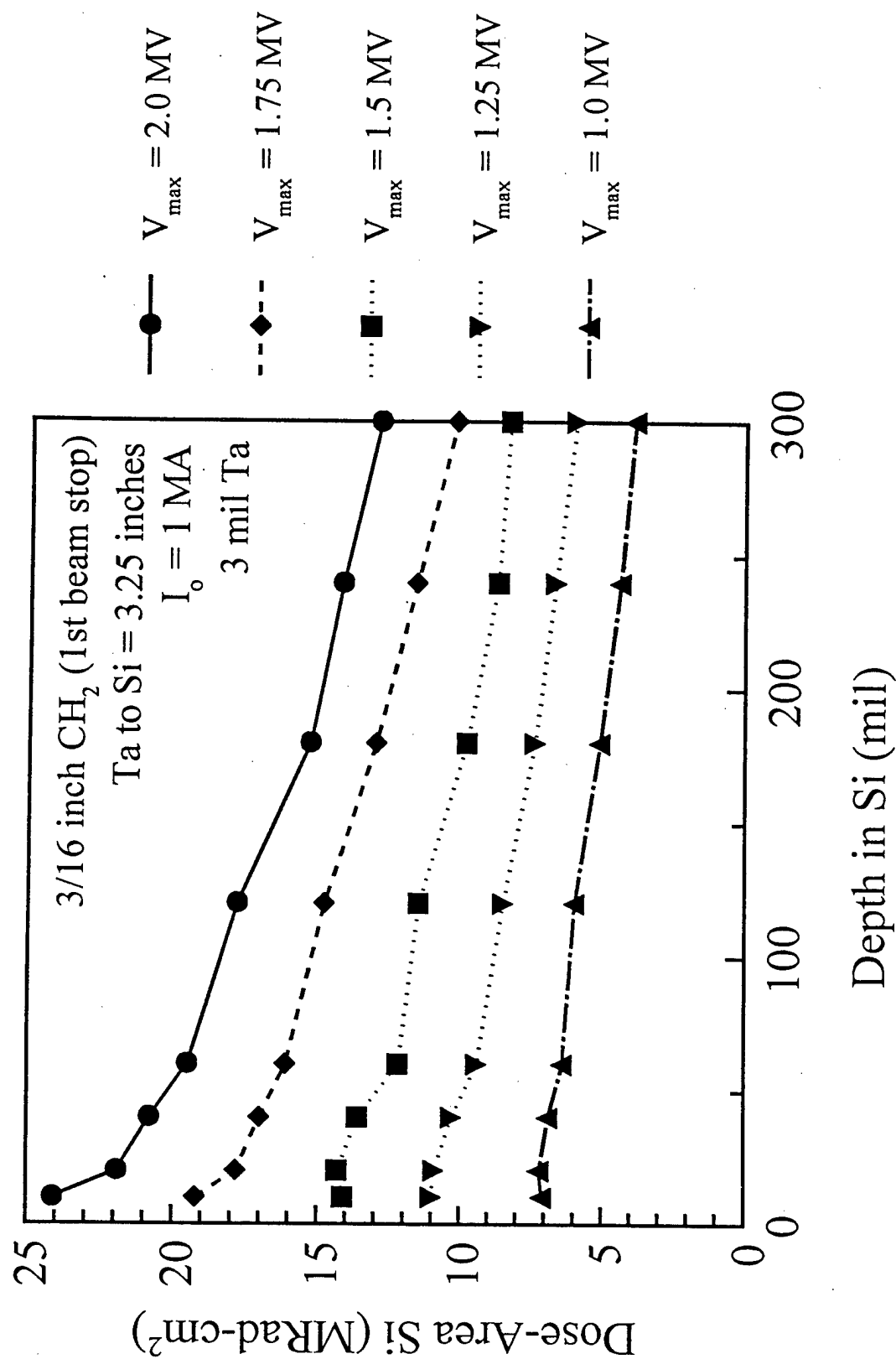


Fig. 14 Plot of DAP versus silicon thickness for several values of  $V_{\max}$ . For these calculations,  $I_o = 1.0 \text{ MA}$ , back-scattering is included, and the converter is 3-mil thick tantalum.

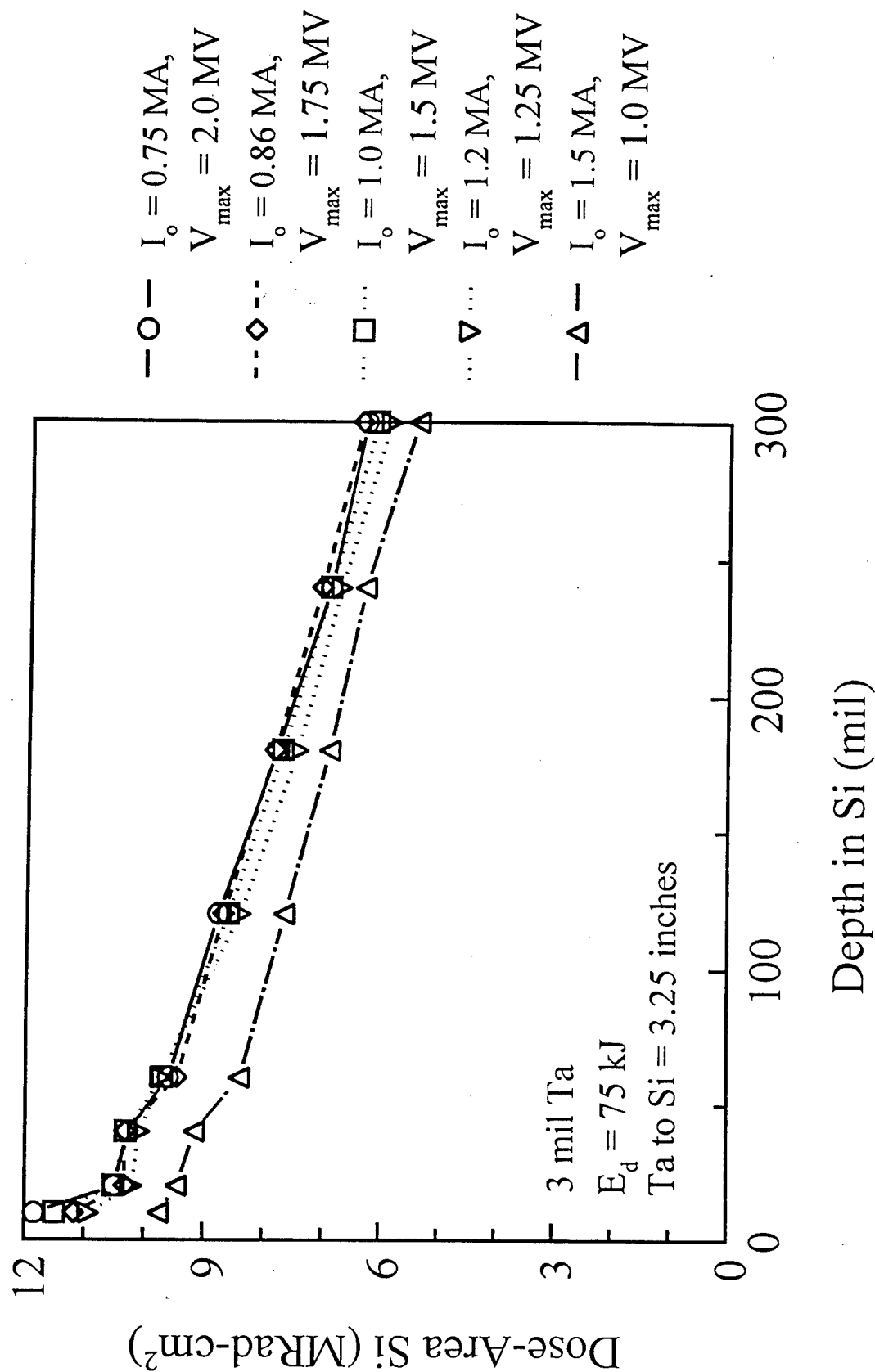


Fig. 15 Plot of DAP versus silicon thickness for  $E_d = 75 \text{ kJ}$ , but with five different combinations of  $I_0$  and  $V_{\max}$ . For these calculations, back-scattering is included, the converter is 3-mil thick tantalum, and  $\tau_o = 100 \text{ ns}$ .

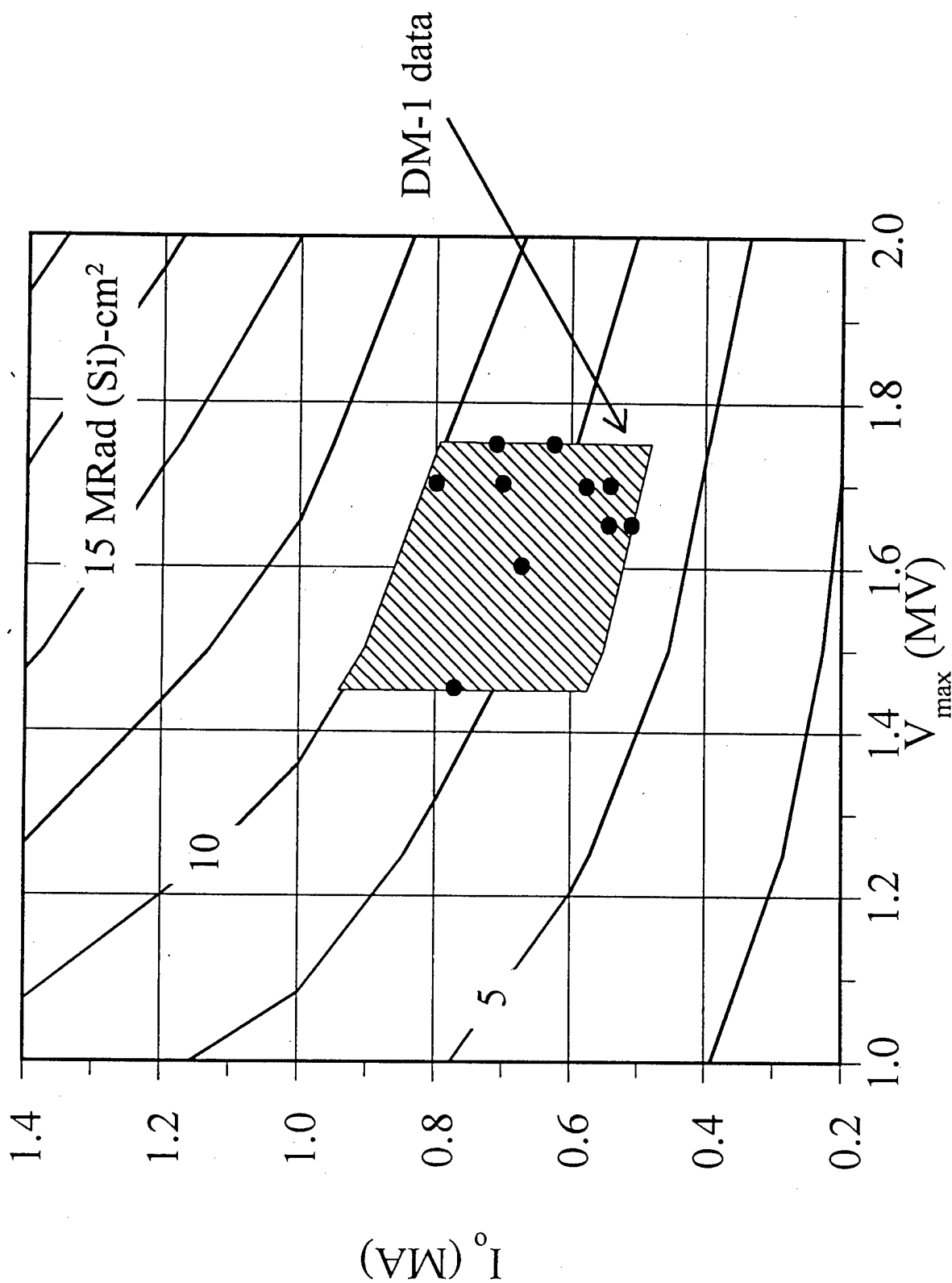


Fig. 16 Contours of iso-DAP in 20 mils of silicon from CYLTRAN calculations with back-scattering for a 3-mil thick tantalum converter and  $\tau_o = 100$  ns. The data points are DM1 results from Table I, column 9, and the shaded box is the DAP "data window" which limits  $I_o$  and  $V_{max}$ .

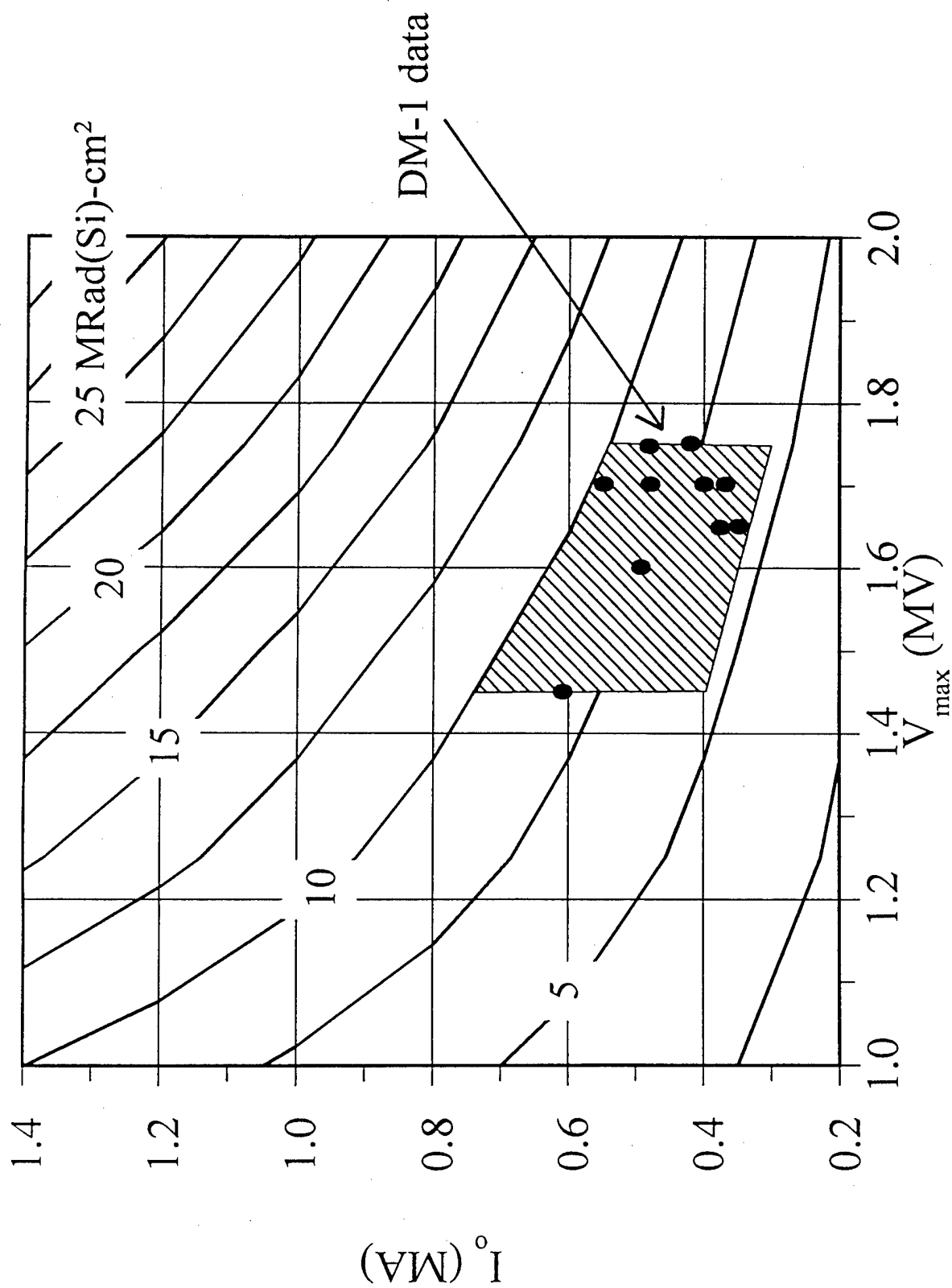


Fig. 17 Contours of iso-DAP in 20 mils of silicon from CYLTRAN calculations with back-scattering and reflexing for a 3-mil thick tantalum converter and  $\tau_o = 100$  ns. The data points are DM1 results from Table I, column 9, and the shaded box is the DAP "data window" which limits  $I_o$  and  $V_{max}$ .



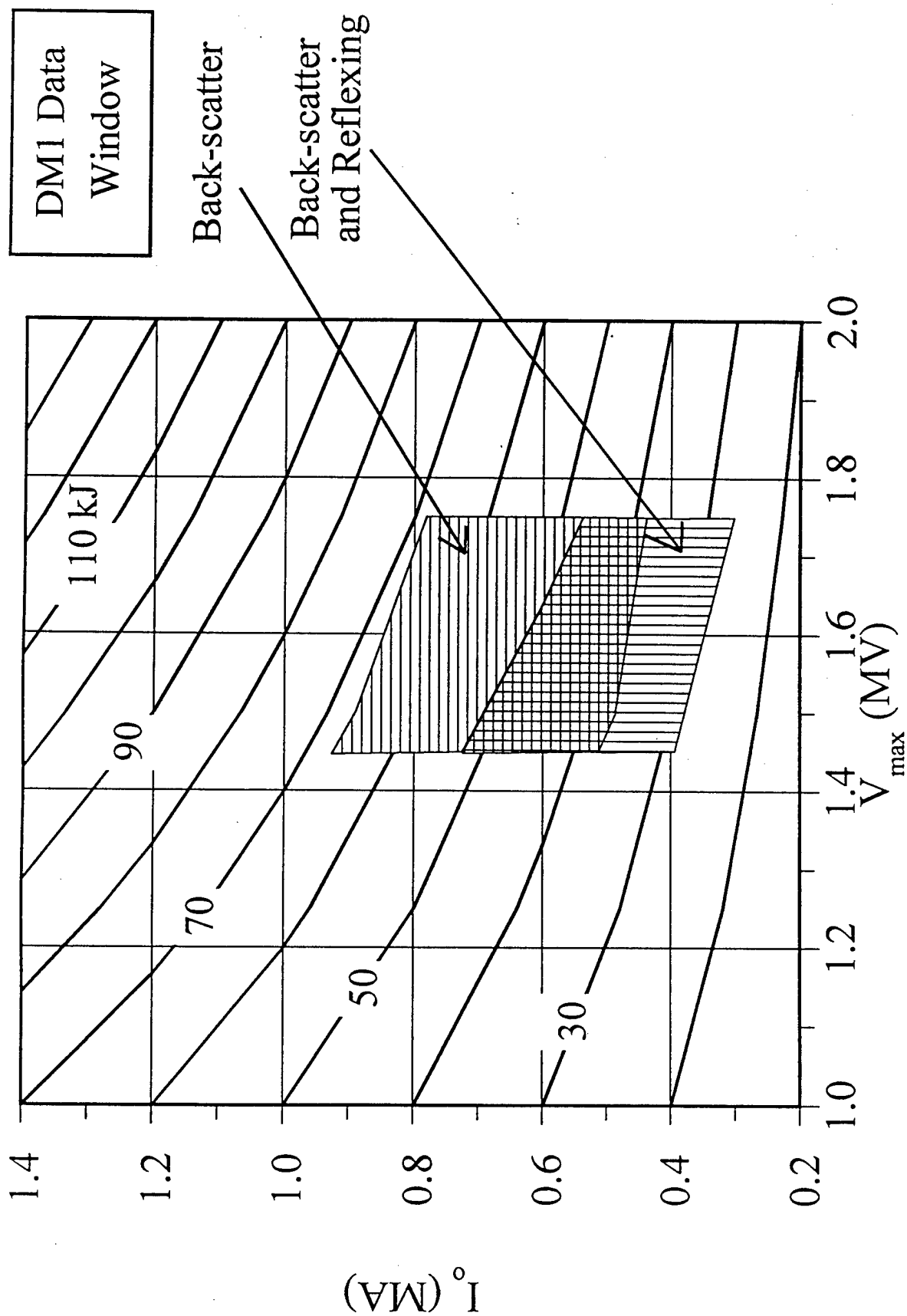


Fig. 18 Contours of iso-energy ( $E_d$ ) compared with the "data windows" from Figs. 16 and 17. These "data windows" place limits on the energy coupled to the diode.

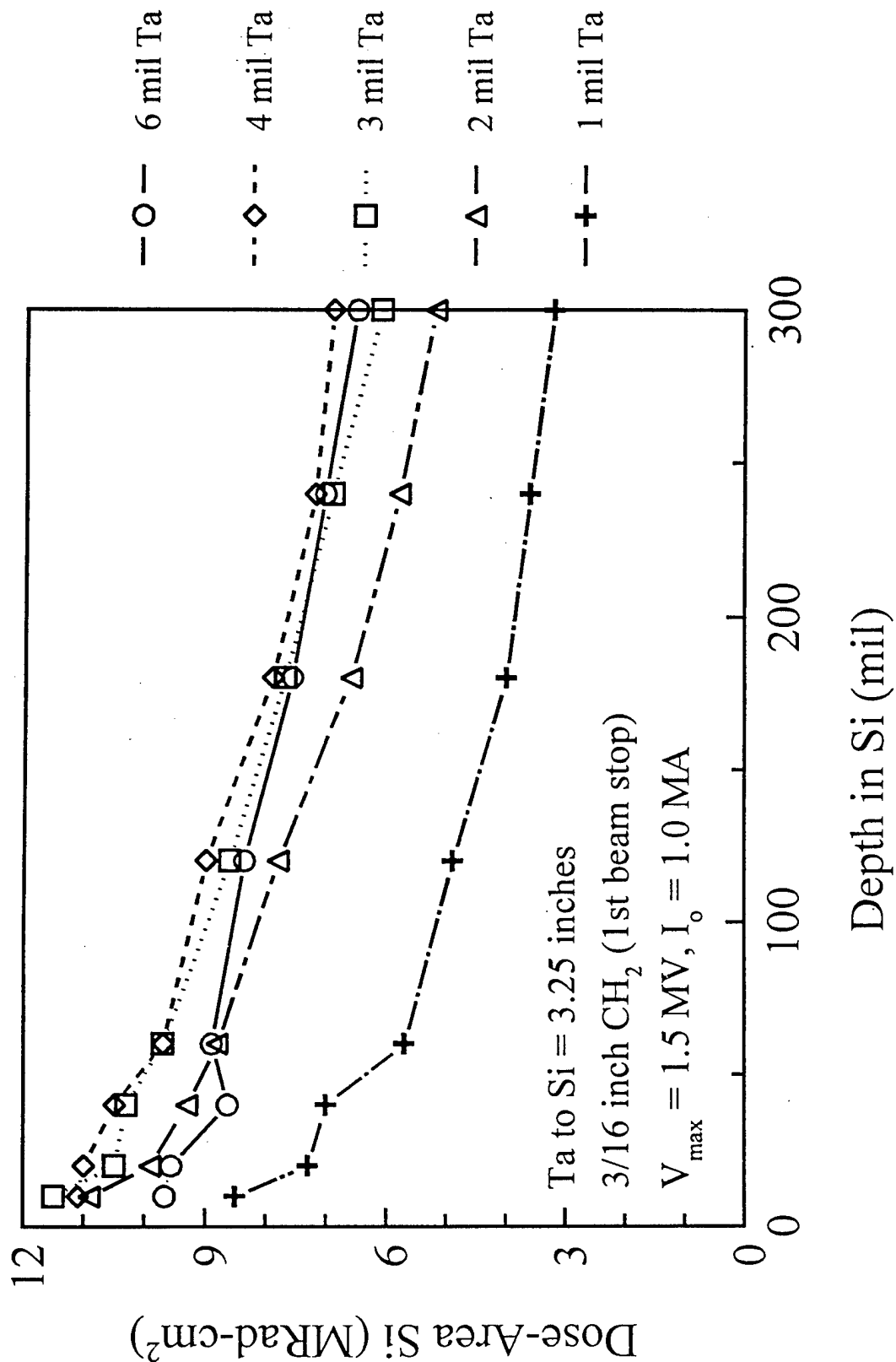


Fig. 19 Plot of DAP verses silicon thickness for 1- to 6-mil thick tantalum converters. For these calculations, back-scattering is

included,  $V_{\max} = 1.5 \text{ MV}$ ,  $I_o = 1.0 \text{ MA}$ , and  $\tau_o = 100 \text{ ns}$ .

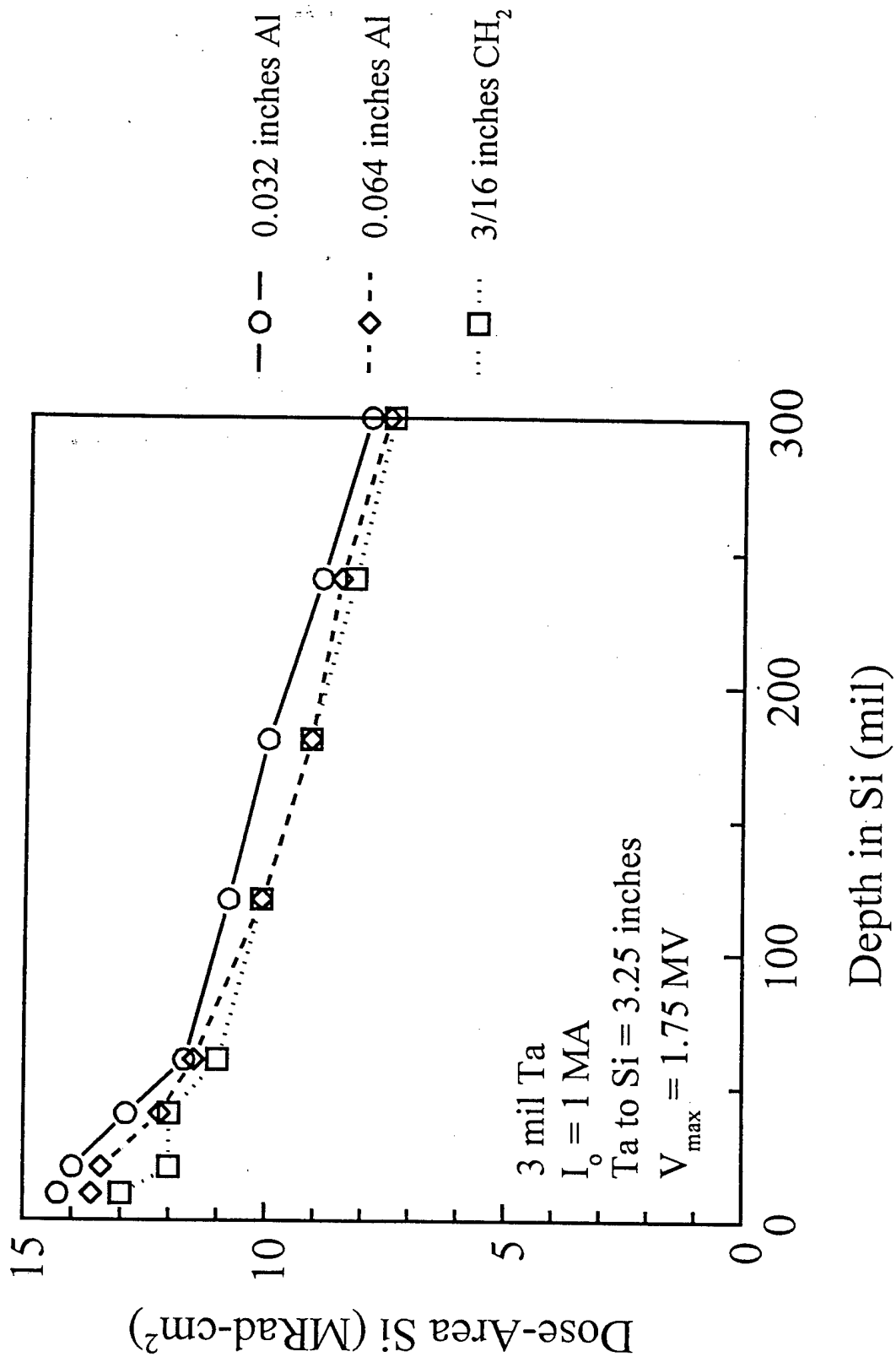


Fig. 20 Plot of DAP versus silicon thickness for different first beam-stops (see Table I and Fig. 5). For these calculations, back-scattering is included,  $V_{\text{max}} = 1.75 \text{ MV}$ ,  $I_0 = 1.0 \text{ MA}$ , and  $\tau_0 = 100 \text{ ns}$ .

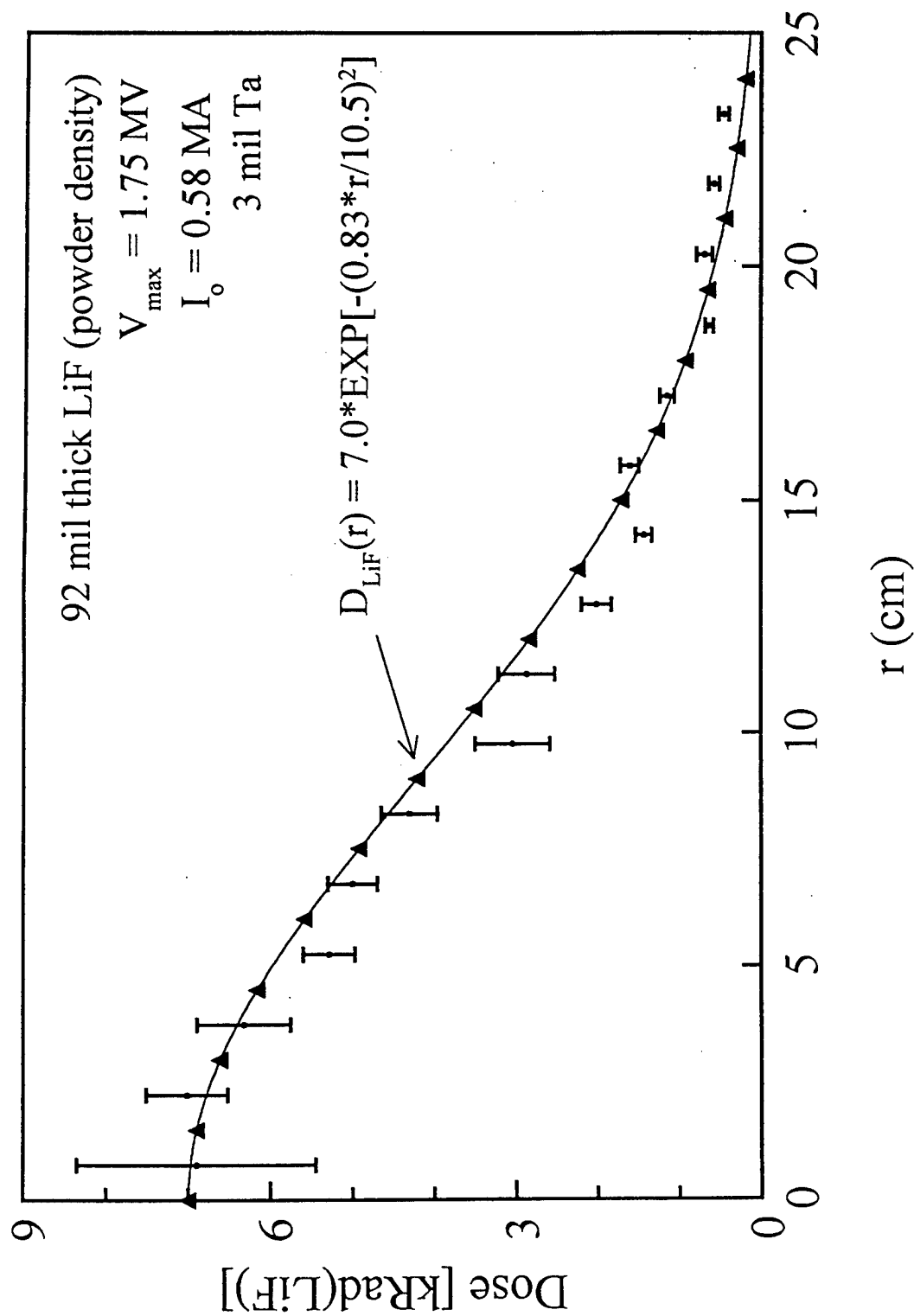


Fig. 21 Comparison of radial dose profiles in lithium fluoride from DM1 measurements (curve) and from a CYLTRAN calculation (points). The curve is a fit to the average dose for eleven shots from Table I with a 3-mil tantalum converter and 3/16-inch  $\text{CH}_2$  first beam-stop. The individual data points are from a CYLTRAN calculation including back-scattering but not reflexing. The calculation is normalized to the measurement at peak dose.

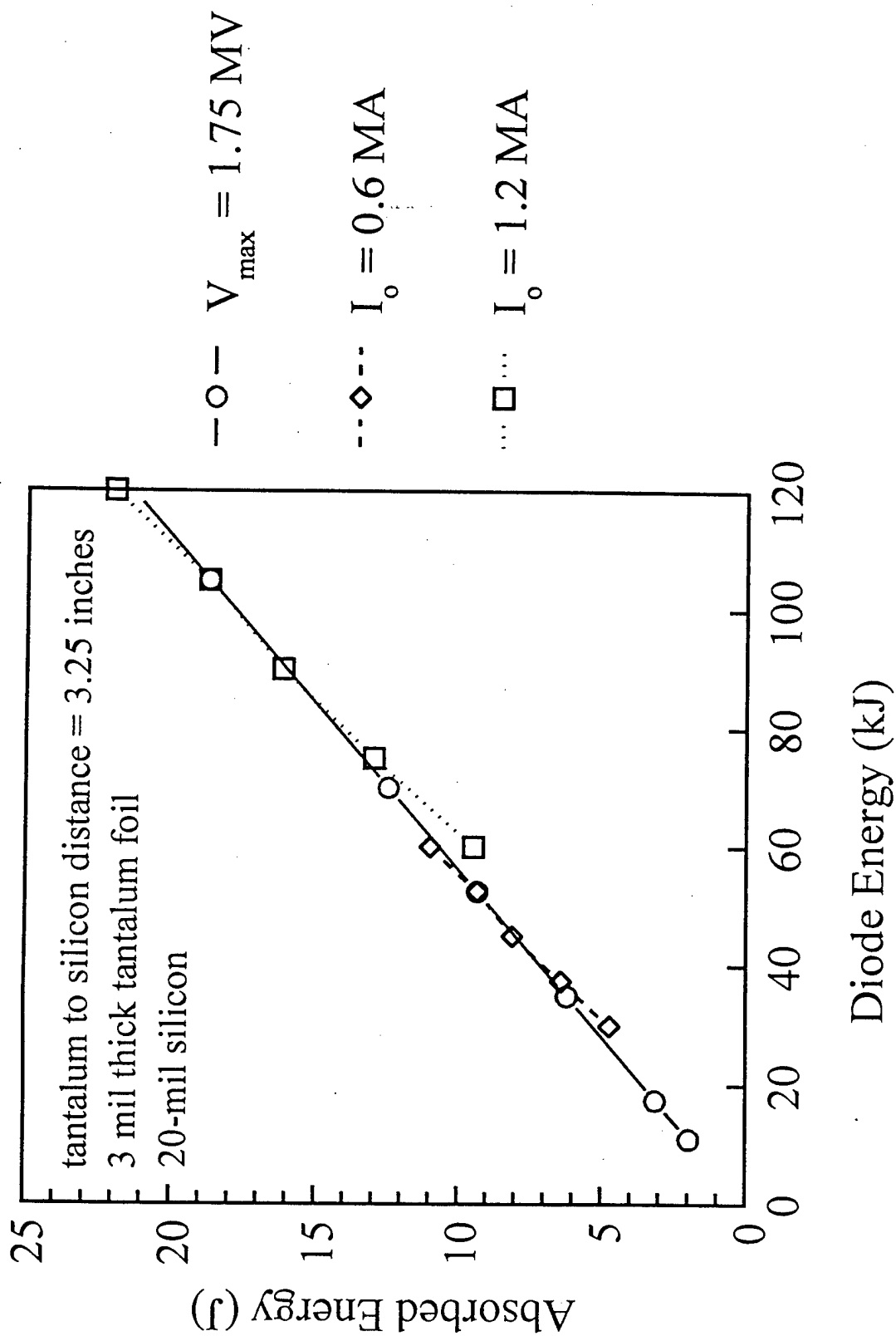


Fig. 22 Plot of energy absorbed in 20 mils of silicon as a function of energy coupled to the diode. Coupled energy is computed by fixing the end-point voltage and varying the current (circles), or by fixing the current and varying the end-point voltage (diamonds and squares). For these calculations, back-scattering is included.



NRL/MR/6770--96-7750

## Circuit Simulations of DM1 with an Electron-Beam Load

R.J. COMMISSO  
J.R. BOLLER

*Pulsed Power Physics Branch  
Plasma Physics Division*

D.V. ROSE  
S.B. SWANEKAMP

*JAYCOR, Inc.  
Vienna, VA*

March 22, 1996

Distribution authorized to U.S. Government agencies and their contractors; critical technology; March 1996. Other requests shall be referred to Commanding Officer, Naval Research Laboratory, Washington, DC 20375-5000.

REPORT DOCUMENTATION PAGE			Form Approved OMB No. 0704-0188	
Public reporting burden for this collection of information is estimated to average 1 hour per response, including the time for reviewing instructions, searching existing data sources, gathering and maintaining the data needed, and completing and reviewing the collection of information. Send comments regarding this burden estimate or any other aspect of this collection of information, including suggestions for reducing this burden, to Washington Headquarters Services, Directorate for Information Operations and Reports, 1215 Jefferson Davis Highway, Suite 1204, Arlington, VA 22202-4302, and to the Office of Management and Budget, Paperwork Reduction Project (0704-0188), Washington, DC 20503.				
1. AGENCY USE ONLY (Leave Blank)		2. REPORT DATE  March 22, 1996		3. REPORT TYPE AND DATES COVERED  Interim Report
4. TITLE AND SUBTITLE  Circuit Simulations of DM1 with an Electron-Beam Load			5. FUNDING NUMBERS	
6. AUTHOR(S)  R.J. Commisso, J.R. Boller, D.V. Rose,* and S.B. Swanekamp*				
7. PERFORMING ORGANIZATION NAME(S) AND ADDRESS(ES)  Naval Research Laboratory Washington, DC 20375-5320			8. PERFORMING ORGANIZATION REPORT NUMBER  NRL/MR/6770-96-7750	
9. SPONSORING/MONITORING AGENCY NAME(S) AND ADDRESS(ES)  Defense Nuclear Agency 6801 Telegraph Road, Alexandria, VA 22310			10. SPONSORING/MONITORING AGENCY REPORT NUMBER	
11. SUPPLEMENTARY NOTES  *JAYCOR, Inc., Vienna, VA 22182				
12a. DISTRIBUTION/AVAILABILITY STATEMENT Distribution authorized to U.S. Government agencies and their contractors; critical technology; March 1996. Other requests shall be referred to Commanding Officer, Naval Research Laboratory, Washington, DC 20375-5000.			12b. DISTRIBUTION CODE  C	
13. ABSTRACT (Maximum 200 words) <p>This report describes results from a circuit analysis of the inductive-energy-store pulsed-power generator DM1, which was built and operated by Physics International (PI). The analysis was performed with the transmission line code, BERTHA, and uses the DM1 equivalent circuit provided by PI along with physics-based circuit models for the plasma opening switch (POS) and electron-beam (e-beam) diode load. The circuit simulations are complemented by calculations of the dose from the DM1 bremsstrahlung converter package using the 2-D, coupled electron-photon transport code CYLTRAN. Together, these tools are used to analyze the DM1 electrical performance during a series of test shots and to suggest methods for increasing the load energy. Agreement is obtained between the circuit simulations and the measured DM1 electrical waveforms up to the POS. Since emphasis was placed on radiation measurements, no electrical measurements were made between the POS and load. The circuit analysis predicts that 12 kJ is delivered to the load for a conducted current of 1.4 MA (220 ns conduction time). This is much lower than the 54 kJ inferred from CYLTRAN analyses of DM1 radiation measurements. The 42 kJ discrepancy likely occurs because the circuit model uses only current flowing in the cathode as load current and does not account for non-cathode, radiation-producing load current. An energy analysis shows that during the load energy delivery time approximately 155 kJ is dissipated by the POS and load combined. To improve the energy coupled to the load for a given conduction current, a higher fraction of this total energy dissipated in the POS-load combination must be delivered to the load (increased load current). Circuit analysis suggests that this can be done by optimizing the load impedance and minimizing the POS-to-load inductance. The circuit simulations show that the energy delivered to the e-beam load is optimized for an initial diode A-K gap of 6.3 mm (<math>Z_L = 2 \Omega</math>), with approximately 37 kJ delivered to the load compared with the 12 kJ delivered with the nominal 25.4-mm A-K gap (<math>Z_L = 11 \Omega</math>) used in the DM1 test series. If, in addition to having an optimized initial A-K gap, the inductance between the POS and load is also reduced from 53 nH to 16 nH, approximately 54 kJ is delivered to the e-beam diode. Assuming, as an upper bound, that the 42 kJ of energy associated with non-cathode, radiation-producing current continues to flow into the load, then the total energy delivered to the optimized e-beam loads would be 79 kJ (63 nH) and 96 kJ (16 nH). An increase in conduction current from 1.4 MA to 1.7 MA (220 ns to 270 ns conduction time) would increase the energy available to drive the POS/load combination by nearly 50%.</p>				
14. SUBJECT TERMS  Pulsed power                      Opening switches			15. NUMBER OF PAGES  36	
			16. PRICE CODE	
17. SECURITY CLASSIFICATION OF REPORT  UNCLASSIFIED	18. SECURITY CLASSIFICATION OF THIS PAGE  UNCLASSIFIED	19. SECURITY CLASSIFICATION OF ABSTRACT  UNCLASSIFIED	20. LIMITATION OF ABSTRACT  SAR	

## CONTENTS

INTRODUCTION .....	1
CIRCUIT DESCRIPTION.....	3
DESCRIPTION OF POS CIRCUIT ELEMENT MODEL .....	6
DESCRIPTION OF E-BEAM DIODE CIRCUIT ELEMENT MODEL .....	8
RESULTS OF DM1 MODELING.....	10
SUMMARY AND CONCLUSIONS .....	19
ACKNOWLEDGMENTS.....	21
REFERENCES .....	21



# CIRCUIT SIMULATIONS OF DM1 WITH AN ELECTRON-BEAM LOAD

## I. INTRODUCTION

The DECADE pulsed power generator<sup>1</sup> comprises 16 independent modules designed to meet a radiation requirement of 20 kRad deposited in a thickness of 20-mil silicon over an area of  $10^4 \text{ cm}^2$  with 2:1 spatial uniformity with a 40 ns full-width half-maximum radiation pulse. The first engineering version of these modules is DECADE Module 1 (DM1),<sup>2</sup> built by Physics International (PI). PI recently completed a series of tests on DM1 for the express purpose of characterizing its performance. In this test series, emphasis was placed on radiation measurements with little attention given to the details of the energy transfer from the POS to the load. As a result, no direct electrical measurements of the current or voltage on the load side (downstream) of the POS was made. This report describes an analysis of the DM1 electrical performance using the transmission line code BERTHA<sup>3</sup>. The circuit simulations are complemented by calculations of the dose from the DM1 bremsstrahlung converter package using the 2-D, coupled electron-photon transport code CYLTRAN.<sup>4</sup> The BERTHA and CYLTRAN simulations are compared with data from the DM1 test series to analyze the overall system operation, characterize the energy delivered to the load, and to suggest methods of increasing the load energy. This work represents an improvement over, and the culmination of, an earlier effort to model DM1 performance.<sup>5</sup> A more thorough CYLTRAN analysis of DM1 radiation measurements using idealized load waveforms and the implications for DM1 performance can be found in Ref. 6. An analysis that combines this work, the work of Ref. 6, and results of initial 2-D PIC simulations of the POS-load coupling can be found in Ref. 7.

The circuit analysis uses the DM1 equivalent circuit provided by PI and physics-based models for the plasma opening switch (POS) and electron-beam (e-beam) diode. The simulations are within 10% of the measured DM1 electrical waveforms. The POS model is based on the flow-impedance concept that can be derived from pressure balance on the vacuum electron flow.<sup>8,9</sup> To obtain the best agreement with the inferred POS voltage pulse width and the time history of the measured x-ray signal, the POS flow impedance was allowed to increase linearly in time to  $1.38 \Omega$  in 28 ns and then decrease exponentially after opening with a  $1/e$  time of 55 ns. In the context of the physical POS model, this corresponds to the formation of a 2.3-mm effective POS gap followed by a closure of this gap. The predicted load energy from BERTHA for the DM1 test series is 12 kJ which is much lower than the 54 kJ inferred from CYLTRAN calculations of DM1 radiation measurements. An additional 520 kA above the calculated load current of 150 kA is necessary to explain this 42 kJ discrepancy. The most likely explanation for this discrepancy is that the circuit model uses only current flowing in the cathode (current in the metal) as load

current and does not account for non-cathode, radiation-producing load current. Such current could be associated with, e.g., vacuum electron flow and/or plasma between the POS and load.

An energy analysis suggests that during the load energy delivery time of 150 ns approximately 155 kJ is dissipated by the POS and e-beam load combined. This 155 kJ is about 72% of the 215 kJ estimated to be available to drive the load power pulse. However, only 54 kJ of the 155 kJ, 35%, is inferred to be dissipated in the load.<sup>6</sup> An increase in conducted current from 1.4 MA to 1.7 MA (220 ns to 270 ns) would increase the estimated energy available to drive the POS/load combination by about 50%. However, limitations in the current DM1 system performance have prevented DM1 from achieving this higher conducted current.

The circuit analysis shows that the load energy is optimized with an initial diode A-K gap of about 6.3 mm corresponding to an optimized load impedance,  $Z_L^*$ , of a little under  $2 \Omega$ . At this optimized impedance the load energy is approximately 37 kJ. In the DM1 test series, a nominal diode A-K gap of 25.4 mm ( $Z_L \approx 11 \Omega$ ) was used. If, in addition to having an optimized diode A-K gap, the POS-to-load inductance is reduced from 63 nH to 16 nH, the circuit simulations predict that 54 kJ is delivered to the optimized e-beam load. Assuming, as an upper bound, that the 42 kJ of energy associated with current non-cathode, radiation-producing load current continues to be delivered to the load, these values become 79 kJ (63 nH) and 96 kJ (16 nH), respectively. The actual response of the DM1 system to reduced load impedance and POS-to-load inductance must be determined from experiment. However, data from Hawk<sup>10</sup> at NRL suggest that the total load energy increases as the diode impedance approaches the optimum value. Improved understanding of POS-to-load coupling issues is currently being obtained through PIC simulations and additional experiments on Hawk and DM1.

The outline of the remainder of the paper is as follows. Section II describes the details of the equivalent circuit. The POS and e-beam diode circuit element models are described in Secs. III and IV, respectively. In Sec. V, results from modeling DM1 with the e-beam diode load are presented. Included here are results from CYLTRAN calculations of the radiation produced using the BERTHA-generated load waveforms. A summary of the important results and conclusions of the paper are presented in Sec. VI.

## II. CIRCUIT DESCRIPTION

The DM1 circuit used for the modeling work reported here changed slightly as the work progressed. The initial circuit modeling was based on an equivalent circuit of the DM1 configuration for shot 1143 as supplied by L. Schlitt.<sup>11</sup> This circuit, shown in Fig. 1, includes resistive losses in the Marx generator and water lines, and skin resistance of the vacuum feed conductors, but does not include losses associated with the propagation of a MITL wave. The diverter switches and their loads were also included. However, they close after the main power pulse and have virtually no effect on the diode load during the time of interest. The initial voltage of 1.02 MV on element No. 1 corresponds to a Marx charge voltage of  $\pm 85$  kV and a stored energy of 570 kJ.

The predicted tube voltage (voltage measured on the oil-side of vacuum insulator, see Fig. 1) and current on the generator side (upstream) of the POS from the BERTHA analysis of the circuit in Fig. 1 are shown in Fig. 2. For comparison, Fig. 2 also shows the predicted tube voltage and upstream current from a simulation performed by Schlitt.<sup>11</sup> Because different POS and load models are used in the two simulations, these comparisons are only valid up to the time the POS opens. The agreement up to this time demonstrates the consistency between the NRL and PI circuit codes. Schlitt's simulations are in agreement with measured waveforms from this shot after some adjustment. The waveforms from both simulations are multiplied by 0.95. Schlitt found this to be necessary to match measurements from this DM1 shot. This correction factor had to be changed slightly for other shots. In an earlier memo,<sup>12</sup> Schlitt wrote: "D. Kortbawi has suggested that a significant portion of this minor discrepancy could be accounted for by the DC voltage drop across the Marx charging resistors."

The circuit in Fig. 1 was modified with updates from S. Ashby<sup>13</sup> to reflect DM1 hardware changes and the revised circuit is shown in Fig. 3. The changes consisted of shortening the 5- $\Omega$  line (transmission line element No. 41) from 8.5 to 5.5 ns and changing the time for closing of the transfer switch to match DM1 Shot 1322. This is also the circuit configuration used for the DM1 test series and for which all further calculations will be made. Shown in Fig. 4 is a comparison between the simulations of Ashby and NRL using this modified circuit. In this figure, comparisons are shown for the transfer capacitor (TC) voltage and the upstream POS current. Note that for this shot, the calculated upstream POS current was multiplied by 0.93 instead of the 0.95 used in Fig. 2 to obtain agreement with the measured current (a reliable measurement, at least during the conduction phase). The calculated TC voltage waveform was multiplied by 1.15 to match experimental data. According to PI, this discrepancy in the TC voltage is a result of a

change in the TC voltage monitor causing a change of calibration that was not accounted for in the experiment.<sup>11</sup> All of the other calculated traces throughout the circuit required the 0.93 correction factor. For the rest of the simulations shown in this report, we assume a Marx charging voltage of  $\pm 85$  kV and a correction factor is simply applied directly to the Marx charging voltage (initial voltage on element #1 of Fig. 3). Simulations using the circuit in Fig. 3, with the corrections noted above, were in agreement with all experimental measurements. This was not the case with earlier modeling<sup>5</sup> where insertion of extra vacuum inductance was required to obtain agreement.

**Table 1. DM1 Front End Inductance and Electrical Length.**

Component	Inductance	Two-way length
Water line *	27.5 nH	110 ns
Oil section to tube	39.8	10
Vacuum transition	15.8	3
5 Ohm MITL	27.5	11
Vacuum transition	13.6	4
7.5 Ohm MITL	30.0	8
Transition to POS	8.0	1
<b>Total to POS</b>	<b>162.2 nH</b>	<b>147 ns</b>
<b>POS-to-load</b>	<b>63.0 nH</b>	<b>3 ns</b>

\* Note, only that part of the water line that is within 75 ns of the load is included in this table.

The inductances and electrical two-way transit times for each section within 75 ns of the load (150 ns two-way time) are shown in Table 1. A length of 75 ns is chosen as a figure of merit; e.g., for statically charged transmission lines, this length would produce a 150 ns output pulse into a matched load. This choice of 75 ns is somewhat arbitrary, and is discussed and to some extent justified in Sec. V.A. and V.B.

Consider an inductive-store/opening switch system with a charging capacitor  $C$ , lumped storage inductance  $L_1$ , output inductance  $L_2$ , and load resistance  $Z_L$ . Assume that the conducted current is  $I_G$  and the current after opening is  $I_L$ . If  $T_{FW}$  is the full width of the POS voltage pulse and  $T_{1/4}$  is the quarter period of the drive circuit, then it can be shown that conservation of flux applies for this circuit provided: (i)  $T_{1/4} \gg T_{FW}$  and (ii)  $L_2/Z_L \gg T_{FW}$ . The first inequality provides the sufficient condition for no additional flux to be added to the circuit during the output

pulse. The second inequality ensures no flux is dissipated in the resistive load during the opening. If, in addition, the POS is ideal ( $R_{pos} \gg Z_L$ ), then flux conservation can be written as

$$I_L = \frac{L_1}{L_1 + L_2} I_G \quad (1)$$

It should be pointed out that none of these conditions apply to DM1 so that Eq. (1) is a figure-of-merit and not an absolute limit. During normal operation, the effective quarter period is about 300 ns while the width of the POS voltage pulse is about 190 ns (see Fig. 5). Therefore, the charging circuit provides additional flux to those elements within the assumed 75 ns of the POS (see Fig. 6 and Sec. V) during the output pulse. DM1 also has a diode load that resistively dissipates energy thereby removing flux from the system ( $L_2/Z_L = 6$  ns for 25.4 mm A-K gap, see Sec. V). In the derivation of Eq. (1), lumped inductances and steady state are assumed, whereas the elements upstream of the POS behave like distributed transmission line elements during the relatively short output pulse. Because of these effects, magnetic flux can be distributed in these elements in such a way that Eq. (1) does not apply. If we take the inductance within 75 ns of the POS from Table 1 to be  $L_1$ , and the POS-to-load inductance from Table 1 to be  $L_2$ , then Eq. (1) predicts that the load current is about 72% of the conducted current. Thus if flux conservation were applicable then, for the typical DM1 operation where  $I_G = 1.4$  MA, (see Fig. 6), one would expect no more than 1 MA of load current.

### III. DESCRIPTION OF POS CIRCUIT ELEMENT MODEL

The circuit element model for the POS is based on the flow-impedance concept<sup>8</sup> for which the flow impedance is defined by

$$Z_f = \frac{V_{SW}}{(I_{AU}^2 - I_{CD}^2)^{1/2}}, \quad (2)$$

where  $V_{SW}$  is the switch voltage,  $I_{AU}$  is the anode current upstream of the POS, and  $I_{CD}$  is the cathode current downstream of the POS. This expression can be derived from pressure balance arguments. The difference between the anode current upstream of the POS and the cathode current downstream of the POS is assumed to be the net current flowing in the form of vacuum electrons. In general, some of this vacuum flow is switch current and some is vacuum electron flow. For the analyses in this report, we assume that all this vacuum electron flow is lost and lumped with the switch losses. Therefore, no vacuum electron flow is counted as load current and the current available for driving the e-beam load, i.e., the load current, is  $I_{CD}$ . Because vacuum electron flow, as well as other processes,<sup>7</sup> can contribute to the load current responsible for the bremsstrahlung radiation produced in the experiment, we expect this POS circuit model to underestimate the load current. With this assumption, the net current in the POS is given by  $I_{SW} = I_{AU} - I_{CD}$ , and the resistance of the switch ( $R_S = V_{SW}/I_{SW}$ ) can be related to the flow impedance by

$$R_s = Z_f \left( \frac{I_{AU} + I_{CD}}{I_{AU} - I_{CD}} \right)^{1/2}. \quad (3)$$

The flow impedance approach has the advantage that the total current (anode current) can be differentiated from the cathode current. However, the time dependence for  $Z_f$  must still be specified. For all but one case (see Sec. V), the flow impedance is assumed to rise linearly in time to a specified maximum in a specified time (28 ns for most of these runs). At that time the impedance may either remain constant or it can be decreased at a given rate to match experimental observations.

A physical interpretation of  $Z_f$  that encompasses a physical model for the POS can be described as follows. If the anode-cathode gap spacing,  $D$ , of a coaxial vacuum transmission line is small compared to the cathode radius,  $R_C$ , then it can be shown that the flow impedance is the vacuum wave impedance between the centroid of the electron space charge and the anode.<sup>14</sup> If the vacuum electrons are very well insulated, the charge centroid is very close to the cathode and the flow impedance is the vacuum wave impedance of the transmission line,  $Z_f \cong 60D/R_C$ . When the vacuum electrons are critically insulated (in "saturated" flow, e.g., when the electrons'

gyroradii are comparable to the anode-cathode spacing of the transmission line), electrons fill the transmission line. In this case, the centroid of the electrons is approximately halfway between the anode and cathode, and the flow impedance is half the vacuum wave impedance of the transmission line. The physical model for the POS used in this report assumes that the vacuum electrons are always critically insulated in the time dependent POS gap,  $D_{crit}(t)$ .<sup>10</sup> It is further assumed that the POS gap forms at the cathode. This last assumption is justified from direct measurements of the POS density before and during opening on Hawk, using the same cable gun plasma sources used on DM1.<sup>15</sup> Under these assumptions, the POS flow impedance can be written as<sup>9</sup>

$$Z_f \cong 30D_{crit}(t)/R_C. \quad (4)$$

A good fit to DM1 Shot 1353 was obtained when the flow impedance for the POS was linearly increased to  $1.38 \Omega$  in 28 ns, then decreased exponentially with a  $1/e$  time of 55 ns. Using Eq. (4) and  $1.38 \Omega$  for  $Z_f$ ,  $D_{crit}$  is 2.3 mm at a radius of 4.95 cm. By comparison, the value for  $D_{crit}$  at peak voltage obtained using the critical current formula [see Sec. V.C., Eq. (9)] at  $R_C = 4.95$  cm is 2.1 mm, confirming the physical interpretation for  $Z_f$ .

#### IV. DESCRIPTION OF E-BEAM DIODE CIRCUIT ELEMENT MODEL

The circuit model for the e-beam load is divided into three phases: 1) an early turn-on phase, 2) a Child-Langmuir (C-L) flow phase, and 3), a critical-current, pinched-beam phase. The input parameters for the diode model are the diode cathode outer radius ( $R$ ), the cathode inner radius ( $R_{in}$ ), the radius of curvature of the cathode edges ( $R_e$ ), the electric field turn-on threshold, the time duration to reach full C-L current, the initial anode-cathode (A-K) gap ( $d$ ), and the gap closure speed ( $v$ ).

During the early turn-on phase, current begins to flow in the diode when the mean electric field reaches a preset threshold. Once the field threshold is exceeded, it is assumed that plasma forms on a fraction of the cathode surface and expands to cover the entire cathode. During the time for the full cathode area to be completely covered with plasma and behave as a zero work function emitting surface, the current rises linearly from zero to the full C-L value.

During the second phase, the model provides a full C-L current and the flow is assumed to originate from both the flat portion of the cathode and from the edges. The total C-L current is determined by adding the perveance from the edges of the cathode and the flat-surface area [ $A = \pi(R^2 - R_{in}^2)$ ] of the cathode. The perveance for the flat cathode surface is given by

$$P_{flat} = \frac{2.33 \times 10^{-6} A}{(d - vt)^2} \quad (A/V^{3/2}), \quad (5)$$

where  $t$  is the time after diode turn-on, and  $vt$  is the distance the gap closes from plasma expansion. The perveance for the cathode edges is given by<sup>16</sup>

$$P_{edge} = \frac{1}{8} (14.66 \times 10^{-6}) \frac{2\pi(R + R_{in})}{d\alpha^2} \quad (A/V^{3/2}), \quad (6)$$

where

$$\alpha \equiv \begin{cases} \beta - 0.4\beta^2 + 0.0917\beta^3 - 0.0142\beta^4 + 0.00168\beta^5 \\ \quad - 0.000161\beta^6, & 0 \leq \beta \leq 2.3 \\ 0.99 & \beta > 2.3 \end{cases},$$

and  $\beta = \ln \frac{d + R_e}{R_e + vt}$ . The truncated power series used for  $\alpha$  in Eq. (6) is a consequence of

cylindrical geometry and is reasonably accurate (within 10%) for all values of  $d/R_e$ . The total diode current is then

$$I_{C-L} = (P_{edge} + P_{flat}) V^{3/2} \quad (A), \quad (7)$$



where  $V$  is the diode voltage.

When the C-L current exceeds critical current, the third phase begins which limits the diode current to the critical current limit for the remainder of the simulation. The critical current is expressed as

$$I_{CRT} = 8500 F_{CR} \frac{R}{d - vt} (\gamma^2 - 1)^{1/2} \quad (\text{A}), \quad (8)$$

where  $F_{CR}$  is a factor that is weakly dependent on voltage and is approximately 1.6 for voltages between 1 and 3 MV,<sup>17</sup> and  $\gamma$  is the ratio of electron energy to electron rest energy.

The best fit to the DM1 shots used 10 kV/cm and 0 ns for the electric field turn-on threshold and duration to full C-L current respectively. Typical values of the electric field turn-on threshold and duration to full C-L current for similar diodes on the NRL Gamble II generator are 200-300 kV/cm and 10-20 ns, respectively. Long conduction time POS shots on Hawk<sup>19</sup> (where POS plasma appears to be in the load region at the time of opening) exhibit the same values as used here for DM1. For all of this work, the closure speed was chosen to be 3.5 cm/ $\mu$ s, typical of similar diodes on Gamble II.

## V. RESULTS OF DM1 MODELING

### A. Modeling for DM1 Experimental configuration.

DM1 shot 1353 was selected for comparing with simulations from a series of identically configured shots (shot numbers 1340 and 1345-1354). The POS voltage, conduction current, x-ray FWHM, and dose-area product for this shot [1.8 MV, 1.4 MA, 20 ns, and 7.8 MRad(Si)-cm,<sup>2</sup> respectively] were close to the average values for the shots in this series [ $1.73 \pm 0.16$  MV,  $1.39 \pm 0.05$  MA,  $32 \pm 9$  ns, and  $7.9 \pm 1.3$  MRad(Si)-cm,<sup>2</sup> respectively]. The POS voltage from the DM1 data was inferred from the voltage monitor located in the oil section close to the vacuum insulator ( $V_{tube}$  in Fig. 3). PI applied inductance and transmission line corrections to the signal from this monitor, using local current measurements, to obtain the voltage at the POS.

The calculated and experimental POS voltage and current immediately upstream of the POS are shown in Fig. 5 for the case where  $Z_f$  rises to  $1.35 \Omega$  in 25 ns and remains a constant after POS opening. An A-K gap of 25.4 mm with a closure speed of 3.5 cm/ $\mu$ s was used in the diode load model for this simulation. The negative going excursion in the POS voltage at about 1.2  $\mu$ s is the result of a “glitch” in the signal from the voltage monitor. This appears on some shots but not others, and is a factor in the uncertainty associated with the inferred POS voltage during and after opening.<sup>18</sup> To obtain the agreement between the calculated and measured current waveforms during POS conduction, it was necessary to apply a correction factor of 0.90 to the nominal 1.02 MV (85 kV charge) initial Marx voltage. This results in roughly a 20% decrease in the initial stored energy to  $\approx 460$  kJ.

While a good match was obtained with the experimental rise of the POS voltage when using a maximum  $Z_f$  of  $1.35 \Omega$  and an opening time of 25 ns, the width of the calculated POS voltage was consistently much wider than that observed on DM1. With the large (25.4 mm) diode gap used in the test series, it is not likely that the diode was shorting out on these time scales (requiring  $\approx 20$  cm/ $\mu$ s closure speed). Therefore, consistent with our physical model for the POS (see Sec. III), it was suspected that the effective POS gap may be decreasing with time after the initial opening, giving rise to a decreasing flow impedance [see Eq. (4)]. To obtain agreement with data from Hawk, where anode and cathode currents between the POS and load were measured, the POS gap also had to decrease with time.<sup>19</sup>

Shown in Fig. 6 are the results obtained using a  $Z_f$  that linearly rises to  $1.38 \Omega$  in 28 ns and then decays exponentially with a  $1/e$  time of 55 ns. Although the details during the fall of the POS

voltage are not replicated in the calculated waveform (nor consistently reproduced in other shots), the overall shape is in much better agreement with the data than the simulation without the decaying  $Z_f$  (Fig. 5). Also shown in Fig. 6 is the calculated current with a short circuit at the POS. This is the current that would be available with later POS opening times. The present DM1 operation utilizes only about 78% of this available current (or about 60% of the available stored energy if the POS conducted the entire current pulse).

The calculated load waveforms and measured x-ray dose rate (from a calibrated PIN diode, provided by JAYCOR, Inc.) are plotted in Fig. 7 for a diode gap of 25.4 mm. The peak load voltage of 1.73 MV is in agreement with the PI end-point monitor value of 1.75 MV for that shot. An estimate of the x-ray waveform from the simulation is shown in Fig 7 by plotting  $IV^{2.8}$  and  $IV$  after normalization to the PIN signal.  $IV^{2.8}$  provides a reasonable match during the fast part of the PIN signal but does not track the late-time tail. The  $IV$  waveform shows a closer agreement to the later times of the x-ray pulse. An  $IV^n$  approximation to the x-ray waveform should not be expected to be accurate with a constant value of  $n$  for all times.

Under the conditions for the calculations shown in Figs. 6 and 7, 12 kJ is delivered to the load by the time the measured x-ray pulse falls to zero, about 150 ns after the POS opens. This is about a factor of 4.5 lower than the 54 kJ believed to be delivered for DM1 shot 1353 based on CYLTRAN analyses.<sup>6</sup> The circuit calculation only uses current flowing in the metal of the cathode and does not include any electron flow in the POS-to-load region. Thus, the POS circuit element model provides a lower bound for the load energy relevant for bremsstrahlung production.

The simulation was also used to provide a time-dependent energy inventory in the various elements of the DM1 generator. The energies in the Marx capacitance and inductance, transfer capacitor, and water line sections are shown in Fig. 8. The energies in the remainder of the sections are shown in Fig. 9 with both the vertical and horizontal axes expanded. The resistive losses in the Marx, transfer capacitor (water losses), diverters, and POS are shown in Fig. 10. Snap shots of the energy distribution at the start of POS opening (beginning of energy delivery to the load) and 150 ns after the start of POS opening are tabulated in Table 2. Also shown in this table are the energies that are within 75 ns (150 ns two-way time) of the load at the time of POS opening. This energy is used as an estimate of the energy available to drive the combined POS and load during the 150-ns output pulse (see following paragraph). The energies shown for the water line consist of roughly equal capacitive and inductive components while the energies stored in the oil and vacuum lines are predominately inductive.

**Table 2. DM1 energy distribution at two different times.**

Component	At POS opening		After 150 ns Total generator
	Within 75 ns of load	Total generator	
Marx capacitance	N/A	67.1 kJ	59.5 kJ
Marx inductance	N/A	4.4	5.9
Marx resistance	N/A	18.9	19.1
Transfer capacitor	N/A	49.3	26.3
Transfer cap. resistance	N/A	36.9	38.3
TC switch section	N/A	11.6	11.8
TC switch loss	N/A	0.6	0.6
Water line	81.5 kJ	133.9	19.2
Diverter, all	N/A	2.5	33.6
Oil line	24.0	24.0	16.0
Vacuum line	108.5	108.5	71.1
Vacuum skin resistance	N/A	0.8	2.3
POS	0	0	143.0
POS-load inductance	0	0	0.1
Load	0	0	12.1
<b>Total</b>	<b>214.7 kJ</b>	<b>458.5 kJ</b>	<b>458.9 kJ</b>

The choice of the 75 ns electrical length is somewhat arbitrary, and is chosen as an estimate of the electrical length in which energy is stored that can be delivered to the load in 150 ns (the calculated relevant energy delivery time). The object is to have a reasonable engineering figure-of-merit to evaluate the design of the pulsed power system up to the POS. Defining this figure-of-merit is difficult to do precisely because the distributed nature of the DM1 circuit results in energy flowing into and out of the elements within 75 ns of the POS during the 150-ns load pulse length. To check our estimate, additional circuit simulations were run with the POS and load replaced with a matched resistive load. These simulations show that about 237 kJ is delivered to the load in 150 ns. The energy stored within 75 ns of the load underestimates this energy by only 10% and is therefore a reasonable figure-of-merit for the energy available to the real POS-load combination. The 215 kJ stored within 75 ns of the load is about 47% of the initial energy stored in the Marx ( $\approx 460$  kJ after the 0.9 correction factor is applied to the charge voltage). The other

53% is either resistively dissipated or remains in the system components, and is unavailable to drive the load during the 150-ns output pulse.

During the 150 ns after the POS starts to open the circuit model predicts that 155 kJ, about 72% of the estimated available energy (defined above), is dissipated by the combined POS and load and, of that, only 12 kJ is delivered to the load. CYLTRAN calculations using idealized load waveforms (which turns out to be a good approximation<sup>7</sup>) were performed to determine the bounds on the energy delivered to the load for the test series.<sup>6</sup> The results indicate that for shot 1353 about 54 kJ (a range of 45 to 75 kJ for the shots considered here) must be delivered to the load to explain the observed radiation. Thus, of the 155 kJ dissipated in the combined POS/load, about 35% is dissipated in the load on DM1. The circuit calculation underestimates the energy delivered to the load on DM1 by 42 kJ. The most likely explanation for this discrepancy is that the model does not account for any non-cathode electron current that hits the Ta anode converter. Vacuum electron flow and current transport in plasma distributed downstream of the POS can increase the load current over that from the cathode alone.<sup>7,20</sup> The agreement between the calculated POS and load voltages and the voltages at the POS and load inferred from the experiment suggest that this non-cathode current is delivered to the load through a very low inductance path. Further experiments, supported by two-D PIC simulations, are required to resolve this issue.

To improve radiation production, a higher fraction of the total energy dissipated in the POS-load combination must be delivered to the load. With the load voltage fixed by DECADE specifications<sup>1</sup> and the POS conduction time limited by the present DM1 performance, an increase in the load energy can only result from an increase in load current (see below). An increase in conduction time of  $\approx 25\%$ , from 220 ns to 270 ns, would increase the estimated energy available to be delivered to the POS/load combination in 150 ns by  $\approx 50\%$  from 215 kJ to 317 kJ. Whether or not a proportionate increase in load energy would result from this increased conducted current must be demonstrated experimentally.

#### B. Modeling with different load configurations.

The results of the previous sections were obtained with a diode A-K gap of 25.4 mm and a vacuum POS-to-load inductance of 63 nH. To determine the optimum load configuration, we carried out simulations for which the diode A-K gap and the POS-to-load inductance were varied.

Simulations were run with the initial diode A-K gap varied from 0 to 25.4 mm to study POS/load coupling issues as a function of load impedance. Figure 11a is a plot of the energy delivered to the load during the first 150 ns after the POS opens and Fig. 11b is a plot of the load voltage and the cathode current at the load at the time of peak load power, both as a function of the diode impedance at peak power. Similar behavior to that illustrated in Fig. 11b was observed on Hawk (see Fig. 6 of Ref. 10), where current was measured at the anode near the load. The optimum load impedance for maximum energy coupling,  $Z_L^*$ , is about  $2\ \Omega$  (6.3 mm initial A-K gap). At this optimum impedance, the energy delivered to the load in 150 ns is 37 kJ. Figure 11b provides an explanation for this optimization. For load impedances greater than  $Z_L^*$ , the system voltage is limited by the POS. The POS voltage is limited by the conducted current and the POS gap size and insensitive to changes in the load impedance. Because the POS voltage is limited by the switch parameters, this regime of POS operation has been termed switch-limited.<sup>10</sup> For values of load impedance smaller than  $Z_L^*$ , the POS voltage is determined by the load impedance and the current transferred from the POS to the load. This regime has been called load-limited because the load controls the POS voltage.<sup>10</sup> The load voltage and current waveforms for the optimum load impedance are shown in Fig. 12. The load current risetime is longer compared with the case shown in Fig. 7. This is probably because of a longer  $L/R$  time from the smaller load impedance. Because the 37 kJ delivered to the load with the 6.3 mm gap is near the lower bound on the CYLTRAN-inferred load energy, a question can be raised that perhaps the diode gap on DM1 is not behaving as modeled. In the experiment, the effective diode gap could be smaller than the vacuum gap either because of POS plasma reaching the diode or because of Ta out-gassing in the diode region causing a local buildup of neutrals. Based on recent Hawk data<sup>21</sup> with a Ta anode, we believe an anomalously small diode A-K gap is not a dominant effect in the DM1 test series described here.

According to Fig. 11b, approximately 520 kA of non-cathode current, in addition to the  $\approx 150$  kA of calculated cathode current, must be delivered to the load to account for the inferred<sup>6</sup> 54 kJ of energy delivered to the load on DM1 shot 1353. Vacuum electron flow alone is probably insufficient to explain this level of non-cathode, bremsstrahlung-producing load current. Also, the calculated and measured POS and load voltage waveforms suggest that this non-cathode current is delivered to the load through a relatively low inductance path. The behavior predicted in Fig. 11 must be determined experimentally on DM1, with anode and cathode current monitors located between the POS and load to measure the partition of anode and cathode current. Direct measurement of the voltage time history near the load would also greatly assist in resolving this issue. If DM1 did behave as predicted by Fig. 11, and taking the 42 kJ associated with non-

cathode current (see above) as an upper bound for non-cathode energy delivered to the load, then when the load impedance is  $Z_L^*$ , a total of 79 kJ at 150 ns would be delivered to the load.

The effects of the inductance between the POS and the load were also investigated. Runs were made with the inductance reduced by factors of two and four from the value implied in the circuit of Fig. 3. The results are shown in Fig. 13, where the energy delivered to the load in 150 ns and the ratio of the peak POS voltage to peak load voltage are plotted with respect to POS-to-load inductance (vacuum value) for two different diode gaps. As might be expected, the figure shows that reducing the coupling inductance has very little effect with a 25.4-mm diode gap because the impedance associated with this gap ( $\approx 11 \Omega$ ) is large enough that changes in the inductive reactance ( $L/\tau$ , where  $L$  is inductance  $\tau$  is the current risetime) have very little effect on the effective impedance seen by the POS. Reducing the coupling inductance does have a large, beneficial effect with the 6.3-mm gap. In this case, the diode load impedance is very near  $Z_L^*$  (see Fig. 11b) and low enough that changes in the coupling inductance can produce large improvements in the coupled energy. The calculated load waveforms for this low-inductance, 6.3-mm gap condition are shown in Fig. 14. The energy delivered to the optimized load with a reduced value of 15.8 nH between the POS and load is 54 kJ

The behavior of DM1 predicted in Figs. 13 and 14 must be demonstrated experimentally on DM1 (with anode and cathode current monitors located between the POS and load). Of particular interest will be power flow and the effects of plasma in the POS-to-load region with reduced POS-to-load inductance. If DM1 did behave as predicted by Fig. 13 and if, as an upper bound, the 42 kJ associated with non-cathode current (see above) was still delivered to the load, then when the load impedance is  $Z_L^*$  and the POS-to-load inductance is reduced to 15.8 nH, a total of 96 kJ would be delivered to the load.

The load current into a short circuit load from Fig. 11b is about 1 MA. This current actually reaches the generator current level, 1.3 MA, but later in time, 100 ns after POS opening. The 1 MA point is reached at a representative time when the load power peaks for non-zero impedance loads, about 50 ns after POS opening. Coincidentally, the value of 1 MA is what would be expected from ideal flux conservation using the inductance ratio discussed in Sec. II, Eq. (1), assuming no additional flux enters the flux conserving boundary and the load is a short circuit (i.e., the conditions for flux conservation to obtain). The discrepancy between the 1-MA flux conservation "limit" and the 1.3 MA calculated for the short circuit load reflects the fact that additional flux is entering the system (see Sec. II). Again, the concept of flux conservation is not particularly useful in these analyses.

### C. Modeling with alternative $Z_f$ time history.

In an attempt to provide better agreement with the late-time history of DM1 Shot 1353, a simulation was performed using a time-varying  $Z_f$  for the POS model that was calculated from the DM1 data. This procedure amounts to prescribing the time history for  $Z_f$  by making use of the relationship between  $Z_f$  and  $D_{CRIT}$ . This was accomplished by calculating  $D_{CRIT}(t)$  from

$$D_{CRIT}(t) = 8500 F_{CR} \frac{R_c}{I_{AU}} (\gamma^2 - 1)^{1/2}, \quad (9)$$

where  $F_{CR}$  is dimensionless, of order unity, and weakly dependent on voltage and  $I_{AU}$  is in amperes.

The inferred POS voltage and measured upstream current from the DM1 data for shot 1353 were used for this computation. The flow impedance,  $Z_f(t)$ , was then calculated according to Eq. (4). Results of this simulation are shown in Figs. 15 and 16. To obtain agreement with the peak DM1 POS voltage, it was necessary to use a value of 1.5 for  $F_{CR}$  in Eq. (9) instead of the customary value of 1.6. This factor may actually vary during the pulse because the calculated and experimental values for the second peaks do not agree. However, the simulation is probably well within the experimental error of the DM1 data. The maximum value of  $Z_f$  was 1.32  $\Omega$ . The calculated POS voltage in Fig. 15 provides a better fit to the DM1 data during the falling edge of the pulse than for the case shown in Fig. 6. The load waveforms shown in Fig. 16 show that this simulation provides slightly more energy into the load in the first 150 ns (15 kJ) than previously observed, mostly due to the second hump in the voltage and current waveforms. For this case, the normalized  $IV$  trace over estimates the height of the measured x-rays during the late-time portion of the pulse. Note that the second peak was not a reproducible feature of all the DM1 shots. Thus, for understanding the system behavior and what might be expected from changes in the load configuration, the assumptions used in Secs. V.A and B for the time dependence of  $Z_f$  are adequate.

It should be noted that in this case, as with all the other cases discussed, there is a discrepancy between the experimental and calculated up-stream currents. We believe that the current as measured by  $B$ -dot loops close to the POS may not be accurate after POS opening. This is also evident when comparisons are made with the inferred current close to the POS derived from monitors located in the vacuum insulator region. Current measurements are also needed in the POS-to-load region of DM1 to provide finer tuning of the simulations.



#### D. Summary of circuit and radiation modeling.

The predicted DM1 bremsstrahlung dose-area product from the four different circuit model waveforms described above is given in Table 3, along with data from the DM1 test series. The first row of Table 3 gives statistics for eleven similarly configured DM1 shots (shot numbers 1340, and 1345-1354). The measured x-ray FWHM and dose-area-product (in 20 mils silicon) given in row 1 are the average and standard deviation for these 11 shots (see Ref. 6, Table I, column 9). The second row of Table 3 applies specifically to shot 1353, which was selected as a typical shot for this series and for which, direct comparisons with the simulations were made. The remaining 4 rows of Table 3 list the parameters and the results of BERTHA and CYLTRAN calculations for the four cases associated with the load waveforms in Figs. 7, 12, 14, and 16, respectively. The BERTHA simulations used parameters for the POS model, POS-to-load inductance and the load A-K gap listed in columns 1-3. The electron energy spectrum resulting from the calculated load current and voltage waveforms was used as input into the CYLTRAN code. The model of the DM1 converter package geometry (converter, beam-stop, and detector) used in the CYLTRAN simulations is described in Ref. 6. The load energy from the four

**Table 3. Summary of experimental data and simulation results.**

POS Model for Simulations	POS-load Induct. (nH)	Load A-K Gap (mm)	X-ray FWHM (ns)	$E_{LOAD}$ @ 150 ns (kJ)	Dose-Area Product (MRad(Si)-cm <sup>2</sup> )
(DM1-11 shots)	63.0	25.4	32 ±9	56.2±8.6*	7.9±1.3
(DM1 Shot 1353)	63.0	25.4	20	54.3*	7.8
1.38 Ω, 28 ns 55 ns 1/e	63.0	25.4	24	12.1	1.8
"	63.0	6.25	37	36.7	4.7
"	15.8	6.25	26	53.9	7.7
30 D <sub>CRIT</sub> (t)/R	63.0	25.4	25	15.1	2.4

\*from Ref. 6, using idealized load waveforms.

BERTHA calculated waveforms at 150 ns is given in columns 5 and 6. CYLTRAN calculations<sup>6</sup> are used to estimate the load energy for the DM1 shots (rows 1 and 2, column 5). Column 7, rows 3-6, lists the dose-area-product in 20-mils Si from the CYLTRAN calculations, performed using the first 150 ns of the BERTHA generated pulses.

The CYLTRAN results for the four cases given in Table 3 (rows 3-6) differ from the DM1 dose-area-product by as much as a factor of 4. In the calculation, all of the energy delivered to the load is associated with cathode current only. As discussed above, this is most likely not the case in the experiment. We believe the agreement between the calculated dose-area product for the 15.8 nH POS-to-load case (fifth data row of Table 3) and the DM1 shots (first and second row) is a coincidence. In the experiment, the POS-to-load inductance and load A-K gap would have to be simultaneously and appropriately reduced from their nominal vacuum values and all of the load current would have to be cathode current to match the simulations.

## VI. SUMMARY AND CONCLUSIONS

Using an up-to-date circuit representation of DM1, physics based circuit element models for the POS and e-beam diode load, and the data base from a recent DM1 test series, we analyzed the DM1 operation with the transmission-line and radiation computational tools, BERTHA and CYLTRAN, respectively. The circuit calculations matched the DM1 waveforms up-stream of the POS when a small correction factor is applied, giving confidence in the DM1 circuit representation. A POS circuit element model incorporating a decaying flow impedance after opening was used and provides agreement with the inferred POS voltage and x-ray signals. In the context of the assumed physical POS model, this corresponds to a closure of the POS gap. The predicted load energy for the DM1 experimental configuration, 12 kJ, is much lower than the 54 kJ estimated from DM1 radiation measurements. An additional 520 kA above the calculated load current of 150 kA is necessary to explain this 42 kJ discrepancy. One likely explanation could be the fact that the circuit model uses only cathode current as load current and does not account for non-cathode, radiation-producing load current associated with vacuum electron flow and/or other effects, such as plasma between the POS and load. The measured and calculated voltage waveforms suggest this additional current is delivered through a relatively small inductance.

An energy analysis suggests that 150 ns after the POS opens in the experiment, approximately 155 kJ is dissipated by the POS and e-beam load combined, compared with the estimated 54 kJ delivered to the load. This 155 kJ is 72% of the estimated energy available to drive the combined POS/load during the 150-ns output pulse. Of the 155 kJ energy dissipated in the combined POS/load only 35% is actually dissipated in the load. The 215 kJ estimated to be available to drive the combined POS/load is less than half of the energy stored initially in the Marx. An increase in conduction time of 25%, from 220 ns to 270 ns, would increase estimated energy available to drive the POS/load combination by about 50% from 215 kJ to 317 kJ.

The BERTHA calculations predict that approximately 37 kJ can be delivered to the load with an optimized e-beam diode A-K gap of 6.3 mm. If, additionally, the POS-to-load inductance is reduced a factor of 4, from 63 nH to 16 nH, 54 kJ is delivered to the load. If, as an upper bound, the approximately 42 kJ of energy associated with non-cathode current continues to be delivered to the load, these values become 79 kJ and 96 kJ, respectively. The optimized A-K gap (6.3 mm) corresponds to an optimized load impedance of a little under  $2\ \Omega$ . In the test series, the diode A-K gap is nominally 25.4 mm. The increase in load energy associated with the reduced inductance can be realized only with the optimum load impedance. Although the actual response of the DM1

system to reduced load impedance and the POS-to-load inductance behavior is not well known and must be determined from experiment, data from Hawk<sup>10</sup> suggest that the total load energy increases as the diode impedance is reduced to the optimum impedance. Guidance on how to better model the POS-to-load coupling awaits results of PIC simulations and additional experiments.

To properly address these issues, well diagnosed experiments are required. Better measurement of the current immediately upstream of the POS on both the anode and cathode side, measurement of cathode and anode currents between the POS and load, direct measurement of the voltage time history near the load, as well as fixing the "glitch" problem associated with the voltage monitor in oil would greatly help in understanding the experiment and in interpretation and analyses of these calculations.

Bremsstrahlung radiation yield calculations using the results of this circuit modeling indicate dose-area-products up to a factor of 4 smaller than average experimental results. Again, these discrepancies can be accounted for, in part, by noting that the circuit calculations only include current carried in the cathode and not all the current that may contribute to the dose.

To improve performance from a circuit point of view, a higher fraction of the total energy dissipated in the POS-load combination must be delivered to the load. For a fixed load voltage, this implies that the current delivered to the e-beam load must increase. From a circuit point of view, this can be done by optimizing the load impedance and minimizing the POS-to-load inductance. Whether or not this can be actually done on DM1 must be demonstrated experimentally.

## VII. ACKNOWLEDGMENTS

The authors express their gratitude to Drs. D. Kortbawi and J. Goyer of PI for willingly providing DM1 data and describing the measurement procedures. Dr. P.F. Ottinger of the Pulsed Power Physics Branch provided many helpful suggestions and a thorough reading of the paper. Many helpful discussions were had with other members of the Pulsed Power Physics Branch at NRL, especially Drs. B.V. Weber, J.M. Grossmann, G. Cooperstein, and F.C. Young. We also acknowledge helpful discussions with Dr. M. Savage of Sandia National Laboratories and Dr. M. Marcus of Kaman Sciences Corporation. The continued support of Dr. J. Rowley of the Defense Nuclear Agency (DNA) is greatly appreciated.

This work was supported by DNA.

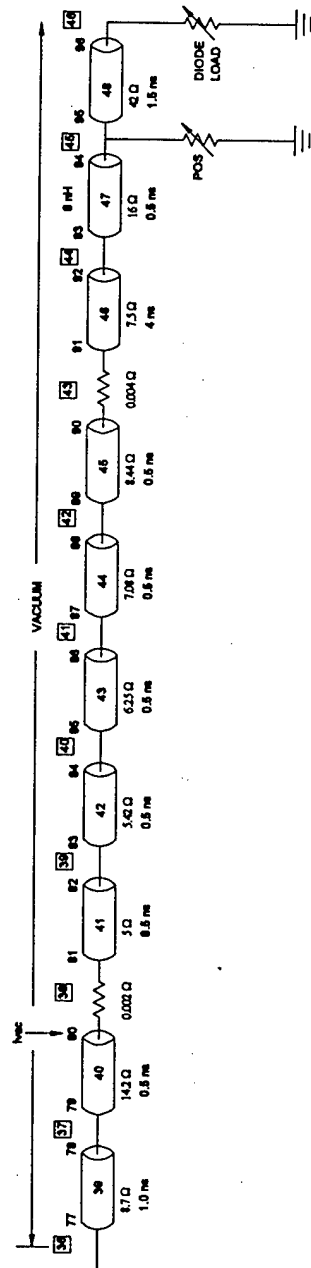
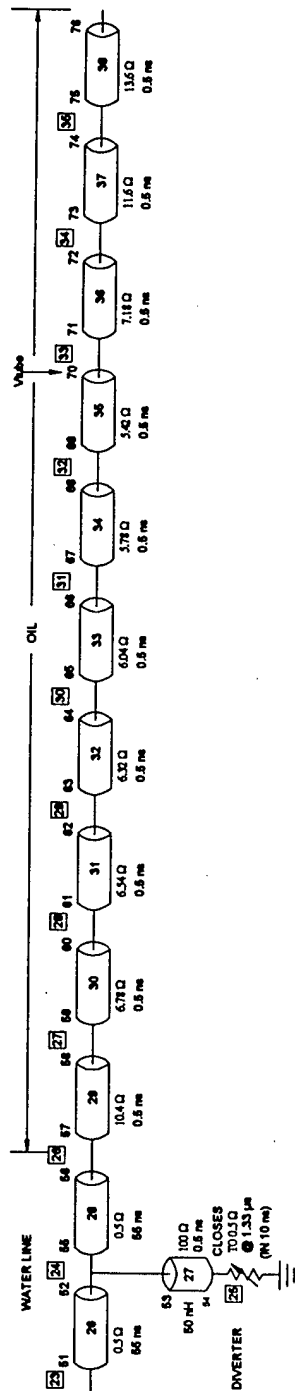
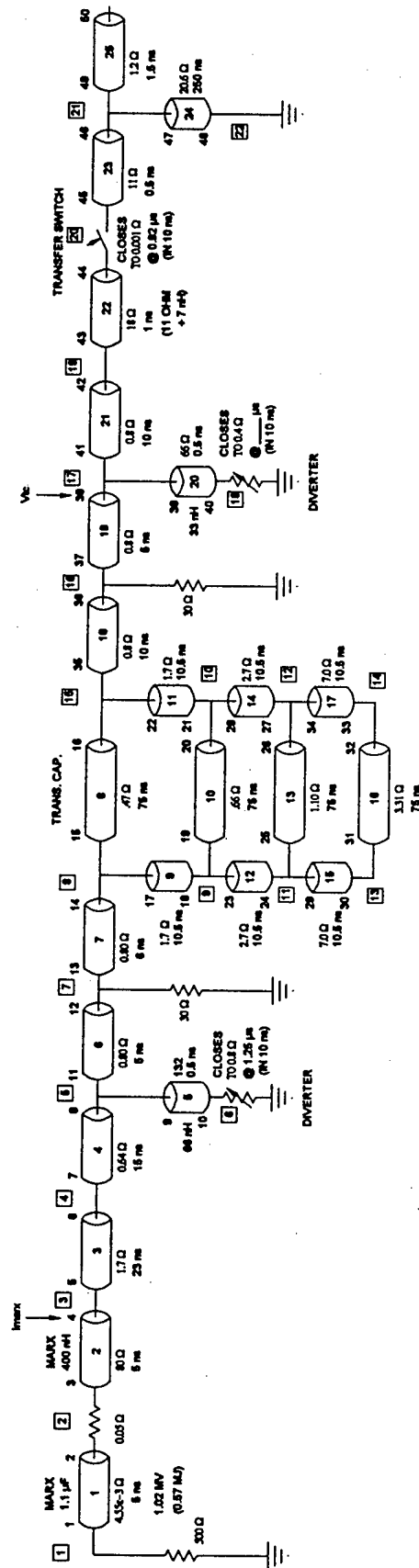
---

## REFERENCES

1. "The DECADE High Power Generator," P. Sincerny, S. Ashby, K. Childers, C. Deeney, D. Drury, J. Goyer, D. Kortbawi, I. Roth, C. Stallings, and L. Schlitt, in Proceedings of the 9th IEEE International Pulsed Power Conference, R. White and W. Rix, eds., San Diego, CA (1993), IEEE Cat. No. 93CH3350-6, p. 880.
2. "Performance of DECADE Module #1 (DM1) and Status of the DECADE Machine," P. Sincerny, S. Ashby, K. Childers, J. Goyer, D. Kortbawi, I. Roth, C. Stallings, J. Dempsey, and L. Schlitt, in Proceedings of the 10th IEEE International Pulsed Power Conference, W. Baker and G. Cooperstein, eds., Albuquerque, NM (1995), paper 12-3, in publication.
3. "BERTHA - A Versatile Transmission Line and Circuit Code," D.D. Hinshelwood, NRL Memorandum Report 5185, (Nov. 1983), unpublished.
4. "ITS Version 3.0: The Integrated TIGER Series of Coupled Electron/Photon Monte Carlo Transport Codes," J.A. Halbleib, R.P. Kensek, T.A. Mehlhorn, G.D. Valdez, S.M. Seltzer, M.J. Berger, Sandia National Laboratories Report SAND91-1634 (1992), unpublished. [Also in Oak Ridge National Laboratory - Radiation Shielding Information Center Report CCC-467, 1994.]
5. "DM1 (DECADE) Circuit Modeling with a Diode Load," J.R. Boller and R.J. Commisso, Pulsed Power Physics Technote No. 94-12 (1994), unpublished.
6. "Bremsstrahlung Yield Simulations for DM1," D.V. Rose, R.J. Commisso, S.B. Swanekamp, and F.C. Young, NRL Memorandum Report 7748 (1995), unpublished.
7. "Modeling of DM1 Performance," R.J. Commisso, J.R. Boller, D.V. Rose, S.B. Swanekamp, F.C. Young, J.M. Grossmann, P.F. Ottinger, B.V. Weber, and G. Cooperstein, in Proceedings of the 10th IEEE International Pulsed Power Conference, W. Baker and G. Cooperstein, eds., Albuquerque, NM (1995), paper 6.6, in publication.
8. "Experiments on a Current-Toggled Plasma-Opening Switch," C.L. Mendel, Jr., M.E. Savage, D.M. Zagar, W.W. Simpson, J.W. Grasser, and J.P. Quintenz, J. Appl. Phys. 71, 3731 (1992).

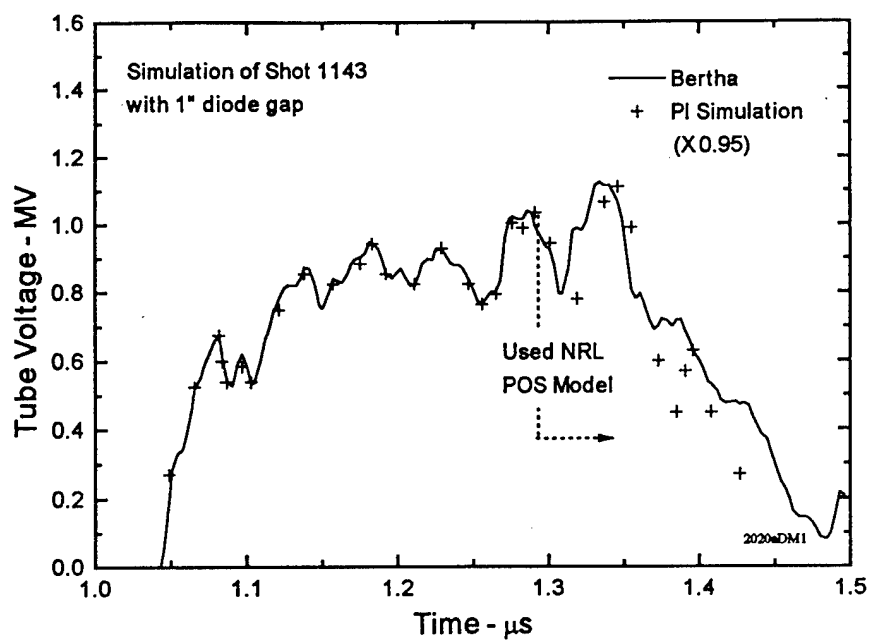
- 
9. "Power Flow between a Plasma-Opening Switch and a Load Separated by a High Inductance Magnetically Insulated Transmission Line," S.B. Swanekamp, J.M. Grossmann, P.F. Ottinger, R.J. Commisso, and J.R. Goyer, *J. Appl. Phys.* 76 2648 (1994).
  10. "Characterization of a Microsecond-Conduction-Time Plasma Opening Switch," R.J. Commisso, P.J. Goodrich, J.M. Grossmann, D.D. Hinshelwood, P.F. Ottinger, and B.V. Weber, *Phys. Fluids B* 4, 2368 (1992).
  11. L. Schlitt, Memorandum to P. Sincerny, 21 June 1994, Subject: Interim Circuit Model for DM1 Shot #1143, unpublished.
  12. L. Schlitt, Memorandum to P. Sincerny, D. Kortbawi, J. Goyer, 15 June 1994, Subject: Interim Circuit Simulations of DM1 Shot #1143 (& #1026), unpublished.
  13. Steven Ashby, PI Memorandum to P. Sincerny, October 6, 1994, Subject: DM1/DECADE Model, unpublished.
  14. C. Mendel, private communication.
  15. "Initial Cable Gun Experiments on Hawk," B.V. Weber, D. Hinshelwood, and R.J. Commisso, Pulsed Power Physics Technote No. 93-06 (1993), unpublished.
  16. "Plasma-induced field emission and the characteristics of high-current relativistic electron flow", R.K. Parker, R.E. Anderson, and C.V. Duncan, *J. Appl. Phys* 45, 2463 (1974).
  17. R.J. Barker and S.A. Goldstein, *Bull. Am. Phys. Soc.* 26, 921 (1981).
  18. D. Kortbawi, private communication.
  19. "Modeling the Hawk POS with Diode Load," J.R. Boller, R.J. Commisso, and B. Weber, Pulsed-Power Physics Technote No. 95-17, unpublished.
  20. "POS-Load Coupling Theory," S. Swanekamp, J. Grossmann, B. Commisso, P. Goodrich, R. Riley, and B. Weber, Pulsed-Power Physics Technote No. 95-11, unpublished.
  21. B.V. Weber, private communication.

CONFIGURATION: DM1  
TS = 0.5 NS

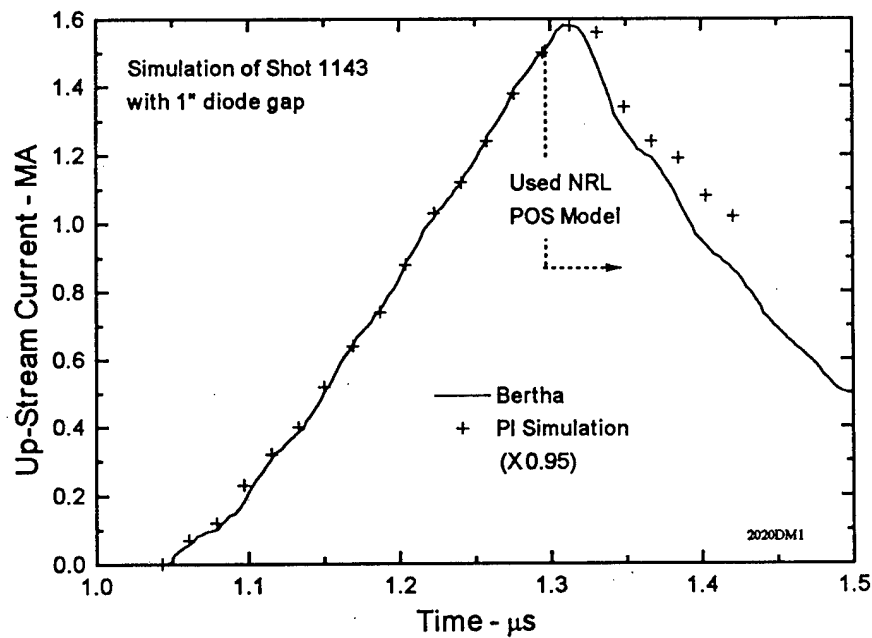


10-12-84

Figure 1. Equivalent transmission-line circuit for DM1.



a. Tube voltage.



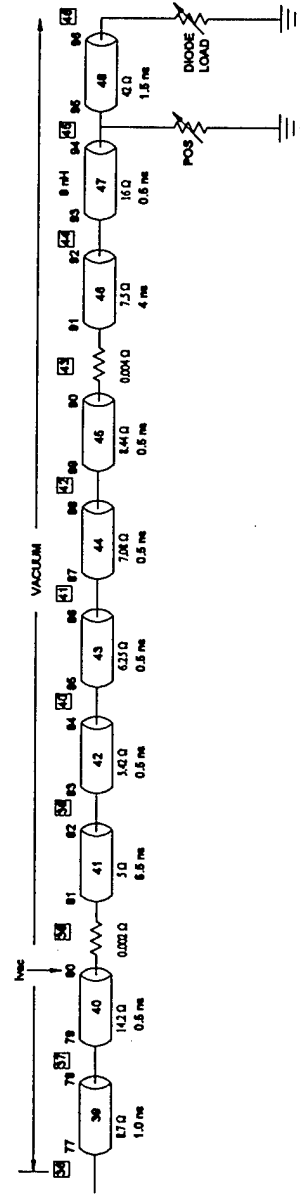
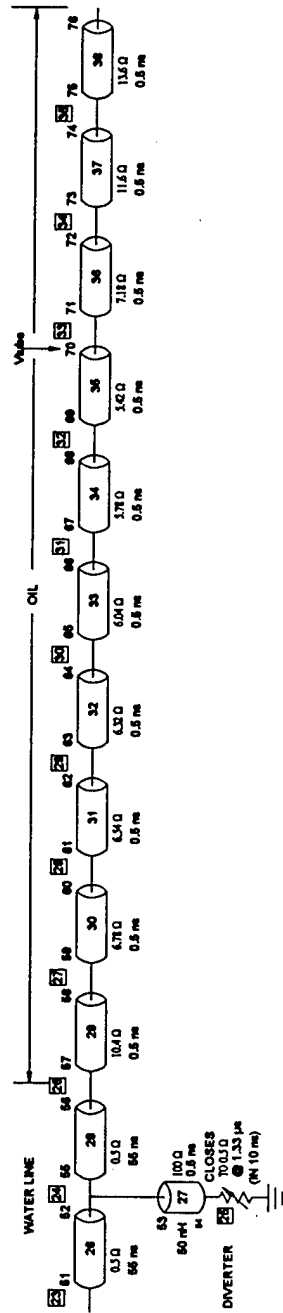
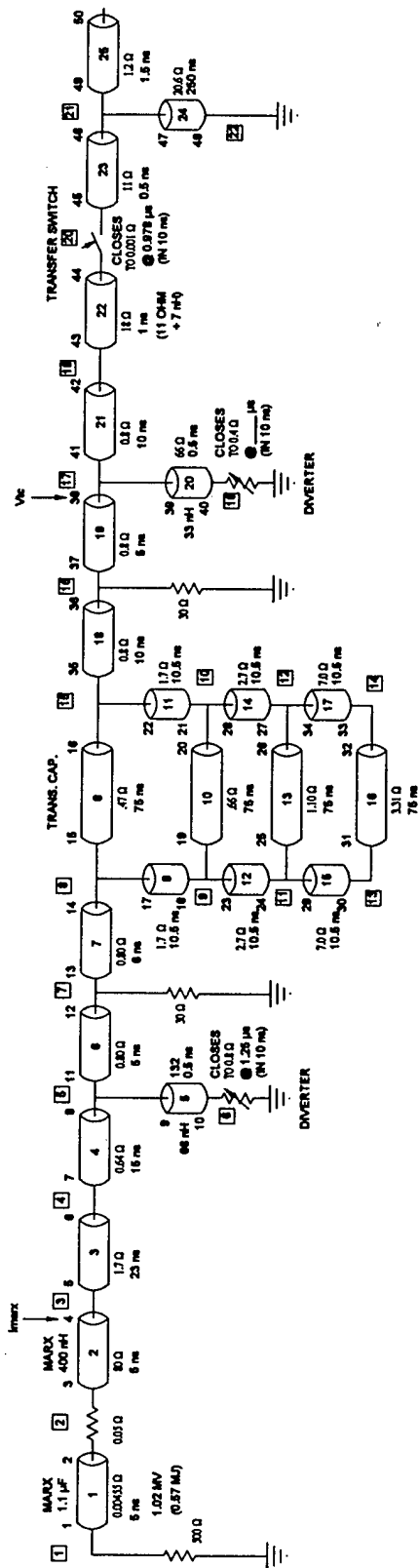
b. Current upstream of the POS.

Figure 2. Comparison of NRL and PI simulations using the circuit of Fig. 1.

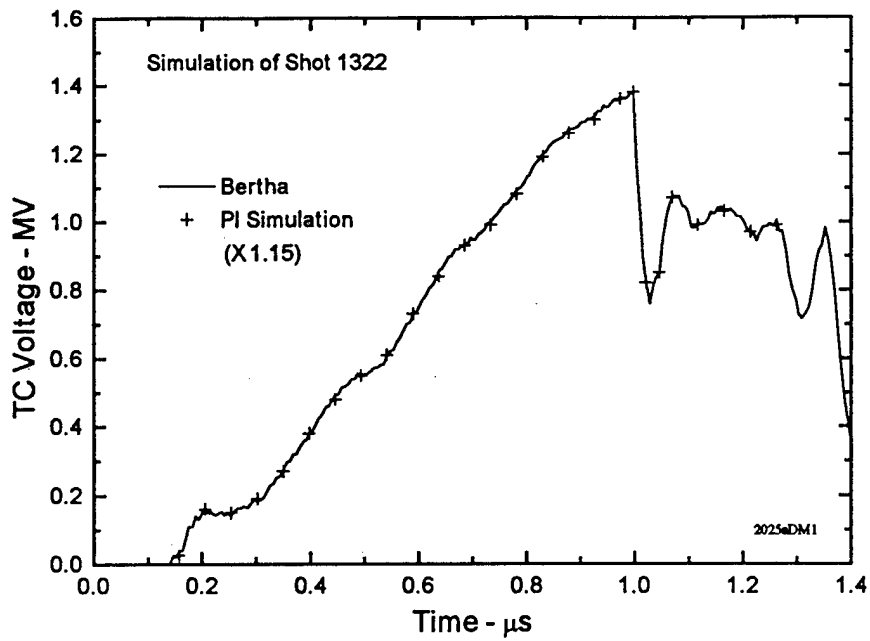


# COMPLETE DM-1 T-LINE CIRCUIT

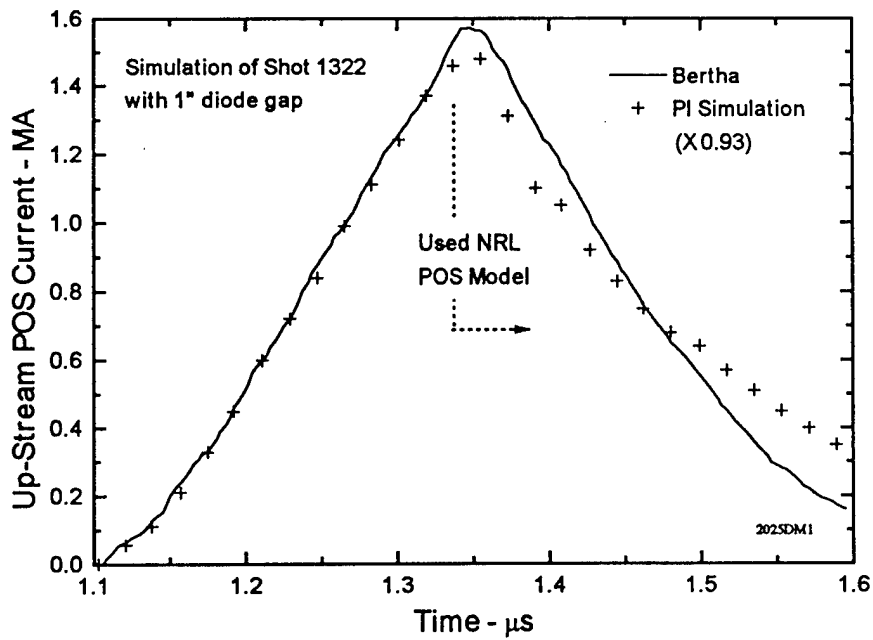
CONFIGURATION: DM1A  
TS = 0.5 NS



**Figure 3. Updated circuit of DML used for test series.**



a. Transfer capacitor voltage.



b. Current upstream of the POS.

Figure 4. Comparison of NRL and PI simulations using the circuit of Fig. 3.

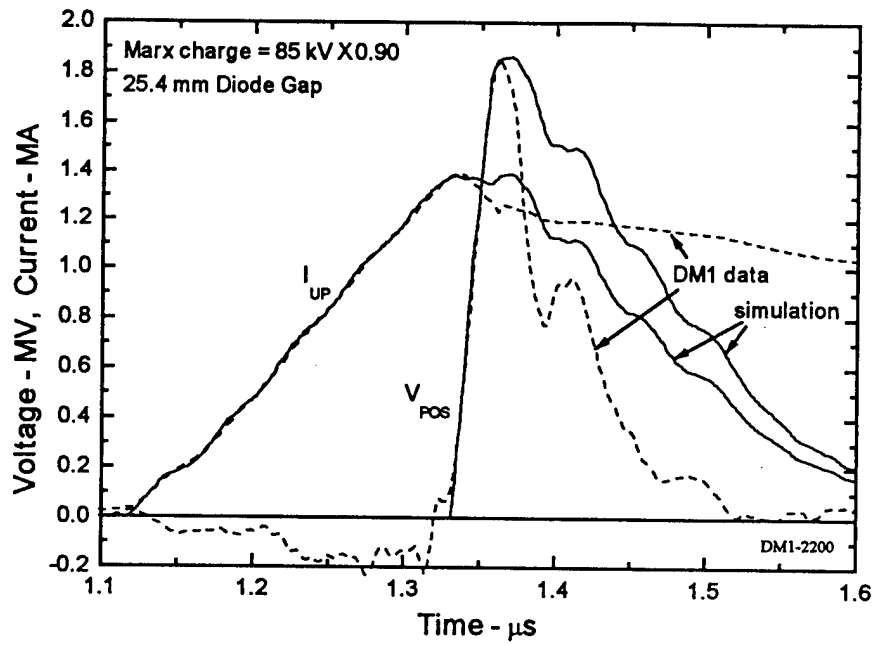


Figure 5. Comparison of simulated waveforms for constant  $Z_f$  after POS opening with measured waveforms from DM1 Shot 1353.

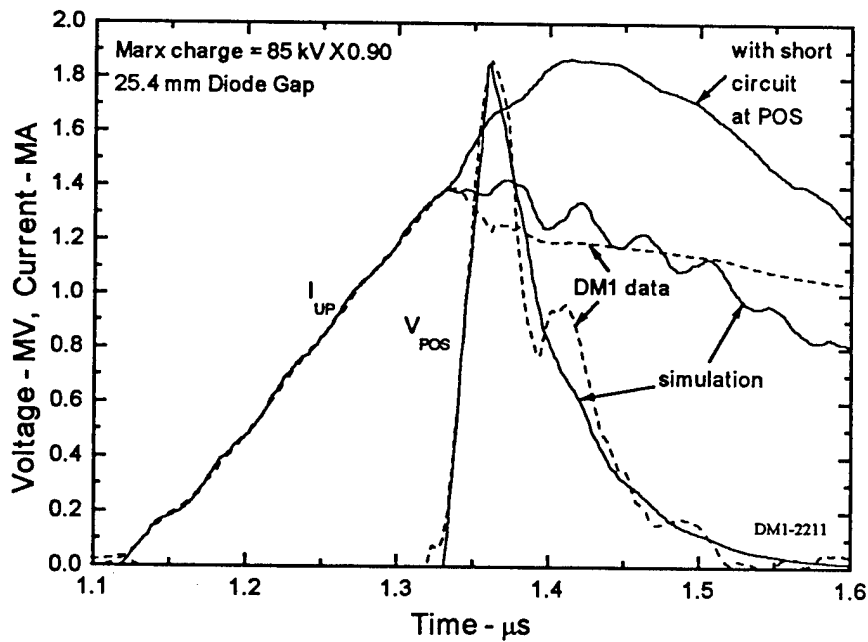


Figure 6. Comparison of simulated waveforms for a decaying  $Z_f$  after POS opening with measured waveforms from DM1 Shot 1353.

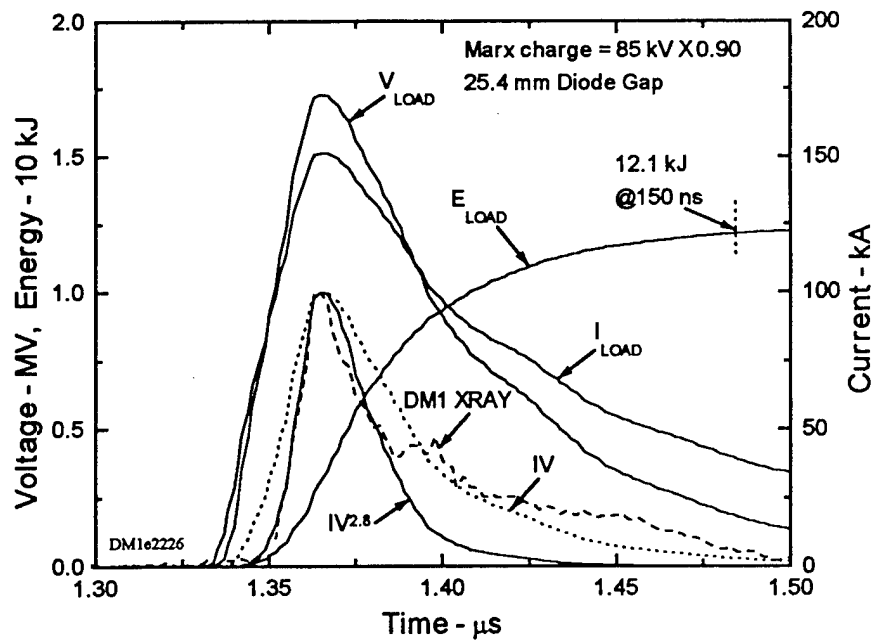


Figure 7. Calculated load waveforms for an initial A-K gap of 25.4 mm and the measured x-ray signal.

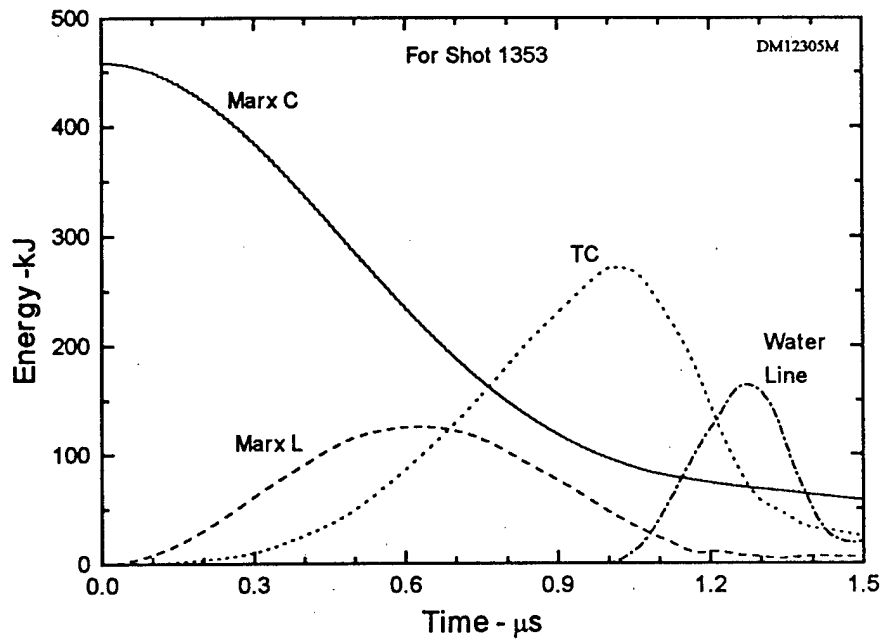


Figure 8. Calculated energy distribution upstream of the transfer capacitor.

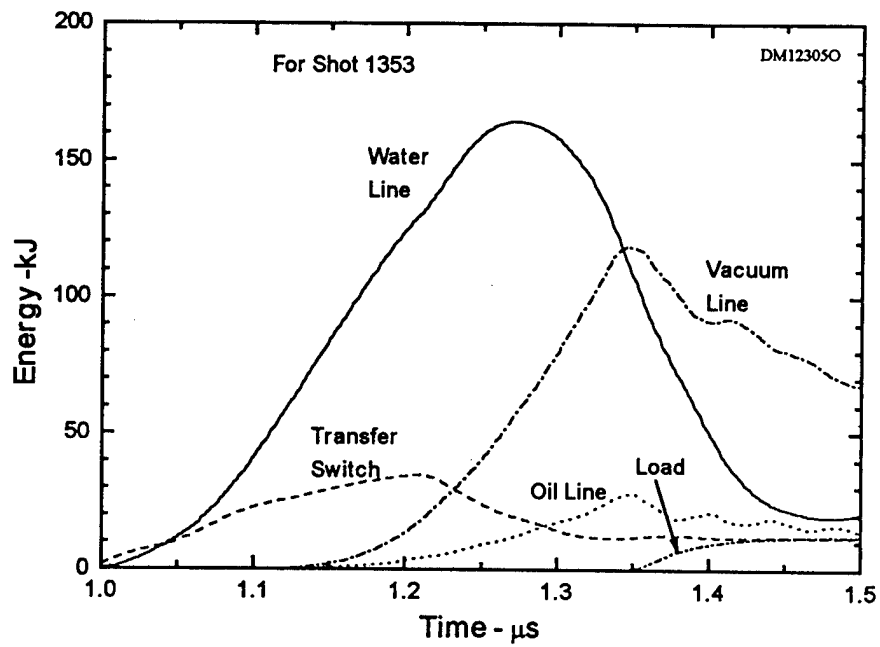


Figure 9. Calculated energy distribution from the transfer switch and forward.

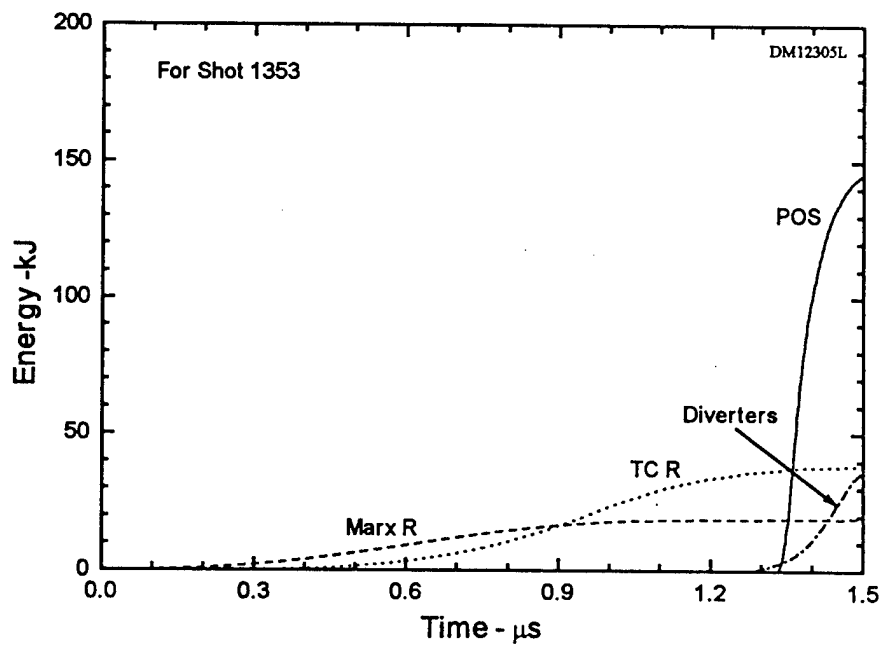
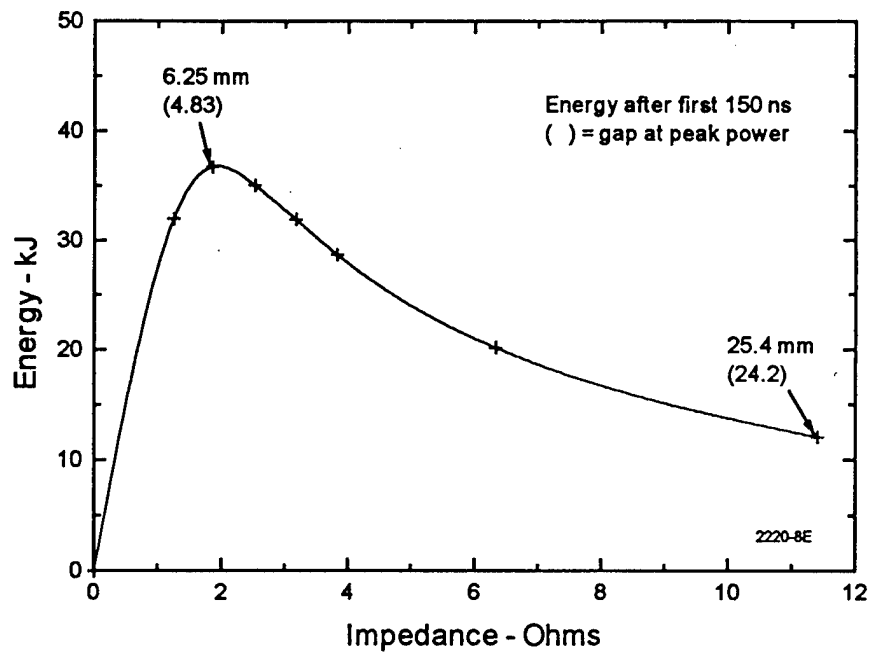
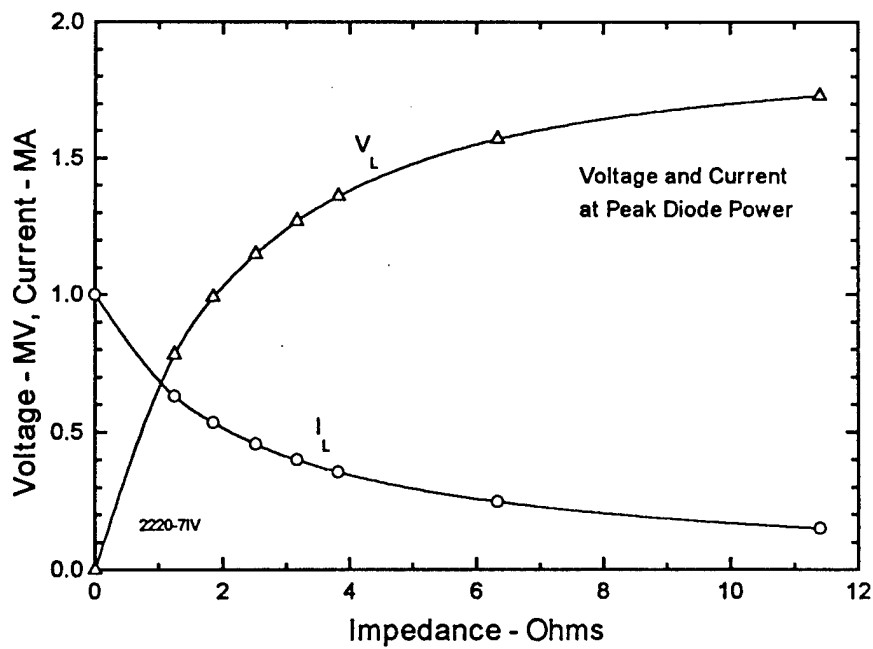


Figure 10. Calculated resistive energy losses.



a. Energy.



b. Load voltage and current.

Figure 11. Calculated load parameters at peak power vs. load impedance.

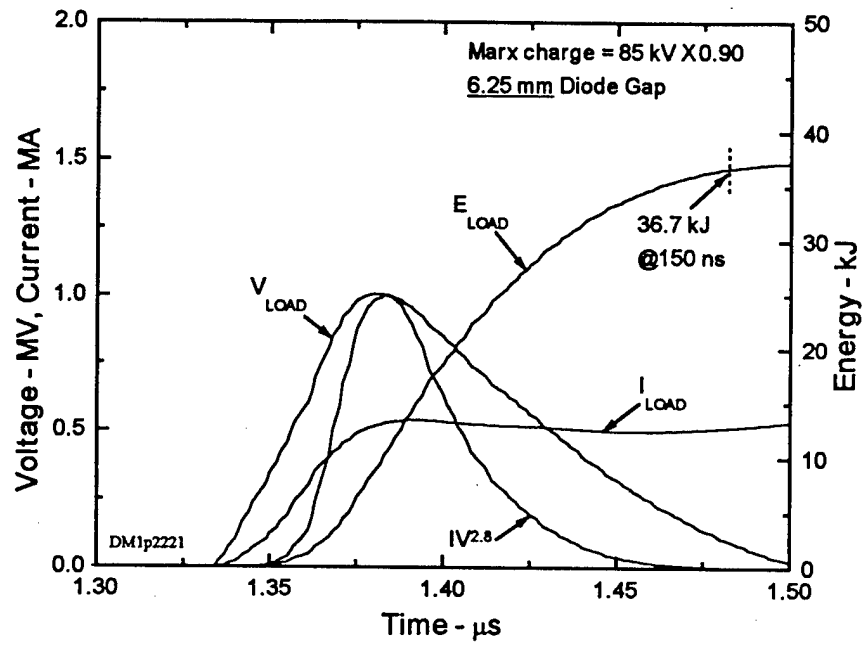


Figure 12. Calculated load waveforms for an initial A-K gap of 6.25 mm.

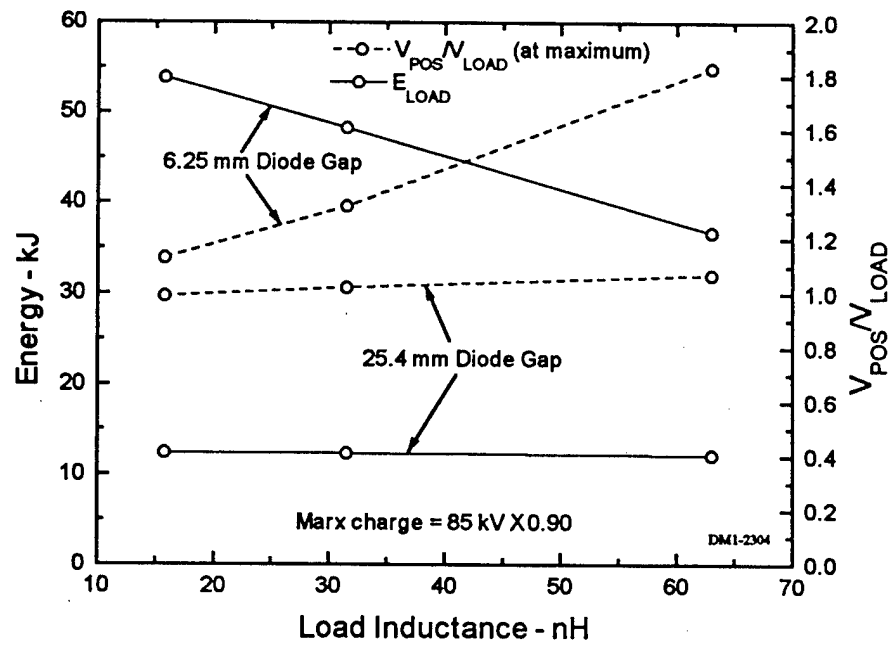


Figure 13. Calculated load parameters at peak power vs. POS to load inductance.

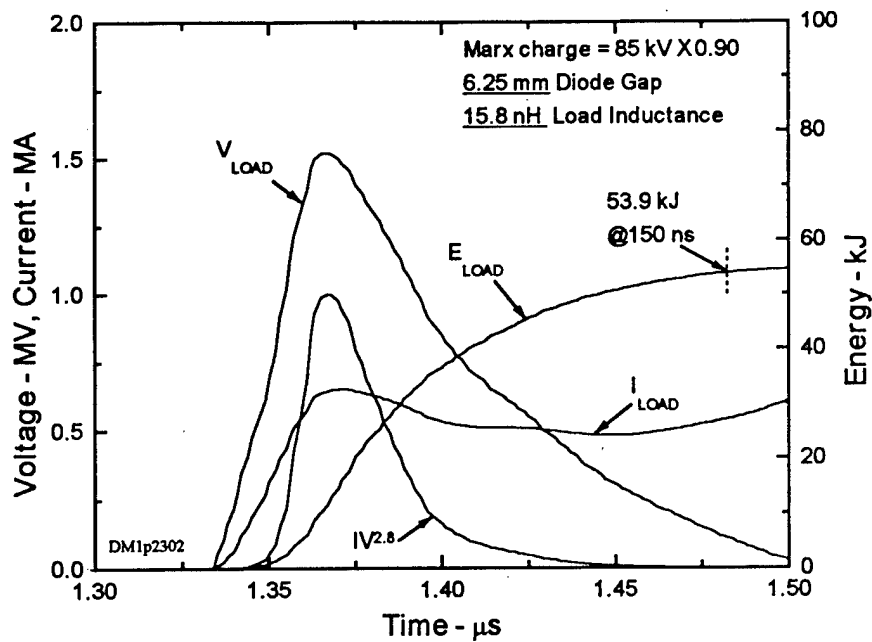


Figure 14. Calculated load waveforms for an initial A-K gap of 6.25 mm and reduced load inductance.

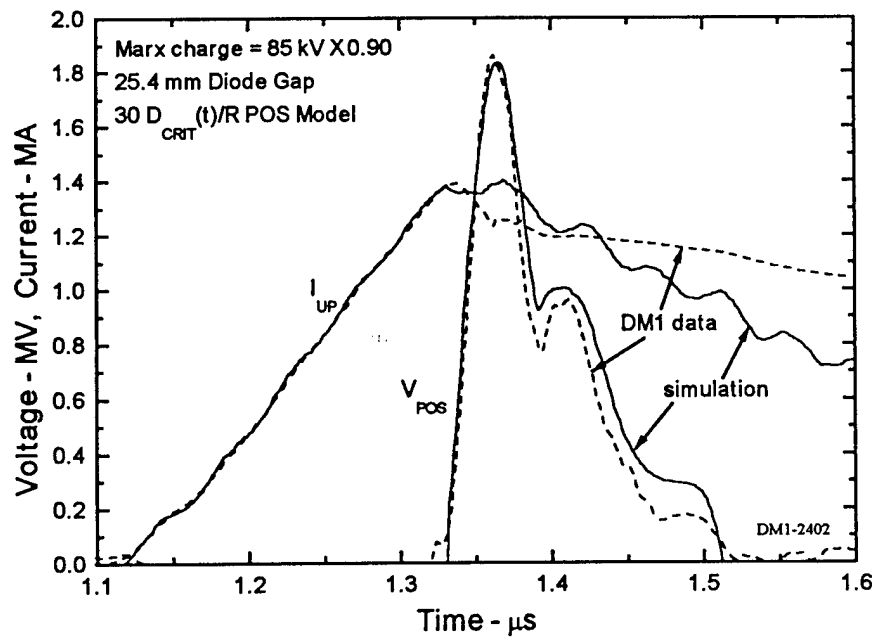


Figure 15. Simulation of DM1 using an empirical POS flow impedance model.



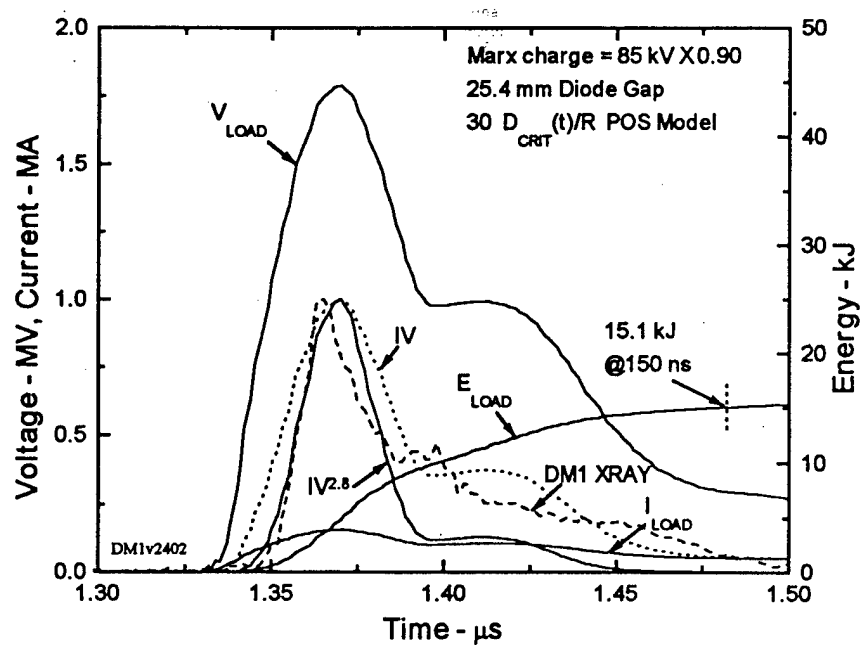


Figure 16. Calculated load waveforms using an empirical POS flow impedance model.

TITLE:       **JOINT NRL/CEG PLASMA FILLED DIODE EXPERIMENT**

AUTHORS:   **B. Weber**

DATE:       19 December 1995

ABSTRACT:       This Technote contains the viewgraphs presented at the US/French Data Exchange Agreement (DEA) meeting on 12 December 1995 at Physics International Co. The presentation summarizes the joint experiment performed on Gamble II at NRL, with French participation, during the two weeks preceding the DEA meeting. The goal of the experiment was to determine the x-ray conversion efficiency for high-density plasma filled diodes (PFDs). Here, "high density" means a PFD that operates at an effective gap many times smaller than the physical AK gap in the diode. Such high density PFDs are potentially attractive sources of low endpoint ( $< 300$  keV) bremsstrahlung because they can be operated, in principle, at higher current density than vacuum diodes thereby providing a higher fluence source than possible by conventional means.

Several PFD variations were examined on Gamble II, and compared with results from low voltage vacuum diode shots. The best PFD radiators were those using a hollow (annular) plasma fill. The worst PFD radiators were those using a solid (circular) plasma fill. The vacuum diode shots result in about three times more radiation than the best PFD shots, where the radiation is normalized by the electrical input to the diode. The causes of this inefficiency may include inductive voltage loss (implosion), ion currents, and collisional losses in the plasma (ionization, heating, etc.).

The last three pages are the proposal for future work we generated at the meeting. In the near term ( $\sim$  six months), the data analysis for the Gamble II experiment should be finished, and a report written for the DEA. (This will be the first of its kind.) Next ( $\sim$  one year time frame), we need to invent and demonstrate a more efficient PFD for low endpoint bremsstrahlung. In the far term ( $> 1$  year), the "sufficiently efficient" PFD should be scaled to high current. The appropriate machine for this scaling demonstration is probably ACE4 with a POS. A 15-cm diameter ring PFD with an effective AK gap of 0.5 mm, for example, may be able to operate at 3 MA, 300 kV, 100 ns, providing the information needed to evaluate this source for testing applications.

THIS REPORT REPRESENTS UNPUBLISHED  
INTERNAL WORKING DOCUMENTS AND SHOULD  
NOT BE REFERENCED OR DISTRIBUTED WITHOUT  
THE AUTHORS' CONSENT

# **Joint NRL/CEG Plasma Filled Diode experiment**

## **NRL participants:**

B. Weber, S. Stephanakis, R. Boller,  
P. Goodrich, F. Young, G. Cooperstein

## **CEG participants:**

M. Vie, A. Porte, J.-P. Bedoch

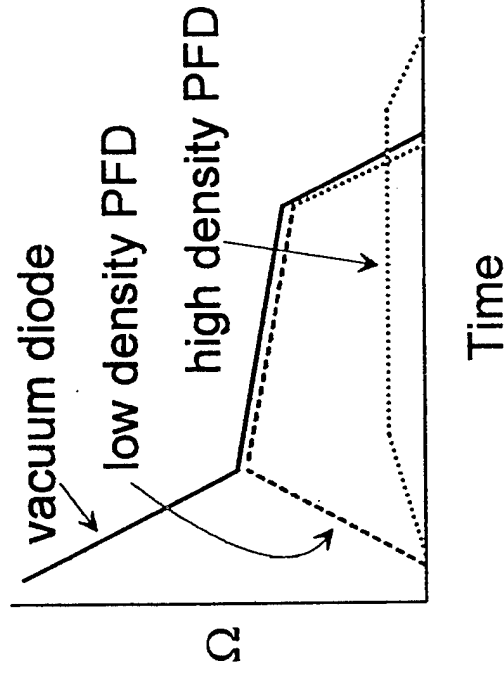
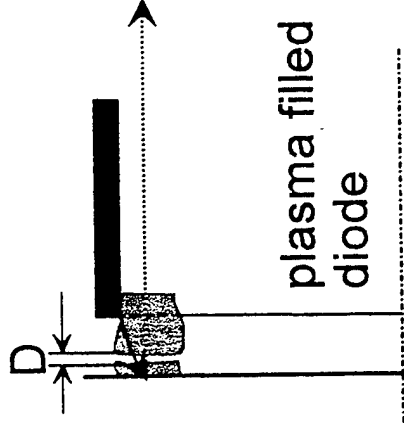
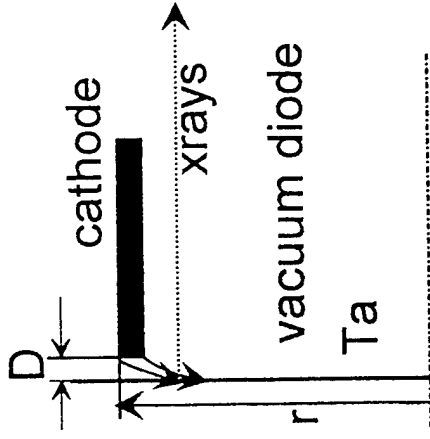
DEA meeting 12 December 1995  
Physics International Co., San Leandro, CA, USA

# **Experimental Objectives**

- Evaluate PFD as a potential source of  $< 300$  keV x-rays for simulation
- Compare efficiency of PFD and vacuum diode
- Make quantitative spectrum measurements
- Evaluate different PFD configurations

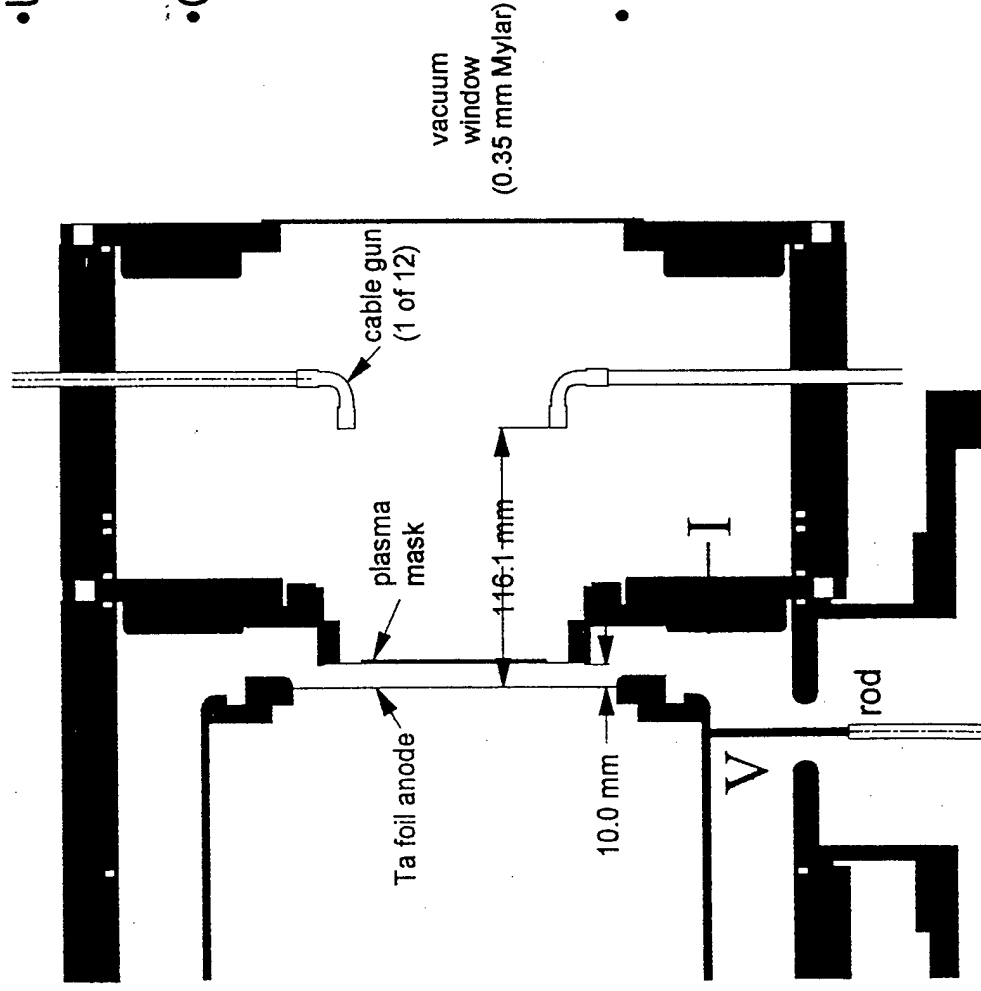
# PFDs have potential advantages over vacuum diodes for 300 kV, high current density applications

- impedance  $\sim D/r$ 
  - small gap ( $D < 2\text{mm}$ ) shorts out by electrode plasmas
  - limits low  $Z$  ( $< 1 \Omega$ ) vacuum diodes to large  $r$
- small gap may form in high density PFD, away from electrode
  - may be useful for  $< 300 \text{ keV}$  radiation source



# Gamble II PFD schematic

- Undermatch Gamble II ( $2\Omega$ )
  - $\sim 1$  MA, 300 kV
- CEG spectrometer
  - time-resolved
  - 8 energy bins
  - total fluence
  - hardness
- Gamble II diagnostics
  - I, V near load
  - scintillator-photodiode
  - time-integrated dose (TLD)
  - pinhole camera

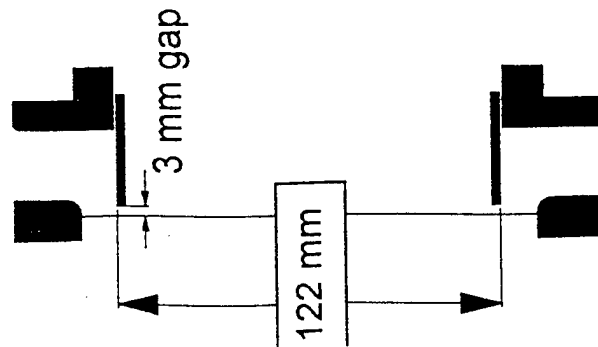


# SPECTROMETER ENERGY BIN DEFINITION

BIN	PASS FILTER	STOP FILTER	BIN WIDTH (KeV)
1	Zn	Ti	5.0 - 9.7
2	Yt	Zn	9.7 - 17
3	Sn	Yt	17 - 29.2
4	Sm	Sn	29.2 - 46.8
5	Ta	Sm	46.8 - 67.4
6	Pb	Ta	67.4 - 88
7	U	Pb	88 - 115.6
8	Sm & Sn		> 70

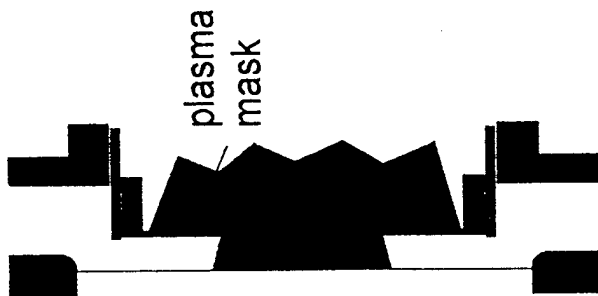
# PFD configurations

vacuum diode



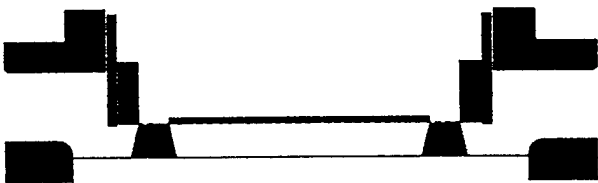
6782-85

solid PFD



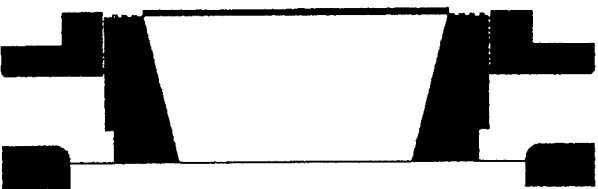
6777-79, 6781

hollow PFD



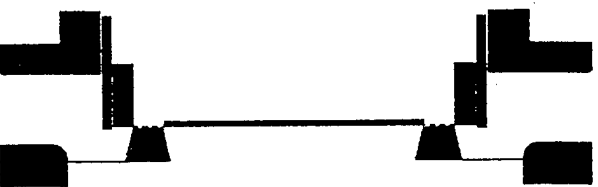
6786-88,  
6791, 6796-7

hollow PFD  
with recessed  
cathode plane



6790

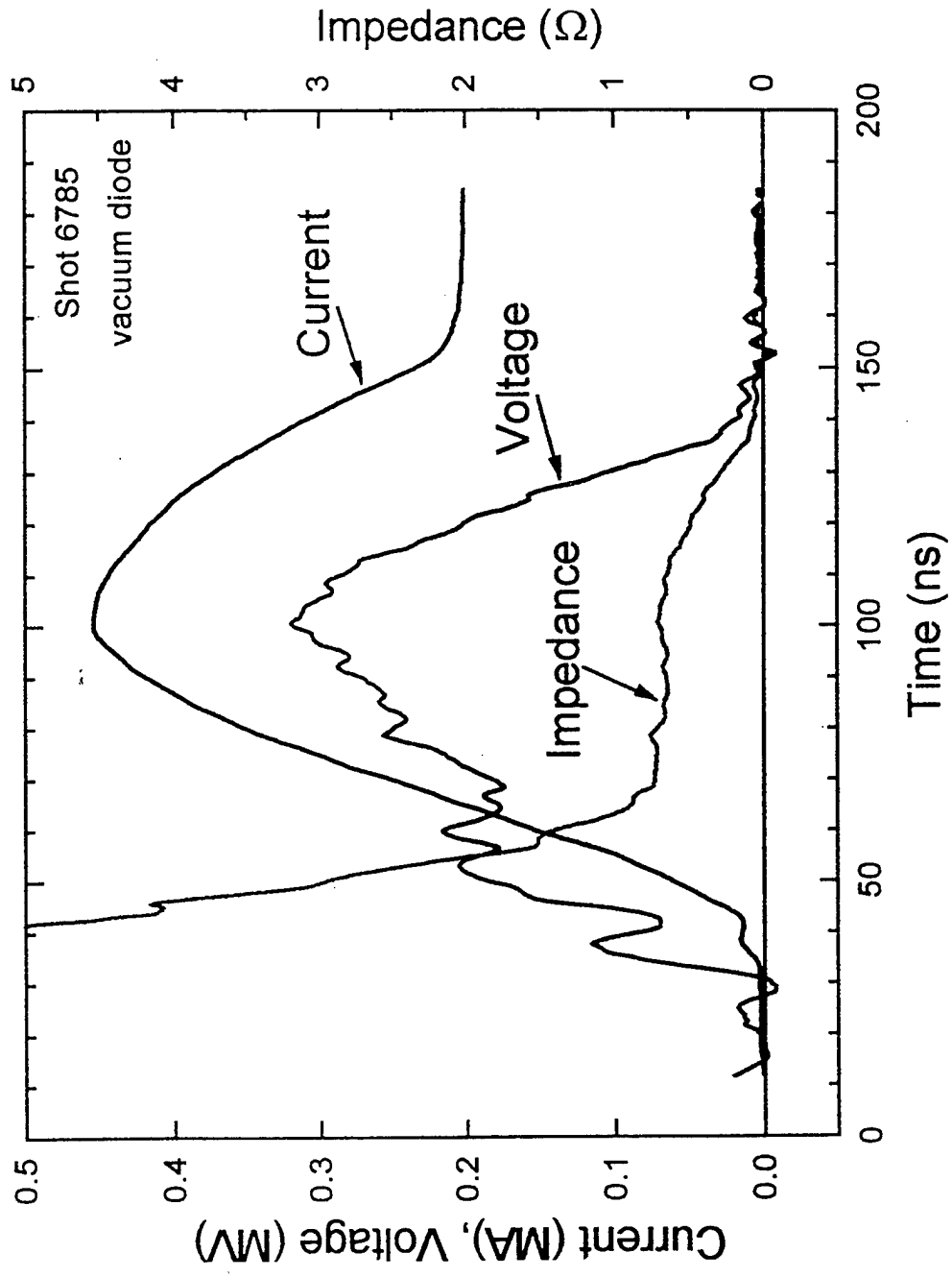
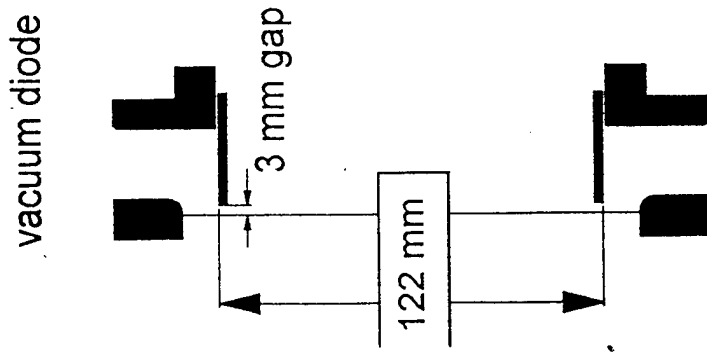
hollow PFD  
with hole  
in anode



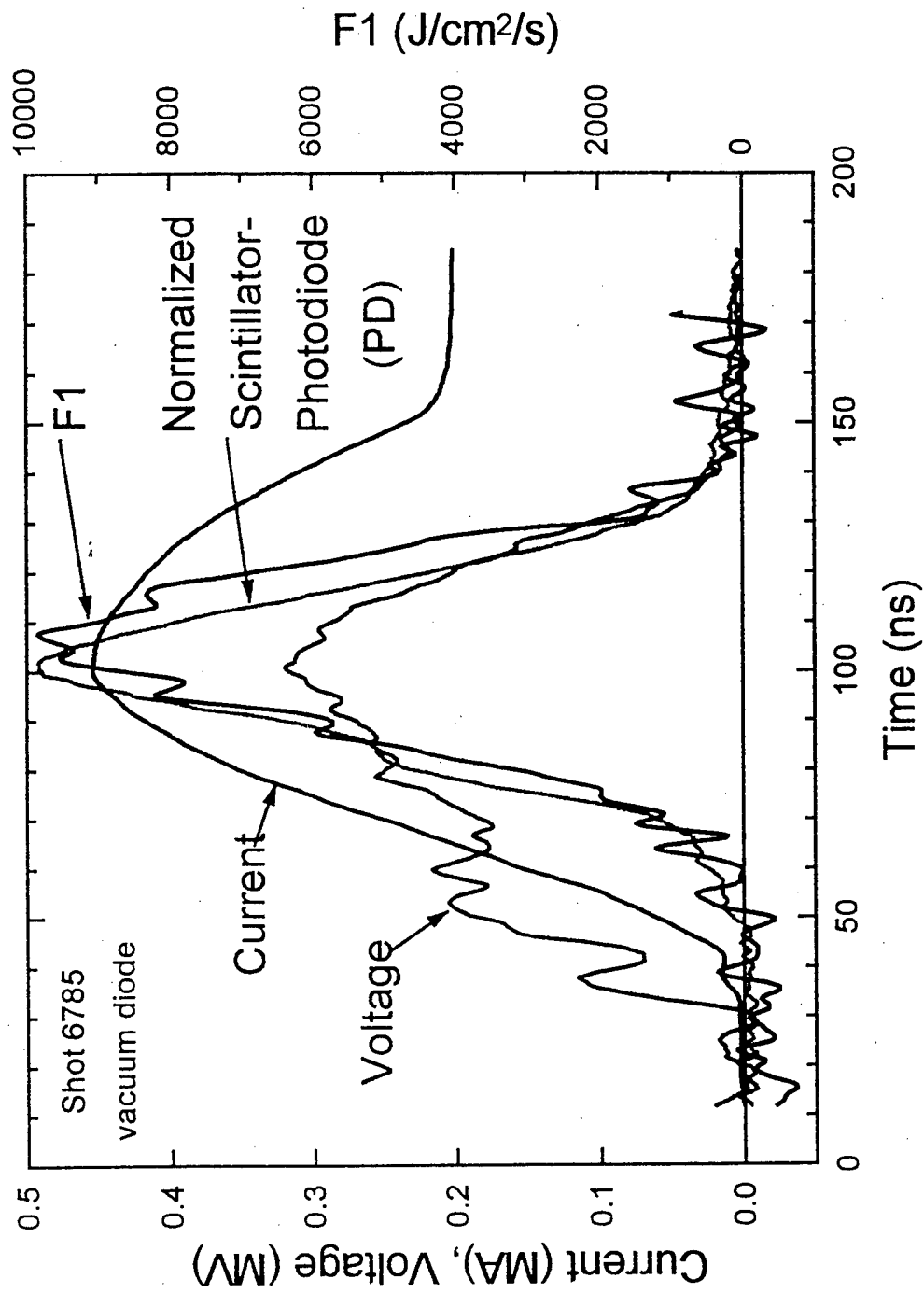
6792-95



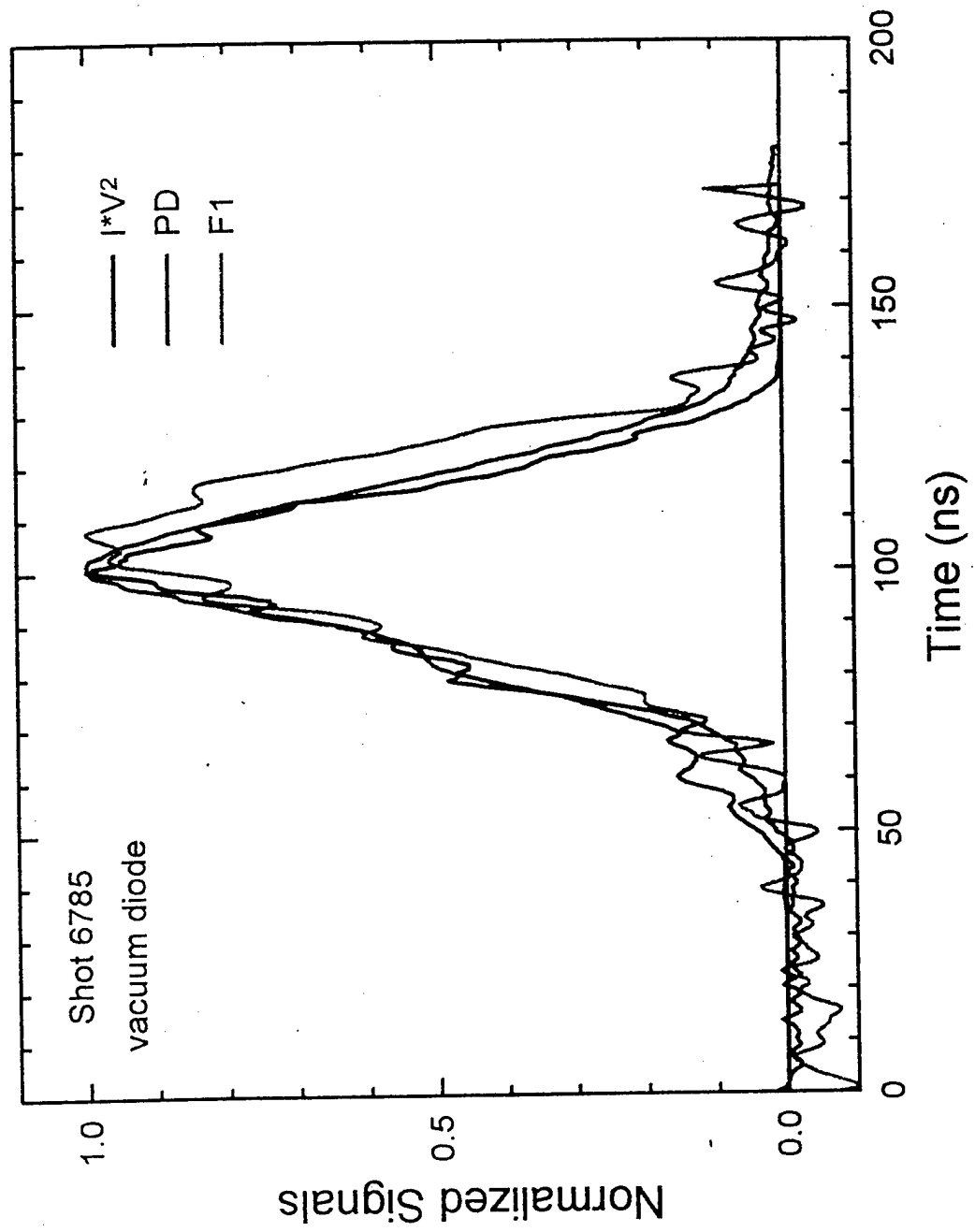
# Low impedance vacuum diode electrical parameters



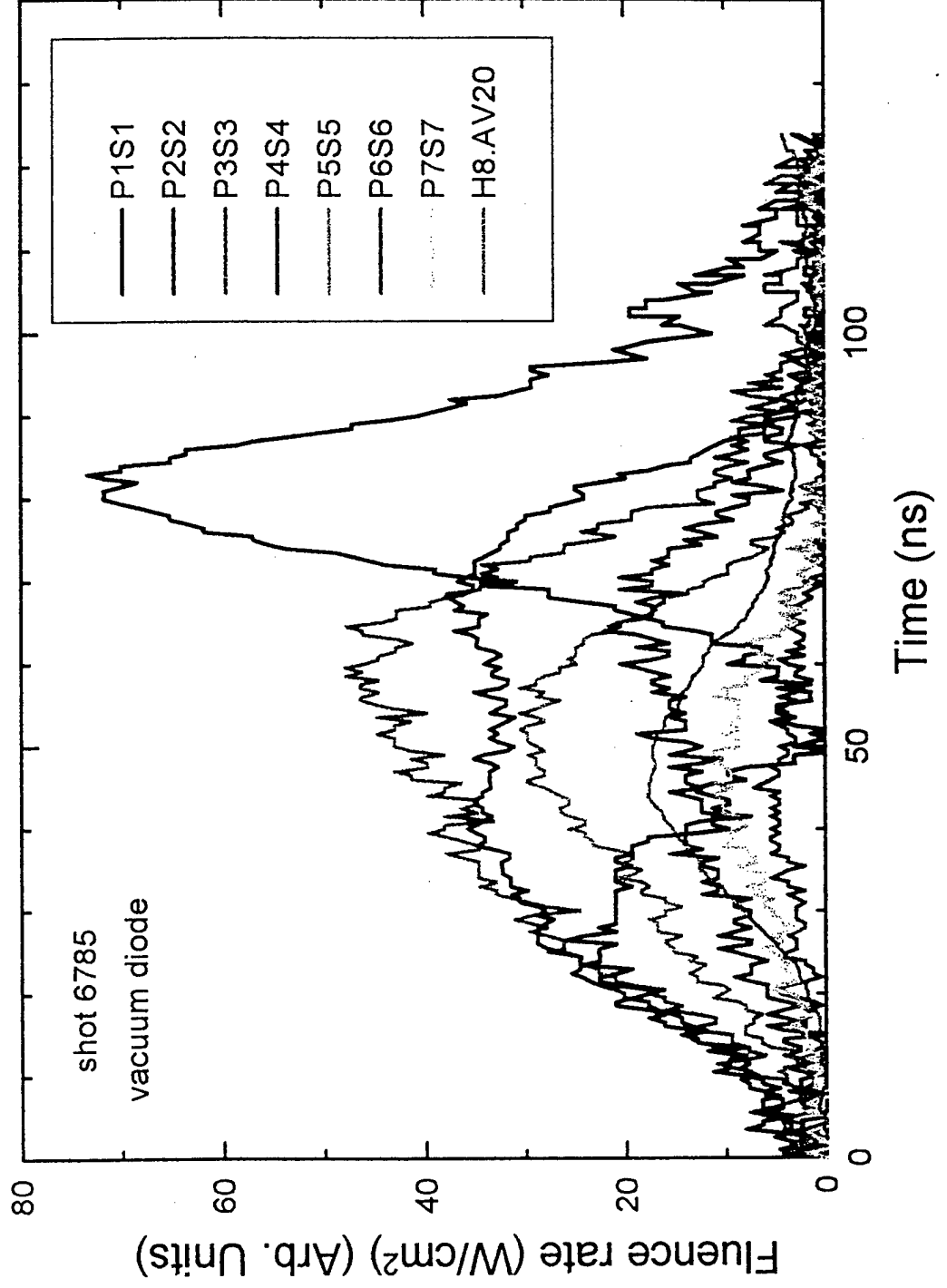
# Maximum radiation occurs at the time of maximum voltage



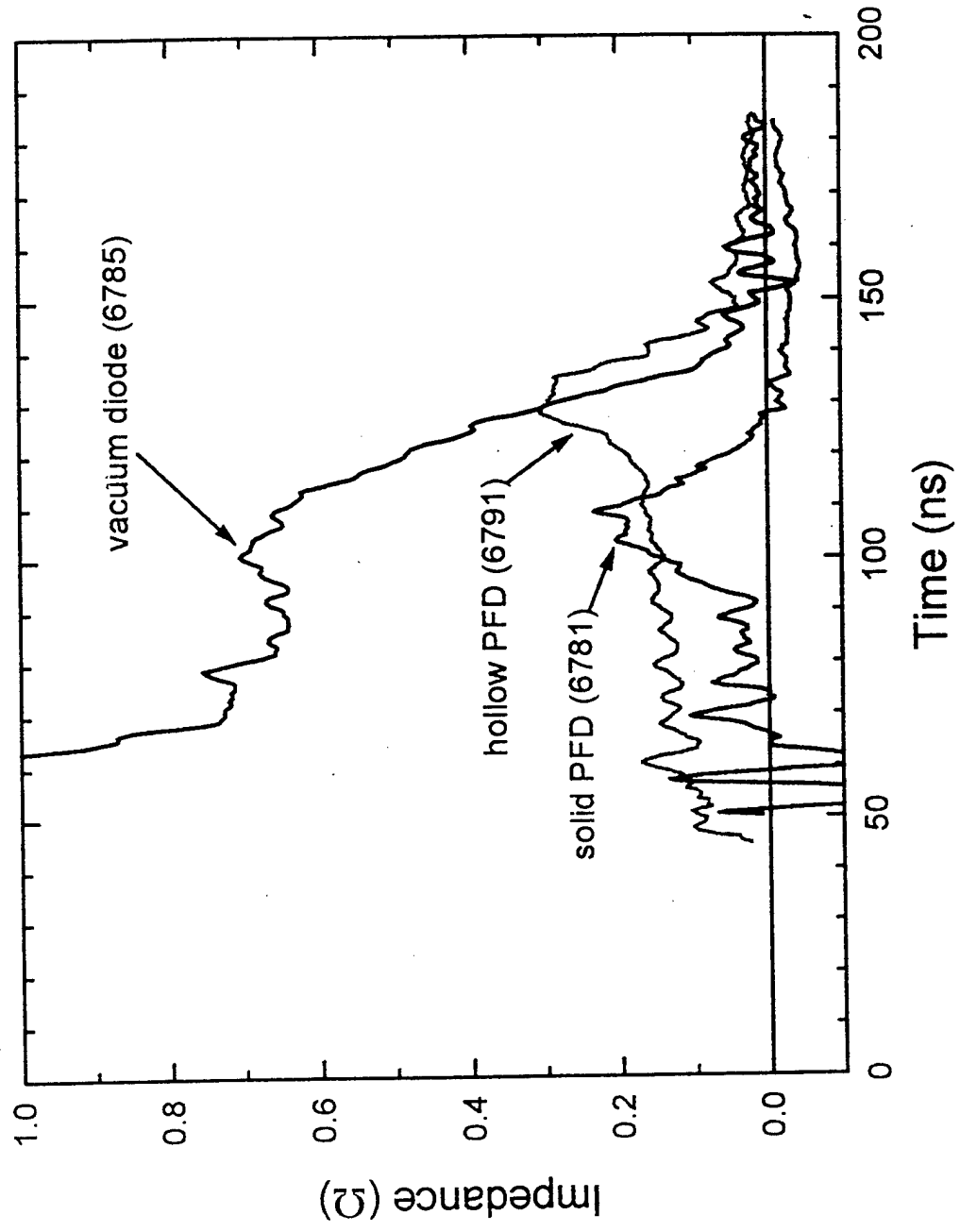
# The radiation signals scale like $I \cdot V^2$



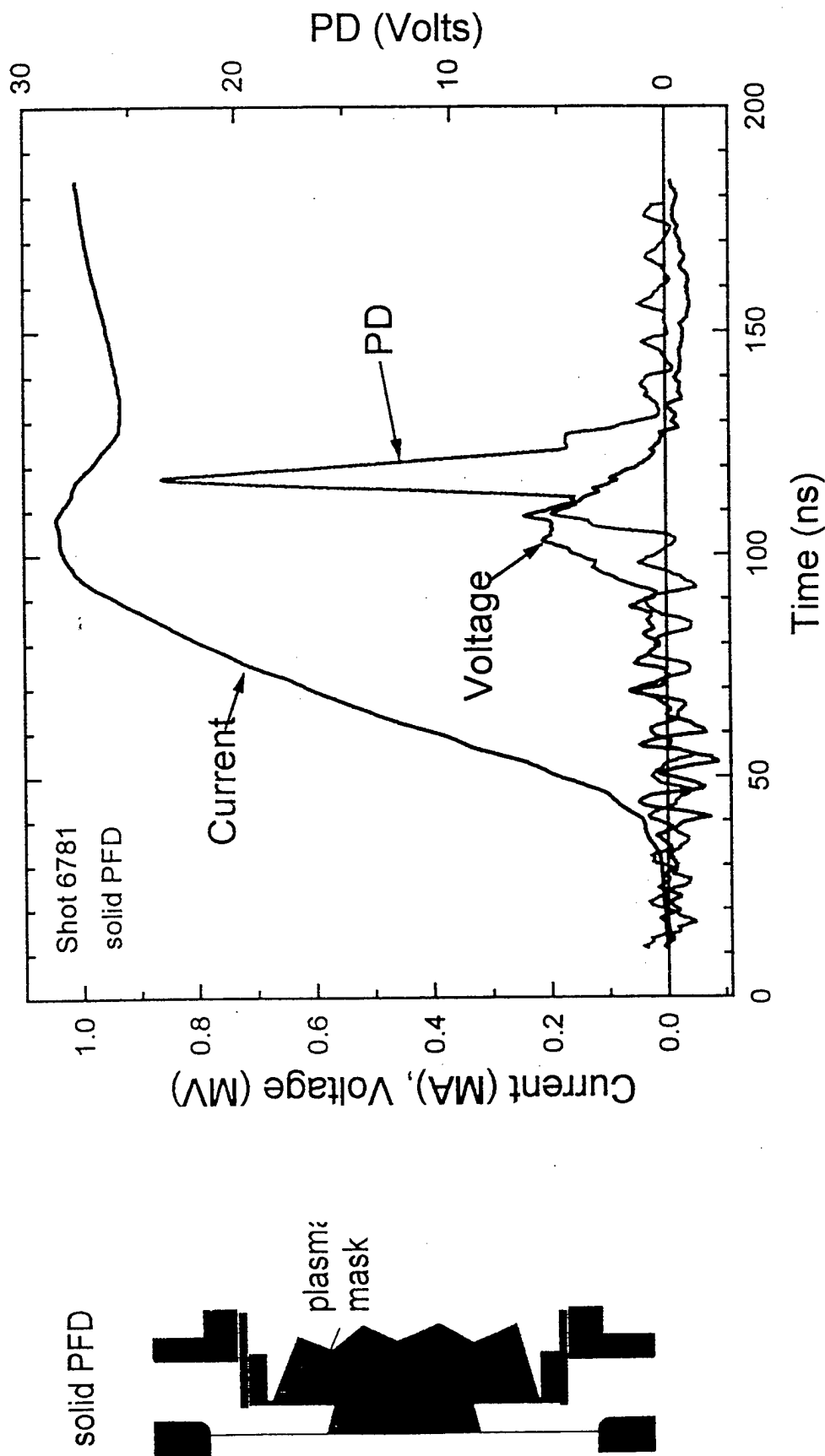
# CEG spectrometer shows temporal evolution of spectrum



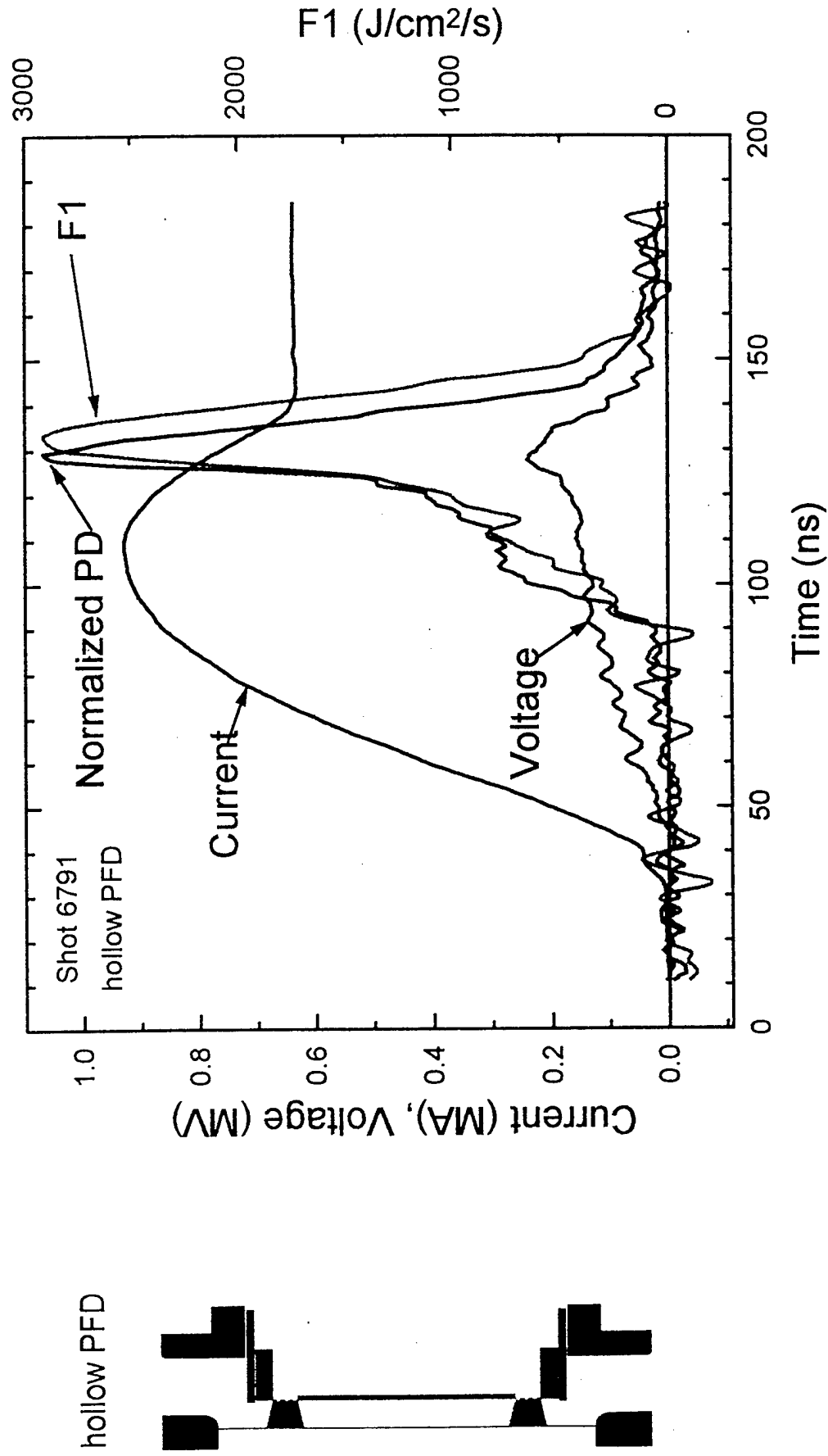
# Very low impedance is possible with high density PFDs



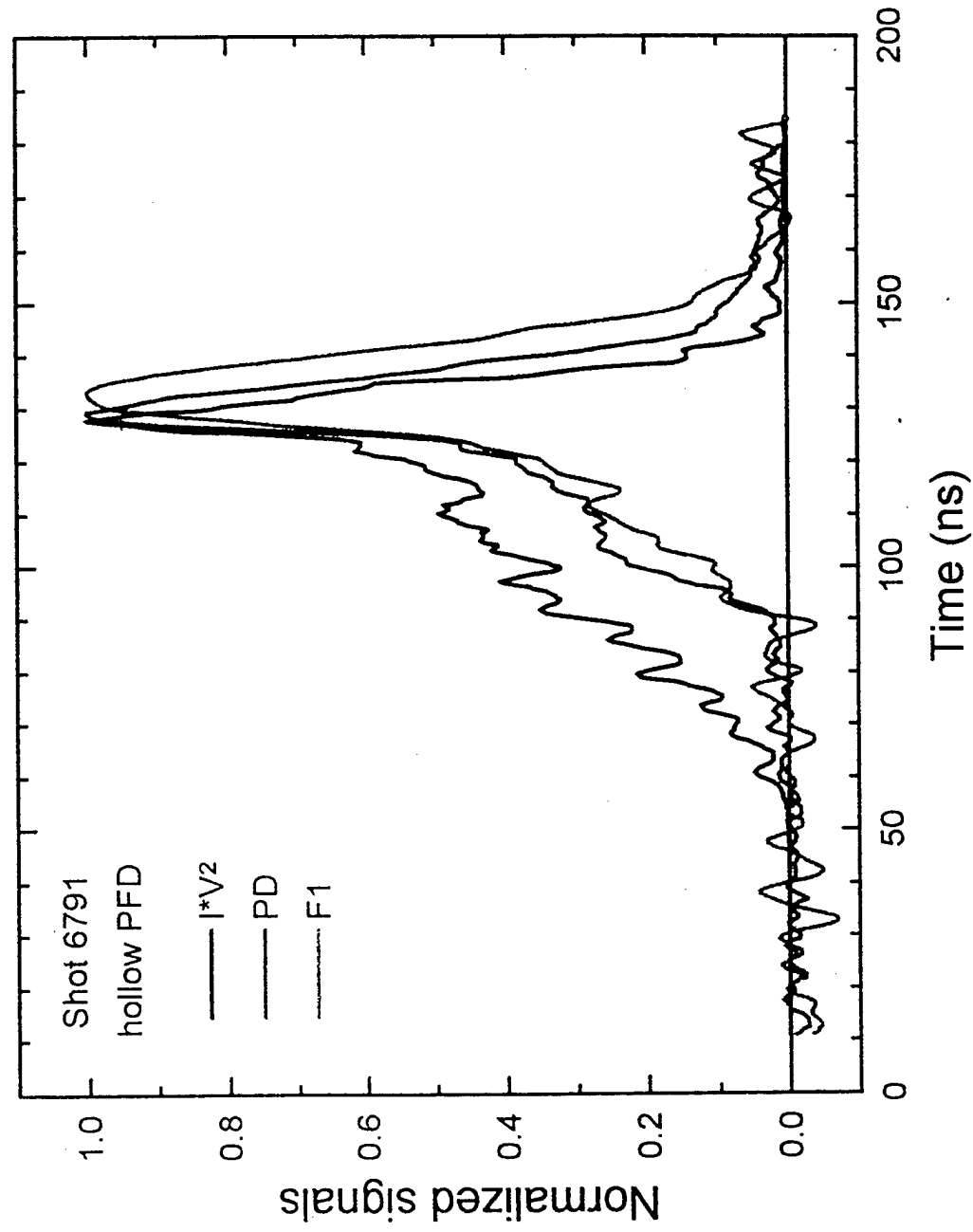
**For solid PFDs, radiation is later than  
voltage (PD not related to  $I \cdot V^2$ )**



# For hollow PFDs, the maximum radiation occurs near the time of maximum voltage

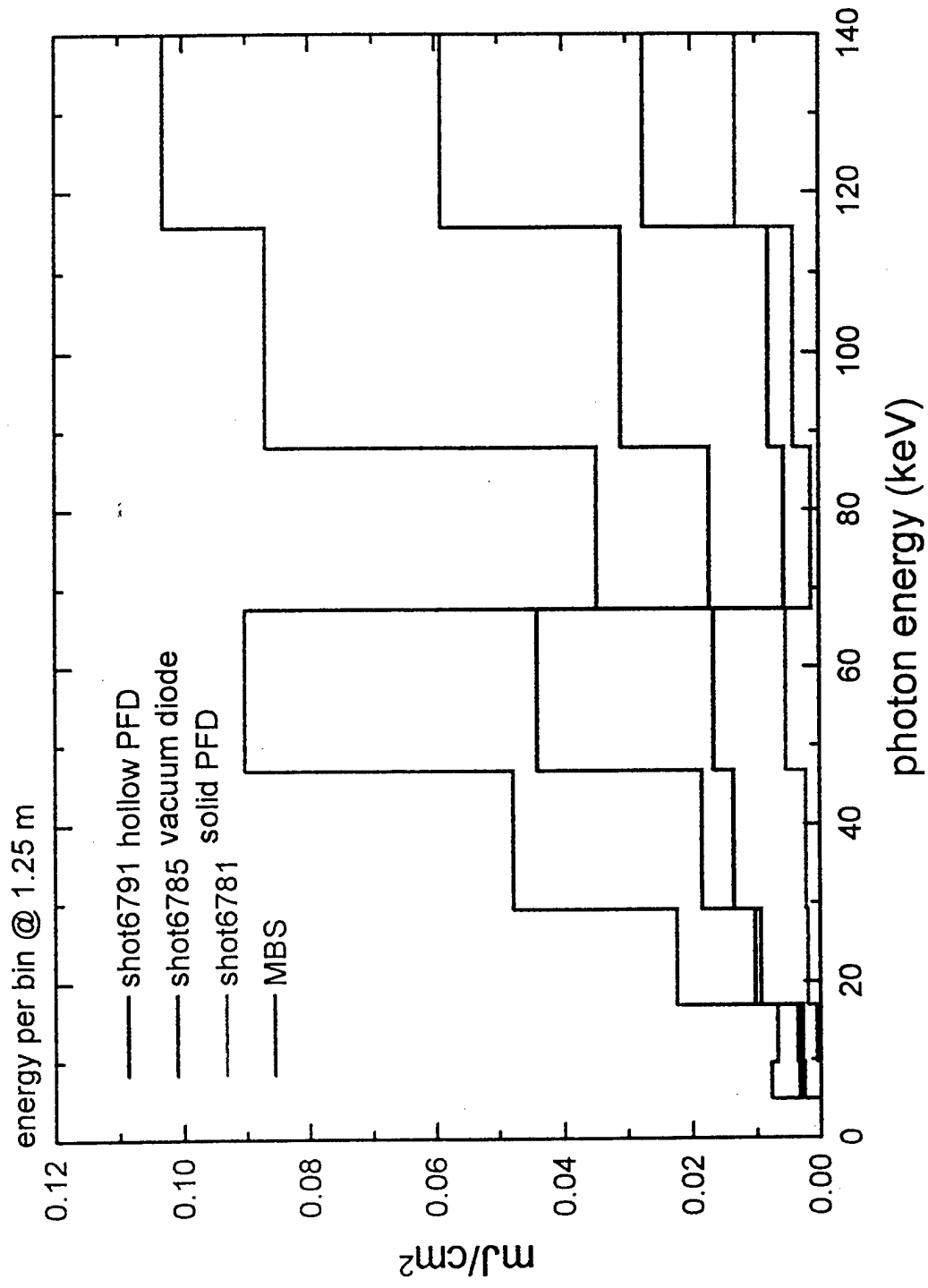


# The radiation signal shapes are different from $I*V_2$

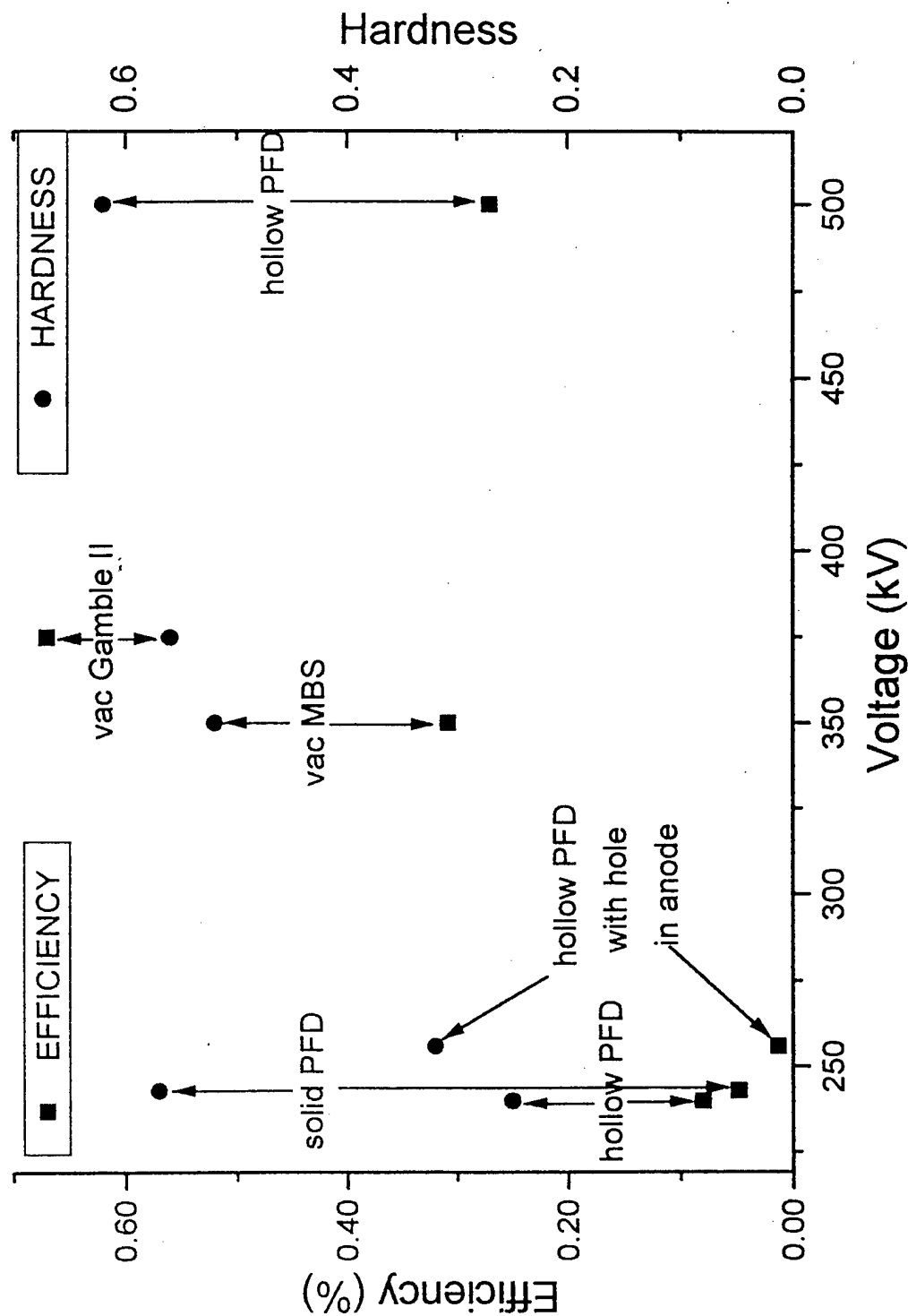




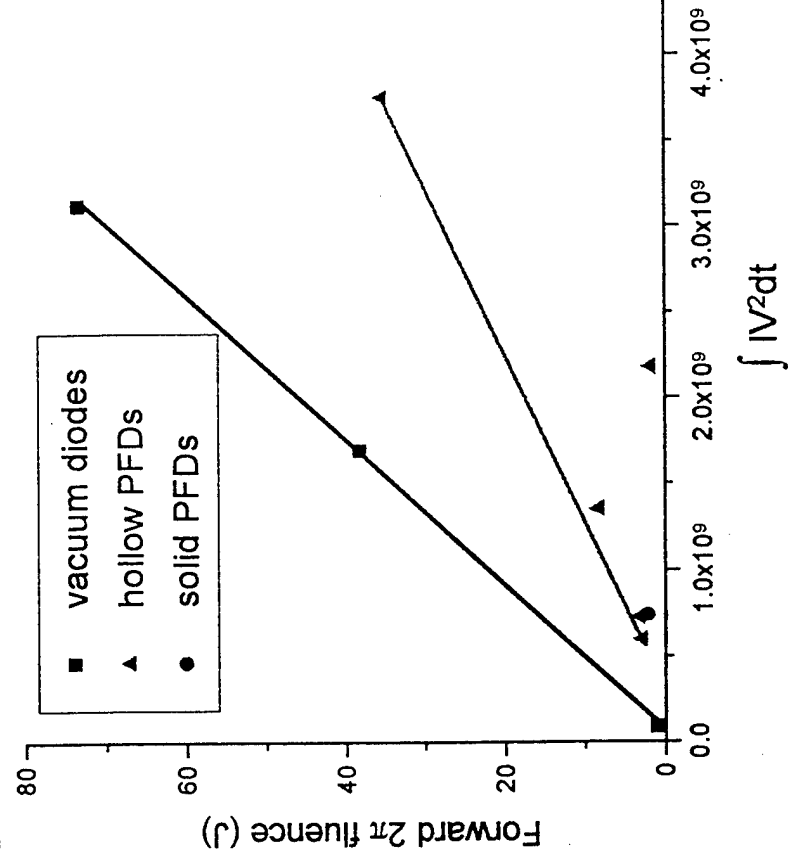
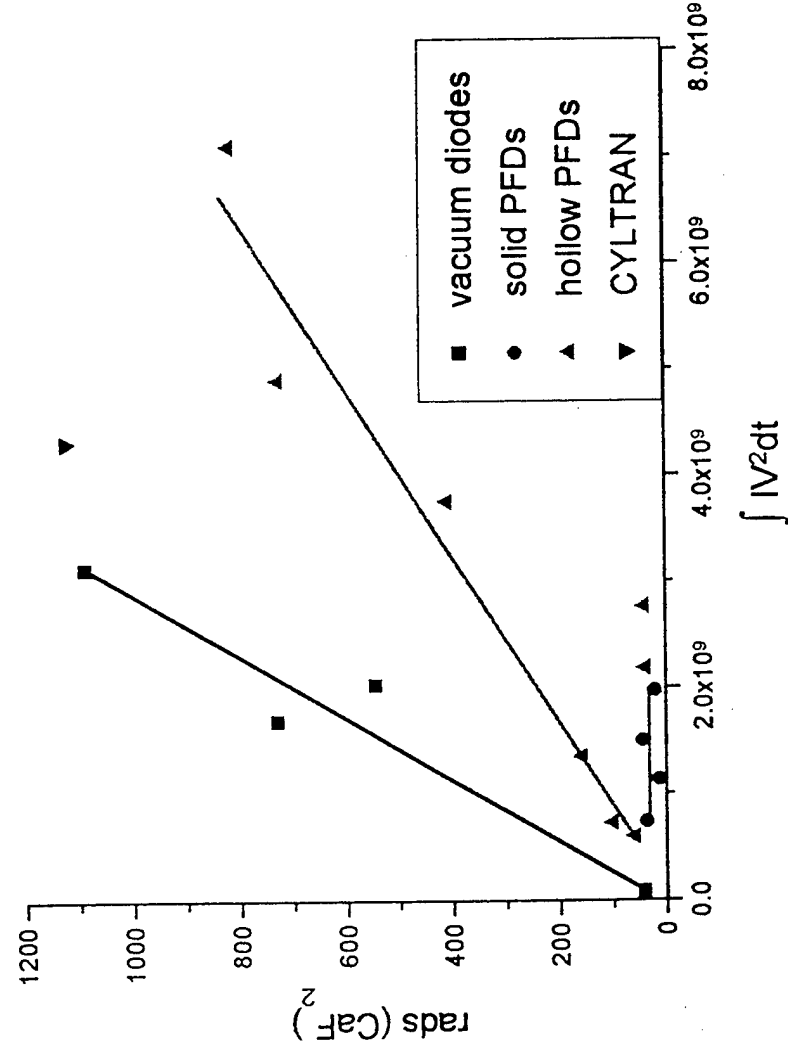
# The spectral shapes are similar for Gamble II and MBS



# PFD efficiency is lower than expected compared with vacuum diodes



# Hollow PFDs produce about 3x less radiation than vacuum diodes (...why?)



# Preliminary conclusions

- The collaborative 2-week experiment was a success
  - hardware, diagnostics, software and people worked well
  - radiation from low impedance PFDs diagnosed and compared with vacuum diodes
- PFDs have possible advantages and disadvantages
  - advantage: PFD can be much lower impedance than possible for vacuum diodes with same area
    - $\ll 1$  mm effective gap sizes with high density PFD, would short out for vacuum diode
    - can it be scaled to  $\gg 1$  MA,  $\sim 300$  kV, small area?
  - disadvantage: radiation efficiency seems low ( $\sim 1/3$ )
    - is this fundamental or can it be improved?

## **Future plans (tentative)**

- Investigate causes of low efficiency
  - inductive voltage (implosion)
  - ion current, other current losses
  - collisional losses (heating, ionization, etc.)
- Improve understanding of PFD radiation efficiency
  - physical model of electron flow in PFD
    - plasma/particle simulations?
- Develop improved efficiency PFD for further investigation
  - different operating point?
  - vary geometry, density, plasma properties?
- Perform experiments on low impedance, high current generator
  - modified Gamble II, high-current MBS, other US, French machines

BREMS Subgroup

DEA meeting Dec 13 1995

Ralph SCHNEIDER

Bruce WEBER

Nichol VIE

Phil SPENCE

Bob COMMISSO

Bill RIX

THE RESULTS OF THIS DISCUSSIONS ARE THREE AREAS FOR FUTURE WORKS.

# 1. SHORT TERM (6 month)

RADIATION CALCULATIONS

CYTRAN <sup>(NRL)</sup> / MONTE CARLO (CEG)

PFD DENSITY MEASUREMENTS

(NRL)

ION CURRENT MEASUREMENTS

(NRC)

PIC PFD SIMULATIONS

(NRL)

ANALYSE / COMPARE GAMBU / MBS

(CEG)

→ write a report.

## 2. MEDIUM TERM ( 12 month )

- USE NEW EXPERIMENTAL CONFIGURATION (S)  
USING DUAL FEED

REDUCE ION CURRENT

REDUCE  $dL/dt$  VOLTAGE

- DEMONSTRATE ON SOME GENERATOR  
CABLE, MBS ?....

## 3 FAR TERM

- SCALING TO HIGH CURRENTS

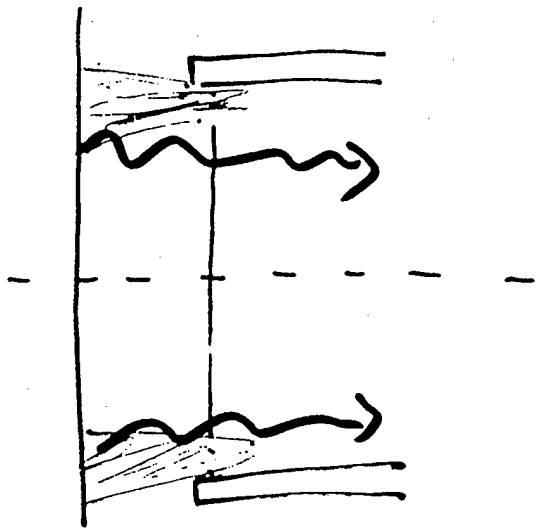
- DEMONSTRATE ON A GENERATOR

ACE 4 WITH POS

SMA/100 ns  $V_{POS} \sim 500$  kV  $L \sim 10$  nH

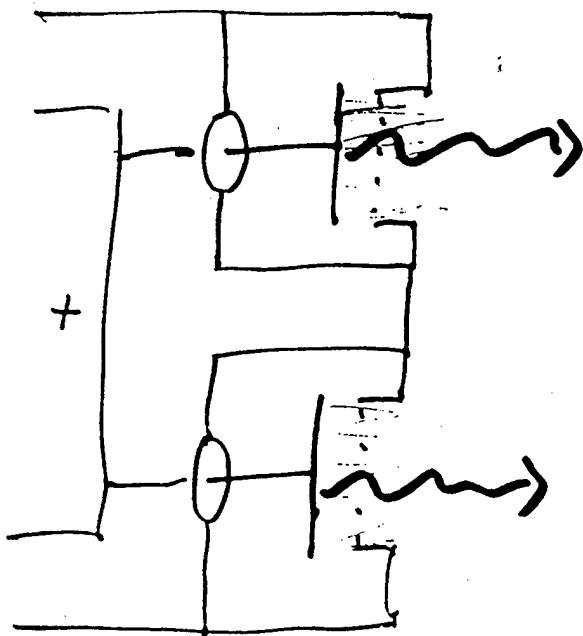
15cm diameter ring diode, .5mm gap

for 300kV, 3MA,  $Z \sim .1 \Omega$



HOLLOW PFD

$\frac{dL}{dt}$  ,  $I_{ion}$  ?



DUAL-FEED PFD

REDUCE  $\frac{dL}{dt}$  ,  $I_{ion}$



PULSED POWER PHYSICS BRANCH TECHNOTE TN95-25.

Title: NUMERICAL SIMULATIONS OF BREMSSTRAHLUNG DIODE  
EXPERIMENTS ON GAMBLE II

Authors: D.V. Rose, R.J. Commisso, F.C. Young, S.J. Stephanakis,  
J.M. Grossmann, J.C. Kellogg, S.B. Swanekamp, and G. Cooperstein.

Date: Oct. 3, 1995, Revised Nov. 4, 1995.

Abstract: A recent bremsstrahlung diode experiment on GAMBLE II is simulated using the integrated TIGER series, Monte Carlo, electron/photon transport code CYLTRAN. A 4-mil tantalum anode in the "backless" diode configuration was used. The radiation dose at 60 cm was measured with an array of  $\text{CaF}_2$  TLDs. Using measured voltage and current waveforms from GAMBLE II as inputs into CYLTRAN, the measured dose is compared with a CYLTRAN model that optionally includes the re-acceleration of electrons back-scattered from the anode. Results indicate good agreement between the measured and computed dose when back-scattering is included in the CYLTRAN calculation. The impact of these conclusions on the results of recently completed simulations of the DM1 experiments is discussed.

**THIS REPORT REPRESENTS UNPUBLISHED INTERNAL  
WORKING DOCUMENTS AND SHOULD NOT BE REFERENCED  
OR DISTRIBUTED WITHOUT CONSENT OF THE AUTHORS**

# NUMERICAL SIMULATIONS OF BREMSSTRAHLUNG DIODE EXPERIMENTS ON GAMBLE II

## I. Introduction

In this note, we present the results of a detailed comparison between the dose measured on axis in the far field on a recent GAMBLE II bremsstrahlung diode shot with calculations performed with the Monte Carlo, electron/photon transport code CYLTRAN [1]. These calculations were carried out, in part, to examine the computational model used in a recently completed study [2]-[4] of the DM1 experiments performed at Physics International. In the DM1 experiments, voltage and current waveforms at the load were not measured, and the analysis presented in Ref. [2] was used to infer magnitudes of the energy delivered to the load from dose measurements in the near field assuming idealized load waveforms. For the GAMBLE II experiment, voltage and current waveforms at the load are measured and used as inputs in the CYLTRAN calculations to compare calculated and measured doses. Good agreement between the measured and computed dose in  $\text{CaF}_2$  is found. This agreement indicates that the back-scattering model used in Ref. [2] for DM1 is consistent with high power bremsstrahlung diodes such as those used on GAMBLE II and DM1.

The GAMBLE II bremsstrahlung diode configuration and measurements are reviewed in Sec. II. The numerical simulations are discussed in Section III, and a summary is presented in Section IV.

## II. Experiment

The GAMBLE II bremsstrahlung diode configuration for shot 6631 uses the "backless" geometry [5]. The significant dimensions are: anode-cathode (A-K) gap of 7 mm, hollow cathode of outer radius 6.1 cm, cathode thickness ( $\Delta r$ ) of 3 mm, and 4-mil thick tantalum anode of 7.4-cm radius. Five  $\text{CaF}_2$  thermoluminescent detectors (TLDs) were located 60 cm from the anode in a linear configuration, centered on axis. The TLDs were spaced 2-cm apart. Each TLD is a 1-mm x 6-mm rectangle, 1-mm thick, and encased in a 2.5-mm thick aluminum cylinder. These TLDs are irradiated from the side of the cylinder through the 2.5-mm aluminum wall. It is assumed that the TLDs are properly equilibrated by this package. The diode voltage and current waveforms for shot 6631 are shown in Fig. 1. For this shot, the peak voltage is 1.3 MV and the peak current is approximately 500 kA. These waveforms are smoothed to remove small amplitude noise and truncated in time at zero voltage for use as inputs into CYLTRAN. For this shot the average measured dose at 60-cm was  $343 \pm 24 \text{ Rad}(\text{CaF}_2)$ , where the error is the standard deviation of the five TLD measurements. For this absolute measurement, the TLD's were calibrated using an intense  $^{60}\text{Co}$  source of known intensity at NRL. The sensitivity of these TLD's is 60% less than the sensitivity determined from a similar calibration in 1990. This decrease is attributed to excessive baking of the TLD's which has reduced their light output. These measurements are consistent with the assumption that 60-cm is in the far field, and therefore no significant radial variation over a 4-cm radius is expected. An x-ray pinhole photograph and measured x-ray pin diode signals for this shot indicate that

most of the radiation is produced in an on-axis pinch of approximately 1.5-cm radius at the anode.

### III. Simulations

The electron spectral distribution incident on the tantalum converter was calculated for ten equally sized voltage bins using the load waveforms from Fig. 1. This electron spectrum is plotted in Fig. 2 and was used as the input spectrum for the CYLTRAN calculations. The diode and TLD detector geometry for this calculation is illustrated in Fig. 3 (drawing not to scale). The  $\text{CaF}_2$  detector geometry is an approximation of the experimental TLD geometry. A large area absorber is required in the simulation to provide meaningful statistics on the calculated dose. Therefore, the TLDs were represented by a 12-cm radius disk of  $\text{CaF}_2$  1-mm thick. This disk was subdivided into 4-cm wide radial zones to give some radial resolution.

Simulations were carried out with and without back-scattering. The term back-scattering [2] refers to the re-acceleration of electrons that are scattered back into the A-K gap from the anode by the diode electric field. In the simulation, these electrons are re-accelerated by a constant, uniform axial electric field in the diode A-K gap. The electrons are injected at the tantalum surface with either a  $\cos(\theta)$  angular distribution about the surface normal *or* with a fixed injection angle,  $\theta_{\text{fixed}} = 60^\circ$ , measured from the surface normal. This model is discussed in more detail in Ref. [2].

Results of the CYLTRAN calculations and the measurement are compared in Fig. 4. Each data point represents the dose in a 4-cm radial zone (0-4 cm, 4-8 cm, and 8-12 cm). The error bar on each calculated dose is the statistical uncertainty of the

calculation. Good agreement between the measurement and the simulation is found for the calculation that includes back-scattering and uses the  $\cos(\theta)$  injected electron distribution. This result *may* be in disagreement with previous Monte Carlo radiation yield calculations for similar GAMBLE II bremsstrahlung diode experiments [6]. Further investigation is required in order to determine how the numerical simulations in Ref. [6] were performed.

This comparison of calculated dose with measured dose is limited by the large uncertainty (29%) on the calculated dose for 0-4 cm. A more stringent comparison can be made by using the dose-area product (DAP). The DAP for  $r = 12$  cm is computed from the CYLTRAN results in Fig. 4. For the  $\cos(\theta)$  electron distribution, the DAP is 87 kRad(CaF<sub>2</sub>)-cm<sup>2</sup> without back-scattering, and 144 kRad(CaF<sub>2</sub>)-cm<sup>2</sup> with back-scattering; an increase of 67%. This increase agrees with an earlier estimate of the increase in the DAP due to back-scattering [7]. For the calculation with back-scattering and  $\theta_{fixed} = 60^\circ$ , the DAP is 112 kRad(CaF<sub>2</sub>)-cm<sup>2</sup>. The statistical uncertainty for these computed DAPs is estimated to be less than 10%. The measured dose corresponds to a DAP of  $155 \pm 11$  kRad(CaF<sub>2</sub>)-cm<sup>2</sup>, provided the measured dose does not vary significantly from 4 to 12 cm. This assumption is valid for this far-field dose measurement. The measured DAP agrees with the simulation result with back-scattering and the  $\cos(\theta)$  electron distribution. Without back-scattering, the calculated DAP is too small, as expected. For a fixed electron injection angle of  $60^\circ$ , the calculated DAP is also somewhat smaller than the measured DAP.

#### IV. Summary

A GAMBLE II bremsstrahlung diode experiment is simulated using the CYLTRAN code. Measured voltage and current waveforms, and source size from x-ray diagnostics are used as CYLTRAN inputs. The calculated dose is in good agreement with the measured dose when back-scattering and a  $\cos(\theta)$  injected electron distribution is included in the calculation.

A recently completed study [2] of the DM1 large-area bremsstrahlung diode experiments used CYLTRAN calculations with back-scattering along with idealized voltage and current waveforms to infer the amount of electrical energy delivered to the diode load. The DM1 diode is similar to the GAMBLE II backless diode except a larger A-K gap (2.54 cm) is used. For the DM1 bremsstrahlung diode, the electron beam does not pinch at the anode, but strikes the anode in an annular ring comparable with the cathode radius, albeit with significant azimuthal non-uniformity as indicated by witness-plate damage patterns and x-ray pinhole camera images. For the DM1 study [2], the injected electron beam was of uniform current density over a radius equal to the cathode radius. In addition, the  $\cos(\theta)$  electron distribution with back-scattering was used. Results of the GAMBLE II experiment in this report imply that this electron distribution is a reasonable model for bremsstrahlung production in these high-power diodes.

Since the time of this analysis, several additional bremsstrahlung diode shots have been taken on GAMBLE II. For these shots, detailed dose measurements were made in planes located at 10, 40, and 70 cm distances from anode. It is the purpose of these shots

to clarify the role of back-scattering and reflexing electrons in high-power bremsstrahlung diodes. Analysis of these shots will be the subject of a future report.

## V. References.

- [1] J.A. Halbleib, R.P. Kensek, T.A. Mehlhorn, G.D. Valdez, S.M. Seltzer, M.J. Berger, "ITS Version 3.0: The Integrated TIGER Series of Coupled Electron/Photon Monte Carlo Transport Codes," Sandia National Laboratories Report SAND91-1634 (1992). [Also in Oak Ridge National Laboratory - Radiation Shielding Information Center Report CCC-467, 1994]
- [2] D.V. Rose, R.J. Commisso, S.B. Swanekamp, and F.C. Young, "Bremsstrahlung Yield Simulations for DM1," NRL Memorandum Report # 7748 (1995).
- [3] R.J. Commisso, J.R. Boller, D.V. Rose, and S.B. Swanekamp, "DM1 Circuit Simulations With an Electron-Beam Diode," NRL Memorandum Report # 7750 (1995).
- [4] R.J. Commisso, J.R. Boller, D.V. Rose, S.B. Swanekamp, F.C. Young, J.M. Grossmann, P.F. Ottinger, B.V. Weber, and G. Cooperstein, "Modeling of DM1 Performance," in the Proceedings of the 10th IEEE International Pulsed Power Conference, W. Baker and G. Cooperstein, eds., Albuquerque, N.M. (1995), paper 6.6.
- [5] S.J. Stephanakis, J.R. Boller, G. Cooperstein, B.V. Weber, and F.C. Young, "Experimental Study of the Pinched-Beam Diode with Thin, Unbacked Foil Anodes," in the Proceeding of the 9th International Conference on High-Power Particle Beams, D. Mosher and G. Cooperstein, eds. (May 25-29, 1992, Washington, DC), Vol. II, p. 871.
- [6] W.F. Oliphant, C.M. Dozier, D.B. Brown, S.J. Stephanakis, J.R. Boller, and G. Cooperstein, "A Characterization and Optimization Study of GAMBLE II as an X-Ray Bremsstrahlung Source," 1982 IEEE Conference on Nuclear and Space Radiation Effects (Las Vegas, NV, July 1982).
- [7] R.J. Adler, "Radiation Production Simulations of the DECADE Simulator," 1994, *unpublished*. See Ref. [2] for more information.

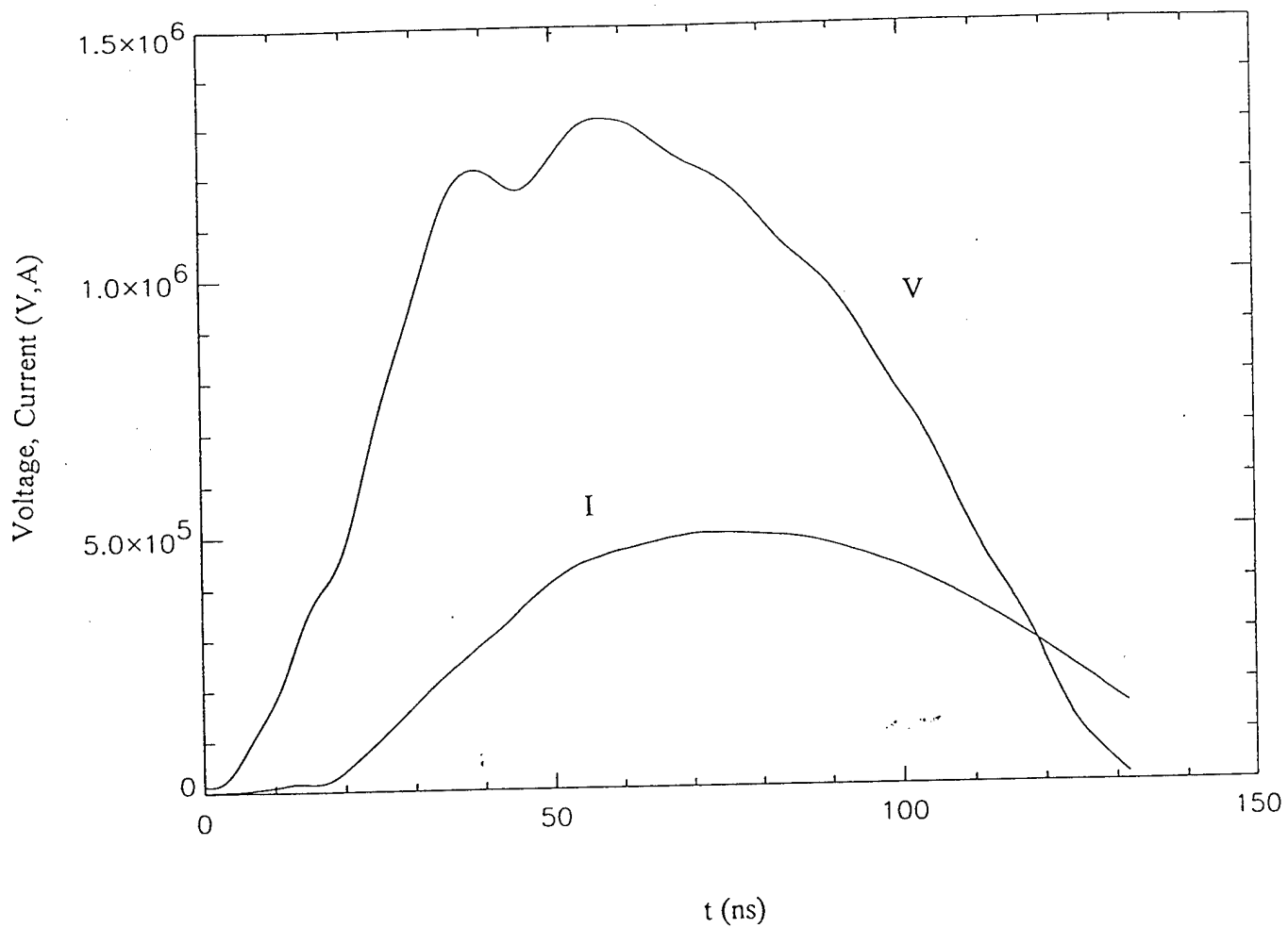


Fig. 1 -Load voltage and current waveforms for GAMBLE II shot 6631. The waveforms have been smoothed and truncated for use in the CYLTRAN calculations.



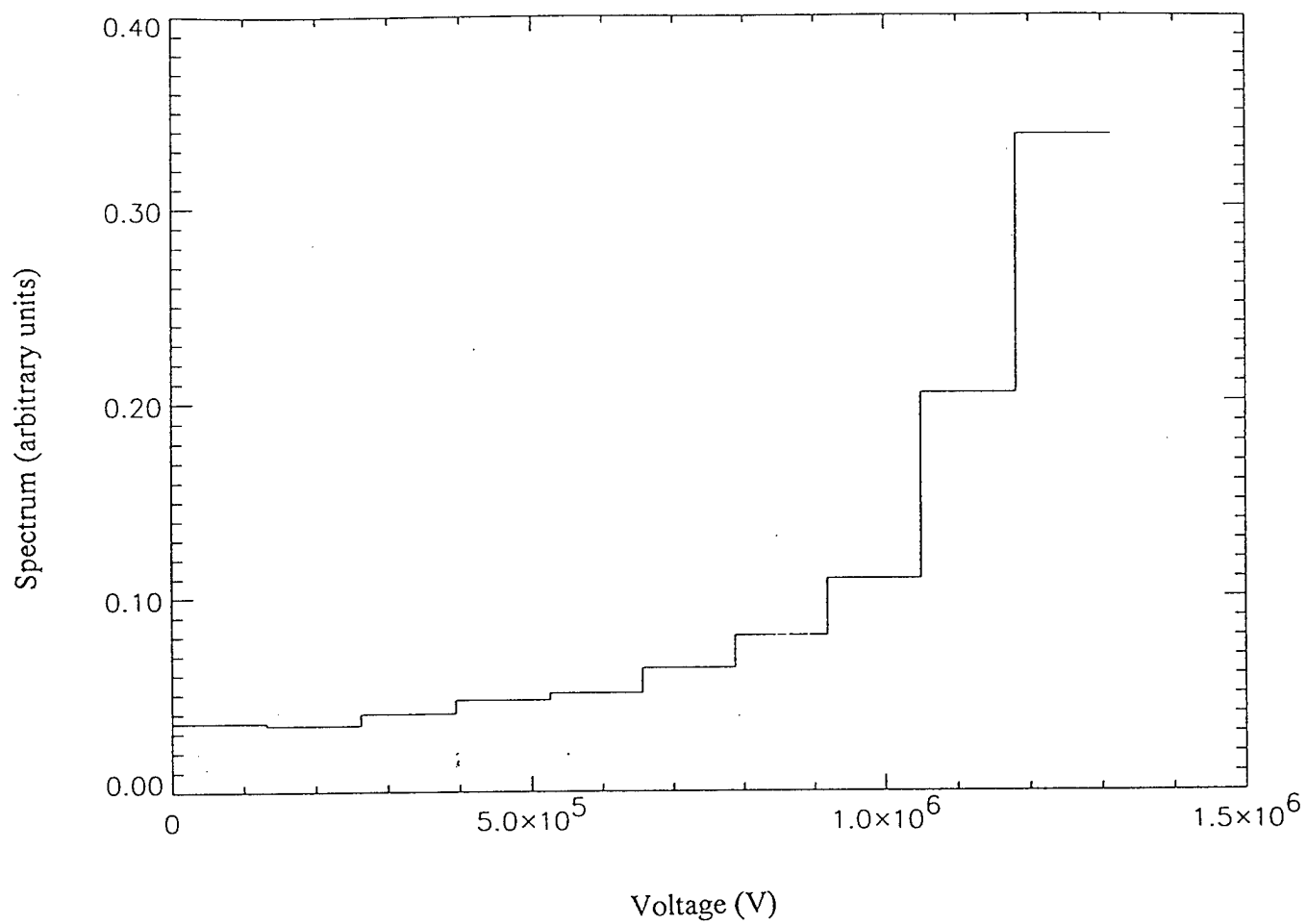


Fig. 2 -Electron spectrum obtained from the waveforms shown in Fig. 1 and used as input into the CYLTRAN calculations.

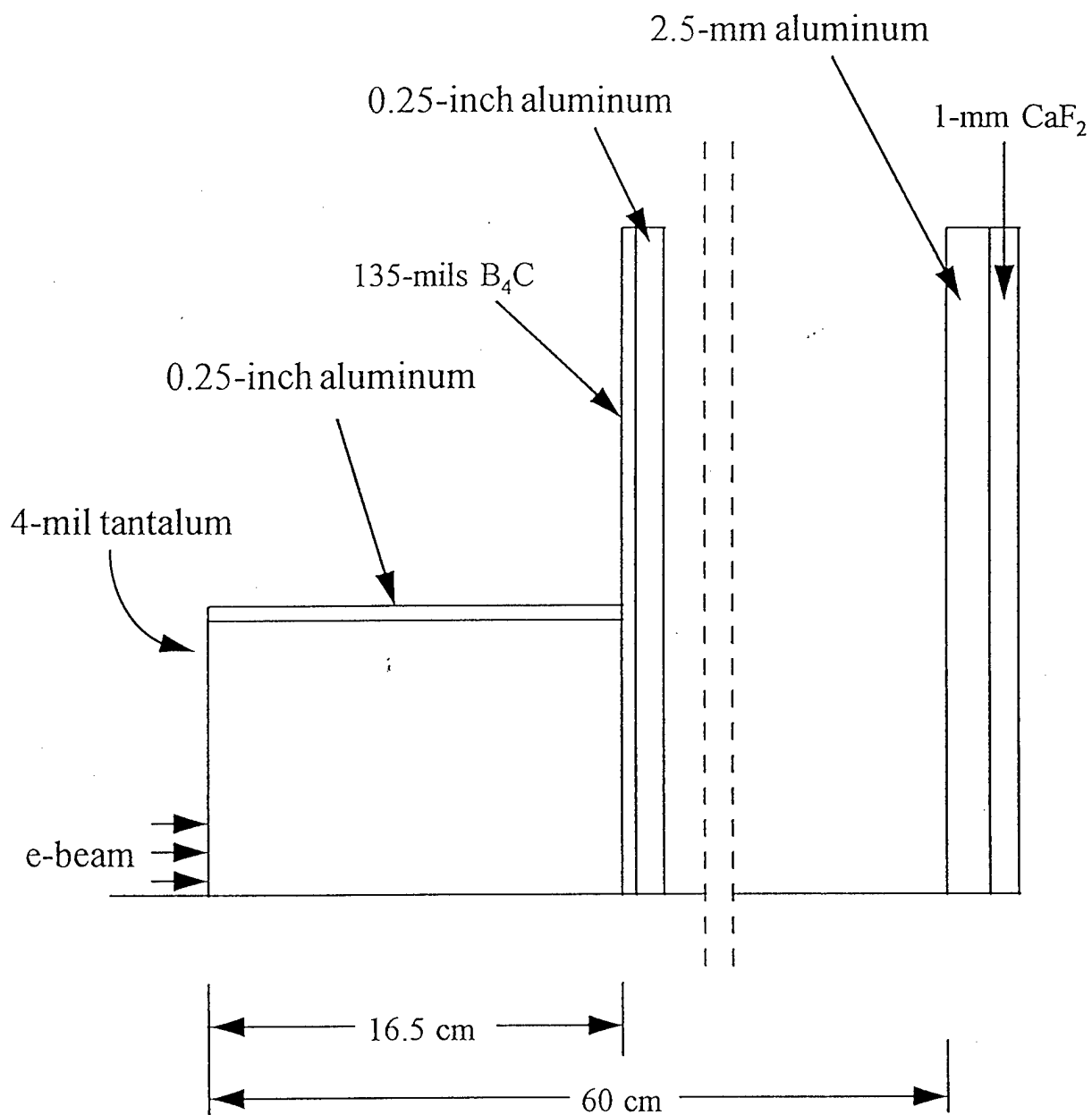
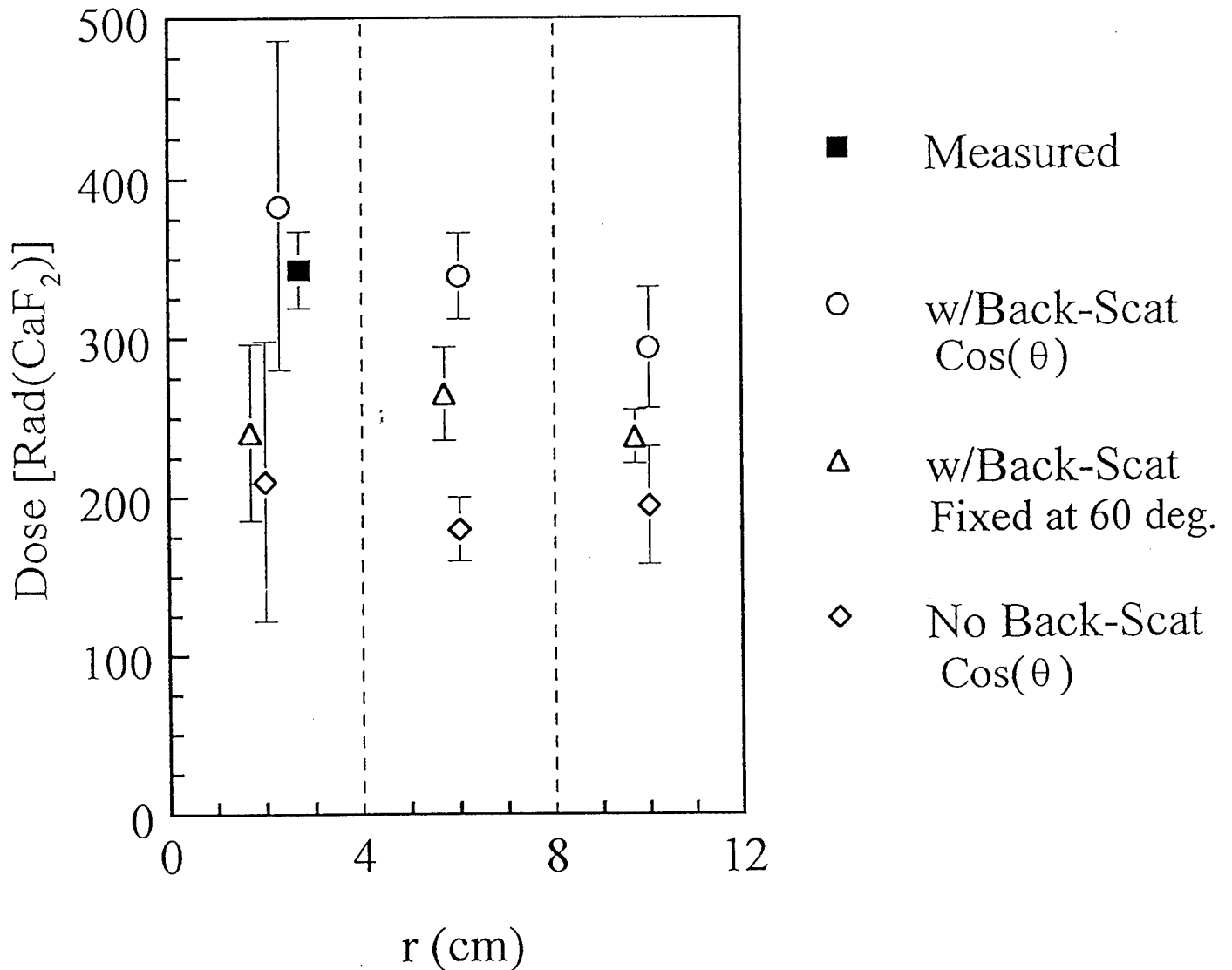


Fig. 3 - Schematic of the anode, beam-stop, and target geometry used in the CYLTRAN simulations. Drawing is not to scale.

# GAMBLE II Shot 6631

Dose measured at 60 cm



Open symbols are CYLTRAN results.

Fig. 4 -Dose in  $\text{CaF}_2$  as a function of radius for the GAMBLE II measurement and the CYLTRAN simulations. Each point represents the average dose in a 4-cm wide radial zone.

TITLE:        KRYPTON DENSITY MEASUREMENTS FOR THE SATURN SOLID  
              PRS NOZZLE

AUTHORS:    B. Weber, J. Kellogg, G. Peterson, R. Spielman<sup>\*</sup>, and M. Sucky

DATE:        2 August 1995

ABSTRACT:        The Kr gas distribution from a Saturn PRS nozzle was measured using one beam from the two-color interferometer on the Hawk vacuum chamber. This nozzle was used previously for Saturn Kr PRS experiments and the results are being modeled by LLNL. An accurate density distribution is required because the modeling turns out to be very sensitive to the distribution. About 250 pulses were used to build up the density profile (at 48 spatial locations) and to determine statistical uncertainties. These line-integrated density measurements are Abel inverted to determine  $n(r,z,t)$ . During the time range of interest for Saturn, most of the gas is located within a 4.5 cm diameter cylinder, the diameter of the nozzle exit, with a slight decrease in density on axis. The mass per unit length is calculated as a function of axial distance and time. Future measurements could include Ar gas with the solid nozzle (for upcoming Saturn experiments), and both Kr and Ar gases with an annular Saturn nozzle. Preionization could also be diagnosed with the two-color interferometer.

THIS REPORT REPRESENTS UNPUBLISHED  
INTERNAL WORKING DOCUMENTS AND SHOULD  
NOT BE REFERENCED OR DISTRIBUTED WITHOUT  
THE AUTHORS' CONSENT

---

<sup>\*</sup> Sandia National Laboratories, Albuquerque, NM

## Experimental Setup

The gas distribution from a Saturn PRS nozzle was diagnosed using one beam of the two-color interferometer. The nozzle produces a "solid" gas distribution, used to study implosion dynamics. The working gas is Kr at a plenum pressure of 1000 Torr. Previous experiments on Saturn are being modeled by LLNL. The model results depend very sensitively on the assumed gas distribution, motivating these measurements.

The Hawk vacuum chamber was used for these measurements. This was convenient because the Hawk vacuum chamber is long enough to avoid gas reflections from the chamber walls and the interferometer was already installed. Future measurements will probably be performed on a separate test stand so they will not interfere with Hawk experiments.

The interferometer technique used here was used previously to diagnose the gas distribution from a Phoenix PRS nozzle (see IEEE Conf. Record-Abstracts, IEEE COPS, June 1995, p. 207). Many of the techniques developed for these measurements apply to the Saturn measurements reported here. The main advantage of this particular interferometer for this application is its superior vibration isolation, allowing small phase change measurements ( $< 1^\circ$ ) during the time scale of interest (a few ms) without spurious phase from vibrations.

The valve/nozzle assembly was moved in vacuum using an x-y translator to probe the cross section; the laser beam was kept in a fixed location. In this way, 48 locations were probed as illustrated in Fig. 1. The exit aperture of the nozzle has a 2.25 cm radius. The measurement locations ( $r, z$ ) are relative to the center of the exit aperture. Measurements were made at five axial locations starting at  $z = 0.2$  cm; with 0.66 cm increments. Close to the axis ( $r = 0$ -1.5 cm), measurements were made with radial increments of 0.5 cm. At greater distances from the axis ( $r > 1.5$  cm), the radial increments were 0.25 cm.

## Measurements

For each shot, the interferometer signal and breakdown pin signals were recorded. The maximum of the breakdown pin signal was used as the  $t = 0$  reference. The interferometer signals were processed to determine the phase shift, and the corresponding Kr integrated gas density (in  $\text{cm}^{-2}$ ). At each location, five consecutive shots were taken to determine an average and standard deviation. An example of the results is shown in Fig. 2. These measurements were made at  $z = 0.2$  cm (close to the nozzle exit) and " $x$ " = 0 (the laser line of sight goes through the nozzle axis). At this location, the phase shift is large. Fig. 2 shows the resulting average and standard deviation of the five shots. A typical Saturn firing time is about 0.75 ms on this scale, during the rise of the gas density. The standard deviation at this time is only a few percent of the average, showing both the reproducibility of the valve and the interferometer.

Results for a location near the edge of the gas distribution are shown in Fig. 3. This location,  $z = 0.2$  cm and  $r = 2.5$  cm, is outside the nozzle aperture (Fig. 1). The standard deviation is greater, in a relative sense, than it is at  $x = 0$ , but in absolute value it is about ten times smaller because the digitizer gain was adjusted for each beam location. At  $t = 0.75$  ms, for example, the line-density is  $2 \times 10^{15} \text{ cm}^{-2}$  at  $x = 2.5$  cm with an uncertainty of 50%, while at the same time at  $x = 0$  the line-density is  $2.5 \times 10^{17} \text{ cm}^{-2}$  with an uncertainty of 2%. For times of interest, the dynamic range is about  $(2.5 \times 10^{17} \text{ cm}^{-2}) / (50\% \times 2 \times 10^{15} \text{ cm}^{-2}) = 250$ . A higher dynamic range of 650 was obtained for the Phoenix measurements, where amplifiers were used to reduce the uncertainty in the low density regions.

The time-dependence of the line-densities in Figs 2 and 3 are interesting. The local maximum at  $t = 1.05$  ms in Fig 2 and subsequent decrease is probably the result of gas dynamics inside the nozzle, and not related to reflections from the chamber walls. A similar feature occurs at  $t = 1.3$  ms outside the nozzle radius as shown in Fig. 3. The Saturn firing time occurs during the initial gas rise, so these features may not be important, but these measurements could be used to benchmark computer simulations, such as those done already by S-cubed.

### Data Analysis

The line-integrated density is plotted vs.  $x$  (distance from the nozzle axis) in Figs. 4-8. Each figure shows the measurements at a single axial location at five times during the density rise:  $t = 0.6, 0.7, 0.8, 0.9$ , and  $1.0$  ms. The error bars correspond to  $\pm$  one standard deviation obtained from five consecutive shots. The curves connecting the data points are special "spline" functions used for the Abel inversion. These splines have the property that the derivative is zero at  $x = 0$ , and at a user-prescribed boundary point, the function and its derivative are zero. This technique has been adopted for these data because the uncertainties are small, so the fitting function can go through the data points without introducing large fluctuations in the results. Alternatively, a fitting function could be used that goes through the error bars. A different curve-fitting approach should be tried to check the sensitivity of the inversion process.

The symbols in Figs 4-8 indicate the measurement locations. The edge of the gas distribution becomes less distinct at greater distances from the nozzle exit and at greater times, as expected. In the interior region,  $r < 1.5$  cm, the measurements vary slowly, justifying the use of larger measurement increments in this region.

The data in Figs 4-8 are Abel inverted using a technique based on the spline fits. The measurement uncertainties (shown as error bars in Figs 4-8) can be used to determine uncertainties in the calculated Abel-inverted densities. (This technique is described in detail in TN 94-05.) The resulting Kr densities and uncertainties are listed in Table I. The  $(r,z)$  locations correspond to measurement locations. Each time column is followed by a column labeled "error" which contains the calculated uncertainty. The row containing zero values for the density and error is the assumed boundary used in the Abel inversion process.

### Results

The data in Table I are plotted in Figs. 9-15. In Figs. 9-13, the density and error bars are plotted as a function of  $r$  for each  $z$  value at the same times as in Figs 4-8. The error bars are noticeably larger relative to the data than for the line-integrated data. The error propagation results in higher error bars at smaller radii, because more measurement locations are used to determine the density. This "amplification" of error is an unavoidable result of the Abel inversion process, and illustrates the need for high precision in the line-integrated measurements.

At all  $z$  locations and at most times, the density drops rapidly outside the nozzle exit aperture ( $r = 2.25$  cm), and is fairly flat in the region inside the nozzle radius. At some times and locations, the plots indicate a depressed density at the axis. Surface plots of the density distribution at  $t = 0.7$  and  $0.8$  ms (relevant times for Saturn) are shown in Figs. 14 and 15, respectively. These plots show the dramatic density decrease outside  $r = 2.25$  cm and the density depression structure on axis (but the error bars at the axis are large as shown in Figs. 9-13 and in Table I).

The mass per unit length is calculated using the Kr radial density distributions. Figure 16 shows the result of this calculation as a function of time at different axial locations. An error

propagation calculation determines the uncertainty in the mass, shown as error bars in Fig. 16. At  $t = 0.75$  ms, for example, the mass per unit length varies from  $100 \mu\text{g/cm}$  at  $z = 0.2$  cm to  $80 \mu\text{g/cm}$ ,  $2.84$  cm from the nozzle.

### Future Measurements

These measurements could be repeated for Ar gas, applicable to upcoming Saturn PRS experiments. Annular nozzle(s) could also be investigated. The results can be used for the implosion and radiation modeling mentioned above, and also for the nozzle design simulations performed by S-cubed.

Another capability of this interferometer is to measure neutral and electron densities simultaneously. To do this, two different lasers are used, one at  $1.06 \mu$  and one at  $0.532 \mu$  (used for these measurements). The phase shift dependence on wavelength is different for neutrals and electrons, so the two densities can be determined independently from the two phase measurements. This technique may be ideal for the preionization of the PRS gas as is done on Saturn shots. To our knowledge, this measurement has never been made, and may be important for understanding and improving PRS sources.

Other techniques may be applicable, and possibly preferable, for gas distribution measurements. A two-dimensional holographic interferometer, developed by HY-Tech, has been used to measure the gas distribution for a Double Eagle nozzle. This technique has the advantage of high spatial resolution and a complete profile at a single time. The limitation is the phase resolution and dynamic range. An x-ray backlighting technique developed by LLNL in support of SNL was used to diagnose an annular Saturn nozzle with Ar gas. A technique under development uses electron-beam attenuation to obtain a 2-D density distribution, under investigation at U.C. Irvine by F. Wessel. These different techniques may complement the measurements described here and lead to improved capabilities to model and predict gas flow from PRS nozzles and the resulting implosion and radiation yields.

Table I. Abel-inverted Kr densities and uncertainties

Abel-inverted Kr densities 7/31/95											
z = 0.2 cm											
r(cm)\t(s)	6.00E-04	error	7.00E-04	error	8.00E-04	error	9.00E-04	error	1.00E-03	error	
0.00E+00	2.80E+16	1.14E+16	2.75E+16	1.54E+16	5.57E+16	1.94E+16	7.83E+16	2.22E+16	1.20E+17	4.13E+16	
5.00E-01	2.76E+16	8.60E+15	4.22E+16	1.06E+16	7.84E+16	1.46E+16	1.06E+17	1.61E+16	1.36E+17	2.83E+16	
1.00E+00	2.39E+16	5.33E+15	5.27E+16	6.93E+15	7.85E+16	7.00E+15	1.06E+17	1.78E+16	1.53E+17	1.67E+16	
1.50E+00	6.40E+15	4.29E+15	5.08E+16	1.05E+16	8.26E+16	7.50E+15	1.04E+17	2.77E+16	1.59E+17	1.51E+16	
1.75E+00	3.08E+15	2.98E+15	3.90E+16	7.74E+15	7.86E+16	6.32E+15	9.85E+16	2.13E+16	1.25E+17	1.28E+16	
2.00E+00	2.58E+15	1.27E+15	1.31E+16	8.23E+14	3.08E+16	1.69E+15	5.19E+16	6.72E+15	7.93E+16	4.45E+15	
2.25E+00	1.20E+15	1.16E+15	2.78E+15	6.21E+14	5.05E+15	7.87E+14	9.60E+15	9.29E+14	1.63E+16	1.13E+15	
2.50E+00	2.09E+14	4.05E+14	9.78E+14	2.53E+14	1.46E+15	2.66E+14	1.17E+15	4.58E+14	7.05E+14	3.68E+14	
3.00E+00	0.00E+00	0.00E+00	0.00E+00	0.00E+00	0.00E+00	0.00E+00	0.00E+00	0.00E+00	0.00E+00	0.00E+00	
z = 0.86 cm											
r(cm)\t(s)	6.00E-04	error	7.00E-04	error	8.00E-04	error	9.00E-04	error	1.00E-03	error	
0.00E+00	1.73E+16	1.36E+16	3.67E+16	1.26E+16	5.58E+16	1.87E+16	9.74E+16	1.53E+16	1.37E+17	3.45E+16	
5.00E-01	2.16E+16	9.08E+15	3.78E+16	6.94E+15	6.74E+16	1.50E+16	9.87E+16	1.18E+16	1.24E+17	2.30E+16	
1.00E+00	2.69E+16	6.20E+15	4.92E+16	7.12E+15	8.64E+16	9.60E+15	1.15E+17	1.31E+16	1.53E+17	1.47E+16	
1.50E+00	5.90E+15	3.67E+15	4.66E+16	8.44E+15	6.59E+16	8.18E+15	8.73E+16	1.47E+16	1.36E+17	1.68E+16	
1.75E+00	2.08E+15	2.39E+15	4.06E+16	5.00E+15	9.08E+16	3.96E+15	1.14E+17	7.49E+15	1.43E+17	1.26E+16	
2.00E+00	1.12E+15	1.27E+15	1.07E+16	1.39E+15	2.91E+16	2.44E+15	4.51E+16	4.05E+15	6.26E+16	3.61E+15	
2.25E+00	3.21E+14	1.03E+15	1.23E+15	1.13E+15	2.66E+15	1.46E+15	6.76E+15	1.67E+15	1.38E+16	2.33E+15	
2.50E+00	4.64E+14	7.28E+14	1.11E+15	1.15E+15	3.14E+15	1.40E+15	3.82E+15	1.51E+15	5.78E+15	1.81E+15	
2.75E+00	5.58E+14	2.44E+14	8.29E+14	4.14E+14	1.83E+15	4.38E+14	2.50E+15	4.44E+14	3.55E+15	5.00E+14	
3.50E+00	0.00E+00	0.00E+00	0.00E+00	0.00E+00	0.00E+00	0.00E+00	0.00E+00	0.00E+00	0.00E+00	0.00E+00	
z = 1.52 cm											
r(cm)\t(s)	6.00E-04	error	7.00E-04	error	8.00E-04	error	9.00E-04	error	1.00E-03	error	
0.00E+00	3.06E+16	1.27E+16	3.21E+16	1.18E+16	6.50E+16	1.08E+16	7.36E+16	1.62E+16	1.14E+17	2.01E+16	
5.00E-01	2.24E+16	8.94E+15	3.90E+16	7.55E+15	6.46E+16	9.83E+15	9.50E+16	1.07E+16	1.34E+17	1.15E+16	
1.00E+00	1.63E+16	5.54E+15	3.69E+16	4.86E+15	6.88E+16	1.16E+16	9.84E+16	9.73E+15	1.38E+17	1.17E+16	
1.50E+00	5.23E+15	2.78E+15	4.36E+16	7.25E+15	7.48E+16	1.48E+16	1.02E+17	1.37E+16	1.26E+17	1.23E+16	
1.75E+00	1.83E+15	1.65E+15	2.65E+16	5.61E+15	6.11E+16	8.55E+15	8.00E+16	1.08E+16	1.12E+17	6.60E+15	
2.00E+00	9.92E+14	1.02E+15	6.91E+15	1.45E+15	2.41E+16	1.54E+15	3.66E+16	3.12E+15	5.20E+16	3.15E+15	
2.25E+00	3.68E+13	8.54E+14	1.16E+15	1.30E+15	5.19E+15	1.46E+15	9.67E+15	1.96E+15	1.45E+16	2.01E+15	
2.50E+00	4.18E+14	6.36E+14	1.59E+15	8.64E+14	3.53E+15	1.09E+15	4.77E+15	1.02E+15	7.90E+15	1.50E+15	
2.75E+00	3.81E+14	9.55E+14	8.78E+14	1.29E+15	1.78E+15	1.29E+15	2.74E+15	1.35E+15	4.17E+15	1.58E+15	
3.00E+00	4.22E+14	5.89E+14	8.46E+14	7.39E+14	1.51E+15	7.27E+14	2.40E+15	8.13E+14	3.49E+15	9.21E+14	
3.50E+00	0.00E+00	0.00E+00	0.00E+00	0.00E+00	0.00E+00	0.00E+00	0.00E+00	0.00E+00	0.00E+00	0.00E+00	
z = 2.18 cm											
r(cm)\t(s)	6.00E-04	error	7.00E-04	error	8.00E-04	error	9.00E-04	error	1.00E-03	error	
0.00E+00	1.53E+16	1.41E+16	2.60E+16	1.77E+16	6.97E+16	2.58E+16	8.85E+16	2.83E+16	1.20E+17	1.94E+16	
5.00E-01	2.26E+16	6.23E+15	4.00E+16	8.91E+15	6.99E+16	1.64E+16	9.38E+16	1.75E+16	1.24E+17	1.44E+16	
1.00E+00	1.44E+16	4.40E+15	3.50E+16	1.08E+16	5.99E+16	1.23E+16	9.27E+16	1.24E+16	1.20E+17	1.34E+16	
1.50E+00	3.62E+15	4.20E+15	3.53E+16	1.27E+16	7.31E+16	1.11E+16	9.04E+16	1.32E+16	1.22E+17	1.35E+16	
1.75E+00	3.01E+15	3.30E+15	2.20E+16	6.30E+15	4.89E+16	5.63E+15	7.25E+16	7.22E+15	9.10E+16	6.61E+15	
2.00E+00	1.25E+15	1.67E+15	6.24E+15	2.81E+15	1.96E+16	3.91E+15	3.27E+16	4.11E+15	4.64E+16	6.07E+15	
2.25E+00	2.42E+14	1.59E+15	2.70E+15	2.30E+15	9.18E+15	2.59E+15	1.67E+16	2.54E+15	2.65E+16	3.55E+15	
2.50E+00	1.19E+15	1.20E+15	2.50E+15	1.50E+15	4.96E+15	2.02E+15	8.63E+15	2.09E+15	1.35E+16	2.11E+15	
2.75E+00	2.56E+14	1.03E+15	6.26E+14	1.40E+15	1.44E+15	1.69E+15	2.37E+15	1.92E+15	4.11E+15	2.28E+15	
3.00E+00	-1.89E+14	3.94E+14	1.66E+14	5.86E+14	9.58E+14	7.20E+14	1.66E+15	8.19E+14	2.83E+15	9.01E+14	
4.00E+00	0.00E+00	0.00E+00	0.00E+00	0.00E+00	0.00E+00	0.00E+00	0.00E+00	0.00E+00	0.00E+00	0.00E+00	
z = 2.84 cm											
r(cm)\t(s)	6.00E-04	error	7.00E-04	error	8.00E-04	error	9.00E-04	error	1.00E-03	error	
0.00E+00	2.63E+16	9.47E+15	1.39E+16	1.50E+16	4.31E+16	1.40E+16	5.17E+16	1.43E+16	9.07E+16	1.70E+16	
5.00E-01	2.11E+16	6.96E+15	3.27E+16	9.21E+15	5.37E+16	5.67E+15	8.50E+16	8.67E+15	1.19E+17	1.09E+16	
1.00E+00	1.01E+16	3.37E+15	3.40E+16	6.32E+15	5.94E+16	5.45E+15	9.11E+16	5.67E+15	1.16E+17	1.09E+16	
1.50E+00	1.57E+15	1.97E+15	2.72E+16	8.76E+15	6.13E+16	8.05E+15	7.74E+16	8.76E+15	1.00E+17	1.15E+16	
1.75E+00	-9.12E+13	1.81E+15	1.87E+16	7.20E+15	4.62E+16	6.56E+15	6.15E+16	7.45E+15	8.25E+16	6.97E+15	
2.00E+00	6.73E+14	1.86E+15	6.64E+15	1.76E+15	2.71E+16	3.22E+15	3.61E+16	4.00E+15	5.15E+16	6.44E+15	
2.25E+00	5.92E+14	1.55E+15	1.41E+15	1.69E+15	9.69E+15	2.28E+15	1.74E+16	4.30E+15	2.65E+16	4.47E+15	
2.50E+00	-7.03E+13	1.00E+15	1.04E+15	1.04E+15	3.89E+15	1.69E+15	7.30E+15	2.82E+15	1.33E+16	2.34E+15	
2.75E+00	3.73E+14	9.24E+14	6.50E+14	9.26E+14	2.12E+15	1.32E+15	3.89E+15	9.71E+14	7.33E+15	1.44E+15	
3.00E+00	-2.69E+14	8.94E+14	9.02E+13	8.95E+14	5.56E+14	1.10E+15	1.59E+15	1.10E+15	2.79E+15	1.65E+15	
3.25E+00	2.34E+14	2.12E+14	8.74E+14	2.58E+14	1.55E+15	1.92E+14	2.33E+15	4.28E+14	3.51E+15	6.84E+14	
4.00E+00	0.00E+00	0.00E+00	0.00E+00	0.00E+00	0.00E+00	0.00E+00	0.00E+00	0.00E+00	0.00E+00	0.00E+00	



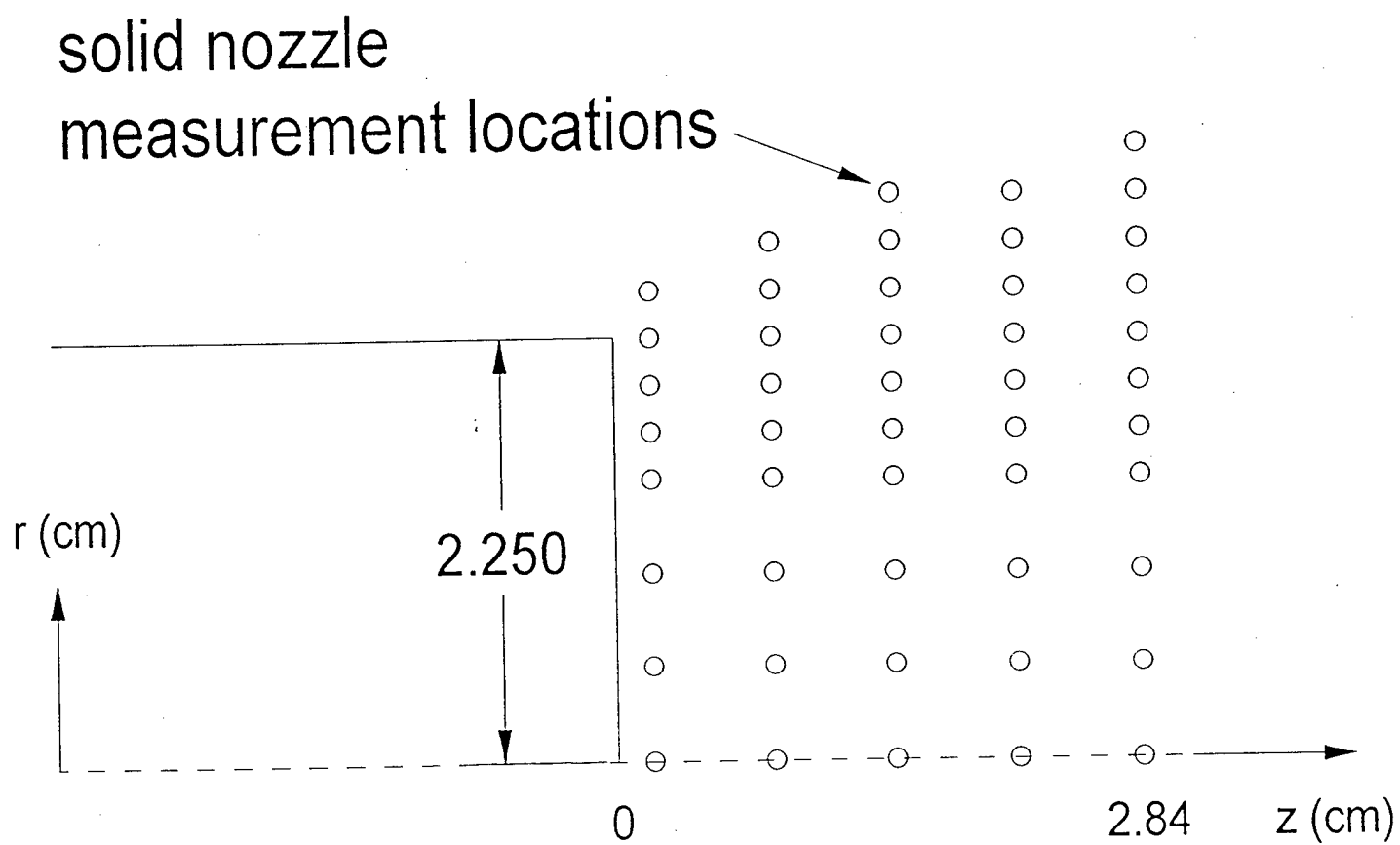


Figure 1. Laser beam locations for Kr gas distribution measurements.

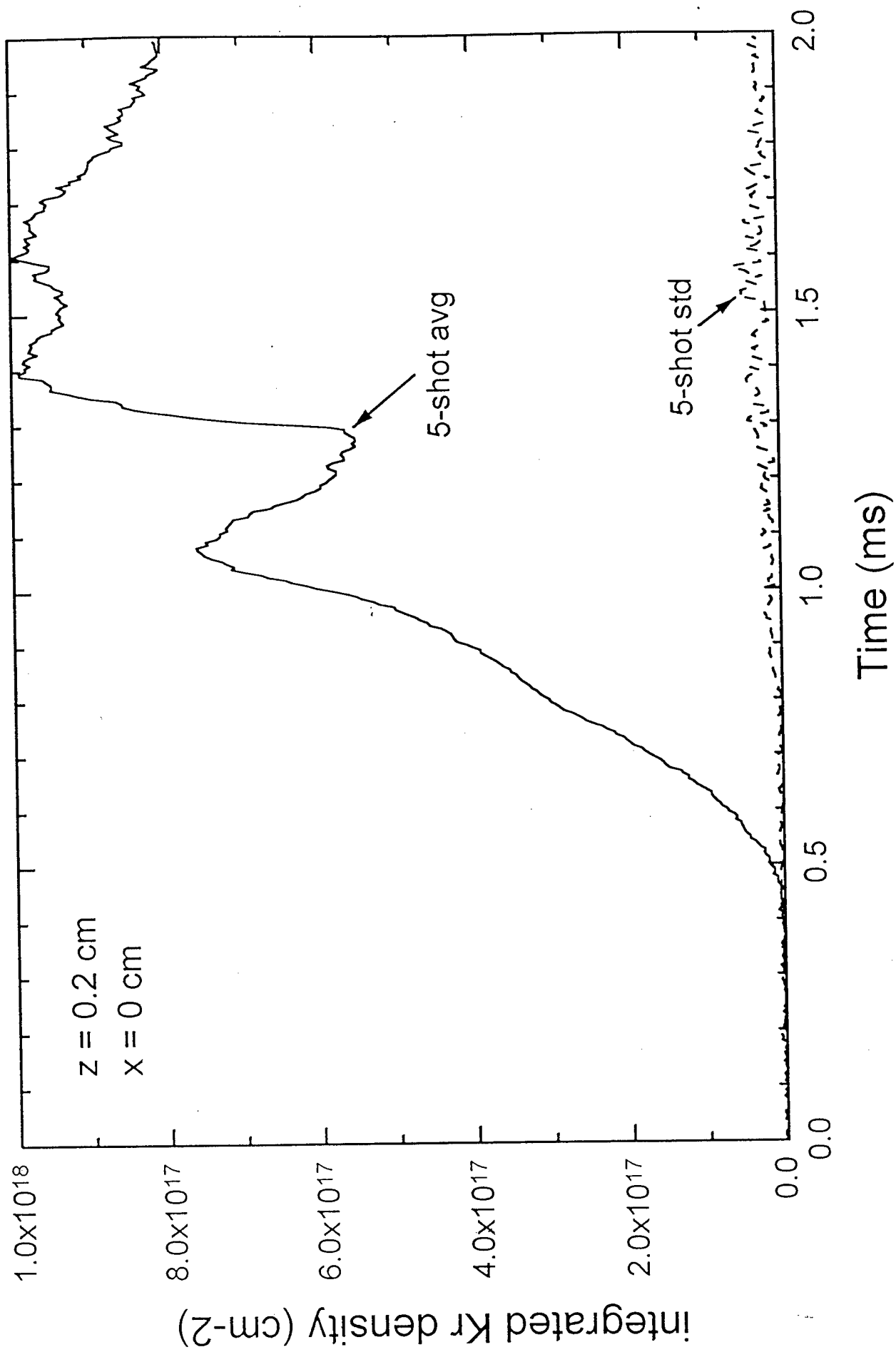


Figure 2. Line-integrated Kr density measured close to the aperture, through a diameter.

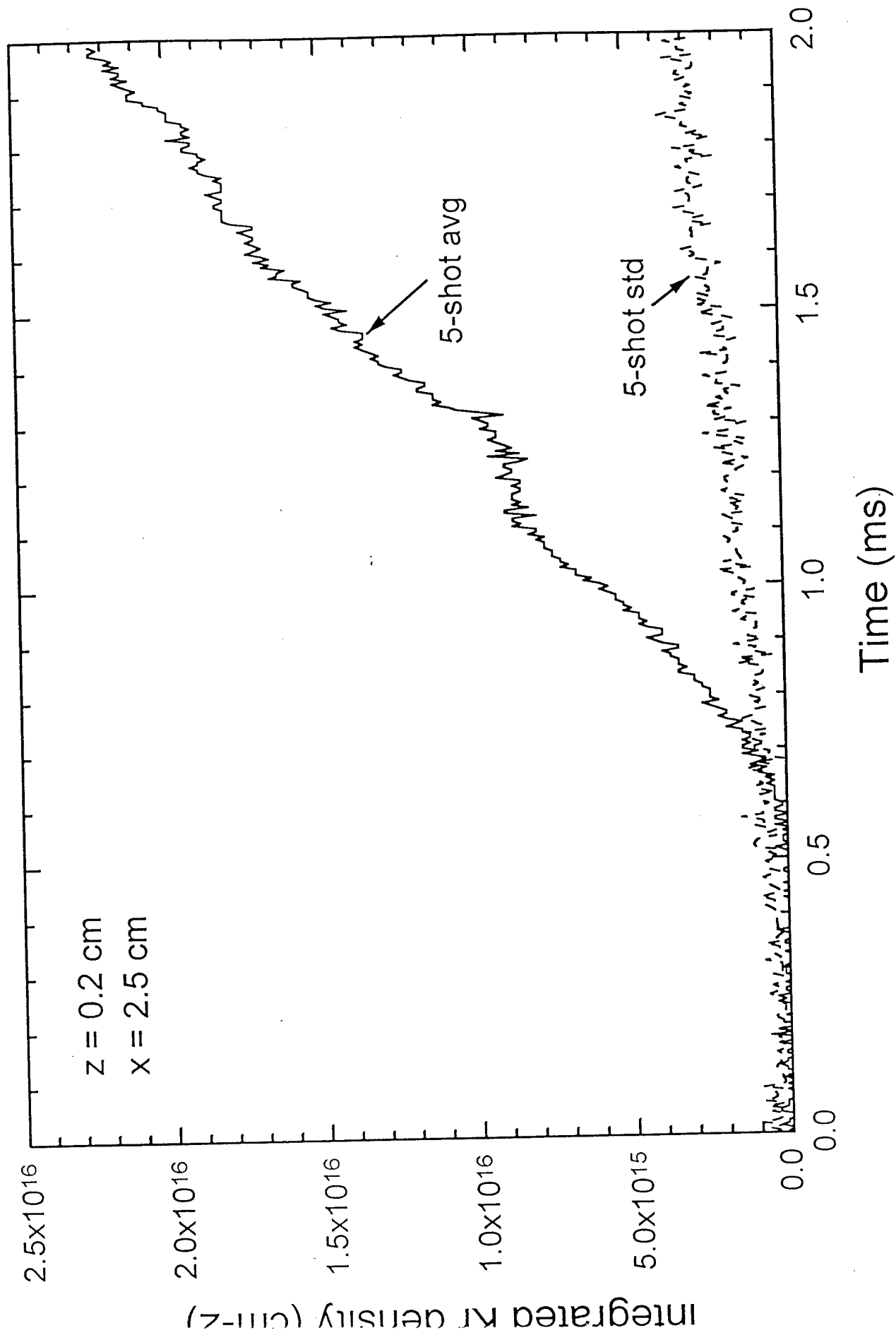


Figure 3. Line-integrated Kr density measured close to the nozzle, outside the radius of the aperture.

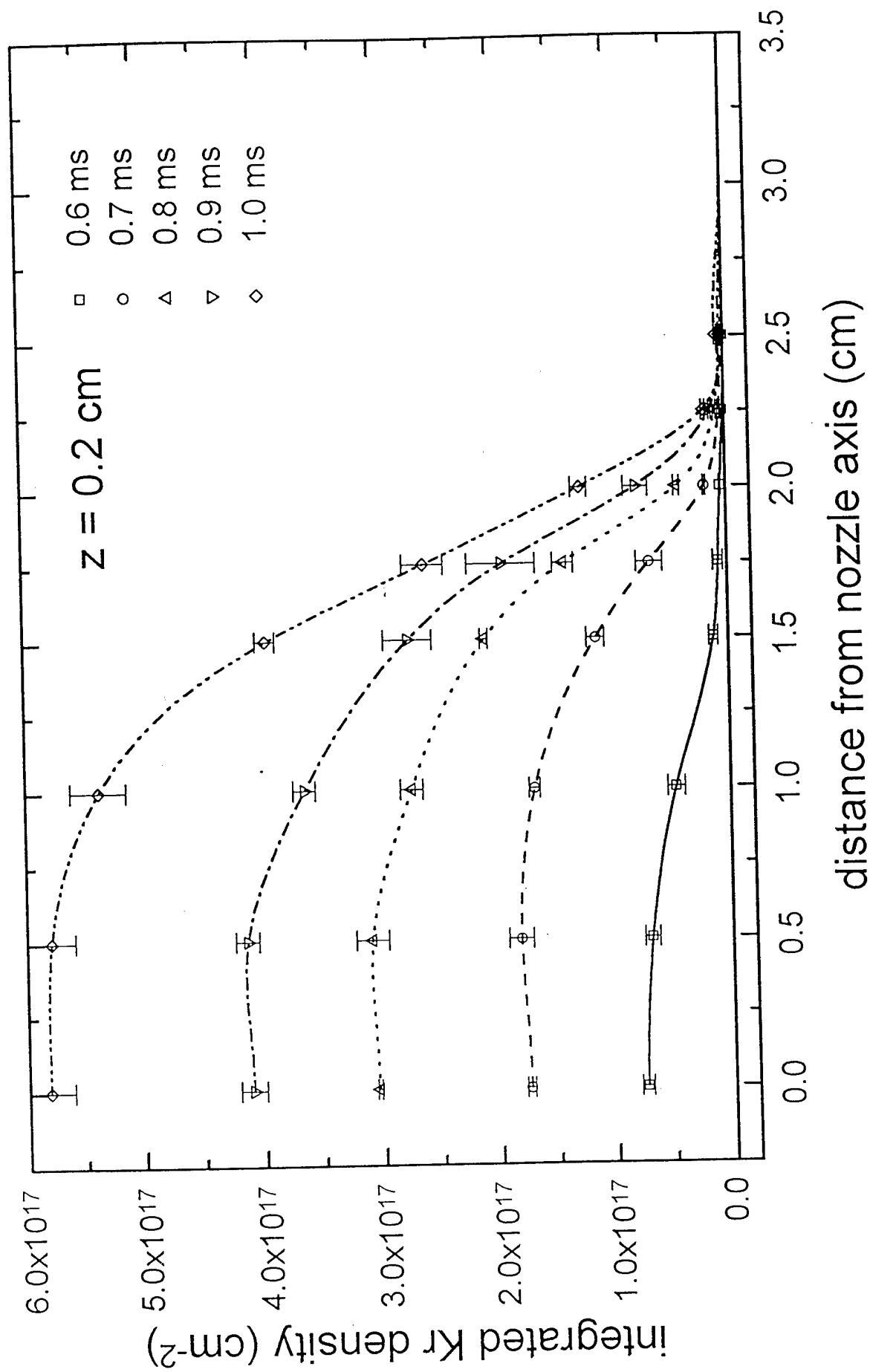


Figure 4. Line-integrated Kr density as a function of  $x$ , at  $z = 0.2 \text{ cm}$ .

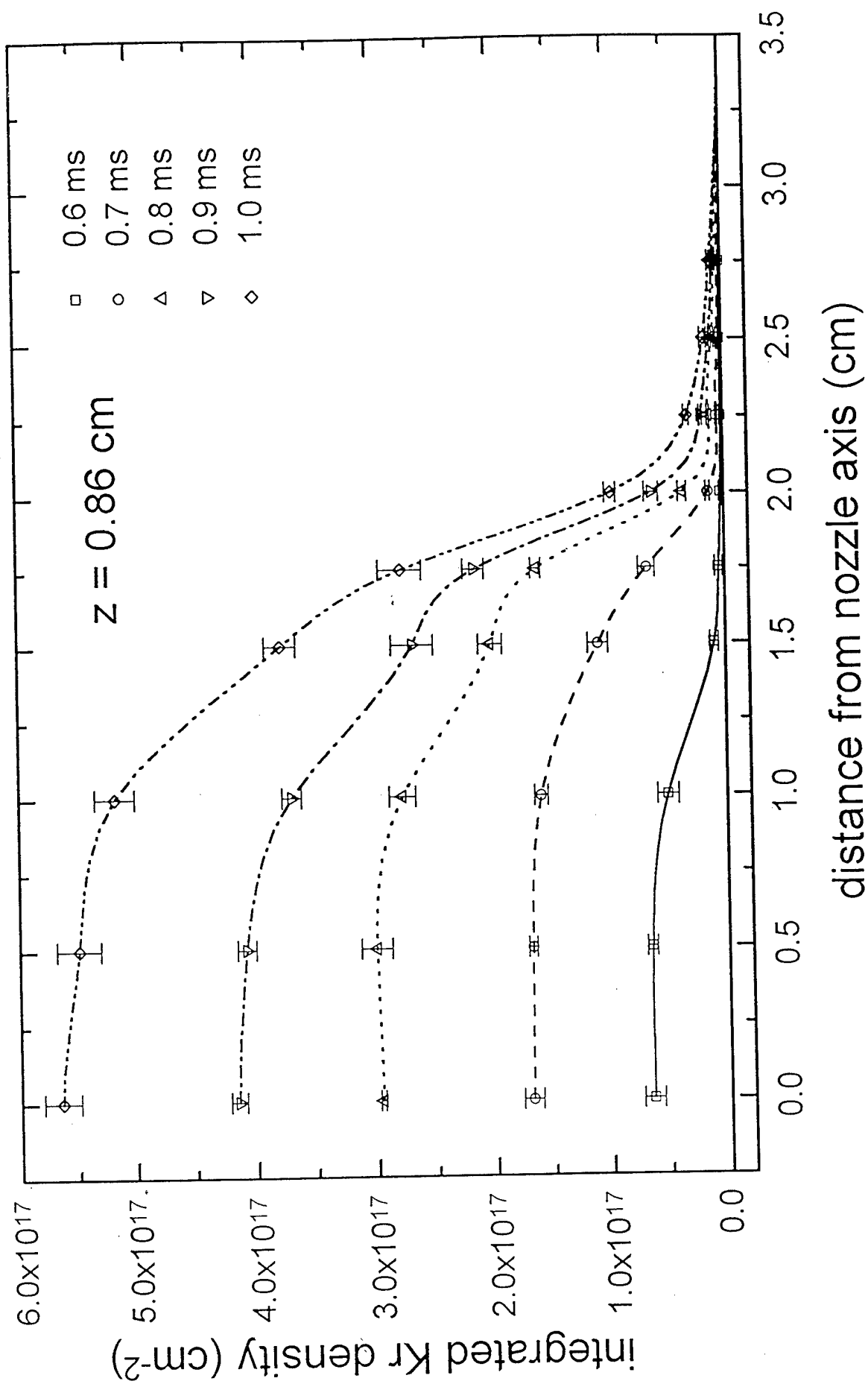


Figure 5. Line-integrated Kr density as a function of  $x$ , at  $z = 0.86 \text{ cm}$ .

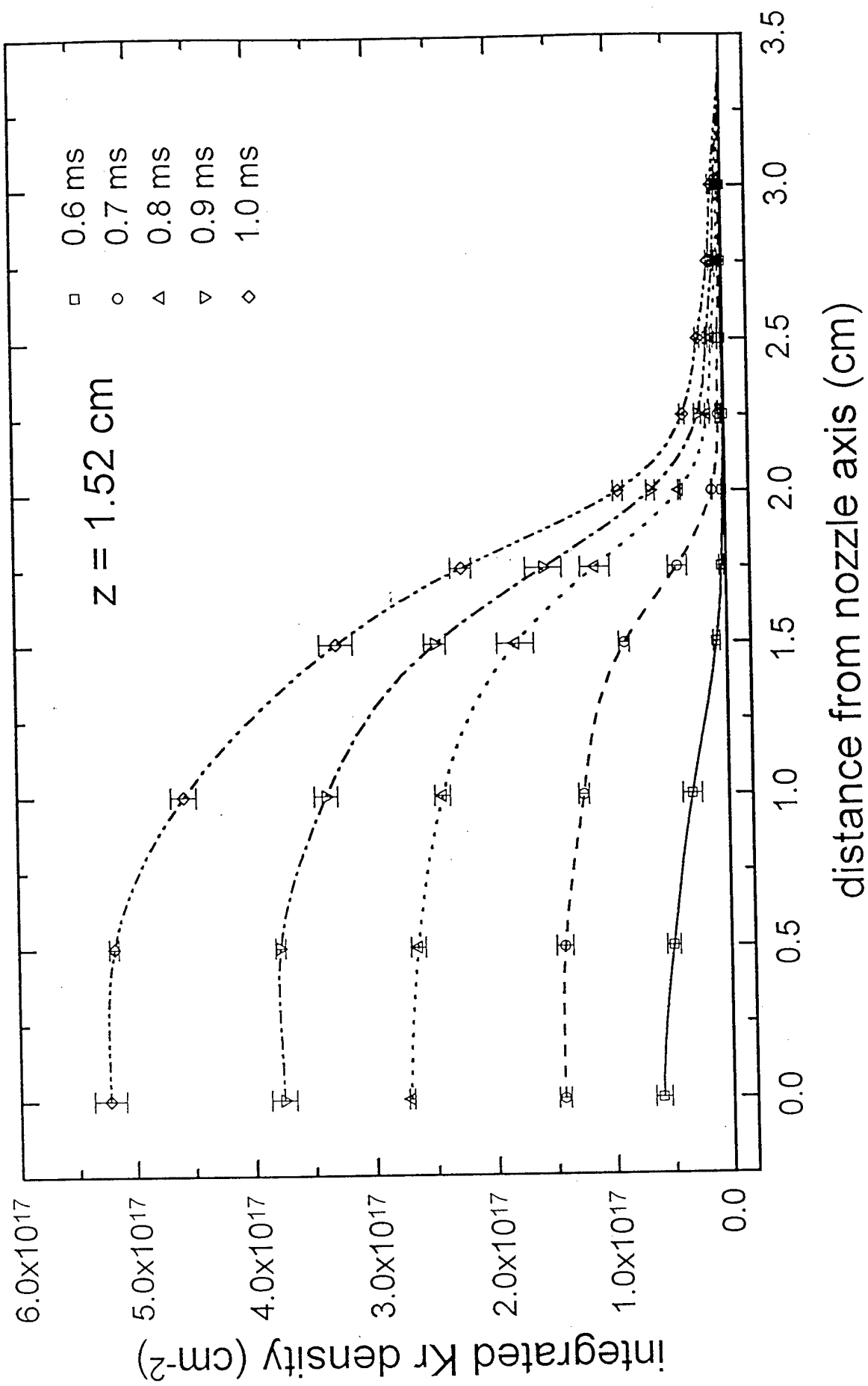


Figure 6. Line-integrated Kr density as a function of  $x$ , at  $z = 1.52 \text{ cm}$ .

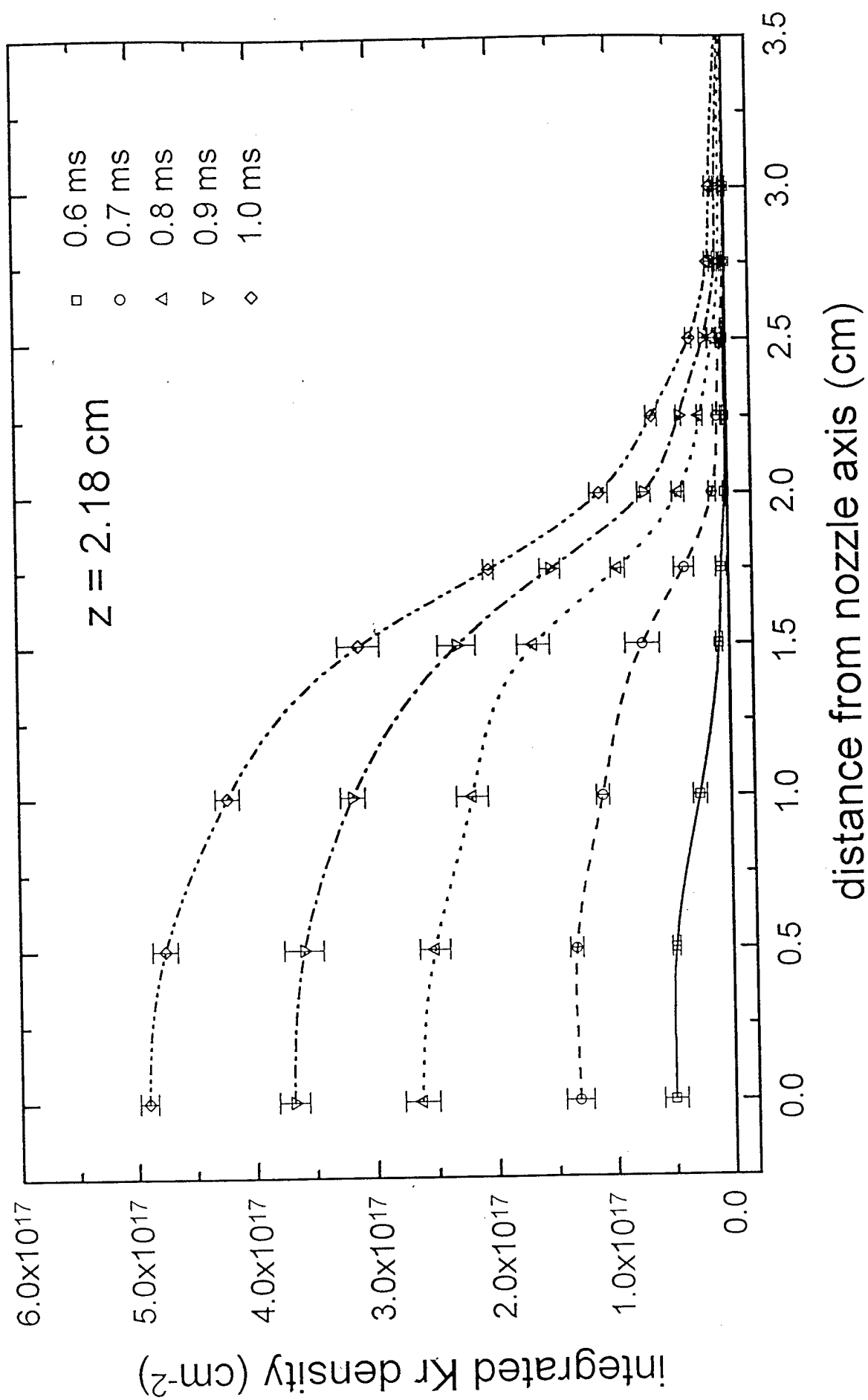


Figure 7. Line-integrated Kr density as a function of  $x$ , at  $z=2.18$  cm.

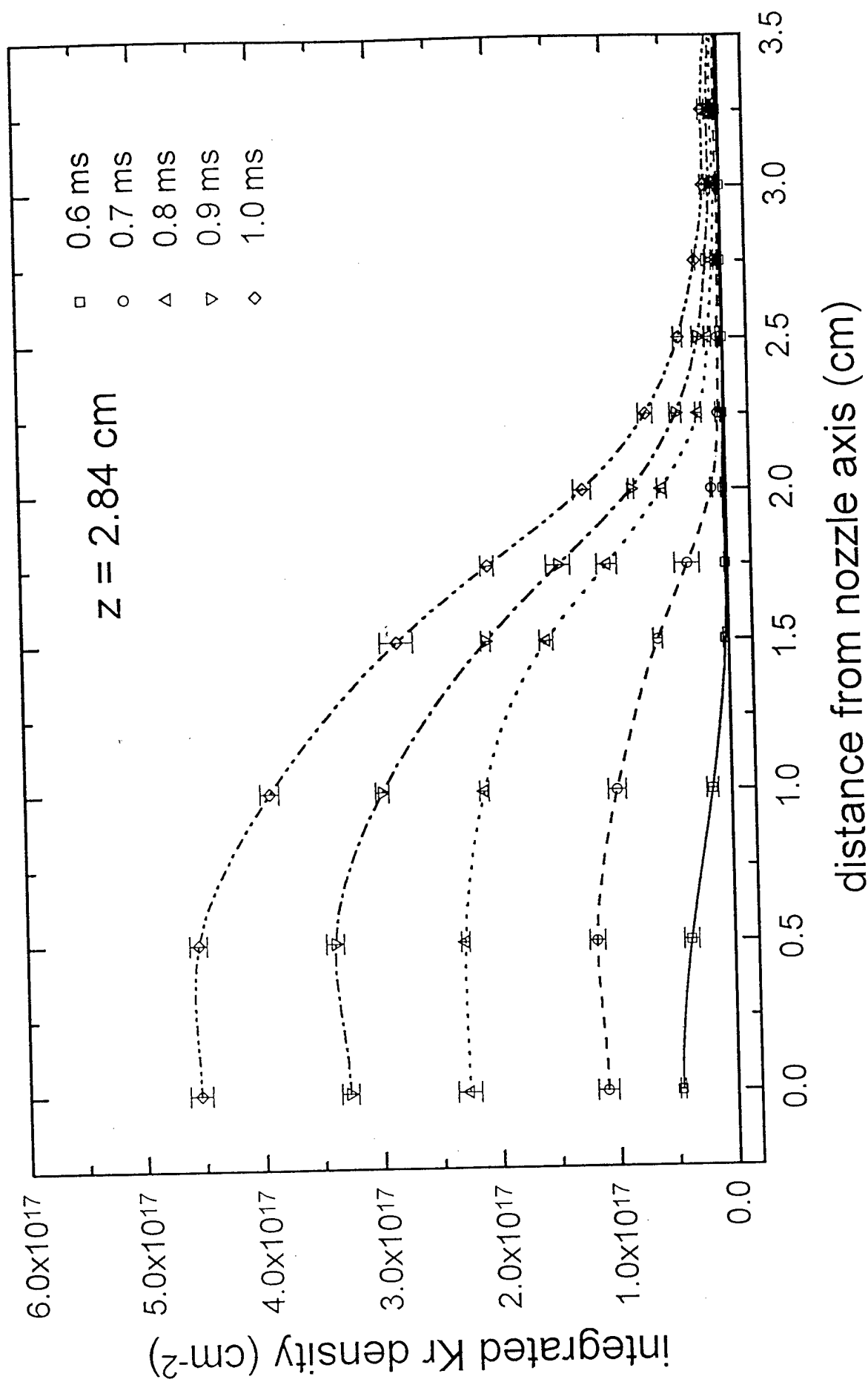


Figure 8. Line-integrated Kr density as a function of  $x$ , at  $z = 2.84 \text{ cm}$ .



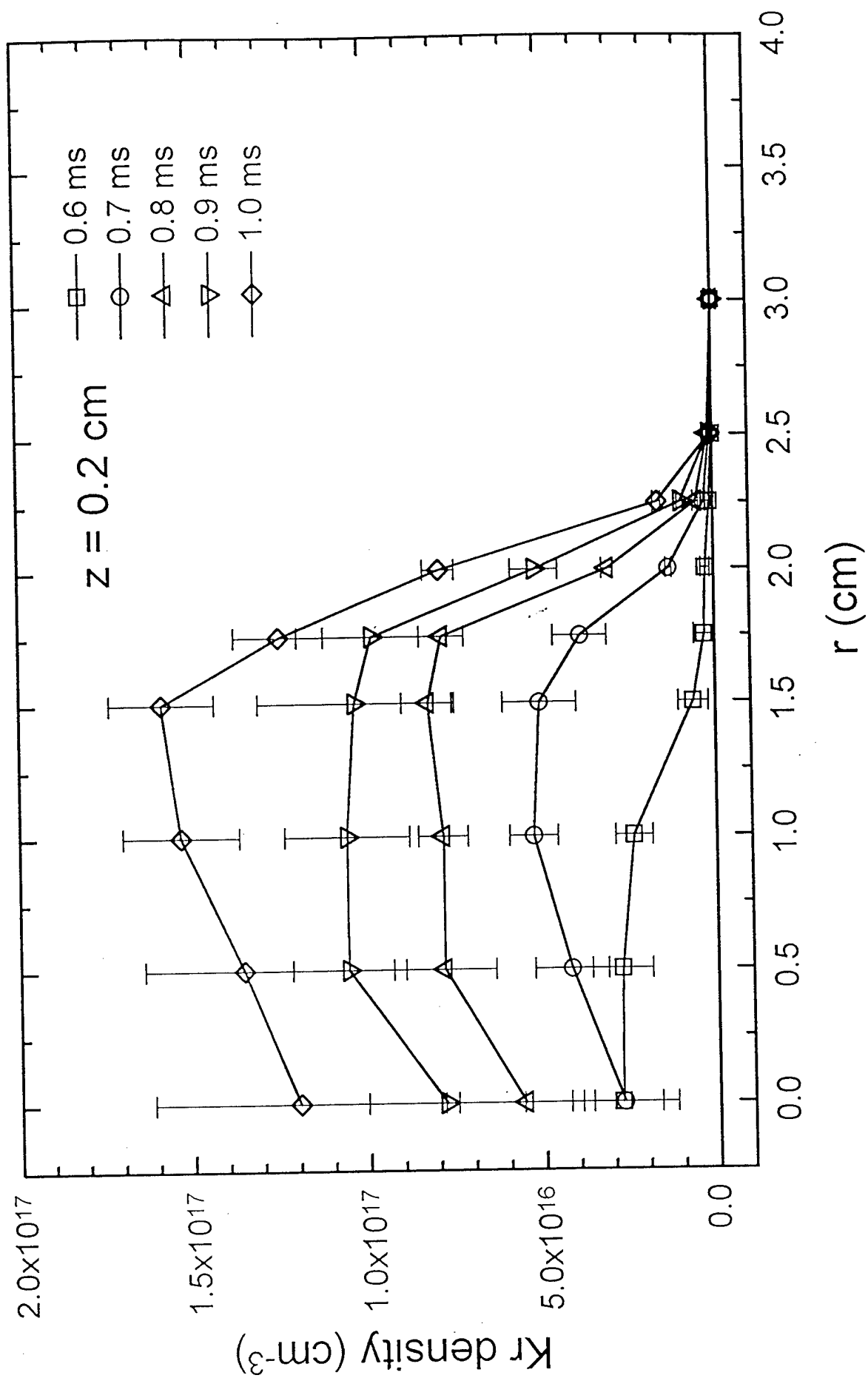


Figure 9. Abel-inverted Kr density as a function of  $r$ , at  $z = 0.2 \text{ cm}$ .

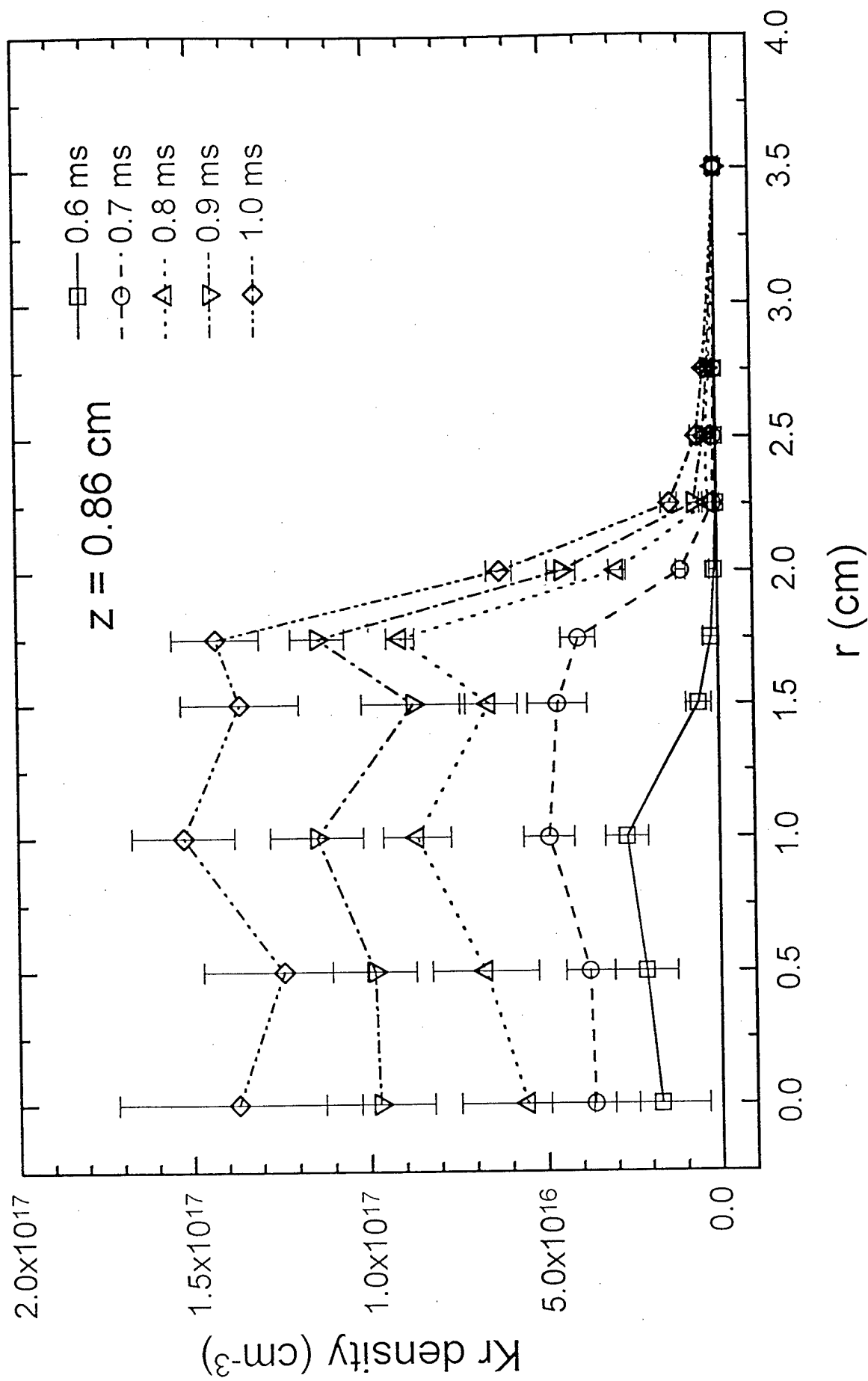


Figure 10. Abel-inverted Kr density as a function of  $r$ , at  $z = 0.86 \text{ cm}$ .

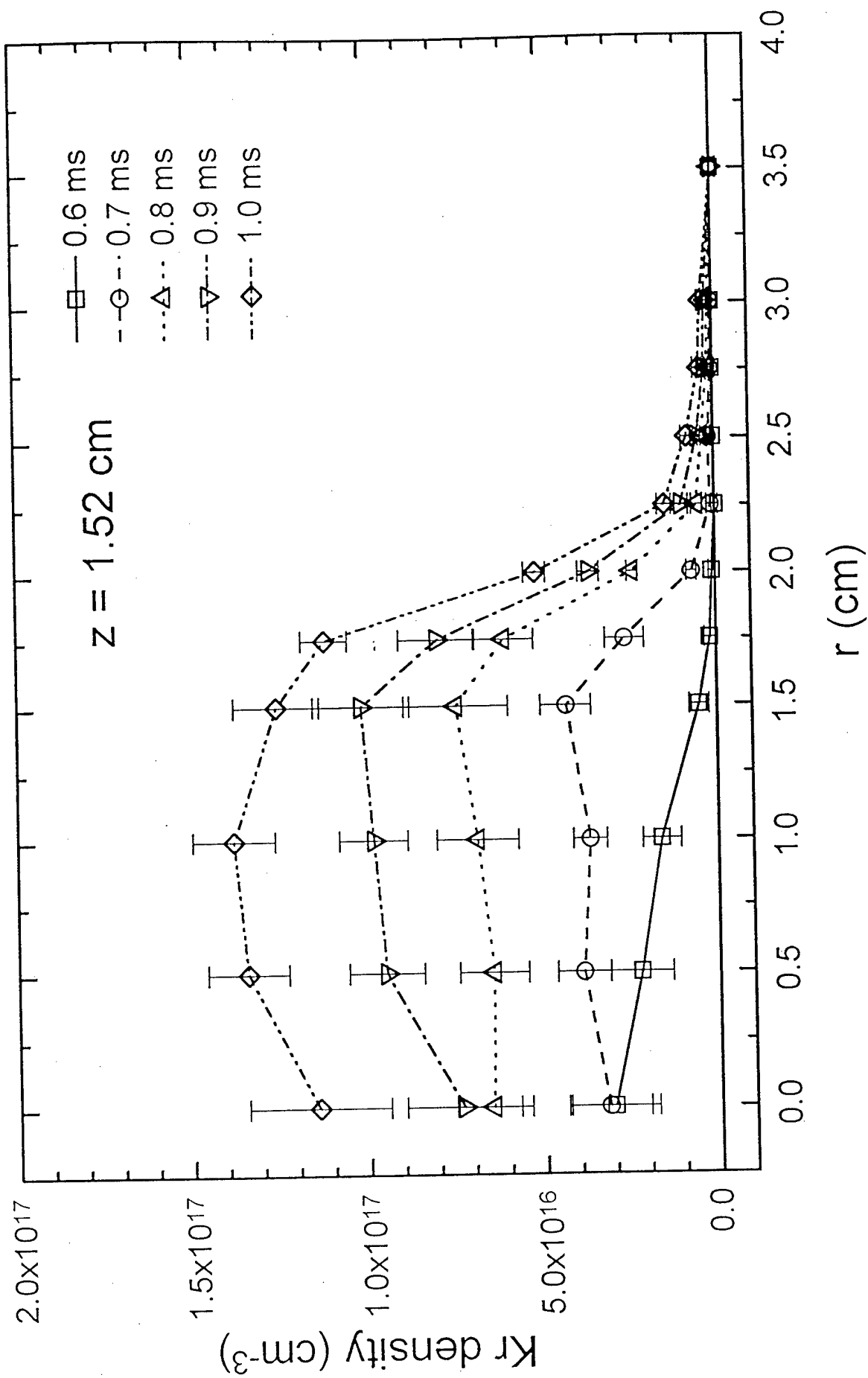


Figure 11. Abel-inverted Kr density as a function of  $r$ , at  $z = 1.52 \text{ cm}$ .

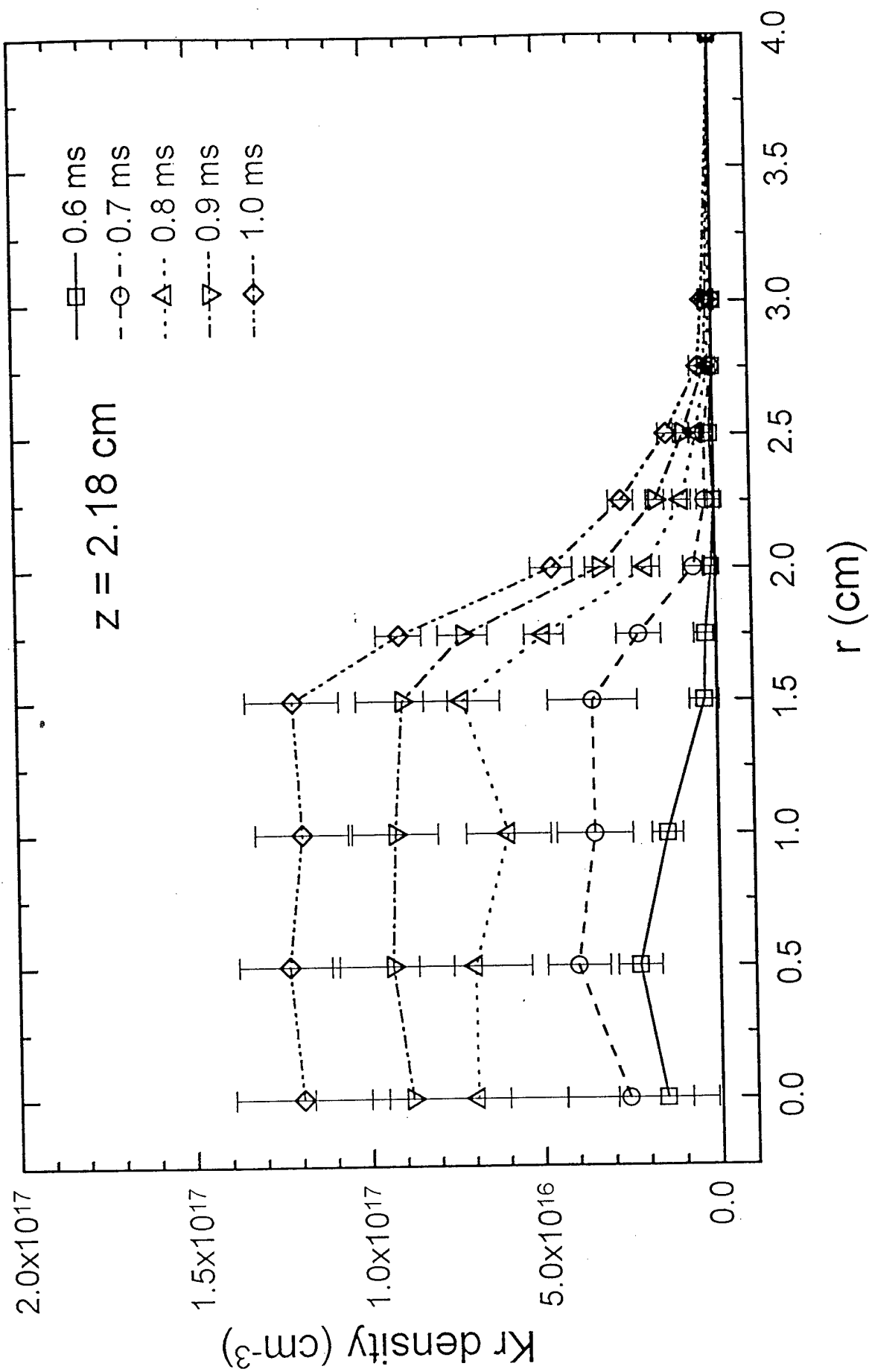


Figure 12. Abel-inverted Kr density as a function of  $r$ , at  $z = 2.18 \text{ cm}$ .

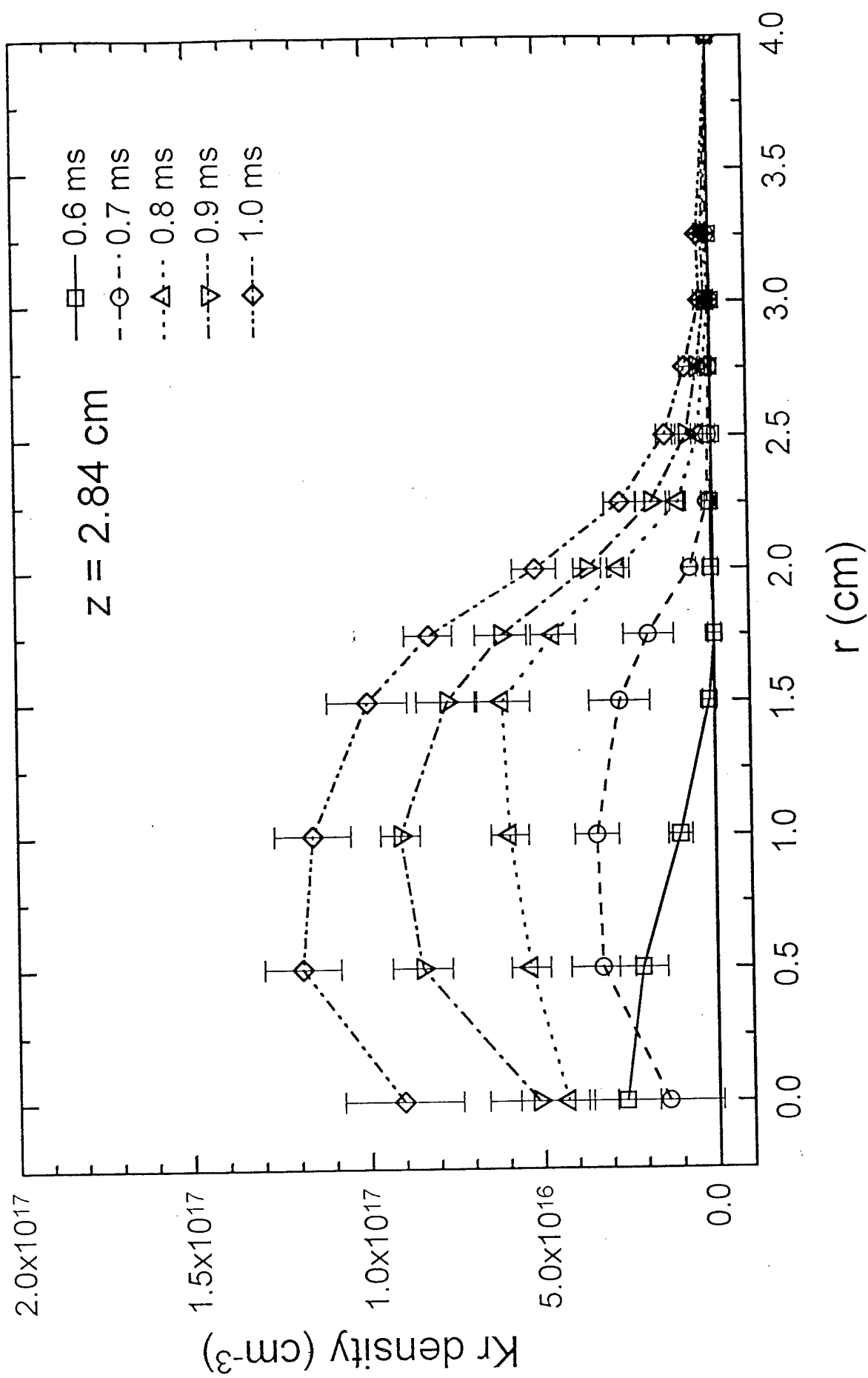


Figure 13. Abel-inverted Kr density as a function of  $r$ , at  $z = 2.84 \text{ cm}$ .

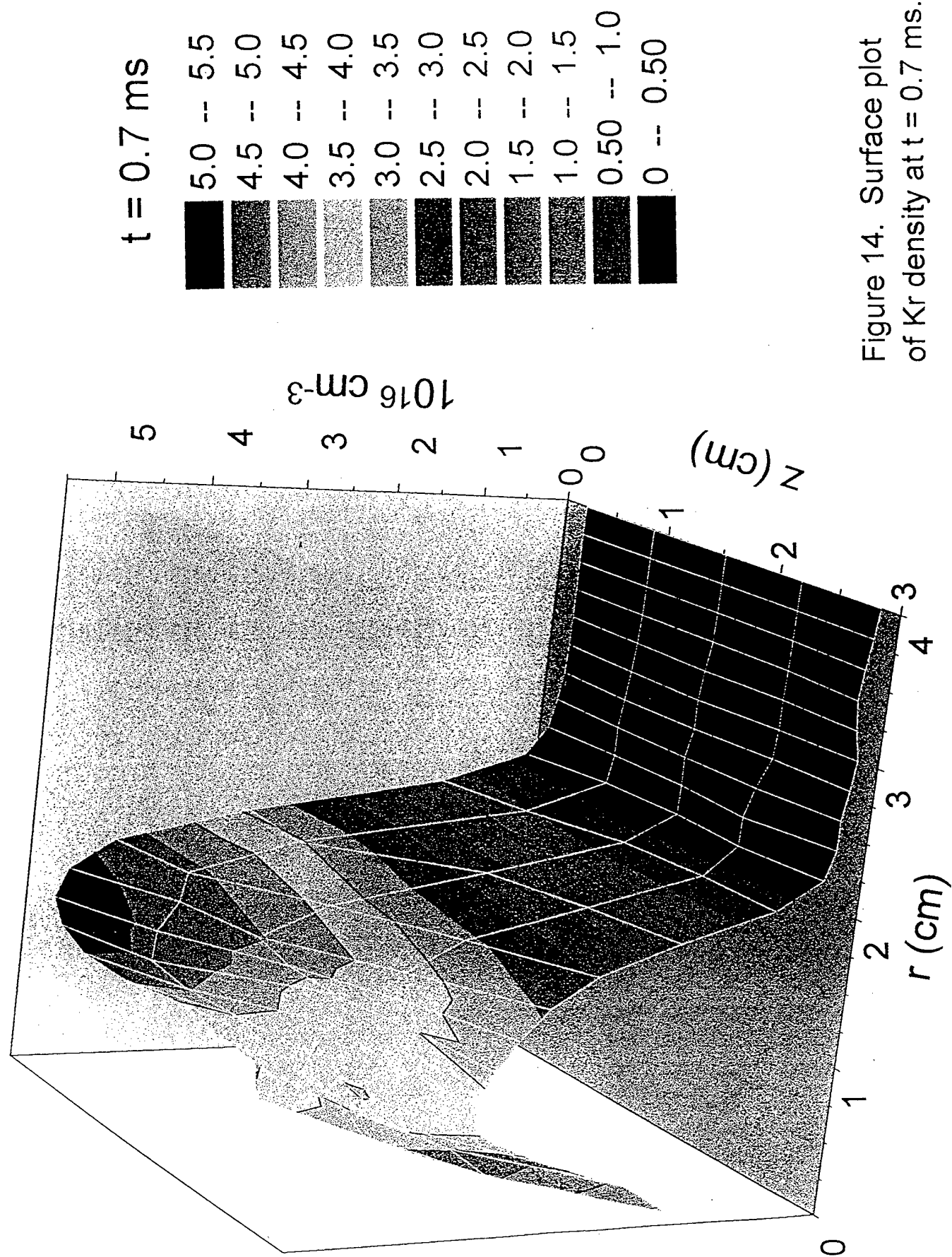


Figure 14. Surface plot of Kr density at  $t = 0.7 \text{ ms}$ .

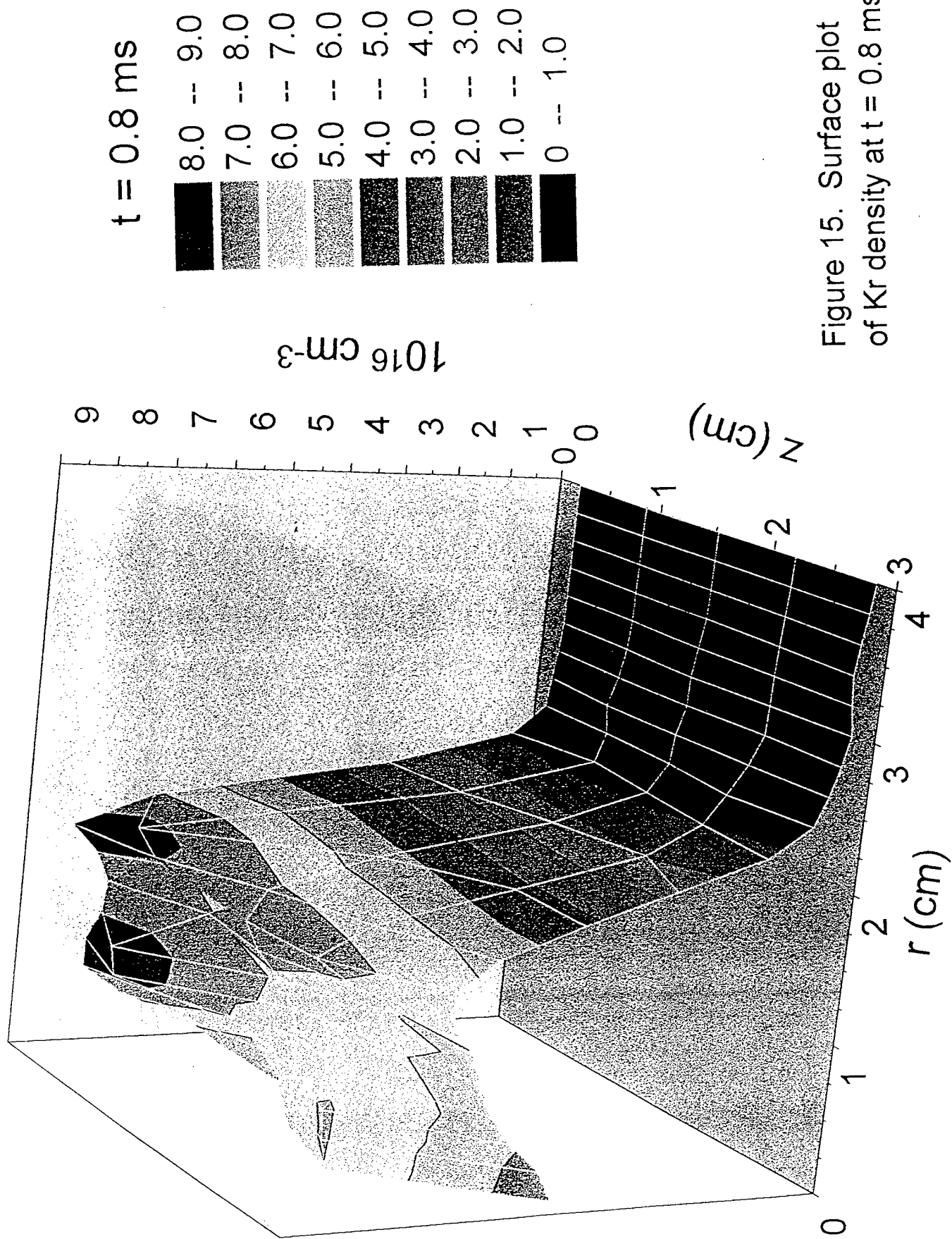


Figure 15. Surface plot of Kr density at  $t = 0.8 \text{ ms}$ .

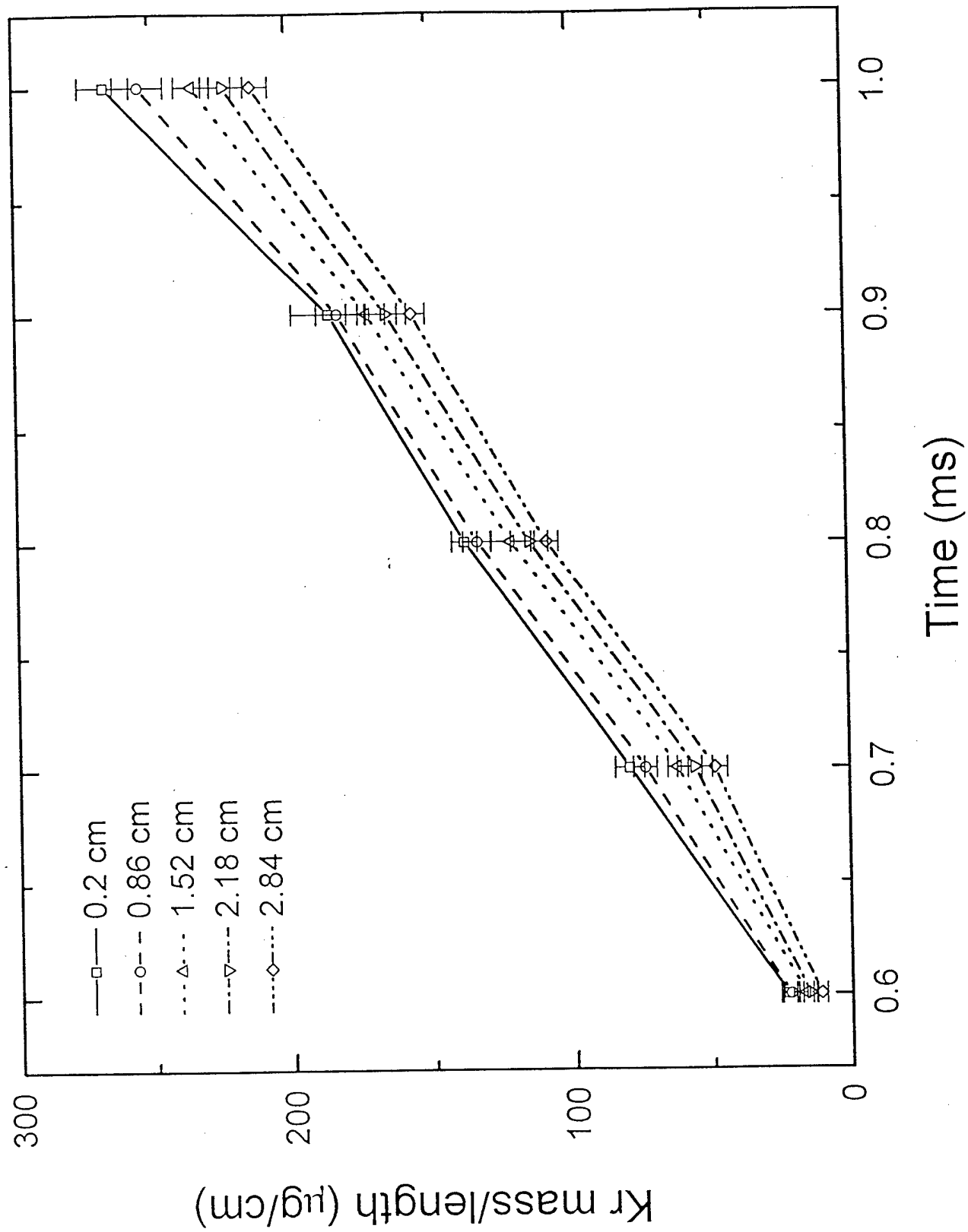


Figure 16. Mass-per-unit-length calculated from the Abel-inverted Kr densities.



PULSED-POWER PHYSICS TECHNOTE NO. 95-22

TITLE: **Experimental and theoretical investigations into 2-D vacuum power-flow**

AUTHORS: Steve Swanekamp<sup>+</sup>, John Grossmann, Dave Hinshelwood<sup>+</sup>, and Bob Commisso

DATE: 21 July, 1995

ABSTRACT: This technote contains the view graphs and notes to a poster that was presented at IEEE Pulsed Power meeting that was held July 10-13, 1995 in Albuquerque, NM. The work presented in this was performed to benchmark vacuum power flow predicted by the PIC code MAGIC with a well diagnosed experiment on Gamble II. Simulations with and without ion emission are compared with each other and to the experimental data. The electron only simulations show large current losses just downstream of the impedance discontinuity. Furthermore it is shown that these losses are determined by the ratio of the gap sizes in the transmission lines. Simulations with ion emission show that the vacuum electron flow transport past an impedance discontinuity is enhanced by the presence of ions. The losses are much more distributed than in the electron only simulations. The experimental data shows a more distributed current loss and is more similar to the case where ion emission is allowed. This suggests that ions may be present and playing a major role in the experiments.

THIS REPORT REPRESENTS  
UNPUBLISHED INTERNAL  
WORKING DOCUMENTS AND  
SHOULD NOT BE REFERENCED  
OR DISTRIBUTED

+JAYCOR, Vienna VA

**Experimental and theoretical investigations into  
~~2-D~~ vacuum power flow**

Steve Swaneekamp\*, John Grossmann, Dave  
Hinshelwood\*, and Bob Commisso  
Plasma Physics Division  
Naval Research Laboratory  
Washington, DC 20375

\*Jaycor, Vienna, VA

## Introduction and motivation

**NRL**

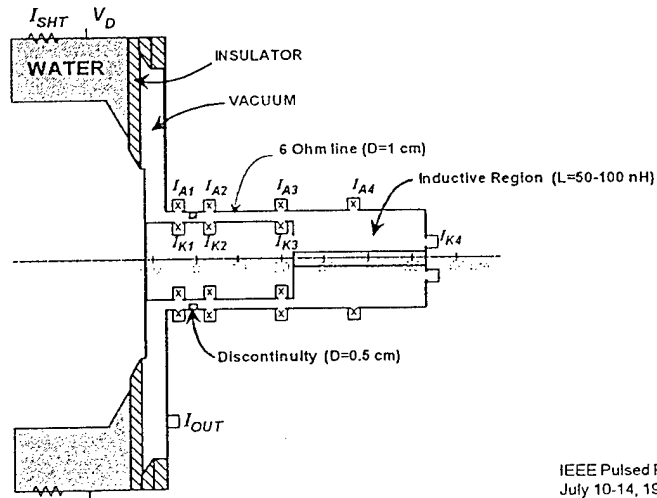
- Power flow in complicated 3-D structures such as convolutes are key to advanced accelerators
- We are modeling simple experiments on Gamble II with the 2-D (MAGIC) and 3-D (Quicksilver) PIC codes
- This paper features the 2-D studies with
  - comparisons with experiment and analytic theory
  - comparisons of results with and without ion emission
- The 3-D work is underway and initial results are presented

IEEE Pulsed Power  
July 10-14, 1995

The goal is to benchmark the 2-D PIC code MAGIC with a well diagnosed experiment on Gamble II. Three-D work is underway but is very preliminary at this point.

## Schematic of power flow experiment on Gamble II

NRL



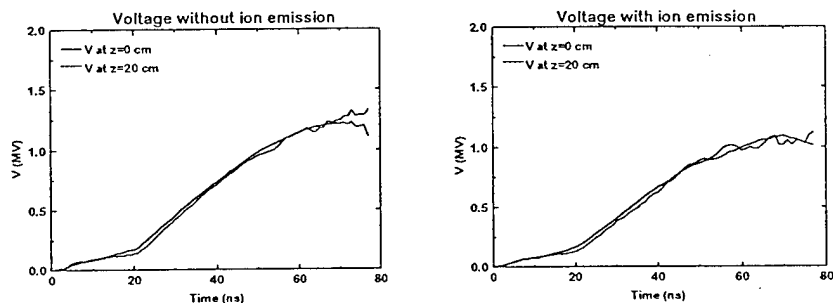
IEEE Pulsed Power  
July 10-14, 1995

This is a schematic of the power-flow experiment that was performed on Gamble II. The goal of these experiments was to benchmark vacuum electron flow predicted by the two-D PIC code MAGIC with a well diagnosed experiment. Vacuum electron flow is launched into the  $6\ \Omega$  line by a localized impedance discontinuity (speed bump) where the A-K gap size decreases from 1 cm to 0.5 cm. Vacuum electron flow is diagnosed by a set of anode and cathode B-dot probes at the locations shown in the figure. The 20 cm long  $6\ \Omega$  line is terminated by a 100 nH inductance which effectively acts as an open circuit during the rise of the current pulse.

## Voltage wave uniform along 6 $\Omega$ line

NRL

- Voltage drops slightly with the emission of ions



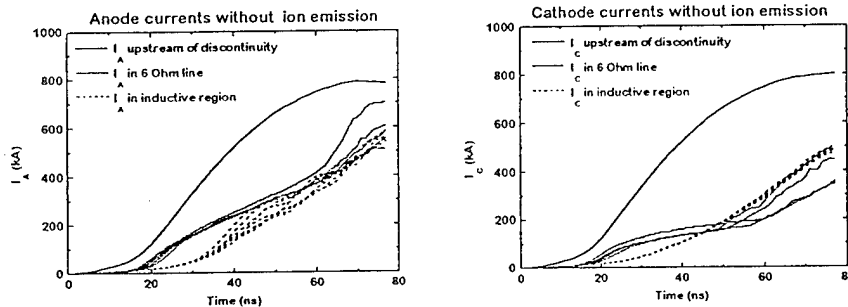
IEEE Pulsed Power  
July 10-14, 1995

Data from the experiments are compared with simulations with and without ion emission from the anode. Ion emission is enabled only in the are allowed only in the 6  $\Omega$  line and electron emission is allowed from the entire cathode. This slide compares the voltage at the speed bump ( $z=0$ ) and at the end of the 6  $\Omega$  line ( $z=20$  cm) from simulations without (left) and with (right) ion emission. Both simulations show a similar voltage at  $z=0$  and  $z=20$  cm. However, the peak voltage is slightly lower for the case when ion emission is allowed than when no ion emission is allowed. This indicates that the inclusion of ions effectively lowers the output impedance.

## Anode and cathode currents without ion emission show large losses near impedance discontinuity

NRL

- Current losses also at transition to inductive region
- Electron retrapping at cathode late in time



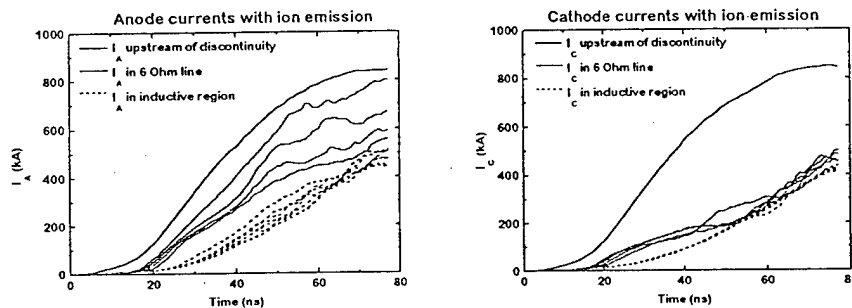
IEEE Pulsed Power  
July 10-14, 1995

This slide shows the anode currents (left) and the cathode currents (right) from the simulation with no ion emission. The largest of the current in both plots is upstream of the speed bump where the simulations show very little vacuum electron flow. The solid curves are taken every 5 cm in the 6  $\Omega$  line and the dashed curves are taken every 5 cm in the inductive load. When there is no ion emission the anode currents show a large current loss in the speed bump and relatively little current loss thereafter. The anode currents also show some current loss at  $z=20$  cm early in time ( $t < 40$  ns). The cathode currents show emission up to 40 ns and then retrapping late in time.

## Anode and cathode currents with ion emission show larger vacuum electron current than without ion emission

NRL

- More current gets past discontinuity and current losses more distributed
- very little retrapping at cathode



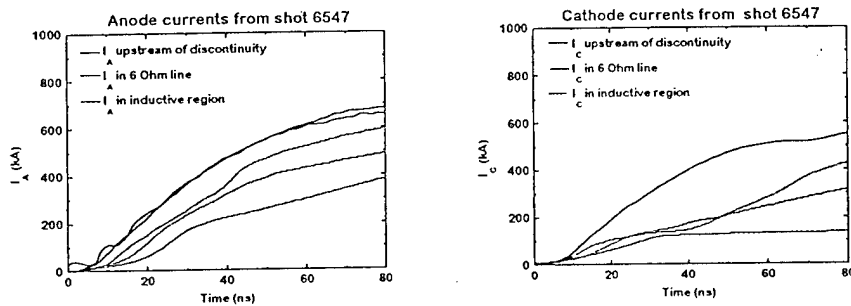
IEEE Pulsed Power  
July 10-14, 1995

This slide shows the anode currents (left) and the cathode currents (right) from the simulation with ion emission. In this case a lot more vacuum electron current is transported past the speed bump and the anode current losses are more distributed. It is speculated that the enhancement of current transport past the speed bump occurs because ions neutralize the electron space charge and allows the magnetic field to better insulate the electrons. Notice that the net current transported to the end of the  $6\ \Omega$  line is lower for this case when compared to the electron only case. It is unknown at this time whether the losses are from electrons or ions. The Child-Langmuir ion current at 1 MV is about 127 kA which is not enough to explain the current loss. However, only a factor of 3 enhancement over Child-Langmuir is necessary to explain the current losses observed in the simulation. The cathode currents for this case is similar to the electron only case except that no retrapping occurs late in time.

## Anode and cathode currents from Gamble II shot 6547

NRL

- Current losses distributed along the anode.
- Measurements more similar to the simulations with ion emission



IEEE Pulsed Power  
July 10-14, 1995

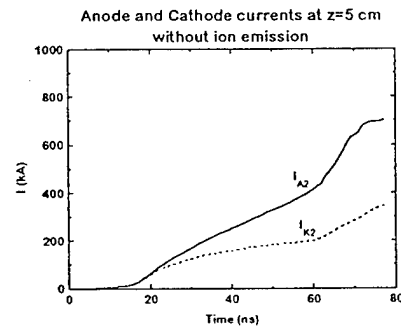
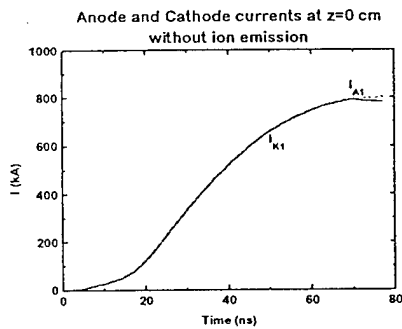
This slide shows the measured anode and cathode currents. The anode currents show a distributed current loss that looks more like the case with ion emission than the electron only case. The cathode current measurements are difficult to interpret. This may be indicative of the difficulty making cathode current measurements.



## Anode and cathode currents near the discontinuity with no ion emission

NRL

- Anode and cathode currents show vacuum electron flow launched at the discontinuity



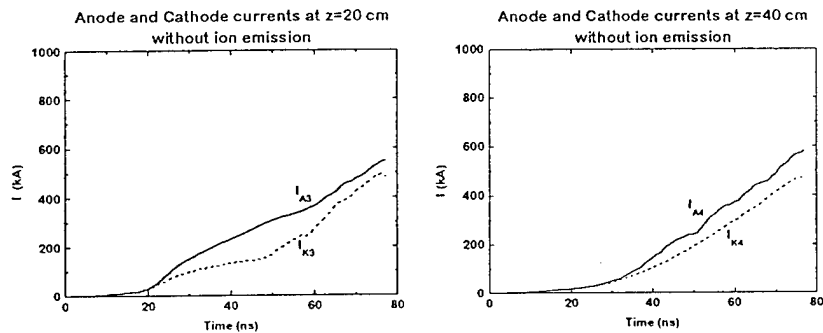
IEEE Pulsed Power  
July 10-14, 1995

This slide shows anode and cathode currents from the electron only simulation at  $z=0$  and  $z=5$  cm where measurements were made in the experiment.

## Anode and cathode currents near the inductive region with no ion emission

NRL

- Anode and cathode currents show that vacuum flow is lost along the  $6\ \Omega$  line



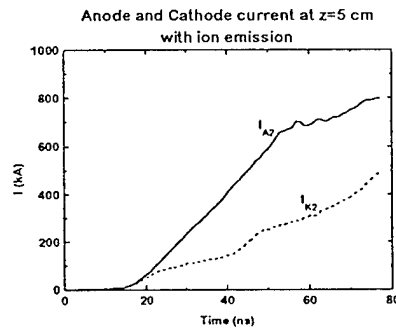
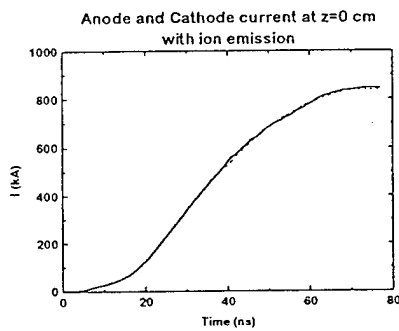
IEEE Pulsed Power  
July 10-14, 1995

This slide shows anode and cathode currents from the electron only simulation at  $z=20$  and  $z=38$  cm where measurements were made in the experiment.

## Anode and cathode currents near the discontinuity with ion emission

NRL

- Ion emission partially neutralizes the electron space charge and allows for enhanced electron current transport past the discontinuity



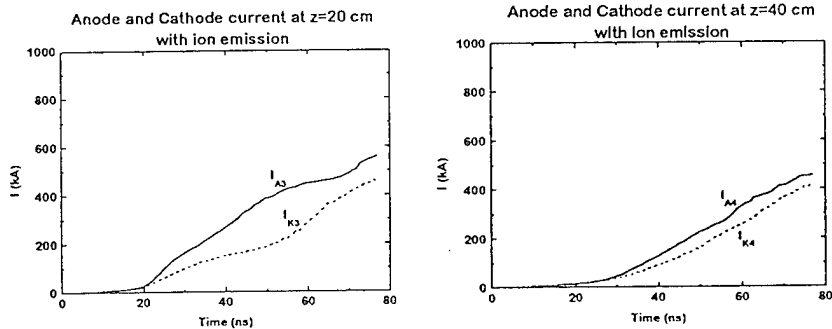
IEEE Pulsed Power  
July 10-14, 1995

This slide shows anode and cathode currents from simulation with ion emission at  $z=0$  and  $z=5$  cm. We see that the vacuum electron flow makes up a much larger fraction of the total current in this case than compared to the electron only case.

## Anode and cathode currents near the inductive region with ion emission

NRL

- Vacuum current losses much larger along the  $6\ \Omega$  line with ion emission than with no emission
- How much current loss is due to ions ?



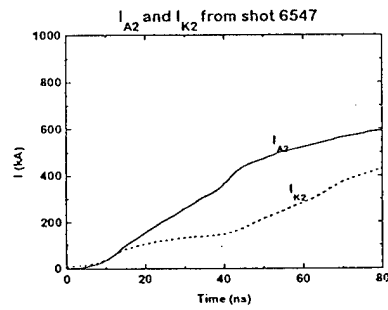
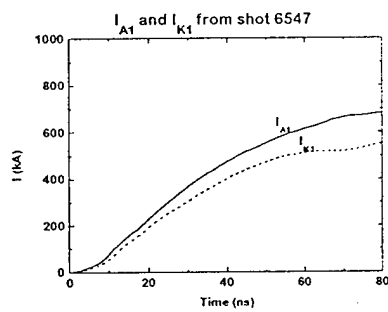
IEEE Pulsed Power  
July 10-14, 1995

This slide shows anode and cathode currents from simulation with ion emission at  $z=20$  and  $z=38$  cm. We see that the vacuum electron flow at the end of the  $6\ \Omega$  line and at  $z=38$  cm is similar to that of the electron only case. However, the total current reaching the end of the  $6\ \Omega$  line is slightly lower when ion emission is included.

## Anode and cathode currents near the discontinuity from Shot 6547

NRL

- Data shows vacuum current upstream of discontinuity

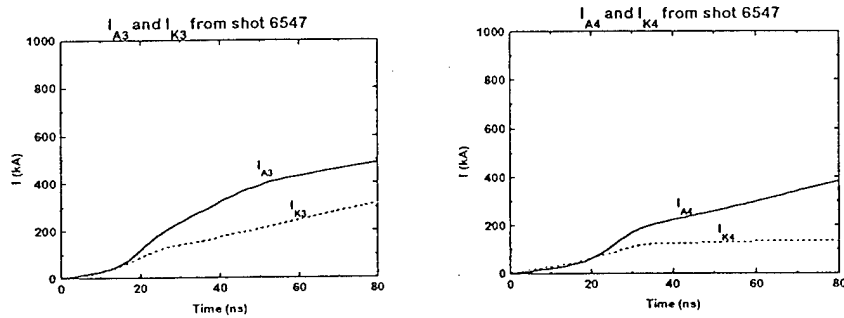


IEEE Pulsed Power  
July 10-14, 1995

This slide shows the measured anode and cathode currents at  $z=0$  and  $z=5$  cm from the Gamble II experiments.

## Anode and cathode currents near the inductive region from Shot 6547

NRL



IEEE Pulsed Power  
July 10-14, 1995

This slide shows the measured anode and cathode currents at  $z=20$  and  $z=38$  cm from the Gamble II experiments.

## The size of the electron cloud can be obtained from the critical current formula

**NRL**

- An estimate for the radial extent for the electron flow can be obtained from the critical current formula
  - when electron flow is fully saturated the formula gives an estimate for the minimum gap size for magnetic insulation

$$D_{\text{crit}} = \frac{1.6 (8500) (\gamma^2 - 1)^{1/2} r_c}{I_A}$$

IEEE Pulsed Power  
July 10-14, 1995

One way to analyze the simulations is from the critical current formula. This is an estimate of the electron Larmor radius and is the minimum A-K gap size necessary to achieve magnetic insulation of the vacuum electron flow. Here  $\gamma \cong 1 + 2V$  is the relativistic factor and  $r_c$  is the cathode radius. When the electron flow fills the A-K gap it is said to be critically insulated or the line is said to be fully saturated.

## Flow impedance a useful concept to analyze MITL flows

**NRL**

- Mendel's definition of Flow impedance is:

$$Z_{\text{flow}} = \frac{V}{(I_A^2 - I_C^2)^{1/2}}$$

- $I_A$ ,  $I_C$ , and  $V$  are local anode and cathode current and voltage

- For a localized impedance discontinuity Mendel's Flow impedance is:

$$Z_{\text{flow}}^{\text{BUMP}} = \frac{V}{(I_{\text{Aup}}^2 - I_{\text{Cdn}}^2)^{1/2}}$$

- $I_{\text{Aup}}$  is the upstream anode current,  $I_{\text{Cdn}}$  is the downstream cathode current,  $V$  is the local voltage

IEEE Pulsed Power  
July 10-14, 1995

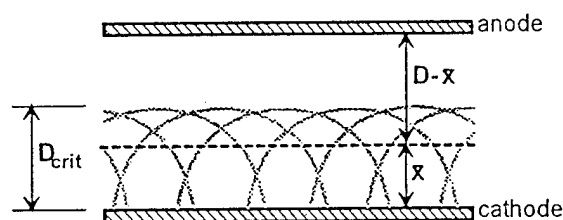
Another concept that is useful in describing magnetically insulated flows is that of the flow impedance which has been developed by Cliff Mendel. The local definition is given by the first equation. In this equation the local voltage, anode and cathode are used. When there is a localized impedance discontinuity in the line such as at the speed bump an alternate definition can be used where the local anode and cathode currents are replaced by the anode current upstream of the discontinuity and the cathode current downstream of the discontinuity.



## Critical gap is a measure of electron Larmor radius, Flow impedance related to centroid of electron space charge

NRL

- Flow impedance is the vacuum wave impedance between the charge centroid and the anode
  - when electron flow is fully saturated  $D_{crit}=D$  and  $Z_{flow}=Z_{vac}/2=30 D/r_c$



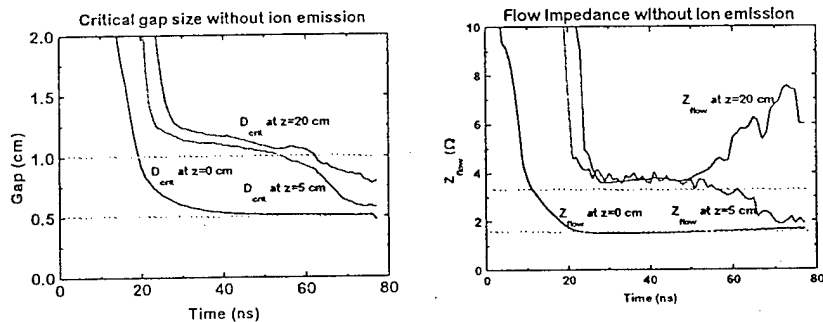
IEEE Pulsed Power  
July 10-14, 1995

To gain some physical insight into the meaning of flow impedance and its relation to the critical gap size consider the cartoon shown in this slide. It can be shown that the flow impedance related to the centroid of the electron charge. In Cartesian coordinates the flow impedance is the vacuum wave impedance between the centroid of the charge and the anode. If the centroid of the charge is close to the cathode then the flow impedance is close to the vacuum wave impedance of the transmission line. If the flow is critically insulated one would expect the centroid to be 1/2 way between the the anode and cathode and the flow impedance should be 1/2 the vacuum wave impedance of the line. Therefore, flow impedance gives you an idea of the average position of the electron charge. However it is limited because it tells you nothing about the details of the distribution. Indeed there are many distributions that have the same charge centroid and therefore the same flow impedance.

## Electron flow is fully saturated in the discontinuity and 6 $\Omega$ line

NRL

- As electrons becomes better insulated Larmor radius decreases
- Decrease in Flow impedance at  $z=5$  indicates that the centroid of charge moves closer to the anode



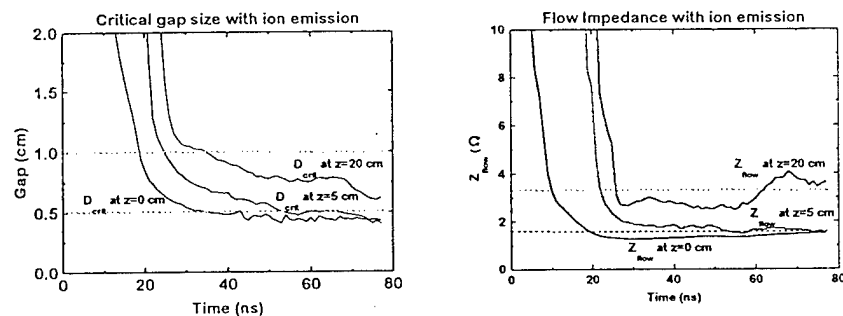
IEEE Pulsed Power  
July 10-14, 1995

This slide shows the critical gap size and the flow impedance for the electron only simulation at several points in the 6  $\Omega$  line. The dashed curve in the critical gap plot indicates the physical A-K gap in the speed bump ( $D=0.5$  cm) and in the 6  $\Omega$  line ( $D=1$  cm). The dashed curve on the flow impedance plot is  $1/2$  the vacuum wave impedance of each of the various sections. Notice that after an initial transient period the electron Larmor radius in each section of the 6  $\Omega$  line is equal to the A-K gap indicating that the electron flow is critically insulated. However, late in time the Larmor radius is reduced as the inductive section fills with magnetic field and the short circuit load begins to express itself. The flow impedance plot shows a similar picture. Late in time the flow impedance rises at  $z=20$  cm indicating that the centroid of the charge moves closer to the cathode. The flow impedance at  $z=5$  cm decreases indicating that the centroid of the electron space charge moves closer to the anode. Evidence for this behavior will be seen in later plots.

## Ion emission causes significant change in both the critical gap and flow impedance

NRL

- Since flow impedance is smaller with ion emission this indicates that the charge centroid moves closer to anode
- Critical gap size is smaller with ions



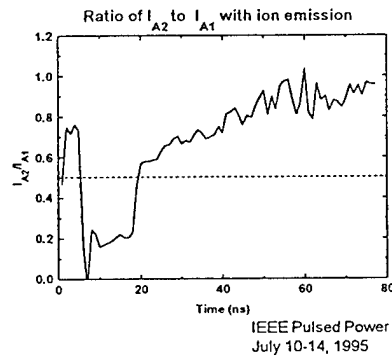
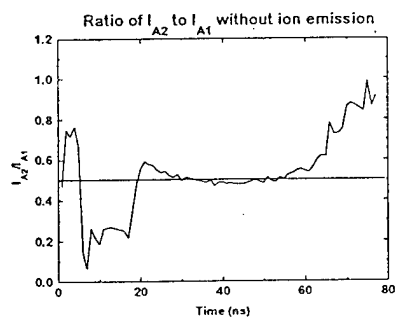
IEEE Pulsed Power  
July 10-14, 1995

This slide shows plots of the critical gap size and flow impedance when ion emission is included. The critical gap plots show that the electron Larmor radius decreases significantly when ion emission is allowed. This means that the electrons are better insulated and can lead to enhanced vacuum electron transport. The flow impedance is smaller than the flow impedance of the electron only case. This means that the centroid of the electron charge is closer to the anode when ion emission is allowed. Evidence for this will be seen in subsequent plots.

## Current loss at the discontinuity is the ratio of the gap sizes

**NRL**

- When both the discontinuity and the line just downstream are fully saturated the critical current formula says  $I_{A2}/I_{A1}=D_1/D_2=0.5$

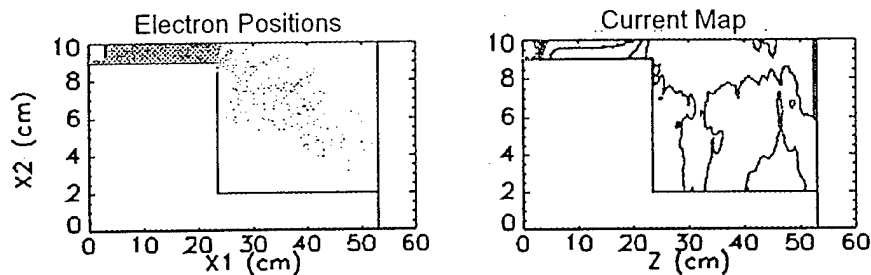


When two sections of transmission line are fully saturated then the critical current formula predicts that ratio of the anode currents on either side of the impedance discontinuity is given by the ratio of the A-K gap sizes. For the example given in this technote the ratio of the gap sizes is 0.5. We see that for the electron only case where the discontinuity and the  $6\ \Omega$  line are fully saturated  $1/2$  the current is lost in the discontinuity. The situation is improved when ion emission is allowed since electrons are better insulated and much more of the current makes it past the discontinuity.

## Electron positions and current map with no ion emission at $t=25$ ns

NRL

- As critical current is exceeded magnetic insulation is quickly achieved in the  $6\ \Omega$  line



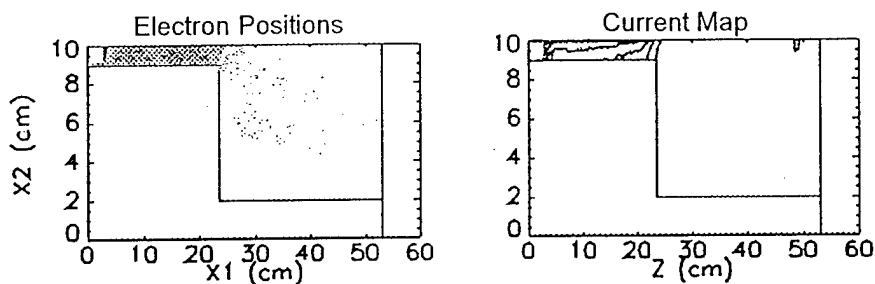
IEEE Pulsed Power  
July 10-14, 1995

This slide shows the electron positions and the current map for the electron only case just after the electron flow becomes magnetically insulated in the  $6\ \Omega$  line. Notice that there is a large current loss near the speed bump and current flow is more or less parallel to the electrodes in the  $6\ \Omega$  line. At this time the inductive region is effectively an open circuit and all vacuum flow is lost to the anode near the end of the  $6\ \Omega$  line.

## Electron positions and current map with ion emission at $t=25$ ns

**NRL**

- Early in time the electron positions and current map for the ion emission case are similar to the no emission



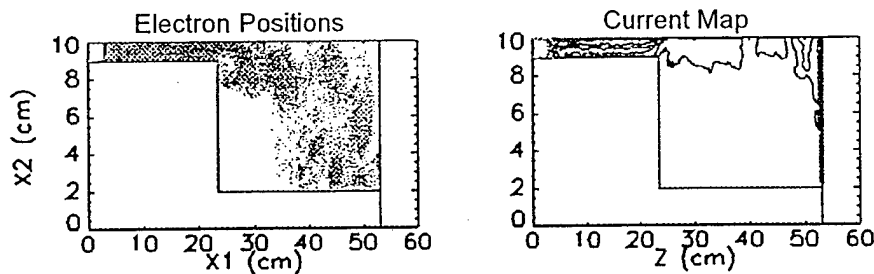
IEEE Pulsed Power  
July 10-14, 1995

This slide shows the electron positions and the current map early in time for the case with ion emission. This plot looks very similar to the electron positions and current flow pattern for the electron only case. This is understandable since very little ion emission has occurred at this time.

## Electron positions and current map with no ion emission at $t=35$ ns

NRL

- While current is rising the inductive region effectively acts as an open circuit
- Electrons flow parallel to the cathode



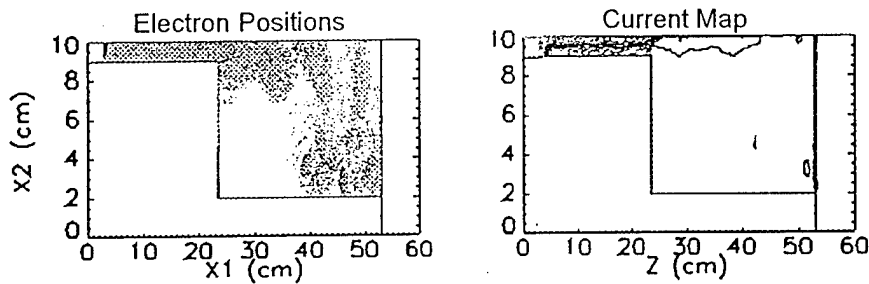
IEEE Pulsed Power  
July 10-14, 1995

This slide shows the electron positions and the current map at  $t=35$  ns for the electron only case. We see that current is more or less uniformly distributed radially in the  $6\ \Omega$  line downstream of the speed bump. Almost all the vacuum flow is lost at the end of the  $6\ \Omega$  line since the inductive section is still effectively a open circuit. We also see the initial stages of the formation of vortices in the inductive section. However, there is very little little current associated these vortices. These vortices are similar to those reported by B. Church et al., Phys. Plasmas 2, 1837 (1995).

## Electron positions and current map with ion emission at $t=35$ ns

NRL

- Electron current more concentrated near the anode with ion emission than without ion emission



July 10-14, 1995

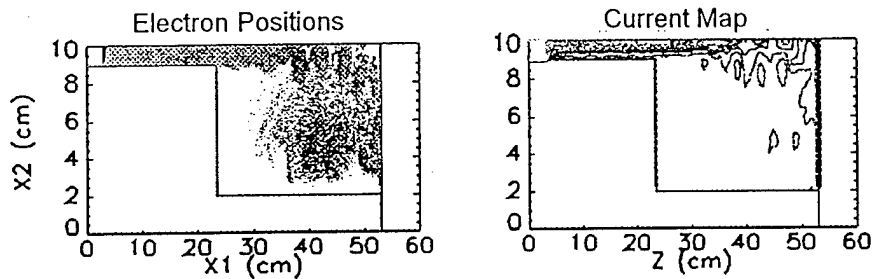
This slide shows the electron positions and the current map at  $t=35$  ns for the case with ion emission. In contrast to the electron only case, we can see somewhat higher currents just downstream of the speed bump. This current is more concentrated near the anode where the ion density is largest. Since electrons are more concentrated near the anode we expect the flow impedance to be smaller than  $1/2$  the vacuum wave impedance. As in the electron only case almost all the vacuum flow is lost at the end of the  $6 \Omega$  line since the inductive section is still effectively a open circuit.



## Electron positions and current map without ion emission at $t=45$ ns

NRL

- Electron flows along the anode in the inductive region
- Large space charge fields allow electrons to  $E \times B$  drift in vortices



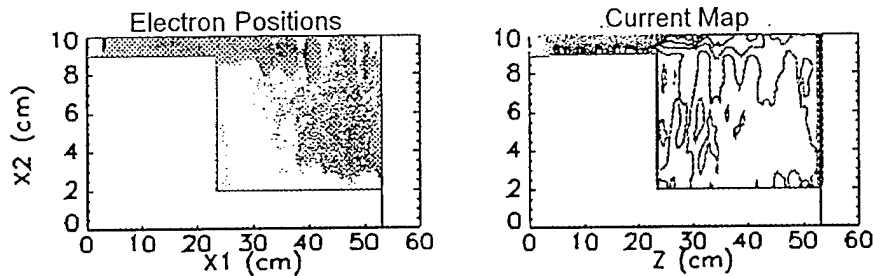
IEEE Pulsed Power  
July 10-14, 1995

This slide shows the electron positions and the current map at  $t=45$  ns for the electron only case. Some current now flows into the inductive region and most of this flow is concentrated near the anode.

## Electron positions and current map with ion emission at $t=45$ ns

NRL

- Current flows along the anode significantly higher with ion emission than without ion emission
- Electron flows enhanced in regions where ions exist. What happens is ions are emitted along entire anode?



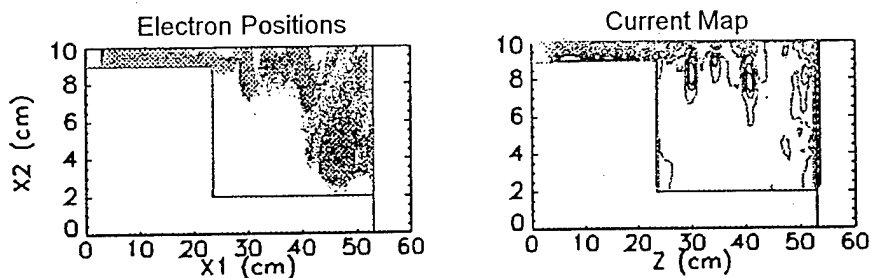
IEEE Pulsed Power  
July 10-14, 1995

This slide shows the electron positions and the current map at  $t=45$  ns for the case when ion emission is allowed. In contrast to the electron only case, the current maps show much higher currents near the anode along the entire length of  $6 \Omega$  line. The current distribution is more concentrated near the anode where the concentration of ions is largest. However, there appears to be large losses of vacuum current near the end of the  $6 \Omega$  line. This is probably due to the fact that no ion emission was enabled in the inductive region thereby losing the space charge neutralization necessary for enhanced transport.

## Electron positions and current map without ion emission at $t=55$ ns

**NRL**

- Electrons flow closer to the cathode near the end of the  $6\ \Omega$  line and closer to the anode near the discontinuity



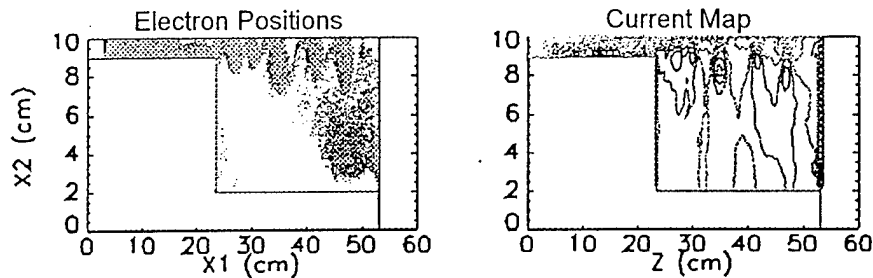
IEEE Pulsed Power  
July 10-14, 1995

This slide shows the electron positions and the current map at  $t=55$  ns for the electron only case. From the current map we can see that the vacuum electron flow near the end of the  $6\ \Omega$  line is more concentrated at the cathode. The flow impedance theory predicts that  $Z_{\text{flow}}$  should be larger than  $1/2$  the vacuum wave impedance. The current map also shows that the flow is more concentrated near the anode just downstream of the speed bump. Since the centroid of charge is closer to the anode the flow impedance should be smaller than  $1/2$  the vacuum wave impedance.

## Electron positions and current map with ion emission at $t=55$ ns

NRL

- Currents along the anode near the discontinuity higher with ion emission (i.e. more current gets past the discontinuity)
- Currents near the inductive section comparable with and without ions

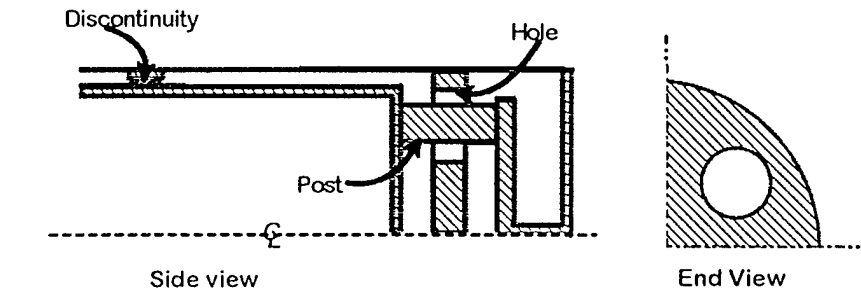


IEEE Pulsed Power  
July 10-14, 1995

This slide shows the electron positions and the current map at  $t=55$  ns for the case when ion emission is allowed. This is similar to the picture for ion emission at  $t=45$  except that the enhanced current transport into the  $6\ \Omega$  line is more pronounced.

Three-D power flow simulations have been  
initiated for comparison with  
future Gamble II experiments

NRL



ALL RIGHTS RESERVED  
July 10-14, 1995

In the future we hope to field a three dimensional geometry on Gamble II. This geometry will be very similar to the 2-D geometry used in this work except that a 3-D structure will be placed at the end of the 6  $\Omega$  line. The 3-D PIC code QUICKSILVER will be used to study the electron flow through this 3-D structure. The goal is to benchmark QUICKSILVER with a well diagnosed experiment.

## Important results and conclusions

**NRL**

- Simulations with no ion emission show that the current loss at an impedance mismatch is determined by the ratio of gap sizes.
  - flow impedance downstream not determined by smallest gap in the system
  - critical gap good estimate for gap size when flow is fully saturated
- Simulations show that ion emission can reduce electron space charge and result in enhanced current transport
  - centroid of electron charge moves closer to the anode and flow impedance decreases
  - electron Larmor radius decreases because enhanced current transport leads to higher magnetic fields
- We have begun 3-D simulations which show similar results to the 2-D simulations

IEEE Pulsed Power  
July 10-14, 1995

TITLE:           **MODELING OF DM1 PERFORMANCE**

AUTHOR(S):   **R.J. Commisso, J.R. Boller, D.V. Rose,\* S.B. Swanekamp,\* F.C. Young, P.F. Ottinger, B.V. Weber, and G. Cooperstein.**

DATE:           18 July 1995

ABSTRACT:       Talk presented at the 1995 Pulsed Power Conference, Albuquerque, NM, 11 -13 July, 1995. The paper reviews the effort at NRL to model the performance of DM1. BERTHA, CLYTRAN, and 2-D MAGIC are used to understand the coupling of a POS to an e-beam load and suggest ways to optimize system performance.

**THIS REPORT REPRESENTS UNPUBLISHED  
INTERNAL WORKING DOCUMENTS AND SHOULD NOT BE REFERENCED OR  
DISTRIBUTED WITHOUT CONSENT OF AUTHORS**

## MODELING OF DM1 PERFORMANCE

R.J. Commisso, J.R. Boller, D.V. Rose,\* S.B. Swanekamp,\*  
F.C. Young, P.F. Ottinger, B.V. Weber, and G. Cooperstein

Pulsed Power Physics Branch  
Plasma Physics Division  
Naval Research Laboratory  
Washington, DC

10th International Pulsed Power Conference,  
11 July 1995  
Albuquerque, NM

\*JAYCOR, Vienna VA

Good afternoon. Today I will be reviewing the status of the effort at NRL to model DECADE Module 1, DM1. DM1 performance and DECADE will be discussed by Peter Sincerny in more detail tomorrow afternoon in Paper 12-3, Pulsed Generators.

I want to take this opportunity to thank the staff at PI, including R. Schneider, J. Goyer, D. Kortbawi, and P. Sincerny for their cooperation in providing the data and answering many questions concerning the data and DM1 operation.



## OUTLINE

NRL

- Analyze DM1 performance with the goals of :
  - understanding POS load interaction
  - optimizing system performance
- Circuit Analysis using BERTHA transmission line code:
  - links pulsed power driver (pre-POS measured waveforms) to the load electrical power delivery from a circuit point of view
  - requires POS circuit model and power flow assumptions:
    - » 2 types of POS model
    - » assumes vacuum inductance between POS and load
- Radiation analysis using CLYTRAN:
  - links the load electrical power delivery to measured dose
- 2-D PIC analysis using MAGIC:
  - links POS to load, i.e., power flow
  - assumes simplifying model for POS/plasma

Pulsed Power  
11 July 1995

The purpose of this effort is to try to improve our understanding of POS/load coupling and to suggest ways the DM1 performance can be improved. Three computational tools are used. In this talk, I will be discussing the results from calculations using these tools. The circuit code, BERTHA (developed at NRL) links the pulsed power upstream of the POS to the electrical power delivery to the load from a purely circuit point of view. For this, the POS is modeled as a circuit element. Also, the inductance between the POS and load is assumed to be the vacuum inductance.

The Monte Carlo, electron/photon transport code CYLTRAN (developed at SNL) is used to link the measured bremsstrahlung radiation to the energy delivered to the e-beam diode, which was not measured in the experiment.

Finally, the 2-D PIC code, MAGIC, is used to better understand the details of the POS coupling to the load.

We will be concentrating on a representative shot from a series of shots done specifically for benchmarking DM1 performance.

## POS AND LOAD MODEL ASSUMPTIONS

NRL

### • POS:

- $Z_{\text{flow}} = V_{\text{sw}} / (I_{\text{UA}}^2 - I_{\text{DC}}^2)^{1/2}$ 
  - » rises linearly to  $1.38 \Omega$  in 28 ns;
  - 1/e decay in 55 ns

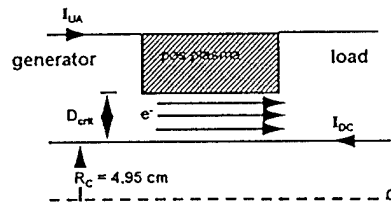
OR

- »  $Z_{\text{flow}}(t) = 30 D_{\text{crit}}(t) / R_C^{**}$
- $D_{\text{max}} = 0.23 \text{ cm}$
- $I_{\text{UA}}$  at opening = 1.39 MA ( $\tau_C = 216 \text{ ns}$ )
- only  $I_{\text{DC}}$  counted as load current!!!

### • Assume vacuum POS-load inductance, 63 nH

### • Diode:

- $R_C = 6.35 \text{ cm}$  (5" diam),  $\Delta R = 0.3 \text{ cm}$
- closure velocity =  $3.5 \text{ cm}/\mu\text{s}$
- initial AK, 0.5 to 2.5 cm



\* C.W. Mendel, et al., J. Appl. Physics **46**, 3731 (1992)

\*\*S.B. Swanekamp, et al., J. Appl. Physics **5**, 2468 (1994)

Pulsed Power  
11 July 1995

The circuit element model for the POS uses the  $Z_{\text{flow}}$  concept of C. Mendel. The biggest advantage of this model is that it allows one to differentiate between cathode and anode current. However,  $Z_{\text{flow}}$  itself must still be prescribed as a function of time. We have assumed two methods to prescribe this time dependence. In the first, we assume a linear rise followed by an exponential decay for  $Z_{\text{flow}}$ . This decay is relatively new and we feel is needed to reproduce the measured upstream waveforms. The values shown here give the best results when compared with the electrical measurements on the generator side, or upstream of the POS. The other method uses the measured upstream waveforms to calculate, using the critical current formula, an effective gap for magnetic insulation,  $D_{\text{crit}}(t)$ , from which  $Z_{\text{flow}}$  is calculated as  $30D_{\text{crit}}(t)/R_C$ . It has been shown that for saturated flow, which is the basic assumption, these two methods are nearly identical. The second method can reproduce details in the waveforms because it uses the measured waveforms to determine  $Z_{\text{flow}}$ . From an energetics point of view, there isn't much difference in these two methods, so to save time we will concentrate mostly on the first method.

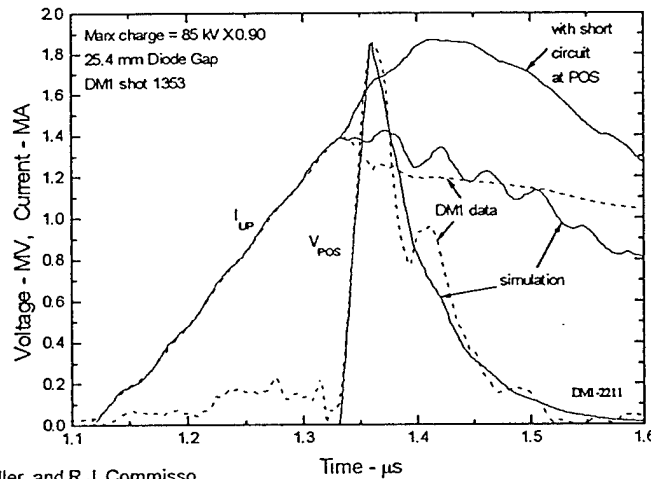
In both cases, the maximum POS gap is about 2.3 mm and we assume the gap forms at the POS cathode. However, these features are often not reproducible from shot-to-shot.

The full vacuum inductance is assumed.

Details of the diode model can be found in the paper. For now, note that the gap closure for large AK gaps is  $3.5 \text{ cm/ms}$  (results not very sensitive to this choice) and the initial gap was varied between 0.5 and 2.5 cm, the latter being the actual value used in the experiment.

## SIMULATION OF MEASURED CIRCUIT PARAMETERS IS ACCEPTABLE

NRL



Shown here, as a function of time for DM1 shot 1353, are the measured (on anode at POS) current into the POS and the inferred (transmission line correction) POS voltage in dotted lines. The BERTHA simulation for this shot is shown in solid lines. Note that the DM1 circuit model and the BERTHA code has been successfully checked against the PI model, as well as measured waveforms further upstream in the system.

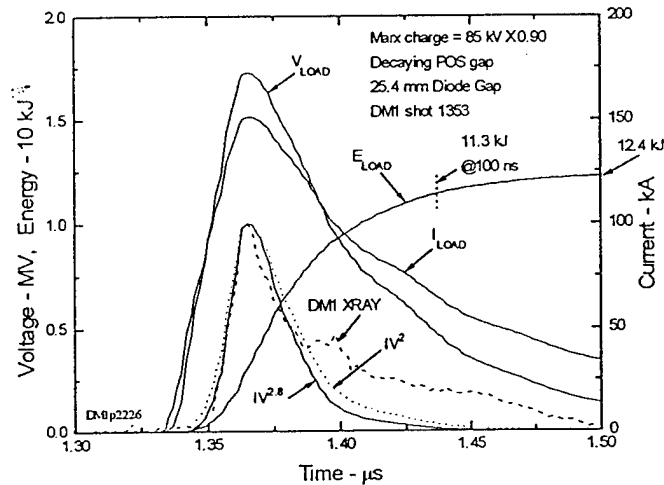
The time dependence of  $Z_{\text{flow}}$  used here is the linear rise followed by an exponential decay. The circuit model predicts the upstream waveforms very well, at least until the time of POS opening. The second method gives the second peak in the POS voltage, but the discrepancy in the upstream current is only partially decreased. This second peak is not seen in all the data shots. We are investigating the discrepancy in the current now.

Both methods for prescribing the time history of  $Z_{\text{flow}}$  infer that the POS gap decreases in size after opening.

The full POS conduction gives 1.8 MA.

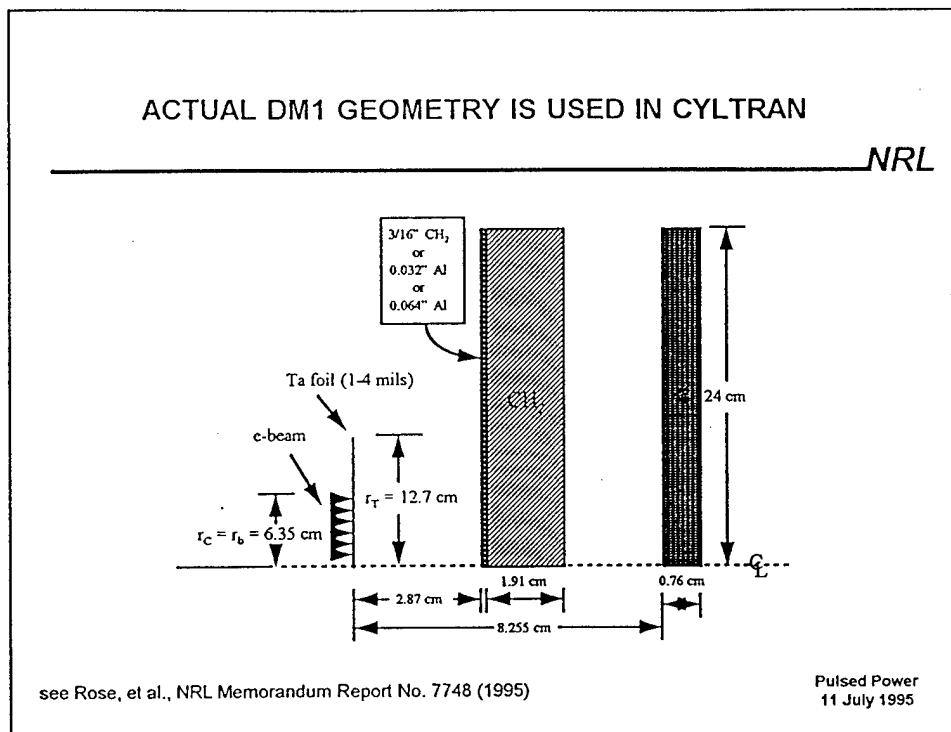
# REASONABLE X-RAY SIGNAL RESULTS FROM PREDICTED LOAD PARAMETERS

NRL



Shown here, as functions of time, are the calculated load voltage and load current for an initial diode AK gap of 25.4 mm, along with measured and inferred x-ray signals. The  $IV^2$  or  $IV^{2.8}$  is only an approximation to the real x-ray signal, and there is no *a priori* reason to assume either should fit, especially at late times. The load energy reaches 11.3 kJ after 100 ns and eventually gets to 12 kJ when the measured x-ray pulse reaches zero. We do not have measured electrical load waveforms to compare with these calculations. The peak load voltage is inferred from de-convolution of a multi-channel, filtered PIN detector array fielded by PI. The peak value here of 1.7 MV agrees with that measurement. We do have measured dose, which can be used to infer a total energy delivered to the load using the electron/photon transport code CYLTRAN.

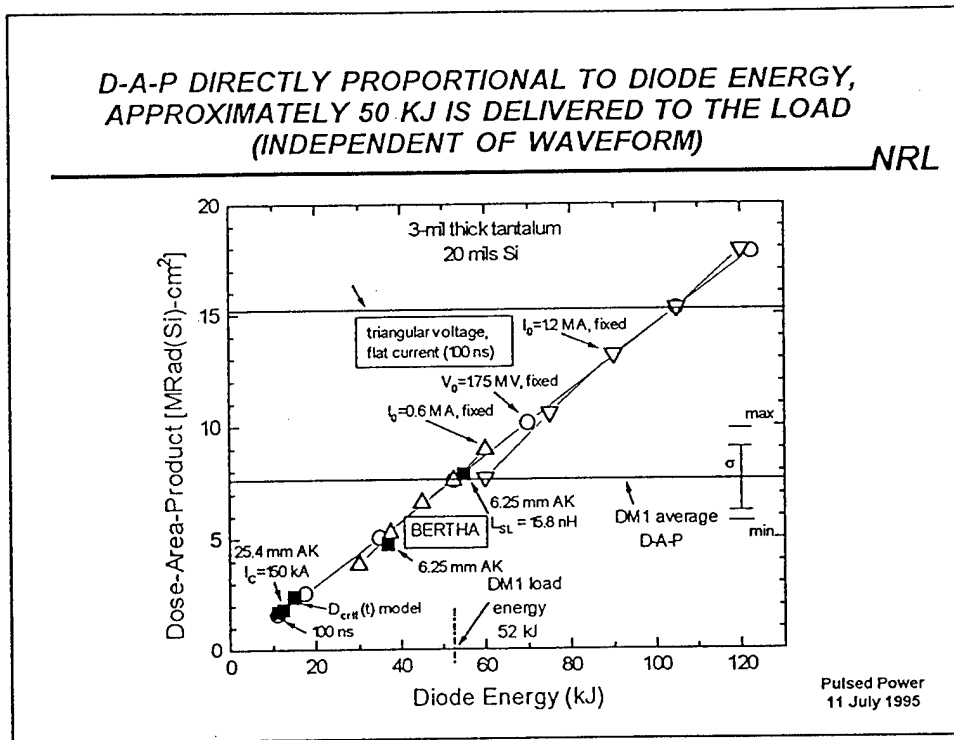
The inferred diode impedance,  $1.75 \text{ MV} / 0.15 \text{ MA} = 11.7 \Omega$ , is very close to the canonical geometrical diode impedance,  $30D_{AK}/R = 12 \Omega$ .



This is a figure showing the geometry used in the CYLTRAN calculations. This geometry is identical to the experimental configuration, except that an array of  $\text{CaF}_2$  and  $\text{LiF}$  TLDs were used in place of the silicon.

Her  $r_c$ ,  $r_b$ , and  $r_T$  are the e-beam diode cathode radius, the e-beam radius, and the tantalum converter radius, respectively.

The electron beam angular distribution was a  $\cos^2\theta$ , which is mostly forward directed [see NRL Memo Report No. 7748 (1995)]. The calculated dose is relatively insensitive to this distribution. The Ta foil thickness used for most of the calculations and data was 3 mil, which turns out to be about optimum for this configuration to produce dose in 20 mils of silicon. The beam stop for the data considered here was a 3/16" thick sheet of polyethylene followed by 3/4" slab of polyethylene.



This is a plot of the CYLTRAN-calculated dose-area-product (DAP) in 20 mils of Si as a function of diode energy for a variety of cases. The horizontal line between 7 and 8 MRad (Si)-cm<sup>2</sup> is the average measured DAP for the DM1 data set. The standard deviation, maximum, and minimum DAP values are also shown. The desired DAP goal for DECADE operation is a factor of two higher.

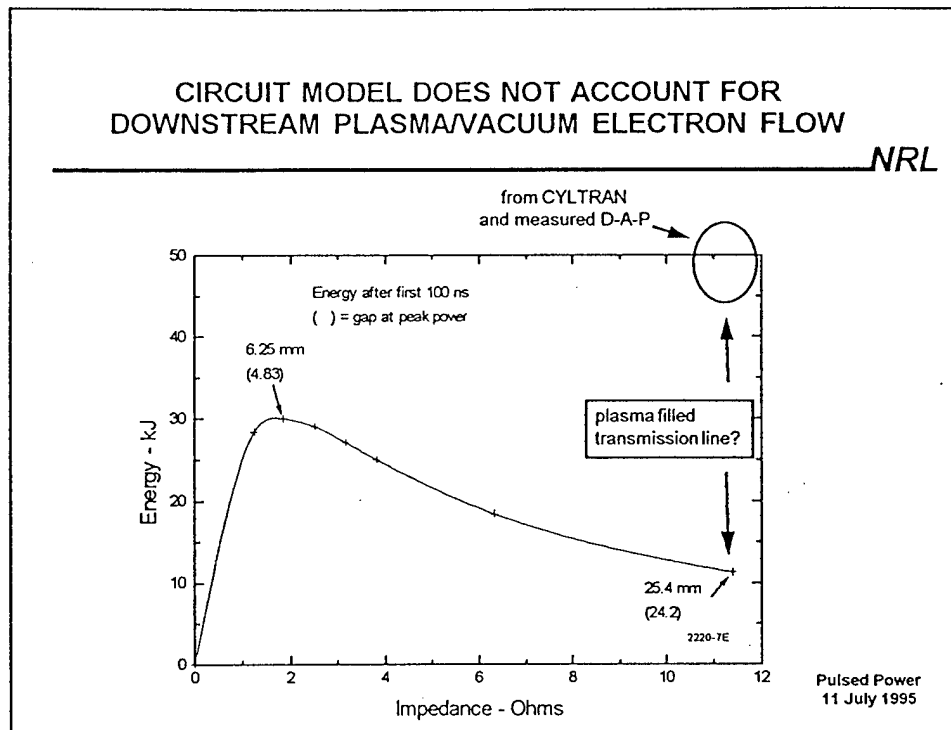
The open symbols in black are CYLTRAN calculations for triangular-voltage, flat-current load waveforms. For the circles, the voltage is fixed at 1.75 MV and the current is varied to generate a curve of calculated DAP as a function of load energy. For the triangles the current is held fixed at either 0.6 MA or 1.2 MA and the voltage is varied between 1 and 2 MV. Note that for these geometries the DAP is an approximately linear function of load energy. This somewhat unexpected result means that electrical energy delivered to the diode is a good parameter for optimizing radiation production.

The filled squares are the calculated DAP for various BERTHA-generated load waveforms. More energy is delivered to the load when the AK gap and switch to load inductance are reduced because the system is not optimized from a circuit point of view (more on this in the next viewgraph). The CYLTRAN results for the BERTHA waveforms fall on the same line as the idealized waveforms indicating that the dose in 20 mils of Si, for this configuration, is independent of waveform.

The energy at which the calculated DAP vs load energy curve intersects the average measured DAP is the energy we infer is producing the observed DAP on DM1 ... a little over 50 kJ. The BERTHA calculation for theoretical configuration under estimates the energy delivered to the load by approximately a factor of 4.

# CIRCUIT MODEL DOES NOT ACCOUNT FOR DOWNSTREAM PLASMA/VACUUM ELECTRON FLOW

NRL

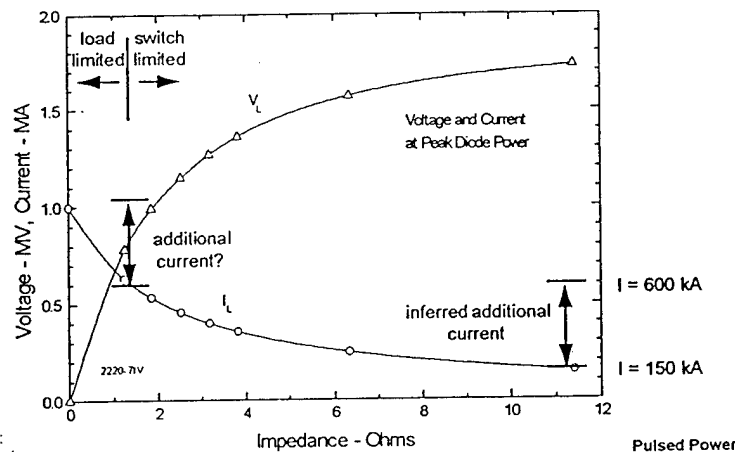


In this figure, the BERTHA-calculated load energy is plotted as a function of load impedance. For the DM1 experimental configuration, the Ak gap is 25.4 mm corresponding to  $Z_L = 11\Omega$ . The 12.4 kJ obtained from the circuit calculation is about a factor of 4 lower than the CYLTRAN-inferred load energy of 50 kJ. Note that only the cathode current is used in calculating the diode energy. The additional energy is most likely a result of additional electron current associated with plasma in the transmission line between the POS and load. Vacuum flow alone cannot explain this result.

Note that as the diode Ak gap, i.e., diode impedance, is reduced, more energy is delivered to the load. The optimum impedance for this configuration is a little less than 2  $\Omega$ . An explanation for this will be given in the next figure.

## CATHODE CURRENT INCREASES WITH LOWER DIODE IMPEDANCE - ANODE CURRENT TOO?

NRL



Plotted here are the BERTHA-calculated load voltage and current (cathode current) as a function of load impedance. At the impedance associated with the experimental configuration, 11  $\Omega$ , only 150 kA is delivered to the load. An additional 450 kA, for a total (cathode current plus current reaching the anode converter that can make bremsstrahlung) of 600 kA is required to explain the data. The additional current is associated with plasma in the vacuum line. Vacuum flow alone cannot explain this result.

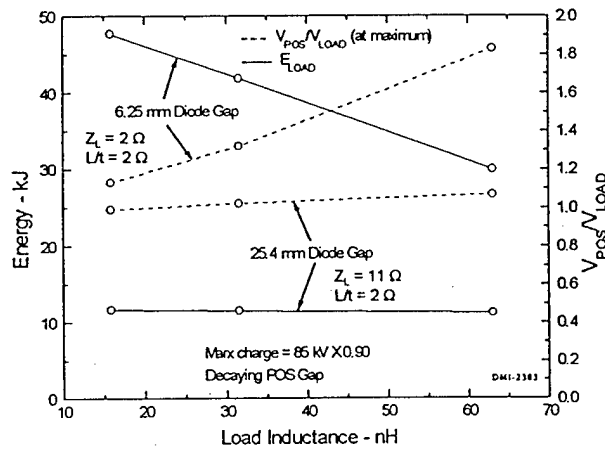
As  $Z_L$  is decreased,  $I_L$  increases and  $V_L$  decreases, but not as much. Thus the optimum power, coupled energy to the load, and radiation occur when  $Z_L$  is a little less than  $\approx 2 \Omega$ . There is a question of what will happen to the additional current as  $Z_L$  is reduced. Will it all turn into cathode current, in which case we have gained nothing, or will the same  $\Delta I$  be available to the load at lower  $Z_L$ ? Similar behavior to this, but for the anode current, was observed on Hawk, at about 1/3 the current and 3 times the conduction time. This is the main reason we believe the DM1 configuration is not optimized. On Hawk, the energy delivered to the load increased as  $Z_L$  was reduced.

Next we will look at some initial 2-D PIC calculations to see if we can gain any insight into the details of the POS-load coupling.



# OPTIMIZING THE SYSTEM MAY BE TRICKY

NRL



Pulsed Power  
11 July 1995

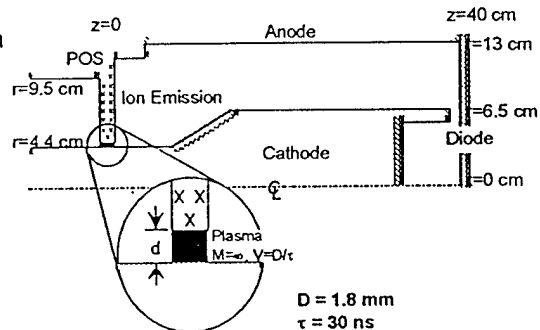
In this figure, the BERTHA-calculated energy coupled to the load and ratio of POS to load voltage (at peak power) are plotted as a function of the POS-to-load inductance,  $L_{SL}$  for diode AK gaps of 25.4 and 6.25 mm. For the larger AK gap, the load energy is nearly independent of  $L_{SL}$ . This results from the fact that the load impedance is so large ( $11 \Omega$ ) it dominates over the inductive loading (approximated by  $L_{SL}/\tau_{open}$ , about  $2 \Omega$  for  $L_{SL} = 63 \text{ nH}$  and  $\tau_{open} = 28 \text{ ns}$ ).

With the diode AK gap reduced to 6.25 mm, the resulting load impedance (about  $2 \Omega$ ) is now comparable to the maximum inductive loading, and the system can deliver more energy to the load as  $L_{SL}$  is reduced.

## GEOMETRY USED IN PIC SIMULATIONS OF DM1 POWER-FLOW

NRL

- POS model
  - pre-formed gap filled with high mass plasma
  - POS opens as ions drift toward cathode
- Entire cathode space-charge limited emitter
- Ion emission in POS region only
- Full generator current flows though POS at  $t=0$

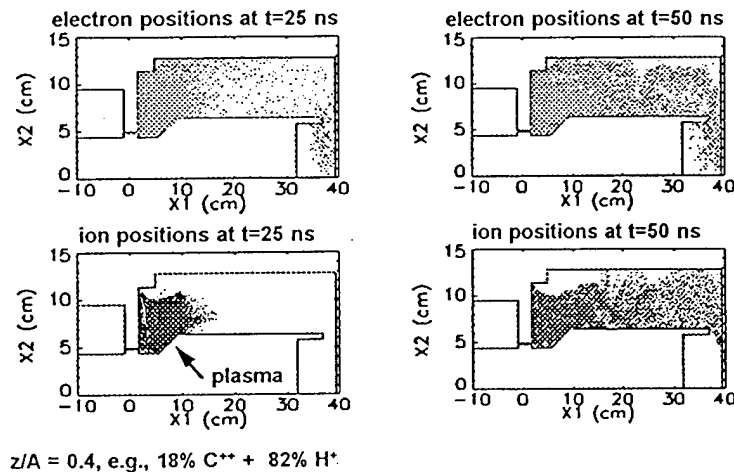


Pulsed Power  
11 July 1995

Geometry for 2-D MAGIC simulations. The POS is modeled by independently moving ions out of a prescribed gap in a prescribed time. The plasma is modeled by allowing ion emission. Under these conditions, the behavior of the particle flow (ions and electrons) is computed using MAGIC.

PLASMA MOVES RAPIDLY DOWN THE MITL  
BRINGING CURRENT WITH IT

NRL



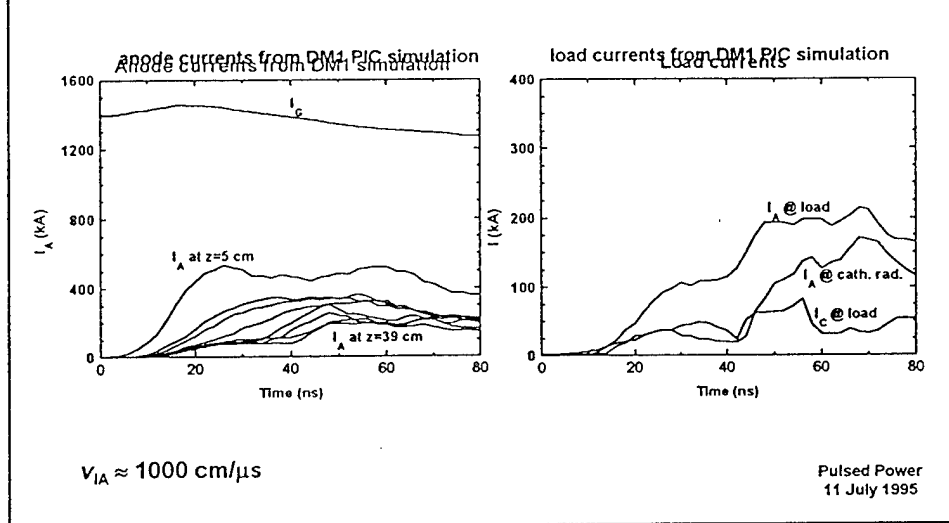
Shown in this figure are four particle plots. Ions and electrons positions are plotted at 2 different times, with  $t = 0$  defining the time of opening. At  $t=25$  ns, the electrons fill the downstream region and are apparently slowly dragging ions into the vacuum line between the POS and load. At  $t=50$  ns, the ions (plasma) also fill the vacuum line. The behavior of the particle flow is distinctly different from that reported in previous simulations [S.B. Swanekamp, et al., J. Appl. Physics 5, 2468 (1994)], where the electron flow hugged the anode of the vacuum line between the POS and load. In this case, the electron flow is more uniformly distributed. The cause of this discrepancy is under investigation.

An increase is observed in the anode current near the load when the plasma reaches the anode (see next figure).

The speed with which the plasma moves depends on  $Z/A$ , which for this simulation was assumed to be  $2/5$  (this corresponds, e.g., to an 18%  $C^{++}$  and 82%  $H^+$  plasma - by comparison, purely  $C^{++}$  ions would have  $Z/A=2/12$ ). This  $Z/A$  was chosen to have the anode current, and therefore the load energy, peak at a reasonable time after opening. The details of this result will depend on how fast this plasma moves and the existence of other plasma, either injected into or generated in the vacuum line. Better plasma measurements are needed to guide the simulation. Work in this area is continuing.

LOAD CURRENT PREDICTED BY 2-D MAGIC IS LARGER  
THAN BERTHA PREDICTION  
( BUT NOT LARGE ENOUGH!)

NRL



Shown in this figure are selected currents obtained from the 2-D particle simulations. Anode currents at different axial locations are plotted as a function of time in the left-hand portion of the figure. When comparing the anode current upstream of the POS to the anode current 5 cm downstream of the POS, a large loss across the POS is inferred (900 kA). The anode current at  $Z = 5$  cm is close to what is required to explain the results of the CLYTRAN analysis. Unfortunately, additional loss is observed at successive axial locations, plotted here in 5 cm intervals up to the axial location of the load. Save a small bias current, the bulk of the current appears to propagate down the vacuum line. The speed of this propagation, about 1000 cm/ $\mu$ s, is determined by the speed of the ions (illustrated on the previous figure) filling the vacuum line.

Currents at the load are plotted in the right hand portion of the figure. Here, the total anode current ( $I_A$  @ load), the total current that reaches the anode converter within a radius equal to the cathode radius ( $I_A$  @ cath. rad.), and the current measured at the tip of the cathode ( $I_C$  @ load).  $I_A$  @ load is about 150 kA, in agreement with the BERTHA calculation. That is the amount of current the diode requires to attain the canonical geometrical impedance (see Fig. 5). The difference between  $I_A$  @ load and  $I_C$  @ load is the current coming from the vacuum line that feeds the diode. An additional 50 kA is delivered to the anode converter a radius that is larger than the cathode radius. While this total anode current is larger than  $I_A$  @ load, it is not enough to explain the the CLYTRAN results.

As stated previously, the question is still open of how plasma in the POS-to-load region should be modeled.

## SUMMARY AND CONCLUSIONS

NRL

- We have made a good start at modeling the DM1 performance:
  - electrical circuit accurately models the pulsed power performance upstream of POS
  - 50 kJ delivered to load (inferred)
- $Z_{\text{flow}}$ /critical-gap model for POS is useful, but limited:
  - To obtain agreement with the measured parameters, the POS gap must decrease after opening
  - For the calculated electrical parameters to predict the energy delivered to the load, additional current (associated with downstream plasma and/or vacuum flow?) is needed
- The anode current predicted by the PIC analysis is too low to give the inferred diode energy (downstream POS plasma not modeled).
  - The roles of plasma and/or vacuum electron flow between the POS and an e-beam diode are not understood
- To improve energy coupled to load:
  - AK gap reduced, better match to R/D of POS gap
  - reduce "inductance" between POS and load (at matched load impedance)
  - increase POS conduction time while maintaining POS performance

Pulsed Power  
11 July 1995

Summary of the results. This is mostly self-explanatory. To obtain agreement with the measured (upstream) electrical waveforms, the POS circuit element model had to include a POS gap closure after opening. Also, the circuit model under estimates the energy delivered to the load, probably because additional electron current reaches the anode converter than the cathode current. The circuit simulations also suggest that the system is not matched for optimum energy delivery to the load. The effects of plasma between the POS and load are still under investigation.

PULSED POWER PHYSICS TECHNOTE NO. 95-12

**TITLE:**            **REVIEW OF HAWK POS POWER FLOW EXPERIMENTS**

**AUTHOR(S):**    R.J. Commisso, B.V. Weber, P.J. Goodrich, J.M. Grossmann, S.B. Swanekamp, P.F. Ottinger, and R.A.Riley.

**DATE:**            4 April 1995

**ABSTRACT:**        Talk presented at the 1995 POS workshop held at NSWC on 28 through 30 march, 1995. Data from Hawk power flow experiments are presented. Shots at short conduction time (300 ns) and long conduction time (800 ns), both with a vacuum e-beam diode, and a long conduction time shot (700 ns) with external plasma fill in the diode are all compared.

**THIS REPORT REPRESENTS UNPUBLISHED  
INTERNAL WORKING DOCUMENTS AND SHOULD NOT BE REFERENCED OR  
DISTRIBUTED WITHOUT CONSENT OF AUTHORS**

## REVIEW OF HAWK POS POWER FLOW EXPERIMENTS

B.V. Weber, R.J. Comisso, P.J. Goodrich, J.M. Grossmann,  
S.B. Swanekamp,\* P.F. Ottinger, and R.A. Riley\*

Pulsed Power Physics Branch  
Plasma Physics Division  
Naval Research Laboratory  
Washington, DC

Opening Switch Workshop, 29 March 1995  
NSWC, Silver Spring, MD

\*JAYCOR, Vienna, VA

\*NRC Research Associate

Title slide. Note that the measurements shown here were were obtained by B. Weber, P. Goodrich, and R. Riley. Some of these data were presented by B. Weber at Beams '94.

## OUTLINE

NRL

- Sample plasma density measurements in the load region
- "Vacuum" electron flow measurements
  - short conduction time, vacuum diode load
  - long conduction time, vacuum diode load
  - long conduction time, deliberate plasma filled diode load
- Summary

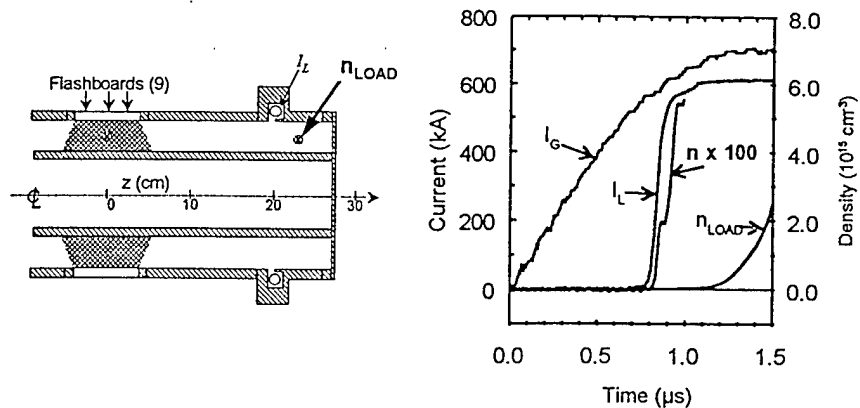
DNA POS WORKSHOP  
29 March 1995

This talk will deal mainly with three shots from Hawk. All three in the same geometry and diagnostics: one shot had a sort conduction time (300 ns), one shot had a long conduction time (700 ns), and one shot had a long conduction time but with a deliberate plasma fill in the diode.



WITH FLASHBOARDS, SHORT POS-TO-LOAD  
DISTANCE, LOW DENSITY PLASMA REACHES  
THE LOAD REGION AFTER  $I_L$  RISES

NRL

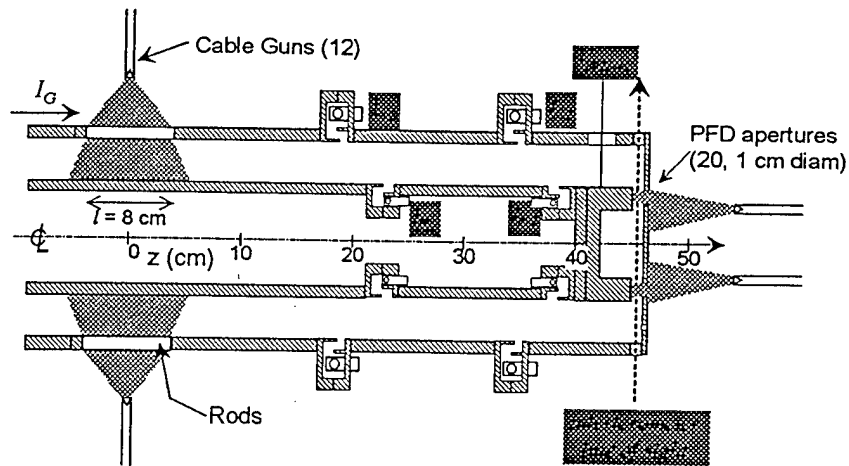


DNA POS WORKSHOP  
29 March 1995

This is one of many geometries investigated (usually incompletely) on Hawk; 9 flashboard plasma sources separated from the load by about 25 cm. When the interferometer is set to have a high sensitivity, plasma is seen to arrive in the load region about the same time (or a twinge later) than the load current. In no cases investigated has plasma been observed in the load region before current. Note, not all cases have been investigated with high sensitivity. (In one case on Pawn, plasma was observed in the region between the POS and load.)

# HAWK POWER FLOW EXPERIMENT EXPERIMENT WITH PLASMA-FILLED DIODE LOAD

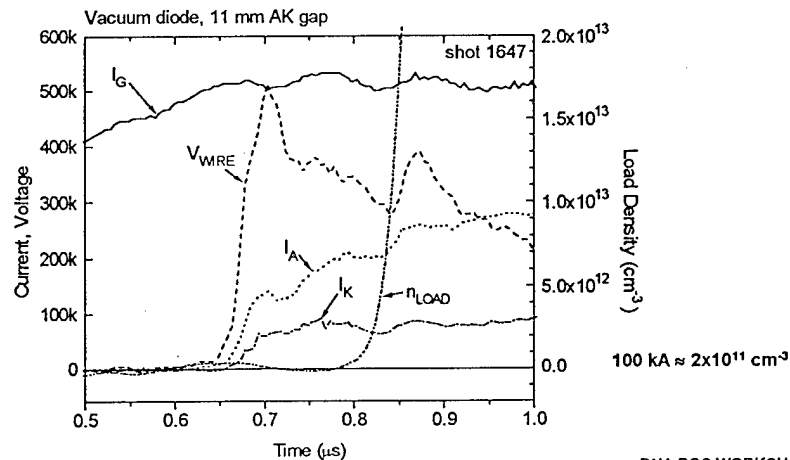
NRL



Setup for the rest of the data in this talk. Two sets of anode and cathode Bdots, separated in azimuth by  $180^\circ$ , are located at two axial positions between that POS and load. A vacuum wire voltmeter measures the load voltage directly. A sensitive interferometer is aligned to view across a diameter between the anode and cathode of the e-beam diode load. The e-beam diode can be plasma filled via an independent plasma source. The distance between the POS and load is extended compared to the previous viewgraph to keep POS plasma from reaching the load region.

## FLOW CURRENT IS PRESENT WITH "NO" PLASMA IN DIODE

NRL

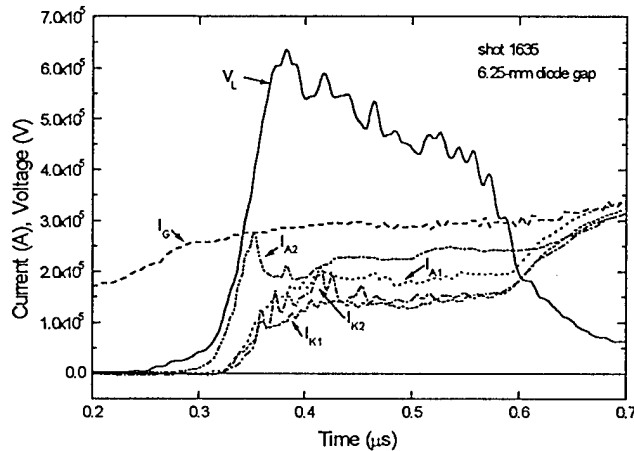


DNA POS WORKSHOP  
29 March 1995

Generator current, load voltage, anode and cathode currents near the load and density in the load as a function of time (here, as with the remainder of the data,  $t=0$  is when the generator current begins). There is no plasma fill from the independent plasma source. On the scale of about  $10^{12} \text{ cm}^{-3}$ , there is no plasma in the e-beam diode. Note, however, 100 kA moving at  $2/3c$  and distributed uniformly across the AK gap between the inner and outer coax corresponds to about  $2 \times 10^{11} \text{ cm}^{-3}$ . This density is below the sensitivity of the measurement.

## SHORT CONDUCTION TIME VACUUM DIODE HAS LITTLE FLOW CURRENT NEAR LOAD

NRL



DNA POS WORKSHOP  
29 March 1995

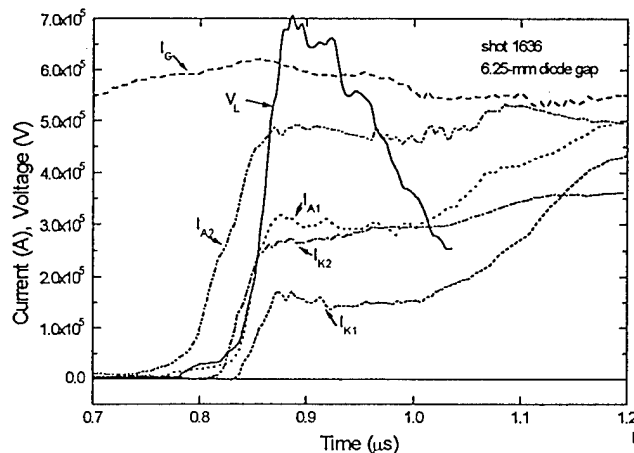
Generator current, load voltage, anode (cathode) Bdot near the POS, denoted with subscript A2 and K2, respectively (A1 and K1, respectively), as functions of time for a short conduction time case (300 ns) with no external plasma fill.  $V_W$  and  $I_{A2}$  start first and at about the same time. The other three Bdots start later and at about the same time.

The distance between the two anode Bdots is about 15 cm and the time delay is about 30 ns giving a speed of 500 cm/ $\mu$ s - too slow for an MITL wave or e-beam propagation through plasma ( $c=30,000$  cm/ $\mu$ s).

Most of the loss appears to be between the the POS and the location of  $I_{A2}$  ( this includes the POS itself). There is little flow current (see bow).

## LONG CONDUCTION TIME VACUUM DIODE HAS FLOW CURRENT EARLY AND EVERYWHERE

NRL



DNA POS WORKSHOP  
29 March 1995

Generator current, load voltage, anode (cathode) Bdot near the POS, denoted with subscript A2 and K2, respectively (A1 and K1, respectively), as functions of time for a long conduction time case (800 ns) with no external plasma fill. Here  $I_{A2}$  (anode Bdot nearest the POS) starts before everything else.  $I_{A1}$  and  $V_W$  begin about 30 ns later, with  $I_{K2}$  and  $I_{K1}$  following sequentially. Under these conditions, the order in which the Bdots start is generally observed to be:  $I_{A2}$ ,  $I_{A1}$ ,  $I_{K2}$ , and  $I_{K1}$ .

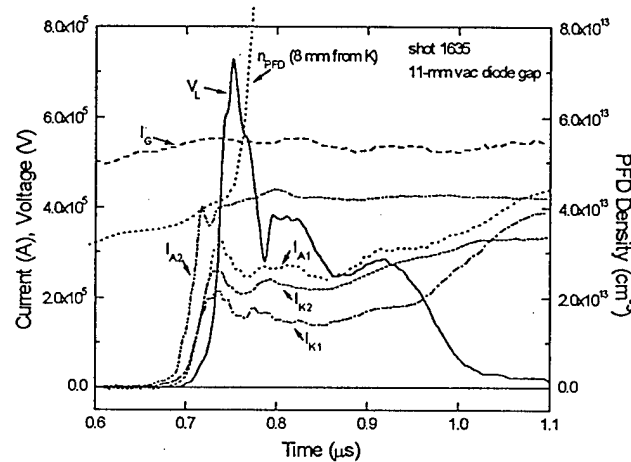
The distance between the two anode Bdots is about 15 cm and the time delay is about 30 ns giving a speed of 500 cm/ $\mu$ s - too slow for an MITL wave or e-beam propagation through plasma ( $c=30,000$  cm/ $\mu$ s). The time delay between  $I_{A1}$  and  $I_{K2}$  is also about 30 ns, and the time delay between  $I_{K2}$  and  $I_{K1}$  is about 20 ns.

Most of the loss appears to be located between the the two anode Bdots (as if the POS "moved" downstream compared to the previous figure). There is substantial current in flow (see below).

Note that this case has many similarities to DM1: POS-to-load length, cable gun plasma sources, and inferred density of about 1/2 DM1.

## PLASMA FILLED DIODE HAS NO INITIAL FLOW CURRENT

NRL



DNA POS WORKSHOP  
29 March 1995

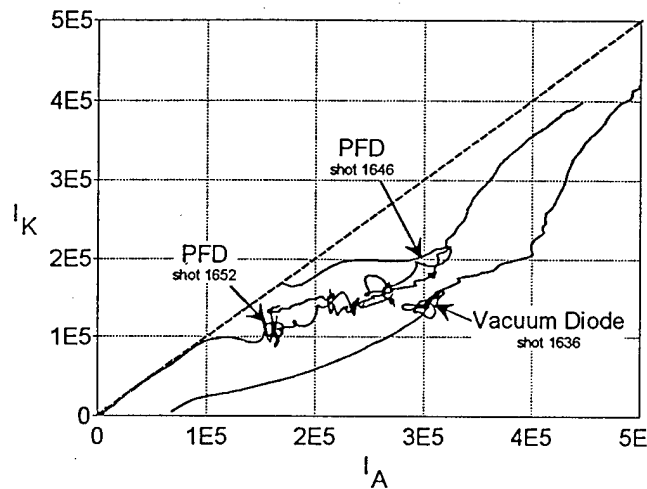
Generator current, load voltage, anode (cathode) Bdot near the POS, denoted with subscript A2 and K2, respectively (A1 and K1, respectively), as functions of time for a long conduction time case (700 ns) with a plasma fill. The density of the PFD is also shown. Again,  $I_{A2}$  (anode Bdot nearest the POS) starts before everything else.  $I_{A1}$ ,  $I_{K2}$ , and  $I_{K1}$  begin at the same time about 15 ns later, with  $V_L$  following some 15 ns after that. This is very different from the previous figure.

The distance between the two anode Bdots is about 15 cm and the time delay is about 15 ns giving a speed of 1,000 cm/μs - too slow for an MITL wave or e-beam propagation through plasma ( $c=30,000$  cm/μs), but faster than the previous case (note, there may be "more plasma" between the POS and load in this case). The time delay between  $I_{A1}$  and  $I_{K2}$  is also about 30 ns, and the time delay between  $I_{K2}$  and  $I_{K1}$  is about 20 ns.

The loss appears evenly distributed between the two anode Bdots. The current in the flow is less than the previous case (but not as small as the short conduction case). (See next figure.)

## CATHODE CURRENT COUPLED TO PFD IS HIGHER THAN FOR VACUUM DIODE

NRL



DNA POS WORKSHOP  
29 March 1995

Cathode current near load vrs anode current near load for a short and long conduction time, PFD case (shots 1652 and 1646, respectively), and a long conduction time, vacuum-diode case (shot 1636). The cathode current is higher for the PFD cases. The short conduction, vacuum-diode case (shot 1635 above, not shown here) has the highest cathode to anode current ratio.

Note, the load voltage was very similar for short (shot 1635) and long (shot 1636) conduction time, vacuum-diode cases and the long conduction time, PFD case (shot 1646).

## SUMMARY AND CONCLUSIONS

NRL

- Probably plasma between the POS and load influences the coupling:
  - short conduction - small influence -  $I_{A2}$  leads other Bdots (low flow)
  - long conduction - big influence
    - »  $I_{A2}$  leads  $V_L$ ,  $I_{A1}$  (big flow)
    - » order of Bdots:  $I_{A2}$ ,  $I_{A1}$ ,  $I_{K2}$ ,  $I_{K1}$  (from POS to load)
  - PFD (plasma in load) - big influence
    - »  $I_{A2}$  leads other Bdots (intermediate flow)
    - » all currents lead voltage
- Future Hawk experiments (relevant to DM1) and simulations will try to:
  - determine dependence of  $I_A$ , ( $I_K / I_A$ ) on  $V$ ,  $\tau_C$ , POS-to-load distance, diode AK gap
  - determine optimum configuration for BDS radiation production
  - investigate coupling for a PRS load
- Future parallel plate experiments and simulations will try to measure plasma distribution between POS and LOAD and characterize neutrals

DNA POS WORKSHOP  
29 March 1995

Conclusions. Self explanatory.



PULSED-POWER PHYSICS TECHNOTE NO. 95-11

TITLE: POS-Load coupling-Theory

AUTHORS: Steve Swanekamp<sup>+</sup>, John Grossmann, Bob Commisso, Phil Goodrich<sup>+</sup>, Ron Riley\* and Bruce Weber

DATE: 4 April 1995

ABSTRACT: This technote contains the view graphs and notes to a talk that was presented at the DNA opening switch workshop which was held at NSWC March 28-30, 1995. The talk describes progress in understanding the vacuum electron flow launched between a POS and a electron beam diode. In this talk particle-in-cell (MAGIC) simulations are compared with data from two experimental geometries. The DPM1 simulations show electron flow concentrated primarily near the anode. In addition to electron flow near the anode, the HAWK simulations suggest that plasma between the POS and the load can be important in determining the current coupling.

THIS REPORT REPRESENTS  
UNPUBLISHED INTERNAL  
WORKING DOCUMENTS AND  
SHOULD NOT BE REFERENCED  
OR DISTRIBUTED

+JAYCOR, Vienna VA

\*NRL-NRC postdoctoral research associate

## POS-Load coupling-Theory

Steve Swanekamp<sup>+</sup>, John Grossmann, Bob Commisso,  
Phil Goodrich<sup>+</sup>, Ron Riley, and Bruce Weber  
Plasma Physics Division  
Naval Research Laboratory  
Washington, DC

Opening Switch Workshop, 29 March 1995  
NSWC, Silver Spring, MD

<sup>+</sup>Jaycor, Vienna, VA

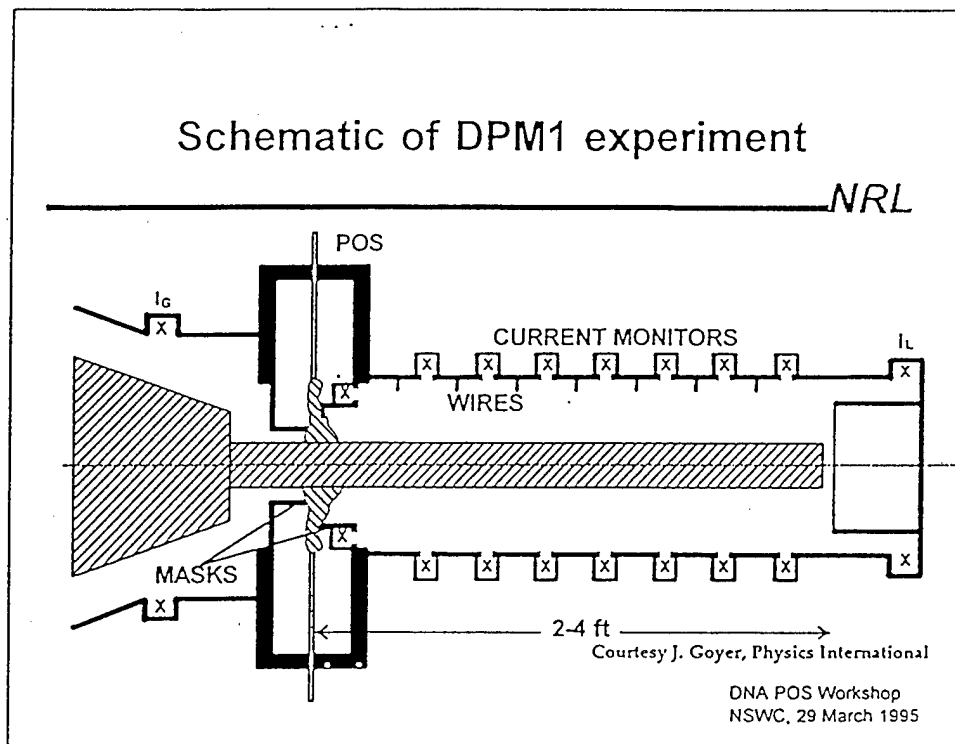
## Outline

NRL

- DPM1 power flow simulations (JAP, 76, 2648 (1994))
  - electrons flow primarily near anode
  - load power maximized when  $Z_L = Z_A(\text{POS})$
  - energy transfer accompanied plasma expansion from the switch into the MITL
- Hawk power flow
  - Comparison of short and long conduction time shots with simulations
  - very little vacuum current where there is no plasma
  - comparison with exp. may indicate low density plasma between POS and load

DNA POS Workshop  
NSWC, 29 March 1995

The talk focuses on simulations of electron flow in the vacuum transmission that separates a POS and a load. The DPM1 simulations show electron flow primarily near the anode downstream of the POS. The transfer of magnetic energy from the primary storage inductor to the load inductance is accompanied by the expansion of plasma from the POS region. The DPM1 simulations show that the load power is maximized when the load impedance is equal to the flow impedance of the POS. The HAWK simulations show very little vacuum electron flow in regions where there is no plasma in the MITL. Comparison with experimental measurements indicate that low density plasma ( $n \sim 10^{12} \text{ cm}^{-3}$ ) may strongly influence the POS-Load current transfer.

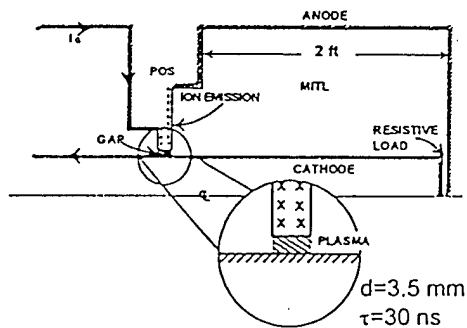


This is a schematic of the DPM1 hardware. Plasma is introduced in the POS region by a series of cable guns. Current monitors were used at several axial locations and a series of wires protruded through the anode to detect the presence of electrons.

## Geometry used in PIC simulations of DPM1 power-flow

NRL

- POS model
  - preformed gap filled with high mass plasma
  - POS opens as ions drift toward cathode
- Entire cathode space-charge limited emitter
- Ion emission in POS region only
- Full generator current flows through POS at  $t=0$

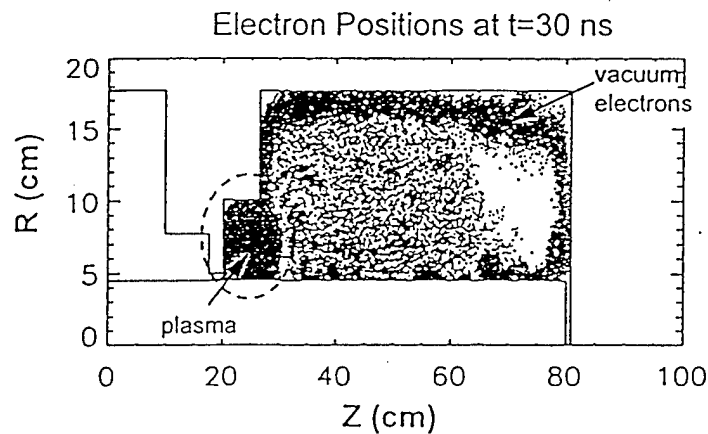


DNA POS Workshop  
NSWC, 29 March 1995

This is a schematic of the simulation setup used to model the DPM1 experiment. A simple model was used for the POS. The model consisted of a 0.35 cm gap prefilled with plasma. The mass of the ions was made artificially large so that they do not respond to electromagnetic fields. To simulate opening, the heavy ions were given an initial velocity so that they clear the gap in 30 ns. The entire cathode surface was modeled as a space-charge limited electron emitter. Because the region of the anode marked by x's would be plasma in the experiment, doubly ionized carbon ions were allowed from this region. The primary storage inductor upstream of the POS was initialized with 1.2 MA. The vacuum electron flow that accompanies opening of the POS was studied with the PIC method.

## DPM1 simulations show electron flow concentrated near anode

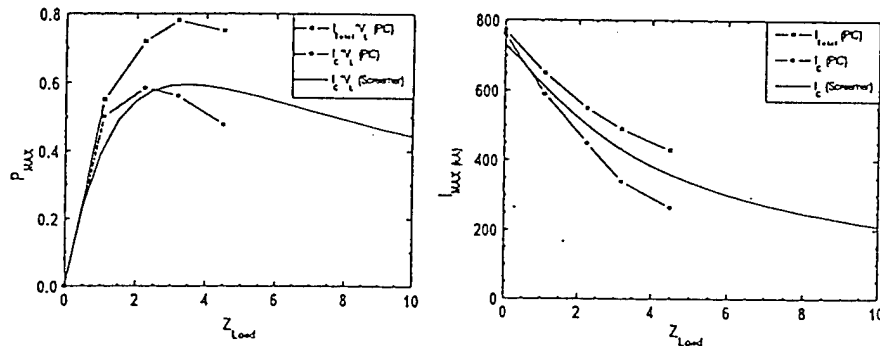
NRL



This shows the electron positions at  $t=30$  ns. We see that the vacuum electron execute an ExB drift primarily near the anode. In the load region the electrons make a 90 degree bend in their drift motion and continue to flow along the anode. Some of these electrons flow directly into the load and some flow back along the cathode. This drift is produced by field reversal at the cathode caused by the excess electron charge that flows into the MITL from the POS. There is also a plasma that expands from the POS region and into the MITL. The characteristics of this plasma might be important for current transfer in other machines. This ions in the plasma (not shown in the figure) are emitted doubly ionized carbon ions.

PIC and Screamer simulations show  
maximum power transfer when  $Z_{\text{Load}} = Z_{\text{flow}}$

NRL

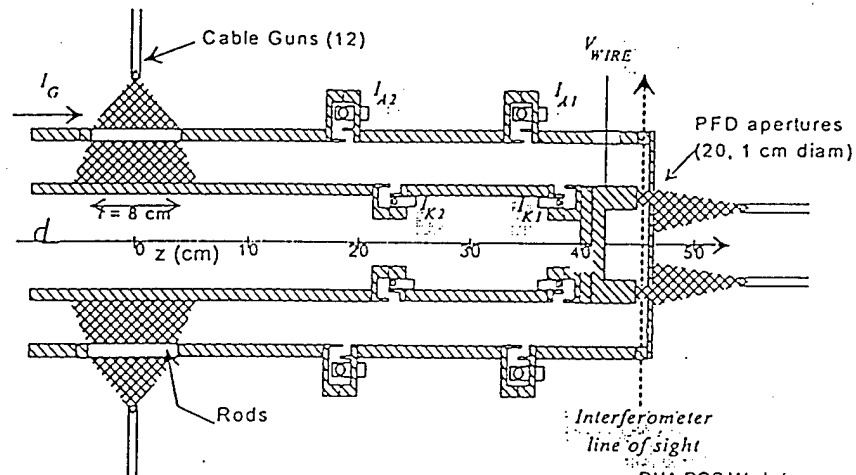


DNA POS Workshop  
NSWC, 29 March 1995

This figure shows a comparison of the peak load powers and currents vs load impedance with a Screamer circuit calculation. The two PIC curves of the load power use the cathode boundary current and the total current load current determined by magnetic probes on the anode. The difference between the cathode boundary current and the net current shown on the right represents the amount of current flowing into the load. We see that the amount of vacuum current flow directly into the load increases dramatically as the load impedance increases. The simulations and the circuit calculation both show that the load power is maximized when the load impedance is equal to the POS flow impedance. The latest experiments on DM1 used a 1" gap with a geometric impedance of about 10 Ohms. If we extrapolate the simulations results to this impedance it seems that nearly all the load current would be in the form of vacuum electron flow and that the system would be far from optimized.

## Schematic of Hawk power flow experiment

NRL



DNA POS Workshop  
NSWC, 29 March 1995

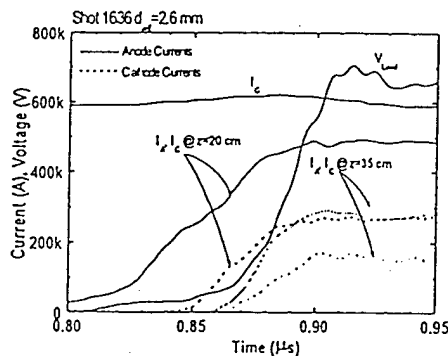
This figure shows a schematic of the power-flow experiment on HAWK. The advantage of the HAWK experiments is the addition of cathode monitors and an independent measurement of the load voltage using the wire voltmeter. The hardware was capable of injecting plasma into the diode but the shots considered here were vacuum diode shots with no plasma deliberately placed in the load.



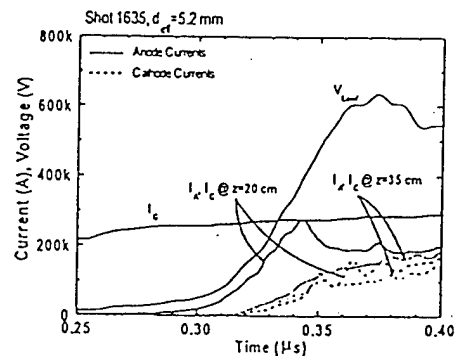
# HAWK long and short conduction time shots suggest plasma may play role in power flow

NRL

Long Conduction Time



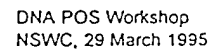
Short Conduction Time



DNA POS Workshop  
NSWC, 29 March 1995

This slide shows the data from a long and short conduction time HAWK shot. The long conduction time shot shows that the anode current at  $z=20$  cm precedes the load voltage and the other current monitors by about 50 ns. This might occur as a result of plasma in the MITL that shunts current and shorts out the transmission line. The anode currents show that there is current losses between the POS and  $z=20$  cm and additional losses between  $z=20$  and  $z=35$  cm. The cathode current monitors show a significant amount of the current exists in the form of vacuum electron flow. The difference between the cathode current at  $z=20$  and 30 cm indicates electron emission from the cathode. The short conduction time shot shows that the load voltage precedes all the current monitors. This may indicate that plasma in the MITL is less important for the short conduction time case. The shot shows some vacuum electron flow at  $z=20$  cm but very little vacuum flow near the load. Further note that most of the losses occur between the POS and  $z=20$  cm. Comparing the two shots we see that the voltages are very similar for the two cases. In addition the cathode currents at  $z=35$  cm are also very similar. However, the anode current at the load is much higher in the long conduction time case. If this current makes it to the load and produces bremsstrahlung then the long conduction time shot is clearly better.

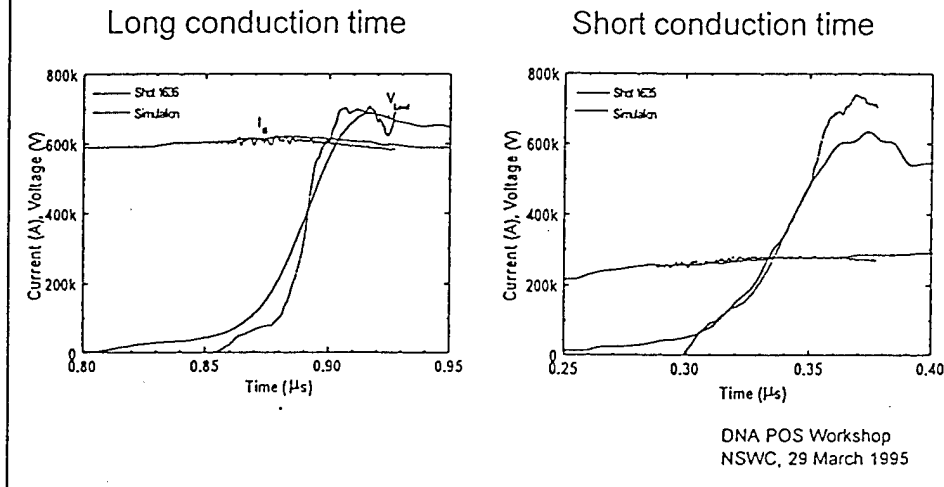
NRL



This slide shows the simulation setup for HAWK. Simulations were performed for both the long and short conduction time shots with the parameters for each simulation given in the figure. Notice that the long conduction time shot used a 2.6 mm gap with an opening time of 40 ns. The short conduction time shot used a 5.2 mm gap with a 60 ns opening time.

## Simulations show good agreement for $I_G$ , and $V_{Load}$

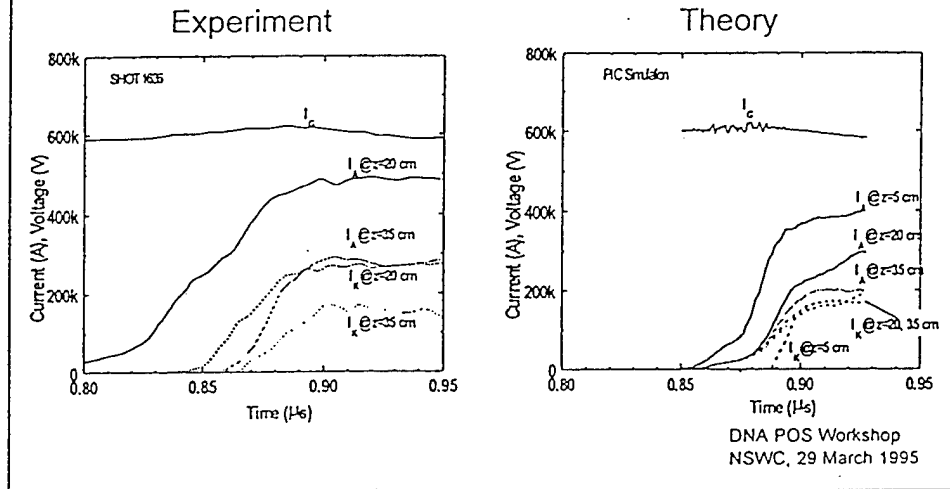
NRL



This slide shows a comparison of the measured generator current and load voltage with simulation for both the long and short conduction time shots. There is good agreement between for the generator currents between simulation and experiments. For the long conduction time shot the load voltage rises more gradually than the simulation but the peak voltage matches nicely. The more rapid voltage rise was compensated for in the short conduction time simulation by going to a 60 ns opening time. For this case we see that the rise time matches nicely but the peak load voltage is about 100 kV lower than the simulation. This could be adjusted for by making the gap a fraction of a mm smaller in the simulation. Neither of the simulations showed the long voltage foot seen in the experiment.

# Vacuum electron flow for long conduction time case shows gap may form downstream of POS region

NRL

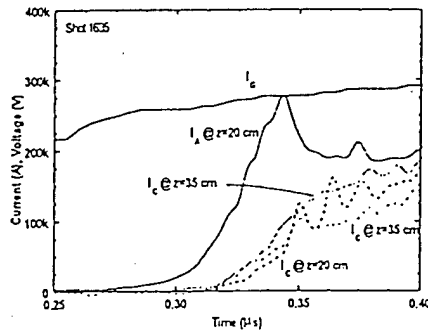


This slide shows a comparison of the measured anode and cathode currents (left) with those predicted by simulation (right) for the long conduction time case. The anode and cathode currents from the simulation at  $z=5$  cm look very similar to the measured anode and cathode currents at  $z=20$  cm. Furthermore, the anode and cathode currents at  $z=20$  cm in the simulation compare well with the measured anode and cathode currents at  $z=35$  cm. This may indicate that the gap may form approximately 15 cm downstream of the POS region. The anode and cathode currents from the simulation at  $z=35$  cm indicate very little vacuum electron flow near the load.

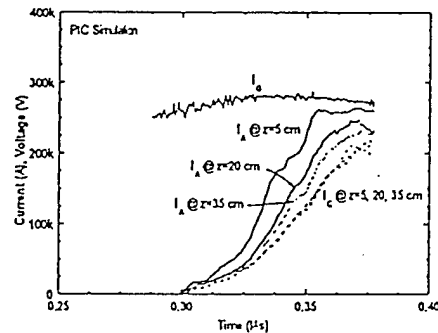
# Vacuum electron flow for the short conduction time case shows plasma plays less of a role

NRL

Experiment



Theory

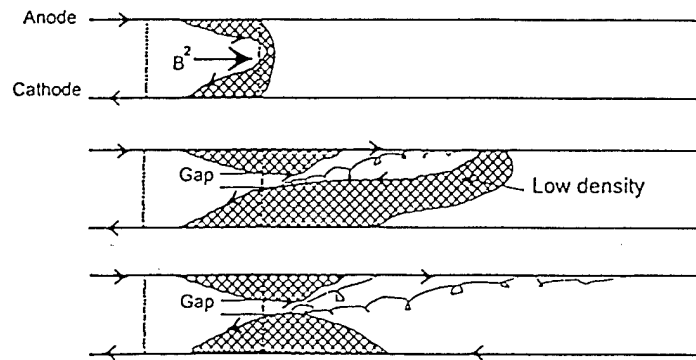


DNA POS Workshop  
NSWC, 29 March 1995

This slide shows a comparison of the measured and simulated currents for the short conduction time case. The simulations again do not predict the anode monitor at  $z=20$  cm very well. This may again be due to plasma in the MITL. However, the downstream current monitors agree with the simulations fairly well. The peak currents in the simulation are slightly higher than the measured currents. This is probably due to the gap being slightly too large.

## Possible current path in HAWK MITL

NRL



DNA POS Workshop  
NSWC, 29 March 1995

This figure gives a cartoon picture of how the power-flow evolution might occur in HAWK. In the top frame the MHD forces displace the plasma during the conduction phase. When the snow-plow front reaches the load end of the plasma a gap forms in the high density plasma and electron flow from the POS is perturbed by a low density plasma in the MITL between the POS and load. This low density plasma also keep the load current and voltage low. Later this plasma is either pushed downstream or to the walls and the load voltage and current rises. During this phase a large fraction of the load current be comprised of vacuum electron flow.

## Summary and future work

*NRL*

- Simple model for POS captures the essence of the measurements
- Examine role of plasma between POS and load on power-flow in PIC simulations (Use Hawk for guidance).
- Measure plasma distribution between POS and load in Hawk (parallel plate ?)
- Apply the understanding to improve DM1 POS-Load coupling

DNA POS Workshop  
NSWC, 29 March 1995

PULSED-POWER PHYSICS TECHNOTE NO. 95-10

TITLE:       **Progress on front to back POS simulation**

AUTHORS: Steve Swanekamp<sup>+</sup>, John Grossmann, Joe Huba, Jim Geary<sup>\*</sup>, Larry Ludeking<sup>\*</sup>, and David Smithe<sup>\*</sup>

DATE:        3 April 1995

ABSTRACT: This technote contains the view graphs and notes to a talk that was presented at the DNA opening switch workshop which was held at NSWC March 28-30, 1995. The talk describes progress in developing a simulation tool that does the conduction phase of a POS with an MHD code and then transitions to PIC to study the opening phase.

THIS REPORT REPRESENTS  
UNPUBLISHED INTERNAL  
WORKING DOCUMENTS AND  
SHOULD NOT BE REFERENCED  
OR DISTRIBUTED

+JAYCOR, Vienna VA

\*MRC, Newington VA



## **Progress on Front to Back POS Simulation**

Steve Swanekamp<sup>+</sup>, John Grossmann, Joe Huba,  
Jim Geary<sup>\*</sup>, Larry Ludeking<sup>\*</sup>, and David Smithe<sup>\*</sup>

Naval Research Laboratory  
Plasma Physics Division  
Washington, DC

Opening Switch Workshop, 30 March 1995  
NSWC, Silver Spring, MD

<sup>+</sup>Jaycor, Vienna, VA  
<sup>\*</sup>MRC, Newington, VA

This talk was presented at the DNA opening switch workshop held on March 28-30 1995 at the Naval Surface Warfare center. The progress made in developing a model that can do both the conduction and opening phases of the POS was presented along with some recent simulations that were done to help understand the transition from conduction to opening.

## Outline

*NRL*

- Comparison of experimental and simulation regimes
  - Conduction phase with MHD
  - Opening phase with PIC
  - Comparison of PIC and MHD
- Can MHD and PIC communicate?
- Conduction current follows  $n^{1/4}$  (MHD) scaling at high density and  $n^{1/2}$  (EMH) at low density
  - EMH effects seen for first time in PIC code
  - Examples from simulations in EMH and MHD regimes

DNA POS Workshop  
NSWC, 29 March 1995

The talk starts with a comparison between the experimental regime of interest with the present simulation capabilities. At present the conduction regime is treated with an MHD code and the opening phase is done with a PIC code. A comparison of PIC and MHD simulations is presented for an identical plasma configurations. This comparison raises the question as to whether MHD and PIC can communicate? Results from simulations where MHD is expected to dominate are compared to simulations where EMH dominates. These results provide insight into the different physics that are expected during the transition from conduction to opening.

## Comparison of experiments to simulation capabilities

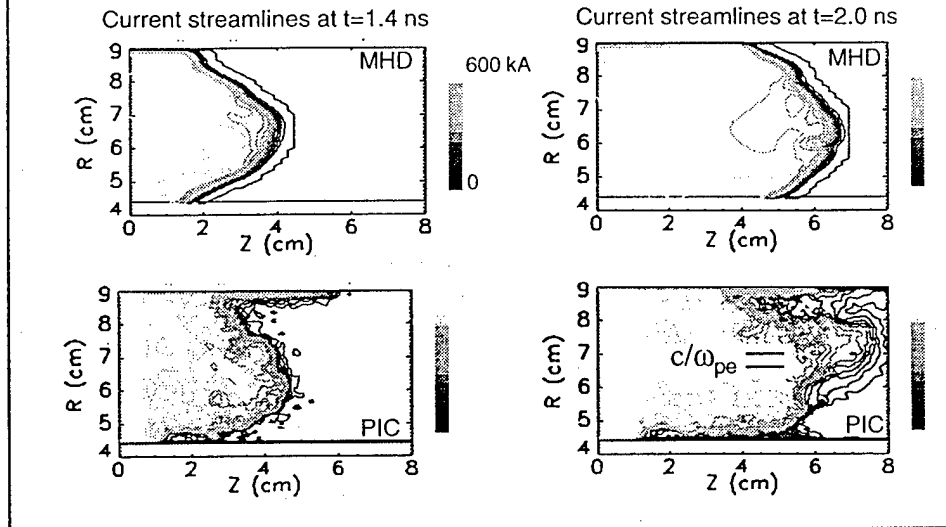
*NRL*

	Strengths	Limitations	Range
<b>Experiments</b>	Has all the right dynamics	Has lots of other stuff going on as well	$n=10^{12}-10^{17} \text{ cm}^{-3}$ $\tau=0.3-1.0 \text{ } \mu\text{s}$ $l=3-10, \Delta r=3-5 \text{ cm}$
<b>MHD</b>	Model ions during cond. phase	<ul style="list-style-type: none"> <li>• Can't do opening</li> <li>• Limited to length scales <math>\gg c/\omega_{pe}</math></li> </ul>	$n \gg 10^{13} \text{ cm}^{-3}$ $\tau < 0.3-1.0 \text{ } \mu\text{s}$ $l=3-10, \Delta r=3-5 \text{ cm}$
<b>Two-fluid</b>	Model electrons & ions during cond. phase	<ul style="list-style-type: none"> <li>• Must resolve <math>c/\omega_{pe}</math> &amp; light waves</li> <li>• Can't treat orbit crossings</li> </ul>	$n=10^{13}-10^{16} \text{ cm}^{-3}$ $\tau < 0.3-1.0 \text{ } \mu\text{s}$ $l=3-10, \Delta r=3-5 \text{ cm}$
<b>PIC</b>	<ul style="list-style-type: none"> <li>• Models opening phase</li> <li>• Allows orbit crossings</li> </ul>	<ul style="list-style-type: none"> <li>• Must resolve <math>\lambda_D, c/\omega_{pe}</math> &amp; light waves</li> <li>• Can't do cond. phase</li> </ul>	$n < 10^{12}-10^{14} \text{ cm}^{-3}$ $\tau < 0.1 \text{ } \mu\text{s}$ $l=1-5, \Delta r=1-3 \text{ cm}$

During the typical operation of a POS densities of interest can vary between  $10^{12}-10^{17} \text{ cm}^{-3}$ . The upper range of densities is expected during the conduction phase while the lower range of density is expected during the opening phase where density thinning in the POS and vacuum electron flow are expected. An MHD code is well suited to do the bulk of the conduction phase but is limited to length scales that are large compared  $c/\omega_{pe}$ . It is important to note that, as the density thins and gaps start to form, length scales in the POS become comparable to  $c/\omega_{pe}$  and it is important to retain the Hall term in Ohm's law. Since gaps on the order of a few mm are expected, an MHD code is limited to densities large compared to  $10^{13} \text{ cm}^{-3}$ . A two fluid code can be used to remove this limitation but it must resolve light waves and  $c/\omega_{pe}$ . This makes run times much longer than MHD. However, a two fluid code can not do orbit crossings and therefore has difficulties treating the vacuum electron flow that accompanies the opening process. In addition to light waves and  $c/\omega_{pe}$  considerations, the PIC code must also resolve the plasma Debye length. This limitation causes the run times for PIC to be much longer than both fluid models. These constraints limit the density range and time scale that can be conveniently simulated with the PIC approach. However, if we compare the regimes where MHD and PIC can operate we see that the two codes complement each other nicely. It seems possible to do the conduction phase with an MHD code and then transition to PIC to do the opening phase.

## PIC and MHD codes show similar behavior during the conduction phase, differ during opening phase

NRL

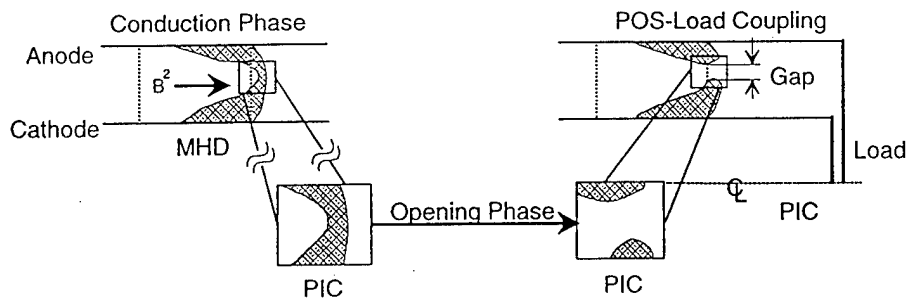


This view graph show a comparison of PIC and MHD for identical initial plasma conditions and the same applied magnetic field. The ion mass is made artificially small so that a lot of MHD motion can be achieved in a short time so that both MHD and PIC run times are short. The left hand pair of plots shows a comparison of the current streamlines from PIC and MHD codes during the MHD dominated conduction phase. Note that the two codes predict very similar behavior. The differences that appear near the anode boundary occur as a result of differences in boundary conditions. This is not a serious problem since we are interested in physics that occurs away from the anode boundary. The right hand pair of plots shows a comparison of the current streamlines from PIC and MHD codes near the time that PIC predicts opening. The PIC result shows that the onset of opening occurs over a scale length comparable to the electron skin depth where the MHD approximation breaks down. While the MHD code at this time shows a smooth snow plow front. Since PIC and MHD show good agreement for most of the conduction time it makes sense to use an MHD model for the conduction phase and then transition to PIC near the time of opening. A possible criteria for transitioning to PIC is to compare the electric pressure ( $E^2/8\pi$ ) with magnetic pressure ( $B^2/8\pi$ ) where  $E$  is estimated from Ohm's law.

## Algorithm for self-consistent modeling of conduction, opening and energy transfer phases

NRL

- Model conduction phase with an MHD or two-fluid code then transition to PIC for opening and energy transfer phases



DNA POS Workshop  
NSWC, 29 March 1995

This slide outlines our strategy for the transition from MHD to PIC. The idea is to do the bulk of the conduction phase with the MHD code and then use the information from the MHD code to initialize the PIC code. One approach is to focus in on the region of the plasma where the gap is expected to form and follow the gap opening from there with the PIC method. Once the gap forms one could then take this information and then transition back to the full scale geometry to study POS-Load coupling. Of course it would be easiest to transform directly from MHD to the full scale PIC to do both the opening and load coupling phases but this may prove to be difficult. We have developed an algorithm for completing the communication link between MHD and PIC. This algorithm is currently being implemented and should be ready to test sometime in the next few weeks.

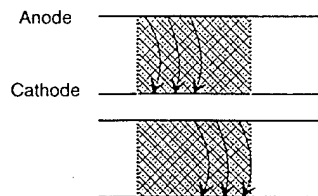
## Conduction current scaling in the EMH limit

NRL

- When ion motion can be ignored ( $\tau \ll \tau_{ci}$  and  $L_n \ll c/\omega_{pi}$ )

$$V_{hall} = \frac{3}{8} \left( \frac{cB}{4\pi en L_n} \right)$$

$$L_n^{-1} = \frac{2}{r} + \frac{1}{n} \frac{dn}{dr}$$



B penetration by  
Hall effect

- Conduction current is defined as the current when the magnetic field penetrates the length of the POS

$$I_{EMH} \sim (r L_n n \ell dI_G / dt)^{1/2}$$

DNA POS Workshop  
NSWC, 29 March 1995

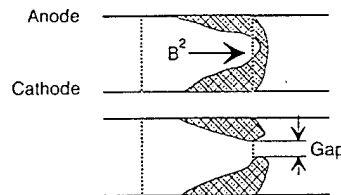
We will now present some results from recent simulations that provide insight into the physics expected to play a role during the transition from conduction to opening. This slide shows the EMH conduction current scaling with the relevant system parameters. The EMH conduction current is defined as the current in the POS plasma when the EMH shock front reaches the load end of the POS.

## Conduction current scaling in the MHD limit

NRL

- When magnetic pressure dominates over the hall term ( $V_{com} \gg V_{hall}$ )

$$\ell n M V_{com} = \int \frac{B^2}{8\pi} dt$$



Plasma distortion by  $J \times B$  forces

- Conduction current is defined as the current when the center-of-mass moves 1/2 the switch length

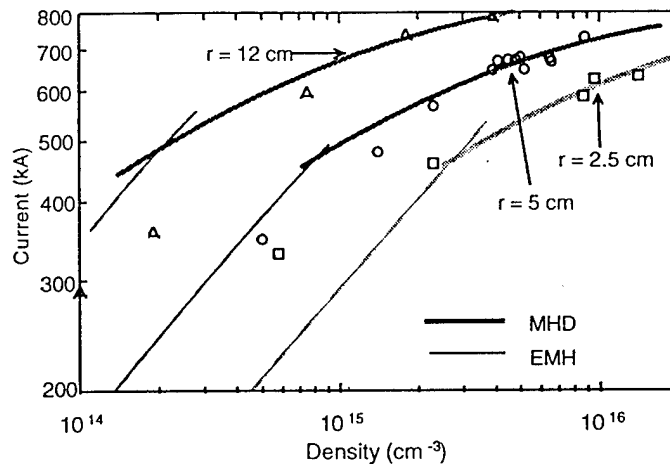
$$I_{MHD} \sim (nM)^{1/4} (r \ell dI_G / dt)^{1/2}$$

DNA POS Workshop  
NSWC, 29 March 1995

This slide shows the MHD conduction current scaling with the relevant system parameters. The MHD conduction current is defined as the current in the POS plasma when the MHD shock front (snow plow) reaches the load end of the POS.

## Conduction current in Hawk follows MHD/EMH scaling

NRL



DNA POS Workshop  
NSWC, 29 March 1995

This slide shows the comparison of the EMH and MHD conduction limits with experiments on HAWK. Note that the conduction scaling follows MHD scaling for large plasma densities but follows EMH scaling more closely at lower densities.



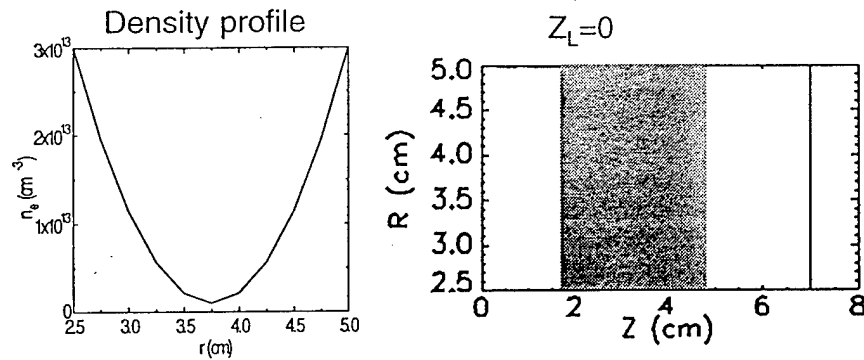
## Simulation Set-up

NRL

$$M_e = m_e/10, M_i = A m_p$$

$$dI/dt \approx 10 \text{ kA/ns}$$

$$Z_L = 0$$

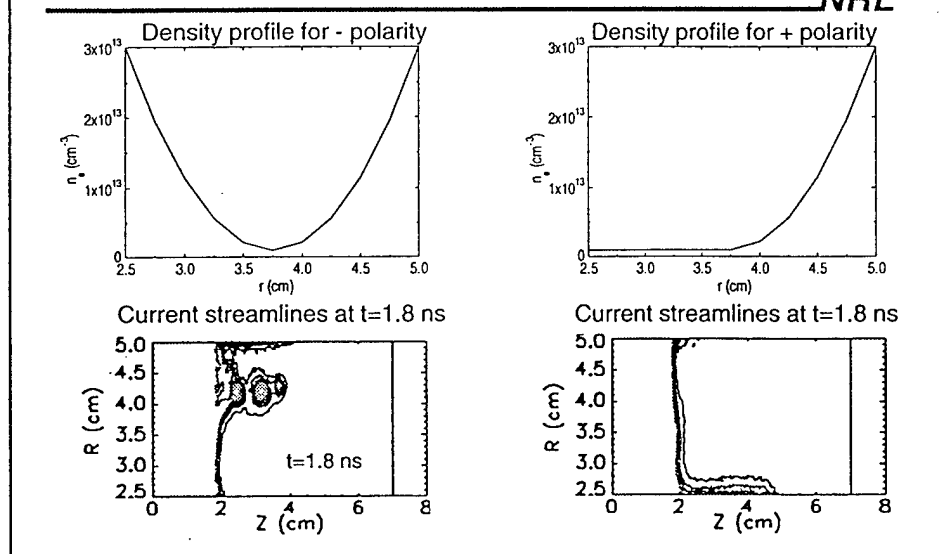


DNA POS Workshop  
NSWC, 29 March 1995

This slide shows the density profile used in the simulation results that will be shown in the subsequent slides. To look at the transition between EMH and MHD we fix the number density and vary the ion mass. At very large ion masses very little MHD motion is expected and EMH is expected to play a role. At very low ion masses MHD motion is expected to dominate. The current rose approximately linear in time at a rate of 10 kA/ns.

## PIC simulations show fast magnetic field penetration due to the Hall effect

NRL

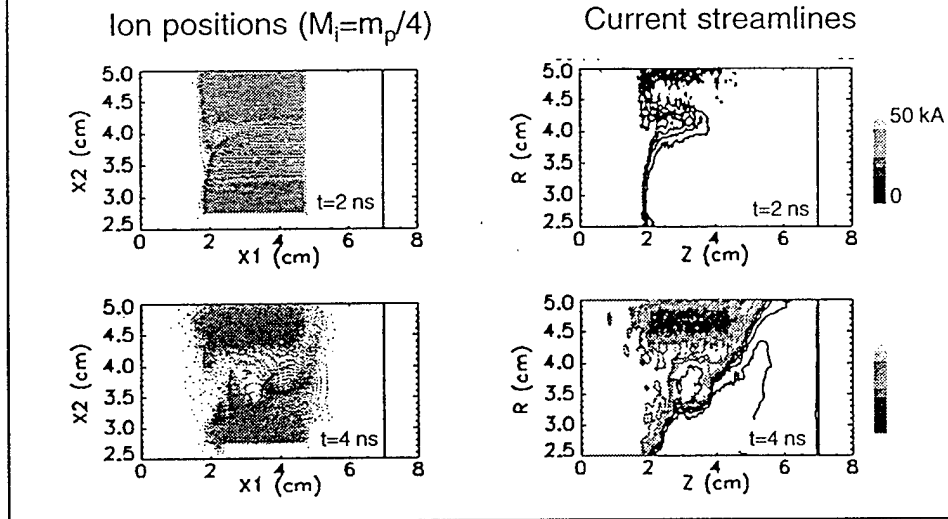


This slide is intended to demonstrate that the penetration of magnetic field into the plasma is related to the Hall penetration that has been published in context of a fluid theory. To our knowledge this is the first time that EMH effects have ever been definitely observed with a PIC code. The ions are infinitely massive in this case so we expect no MHD motion. The left hand side shows that when the density profile is parabolic the current penetrates into the plasma at the radius where the Hall speed is a maximum. This penetration is accompanied by the formation of vortices in the electron flow behind the shock front. These vortices are paramagnetic and almost a factor of two larger than the driving magnetic field. To show that this is related to the Hall effect, a run with the radial profile shown in the top right was done in positive polarity. In this case the theory predicts that magnetic field should be excluded from the bulk plasma. This is seen in the simulation results shown in the lower right. The penetration that occurs near the anode is due to the boundary condition. It is important to note that the penetration speed observed in the simulation is about 50 % slower than that predicted by theory.

**PIC simulations with  $M_i = m_p/4$  show  
penetration due to EMH and gap opening  
due to radial  $J \times B$  forces**

---

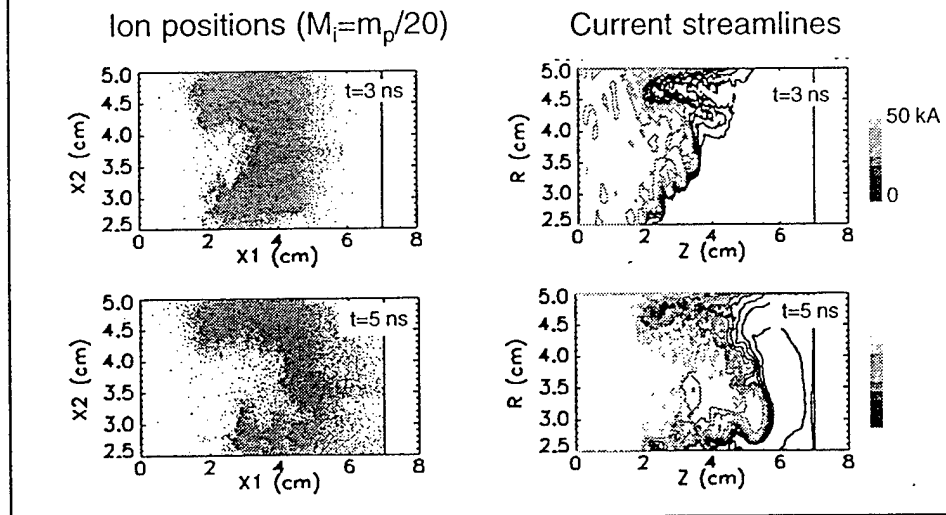
*NRL*



This slide shows the ion positions and the current streamlines for the parabolic profile for an ion mass that is 1/4 that of a proton. In this case we see axial penetration of magnetic field followed by radial  $J \times B$  motion of the ions. This is a mechanism that can produce gaps and may be responsible for the gaps that form in experiments.

## PIC simulations with $M_i=m_p/20$ show plasma distortion due to $\mathbf{J} \times \mathbf{B}$ forces

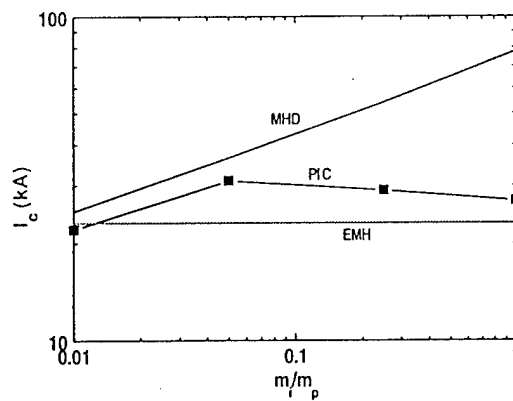
NRL



This slide shows the ion positions and current streamlines for the case where the ion mass is  $1/20$  that of a proton. The behavior of the plasma is very different between this case and the previous two cases where the ion mass is large. In this case we see primarily axial  $\mathbf{J} \times \mathbf{B}$  pushing and a large amount of axial displacement of the center of mass. The gap opening process is much more complicated in this case since the initial plasma distribution has been greatly altered by the large MHD forces.

## Conduction current in simulations follows MHD/EMH scaling

NRL



DNA POS Workshop  
NSWC, 29 March 1995

This slide shows that the simulations predict MHD scaling at low ion masses and that the scaling transitions from MHD to EMH scaling at high densities. This is in qualitative agreement with the experimental measurements.

## Summary and conclusion

*NRL*

- Progress has been made in understanding the transition from MHD dominated conduction phase to non-MHD opening phase
  - Gap probably forms in regions where scale lengths drop below  $c/\omega_{pe}$
- EMH effects observed in PIC codes for first time
  - EMH regime shows axial penetration of magnetic field followed by radial JxB gap opening
  - MHD regime dominated primarily by axial JxB pushing
- Work is underway to use MHD code for conduction phase and then initialize PIC to model gap formation

DNA POS Workshop  
NSWC, 29 March 1995

TITLE:           **DECADE CIRCUIT MODELING WITH A PRS LOAD**

AUTHOR(S):   J.R. Boller, R.J. Comisso, D. Mosher, P.F. Ottinger, and S.B. Swanekamp

DATE:           21 June 1994

ABSTRACT:       The purpose of this note is to use a revised, more complete DECADE electrical circuit model to determine and compare the kinetic energy delivered to an annular imploding z-pinch load (PRS) for DECADE configured both with and without a POS. Based on this kinetic energy, Al and Ar K-shell radiation are crudely estimated using two different analytic approaches for a range of initial radii from 0.5 to 5.0 cm. In these analyses, the implosion times are fixed by adjusting the initial Z-pinch mass and a 10:1 implosion compression ratio is assumed.

With the POS, a peak current of 15 MA is delivered to a PRS that implodes in 150 ns with a current bite of about 30%, resulting in 0.7 to 0.8 MJ of PRS kinetic energy, depending on the POS operation. Without a POS, implosion times of 150 ns or 300 ns result in peak currents of 6.1 MA or 15.6 MA with current bites of 13% or 17%, resulting in total kinetic energies of 0.1 or 0.9 MJ, respectively. Increasing the PRS length from 2 to 3 cm increases the kinetic energy by 15% and 19% for the cases with and without a POS, respectively. Results using this detailed electrical circuit model differ significantly from calculations with a simplified circuit model.

The K-shell yield estimates, an upper bound, suggest that DECADE with a POS can minimally satisfy the DECADE soft radiation requirements for Al and Ar K-shell emission (400 kJ and 200 kJ, respectively), if stable, 150-ns, 2.5- to 4-cm radius implosions can be realized. Because of the increased kinetic energy, a PRS length of 3 cm has higher K-shell yield compared to a 2-cm length. Without the POS, the yields are roughly the same as with the POS, but here the imploding load must be stable for 300 ns and start at an initial radius of 5 cm. Additional research must be carried out and new stabilization techniques investigated to better assess the stability limits for the PRS.

The initial mass for Ar is about an order of magnitude larger than what has been achieved with conventional gas puffs. To achieve such a gas fill may require additional gas injector development.

**THIS REPORT REPRESENTS UNPUBLISHED INTERNAL WORKING DOCUMENTS AND SHOULD NOT BE REFERENCED OR DISTRIBUTED WITHOUT CONSENT OF AUTHORS**

## DECADE CIRCUIT MODELING WITH A PRS LOAD

J.R. Boller, R.J. Comisso, D. Mosher,

P.F. Ottinger, and S.B. Swanekamp

### I. INTRODUCTION AND SUMMARY

Several, in depth, studies have been carried out to assess the potential of DECADE as a pulsed power driver for a plasma radiation source (PRS) for soft ( $< 10$  keV) x-rays to be used in Nuclear Weapons Effects Simulation.<sup>1,2</sup> These studies have used some form of electrical circuit model in conjunction with a sophisticated radiation treatment to identify the optimum PRS design and, thus, the potential utility of DECADE to provide PRS radiation. Since the completion of those studies, the DECADE circuit, as well as the models for the plasma opening switch (POS) have matured. The purpose of this note is to use a revised, more complete, DECADE electrical circuit model to determine and compare the kinetic energy delivered to an annular imploding z-pinch load for DECADE configured both with and without a POS. Based on this kinetic energy, Al and Ar K-shell radiation are crudely estimated using two different analytic approaches for initial radii of 0.5 to 5.0 cm. In these analyses, the implosion times are fixed by adjusting the initial PRS mass and a 10:1 implosion compression ratio is assumed. The results of this study are also useful in evaluating the utility of a DECADE PRS option in an advanced simulator development program.

For a 2-cm long PRS, the results indicate that with the POS, DECADE delivers a peak current of 15 MA to a PRS that implodes in 150 ns, with a current bite (defined for the PRS current as the ratio of the difference between peak current and final current at implosion to the peak current) of about 30%, resulting in 0.7 to 0.8 MJ of final PRS kinetic energy, depending on the POS operation. Without a POS, for implosion times of 150 or 300 ns, peak currents of 6.1 MA or 15.6 MA are delivered to the PRS with current bites of 13% or 17%, resulting in total kinetic energies of 0.1 MJ or 0.9 MJ, respectively. Increasing the PRS length from 2 to 3 cm increases the kinetic energy by 15% and 19% for the cases with and without the POS, respectively. It is important to note that the results using this detailed electrical circuit model differ significantly from calculations with a simplified circuit model. The detailed model should always be used in preference to the simplified model.

Although the estimated K-shell yields must be considered an upper bound, they suggest that DECADE with a POS can just about satisfy the DECADE soft radiation requirements for Al and Ar K-shell emission (400 kJ and 200 kJ), if stable, 150-ns, 2.5- to



4-cm radius implosions can be realized. Because of the increased kinetic energy, a PRS length of 3 cm has higher K-shell yield compared to a 2-cm length. Without the POS, the yields are roughly the same as the POS case, but here the implosion must be stable for 300 ns and start at an initial radius of 5 cm. Additional research must be carried out and new stabilization techniques investigated to better assess the stability limits for the PRS. Note that the initial mass for Ar is about an order of magnitude larger than what has been achieved with conventional gas puffs. To achieve such a gas fill may require additional gas injector development.

It is important to note that even as this report is being prepared, the DECADE circuit is evolving - especially the choice for the vacuum transmission lines. Thus, the results herein are subject to change. This is particularly true if modifications result in lower output current, because the radiation yield is a strong, non-linear function of the current delivered to the PRS.

## II. CIRCUIT DESCRIPTION AND CHOICE OF MODEL

We began modeling the DECADE generator with a PRS load using a simplified equivalent circuit supplied by PI<sup>3</sup> as shown in Fig. 1. Circuit values for both a single module and the equivalent values for 16 parallel modules are shown in this figure. Figure 2 shows how this circuit was configured for use with the NRL BERTHA transmission line program.<sup>4</sup> In this model, the Marx and transfer capacitor (TC) are represented by short line segments (5 ns), essentially treating them as lumped circuit elements. The initial voltage on element number 1 corresponds to  $\pm 85$  kV charge on the Marx. The remaining sections up to the POS use realistic lengths. The electrical length of element 9 in Fig. 2, representing the PRS, is 1 time step long, i.e., 0.2 ns. The initial impedance of this element is adjusted so that its inductance ( $L = Z_0 \Delta t$ ) is equal to the sum of the feed inductance, inclusive from the POS, and the initial inductance of the load. C. Deeney of PI has estimated that, for the 16 module system, this inductance may range from 6.5 to 9.5 nH for a 2-cm long pinch depending on the final configuration. A conservative value of 10 nH was used for the analysis presented here.

This simplified circuit was used to obtain estimates of PRS performance using the kinetic energy at implosion as a figure of merit, both with and without the POS. The case without the POS was reported in Ref. 5. To check if significant errors were incurred by using the simplified model, a more detailed analysis was performed. Recently, PI provided the more detailed circuit shown in Fig. 3 (single module circuit values).<sup>3</sup> This circuit was transformed into a correspondingly detailed transmission-line circuit, shown in Fig. 4, for

use with BERTHA. The diverter switches and their loads were not included because they switch after implosion and should have no effect on the load during the time of interest. This more detailed model also includes resistive losses in the Marx generator and water lines and skin resistance of the vacuum feed conductors, but not MITL losses. Elements 33 and 34 in Fig. 4 correspond to a 8-ns, 3- $\Omega$  and a 4-ns, 5.7- $\Omega$  line, respectively, for each module. This is the assumed vacuum transmission line configuration for all that follows. In the detailed model, the TC is switched at 1.05 MV.

A comparison of the simplified and more detailed models is shown in Fig. 5 where the current into a short circuit at the POS is plotted for each model. The difference in the two waveforms is significant and is attributed to: (1) no resistive losses in the simplified model, (2) revised circuit parameters in the more detailed model based on recent measurements on DM1, and (3) a more accurate representation of the machine by the detailed model. The increased inductance from the water line to the first MITL (2.5 to 3.7 nH) is one example of differences between the two models. The simple model was modified in an attempt to provide closer agreement with the results of the more detailed model; however some differences were still observed, especially in the current downstream of the POS, which could effect the PRS yield. Because of these discrepancies and the fact that the even more detailed model runs very quickly on BERTHA, it was decided to use the more detailed model (Figs. 3 and 4) for all DECADE modeling. Note that the exact configuration for the vacuum transmission lines on DECADE is still evolving. When a final configuration is determined, the calculations below should be re-visited.

### III. LOAD MODEL

An imploding load routine is included in the BERTHA transmission-line program. The input parameters for this routine are initial radius, mass, length, and initial inductance. The mass is treated as a thin annulus at the initial radius, i.e. a slug model. The load is represented as a varying-impedance transmission-line element with an electrical length of one time step. A new radius, velocity, and inductance are calculated at each time step in accordance with a JXB radial implosion. The calculation is terminated when the radius is 1/10 of the initial radius. Except where noted, the load is a 2-cm long PRS with a 2.5-cm initial radius. In all cases but two, the mass is chosen to give an implosion time of 150 ns. This choice is somewhat arbitrary and reflects a subjective estimate of a maximum implosion time before significant Rayleigh-Taylor instability growth. For the case of no POS (Sec. V. A., below), the mass is also chosen to give a 300-ns implosion time for either 2- or 3-cm long loads.

#### IV. DESCRIPTION OF POS MODEL

The POS was modeled by using a flow-impedance concept<sup>6,7</sup> for which the flow impedance is defined by

$$Z_f = \frac{V_{SW}}{(I_{AU}^2 - I_{CD}^2)^{1/2}}, \quad (1)$$

where  $V_{SW}$  is the switch voltage,  $I_{AU}$  is the anode current upstream of the POS, and  $I_{CD}$  is the cathode current downstream of the POS. The difference between the anode current upstream of the POS and the cathode current downstream of the POS is the net current flowing in the form of vacuum electrons. This expression can be derived from pressure balance arguments.<sup>6,7</sup> In general, some of this vacuum flow is switch current and some is MITL electron flow. If it is assumed that all the MITL electron flow is lost and lumped with the switch current, then the net current in the POS is given by  $I_{AU} - I_{CD}$ . With this approximation, the resistance of the switch [ $R_S = V_{SW}/(I_{AU} - I_{CD})$ ] can be related to the flow impedance by

$$R_s = Z_f \left( \frac{I_{AU} + I_{CD}}{I_{AU} - I_{CD}} \right)^{1/2}. \quad (2)$$

In this model, the flow impedance is assumed to rise linearly in time to a specified maximum flow impedance in a specified time (30 ns for most of these runs) and subsequently remain constant. The current available for driving the PRS, i.e., the load current, is  $I_{CD}$ .

In general, the flow impedance is the vacuum wave impedance between the centroid of the electron space charge and the anode in the switch region.<sup>8</sup> Therefore, the flow impedance must remain smaller than the local vacuum impedance of the transmission line,  $Z_0$ . When the electron flow uniformly fills the MITL it can be shown that  $Z_f \cong Z_0/2$  is a reasonable approximation.<sup>7</sup> When the electron flow is very well insulated (i.e. confined very close to the cathode surface), the flow impedance increases to the vacuum impedance of the transmission line. For the analysis reported here,  $Z_f$  was chosen to be  $30D/R$ , where  $D$  is the effective gap for magnetic insulation<sup>9</sup> and  $R$  is the center conductor radius. Except where noted,  $R$  was 6.35 cm (as currently being planned for DM-1) and  $D$  is 0.5 cm (representing expected DM-1 POS performance).

## V. ELECTRICAL PERFORMANCE

### A. Without the POS

The Decade circuit in Fig. 4 was used to directly drive an imploding load without the POS. Results of BERTHA modeling are shown in Fig. 6. Load currents,  $I_{PRS}$ , and kinetic energies, KE, for 150- and 300-ns implosion times are shown. Also shown is the current,  $I_{SC}$ , delivered to a short circuit at the initial PRS radius. The mass was chosen to obtain 150- and 300-ns implosion times. For implosion times of 150 or 300 ns, a peak current of 6.1 MA or 15.6 MA is delivered to the PRS with a current bite of 13% or 17%, resulting in a total kinetic energy of 0.14 or 0.92 MJ, respectively. These energies compare with 0.25 or 1.32 MJ for the simplified circuit.<sup>5</sup> The voltage developed across the PRS and 10-nH feed inductance (the POS position, junction 31 in Fig. 4) is  $\cong 700$  kV during the early phase of the current pulse, then rises to 1.6 MV at the time of implosion for the 150-ns case. For the 300-ns implosion time case, equivalent voltages of 800 kV and 2.1 MV are calculated. If the PRS length is increased to 3 cm (with appropriate load inductance change, see below), the kinetic energy increases by 19% to 1.09 MJ. The electrical performance of DECADE without a POS is summarized in the last three rows of Table 1 for PRS loads of 2-cm and 3-cm length.

### B. With the POS

Numerous modeling runs were made with a POS-driven PRS load using a variety of POS parameters. Figure 7 shows the typical output of a BERTHA calculation. The POS and PRS parameters shown in the figure are baseline values. The waveforms in Fig. 7a are the current upstream of the POS ( $I_{POS}$ ), the PRS current ( $I_{PRS}$ ), and PRS kinetic energy (KE). The POS conduction time is about 250 ns. Figure 7b shows the voltage at the POS ( $V_{POS}$ ),  $I_{PRS}$ , and the PRS radius for the same conditions as in Fig. 7a. Note that the voltage at the POS reaches 3 MV during the rise of the PRS current - much higher than the voltage levels for the no-POS case, while the voltage at maximum compression, 1.1 MV, is lower than the no-POS case. Runs were also made with the POS opening time ( $T_o$ ) increasing from 30 to 50 ns, the POS conduction current ( $I_C$ ) decreasing from 32 MA (2 MA/module) to 27.2 MA (1.7 MA/module), and the POS effective gap (D) decreasing from 0.5 to 0.35 cm. One run was also made for a PRS length of 3 cm. For this case, the initial inductance was increased by 0.75 nH representing a 50% increase in the PRS portion of the total load inductance. Results of these calculations are

summarized in Table 1, along with the case for no POS. The first row in Table 1 corresponds to the baseline case shown in Fig. 7. In subsequent rows, changes in the baseline values are bolded and underlined. In summary, DECADE with a POS should deliver about 15 MA to a z-pinch that implodes in 150 ns with a current bite of about 30%, resulting in 0.68 to 0.83 MJ of PRS kinetic energy, depending on POS performance. If the PRS length is increased to 3 cm, the kinetic energy should increase by 15% to 0.91 MJ.

Table 1. Summary of PRS Modeling

POS				PRS							
gap cm	R cm	T <sub>o</sub> ns	I <sub>c</sub> MA	R <sub>i</sub> cm	length cm	mass mg	t <sub>impl</sub> ns	I <sub>max</sub> MA	I <sub>impl</sub> MA	KE MJ	V <sub>impl</sub> cm/ $\mu$ s
0.5	6.35	30	32.0	2.5	2	5.4	152	15.1	10.6	0.79	54.0
<b><u>0.35</u></b>	6.35	30	32.0	2.5	2	4.0	151	14.1	10.0	0.68	58.3
<b><u>0.65</u></b>	6.35	30	32.0	2.5	2	6.0	150	15.9	10.9	0.83	52.6
0.5	6.35	<b><u>50</u></b>	32.0	2.5	2	4.4	151	15.0	10.4	0.74	58.1
0.5	6.35	30	<b><u>27.2</u></b>	2.5	2	4.6	150	14.9	10.6	0.78	58.1
0.5	6.35	30	32.0	2.5	<b><u>3</u></b>	6.9	152	14.0	8.8	0.91	51.3
-	-	-	-	2.5	2	0.54	151	6.1	5.3	0.14	72.5
-	-	-	-	2.5	2	10.0	301	15.6	13.0	0.92	42.8
-	-	-	-	2.5	<b><u>3</u></b>	13.2	300	14.0	10.9	1.09	40.6

### C. Estimates using Flux Conservation

Values for the peak PRS current and PRS current at implosion (9th and 10th columns in Table 1) are compared with estimates based on flux conservation arguments. In applying flux conservation, it is assumed that the relevant upstream inductance is that inductance electrically separated from the PRS by half the implosion time and that with the POS, a 2-step process (POS opening followed by implosion) is appropriate. With the POS, this upstream inductance is 8.34 nH. Without a POS, the inductances upstream of the PRS are 18.34 or 23.26 nH (150- or 300-ns implosion time, respectively). These inductances include the 10-nH feed and initial inductance of the PRS. The results indicate that currents computed from the more detailed model are, in general, about 10 to 30% higher than predicted by flux conservation. The larger currents result from the fact that

current is still being driven into the system from the upstream circuit during the POS opening and PRS implosion. Therefore, there is a source of flux increase and flux is not rigorously conserved.

## VI. ESTIMATED K-SHELL RADIATION YIELDS:

K-line yields calculated for some BERTHA modeling runs are summarized in Table 2, below. In all cases, it is assumed that the total current conducted by the POS is 32 MA (2 MA/ module) and that the POS opens to an effective gap of 0.5 cm in 30 ns (baseline case). The kinetic energy and  $mr^2$  values from the BERTHA runs were used to predict radiation yields of both Al and Ar K-lines for initial radii ranging from 0.5 cm to 5 cm.  $Y_M$  is the yield calculated from Mosher's 2-level model<sup>10</sup> and  $Y_W$  is the yield calculated from the Whitney-Giuliani model.<sup>11</sup> The table shows yields for the 2.5-cm radius used in the BERTHA runs as well as the maximum yields at their corresponding radii.

Table 2. Predicted Al and Ar K-Line Yields

POS y/n	$T_{impl}$ ns	length cm	KE MJ	Aluminum K-Shell				Argon K-Shell			
				$R_i$ cm	mass mg	$Y_M$ kJ	$Y_W$ kJ	$R_i$ cm	mass mg	$Y_M$ kJ	$Y_W$ kJ
y	152	2	0.79	2.5	5.40	340	237	2.5	5.40	244	97
				4.0	2.11	392	237	4.0	2.11	294	237
y	152	3	0.91	2.5	6.90	382	273	2.5	6.90	255	95
				4.0	2.70	444	273	4.0	2.70	314	273
n	151	2	0.14	2.5	0.54	61.5	42.6	2.5	0.54	35.4	38.2
n	301	2	0.92	2.5	10.0	335	176	2.5	10.0	209	50.3
				5.0	2.50	459	275	4.5	3.09	336	275
n	300	3	1.09	2.5	13.2	371	180	2.5	13.2	210	46.5
				5.0	3.30	531	326	5.0	3.30	373	326

Although these calculations must be considered an upper bound on the K-shell yield, they suggest that DECADE with a POS can marginally satisfy the DECADE soft radiation requirements for Al and Ar K-shell emission (400 kJ and 200 kJ, respectively), if stable, 150-ns, 2.5- to 4-cm radius implosions can be realized. A PRS length of 3 cm increases the PRS kinetic energy and therefore the K-shell yield, compared to a 2-cm length. Without the POS the yields are roughly the same as with the POS, but here the imploding load must be stable for 300 ns and start at an initial radius of 5 cm. Additional research

must be carried out and new stabilization techniques investigated to better assess the stability limits for the PRS.

Note that the initial PRS mass for Ar is about an order of magnitude larger than what has been achieved with conventional gas puffs. To achieve such a gas fill may require additional gas-injector development.

## VII. ASIDE - OUTPUT CURRENT WITHOUT 0.5-OHM WATER LINE

Out of curiosity, a BERTHA calculation was made without the 100-ns, 0.5- $\Omega$  (0.031- $\Omega$  total parallel value) output water line in the circuit. This component is represented by element 5 in Fig. 2, and elements 24 and 25 in Fig. 4. Figure 8 shows the short-circuit currents into the POS for both configurations. The water line provides a little faster overall rise time but achieves about the same peak current amplitude. However, this comparison may not be realistic because for proper front-end geometrical convergence, the water line may have to be replaced with a coaxial section of finite length and impedance, and this was not included in the analysis. This would lower the current amplitude and increase the current rise time over what is shown in Fig. 8 for the no output-water-line case. On the other hand, if the convergence issue could be circumvented, the benefits of the water-output-line are not entirely obvious. The oscillations in the waveform without the water line are due to the inductive coupling (7.06 nH) provided by the transmission-line elements between the transfer capacitor and the 8-ns MITL section, which is equivalent to a 48-nF capacitor on a long time scale. The period of this LC ringing is 116 ns, which is in agreement with the ringing observed on the waveform in Fig. 8.

## VII. ACKNOWLEDGMENTS

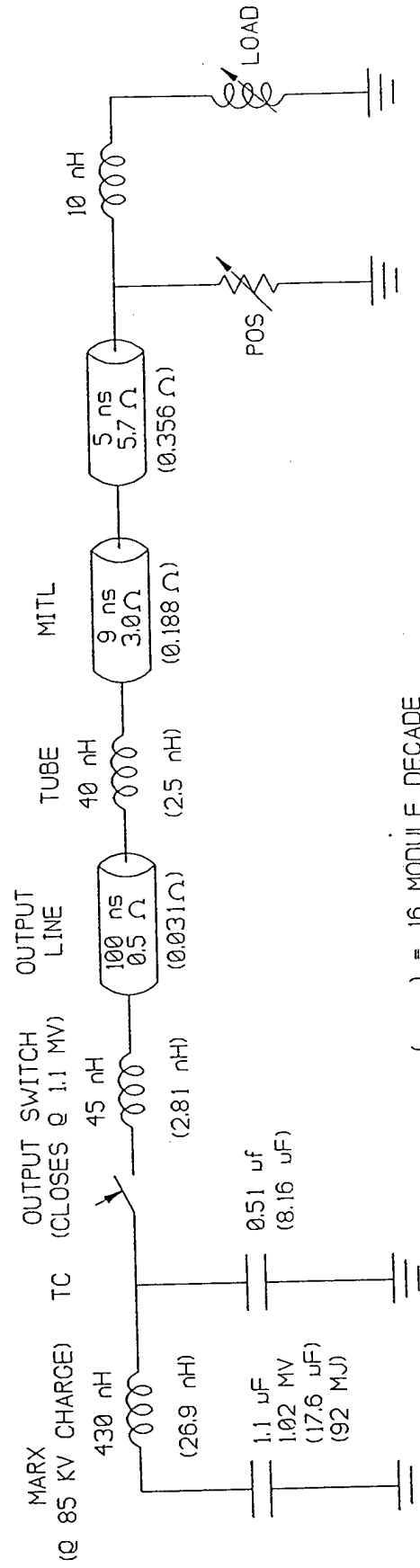
The assistance of Dr. J.L. Giuliani, Jr., NRL Code 6720, in reviewing our calculations and Dr. F.C. Young in reading the text is greatly appreciated.

## IX. REFERENCES

1. "Numerical Simulations of PRS Yields For a Pulsed Power, Decade-Class Generator," J.L. Giuliani, Jr., M. Mulbrandon, J. Davis, P.F. Ottinger, R.J. Commisso, C. Deeney, and P.A. LePell, to be published in JREERE (1994).
2. "PRS Projections for DECADE," K.G. Whitney, J.W. Thornhill, J.L. Giuliani, Jr., and J. Davis, NRL Memorandum Report NRL/MR/6722--94-7459 (1994).
3. Steve Ashby, private communication
4. "BERTHA - A Versatile Transmission Line and Circuit Code," D.D. Hinshelwood, NRL Memorandum Report 5185, Nov. 1983.
5. "Comments on DECADE PRS with no POS," R.J. Commisso, J.R. Boller, D. Mosher, and K. Whitney, presentation at the Dec. 1994 DECADE Technical Exchange Meeting at PI.
6. "Experiments on a Current-Toggled Plasma-Opening Switch," C.L. Mendel, Jr., M.E. Savage, D.M. Zagar, W.W. Simpson, J.W. Grasser, and J.P. Quentenz, J. Appl. Physics, 71, 3731 (1992).
7. "Power Flow between a Plasma-Opening Switch and a Load Separated by a High Inductance Magnetically Insulated Transmission Line", S.B. Swanekamp, J.M. Grossmann, P.F. Ottinger, R.J. Commisso, and J.R. Goyer, J. Appl. Physics, (accepted for Pub. 1994).
8. B.V. Weber, private communication.
9. "Characterization of a Microsecond-Conduction-Time Plasma Opening Switch," R.J. Commisso, P.J. Goodrich, J.M. Grossmann, D.D. Hinshelwood, P.F. Ottinger, and B.V. Weber, Phys. of Fluids B 4, 2368 (1992).
10. "K-Line Yield Scaling for the Plasma Radiation Source," D. Mosher, J. Giuliani, N. Qi, and M. Krishnan, Bull. Am. Phys. Soc. 38, 2013 (1994), and to be submitted for publication.
11. "PRS Scoping Study I: Scaling Law Estimates for K-Shell Radiation Yields on JUPITER-Class Generators," J.L. Giuliani, Jr., J. Davis, M. Mulbrandon, K. Whitney, and J.W. Thornhill, Naval Research Laboratory Memorandum Report NRL/MR/6720--94-7466 (1994).



# EQUIVALENT CIRCUIT DIAGRAM FOR DECADE WITH PRS LOAD



DECPRS1

3-22-94

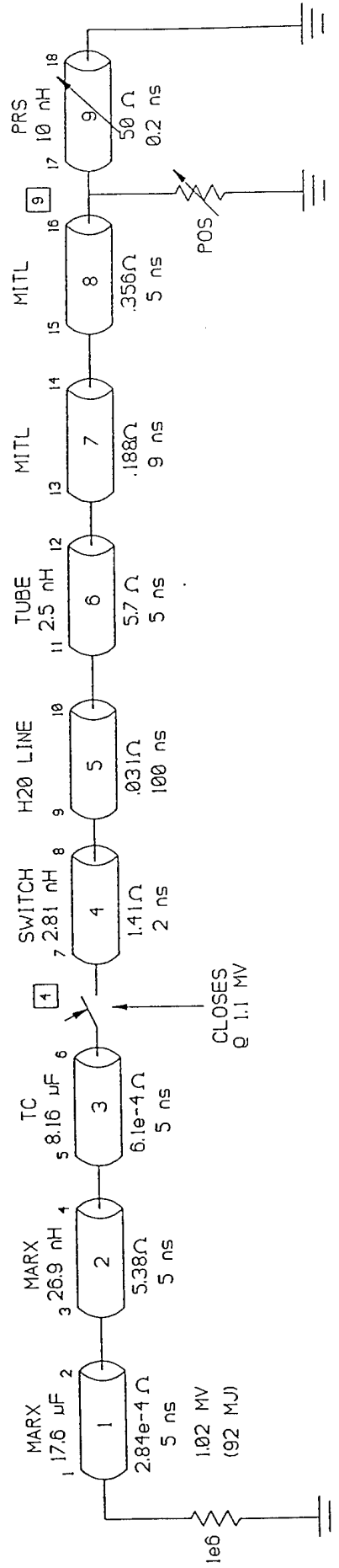
COURTESY OF STEVE ASHBY, PI

Figure 1. Simplified decade circuit diagram with PRS load.

# DECADE T-LINE CIRCUIT WITH POS & PRS

CONFIGURATION: DEC1

TS = 0.2 NS



3-22-94

Figure 2. Simplified transmission-line circuit of decade.

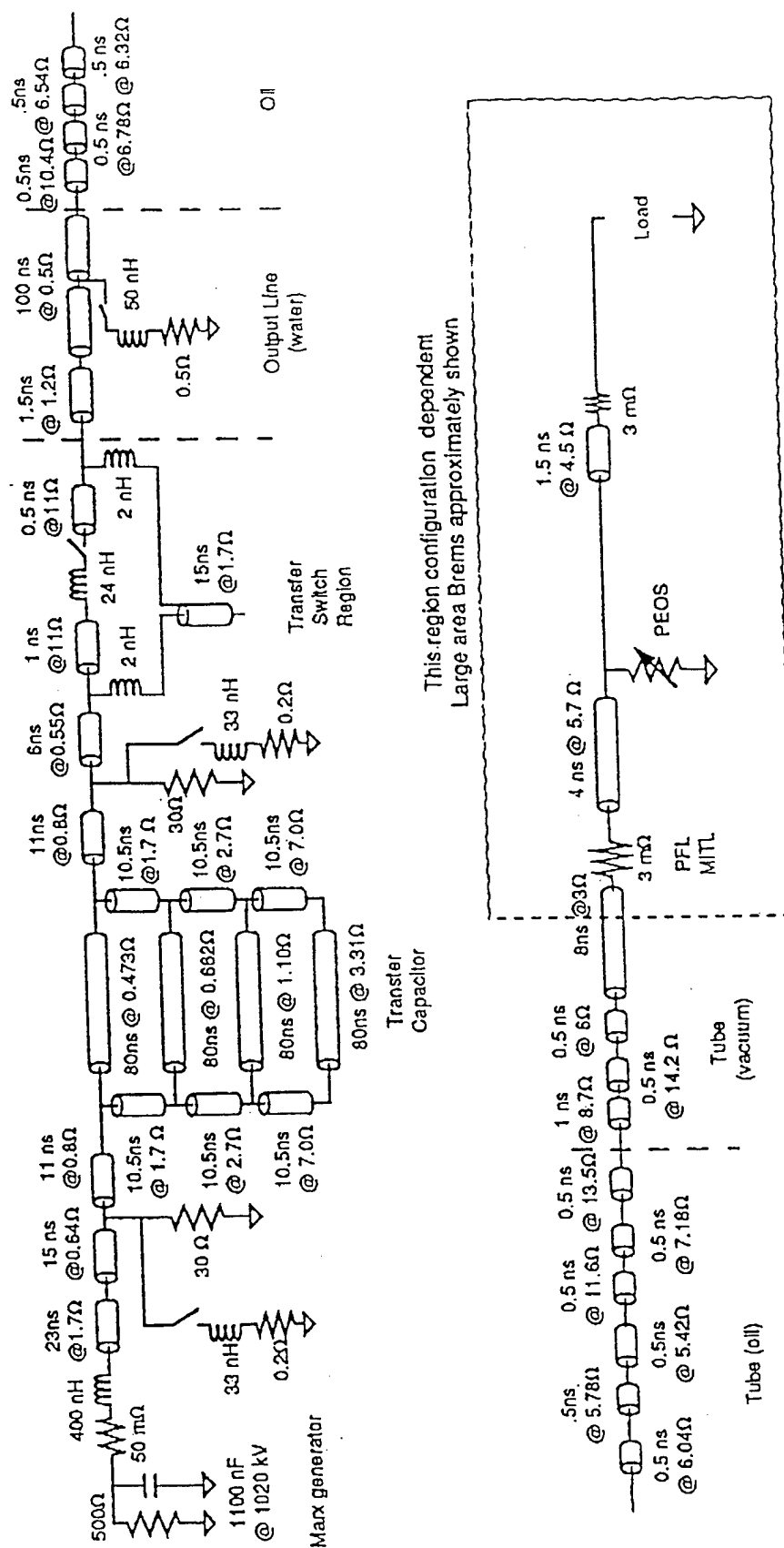
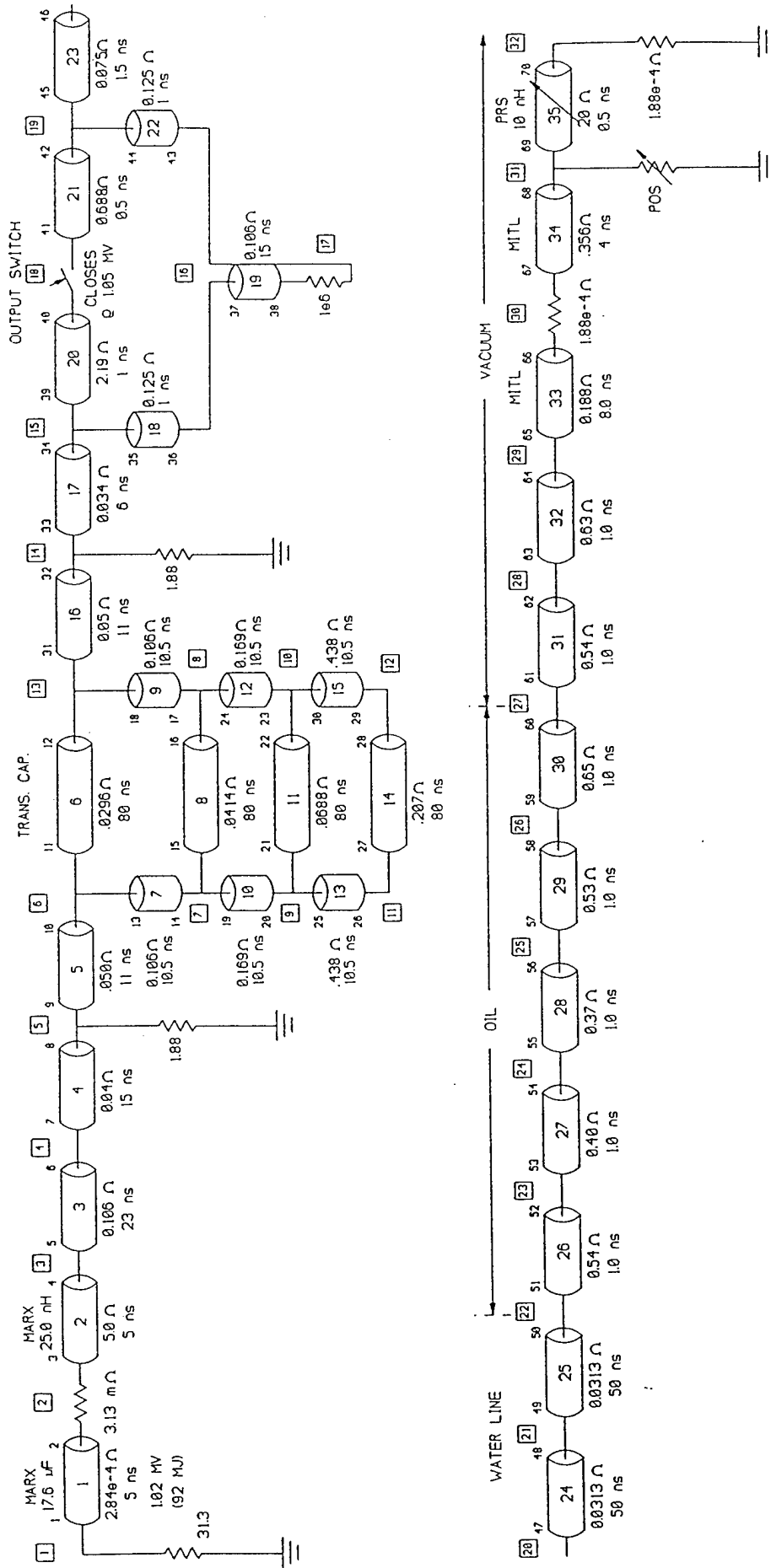


Figure 3. Detailed decade circuit diagram.

# COMPLETE DECADE T-LINE CIRCUIT WITH POS, PRS, & LOSSES

CONFIGURATION: DECF  
TS = 0.5 NS



3-30-91

Figure 4. Detailed transmission-line circuit of decade.

# DECADE CURRENT INTO POS USING SIMPLE AND DETAILED MODELS

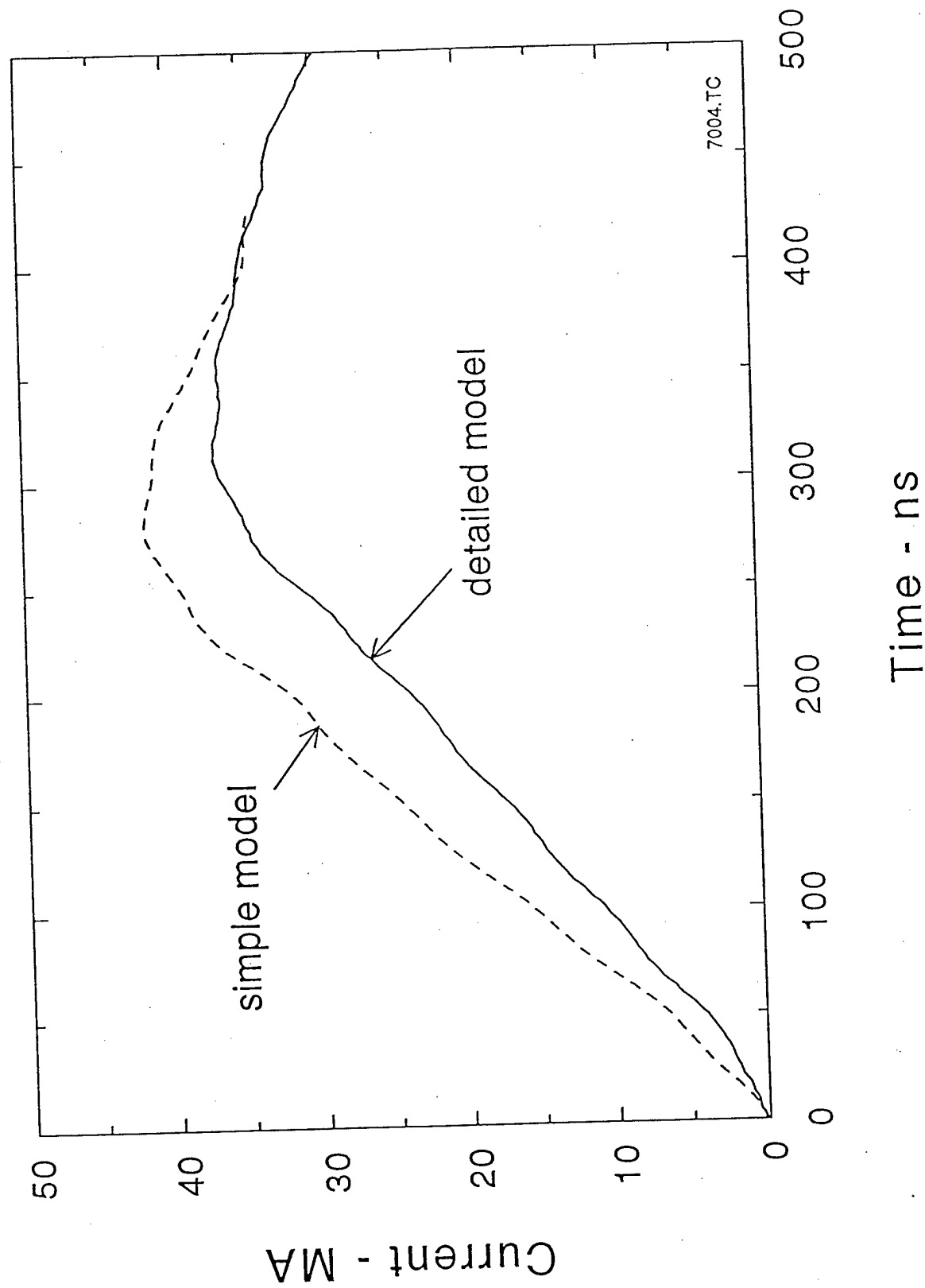


Figure 5. Comparison of currents into the POS using the simplified and detailed circuit models.

# DECADE WITH PRS LOAD AND NO POS

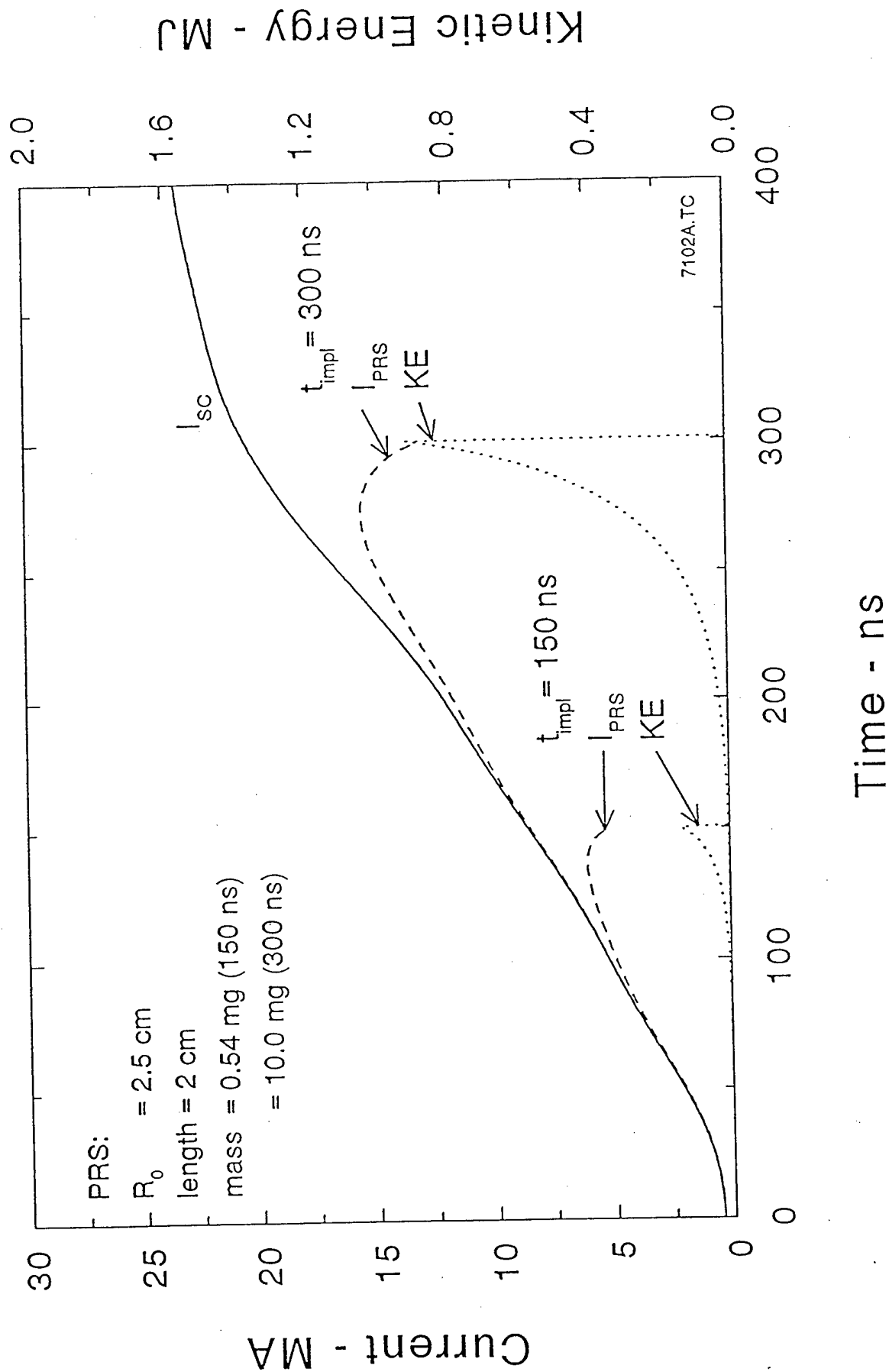
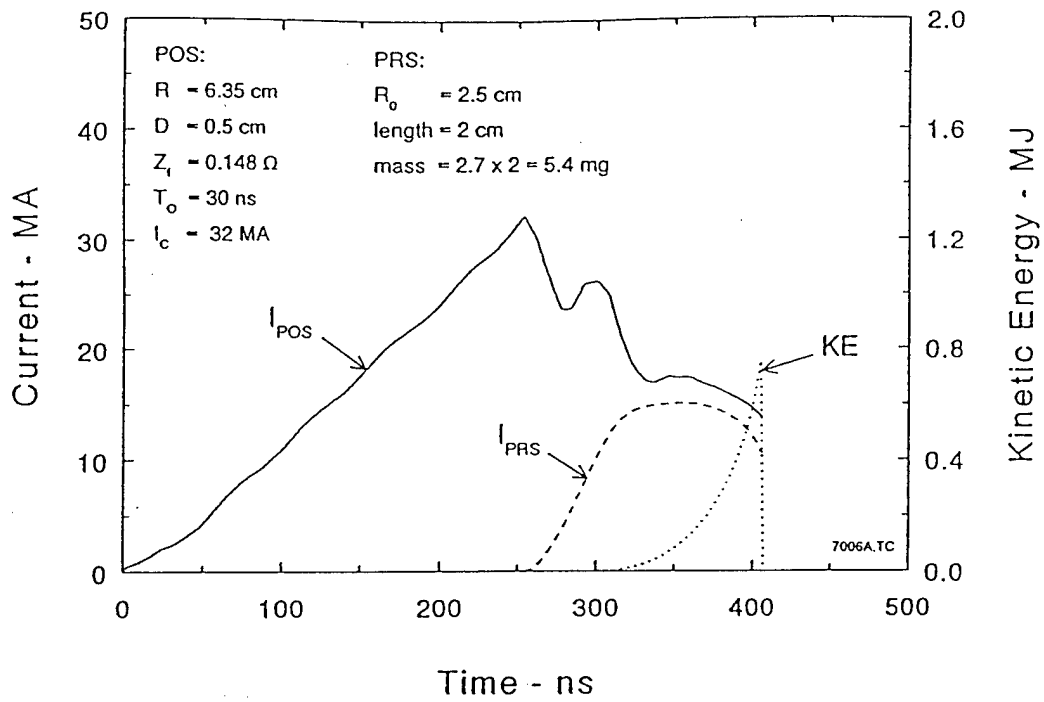
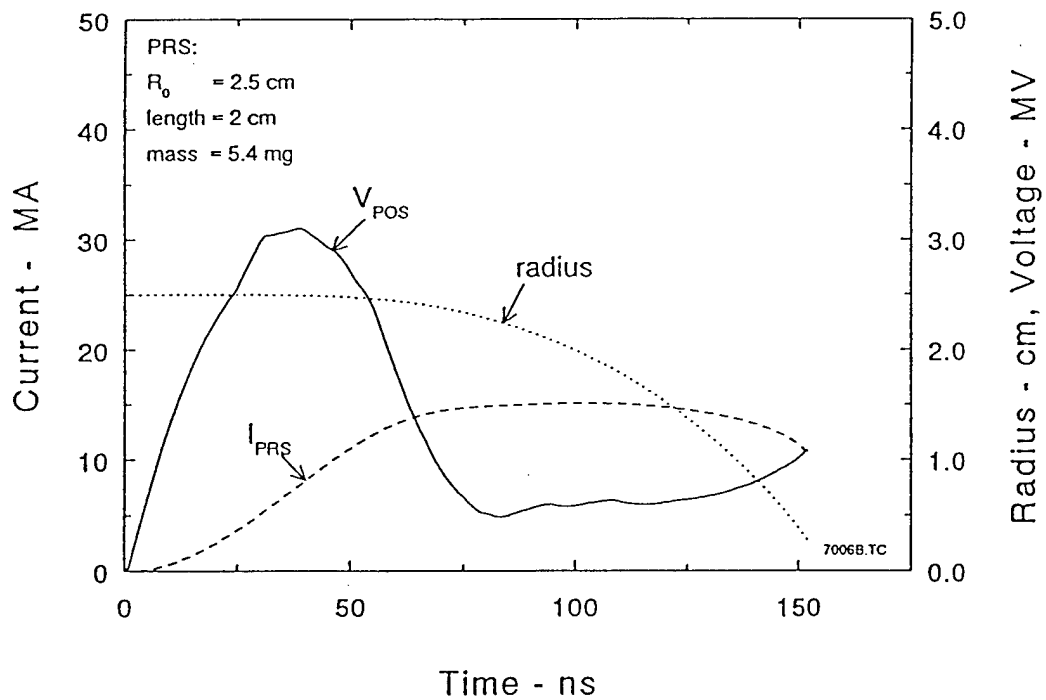


Figure 6. PRS Performance for 150 and 300 ns implosion times without a POS.



a. POS and PRS currents and kinetic energy.



b. POS voltage and PRS current and radius.

Figure 7. Typical PRS waveforms with POS for baseline case.

# DECADE CURRENT INTO POS WITH AND WITHOUT WATER LINE

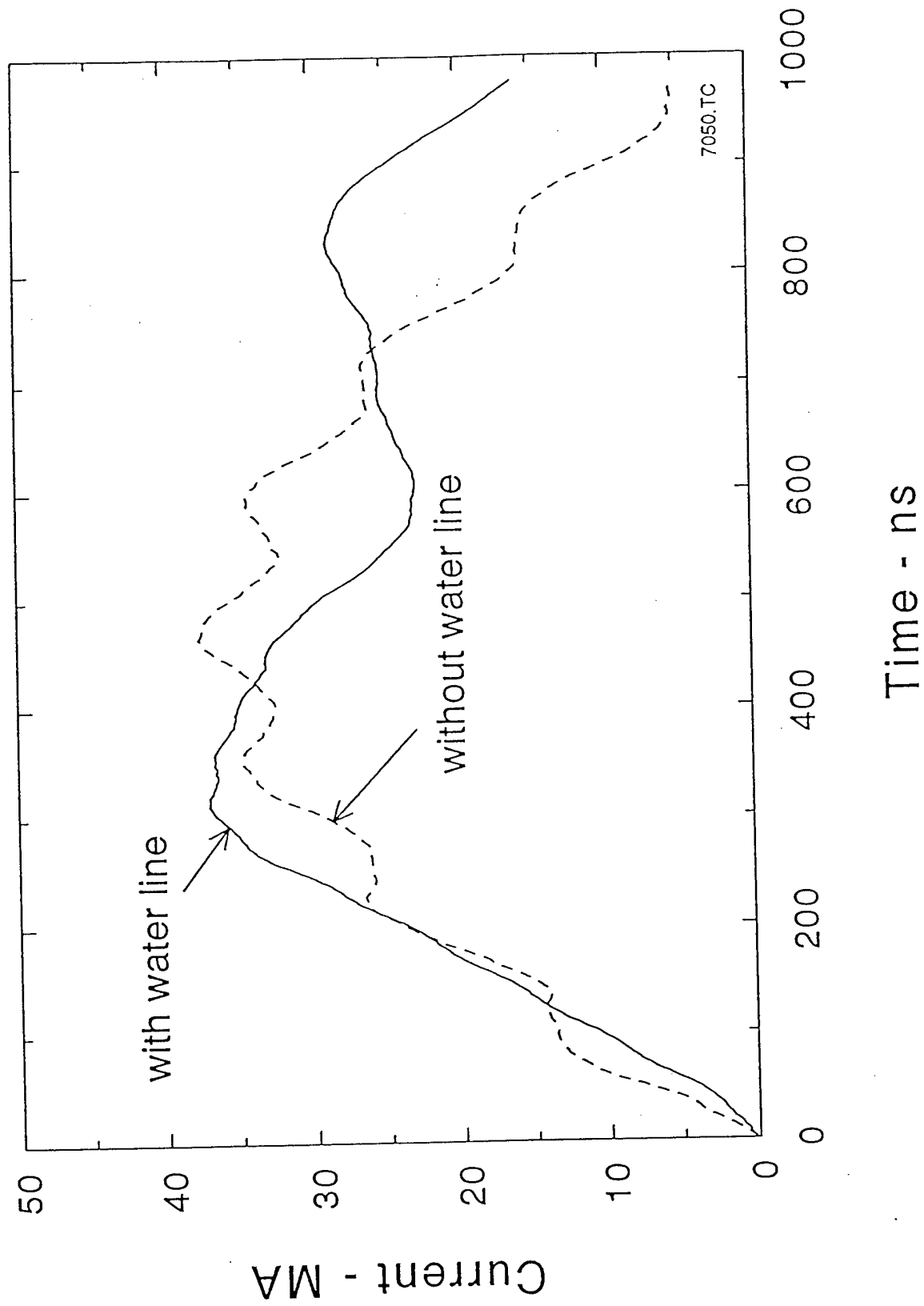


Figure 8. Currents into the POS with and without a water line.



TITLE: CATHODE CURRENT MEASUREMENTS ON HAWK

AUTHORS: B. Weber, M. Sucky

DATE: 19 May 1993

ABSTRACT: Initial results of cathode current measurements with a diode load are reported and compared with similar measurements using a short circuit load. The B-dot probe technique is complicated by plasma shielding in some cases; further experimental tests are required to determine the limitations of these current monitors. For long conduction time (1  $\mu$ s), shielding of probes near the switch is evident, even with short circuit loads. The cathode current near the load indicates a large electron flow current (200 kA). A diode load shot with shorter conduction time (700 ns) shows reasonable currents at all locations, although some shielding may occur in this case too. Interpreting the signals literally, electron losses are divided between the switch region and the load region. The load current measured on the outer conductor is a little higher than the cathode current near the load. A center-fed diode (power symmetrizing technique) may be responsible for the highly symmetric up/down load current waveforms on these shots. The diode impedance behavior is interesting on these shots because high current, hollow beams are formed that evidently do not pinch. This phenomenon is consistent with the idea that the impedance is determined by Child-Langmuir emission instead of a critical-current relation. This experiment will continue with the goal of improving our understanding of POS/load power flow for comparison with numerical calculations and ongoing experiments at PI.

THIS REPORT REPRESENTS  
UNPUBLISHED INTERNAL  
WORKING DOCUMENTS AND  
SHOULD NOT BE REFERENCED  
OR DISTRIBUTED

## Setup

The experimental setup on Hawk is illustrated in Fig. 1. The center conductor radius is 5 cm (4 inch diameter). The plasma injection aperture is masked to a length of 2.5 cm for the data presented below. The 12 cable guns are located 9 cm from the center conductor. The anode current monitors consist of sets of B-dot loops at three locations: near the switch ( $I_{SU}$  and  $I_{SL}$ ), between the switch and load ( $I_{LU}$  and  $I_{LL}$ ), and at the load ( $I_{LU2}$  and  $I_{LL2}$ ).

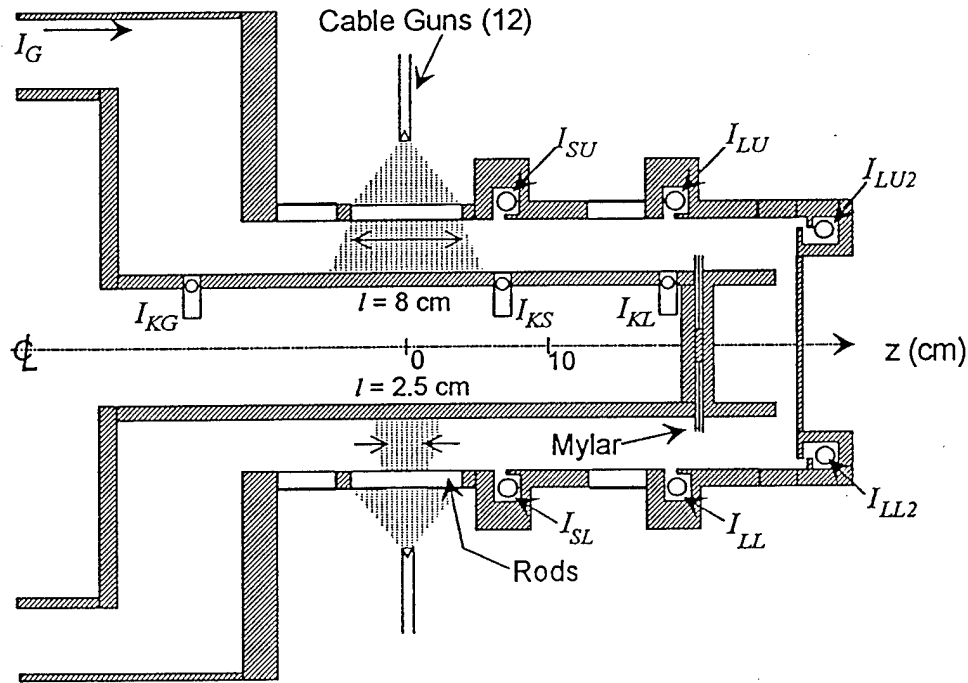


Figure 1. Hawk POS setup and cathode current monitors

New cathode current monitors were installed for these experiments, located on the generator side of the switch ( $I_{KG}$ ), near the switch ( $I_{KS}$ ), and near the load ( $I_{KL}$ ). The cathode monitors  $I_{KS}$  and  $I_{KL}$  are located opposite probes on the anode as shown. The B-dot loops are potted inside insulating (urethane) holders, and supported flush with the center conductor surface, as shown. The loops respond to magnetic field that dips into the 1/2" diam holes, resulting in a signal reduction of about a factor of ten compared with the signal expected if the loops were exposed to the vacuum field. The cathode current cables were fed to the screen room using an inductive isolator built by Rick Fisher and Dave Hinshelwood. The isolator worked well, with no obvious pickup from ground currents, etc. Calibration was accomplished by measuring the signals using a short circuit load without any plasma. Comparing the signals with the standard generator current measured at the door ( $I_G$ ) determined the time shift, calibration factor, and the effective RC constant (about 1  $\mu$ s) needed to match the shape and magnitude of the  $I_G$  signal.

The diode load used in these experiments is a center-fed, hollow ( $\Delta r = 1/4$ ") cylindrical cathode opposite a 1/4" thick steel anode. The current is forced through a washer ( $\sim 1$  cm diam) to improve the symmetry of the power to the cathode. Mylar insulation is used to prevent breakdown between the small gap. There is evidence that this technique improves the symmetry

of the electron beam, but the evidence is not definitive. (After about 15 shots, the current contact erodes to the point that the bolt breaks and has to be replaced.)

These experiments are intended to develop a believable cathode current monitor technique and eventually use the information to study electron flow and current losses in the Hawk POS. Any technique of this kind will be limited by shielding effects. Surface plasmas can cover the probe, decreasing the signal and implying a lower current than the current of interest. This is a problem especially on the cathode side of the system. It is assumed that the cathode monitors are at least a lower bound for the current of interest. These first measurements will be illustrated using a short circuit load shot (1366) and a diode load shot (1374).

### Short circuit load shot

The center-fed diode was shorted to the anode to calibrate the probes and to measure currents during POS shots for comparison with diode shots. Figure 2 shows currents measured on the outer conductor:  $I_G$  is the generator current measured at the door (also known as  $I_{OUT}$ ). The cathode current measured on the generator side of the POS,  $I_{KG}$ , is almost identical to  $I_G$  for all shots so far.  $I_S$  is the average of  $I_{SU}$  and  $I_{SL}$ ,  $I_L$  is the average of  $I_{LU}$  and  $I_{LL}$ ,  $I_{L2}$  is the average of  $I_{LU2}$  and  $I_{LL2}$ . The plasma delay was about 5.3  $\mu s$  for this shot, resulting in a conduction current of 670 kA and a conduction time of 980 ns (ignoring the foot in the load currents). The delay between  $I_S$  and  $I_L$  is about 70 ns, a typical value (see TN 93-06). The low amplitude of  $I_S$  is probably the result of shielding. It is difficult to imagine a physically acceptable electron flow to explain the low value of  $I_S$ . It is possible that plasma moves over the measurement slot and "crowbars" the probes. Another possibility is that electrons bombard the probe and slot surfaces

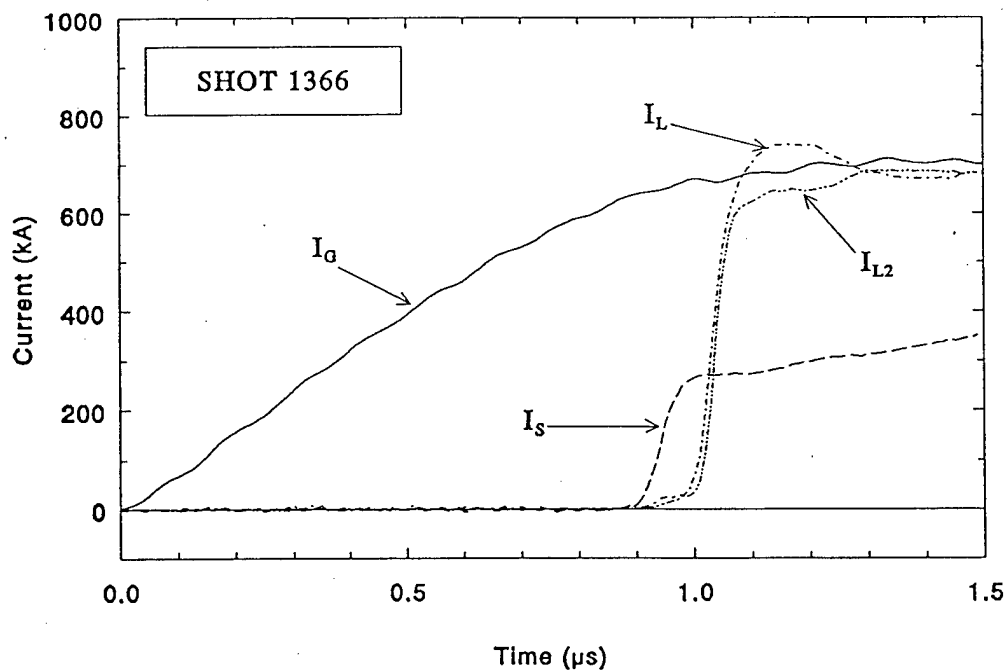


Figure 2. Averaged anode currents for a 1- $\mu s$  conduction time POS shot

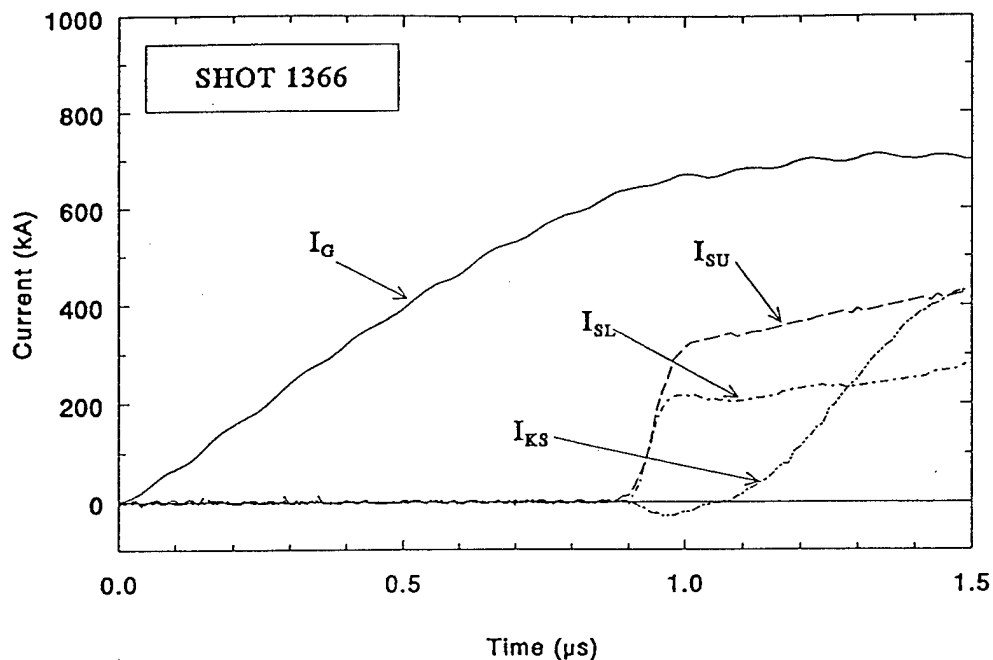


Figure 3. Currents measured near the switch

and generate a localized conduction path that shields the probes. Variations in probe design may shed some light on this problem. The "load currents,"  $I_L$  and  $I_{L2}$ , are almost synchronous, and rise to the generator current (or greater because of asymmetry, see Fig. 4 below).

Figure 3 compares currents measured near the downstream side of the POS. All three monitors ( $I_{SU}$ ,  $I_{SL}$ ,  $I_{KS}$ ) seem to suffer from shielding, especially the cathode monitor,  $I_{KS}$ . The three signals begin at the same time, although the cathode signal is initially negative. Differences

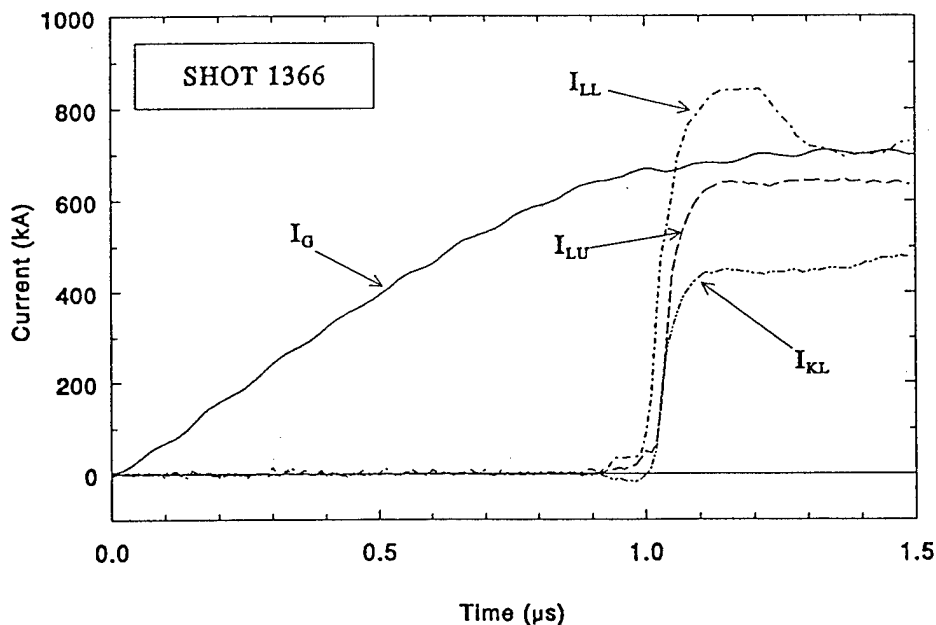


Figure 4. Currents measured at the intermediate location

in the signals could be the result of a gross asymmetry, confused by shielding.

Figure 4 compares the currents measured in the intermediate location. The high value of  $I_{LL}$  is the cause of the overshoot in the average anode current at this location shown in Fig. 2. There is a small time delay between the upper and lower anode currents, and a difference in their magnitudes that may be a manifestation of upstream asymmetry. The cathode current  $I_{KL}$  rises at the same time as the local anode current  $I_{LU}$  and has a lower magnitude. The difference between  $I_{KL}$  and  $I_{LU}$  is about 200 kA, which is the electron flow current unless the cathode monitor is shielded by surface plasma.

The currents measured at the short circuit load are virtually identical as shown in Fig. 5. The center-fed diode may have smoothed the asymmetry evident in the upstream probes. The small difference between the load currents and the generator current could be a loss to the outer conductor in the load region.

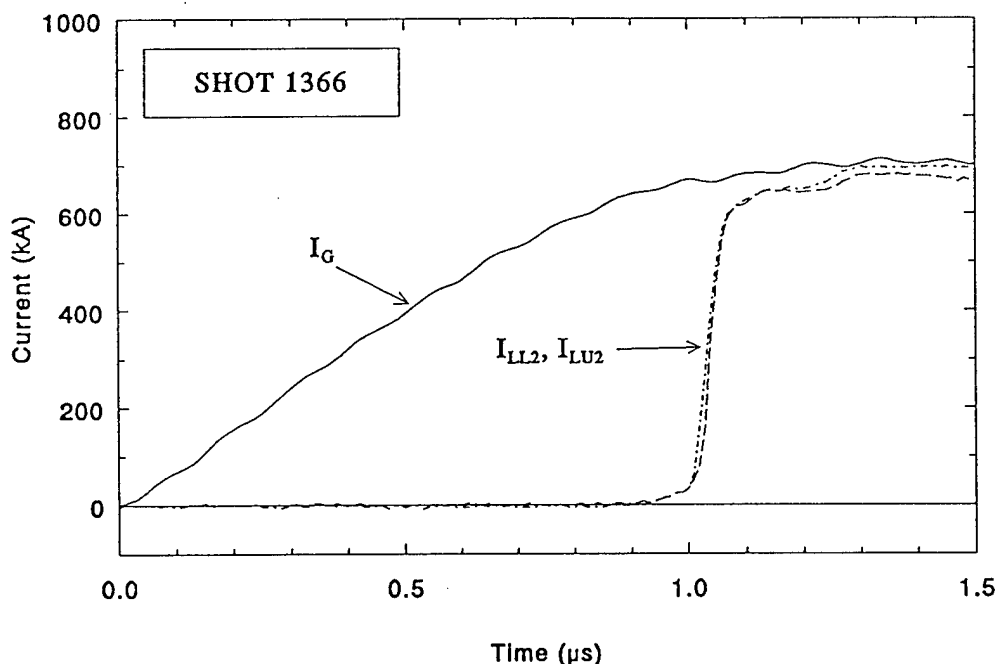


Figure 5. Currents measured at the load

#### Diode load shot

A diode shot (1374) was chosen to illustrate the difference in the current monitors under high voltage conditions. This shot used an AK gap of 10 mm and a plasma delay of about 3.3  $\mu$ s resulting in a conduction current of 500 kA and conduction time of 700 ns. The averaged outer conductor currents are shown in Fig. 6. The insulator flashed when the switch voltage reached 900 kV (see Fig. 9). The  $I_s$  current is greater than the load currents, perhaps because it is not shielded for this shorter conduction time. The time delay between  $I_s$  and  $I_L$  is about 70 ns. Taken literally, these measurements indicate a current loss of about 300 kA out of 500 kA between the generator and the load, with about half of the loss localized between the load monitors  $I_L$  and  $I_{L2}$ ,

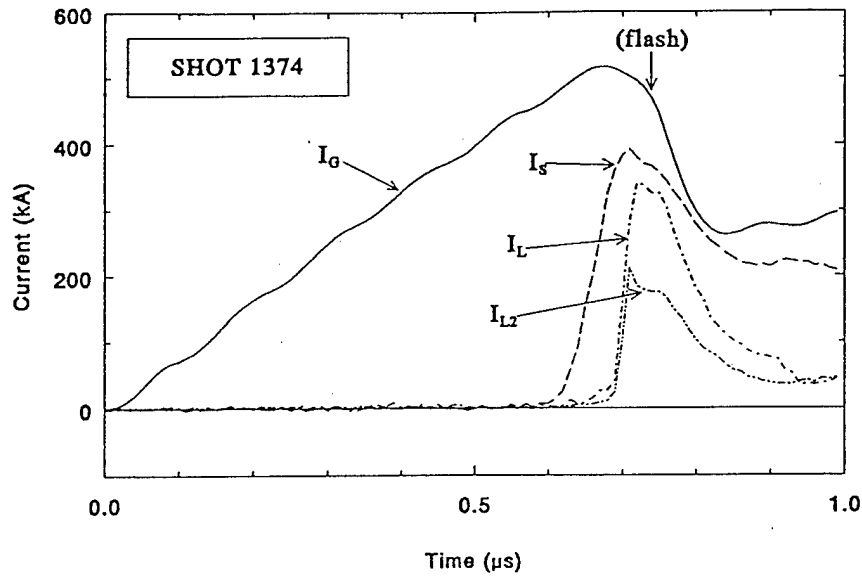


Figure 6. Averaged anode currents for a diode shot

and the other half of the loss localized in the switch region. The two load currents are almost simultaneous.

The individual current signals measured at the three axial locations are shown in Figs. 7-9. Figure 7 shows waveforms from the monitors near the switch. The outer conductor signals are synchronous and symmetric. The cathode current,  $I_{KS}$ , is reasonable, indicating a significant electron flow current of about 150 kA. Figure 8 shows the corresponding measurements at the intermediate location. Here, the electron flow current is about the same, and all three currents have decreased a little. The load currents and switch voltage are shown in Fig. 9. The two load current signals indicate very good symmetry, possibly the result of the center-fed diode. The peak

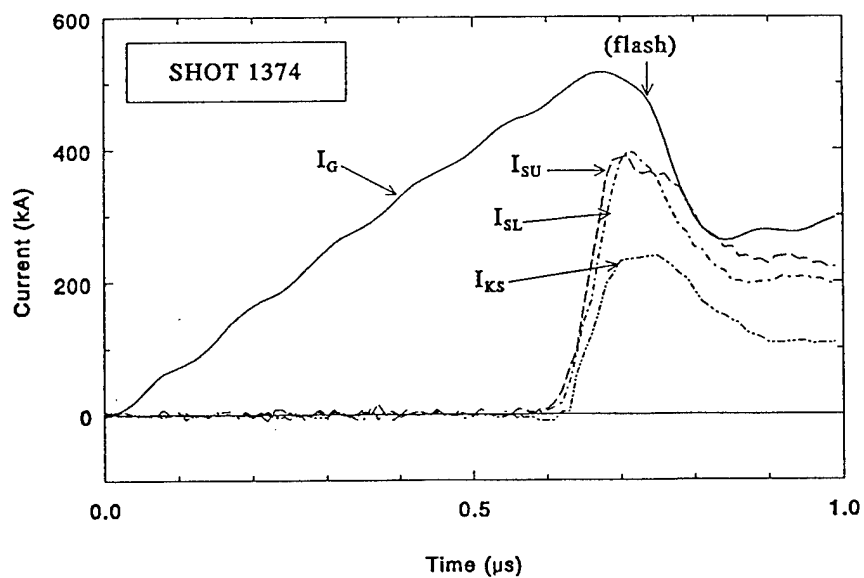


Figure 7. Currents measured near the switch for a diode shot

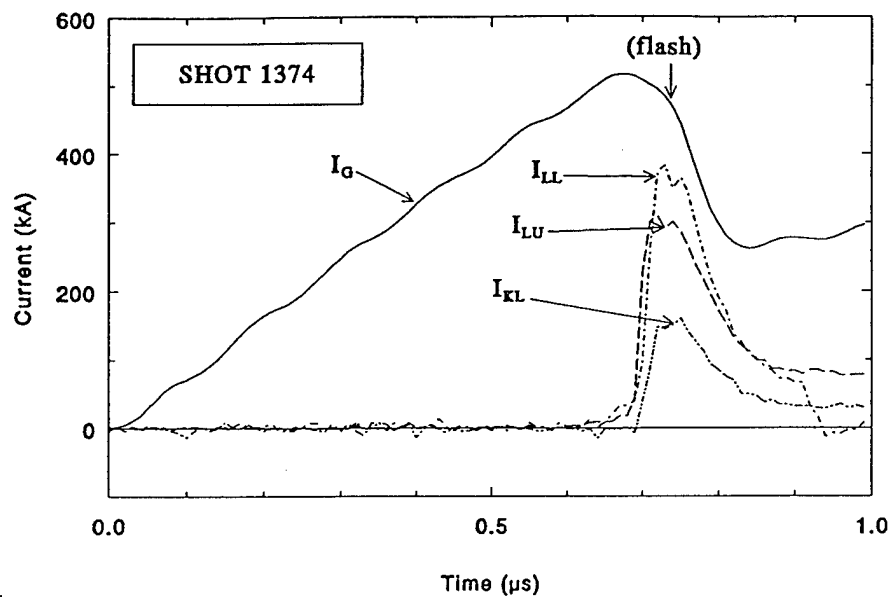


Figure 8. Currents measured at the intermediate location for a diode load

load current is about 200 kA, a little higher than the peak cathode current measured near the load, 150 kA.

The switch voltage in Fig. 9 is calculated by inductively correcting the voltage measured at the insulator (VD). The inductive correction increases the maximum voltage from 830 kV to 910 kV. The voltage inferred from the ratio of two filtered PIN diode signals was 810 kV. The diode impedance, calculated by dividing the switch voltage by the load current  $I_{L2}$ , is about  $4 \Omega$ . The end-on x-ray photo indicates a hollow beam that evidently does not pinch. This may be an

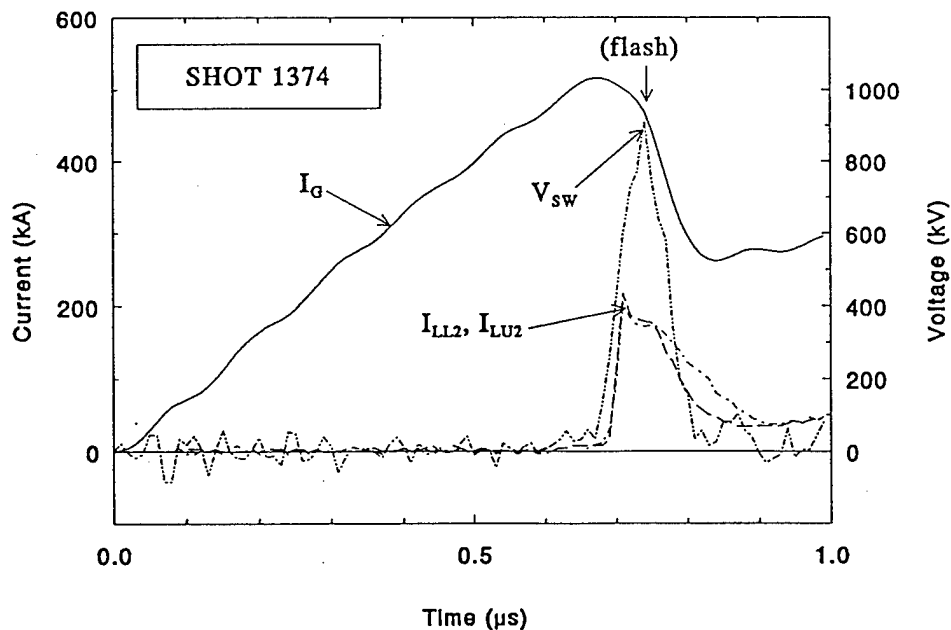


Figure 9. Currents at the load and switch voltage for a diode shot

example of a high current (200 kA) hollow beam that is below critical current. A simple comparison of Child-Langmuir and critical current formulae can explain the diode behavior (using reasonable parameters). A major "fudge" factor in this analysis is an adjustment to increase the CL emission area to account for beam spreading (Gerry Cooperstein recommends  $45^\circ$ , or an increase in the effective  $\Delta r$  by  $2D$ ). For parameters  $r = 5$  cm,  $D = 7$ -8 mm (allowing some gap closure),  $\Delta r = 6$  mm +  $2D$ , and a 1.6 multiplier in the critical current formula, the diode should operate in a CL mode with a  $4 \Omega$  impedance, consistent with the experimental observations. In this case, critical current overtakes CL current when the voltage exceeds 1 MV. This diode behavior is probably different from previous Hawk experiments, where pinching was more common. It would be interesting to compare these new results with previous experiments to refine our understanding of the diode behavior.



PULSED POWER PHYSICS TECHNOTE NO. 95-19

TITLE: Aluminum Wire Array Implosions on ZFX

AUTHOR(S): G.G. Peterson\*, J.R. Boller, R. Fisher<sup>†</sup>, J.C. Kellogg, D. Mosher, F.C. Young,  
R.J. Comisso

DATE: 14 June 1995

ABSTRACT: Aluminum wire PRS experiments were undertaken on ZFX as a demonstration of capability and as part of performance testing. The loads consisted of eight 1.1 mil diameter Al wires placed symmetrically in a 2-cm diameter array. The A-K gap was 2.7 cm. No attempt was made to optimize the load geometry. The total mass/length was 126  $\mu\text{g}/\text{cm}$ . The PRS loads were driven using a Marx charge of 40 kV, generating 650 kA in 450 ns (the implosion time). Diagnostics included system voltage and current monitors, two time integrated x-ray pinhole cameras, and three filtered x-ray photo diodes (XRDs). On the second shot the diverter switched late and the transfer capacitor broke down.

THIS REPORT REPRESENTS  
UNPUBLISHED INTERNAL  
WORKING DOCUMENTS AND  
SHOULD NOT BE REFERENCED  
OR DISTRIBUTED

\* NRL/NRC Associate

<sup>†</sup> Jaycor

Two aluminum wire PRS shots were fired on ZFX with a Marx charge of 40 kV. Shot 103 was fired on 28 September 1994, and shot 104 on the 30th. The loads consisted of eight 1.1 mil diameter Al wires placed symmetrically in a 2-cm diameter array (Fig. 1). The A-K gap was 2.7 cm. The total mass/length was 126  $\mu\text{g}/\text{cm}$ . Diagnostics included system voltage and current monitors, two time integrated x-ray pinhole cameras, and three filtered x-ray photo diodes (XRDs).

The wire arrays were imploded to demonstrate machine capability for driving a PRS load. Wire implosions were chosen over gas-puff for ease of fielding. Optimization of x-ray yield was not a priority therefore we did not try to reduce the machine's rather high front end inductance or try to attain  $\eta \geq 1$ . Transmission line modeling of ZFX with an imploding annular load was done using NRL's BERTHA code to help determine a load mass and array diameter to produce a reasonably high quality implosion, with an implosion time between 400-500 ns (Fig. 2).

Power scaling laws were used to estimate x-ray yields to guide the design of x-ray diagnostics. Modifications were made to existing pinhole cameras and XRDs. New filters and pinholes were installed and internal baffles were added to the inside of the diagnostic extension vacuum tubes to prevent grazing x-rays from scattering into the XRDs. The XRDs were 0.5 inches in diameter, covered with aluminum foil and were placed 80 cm from the PRS. A bias charge of -1 kilovolt was used. Filters were placed 7 cm from the XRDs. The first XRD configuration consisted of a bare XRD, attenuated by a pinhole array located 50 cm from the PRS. The pinhole array consisted of 3, 0.25 mm diameter pinholes 1.8 mm apart, perpendicular to the z-pinch axis. The second XRD was filtered with 2  $\mu\text{m}$  Kimfol, attenuated with a similar array of 0.8 mm diameter pinholes. The third XRD was filtered with 0.5 mil Saran, allowing measurements of Al K-shell x-ray emission. Tables and graphs of filter attenuations and XRD responses from earlier NRL work were used to design the diagnostics and to calculate x-ray yields.

The time-integrated pinhole cameras used 200-800  $\mu\text{m}$  diameter pinholes, filter combinations of 6.4  $\mu\text{m}$  Al-mylar (Al thickness of 0.13  $\mu\text{m}$ ) and 2  $\mu\text{m}$  Al foil, and RAR 2492 x-ray film. The pinholes were roughly 55-cm from the PRS; the x-ray film was 33 cm beyond that (see Fig. 3).

Both shots had implosion times of 450 ns, currents at peak compression of 650 kA, and very similar x-ray pulses. The x-ray FWHMs on both shots were 175-200 ns. Total x-ray yield calculated from XRD traces ranged between 0.8-8 kJ and Al K-shell yield (energy above 1.5 keV) was about 50 Joules (Figs. 4 and 5). The kinetic energy delivered to the load as calculated with Bertha was 2 kJ.

The measure of x-ray energy with the three XRDs was rather crude, especially for energies below the Al K-shell. Calculation of the energies went as follows:

$$V_{\text{XRD}} = \left( \begin{array}{c} \text{anode} \\ \text{screen} \\ \text{transparency} \end{array} \right) \left( \begin{array}{c} \text{solid} \\ \text{angle} \\ \text{fraction} \end{array} \right) \left( \begin{array}{c} 50 \Omega \text{ cable} \\ \text{impedance} \end{array} \right) \left( \begin{array}{c} \text{x-ray} \\ \text{power} \end{array} \right) \left( \begin{array}{c} \text{filtered} \\ \text{XRD} \\ \text{response} \end{array} \right)$$

$$\text{Energy} = \int P \times dt \approx \left( \begin{array}{c} \text{x-ray} \\ \text{power} \end{array} \right) \left( \begin{array}{c} \text{time} \\ \text{fwhm} \end{array} \right)$$

The anode screen transparency = 0.33.

The solid angle fraction was different for each filtered XRD.

Further attenuation was required for the Kimfol and Bare filtered XRDs due their large response. In the path of these XRDs were placed pinhole arrays consisting of three pinholes each. This was an easy but not desirable fix, as the pinhole attenuated XRDs could see only about 70% of the radiating pinch axis. This was taken into account when calculating the solid angle fraction for the Kimfol and bare filtered XRDs (0.7 multiplication factor).

XRD filter	XRD sensitivity range (keV)	solid angle fraction	range of XRD response (A/MW)	x-ray FWHM (ns)	V <sub>XRD</sub> (V)	range of x-ray energy
0.5 mil Saran	1.56-2.82	1.6 x 10 <sup>-5</sup>	4.5-5.2	175	0.4	50-60 J
1.8 μm Kimfol	0.150-0.280	3.4 x 10 <sup>-7</sup>	70-100	200	4.0	1.4-2 kJ
Bare	0.010-0.073	3.3 x 10 <sup>-8</sup>	800-8000	175	20	0.8-8 kJ

Table 1. Filtered XRD parameters and estimated x-ray yields for shots 103 and 104.

The shots revealed no surprises. The large front end inductance of ZFX provided a stiff driver for the implosions. The load current had no noticeable inductive bite. The stiffness allowed current to continue to flow at maximum compression possibly transferring energy to the Al plasma through ohmic heating. The second x-ray pulse after the main pulse may indicate that the plasma bounced, implying continued current flow through the compressed load after the first implosion. The time-integrated pinhole photos show a somewhat unstable pinch as expected for the large initial wire radius and the long implosion time. The yield estimates in Table 1 are limited by the variations in XRD responses for the filters used on these detectors. The XRD responses for the Kimfol and bare XRDs vary widely over the range of sensitivity, requiring knowledge of the energy spectrum intensity in order to determine more precise x-ray yields.

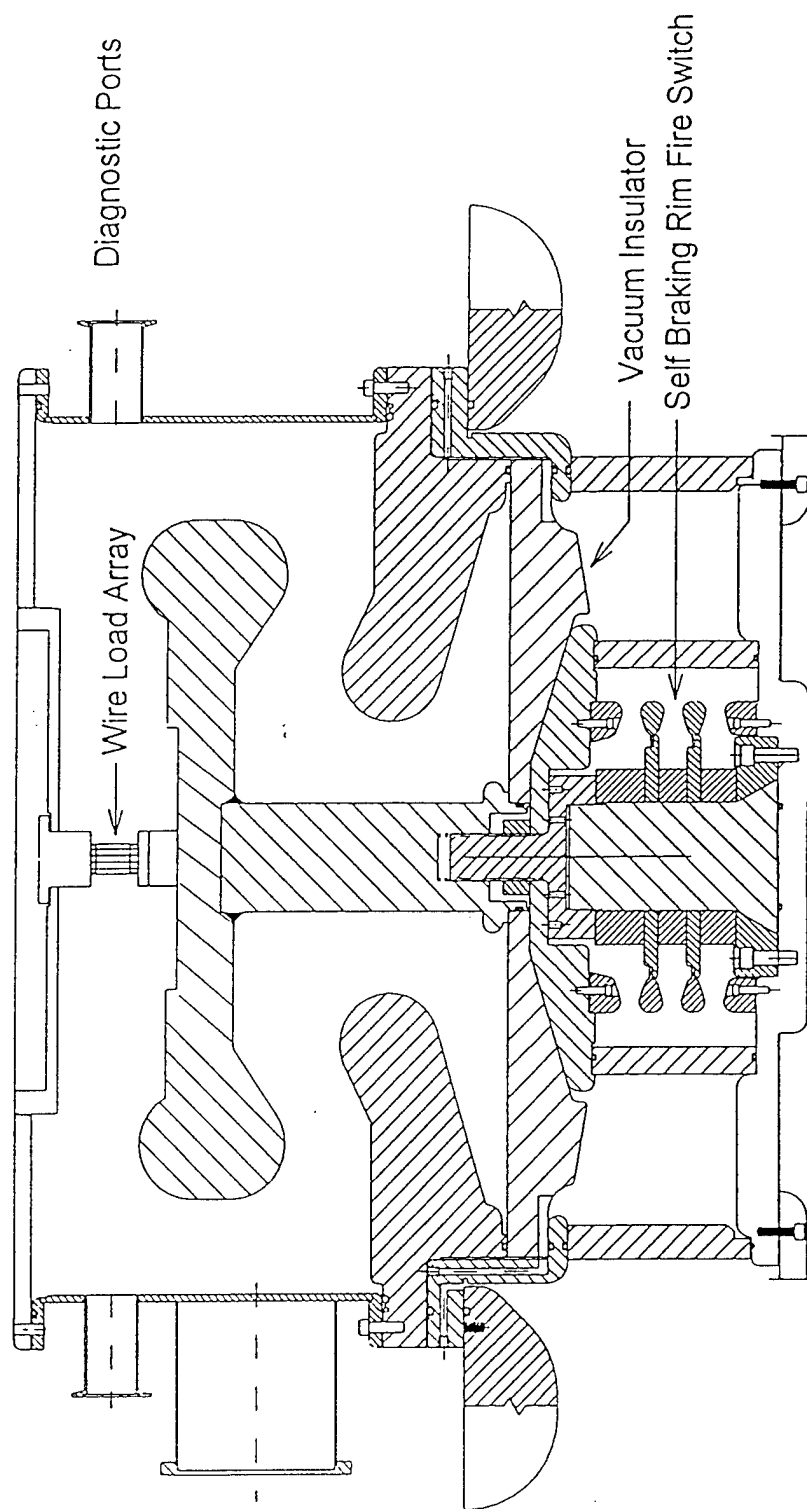


FIG. 1. ZFX Front End

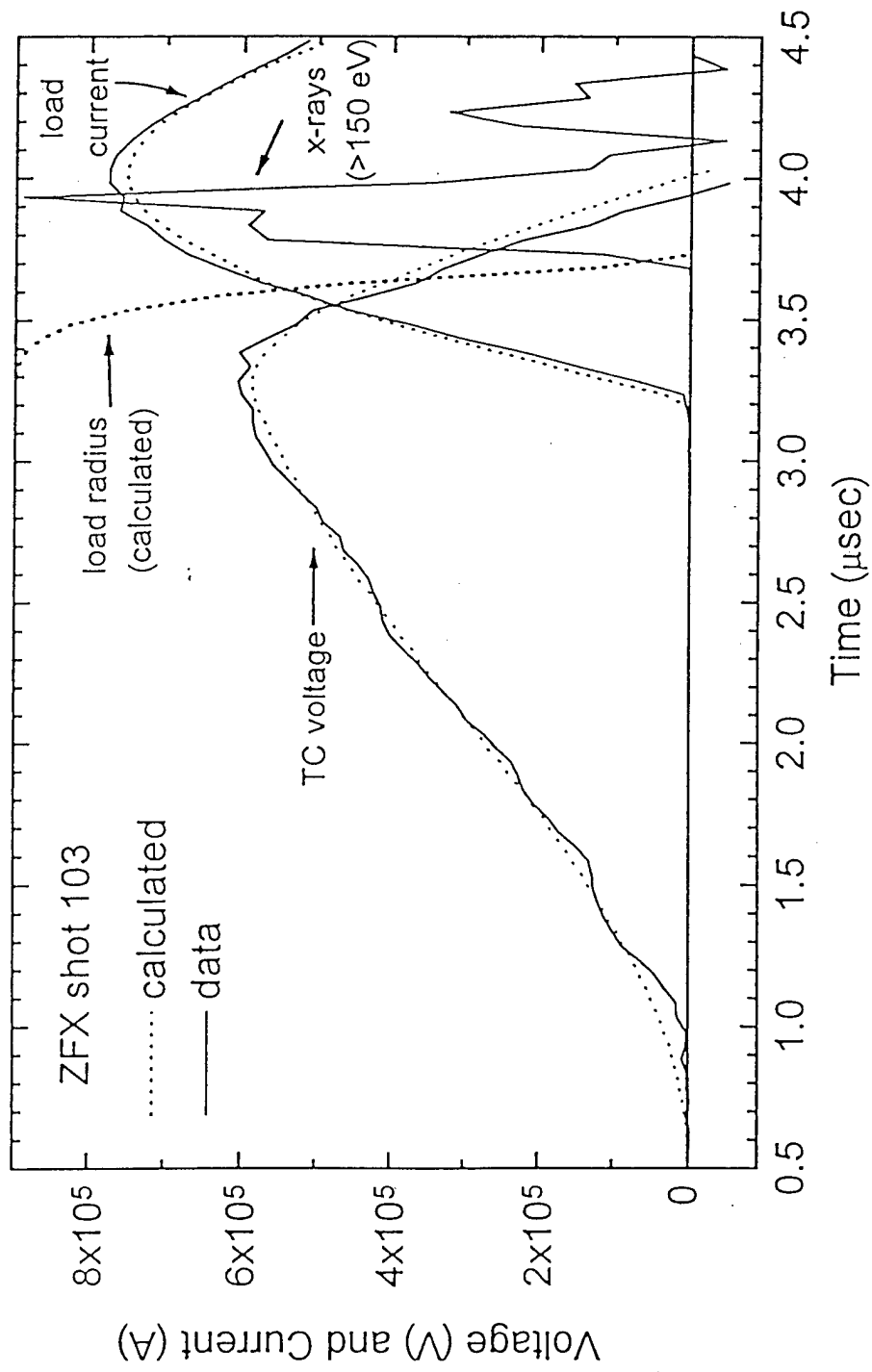
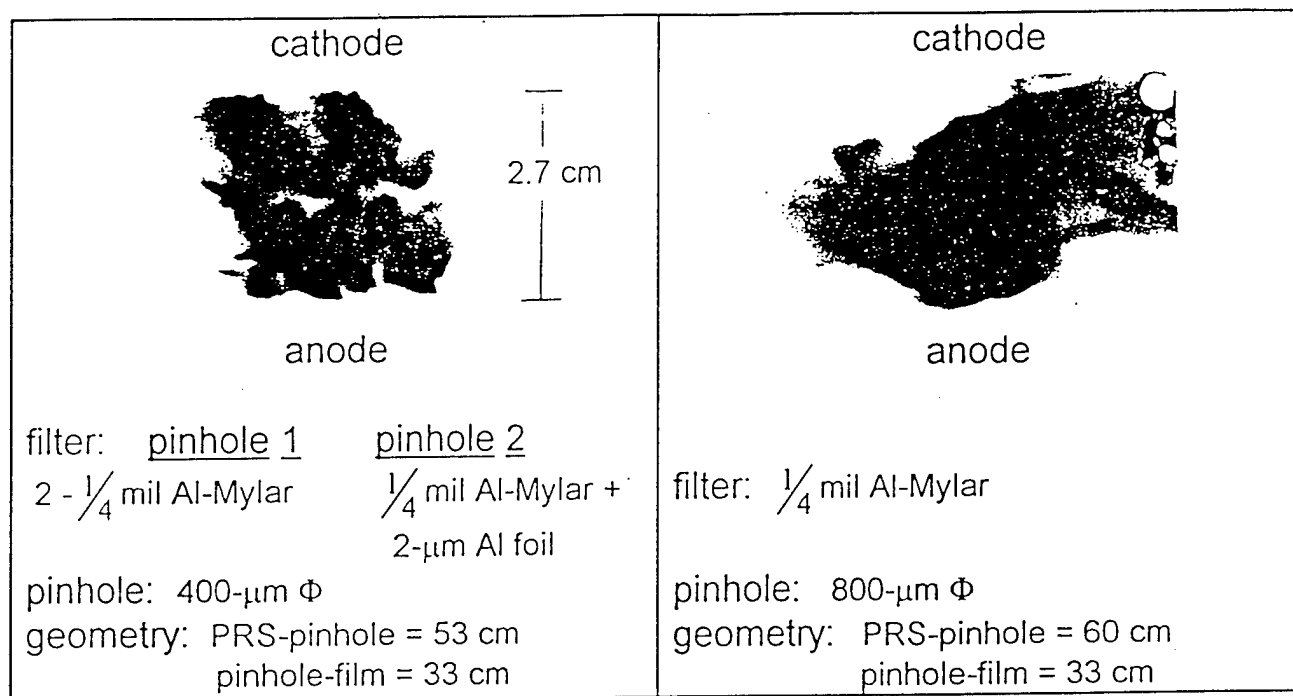
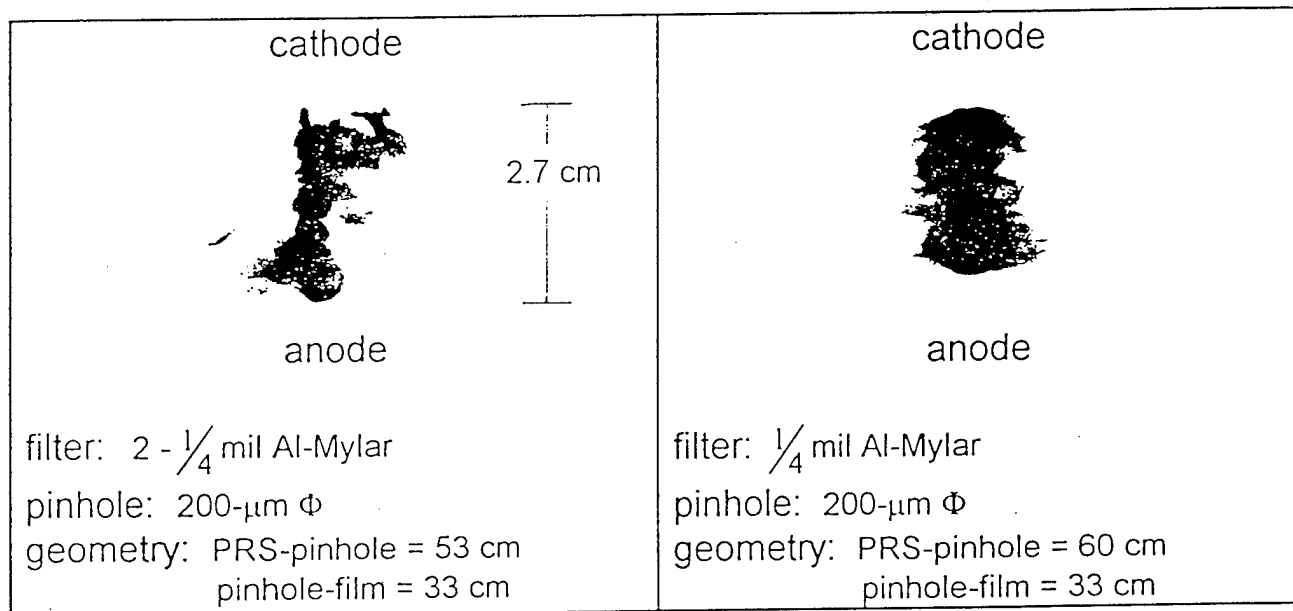


FIG. 2. BERTHA Simulation Compared with Experiment



Shot 103



Shot 104

FIG. 3. X-Ray Pinhole Photos (2492 film)

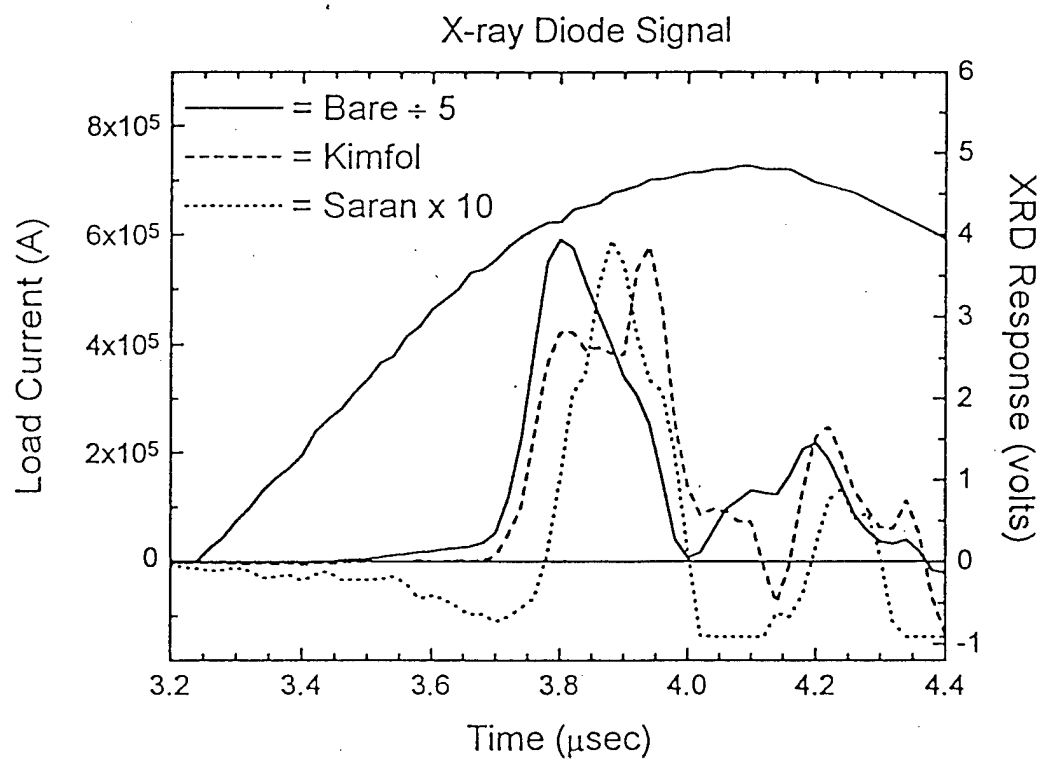
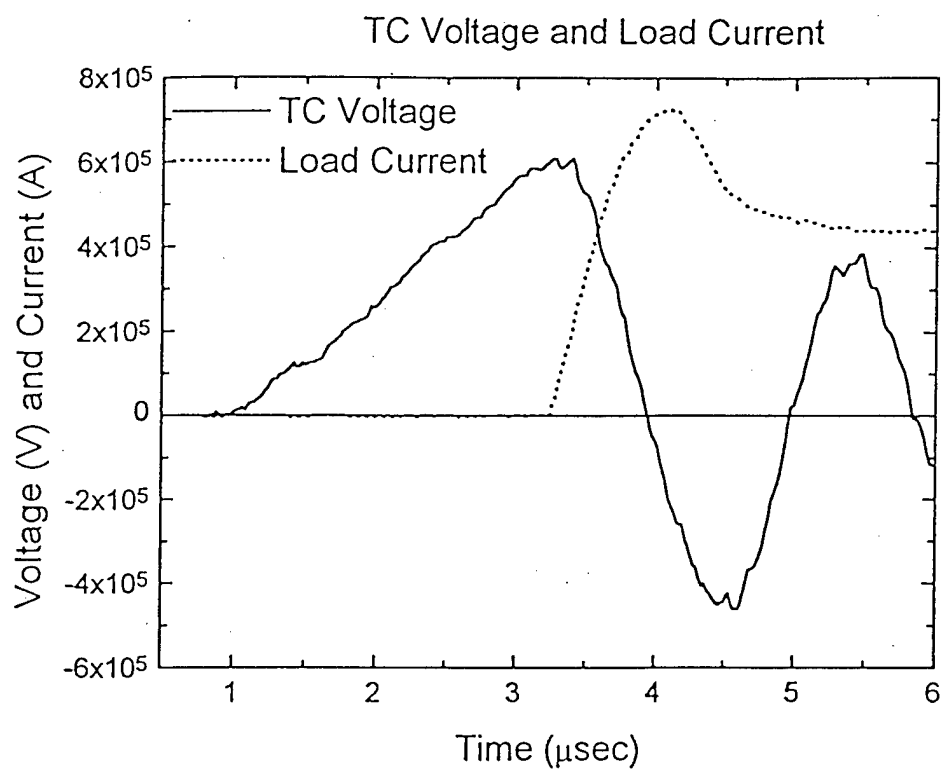


FIG. 4. ZFX Shot 103, Al Wire PRS

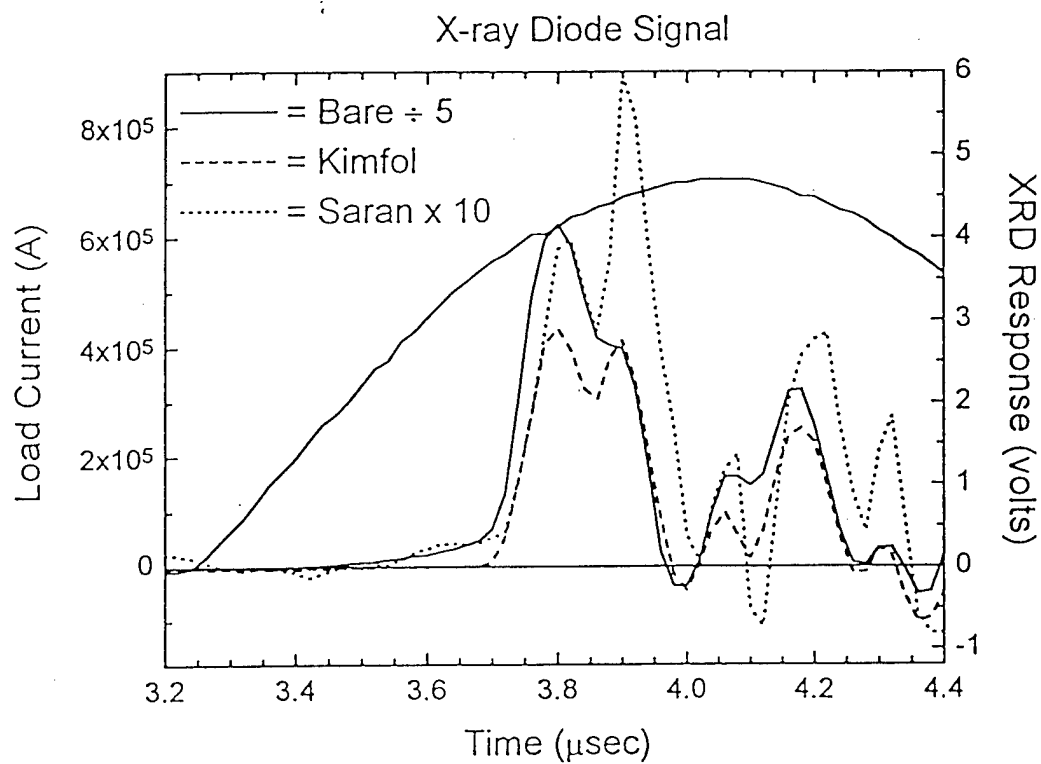
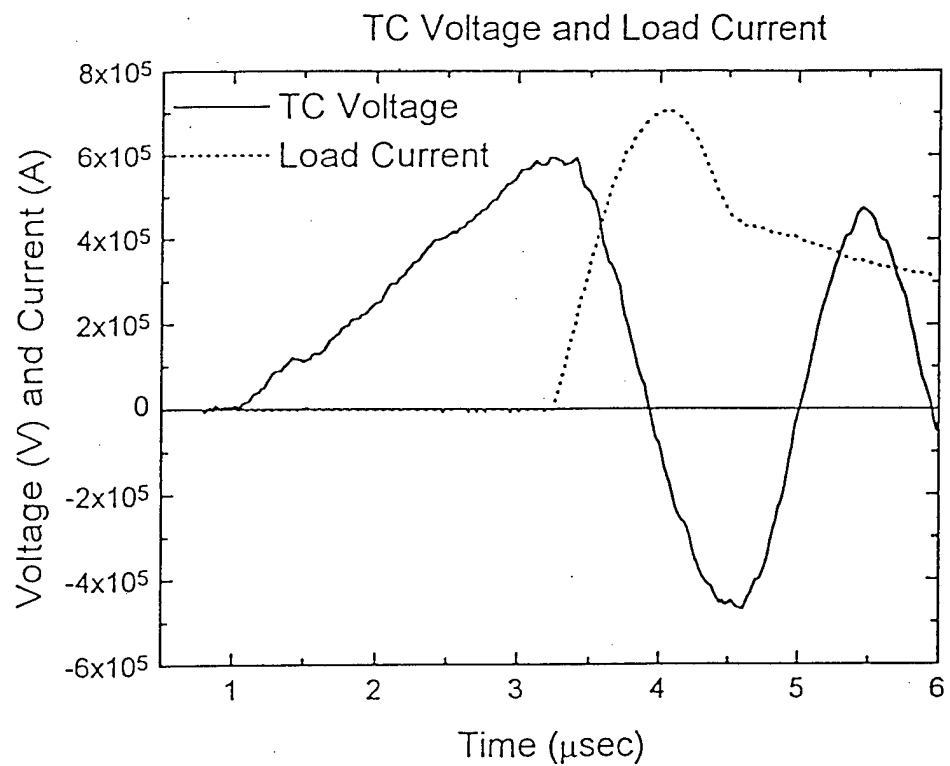


FIG. 5. ZFX Shot 104, Al Wire PRS



# EVALUATION OF THE ZFX 240-kJ PARALLEL-PLATE WATER CAPACITOR: LESSONS LEARNED<sup>†</sup>

J.C. Kellogg, J.R. Boller, R.J. Commisso, K.A. Gerber, and J.D. Sethian  
Plasma Physics Division, Naval Research Laboratory, Washington DC

G.G. Peterson  
NRL/NRC Research Associate, Washington DC

S.B. Swanekamp  
Jaycor, Inc., Vienna VA

## ABSTRACT

The ZFX pulsed-power generator employed a unique intermediate store capacitor; a 0.58- $\mu$ F water-dielectric parallel-plate transfer capacitor (TC) designed for a maximum voltage of 940 kV. To lower the cost and overall size of the TC, plastic field attractors (PFAs) were used to reduce the electric field in the water at the plate edges. The TC was operated successfully at the 750 kV level for several discharges, but a damaging electrical breakdown in the TC ended operations. Electrical stress in the TC was well below the predicted failure level at the time of the breakdown; it was probably caused by debris in the water. Debris was particularly difficult to remove because of the complicated geometry of the TC, a factor which also impeded removal of trapped air bubbles and limited accessibility of the TC interior. PFAs had poor survivability when a fault occurred. The extensive engineering and fabrication effort required to correct these problems would reduce the possible cost savings of the configuration.

## DESIGN RATIONALE

ZFX was a 250-kJ pulsed power generator,<sup>1,2</sup> designed and partially built as a driver for z-pinch fusion experiments. It was later completed in anticipation of its use for plasma opening switch (POS) work. The initial projection of the generator's performance was 1 MA delivered to a load in 500 ns, based on circuit modeling<sup>3,4</sup> with estimated electrical parameters. The novel feature of ZFX was its intermediate-store capacitor, a parallel-plate water-dielectric transfer capacitor (TC).<sup>2</sup> This design offered low inductance, low cost, and was relatively compact. In fact, it was the only design that could provide the desired performance and fit the budget and space constraints. It also represented a high technical risk, as the chosen configuration was unproven on such a large scale. Unfortunately, the TC suffered a damaging electrical breakdown before reaching its desired performance. Many practical difficulties were discovered and overcome in bringing the TC into operation; this experience is presented here.

Cross-sections of three possible configurations for a water capacitor are compared in Fig. 1. The single co-axial line is well understood and relatively simple in construction. However, the large volume inside its center conductor does not store energy, and thus is wasted space. An array of many coaxial lines in parallel, as used on DECADE,<sup>5</sup> is a more space-efficient arrangement than a single line, allowing a more compact, low-inductance TC. But the fabrication and assembly of such a complex device would appear to make this the most expensive option. A third possibility is the parallel plate capacitor, with flat high-voltage and ground vanes arranged in an open-topped rectangular water tank. This configuration is the most compact for a given stored energy; compared with a DECADE-module water capacitor, a comparable parallel-plate water capacitor could be 20% smaller in volume.<sup>4</sup> Most of its components could be easily fabricated from standard-size metal and plastic stock. The difficulty with a parallel plate configuration is the enhancement of the electric field at the plate edges. This must be reduced to prevent electrical arcing through the water and to take full advantage of the configuration's space efficiency.

ZFX used plastic field attractors<sup>2</sup> (PFAs) to reshape the electric field at the edges of thin high-voltage vanes.

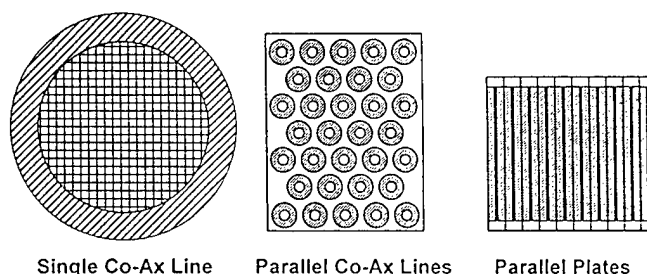


Figure 1. Three possible water capacitor configurations.

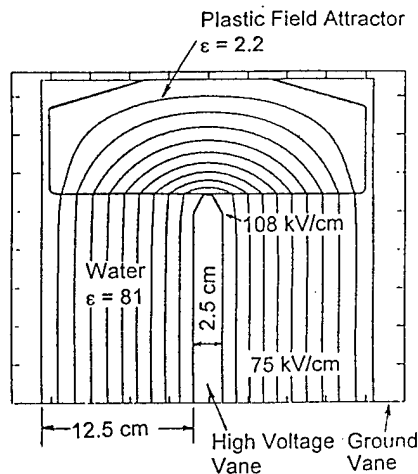


Figure 2. Electric field at a ZFX high-voltage vane edge and plastic field attractor; applied voltage is 940 kV.

The ZFX TC was constructed in two mirror-image halves, each a 2.9-m long by 2.4-m wide by 1.5-m high rectangular tank with an open top. Figure 4 is a photograph of the TC halves; between them can be seen a smaller tank which holds current collector plates, the transfer and divertor switches, and the load region. Eight high voltage vanes are supported vertically in each half. Figure 5 shows a cutaway drawing of a portion of the left TC half. The edges of the high voltage vanes are surrounded by the PFAs: solid blocks of plastic with a cross section of 10.2-cm high by 27-cm wide. Ground vanes separate each high-voltage vane and its respective PFAs. All vanes were of irridite-coated aluminum plate, 2.5-cm thick for the high voltage vanes, and 1.3-cm for the ground vanes. These thicknesses were chosen to ensure that the vanes had sufficient mechanical strength to survive a water breakdown without distortion. The ground vanes are bolted to the tank walls. The high-voltage vanes of each TC half are electrically interconnected through the ground vanes by insulated cylindrical feed-throughs. Parallel-plate current feeds, with their edges surrounded by PFAs,

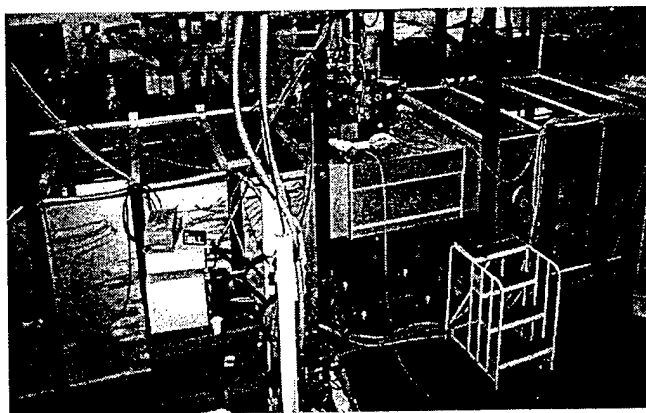


Figure 4. Photograph of ZFX transfer capacitor; the collector region is at center, Marx feed is at right.

The much lower dielectric constant of the plastic (2-3 versus 81 for water) redistributes, or "attracts," the electrostatic equipotential surfaces, reducing the field in the water. Figure 2 shows the equipotential lines around a vane edge and PFA, as generated by an electrostatic field solver. The field values shown correspond to the initial-design maximum TC voltage of 940 kV. Without the PFA, the electric field at the vane tip would be 340 kV/cm in the water. With the PFA in place, this field is reduced to 170 kV/cm, and it now occurs inside the plastic rather than in the water. The highest field in the water (108 kV/cm) occurs at the end of the vane edge-taper. The field away from the edges is very uniform; 75 kV/cm over the  $10^{-6}$ -cm<sup>2</sup> area between the vanes.

## DESIGN DESCRIPTION

The equivalent circuit for ZFX (Fig. 3) is quite conventional; a 14-stage oil-insulated Marx generator stores 245 kJ at 50 kV charge. At this charge voltage the Marx charges the TC to about -750 kV in 2.5  $\mu$ s. The transfer switch, a self-breaking rimfire-type gas switch, then closes and transfers current through an insulating vacuum feed-through to the load: 800 kA in 650 ns. As the TC discharges, an externally-triggered divertor switch is fired to damp-out ringing between the TC and the load.

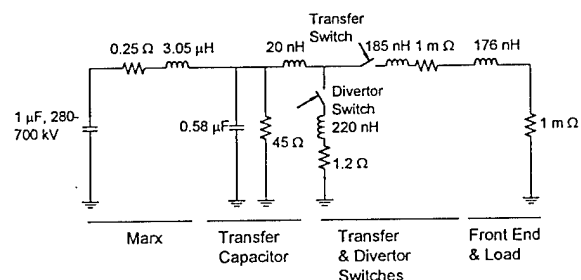


Figure 3. ZFX equivalent circuit.

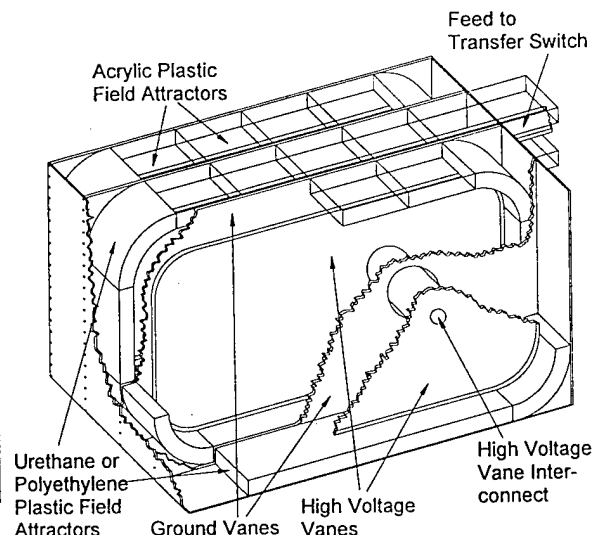


Figure 5. Cutaway of ZFX transfer capacitor.

lead into the collector plate in the central tank between the two TC halves. The transfer switch, vacuum insulator, and load region rose vertically from this plate in a coaxial configuration. The divertor system was connected to the bottom of the collector plate. The Marx generator fed into the high voltage vanes at the outside end of one of the TC halves, through an acrylic insulator.

### ELECTRICAL BREAKDOWN LIMITS IN WATER

The empirically derived expressions for maximum allowable electrical stress in deionized water, formulated by J.C. Martin and others,<sup>6</sup>

$$E_+ = \frac{230}{\tau_{\text{eff}}^{1/3} A^{.058}} \text{ (kV / cm)} \quad (1)$$

$$E_- = \frac{560\alpha}{\tau_{\text{eff}}^{1/3} A^{.069}} \text{ (kV / cm)}, \quad (2)$$

$$\text{where } \alpha = 1 + 12\sqrt{E_{\text{max}}/E_{\text{mean}}} - 1,$$

were used to determine the operational voltage limit of the TC.  $E_+$  and  $E_-$  are the electric field levels, at the positive and negative electrodes respectively, that will cause a breakdown through the water.  $A$  is the electrode area under consideration (in  $\text{cm}^2$ ) and the "effective time,"  $\tau_{\text{eff}}$ , is the time (in  $\mu\text{s}$ ) that the absolute value of the applied voltage,  $V$ , is above 63% of  $V_{\text{max}}$ , its maximum value.  $E_{\text{max}}$  and  $E_{\text{mean}}$  are the maximum and mean electric fields present for a given geometry.

In applying equations (1) and (2) to an oscillatory system, it is assumed that a streamer will form during the first half-cycle of the TC voltage oscillation, and will continue to grow during each subsequent half-cycle without collapsing at the voltage zero-crossing points. To model this, a total  $\tau_{\text{eff}}$  is determined for the entire oscillatory pulse. Each half-cycle (numbered in sequence as integer  $i$ ) is first considered separately. For the first ( $i = 1$ ) half-cycle, a value of  $\tau_{\text{eff}}(i = 1)$  is calculated as the time that  $V > 63\%$  of  $V_{\text{max}}$  during this half-cycle. Then a  $\tau_{\text{eff}}(i > 1)$  is calculated for each subsequent half-cycle as the time during that half-cycle that  $V > 63\%$  of  $V_{\text{max}}$ . In each case,  $V_{\text{max}}$  is taken as the peak TC voltage from the first half-cycle. Later half-cycles in which the voltage damps out to the point that  $V$  never exceeds 63% of  $V_{\text{max}}$ , are neglected. A total  $\tau_{\text{eff}}$  is calculated for the entire voltage pulse by summing the individual  $\tau_{\text{eff}}$  values, after applying a scaling factor<sup>4</sup> to the  $\tau_{\text{eff}}$  values derived from the voltage reversal half-cycles. An example of this procedure follows.

The likelihood of breakdown is considered separately in two different electrode-surface regions of the TC, with  $V_{\text{max}} = 940 \text{ kV}$  as in Fig. 2. First, the parallel-plate electrode surfaces are of concern because of their very large surface area ( $A = 10^6 \text{ cm}^2$ ). The associated field in this region is uniform and perpendicular to the plates. Because the electric fields are equal (75 kV/cm) on both electrodes, the lower value of the breakdown field,  $E_+$ , is used as an estimate of the breakdown level between the plates. Since the first voltage half-cycle on the TC is negative, this assumes that an ionized streamer will originate from a ground electrode.

In the first half-cycle,  $V_{\text{max}} = 940 \text{ kV}$ ; the time that  $V > 590 \text{ kV}$  (63% of  $V_{\text{max}}$ ) is  $1.45 \mu\text{s} = \tau_{\text{eff}}(i = 1)$ . In the second half-cycle,  $V > 590 \text{ kV}$  for  $0.40 \mu\text{s} = \tau_{\text{eff}}(i = 2)$ . None of the subsequent half-cycles exceed 590 kV. While  $E_+$  is valid during the first half-cycle,  $E_-$  describes the conditions in the second half-cycle, so  $\tau_{\text{eff}}(i = 2)$  is multiplied by a scaling factor,  $s_-$ , to compensate for the different coefficients in equations (1) and (2). The total  $\tau_{\text{eff}}$  is  $\tau_{\text{eff}}(i = 1) + s_- \times \tau_{\text{eff}}(i = 2)$ , where  $s_- = (230A^{.069}/560\alpha A^{.058})^{1/3}$ .  $A = 10^6 \text{ cm}^2$ , and since the field here is uniform,  $E_{\text{max}} = E_{\text{mean}} = 75 \text{ kV/cm}$ , giving  $\alpha = 1$ . The scaling factor is  $s_- = 0.78$ , and the total  $\tau_{\text{eff}} = 1.76 \mu\text{s}$ . Using this in Eq. (1) gives a breakdown level of  $E_+ = 85 \text{ kV/cm}$  at  $V_{\text{max}} = 940 \text{ kV}$ . The ratio  $E_{\text{max}}/E_+ = 0.88$ . Thus, at a TC voltage of 940 kV, the transfer capacitor is operating at 88% of its breakdown limit between the parallel plates.

The second electrode-surface region of concern is the  $A = 5000 \text{ cm}^2$ -area of the high-voltage vane edges, where the highest electric field in the water is present ( $E_{\text{max}} = 108 \text{ kV/cm}$ , see Fig. 2). Here, the field is not uniform between the electrodes; it drops to the  $E_{\text{mean}} = 75 \text{ kV/cm}$  level a few centimeters away from the vane edge. In this case the high voltage vane is the negative electrode during the first half-cycle, so  $E_-$  is applied to model a streamer originating from this region. From Eq. (2),  $\alpha = 1.08$ , so  $\tau_{\text{eff}}(i = 2) = 0.40 \mu\text{s}$  for the reversal is corrected by  $s_+ = (560\alpha A^{.058}/230A^{.069})^{1/3} = 1.34$  to scale it to  $E_-$ . The total  $\tau_{\text{eff}}$  is  $2.00 \mu\text{s}$ . Substituting this total  $\tau_{\text{eff}}$  in Eq. (2) results in  $E_- = 267 \text{ kV/cm}$ . This gives a ratio of  $E_{\text{max}}/E_- = 40\%$  at the high-voltage vane edges, much lower than that for the area between the parallel plates. Thus it should be the large area between the plates that will dominate the TC breakdown characteristics.

One other area of concern in the TC was the effect of water-filled gaps between adjoining PFA segments. These gaps would inevitably be present because of machining and assembly tolerances on the PFAs. In fact, a water-filled gap of some width is essential because it would be virtually impossible to remove trapped air from between PFA segments that are in direct contact with each other. A half-scale model of the corner of a high voltage vane and its PFAs (Fig. 6) was pulsed to high voltage to determine experimentally the maximum permissible gap size. The results were difficult to interpret clearly; the model would sometimes stand off many pulses at a voltage equivalent to 1 MV on the full size ZFX. On other occasions the system would breakdown at an equivalent voltage as low as 750 kV. However, these breakdowns were not necessarily in the PFA gap.

Three-dimensional electrostatic computer-simulation of a vane and PFA assembly showed that the electric field in such a gap rises rapidly with increasing gap size. Compared to a region with no gap, the field is 18% greater in a 3 mm gap and 28% greater in a 6 mm gap. Guided by the computer simulation results, and by the qualitative results from the half-scale test model, the PFAs were machined so as to maintain a water-filled gap of 1.3-mm between each segment. This was the minimum size that permitted the gaps to be inspected and cleared of trapped air bubbles. Care was taken to ensure that the machined surfaces of the PFAs were free of tool marks or other scratches, because it was observed that breakdowns on the half-scale model tended to follow machining grooves on the plastic surface. Also, it was decided to limit the TC voltage to about 750 kV for the first operational runs on ZFX.

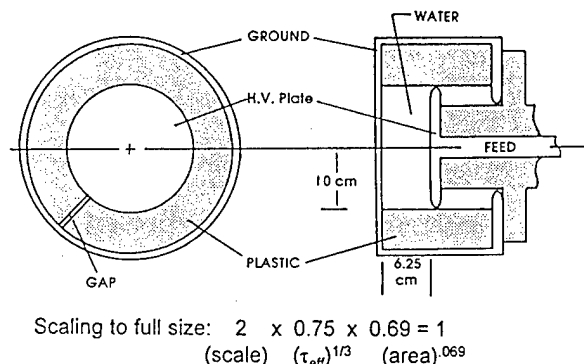


Figure 6. Half-scale test model of plastic field attractor.

### ENGINEERING DEVELOPMENT ISSUES

A lesson learned early in the process of bringing ZFX into operation was that the TC and PFAs were very sensitive to small imperfections. Air bubbles in the TC were a constant problem; circulating the water through a vacuum deaeration system was inadequate. The locations where PFA segments came together in a horizontal plane inevitably trapped air when the tank was filled. By introducing a 1.3 mm gap in these locations, the joints could be inspected for bubbles with a commercially-available underwater viewing-scope. Bubbles could be swept out of the gaps with a small custom-built water jet.

Bubbles regularly appeared in the TC during operations. One source of bubbles was gas evolved at the current-carrying joints of the high-voltage vane interconnect. These bubbles were generally seen trapped beneath the upper PFAs, which were made from clear acrylic sheet to allow visual inspection of the TC interior. The other PFA segments were polyurethane, used for custom molded sections, or pressure-cast ultra-high molecular-weight (UHMW) polyethylene sheet. Lower cost materials, such as low density polyethylene, were subject to voids in the interior that resulted in an arc through the plastic.

Access to the interior of the TC was a major problem; very little of it could be reached directly by hand. When interior parts had to be removed or replaced, it was often necessary to disassemble large portions of the device. This was not uncommon because when a breakdown occurred across a PFA, it caused the plastic surface to become carbonized, necessitating repair by remote handling techniques or replacement. Because the original design did not take into account rapid assembly and disassembly, these operations could take several weeks. If the TC had to be drained, the process of removing air bubbles upon refilling was extensive. The convoluted nature of the vanes, PFAs, current feeds, switches, and tank support structure was one reason for the poor accessibility of the TC; another cause was limited funds that had precluded a more amenable engineering design.

Another difficulty was the buildup of debris in the water. The constant need for inspection and bubble removal meant that permanently closing over the top of the tank was not an option. Debris was observed in the tank, usually settled out on the upper surfaces of the bottom PFAs. Vacuum cleaning of this area was awkward and only marginally effective. Filters in the water circulation system were also ineffective. The close fit between the PFAs and the vanes (see figures 2 and 5) effectively divided the TC into a series of baffle chambers; water could only be injected or exhausted from outside these baffles. Water had to circulate around the edges of the PFAs, making it impossible to have a sufficient flow rate in the interior volumes to entrain and flush out trapped debris.

## TRANSFER CAPACITOR OPERATION

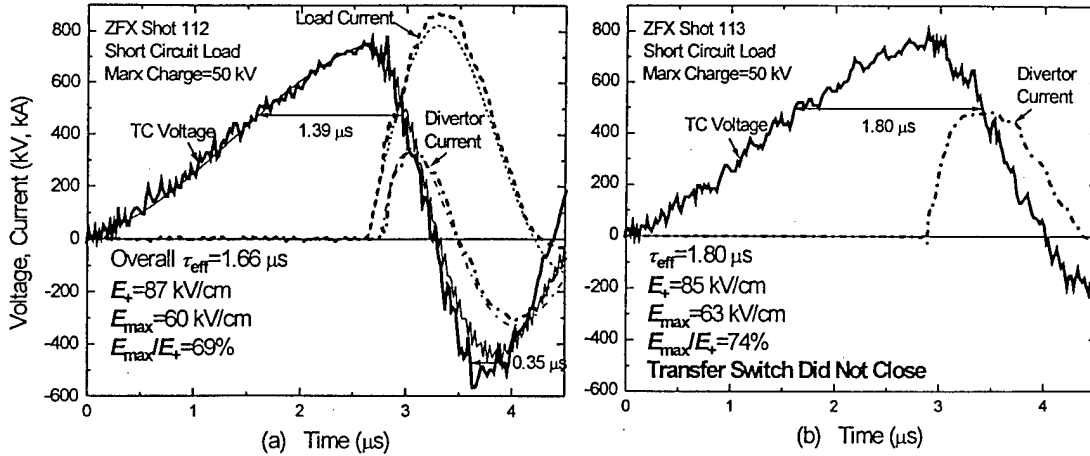


Figure 7. ZFX transfer capacitor voltage, load and divertor currents for shots with no water breakdown. Thin lines in figure 7a represent circuit modeling of shot 112.

ZFX was operated with an aluminum-wire array plasma-radiation-source (PRS) load, and a short circuit load of comparable inductance. Shot 112 is illustrated in Fig. 7a; the peak TC voltage,  $V_{\text{max}}$ , reached 750 kV without a breakdown. Applying equations (1) and (2) to this shot as described above,  $E_{\text{max}}/E_+ = 69\%$  between the parallel plates. On shot 113 (Fig. 7b) the transfer switch failed to close, resulting in the highest electrical stress ever placed on the TC:  $E_{\text{max}}/E_+ = 74\%$  with  $V_{\text{max}} = 790$  kV. Again, no breakdown occurred. Two shots which did have TC breakdowns are illustrated in Fig. 8. The operating conditions for shot 121 (Fig. 8a) were identical to those of shot 112, but jitter in the transfer switch closing lengthened the first voltage half-cycle on the TC. The TC broke down at the first voltage reversal.  $E_{\text{max}}/E_+ = 69\%$  at this time, as on shot 112;  $V_{\text{max}} = 765$  kV for this shot, and  $\tau_{\text{eff}} = 1.6 \mu\text{s}$  before the breakdown. Shot 104 (Fig. 8b) was fired with a lower Marx charge than the other shots in figures 7 and 8;  $V_{\text{max}}$  reached only 590 kV. However, a divertor switch triggering problem permitted the TC voltage to ring through two complete cycles, and the TC broke down late in time;  $E_{\text{max}}/E_+$  was only 59% in this case. After a PFA was destroyed on shot 121, ZFX operations ceased. The machine has since been dismantled.

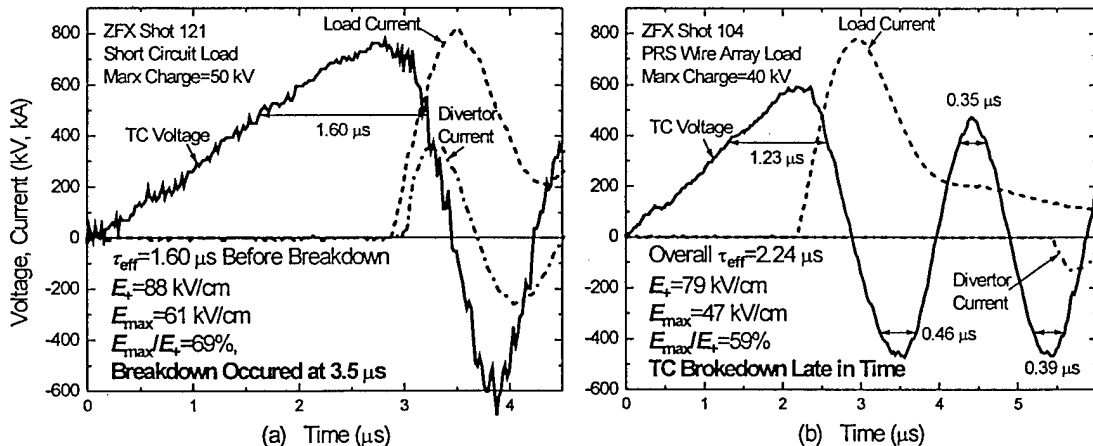


Figure 8. ZFX transfer capacitor voltage, load and divertor currents for shots with water breakdowns.

Triggering the divertor switch at the required time was difficult because of the shape of the TC voltage waveform and the fact that there was no inductive isolation between the divertor and the transfer switch. The divertor switch had to standoff the maximum TC voltage, then breakdown while the TC voltage was dropping rapidly. Jitter in the operation of the self-triggered transfer switch made the timing of this event difficult to predict.

Premature triggering of the divertor caused a significant reduction in load current, but late triggering could result in excessive voltage ringing on the TC, leading to water breakdown. On some shots the divertor trigger command came too late, and the divertor did not fire until the first or second TC voltage reversal. A method of generating the divertor trigger command by sensing the rise of the load current was being developed when ZFX operation ceased. This required a backup trigger command timed from the beginning of the shot, in the event that the transfer switch failed to close.

While the parallel plate TC achieved its low-inductance goal of 20-nH, the performance of the transfer switch was disappointing. Its inductance was originally estimated at 50 nH, but circuit modeling<sup>3</sup> (see Fig. 7a) showed that its actual inductance was 185 nH. This, along with the reduced charge voltage, prevented ZFX from achieving its desired load current performance.

## CONCLUSIONS

The most likely cause of the TC breakdowns on shots 104 and 121 was debris on the surface of the PFAs. Both breakdowns occurred at the upper surface of the polyethylene PFAs on the bottom of the tank, where debris had been seen to accumulate. In both instances the breakdown track damage was across the surface of the PFA, rather than penetrating through it, and arc damage was seen on the high voltage vane about 5 cm above the PFA surface. This would be near the location of the maximum electric field present in the water.

Keeping the water of the TC clear of debris and bubbles is greatly complicated by the convoluted geometry of a parallel-plate water capacitor with PFAs. To properly circulate and filter the water, it is vital to establish a flow rate sufficient to flush out debris in the otherwise stagnant water pockets. One possible approach to this problem would be a system of inlet and outlet manifolds built inside the ground vanes, but this would make them thicker and more complex. Another method would be to reshape the cross-section of the PFAs, creating a gap between their outside edges and the ground vanes that would be sufficient to circulate water at a high flow rate. The electrical requirements of redistributing the electric field would still have to be met by the new PFA shape. As long as access is required through the top of the TC, it might also be necessary to build the device in a clean room environment to reduce the introduction of debris. None of these solutions was practical on ZFX, and the need for them was not fully understood until after it was learned how sensitive the PFA system is to small imperfections.

The problem of removing air bubbles from the TC was solved on ZFX, but at a very high cost in labor. By making PFAs in large segments rather than from multiple smaller pieces, the air-trapping horizontal PFA joints could be eliminated. These large segments could be custom cast from polyurethane, but they would be much more expensive and more awkward to handle than the ZFX PFAs. Another vital improvement needed for a parallel plate TC is improved access to the interior. TC construction should be modular, so that a single vane, PFA, or switch can be removed or serviced without significant disassembly of the rest of the machine.

The parallel-plate water capacitor is an attractive idea for high energy systems. However, the advantages of compactness and the perceived simplicity of its components must be weighed against the inherent complexities of the design. The tight spaces, trapped water volumes, susceptibility to debris, and the non-self healing nature of surface discharges on plastic make this task a challenge. The expense of the engineering and fabrication effort required to create a practical, maintainable device could significantly reduce the cost benefits that the configuration holds. Also, the electrical breakdown characteristics of a large-area PFA-equipped parallel-plate water capacitor have yet to be tested in a debris-free environment. Unfortunately, work on this concept has ceased and these issues remain unresolved.

The authors gratefully acknowledge the technical support of E. Featherstone, R. Fisher, J. Picciotta, B. Roberts, and M. Sucky.

<sup>†</sup>Work supported by Defense Nuclear Agency

## REFERENCES

1. J.D. Sethian and A.E. Robson, *Seventh IEEE Pulsed Power Conference*, (Monterey CA, 1989), pp. 732-735.
2. J.D. Sethian, *Eighth IEEE Pulsed Power Conference*, (San Diego CA, 1991), pp. 170-172.
3. D.D. Hinshelwood, NRL Memorandum Report 5185, (November 1983), unpublished.
4. J.D. Sethian, unpublished notes, April 1993.
5. P. Sincerny et al, *Eighth IEEE Pulsed Power Conference*, (San Diego CA, 1993), pp. 880-883.
6. R.J. Adler, *Pulse Power Formulary*, North Star Research Corporation, revised August 1991, p. 21.

**PULSED POWER PHYSICS TECHNOTE NO. 94-26**

**TITLE: ZFX SMALL-SCALE MODULE TESTS**

**AUTHOR(S): J.R. Boller, J.C. Kellogg, R.C. Fisher, M.M. Sucky, and R.J. Commisso**

**DATE: 29 November 1994**

**ABSTRACT:** The ZFX water capacitor utilizes a parallel plate geometry with plastic field attractors (PFA) to reduce the field enhancement at the edges of the plates. This note reports the results of additional tests conducted in May 1994 with a small-scale module consisting of a single 8-in dia. high-voltage plate to determine the electrical breakdown levels of the PFA concept. The test module experienced a wide range of breakdown levels, from 744 kV to 1.04 MV. These results indicate that a voltage of 700 kV is a safe operating level for the water capacitor of ZFX and that under some circumstances, operation at 800-900 kV may also be possible.

**THIS REPORT REPRESENTS UNPUBLISHED INTERNAL WORKING DOCUMENTS AND SHOULD NOT BE REFERENCED OR DISTRIBUTED WITHOUT CONSENT OF AUTHORS**

## ZFX SMALL-SCALE MODULE TESTS

J.R. Boller, J.C. Kellogg, R.C. Fisher, M.M. Sucky, and R.J. Comisso

### INTRODUCTION AND SUMMARY

The ZFX<sup>1</sup> water capacitor utilizes a parallel plate geometry with plastic field attractors (PFA) to reduce the field enhancement at the edges of the plates. This note reports the results of additional tests conducted in May 1994 with a small-scale module consisting of a single 8-in dia. high-voltage plate to determine the electrical breakdown levels of the PFA concept. The test module experienced a wide range of breakdown levels, from 744 kV to 1.04 MV. These results indicate that a voltage of 700 kV is a safe operating level for the water capacitor of ZFX and that under some circumstances, operation at 800-900 kV may also be possible..

### MOTIVATION

The PFA concept used in the ZFX generator is probably the highest-risk component of the machine and may determine the maximum energy level at which ZFX can be operated. During the design phase of ZFX, John Sethian tested the concept by measuring breakdown levels on a small-scale test module<sup>1</sup>. Although the results of these tests were encouraging, additional questions recently arose concerning maximum permissible gaps between plastic sections. This is important because it has been observed that a gap is necessary to allow the removal of air bubbles trapped between the plastic pieces<sup>2</sup>

Three dimensional electrostatic simulations of the ZFX water capacitor were performed by Steve Swanekamp<sup>3</sup> to study the dependence of the electric field on the size of the gap in the plastic. These results showed an increase in electric field of 18% for a 0.125 in gap and 28% for a 0.25 in gap as compared to regions without a gap.

Because of these concerns, additional tests to determine the effect of gaps in the plastic were conducted using Sethian's test module.

### DESCRIPTION OF EXPERIMENTAL SETUP

Figure 1 shows the module used for these tests. The H.V. plate is 8-in dia., 0.5-in thick aluminum with a tapered edge similar to the edges of the vanes in ZFX. The spacings between the H.V. plate and the ground plates are 2.5 in. The plastic pieces surrounding the H.V. plate and the high voltage feed are polyethylene. Note that the plastic surrounding the high voltage feed



also serves as a PFA to reduce the field enhancement on the edge of the ground (positive) electrode in the feed region.

The plastic surrounding the H.V. plate is cut into two pieces, providing a gap at the top and bottom as shown in the figure to simulate the gaps between plastic pieces in ZFX. The width of these gaps were varied from 0 to 0.065 in. Because the dimensions of the module are half-scale of ZFX, these gaps would correspond to gaps of up to 0.130 in on ZFX. The scaling of the gap width was also verified by the three dimensional electrostatic simulations described above. This is illustrated in Fig. 2 where the maximum electric field vs. gap is plotted for both the module and ZFX. This figure shows that when one-half of the ZFX voltage is applied to the module with a gap of one-half of the ZFX gap, the fields on the module and ZFX are the same.

A capacitive voltage monitor is mounted at the center of the ground end of the test module (see Fig. 1) to measure the applied voltage. This monitor was calibrated by the conventional method of resonantly charging the module from a 2  $\mu$ F capacitor at a measured dc charge level of about 20 kV. With the capacitance of the module being  $\cong$  650 pF, the voltage ring-up is essentially a factor of 2 (resistive damping of the waveform is accounted for in the calibration).

Two windows in the top of the tank wall provided a visual means of inspecting the top gap and taking open-shutter photographs during the testing. The presence of a bright light from the windows provided verification of an electrical breakdown within the module.

The test module was filled with de-ionized, de-aerated water from the ZFX water conditioning system. Several methods were used in an attempt to fill the module without entrapping air, such as evacuating and then back-filling with water. The most successful technique was to simply assemble the module under water, carefully removing bubbles from each piece during the assembly process.

The electrical driver used for these tests was a marx generator located in the Building 71 laboratory area of Code 6750. This marx consists of 18 stages of 0.08- $\mu$ F, 100-kV capacitors in a SF<sub>6</sub> insulated housing. A resistive voltage divider is provided with the marx to monitor the output voltage. The marx was connected through a 154- $\mu$ H coil (73 turns of #10 insulated wire on a 3.75-in dia. form) to the high voltage feed of the test module. This provided an under-damped discharge from the marx with a ringing period of 1.9  $\mu$ s. The marx charging voltage ranged from 30 to 44 kV, providing peak voltages on the test module of more than 1 MV. The current through the module was monitored by a Pearson Model 110A current transformer. The coil and module were submerged in a 2 ft x 2 ft x 3 ft plastic tank filled with transformer oil for high voltage insulation.

The marx voltage and the module voltage and current were recorded on a Gould model 4074, 4-channel digital storage oscilloscope, with selected shots downloaded to the "Fermi" micro-vax for processing.

## EXPERIMENTAL RESULTS

A total of 171 shots were taken on the test module with applied voltages ranging from 600 to 1040 kV. A typical module voltage waveform is shown in Fig. 3. The effective time (time that the voltage is above 63% of maximum) of the first cycle is about 0.75  $\mu$ s. Figures 4 and 5 show an example of waveforms with breakdowns after the first and second peaks respectively. A graphical summary of all shots are shown in Figs. 6 and 7. These figures show the peak applied voltage for each shot as well as identifying the shots which had a breakdown and the timing of the breakdown. The shots in Fig. 6 exhibited a wide range of breakdown levels ranging from 744 to 1020 kV. Five of the ten shots shown in this figure that broke down had breakdown paths that were either through the water in areas not associated with gaps, or in a gap that had minimal width. Four had breakdown paths in gaps of 0.045 to 0.065 in and the breakdown path for one shot was not determined.

Figure 7 shows a series of 50 consecutive shots at  $\approx 700$  kV without a breakdown (shots 69 - 118) and then another series of 50 consecutive shots where the voltage was slowly increased to over 1 MV. These shots had a top gap of 0.065 in and a bottom gap of 0.02 in. The last shot, which broke down at 1040 kV, did not break down from the edge of the high voltage disc but instead tracked along the feed insulator. The damage to this insulator was un-repairable, thus ending this series of tests. We do not understand why the performance on this series of shots was superior to the shots in Fig. 6.

## SCALING TEST-MODULE RESULTS TO ZFX

The results from the module tests must be scaled properly when used to predict the performance of ZFX. Voltages from the half-scale module should be doubled to produce the same electric fields on ZFX. However because of the familiar JCM scaling laws of electrode areas and effective times of the voltage pulses, the predicted breakdown field levels on ZFX will be reduced. The effective time of the pulses applied to the module were 0.75  $\mu$ s while the same value for ZFX is 1.5  $\mu$ s. Thus with a scaling factor of  $t^{1/3}$ , the breakdown field levels observed on the module should be multiplied by  $(0.75/1.5)^{1/3} = 0.79$  due to the time factor alone.

The area scaling produces further reductions in the breakdown levels. For breakdowns from the enhanced negative (hot) edge of the electrodes, an  $A^{0.069}$  scaling prevails. With the length of the edges of the ZFX high voltage vanes being 180 times longer and each vane being 2 times wider than the vane in the module, a factor of  $(1/(180 \times 2))^{0.069} = 0.67$  must be applied. Thus a total scaling factor of  $0.79 \times 0.67 = 0.53$  must be used for calculating the allowable electric fields on the negative electrodes of ZFX. Overall then, the measured voltages on the half-scale module

would be almost the same as the equivalent voltages for ZFX as far as the likelihood of breakdown from the negative electrodes is concerned.

The area scaling for breakdown from the positive (ground) electrodes follows an  $A^{0.058}$  relation. This results in an area scaling factor of  $(A_{\text{MOD}}/A_{\text{ZFX}})^{0.058} = (478 \text{ cm}^2/1.05 \times 10^6 \text{ cm}^2)^{0.058} = 0.64$ . The total scaling factor for positive breakdown is  $0.79 \times 0.64 = \underline{0.51}$ , similar to the negative electrode case.

## CONCLUSIONS

The test module experienced a wide range of breakdown levels, from 744 kV to 1.04 MV. No explanation could be determined for this effect. A voltage of 700 kV appears to be a safe level for both the test module and ZFX. Voltages above this level on ZFX would probably be very risky until a better understanding of the data from the test module is obtained. However, under circumstances that are not understood, 800-900 kV operation may be possible. Note that Marx series resistance limits the maximum charge voltage on the ZFX water capacitor to  $\leq 800$  kV. Understanding the cause of the observed breakdown behavior would probably require many more shots to investigate the results of systematic changes made to surface preparation and assembly procedures.

## REFERENCES

1. "A Compact Parallel Plate Water Capacitor," J.D. Sethian, 8th IEEE Pulsed Power Conference, 1991, p 170.
2. "Failure Analysis of ZFX Shot #36," J.C. Kellogg, J.R. Boller, R. Fisher, and M. Sucy, Pulsed-Power Physics Technote No. 94-07.
3. "Three Dimensional Electrostatic Simulations of the ZFX Water Capacitor," S. Swanekamp, R. Boller, and J. Kellogg, Pulsed-Power Physics Technote No. 94-03.

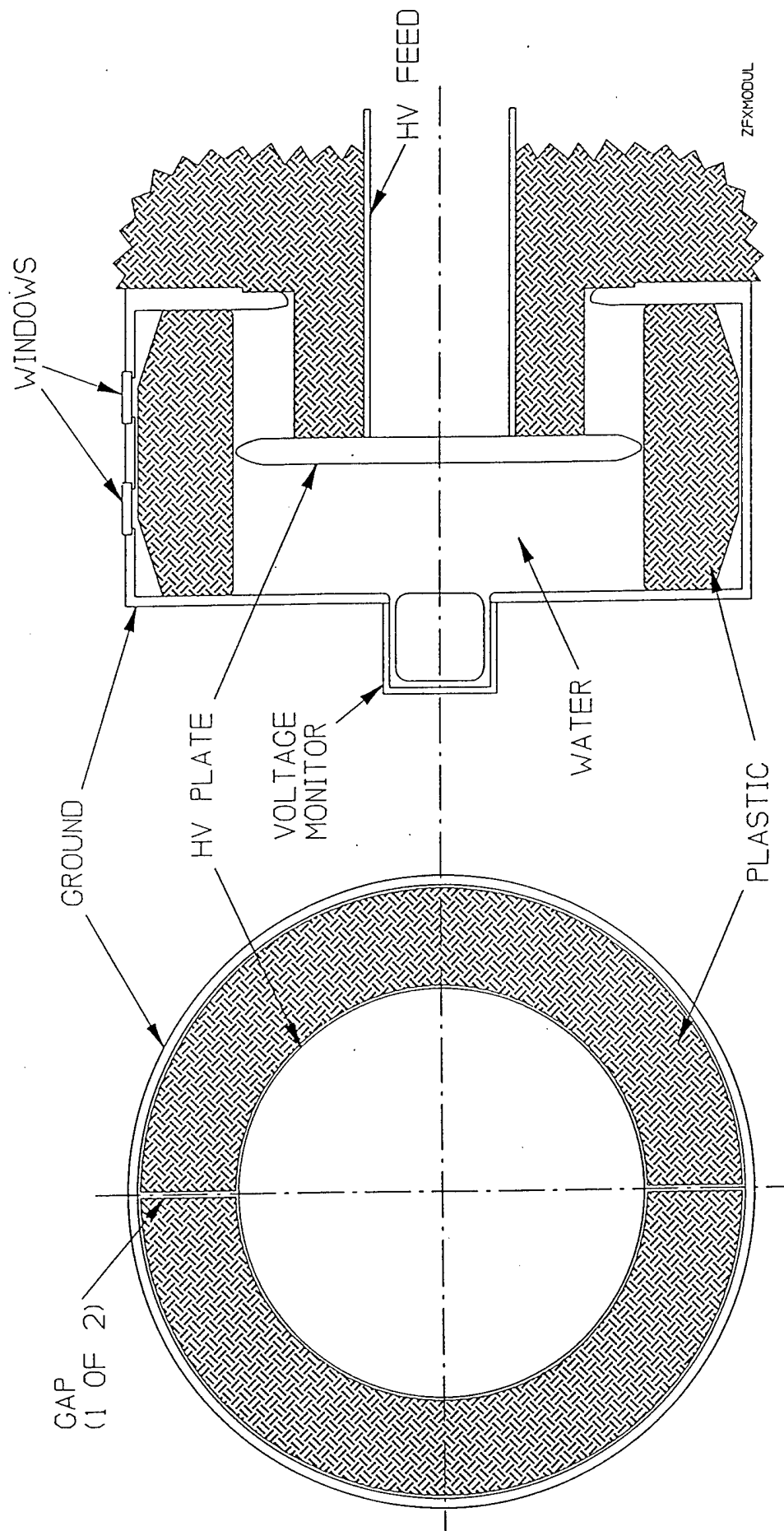


Figure 1. ZFX test module.

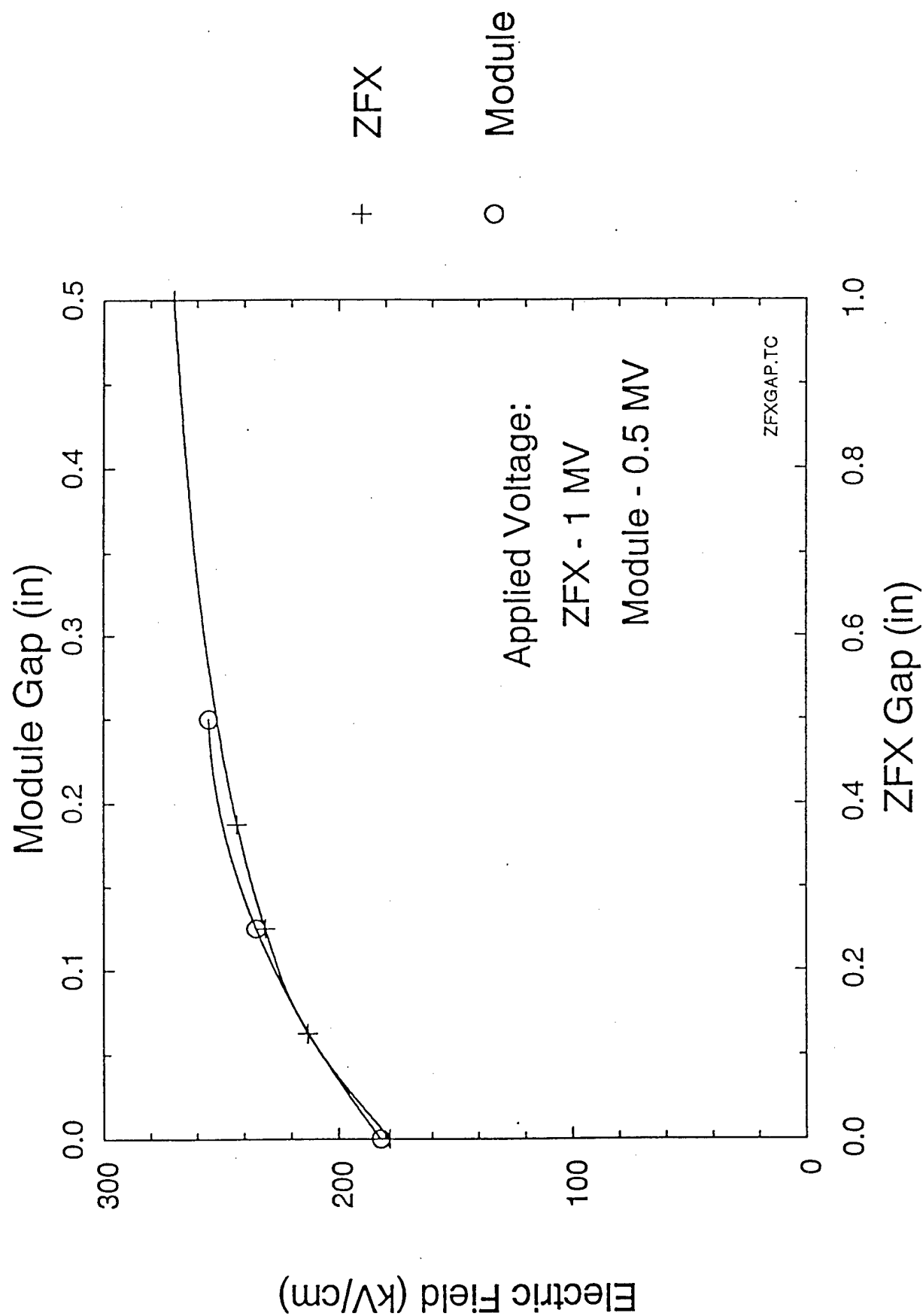


Figure 2. Maximum electric field on the high voltage vane vs. the length of the gap in the PFA.

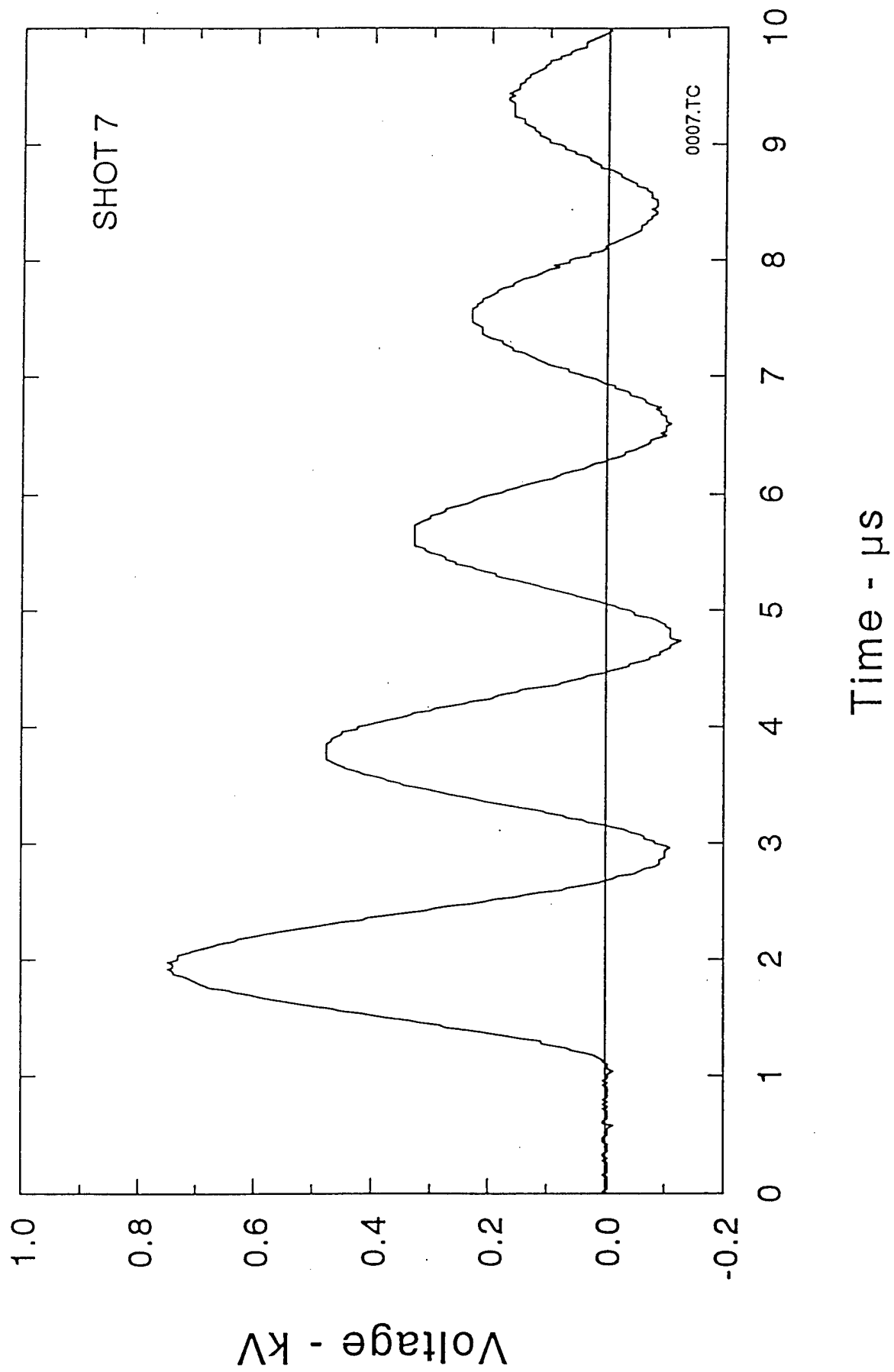


Figure 3. Typical test module voltage.

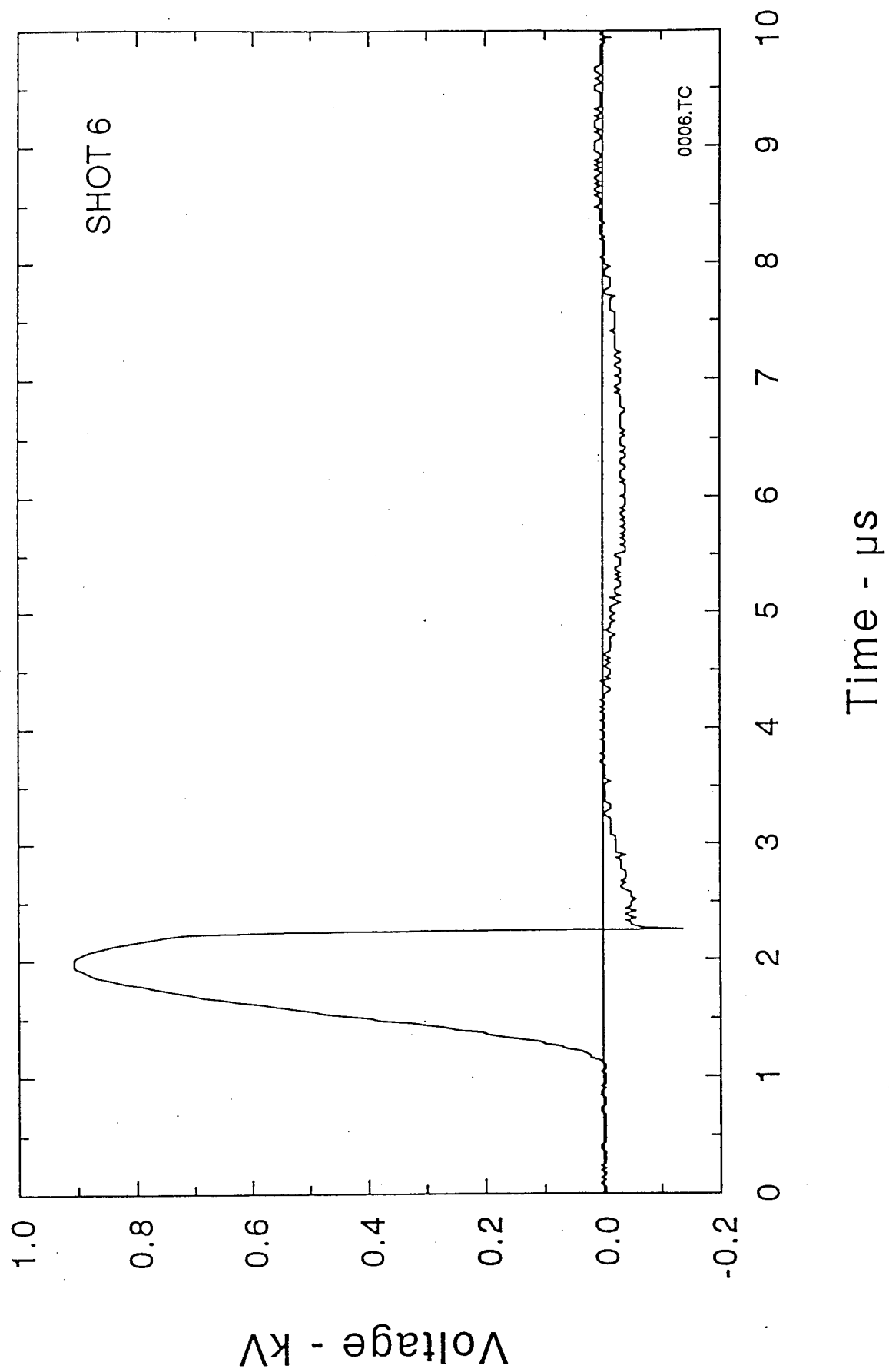


Figure 4. Test module voltage with a breakdown after the first peak.

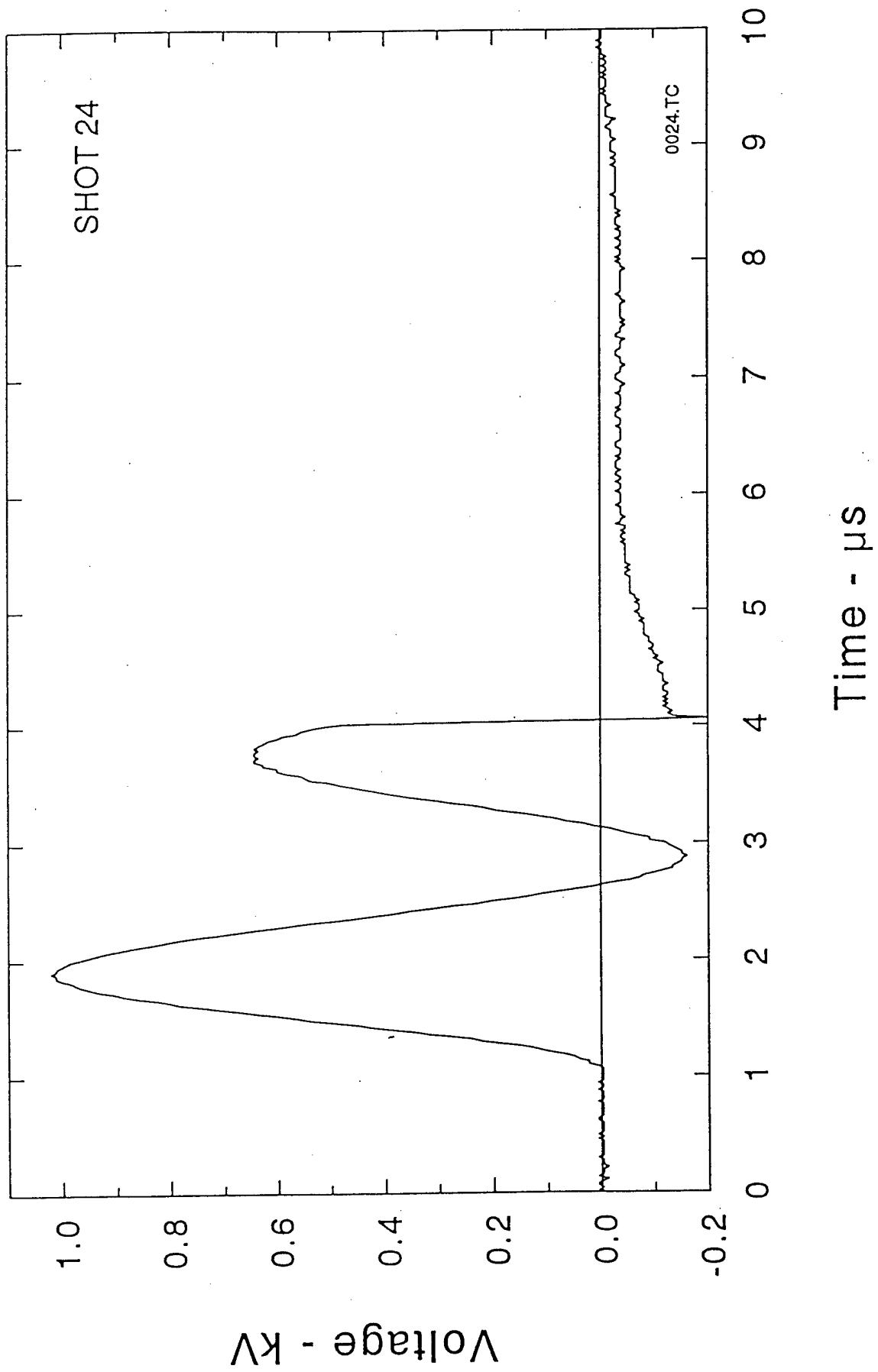


Figure 5. Test module voltage with a breakdown after the second peak.



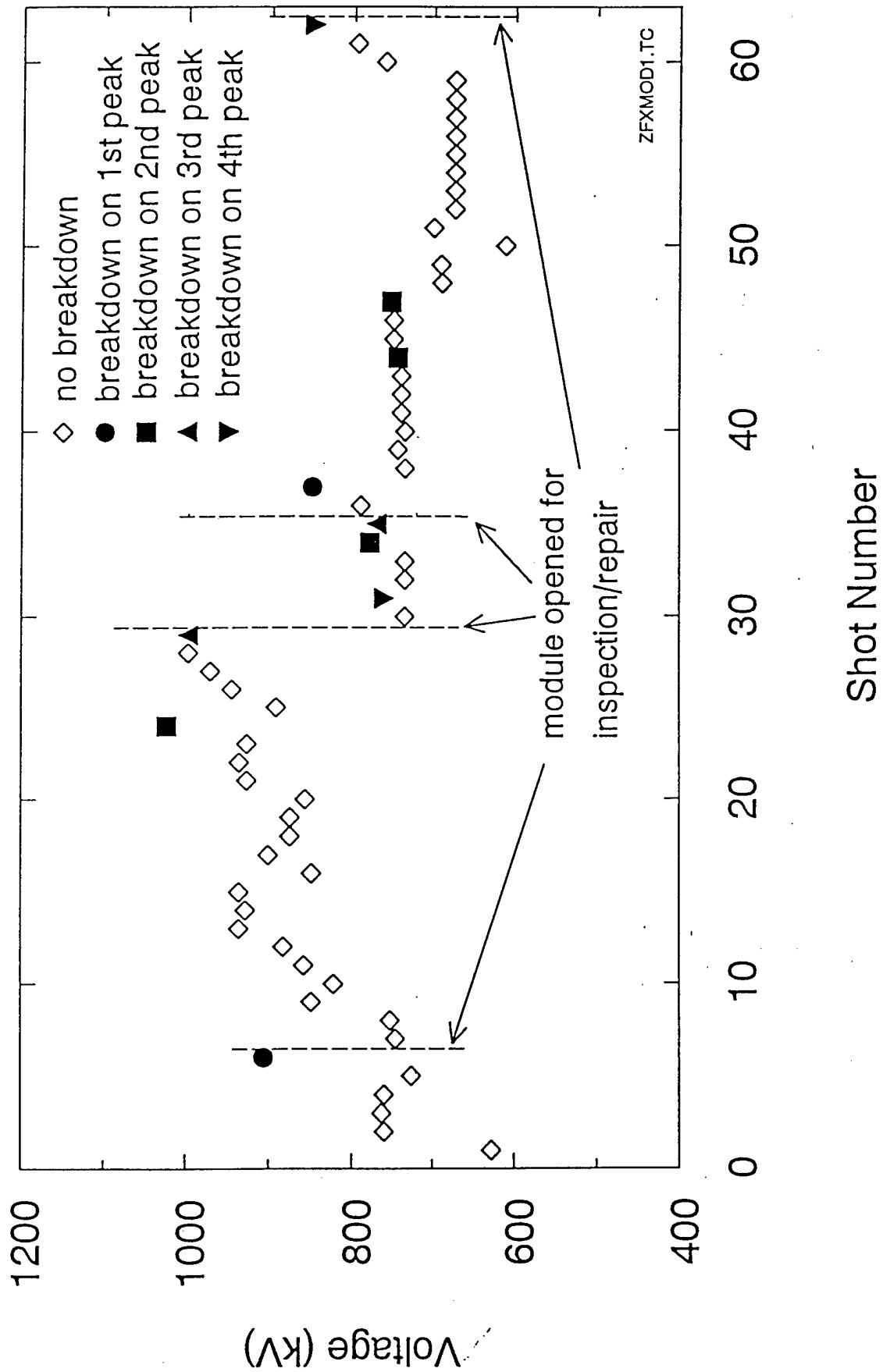
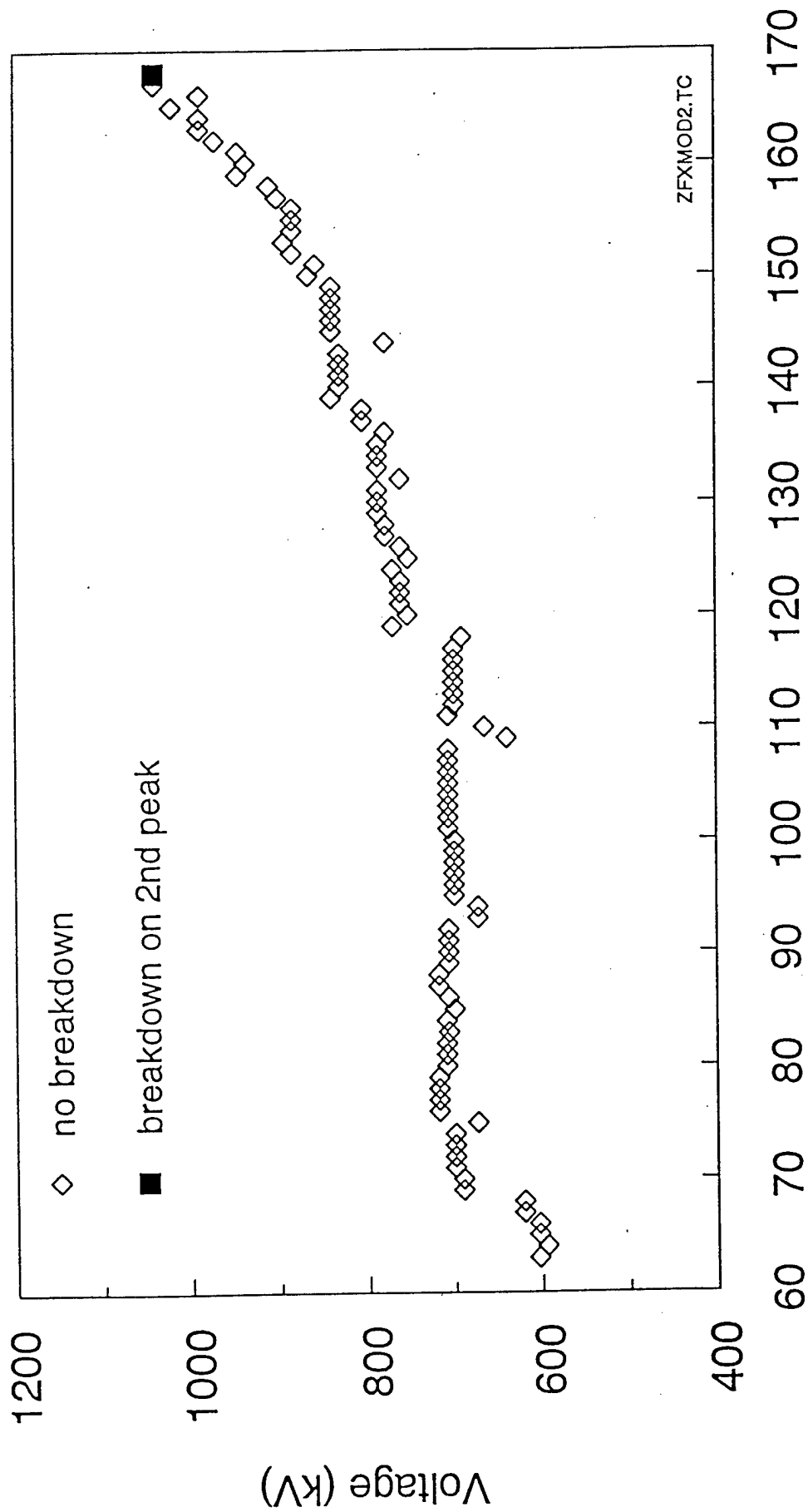


Figure 6. Summary of ZFX module tests for Shots 1 - 62.



### Shot Number

Figure 7. Summary of ZFX module tests for Shots 63 - 168.

PULSED POWER PHYSICS TECHNOTE NO. 94-07

TITLE: FAILURE ANALYSIS OF ZFX SHOT #36

AUTHORS: J.C. KELLOGG, J.R. BOLLER, R. FISHER\*, M. SUCY\*

DATE: 25 APRIL 1994

ABSTRACT: The first shot on ZFX since the new plastic components were installed resulted in two breakdowns in the water dielectric of the transfer capacitor. Maximum voltage on the transfer capacitor for this shot was 186 kV. At least one breakdown occurred late in time, in the third full cycle of the transfer capacitor voltage. The divertor switch was installed, but did not trigger properly. The physical locations for both breakdowns was at the interface between two blocks of plastic, where a polyethylene and a polyurethane piece were in contact with each other. These interfaces are in a horizontal plane, and could easily have trapped air. Air was found after the shot trapped in other, similar places on the machine. Trapped air is believed to have been the cause of the breakdowns. This failure mode differs from the first failure (March 1993), which resulted from voids in the plastic field attractors.

THIS REPORT REPRESENTS  
UNPUBLISHED INTERNAL  
WORKING DOCUMENTS AND  
SHOULD NOT BE REFERENCED  
OR DISTRIBUTED

\*JAYCOR, Vienna, VA

On 31 January 1994, ZFX fired shot 36; the first shot since being reassembled with new UHMW-polyethylene and polyurethane components for its plastic field attractors. The new plastic was necessary because voids in the original polyethylene led to breakdowns in the transfer capacitor (TC), during initial tests in March 1993. On shot 36, breakdowns occurred at two locations in the water dielectric of the TC, one each in its north and south halves. Both breakdowns occurred at the horizontal interface between a polyethylene and a polyurethane component of the plastic field attractors. The cause of these breakdowns is believed to be bubbles of air trapped between horizontal plastic surfaces.

Shot 36 was to be a repeat of shot 32, which did not have a water breakdown. The load was a short circuit, with 2 psi of pure SF<sub>6</sub> in the front end. The Marx charge was 20 kV, giving an erected voltage of 280 kV, which is one-third of the expected operating charge. The ZFX transfer switch was pressurized with 2.1 psi of 14.5% SF<sub>6</sub>/Argon, so that self-break was expected at ~200 kV on the TC (about 2  $\mu$ s into the TC ring-up). The resistivity of the water was 1.45 M $\Omega$ -cm. The de-aeration system had been operating off and on for about two weeks prior to the shot, but extremely cold weather had limited its time of operation. All visible bubbles had been removed from the tank. The divertor system was installed for the first time on shot 36. This consisted of an externally-triggered gas switch and a 1.8  $\Omega$  damping resistor. The trigger time was set for 1  $\mu$ s after Marx erection—well before the expected self-break of the transfer switch.

An equivalent circuit diagram for ZFX is shown in figure 1. Figure 2 compares the TC voltage and output current for shots 36 and 32. The two shots are virtually identical until about 8  $\mu$ s, when a perturbation can be seen in both the current and voltage of shot 36. This indicates that the breakdowns occurred late in time, with at least one in the third full cycle of the TC voltage.

Both of the locations where breakdown occurred have the same geometry (see figure 3). A small, right-angle elbow of cast polyurethane was butted against the end of a polyethylene wall piece, with the two contacting surfaces making a horizontal plane of about 10 cm by 27 cm. The upper surface was the polyurethane, and the lower was polyethylene. The polyurethane surfaces were quite smoothly finished, but had a slight concavity. The center of the surface was recessed about 0.15 cm inside the edges. The polyethylene surface was fairly rough, with grooves of 0.08-0.15 cm depth across it, due to its being cut with a large diameter circular saw blade. Air bubbles were almost certainly trapped between the two plastic surfaces, in such a way that the de-aerated water in the tank could not circulate through the interface to absorb the air. There are nine such locations in ZFX. Two of these broke down on shot 36; one at the raft side of the south TC half, the other at the Marx feed on the north TC half, with the former showing slightly more damage than the latter. When some of the other identical interfaces were examined after the shot, at least one held trapped air.

In both locations, the breakdown track followed the pattern of saw-cut grooves on the plastic surface (see figure 4). The most likely explanation for this is that the trapped bubbles assumed the shape of the grooves that they filled. We know that bubbles were present *after* the shot; but we cannot be absolutely certain that the bubbles were there *before* the shot. If we had known the bubbles were present, we would have removed them.

On shot 36, the ZFX Marx erected  $\sim 4 \mu\text{s}$  later than expected. This caused a timing problem with the mini-Marx that triggers the divertor switch; the divertor-switch trigger pulse arrived before there was any voltage on the TC. With no voltage across it, the switch could not conduct. Figure 5 compares the TC voltage on shot 36 with two Bertha simulations of the shot, which used the transmission line model shown in figure 1. In the first simulation, the divertor switch was not fired. Agreement is good between this simulation and the actual shot. In the second simulation, the divertor switch closed at  $1 \mu\text{s}$ . The TC voltage of this simulation is markedly more damped than the TC voltage measured on shot 36. It is evident that the divertor switch did not trigger on this shot. To prevent this sort of problem in the future, the divertor-switch trigger command will be generated by a level crossing detector that will monitor the TC voltage.

It is almost certain that air trapped between the plastic surfaces was the cause of the breakdowns on shot 36. We had already known that bubbles trapped in such spaces could not be tolerated; now we know that the de-aeration system alone cannot be relied upon to remove such bubbles. We are now modifying the plastic interfaces so that a thin water gap will separate all the plastic blocks. These gaps will be cleared of air by installing the blocks underwater whenever possible, and by squirting a high-velocity jet of water through the interfaces. We will take particular care in places where the interfaces between blocks are horizontal. When ZFX is put back into operation we will be able to address another question: do bubbles only form when the tank is initially filled, or will we have ongoing problems with bubbles appearing between successive shots?

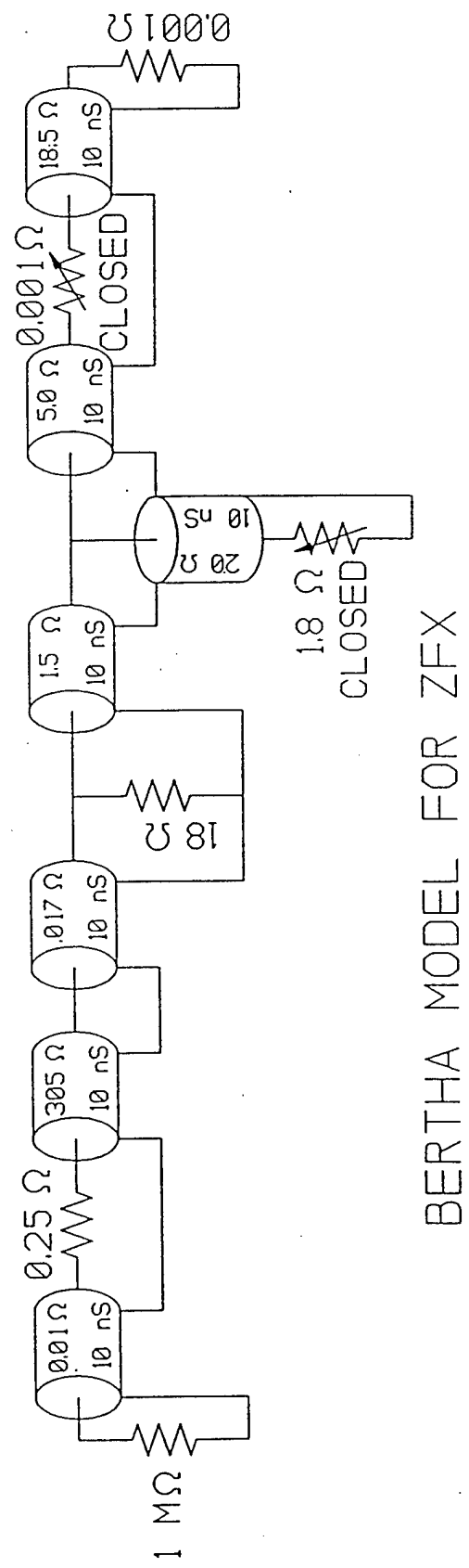
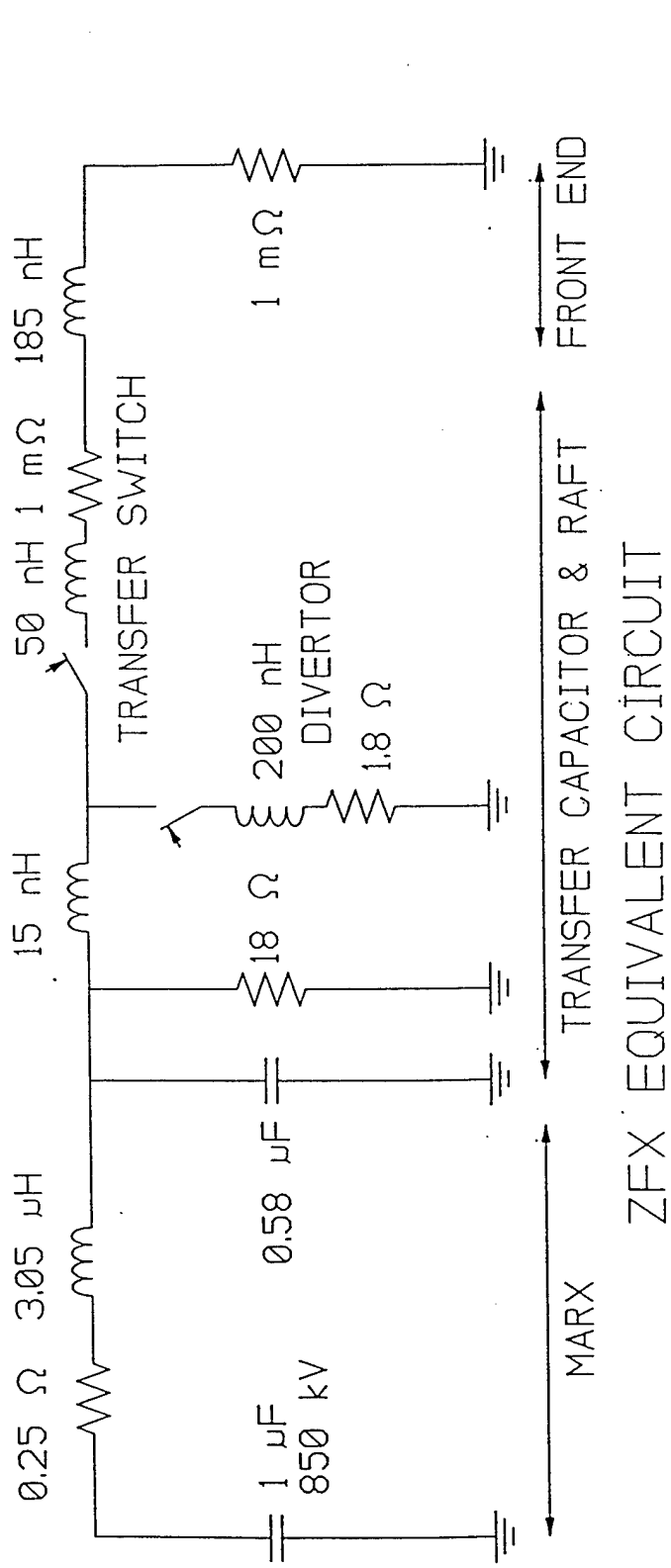
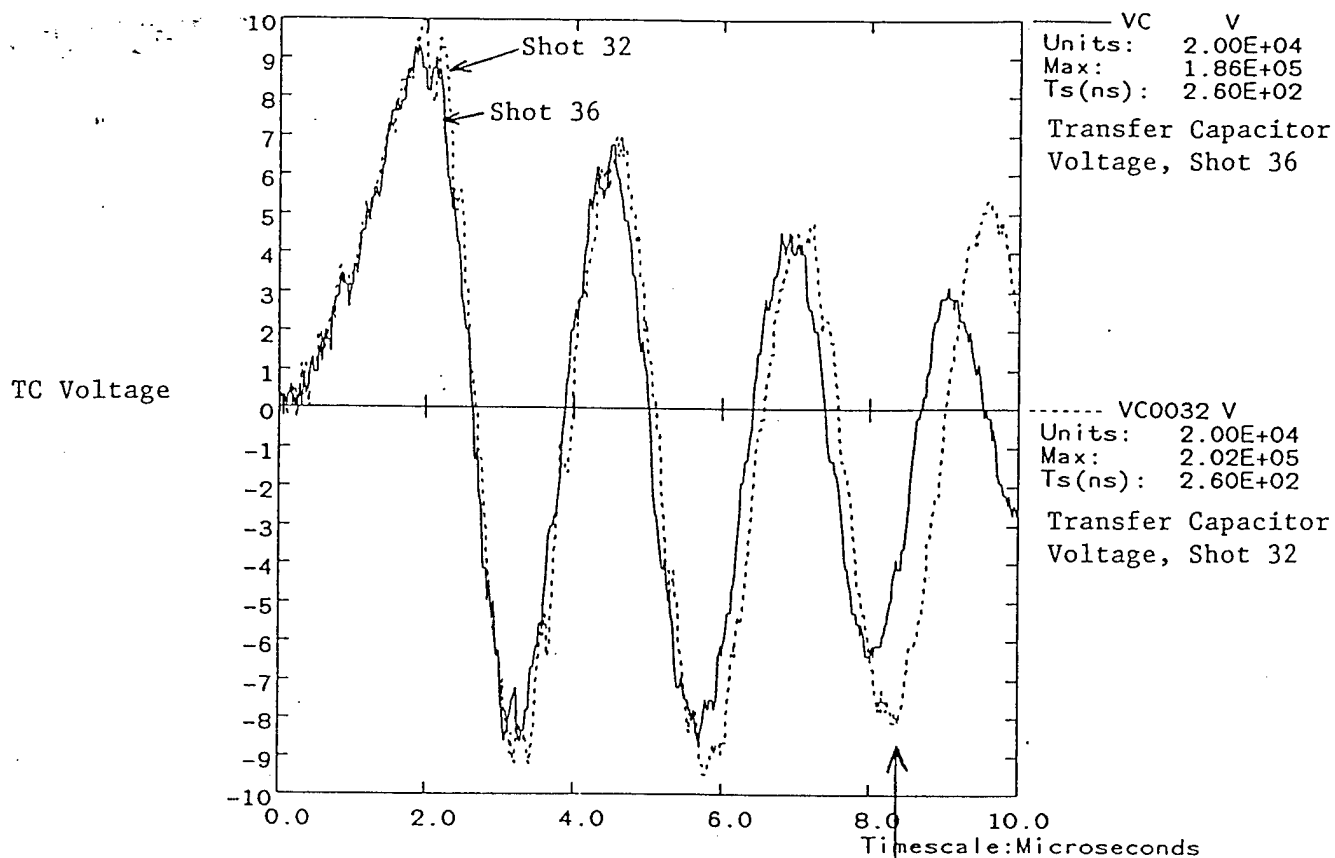


Figure 1. ZFX equivalent circuit and transmission line model.

Shot 0036



Shot 0036

Breakdown

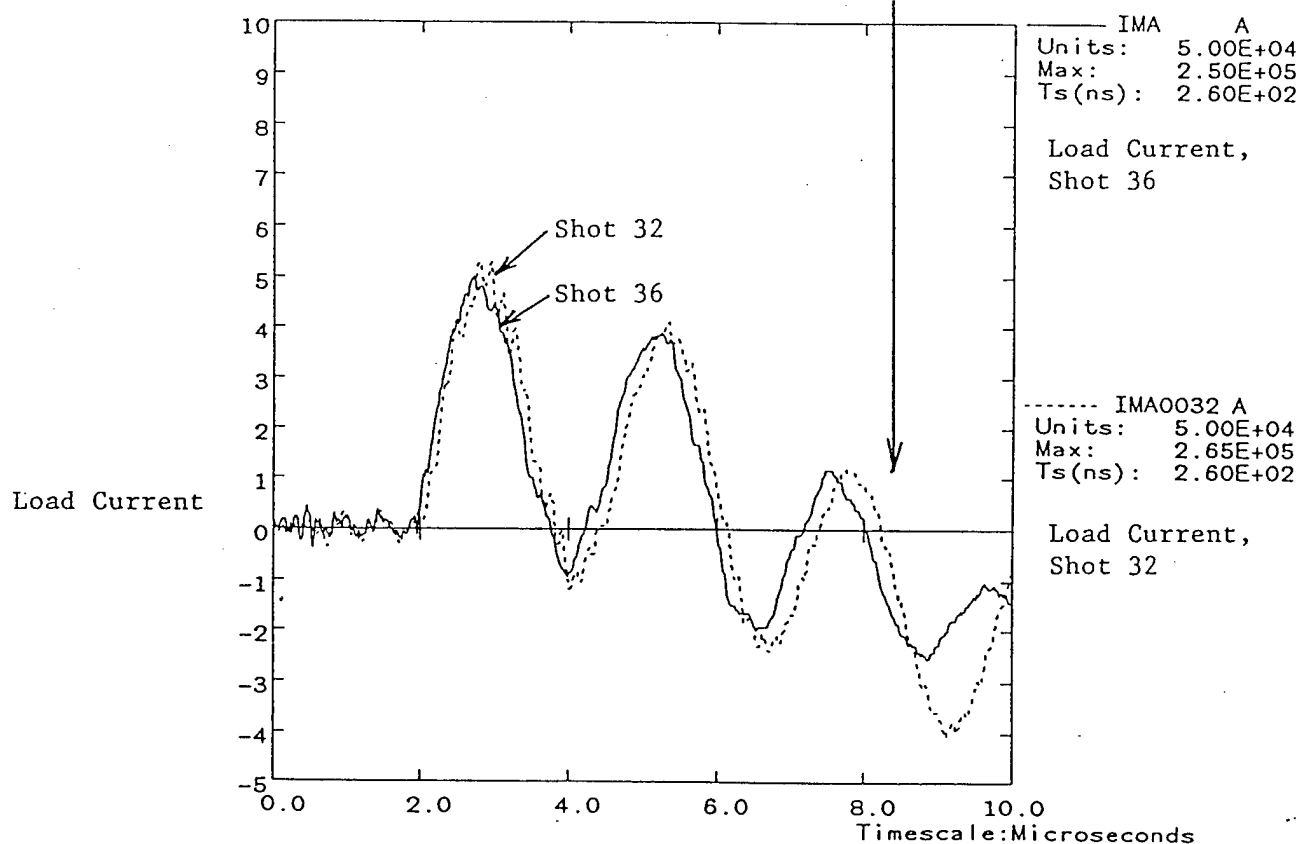


Figure 2. Comparison of TC performance, ZFX shots 32 and 36.

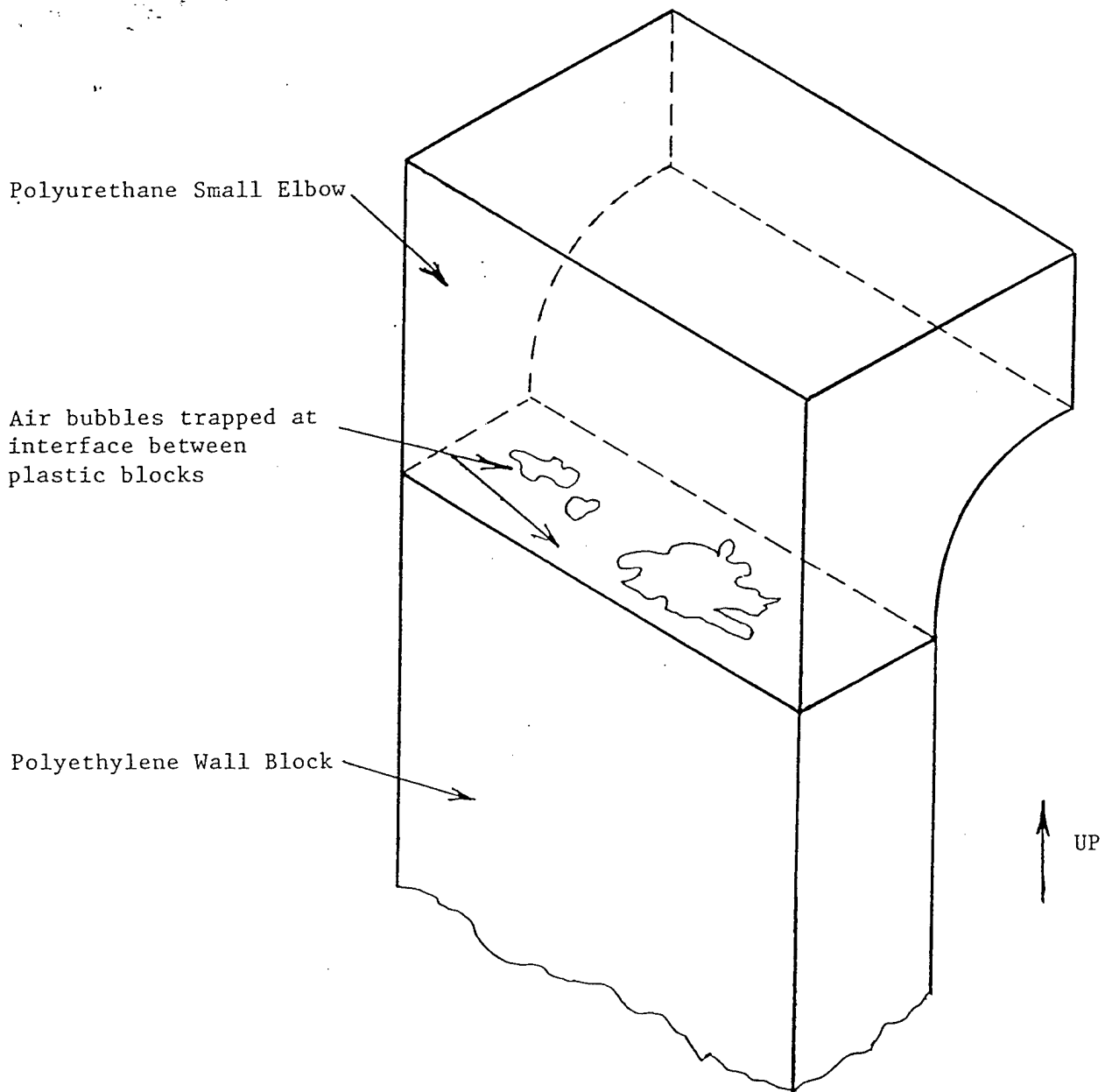


Figure 3. Arrangement of plastic field attractors in the locations where breakdowns occurred. Air bubbles were found in the location shown after the shot, not only in the interfaces that broke down, but in other similar locations.



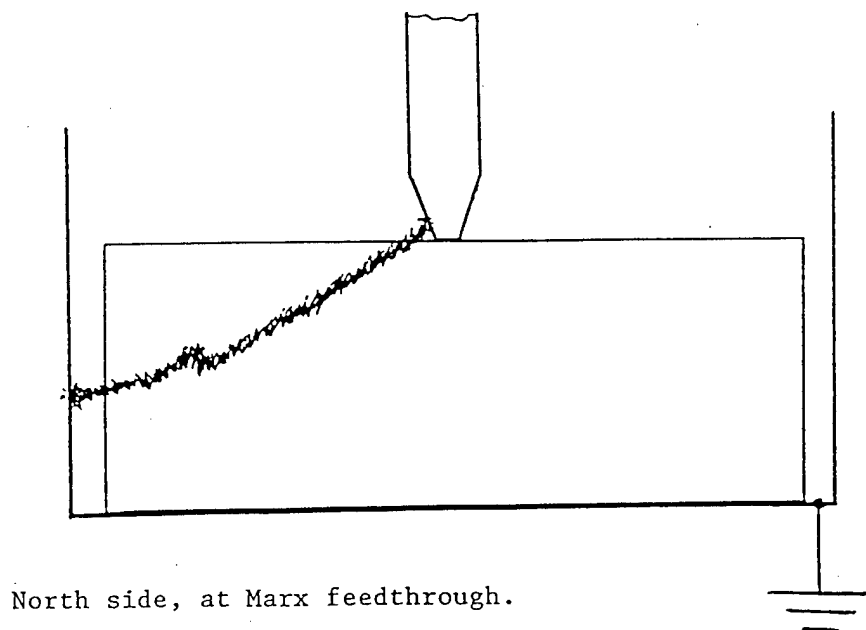
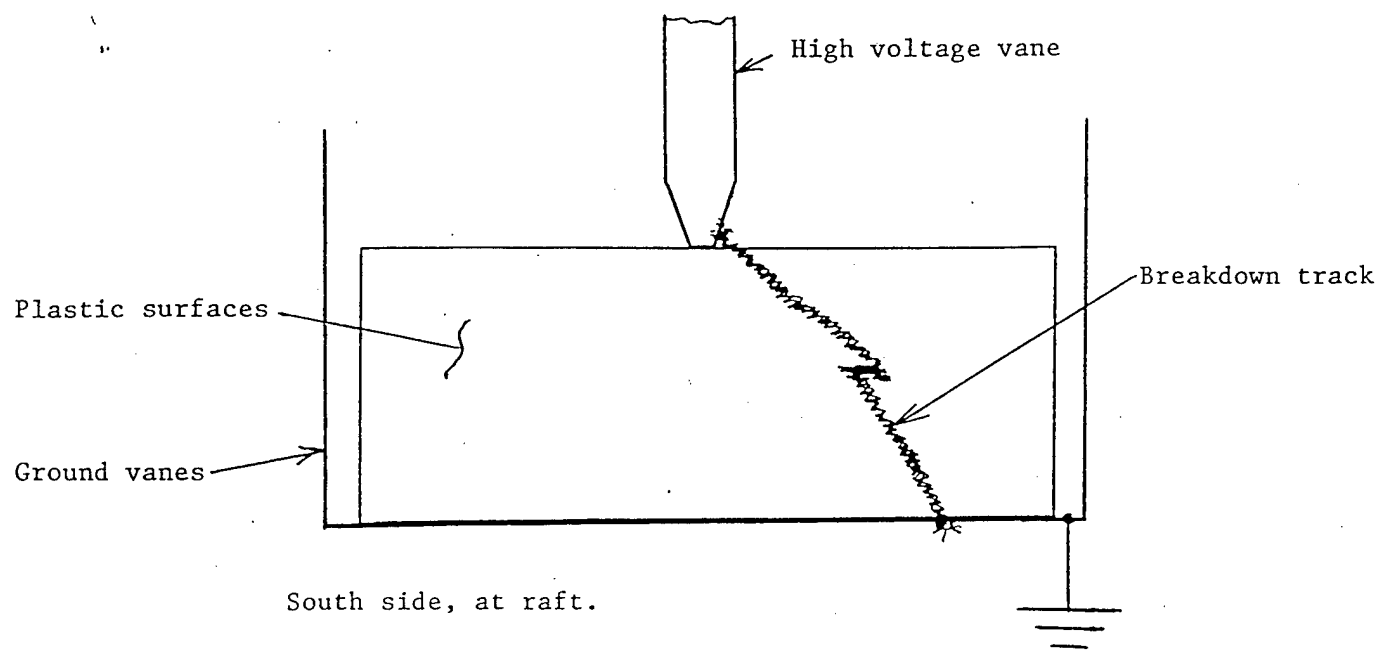
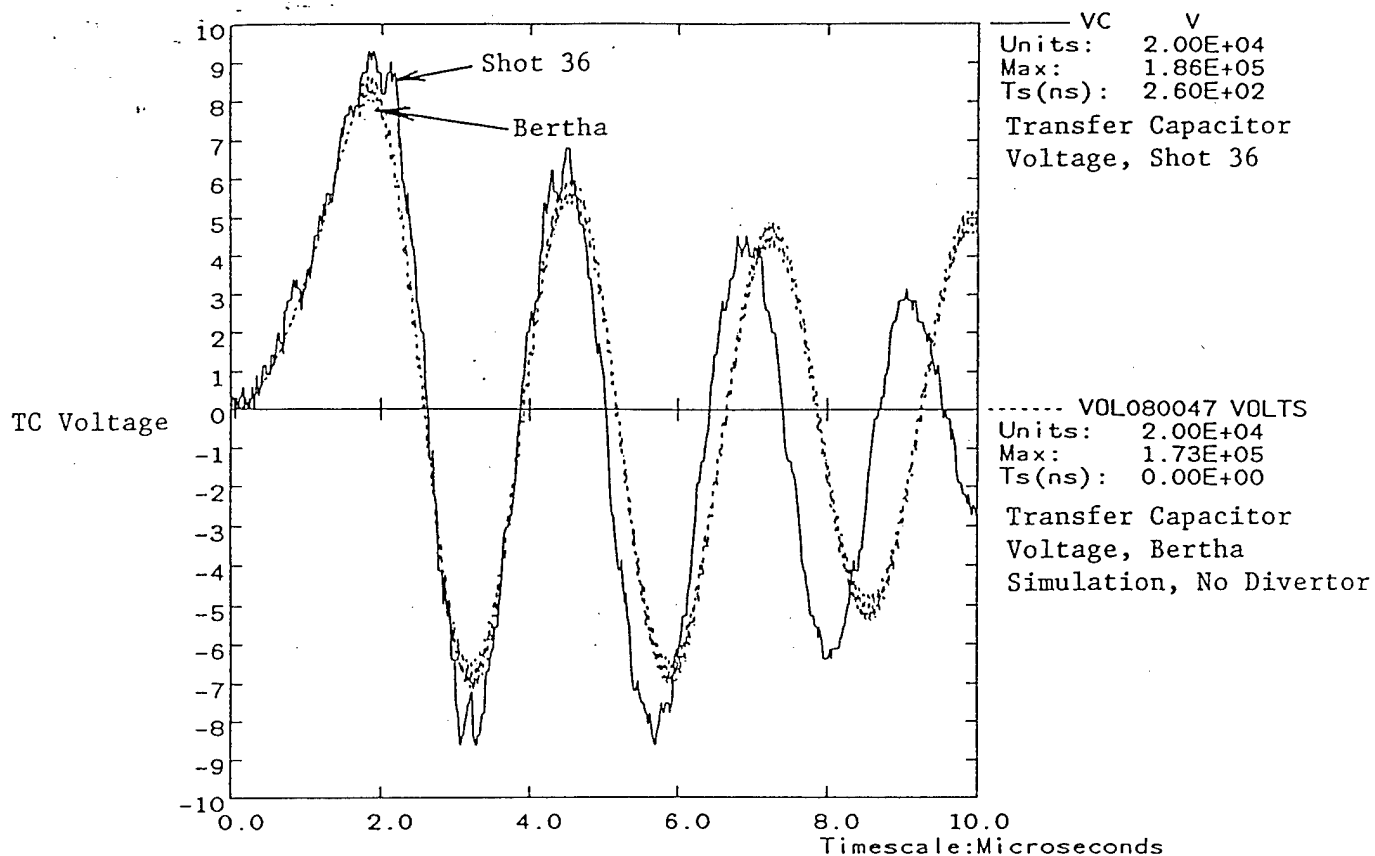


Figure 4. Cross section of the two breakdown paths found after the shot. The surface of the polyethylene was carbonized, and small arc marks were found on the hot and ground vanes as shown.

Shot 0036



Shot 0036

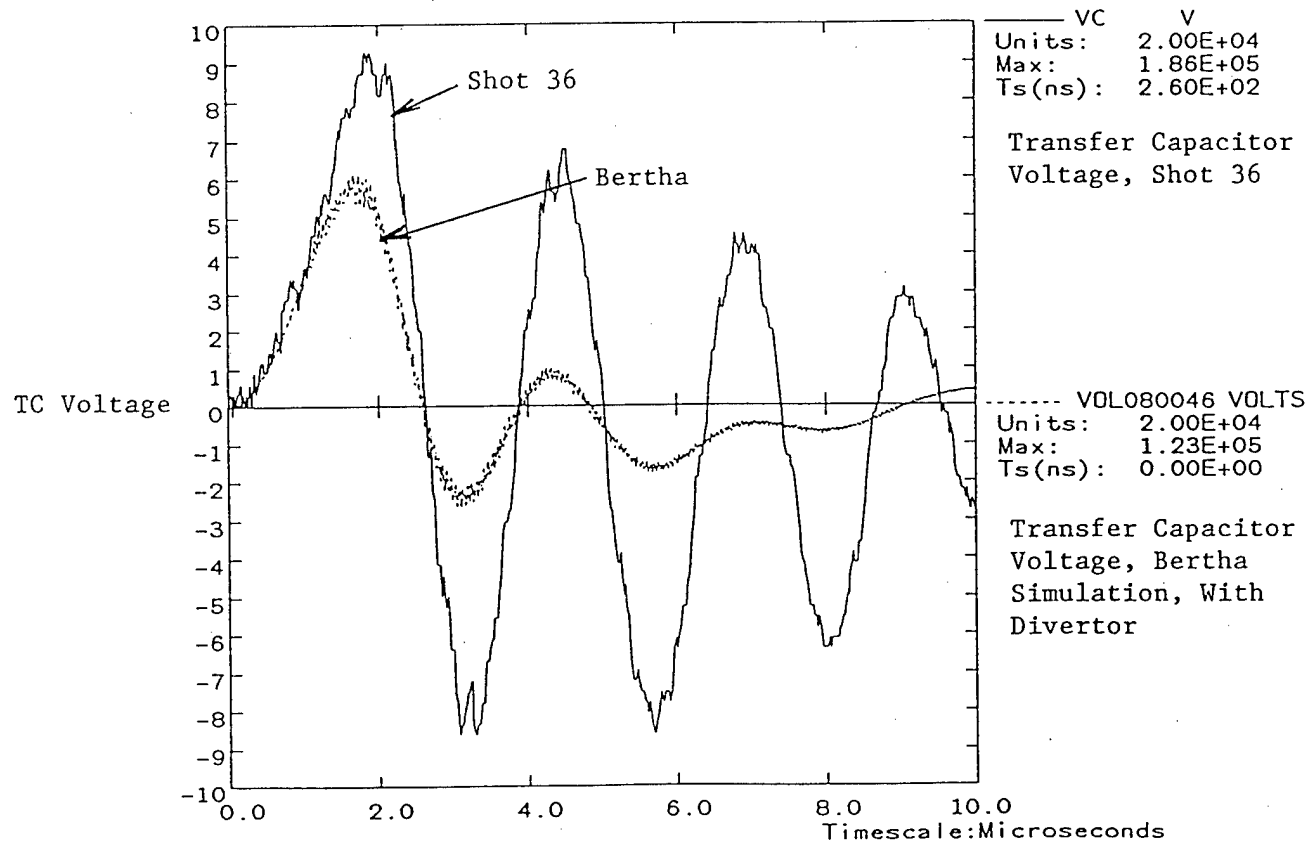


Figure 5. Transfer capacitor voltage for shot 36, compared with Bertha transmission line model simulations. Shot 36 clearly resembles the simulation without a divertor.

PULSED POWER PHYSICS TECHNOTE NO. 93-13

**TITLE:**           **ZFX--A PULSED POWER DRIVER USING A PARALLEL PLATE WATER CAPACITOR** (Summary of the oral presentation at the 9<sup>th</sup> Pulsed Power Conference, 21-23 June 1993, Albuquerque, NM)

**AUTHOR(S):**   J.D. Sethian, J.R. Boller, R.J. Comisso, J.C. Kellogg, B.V. Weber, P.J. Goodrich, and D.D. Hinshelwood

**DATE:**           21 July 1993

**ABSTRACT:**    A new pulsed power generator that uses a thin parallel plate water capacitor as the intermediate store is nearing completion at the Naval Research Laboratory. The plates are made of relatively thin (2.54 cm thick) aluminum sheets and rely on "plastic field attractors" to reduce the field enhancement at the plate edge.

The water capacitor is pulse charged by a conventional 340 kJ Marx, and then discharged by a self-break rimfire-type switch into the load. Because the plates are thin, over 70% of the stored water is used to store energy, and thus the system is very compact. Other potential advantages of this system might be cost and ease of fabrication and maintenance.

The first experiments on ZFX, will be to drive current through a plasma opening switch. It is anticipated that ZFX should be able to deliver a current of 1 MA with a risetime of 300 nsec to the switch. Peak current would be 1.4 MA at 625 nsec.

THIS REPORT REPRESENTS  
UNPUBLISHED INTERNAL  
WORKING DOCUMENTS AND  
SHOULD NOT BE REFERENCED  
OR DISTRIBUTED

- Figure 1: Title
- Figure 2: Schematic layout of the system showing the system architecture, the electrical parameter range, and the power conditioning times scales appropriate for the ZFX water capacitor.
- Figure 3: Comparison of two approaches for storing electrical energy using water capacitors; In the coaxial system (left) a large fraction of the water, namely that inside the inner conductor, does not store energy and hence a significant volume wasted. In contrast, a parallel plate water capacitor (right) can be much smaller because a greater fraction of the water is used to store energy. The problem with the coaxial construction can be ameliorated somewhat by using multiple parallel coaxes, as described below. The problem with a parallel plate arrangement is what to do about the field enhancement at the edges. By using the techniques described below, we show that the parallel plate construction results in more efficient use of the water compared with an optimized multiple coax system.
- Figure 4: The enhancement at the edges is shown in graphic detail in this plot. This is an equipotential plot of the circled area shown in Figure 3, for a parallel plate capacitor charged to 950 kV and an interplate spacing of 12.5 cm. Note that while the field between the plates is uniform at 75 kV/cm, that at the edges is 360 kV/cm, which will exceed the breakdown strength in water.
- Figure 5: If however, one places a plastic block at the edge of the plate, the lower dielectric constant of the plastic (2.2 vs 81 in the water) causes the equipotential lines to be pulled away from the plate edges. In a sense the plastic is "attracting" field lines into it, and hence can be thought of as a "Plastic Field Attractor" (PFA). Note that in this example the field between the plates is uniform at 75 kV/cm, except at the transition to the curved edge of the plate where it increases to 108 kV/cm. This is still below breakdown. The field in the bulk plastic is 184 kV/cm and should also be well below breakdown, provided the plastic is free of voids and impurities. This technique using shaped plastic to locally reduce field stresses in water is not new, however, this is the first time that it has been proposed as the basis for an entire system. Note that these plastic pieces are essential for the parallel plate capacitor to be a viable concept. Otherwise the plates would have

to be so thick (in order to have a large enough radius to reduce the field enhancement) that the volumetric efficiency would be dismal.

Figure 6: Experimental apparatus used to test the PFA concept on a small scale. This tests the PFA concept for both positive and negative high voltage plates (see the ground aperture at the feed), and it tests the more severe conditions where the corners of the plates must be rounded.

Figure 7: Data from the test apparatus show the concept should be viable; According to these results it should be possible to operate a full scale water capacitor at 14% above its design value of 1000 kV. Autopsies indicated the system was as likely to break along the plastic as in the water gap itself, implying the plastic/water interface was no weaker than the rest of the system. During these tests a number of "construction faults" were deliberately introduced in order to determine the robustness of the system. These included gaps in the plastic (perpendicular to the plate edge), gaps between the plastic and the edge of the plate, holes drilled into the plastic to simulate voids, and trapped air in the water. Only the latter two caused a problem, which was taken as a clear warning of the importance of removing all trapped air.

Figure 8: Line drawing of the ZFX water capacitor. The water capacitor is housed in two boxes, each 8 feet wide x 10 feet long x 5 feet high, situated on either side of the switch load region. The latter is mounted on a "raft" that bridges the two water capacitors. The plates are oriented so they behave as several parallel plate transmission lines feeding into a common collector.

Figure 9: Photo of a model of the ZFX water capacitor.

Figure 10: Photo of the ZFX water capacitor under construction

Figure 11: Photo of the ZFX water capacitor under construction

Figure 12: Performance of ZFX as modelled with a simple transmission line code. Maximum predicted current is 1.5 MA @ 600 nsec.

- Figure 13: Calculations show that ZFX should operate well below the limits of electrical breakdown in water, provided a divertor switch is incorporated in the system. These breakdown strengths were calculated using rather pessimistic assumptions: It was assumed that the  $A^{.058}$  dependence holds for large areas, and that the breakdown is a cumulative process; i.e. once a streamer is launched, it will continue independent of the polarity of the surface.
- Figure 14: Using available data, the surface of the plastic should also be operating well below breakdown.
- Figure 15: Equivalent circuit of ZFX as it was configured for the first, low voltage power tests. The switch inductance in this circuit is about a factor of 2.4 higher than in the circuit used to compute the maximum performance shown in Figure 12. This reflects the reluctance of the switch to multichannel at lower voltages.
- Figure 16: Comparison of calculated and measured water capacitor waveforms.
- Figure 17: Comparison of calculated and measured output current waveforms. Load is a 1" diameter bolt.
- Figure 18: A comparison between a multiple coaxial tube water capacitor (based on the PI Decade design) and a parallel plate arrangement. The parallel plate arrangement can store the same amount of energy but in 75% of the volume.
- Figure 19: Summary

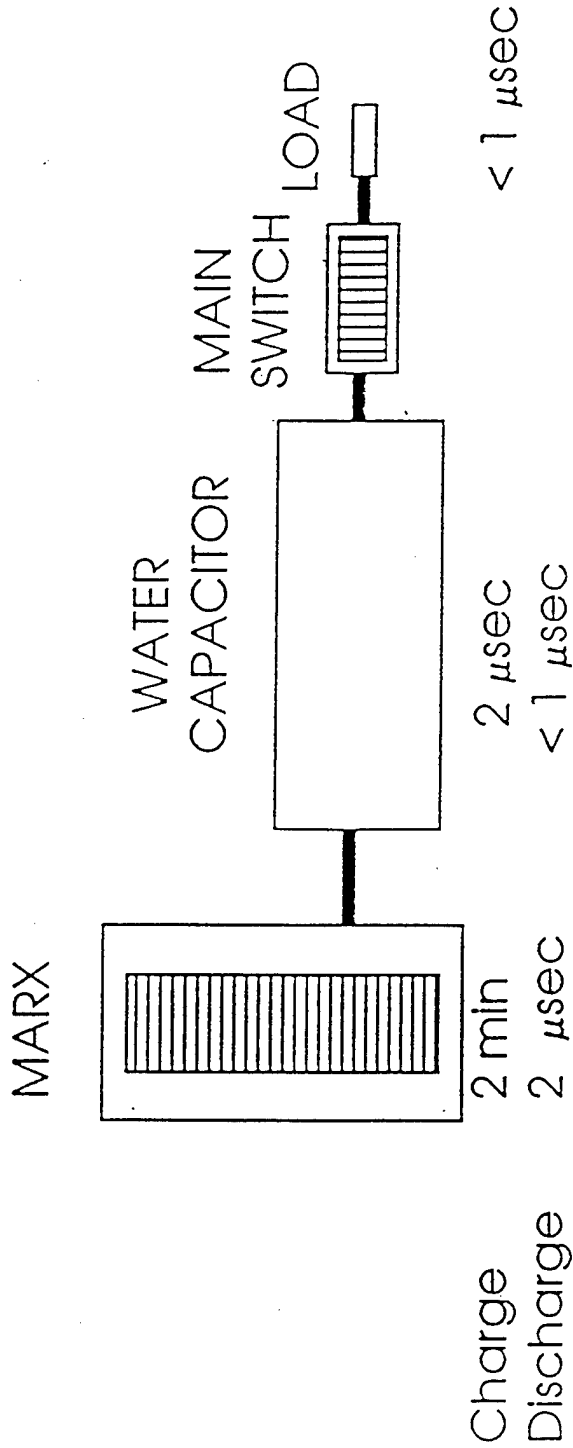
ZFX -- A PULSED POWER DRIVER USING  
A PARALLEL PLATE WATER CAPACITOR

J.D. Sethian, J.R. Boller, R.J. Commisso, J.C. Kellogg and B.V. Weber  
*Naval Research Laboratory*  
*Plasma Physics Division*  
*Washington, D.C. 20375-5346*

P.J. Goodrich and D.D. Hinshelwood  
*JAYCOR, Inc*  
*Vienna, VA 22180-2270*

Water Capacitor is used as an Intermediate Store between Marx and Load

System Energy: ~ 300 kJ, Voltage ~ 500 - 1000 kV, Current 1 - 2 MA

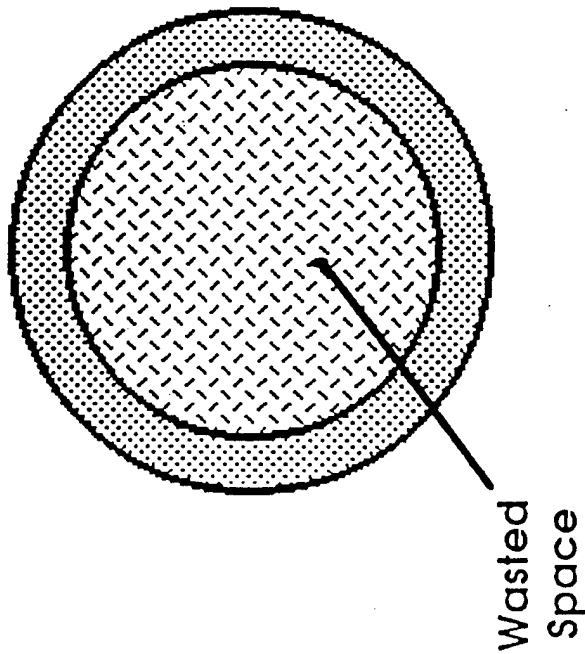




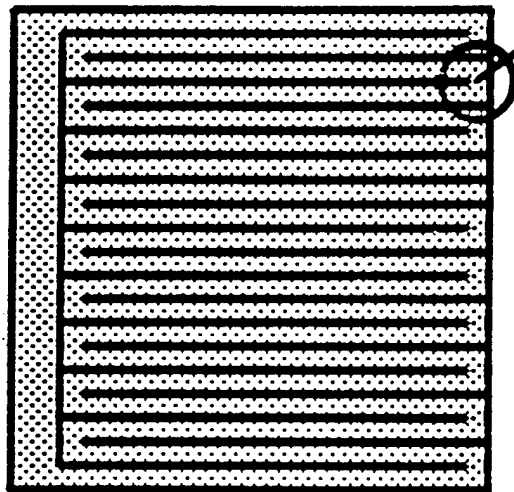
A Parallel Plate Water Capacitor can have a Very High Volumetric Efficiency

---

Coaxial Line  
(Inefficient)

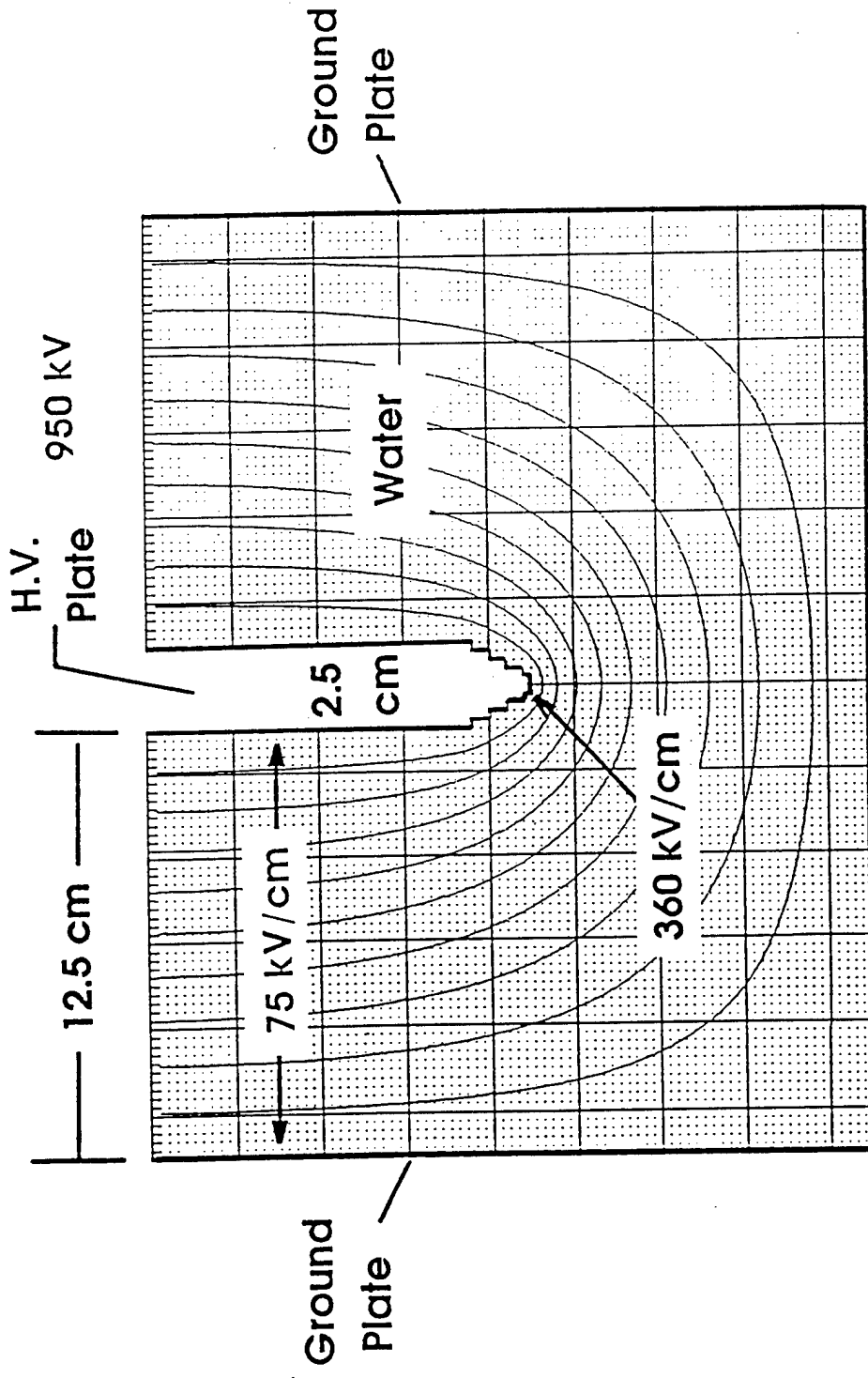


Parallel plate capacitor  
(Efficient)

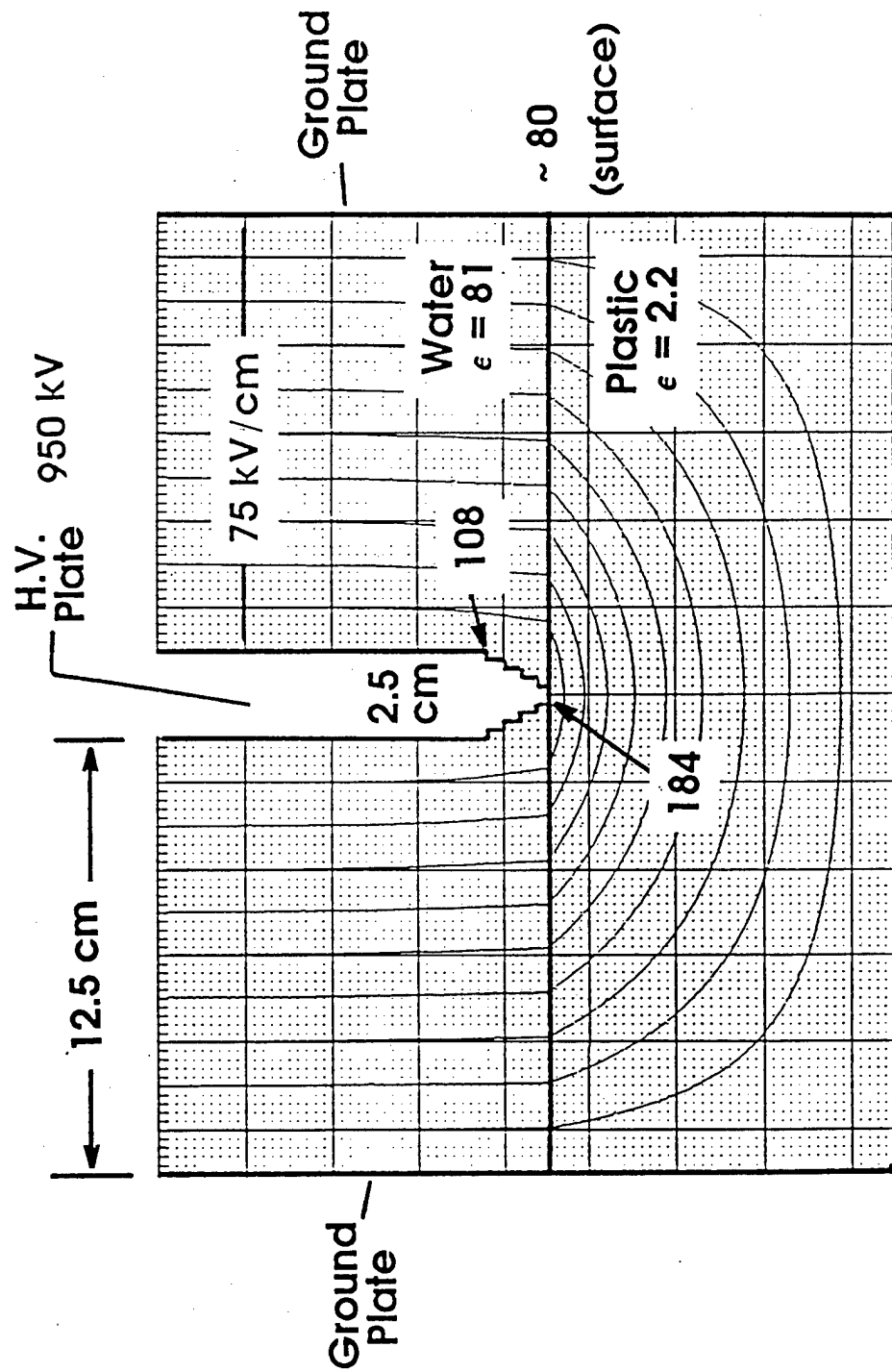


**BIG PROBLEM:  
WHAT ABOUT THE EDGES?**

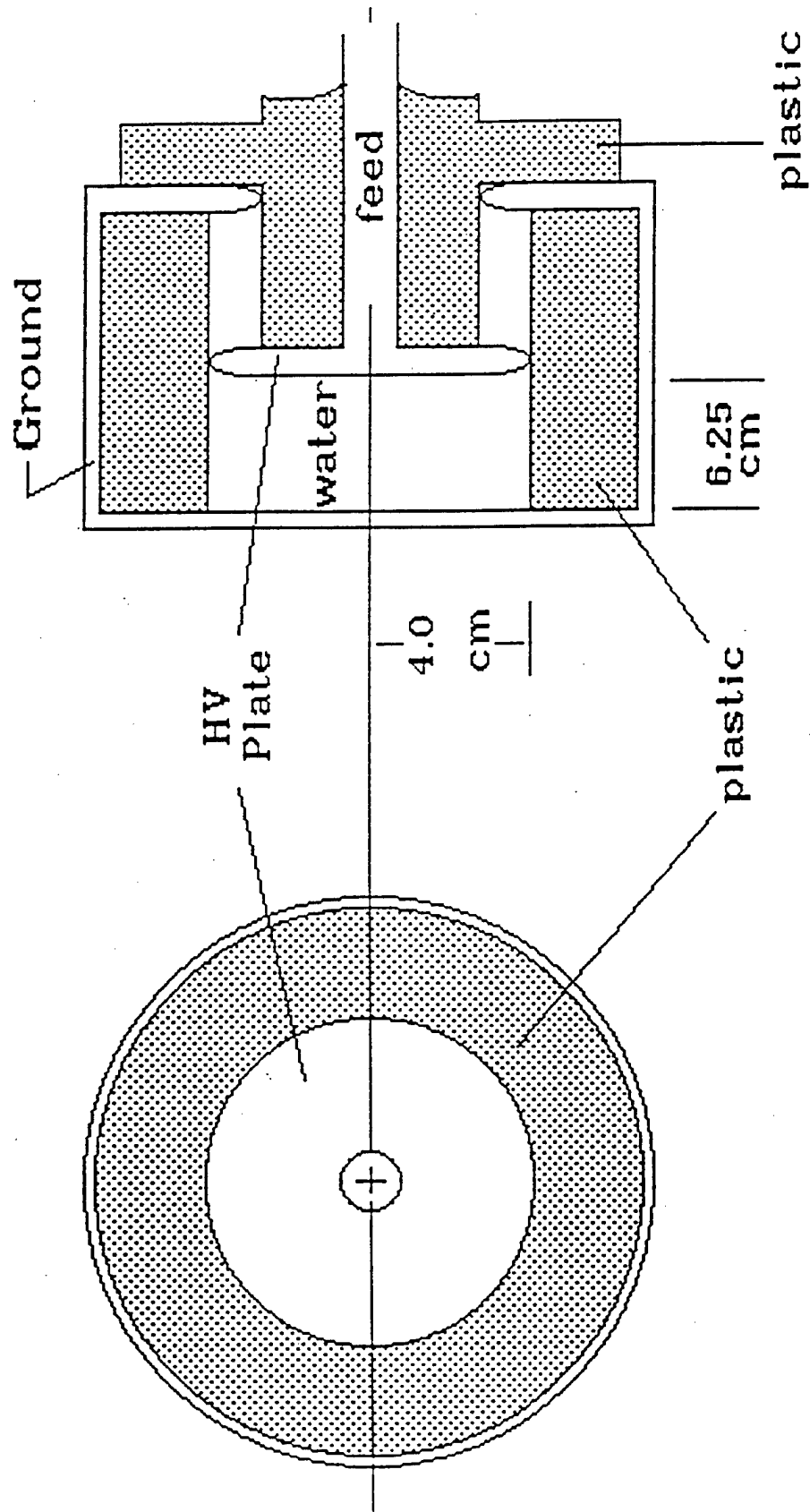
Fundamental problem is field enhancement at the edges of the plates



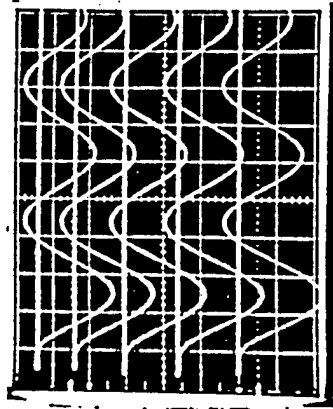
# Plastic Field Attractor (PFA) reduces field enhancement in water



PFA Concept has been tested with a half-scale module



# Module results predict good electrical performance

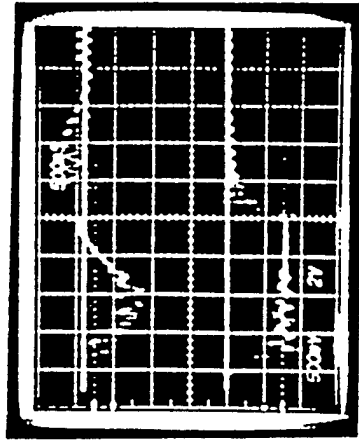


635 kV  
~ 100 shots  
No breakdown

All data:

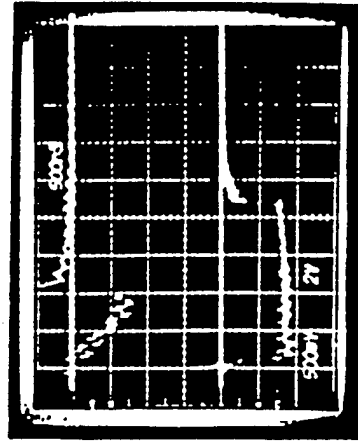
$$\tau_{\text{eff}} = 1.2 \mu\text{sec}$$

1  $\mu\text{sec/div}$



892 kV  
No breakdown

.5  $\mu\text{sec/div}$



1040 kV  
50% breakdown

.5  $\mu\text{sec/div}$

Predicted performance:

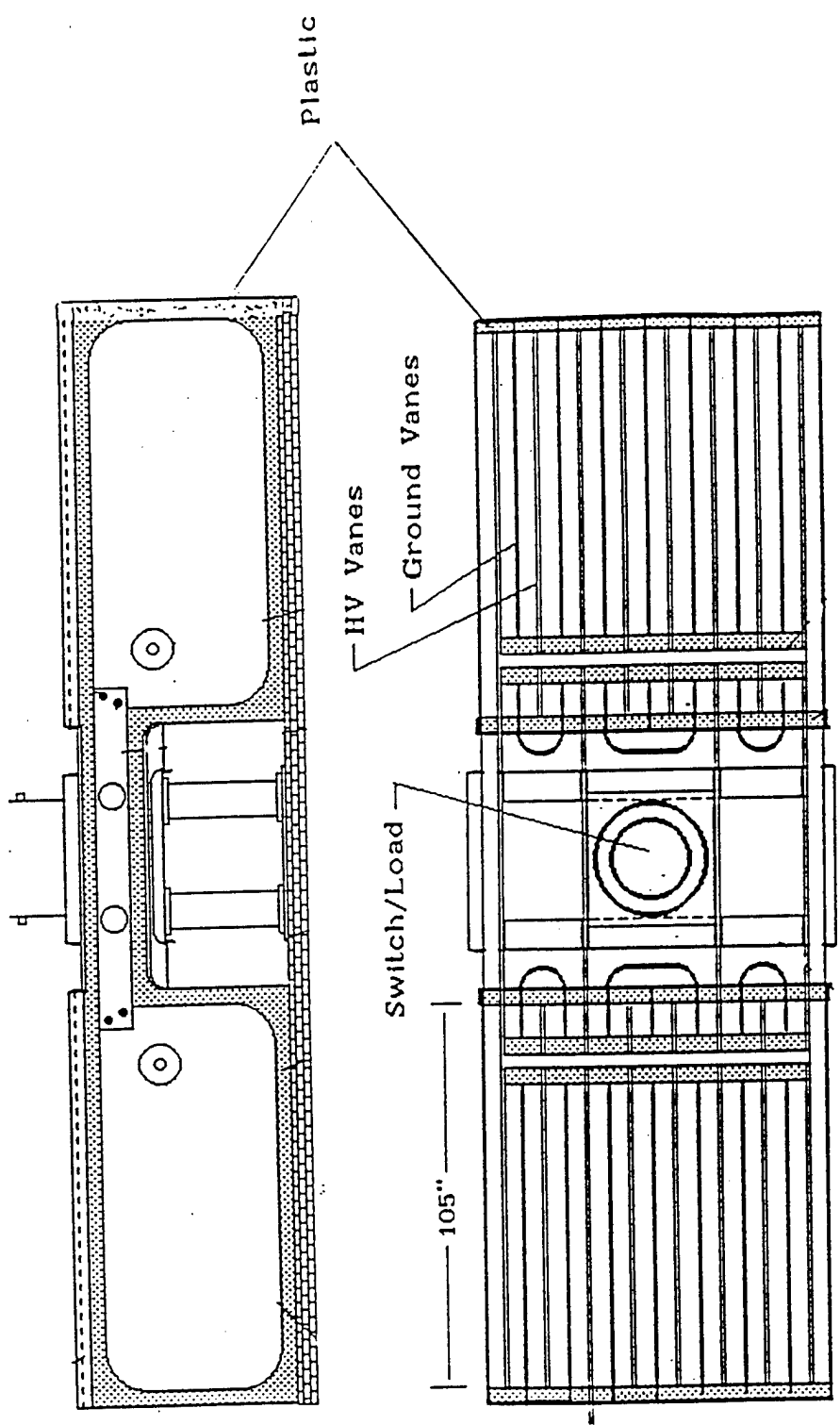
$$V = 892 \times (648/106)^{.058} \times 2 = 1165 \text{ kV}$$

area scaling      half scale  
module voltage

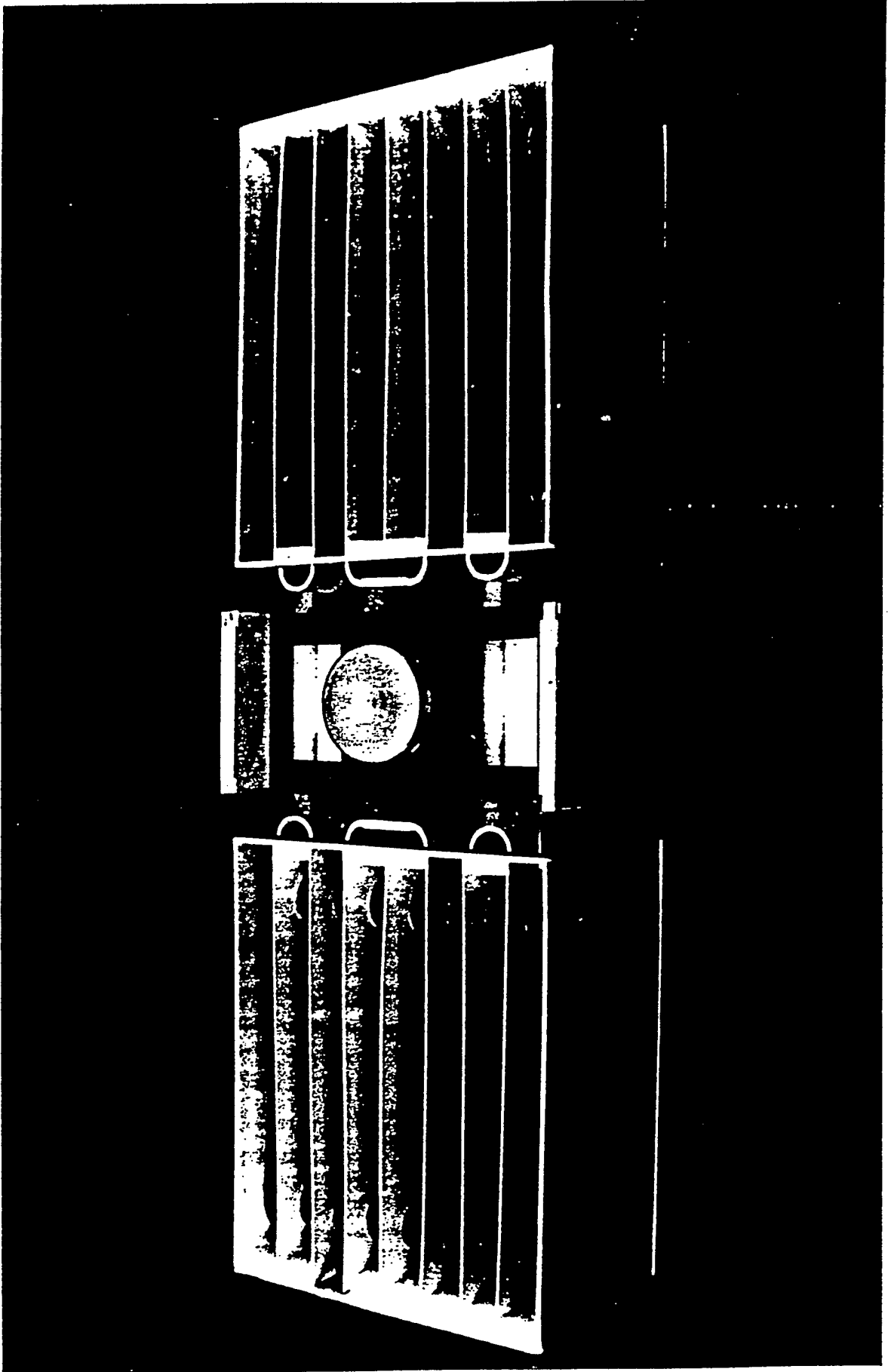
Require 1000 kV (86% of max)

(8)

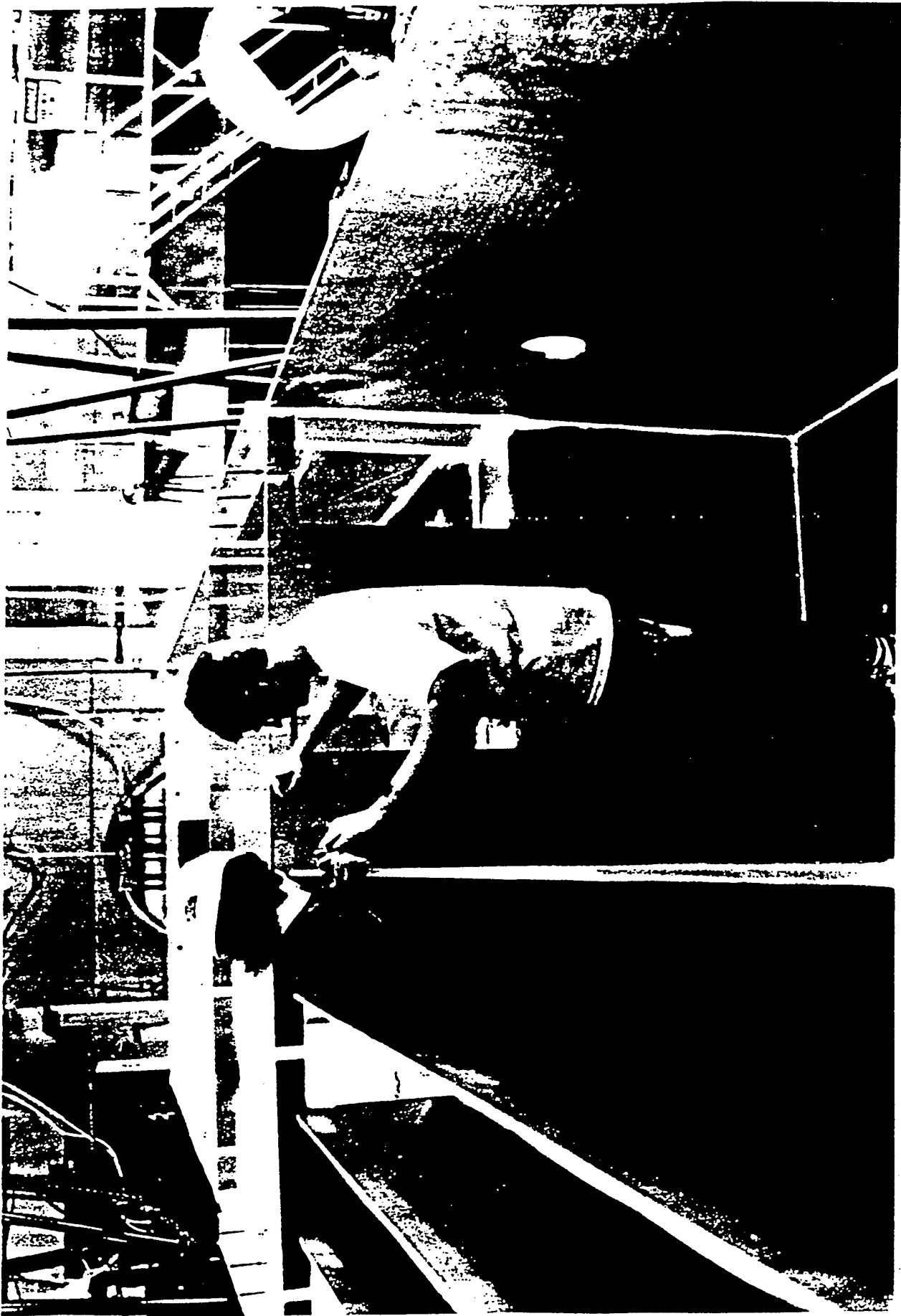
# ZFX, A 1 MV, .58 $\mu$ F PARALLEL PLATE WATER CAPACITOR



(9)



(10)



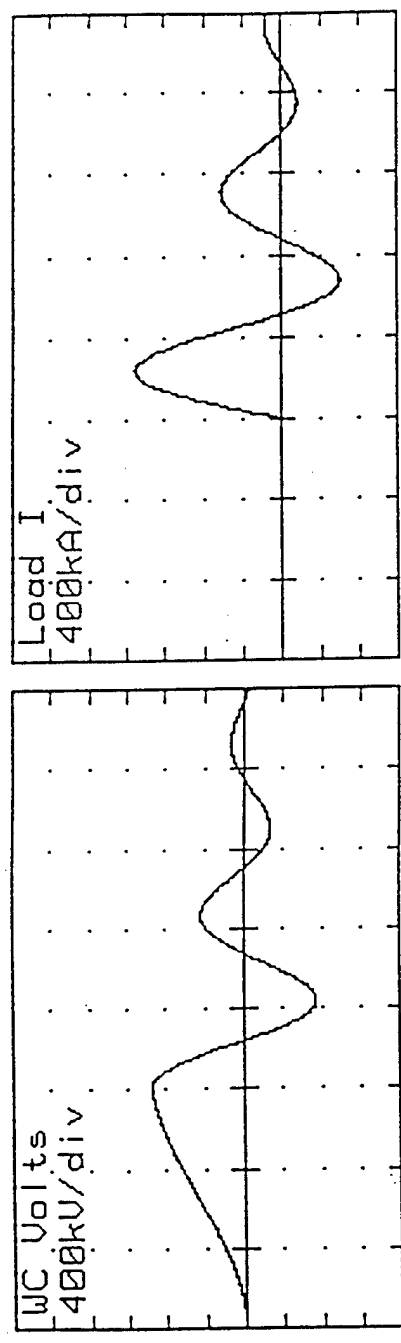


(11)

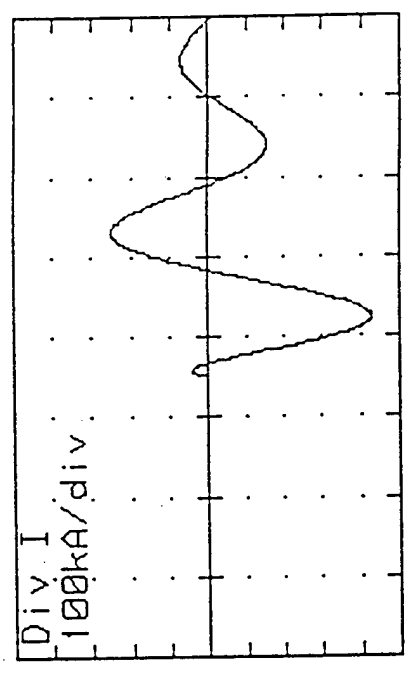


9)

# PERFORMANCE OF ZFX shows 1.5 MA at 600 nsec



DIVIDER - 350 NS  
MAIN SW - 3000 NS



TIME: 1000 ns/div

WC volts	:	Max V	=	946.31 kV	at	T = 3030 ns
(at Node 6)	:	Min V	=	-740.02 kV	at	T = 4090 ns
Load I	:	Max I	=	1.51 MA	at	T = 3600 ns
(at Node 12)	:	Min I	=	-605.39 kA	at	T = 4660 ns
Div I	:	Max I	=	251.97 kA	at	T = 5290 ns
(at Node 14)	:	Min I	=	-426.41 kA	at	T = 4230 ns

Calculations show ZFX should operate well within the limits of electrical breakdown

---

$$E_{ave} = 75 \text{ kV/cm}$$

$$E_{+br} = 230/\tau_{eff}^{1/3} A^{.058} \text{ [kV/cm]}$$

$$= 100/\tau_{eff}^{1/3} \text{ [kV/cm]} @ 10^6 \text{ cm}^2$$

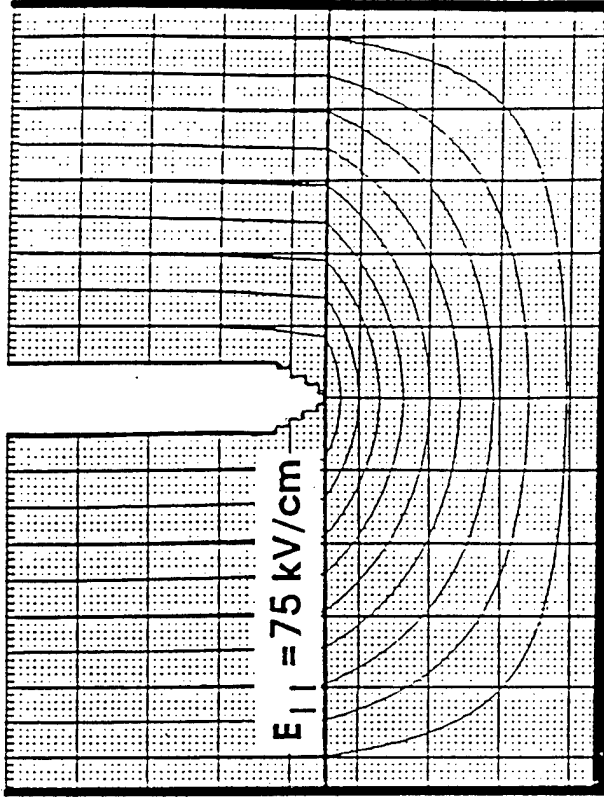
CASE	$\tau_{eff}$	$E_{+br}$	$75/E_{+}$
Normal Switch & Diverter	$1.45 + (.75 \times .2) = 1.60$	87 kV/cm	86%
Diverter only	2.02	79 kV/cm	95%
Switch only	$2.03 + (.75 \times 1.00) = 2.780$	71.3 kV/cm	105%
Nothing fires	5.90 (two cycles)	55 kV/cm	135%

Stress on water/plastic interface also below breakdown

From I.D. Smith, MBS device ran successfully with

$$E_{II} = 165 \text{ kV/cm @ } \tau = 0.3 \text{ } \mu\text{sec}$$

I.D. Smith also suggests  $\tau^{.33}$  scaling

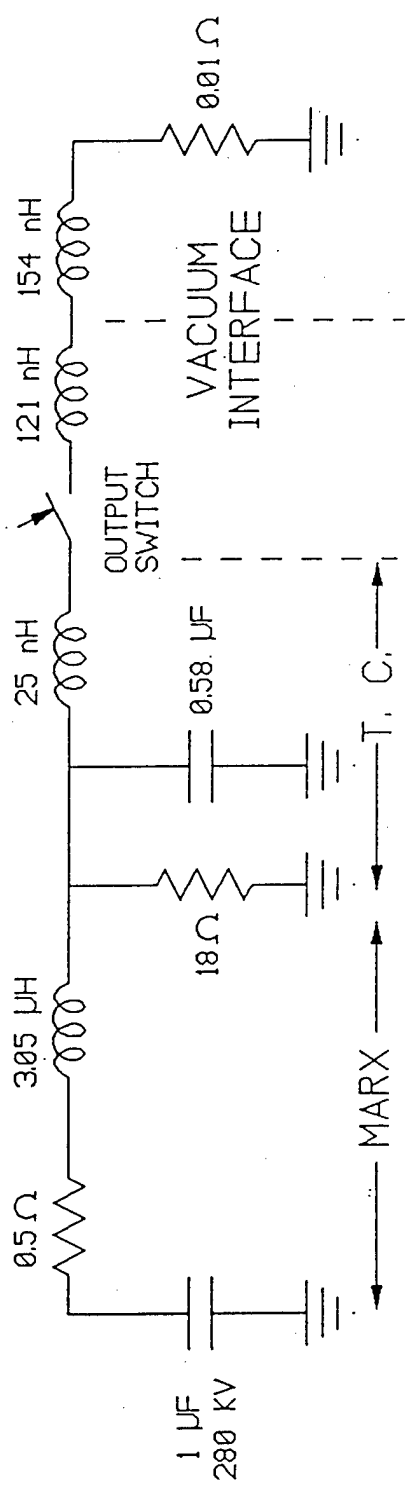


I	Normal switch and diverter	$\tau = 1.6 \text{ } \mu\text{sec}$	80%
II	Diverter, no switch:	$\tau = 2 \text{ } \mu\text{sec}$	85%
III	Switch, no diverter	$\tau = 2.8 \text{ } \mu\text{sec}$	96%
IV	No switch or diverter	$\tau = 5.9 \text{ } \mu\text{sec}$	122%

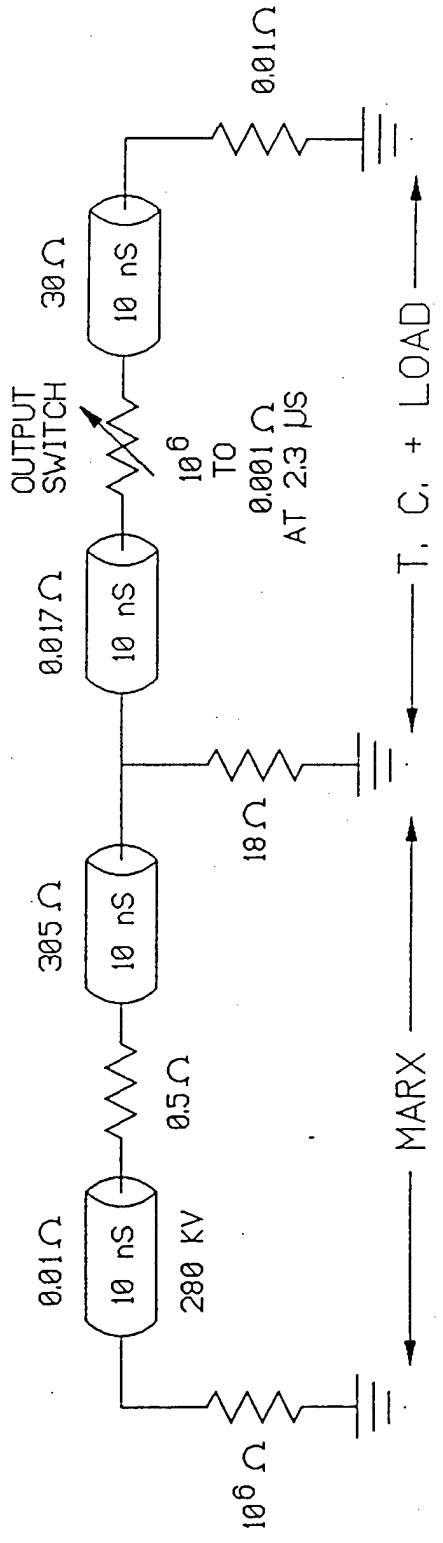
Since the MBS device worked successfully, it is safe to assume that we are well below breakdown

(S)

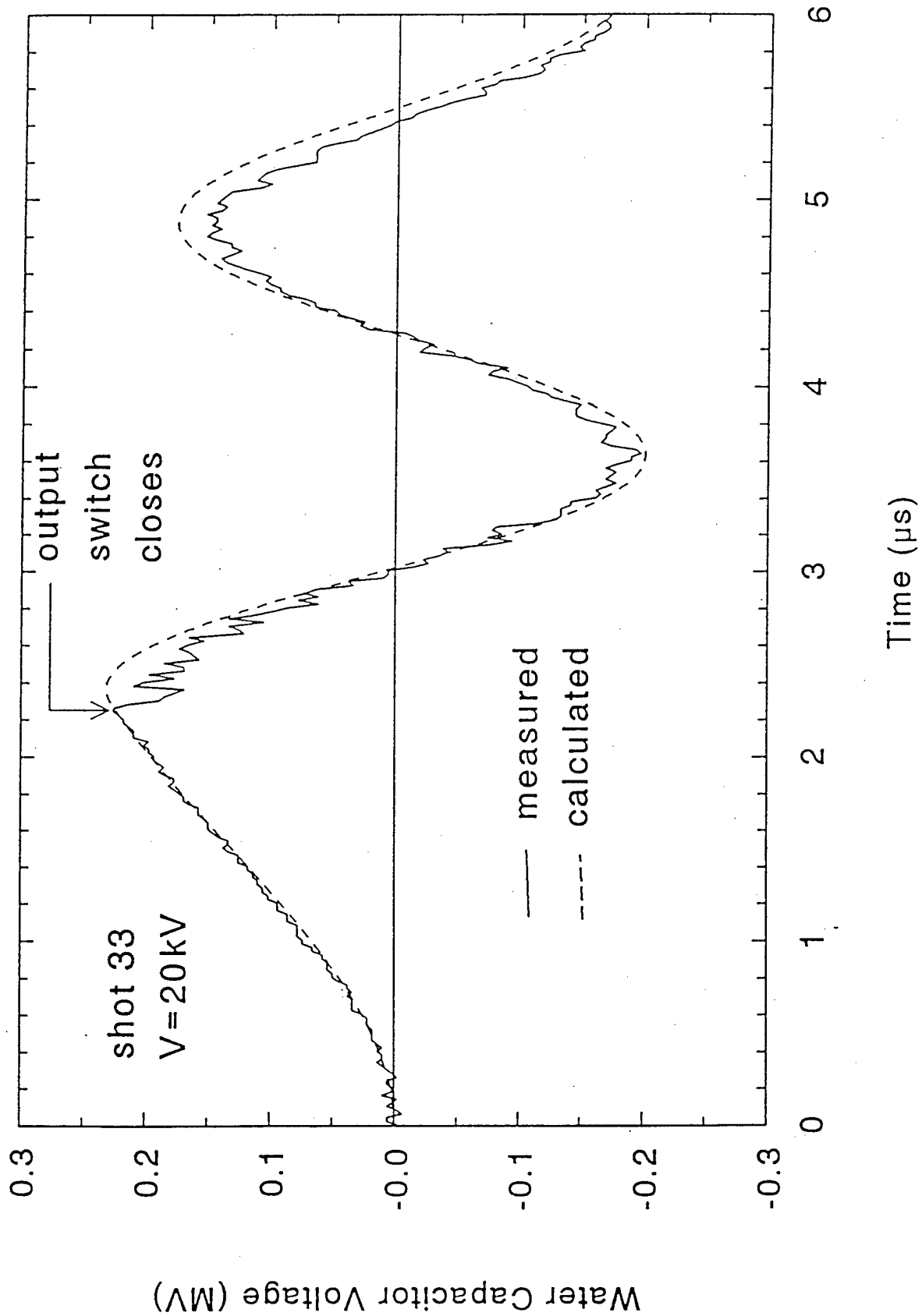
# ZFX EQUIVALENT CIRCUIT FOR S.C. SHOT 33



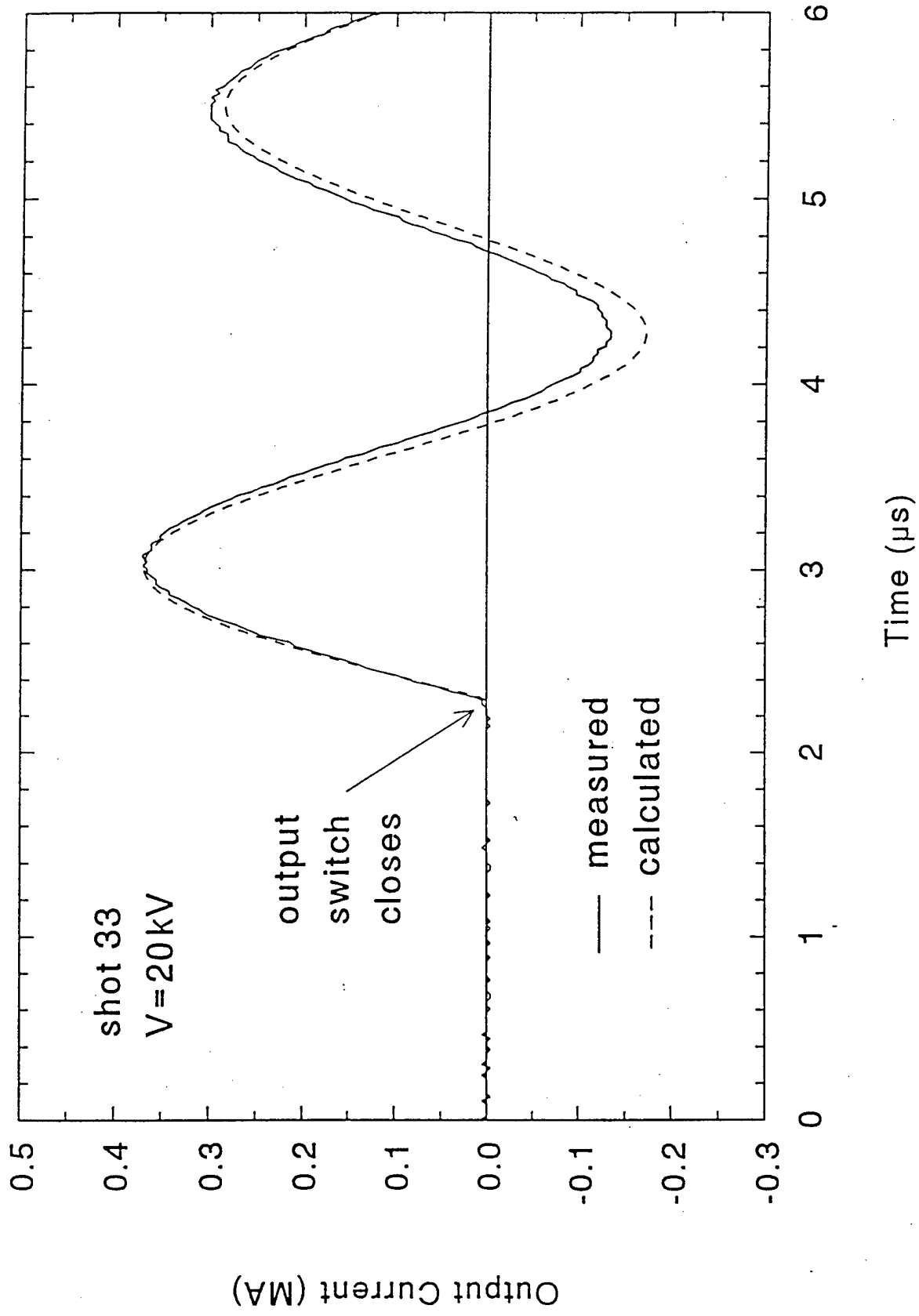
# EQUIVALENT TRANSMISSION LINE CIRCUIT



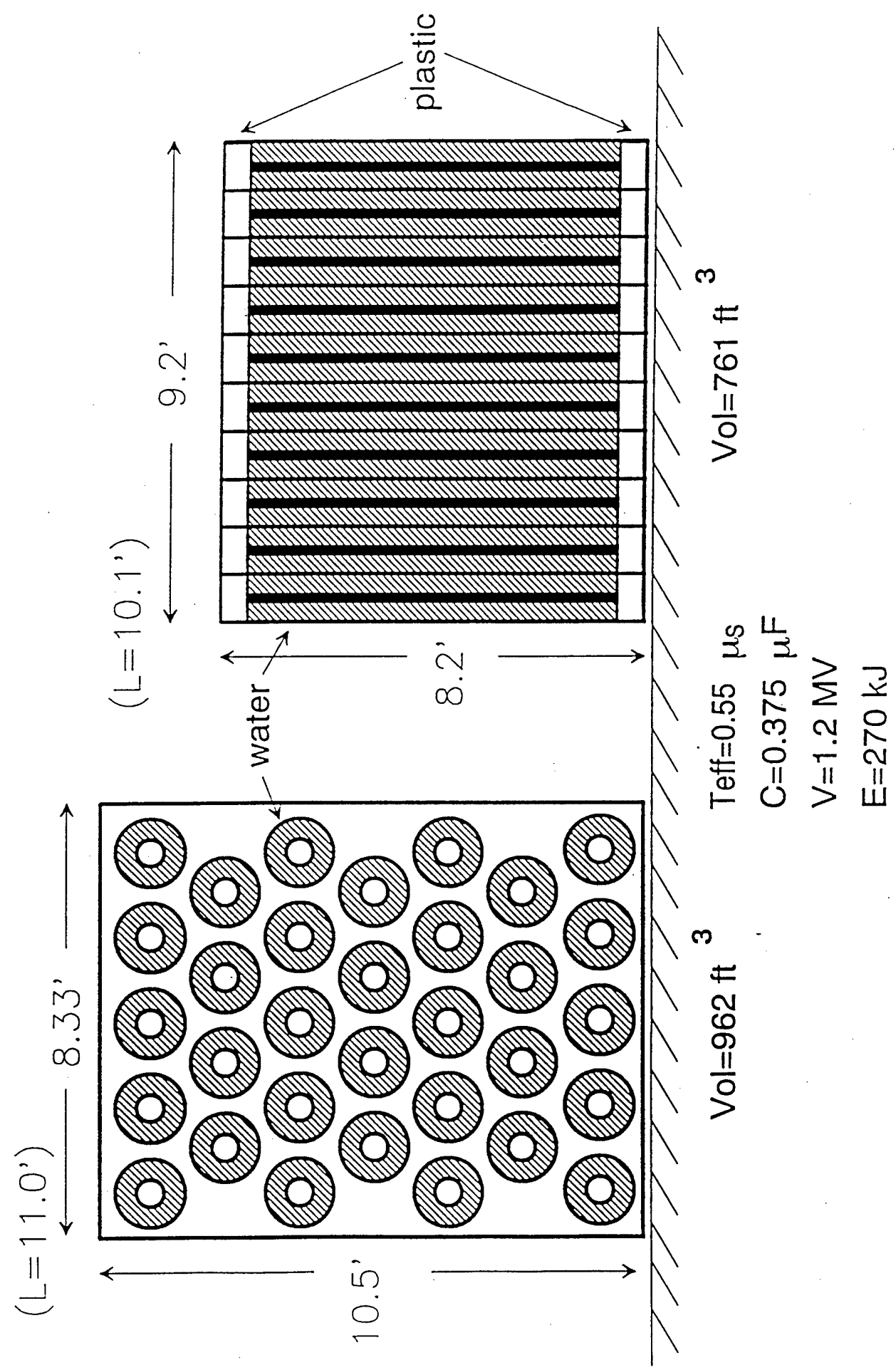
CALCULATED AND MEASURED ZFX  
WATER CAPACITOR VOLTAGE AGREE



# CALCULATED AND MEASURED ZFX OUTPUT CURRENT AGREE

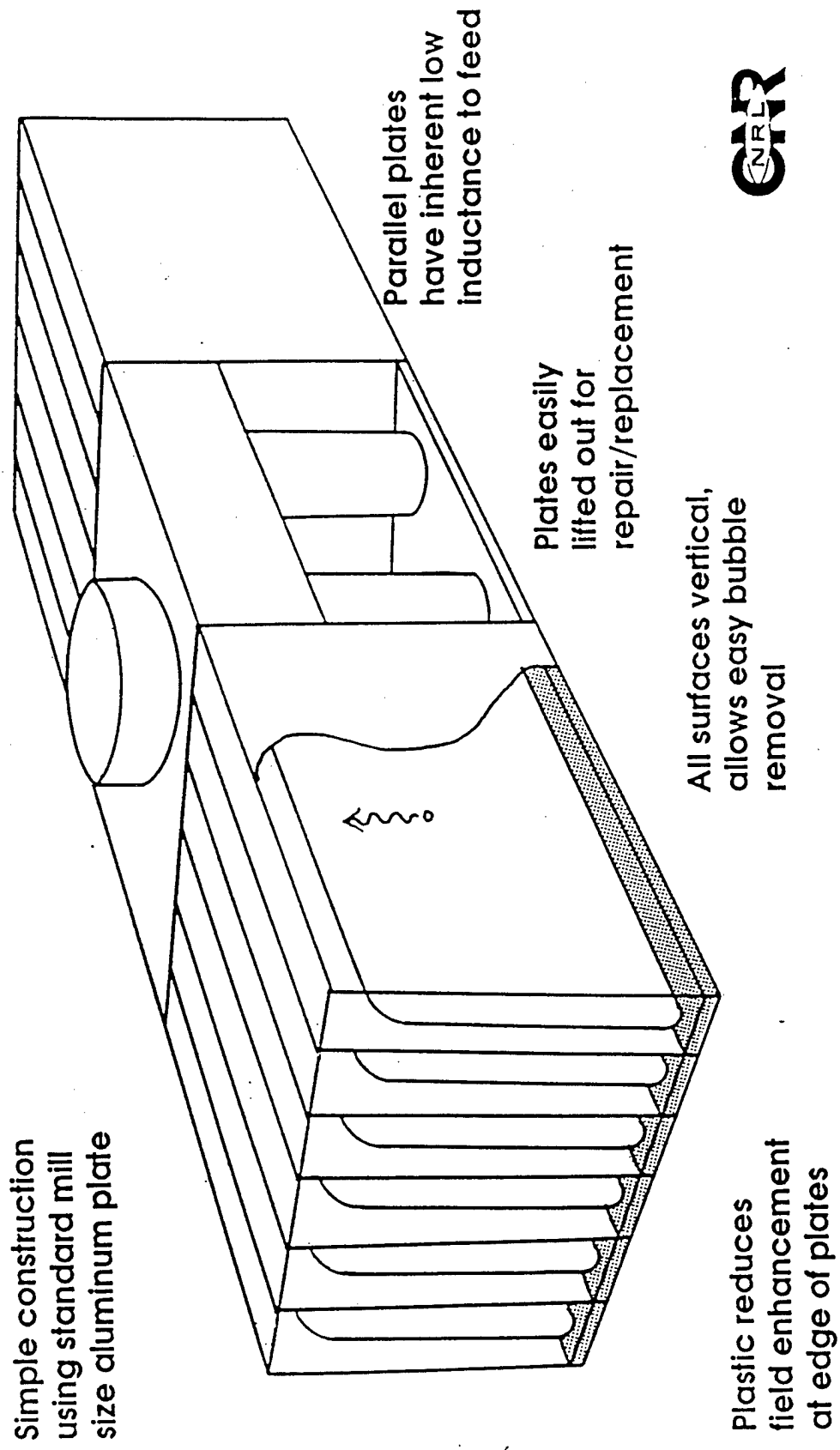


MULTIPLE COAX LINES and PARALLEL PLATES -  
TWO DESIGN OPTIONS for WATER CAPACITORS





The ZFX Parallel Plate Water Capacitor could be a compact, relatively inexpensive, easy to operate/maintain alternative for an intermediate store



TITLE:       **INITIAL CABLE GUN POS EXPERIMENTS ON HAWK**

AUTHORS:   **B. Weber, D. Hinshelwood, R. Commisso**

DATE:       **29 March 1993**

ABSTRACT:       Experiments have begun on Hawk using the cable gun plasma sources developed for use on DPM1 at PI. These plasma sources have resulted in impressive POS performance (high voltage and low jitter) on DPM1, and have been chosen as the probable plasma source for the Decade machine. The experimental objective on Hawk is to discover how the cable-gun POS operates, and how it is different from the flashboard POS. It is known, for example, that the cable gun plasma is about ten times slower than the flashboard plasma. This property may have beneficial effects, including: less secondary plasma at surfaces, reduced gap closure rate, and less plasma spreading away from the injection region.

This technote describes results using short circuit loads in the "standard" configuration ( $r = 5$  cm,  $l = 8$  cm, switch-load distance = 26 cm) with a He-Ne interferometer to measure the line-integrated electron density during shots. The density is measured at different radii for shots with conduction times of about 0.95  $\mu$ s. At all radii, the density increases during conduction above the level that would be measured by firing the sources alone. This is in contrast to the flashboard case, where the density follows the source-only density for the first part of the conduction phase, then decreases prior to opening (except near the conductors). The measured density is non-zero at all radii during opening; the trend suggests that opening actually occurs near the center conductor, closer than the 3 mm displacement of the laser beam. This is consistent with the expected MHD distortion of the approximately constant (initial) radial plasma distribution. The conduction time is longer for a given electron density than for flashboards, suggesting that the effective  $M/Z = 10-14$ , about a factor of two higher than for the flashboard plasma.

THIS REPORT REPRESENTS  
UNPUBLISHED INTERNAL  
WORKING DOCUMENTS AND  
SHOULD NOT BE REFERENCED  
OR DISTRIBUTED

## I. Experimental Setup

The experimental arrangement on Hawk is shown in Fig. 1. The cable guns are constructed from 1/4" diam semi-rigid coax by drilling a 60° conical hole at the end. The gun is powered by a 0.6  $\mu$ F capacitor charged to 25 kV (the same as is typically used for a flashboard). The plasma composition may be somewhat different from flashboards because the flashover surface is Teflon ( $C_2F_4$ ) instead of carbon-coated Kapton ( $C_{22}H_{10}N_2O_5$ ). Twelve guns are arranged at the distance shown, 9 cm from the surface of the 5-cm radius center conductor. The plasma flows through the transparent rod region. The 8-cm long rods are located azimuthally between guns. The POS configuration is the same as for previous flashboard POS experiments using this "standard" configuration; that is,  $l = 8$  cm,  $r = 5$  cm,  $\Delta r = 2$  cm in the plasma injection region, and the switch-load distance is 26 cm.

The He-Ne laser beam is indicated by the heavy dashed line in Fig. 1. The radial location of the beam can be changed shot to shot. The beam is located azimuthally under a gun. The line-integrated electron density is measured directly by this technique, and converted to an average density by dividing by the plasma injection length, 8 cm. For these experiments, the entire laser beam was recorded at the detector. This limits the spatial resolution of the measurement to the beam diameter in the plasma region, about 4-5 mm; This approach resulted in an excellent signal-to-noise ratio. The uncertainty in the average density is about  $1 \times 10^{14} \text{ cm}^{-3}$ . A short circuit load is used to simplify the density measurement and to reduce debris and x rays.

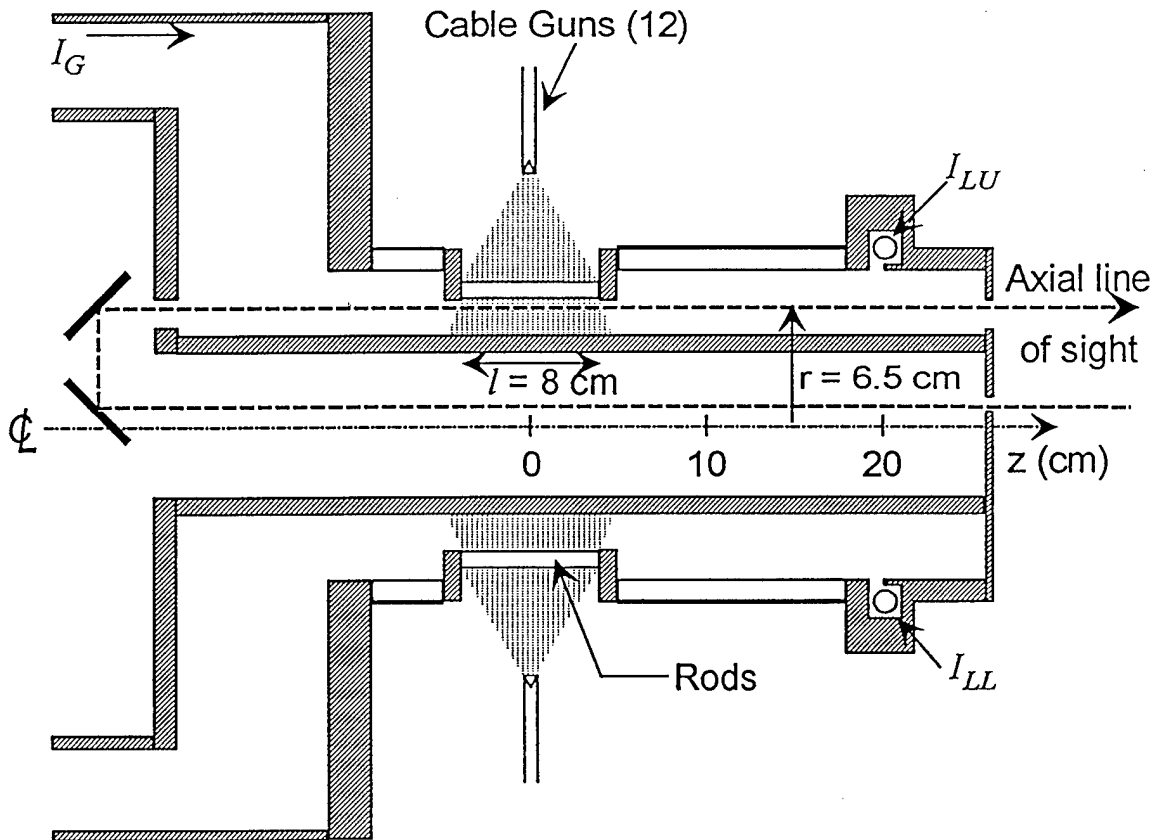


Figure 1. Cable Gun POS on Hawk

## II. Radial Density Scan

POS shots were taken for the case of  $0.95\ \mu\text{s}$  conduction time. This required a delay time between firing the guns and firing Hawk of  $3.7\ \mu\text{s}$ . For comparison, the same conduction time using 18 flashboards 12.5 cm from the center conductor requires only a  $1.5\ \mu\text{s}$  time delay. The difference in required delay times is primarily the result of different flow velocities, and secondarily the result of different secondary plasma generation at the conductors. This conduction time was chosen for comparison with our published density data using flashboards (Phys. Rev. Lett. 68, 3567 (1992)), and because this conduction time results in maximum power with diode loads using flashboards.

Data taken at six different radial locations of the laser beam are shown in Fig. 2. For each beam location, the generator and load currents are plotted along with the average electron density measured during the shot and before the shot firing the guns alone. The radial location of the beam center is indicated in the upper left corner of each plot. The conduction time for all six shots is in the  $0.9\text{-}0.95\ \mu\text{s}$  range. The initial density is within 10% of  $1 \times 10^{15}\ \text{cm}^{-3}$  for all six shots. The load currents rise in about 50 ns to the full generator current. This set of shots is assumed to be reproducible enough to estimate the density distribution for comparison with the flashboard case.

At all six locations, the density increases during conduction. This differs from the flashboard case, where the density follows the flashboard-only density for the first part of the conduction phase, then decreases prior to opening at most locations in the cross section. The density increase with the cable guns could result from several sources. During conduction,  $J \times B$  forces can move plasma in the radial direction, increasing the line-density at a given radius and decreasing it at others. Plasmas can evolve from the surfaces during conduction and increase the local density, and eventually contribute to the density in regions away from the conductors. Another possibility is ionization of plasma ions and neutrals during conduction. The density increase during conduction is a major difference between these cable gun experiments and flashboard experiments, and should be investigated further with more experiments and theoretical calculations.

The density decreases prior to opening beginning near the center conductor and propagating toward the outer conductor. Density cross plots for selected times are shown in Fig. 3. During the rise of the load current, the density is smallest close to the center conductor, but is still finite (a few times  $10^{14}\ \text{cm}^{-3}$ ). The density reaches zero (less than  $10^{14}\ \text{cm}^{-3}$ ) at the 6 mm, 9 mm, and 12 mm locations, but well after switching. (For the corresponding flashboard case, the density decreased essentially to zero at the 15 mm location at the onset of opening, and the density remained negligible at this location until 300 ns after opening.) For the cable guns, opening may begin close to the center conductor, assuming a vacuum gap is needed to explain the observed switching. The interferometer may not reveal a vacuum gap if it is smaller than the beam diameter (4-5 mm) or if it is not parallel to the beam.

The density distribution from the cable guns is relatively constant as a function of  $r$ . As current is conducted through this plasma, the magnetic forces will displace plasma near the center conductor farther in the axial direction. The distortion of the plasma would then allow radial magnetic forces to decrease the line density there. Opening could then begin in the rarefied plasma near the center conductor. The flashboard density distribution increases near the center conductor because of the surface interaction with the high velocity plasma. Opening (or at least

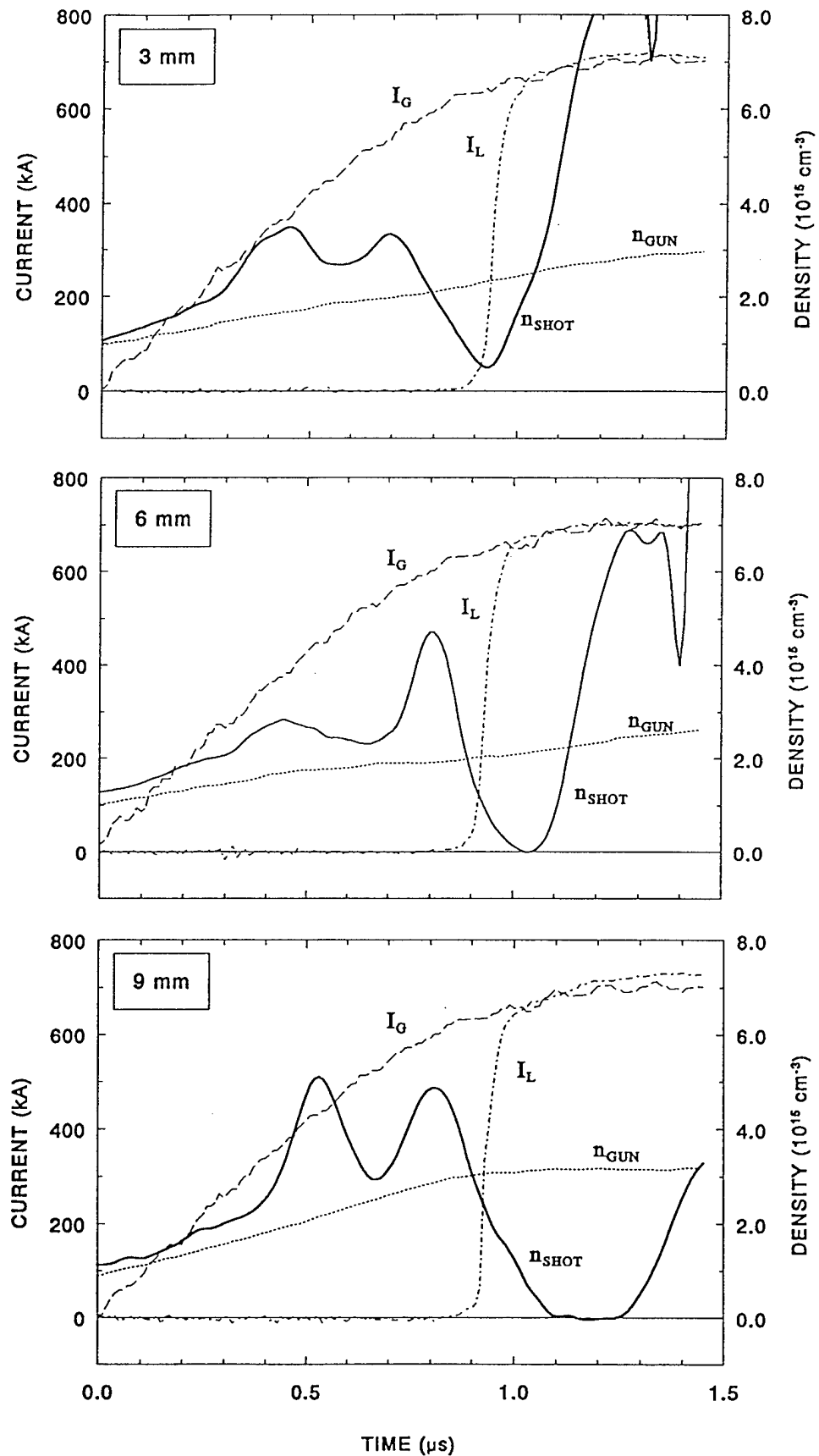


Figure 2. Density and current measurements on Hawk using cable guns.

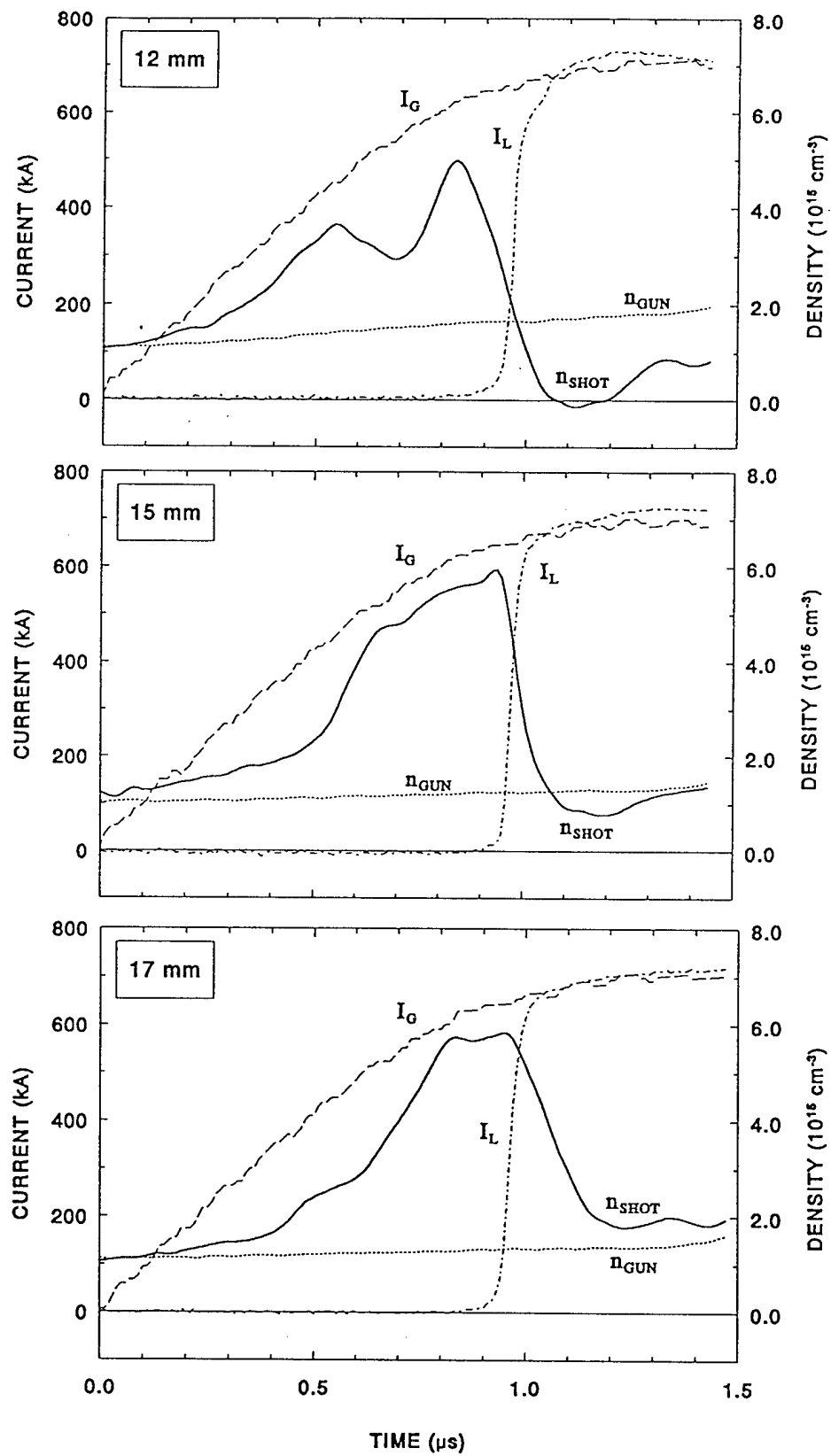


Figure 2 (continued)

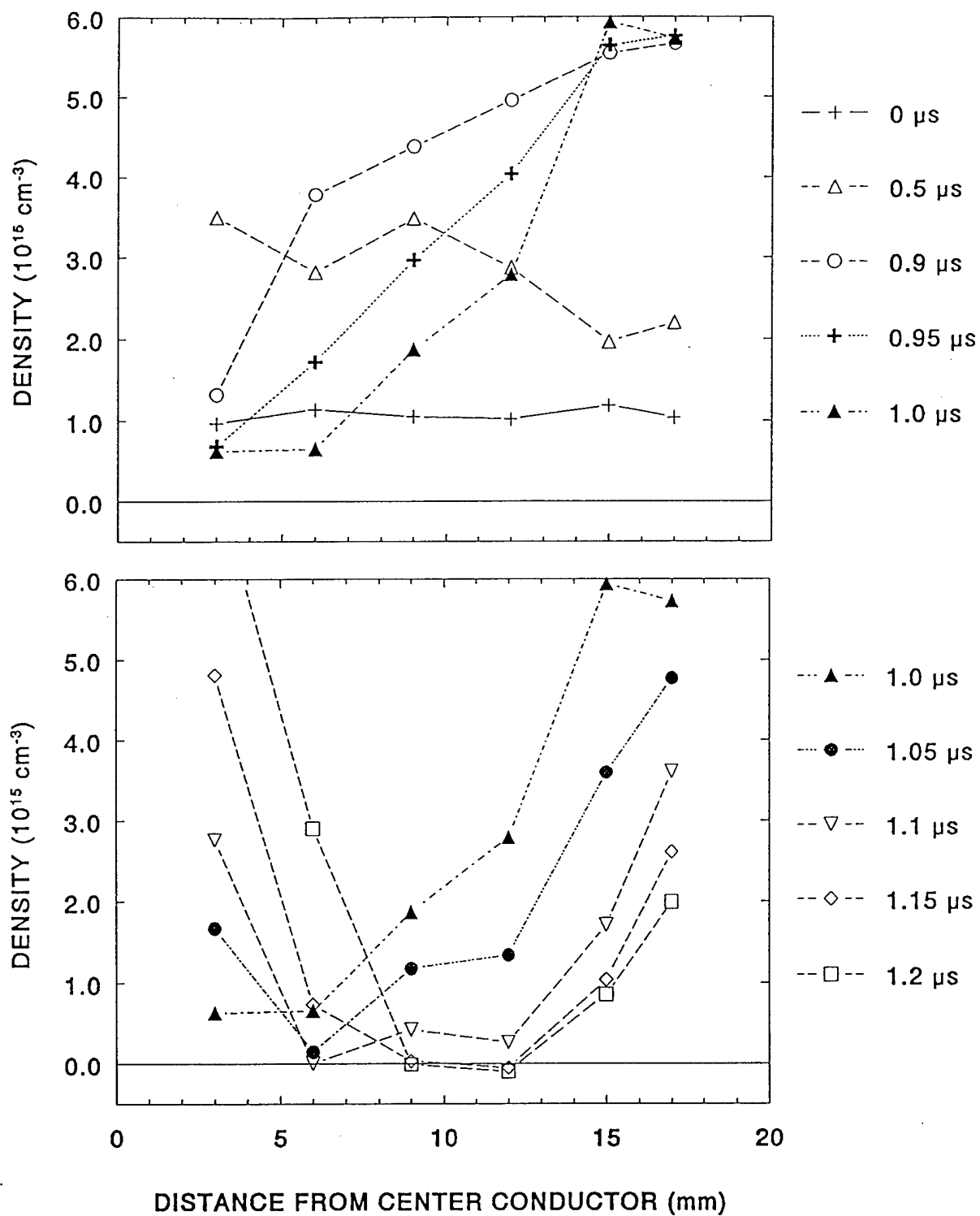


Figure 3. Cross plots of density for selected times:  $t = 0 \mu\text{s}$  (start of conduction),  $0.5 \mu\text{s}$  (during conduction),  $0.9 \mu\text{s}$  (start of opening),  $0.95\text{--}1.0 \mu\text{s}$  (during opening) and  $1.05\text{--}1.2 \mu\text{s}$  (after opening)

density thinning) occurs 15 mm from the center conductor, in agreement with fluid calculations of the plasma distortion.

### III. MHD Scaling

The plasma density required for conduction in this case can be estimated from the data in Fig. 2. Assuming opening begins near the center conductor and that the density increase during conduction contributes to the conduction time, the peak density during conduction at the 3 mm location,  $3.5 \times 10^{15} \text{ cm}^{-3}$ , will be taken to be "the density" for scaling purposes. The MHD conduction limit asserts that switching begins at the time the plasma center-of-mass is axially displaced by half the switch length (or equivalently, the time for a snowplow to reach the load end of the plasma). This model works remarkably well for Hawk flashboard experiments assuming a  $\text{C}^{++}$  plasma, for which  $M_i/Zm_p = 6$ . Applying the same argument to the cable gun data, and using as input the parameters:  $r = 5 \text{ cm}$ ,  $l = 8 \text{ cm}$ , and  $\iint I^2 dt^2 = 3 - 4 \times 10^{-2} \text{ C}^2$ , a value of  $M_i/Zm_p = 10-14$  is derived for the cable gun plasma. This is (very indirect) evidence that the cable gun plasma species is different from the flashboard plasma. For example, the cable guns may produce Fluorine (atomic weight 19) ions, more  $\text{C}^+$  ions, and fewer protons than flashboards, increasing the effective  $M_i/Z$ .

If the cable gun plasma is filling only a fraction of the 8 cm injection aperture, then the calculated  $M_i/Z$  would be even greater by the factor  $(8 \text{ cm}/l)$ . Another source of uncertainty in these estimates is the actual plasma displacement,  $\Delta z$ , during conduction. If the displacement is different from  $l/2$ , the corresponding value of  $M_i/Z$  would change by a factor of  $(l/2\Delta z)$ .

### IV. Conclusions

These initial experiments have shown several differences between flashboard and cable gun POSs that may be important for future work. For the specific case of  $\sim 1 \mu\text{s}$  conduction on Hawk, the cable gun POS requires a longer delay time than the flashboard POS, consistent with the slower flow velocity of the cable gun plasma ( $2-3 \text{ cm}/\mu\text{s}$  versus  $15-30 \text{ cm}/\mu\text{s}$ ). Density measurements during shots show that the density increases during conduction, very different from the flashboard case. It is unclear what causes the density increase, but it is probably a combination of MHD displacement, plasmas evolving from surfaces, and ionization of the plasma ions and neutrals. During opening, the density is smallest near the center conductor. This is not unexpected based on the relatively constant radial density distribution and an MHD conduction limit. The measured density is finite at all radial locations during opening, possibly because a vacuum gap forms at a location closer to the center conductor, or because the gap is smaller than the beam or not parallel to the beam. In any case, the dynamics of the plasma are notable different from the flashboard case, where opening appears to happen at a large distance from the center conductor, 15 mm for the analogous flashboard case. Applying the MHD conduction limit argument to the cable gun POS, agreement between measurements and the simple theory requires the plasma species to have an  $M_i/Z$  value about two times higher than the flashboard plasma. This is indirect evidence that the plasma composition is different for the cable gun plasma, possibly including fewer protons, and more  $\text{C}^+$  and F ions. Future experiments will examine



switching into loads and power flow between the POS and load to determine promising POS configurations that will then be examined using interferometry.

PULSED-POWER PHYSICS TECHNOTE NO. 94-03

TITLE:       **Three Dimensional Electrostatic Simulations of the ZFX Water Capacitor**

AUTHORS:   **Steve Swanekamp+, Ron Boller, and Jim Kellogg**

DATE:       18 March 1994

ABSTRACT: The ZFX water capacitor has experienced some technical difficulties where two different pieces of plastic are fitted together. This problem arises because the seam where the two pieces of plastic are joined can trap air which can cause electrical breakdown of the capacitor. One way which has been suggested to alleviate this problem is to separate the plastic pieces to allow the air bubbles to escape. However, this can also cause problems since the electric field increases in the vicinity of the high voltage plate where there is a gap in the plastic. Three dimensional electrostatic simulations of the ZFX water capacitor were performed to study the dependence of the electric field on the plastic gap size. These simulations show that the electric field on the high voltage plate increases from 180 kV/cm when there is no gap in the plastic to approximately 230 kV/cm for a 1/4" gap in the plastic and about 310 kV/cm when there is no plastic at all.

THIS REPORT REPRESENTS  
UNPUBLISHED INTERNAL  
WORKING DOCUMENTS AND  
SHOULD NOT BE REFERENCED  
OR DISTRIBUTED

+SAIC McLean, VA

The heart of the ZFX machine is an advanced water capacitor designed with a parallel plate geometry. A schematic of the ZFX water capacitor is shown in Fig. 1. As shown in this figure the capacitor consists of several high-voltage plates that are interleaved between several ground plates. The majority of the region between the plates is filled with water ( $\epsilon_r=80$ ) except between the end of the high-voltage plate and the ground plate where plastic ( $\epsilon_r=2.2$ ) is used to reduce electric field enhancements. The plastic consists of many separate pieces that are butted against one another. When two pieces of plastic meet a seam is formed that can trap an air bubble near the end of the high-voltage plate that can cause electrical breakdown. One way to alleviate this problem is to separate the plastic pieces enough to allow the trapped air bubbles to escape. However, separating the plastic can cause the electric field at the end of the high-voltage plate in the vicinity of the gap in the plastic to increase beyond that which causes electrical failure. To study the increase in the electric field around the high-voltage plate as the gap in the plastic increases a three-dimensional (3-D) electrostatic simulation of the ZFX water capacitor was performed using the general purpose 3-D electromagnetic/electrostatic code ARGUS.

A schematic of the simulation region is shown in Fig. 2. As seen in this figure, only one of the high voltage plates of the capacitor is considered. In addition, only a 11"x16"x10" portion of the capacitor was simulated. The majority of the capacitor is filled with water except at the ends of the high-voltage plate where plastic is used to reduce electric field enhancements. A Neumann boundary condition (i.e. normal component of electric field set to zero) was used at the  $y=0$ ,  $z=0$ , and  $z=10$ " boundaries. A voltage of 1 MV was applied to the high voltage plate. Gaps in the plastic of 0.0, 0.125, 0.250, 0.375, 1.0, and 10.0 inches were simulated. The gaps were centered about  $z=5$ " and in each case it was assumed that water filled the gap in the plastic.

The potential contours and the y-component of the electric field as a function of y at the middle of the high-voltage electrode ( $x=0$ ) and at  $z=5$ " for the case where there is no gap in the plastic are shown in Figs. 3a and 3b. For contrast the potential contours and electric field when the gap in the plastic extends along the entire 10" axial length of the simulation is shown in Figs. 4a and 4b. A comparison of Figs. 3a and 4a shows that the potential contours near the high-voltage plate more closely follow the electrode shape when there is no plastic. When the plastic is added the potential contours are pulled away from the high-voltage electrode and enter the plastic nearly perpendicular to the plastic/water interface. In the plastic the contours are not as closely packed at the end of the high-voltage electrode. This has the desired effect of reducing the electric field at the high-voltage electrode. This is seen in Figs. 3b and 4b which show that the addition of the plastic has reduced the peak electric field from approximately 310 kV/cm to approximately 180 kV/cm.

As mentioned above, trapped air near the seams in the plastic can lead to electrical failure of the capacitor. One way to alleviate this problem is to open up a gap in the plastic that is wide enough for the trapped air to escape. The potential contours and electric fields for gaps in the plastic of 0.125, 0.250, 0.375, and 1.0 inches are shown in Figs. 5-8. A plot of  $E_y$  on the end of the high-voltage plate at  $x=0$ ,  $y=12.0$ ", and  $z=5.0$ " for gap sizes between 0.0 and 1.0" are shown in Fig. 9. This figure shows that the electric field increases as the gap in the plastic increases from about 180 kV/cm when there is no gap in the plastic to about 270 kV/cm when there is about a 1" gap in the plastic. When there is no plastic (i.e. the gap extends along the entire 10" axial length) the electric field on the end of the high-voltage plate increases to about 310 kV/cm.

The NRL ZFX Generator can drive 1.5 MA in 580 nsec through a 200 nH load, and features a simple parallel plate water capacitor as the intermediate stor

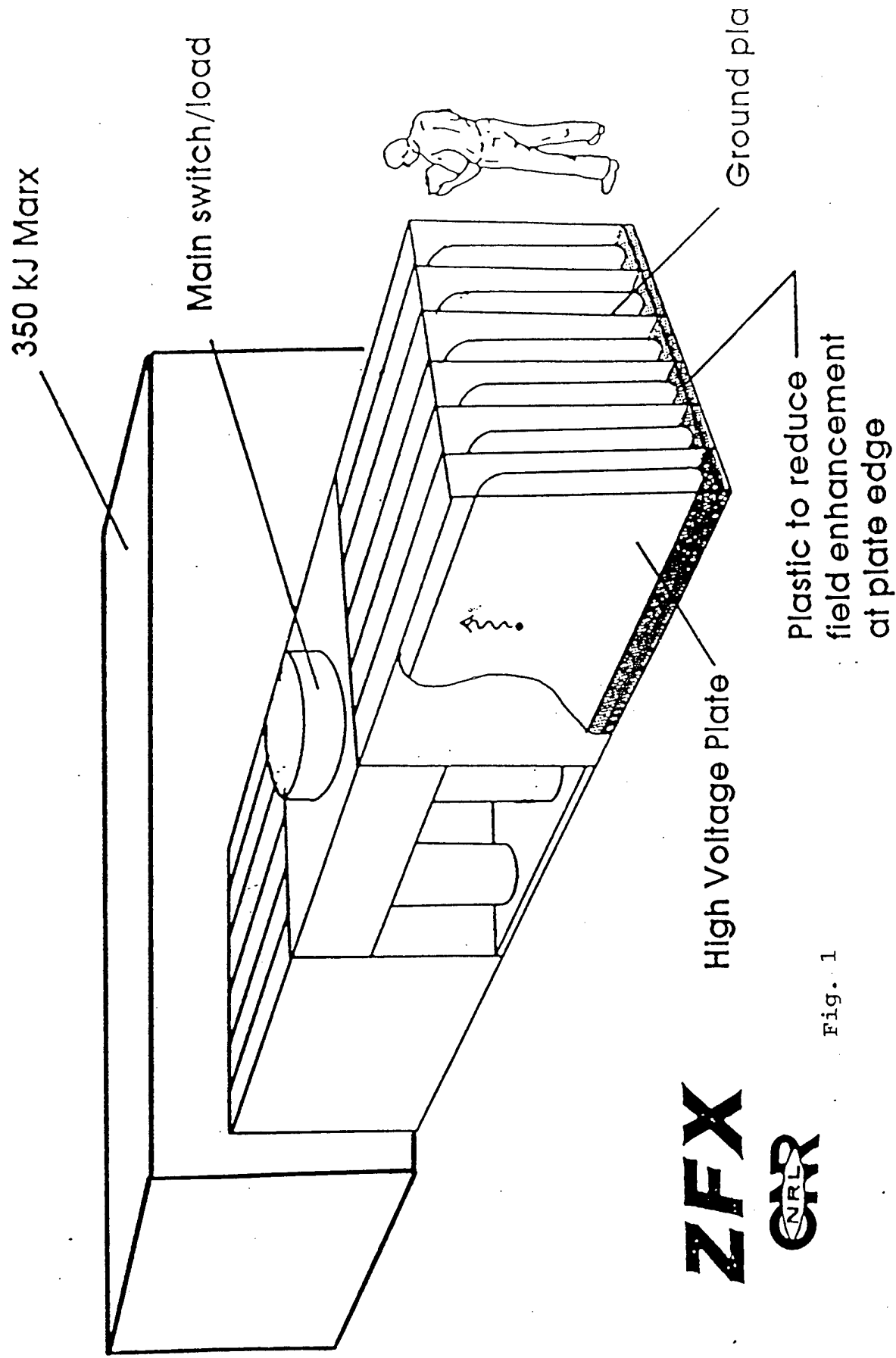


Fig. 1

# MODEL USED IN SIMUALTIONS OF THE ZFX CAPACITOR

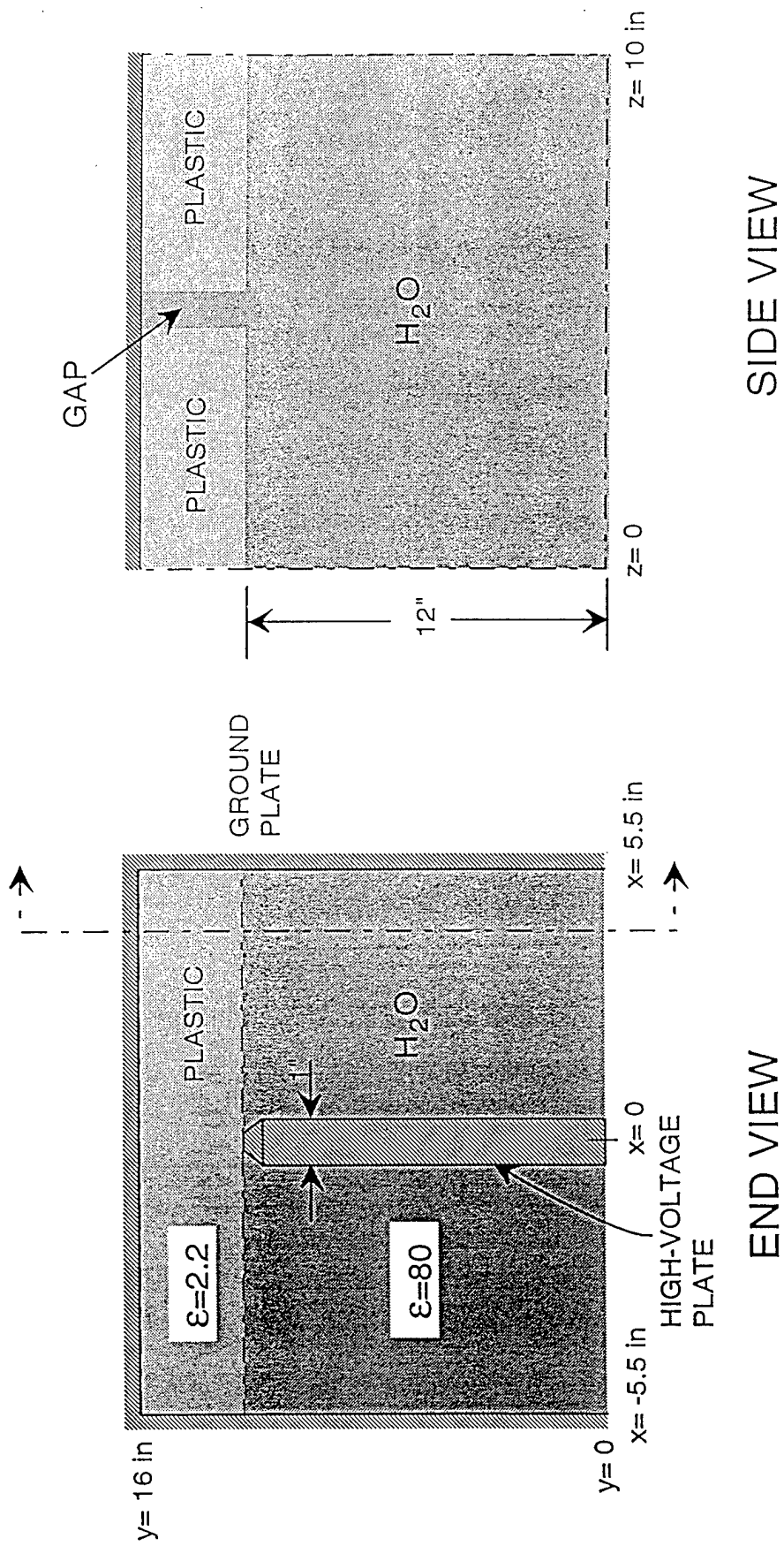
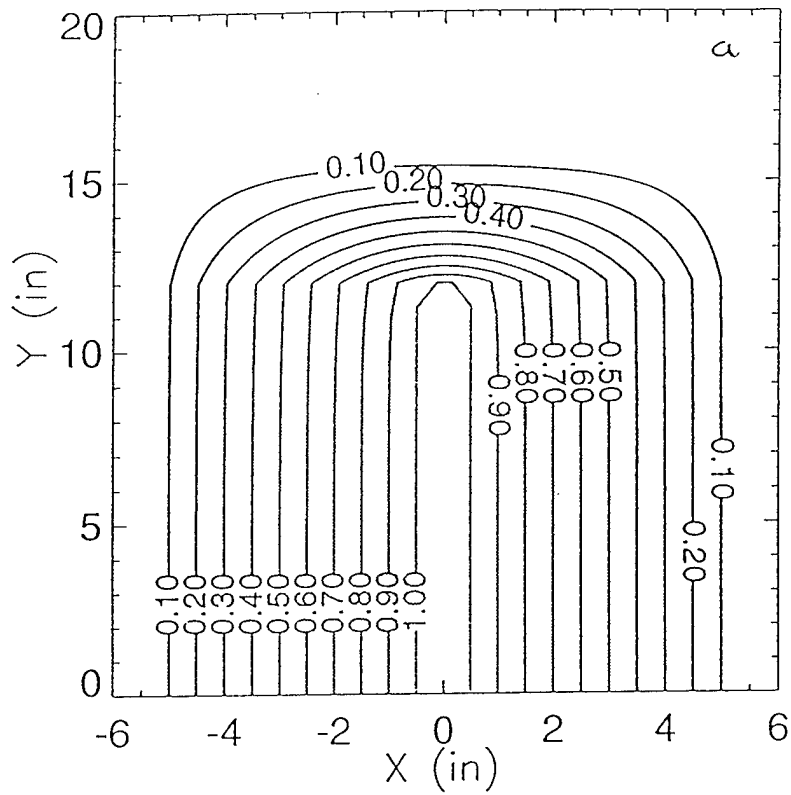


Fig. 2

# ZFX Potential Contours:

Z: 5.00000 Inches

Gap in Plastic: 0.00000 in



Ey at X=0.0 and Z=5.0 in,

Gap in Plastic: 0.00000 in

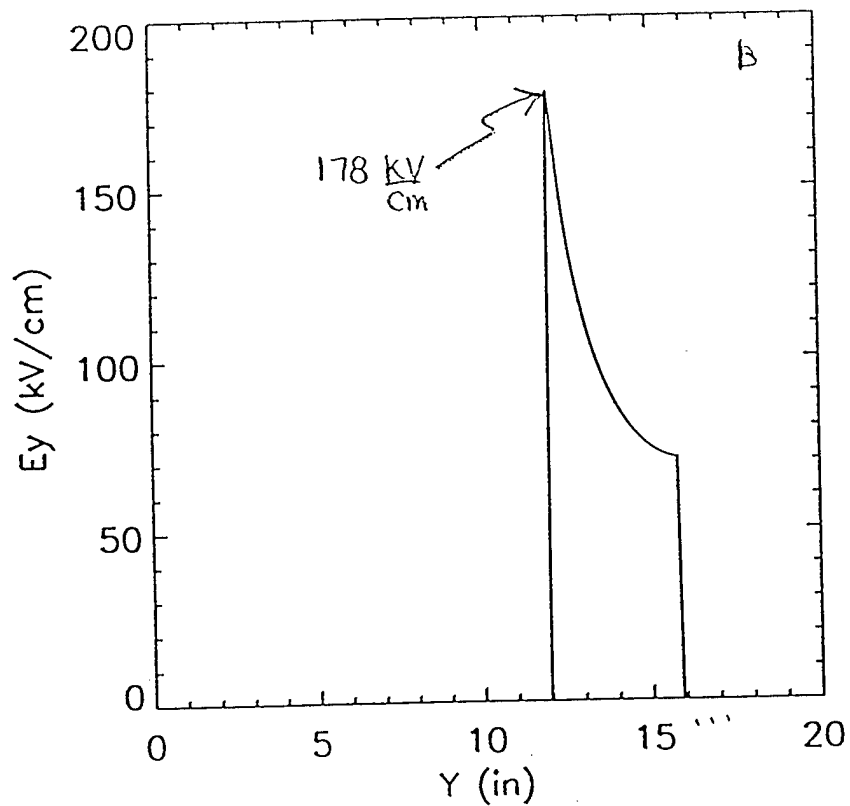
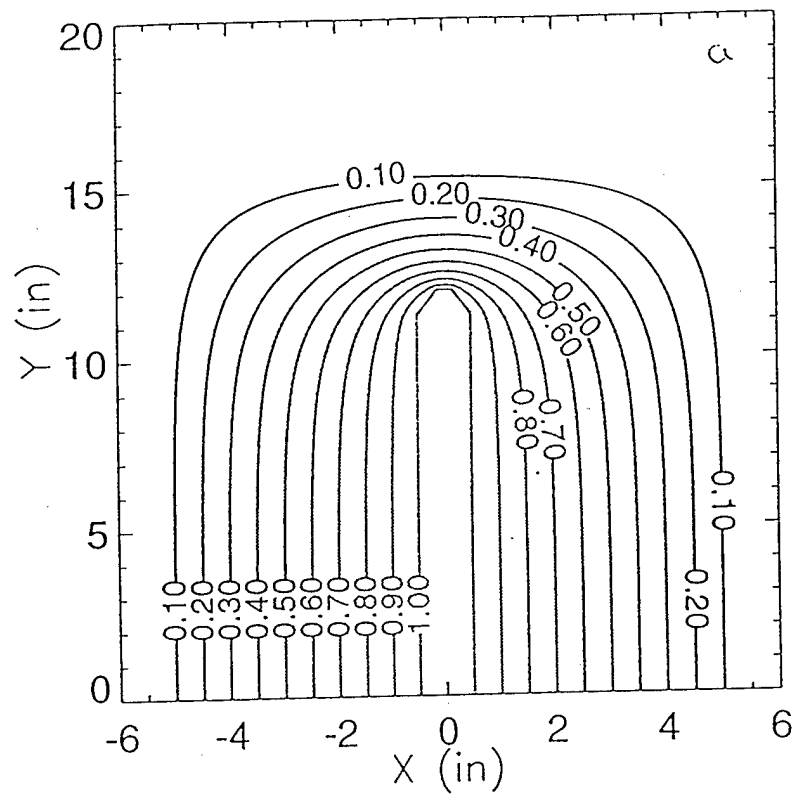


Fig. 3

# ZFX Potential Contours:

Z: 5.00000 Inches

Gap in Plastic: 10.0000 in



Ey at X=0.0 and Z=5.0 in,

Gap in Plastic: 10.0000 in

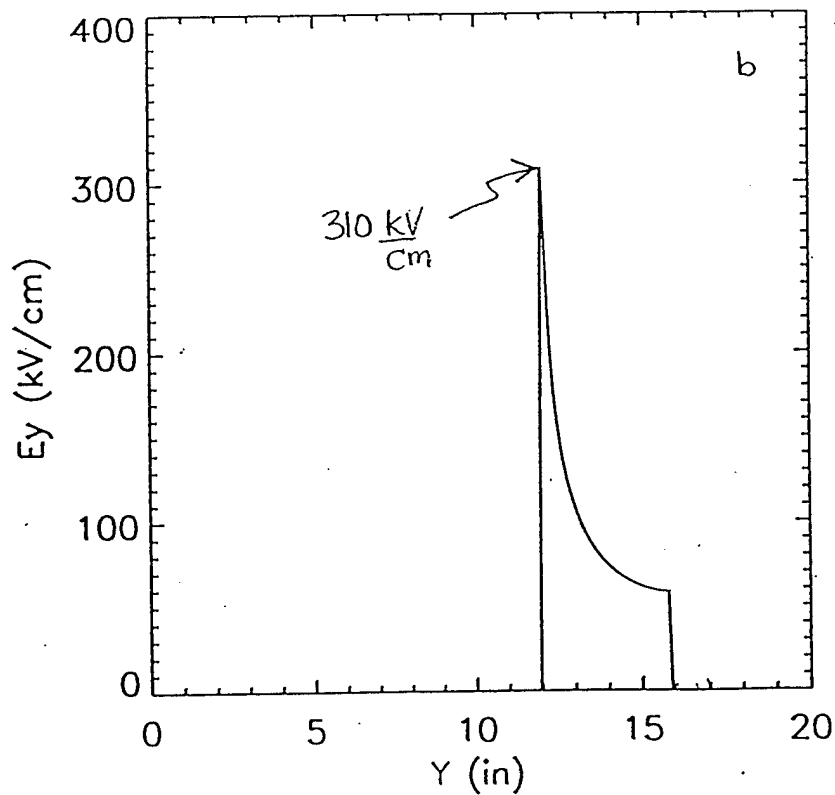


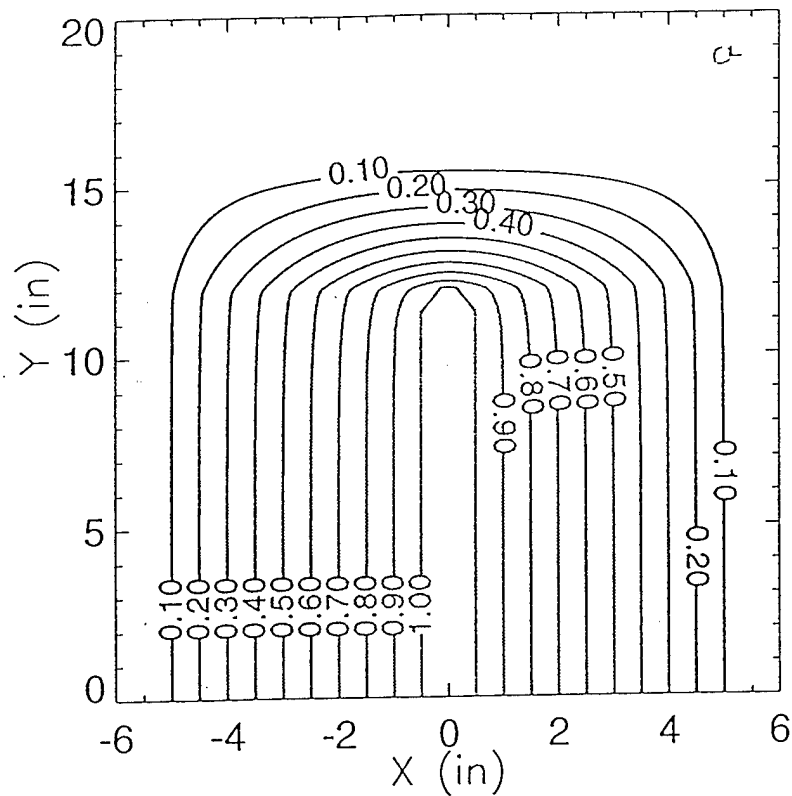
Fig. 4



# ZFX Potential Contours:

Z: 5.00000 Inches

Gap in Plastic: 0.125000 in



Ey at X=0.0 and Z=5.0 in,  
Gap in Plastic: 0.125000 in

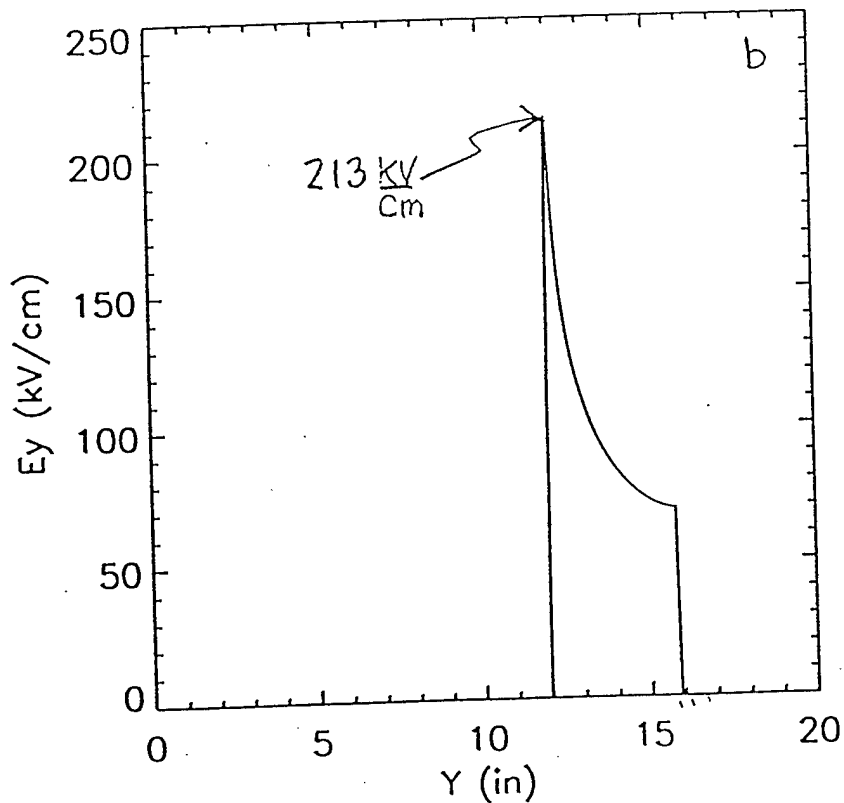
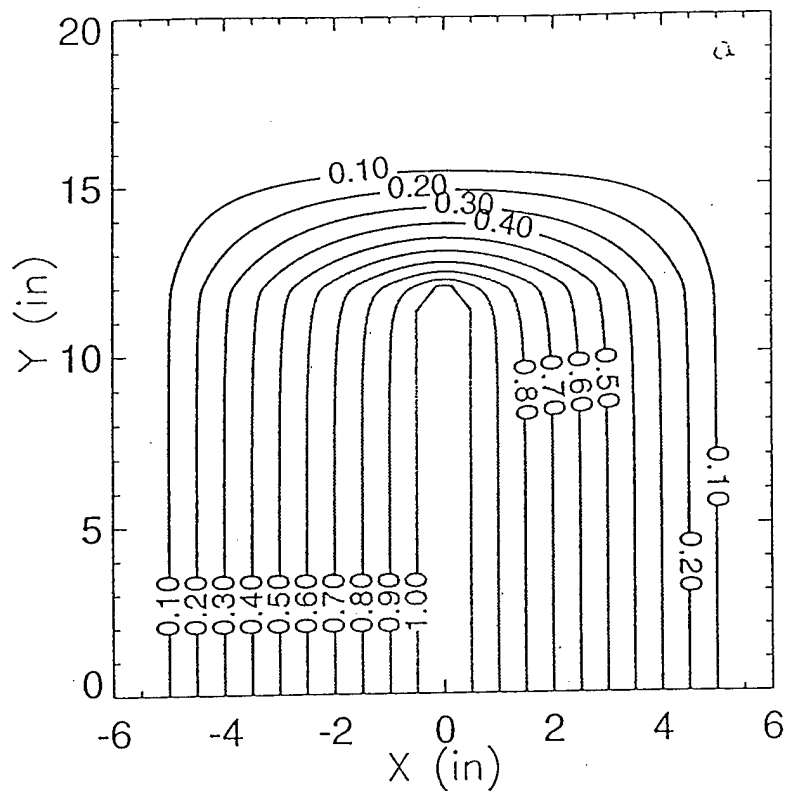


Fig. 5

# ZFX Potential Contours:

Z: 5.00000 Inches

Gap in Plastic: 0.250000 in



Ey at X=0.0 and Z=5.0 in,

Gap in Plastic: 0.250000 in

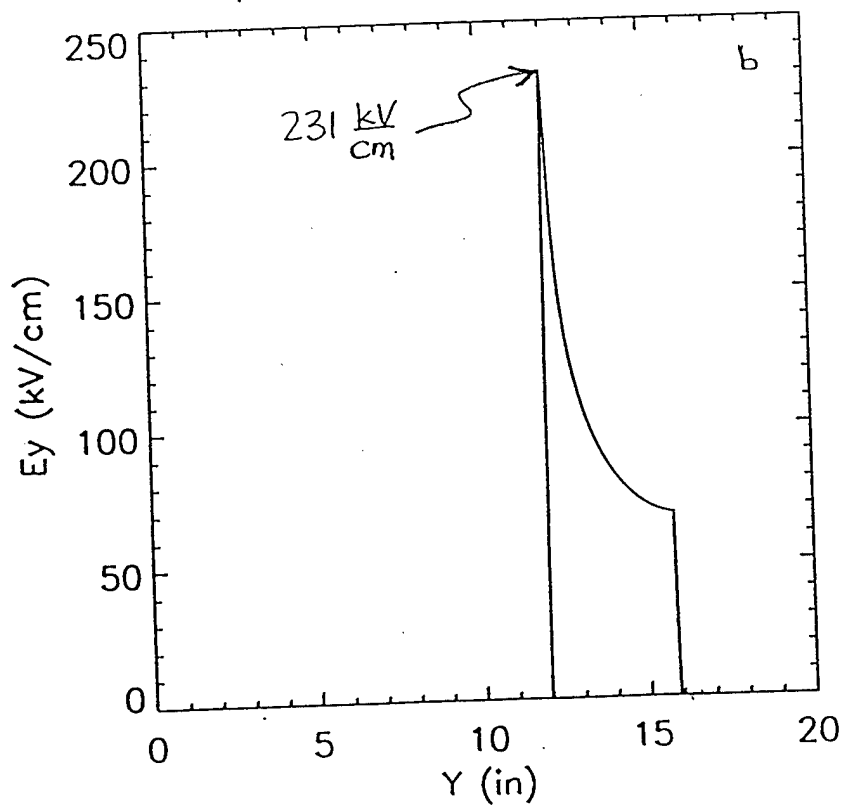
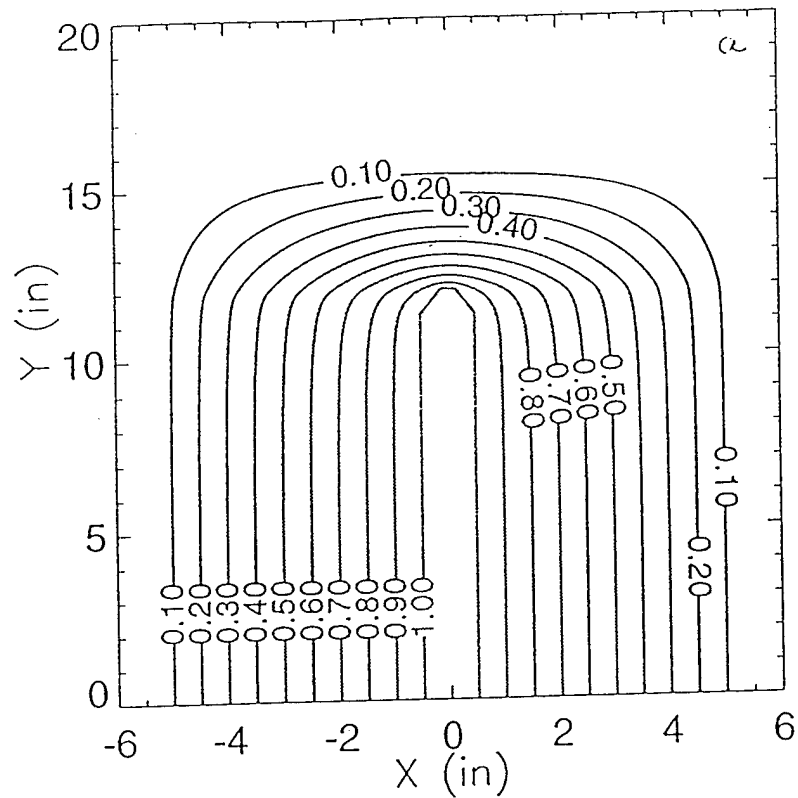


Fig. 6

# ZFX Potential Contours:

Z: 5.00000 Inches

Gap in Plastic: 0.375000 in



Ey at X=0.0 and Z=5.0 in,

Gap in Plastic: 0.375000 in

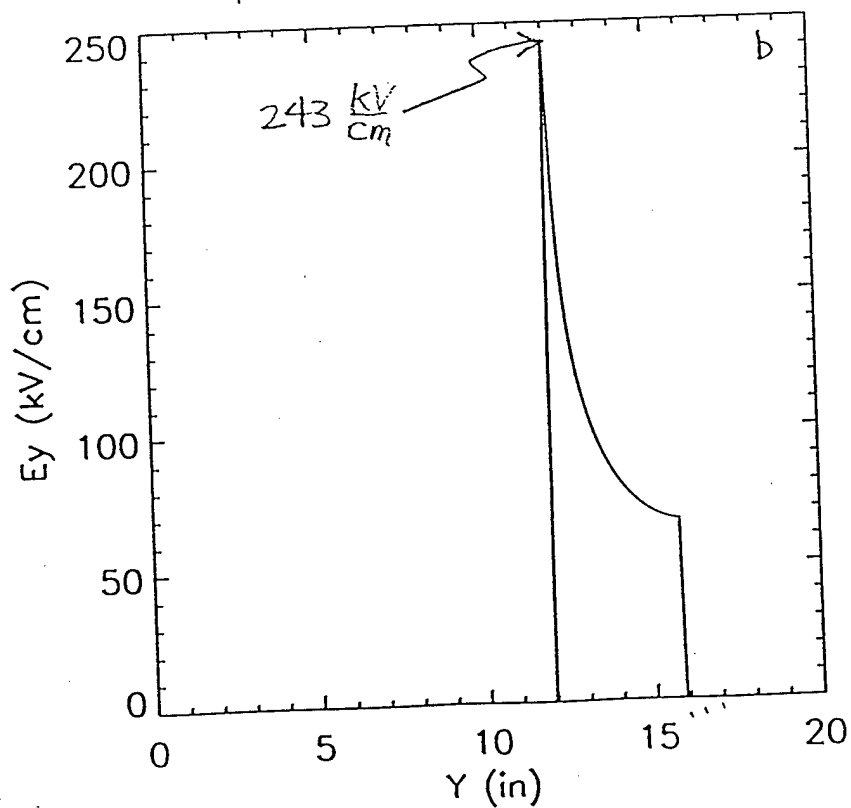
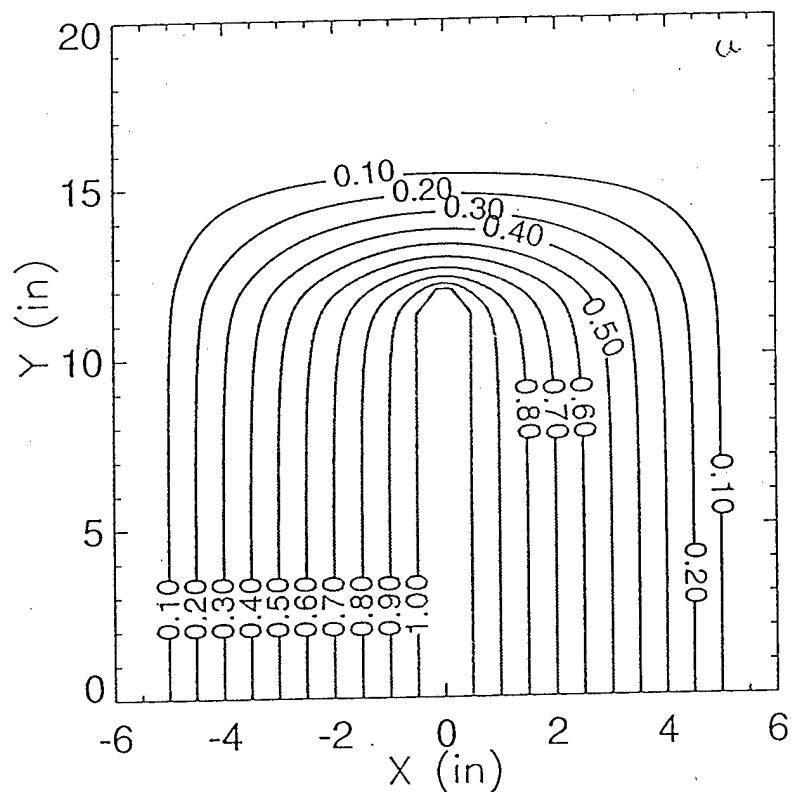


Fig. 7

# ZFX Potential Contours:

Z: 5.00000 Inches

Gap in Plastic: 1.00000 in



Ey at X=0.0 and Z=5.0 in,

Gap in Plastic: 1.00000 in

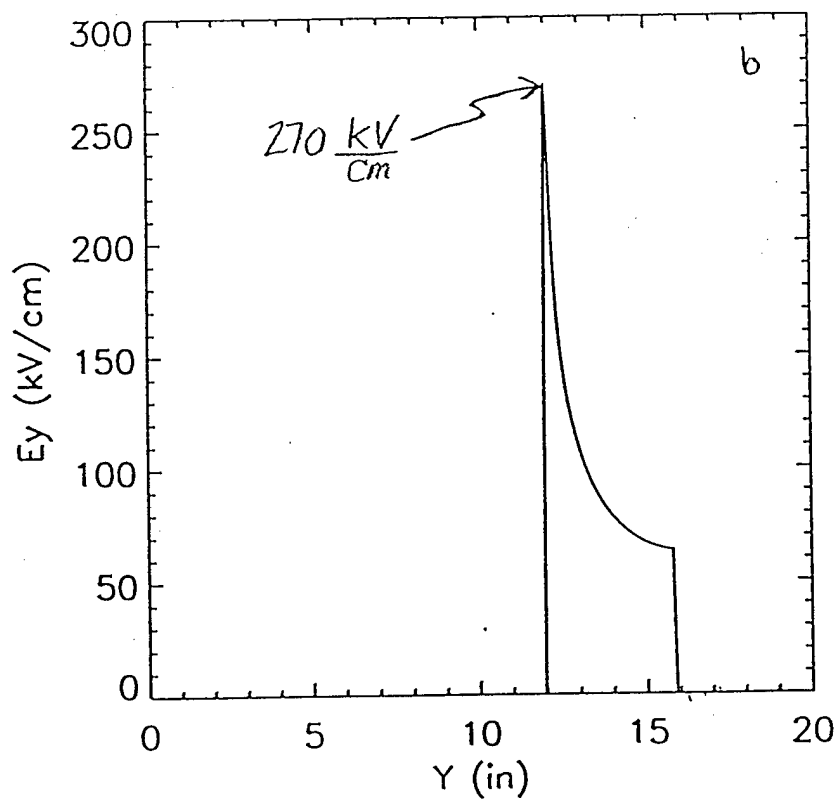


Fig. 8

$E_y$  at  $X=0.0$ ,  $Y=12.0$ ,  $Z=5.0$  in

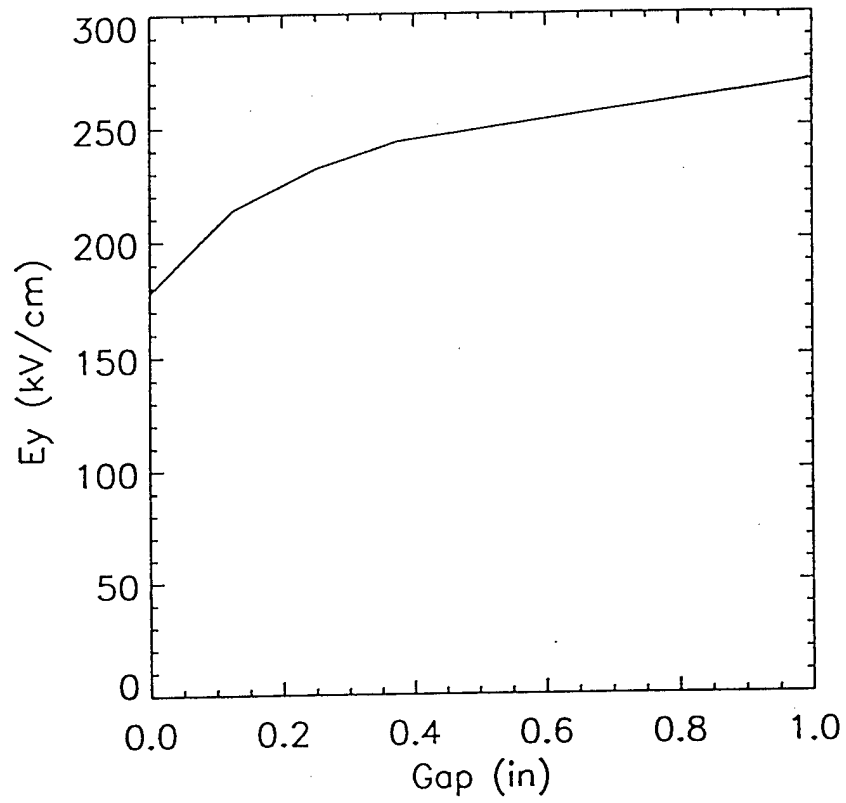


Fig. 9

$E_y$  at  $X=0.0$ ,  $Y=12.0$ , and  $Z=5.0$  in

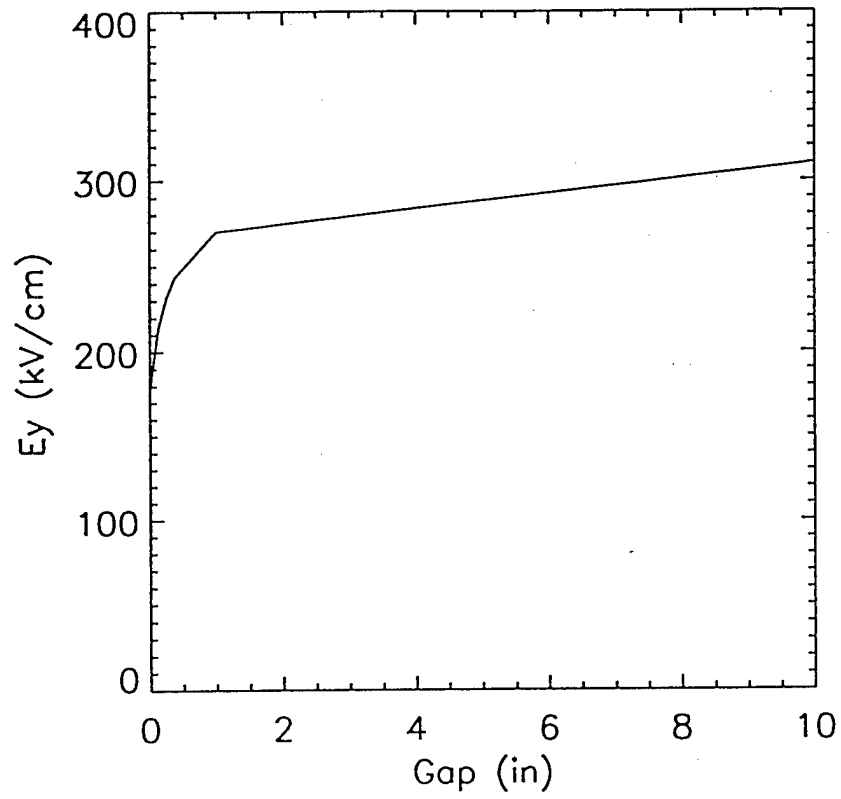


Fig. 10